SGSMP
SSRPM
SSRFM

DGMP

ÖGMP

Joint Conference
of the SSRMP, DGMP, ÖGMP

Dreiländertagung
der Medizinischen Physik

Abstractbook

Editor: Stephan Klöck

UniversitätsSpital Zürich

Universität Zürich[UZH]

ISBN: 987-3-9816508-5-3

Joint Conference
of the SSRMP, DGMP, ÖGMP

Dreiländertagung
der Medizinischen Physik

7–10 September 2014 • Zurich/CH

Editor: Dr. Stephan Klöck
UniversityHospital Zurich
Division of Radio-Oncology
Medical Physics
Rämistrasse 100
8091 Zurich, Switzerland

The review process of all submitted abstracts was undertaken by the chairs and invited lecturer.

Scientific committee
Dr. Maria Mania Aspradakis (Luzern/CH)
Prof. Dr. Christoph Bert (Erlangen/DE)
Prof. Dr. Thomas Beyer (Zurich/CH)
Prof. Dr. François Bochud (Lausanne/CH)
Prof. Dr. Michael Bock (Freiburg i. Br./DE)
Dr. Markus Borowski (Braunschweig/DE)
Dr. Konrad Buchauer (St. Gallen/CH)
Prof. Dr. Markus Buchgeister (Berlin/DE)
Prof. Dr. Paola Coan (Munich/DE)
Dr. Georg Dobrozemsky (Vienna/AT)
Prof. Dr. Wolfgang Enghardt (Dresden/DE)
Prof. Dr. Martin Fiebich (Giessen/DE)
PD Dr. Michael K. Fix (Bern/CH)
Daniel Frauchiger (Bern/CH)
Dr. Thorsten Frenzel (Hamburg/DE)
Prof. Dr. Gerhard Glatting (Heidelberg/DE)
Dr. Ewald Guni (Nuremberg/DE)
Dr. Michael Hentschel (Bern/CH)
Prof. Dr. Oliver Jäkel (Heidelberg/DE)
Prof. Christian Kirisits (Vienna/AT)
Dr. Stephan Klöck (Zurich/CH)
Dr. Goetz Kohler (Basel/CH)
Prof. Dr. Sebastian Kozerke (Zurich/CH)
Dr. Gabriele Kragl (Vienna/AT)
Prof. Dr. Roland Kreis (Bern/CH)
Prof. Thomas Künzler (Feldkirchen/AT)
Prof. Dr. Mark E. Ladd (Heidelberg/DE)
Dr. Stephanie Lang (Zurich/CH)
Prof. Dr. Antony John Lomax (Villigen, Zurich/CH)
Dr. Gerd Lutters (Aarau/CH)
Dr. Jürgen Machann (Tübingen/DE)
PD Dr. Andreas Mack (Zurich/CH)
Vera Magaddino (Lausanne/CH)
Dr. Peter Manser (Bern/CH)
PD Dr. Raphaël Moeckli (Lausanne/CH)
Prof. Dr. Reinhold Müller (Erlangen/DE)
Dr. Simeon Nill (London/GB)
Prof. Dr. Fridtjof Nüsslin (Munich/DE)
Prof. Dr. Uwe Oelfke (London/GB)
Prof. Dr. Katia Parodi (Munich/DE)
Dr. Peter Pemler (Zurich/CH)
Prof. Dr. Martin Pruschy (Zurich/CH)
Prof. Dr. Klaas Paul Prüssmann (Zurich/CH)
Prof. Dr. Harald Quick (Duisburg/DE)
Prof. Dr. Jürgen R. Reichenbach (Jena/DE)
Sigrid Richter (Augsburg/DE)
Dr. Karl Ludwig Rittmann (Chur/CH)
Dr. Hans W. Roser (Basel/CH)
Prof. Dr. Otto Sauer (Würzburg /DE)
Dr. Andrea Schäfer (Homburg, Saar/DE)
Prof. Dr. Wolfgang Schlegel (Heidelberg/DE)
Prof. Dr. Laura Maria Schreiber (Mainz/DE)
Wolf Seelentag (St. Gallen/AT)
Dr. Ferid Shannoun (Vienna/AT)
Roland Simmler (Zurich/CH)
Dr. Gabriele Sroka-Perez (Heidelberg/DE)
Prof. Dr. Marco Stampanoni (Villigen, Zurich/CH)
Prof. Dr. Markus Stock (Vienna/AT)
Dr. Tino Streller (Zurich/CH)
Prof. Dr. Georg Stücklschweiger (Graz/AT)
Dr. Dario Terriblini (Bern/CH)
PD Dr. Harald Treuer (Cologne/DE)
Dr. Daniel Vetterli (Biel/CH)
Prof. Dr. Jan Wilkens (Munich/DE)
Dr. Peter Winkler (Graz/AT)
Prof. Dr. Ulrich Wolf (Leipzig/DE)
Dr. Uwe Wolff (Vienna/AT)
Dr. Michael Wucherer (Nuremberg/DE)
Prof. Dr. Sibylle Ziegler (Munich/DE)
Prof. Dr. Klemens Zink (Giessen, Marburg/DE)

© Swiss Society of Radiobiology and Medical Physics (SSRMP)
German Society of Medical Physics (DGMP)
Austrian Society for Medical Physics (ÖGMP)

Table of Contents

Session 1 – Dosimetry in radiation therapy I: Interactions

Chairs: M. M. Aspradakis (Luzern/CH), O. Sauer (Würzburg/DE)

1 Introductory lecture: GafChromic dosimetry and the status of the GafChromic detector in clinical small field dosimetry

K. Buchauer[1]
[1] Kantonsspital St. Gallen, Klinik für Radio-Onkologie, St. Gallen, Switzerland

Purpose: Technological advancements of Radiation Therapy included IMRT and VMAT. Treatment technologies that are utilizing a huge amount of small field contributions to deliver highly complex, conformal, organ at risk sparing radiation treatments. In the same time the technical ability to perform a considerable range of stereotactic treatments with a Linear Accelerator was established and adopted in many clinics. Small field dosimetry traditionally is the dosimetry discipline with the closest relation of physical properties of radiation and particles and interactions with matter. Detector choice has always been crucial for reliable small field dosimetry, and the best detector is still to be found.

Methods: Following the structure of Radiochromic film dosimetry Recommendations of AAPM Radiation Therapy Committee Task Group 55 [2] the current status of Gafchromic EBT-x dosimetry is reviewed. Furthermore the question is discussed whether improvements in Gafchromic film dosimetry methods of the last years have changed the role of film in small film dosimetry.

Results: Within a lunch breaks time a set of smallest field 2D dose distributions can be acquired with Gafchromic EBT3 film in impressive high detail and resolution with or without commercially available software. Fig. 1 and Fig. 2 give an example, solely utilizing the red color channel without advanced artifact correction algorithms. Absolute dose readings fit in uncertainty ranges published for point based detectors [1].

Conclusion: Technology advancements in IMRT/VMAT/SBRT/SRS planning and delivery contribute to increasing importance of small field dosimetry. Radiochromic film has a very high spatial resolution and absolute dose measurement capability. New techniques of evaluation overcome the artifacts commonly associated with Radiochromic film dosimetry. A protocol for Radiochromic film based general small field dosimetry or an update on existing recommendations is desirable as basis of feasible results obtained in clinical dosimetry.

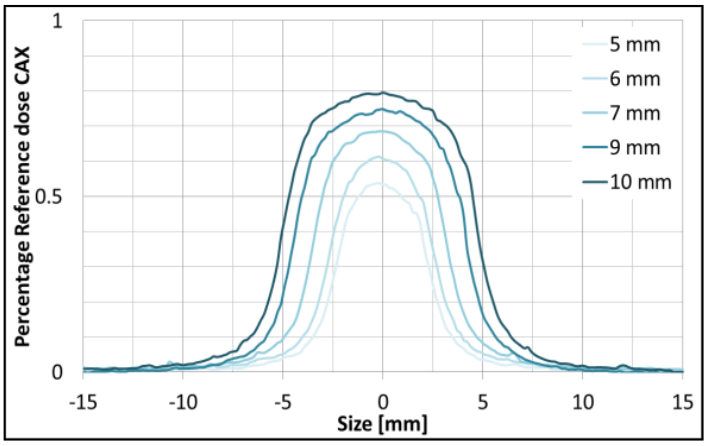

Fig.1: Inplane profiles field size 5-10 mm

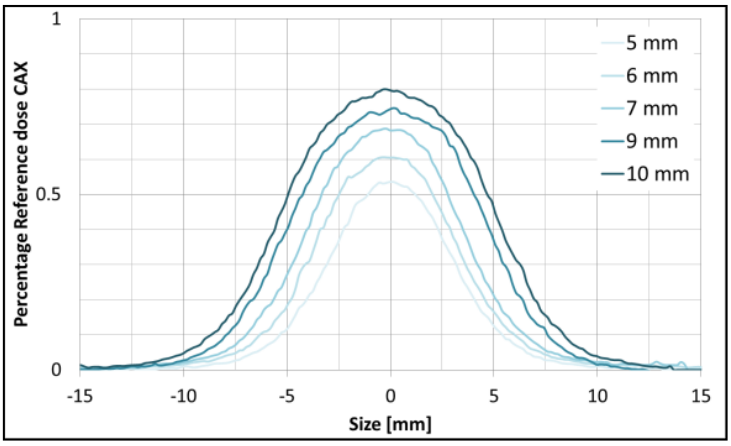

Fig.2: Crossplane profiles field size 5-10 mm

References

[1] Huet C, Dagois S, Derreumaux S et al (2012) Characterization and optimization of EBT2 radiochromic films dosimetry system for precise measurements of output factors in small fields used in radiotherapy. Radiation Measurements 47:40-49

[2] Niroomand-Rad A, Blackwell CR, Coursey BM et al (1998) Radiochromic film dosimetry: Recommendations of AAPM Radiation Therapy Committee Task Group 55. Medical physics 25:2093-2115

2 The volume-dependent correction factor *k*V – its derivation from the convolution model, some numerical examples and its relationship with the IAEA nonstandard field formalism

H. K. Looe[1], D. Harder[2], B. Poppe[1]
[1]Pius-Hospital and Carl von Ossietzky University, WG Medical Radiation Physics, Oldenburg, Germany
[2]Georg August University, Medical Physics and Biophysics, Göttingen, Germany

Introduction: In narrow photon beam dosimetry, the size of a probe-type dosimetric detector, e.g. of a small ionization chamber, a Si p-n diode, a diamond detector or a TLD probe embedded in phantom material, has to be accounted for by a suitable correction factor added to the fundamental equation of probe-type dosimetry. According to this equation, the absorbed dose to water, $D(x)$ at the point of measurement x, is determined by the signal $M(x)$ of the detector, whose EPOM is placed at coordinate x, the detector's calibration factor N, the product of all other correction factors k_i and the new correction factor k_V, the "volume-dependent correction factor":

$$D(x) = M(x) \times N \times \prod_i k_i \times k_V \tag{1}$$

Factor k_V represents more than just dose averaging over the detector's sensitive volume since secondary electron generation and transport inclusive of the disturbance of the field of secondary electrons are playing their part, but index V as well as the term "volume-dependent correction factor" shall illustrate the important role of the detector's volume. Based on the "convolution model" of the detector size and secondary electron transport influence, factor k_V will be derived, numerical examples will be given, and its relationship with the IAEA nonstandard field formalism will be clarified.

Materials and methods: Mathematical convolutions and Fourier's convolution theorem have been used for the derivation of the volume effect correction factor. Monte Carlo simulations of photon pencil beams were performed using EGSnrc to obtain the response functions of four clinical detectors: Semiflex 31010, PinPoint 31014, unshielded diode 60012 and microDiamond 60019 (all from PTW-Freiburg). Detector constructions were adapted from manufacturers' information. Using these convolution kernels, numerical examples of factor k_V have been derived. We will discuss in this work the role of factor k_V in the proposed dosimetry protocol for small photon fields (DIN 6809-8) and we will compare this factor with the formalism proposed by an IAEA working group for the dosimetry under non-reference conditions [1].

Results: In accordance with the recent literature [2, 5, 7-13], the volume effect of probe-type detectors of non-negligible size can be described by a set of three convolutions. The first of these is

$$M(x) = K_M(x) * \Phi(x) \tag{2}$$

where M(x) is the lateral signal profile of the detector and Φ(x) the lateral photon fluence profile. Convolution kernel KM(x) can be measured or simulated by scanning a photon slit beam over the detector. Secondly, the true dose profile D(x) in the undisturbed absorber medium is resulting from the convolution of Φ(x) with the "dose deposition kernel" KD(x):

$$D(x) = K_D(x) * \Phi(x) \tag{3}$$

And thirdly, the signal profile M(x) and the true dose profile D(x) can be formally correlated by a convolution with the "lateral dose response function" or "dose response kernel" K(x):

$$M(x) = K(x) * D(x) \tag{4}$$

Applying Fourier's convolution theorem to eqs. (2) to (4) and eliminating FT[Φ(x)], the relationship

$$\mathrm{FT}[K(x)] = \frac{1}{\sqrt{2\pi}} \frac{\mathrm{FT}[K_M(x)]}{\mathrm{FT}[K_D(x)]} \tag{5}$$

is obtained, with the symbol FT denoting the Fourier transform [7]. Eq. (5) is a useful instrument for deriving K(x) from Monte-Carlo simulated kernels KM(x) and KD(x), as will be shown below.

Correction factor kV(x) can be formally derived from eqs. (1) and (4) by the consideration that, for an ideal, point-like detector, its dose response function Kpoint(x) is proportional to a Dirac delta function:

$$k_V(x) = \frac{M_{point}(x)}{M(x)} = \frac{\int_{-\infty}^{+\infty} K_{point}(x - x) D(x) dx}{\int_{-\infty}^{+\infty} K(x - x) D(x) dx} \quad (6)$$

so that in the numerator factor D(x) can be drawn before the integral. By expressing the true dose profile as D(x) = Dmax p(x), eq. (6) can be written as

$$k_v(x) = \frac{M_{point}(x)}{M(x)} = \frac{p(x)}{\int_{-\infty}^{+\infty} K'(x - x) p(x) dx} \quad (7)$$

where K'(x) is the area-normalized lateral dose response function, and p(x) the relative dose profile. Eq. (7) is also what would be intuitively expected.

By substitution of eq. (7) in eq. (1), the basic equation of probe-type dosimetry is taking the form

$$D(x) = M(x) \times N \times \sum_i k_i \times \frac{p(x)}{\int_{-\infty}^{+\infty} K'(x - x) p(x) dx} \quad (8)$$

where the last term represents the sought correction factor kV(x), accounting for the shapes of the area-normalized convolution kernel K'(x-ξ) as well as the relative dose profile p(x).
Particularly, the correction for the reduction of the dose maximum on the central axis (x = 0) of a symmetric photon fluence profile, where p (x = 0) = 1, is given by

$$k_V(x = 0) = \frac{1}{\int_{-\infty}^{+\infty} K'(x - x) p(x) dx} \quad (9)$$

This correction compensates, e.g., the numerical error in a measured accelerator output factor owed to finite detector dimensions.

Fig. 1 shows four Monte-Carlo calculated examples of kernels KM(x) and K(x) in maximum-normalized plots, whereas kernel KD(x) – not shown here – is essentially a Lorentz distribution [6] with full half width 0.50 mm at 6 MV. The striking effect is that the wide tails of KM(x), owed to secondary electron transport, largely disappear in K(x), because K(x) is the kernel convolved with the dose deposition kernel KD(x) which in itself comprises wide tails due to secondary electron transport. The slightly negative valleys of K(x) for silicon resp. diamond detectors are significant and are the expression of the density-dependent secondary electron disequilibrium at the interface between these detectors and the surrounding water.

Given these convolution kernels, it is easy to calculate the correction factor kV(x) from eq. (7) for arbitrary photon beam profiles. For p(x) we have taken the transverse profiles of the absorbed dose to water at depth 5 cm resulting from photon beams with variable rectangular photon fluence profiles, and we are here focusing on the special case x = 0 (see eq. (9)), i.e. when the detector is centered on the beam axis. Fig. 2 (left panel) shows the values of correction factor kV(x=0) for the four detectors in dependence upon the FWHM of the dose profiles in water. When the beam becomes narrower than the convolution kernel, kV(x=0) can achieve very large values.

It is interesting that these large correction factors basically reflect the desire to know the exact dose value in the centre of a narrow dose profile although the applied detector is too large to really resolve the profile. One should, however, consider that – under radiobiological viewpoints – the central value of the true dose profile might probably appear as less interesting than the mean dose value averaged over a small volume. We have therefore also calculated kV, water(x=0) for water-filled volumes with dimensions identical to those of the sensitive volumes of the four detectors, and have computed the ratios kV(x=0) / kV, water(x=0) (Fig. 2, right panel). These ratios are larger than unity for air-filled ionization chambers with density lower than of water and smaller than unity for the Si diode and microDiamond detectors with density higher than of water; for the diamond detector this ratio is very close to unity. The values kV(x=0) / kV, water(x=0) of the ionization chambers somewhat decrease at very narrow field widths corresponding to the dimensions of their aluminum central electrodes with density (2.3 g/cm3) higher than of water.

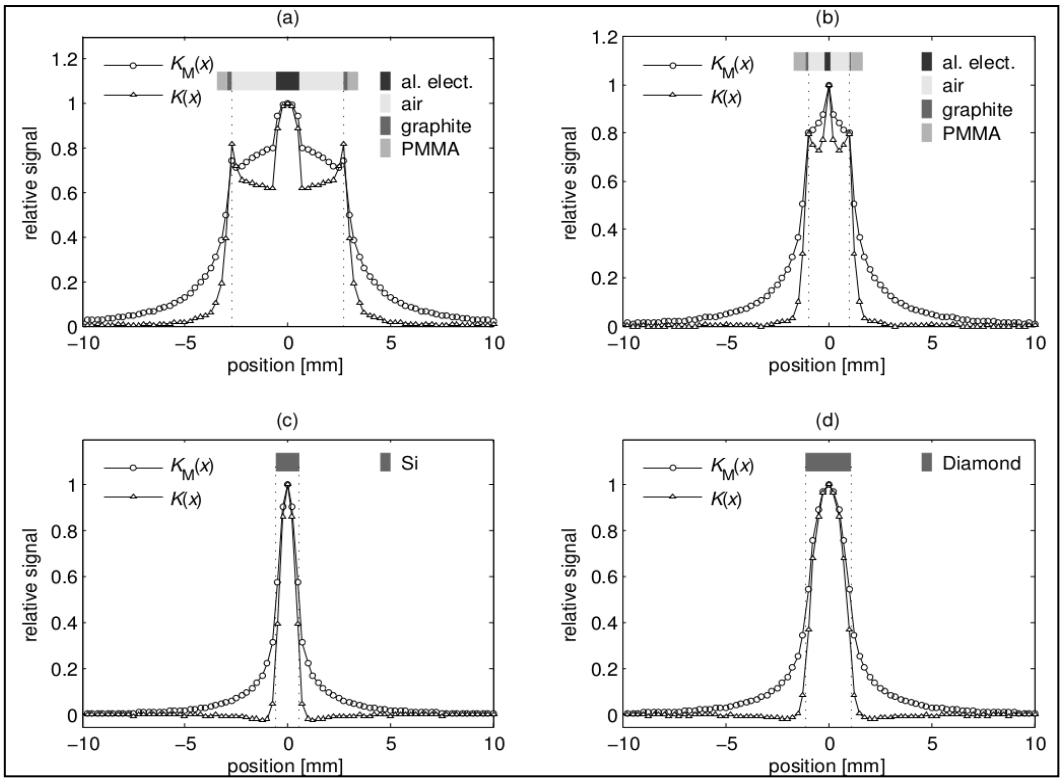

Fig. 1 Monte-Carlo-calculated kernels KM(x) and K(x) for (a) Semiflex PTW 31010; (b) PinPoint PTW 31014; (c) Si diode PTW 60012; (d) microDiamond PTW 60019, at 5 cm depth in water, irradiated with 6 MV photons. The extension of the sensitive volume for each detector in mm is shown by the dotted lines.

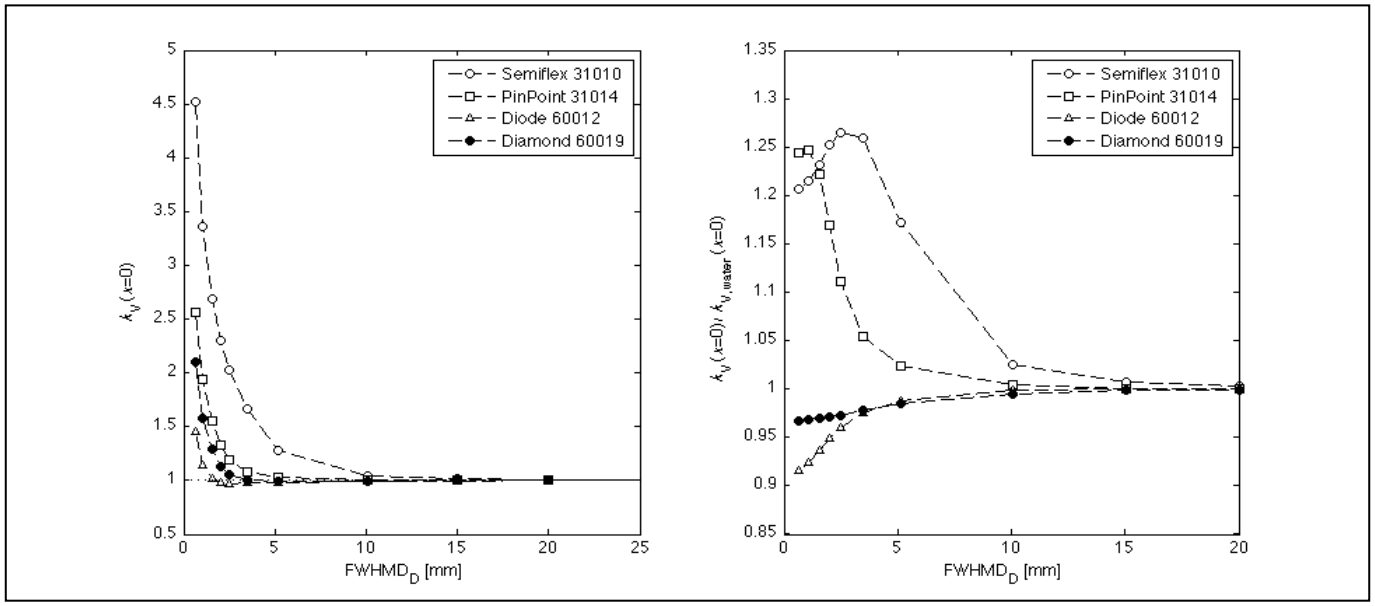

Fig. 2. Left panel: Volume-dependent correction factor kV(x=0), calculated by eq. (9), for four detectors as function of the full width at half maximum, FWHM, of the dose profile generated by a photon beam with rectangular fluence profile. Right panel: Relative values kV(x=0) / kV,water(x=0), where kV,water(x=0) is valid for a water-filled volume identical with the detector's sensitive volume.

In the proposed standard DIN 6809-8 on “Dosimetry in small photon fields”, it is recommended that detectors with sufficient spatial resolution such as Si diodes, diamonds, compact ionization chambers or films should be used for small-field dosimetry. These high-resolution detectors can be cross-calibrated in a "small reference field" 4 cm × 4 cm by comparing the measured signal of the high-resolution detector Mhigh-res to the dose in water Dic measured by a calibrated standard ionization chamber according to eq. (1). The "cross-calibration factor" is then given by: Nhigh-res = Dic / Mhigh-res. Using the thereby calibrated high-resolution detector, the absorbed dose to water in any clinically given narrow photon field, Dclin, can be determined using eq. (10):

$$D_{\mathrm{clin}}(x) = M(x) \cdot N_{\mathrm{high\text{-}res}} \cdot \prod_{\mathrm{i}} k_{\mathrm{i}} \cdot k_{\mathrm{NR,CC}} \cdot k_{\mathrm{V}} \qquad (10)$$

where M(x) is the detector reading in the given application situation and kNR,CC is the factor correcting for the change in the detector's energy-dependent dose response between the cross calibration conditions and the application situation

[3,4]. In this case the product of the ki's does not comprise the kQ under small-field reference conditions, since the latter is part of the cross calibration factor Nhigh-res. This approach was chosen in order to keep factor kNR,CC close to unity.

With regard to the product kNR,CC·kV it is appropriate to consider that an IAEA working group [1] has proposed a similar approach for the dosimetry in small and non-standard fields, which also requires the establishment of a machine specific reference field fmsr. The absorbed dose to water under clinical small field conditions fclin is in [1] determined according to eq. (11):

$$D_{w,Q_{\mathrm{clin}}}^{f_{\mathrm{clin}}} = D_{w,Q_{\mathrm{msr}}}^{f_{\mathrm{msr}}} \Omega_{Q_{\mathrm{clin}},Q_{\mathrm{msr}}}^{f_{\mathrm{clin}},f_{\mathrm{msr}}} = D_{w,Q_{\mathrm{msr}}}^{f_{\mathrm{msr}}} \cdot [M_{Q_{\mathrm{clin}}}^{f_{\mathrm{clin}}} / M_{Q_{\mathrm{msr}}}^{f_{\mathrm{msr}}}] \cdot k_{Q_{\mathrm{clin}},Q_{\mathrm{msr}}}^{f_{\mathrm{clin}},f_{\mathrm{msr}}} \qquad (11)$$

Factor Ω is the "field factor" described in the second part of eq. (11) as the quotient of the dosimeter readings per monitor unit at fclin and fmsr conditions, multiplied with the "four-parameter factor" $k_{Q_{\mathrm{clin}},Q_{\mathrm{msr}}}^{f_{\mathrm{clin}},f_{\mathrm{msr}}}$, the ratio of the Dw/Ddet values under fclin and fmsr conditions [5]. In applications of this equation is useful to consider that the symbol M is here used with a meaning different from eq. (10). Moreover, quantities D(fclin,w,Qclin) and D(fmsr,w,Qmsr) are understood as absorbed doses to water per monitor unit.

Basically, the meaning of the "four-parameter factor" in eq. (11) is the same as the product kNR,CC·kV in eq. (10). However it is important to note that the tabulated values of this factor are valid for special cases – the chosen fclin conditions (specified accelerator, SSD = 90 cm, central axis of a symmetrical field, depth 10 cm in water, variable field size) – whereas the energy-dependent factor kNR,CC and the volume-dependent correction kV according to eqs. (7) and (9) are generally applicable to any photon spectrum and any fluence profile as determined by the prevailing accelerator setting and given absorber conditions (material, field size, depth, etc., including nonuniform dose profiles and out-of-field conditions). Moreover intrinsic effects which may affect the responses of solid-state detectors such as Si diodes [3, 4] are accounted for in calculations of kNR,CC, but so far not in the "four-parameter factor".

We will compare applications of eqs. (10) and (11). Fig. 2 deals with the special example of a flat fluence profile of the photons, whereas most small clinical photon fields have "peaked" photon fluence profiles.

Conclusions: In order to account for the sizes of dosimetric detectors in narrow photon beams, the "volume-dependent correction factor" kV has been introduced into the fundamental equation of probe-type dosimetry, and the convolution method has proven to be a helpful and flexible tool for the derivation of its numerical values. For photon beam widths comparable to secondary electrons' ranges, kV can reach very high values. However, it can be shown that the signals of small diamond detectors are well representing the absorbed dose to water averaged over the detector volume. A comparison of the DIN and IAEA approaches has illustrated the close relationship between the formulations describing a detectors' energy-dependent dose response and its volume-dependent response function.

References

[1] Alfonso R, Andreo P, Capote R, Huq MS, Kilby W, Kjäll P, Mackie TR, Palmans H, Rosser K, Seuntjens J, Ullrich W, Vatnitsky S. *Med.Phys.* 35 (2008) 5179-5186

[2] Bouchard H, Seuntjens J, Carrier JF, Kawrakow I. *Med. Phys.* 36 (2009) 4654 – 4663

[3] Chofor N, Harder D, Poppe B. *Z. Med. Phys.* 22 (2012) 181-196

[4] Chofor N, Harder D, Poppe B. *Z Med Phys.* (2014) 27-37

[5] Czarnecki D, Zink K. *Phys.Med.Biol. 58* (2013) 2431-44

[6] Djouguela A, Harder D, Kollhoff R, Foschepoth S, Kunth W, Rühmann A, Willborn K and Poppe B. *Phys. Med. Biol.* 54 (2009) 2807-2827

[7] Fox C, Simon T, Simon B, Dempsey JF, Kahler D, Palta JR, Liu C, Yan G. *Med. Phys.* 37 (2000) 477-84

[8] Francescon P, Cora S, Satariano N. *Med Phys.* 38 (2011) 6513-6527

[9] Gago-Arias A, Brualla-González L, González-Castaño DM, Gómez F, García MS, Vega VL, Sueiro JM, Pardo-Montero J. Phys. Med. Biol. 57 (2012) 2005-20

[10] Looe HK, Stelljes TS, Foschepoth S, Harder D, Willborn K and Poppe B. *Z. Med. Phys.* 23 (2013) 129-143.

[11] Scott AJD, Kumar S, Nahum E and Fenwick J *Phys. Med. Biol.* 57 (2012) 4461-4476

[12] Ulmer W. *Inverse Problems* 26 (2010) 085002

[13] Underwood TS, Winter HC, Hill MA, Fenwick JD. *Med Phys*. 40 (2013) 082102

3 A study on ionization chamber perturbation corrections in flattening filter free beams

D. Czarnecki[1], P. von-Voigts-Rhetz[1], K. Zink[1,2]
[1]University of Applied Sciences, Institute for Medical Physics and Radiation Protection – IMPS, Giessen, Germany
[2]University Medical Center Marburg, Department of Radiotherapy and Radiation Oncology, Marburg, Germany

Introduction: The determination of absorbed dose to water in photon radiation fields requires the application of beam quality correction factors k_Q to take the difference between the ionization chamber's response in the calibration radiation field of a ^{60}Co source and the clinical photon field into account. The beam quality correction factor k_Q is related to the restricted water-to-air mass collision stopping-power ratio and ionization chamber perturbation corrections p_i as shown in equation (1) [1].

$$k_Q = \frac{\left[\left(\frac{\bar{L}}{\rho}\right)_a^w \prod_i p_i\right]_Q}{\left[\left(\frac{\bar{L}}{\rho}\right)_a^w \prod_i p_i\right]_{^{60}Co}} \quad (1)$$

In current dosimetry protocols [1,2] the beam quality correction factor and the restricted water-to-air mass collision stopping power ratio are given for several ionization chambers as a function of beam quality specifiers for conventional linear accelerator with flattening filter (WFF). However, these beam quality specifiers do not include energy spectrum variations which occur in modern linear accelerators with flattening filter free modes (FFF). Monte Carlo calculations by Xiong and Rogers [3] show an influence of the flattening filter on the relationship between the water-to-air stopping-power ratio and the beam quality specifiers $TPR_{20,10}$ and %dd(10).

In this Monte Carlo simulation based study the influence of the flattening filter on the relationship between the beam quality specifiers and perturbation factors of the thimble ionization chamber PTW 31010 (PTW, Freiburg) respectively k_Q were investigated.

Materials and methods: The beam quality correction factor k_Q was calculated according to equation (2)

$$k_Q = \frac{\left[\frac{D_w}{D_{det}}\right]_Q}{\left[\frac{D_w}{D_{det}}\right]_{^{60}Co}} \quad (2)$$

where D_w describes the point dose in 10 cm water depth and is determined in good approximation by the absorb dose in a small cylindrical water voxel (radius = 2 mm, height = 0.5 mm). Perturbation corrections were determined from Monte Carlo simulations of a 10 x 10 cm² open photon field defined by the position of jaws according to the formalism described in [4, 5]. The central electrode, wall, fluence, density and volume perturbation factors p_{cel}, p_{wall}, p_{fl}, p_ρ and p_{vol} were calculated as a function of beam quality specifier $TPR_{20,10}$ in 10 cm water depth for photon fields of FFF and WFF linear accelerators with nominal energies in the range from 4 MV to 20 MV. The overall perturbation factor was calculated according to equation (3).

$$p = \frac{D_w}{D_{det}\left[\frac{\bar{L}}{\rho}\right]_a^w} \quad (3)$$

All Monte Carlo calculations were performed with the EGSnrc/BEAMnrc code system [6]. The radiation transport through nine different linear accelerator heads from three major manufactures (Varian, Elekta and Siemens) was simulated with the user code BEAMnrc [7]. The reference radiation field was simulated using the BEAMnrc model of an Eldorado 6 teletherapy unit developed by Muri *et al* [8]. The thimble ionization chamber PTW-31010 (PTW, Freiburg) was modeled in detail according to manufactory drawings using the egs++ class library [9]. Dose to water and dose calculations within the active volume of the ionization chamber were performed with egs_chamber [10]. The restricted water-to-air mass collision

stopping-power ratio was calculated applying the user code SPRRZnrc [11]. The transport threshold/cutoff energies in all Monte Carlo simulations were set to AE = ECUT = 521 keV and AP = PCUT = 10 keV.

Results and discussion: In Figure 1 the over-all perturbation corrections and the single perturbation corrections for FFF and WFF beams are presented as a function of $TPR_{20,10}$. Figure 2 shows the beam quality correction factor k_Q for the thimble ionization chamber PTW31010 and the restricted water-to-air mass collision stopping-power ratio as a function of $TPR_{20,10}$ for FFF and WFF beams. The Monte Carlo calculated stopping-power ratio has been compared to the cubic polynomial fit published in the IAEA dosimetry protocol [1]. In Figure 2 the Monte Carlo calculated k_Q values are compared with typical values taken from [1]. The Monte Carlo calculated stopping power ratio and beam quality correction factor k_Q for conventional linear accelerator (WFF) are in good agreement with the published data [1].

Conclusion: The results conform the expected bias between the water-to-air stopping power ratio of FFF and WFF beams. Nevertheless the perturbation due to the components of the ionization chamber PTW 31010 such as stem, central electrode and wall showed no deviation between FFF and WFF beams. Despite the inhomogeneous photon field of the FFF beam, the volume perturbation factors showed no significant difference to the volume perturbation factors of the homogeneous WFF beam. The fluence and density perturbation corrections for FFF beams are systematically slightly below respective above the values for WFF beams. A bias between the over-all perturbation correction for WFF and FFF beams is not significant due to a relative high statistical uncertainty. Therefore, it cannot be said clearly that a bias between the beam quality correction factor for FFF and WFF beams is caused by the restricted mass collision stopping-power ratio only. Further calculations have to be performed to confirm this statement.

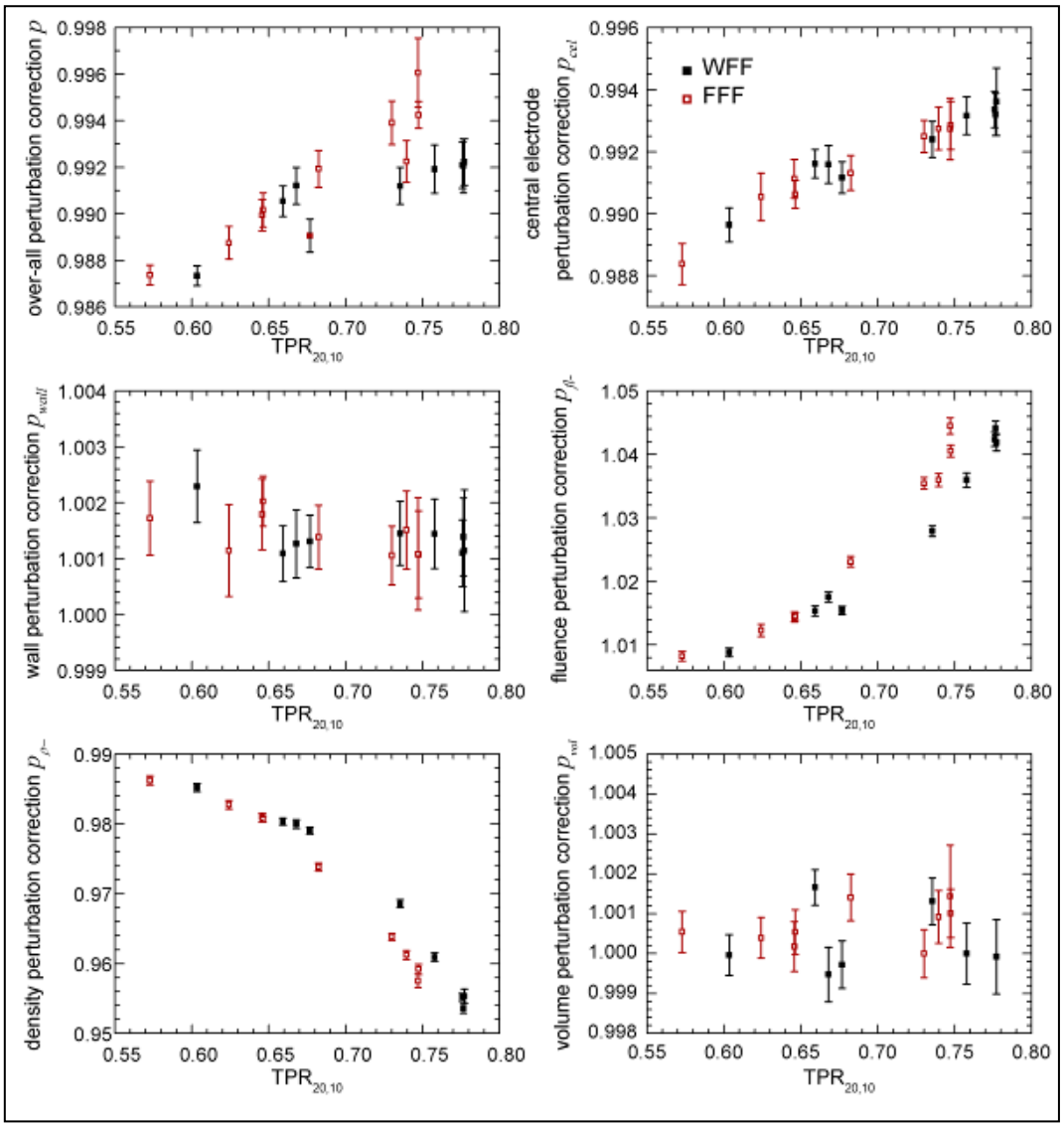

Fig. 1: Monte Carlo calculated perturbation factors in 10 cm water depth for the ionization chamber PTW 31010 as a function of $TPR_{20,10}$.

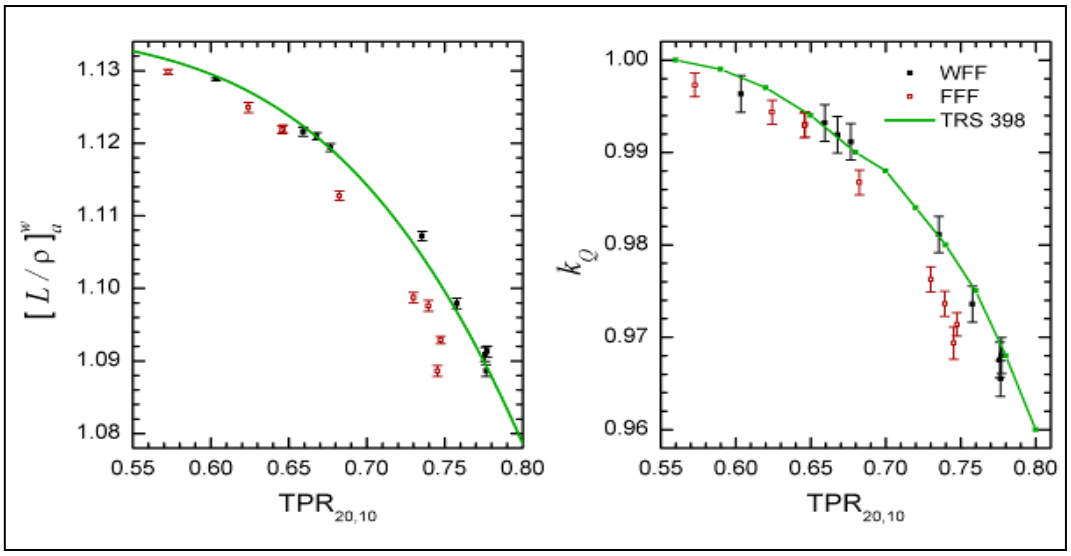

Fig. 2: Monte Carlo based calculations of water-to-air restricted mass collision stopping-power ratio (left) and beam quality conrrection factor kQ (right) as a function of TPR20,10 at the point of measurement within the water phantom (depth z = 10 cm) for FFF (red) and WFF (black) beams. The solid line give the data according to IAEA TRS 398 [1].

References

[1] Andreo P, et al., (2000) IAEA Technical Reports Series no 398 Vienna: International Atomic Energy Agency
[2] Norm DIN 6800-2 (2008). Berlin: Beuth Verlag
[3] Xiong, G., & Rogers, D. W. O. (2008). Med. Phys. 35(5), 2104-2109
[4] Bouchard, H., Seuntjens, J., Carrier, J. F., & Kawrakow, I. (2009). Med. Phys. 36(10), 4654-4663
[5] Fenwick, J. D., Kumar, S., Scott, A. J., & Nahum, A. E. (2013). Phys. Med. Biol., 58(9), 2901.
[6] Kawrakow, I., Rogers, D. W. O., Tessier, F., & Walters, B. R. B. (2013). NRCC Report PIRS-701, National Research Council of Canada, Ottawa, Canada
[7] Rogers, D. W. O., Walters, B. R. B., & Kawrakow, I. (2013). NRCC Report PIRS-0509(A)revL, National Research Council of Canada, Ottawa, Canada
[8] Muir, B., Xiong, G., Selvam, T. P., & Rogers, D. W. O. (2009). CLRP-Report CLRP-09-01
[9] Kawrakow I. (2006). NRCC Report PIRS-898, National Research Council of Canada, Ottawa, Canada
[10] Wulff, J., Zink, K., & Kawrakow, I. (2008). Med. Phys. 35(4), 1328-1336
[11] Rogers, D. W. O., Kawrakow, I., Seuntjens, J. P., Walters, B. R. B., & Mainegra-Hing, E. (2013). NRC user codes for EGSnrc. NRCC Report No. PIRS-702(revC), National Research Council of Canada, Ottawa, Canada

4 Comparison of the number of MU and out-of-field radiation for different delivery techniques

M. Jäckel[1]
[1]Universitätsklinikum Hamburg-Eppendorf, Strahlentherapie und Radioonkologie, Hamburg, Germany

Introduction: The development of linear accelerators in recent years has made it possible to deliverradiation in a variety of techniques. Differences between static and intensity modulated fields as well as high and low photon energy need to be considered when deciding which technique is the best for the individual patient. Meanwhile it is not enough to analyze a DVH when choosing a treatment plan, as often several intensity modulated plan variations give similar DVHs [1]. This work investigates the influence of different delivery techniques on the number of MU and out-of-field secondary radiation.

Materials and methods: Following plans were calculated in Eclipse Treatment Planning System for a Varian True Beam linear accelerator for 6 and 15 MV and for a 2 Gy fraction dose:

1) single arc (1RA),
2) double arc (2RA),
3) 7 field IMRT with dose rate 300 MU/min (IMRT DR300),
4) 7 field IMRT with dose rate 600 MU/min (IMRT DR600),
5) 4 static fields with gantry angles 0°, 90°, 180°and 270° (4F),
6) 3 static fields with gantry angles 0°, 90 and 270° of which 2 lateral fields modulated with field in field technique (3F FinF),
7) 3 static fields with gantry angles 0°, 90 and 270° of which 2 lateral fields modulated with dynamic wedge (3F DW).

All these 14 plan variations were calculated for 4 cases (the 2nd and the 4th are depicted in Fig. 1):

1) prostate cancer patient,
2) Alderson Radiation Therapy phantom,
3) rectangular box solid phantom,
4) rectangular box solid water (RW3) phantom with a square axial cross-section.

Each plan was normalized to 100 % mean dose in the target volume. For inversed planning techniques (1-4), the same optimization objectives were used. For forward planning techniques (5-7), field weights were adjusted to minimize the differences in DVHs. The numbers of MU, which resulted from plan calculation, were compared according to applied energy and planning modality.Out-of-field point dose was measured for the case number 4 in a solid phantom with an ionization chamber. The isocenter and the measuring point were on the longitudinal axis of the accelerator and in the middle of phantom's axial cross-section. The measuring point was 18 cm away from the isocenter towards the target. Each of the plans 1-4 was irradiated 5 times and the plans 5-7 were rescaled to a fraction size 10 Gy.

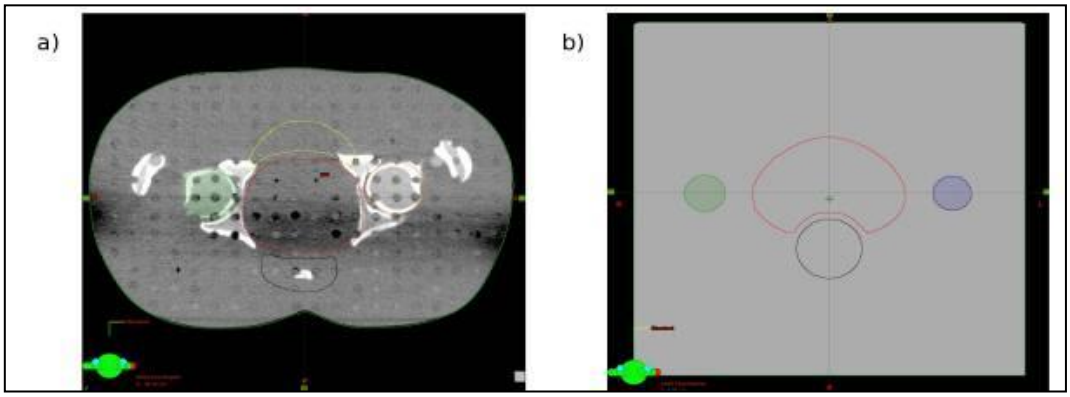

Fig. 1: a) the case number 2, Alderson Radiation Therapy phantom, b) case number 4, square solid phantom for which the out-of-field dose was measured.

Results: The computed number of MU and the measured out-of-field dose are presented in Tab. 1. The comparison of the number of MU revealed the following results:

- all 6 MV plans have 22 ± 5% more MUs than the 15 MV plans obtained with the same technique,
- IMRT DR600 have 12 ± 3 % more MUs than IMRT DR300 (in cases 2-4 the difference was larger for 15 MV plans than for 6 MV plans),
- 2RA have 7.5 ± 2.5% and 5.2 ± 0.4 % more MUs than 1RA for 6 and 15 MV respectively,

- the difference in the number of MU between IMRT and RA is not as high as reported in [1] and in the case number 1 both RA plans have more MUs than both IMRT plans of the same energy,
- within forward planning techniques 3F DW needs the highest number of MUs and the 4F the lowest, when comparing plans of the same energy.
-

The results of out-of-field measurement show that the measured dose is:

- proportional to the number of MU,
- dose per MU does not depend on used beam energy,
- there is 8.5 % increase in measured dose per MU for IMRT plans in comparison to RA plans,
- within forward planning techniques the dose per MU for 4F and 3F FinF is 53 % higher than for 3F DW.

Conclusion: Considering out-of-field dose, 15 MV plans have a serious advantage over 6 MV plans as they have less MUs and therefore produce less out-of-field radiation. Nevertheless, this work does not take into account the scattered neutron dose which is approximately the same throughout the whole body [2]. It should be further investigated if the benefit of less out-of-field dose in 15 MV plans outweighs the risks of additional dose from scattered neutrons.

If the treatment time is not of importance, it is advantageous to use IMRT with lower dose rate instead of higher dose rate as it has less MUs.

When considering forward planning techniques, the use of a dynamic wedge for dose modulation decreases the out-of-field dose, despite requiring more MUs. This is most likely due to the fact that the radiation scattered from the dynamic wedge, which is the upper jaw, is blocked by the lower jaw and the MLC.

	Number of MU for 2 Gy				Measured out-of-field
Technique	**case 1**	**case 2**	**case 3**	**case 4**	**dose for 10 Gy [mGy]**
1 RA 6 MV	892	735	715	620	34.01
1 RA 15 MV	695	596	608	552	29.51
2 RA 6 MV	940	779	793	668	35.42
2 RA 15 MV	728	630	640	580	30.77
IMRT DR300 6 MV	752	698	878	613	35.75
IMRT DR300 15 MV	620	578	699	529	30.51
IMRT DR600 6 MV	838	795	1010	695	40.01
IMRT DR600 15 MV	660	679	845	607	35.84
4F 6 MV	345	296	274	249	37.88
4F 15 MV	269	238	225	213	34.08
3F FinF 6 MV	374	329	312	265	36.86
3F FinF 15 MV	292	262	253	229	34.78
3F DW 6 MV	401	357	323	284	28.29
3F DW 15 MV	303	280	256	237	23.12

Table 1: The results of plan computation and out-of-field dose measurement.

References

[1] Teoh, M., Clark, C. H., Wood, K., et al. "Volumetric modulated arc therapy: a review of current Literature and clinical use in practice." *British Journal of Radiology,* 84(1007): 967-996, 2011.

[2] Kry, S. F., Salehpour, M., Followill,, et al. "Out-of-field photon and neutron dose equivalentsfrom step-and-shoot intensity-modulated radiation therapy." *International Journal of Radiation Oncology* Biology* Physics,* 62(4): 1204-1216, 2005.

5 Mass attenuation coefficients of typical phantom materials for X-rays with energies between 7 keV and 70 keV

D. Radeck[1], T. Schneider[1]
[1]Physikalisch-Technische Bundesanstalt, Braunschweig, Germany

Introduction: Data on attenuation coefficients of phantom materials are relevant for fundamental and reference radiation dosimetry. Radiation transport calculations – an important tool in dosimetry – use data bases for fundamental physical quantities. The accuracy of simulation results, however, is strongly dependent on the correctness of the values in the data bases. Several data bases on mass attenuation coefficients exist that were theoretically and/or semi-empirically evaluated. In particular for low-energy photons the data bases show discrepancies. Thus, the results of Monte Carlo calculations depend on the choice of data base and this can cause high uncertainties of calculated correction factors needed in dosimetry. For the realization of the measurand of absorbed dose to water for low-energy brachytherapy sources, i.e. for I-125 and miniature X-ray tubes, the PTB primary standard is currently under further development. In this context a review of existing values on mass attenuation coefficients for dosimetrically relevant materials was carried out as well as an experimental determination of monoenergetic coefficients between 7 keV and 70 keV.

Materials and methods: For the experimental investigation, a narrow-beam setup was used. Fluorescence lines induced by the irradiation of different thin deflection foils at an X-ray facility were applied in order to determine monoenergetic attenuation coefficients of different materials at energies between 7 keV and 70 keV. The reduction of beam intensity dI/I is proportional to the mass attenuation coefficient and slab thickness. The investigated materials were water, graphite, PMMA, PE, Makrolon, and RW1. The absorber was a slab of the phantom material of interest and aligned with plane parallel faces normal to the beam.

Results and Conclusion: Values of low-energy attenuation coefficients for typical phantom materials were determined with small uncertainties and are compared with data evaluated by Storm and Israel [1], Hubbell [2], and the web-based National Institute of Standards and Technology (NIST) database xcom [3]. A discussion on reasonable uncertainties in the low-energy range is presented. The results are needed for the realization and dissemination of absorbed dose to water for low-energy brachytherapy sources as well as for other dosimetric investigations.

References

[1] Storm, E. and Israel, H.I. (1970), ‘Photon Cross Sections from 1 keV to 100 MeV for elements Z=1 to Z=100‘, Nucl. Data Tabl. A 7, 565-581.
[2] Hubbell, J.H. (1977), ‘Photon Mass Attenuation and Mass Energy-Absorption coefficients for H, C, N, O, Ar, and seven mixtures from 0.1 keV to 20 MeV‘, Rad. Res. 70, 58-81.
[3] Berger, M.J., Hubbell, J.H., Seltzer, S.M., Chang, J., Coursey, J.S., Sukumar, R.,Zucker, D.S., and Olsen, K. (2010), XCOM: Photon Cross Section Database (version 1.5).
[Online] Available: http://physics.nist.gov/xcom, National Institute of Standards and Technology, Gaithersburg, MD.

6 Investigation on the influence of radiotherapy on pacemakers considering photons, neutrons and EMI – effects

V. M. Schneider[1,2], C. Wilhelm[1], J. Bummer[1], J. Müller[1], M. Treiber[1], M. Möller[2]
[1]Caritasklinikum Saarbrücken, Saarbrücken, Germany
[2]Hochschule für Technik und Wirtschaft, Saarbrücken, Germany

Introduction: The number of patients with cardiac pacemakers is increasing every year, about 140.000 in Germany in 2010. The number of patients suffering from cancer is also increasing, 490.000 every year are expected in Germany. Experts expect 30 percent more malignant diseases up to 2050. Therefore there is a greater probability that patients with pacemakers have to be treated with radiotherapy.

The effect of radiation therapy on cardiac pacemakers has already been discussed in various studies where different causes for malfunctions or damage of pacemakers were discussed [1, 2]. Here, we study the influence of various treatment parameters – in particular, the acceleration energy in connection with the influence of neutrons – as well as electromagnetic interference (EMI) on a selection of pacemakers connected to an arrhythmia simulator.

Materials and methods: A selection of 6 BIOTRONIK pacemakers (Axios DR (2 specimens), Cylos DR, Philos DR, Talos DR and Talos SLR) were operated in DDD resp. VDD mode. The pacemakers were connected to an arrhythmia simulator programmed to simulate a 2nd-degree a-v block, thus correct pacemaker performance should result in a ventricular stimulation in every other cardiac period. The atrial and ventricular electrode signals and the simulated ECG (see Fig. 2) were recorded continuously by an analog-to-digital converter placed outside the treatment room. In order to determine early battery depletion and parasitic errors which might occur afterwards, measurements were continued for long periods of time after irradiation. Irradiation was performed on two Varian Clinac 2300 DHX linear accelerators at the Caritas Hospital St. Theresia (Saarbrücken, Germany). Both photon radiation at 6 MV or 18 MV and electrons with energies of 6 MeV, 9 MeV or 22 MeV were applied. Malfunctions due to reversible damage are discussed in the literature. Thus, two devices were irradiated until a malfunction occurred (Cylos DR-T, Philos DR). With one device (Cylos DR-T) we carried out measurements continuously increasing dose rates from 1 Gy/min to 6 Gy/min, using 6 MV in order to minimize the influence of neutrons. The other four devices were to be checked for malfunctions after irradiation with radiation doses as commonly used in clinical practice: 72 Gy (Axios DR#2), 20 Gy (Axios DR#1) and 30 Gy (Talos DR , Talos SLR). Four pacemakers (2 Axios DR, Cylos DR–T, Philos DR) were irradiated directly with a SSD of 100 cm and 10x10 cm² field. For the other two pacemakers (Talos DR and Talos SLR) a PMMA body phantom was used to simulate a realistic radiation situation: The pacemakers were modeled in a flap and placed anatomically correct on the phantom. Then planning computer tomography and treatment planning followed analogous to common patient treatment. The target volume of a bone metastasis was created to be irradiated with a total dose of 30 Gy at 3 Gy/fraction using VMAT technology. The objective for the pacemaker was chosen not to exceed 5 Gy for the complete treatment. A check of the pacemaker using the Biotronik PMS 1000plus programmer was carried out before and after every treatment. EMI is described to be able to cause temporary damage which should occur immediately under irradiation. Here, we measured EMI field strengths using a NARDA SRM with a field probe ranging from 27 MHZ to 3 GHZ. The pacemakers were placed in the treatment area with the photon resp. electron radiation blocked by the completely closed multileaf collimator (MLC). Again, the pacemaker electrode signals were monitored continuously in order to detect irregularities. Neutron contamination of the photon radiation was measured with a Berthold neutron dosimeter placed close to the treatment area outside the radiation field (see Fig. 1) during irradiation. Neutron activation of the pacemaker was measured after irradiation by taking the device outside the treatment room and measuring the emitted radiation using an Automess photon dosimeter.

Results: No malfunctions were observed during or after irradiation of the Axios DR#1, the Axios DR#2 and the Talos SLR. The Cylos DR-T lost stimulation in the ventricle after a dose of 66 Gy (6 MV). After some weeks the pacemaker recovered and continued to work without malfunctions. The Philos DR showed a total loss of stimulation comparable to the one of the Cylos DR-T after a dose of 135 Gy (18 MV). Again, the device was reconnected one week after irradiation and showed flawless performance. The Talos DR exhibited a total loss of stimulation at a dose of 0.7 Gy (18 MV) at the device The subsequent check with the programmer showed the devices' RAM data to be corrupt, thus re-initialization by the programmer had to be performed. After that, long term measurement confirmed the recovery of the device. Irradiation of a similar type of pacemaker (Talos SLR) at 6 MV showed no malfunction, even after a dose of 4.1 Gy at the device. EMI measurements were started when the accelerator was ready to beam. The RF driver signal could be observed at 2.856 GHz with a field strength ranging from 85 mV/m to 183 mV/m, depending on the selected energy. In the pacemaker electrode signals, no irregularities were observed. Neutron measurements at 18 MV showed a neutron dose of about 16.45 mSv after a photon radiation dose of 135 Gy (Philos DR), about 8.84 mSv after a dose of 72 Gy (Axios DR #2) and 836 µSv after a dose of 30 Gy (Talos DR). Activation measurements resulted in a dose rate of 4.1 µSv/h from the Axios DR #2 after an irradiation dose of 72 Gy and 0.12 µSv/h from the Talos DR after 0.7 Gy at the device, both at 18 MV, thus confirming neutron activation of the materials.

Conclusion: A relevant influence of EMI on pacemaker operation could not be determined in this work. Probably, there will be minimal voltage drops or voltage rises on some component of the pacemaker, but this is not detectable with this measurement setup. Malfunctions in the form of a decrease of the stimulation amplitude below the stimulation threshold

occurred in 3 of the 6 pacemakers during treatment. Two of these devices had been irradiated with 18 MV, one with 6 MV photon radiation. In one of the 18 MV cases, even the devices' RAM data was corrupted; here, comparison with a similar device at 6 MV showed no malfunction, even after a considerably higher dose. All damaged pacemakers completely recovered within intervals ranging from days to weeks. After recovery, no other malfunctions were observed. Confirmed by neutron dose measurements, it can be assumed that in the two 18 MV cases the adverse effect of radiotherapy on pacemaker function is at least partially caused by neutrons, even in the low dose range. At 6 MV, the influence of the neutrons might be insignificant; here the influence of various dose rates and MUs might still be investigated with a higher number of specimens. Nevertheless, neutrons are generated even at low photon energies. Additionally, the effect of activation of the pacemaker should be investigated as well. Furthermore, accelerators with Flattening-Filter-Free (FFF) mode are being used more and more in practice. This mode allows higher dose rates, which may result in an increased adverse effect on pacemakers. In conclusion (and in agreement with the recommendations of the pacemaker manufacturers): don´t irradiate pacemakers with energies higher than 6 MV! The authors would like to thank BIOTRONIK SE & Co. KG, Berlin, for providing the pacemaker samples.

References

[1] M. Dorenkamp: Strahlentherapie bei Patienten mit Herzschrittmachern oder implantierbaren Kardioverter-Defibrillatoren, Strahlentherapie und Onkologie 1 2013

[2] Coen W. Hurkmans: Management of radiation oncology patients with a pacemaker or ICD: new comprehensive practical guideline in The Netherlands, Radiation Oncology 2012

Fig. 1: Neutron measurement setup

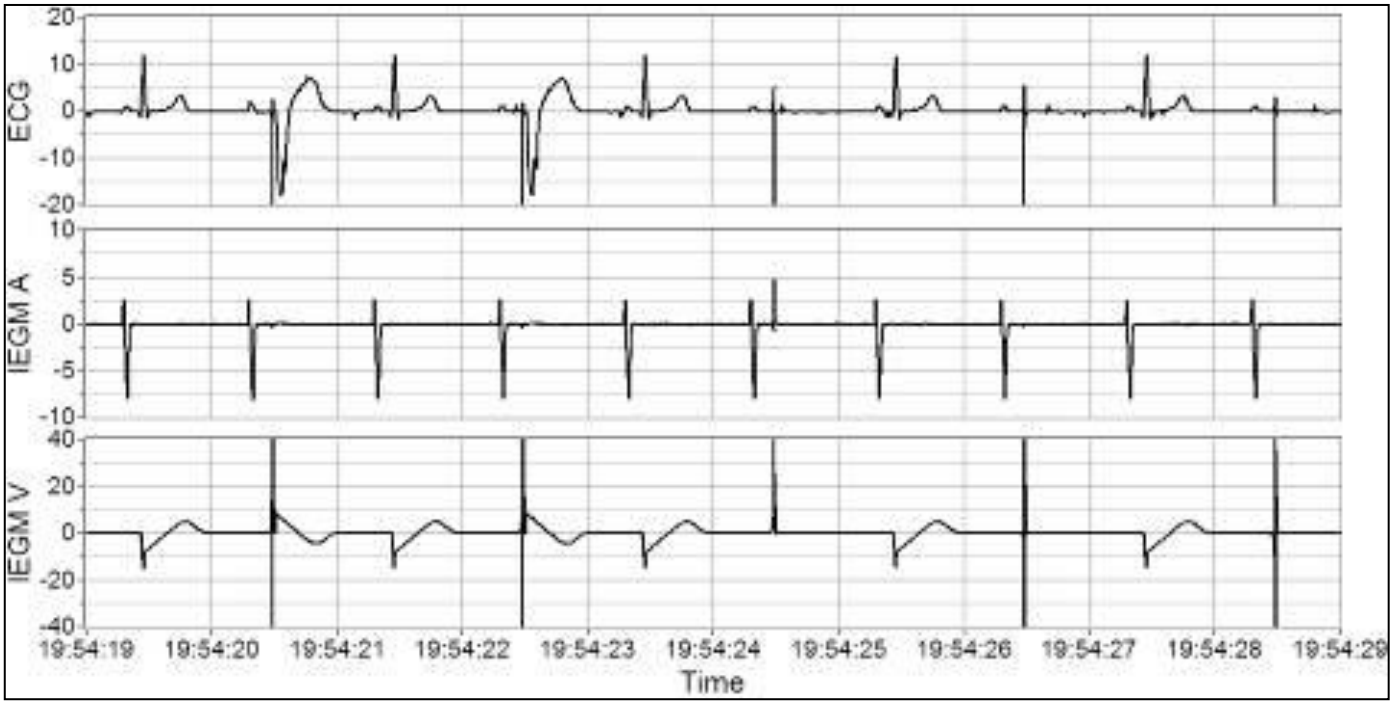

Fig. 2: Pacemaker operation showing stimulation failure (starting at 19:54:24) after exposure to 135 Gy / 18 MV.

Session 2 – Particle radiation therapy I: Systems

Chairs: O. Jäkel (Heidelberg/DE), A. J. Lomax (Villigen, Zurich/CH)

7 Introductory lecture: Particle Beam Radiotherapy – Quo vadis

O. Jäkel[1]
[1]Heidelberg, Germany

8 Development of a Compact Particle Therapy Facility with Laser-driven Ion Beams via Novel Pulse Powered Gantry Systems

U. Masood[1], M. Bussmann[2], M. Baumann[1,3,4,5], T. E. Cowan[2,6], W. Enghardt[1,3,4], T. Herrmannsdörfer[7], K. M. Hofmann[8] M. Kaluza[9], L. Karsch[1], F. Kroll[2], U. Schramm[2,6], M. Schürer[1], J.J. Wilkens[8], J. Pawelke[1,2]
[1]OncoRay-National Center for Radiation Research in Oncology, Faculty of Medicine C.G. Carus, Technische Universität Dresden, Dresden, Germany
[2]Helmholtz-Zentrum Dresden-Rossendorf, Institute of Radiation Physics, Dresden, Germany
[3]University Hospital C.G. Carus, Department of Radiation Oncology, Dresden, Germany
[4]Helmholtz-Zentrum Dresden-Rossendorf, Institute of Radiation Oncology, Dresden, Germany
[5]German Consortium of Translational Cancer Research (DKTK), Dresden, Germany
[6]Technische Universität Dresden, Dresden, Germany
[7]Helmholtz-Zentrum Dresden-Rossendorf, Hochfeld-Magnetlabor Dresden, Dresden, Germany
[8]Technische Universität Munich, Klinikum rechts der Isar, Department of Radiation Oncology, Munich, Germany
[9]Friedrich-Schiller-Universität Jena, Institute of Optics and Quantum Electronics, Jena, Germany

Introduction: The recent progress in laser-driven particle acceleration has made Laser-based Ion Beam Therapy (L-IBT) an attractive alternative to existing Ion Beam Therapy (IBT) facilities for size and cost reduction [1, 2]. In laser-driven ion acceleration, an ultra-intense laser pulse interacts with thin targets and accelerates intense ion bunches on µm scale. Protons and carbon ions can be generated from different targets with the same laser system. However, in contrast to narrow mono-energetic beams from conventional accelerators, laser-driven ion beams are characterized by short pulses of high particle flux with peak dose rate exceeding conventional values by 8-9 orders of magnitude, low repetition rate, broad energy spectrum and large divergence. In addition to laser particle accelerator development for achieving therapeutic ion beams, the aforementioned distinct features demand novel techniques for dose delivery system. The conventional solutions cannot be applied directly to L-IBT and new approaches are needed for beam transport including ion capturing and energy selection [1], beam monitoring and dosimetry [3], irradiation field formation and optimized treatment planning [4]. Oncooptics is a German joint research project of several institutions in Jena and Dresden aiming to develop and establish L-IBT. We have designed a compact 360° rotatable iso-centric gantry system with integrated beam capturing and energy selection system for laser-driven proton and carbon beams. Our first design was presented at DGMP 2012. Now we would focus on our advancement in improving the design and its practical realization.

Materials and methods: The pulsed nature of laser-driven ion beams allowed us to utilize pulse powered air-core magnets for the gantry design. Unlike conventional iron-core magnets, pulsed magnets are not limited by iron's saturation of magnetization to 2 T and provide higher magnetic fields which can bend high energy ions in smaller radius and hence compact designs are achievable. The general gantry design is characterized by capturing and focusing the divergent laser-driven beam by a solenoid lens. Then, energy selection is achieved by 90° sector (dipole) magnet in combination with quadrupole lenses. The magnetic element arrangement in the beamline, allowed shaping the beam according to the patient field requirements. Optimization of the previously presented design aimed to reduce the overall size of the gantry, to lower the number of necessary magnetic elements and to increase beam transport efficiency and energy selection resolution. The realization of the gantry has been started. Due to missing iron-core and higher current values, the pulse magnetic elements of the gantry, namely solenoid, dipole and quadrupole, are non-trivial and challenging to develop and realize. They require complex multi-layer winding geometries. Also, higher magnetic field introduces intense magnetic pressure which needed to be compensated by mechanical strength of the construction. Moreover, heat dissipation and vacuum requirements were essential parameters to be considered. After construction magnetic elements are required to be characterized at reference beams of conventional accelerators followed by tests at laser-driven beams. Moreover, in order to investigate the quality of treatment plans for laser-driven protons, deliverable via our gantry, a dedicated 3D treatment planning system (TPS) is being developed under collaboration with Technical University Munich, Germany.

Results: The optimization of the first double-achromatic pulsed gantry design has resulted in reduction of size to 3 m in diameter, which is about 2.5 times smaller than conventional gantries. The improved integrated high resolution and high acceptance energy selection system has resulted in transport efficiencies of ~22 %. Also, with the 3D TPS, we were able to produce treatment plans with plan qualities of clinical relevance by using broad energetic beams [5]. For the realization of the gantry design, development and testing of pulsed magnets are in-progress. A first prototype of 20 T pulsed solenoid, as particle capturing and focusing device, has been designed and manufactured and has been successfully tested at laser-driven proton beams. A prototype 10 T compact pulsed 45° sector magnet has also been designed and manufactured. This has a non-conventional complex multi-layer (6+8+6) winding structure, which was necessary for achieving high magnetic flux values. The first electrical and vacuum tests were successfully performed and characterization of the dipole with reference proton beams at conventional Tandem accelerator is in progress. Furthermore, a pulsed large acceptance quadrupole with high gradient (~250 T/m) has been designed and simulated. The design, construction process and current status will be presented.

Summary: Our pulsed gantry systems provide a compact solution for L-IBT. The realization and tests of pulsed gantry magnetic elements are being continued. The conventional proton therapy facility at OncoRay Dresden, Germany (under commissioning) is additionally equipped with a high-intensity laser laboratory and an experimental irradiation bunker. This will be used for further L-IBT development, including pulsed gantry elements, towards clinical applicability side-by-side with the conventional therapeutic proton beams as reference.

Acknowledgment: This work is supported by the German Ministry of Education and Research (BMBF) under grant numbers 03ZIK445, 03Z1N511 and 03Z1O511 and DFG Cluster of excellence: Munich-Centre for Advanced Photonics.

References

[1] U Masood et al., Appl. Phys. B, 1-12 (2014)
[2]]K W D Ledingham and W Galster. New J. Phys. 12, 045005 (2010)
[3] C Richter et al., Phys. Med. Biol., 56:1529-1543 (2011)
[4] S Schell et al., Med. Phys., 37:5330-5340 (2010)
[5] K M Hofmann et al., Dreiländertagung Medizinische Physik (abstract, submitted) (2014)

9 A treatment planning study to assess the feasibility and the limitations of laser-driven proton therapy

K. M. Hofmann[1], U. Masood[2], J. Pawelke[2,3], J.J. Wilkens[1]
[1]Technische Universität Munich, Klinikum rechts der Isar, Department of Radiation Oncology, Munich, Germany
[2]OncoRay, National Center for Radiation Research in Oncology, Dresden, Germany
[3]Helmholtz-Zentrum Dresden-Rossendorf e. V., Dresden, Germany

Introduction: Laser-driven proton acceleration may develop as an efficient alternative for producing protons with energies relevant for radiation therapy. The bunch structure of laser-accelerated protons is fairly different compared to conventionally accelerated protons in radiotherapy since the bunch length is much shorter and the number of protons per bunch is much higher than in current facilities. Hence, laser-driven proton bunches cannot be modulated easily during irradiation as commonly done in proton therapy. Therefore, the aim of this study is to investigate the quality of treatment plans gained by utilizing full shots of laser-accelerated protons and whether a laser-driven treatment unit would be feasible for future proton therapy centers.

Materials and methods: A proton spectrum measured in a current laser experiment was extrapolated and utilized as “initial spectrum” in which the contained “initial proton number” was a free parameter. This exponentially decaying spectrum was tracked through a compact gantry and energy selection design based on pulsed magnets [1] to simulate various possible resulting proton spectra. These were fed into a treatment planning system (TPS) adapted to handle laser-driven proton beams [2]. The spectra are centered on numerous nominal energies (50 MeV – 250 MeV) with several energy widths (4 % – 24 % of the nominal energy) and, therefore, contain a well known proton number depending on the initial proton number. To evaluate the feasibility and limitations of the design we calculated treatment plans for an astrocytoma patient, previously treated in our department (prescribed dose Dp = 2 Gy per fraction), by varying the initial proton number and the lateral width (full width at half maximum, FWHM) of the beam at the entrance of the patient. Since the laser can only deliver full shots the required numbers of shots were rounded to the next integer after optimization. The resulting plans were evaluated depending on their dosimetric quality and in terms of treatment time. A plan was defined to be clinically acceptable if the target coverage TC ≥ 98 %, the conformation number CN ≥ 90 %, Dmin(1cm³) ≥ 95 % of Dp and Dmax(1cm³) ≤ 105 % of Dp. A plan was declared to be not acceptable if one of the following is true: TC < 95 %, CN < 82 %, Dmin(1cm³) < 92.5 % of Dp or Dmax(1cm³) > 107.5 % of Dp. Plans of intermediate quality according to these criteria would need a detailed plan review.

Results: The analysis showed that good dose distributions could be achieved with laser-driven proton beams even with energy widths up to 24 %. We observed that clinically relevant plans could be produced with lateral beam widths smaller than 2.0 cm FWHM and initial proton numbers less than 6*108. For a higher proton number or a greater beam width only non-acceptable dose distributions were obtained. Besides the dosimetric quality, the required total number of laser shots was studied. Obviously, a lower initial proton number per laser shot requires a higher number of laser shots to irradiate the patient. To deliver a good plan, we found that 5*104-106 laser shots are required for initial proton numbers of 107-108 per shot. Considering an optimistic repetition rate of the laser system of 10 Hz would imply an upper clinical limit of 104 shots, as this corresponds to a delivery time of roughly 15 minutes.

Conclusion: With the simulated beam line and the assumed shape of the initial proton spectrum it was possible to produce clinically relevant plans in terms of plan quality, if the initial proton number per laser shots can be tuned to be below a certain limit. However, the resulting treatment time limits the clinical feasibility, as good quality plans need too many shots. Therefore, a method or device to modulate the proton fluence during the treatment will be essential. If this becomes possible with the laser itself or in the beam line, radiotherapy with laser-driven protons can be comparable to state-of-the-art proton therapy.

References

[1] U. Masood et al., Proc. SPIE 8779B, 8779-53 Session 11 (2013).
[2] S. Schell and J. J. Wilkens, Med. Phys. 37, 5330-5340 (2010).

10 Evaluation of new 2D Ripple Filters for Particle Therapy Facilities

T. Printz Ringbæk[1,2], S. Brons[3], J. Naumann[3], B. Ackermann[3], B. Thomsen[2], N. Bassler[2,4], K. Zink[1,5], U. Weber[5,6]
[1]Technische Hochschule Mittelhessen (THM), Gießen, Germany
[2]Aarhus University, Physics and Astronomy, Aarhus, Denmark
[3]Heidelberg Ionentherapiezentrum (HIT), Heidelberg, Germany
[4]Aarhus University Hospital, Department of Experimental Clinical Oncology, Aarhus, Denmark
[5]Universitätsklinikum Gießen und Marburg, Darmstadt, Germany
[6]University of Applied Science, Gießen-Friedberg, Germany

Introduction: A ripple filter (RiFi) broadens the Bragg peak (BP), which leads to fewer energy steps from the accelerator required to obtain a homogeneous dose coverage of the PTV[1]. This reduces treatment time and interplay problems. At the Universitätsklinikum Gießen und Marburg, Germany, a new second generation RiFi has been developed with two-dimensional groove structures using rapid prototyping technology. This new design has a stronger modulation compared to already existing RiFis allowing step sizes of up to 6 mm for raster scanning treatments, and has no non-modulating material, thereby minimizing the undesired lateral scattering. The new design should effectively make RiFis usable in proton treatments. However, RiFis can cause fine structures in the dose distribution at insufficient distances from the RiFi[2]. These structures are due to the inhomogeneous scattering strength caused by the alternating thickness of the RiFi. For heavy ions and specific ion optical settings, inhomogeneities are even observed at the isocenter. Also, the alternating particle ranges in the target due to the inhomogeneous RiFi mass distribution can result in dose inhomogeneities inside the target.

Materials and methods: The beam application and monitoring system (BAMS) originally from GSI, Darmstadt, Germany, is modelled. Using SHIELD-HIT12A[3] RiFi-induced inhomogeneities for variable distances from the RiFi to the target surface have been investigated for various ion types, initial particle energies, RiFis, ion optical focusing configurations and raster scanning step sizes. In addition, the lateral scattering of various RiFis of the old and new design as well as for no RiFi have been simulated and investigated.

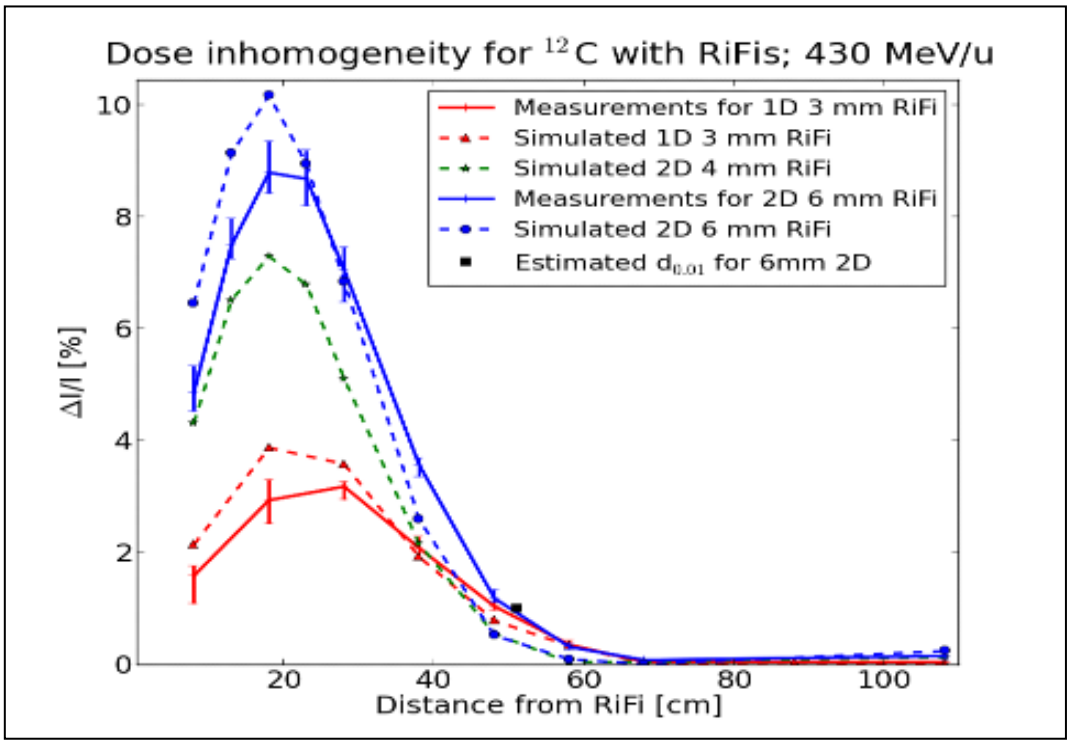

Fig. 1: Dose inhomogeneity as a function of distance from the RiFi for different RiFis. Experimental values are obtained with fits to fluence profile plots from exposure films. Simulated values are obtained with fits to simulated fluence profiles from SHIELD-HIT12A. The distance d0.01 is the threshold distance at which the measured inhomogeneity is below 1 %.

Experimental data have been obtained at PTZ, Marburg, as well as at HIT, Heidelberg, and compared with simulated data (see figure 1). To evaluate the PTV dose coverage performance of the new RiFi design, the heavy ion treatment planning system TRiP98 has been used for dose optimization with SHIELD-HIT12A used to prepare the facility-specific physical dose kernels needed by TRiP and for recalculating the physical dose distribution after optimization.

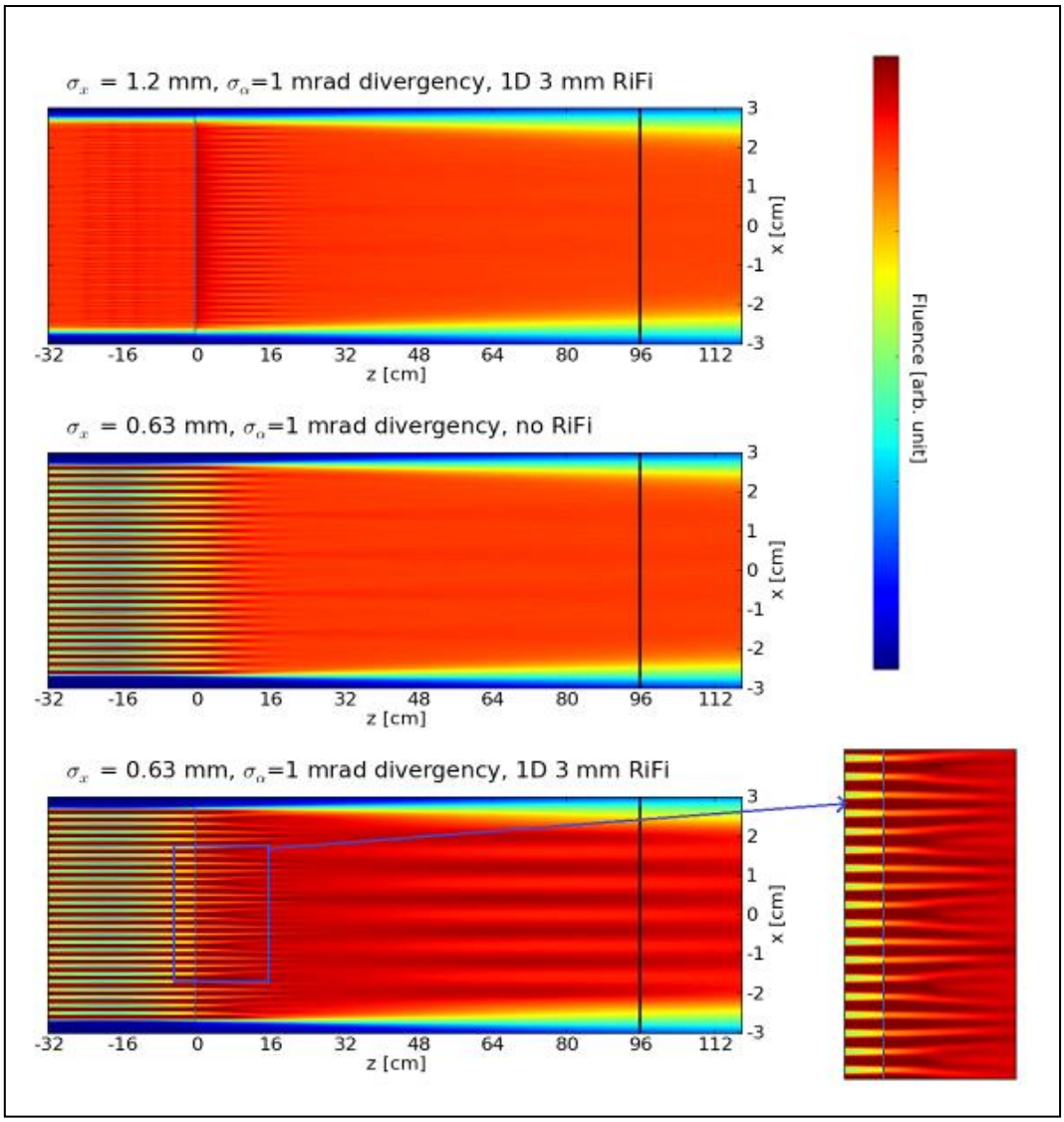

Fig. 2: 2D fluence distributions for 150 MeV/u carbon-12 pencil beams with various parameters as described in the titles above. The values of σx given are in the RiFi-plane. The RiFi is placed at z=0, meaning that negative values of z indicates positions within the BAMS. At z=96 mm the black lines mark the HIT-isocenter. The lower "zoom" shows the development of the Moiré-effect in the fluence distribution.

Results: For various RiFis, ion types and initial particle energies the distance from the RiFi at which maximum dose inhomogeneity occurs and a threshold distance where the inhomogeneity is less than 1 % are found. Analytical expressions for the distances are found which fit the MC data; both distances are inversely related to the angular distribution and proportional to the RiFi period. When focusing sharply on the RiFi plane (width of the pencil beams much smaller than the raster scanning step size) the resulting inhomogeneous fluence distribution at the RiFi will interfere with the inhomogeneous mass distribution of the RiFi causing inhomogeneities at the isocenter of up to 7 % (see figure 2). It is concluded that the dose inhomogeneity at target surface is much more critical than the inhomogeneity in depth. If one avoids the former, the latter is not seen. Simulated Spread-out Bragg peaks with RiFis have a satisfactory homogeneous PTV dose coverage as long as the RiFi thickness in water-equivalent path length times 1.2 matches the energy step size.

Conclusion: Our findings clearly indicate that the inhomogeneity induced by RiFis does not add uncertainties to the dose distribution in the clinical setting for normal treatment configurations. The new RiFi design can be used in treatments to obtain homogeneous PTV dose coverage with fewer energy steps while improving the lateral penumbra.

References

[1] Weber U, Kraft G. Design and construction of a ripple filter for a smoothed depth dose distribution in conformal particle therapy. Phys Med Biol. 1999;44:2765–2775

[2] Ringbæk TP, Weber U, Thomsen B, Petersen JBB, Bassler N. Monte Carlo Simulations of New 2D Ripple Filters for Particle Therapy Facilities. Acta Oncol. 2014;53:40–49.

[3] Hansen DC, L˙hr A, Sobolevsky N, Bassler N. Optimizing SHIELD-HIT for carbon ion treatment. Phys Med Biol. 2012;57(8):2393–2409.

11 Open source anatomy of the MedAustron particle therapy accelerator medical frontend

D. Kellner[1,2], H. Deutschmann[1,3,2], F. Sedlmayer[1,3], P. Steininger[1,2]
[1]Paracelsus Medical University (PMU), Institute for Research and Development on Advanced Radiation Technologies (radART), Salzburg, Austria
[2]medPhoton GmbH, Salzburg, Austria
[3]Paracelsus Medical University (PMU), University Clinic for Radiotherapy and Radio-Oncology, Salzburg, Austria

Purpose/objective: Reoccurring radiotherapy-specific algorithmic issues as well as the existence and complexity of different data formats in the field aggravate the development of software tooling that helps simplifying the daily routine and contributes to cutting-edge research. We present the open-source software library SORRY (Software for Open Research in Radiation therapY) that provides a framework for radiotherapy applications. For example, the MedAustron Delivery and Allocation Manager (MADAM) makes excessive use of SORRY for controlling the particle therapy accelerator at the emerging heavy ion facility MedAustron (Austria). Similarly, SORRY provides rapid software development opportunities for daily particle therapy quality assurance and associated research.

Framework: The C++-based SORRY library comprises a range of functionalities, starting from communication protocols up to dedicated frameworks for adaptive Image Guided Radiation Therapy. In the scope of MADAM, the following modules play a major role: The central logging service (CLS) aggregates facility-wide logging records, the Distributed Inter-Process Communication (DIPC) enables type-safe, object-oriented interaction between software components and third-party components, utility tools and testing frameworks are indispensable for rapid development. The RTCore framework is a hierarchical data container that also allows translations from and into different data formats. As such, it enables the conversion from a DICOM RT Ion Plan format that is sent by the treatment planning system into a machine-specific low-level format that is understood by the accelerator. It is worth being noted that the data input and output could be in any format, since data format and data container are entirely separated. The data container framework is accessible with a range of scripting languages (e.g. Java, JavaScript, Python, Ruby) to enable interested users interfacing without caring about programming details in C++.

Architecture: MADAM consists of so-called facades, where an instance of a facade is responsible for interfacing and controlling a certain hardware component. There are facades for controlling the accelerator allocation components, the dose delivery systems, timing and interlock gateways, the beam interlock system, the energy verification system and an independent termination system. All relevant parameters and commands are accessible via a central core application that also implements a hierarchical state machine for safely orchestrating the treatment micro-workflow. Irradiation prescriptions (i.e. beam delivery and meta data) are coordinatedly distributed to the accelerator, verification systems and the dose delivery system. MADAM itself can be seen as managing black box that has only one object-oriented DIPC-based interface to the Record-and-Verify-System (RVS) that manages the scheduling and occupation of beam lines. The status and important parameters of all subcomponents are frequently pushed to the RVS in order to enable safe treatment recording and visualization.

Conclusions: The design of MADAM has shown that the SORRY library can be used for demanding software components as well as for rapid in-house developments using the scripting interfaces. The data container can be easily extended to also provide the import and export of formats to other environments as for example Monte Carlo frameworks. We focused on creating a framework that is easy to use without profound programming skills.

License: SORRY is open-source and released under the terms of a clean BSD License. SORRY is available at www.open-radart.org.

12 Assessment of the performance of proton computed tomography for use in proton therapy treatment planning: Monte Carlo study

G. Dedes[1], N. Arbor[2,3], D. Dauvergne[2], J.-M. Létang[3], K. Parodi[1], C. T. Quinones[3], E. Testa[2], S. Rit[3]
[1]LMU Munich, Faculty of Physics – Department of Medical Physics, Garching, Germany
[2]Université de Lyon, IPNL Lyon, Lyon, France
[3]Université de Lyon, CREATIS, France, France

Related questions: Proton therapy treatment planning is currently performed on the tissue attenuation coefficients obtained with X-ray CT data and converted to relative stopping power (RSP) maps using a calibration procedure. This process introduces a proton range uncertainty and therefore clinical margins ranging from 2.5 %+1mm to 3.5 %+3mm [1] are used, preventing the full exploitation of the steep dose gradients achievable with proton irradiation.

Proton computed tomography (pCT) could offer a more accurate estimation of the RSP maps with a lower dose compared to X-ray CT.

Material and procedure: The assessment of proton CT for use in treatment planning is performed in a twofold way: basic studies of the intrinsic proton CT performance and the comparison with X-ray CT in terms of calculated dose maps. For the purpose of the studies, GATE/Geant4 Monte Carlo simulations are used. X-ray CT images are reconstructed using a 2D filtered backprojection algorithm. Proton CT reconstruction is performed by a filtered backprojection algorithm taking into account curved proton paths [2].

For the basic studies, cylindrical water phantoms with tissue equivalent inserts based on ICRP 110 report were simulated. The RSP accuracy of proton CT is estimated for different insert sizes and imaging doses, assuming an ideal scanner setup. Furthermore, the influence of detector effects (finite energy and spatial resolution) is also calculated. The impact of the above effects on a single proton pencil beam range is also investigated.

The full clinical impact of proton CT on proton therapy treatment planning is assessed via the comparison of X-ray CT and proton CT. Using the ICRP 110 anthropomorphic phantom, X-ray and proton tomographies are simulated and reconstructed. Both photon CT RSP map (computed from the reconstructed attenuation map) and proton CT RSP map are transformed into chemical composition maps through the same process. The resulting material maps are then used for a proton therapy dose calculation [3] and compared to the initial ICRP 110 phantom.

Result: Results show that with an ideal proton CT scanner, very accurate RSP maps can be produced. For a dose of 3mGy, RSP resolution between 1-2 % is achieved for a variety of tissue equivalent materials. An example comparison between X-ray CT and proton CT obtained RSP maps of the ICRP 110 anthropomorphic phantom is shown in Figure 1. Furthermore, when detectors' finite resolution is taken into account, the results based on an ideal scanner deteriorate, ie a 2 % energy resolution deteriorates the RSP resolution by 3 % (Figure 2), providing hardware specifications for a potential prototype.

Summary: The above presented analysis is quantifying the clinical benefit from proton CT, in terms of reducing range uncertainties. The principal performance of an ideal proton CT scanner is investigated and a comparison with X-ray CT is performed. Finally, the obtained results are put into the perspective of a real-world scanner by estimating the impact of basic detector effects.

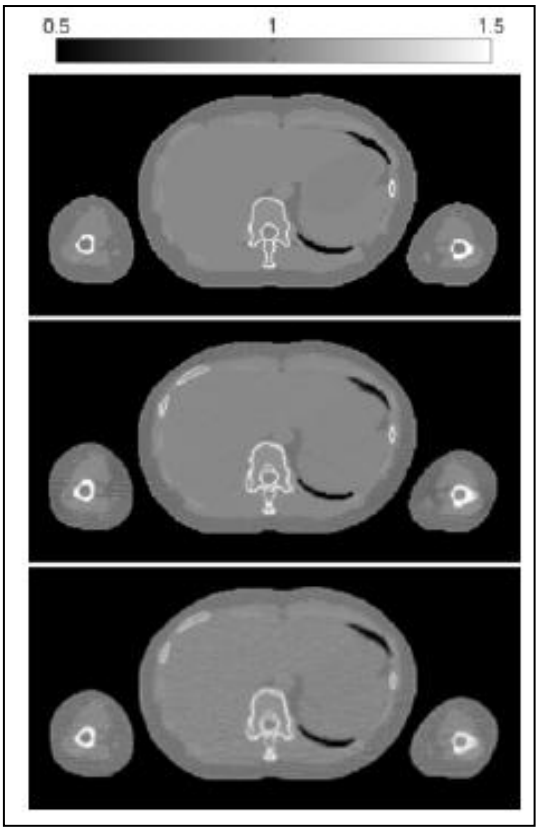

Fig. 1: RSP maps from ICRP phantom (top), RSP X-ray (middle), proton CT (bottom)

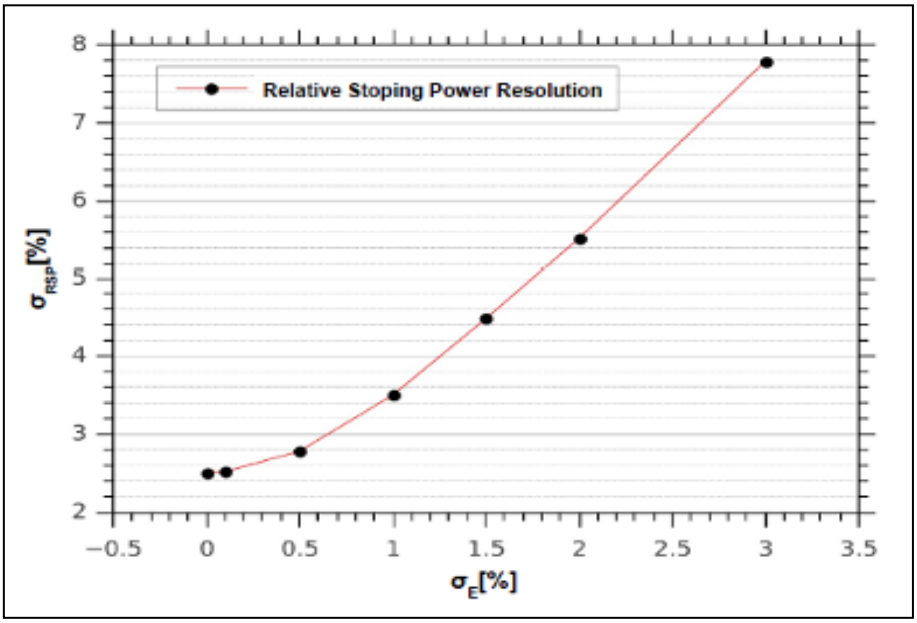

Fig: 2: Detector energy resolution impact on resolution

References

[1] H. Paganetti (2012), “Range uncertainties in proton therapy and the role of Monte Carlo simulations”, Phys. Med. Biol. 57(11)

[2] S. Rit et al. (2013), “Filtered backprojection proton CT reconstruction along most likely paths”, Med. Phys. 40(3)

[3] L. Grevillot et al. (2012), “GATE as a GEANT4-based Monte Carlo platform for the evaluation of proton pencil beam scanning treatment plans: Phys. Med. Biol. 57(13)

Session 3 – Magnetic resonance imaging I: systems and methodology

Chairs: L. M. Schreiber (Mainz/DE), K. P. Prüssmann (Zurich/CH)

13 Introductory lecture: Current advances in MRI technology

K. P. Prüssmann

14 64-Channel Cardiac Phased Array Coil at 3T: Preliminary Results

M. Schuppert[1], K. F. Kreitner[2], S. Fischer[1], B. Keil[3], B. Guerin[3], R. Schmidt[1], S. Wein[2], L. L. Wald[3,4,5], L. M. Schreiber[1]
[1]Johannes Gutenberg University Medical Center Mainz, Department of Radiology, Section of Medical Physics, Mainz, Germany, Germany
[2]Johannes Gutenberg University Medical Center Mainz, Department of Radiology, Mainz, Germany, Germany
[3]A.A. Martinos Center for Biomedical Imaging, Department of Radiology, Massachusetts General Hospital, Charlestown, MA, USA, United States
[4]Harvard Medical School, Boston, MA, USA, United States
[5]Harvard-MIT Division of Health Science and Technology, Cambridge, MA, USA, United States

Introduction: Cardiac magnetic resonance imaging (CMRI) is a frequently used method to evaluate cardiac morphology and function. CMRI requires fast imaging due to cardiac and respiratory motion. Strong gradient systems and phased array coils in association with parallel imaging strategies have a major impact on imaging speed. Phased array coils [1] consist of multiple receive elements and allow simultaneous detection of the MR signal. Distribution of multiple receiver elements over the imaged volume yields an increase in SNR due to the superposition of the sensitivity profiles of the individual receiver elements. The dense coverage with coil elements of the imaged volume thereby provides subsidiary spatial encoding which is the major requirement for accelerated imaging. Applying sophisticated reconstruction algorithms [2; 3] this spatial information can be utilized to calculate full images even from undersampled data. Undersampling data to a high degree, thus reduction of phase encoding steps, accelerates imaging substantially if the multi-channel receive coil is properly adapted to the imaged volume, i.e. the thorax. In this pilot study we investigate the accelerated imaging performance of an in-house built 64-channel cardiac phased array coil prototype [4]. Additionally, preliminary signal-to-noise ratio (SNR) analysis was performed to evaluate the SNR in the heart in dependency of coil element distance to the heart.

Materials and methods: 6 healthy volunteers (3 females, 3 males, ages 28±4 years, heights 172±14cm, weights 67±12kg) were examined using accelerated cardiac cine imaging in four-chamber (4CH) and short-axis (SAX) orientation on a 3T Siemens MAGNETOM Prisma (Siemens AG, Erlangen, Germany) after obtaining informed consent of the local ethics committee. All MR examinations were conducted with the in-house built 64-channel cardiac receive-only phased array prototype coil which is strongly adapted to the shape of the human thorax. Accelerated functional cardiac imaging was performed at acceleration factors R = 3, R = 5, R = 7, and R = 8 using a retrospectively triggered 2D bSSFP cine pulse sequence and tGRAPPA [5]. An independent radiologist scored all CMR data to assess the image quality (1 = Excellent, 2 = Good, 3 = Satisfactory, 4 = Fair, 5 = Fail) and artifacts (0 = none, 1 = minor, 2 = strong). In one volunteer (male, age 25 years, height 172cm, weight 71kg) un-accelerated cine data including a noise-only dataset was acquired in 4CH orientation. The images were cropped to a square matrix after Fourier transformation to calculate image SNR in SNR units [6]. At first, only the SNR contribution of the coil element centered over the heart was calculated. Subsequently, further coil elements in concentric rings around the center coil element were included in the SNR calculation (Fig.1).

To evaluate the SNR dependency of the coil element distance from the center coil element, SNR was calculated in two ROIs containing 24 pixels each in the apex and the posterior wall (Fig.2a). This calculation was done for the 40-channel chest part of the coil only, the 24-channel back part of the coil only, and the total 64-channel cardiac phased array coil to assess SNR contributions of both coil parts.

Results: A total of 41 cine image series were scored for image quality and artifacts in 4CH and SAX (Fig.3) orientation. 41 % of all image series were of excellent or good image quality. 39 % of all image series were of satisfactory quality. One image series (4CH, tPAT = 8) was scored with a score value of “5”. Image quality in SAX orientation was scored to be superior (lower score value) to 4CH orientation in 50 % of all image series including all acceleration factors. Observed artifacts were off-resonance artifacts and reduced SNR due to high acceleration factors. 22 % of all image series were without artifacts. Thereby 89 % of all “0” scores were obtained in SAX orientation. 61 % of all image series exhibit minor artifacts. Seven out of 41 image series possessed major artifacts at maximum acceleration factors R = 7 or 8. Score values of image quality are in agreement with formerly scored cine image datasets acquired on a scanner with 70cm bore diameter [7]. Overall slightly better scores were achieved which might be due to improved B_0 homogeneity as a result of the smaller bore diameter.

Pixel-wise SNR maps in SNR units were calculated based on un-accelerated cine images and pre-scan noise-only measurements using sum-of-squares reconstruction (Fig. 2a). Maximum SNR in the heart was achieved in the apex closest to the coil elements. In the myocardium the SNR of the posterior wall was about 40 % lower compared to the apex when comparing both ROIs (Fig.2b). The SNR analysis of the 40-channel chest part and the total 64-channel coil reveal increased SNR with additional coil elements from the concentric rings and reached a plateau at four coil elements diameter distance from the center coil element in the apex and the posterior wall. The SNR analysis of the back part only did not show a plateau. The SNR differences between 40-channel only and the total 64-channel coil in the plateau were below 1 % in the apex and 4 % in the posterior wall (Fig.2b).

Conclusion: As shown in [4] the critical area for SNR is the posterior wall. This could be confirmed in this study by calculating pixel-wise SNR maps from un-accelerated cine images. The obvious reason for this is that the apex is much closer to coil elements compared to the posterior wall which is deep within the body. The same explanation is valid for the negligible SNR increase in the apex when using the 40-channel chest part only compared to all 64-channels. The coil elements of the back part are too far away from the apex to contribute substantially to the local SNR. Thus, the result that there is a plateau in the SNR is not surprising, meaning coil elements distant from the ROIs do not contribute substantially to SNR. An interesting result is that the SNR did not reach a plateau for the back part only which might suggest to arrange further coil elements on the back.

Highly parallel array coils are built to accelerate imaging by applying parallel imaging (PI) strategies. High SNR is mandatory because higher reduction of phase encoding steps in PI results in overproportional SNR reduction. With regard to SNR the lateral coil elements of this coil prototype seem to not be of high influence. When omitting the outer eight coil elements the SNR is reduced by around 1 % in the heart. In further investigation it is important to understand and analyze the impact on accelerated imaging if specific coil elements are removed. Based on the scoring, the in-house built 64-channel cardiac phased array coil prototype achieves images of high quality even at very high acceleration factors. This suggests that the sensitivity information of the lateral coil elements is of higher influence for accelerated imaging compared to their SNR contribution.

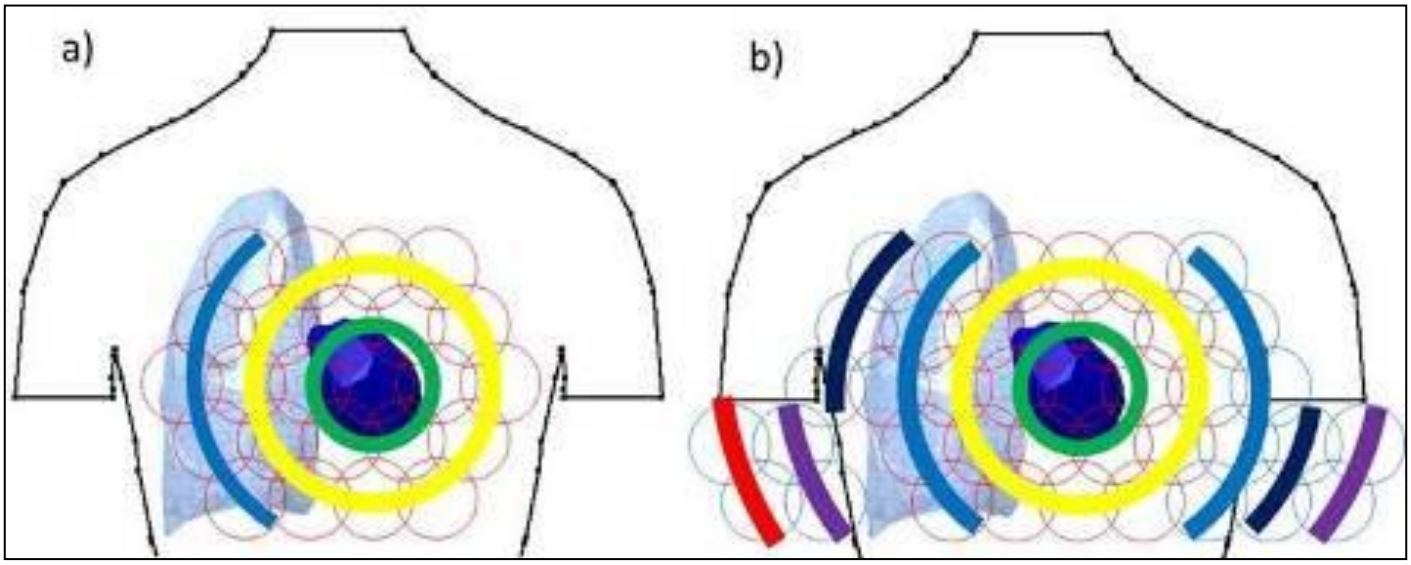

Fig. 1:(a) Coil element layout of the back part with three concentric coil element rings (b) and chest part with six concentric coil element rings

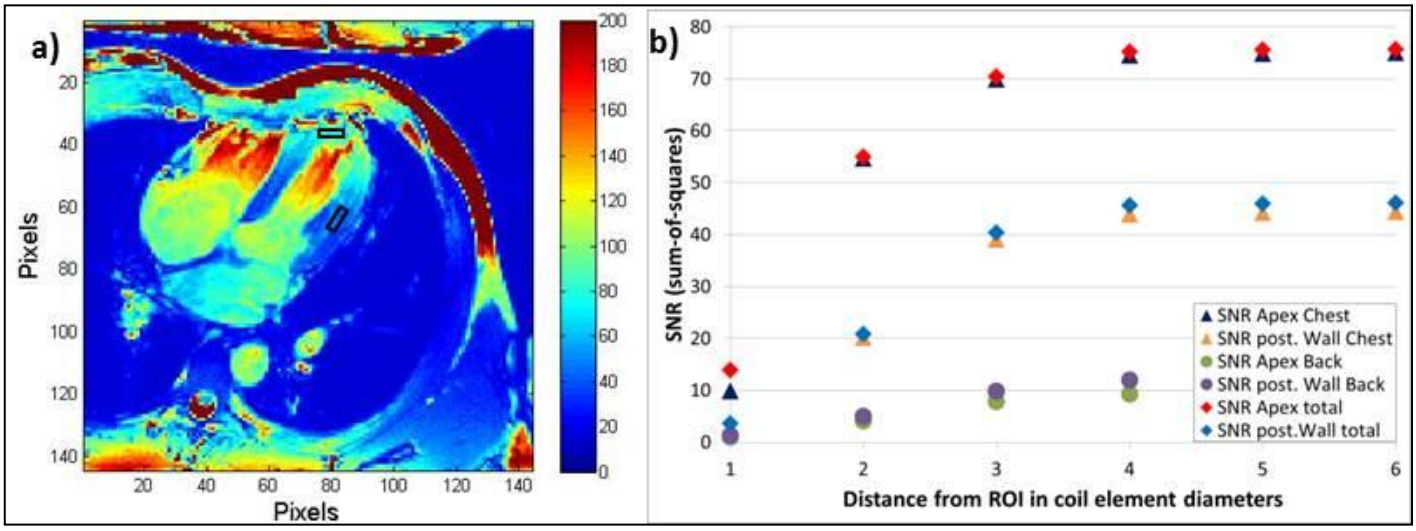

Fig. 2:(a) Pixel-wise SNR map with apex and posterior wall ROIs (black rectangles) (b) and SNR as a function of the distance from the central coil element

Fig. 3:2D TrusFISP Cine short-axis orientation, tPAT=5; FA / Res / FoV / Slice = 54° / 139x208 / 250mm x 300mm / 6mm; TR (estimated) / TE = 3.6ms / 1.47ms

References

[1] Roemer PB, Edelstein WA, Hayes CE, Souza SP, Mueller OM (1990) The NMR phased array. Magnetic Resonance in Medicine 16:192-225

[2] Griswold MA, Jakob PM, Heidemann RM et al (2002) Generalized autocalibrating partially parallel acquisitions (GRAPPA). Magnetic Resonance in Medicine 47:1202-1210

[3] Pruessmann KP, Weiger M, Scheidegger MB, Boesiger P (1999) SENSE: Sensitivity encoding for fast MRI. Magnetic Resonance in Medicine 42:952-962

[4] Schuppert M, Keil B, Guerin B, Fischer F, Schreiber LM, Wald LL (2013) Concept for the Geometrical Arrangement of Coil Elements in a 64-Channel Cardiac Phased-Array Coil for Optimized SNR and g-Factors at 3T, Proceedings of the 21th Annual Meeting of ISMRM, Salt Lake City, UT, USA,

[5] Breuer FA, Kellman P, Griswold MA, Jakob PM (2005) Dynamic autocalibrated parallel imaging using temporal GRAPPA (TGRAPPA). Magnetic Resonance in Medicine 53:981-985

[6] Kellman P, McVeigh ER (2005) Image reconstruction in SNR units: A general method for SNR measurement. Magnetic Resonance in Medicine 54:1439-1447

[7] Schuppert M, Schmidt M, Kreitner KF et al (2014) A Dedicated 64-Channel Cardiac Receive-Only Phased Array Coil: Initial Experience, Proceedings of the 22th Annual Meeting of ISMRM, Milan, Italy,

15 On electromagnetic power balance calculations in MRI transmit coil arrays

A. Kuehne[1,2], S. Goluch[1,2], E. Moser[1,2], E. Laistler[1,2]
[1]Medical University of Vienna, Center for Medical Physics and Biomedical Engineering, Vienna, Austria
[2]Medical University of Vienna, MR Center of Excellence, Vienna, Austria

Target Audience: Researchers interested in electromagnetic simulation, safety evaluation and optimization of MRI parallel transmission coil arrays.

Purpose: The power balance of an MR coil is an important performance metric. In this work we aim to extend the quadratic form power correlation matrix (PCM) formalism [1] used for estimation of deposited power in lossy materials by a transmit coil array used in Magnetic Resonance Imaging. A distinct PCM is derived for each term of the power balance – forward, reflected, absorbed, radiated, and lumped element loss power. The goal is to enable a straight-forward calculation of losses for arbitrary excitations, transmit array worst-case loss analysis; and also to verify EM simulation integrity, which is imperative especially for complex workflows that are prone to mistakes.

Theory: The approach is based on the calculation of absorbed power P via quadratic forms $P = v^H Q v$ for each term in the balance. In an N-channel array, Q denotes an $N \times N$ PCM, v the applied coil voltage column vector and H the hermitian transpose. Knowledge of the coil array scattering matrix S, 3D E- and H field distributions and lumped element (capacitor, inductor, resistor…) currents and voltages is assumed. All values are normalized to a unit excitation of 0.01W forward power, i.e. 1V amplitude applied voltage at a source impedance $Z_0 = 50\,\Omega$. The forward PCM, $Q_F = (2Z_0)^{-1}1$, used to calculate the power incident into the coil, is a scaled identity matrix. Any power loss due to coupling or imperfect matching is computed using the coupling loss matrix derived from the scattering matrix as $Q_C = (2Z_0)^{-1}(S^H S)$. For an N channel coil with M discrete lumped elements, the element voltages and currents can be arranged in $N \times M$ matrices U and I, in which the Nth column contains the normalized voltages or currents of each lumped component for the excitation of coil element N. The resulting power loss is given as $P = 1/2\,\mathrm{Re}(v^H I^H U v)$, and resolving the real part yields $Q_L = 1/4\ (I^H U + U^H I)$ as the lumped element loss matrix. Power dissipated inside lossy materials is derived from the originally proposed PCM Q_D, with its entries defined as $q_{ij} = 1/2 \int \sigma E_i^* E_j dV$, with the conductivity σ and E_i denoting the electric field produced by a unit excitation of coil element i. By restricting the integration volume to certain materials (body, metal, substrate…), power correlation matrices can be obtained for each material of interest. A similar approach is taken for calculating the radiated power by integration of the pointing flux through a box enclosing the problem space. The radiated power of multiple interfering fields can be obtained via $P = 1/2\ \mathrm{Re}\left(v^H \tilde{Q}_R v\right)$, with the elements of $\tilde{Q}_R$ defined as $q_{ij} = \oiint E_j \times H_i^* d\vec{A}$. Again resolving the real part yields

$Q_R = 1/4\left(\tilde{Q}_R + \tilde{Q}_R^H\right)$ for the radiated PCM. The power balance can now be written as $Q_F = Q_C + Q_L + Q_D + Q_R$. Any residual imbalance of this equation can be attributed to factors such as non-convergence of FDTD simulations, insufficient sampling frequency, loss of precision due to simulation methodology or simply user errors. The by magnitude largest (smallest) Eigenvalue of the residual imbalance matrix represents the maximum (minimum) power balance error.

Methods: The presented theory was applied to an 8-channel array at 297.2 MHz (Fig. 1). Individual elements measuring 9x22 cm, constructed of 5mm wide copper strips, were arranged conformally on a cylindrical acrylic former (27 cm outer diameter, thickness 1 cm) with a copper RF shield of 31 cm diameter. Nearest-neighbor decoupling (≈ -15 dB) was achieved using counterwound inductors [2]. The magnet bore was modeled as a 2.45 m long, 89.5 cm diameter steel cylinder. A spherical phantom, comparable to the human brain in dimensions as well as in dielectric properties $(d = 18\ \mathrm{cm}, \epsilon = 50.6, \sigma = 0.66\ \mathrm{S/m})$, was used as the coil load. Coil simulation was done with XFdtd (Remcom, State College, PA, USA) being used for 3D EM simulations and ADS (Agilent, Santa Clara, USA) for tuning, matching and decoupling [3]. Particular care was taken to ensure accurate loss modeling. Metal losses were approximated by enabling a good conductor approximation in XFdtd [4]; and capacitors assigned an ESR of appropriate ATC 100E series models (American Technical Ceramics Inc., Huntington Station, NY, USA). Air core solenoid losses were estimated using wcalc (http://wcalc.sourceforge.net/) [5], and solder joint resistances were extrapolated from literature data [6] based on a $\sqrt{f}$ frequency dependence. The loss tangent of the acrylic former was provided by XFdtd. Single channel fields and all power correlation matrices were calculated using MATLAB (The MathWorks, Natick, MA, USA). Finally, power imbalance, worst-case losses and the complete power balance for five different excitation modes were analyzed to demonstrate the method.

Results: The maximum and minimum power imbalances for the investigated array were 0.018 % and 0.002 %, respectively. The worst- and best-case losses for each power balance term are detailed in Table 1. Figure 2 shows the complete power balance for the four clockwise rotating excitations (“Birdcage”-Modes) and the “Maxwell”-Mode (equal phase for all coil elements).

Discussion: The maximum power imbalance is negligible and thus in excellent agreement with theory. The small residual error can be attributed to multiple factors. Determination of radiated power in FDTD simulations is prone to minor errors

due to the use of a non-uniform mesh combined with the need to co-locate E- and H fields for Poynting vector estimation via interpolation [7]. Furthermore, the complex simulation workflow and interplay of various calculation and post-processing routines can lead to additional errors due to limited precision of each computation and the exchanged data, such as S-Parameters. As care was taken to reach simulation convergence down to the numerical noise level (<-95 dB) and obey the sampling theorem w.r.t. the input pulse, these factors are not expected to contribute to the error. The reported imbalance can be regarded as a lower-limit error for simulations of comparable complexity. Power balance calculations for different excitation modes show a strong variation of the individual terms for different excitation patterns. The radiated power component is negligible in all investigated excitations but the common CP1+, for which it is similar to previously published results of comparable geometries [8]. Minimum and maximum absorbed powers are significantly different, and can vary by orders of magnitude for the radiated power component. Conductor metal losses still have an uncertainty attached, especially concerning the correct approximation of lateral skin effect contributions [9] in copper strip conductors. It may be advantageous to instead model coil conductor losses as lumped resistors derived from analytical considerations for the given conductor geometry and coil size, which has been shown to provide accurate estimates for intrinsic coil losses [6].

Conclusion: The presented theoretical framework has been shown to reliably provide access to the power balance for arbitrary excitations using simple matrix calculations. Worst case power imbalance estimates allow a straight-forward plausibility check for EM simulations of arbitrary complexity. Losses have been shown to vary significantly between different excitations, allowing a deeper insight into loss mechanisms than considering only a single mode.

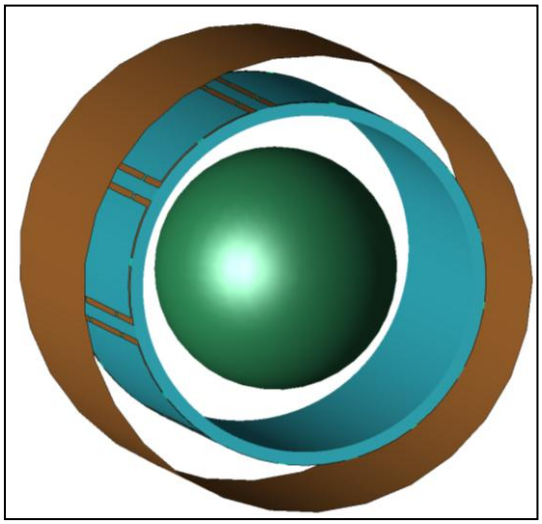

Fig. 1: Setup of the simulated coil array showing coil elements, acrylic former, phantom load and RF shield.

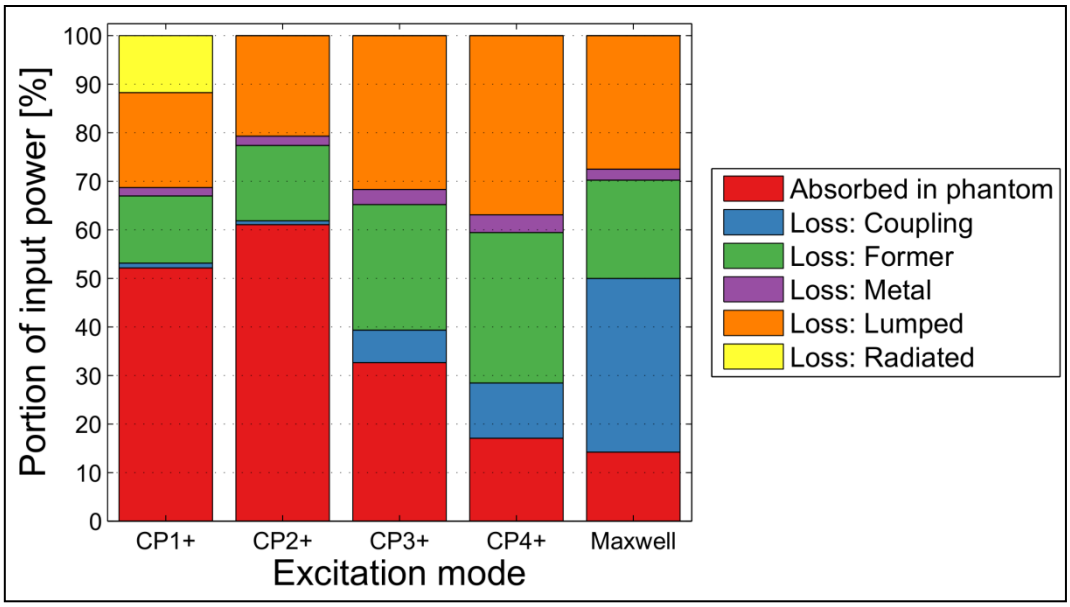

Fig. 2: Power balance for five different excitation modes of the array. The power distribution between different loss terms varies significantly between excitation modes and, as is to be expected, adds up to 100 % within a negligible margin of error.

	Phantom	Coupling	Former	Metal	Lumped	Radiated
max [%]	61.7	35.9	31.1	3.7	36.9	11.8
min [%]	14.2	0.6	13.8	1.7	19.5	1e-6

Tab. 1: Maximum and minimum absorbed power for each term in the power balance, as given by the largest (smallest) Eigenvalue of the respective power correlation matrices.

References

[1] Zhu, Y. (2004), *MRM*, 51(4), 775–84
[2] Avdievich, N. I. (2011), *Appl Magn Reson*, 483–506
[3] Kozlov et al. (2009), *JMRI*, 147–152.
[4] Chamberlin, K. et al. (1995), IEEE *Trans. EM Compat.* 210–216
[5] Geffe, P., *MW Journal* (1996), 70–76
[6] Kumar, A. et al. (2009), *MRM*, 1201–1209
[7] De Moerloose, J et al., *MW Opt. Techn. Let.*, 257–260
[8] Liu, W. et al. (2013) *MRM*, 290–4
[9] Giovannetti, G et al. (2012). *CMR B*, 57–61.

Acknowledgements: This work was funded by the Austrian BMWFJ, FFG Project Nr. 832107

16 Are peak velocities determined by 2D phase-contrast MRI comparable to those assessed by real-time phase-contrast MRI and pulse wave echocardiography?

H. Körperich[1], P. Barth[1], A. M. Lehne[1], K. T. Laser[1], W. Burchert[1], J. Körfer[1]
[1]Heart and Diabetes Center NRW, Ruhr-University of Bochum, Institute for Radiology, Nuclear Medicine and Molecular Imaging, Bad Oeynhausen, Germany

Introduction: In clinical routine work accurate determination of peak velocities is an important diagnosic measure for e.g. (I) estimation of the severity of stenosis[1], (II) analysis of arterial stiffness[2, 3] and (III) assessment of the pulmonary flow pattern to classify the different levels of development of LV diastolic dysfunction[4]. Due to its widespread availability echocardiographic methods such as pulse wave (PW) tissue Doppler imaging are commonly used. In recent years, magnetic resonance imaging (MRI) is increasingly accepted as a valuable noninvasive tool for evaluation of aortic distensibility and PW velocity based on its high accuracy and reproducibility[3, 5]. Whereas MRI is known to underestimate peak velocities due to averaging of flow information related to the typical long data acquisition times, echocardiography is considered as highly operator dependent.

Thus, the aim of this study was to compare peak velocities (Vmax) assessed by two-dimensional (2D) phase-contrast velocity mapping (PC-MRI), real-time PC-MRI and pulse wave echocardiography regarding the degree of discrepancy.

Materials and methods: Quantitative through-plane PC-MRI flow/peak velocity measurements were performed in the ascending aorta of 11 healthy subjects (mean age = 42.6±13.7years; 6 male) with a 3.0T-TX system (Achieva, Philips Healthcare) equipped with parallel radiofrequency signal transmission technology using (a) retrospectively gated standard 2D PC-MRI (=MR_ref; TE/flip = 5.2ms/30°, 36-42 heart phases, flow encoding = main blood flow direction, scanning time ~1.5 min); (b) 2D PC-MRI (=MR_3D; comparable to a) but with flow encoding in 3 spatial directions for 3D vector calculating); (c) real-time PC-MRI (=MR_RT; TR/TEeff/excitation angle = 12-14ms/3.3ms/40°, temporal resolution 24-28 ms; scanning time = 1 heart beat) and (d) pulse wave echocardiography (=Echo; Vivid 9, GE). To avoid physiological variations all measurements were performed in the same examination unit without repositioning of the subject. The normally distributed data were analyzed by paired Student-t-test regarding a p-value of 0.05 as statistically significant, Bland-Altman statistics and by calculating of regression coefficients.

Results and discussion: As expected, on average Vmax(MR_3D) exceeded Vmax(MR_ref) by 4,4 % (=mean, limits-of-agreement: +14.1 % to -5.3 %, r~0.96, p<0.05). This may be related to the occasionally non-perpendicular blood flow direction in a curved vessel underscoring the need for calculating of three-dimensional velocity vectors. Peak velocities were higher applying real-time PC-MRI compared to MR_ref (28.1 %; +51.4 % to +4.9 %, r~0.64, p<0.05), which can be explained by the non-averaging character of this technique representing a snap-shot of the actual blood flow in the region-of-interest (Abb. 1). Accordingly, Vmax(echo) was increased by 25.2 % in relation to Vmax(MR_ref) (+69.0 % to -18.5 %, r<0.5, p<0.05). Comparing real-time PC-MRI and pulse wave echocardiography high agreement was observed between both methods (2.7 %; +44.5 % to -39.2 %, r<0.5, p<0.05) but with substantial scatters and a low correlation coefficient. Short-term effects influencing blood flow velocities such as respiration of the subject, varying heart rates or slightly different measuring positions between the two different techniques may be responsible for this behavior.

Conclusion: Peak velocities assessed by standard quantitative two-dimensional PC-MRI were underestimated by 25-30% in comparison to real-time PC-MRI and pulse wave echocardiography.

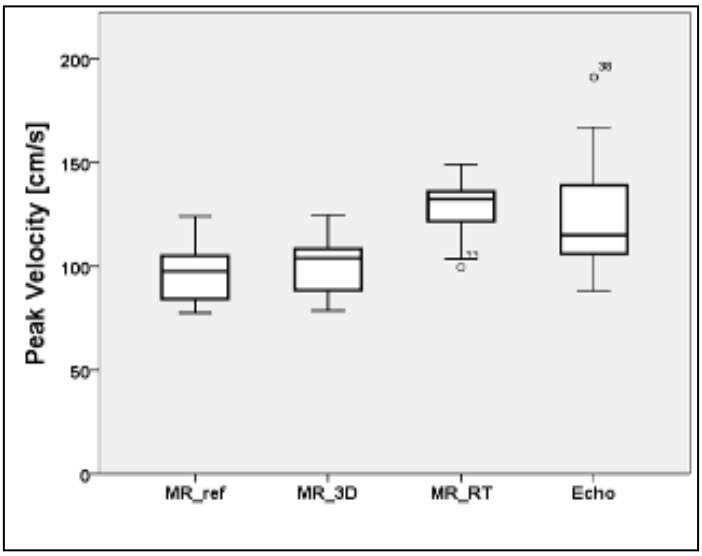

Fig1: Peak velocities assessed by phase-contrast MRI and pulse wave echocardiography

References

[1] Beach KW, Leotta DF, Zierler RE. Carotid Doppler velocity measurements and anatomic stenosis: correlation is futile. Vasc Endovascular Surg. 2012 Aug;46(6):466-74.

[2] AlHuzaimi A, Al Mashham Y, Potts JE, De Souza AM, Sandor GG. Echo-Doppler assessment of arterial stiffness in pediatric patients with Kawasaki disease. J Am Soc Echocardiogr. 2013 Sep;26(9):1084-9.

[3] Voges I, Jerosch-Herold M, Hedderich J, Pardun E, Hart C, Gabbert DD, et al. Normal values of aortic dimensions, distensibility, and pulse wave velocity in children and young adults: a cross-sectional study. J Cardiovasc Magn Reson. 2012;14:77.

[4] Rusconi C, Sabatini T, Faggiano P, Ghizzoni G, Oneglia C, Simoncelli U, et al. Prevalence of isolated left ventricular diastolic dysfunction in hypertension as assessed by combined transmitral and pulmonary vein flow Doppler study. Am J Cardiol. 2001 Feb 1;87(3):357-60, A10.

[5] Markl M, Wallis W, Strecker C, Gladstone BP, Vach W, Harloff A. Analysis of pulse wave velocity in the thoracic aorta by flow-sensitive four-dimensional MRI: reproducibility and correlation with characteristics in patients with aortic atherosclerosis. J Magn Reson Imaging. 2012 May;35(5):1162-8.

17 Optimisation of parameters for thermometry in deep hyperthermia treatments using MR-spectroscopy methods

J. Hartmann[1], S. Pyatykh[2], J. Hesser[2], O. Ott[1], R. Fietkau[1], C. Bert[1,3]
[1]University Clinic Erlangen and Friedrich-Alexander University Erlangen-Nürnberg, Department of Radiation Oncology, Universitätsstraße 27, 91054 Erlangen – Germany, Germany
[2]University Medical Center Mannheim, University Heidelberg, Experimental Radiation Oncology, Germany
[3]GSI – Helmholtz Centre for Heavy Ion Research, Department of Biophysics, Germany

Introduction: The University Hospital Erlangen is equipped with devices for phased array deep hyperthermia treatments. During these treatments the patient lies inside a water-filled applicator. The implemented antennas in the applicator send steered microwaves to heat the tissue, preferably the tumour area. Therefore, thermometry is essential to protect the surrounding healthy tissue and to offer the option of optimal temperature control in the target tissue. Thermistors with high-resistance, carbon-imbedded plastic leads (Bowman probes [1]) measure absolute values reliably at the cost of invasiveness and only local temperature values. MR-guided hyperthermia offers another option for temperature control. Using the proton resonance frequency (PRF) shift method, temperature values for every voxel in the MR-image can be determined [2]. The potential of online imaging and tumour control during treatments is another advantage of this technique. While the PRF shift method yields only relative temperature values, absolute temperature measurement can be investigated using the temperature induced proton chemical shift in MR-spectroscopy. This study investigated parameters used for the MR-sequence including peak fitting methods.

Materials and methods: A BSD-2000/3D/MR (BSD Medical Corporation, Salt Lake City, Utah, USA) combined with a Magnetom Symphony 1.5T MRT scanner (Siemens, Erlangen, Germany) was used for the measurements. The single voxel technique was applied for MR-spectroscopy using a PRESS sequence, which consists of one 90° excitation and two 180° refocusing pulses. Different phantoms of mayonnaise and pork were measured. The phantom inside the hyperthermia applicator was placed in the MRT scanner. The single voxel for the MR-spectroscopy had to be positioned in a suitable region in the MR-images. The voxel size was the first investigated parameter, which was varied between 20x20x20 mm³ to 40x40x40 mm³. The flip angle was the second investigated parameter and was varied from 30° to 90° to optimise the signal quality. For temperature calculation, precise determinations of fat and water peaks were necessary due to the tiny change of the chemical shift per degree Celsius. Fitted Lorentz peaks using a Matlab tool (Mathworks, Natick, MA, USA) with the Nelder-Mead simplex method, integrated spectroscopy peak fitting using syngo MR A35 software (Siemens, Erlangen, Germany) and a peak finding method using the singular value decomposition (SVD) of a Hankel matrix [3] were compared. After the peak finding process, the peak difference between fat and water peaks in ppm was calculated. The results of the different processes were then compared.

Results: As expected, the signal to noise ratio decreased with smaller voxel size. However, the measured area was more homogeneous in tissue composition and temperature when the voxel size decreased. The optimised flip angle was 90° so that the loss of signal due to the reduced voxel size could be compensated. The peak finding process was satisfactory by detecting two peaks; an additional third peak was determined by fitting in Matlab, but could not improve the calculation of the chemical shift. Although the resulting peak positions of the syngo software tool gave only one decimal place, the peak difference to the Matlab fitting was comparable. Only the resulting values of the Hankel matrix SVD showed a small but constant shift relative to the two other methods.

Conclusion: The acquisition parameter optimisation resulted in an optimal voxel size of 20x20x20 mm³ and a flip angle of 90°. Using these values for MR-spectroscopy single voxel sequence simplified the evaluation of the peak difference. The two peak fitting method yielded reliable peak positions and peak differences as does the SVD. However, the occurring constant shift is going to be investigated in more detail before the time consuming Matlab tool method will be replaced. In summary these results formed a good basis for currently ongoing clinical studies with non-invasive absolute thermometry by MR-spectroscopy.

References

[1] Bowman RR. A probe for measuring temperature in radio-frequency-heated material (short papers). Microwave Theory and Techniques, IEEE Transactions on 1976;24:43-45.
[2] Depoorter J, Dewagter C, Dedeene Y, Thomsen C, Stahlberg F Achten E. Noninvasive MRT thermometry with the proton-resonance frequency (PRF) method – in-vivo results in human muscle. Magnetic Resonance in Medicine 1995;33:74-81.
[3] Laudadio T, Mastronardi N, Vanhamme L, Van Hecke P Van Huffel S. Improved Lanczos algorithms for blackbox MRS data quantitation. Journal of Magnetic Resonance 2002;157:292-297.

18 Reproducible and Accurate Automatic Correction of Intensity Non-Uniformity in MRI Data

S. Leger[1], S. Löck[1], V. Hietschold[2], R. Haase[1], H. J. Böhme[3], N. Abolmaali[4]
[1]OncoRay – National Center for Radiation Research in Oncology, Faculty of Medicine and University Hospital Carl Gustav Carus, Technische Universität Dresden, Helmholtz- Zentrum Dresden – Rossendorf, Dresden, Germany
[2]University Hospital Carl Gustav Carus, Institute and Policlinic for Radiology, Dresden, Germany
[3]University of Applied Science, Department of Artificial Intelligence, Faculty of Computer Science/Mathematics, Dresden, Germany
[4]University Teaching Hospital, Clinic for Radiology, Dresden, Germany

Introduction: Magnetic resonance imaging (MRI) is an established and widely applied non-invasive imaging technique for clinical diagnostics such as tissue characterization, therapy planning and response monitoring. However, artifacts, such as intensity non-uniformity or motion artifacts, disturb the performance of image analysis, e.g. in the segmentation process. For the correction of intensity non-uniformity we present a novel approach**,** with the aim to maximize the sum of the squared two-dimensional histogram of a pair of MR images to estimate a correction function. A detailed evaluation was performed to determine, if the new approach outperforms the established N4 correction algorithm.

Material and methods: An established correction model for intensity non-uniformity in MRI is a simplified multiplicative approach [1] where *x* is the spatial position, *S* is the measured signal, *t* is the unbiased signal emitted by the tissue, *f* is the unknown non-uniformity function and *n* describes the additive noise. Furthermore we assume that the effect of intensity non-uniformity in MRI occurs due to the fact that the signal emitted by the tissue is slowly decreasing. This is caused by the increasing spatial distance between the head of the patient and the coil segments as well as by attenuation effects. We describe the gradually decreasing signal for a typical MR head coil, consisting of eight single segments, i.e. coils, by an exponential model. We combine a pair of T1- and T2-weighted MR images to estimate the unknown function *f* using the joint histogram of two MR-Images. The sum of the squared histogram bins is minimal for images with constant gray values and maximal for images with the same average gray values in which just one pixel differs from zero. Thus, maximizing the joint histogram function leads to more clustered gray value distributions in the histogram, reducing the non-uniformity in the images. Figure 1 shows uncorrected and corrected MR images, a corresponding joint histogram and the influence of intensity non-uniformity on the segmentation process. In order to determine the optimal parameters for the unknown function *f,* the joint histogram function is maximized using an Artificial Bee Colony algorithm [2].

The proposed correction algorithm was evaluated using brain MR images from six patients. In addition, the performance of the new algorithm was compared to the N4 algorithm [3], with two parameter configurations: ($N4_{50}$) with a spline distance of 50 mm and ($N4_{100}$) with a spline distance of 100 mm. As a comparison criterion we calculated the coefficient of variation *cv* of three regions of interest: white matter (wm), grey matter (gm) and cerebro-spinal fluid (csf). A smaller *cv* value indicates a correction result of higher quality. We repeated the correction of each dataset for five times to investigate the reproducibility of the new algorithm. Finally we used different parameter configurations for colony size and number of iterations of the ABC, to achieve an optimal parameter configuration.

Results: Figure 2 shows the *cv* of the new approach and the N4 algorithm for the T1- and T2-weighted datasets, respectively. The average correction performances for the T1-weighted datasets was 13.2, indicating a better performance in comparison to 13.6 for the N4 algorithm with a spline distance of 50 mm. The correction performance for the T2-weighted datasets were similar (16.9) to the results (16.7) of $N4_{50}$ algorithm. The correction results of the $N4_{100}$ algorithm for all T1- and T2-weighted datasets were inferior to the proposed method. Figure 2 also shows the reproducibility of the novel correction method. The average standard deviation of the *cv* for all patient datasets after five repetitions was 0.20 for the T1- and 0.09 for the T2-weighted datasets. The best correction performance was achieved with a colony size of 30 and a maximal number of iterations of 30. For colony sizes of 10 , 15 and 20 the *cv* was larger. Further increasing the colony size, e.g. to 50, did not reveal better correction performance but higher computation times.
Summary: In this study we present a novel method to correct intensity non-uniformity in MRI data. The evaluation showed that the coefficient of variation of gray values for several tissue types as a measure of the performance of the correction were smaller or similar in comparison to the established N4 algorithm. These results indicate that the new correction method is able to correct the intensity non-uniformity in MRI data. Furthermore the reproducibility of the novel method was demonstrated, confirming the algorithm applicability. Finally, an optimal parameter configuration of the ABC could be identified for an optimal correction performance.

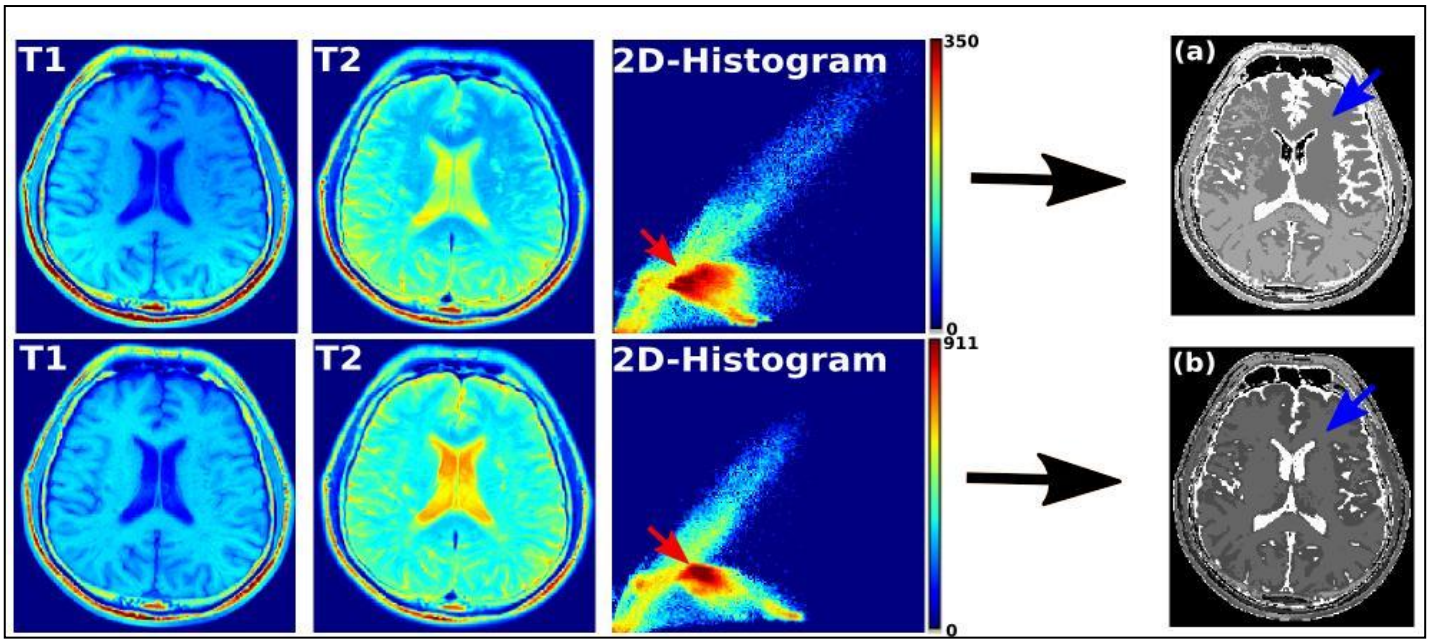

Fig. 1: Example of uncorrected T1- and T2-weighted images and the joint two-dimensional histogram as well as the corresponding segmentation result (top row). The histogram of the uncorrected images appears blurred (red arrow). In (a) the influence of the intensity non-uniformity on the segmentation result is visible (blue arrow). The bottom row shows the same T1- and T2-weighted images after the intensity non-uniformity correction. The histogram of the corrected images is more clustered (red arrow). In (b) the improved segmentation result is shown (blue arrow).

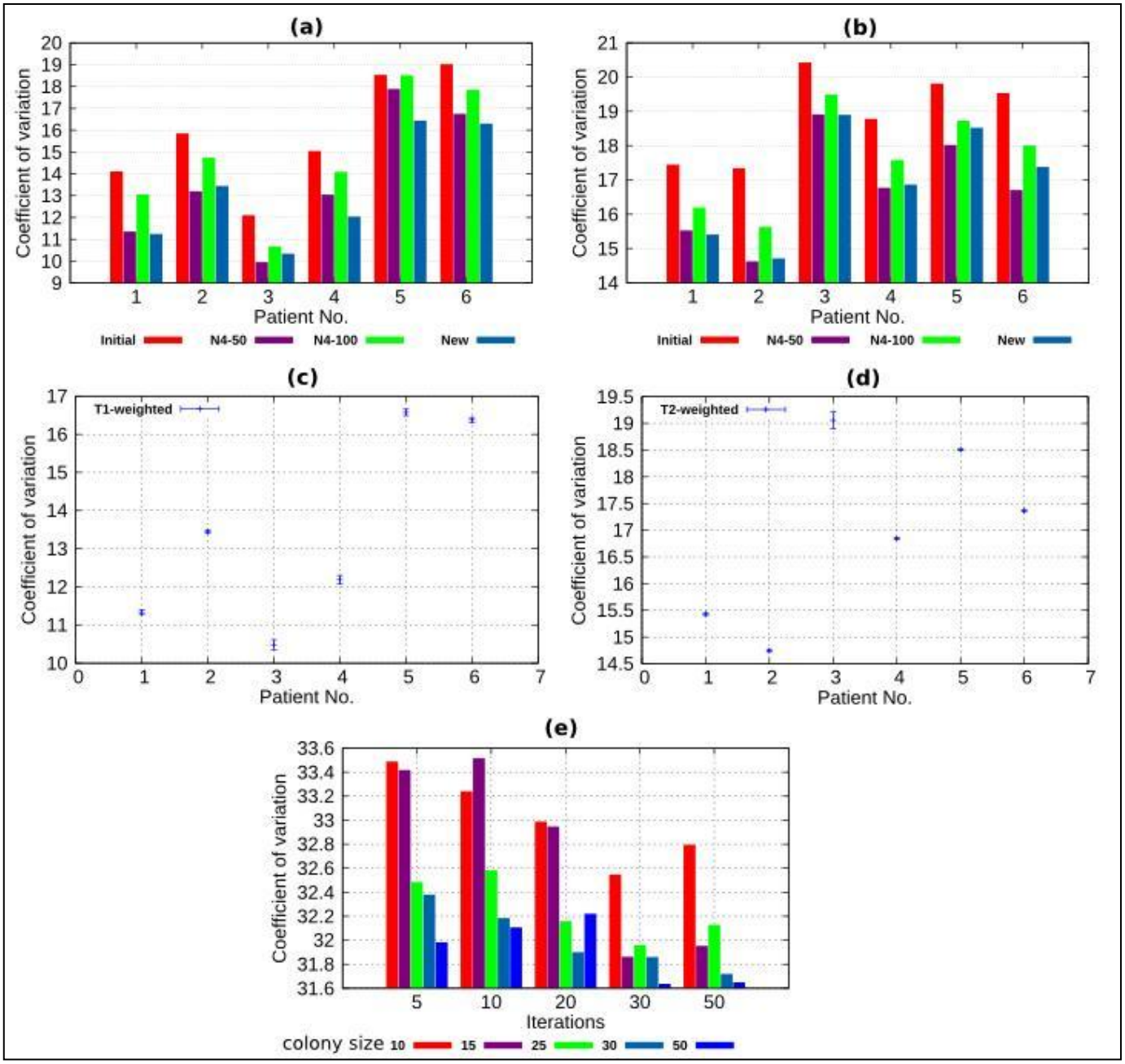

Fig. 2: The coefficient of variation analysis (a) and (b) of the new method and the N4 algorithm is shown for six T1- and T2-weighted patient datasets. The performance of the new approach was similar or even better in comparison to the N4 algorithm. The measured reproducibility of the new correction approach is shown in (c) and (d). The influence of different parameter configurations of the ABC on the coefficient of variation is visualized in (e).

References

[1] Dawant, B. M., Zijdenbos, A. P. , Margolin, R. A.: Correction of intensity variations in MR images for computer aided tissue classification. In: IEEE Transaction on Medical Imaging, vol. 12, 1993, pp. 770781

[2] Karaboga, D.: An Idea Based on Honey Bee Swarm For Numerical Optimization. In: Technical Report-TR-06 2005

[3] Tustison, N.J., Avants, B.B., Cook, P.A., Zheng, Y., Egan, A., Yushkevich. P.A., Gee, J.C.: N4ITK: improved N3 bias correction. In: IEEE Transaction on Medical Imaging, vol. 29, 2010, pp. 1310-1320

Session 4 – Dosimetry in radio diagnostics and nuclear medicine I: Nuclear medicine

Chairs: F. Bochud (Lausanne/CH), G. Glatting (Heidelberg/DE)

19 Introductory lecture: Dosimetry in nuclear medicine therapy – quantitative imaging and dose calculation

A. Schäfer[1]
[1]Department of Nuclear Medicine; University Medical Centre, Homburg/Saar, Germany

In nuclear medicine therapy tumours are treated by internal radiation exposure from a radionuclide or a radioactively labelled pharmaceutical administered to the patient. To permit the efficient delivery of high amounts of radiation dose to tumours while limiting the radiation dose to critical organs dosimetry calculations need to be performed. Moreover, patient-specific dosimetry is needed to provide an estimation of the radiation dose to tissues for an individual patient.

Individual treatment planning in nuclear medicine is performed by use of a diagnostic pre-treatment test dose of the radiopharmaceutical administered to the patient. This approach allows to quantify the relationship between administered activity and absorbed radiation dose in the critical organs and to estimate the radiation absorbed dose to both the tumour and the normal organs. The objective of treatment planning is to determine the amount of activity administered which maximizes tumour cell sterilization while minimizing normal tissue toxicity.

Treatment planning in nuclear medicine comprises the following steps:

(i) Measurement of the biodistribution of the radiopharmaceutical within the patient, that is to determine the percentage of administered activity for the accumulating organs. This step mainly requires the implementation of quantitative imaging procedures which can be performed by serial planar gamma-camera scans or with considerably increased accuracy – by tomographic measurements using SPECT(/CT) or PET(/CT). (ii) The quantitative imaging procedure needs to be repeated at appropriate points in time in order to assess the biokinetics of the radiopharmaceutical. This data is used to calculate the number of disintegration in the source organs and the respective residence times (time-integrated activity coefficients). (iii) The absorbed doses need to be estimated relying on the physical properties of the radionuclide and the measured biokinetics. Several methods have been developed for estimating radiation dose in the patient ranging from reference tables derived from anthropomorphic phantoms to direct, stochastic simulation of radiation dose deposition in the patient using a CT-based representation of the patient. Each step of the treatment planning process implies uncertainty in the assessment of radiation absorbed dose to normal organs which will be addressed in the lecture.

20 Optimization of the dosimetry prior to radioiodine therapies of the thyroid in a clinical setting

M. Borowski[1], S. Meins[1]
[1]Klinikum Braunschweig, Institut für Röntgendiagnostik, Braunschweig, Germany

Motivation: The application of the radioactive isotope I-131 is a common therapy option for diseases of the thyroid like goiter or hyperthyroidism. Prior to the therapy the I-131 uptake to the thyroid as well as the outflow and corresponding retention time have to be determined. Normally the uptake and effective half life period are estimated from few measurements within the first two days after application of a test dose of activity. This proceeding, however, suffers from the fact that especially the half life period only can be estimated with a large uncertainty. As a result the therapeutic aim cannot be reached precisely. Further the planning of the length of the stay of patients within the radioiodine therapy ward is subject to an increased uncertainty. Both consequences are to be avoided as far as possible. In 2013 a recommendation of the European Association of Nuclear Medicine (EANM) was published, which takes the physiological processes of the I-131 dynamic better into account [1]. The full use of this recommendation, however, easily results in an increased effort to the staff and patient. Within this work the effect of the EANM recommendation on the therapy outcome was studied in a clinical environment. Further, optimization strategies have been determined to minimize the effort of the pre-therapeutic dosimetry.

Materials and methods: Within the study data from pre-therapeutic dosimetry as well as from I-131 therapies of the thyroid have been analyzed for about 60 patients. According to the EANM recommendation the I-131 uptake to the thyroid was measured at least up to 6 to 7 days after application. We determined the effect of the measurements at different points in time on the estimated overall I-131 uptake, the half life and the activity to be administered under therapy conditions. The correlation between the prediction based on the different test scenarios and the therapeutic behavior of the thyroid have been analyzed. The analysis was conducted on different subgroups of diseases of the thyroid.

Results: It could be verified under clinical conditions that measurements at about one week after application of the test activity have a substantial effect on the predicted half life for diseases with an average effective half life of about 6 days or below as well as diseases where the individual effective half life time varies relevantly. Especially for Grave's disease the uncertainty of the half life can be lowered with the use of the EANM approach by a factor of 1.5 compared to common used procedures. For diseases with an average effective half life of around 7 days, like goiter, the effect of the more elaborated dosimetry approach was smaller with only limited benefit in comparison to a simple 'Marinelli approach'. It also got obvious that it is fully sufficient to sample the I-131 uptake on the basis of three measurements only, one after about four hours after application, one after one to two days and one after about one week. A further increase of effort does not positively affect the precision of the pre-therapeutic dosimetry. Further there are hints that even with measurements at the first and last point in time the activity to be administered can be predicted with sufficient precision.

Conclusion: We studied the effect of more elaborated pre-therapeutic I-131 uptake tests on the precision of the prediction of the therapeutic behavior of the thyroid. It showed up that the use of a measurement at a delayed point in time has a clear effect on the quality of the prediction. There is, however, a chance to optimize the tests by performing measurement at no more than two to three points in time.

References

[1] H. Hänscheid et. al., Eur. J. Nucl. Med. Mol. Imaging: 2013 Jul; 40(7):1126-34 , "EANM Dosimetry Committee Series on Standard Operational Procedures for Pre-Therapeutic Dosimetry II. Dosimetry prior to radioiodine therapy of benign thyroid diseases"

21 Optimal Sampling Schedule: Investigating the effect of a reduced data set on the time-integrated activity coefficients in peptide receptor radionuclide therapy (PRRT)

C. Maaß[1], P. Kletting[2], F. Mottaghy[3], G. Glatting[1]
[1]University Medical Centre Mannheim, University Heidelberg, Medical Radiation Physics/Radiation Protection, Mannheim, Germany
[2]Ulm University, Medical Physics, Ulm, Germany
[3]University Medical Centre Aachen, Nuclear Medicine, Aachen, Germany

Aim: The aim of this study was to investigate the effect of a reduced number of measurement points on the estimation of the time-integrated activity coefficients in PRRT with 111In-labelled DTPAOC.

Materials and methods: Ten patients with proven neuroendocrine tumours (NETs) were investigated. Planar whole-body scans using a double-head γ-camera (Siemens, Erlangen, Germany) were performed at 0.75, 4 h, 1, 2, and 3 d after the injection of 111In-DTPAOC for prediction of absorbed doses [1]. A physiologically based pharmacokinetic (PBPK) model [1] was implemented describing the main physiological processes, i.e. absorption, distribution, internalization and excretion (ADME). To investigate the effect of neglecting the last measurement point on the optimized biodistribution (Fig. 1) and thus the time-integrated activity coefficient both the full and the reduced data sets were fitted to the model. The relative difference RD of the resulting time-integrated activity coefficients was calculated using the area under the curve (AUC) individually for all organs according to

$$\mathrm{RD} = 100 * \frac{\mathrm{AUC(reduced\ dat)} - \mathrm{AUC(full\ data)}}{\mathrm{AUC(full\ data)}} \quad (1)$$

Results: The time-integrated activity coefficients for the full data sets are as follows: serum = (0.8 ± 0.3) h, liver = (2.2 ± 0.8) h, tumour = (5.8 ± 1.3) h, spleen = (1.45 ± 2.1) h, kidney = (1.1 ± 0.5) h, whole body = (13.1 ± 4.0) h. The mean relative differences between the time-integrated activity coefficients are showing an overestimation on average for serum, spleen, kidney and whole body (Table 1). For tumour and liver the AUC is underestimated on average (Table 1). The differences for tumour and serum are significant ($p < 0.05$, Wilcoxon t test).

Organ	Mean ± STD [%]	Median [%]	Min [%]	Max [%]
Tumour	-32 ± 42	-24	-99	33
Kidney	14 ± 24	16	-20	64
Liver	-0.5 ± 14	-2	-19	26
Spleen	38 ± 59	16	-49	139
Whole Body	18 ± 26	4	-12	56
Serum	47 ± 50	46	-21	110

Tab. 1: Relative differences of the estimated time-integrated activity coefficients between both data sets (full and reduced) for all patients.

Conclusion: The results of the herewith investigated case using less data on the time-integrated activity coefficients suggest a considerable effect of the last measurement point on the quantitative estimation accuracy of the absorbed dose. The effect has a major influence on the AUC. A positive difference is indicating an overestimation of the actual AUC and thus the absorbed dose to the organ at risk. Overall, in this patient group the last measurement point is necessary to avoid an inaccurate estimation or prediction of the actual absorbed dose.

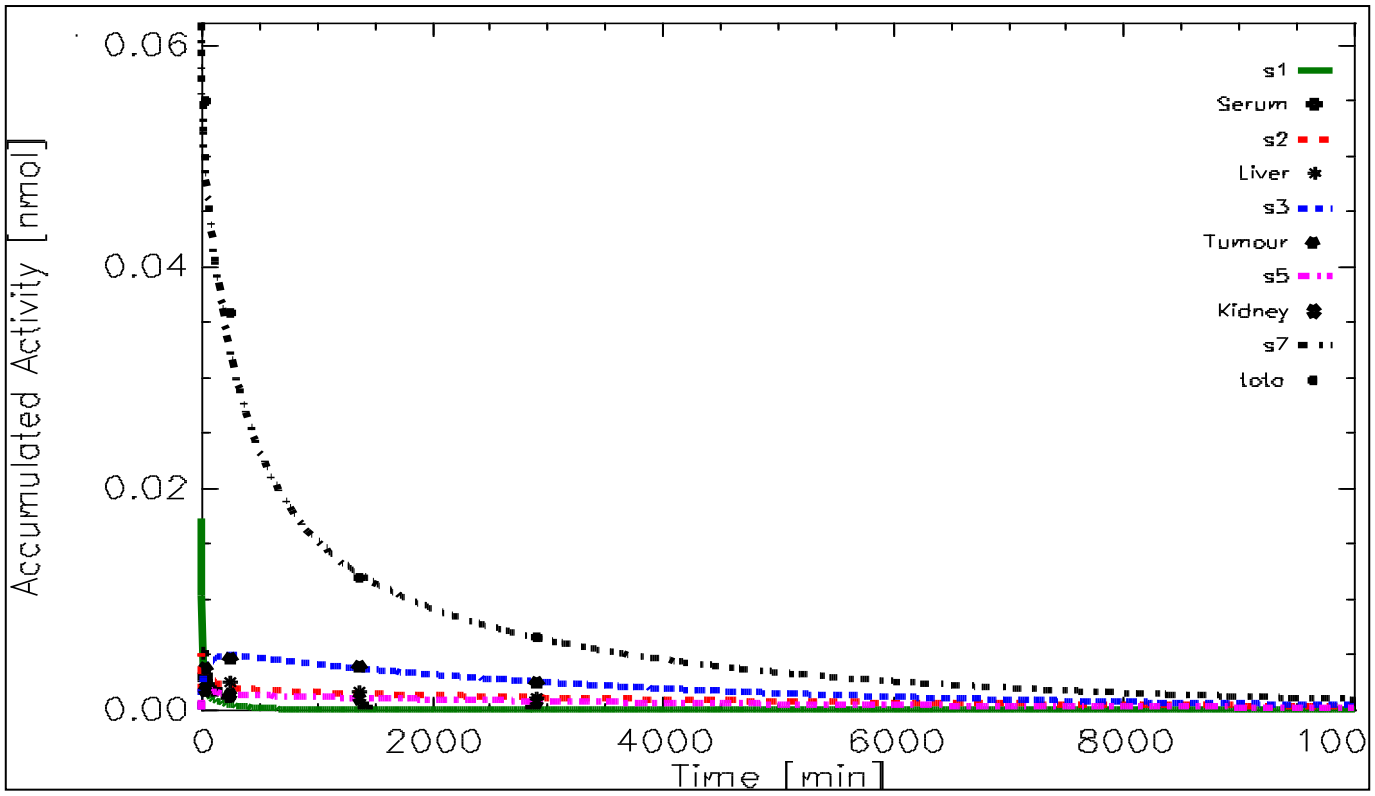

Fig. 1: A typical measured biodistribution (black dots) and the fit (colored lines) by the model for serum, liver, tumour, kidney and whole body (total).

References

[1] Kletting P, Müller B, Erentok B, Schmaljohann Jr, Behrendt FF, Reske SN, Mottaghy FM, Glatting G. Differences in Predicted and Actually Absorbed Doses in Peptide Receptor Radionuclide Therapy. Med Phys 2012; 39: 5708.

22 The NUKDOS Software for Dosimetry in Molecular Radiotherapy

P. Kletting[1], S. Schimmel[1], H. Hänscheid[2], M. Luster[3], M. Fernandez[2,3], D. Noßke[4], M. Lassmann[2], G. Glatting[5]
[1]Universität Ulm, Klinik für Nuklearmedizin, Ulm, Germany
[2]Universtität Würzburg, Klinik für Nuklearmedizin, Würzburg, Germany
[3]Universität Marburg, Klinik für Nuklearmedizin, Marburg, Germany
[4]Bundesamt für Strahlenschutz, Oberschleißheim, Germany
[5]Universität Heidelberg, Mannheim, Germany

Questions: For dosimetry in molecular radiotherapy there is no software tool available which allows a seamless workflow from 2D/3D data processing to the actual calculation of the activity to administer and the absorbed doses. In addition, current software lacks providing errors for the results. Therefore, dosimetry software for molecular radiotherapy was developed which includes all relevant methods for calculating the activity to administer and the pertaining absorbed doses (with the corresponding error) using a series of 2D images and one 3D image or external counter data as input.

Materials und methods: NUKDOS follows the MIRD formalism on a voxel-level (1) and was developed in MATLAB. To determine the kinetics of the radiolabeled substance the time activity curve of organs of interest can be derived from a series of gamma camera images using the 2D image processing tool. In addition, counter data from urine, serum, blood or probe can be processed. To estimate the time-integrated activity coefficients the data can be fitted to a list of pre-defined functions (sums of exponentials). The integration of the functions with the corresponding fit parameters is conducted analytically (2). To determine the absolute activity and the time-integrated activity coefficients in each organ on a voxel level one SPECT/CT image is required. The absorbed dose coefficients are calculated by convolution of the time-integrated activity coefficient matrix and an S-value kernel. S-Value kernels are provided for Y-90, I-131 and Lu-177 and are automatically constructed based on the voxel size of the image (3). From the mean value of the absorbed dose coefficients of the organ at risk the activity to administer is calculated. Subsequently the absorbed doses and/or the biologically equivalent dose of the organs of interest are computed. The error of the absorbed doses is estimated by Gaussian error propagation taking into account the errors of all contributing variables. In addition, NUKDOS supports the latest EANM SOP formalisms provided for dosimetry in the treatment of thyroid diseases (4).To validate NUKDOS, the results of dosimetry in receptor radionuclide therapy were compared to the output of other software (OLINDA/EXM (5), SAAM2 (6) and UlmDOS (7)). An example from radioiodine therapy was also used to test for accuracy and reproducibility of the results.

Results: The time activity curves of NUKDOS and UlmDos were very similar considering the problem of drawing the same ROI with different software tools. For each time point and organ the difference was < 5 %. The fitting results (based on the same data) of SAAM2 were identical. For a maximal dose of 12 Gy for the kidney, the difference between OLINDA/EXM (mass corrected) and NUKDOS were < 5 % for the activity to administer based on the same time-integrated activity coefficients.

Conclusion: For treatment planning in molecular radiotherapy NUKDOS provides an objective estimate of the activity to administer and the pertaining absorbed doses for several radionuclides. Presently it is based on a series of gamma camera images and one SPECT/CT (PET/CT) as well as external counter data. In addition, the errors of the absorbed doses are provided.

References

[1] Bolch WE, Bouchet LG, Robertson JS, et al. MIRD pamphlet No. 17: the dosimetry of nonuniform activity distributions--radionuclide S values at the voxel level. Medical Internal Radiation Dose Committee. J Nucl Med. 1999;40(1):11S-36S.
[2] Kletting P, Schimmel S, Kestler HA, et al. Molecular radiotherapy: The NUKFIT software for calculating the time-integrated activity coefficient. Med Phys. Oct 2013;40(10):102504.
[3] Fernandez M, Hanscheid H, Mauxion T, et al. A fast method for rescaling voxel S values for arbitrary voxel sizes in targeted radionuclide therapy from a single Monte Carlo calculation. Med Phys. Aug 2013;40(8):082502.
[4] Hanscheid H, Canzi C, Eschner W, et al. EANM Dosimetry Committee series on standard operational procedures for pre-therapeutic dosimetry II. Dosimetry prior to radioiodine therapy of benign thyroid diseases. Eur J Nucl MEd Mol Imaging. Jul 2013;40(7):1126-1134.
[5] Stabin MG, Sparks RB, Crowe E. OLINDA/EXM: The Second-Generation Personal Computer Software for Internal Dose Assessment in Nuclear Medicine. J Nucl Med. 2005;46(6):1023-1027.
[6] Barrett PH, Bell BM, Cobelli C, et al. SAAM II: Simulation, Analysis, and Modeling Software for tracer and pharmacokinetic studies. Metabolism. 1998;47(4):484-492.
[7] Glatting G, Landmann M, Kull T, et al. Internal radionuclide therapy: The UlmDos software for treatment planning. Med Phys. 2005;32(7):2399-2405.

23 Increasing the accuracy of the predicted absorbed dose in radioimmunotherapy with anti-CD66 antibody using a physiologically based pharmacokinetic model

P. Kletting[1], C. Maaß[2], A. Beer[1], G. Glatting[2]
[1]Universität Ulm, Klinik für Nuklearmedizin, Ulm, Germany
[2]Universität Heidelberg, Mannheim, Germany

Introduction: Radioimmunotherapy (RIT) is employed in conditioning before blood stem cell transplantation of acute (myeloid and lymphoblastic) leukemia patients (*1, 2*). To achieve the desired absorbed dose, therapy planning is conducted based on pretherapeutic measurements, a pharmacokinetic and physical model. In the past, equal pretherapeutic and therapeutic biodistribution was assumed. However, it has been shown that this assumption is not justified and that a physiologically based pharmacokinetic (PBPK) model is required to predict the time-integrated activity coefficients (residence times) for the calculation of the absorbed dose (*1*). The introduction of a PBPK model in RIT with radiolabelled anti-CD66 antibody allowed individual dosimetry while including *a priori* knowledge of physiological parameters. Here, this PBPK model is improved using more patient data and including additional *a priori* knowledge.

Material and methods: The recently developed model was modified by adding sub-models for half and non-immunoreactive fractions of the antibody. In addition, it was assumed that the number of antigens in the liver and spleen together are equal to the antigens on the circulating granulocytes (*3*) and 38 fold lower than in the red marrow (*4*). Gamma camera and serum measurements of 28 patients with acute myeloid or lymphoblastic leukemia were available. The prediction accuracy was evaluated by comparing the predicted and the measured serum activity curve during therapy. In addition, the time-integrated activity coefficients τ_i for all organs were investigated.

Results: Visual inspection showed good fits for all models and data, except the red marrow time-activity curve (TAC) for one patient. All elements of the correlation matrix were < 0.9 and the coefficients of variation of the estimated time-integrated activity coefficients τ_i were < 0.2 for all organs and patients (*5*). The median relative deviation of the time-integrated activity coefficient based on the predicted and measured therapeutic serum TAC was 11 % (range: 0.1-64 %). The pretherapeutic and therapeutic τ_i for serum and red marrow differed by a factor of 0.76±0.15 and 1.2±0.2, respectively. The amount of injected substance and the number of available antigens are the most important determinants for biodistribution.

Summary: The prediction accuracy is in a reasonable range considering the alternative of assuming equal biodistribution for the pretherapeutic measurements and therapy. Therefore, it is recommended to use the presented PBPK model for estimating the time-integrated activity coefficients in RIT with anti-CD66 antibody from pretherapeutic measurements. Further validation of the model is ongoing.

References

[1] Kletting P, Kull T, Bunjes D, et al. Radioimmunotherapy with anti-CD66 antibody: Improving the biodistribution using a physiologically based pharmacokinetic model. J Nucl Med. 2010;51(3):484-491.
[2] Schulz AS, Glatting G, Hoenig M, et al. Radioimmunotherapy based Conditioning for Hematopoietic Cell Transplantation in Children with Malignant and Non-Malignant Diseases. Blood. 2011;117(17):4642-4650.
[3] Peters AM, Saverymuttu SH, Bell RN, Lavender JP. Quantification of the distribution of the marginating granulocyte pool in man. Scand J Haematol. Feb 1985;34(2):111-120.
[4] Donohue DM, Reiff RH, Hanson ML, Betson Y, Finch CA. Quantitative measurement of the erythrocytic and granulocytic cells of the marrow and blood. J Clin Invest. Nov 1958;37(11):1571-1576.
[5] Kletting P, Schimmel S, Kestler HA, et al. Molecular radiotherapy: The NUKFIT software for calculating the time-integrated activity coefficient. Med Phys. Oct 2013;40(10):102504.

Session 5 – Treatment planning and dose calculation in radiation therapy I: Dosimetry

Chairs: T. Frenzel (Hamburg/DE), J. Wilkens (Munich/DE)

24 Non-coplanar IMRT class solutions for organs at risk of different symmetries: A planning study

K. Bratengeier[1]
[1]Universität Würzburg, Klinik für Strahlentherapie, Würzburg, Germany

Purpose: Intensity modulated radiation therapy (IMRT) uses optimization procedures to achieve desired dose distributions. However, the problem of finding an optimal gantry angle configuration can hardly be solved by linear optimization even for coplanar beams (Meedt et al., 2003), more so for the non-coplanar beam arrangements. Therefore, it could be helpful to utilize other approaches such as class solutions. The purpose of this study was to evaluate different non-coplanar class solutions for simplified organ at risk (OAR) / planning target volume (PTV) topologies resembling different clinical cases.

Methods: The optimal fluence distribution of IMRT fields depend strongly on the topology of OARs and PTVs. For example, concave PTV structure surrounding an OAR requires solutions completely different from those for convex PTV (Brahme et al., 1982; Bratengeier, 2005; Bratengeier et al., 2012b). To model clinical situations where non-coplanar beam arrangements may be useful, we used three types of PTV-OAR topology (see Fig. 1). Spherical embedded OAR (Fig. 1a) simulated such compact objects as eyeballs, lenses, parotid glands, pituitary glands, etc. Cylindrical OAR (Fig. 1b) modelled elongated OARs such as spinal cord and optic nerves in the head and neck cases. A curved elongated OAR (Fig. 1c) modelled more complex objects such as the rectum in the prostate cases. Note that for Fig. 1 a) and 1 c) no beam direction can be found to spare the OAR without also blocking out parts of the PTV.

For the PTV-OAR topologies in Fig. 1, a reference coplanar and a number of non-coplanar IMRT class solutions were planned in Pinnacle3D 9.1 using direct machine parameter optimization (DMPO) and, for comparison, fluence optimization.

For each OAR shape (a: ball, b: cylinder with rounded ends, c: banana), a cutting plane through phantom centre (upper row) combined with a perspective view (lower row) of the green OAR embedded in the transparent red PTV is depicted. The orientation is the same as for the patient with inferior (I)-superior (S)-direction parallel to the couch. The Phantom surface (sphere, diameter 20 cm) is represented by brown contours.

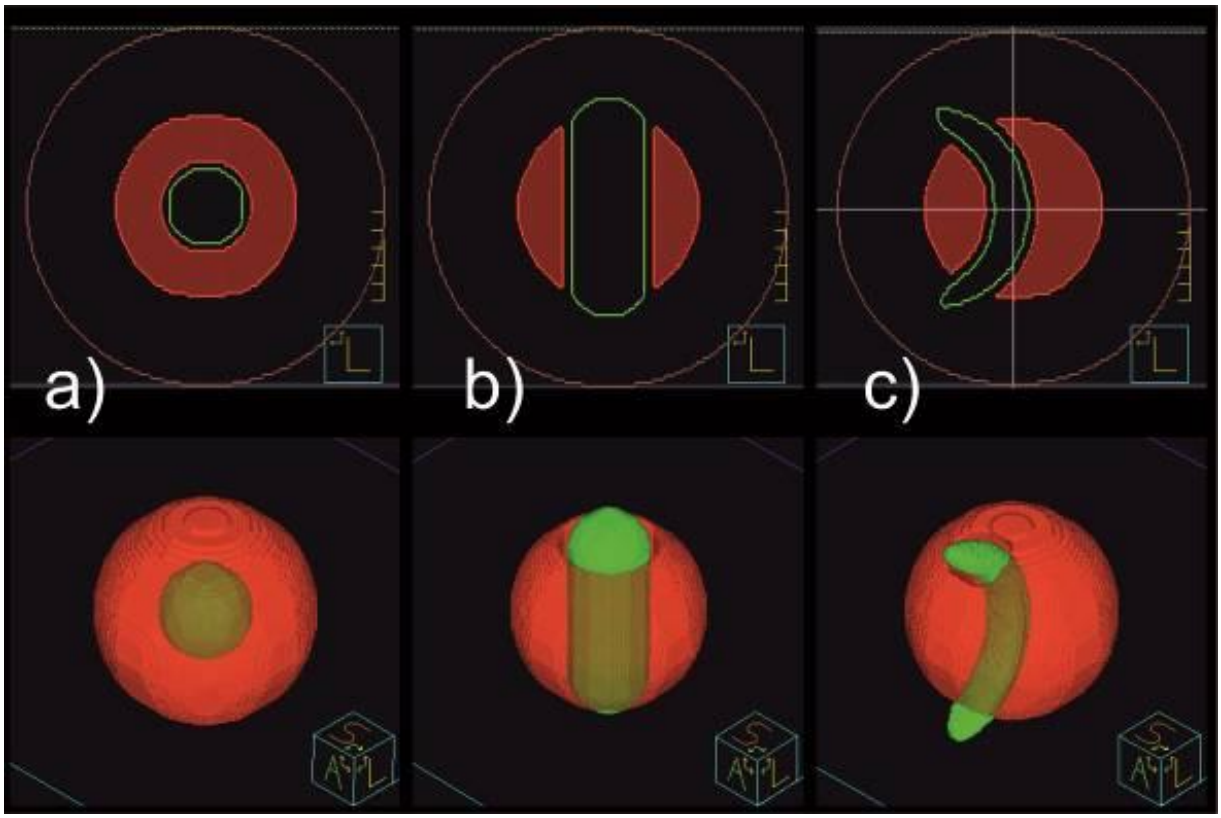

Fig1: employed PTV-OAR topologies

Several factors that potentially influence clinical applicability of the results were assessed: number of beams, maximum number of allowed segments (64 or 120) or raw fluence distributions, differently weighted OAR sparing, different collimator angles, variation of the dose grid, different collimator types and leaf widths (4 mm, 10 mm).

The following class solutions were compared:

1. Coplanar equidistant IMRT (Co) – the reference technique
2. Non-coplanar Quasi-isotropical, with central axes in 5 planes (NonCo *)
3. Coplanar technique with additional orthogonal field (Co+1)
4. Non-coplanar with central axes in 2 planes (2P); same as coplanar, but half of the beams used 90° turned patient couch

Further non-coplanar plans planned by experienced IMRT planners (*) central axes through the vertices of icosahedron and/or dodecahedron (Bratengeier et al., 2012a). The resulting plans were compared using mean dose to the OAR and minimum dose to the PTV. Additionally, more comprehensive summarizing evaluation methods were used.

Results: For all techniques more segments, particularly more beam directions enabled better plan quality. Spherical OARs are best treated using Quasi-isotropical NonCo technique; however, the number of beams and segments should be high: minimum 16 beams and 120 segments had to be used. 2P-techniques turned out to be almost equivalent to NonCo. If less beams and segments were allowed, they actually were preferable.

For cylindrical OARs, coplanar IMRT with an additional beam along the cylinder axis (Co+1) achieved best results – also for a limited number of allowed beams and segments. 2P plans were second best for cylindrical OARs; they were almost equivalent, if few segments were allowed.

For the most irregular (banana) shape Co+1 delivered best plans, also for a reduced number of beams. The coplanar techniques were almost of the same quality. However, Co+1 and particularly 2P plans were less sensitive to the reduction of the number of segments.

Individually generated plans could compete with other techniques in cases b) and c) only if additional non-coplanar beams were used along the OAR axis.

Discussion and conclusion: Non-coplanar IMRT seems to be clinically effective solely if beam arrangement is dense enough towards two neighboured beams, at least for a subgroup of the beams. For all techniques, this subgroup has to be extended over a wide angular range, as for 2P-techniques or single beams additional to a coplanar beam arrangement. The latter case shows that not every beam needs dense neighbours. For cylindrical OARs, coplanar beam arrangements with additional beams along the OAR axis increase plan quality considerably. Such techniques are even successful for curved OARs that do not have an obvious OAR-sparing direction (case c).

Planning studies for real clinical cases will follow.

References

[1] Brahme A, Roos J E and Lax I 1982 Solution of an integral equation encountered in rotation therapy. Phys.Med.Biol. 27 1221-9
[2] Bratengeier K 2005 2-Step IMAT and 2-Step IMRT: a geometrical approach Med Phys 32 777-85
[3] Bratengeier K, Seubert B, Holubyev K and Schachner H 2012a Considerations on IMRT for quasi-isotropic non-coplanar irradiation Phys Med Biol 57 7303-15
[4] Bratengeier K, Seubert B and Schachner H 2012b Quasi-isotrope non-koplanare IMRT im Vergleich zu koplanarer IMRT. In: Medizinische Physik, (Jena: DGMP)
[5] Meedt G, Alber M and Nusslin F 2003 Non-coplanar beam direction optimization for intensity-modulated radiotherapy Phys Med Biol 48 2999-3019

25 Modeling of the new accelerator head agility and subsequent validation by measurements

U. Kuck[1,2], N. Escobar-Corral[1], S. Lotze[1], K. Laihem[1,2], A. Schmachtenberg[1], A. Stahl[2], M. J. Eble[1]
[1]University Hospital Aachen, Clinic for Radiooncology and Radiotherapy, Aachen, Germany
[2]RWTH Aachen University, III. Physical Institute B, Aachen, Germany

Introduction: In radiotherapy it is possible to obtain highly accurate dose calculations by using Monte Carlo (MC) algorithms, even in regions with inhomogeneous densities. However, because of the required high computing power, MC algorithms are not common in commercial planning systems yet.

This work aims to construct a highly accurate geometric model of one of the linear accelerators available at our clinic using the MC toolkit GEANT4 [1,2]. With this model, simulations of energy depositions can be made and verified by measurements. A geometric calibration is necessary to take the curvature of the collimator tips into account [3].

Materials and methods: For the modeling the MC toolkit GEANT4 is used. It features a high flexibility for the choice of primary particles and in the creation of geometries being also suitable for the generation of time-dependent geometries.

The modeled linear accelerator is the Axesse (Elekta) with Agility head. This head provides accurate dose delivery to tumors due to a multileaf collimator (MLC) containing 160 tungsten leaves split up into two opposing leaf banks. These leaves have a projected thickness of 5mm in the isocentric level and can be moved individually, enabling highly precise and rapidly varying radiation fields. In X-direction the field is limited by two opposing, movable X-collimators.

The accelerator head is modeled in GEANT4 from target to collimators in collaboration with the manufacturer. To validate the simulation several dose profiles are measured using a diode (PTW 60017) in a water phantom. These measurements are compared to dose profiles which have been simulated with the same geometry. The measurements are taken in the isocenter with a source surface distance of 90cm. The calibration of the simulation is done for photons at energies of 6MV and 15MV. Individual calibration functions are made for both MLC leaf banks and the X-collimators.

Results: With the calibrated model several fields are simulated. The simulated fields are compared to measured fields by means of the one dimensional gamma index criterion. Simulation and measurement show a very good agreement, validating our model.

Conclusion: The simulation has been dosimetrically and geometrically verified and we have obtained a model of our linear accelerator in GEANT4 which enables us to make highly accurate calculations of energy depositions. With this model it is possible to perform 4D simulations and dose calculations in patients for advanced radiation techniques which require this high precision.

References

[1] Agostinelli, S. et al., G4-a simulation toolkit, Nuclear Instruments and Methods in Physicis Research A, 506(3),250-303 (2003)
[2] Allison, J. et al., Geant4 developments and applications, Nuclear Sciece, IEEE Transactions on, 53(1), 270-278 (2006)
[3] Philip Vial, Lyn Oliver, Peter B Greer, Clive Baldock (2006), An experimental investigation into the radiation field offset of a dynamic multileaf collimator, Physics in Medicine and Biology 510(21) p. 5517-38

26 Precise characterisation of the beam parameters of a research electron accelerator

F. Renner[1], R.-P. Kapsch[1], A. Schüller[1], C. Makowski[1]
[1]Physikalisch-Technische Bundesanstalt Braunschweig, Braunschweig, Germany

Introduction: The national metrology institute of Germany, the Physikalisch-Technische Bundesanstalt (PTB), operates an electron linear accelerator for fundamental research in dosimetry for radiation therapy [1]. The accelerator consists of two sections: A low-energy section (0.5 MeV – 10 MeV) and a high-energy section (6 MeV – 50 MeV). At the end of both accelerator sections the electron beam can be deflected into the irradiation rooms where the experimental beamlines are located. Both experimental beamlines are set up with devices for a precise characterisation of the electron beam. In connection with a benchmark experiment for the verification of Monte Carlo codes, e.g. EGSnrc [2], measurements with these devices have been performed at the high-energy beamline for a nominal energy of about 25 MeV. Results of these measurements are presented in the following.

Materials and methods: The high-energy experimental beamline is equipped with beam profilers, beam current monitors and a magnetic spectrometer to characterise the electron beam. The beam profilers and the beam current monitors are commercial products available from National Electrostatic Corporation (NEC) and BERGOZ Instrumentation, respectively. The beam current monitors installed at the beamline have been calibrated by means of a Faraday cup developed by PTB. This means that an absolute and non-destructive measurement of each beam charge pulse is possible for high-energy electron beams. The energy spectrum of the electron beam can be evaluated precisely by a system based on magnetic spectrometry [3].

Results: Figure 1 shows an example of a horizontal beam profile measured with one of the NEC profilers which is located near the end of the beamline. The profilers always measure a vertical profile, too. This provides information about the widths of the electron beam. There are two more profilers installed along the experimental beamline in order to obtain additional geometrical information, e.g. beam divergence. By measuring of the beam pulse charge, the number of electrons per beam pulse can be specified with an uncertainty < 0.3 %. The number of electrons is used for the normalisation of quantities calculated with a Monte Carlo code and therefore it is information necessary in the benchmark experiment. Additionally, with a recording of the beam pulse charge the stability of the accelerator can be evaluated. Figure 2 shows results of a measurement of the beam pulse charge for a time scale of 10 hours. With the magnetic spectrometer a Gaussian-shaped energy spectrum of the beam with a mean energy of 27.120 MeV and a full width at half maximum of less than 1 % of the mean energy was determined. The standard uncertainty of the mean energy was 0.125 %.

Conclusion: At the experimental beamline of the high-energy section of the research electron accelerator installed at PTB, the electron beam can be characterised by measurements with regard to beam geometry, beam pulse charge and energy spectrum. This is a precondition for benchmark experiments which aim at the absolute verification of Monte Carlo codes, e.g. EGSnrc. A first experiment for high-energy photon radiation produced by an X-ray target was carried out successfully in 2013.

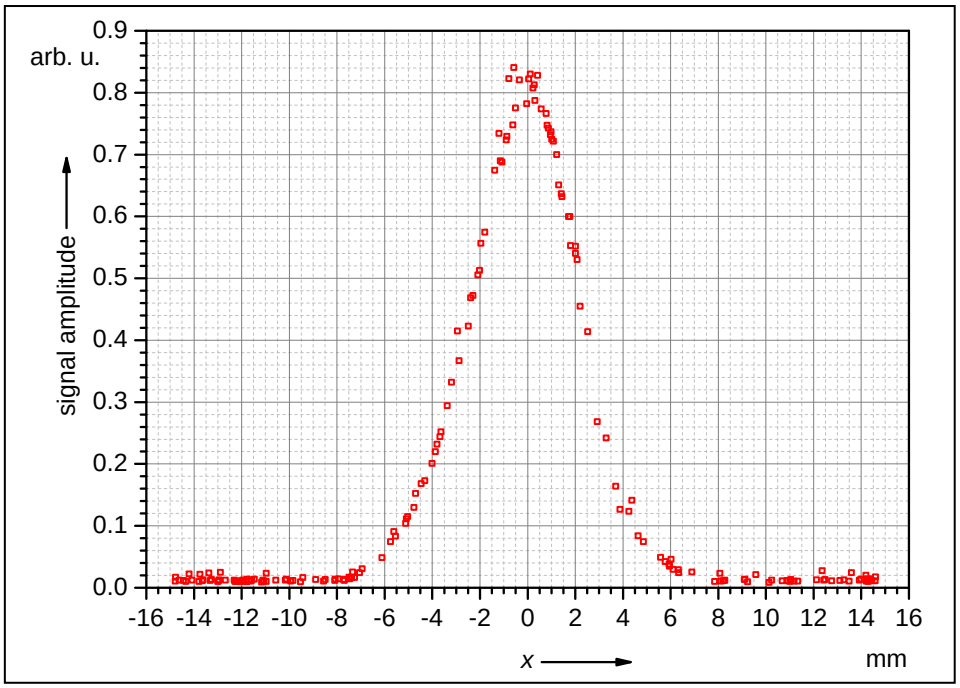

Fig. 1: Measured horizontal beam profile near the end of the experimental beamline. The full width at half maximum of the signal amplitude is about 5 mm.

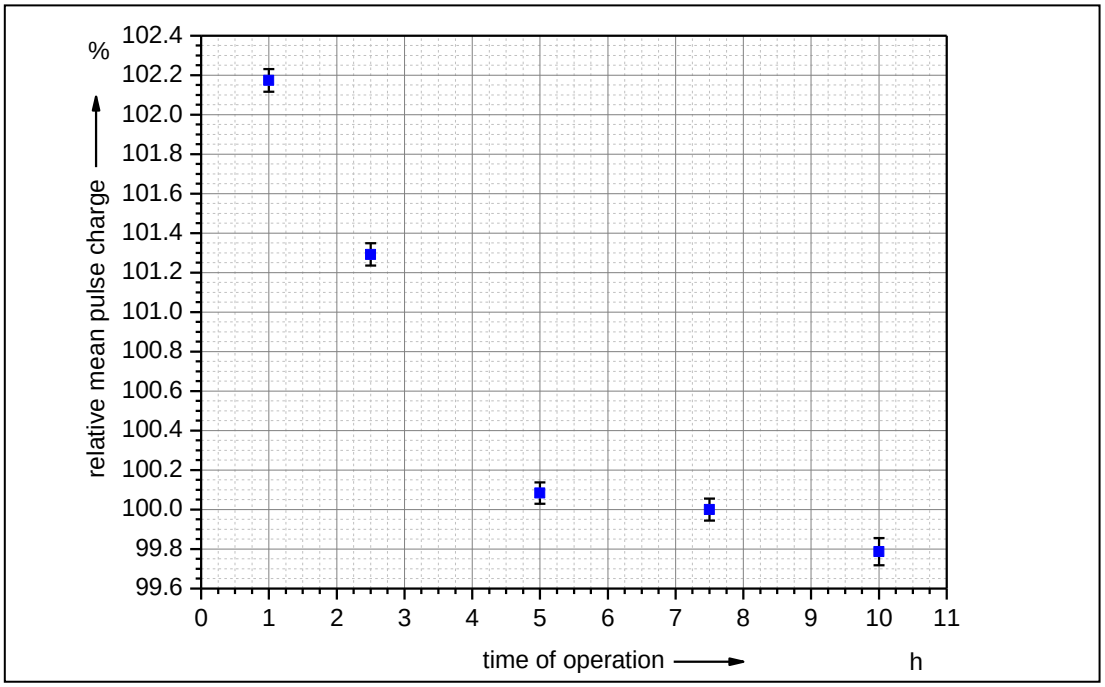

Fig. 2: Temporal development of the beam charge during the operation of the linac. After 5 hours of operation the mean pulse charge just changes by less than 0.3 % during the next 5 hours.

References

[1] Derikum, K.: A Dedicated Irradiation Facility for Radiotherapy Dosimetry, in: O. Dössel and W. C. Schlegel (Eds.) WC 2009, IFMBE Proceedings 25/I (2009) 53

[2] Kawrakow, I. et al.: The EGSnrc Code System: Monte Carlo Simulation of Electron and Photon Transport. NRCC Report PIRS-701, Ottawa, Canada, 2009

[3] Renner, F. et al.: An approach to an accurate energy determination of the energy spectrum of high-energy electron beams using magnetic spectrometry, Journal of Instrumentation, Vol. 9, P030904, 2014, doi:10.1088/1748-0221/9/03/P03004

27 Impact of small Gantry Angle Changes in Helical Tomotherapy: Recalculation of Dose Distributions with VOXELPLAN

S. Klüter[1], K. Schubert[1], S. Lissner[1], D. Oetzel[1], S. Nill[2]
[1]Universitätsklinikum, Abteilung Radioonkologie, Heidelberg, Germany
[2]Institute of Cancer Research, Joint Department of Physics, Sutton, United Kingdom

Introduction: Helical Tomotherapy offers the possibility to correct a rotational setup error of the patient via adaption of the gantry angles of a treatment plan (roll correction). This is only possible in combination with image guidance, i.e. if MVCT setup scans are performed. We present an analysis of the dosimetric impact of small gantry angle changes on dose distributions for helical tomotherapy treatment plans. The goal was to estimate the expectable effects in case daily image guidance is not performed and thus a roll correction is not applied.

Materials and methods: In Image Guided Radiotherapy (IGRT), an incorrect patient position can be corrected by repositioning of the treatment couch. If no robotic couch is available, as is the case for most linacs, the correction is limited to a shift in X-, Y- and Z-direction. For helical tomotherapy treatments, an additional roll correction that can correct a rotation of the patient about the longitudinal axis (IEC Y) is possible. The value for the roll correction is determined by matching the rotation of the MVCT scan to the planning CT, and it is then applied to the treatment plan by shifting the gantry angle at which the treatment starts (and all following gantry angles accordingly). At our institution, typical values for the roll correction range from 0° to 2°, sometimes 3°.

A method for recalculation of dose distributions for helical tomotherapy with VOXELPLAN, a treatment planning system developed at the German Cancer Research Center DKFZ, has been established. CT, Structure Set and dose distributions calculated in the tomotherapy TPS can be imported via Dicom Export into VOXELPLAN. The treatment plans are then converted into a format readable by VOXELPLAN by assignment of one static treatment field for each projection and a target point-shift for each field, and dose is recalculated with a pencil beam algorithm. Details regarding the algorithm and validation of the dose calculation for static tomotherapy beams have already been presented [1]. The individual dose calculation furthermore has been validated using several phantom and patient treatment plans.

In this work, dose was recalculated in VOXELPLAN for 4 different tomotherapy patient cases. For a prostate case, a breast case and a head and neck case, gantry angle shifts of 0°, 0.5°, 1° and 2° were used. Additionally, for a scalp case, gantry angle shifts of 0° and 2° were used. All dose distributions were compared against the recalculated 0° dose distribution, and dose differences as well as dose-volume histograms (DVH) and corresponding statistics were evaluated.

Results: The DVH comparisons for all 4 cases between no gantry shift and a 2° gantry shift are shown in figure 1 (a)-(d). For the target volumes of the prostate and the scalp case, the DVHs show no variations. For the head and neck case, the minimal dose to the boost volume dropped from 88.2 to 80.4 percent of the prescribed dose For the breast case, the minimal dose to the supraclavicular volume decreased by 3.1 % while the mean dose to the PTV increased by 0.6 %. Dose statistics for selected organs at risk are shown in table 1 for all gantry angle shifts and all patient cases. It should be noted that the use of a pencil beam algorithm for dose recalculation might lead to a systematic error of the reported change in lung dose for the breast case [2].

Conclusion: Small changes of the gantry angle of the order of 1 – 2 degrees can have an impact on dose distributions in helical tomotherapy, especially for organs at risk. It could be shown that the extent of the effect is dependent on the treatment indication, as the indication determines the position of the target volumes with respect to the machine isocenter as well as sizes and positions of organs at risk. The fact that a patient rotation can be corrected in helical tomotherapy contributes to a higher accuracy in patient positioning. In order to exploit this advantage, daily MVCT scans are necessary.

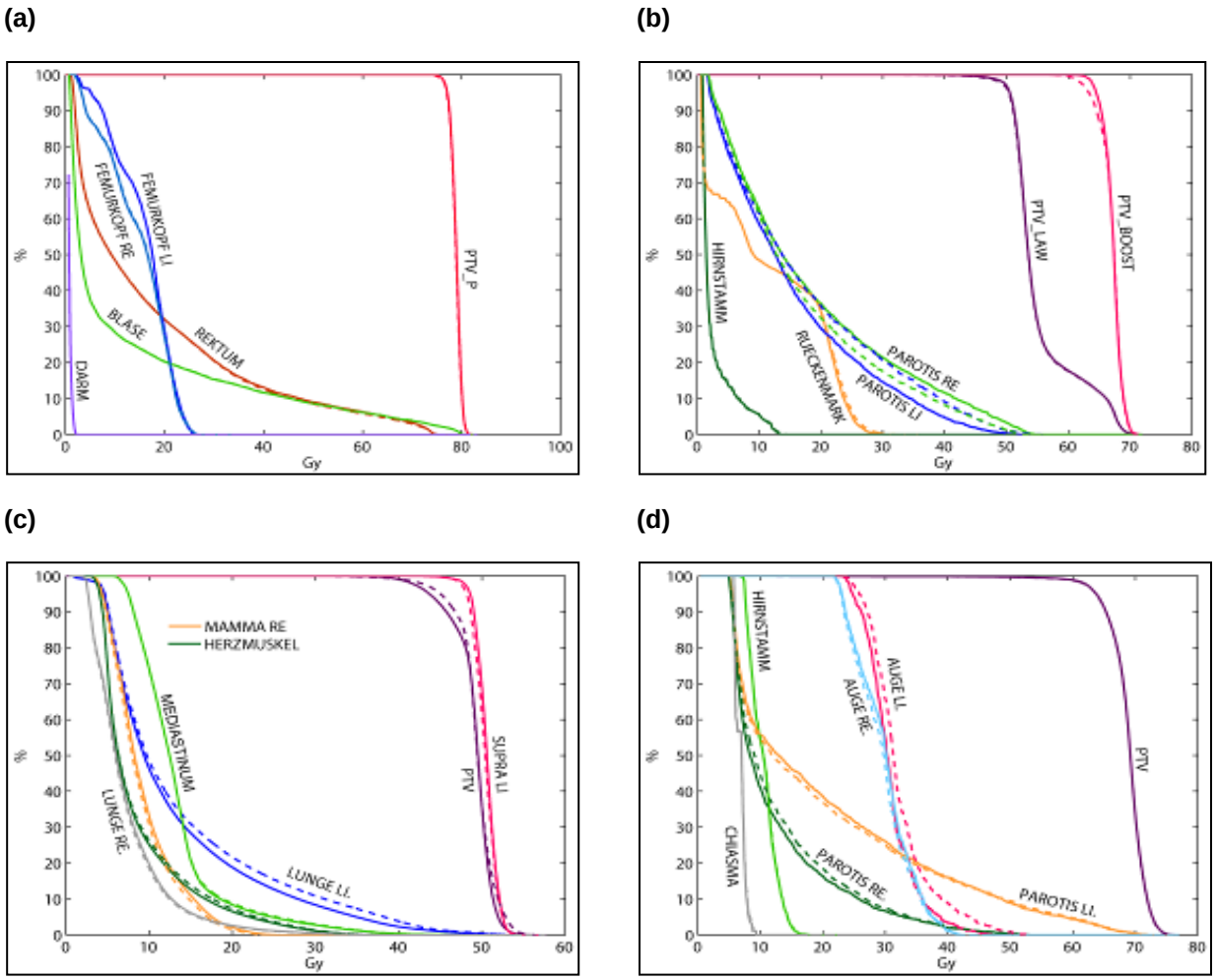

Fig. 1: DVH comparisons for all 4 patient cases between no gantry angle shift (solid lines) and a 2° gantry angle shift (dashed lines). (a) prostate case, (b) head and neck case, (c) breast case, (d) scalp case.

		0.5° shift	1° shift	2° shift
Head and Neck				
Right Parotid:	V_30%	-3.4%	-6.6%	-11.4 %
Right Parotid:	D_mean	-2.3 % (-0.8 %)	-4.1 % (-1.4 %)	-7.9 % (-1.4 %)
Right Parotid:	D_max	-0.6 % (-0.5 %)	-1.8 % (-1.4 %)	-2.8 % (-2.2 %)
Left Parotid:	V_30 %	+4.9 %	+9.5 %	+22.6 %
Left Parotid:	D_mean	+2.6 % (+0.8 %)	+5.7 % (+1.6 %)	+12.8 %(+3.6 %)
Left Parotid:	D_max	+2.6 % (+2.0 %)	+5.0 % (+3.8 %)	+6.3 % (+4.8 %)
Breast				
Left Lung:	D_mean	+1.5 % (+0.4 %)	+3.5 % (+0.9 %)	+6.9 % (+1.8 %)
Left Lung:	V_30 %	+2.5 %	+5.0 %	+9.6 %
Scalp				
Right Eye:	D_mean	-	-	-1.4 % (-0.6 %)
Right Eye:	D_max	-	-	+0.2 % (+0.1 %)
Left Eye:	D_mean	-	-	+5.0 % (+2.2 %)
Left Eye:	D_max	-	-	+13.7 %(+9.2 %)

Tab. 1: Dose statistics for selected organs at risk. Differences in mean dose (D_mean) and maximum dose (D_max) are given as local percentage deviations, and additionally in brackets in percent of the prescribed dose. V_30 % is the volume that received at least 30 % of the prescribed dose.

References

[1] Klüter, S., Siggel, M., Schubert, K., Lissner, S., Nill, S.: Validierung eines Pencil-Kernel Algorithmus zur Dosisberechnung für Tomotherapie. Abstractband der 43. Jahrestagung der Deutschen Gesellschaft für Medizinische Physik, Jena, 2012, S.424

[2] Knöös, T., Wieslander, E., Cozzi, L., Brink, C., Fogliata, A., Albers, D., Nyström, H., Lassen, S.: Comparison of dose calculation algorithms for treatment planning in external photon beam therapy for clinical situations. Phys. Med. Biol. (51) 2006, S.5785-5807

28 On the dose to air cavities in SBRT lung treatments

M. F. Belosi[1], A. Fogliata[1], G. Nicolini[1], E. Vanetti de Palma[1], A. Clivio[1], L. Cozzi[1]
[1]Oncology Institute of Southern Switzerland, Radiotherapy, Bellinzona, Switzerland

Object/purpose: To investigate the possible impact of the presence of air cavity regions in lung, which surround a CTV to be treated for early stage of NSCLC in stereotactical regimen.

Material and methods: Five patients presenting NSCLC and treated with 3 sessions of 18 Gy each where selected. They presented air cavities in the lung (HU<-950), in small regions surrounding the GTV, and included in the PTV. Targets were delineated based on ITV on 4DCT datasets. VMAT (RapidArc) plans with two partial arcs by 6 MV FFF beams were optimized with PRO3 algorithm, running the optimization twice, with the second accounting for the accurate final dose calculated after the first optimization run; this allowed to obtain a good target coverage also in presence of air cavities. Doses were calculated with Acuros XB (vers. 11). In the present work doses were reported as both dose to medium and dose to water, as well as using different ranges of densities (and HU) to discriminate lung and air tissue in the very low density region. The default “physical material table” used by Acuros XB included air from 0.0 to 0.0204 g/cm3, lung from 0.011 to 0.6242 g/cm3 (with linear interpolation in the overlapping range); a customized table included only lung from 0.0 to 0.6242 g/cm3. The same optimization was used for all the dose calculations, and was based on dose to medium using the default material table; the same MU were set for all plans. Structures were delineated to distinguish the PTV region with HU<-900 and HU<-950.

Results: The dose to the target composed by soft tissue did not show significant differences for both dose to medium and dose to water, as well as using the two material tables, using the same MLC movement and MU. Differences were presented in the air cavities (PTV with HU<-950 and in some cases where HU<-900). Dose to water reported doses in such regions higher than dose to medium in a range of 3 to 10 %, depending on the PTV volume, on the air cavity size, on their location relative to the GTV in soft tissue. Results similar to those obtained with dose to water reporting were shown for the customized material table excluding air.

Conclusion: Particular attention on dose distribution should be paid when air cavities surround the GTV in NSCLC to be treated with stereotactical targets. The meaning of the dose delivered to such regions when dose to medium or dose to water are reported should be deeply understood when prescribing a treatment. This concept should be related to a multiplicity of factors, from the pure medium density and probability to have clonogenic cells in such regions, to the clinical need to which dose level such air cavities should be treated, in relation to the possible microscopic spread of the disease. The choice of margins from GTV to CTV should refer also to such a concept. From a more physical and pragmatical perspective, care has to be paid to the delivered dose also in correlation with movement (4DCT) and possible patient mispositioning.

29 Analytical uncertainty quantification for scanned proton pencil beams in heterogeneous media

M. Bangert[1], F. Zimmermann[1], P. Hennig[2]
[1]DKFZ – German Cancer Research Center, Medical Physics in Radiation Oncology, Heidelberg, Germany
[2]Max Planck Institute for Intelligent Systems, Empirical Inference, Tübingen, Germany

Introduction: Proton dose distributions which are calculated during planning usually do not correspond to the dose distributions which are delivered during treatment. Patient motion, range uncertainties, and deficient immobilization may compromise the validity of the original dose calculation. In the presence of lateral inhomogeneities, setup uncertainties are particularly challenging as small misalignments of the patient may result in substantial alterations of the geometrical proton range within the patient anatomy.

We have recently introduced the concept of analytical probabilistic modeling (APM) for uncertainty quantification in radiation treatment planning [1]. APM enables the analytical calculation of the mean and (co)variance of intensity-modulated dose distributions subject to range and setup uncertainties at realistic computational cost. It accounts for the complex dosimetric interplay of random and systematic errors in fractionated radiotherapy and incorporates structured correlations in the underlying sources of uncertainty.

Here, we present work in progress regarding a conceptual extension of APM for probabilistic proton dose calculations which are subject to setup uncertainties in the presence of pronounced lateral inhomogeneities.

Materials and methods: The basis of APM for proton dose calculation is a functional representation of the dose distribution $d(X)$ which can be integrated analytically against a Gaussian probability distribution $\mathcal{N}(X)$ over the uncertain input parameters X. Hence, the integrals required for expectation value and (co)variance calculation remain analytically tractable and can efficiently be evaluated without sampling.

$$E[d(X)] = \int dX\, \mathcal{N}(X) d(X) \quad \text{and} \quad Var[d(X)] = \int dX\, \mathcal{N}(X) d(X)^2 - E[d(X)]^2$$

For protons, this approach has recently been validated with a pencil beam algorithm [2] that parameterizes the lateral dose profile $L(X)$ with one Gaussian $\mathcal{N}^L(X)$ and the depth dose $Z(X)$ with a superposition of ten Gaussians $\mathcal{N}_i^Z(X)$ [1]. To overcome the limitations of pencil beam algorithms in heterogeneities, we suggest a Gaussian fine sampling of the lateral proton dose distribution according to [3] (Figure 1).

$$L(X) = \mathcal{N}^L(X) = \sum \omega_i \mathcal{N}_i^L(X) = \sum \mathcal{N}_i^\omega(\Delta)\, \mathcal{N}_i^L(X)$$

Thereby, we incorporate off-axis density scaling into the dose calculation. The APM formalism remains valid as both the fine sampling base functions $\mathcal{N}_i^L(X)$and their weights ω_i are of Gaussian form (Figure 1) and can consequently be integrated analytically against Gaussian uncertainties. In particular, it is possible to simulate a lateral shift of the proton dose, i.e., setup uncertainties, simply by changing the weights of the contributing sub pencil beams according to a Gaussian function (Figure 1). Additional ray tracings to compute the radiological depths for shifted scenarios are not necessary.

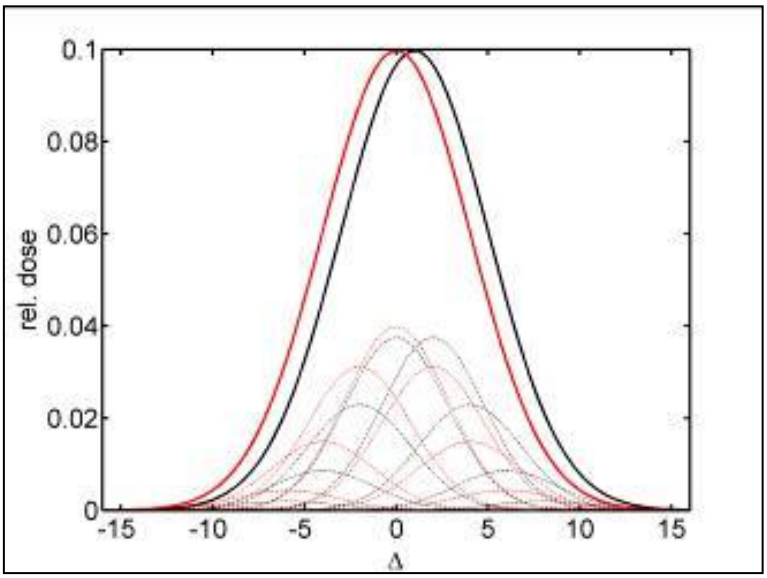

Fig. 1: A lateral proton dose profile (solid black) of Gaussian shape can be decomposed into Gaussian components (dashed black). By changing the relative weights of these components (dashed red), it is possible to model a lateral shift of the original dose (solid red). Here, we use a fine sampling distance of 0.33mm *of the individual components.*

Our analytical calculations are evaluated against Monte Carlo simulations [4] for a single pencil beam in a 2D water phantom featuring a lateral $20.0mm$ air inhomogeneity at $50.0mm$ depth (Fig. 2). We assume a proton energy of $128.0MeV \pm 0.9\,\%$ [5] and an initial proton fluence of Gaussian shape with $\sigma = 3.4mm$ [6]. For the simulation of setup uncertainties we assume a Gaussian distribution over the lateral patient position with $\sigma_S = 3.0mm$. For benchmarking, 73 Monte Carlo simulations with 10^5 histories are performed on a regular grid covering $\pm 3\sigma_S$ and weighted according their probability to estimate the expectation value and the standard deviation of the dose.

Results: Figure 2 (a) compares APM versus Monte Carlo simulations for (a) the nominal proton dose calculation. Figures 2 (b) and (c) compare the expectation value and the standard deviation under the influence of lateral setup uncertainties. Corresponding □-index calculations applying a global 3 % dose and 2mm distance criterion yield pass rates of 98.7 %, 99.4 %, and 99.1 %. At the lateral dose fall-offs of the two peaks towards the central axis (indicated by the two arrows in figure 2(a)) we observe maximum deviations of up to 12 %, 10 %, and 6 % for the nominal dose, the expectation value, and the standard deviation, respectively. While the Monte Carlo simulations [4] require more than 10h of computation time, APM requires only a couple of seconds with a Matlab prototype.

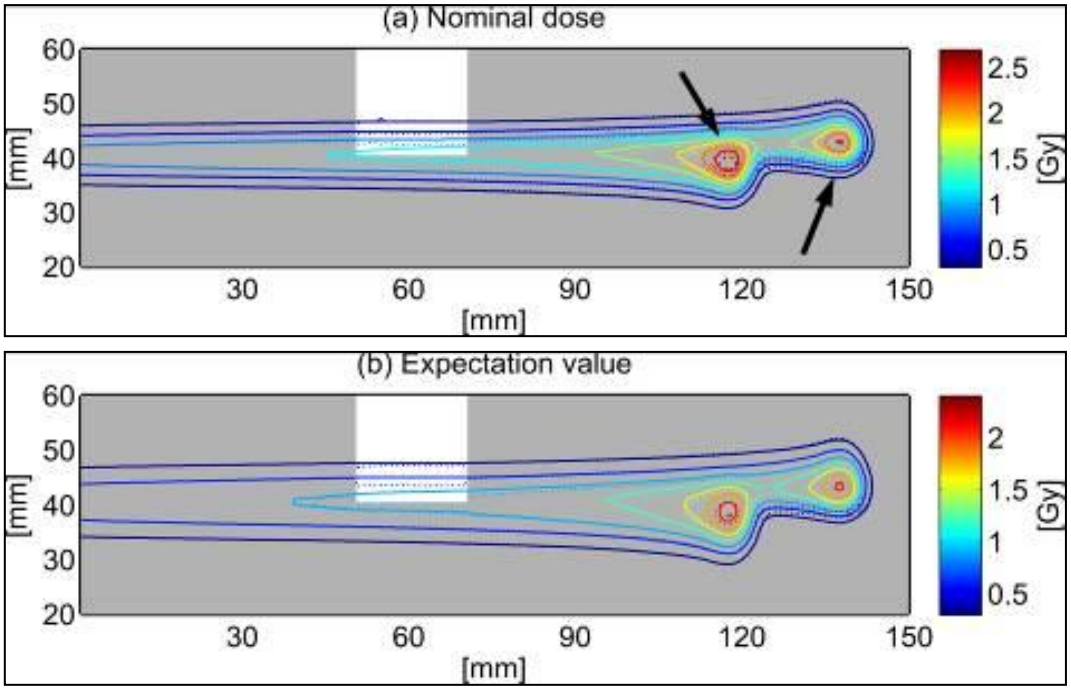

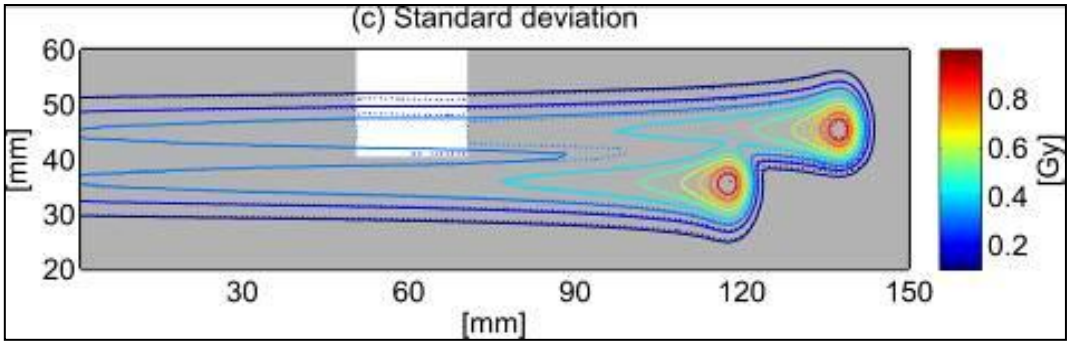

Fig. 2: Monte Carlo simulations (dotted) vs. analytical calculations (solid) in a water tank (grey) featuring a lateral air inhomogeneity (white). The nominal dose distributions are shown in (a), the expectation values of the dose assuming a Gaussian setup error in lateral direction with 3mm standard deviation are shown in (b), and the standard deviations of the dose are shown in (c). Arrows indicate regions of maximum discrepancy.

Discussion and conclusion: We demonstrated that APM can be applied for proton dose calculations facilitating pencil beam decomposition. Compared to conventional pencil beam algorithms, fine sampling improves the dose calculation accuracy in heterogeneous anatomies. APM uncertainty quantification was orders of magnitude faster than the benchmarking Monte Carlo simulations [4]. The observed deviations between analytical calculation and Monte Carlo simulation, however, suggest further refinements of the APM algorithm to include nuclear corrections [3] and two-dimensional scaling [7] for the lateral scattering model. Incorporating these refinements is conceptually unproblematic and subject of ongoing work in our research group. As the discrepancies between Monte Carlo simulations and APM are likely to decrease when going from challenging toy problems to realistic patient cases featuring thousands of superimposing pencil beams, we envisage manifold applications of APM in the context of robust planning in the future.

References

[1] M Bangert et al.: Analytical probabilistic modeling for radiation therapy treatment planning 2013 Phys. Med. Biol. 58
[2] L Hong et al.: A pencil beam algorithm for proton dose calculations 1996 Phys. Med. Biol. 41
[3] M Soukup et al.: A pencil beam algorithm for intensity modulated proton therapy derived from Monte Carlo simulations 2005 Phys. Med. Biol. 50
[4] J Perl et al.: TOPAS – An innovative proton Monte Carlo platform for research and clinical applications 2012 Med. Phys. 39
[5] H Paganetti et al.: Clinical implementation of full Monte Carlo dose calculation in proton beam therapy 2008 Phys. Med. Biol. 53
[6] S Safai et al.: Improving the precision and performance of proton pencil beam scanning 2012 Translational Cancer Res. 1
[7] H Szymanowski & U Oelfke: Two-dimensional pencil beam scaling: an improved proton dose algorithm for heterogeneous media 2002 Phys. Med. Biol. 47

Session 6 – Hybrid systems for imaging (PET/MR, PET/CT, X/MR)

Chairs: S. Ziegler (Munich/DE), H. Quick (Duisburg/DE)

30 Introductory lecture: Current challenges in PET/MR hybrid imaging

H. Quick[1]
[1]University of Duisburg-Essen, Erwin L. Hahn Institute for MR Imaging, Essen, Germany

Following PET/CT and SPECT/CT, PET/MR hybrid imaging, with its clinical introduction in the year 2010, is the most recent addition to the palette of hybrid imaging modalities. PET/MR synergistically combines excellent soft tissue contrast and various functional imaging parameters provided by MR with high sensitivity and quantification of radiotracer metabolism provided by PET. Integrated PET/MR systems furthermore offer the ability to acquire hybrid imaging data simultaneously.

While clinical evaluation of PET/MR in oncology, neurology, pediatric oncology and cardiovascular disease now is under way; integrated PET/MR demands for new technologies and innovative solutions, currently subject to interdisciplinary research. To fully assess the diagnostic potential of PET/MR, several technical challenges have to be considered: attenuation correction (AC) of the patient tissues in PET/MR has to be based on MR-images since CT attenuation information is missing. MR-based AC of patient tissues is currently hampered by a limited number of tissue classes and undercorrection of bone tissue. In the context of MR-based AC, the limited field-of-view of the MR system component may lead to MR signal truncation in body parts where the patient anatomy exceeds these spatial constraints of the MR field-of-view (e.g. the arms). This may lead to an undercorrection of patient tissues and, consequently, quantification of PET data might be biased in these regions. Not only the patient tissues but also hardware components in the PET field-of-view, such as radiofrequency (RF) coils and the system patient table, need to be corrected as well. Here, CT-based templates of the individual hardware components are used for AC in PET/MR.

The current challenges in PET/MR hybrid imaging will be introduced and recent solutions and developments will be discussed in this introductory lecture.

References

[1] Quick HH, Integrated PET/MR. J Magn Reson Imag. 2014; 39:243-58.

31 Brain PET attenuation correction using MR UTE pulse sequences

J. Cabello[1], S. G. Nekolla[1], S. I. Ziegler[1]
[1]Klinikum rechts der Isar, Nuklearmedizin, Munich, Germany

Introduction: With the current advent of PET/MR scanners attenuation correction (AC) has to be performed with image data obtained from the MR. This task is not as simple as with CT since the MR provides information about the tissue proton density, which is not directly related to tissue density. Currently a Dixon pulse sequence is used in clinical routine. The Dixon pulse sequence provides high contrast between soft tissues, but signal from bone tissue is not obtained. Such classification is acceptable for full body scan, but for brain PET/MR it has been shown that 15 %-30 % error can occur, more enhanced near the bone [1]. Another comparison between quantitative results obtained using a Dixon pulse sequence and ultra-short echo-time (UTE)-based AC showed 15 %-20 % activity underestimation errors compared to CT [2]. Several approaches using a combination of MR sequences have shown highly quantitative results [3-5]. The purpose of this study is to show the accuracy of an attenuation map based on UTE sequences information from MR for AC in brain PET.

Materials and methods: The Biograph mMR (Siemens Healthcare) scanner is a PET/MR tomograph that simultaneously acquires PET and MR information. An UTE sequence is an MR sequence with very short echo-time (TE) to detect measurable signal from tissues with short T2 relaxation component. In this work we delineated the location of the bone tissue from the R2 map [6], defined as

$$R2 = \frac{\ln I_{E1} - \ln I_{E2}}{TE2 - TE1}, \quad [1]$$

obtained from two consecutive UTE echoes. I_{E1} and I_{E2} are the intensity images of each echo image, UTE1 and UTE2, and TE1 and TE2 are the echo-times of each image, 0.07 ms and 2.46 ms in the mMR.

Before calculating the R2 map, a binary mask ($B_{air,ext}$), corresponding to air and represented as the non-zero voxels outside the head, was calculated by automatic histogram-based thresholding. Then, the R2 map was calculated. All those voxels in the R2 map with values below zero were set to zero because they correspond to soft tissue.

Differentiating bone and air, has been agreed by several studies [1,6], is the most challenging task. The R2 map does not show differences between bone tissue and air. Therefore, air information inside the head was extracted as an additional step. By looking at the statistical properties of the non-zero voxels in UTE1 outside the head contained in $B_{air,ext}$, we characterized the voxels that correspond to air inside the head, appending these voxels to $B_{air,ext}$. The mean (μ_{air}) and the standard deviation (σ_{air}) of the voxels in the UTE1 image included in $B_{air,ext}$ were calculated. Subsequently, those voxels inside the head with intensity value below $\mu_{air}+\sigma_{air}$ were used to create an additional binary air mask ($B_{air,int}$) which was merged to $B_{air,ext}$, producing a general air mask (B_{air}). Small blobs contained in B_{air} were removed using binary operations.

To scale the intensity values of the R2 map to the attenuation coefficients required for AC, the voxels corresponding to hard tissue and soft tissue have to be classified. After normalizing the R2 map (maximum value of R2 map is set to 1), since the intensity histogram of the R2 map is highly skewed, the mode represents the intensity distribution better than the mean. Therefore, the mode (M_{R2}) and the standard deviation (σ_{R2}) of the non-zero voxels contained in the R2 map were calculated. All those voxels with intensity above $M_{R2}+\sigma_{R2}$ were classified as hard tissue; otherwise they were classified as soft tissue. The R2 map voxels corresponding to hard tissue were scaled so the mean value is 0.151 cm^{-1}, and the R2 map voxels corresponding to soft tissue were scaled so the mean value is 0.096 cm^{-1}, producing the μ-map to be used for reconstruction.

The noise in the resulting hard tissue from the R2 map was higher than that observed in typical CT data. Hence, the μ-map was smoothed with a Gaussian mask to reduce the noise and to match the image resolution of the MR data (UTE1) to the PET data. Since the point spread function of the PET scanner is 4.2 mm [7], and the voxel size of the MR data is 1.56 mm/voxel, the σ of the Gaussian mask was set to 3 voxels.

For comparison purposes a PET/CT scan of the same patient was acquired prior to the PET/MR scan. The CT scan was resampled and registered rigidly to match the UTE images.

Reconstruction was performed using OS-EM (21 subsets, 3 iterations) using no AC, a Dixon—based μ-map (routinely used in clinic), a CT—based μ-map and the proposed UTE—based μ-map.

Results: Figure 1 shows two representative axial slices from the CT scan, the same two slices from the R2 map and the corresponding two slices of the post-processed μ-map.

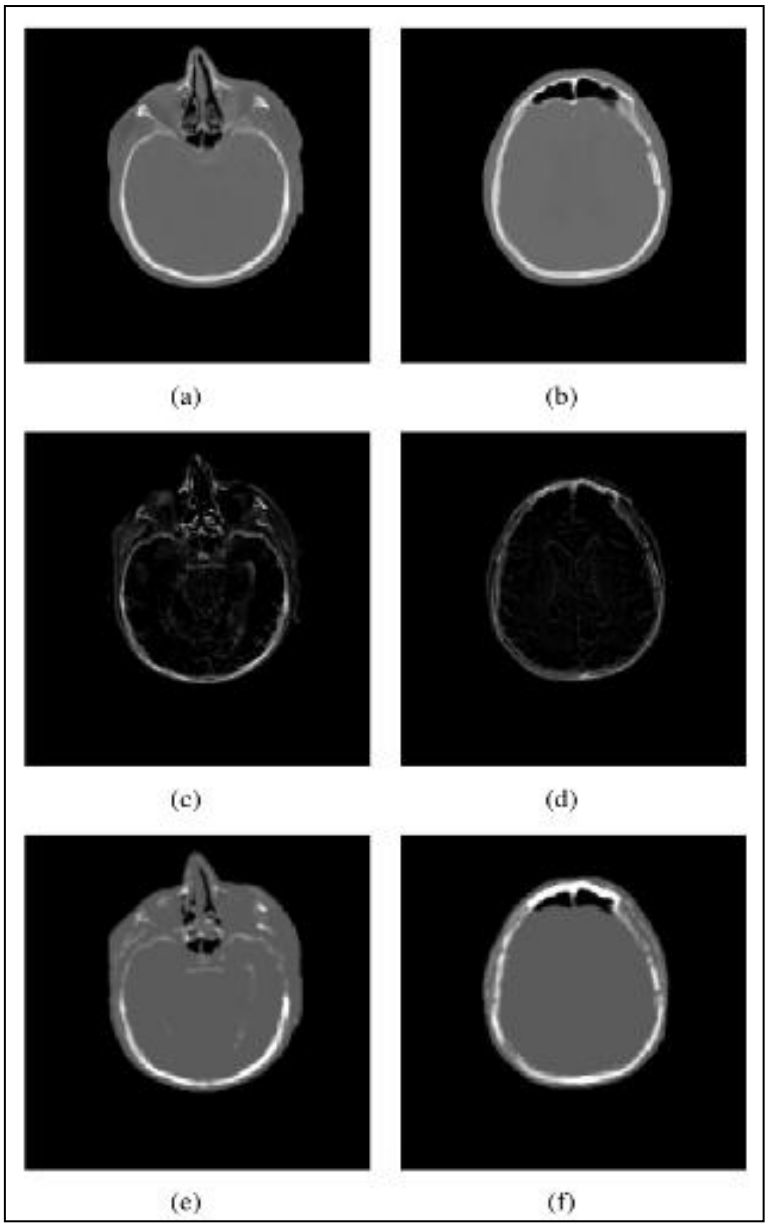

Fig. 1: CT (a,b), R2 map (c,d) and MR-based µ-map (e,f) of two representative axial slices.

Figure 2 shows an axial slice of the reconstructed images using the different µ-maps mentioned above, including the µ-map shown in Figure 1. To assess the quantitative accuracy a region of interest (RoI) was manually drawn at the level of the cerebellum in the image reconstructed using the CT—based µ-map. Using the same RoI in every reconstructed dataset Figure 3 shows the activity measured in each case. Using the CT—based µ-map image as reference, the relative difference was 34 % for the non AC case, 13 % for the Dixon—based µ-map, 12 % for the UTE—based µ-map provided by the mMR scanner, and 0.8 % for the proposed UTE—based µ-map.

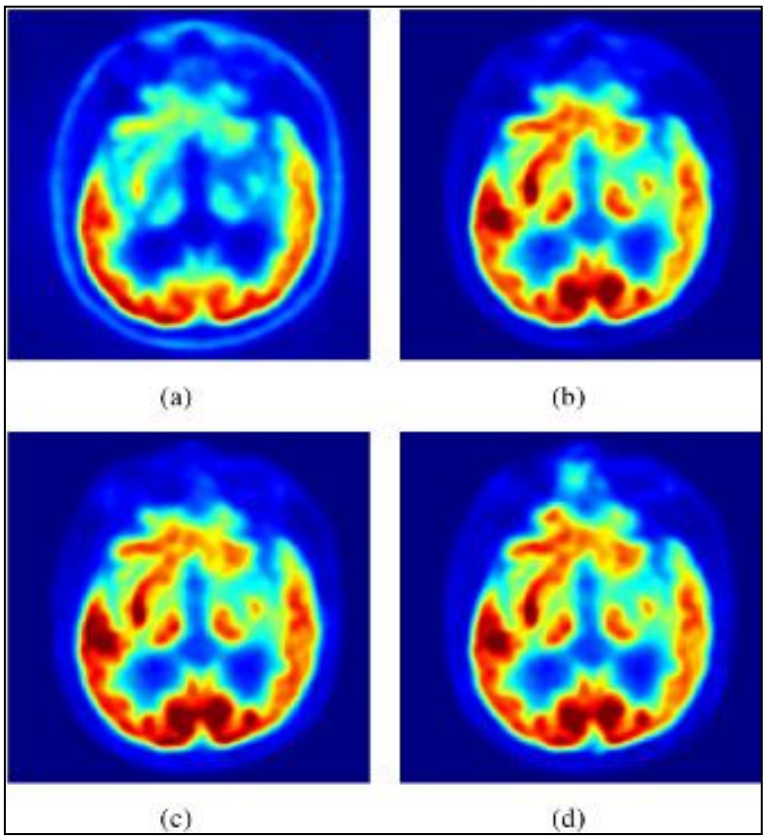

Fig. 2: Axial slice reconstructed without AC (a), with Dixon—based μ-map (b), with CT—based μ-map (c) and with the proposed UTE—based μ-map (d).

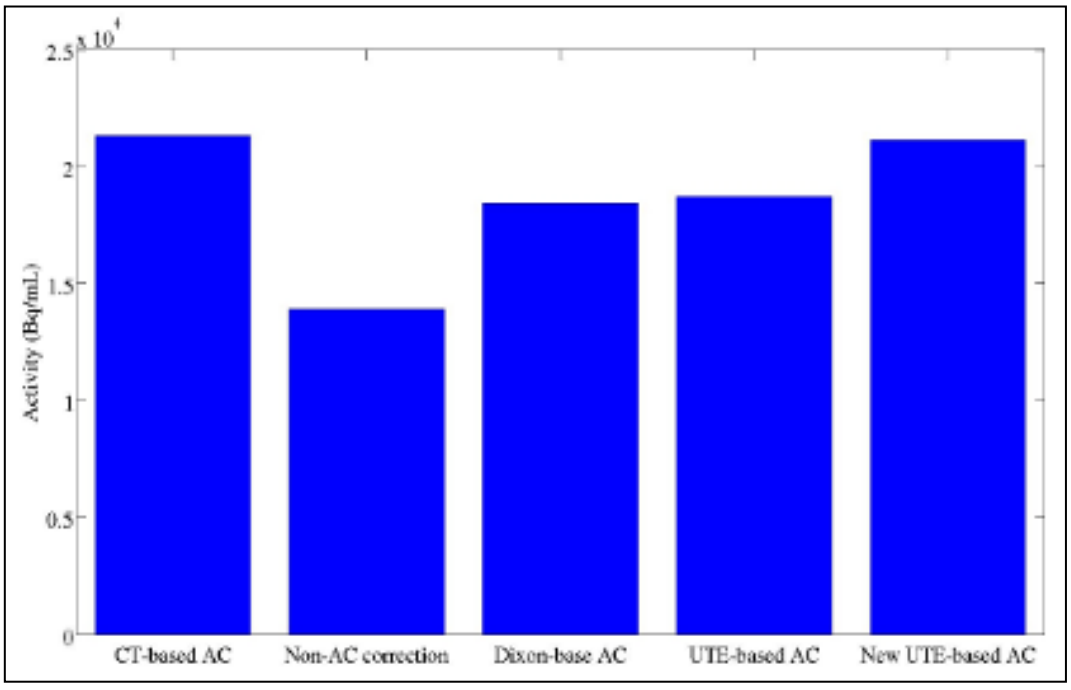

Fig. 3: Activity measured in the area of cerebellum in reconstructed images using the different μ-maps.

Summary: Compared to CT data, a visually similar MR-based attenuation map was obtained. Small structural differences were observed which could be due to registration inaccuracies. The air mask matched well in general to the one measured with CT. After reconstruction using the different μ-maps, quantitative comparison showed that the proposed UTE—based μ-map produced the most accurate results compared to CT—based μ-map with a relative difference of 0.8 % in the cerebellum.

References

[1] C. Catana et al., “Is Accurate Bone Segmentation Required for MR-based PET Attenuation Correction?” in Proceedings of the International Society for Magnetic Resonance in Medicine, no. 17, 2009.

[2] J. Dickson et al., “A comparison of CT- and MR-based attenuation correction in neurological PET,” European Journal of Nuclear Medicine and Molecular Imaging, pp. 1–14, 2014.

[3] A. S. Ribeiro et al., “Hybrid approach for attenuation correction in PET/MR scanners,” Nuclear Instruments and Methods in Physics Research Section A, vol. 734, Part B, no. 0, pp. 166 – 170, 2014.

[4] V. Schulz et al., “Automatic, three-segment, MR-based attenuation correction for whole-body PET/MR data,” European Journal of Nuclear Medicine and Molecular Imaging, vol. 38, no. 1, pp. 138–152, 2011.

[5] Y. Berker et al., “MRI-Based Attenuation Correction for Hybrid PET/MRI Systems: A 4-Class Tissue Segmentation Technique Using a Combined Ultrashort-Echo-Time/Dixon MRI Sequence,” Journal of Nuclear Medicine, vol. 53, no. 5, pp. 796–804, 2012.

[6] V. Keereman et al., “MRI-Based Attenuation Correction for PET/MRI Using Ultrashort Echo Time Sequences,” Journal of Nuclear Medicine, vol. 51, no. 5, pp. 812–818, 2010.

[7] G. Delso et al., “Performance measurements of the Siemens mMR integrated whole-body PET/MR scanner,” Journal of Nuclear Medicine, vol. 52, no. 12, pp. 1914–1922, 2011.

32 Automatic delineation of tumor volumes by co-segmentation of hybrid PET/MRI data

S. Leibfarth[1], C. Siegel[2], S. Welz[2], F. Eckert[2], H. Schmidt[3], N. Schwenzer[3], D. Zips[2], D. Thorwarth[1]
[1]University Hospital Tübingen, Section for Biomedical Physics, Tübingen, Germany
[2]University Hospital Tübingen, Department of Radiation Oncology, Tübingen, Germany
[3]University Hospital Tübingen, Department of Diagnostic and Inverventional Radiology, Tübingen, Germany

Introduction: Combined PET/MRI systems may be highly beneficial for tumor delineation and characterization due to the provided anatomical, molecular and functional information. In this study, an automatic algorithm for the segmentation of head and neck (HN) tumors on basis of PET/MRI data was developed to integrate the complementary information provided by MRI and PET into radiotherapy treatment planning [1].

Materials and methods: N=10 HN patient datasets from FDG-PET/MRI were available. Tumor sites were oropharynx (N=4), hypopharynx (N=2), nasopharynx (N=1), sinunasal (N=1), cervical lymph node (N=1) and mandibula (N=1). The FDG-PET and a clinical T2-weighted MRI acquisition (STIR) were used for tumor volume delineation. Voxel spacings for PET and MRI were 2.8 x 2.8 x 2.0 mm^3 and 0.7 x 0.7 x 4.8 mm^3, respectively.

First, a sigmoidal mapping function assigning PET voxel information to tumor probability (PMF_{pet}) was defined, where the location of the inflexion point corresponding to a probability of 0.5 was set to 40 % SUV_{max} (Fig. 1II). From the respective tumor probability map (Fig. 1III) a PET tumor volume (V_{petGTV}) was automatically derived using a probability of 0.5 as threshold, being equivalent to a relative threshold segmentation of the PET data with 40 % SUV_{max}. Moreover, a margin of 10 mm extending this volume was defined ($V_{petMarg}$) (Fig. 1A). Histograms of MRI values in both V_{petGTV} and $V_{petMarg}$ were generated, and corresponding probability density functions PDF_{mrGTV} and PDF_{mrMarg} were derived by kernel density estimation (Fig. 1B). Using these PDFs, a function mapping MR values to tumor probabilities (PMF_{mr}) was defined by a combination of two sigmoidal functions (Fig. 1C), and the corresponding MR tumor probability map was derived (Fig. 1D). Finally, a combined probability map was defined by a weighted sum of the PET and MR derived probability maps (Fig. 1E). On this combined map, the tumor volume was derived by a threshold Level Set (thLS) segmentation method [2] ($thLS_{cb}$) (Fig. 1Fbc). For evaluation purposes, also a thLS segmentation on the MR probability map only was performed ($thLS_{mr}$) (Fig. 1Fmr).

To evaluate segmentation accuracy, manual delineations of the tumor volume were provided by three experienced radiation oncologists for each patient. The radiation oncologists were advised to delineate for each patient both a volume considering PET data only and a volume considering MRI data only. For evaluation of both inter-observer variability and variability between observers and automatic segmentation method, mutual Dice Similarity Index (DSI) values were determined comparing the union of the PET and MRI volumes derived by each observer to method $thLS_{cb}$. An additional evaluation compared the manual MRI volumes to method $thLS_{mr}$.

Results: Results of the quantitative evaluation of the variability between tumor volumes are shown in Fig. 3A for MR-based volumes and in Fig. 3B for PET/MR-based volumes. Median DSI values around 0.7 were obtained for both the mutual comparison of manually derived volumes and the comparison of manually versus automatically derived contours, which shows that significant differences in tumor delineation occur in both cases. The highest differences were obtained for patients for which the MR image only showed low contrast between tumor and surrounding normal tissue.

The variabilities between automatic and manual contours are comparable with the inter-observer variabilities, which confirms the validity of the proposed segmentation method.

Conclusion: PET and MR imaging data exhibit complementary information. However, this study shows that information from PET data can be used to derive an appropriate MRI tumor probability mapping function. The proposed algorithm for PET/MRI tumor volume segmentation yields accurate results with respect to inter-observer variability.

The observed variabilities could probably be reduced by including additional complementary imaging data (e.g. additional MRI sequences). Such complementary imaging information can easily be integrated in the proposed segmentation algorithm by corresponding probability maps.

Using this probability-based segmentation method in combination with an accurate image registration algorithm allows for the integration of PET/MR imaging data into radiotherapy treatment planning.

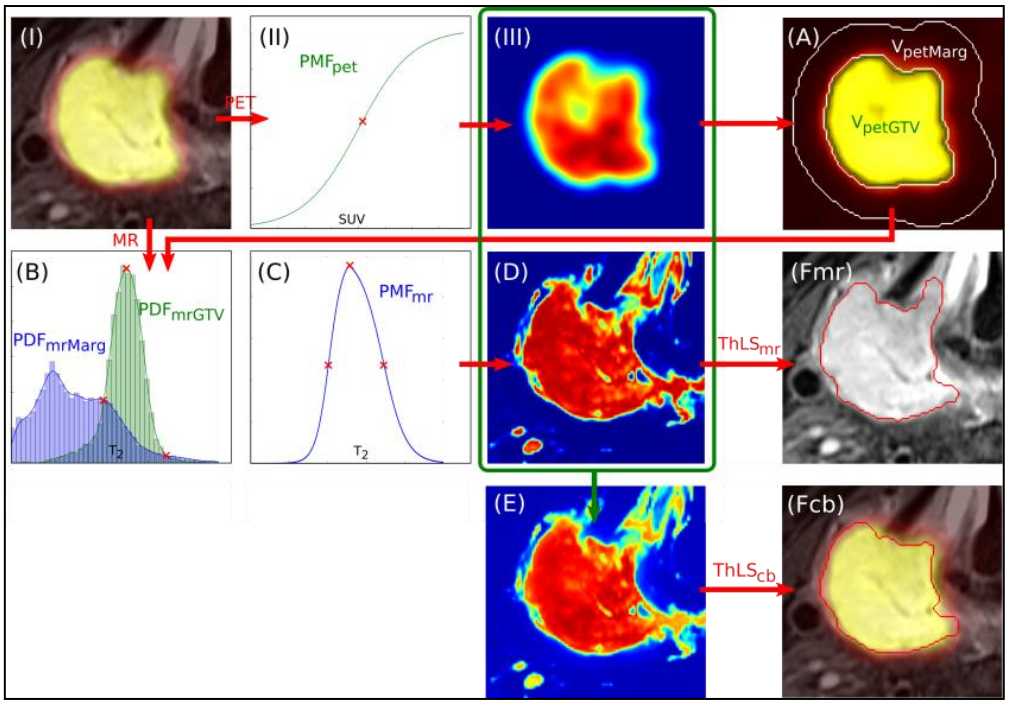

Fig. 1: Schematic illustration of the proposed automatic segmentation methods to create a contour derived from a MRI-based tumor probability map (Fmr) and the combination of a PET- and a MRI-based probability map (Fcb). The respective steps are explained in the text above.

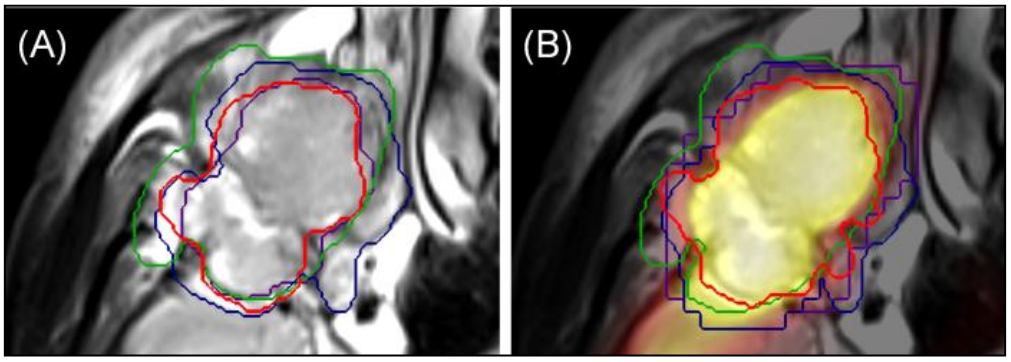

Fig. 2: Segmentations for exemplary patient with nasopharyngeal carcinoma. Tumor volumes are shown for (A) MR-based volumes from the three observers (purple, blue, green) and automatically derived volume with $thLS_{mr}$ (red) and (B) PET/MR-based volumes from the three observers (purple, blue, green) and automatically derived volume with $thLS_{cb}$ (red).

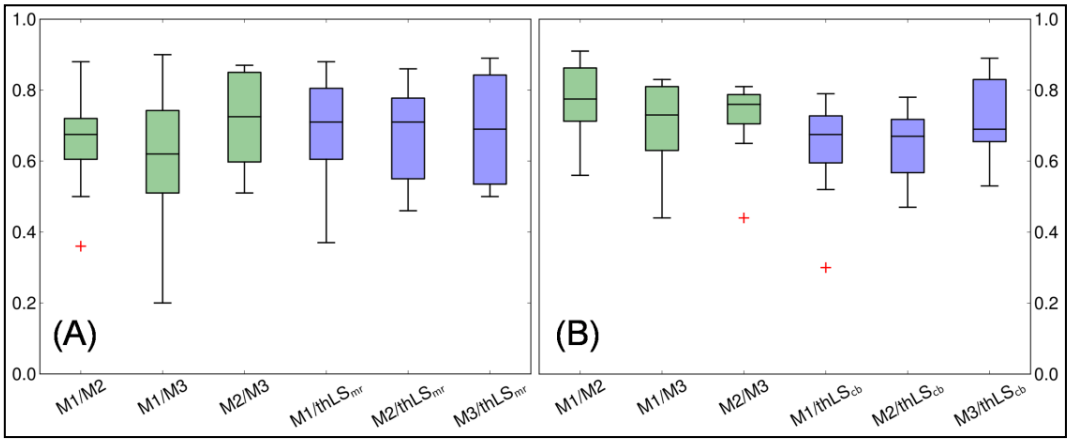

Fig. 3: Boxplots showing the distribution of mutual DSI values of tumor volumes from the three different observers (M1/M2/M3) and the automatic method (A) for the MRI derived tumor volumes (with $thLS_{mr}$ as automatic method), (B) for the PET/MRI derived tumor volumes (with $thLS_{cb}$ as automatic method). Each boxplot represents the distribution within the patient cohort (N=10).

References

[1] Becker, Zaidi; *Br J Radiol* 2014; 87(1036): 20130677

[2] Insight Segmentation and Registration Toolkit, *www.itk.org*

33 First pre-clinical measurements using Traveling Wave Magnetic Particle Imaging

P. Vogel[1,2], S. Herz[3], M. A. Rückert[1], C. Brede[4], T. Kampf[1], S. Veldhoen[3], P. M. Jakob[1,2], A. Beilhack[4], T. A. Bley[3]
V. C. Behr[1]
[1]University of Würzburg, Experimental Physics 5 (Biophysics), Würzburg, Germany
[2]Research Center for Magnetic Resonance Bavaria e.V., MRB, Würzburg, Germany
[3]Würzburg University Hospital, Diagnostic and Interventional Radiology, Würzburg, Germany
[4]Würzburg University Hospital, Medicine II, Würzburg, Germany

Introduction: Multimodal imaging systems like PET/CT and PET/MRI have become increasingly important in pre-clinical research and clinical practice. MRI and CT provide tissue contrast at high spatial resolution, whereas functional imaging methods such as PET or SPECT offer high sensitivity using radioactive substances, which provides a better and more specific diagnosis and monitoring of physiological processes and diseases.

A novel imaging modality, magnetic particle imaging (MPI), is a very sensitive and fast way of directly detecting superparamagnetic iron-oxide nanoparticles (SPION) in 3D. As PET or SPECT, MPI also relies on anatomical background information obtained by MRT or CT, but offers the benefit of a radiation-free tracer. The combination of MPI and novel approaches for functionalizing markers with iron-oxide nanoparticles provides the opportunity for a better understanding of diseases and improved diagnostics.

In a pre-clinical test the feasibility of TWMPI/MRI fusion imaging was investigated to visualize immune cells labeled with specific antibodies conjugated to SPIONs in a murine graft-versus-host disease (GVHD) model using MPI and MRI fusion imaging.

Materials and methods: Acute GVHD was induced in myeloablated (9 Gy) BALB/c mice (H-2d, CD90.2) by transplantation of allogeneic luciferase (luc+) CD90.1+ T cells from transgenic C57BL/6.L2G85 mice with T cell depleted bone marrow cells from C57BL/6 wild type mice. Controls received T cell depleted bone marrow [1]. Three days after transplantation *in-vivo* bioluminescence imaging (BLI) was performed before i.v. application of a donor T cell specific CD90.1 monoclonal antibody conjugated to SPIONs (see fig. 1 a). After 3 h and 6 h respectively *ex-vivo* MPI and MRI measurements were performed using the same animal holder to ensure identical positioning of mice for both modalities (fig. 1 b).

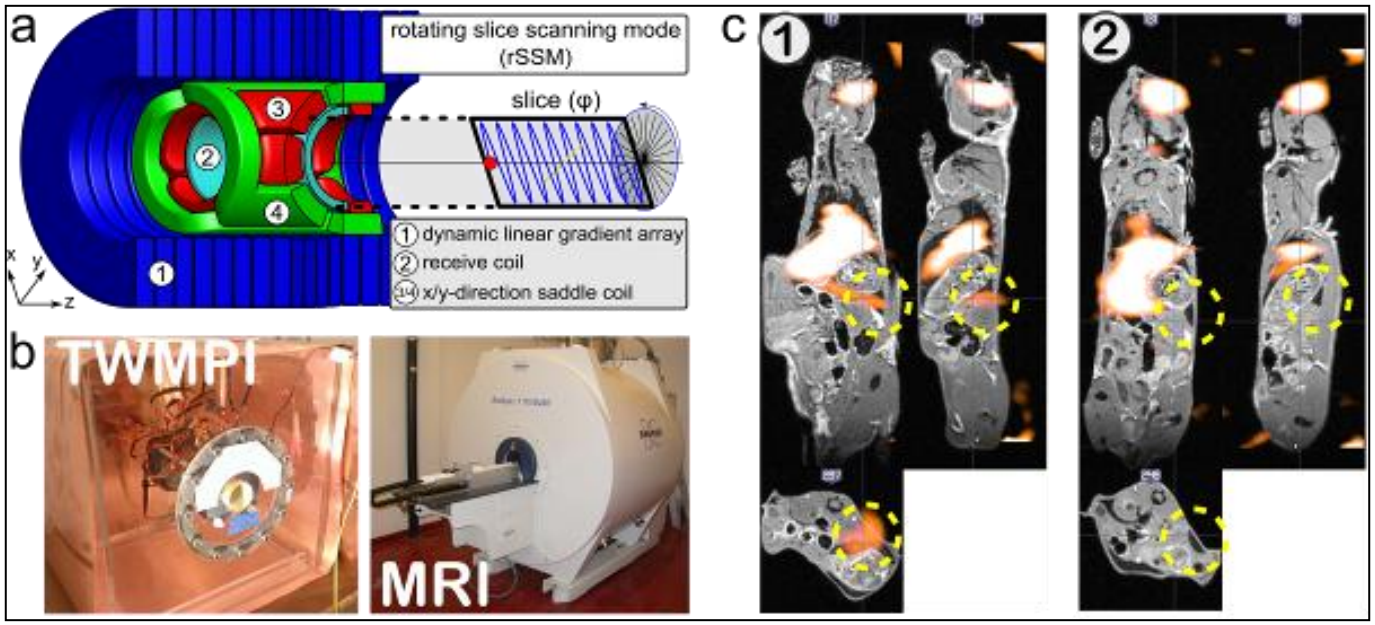

Fig. 1: ***(a)*** *Sketch of the traveling wave MPI scanner:* ***(1)*** *the dynamic linear gradient array (dLGA) and two saddle coil pairs* ***(3/4)*** *generate and move the field free point (FFP), which is necessary for the signal generation and the encoding of the MPI signal. For scanning a whole 3D volume a rotating slice scanning mode (rSSM) is used.* ***(b)*** *Images of the TWMPI and MRI scanner: After the injection of the labeled antibodies the mice were sacrificed and measured subsequently.* ***(c)*** *MPI/MRI fusion images:* ***(1)*** *High MPI signal in the spleen of a BALB/c mouse during acute GVHD.* ***(2)*** *Control shows only baseline signal.*

The 3D MPI measurements were performed using a homemade traveling wave MPI (TWMPI) scanner with an isotropic resolution of about 2 mm (gradient: 4 T/m, FOV: 65 x 25 x 25 mm^3) [2]. Figure 1 a shows a sketch of the TWMPI scanner, which uses a dynamic linear gradient array (dLGA) (1) and two perpendicular saddle coil pairs (3/4) for generating and moving a field free point (FFP) with a high gradient through the 3D volume. The MPI signal can be detected while moving

the FFP over a SPION ensemble. The changing of the magnetic field flips the magnetization of the SPIONs, which induces a signal in the receive coil (2). For a 3D TWMPI dataset 72 slices over an angle of 180° were taken in a total acquisition time of 7.2 s (rotating slice scanning mode – rSSM) [3].

MRI was performed on a 7 T scanner with a 300 mm horizontal bore (Bruker Biospin with BGA12 gradient system). A 3D T2-weighted rapid acquisition with relaxation enhancement (RARE) sequence was used to provide anatomical background. MPI and MRI data were reconstructed and fused manually using markers for co-registration.

Results: In figure 1 c the co-registered TWMPI and MRI measurements of the BALB/c mouse during acute GVHD (1) and the control mouse (2) are shown. The TWMPI data (yellow overlay) shows high signal in liver and spleen (1), whereas the bone marrow controls only show signal in liver. All mice also show high signal in the region of the right eye (orbita) coming from residues of the retroorbital injection of the labeled antibodies. *In-vivo* BLI as reference standard showed high signals in the cervical, mesenteric and splenic region indicating alloreactive T cells within secondary lymphoid organs during acute GVHD.

Conclusion: MPI is a promising imaging that can provide background-free visualization of the distribution of targeted SPIONs. These first results successfully demonstrate the feasibility of visualizing antibody-labeled alloreactive T cells in a murine graft-versus-host disease model.

References

[1] C. Brede, et al.: Mapping immune processes in intact tissues at cellular resolution, *J Clin Invest*, 122(12), 4439-46, Dec. 2012.

[2] P. Vogel, et al.: Traveling Wave Magnetic Particle Imaging, *IEEE Trans. Med. Imaging*, vol. 33(2), p. 1-8, Feb. 2014.

[3] P. Vogel, at al.: Rotating Slice Scanning Mode for Traveling Wave MPI, *IEEE Proceedings on IWMPI 2014*, Berlin.

34 Carbon ion radiography and tomography using beam scanning and a range telescope

I. Rinaldi[1,2], T. Marcelos[1], L. Magallanes[1,2], S. Brons[3], O. Jäkel[2], M. Takechi[4], B. Voss[4], K. Parodi[1]
[1]Ludwig Maximilians University, Dept. of Medical Physics, Garching/Munich, Germany
[2]Heidelberg University Hospital, Dept. of Radiation Oncology, Heidelberg, Germany
[3]Heidelberg Ion Beam Therapy Center, Heidelberg, Germany
[4]GSI Helmholtzzentrum für Schwerionenforschung, Detector Laboratory, Darmstadt, Germany

Problem: Range uncertainties still represent a major obstacle to the full clinical exploitation of the superior physical selectivity offered by ion beams for highly conformal tumour therapy. Hence, increasing efforts are being devoted to the development of novel imaging techniques, which could replace or enhance X-ray CT imaging for determination of the patient stopping power properties at the treatment site. This work addresses the feasibility and imaging performances of a dedicated and relatively cost-effective setup based on a range telescope, coupled to actively scanned carbon ion beam delivery.

Materials and methods: Experimental investigations have been carried out to characterize the performances of a prototype range telescope setup based on a stack of 61 parallel-plate ionization chambers (PPIC), interleaved with 3 mm absorber plates of PMMA and read out synchronously to the scanned carbon ion beam delivery [1]. Targets of increasing complexity have been imaged, and the experimental results have been complemented by extensive Monte Carlo simulations addressing the effect of different acquisition parameters (e.g., number of particles and raster scan step size) on the water-equivalent-thickness (WET) quantification of radiographic projections.

Results: For a clinical-like scenario of an anthropomorphic Alderson head phantom, the experimental setup with a dedicated data analysis scheme demonstrated a reasonable WET agreement with respect to a calibrated X-ray digitally reconstructed radiography, resulting in 87 % passing ratio for a 3 % - 3 mm □-index analysis. Larger deviations especially encountered in high density regions hinted to a potential improvement of the stopping power calibration curve when using carbon ion based imaging. Initial simulations of carbon ion radiographies in controlled phantom arrangements also suggest a rather robust range assessment even for low dose (ca. 0.2 mGy) irradiation scenarios, which are not yet experimentally accessible.

Conclusion: Initial experimental and simulation results support the feasibility of the prototype range telescope for carbon ion radiography applications at reasonable dose levels. Ongoing efforts aiming at further improvements of the experimental setup and of the data processing scheme will be also discussed.

Acknowledgement: This project is supported by the German Research Foundation (DFG). T.M. also acknowledges funding from the European Commission under the ERASMUS exchange program.

References

[1] I Rinaldi, S Brons, J Gordon, R Panse, B Voss, O Jäkel and K Parodi, “Experimental characterization of a prototype detector system for carbon ion radiography and tomography”, Phys. Med. Biol. 58 413, 2013

35 Analysis of ^{90}Y distribution with a Biograph mCT

A. A. Attarwala[1], F. Molina-Duran[1], K. Anett Büsing[1], M. Tapner[2], S. Schönberg[1], K. Willowson[3], G. Glatting[1]
[1]Medizinische Fakultät Mannheim der Universität Heidelberg, Strahlentherapie und Radioonkologie, Mannheim, Germany
[2]Sirtex, Sydney, Australia
[3]University of Sydney, Sydney, Australia

Aim: Yttrium-90 is known to have a low positron emission decay of 32 ppm that may allow for personalized dosimetry of liver cancer therapy with ^{90}Y labelled microspheres. The aim of this work was to image and quantify ^{90}Y so that accurate predictions of the absorbed dose can be made.

Introduction: Liver cancer is one of the fifth most often detected cancer worldwide and has a poor prognosis for both primary and secondary tumors. Treatment options include a surgery or external beam therapy. However, multiple tumors in the liver are very challenging to remove by surgery and normal liver parenchyma has a lower tolerance for radiation compared to tumors. Therefore, Selective Internal Radiation Therapy (SIRT) has been developed. This procedure is based on microspheres containing ^{90}Y that are transported to the tumor via the arterial blood flow thus providing a highly localized dose to shrink the tumor. Post treatment activity quantification until recently was performed using the bremsstrahlung spectrum of ^{90}Y captured with single photon emission computed tomography (SPECT) [1, 2]. However, this method suffers from inaccurate quantification due to the continuous energy spectrum of ^{90}Y. In 2010, Lhommel et al. performed a feasibility study to obtain the biodistribution of ^{90}Y using its very low fraction (32 ppm) of positron production. The study showed higher accuracy for dose distribution assessments imaging with a time-of-flight (TOF) PET/CT [3]. Activity quantification with PET is challenging due to the low statistics of positron emission decay of ^{90}Y combined with the high additional background from the bremsstrahlung and the limited system resolution.

In 2012, Willowson et al. performed a quantitative experimental study with the IEC NEMA phantom to analyze these factors and concluded that the method of imaging ^{90}Y with a PET/CT has potential for deriving accurate dosimetric data [4].

Materials and methods: The measurements were performed within the QUEST study (University of Sydney, Australia). A NEMA IEC body phantom containing 6 fillable spheres (diameter range 10-37 mm) and a cold insert was used to measure the ^{90}Y distribution with a Biograph mCT PET/CT (Siemens, Erlangen, Germany). The phantom was prepared with a sphere to background ratio of 8:1 and contained a total ^{90}Y activity of 3 GBq. Measurements were conducted over a period of one week (0, 3, 5 and 7 d). The acquisition protocol consisted of 2 bed positions at 15 min/bed.

Images were reconstructed with 3D ordered subset expectation maximization (OSEM) and resolution recovery (TrueX) for iteration numbers of 1-12 with 21 subsets, both with and without TOF and with CT based attenuation and scatter correction. Convergence of algorithms was assessed based on regions-of-interest (ROI) analysis of the background (100 voxels) and lung insert (25 voxels). The activity recovery was assessed using 4 voxels centred in the 17 mm diameter sphere, as it was the smallest sphere to offer adequate visibility. Percent contrast and background variability were assessed equivalent to NEMA Nu 2-2007 definitions.

Results: All algorithms converged with 1 iteration and 21 (TOF) and 24 (non-TOF) subsets. With higher iterations the images became noisier and the 13 mm sphere was no longer discernible. The 17 mm sphere on Day 0 and the 22 mm sphere on Day 3 were the smallest spheres to offer adequate visibility for analysis. Table 1 below shows the effect of different reconstruction algorithms on the percentage of contrast recovered for the 17 mm hot sphere, the cold insert and the corresponding percentage of the background variability.

Algorithm	% Contrast 17 mm sphere	% Contrast cold insert	% Background variability
TrueX TOF	64 ± 21	73 ± 22	21 ± 11
OSEM TOF	67 ± 35	79 ± 46	42 ± 25
TrueX	37 ± 18	72 ± 58	18 ± 7
OSEM	27 ± 19	68 ± 60	29 ± 15

Tab. 1: Contrast and background variability for Day 0 image acquisition for different reconstruction algorithms.

Conclusion: Of the investigated algorithms, for quantitative image reconstruction the TrueX-TOF algorithm (1 iteration, 21 subsets) seemed to offer advantages over the other algorithms.

References

[1] Minarik D, Ljungberg M, Segars P, Gleisner KS. Evaluation of Quantitative Planar ^{90}Y Bremsstrahlung Whole-Body Imaging. Phys Med Biol 2009; 54: 5873-83.

[2] Minarik D, Sjogreen-Gleisner K, Linden O, Wingardh K, Tennvall J, Strand SE, Ljungberg M. ^{90}Y Bremsstrahlung Imaging for Absorbed-Dose Assessment in High-Dose Radioimmunotherapy. J Nucl Med 2010; 51: 1974-8.

[3] Lhommel R, Elmbt L, Goffette P, Eynde M, Jamar F, Pauwels S, Walrand S. Feasibility of ^{90}Y TOF PET-Based Dosimetry in Liver Metastasis Therapy Using SIR-Spheres. Eur J Nucl Med Mol Imaging 2010; 37: 1654-62.

[4] Willowson K, Forwood N, Jakoby BW, Smith AM, Bailey DL. Quantitative ^{90}Y Image Reconstruction in PET. Med Phys 2012; 39: 7153-9.

36 Variation of PET/CT performance, quality control standards and adherence to FDG-imaging guidelines in Austria

I. Rausch[1,2], H. Bergmann[1], B. Geist[2], A. Hirtl[2], M. P. Schaffarich[1], M. Hacker[2], T. Beyer[1]
[1]Medical University Vienna, Centre for Medical Physics and Biomedical Engineering, Vienna, Austria
[2]Medical University Vienna, Division of Nuclear Medicine, Department of Biomedical Imaging and Image-guided Therapy, Vienna, Austria

Introduction: Combined PET/CT has become a standard method in clinical imaging and clinical trials. Nevertheless, diagnostic quality and quantitative accuracy of PET/CT images are sensitive to various parameters such as reconstruction settings or acquisition protocols. Therefore, adequate quality control (QC) mechanisms and protocol standardization are essential for inter- and intra-scan accuracy. Despite efforts of aligning PET/CT users on a common standard [1–4], large variability has been observed [5,6]. Our goal was to gather information on clinical operations among all clinical PET/CT users in Austria to get an overview on the adherence to published imaging and quality control guidelines.
Materials and methods

A written survey composed of 68 questions related to A) PET/CT centre and installation, B) FDG oncology imaging protocols and C) standard QC procedures was conducted between November and December of 2013 among all 12 Austrian PET/CT centres. In addition, a NEMA-NU2 2012 image quality phantom test was performed using standard whole-body imaging settings on all PET/CT systems with a sphere-to-background ratio of 4. Recovery Coefficients (RC) were calculated for each sphere and PET/CT system.

Results : A) 13 PET/CT systems are installed in 12 Nuclear Medicine departments of public hospitals. 8/12 centres have min. 5-y experience in PET. Over 86 % of PET/CT examinations are performed for oncology indications.

B) Average fasting prior to FDG-PET/CT is 7.2 (4-12) h. All sites measure blood glucose levels while using different cut-offs (64 %: 150 mg/dL). Weight-based activity injection is performed at 81 % sites with a mean FDG activity of 4.1 MBq/kg. Average FDG uptake time is 57 (45-75) min. All sites employ CT contrast agents (variation from 1 %-95 % of the patients). All sites report SUVmax.

C) A large variation in the frequency of performed QC measurements was observed. QC phantom measurements revealed significant differences in RCs (see figure 1) with the RCs being at the upper acceptance limit [7].

Conclusion: Variations in FDG-PET/CT protocol parameters among all Austrian PET/CT users were observed, but less pronounced than those reported in 2011 [5,6]. However, standardized QC procedures need to be implemented to improve quantitative accuracy across the centres.

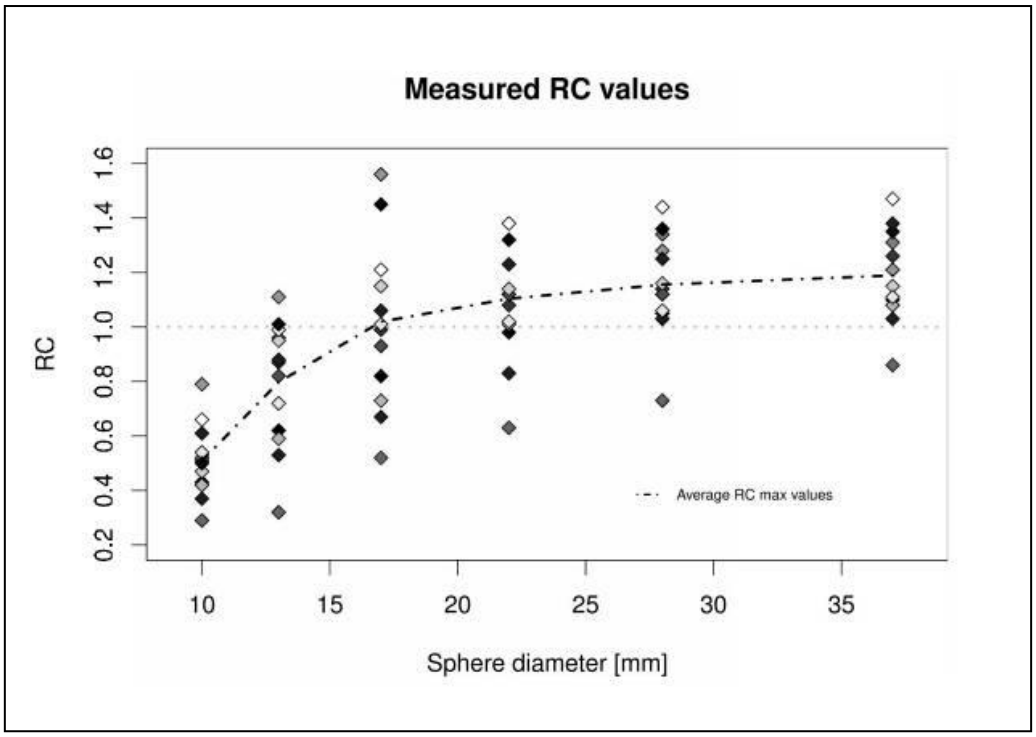

Fig. 4: Variability of measured, maximum RC values among Austrian PET/CT centres; the points represent the 13 PET/CT systems.

References

[1] Boellaard R, O'Doherty MJ, Weber WA, Mottaghy FM, Lonsdale MN, Stroobants SG, et al. FDG PET and PET/CT: EANM procedure guidelines for tumour PET imaging: version 1.0. Eur J Nucl Med Mol Imaging [Internet]. 2010;37:181–200. Available from: http://dx.doi.org/10.1007/s00259-009-1297-4

[2] Delbeke D, Coleman RE, Guiberteau MJ, Brown ML, Royal HD, Siegel BA, et al. Procedure guideline for tumor imaging with 18F-FDG PET/CT 1.0. J Nucl Med. 2006;47:885–95.

[3] Shankar LK, Hoffman JM, Bacharach S, Graham MM, Karp J, Lammertsma AA, et al. Consensus recommendations for the use of 18F-FDG PET as an indicator of therapeutic response in patients in National Cancer Institute Trials. J Nucl Med. 2006;47:1059–66.

[4] Krause BJ, Schwarzenböck S, Souvatzoglou M. FDG PET and PET/CT. Recent Results Cancer Res [Internet]. 2013;187:351–69. Available from: http://dx.doi.org/10.1007/978-3-642-10853-2_12

[5] Graham MM, Badawi RD, Wahl RL. Variations in PET/CT methodology for oncologic imaging at U.S. academic medical centers: an imaging response assessment team survey. J Nucl Med [Internet]. 2011;52:311–7. Available from: http://dx.doi.org/10.2967/jnumed.109.074104

[6] Beyer T, Czernin J, Freudenberg LS. Variations in clinical PET/CT operations: results of an international survey of active PET/CT users. J Nucl Med [Internet]. 2011;52:303–10. Available from: http://dx.doi.org/10.2967/jnumed.110.079624

[7] Boellaard R. Part 1: The EARL FDG-PET/CT Accreditation Programme & Guideline Developments: Results of more than 65 Successfully Accredited Sites and Future Perspectives. EANM´13, Lyon, Fr. 19.10-23.10.2013 [Internet]. Online (25.02.2014); Available from: http://earl.eanm.org/html/img/pool/EARL_2013_Boellaard_Part1.pdf

Session 7 – Radiation protection – medical physics service in clinical radio diagnostics and nuclear medicine

Chairs: G. Lutters (Aarau/CH), M. Wucherer (Nuremberg/DE)

37 Introductory lecture: Implementation of “Art. 74 StSV” and related requirements to the organisation of radioprotection

R. Simmler[1]
[1]Zurich, Switzerland

38 Medical physicists' implication in diagnostic CT in Switzerland: results on 45 CT-units

N. Ryckx[1], J. Bize[1], C. Elandoy[1], F. R. Verdun[1]
[1]Lausanne University Hospital, Institute for Radiation Physics, Lausanne, Switzerland

Purpose: Since January 1st 2008, the Swiss ordinance on radiation protection requires the involvement of a medical physicist to support the optimization process of medical imaging techniques using ionizing radiation. After a long process of implementation, this requirement is satisfied all over the country since the beginning of 2013. The goal of this contribution is to summarize the main results obtained in this first year of experience in computed tomography (CT).

Objectives and methodology: We assessed the output and clinical use of 45 CT units (18 % of all units installed in Switzerland) using a three-pronged approach. First, we assessed the output of the device in terms of effective vs. calculated CTDIvol, effective vs. predicted primary beam collimation and stability of Hounsfield numbers (HU) in water at different tube tensions. Secondly, we characterized the local chest and abdomen acquisition and reconstruction protocols using the Catphan® 600 phantom. Alongside, we set up a benchmarking protocol (15mGy CTDIvol, 2.5mm slice thickness, soft tissue convolution kernel, FBP) for machine cross-comparison. Lastly, we assessed the clinical use of the machine by analyzing an extract of a dozen clinical examinations per unit from the point of view of dosimetry (mean CTDIvol, mean and cumulated DLP, number of phases and estimated effective dose).

Results: We showed that there is a large disparity in the clinical use of the devices. 9 out of 45 units showed incorrect collimator settings, e.g. 4mm instead of 1mm. 21 out of 45 devices showed incorrectly- or non-calibrated HU, especially at lower kV settings. We witnessed also a large spread in reconstruction parameters, especially for reconstructed slice thickness, thus showing notable variations in low contrast detectability performances. Finally, the clinical use of the devices showed a rather large spread in the clinical practice. For example, estimated patient effective dose per abdomen examination lies at 18.7+/-12.7mSv (min: 2.0mSv – max: 112.0mSv). Chest and brain scans have a narrower dispersion, but patient effective dose is also spread by about a factor of 10 to 20 (between 1.4 and 20.3mSv for chest examinations, 1.0 and 6.6mSv for brain).

Conclusion: This protocol is aimed to be low time-demanding hence compatible to the clinical workflow of the visited centers. It appears of crucial importance to communicate the most common pitfalls reported to physicians and technologist thus promoting rising awareness. The lack of statistical precision (restricted subset of clinical examinations), however, will imply that we collaborate more closely with radiologists and technologists to assess clinical practice following a clinical demand rather than an anatomical region. Furthermore, low contrast sensitivity being a crucial parameter, even more since the introduction of iterative reconstruction techniques, an objective method using a model observer will be used to assess low contrast sensitivity.

39 Adherence to diagnostic reference levels in clinical CT imaging: An institutional review from Switzerland

M. Hentschel[1], I. Rausch[2], C. Kuderer[3], T. Beyer[2]
[1]Inselspital Bern, Department of Nuclear Medicine, Bern, Switzerland
[2]Medical University Vienna, Centre for Medical Physics and Biomedical Engineering, Vienna, Austria
[3]Landesklinikum Wiener Neustadt, Nuclear Medicine, Vienna, Austria

Purpose: The mean annual per capita effective dose in Switzerland is about 4 mSv, of which 1.2 mSv are attributed to medical imaging. In 2010 the Federal Office of Health (FOH) published diagnostic reference levels (DRL) for 21 common CT examinations related to the skull (4), neck (3), thorax (3), abdomen (4), pelvis (2), whole-body (1), skeletal system and extremities (2) and myocardium (2). There were 240 operating Radiology centres in Switzerland in 2012, all of which utilize CT scanners. Since 2012 all Swiss radiology centres are required to consult medical physicists on a regular basis with regards to radiation safety aspects of their clinical practice. As part of this task we report on the clinical use of CT and resulting routine patient exposure levels in imaging centres in Switzerland in relation to published DRL.

Materials and methods: 16 radiology centres were included in this survey. All centres were asked to document their CT practice over a minimum of 4 weeks of service. Documentation included the type of the CT system, deviations from standard CT protocols and DLP (mGy*cm) per scan series and FOH category. We report %-examinations that deviate from pre-defined standard and mean DLP for each category averaged across centres.

Results: All centres employed multi-slice spiral CT: 4-slice (2), 16-slice (6), 64-slice (6) and 128-slice (2); all with standard tube-current modulation (TCM) but only 2 with iterative CT reconstruction (IR) and 2 with automatic tube voltage selection (AVS). All centres reported deviations from standard protocols in 19 % (3 %-40 %) examinations leading to significantly increased and reduced patient exposure in 5 % (0.4 %-9 %) and 5 % (0 %-18 %), respectively.

Across all centres DRL of the skull, neck, thorax, whole-body and skeletal system were adhered to. Multi-centre dose levels exceeded the DRL for examinations of the abdomen (by 4 %-40 %), pelvis (6 %-22 %) and the heart (11 %-15 %).

Pilot evaluation of dose levels after on-site training, protocol optimization and the installation of TCM, AVS or IR indicate the potential to reduce patient exposure in thoracic and abdominal body regions.

Conclusion: This study indicates a tendency towards overdosing patients in selected routine CT imaging protocols performed at public and private radiology imaging centres in Switzerland. Subsequent operator training and the adoption of state-of-the-art dose reduction schemes helps reduce patient exposure. Recent advances in automatic dose tracking may support a refined, routine observation of exposure rates in clinical practice and, thus, help monitor and improve radiation hygiene in radiology practices.

Clinical relevance statement: Monitoring CT dose levels in clinical routine supports protocol optimization and dose reduction schemes.

40 Reduction of uterus dose in chest computed tomography by using a lead apron

E. Bohrer[1], M. Fiebich[1]
[1]Technische Hochschule Mittelhessen, Institut für medizinische Physik und Strahlenschutz, Gießen, Germany

Introduction: While in diagnostic radiography lead apron and gonad shielding are commonly used it is often ignored in CT examinations although it is required, [1, 2]. A study showed that in clinical chest CT scans the uterus dose could be reduced about 34 % [3]. However the aspect of shielding during the localizer radiograph was not included in this work as well as the use of different scanner settings for the localizer and the influence on patient dose. The aim of this study is to show that using lead apron in a chest CT examination including the localizer radiograph could lead to further dose reduction. Therefore the exposure during a female chest examination considering the localizer and shielding was calculated with Monte Carlo simulations.

Materials and methods: The chest CT examination was simulated by using GMctdospp [4], a graphical user interface especially for CT simulations based on the Monte Carlo user code EGSnrc. Therefore a Model of a 64 slice MDCT scanner (Somatom Definition DS, Siemens Healthcare, Forchheim, Germany) was implemented. Simulations were realized on the ICRP voxelphantom of the adult female. To examine the influence of shielding to the uterus and effective dose a lead apron over the pelvis with 0.25 mm Pb equivalent and an elliptical shape was integrated in the ICRP phantom in three ways, first covering the phantom and second with the phantom enveloped in the lead apron (Fig. 1) and third without apron. The CT scans were performed with 120 kVp, 90 effective mAs, 1 x 10 mm collimation, 1.5 pitch and a scan length of 220 mm. Additional localizer radiographs were simulated with factory setting of 120 kVp, 34 mA, 6 x 0.6 mm collimation, 5.4 s scan time, 512 mm scan length, with and without shielding and in different tube positions (ap, pa, lateral). The localizer doses were also calculated with lowest scanner settings of 80 kVp and 20 mA.

Results: There was no significant change in effective dose of 1.56 mSv when using lead apron. However the use of lead apron decreased the effective dose of the localizer radiograph up to 60 % when using the factory settings and up to 93 % using minimal scanner settings (Fig. 2). This caused a reduction of the effective dose of 6 % by factory settings and 9% by lowest scanner settings. The uterus dose in the localizer radiograph was higher than in the spiral CT scan when no shielding was used and when the ap- tube position was used while the phantom was covered with lead apron (Fig. 3). There the uterus dose was about 10 µSv. In the spiral CT scan the uterus dose decreased about 18 % when the phantom was wrapped in the lead apron. In the total chest examination with factory settings of the localizer radiograph the uterus dose decreased about 60 % and with minimal settings for the localizer about 73 %.

Conclusion: The localizer has the main contribution to the uterus dose. This is caused by the long scan range. For chest and abdomen-pelvis examinations the lateral localizer radiograph should be favored [5]. This also causes lower doses in the chest CT scan when using tube current modulation (TCM) [6]. Due to backscatter effects a localizer in pa- tube position should not be used when the patient is just covered with a lead apron. The spiral CT scan showed less reduction effect compared to the study of Danova et. al [3]. This was mainly caused by the shorter scan length and longer distance of the scan region to the uterus. The use of lead apron had to be handled carefully. If the lead apron is used during the localizer and in a CT scanner with TCM the shielding had to be far enough from the following CT scan range and when the modulation function is based on the localizer radiograph the lowest scanner settings may not be applicable. However in CT scanners with fixed localizer scan length the unnecessary exposure caused by the long scan length could be reduced with lead apron. Shielding and optimized scanner settings for the localizer radiograph could reduce patient dose significantly and had to be used especially for pregnant women.

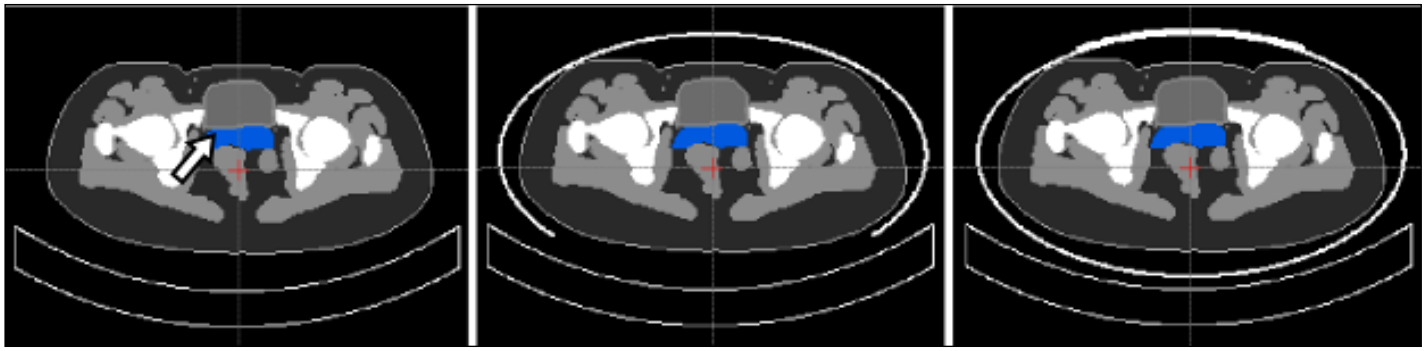

Fig. 1: The ICRP female Voxelphantom with implemented table without a lead apron (left), covered with a lead apron (centre) and enveloped in a lead apron (right). The uterus is marked with an arrow (left).

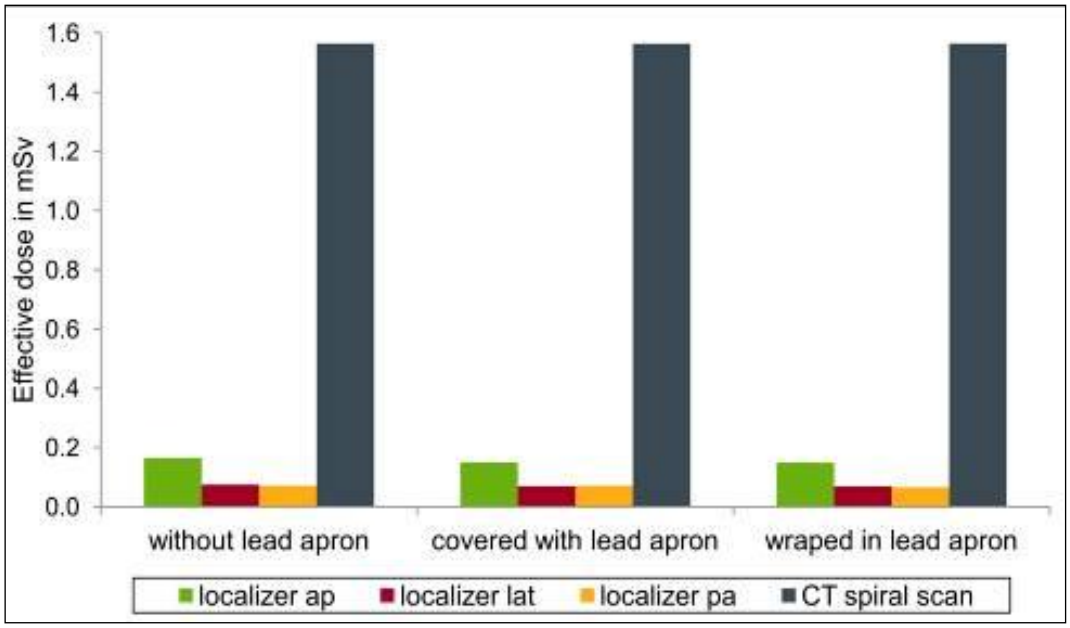

Fig. 2: The influence of shielding to the effective dose of spiral CT scan and localizer radiograph with factory settings.

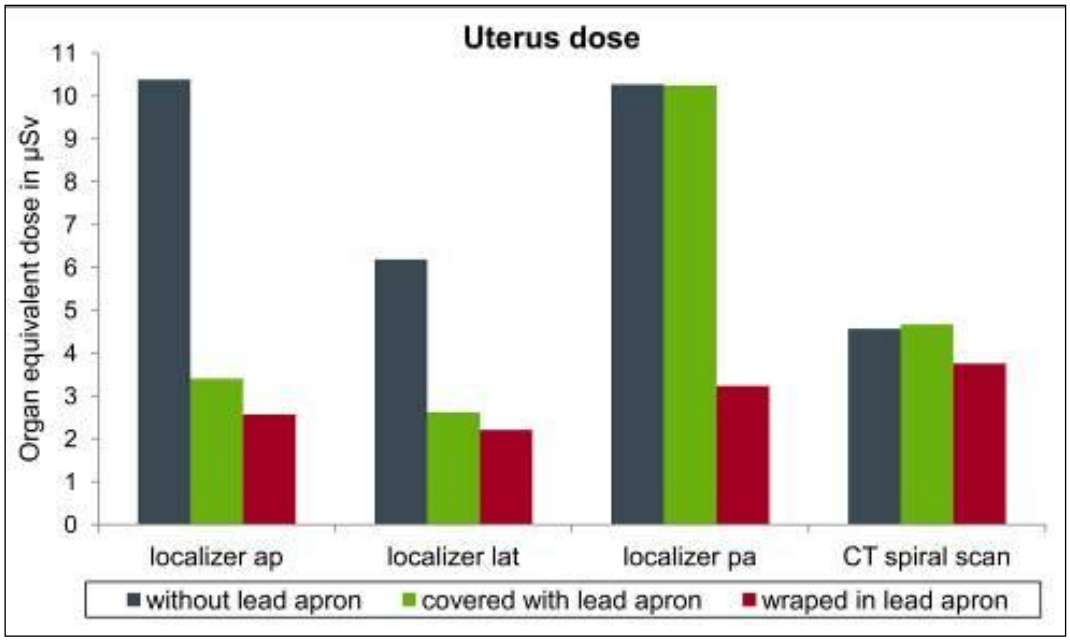

Fig. 3:The influence of shielding to the uterus dose of spiral CT scan and localizer radiograph with factory settings.

References

[1] Verordnung über den Schutz vor Schäden durch Röntgenstrahlung (Röntgenverordnung – RöV § 25), http://www.bfs.de/de/bfs/recht/rsh/volltext/1A_Atomrecht/1A_14_RoeV_1011.pdf (10.04.2014)

[2] Verordnung vom 20. Januar 1998 über den Strahlenschutz bei medizinischen Röntgenanlagen (Röntgenverordnung – Anhang 2, Art. 2), http://www.gesetze.ch/inh/inhsub814.542.1.htm (10.04.2014)

[3] Danova, D., Keil B., Kästner B., et al.,Reduction of uterus dose in clinical thoracic computed tomography, Fortschr Röntgenstr 2010

[4] Schmidt R., Wulf J., Kästner B., et al., Monte Carlo based calculation of patient exposure in X-ray CTexaminations, 4th European Conference of the International Federation for Medical and Biological Engineering, 2009; Vol. 22: 2487-2490

[5] Schmidt, B., Saltybaeva, N., Kolditz, D. Kalender, W. A., Assessment of patient dose from CT localizer radiographs,Med. Phys. 40 (8), 2013, 084301-1 – 084301-8

[6] Bang DH, Lim D, Hwang WS, Park SH, Jeong OM, Kang KW, Kang H. Lateral Topography for Reducing Effective Dose in Low-Dose Chest CT. AJR Am J Roentgenol. 2013; 200 (6): 1294-1297

41 Introductory lecture: Personal dosimetry – reasonably using the existing resources

M. Borowski[1]
[1]Klinikum Braunschweig, Institut für Röntgendiagnostik, Braunschweig, Germany

Personal working in controlled areas is expected to be exposed to an increased level of ionizing radiation. Apart from whole body exposure in particular extremities or the eye lenses can be exposed to considerable up to critical levels. To monitor the possible radiation exposure all persons entering controlled areas are obliged to personal dosimetry. Within legal dosimetry persons normally are asked to wear film or TLD based dosimeters for whole body monitoring. Personal with an expected increased exposure of the extremities, e.g. within nuclear medicine departments, are asked to use finger dosimeters. Because of an ongoing debate on the detrimental effects of ionizing radiation on the eye lens in future the requirement of a dosimetric surveillance of the eye lens, at least for interventionalists, can be anticipated. Each year there are several million euro spend for personnel dosimetry within the EU. On the other hand more than 95% of all persons monitored with whole body dosemeters are exposed to dose levels below the detection threshold. Extremity dosimetry, as became obvious from the EC funded ORAMED project, suffers from large uncertainties. For the dosimetry of the eye lens not even the basic scientific research is done jet. Thus, actually most of the persons do not benefit from the large effort. There are, however, alternate approaches to enhance the effectiveness and acceptance of the personal dosimetry. These are e.g. an exchange rate of whole body dosemeters, which is adapted to the height of the person's exposure within history or the two dosimeter approach, which provides a by far more realistic estimate of the person's effective dose. Another approach is the use of active electronic dosemeters (EPD). EPD give a direct feedback to individual actions and provide thereby the necessary basic information for teaching or optimization processes. EPDs, however, suffer from the fact that they can get blinded from too high dose rates. The extra information, also, are accompanied with an increased effort to analyse the data.

Within the talk the usability and cost-effectiveness of different dosimetric approaches will be discussed. The audience shall leave the session with a well-founded basis for their own justified decisions. The talk shall open the view to question normally unquestioned personal dosimetry practices and point out reasonable alternative approaches.

42 Real Time Dosimetry System in Interventional Radiology: Utility as an Optimization Tool in Radiation Protection.

M. Pinto[1]
[1]Kantonsspital Aarau, Aarau, Switzerland

Related questions: Workers at the catheter laboratory are among the most exposed to ionizing radiation in hospitals. However, it is difficult to know with certainty the staff radiation doses, as personal dosimeters are often misused [1, 2]. Morover, the information provided by thermoluminiscent dosimeters (TLD) corresponds to the monthly accumulated dosis, so corrective actions cannot be taken on short time. Real time dosimetry can help to make the staff aware of the radiation they are receiving as well to motivate them to use the radiation protection material. The purpose of this work is to evaluate a real time dosimetry system as an optimization tool in radiation protection.

Material and procedure: A real time dosimetry system consisting of several solid-state detectors connected wirelessly to a real time display has been used. The system has been initially tested in 8 interventional procedures at two interventional radiology (IR) suites, one dedicated to neuroradiology interventions and other dedicated to angiography. Each participant carried a dosimeter at chest level over the apron. Simultaneously, all interventions were video recorded. A retrospective analysis was carried out. High dose rates were investigated and analyzed through the recorded images. A radiation protection learning session was prepared for the IR team with the results and most important findings.

Results: A total of 3 staff members usually participate in the interventional procedures. During the whole procedure a doctor and a technician stay in the room. A second technician helps during specific parts of the procedure, normally when specific handling of patient or new material is needed. The normal working position would be: the doctor situated the closest to the patient and x-ray equipment separated by the ceiling suspended shielding and the lower shielding; next to the doctor would be the main technician; the second technician would come in and out as he is needed moving through the room.

				Accumulated dose (μSv)		
	Total Fluoroscopy Time (min)	Number Image	Total DAP (Gy cm2)	Radiologist	Technician	Tecnician II
Average	***44.24***	***632***	***332.88***	***124.5***	***9.13***	***22***
Max	107.3	1100	1275.48	642	25	148
Min	4.3	105	11.14	7	2	0
STD	39.8	434	434.58	229.15	8.28	59.94

Tab. 1: Summary of results: average, maximum and minimum values and standard deviation of the fluoroscopy time, number of images and dose-area-product (provided by the equipment) and cumulative dose during the interventions from the radiologist, and technicians.

Preliminary results (cumulative dose, fluoroscopy time, dose area product and number of images) from eight interventions are summarized on table I. An incorrect positioning of the ceiling suspended shield was found at the beginning of the intervention several times (see figure 1a). Several situations were found where a technician received the highest dose rates, when he was either handling the patient or material with no other shield but the protective apron (see figure 1b). Recommendations were made to avoid, when possible, irradiation while short manipulating the patient without shielding. Significant differences in the dose rate registered by the dosimeters were found between fluoroscopy and cinema mode. When possible, it was recommended to use fluoroscopy images for documenting the procedure, leaving high dose image modalities when high image quality is required.

Fig. 1: a. Example of snapshots from the video recording of a stent placement intervention. At the left side an incorrect position of the ceiling suspended shielding is noticed. b. At the right side the anaesthesiologist manipulates the patient at high scattered radiation area without any additional shielding.

Summary: The real time dosimetry system has shown to be a valuable learning and optimizing tool for radiation protection purposes. On the one hand, its solely use allows the staff to be aware of their radiation dose and take protective actions, if needed, on the go. On the other hand, through the simultaneous video recording of the interventions and its retrospective analysis, it is a powerful tool to improve radiation protection with own staff quantitative examples. The staff showed high satisfaction with the system.

References

[1] Vañó E, Fernández JM, Sánchez R. Occupational dosimetry in real time. Benefits for interventional radiology. Radiation Measurements 2011; 46(11):1262-1265.

[2] Sánchez R, Vañó E, Fernández JM, Gallego JJ. Staff Radiation Doses in a Real-Time Display Inside the Angiography Room. Cardiovasc Intervent Radiol 2010; 33:1210-1214.

43 Impact of Radiation Protection Means on the Eye Lens Dose while Handling Radionuclides in Nuclear Medicine

I. Bruchmann[1], B. Szermerski[1], L. Geworski[1]
[1]Hanover Medical School, Department of Radiation Protection and Medical Physics, Hanover, Germany

Aim: Recent epidemiological studies suggest that the human eye lens is more radio sensitive than previously assumed. The reduction of the dose threshold for the eye lens to 20 mSv per year has been passed in the current Euratom Directives (2013). Handling especially high-energy beta-emitter may induce high doses in the eye lens. The aim of this work was to investigate the attenuation impact of different radiation protection means to the eye lens dose while handling radionuclides in nuclear medicine.

Methods: Using laboratory glasses and X-ray protective goggles, attenuation factors for different nuclides (Tc-99m, I-131, Y-90, F-18, Ga-68) were determined. The radionuclides in typical geometry (syringe, vial, applicator) were positioned in a distance of 50 cm to the eyes of four Alderson-Head-Phantoms. Different dosimeters measuring $H_p(3)$ respective $H_p(0.07)$ were fixed to the eyes of the phantoms as nearby as possible behind respective without any protective means.

Results: The protection means-dependent mean attenuation factors for the $H_p(3)$- measure were determined to be 1 (no attenuation effect) for F-18 using laboratory glasses and 370 for Y-90 using X-ray protective goggles. The other results take values between these ranges. For the measure $H_p(0.07)$, the mean attenuation factors range between 1 (I-131, X-ray protective goggles) and 71 (Y-90, X-ray protective goggles).

Conclusion: The attenuation factors of the different protection means vary with the choose of the nuclide.

Prospective eye lens doses can be dramatically reduced by using protection means, especially for those dose-relevant nuclides such as Y-90.

Session 8 – Miscellaneous topics

Chairs: F. Nüsslin (Munich/DE), W. Seelentag (St. Gallen/CH)

44 Opening Laudation: Fritz Hawliczek: A Pioneer for Medical Physics in Austria 1950 – 1990

W. Schmidt[1], F. Steger[1]
[1]Institute for Radiooncology, Donauspital Vienna, Vienna, Austria

Fritz Hawliczek (1920 – 1992) was born (and spent most of his life) in Vienna. After war he studied physics at the University of Vienna and was employed at the famous "Institut für Radiumforschung" in Vienna from 1945 – 1955; in this time he made his first experiences with "Medical Physics":

"…in 1950 H. Vetter read an article about injection of sodium-24, whose passage through heart ventricles could be measured with a Geiger-Müller counter… Since this equipment was not commercially available at this time, Fritz Hawliczek freely offered his help to find a solution to this problem. Hawliczek himself built a gamma-ray counter with an argon-alcohol filled brass-cylinder fashioned after a Geiger-Müller counter, a mechanical impulse counter, and a lead collimator with a special "gallows" for positioning the apparatus over the patient; this was so heavy, that one had to take constant care that the lead shielded counter would not fall and injure one of the patients…" [1].

Another paper from this time titles: "Use of an electrocardiograph as registration unit for a Geiger-Müller counter in radiocardiography" [2] (1952).

From 1955 to 1986 he was head of the "Radiumtechnische Versuchsanstalt" (later: „Physikalisch-technische Prüfanstalt für Radiologie und Elektromedizin, Prüfstelle Lainz") in Vienna. In this time more than 20 published papers prove his scientific career. He built up his institute to a well-known institution in German speaking countries. The first Austrian installations of telecobalt (1959) and a betatron (1964) as well as a new isotope laboratory (1970) also fell under his responsibilities. His work included compilation of radioprotection expertises in all fields of medical physics and he contributed to the Austrian Radioprotection Law in 1972 as an expert.

As a genius inventor he developed measurement devices, among them a patented semi-automatic isodose-writer which was licensed to BBC in 1970. Up to 1972 he was designated as consultant to the IAEA; at this time the "young" agency needed irradiation devices "in place" for radiobiology, chamber calibration and dosimetry services. He also was in close contact (radioprotection as well as nuclear medicine issues) with the Austrian Research Center Seibersdorf (opened 1956) and the Atominstitut of the Austrian Universities (opened 1961), each equipped with a research reactor.

At the age of 67 he presented a self-written depth-dose calculation program for mini-computers at the "First Congress of the European Federation of Organisations of Medical Physics (EFOMP)" ([3]; Innsbruck 1987; to our knowledge his last publication).

1980 he was cofounder of the "Gesellschaft für Krankenhausphysik" (renamed to ÖGMP 1985) and first president (1981-1984). In this time the society joined EFOMP (1981) and IOMP (1982), organized scientific annual meetings in Munich (1981) and Nürnberg (1984, both together with the German society), Vienna (1982) and Salzburg (1983). In 1987 his dedication was honored with the Honorary Membership of the ÖGMP.

Remarkable stations of his life, the growing role of medical physics in Austria in the second half of the 20th century as well as his contacts to other Austrian medical physicists at this time can be presented in a lecture or a poster.

References

[1] History of Nuclear Medicine in Europe, H. Schicha et al. (ed.), p. 12-13; Schattauer, 2003
[2] Über die Verwendung des Elektrokardiographen als Registriergerät in der Radiokardiographie. Fritz Hawliczek, MIR 161 (7+8), Nr. 486, 1952 (in German)
[3] Ein Kleincomputerprogramm zur Berechnung von Tiefendosen am Beispiel eines 6MeV Linear-beschleunigers. Hawliczek, R., Hawliczek, F., Binder, W. Medizinische Physik ' 87, p. 115-120, 1987, ISBN 3-925218-04-1 (in German)

45 Observers needs in diagnostic CT image quality

J. M. Voigt[1], C. Güldner[1], M. Fiebich[1]
[1]Technische Hochschule Mittelhessen, Institut für Medizinische Physik und Strahlenschutz, Gießen, Germany

Purpose: When running a CT scanner it is required by law to use reasonable patient exposures. Specific dose reduction methods or techniques are not mentioned. The only advice given is to follow ALARA-principle (as low as reasonably achievable). But what does that mean? Finding the minimum dose is an observer dependent and iterative process. This study shows an unified approach on the example of paranasal sinus scans to correlate subjective image quality with displayed $CTDI_{vol}$. Image quality was evaluated by three observer, using three different cadaveric heads. To determine the effect of the reconstruction on image quality, four different convolution kernels had been used.

Materials and methods: Three cadaveric heads were scanned using a Siemens Definition (Siemens, Forchheim/Germany) dual source CT scanner. The scan was performed with variied exposure parameters. Three different kVp settings were used (80 kVp, 100 kVp and 120 kVp). For all kVp settings tube current time product (mAs) was changed from scanner minimum (7 mAs) to the value that leads to a $CTDI_{vol} \leq 9$ mGy, which is the german diagnostic reference value for paranasal sinus scans. Logically different number of scans were taken for each kVp. Table 1 shows the total number of scans for each kVp. All acquired series were reconstructed using four different convolution kernels: H47, H50, H60 and H70. H47 and H50 are defined as “middle sharp”, H60 as “sharp” and H70 as “extra sharp”. It is worth mentioning that H70 is only available for scans ≥ 20 mAs. Kernels below H47 were excluded in preliminary studies because of too low spatial resolution and to low contrast. The reconstructed series were randomized and anonymized. In total the observer had to evaluate 160 series. The randomized images were reviewed by three ENT specialists that gave marks from 1 (best) to 4 (worst) (table 2) on different anatomic structures. The mean value of all marks was calculated and displayed as function of the displayed $CTDI_{vol}$. After all a threshold (ALARA-Point) was defined that no mean score > 2.0 should appear. The threshold defined as 2.0 ensures that all observers are able to confirm diagnostic findings.

kVp	No. of mAs settings
80	25
100	14
120	9

Tab. 1: Number of different mAs settings for each kV to reach the diagnostic reference value of $CTDI_{vol}$ = 9.0 mGy.

Grade	Explanation
1	excelent
2	good
3	with restrictions
4	not visible

Tab. 2: Scale used for the evaluation of the image quality.

Results and discussion: Table 3 shows the minimum $CTDI_{vol}$ that leads to a mean score ≤ 2.0 depending on kVp and convolution kernel. The best result was reached with the combination of H47 kernel and 100 kVp ($CTDI_{vol}$ = 0.93 mGy). The second best was achieved with a $CTDI_{vol}$ = 1.52 mGy by use of 120 kVp and the H50 convolution kernel. The minimum $CTDI_{vol}$ for the other kernels (H60 and H70) is too high. These kernels are very sharp and enhance image noise dramatically. As expected and displayed in figure 1 the image quality score is better at higher dose. But figure one shows a significant saturation and no trend to exactly 1.0. This means that it is impossible to reach the optimum (score of 1.0) in diagnostic image quality in this case. The best reachable image quality is still a compromise. This compromise exists between a $CTDI_{vol}$ of about 3.5 mGy to the diagnostic reference level of 9.0 mGy.

	minimal $CTDI_{Vol}$ in mGy			
kVp	H47	H50	H60	H70
80	2.2	2.64	3.09	6.15
100	**0.93**	2.31	6.48	7.41
120	2.28	**1.52**	3.81	7.61

Tab. 3: Minimal $CTDI_{vol}$ at which the mean score is ≤ 2.0

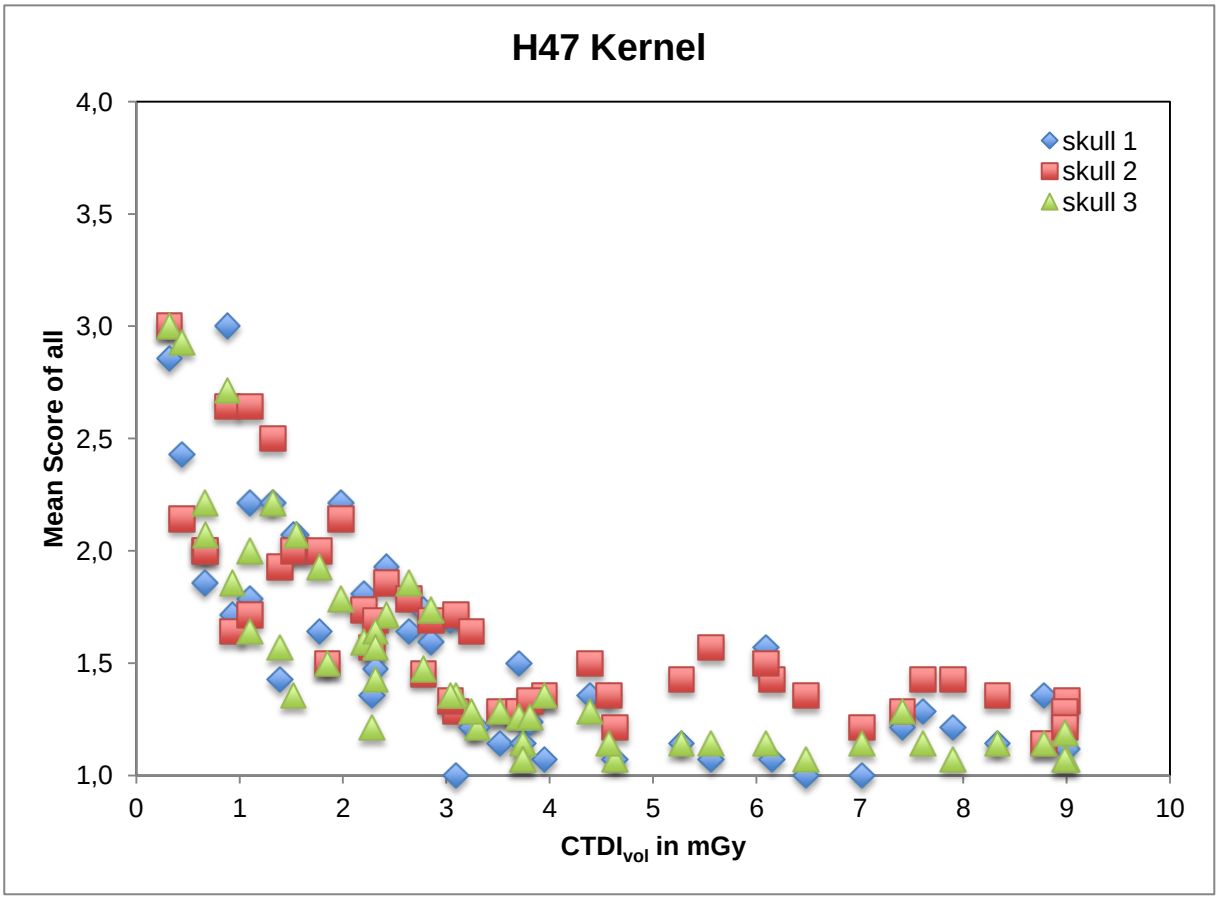

Fig. 5: Mean score as function of indicated CTDIvol over all kV. As expected the image quality score gets better with higher dose. A saturation effect is visible.

Conclusion: Dose optimizations following a consequent ALARA-approach are extremely time consuming and subordinate to a significant observer dependent variation. This makes it difficult to find a common protocol that fits all observers needs in diagnostic imaging and represents ALARA at its best. A more common approach would be to define needs in diagnostic image quality that should be achieved by the image. This needs enable each observer to secure diagnostic findings and represent the image quality that is as high as reasonably achievable (AHARA-approach). However, this approach is also time consuming and depends on variations between observers.

46 Incorporation of prior information and their reliability into the Prior Image ConstrainedCompressed Sensing (PICCS) framework

S. Vaegler[1], D. Stsepankou[2], J. Hesser[2], O. Sauer[1]
[1]University of Würzburg, Department of Radiation Oncology, Würzburg, Germany
[2]University Medical Center Mannheim, Department of Experimental Radiation Oncology, Mannheim, Germany

Introduction: The reduction of dose in cone beam computer tomography (CBCT) is achievable by image acquisition protocols that reduce the current for each projection as well as the number of projections. Reconstructing images from projections obtained by such protocols necessitates sophisticated image reconstruction techniques in order to maintain good image quality. The Prior Image Constrained Compressed Sensing (PICCS, [1]) framework incorporates prior information into the reconstruction algorithm and outperforms the widespread used Feldkamp-Davis-Kress-algorithm (FDK) when the number of projections is reduced. However, major differences between the prior and current images are so far not appropriately considered in the PICCS algorithm. We therefore propose a problem-specific extension of the PICCS method such that the reliability of the prior information is incorporated additionally.

Materials and methods: We assumed that the prior images are composed of areas with large and small deviations. Accordingly, a weighting matrix considered the reliability of assigned areas in the objective function. Objective function minimization was based on the ASD-POCS framework [2, 3].
Simulations were performed with the Shepp-Logan-phantom as well as on clinical CBCT projections from a head-and-neck case. All prior images contained large local variations compared to the reference image (Fig. 1). We applied our method to the problem of image reconstruction from few projections. The reconstructed images were compared to the reconstruction results by the FDK-algorithm, the total variation (TV) minimization and the conventional PICCS-method.
In order to show the improvement of image quality we compared image details with the reference image and determined the root-mean-square error (RMSE) and the contrast-to-noise ratio (CNR).

Results: In all investigated cases our reconstruction method yielded images with substantially improved quality compared to the images reconstructed by the FDK algorithm, by the TV-minimization or by the conventional PICCS-method, respectively. Accordingly, these images contained strong artefacts such as streaking, blurring and inaccurate reconstructed structures when the number of projections was very small. In Fig. 2 the reconstruction results of the Shepp-Logan phantom are exemplarily displayed. These results were achieved by using 5 projections.

Conclusions: We propose a problem-specific extension of the PICCS-method. Besides prior images we included local dependent information about the reliability of the prior image. Using this information, we could demonstrate reconstruction results with substantially improved image quality for the computer phantom as well as for the experimental data simulations. This concept indicates the potential for dose reduction while maintaining good image quality. Further development concerning registration of the prior image during the image reconstruction process is currently in preparation.

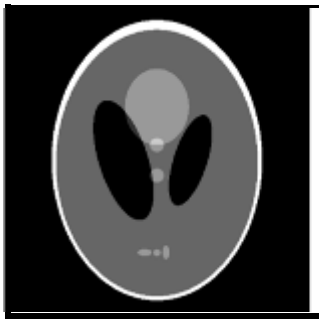

Fig. 1: The reference image (left) and the prior image (right) used for the computer phantom simulations. The arrows indicate the strong local variations.

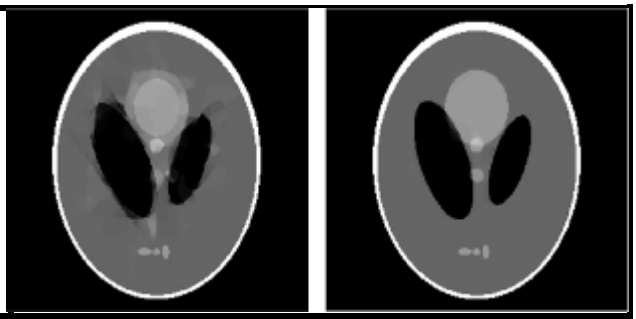

Fig. 2: Reconstructed images by the conventional PICCS (left) and by our method (right) using 5 projections.

References

[1] Chen, G.H., J. Tang, and S.H. Leng, Prior image constrained compressed sensing (PICCS): A method to accurately reconstruct dynamic CT images from highly undersampled projection data sets. Med Phys, 2008. **35**(2): p. 660.
[2] Sidky, E.Y. and X.C. Pan, Image reconstruction in circular cone-beam computed tomography by constrained, total-variation minimization. Phys Med Biol, 2008. **53**(17): p. 4777.
[3] Sidky, E.Y., et al., A constrained, total-variation minimization algorithm for low-intensity x-ray CT. Med Phys, 2011. **38**: p. S117.

47 Image processing system for the evaluation of fungal infections of the skin in fluorescence microscopy images

U. Mäder[1], N. Quiskamp[2], P. Mayser[3], F. Runkel[1], M. Fiebich[1]
[1]Technische Hochschule Mittelhessen, Gießen, Germany
[2]Helmut Hund GmbH, Wetzlar, Germany
[3]University of Gießen, Gießen, Germany

Introduction: The diagnosis of fungal infections of the skin is a main task of dermatologists. For a fast assessment of potential infections, microscopy of extracted skin samples is used. Frequently, antifungal ointments are prescribed for therapy whenever fungal hyphae are found. In fact, a single positive diagnostic finding can be sufficient to initiate therapy.

While the contrast of fungal hyphae is low in brightfield microscopy, it is possible to enhance contrast with fluorescent markers. Therefore, fluorescence microscopy is a main approach for a reliable diagnosis [1,2]. However, the fluorescent markers stain other structures like cellulose of clothing as well, which can lead to false-positive diagnoses.

To support the dermatologists, an image processing methodology was developed that evaluates digital microscopic images of skin samples to detect fungal hyphae.

Materials and methods: Samples consisting of small skin flakes of infected patients were provided by the Department of Dermatology of the University of Giessen. Here, positive samples were gathered during routine examination where fungal infections were diagnosed by the clinical staff. The sample preparation was performed at our lab and included staining with commercially available Mykoval (Helmut Hund GmbH, Wetzlar).

The imaging was performed using an automated fluorescence imaging system that provided a complete 1 cm² area scan (consisting of 100 single images) of the specimen on which the skin flakes were randomly located. The system is equipped with a monochrome camera, an objective (10x magnification) and a LED illumination unit (Helmut Hund GmbH, Wetzlar).

For image processing, a framework was developed that is able to load image data and to visualize the results. The following processing steps were developed:

- image preprocessing: background reduction and binarization
- image segmentation: separating objects for classification based on preprocessing
- classification analyzing intensity-based and morphological parameters

Results: Figure 1 shows an original sample image before and after preprocessing. After separation of the objects, the classification algorithm analyzes a set of parameters to reduce false-positive structures. The parameters are derived from the specific morphological characteristics of fungal hyphae that distinguish these objects from other objects. Hyphae are small fibrous structures with a uniform width (see figure 2) that could fork or build net-like objects.

The algorithm marks and presents an image to the dermatologist whenever an infection is found. Using this automated scanning system and the image processing methodology only the images containing possible infections must be determined. Images without infection must not be read. For every examined sample an infection was found with low false-positive findings.

Conclusion: The developed image processing methodology is capable of detecting fungal hyphae in digital fluorescence microscopy images. In combination with the automated imaging system the dermatologists can reliably evaluate the whole sample area without reading every image, as only images where infections can be seen are presented. A sample is positive when one hypha is found. In the case of an infection, a high number of hyphae are typically present and therefore it is theoretically not necessary to reliably detect all hyphae in the sample. Hence, the required sensitivity of the method for a single object is not as high as for computer aided diagnose systems in other medical fields (for example lung nodule detection in computed tomography).

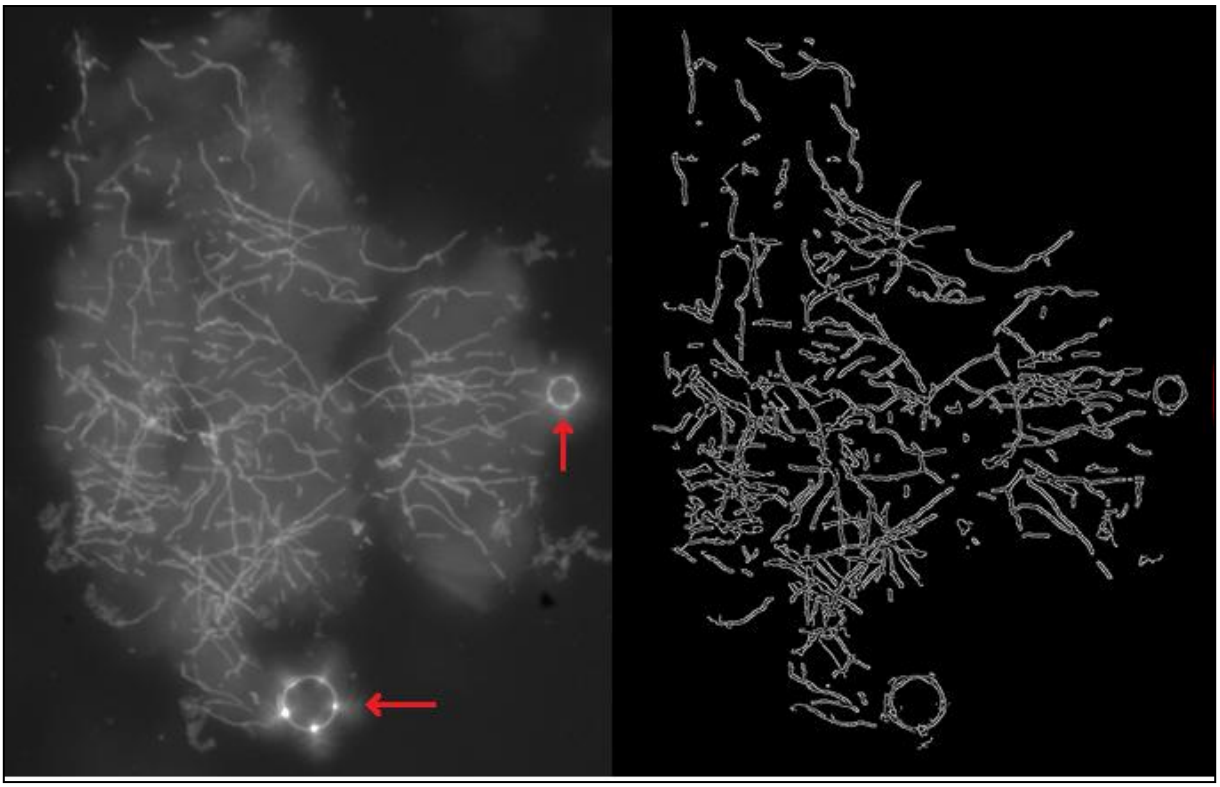

Fig. 1: Original and pre-processed microscopy image of skin flake with hyphae and two circular false-positive reflections of the LED illumination (arrows).

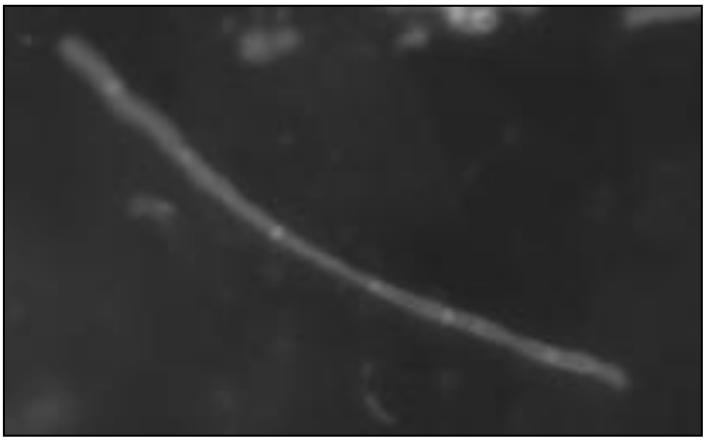

Fig. 2: Detected Hypha with characteristic uniform width.

References

[1] Ruechel, R.; Dellmann, A.; Schaffrinski, M.; Donhuijsen, K.: Vereinfachte Pilzdetektion; Screeningmethode mit optischem Aufheller. In: Pathologe 25 (2004), S. 235-237

[2] Hoch, H.C.; Galvani, C.D.; Szarowski, D.H.; Turner, J.N.: Two new fluorescent dyes applicable for visualization of fungal cell walls. In: Mycologia 97 (2005), S. 580-588

48 Experience in online teaching – the Master Online in "Advanced Physical Methods in Radiotherapy" (APMR) at Heidelberg University

M. Schaefer[1], J. Debus[2], L. Gebauer-Hötzel[1], O. Jäkel[1], W. Schlegel[1]
[1]DKFZ Heidelberg, Department of Medical Physics in Radiation Oncology, Heidelberg, Germany
[2]University Hospital Heidelberg, Department of Radiation Oncology, Heidelberg, Germany

Purpose: In October 2013 the first group of APMR students was awarded with the Master of Science (MSc.) degree in "Advanced Physical Methods in Radiotherapy", the first online master program at Heidelberg University, Germany. Furthermore, three additional study groups of international students are currently enrolled to the program. Besides Master students, we also accept medical physicists who want to study a subset of the modules in the frame of continuous professional development (CPD).

Materials and methods: The program is designed for graduates in physics or biomedical engineering with a clear background in medical physics and one to two years of professional working experience in the same field. It concentrates on modern treatment techniques such as IMRT, IGRT and radiotherapy with proton and ion beams and is supplemented by advanced anatomy, an update of modern imaging techniques, special quality assurance and dosimetry methods needed for the new modalities.

During the first three semesters students participate in five online modules, mainly covering the theoretical knowledge of the above mentioned topics. The online modules are terminated by attendance phases of 2-4 days in Heidelberg. Finally, the students join the on-site internship module (7-10 days) in order to apply their knowledge and to deepen their practical experience in the respective fields. These practical sessions take place at the University Hospital of Heidelberg, the German Cancer Research Center (DKFZ) and the Heidelberg Ion Beam Therapy center (HIT). The forth semester is dedicated to writing the final master thesis.

During the online modules, students listen to recorded video lectures, read ejournals and ebooks and work on written assignments and discussions. Periodic online meetings take place every two to three weeks. All national and international teachers (+70) have long-lasting on-site teaching experience but no one ever taught online before. Furthermore, all students studied on-site first, before joining the online program APMR.

Results: The curriculum design demonstrates one possibility of an online program which fulfills the need of teachers and students, both new to online teaching and learning. Comparing the beginning and the current status of the program, the combination of cooperative learning methods, periodic online meetings, recorded video lectures and their flexible use are considered to be very important from a student perspective in order to successfully pass an online program over two years. Moreover, from the teachers perspective, the curriculum design integrates their numerous and different on-site teaching experiences and allows them to find their individual online approaches.

Conclusion: With increasing experience in online teaching we were able to substantially optimize the study program during the last four years. Started with teacher-centered methods only, (e.g. recorded video lectures) we moved towards learner-centered learning approaches such as problem-based discussions or online case study sessions. This new settings require a continuous supervision of both students and teachers but enable both to successfully participate in an online master course with their own individual needs.

References

[1] Kerres, Michael: Mediendidaktik. Konzeption und Entwicklung mediengestützter Lernangebote. 3. Aufl. Munich 2012.
[2] Nolda, Sigrid: Einführung in die Theorie der Erwachsenenbildung. 2. Aufl. Darmstadt 2012.
[3] Reich, Kersten: Konstruktivistische Didaktik. Das Lehr- und Studienbuch mit Online-Methodenpool. 5. Aufl. Weinheim, Basel 2012.

Session 9 – Motion management in imaging and radiation therapy

Chairs: C. Bert (Erlangen/DE), R. Moeckli (Lausanne/CH)

49 Introductory lecture: Motion management

K. Parodi[1]
[1]Ludwig-Maximilians-Universität München, Lehrstuhl für Experimentalphysik-Medizinische Physik, Garching/Munich, Germany

Physiological motion such as respiration and heart beat still represents a major challenge for artifact-free imaging in diagnostics and highly conformal dose-delivery in radiation therapy. In particular, the tremendous advances achieved over the last decade in the degree of tumour-dose conformality with modern radiotherapy techniques using electromagnetic or hadronic radiation have demanded the development of sophisticated technologies for motion monitoring and management in the entire radiotherapy workflow, from initial diagnostic imaging to treatment planning and beam delivery.

This talk will specifically address the role of time-resolved imaging (with emphasis on four dimensional computed tomography) in the pre-treatment assessment of the tumour motion for identification of the appropriate treatment strategy, and of dedicated motion monitoring sensors and beam delivery systems for assessment and compensation of the motion during the actual beam delivery.

Remaining challenges and ongoing research trends will be also highlighted, together with an overview of novel perspectives of motion management in the near future.

50 Prospective slice tracking to correct respiratory motion in free-breathing myocardial perfusion MRI

S. Wein[1], S. Weber[1], J. F. Dechent[1], K.-F. Kreitner[2], C. Düber[2], L. M. Schreiber[1]
[1]Johannes Gutenberg University Medical Center Mainz, Section of Medical Physics, Department of Radiology, Mainz, Germany, Germany
[2]Johannes Gutenberg University Medical Center Mainz, Department of Radiology, Mainz, Germany, Germany

Introduction: The acute effect of coronary heart diseases is a reduced perfusion of myocardium [1]. Therefore, measuring myocardial perfusion is of great interest in order to diagnose coronary heart diseases. A promising non-invasive method to determine the current state of myocardial perfusion represents magnetic resonance imaging (MRI). By using the contrast-enhanced first-pass perfusion imaging method (FPP) it is possible to determine the perfusion of the heart in a quantitative way [2, 3]. One of the main challenges of this technique is the motion of the heart caused by respiration. Even during breath-holding a slow cranio-caudal directed motion is observed because of oxygen consumption. Hereby the accurate determination of myocardial perfusion is affected by respiratory motion both during breath-holding and during free-breathing FPP. Thus, this can result in false diagnostic assessment. The aim of this study was therefore to develop and implement a prospective slice tracking method correcting the respiratory motion during FPP.

Materials and methods: A navigator based technique for prospective slice tracking (PST) was developed on 3-Tesla magnetic resonance systems (Magnetom Skyra and Prisma, Siemens Medical Solution, Erlangen, Germany). The first PST approach for FPP was proposed by Pedersen et al. [4] using the standard navigator based technique to compensate for cardiac motion. In this standard approach it is assumed that the motion of the heart caused by respiration correlates with the motion of the diaphragm. However, the deviation between cardiac motion and the motion of the diaphragm varies individually for every patient and has to be measured before FPP. In contrast to this, in our study not the diaphragm was monitored, but the real position of the heart was measured to track the slice depending on its current position. For that purpose the position of the heart was determined by monitoring the change of contrast in the heart-lung interface using a fast one dimensional RF excitation. With the result of this, the position of the perfusion slice was corrected immediately before data acquisition. Thus, contrary to the approach of Pedersen et al., no additional underlying model calculations connecting diaphragm and cardiac motion were needed. Therefore a more direct and straightforward approach was proposed in this study. The developed navigator based technique was implemented in a SR-TrueFISP [5] perfusion sequence.

With the aim to adjust the optimal anatomical position of the navigator across the heart in order to obtain a reliable relation between the observed navigator signal and the motion of the heart, several subjects were investigated using two different approaches. In the first approach, the apex of the heart was monitored to compensate for the motion through the perfusion slice (Fig. 1A). Under this condition all further remaining motion can be compensated in a post processing in-plane motion correction algorithm. In a second approach, the motion of the heart was monitored by the navigator along the biggest motion amplitude in cranio-caudal direction. In that measurement the readout direction of the navigator was tilted to the through-plane direction of the perfusion slice (Fig. 1B).

Furthermore the quality of the developed navigator based PST method was investigated in a pilot study with volunteers by determination of both the absolute quantitative perfusion of the myocardium by using the MMID4 model and the residual movement of the heart inside the perfusion slice. For this purpose three measurements (flip angle, TR, TE, TI, FOV, slice thickness were 40°, 173 msec, 1.17 msec, 100 msec, 379 x 284 mm², 8 mm) were done at each subject: a reference measurement under breath-holding condition and two further measurements under free-breathing conditions both with and without navigator based motion correction.

Results: As a result of the first approach, where the navigator was positioned perpendicular to the perfusion slice across the heart, the contrast between the apex of the heart and the lung was not sufficiently high to guarantee a stable prospective slice tracking algorithm. Furthermore, the correlation between the motion of the apex in the signal of the navigator and the through-plane motion of the heart was not sufficient because of physiological deformation of the heart's apex during the breathing cycle. In the second approach, where the motion of the heart was monitored along cranio-caudal direction, the contrast in the upper heart-lung interface both correlates perfectly with the motion of the heart and was high enough to allow for the edge-detection algorithm to determine the current position of the heart.

In a pilot study the effectiveness of the navigator based PST method appeared in the reduction of motion inside the perfusion slice. To evaluate the remaining motion of the heart, distinctive points of the heart were selected manually in the perfusion slice. In comparison to a free-breathing measurement the interquartile range of the variation of these points was reduced by about 51 % by using the navigator based PST method. Even in comparison to the reference measurement under breath-holding condition the measurement under free-breathing condition with PST showed less variation (Fig. 2).

In summary the standard derivation (SD) of the determined myocardial blood flow (MBF) of six different regions of the myocardium was reduced by using PST in comparison to a measurement without the navigator. Moreover the difference

of the SD between the reference measurement and the measurement under free-breathing was sightly smaller when using the PST method (Tab. 1).

Discussion: Overall the cardiac motion of the heart was reduced by about 51 % within the perfusion slice using the PST method in comparison to an uncorrected measurement. Furthermore, the interquartile range of the heart´s position under free-breathing condition with PST was about 23 % smaller than the interquartile range in the reference measurement under breath-holding condition. The reason for this might be that the oxygen consumption while measuring the perfusion under breath-holding condition additionally influences the motion of the heart. Therefore the accuracy of the MBF might also be affected under this condition. In further measurements it has to be clarified if the determination of the MBF under breath-holding condition benefits from the navigator based PST method as well.

Caused by residual contrast agent in the bloodstream the determined MBF values increased with each measurement. Therefore a direct comparison of these values was not possible. However the derivation of the MBF values of the six different regions of the myocardium was more homogeneous by using the PST method in comparison to a not corrected slice. This corresponds well to the results of the animal studies of Cleppien el al. [6]. Furthermore the difference of the standard derivation between the measurement under free-breathing condition and the reference measurement was sightly smaller when using the PST method. This indicated an increased accuracy of the measured MBF values by using the PST method.

In summary, the results correspond well with the results found by Pedersen et al. [4] that the determination of myocardial perfusion is improved by reducing through-plane motion under free-breathing conditions. In their study, the position of the diaphragm was monitored by the standard navigator approach. Therefore an underlying motion model connecting diaphragm and cardiac motion was needed, which was a major source of error due to the poor signal intensity of the navigator. All this affected in a reduced accuracy of the motion correction. In our study, the position of the heart was measured directly, thus the main source of error by the standard navigator approach was avoided. In consequence, the approach presented in this study provided a more straightforward way for correcting the respiratory motion during FPP.

A further study with a higher number of subjects will be performed to demonstrate the results with higher statistical and systematic evidence.

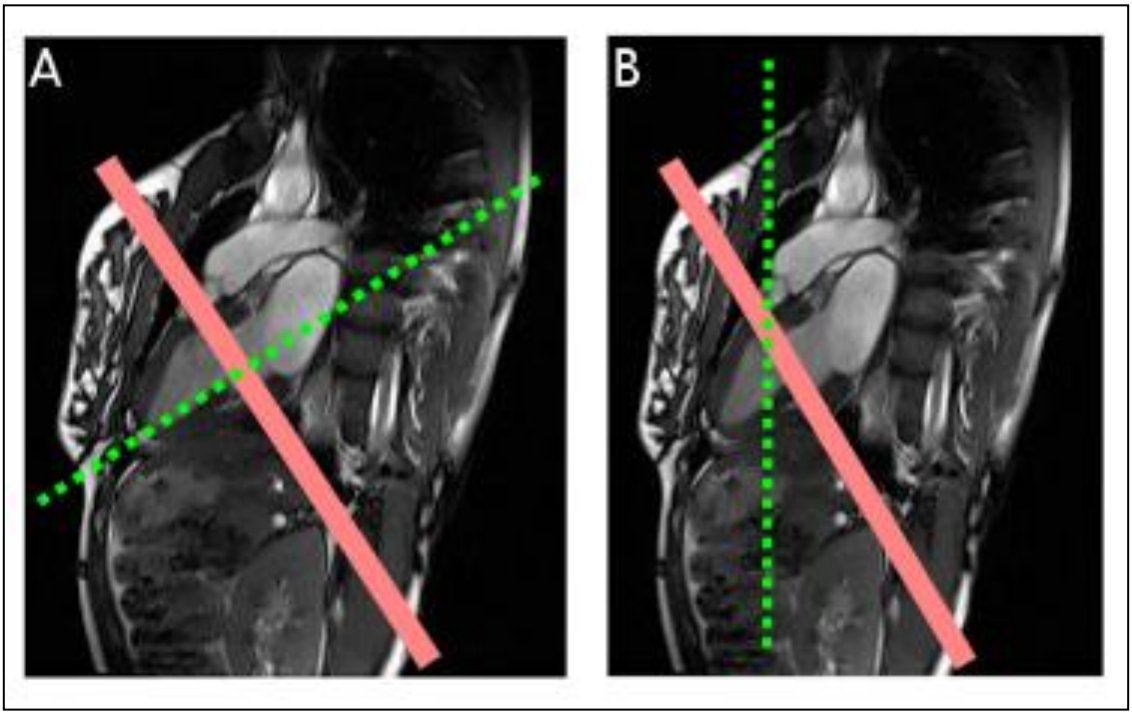

Fig. 1: The Perfusion slice (red) and readout direction of the navigator (green) A: along the through-plane direction of the perfusion slice and B: along the biggest amplitude in cranio-caudal direction.

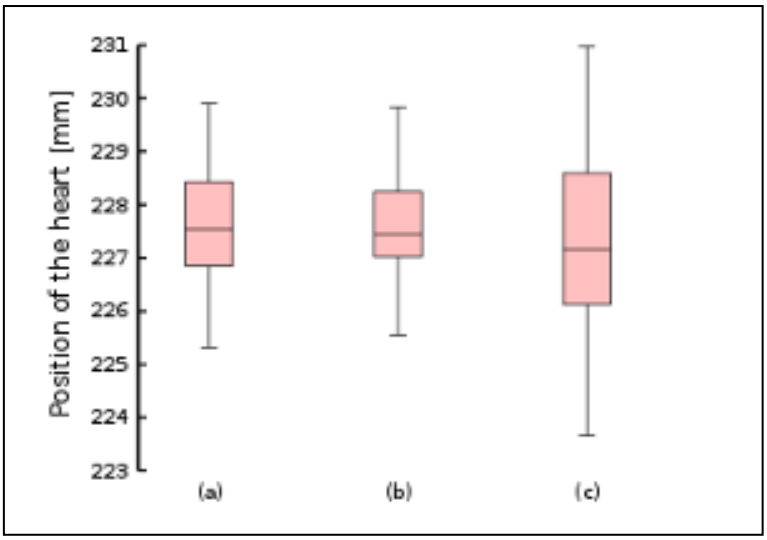

Fig. 2: Derivation of the position of the heart within a FPP a) under breath-holding condition, b) under free-breathing condition with PST and c) under free-breathing condition without using PST.

Region	**M1** $\frac{ml}{\min \cdot g}$	**M2** $\frac{ml}{\min \cdot g}$	**M3** $\frac{ml}{\min \cdot g}$
1	0.54	0.79	0.79
2	0.38	0.56	0.65
3	0.40	0.57	1.11
4	0.35	0.70	0.89
5	0.58	0.71	0.68
6	0.53	0.74	0.98
Median	0.465	0.705	0.840
SD	0.098	0.093	0.178

Tab. 1: MBF values of different regions of myocardium M1: under breath-holding condition, M2: under free-breathing condition with PST and M3: under free-breathing condition without using PST.

References

[1] Nesto RW, Kowalchuk GJ. The ischemic cascade: temporal sequence of hemodynamic, electrocardiographic and symptomatic expressions of ischemia. Am J Cardiol 1987;59(7):23C-30C.

[2] Jerosch-Herold M, Wilke N, Stillman AE. Magnetic resonance quantification of the myocardial perfusion reserve with a Fermi function model for constrained deconvolution. Med Phys 1998;25(1):73-84.

[3] Schmitt M, Viallon M, Thelen M, Schreiber WG. Quantification of myocardial blood flow and blood flow reserve in the presence of arterial dispersion: a simulation study. Magn Reson Med 2002;47(4):787-793

[4] Pedersen H, et al. "Quantification of myocardial perfusion using free-breathing MRI and prospective slice tracking." *Magnetic Resonance in Medicine*61.3 (2009): 734-738.

[5] Schreiber, WG, et al. "Dynamic contrast-enhanced myocardial perfusion imaging using saturation-prepared TrueFISP." Journal of Magnetic Resonance Imaging 16.6 (2002): 641-652.

[6] Cleppien, D. E. J., Horstick, G., Abegunewardene, N., Weber, S., Müller, C. E., Heimann, A., Kreitner oK.F., Kempski, and Schreiber, L. M. (2010). Comparison of the quantitative first pass myocardial perfusion MRI with and without prospective slice tracking: Comparison between breath-hold and free-breathing condition. *Magnetic* Resonance in Medicine, 64(5), 1461-1470.

51 Restoration of motion-blurred images in digital radiography: a feasibility study

K. Loot[1,2,3], A. Block[1]
[1]Klinikum Dortmund, Institut für Medizinische Strahlenphysik und Strahlenschutz, Dortmund, Germany
[2]Heinrich-Heine-Universität, Düsseldorf, Germany
[3]Technische Universität, Dortmund, Germany

Introduction: In digital radiography, the patient is usually asked to remain immobile and refrain from breathing during the exposure. This minimizes motion artifacts sufficiently so that they have negligible influence on the image quality. However, for patient groups which are unable to control their breathing or limb movements (patients in intensive care or suffering from Parkinson disease, infants, etc.) the image resolution suffers from motion blur. We show that image processing with restoration algorithms (originally developed for digital photography) can be implemented for digital radiography to increase the spatial resolution. We use the modulation transfer function (MTF) to quantify the improvement in image quality.

Materials and methods: System theory describes the motion-blurred image as a convolution of the original image with the point spread function (PSF) of the motion. The PSF contains information about the blur extent and the direction of the motion. The Fourier transform of the PSF is the MTF, which gives valuable information about the spatial frequency dependence of contrast in the image. The convolution process involves information loss, making deconvolution ill-posed. Restoration algorithms are able to produce an estimate of the original image, provided they are given the PSF along with the blurred image.

PSF and MTF can be calculated analytically for any motion function [1]. Due to the short exposure duration (~ms), there will be little change in velocity during the exposure and uniform linear motion is assumed in the first instance. The PSF of linear motion along the x-axis is $PSF(x) = \mathrm{Rect}\left(\frac{x}{v \cdot \tau}\right)$, the product of velocity v and exposure duration τ describes the blur extent.

Using a computational software program (Mathematica, Wolfram Research), we employed a Wiener filter (representing spectral deconvolution), the Richardson-Lucy restoration algorithm (representing iterative deconvolution) and a total variation regularization algorithm. To quantify the effect of the restoration, we compared the MTFs of the images. For this, an analysis program was written, which calculates the MTF based on the image of an edge transition as described in [2]. As a starting point, we examined the behavior of simulation images. These images were also created with Mathematica and featured an edge transition similar to that of the experimental images, including influences of the sampling aperture, object motion and Poisson noise. The experimental images were obtained with a commercial radiography system (Axiom Multix M, Siemens) by mounting a suitable edge device onto a motion simulator (MotionSimXY/4D, Sun Nuclear Corporation).

Results: The simulation images were used to examine the influence of motion blur at different velocities compared to other degrading influences like scattering and geometrical unsharpness. It was shown that there is no lower limit for the velocity below which the object motion goes unnoticed. The restoration methods all performed well for noiseless images but showed great differences in the handling of noisy data. Of the three, the total variation regularization algorithm performed best in the presence of noise (Fig. 1). It significantly lessened the impact of the first zero in the motion MTF at $\xi = \frac{1}{v \cdot \tau}$ and furthermore decreased the overall noise level. We subsequently employed this algorithm for treatment of an experimental image. In this case, the velocity and the exposure duration caused a blur extent of 1.9 pixel. Restoration with a PSF assuming a blur extent of 2 pixel resulted in an increase of the MTF over the whole frequency range (Fig. 2). This leads to the promising conclusion that the image restoration returns satisfactory results even when the blur extent is only approximately known.

Conclusion: This work demonstrates the restoration of motion-blurred radiographs for the first time to the best of our knowledge. Established restoration algorithms were used to enhance spatial resolution and contrast of the images. Particularly promising is the result that the blur extents and thereby the velocities need only to be known approximately to accomplish significant improvements. Measurement of the blur extent and direction could easily be implemented in a clinical environment by use of motion sensors or video recording. Further investigations should include detailed determination of the most appropriate restoration method, mapping of patient movements and clinical studies judging the subjective increase in image quality.

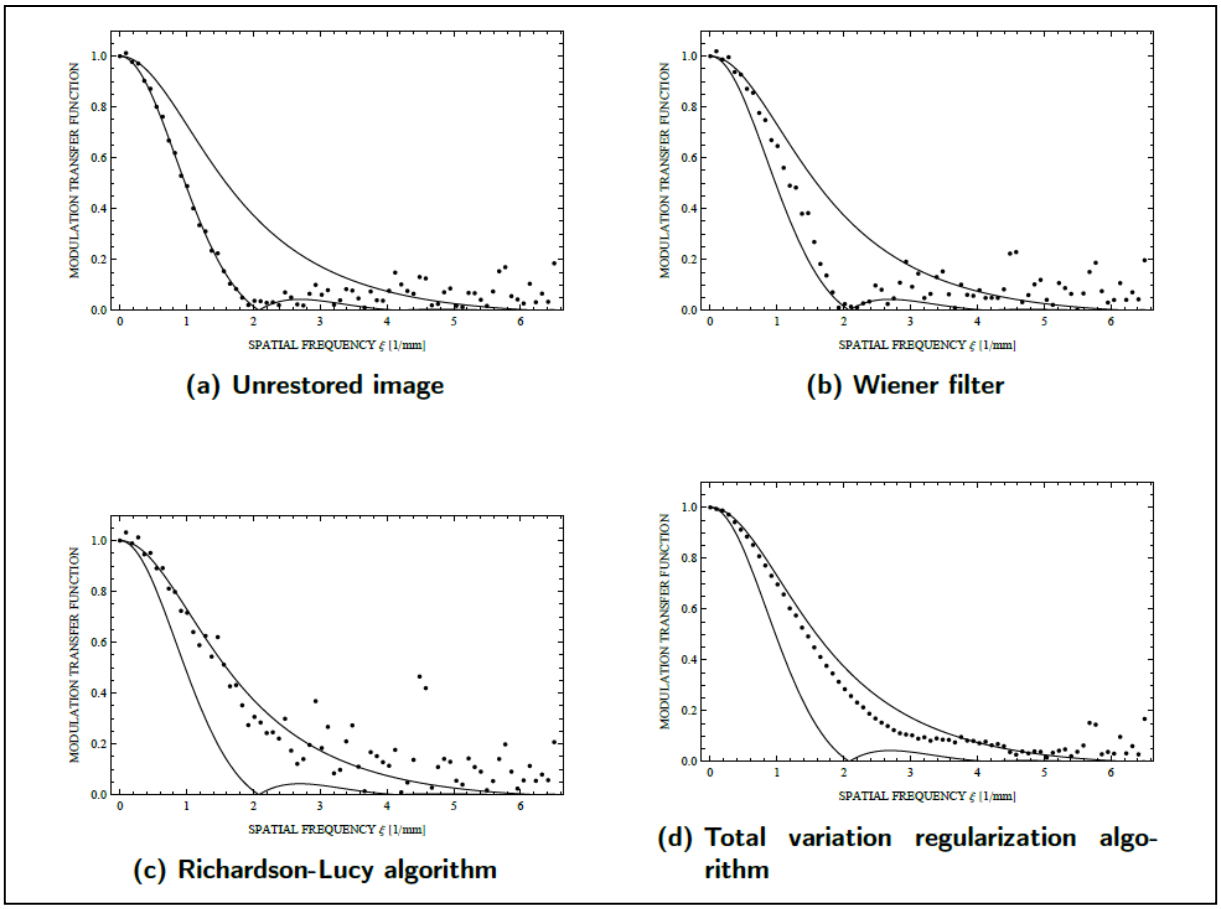

Fig. 1: Comparison of the performance of three restoration algorithms in the presence of Poisson noise by means of the MTF. Continuous curves show analytical MTF with (below) and without (above) a motion blur of 3 pixel width.

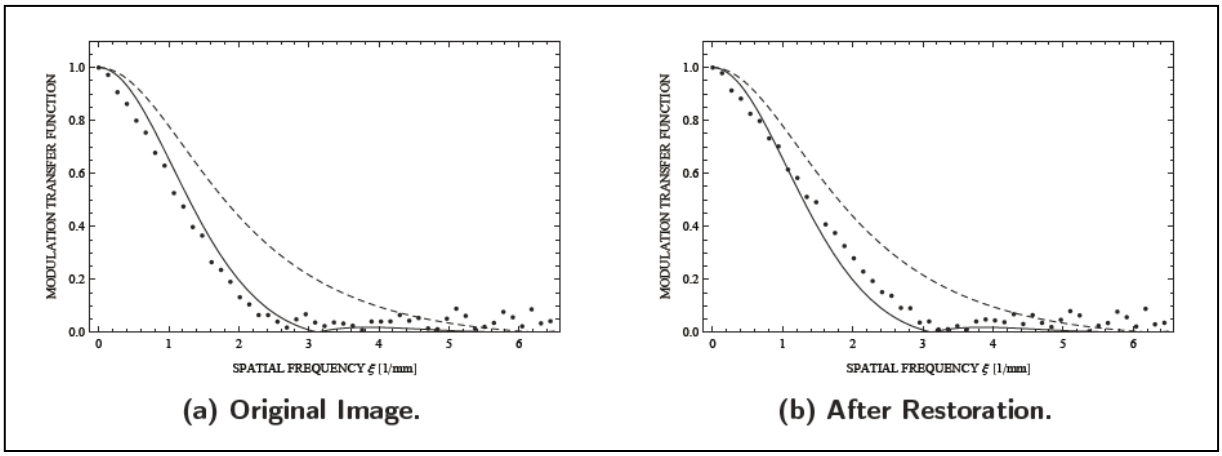

Fig. 2: MTF of a motion-blurred edge (a) before and (b) after restoration with a total variation regularization algorithm. Actual blur extent was 1.9 pixel, restoration was performed with 2 pixel.

References

[1] Stern, A. and Kopeika, N.: Analytical method to calculate optical transfer functions for image motion and vibrations using moments. Journal of the Optical Society of America A, 14(2), 1997.

[2] IEC 62220-1: Medical Electrical Equipment – Characteristics of Digital X-ray Imaging Devices – Part 1: Determination of the Detective Quantum Efficiency. IEC, 2003.

52 Localization of lung tumors despite limited tumor visibility: Tracking anatomical structures in near proximity to model the tumor motion

H. Teske[1,2], K. Giske[1], R. Bendl[1,]
[1]DKFZ Heidelberg, Division of Medical Physics in Radiation Oncology, Heidelberg, Germany
[2]Heilbronn University, Department of Medical Informatics, Heilbronn, Germany

Introduction: In the context of the increasingly precise and conformal radiotherapy, the handling of intra-fractional tumor motion gains crucial relevance. With the potential to tailor the dose distribution to the shape of the target volume, an exact localization of moving tumors during treatment is of increasing interest. The aim to deliver high dose to the target volume while sparing the surrounding healthy tissue requires a concept to compensate for such motion. Hence, the motion detection of the tumor during radiation therapy, especially for lung tumors, plays an essential step towards that direction. Tumor tracking in image-based approaches might fail when the projection of the tumor is either temporary overlapped by ribs or is lacking in visibility due to poor contrast settings. To remedy that, a model-based approach in combination with tracking of anatomical surrogates is presented which does not rely on tumor visibility.

Materials and methods: Fluoroscopic image sequences of 4 patients recorded during 5-9 breathing cycles were retrospectively analyzed to automatically localize the tumors. Four experts manually determined the position of the tumor in each fluoroscopic image for each patient by dragging the projected GTV of the planning-CT on top of the tumor within the fluoroscopic image data. The mean of these positions was then considered as the ground-truth.

Since diaphragm motion is known to be highly correlated with the motion of lung tumors as well as providing high visibility in fluoroscopic images, this anatomical structure is used as a surrogate to deduce the tumor position from its motion pattern [1]. To do so, a thin plate spline interpolation model is adopted. The model consists of a potential function and supporting points, which are represented by correspondence points at different times. Those positions are obtained from the projected diaphragm contour, defined through geodesic distances from the left and right endpoints of that contour. For that purpose, the diaphragm contour was manually delineated in each fluoroscopic image for each patient. Based on the motion of the highly visible anatomic surrogate, represented by the supporting points, the thin plate spline interpolation creates a vector field that defines the spatial displacement of every position in respect to the distance to each supporting point and the underlying potential function (Fig. 1).

While the motion of tumors located in the lower lobes of the lung are stronger affected by the diaphragm movement, more superior located tumors have a smaller motion range [2]. For that purpose, the displacement of the upper lung border was incorporated to limit the modeled motion of tumors within the upper lobes. An optimal parameterization of the model concerning the used potential function, as well as the amount and position of the used supporting points was sought to achieve a more general modeling approach.

Results: Compared to the ground-truth, the accuracy of the presented approach in its optimal per-patient parameterization results in a mean RMSE of 1.4 mm ± 0.6 mm in left-right and 1.8 mm ± 1.1 mm in superior-inferior direction (Tab. 1). Even though one single parameterization of the thin plate spline interpolation model yielding best results for each patient could not be found, the achieved accuracy lies within the mean inter-observer standard deviation of 1.6 mm in left-right and 2.8 mm in superior-inferior direction.

Conclusion: The presented model-based approach is capable of accurately localizing the tumor position irrespective of whether the tumor has a poor visibility or is temporary overlapped by ribs. Given that the model does not rely on a fixed training set of known tumor motion, the thin plate spline interpolation model combines a pretty general modeling procedure with the capability to incorporate patient and fraction specific motion characteristics. Therefore, the tumor motion can be individually modeled for different patients and conditions.

Acknowledgements: This presented work was carried out with the support of the German Research Foundation (DFG), SFB/TRR 125 “Cognition-Guided Surgery”.

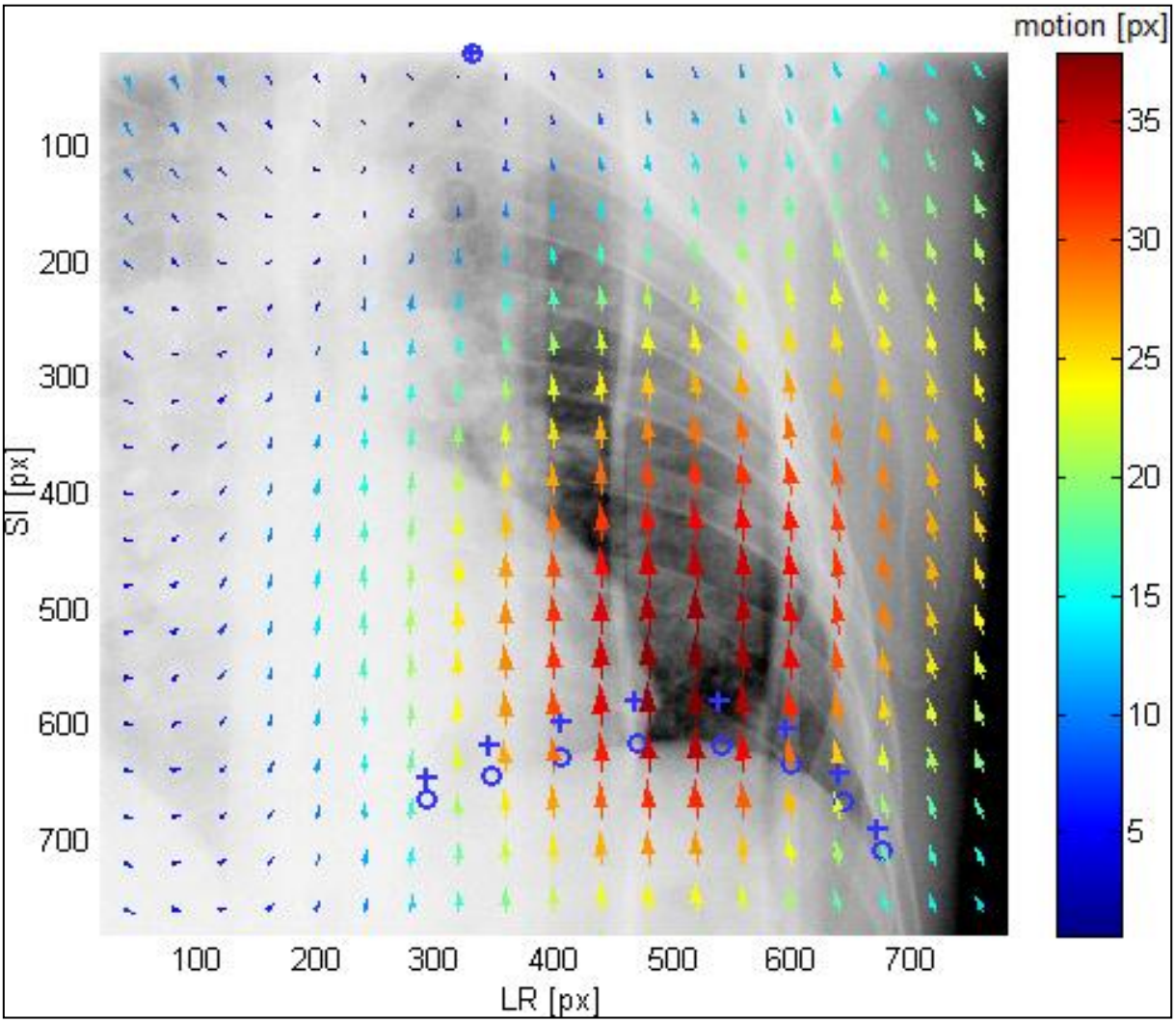

Fig. 1: Vector field generated by the thin plate spline interpolation model with the use of supporting points on the diaphragm contour, as well as on the superior located lung contour. Those points are represented as circles in the inhale phase and as crosses in the exhale phase. Positions near the diaphragm receive a larger spatial displacement than positions located in the upper lobe of the lung. The displacement of the initial supporting points ranges from the encircled points to the nearest crosses.

Patient	Thin plate spline interpolation with optimal parameterization	
	RMSE in LR [mm]	RMSE in SI [mm]
1	1.5	1.3
2	2.3	0.7
3	1.1	2.1
4	0.9	3.2

Tab. 1: Accuracy of the modeled tumor positions compared against the ground-truth in left-right and superior-inferior direction. Errors achieved with the use of the thin plate spline interpolation model and an optimal parameterization on a per-patient basis.

References

[1] Cerviño, L.I., Chao, Alvin K Y, Sandhu, A., Jiang, S.B.: The diaphragm as an anatomic surrogate for lung tumor motion. Phys. Med. Biol. 54, 3529–3541 (2009)

[2] Seppenwoolde, Y., Shirato, H., Kitamura, K., Shimizu, S., van Herk, M., Lebesque,

[3] J.V., Miyasaka, K.: Precise and real-time measurement of 3D tumor motion in lung due to breathing and heartbeat, measured during radiotherapy. Int J Radiat Oncol Biol Phys 53, 822–834 (2002)

53 Prediction filter for Real-Time Tumor Tracking using the Treatment Couch

A. Jöhl[1,2], J. Zeimetz[1,2], S. Lang[1], G. Ochsner[1,2], M. Schmid Daners[2], S. Klöck[1]
[1]University Hospital Zurich, Zurich, Switzerland
[2]Eidgenössische Technische Hochschule Zurich, Institute for Dynamic Systems and Control, Zurich, Switzerland

Purpose: The objective is to develop a tumor tracking system, which maximally reduces the radiation dose on healthy tissue while keeping the patient comfortable. The available hardware has large time delays and to mitigate the, thereby introduced, inaccuracies, a breathing motion prediction filter is needed. A survey of different filters used on several hardware configurations was performed.

Materials and methods: A simulation environment was developed using MATLAB/Simulink R2014a (The MathWorks, Inc., Natick, MA, USA) including the couch dynamics, the patient breathing motion signal, the sensors, the breathing motion prediction filter and the controller. This enables quick testing of different controllers and prediction filters with varying parameters. Additionally in a virtual testing environment there is no risk of hardware failure. For testing with real hardware the Protura Robotic Patient Positioning System (CIVCO Medical Solutions, Kalona, IA, USA) was used together with the Hexapod H 840 (Physik Instrumente GmbH & Co. KG, Karlsruhe/Palmbach, Germany) as the breathing phantom. The sensor systems used are the laser triangulation system (LTS) optoNCDT 1302-100 (MICRO EPSILON MESSTECHNIK GmbH & Co. KG, Ortenburg, Germany) and the Topometrical Positioning System (TOPOS) (cyberTECHNOLOGIES, Ingolstadt, Germany). The hardware is controlled using MATLAB/Simulink R2014a with Real-TimeWindows Target (The MathWorks, Inc., Natick, MA, USA). The breathing motion patterns have been obtained from different patients. Two prediction filters were implemented a MULIN algorithm and a normalized least mean square algorithm. Both were tested on four different tracking systems:

1) LTS with 500 Hz measuring frequency and 100 ms delay
2) LTS with 500 Hz measuring frequency and 360 ms delay
3) LTS with 10 Hz measuring frequency and 360 ms delay
4) TOPOS with 10 Hz measuring frequency and 360 ms delay

Results: The MULIN algorithm outperformed the nLMS algorithm and predicted the respiratory motion with a measuring rate of 500Hz for 100ms with a standard error of the mean of 0.3 ± 0.01µm and with a measuring rate of 10Hz for 360ms with a standard error of the mean of 1.9 ± 0.5µm. For a small time delay of 100ms the control structure has no influence on the tracking results. For a large time delay of 360ms the Smith Predictor combined with the prediction of respiratory motion outperformed the standard feedback control structure.

Conclusion: The Smith Predictor combined with the prediction of the respiratory motion increased the accuracy of tumor tracking systems with a time delay of 360ms. However, for time delays smaller than 100ms this implementation showed no advantage over the standard feedback control structure with a PID controller.

54 Respiratory pattern changes of volunteers due to couch tracking

S. Lang[1], J. Zeimetz[1], G. Ochsner[2], M. Schmid Daners[2], S. Klöck[1], O. Riesterer[1]
[1]University Hospital Zurich, Radiation Oncology, Zurich, Switzerland
[2] ETH Zurich, Institute for Dynamic Systems and Control, Zurich, Switzerland

Motivation: Tumor motion due to breathing leads to large clinical target volume (CTV) to planning target volume (PTV) margins and increased dose to organs at risk (OAR). The three motion management techniques currently used in clinical settings are motion encompassing treatment, gating and tracking. In comparison to motion encompassing treatment, gating allows treatment to a smaller volume; however, at the cost of substantially increased treatment time. The most sophisticated treatment technique appears to be tracking because it confines the high dose to the tumor (small volume) and is time efficient. Tracking can be realized on a conventional linear accelerator by dynamically compensating the tumor motion with the treatment couch. However little evidence exists on the tolerance and the effect of couch tracking upon the patients. Therefore the goal of this study was to assess the effect of a one-dimensional motion tracking system using the treatment couch upon a group of 20 volunteers. Additionally, the accuracy of the tracking system was evaluated.

Materials and methods: Our in-house developed treatment couch tracking system is able to compensate for vertical respiratory motion. Respiratory motion is detected by a laser triangulation sensor and compensated for using the Protura treatment couch. A proportional-integral-derivative control system is used with a complete system delay of approximately 60 ms. 20 volunteers were recruited to test the system. Respiratory curves of the volunteers were assessed before, during, and after motion compensation to assess the influence of tracking upon breathing. Additionally, all volunteers were asked to complete a motion sickness assessment questionnaire (1) evaluating four dimensions of motion sickness: gastrointestinal, central, peripheral, and sopite-related. Motion sickness subscale scores in the four dimensions were calculated (0 % no signs of motion sickness, 100 % severe signs of motion sickness). The mean absolute deviation of residual motion with and without tracking was calculated.

Results: Comparing respiratory curves, 16 of 20 volunteers demonstrated an increased amplitude of breathing (mean increase 12 %) when tracking was applied (figure 1). There was no systematic change in respiration frequency. Some volunteers reported that they felt forced to breathe faster due to the vibrations which occurred at the extremes of inhalation and exhalation. Others however, found it easier to breathe regularly and slowly during tracking due to the regular sound of the couch motors.

15 of 20 volunteers reported no signs of motion sickness. Four volunteers reported mild motion sickness in the sopite-related dimension (subscale score 16.6 % to 19.4 %). One volunteer reported mild symptoms in the central dimension (subscale score 31 %).

Tracking reduced the mean absolute deviation of residual motion by a factor of 7.2 +/- 3.1 compared to no tracking. Figure 1 shows the reduction for one volunteer.

Discussion: One dimensional tracking was well tolerated by all volunteers, with mild motion sickness reported by five of 20 volunteers. All respiratory curves could be successfully tracked. However, we must further investigate why the amplitude of breathing often increased when tracking was applied. An adaptation period for patients may be of value, or further improvements to reduce vibration during extremes of inhalation and exhalation.

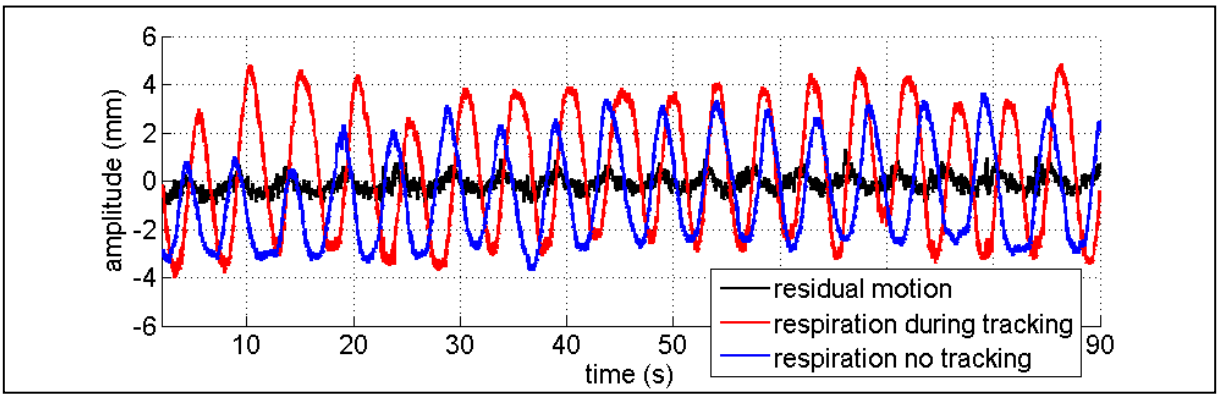

Fig. 1: Change in respiratory pattern for one volunteer during couch tracking, as well as residual motion if tracking is applied.

References

[1] Gianaros et al, Aviat Space Environ Med. 2001 February ; 72(2): 115–119

Session 10 – Brachytherapy

Chairs: D. Terriblini (Bern/CH), U. Wolff (Vienna/AT)

55 Introductory lecture: Clinical implementation of a HDR brachytherapy treatment programme

V. Magaddino[1]
[1]Institute of Radiation Physics, CHUV and University of Lausanne, Lausanne, Switzerland

Brachytherapy is an important modality in the radiation therapy treatment of cancer patients. Radioactive sources are placed into the tumour or immediately adjacent to it, thus combining the advantage of a very high and accurate dose delivery to the target volume while sparing the surrounding healthy tissues. Common brachytherapy techniques are high dose rate (HDR), low dose rate (LDR) and pulse dose rate (PDR), differing for the treatment dose rate (>12Gy/h in the former, ranging between [0.4; 2] Gy/h the latter).

The attention will be focused on the HDR brachytherapy, being the most diffused modality. The steps involved in the implementation of a HDR brachytherapy program are discussed.

After a short introduction on air kerma strength and calibration procedures, an overview of the brachytherapy dose calculation formalism based on the AAPM Task Group 43 report (1994) and its revised version (TG-43U1 2004) is presented. The generalities of remote afterloading equipment used to drive the source to and from the patients through catheters are discussed. Imaging techniques used for contouring, catheters reconstruction and planning, such as CT, MRI, ultrasound, fluoroscopy, are shown along with some indication site for HDR treatments. A short overview of the planning process is also presented, from source activation, to optimization and normalization accordingly to the dose requirements on target and organs at risk. Eventually, plan evaluation by means of dose volume histogram (DVH) is discussed. In conclusion, an overview of the different aspects of routine quality control, ranging from safety test to positional and temporal accuracy, is presented.

56 Introductory lecture: Clinical needs for accurate brachytherapy dose delivery

C. Kirisits[1]
[1]Vienna, Austria

57 Determination of a radiation quality correction factor k_Q for well-type ionisation chambers for the measurement of the reference air kerma rate of ^{60}Co HDR Brachytherapy sources

A. Schüller[1], U. Ankerhold[1]
[1]Physikalisch-Technische Bundesanstalt, Braunschweig, Germany

Introduction: About 11 years ago, a miniaturized ^{60}Co high-dose-rate (HDR) brachytherapy source, with similar geometrical dimensions to the commonly used ^{192}Ir HDR sources, was introduced into the clinics. Because of the long half life of ^{60}Co ($t_{1/2}$ = 5.3 a), afterloader systems based on ^{60}Co require a source replacement at the most every five years while systems based on ^{192}Ir ($t_{1/2}$ = 73.8 d) require a replacement at least every four months [1]. In particular for hospitals in developing countries the source exchange frequency is a crucial factor. The relatively small differences in radial dose distribution of ^{60}Co sources compared to ^{192}Ir sources do not result in clinically significant differences [1-3]. At present already more than 200 afterloader systems equipped with ^{60}Co are in service worldwide with a clearly increasing tendency [4, 5].

On the other hand, the dosimetric verification of ^{60}Co sources in the hospitals may be error-prone [7, 8], among others, due to the absence of measuring devices calibrated traceable to a national standard. For ^{192}Ir HDR brachytherapy sources the traceability has been well established by several national metrological institutes by means of traceable calibrated well-type ionization chambers, whereas in the case of ^{60}Co only PTB offers a calibration service.

In this work, within a framework of a research cooperation, it was investigated whether a chamber type-specific radiation quality correction factor k_Q can be determined in order to enable the measurement of the reference air kerma rate (RAKR) of ^{60}Co HDR brachytherapy sources with acceptable uncertainty by means of a well-type ionization chamber calibrated for ^{192}Ir-radiation.

Materials and methods: A total number of 29 well-type ionization chambers were studied: six of the type HDR 1000 Plus from Standard Imaging Inc., Wisconsin, USA, with the applicator REF 70110, and 23 chambers of the type Tx33004 from PTW, Freiburg, Germany in connection with the applicator T33002.1.009. The latter chamber type is also distributed by Nucletron, Veenendaal, The Netherlands, as “Source Dosimetry System” SDS under reference number 077.0xx together with the applicator (reference number 077.095).

Four ^{60}Co brachytherapy sources have been used: one of the type GK60M24 provided by Nucletron under reference number 136.002, furthermore one source of the type GK60M21 and two sources of the type GK60M23, all three provided by Eckert & Ziegler BEBIG GmbH, Berlin, Germany under the product code Co0.A86. In order to investigate a possible influence of the activity to the correction factors k_Q a source with an activity of about 75 GBq and one with about 35 GBq were used. Thereby the whole clinically relevant activity range given by the source replacements every five years are covered. All ^{60}Co source types have a similar design; its geometry of the radioactive part (about 3.5 mm length and 0.5 mm in diameter) is nearly identical [6].

The surveyed ^{192}Ir brachytherapy source types are: the Microselectron-HDR classic and the Microselectron V2 manufactured on behalf of Nucletron by Mallinckrodt Medical B.V., Petten, The Netherlands, as well as the GammaMed 232 distributed by NTP Radioisotopes, Fleurus, Belgium. For one and the same Microselectron V2 source with initial activity of about 470 GBq the measurements were repeated after approximately three half-life periods at about 60 GBq, which covers more than the clinically relevant activity range between the source replacements every four months.

The experiment was performed as follows: First the determination of the RAKR of the ^{60}Co and the ^{192}Ir brachytherapy sources was carried out with the PTB calibration facility for HDR brachytherapy sources [9] which is based on a secondary standard ionization chamber calibrated traceably to PTB’s primary standards in terms of air kerma [10]. Subsequently the calibration factors of the well-type ionization chambers for radiation fields of ^{192}Ir and ^{60}Co HDR brachytherapy sources $N_{\text{Ir-192}}(i)$ and $N_{\text{Co-60}}(i)$ were determined for each chamber (i) using the calibrated sources. Then the individual radiation quality correction factors $k_Q(i) = N_{\text{Co-60}}(i) / N_{\text{Ir-192}}(i)$ are analyzed with respect to their variation. For a certain range of validity a type specific radiation quality correction factor k_Q is derived from the average over the individual correction factors $k_Q = \langle k_Q(i) \rangle$.

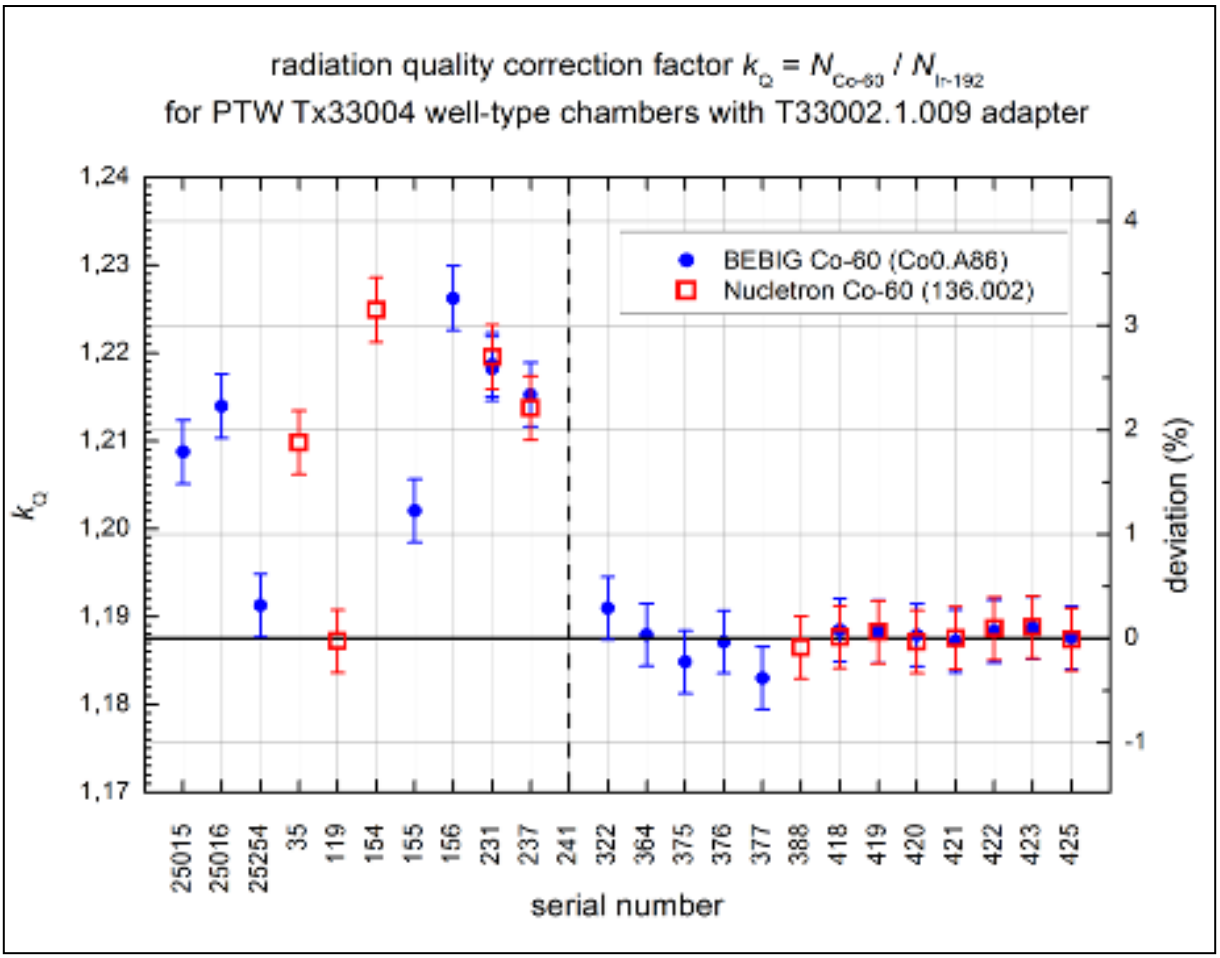

Fig. 1: Individual radiation quality correction factors $k_Q(i)= N_{Co-60}(i) / N_{Ir-192}(i)$ for PTW Tx33004 well-type ionization chambers in connection with a T33002.1.009 adapter as function of serial number of device under test. Full circles: $k_Q(i)$ determined with BEBIG ^{60}Co Co0.A86 sources. Open squares: $k_Q(i)$ determined with a Nucletron ^{60}Cosource. Dashed vertical line: lower limit for up-to-date chambers built without technical changes [11]. Continuous horizontal line: type specific radiation quality correction factor $k_Q=<k_Q(i)>$ from average of chambers with SN > 241.

Results: Figure 1 shows the individual radiation quality correction factors $k_Q(i) = N_{Co-60}(i) / N_{Ir-192}(i)$ of 23 PTW Tx33004 well-type ionization chambers in connection with a T33002.1.009 adapter as a function of the serial number (SN) of the chamber. For the same chamber, the $k_Q(i)$ values obtained with the ^{60}Co sources of BEBIG (full circles) and of Nucletron (open squares) agree within the experimental uncertainty. Chambers with higher SN feature $k_Q(i)$ values which agree within 0,3 % (k=2) whereas specimens with a lower SN vary up to about 3 %. At the request of PTB, the manufacturer PTW states that well-type chambers of the type 33004 are up to date and were built without technical changes from PTW serial number 241 (and Nucletron SDS serial number 463) onwards [11]. Chambers built before July 2008 with SN < 241 as well as with the old serial number notation 25xxx (left of dashed vertical line in Fig. 1) differ from the up-to-date chambers. From the average of all investigated chambers with SN > 241, a type specific radiation quality correction factor of k_Q = 1.188 +/- 0.3 % is determined (continuous horizontal line in Fig. 1). The chamber with SN 25254 was updated during a repair [12] and feature therefore a similar $k_Q(i)$ to the new chambers. The radiation quality correction factor currently used by PTW is derived from measurements with old chambers with SN < 241. This results in a deviation of the measured ^{60}Co calibration factor of more than 2 % from the manufacturer's data, i.e. an overestimation of the RAKR of ^{60}Co sources for new chambers with SN > 241.

From the individual radiation quality correction factors of six HDR 1000 Plus well-type chambers from Standard Imaging with widely spread serial numbers the type specific radiation quality correction factor k_Q = 1.052 +/- 0.3 % has been derived. No statements are given by the manufacturer with respect to a ^{60}Co calibration factor.

Conclusion: A type specific radiation quality correction factor k_Q was determined for well-type ionization chambers of the type Tx33004 and HDR 1000 Plus, respectively. Thus the calibration factor in terms of RAKR of a chamber for radiation fields of ^{60}Co brachytherapy sources $N_{Co\text{-}60} = k_Q \cdot N_{Ir\text{-}192}$ can be calculated from a given calibration factor $N_{Ir\text{-}192}$ for an ^{192}Ir HDR source. In the case of PTW's Tx33004 chamber the derived k_Q value is valid for up-to-date chambers with SN > 241 (Nucletron SDS SN > 463) onwards only. For chambers with SN < 241 or the notation 25xxx, deviations of more than 3 % have been observed. For these chambers a direct calibration with a ^{60}Co source is necessary. For both chamber types the uncertainty of k_Q is small compared to the typical uncertainty of the calibration factor $N_{Ir\text{-}192}$ of about 2.5 % ($k = 2$).

Hence the uncertainty of the ^{60}Co calibration factor calculated from $N_{Co60} = k_Q \cdot N_{Ir\text{-}192}$ is dominated by the uncertainty of $N_{Ir\text{-}192}$.

References

[1] Palmer, A., Hayman, O., Muscat, S.: Treatment planning study of the 3D dosimetric differences between Co-60 and Ir-192 sources in high dose rate (HDR) brachytherapy for cervix cancer, J. Contemp. Brachytherapy. 4 (2012) 52

[2] Baier, K., Richter, J., Flentje, M.: Vergleich von ^{60}Co und ^{192}Ir im Einsatz beim Afterloading,Tagungsband der 37. Jahrestagung der DGMP, Regensburg (2006) 235

[3] Strohmaier, S., Zwierzchowski, G.: Comparison of ^{60}Co and ^{192}Ir sources in HDR brachytherapy, J. Contemp. Brachytherapy 3 (2011) 199

[4] Andrássy, M., Niatsetsky, Y., Pérez-Calatayud, J.: Co-60 versus Ir-192 in HDR brachytherapy: Scientific and technological comparison, Rev. Fis. Med. 13 (2012) 125

[5] Marketing Department Eckert & Ziegler BEBIG

[6] Approval certificate for special form radioactive material RUS/5900/S-96, ROSATOM State Corporation for Atomic Energy, Russian Federation (2011)

[7] Zakaria, G. A., Schütte, W.: Dosimetrie in der HDR-Afterloading-Brachytherapie mit Ir-192 und Co-60: Vergleich verschiedener internationaler Dosimetrieprotokolle, Tagungsband der 39. Jahrestagung der DGMP, Oldenburg (2008)

[8] Azhari, H. A., Hensley, F., Schütte, W., Zakaria, G. A.: Dosimetric verification of source strength for HDR afterloading units with Ir-192 and Co-60 photon sources: Comparison of three different international protocols, J. Med. Phys. 37 (2012) 183

[9] Selbach, H.-J: Neue Kalibrieranlage für ^{192}Ir- und ^{60}Co-Brachytherapie-Strahlungsquellen, Tagungsband der 37. Jahrestagung der DGMP, Regensburg (2006) 244

[10] Selbach, H.-J.; Büermann, L.: Vergleich zweier Verfahren zur Darstellung der Einheit der Kenndosisleistung für ^{192}Ir-HDR-Brachytherapiequellen, Tagungsband der 35. Jahrestagung der DGMP, Leipzig (2004)

[11] official letter from Dr. E. Schüle, PTW-Freiburg to PTB dated 24.9.2013

[12] private communication by Dr. H. Georg, PTW-Freiburg

58 Dose measurement with Octavius SRS 1000 Array in brachytherapy. Principle suitability for system checks and dosimetry – First Results

M. Kollefrath[1], M. Gainey[1]
[1]Universitätsklinikum Freiburg, Klinik für Strahlenheilkunde, Freiburg, Germany

Introduction: Brachytherapy dosimetry is complicated by the steep absorbed dose gradients proximal to the source. There is currently a paucity of dosimetric system checks in brachytherapy, which has been criticised from many parties, for example the SSK.

Is it possible to verify HDR (^{192}Ir, Microselectron V2) brachytherapy treatment plans, on the basis of independent dose calculation based upon TG-43 [2], using a commercially available high resolution 2D measurement array?

Materials and methods: The Octavius SRS 1000 (PTW Freiburg) is a measurement array comprising 977 liquid filled ionisation chambers, distributed over an area of 110mm x 110mm. Each ionisation chamber has a thickness of 0,5mm and an area of 2.3mm x 2.3mm. The array has great potential for brachytherapy due to the large number of measurement chambers with small dimensions in the direction of steepest dose gradient. A mechanical jig is placed in direct contact with the upper surface of the array (Figure 2), which can accomodate up to 8 cathethers (clinical 4 French steel needles). This arrangement was reconstructed in the treatment planning system, TPS, (Oncentra Masterplan, Elekta AG Sweden) and the dose subsequently calculated in the plane of the measurement chambers in accordance with the TG-43 formalism.

Subsequently the fundamental suitability of the array for measurements with Irradiation with a ^{192}Ir source will be investigated. The dependence of the measured value with respect to direction and energy-variation with depth will be investigated with a single dwell position located above the geometric centre of the array. By employing a plan comprising more catheters the dependence on the radiation quality, kQ, will also be investigated.

Results: The preliminary measurements with the array confirm its suitability for quality assurance in brachytherapy. For the measurement of a single dwell-position an excellent agreement between measurement and dose calculation was observed, Moreover the dose varied by more than a factor of 50 due to the inverse square law (Figure 1).

Conclusion: After completing the initial measurement one can conclude that the array is suitable for measurement in brachytherapy with ^{192}Ir. Further investigations and consideration for application for quality assurance can be found in the presentation by Mr. Gainey.

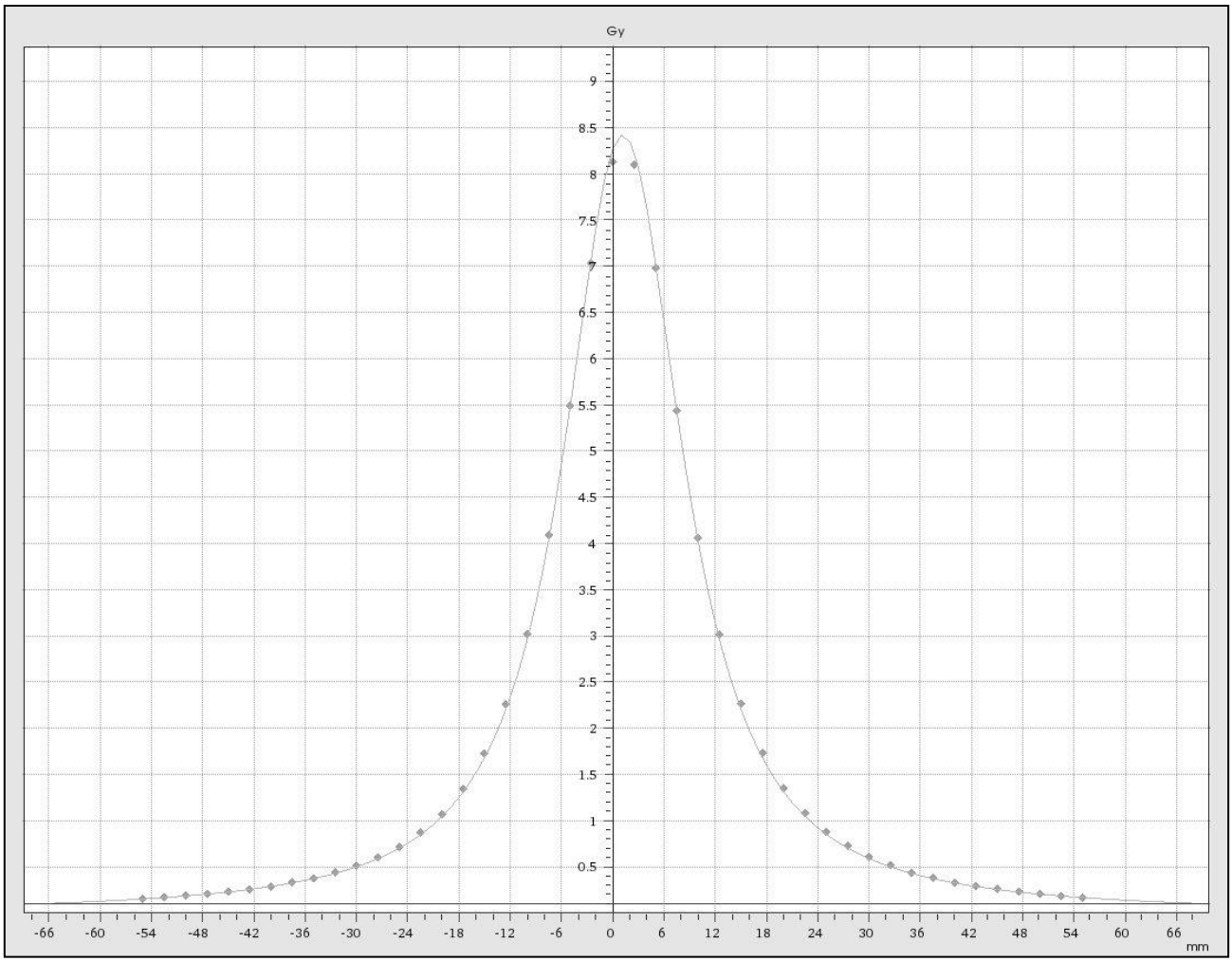

Fig. 1: Dose measurement with a single through the dwell position. Solid line (TPS), points (SRS 1000 Array).

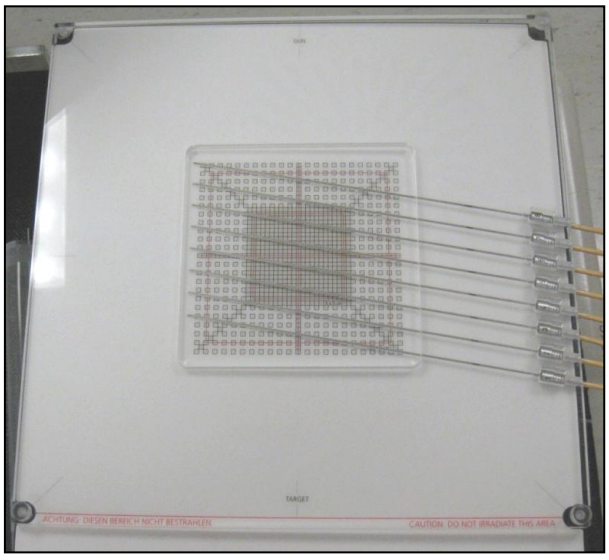

Fig. 2: Photo showing the catheter- source dwell position: orthogonal dose profile holder fixed on top of the SRS 1000 array.

References

[1] Physikalisch-technische Qualitätssicherung in der Strahlentherapie – Vorschläge zur Prüfung des gesamten Behandlungssystems, Empfehlung der Strahlenschutzkommision, (2010), S. 29

[2] Mark J. Rivard, Update of AAPM Task Group No. 43 Report: A revised AAPM protocol for brachytherapy dose calculations, AAPM (1995 und update 2003)

59 Brachytherapy dosimetry using a high resolution commercial liquid-filled ionisation chamber array: initial experience and limitations

M. Gainey[1], M. Kollefrath[1]
[1]Universitätsklinikum Freiburg, Klinik für Strahlenheilkunde, Freiburg, Germany

Introduction: Brachytherapy dosimetry is complicated by the steep absorbed dose gradients proximal to the source. Whilst it is possible to verify simple 2D geometrically based brachytherapy treatment plans, such as a vaginal cylinder or ring-tube, on the basis of empirical fitting or independent dose calculation based upon TG-43, the situation is non-trivial for complex 3D brachytherapy plans, such as the interstitial ring-tube. Thus the question arises whether it is possible to verify complex 3D HDR brachytherypy plans using a commercially available high resolution 2D measurement array.

Material and methods: We describe a method using the Octavius 1000 SRS 2D (PTW Freiburg, Germany) array comprising 977 liquid-filled ionisation chambers covering an area of 110 x 110 mm² [1]. This array was designed to perform dosimetric verification of SRS/SBRT treatment plans with high spatial resolution. 3D brachytherapy patient plans were employed to irradiate the 1000 SRS array using an in-house PMMA jig which fixes up to 8 application needles (4-French) at a constant separation of 9.65 mm above the upper surface of the detector array (Fig. 1). The needles run parallel to each other, separated by 12.80mm, but rotated by 10 degrees relative to the axial axis of the detector array, thereby avoiding irradiating the detector electronics. In a first step a homogeneous plan employing all 8 needles was generated: one catheter point was defined per dwell position but displaced in the reference plane. Patient plans were copied manually from the patient CT study and entered into an empty CT study within the brachyhtherapy module of OTP (Nucletron/Elekta AG Sweden) treatment planning system: the needle geometry was reproduced using cathether reconstruction. Dose is calculated in accordance with TG-43, viz. within an infinite homogeneous water tank. The resulting dose distribution was calculated and compared with the measured dose distribution using the Verisoft 6.0 software (PTW Freiburg, Germany).

Results: Initial results indicate that the PMMA jig is mechanically stable, viz. the repeated measurement showed a maximal dose difference of 0.6 % using the most stringent absolute local analysis criterion (local percentage difference ≤ 3 %), median 0.07 %. Comparison of the calculated and measured dose distribution using the aforementioned local analysis criterion was excellent: 95.9 % agreement (Fig. 2).

Summary: This work builds upon the work described in our other submitted abstract (abstract-ID:32). The initial results presented using the Octavius SRS1000 array are very promising. Further work needs to be performed to evaluate the effect of systematic shifts of the source on the analysis. Currently the dwell time pattern are entered manually into the empty base plan. It is hoped that this will be automated in the near future.

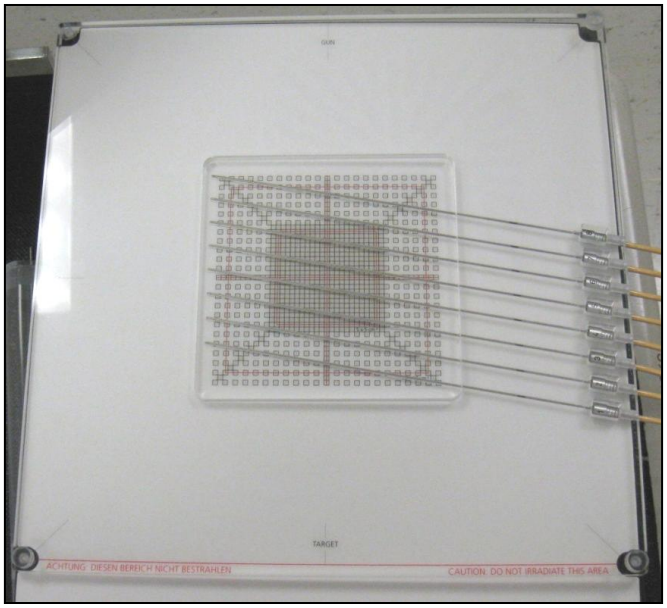

Fig. 1: Photograph showing the 2D array, the jig and 8 needles inserted

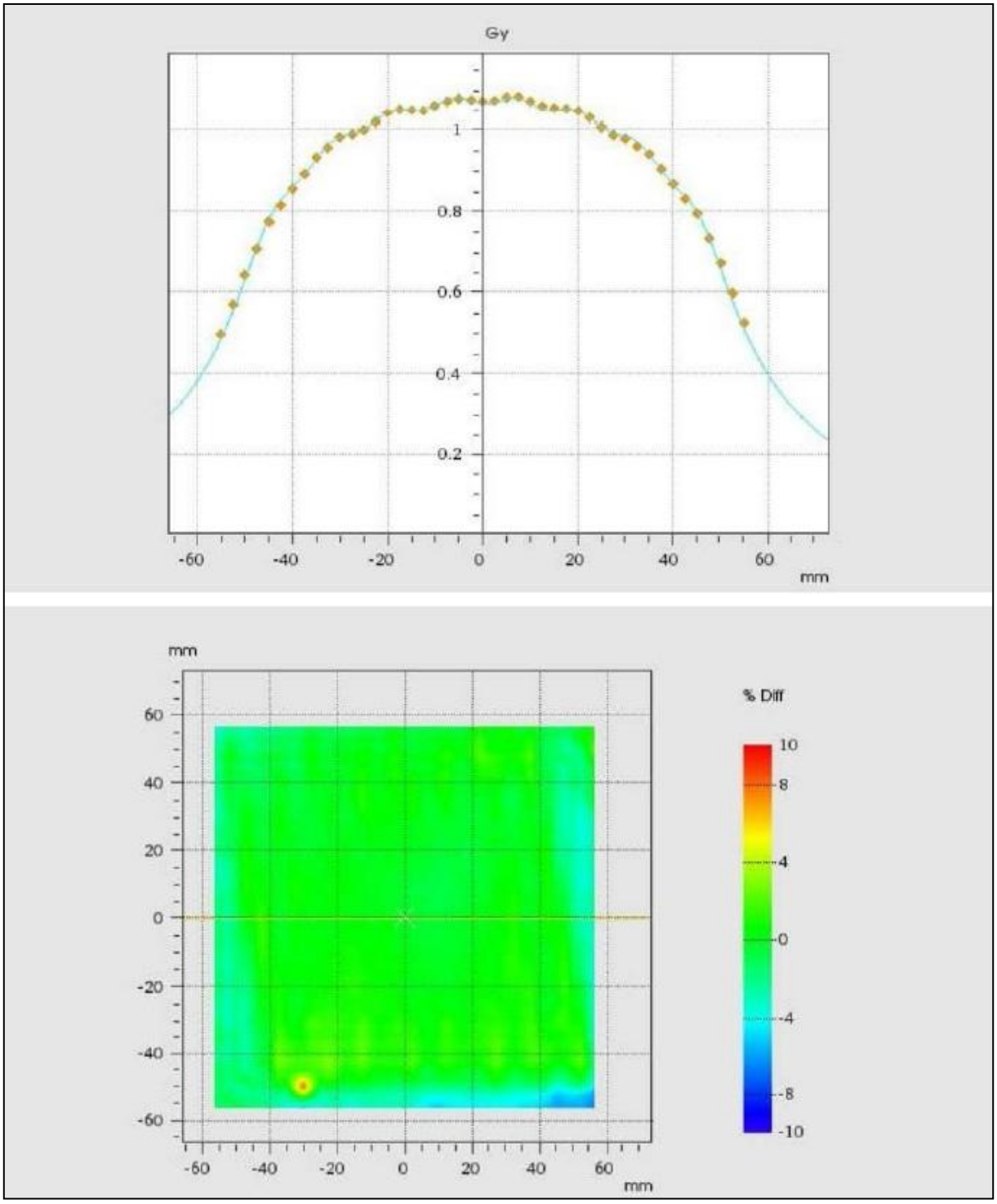

Fig. 2: Initial results showing the left-right profile : measured (points) and calculated dose profile (continuous line)

References

[1] Poppe B, Stelljes T S, Looe H K, Harder D and Willborn K, Dosimetric Properties of the Octavius 1000SRS Liquid Filled Ionization Chamber Array, (2013) 40, Med. Phys 217

60 Measurement of mean photon energy E_m at points in a ^{192}Ir HDR source brachytherapy field by the twin-detector method

N. Chofor[1], D. Harder[2], B. Poppe[1]
[1]Pius-Hospital Oldenburg, Strahlentherapie, Oldenburg, Germany
[2]Georg-August-University, Medical Physics and Biophysics, Göttingen, Germany

Introduction: In previous work we have shown by Monte Carlo calculation that the radiation quality correction factor k_Q under brachytherapy conditions depends on a single parameter, the mean photon energy E_m at the point of measurement [1]. We have also shown that the *signal ratio* of a pair of detectors comprising an unshielded p-type silicon diode 60012 (PTW Freiburg, Germany) and the synthetic single crystal microDiamond detector 60019 (PTW Freiburg, Germany) can be used to determine E_m at any point of measurement. The method takes advantage of the enhanced response of the Si diode detector to low-energy photons and the comparatively flat energy response of the diamond detector [1]. In the present study we will more closely describe how the normalized signal ratio *NSR* can be calibrated in terms of E_m and how it can be applied under clinical conditions.

Materials and methods

The spectral fluence $\Phi_E(E)$ of the primary and scattered photons at points of interest in a water phantom was modeled using FLURZnrc/egsnrc. Using a realistic model of a ^{192}Ir HDR GammaMed Plus source, the mean photon energy,

$$E_m = \int E\, \Phi_E(E)\, dE \,/\, \int \Phi_E(E)\, dE \qquad \ldots\ldots\ldots\ldots \qquad (1)$$

was calculated for different off-axis positions within a cylindrical water phantom with dimensions of either R = 30 cm, H = 60 cm or R = 20 cm, H = 40 cm. Similarly, measurements of the silicon diode/microDiamond signal ratio were performed at a ^{192}Ir HDR GammaMed Plus unit within a water tank with dimensions of either 50×50×50 cm³ (the PTW-Freiburg MP3 water tank) or R = 20 cm, H = 40 cm. The smaller cylindrical phantom was placed within the PTW-Freiburg MP3 water tank, taking advantage of the MEPHYSTO software for stepper motor control and data acquisition. Each detector was positioned with its longitudinal axis aligned in the source's midplane and pointing towards the longitudinal axis of the source, and with its EPOM at the point of measurement. The EPOM was 1.2 mm below the front surface for the diode detector and 1.7 mm for the diamond detector. With the two detectors, lateral signal profiles were obtained in the midplane of the source as functions of the distance from the longitudinal axis of the source.

The normalized signal ratio *NSR* is defined as the quotient of the signal ratio under any given application condition x to that at the brachytherapy reference position r_{ref} = 1 cm away from the longitudinal axis of the source along a plane perpendicular to it:

$$NSR_x = SR_x \,/\, SR_{ref} \qquad \ldots\ldots \qquad \ldots\ldots \qquad (2)$$

Theoretically, the signal ratio *SR* of a pair of radiation detectors under condition x can be described as:

$$SR(x) = \frac{\sum_{i=1}^{n} r_1(E_i) \left(\frac{\mu_{en}(E_i)}{\rho}\right)_w \phi_E(E_i)\, E_i\, \Delta E_i}{\sum_{i=1}^{n} r_2(E_i) \left(\frac{\mu_{en}(E_i)}{\rho}\right)_w \phi_E(E_i)\, E_i\, \Delta E_i} \qquad (3)$$

where $r_1(E_i)$ and $r_2(E_i)$ represent the energy dependent responses of detectors 1 and 2 respectively and $\Phi_E(E)$ is the spectral photon fluence under condition x. We can here use the kerma approximation because for the whole range of photon energies concerned in brachytherapy dosimetry at a ^{192}Ir unit, the $r(E_i)$ data come from measurements under conditions of secondary electron equilibrium, and secondary electron equilibrium in water can as well be assumed in a very good approximation at points of measurement in a surrounding large phantom.

Results: Figure 1a shows how the Monte Carlo calculated values of E_m in a large cylindrical phantom [dimensions: R = 30 cm, H = 60 cm] (full curve) have been correlated with the values of the *NSR* measured in the MP3 water tank [dimensions: 50 × 50 × 50 cm³] (points) at the same distances from the source axis for which the values of E_m had been calculated. Thereby the correlation function

$$E_m = 105.3 \exp(-7.108\, NSR) + 0.4311 \exp(-0.5885\, NSR) \qquad (4)$$

(with E_m in MeV) was obtained, which has the meaning of a *calibration* of the *NSR* in terms of E_m.

The pair of detectors thereby calibrated to measure E_m was then placed in the smaller cylindrical phantom (R = 20 cm, H = 40 cm) and values of E_m were measured at off-axis positions. Fig. 1b shows that they closely approximate the Monte Carlo values calculated for control.

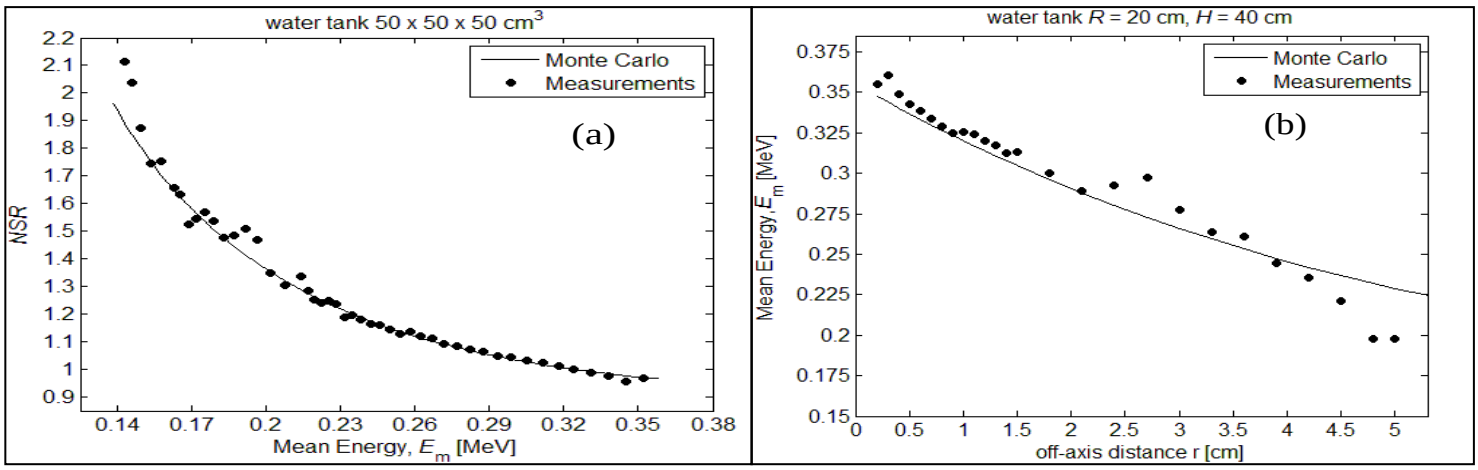

Fig. 1: Variation of the normalized signal ratio, NSR, with mean photon energy E_m at a ^{192}Ir source HDR GammaMed Plus unit. (a) Monte Carlo calculations of the NSR according to equation 3 are compared with measurements of the NSR with the diode/diamond detector pair. Thereby the NSR is calibrated in terms of E_m. This calibration is expressed by Eq. (4). (b) Comparison of measured values of E_m in a smaller phantom (R = 20 cm, H = 40 cm) with Monte Carlo calculated control values.

Fig. 1b: also illustrates the variation of the results from measurement sessions on three different days, due to repositioning the detectors with respect to the source. The overall detector positioning precision (repeatability) in the direction of scan is thereby estimated to be within ± 0.3 mm. This entails the positioning accuracy of the stepper motors of the MP3 unit, reported by the manufacturer to be within ± 0.1 mm, which value was confirmed by repeated measurements during a single measurement session. An additional source of uncertainty may come from a small variation of the angular alignment of the detector with respect to the direction towards the mid-point of the source. Thus the results in fig. 1b indicate the magnitude of daily positioning errors and the resulting accuracy in determining the mean photon energy. For points up to 5 cm from the source, the overall uncertainty of E_m determinations by this method is estimated to lie within limits of ± 5 %. When such E_m values are applied to determine k_Q with the help of the earlier published fitting equations of the form [1]

$$k_Q = a \exp(b E_m) + c \exp(d E_m) \qquad (5)$$

the resulting uncertainty of k_Q e.g. at E_m = 0.32 MeV (i.e. at 1 cm from the center of a ^{192}Ir source) is ± 2.2 % in the worst case (a silicon diode) and ± 0.1 % in an advantageous case (diamond detector)

Conclusions: Using the normalized signal ratio, *NSR*, of a diamond/diode detector pair calibrated to measure the mean photon energy E_m, the mean photon energy under application conditions has been measured with an uncertainty of ± 5 % for off-axis points up to 5 cm from a commercial HDR GammaMed Plus ^{192}Ir source. Indirectly, this means that the k_Q value at a point of measurement in the field of an ^{192}Ir source 1 cm away from the source axis can be determined with an uncertainty of ± 2.2 % for a Si diode and ± 0.1 % for a diamond detector. Despite the remaining accuracy challenges with regard to detector and source positioning, the *NSR* measured by the twin-detector method is hereby confirmed as a practical approach to determine the mean photon energy E_m and thereby k_Q at any given point of measurement under brachytherapy applications. In future work we shall concentrate on furthermore reducing positioning errors in order to improve the accuracy of the method.

References

[1] Chofor N, Harder D, Nebah FP, Selbach H-J, Poppe B. In ^{192}Ir brachytherapy dosimetry, detector-specific radiation quality correction factor k_Q depends on mean photon energy E_m at point of measurement. Med Phys 2014, submitted.

61 Dosimetric characterization of three types of ^{106}Ru eye-plaques for uveal melanoma with different detectors

G. Heilemann[1], N. Nesvacil[1], M. Blaickner[2], D. Georg[1,3]
[1]Medical University of Vienna, Department of Radiation Oncology, Vienna, Austria
[2]Austrian Institute of Technology GmbH, Health & Environment Department Biomedical Systems, Vienna, Austria

[3]Medical University of Vienna, Christian Doppler Laboratory for Medical Radiation Research for Radiation Oncology, Vienna, Austria

Introduction: Due to steep dose gradients and the confined geometry quality assurance of ^{106}Ru/^{106}Rh eye-plaque applicators (BEBIG, Germany) is challenging. For this study relative dose distributions as well as reference dose rates were measured with different dosimetric detector systems and were compared with Monte Carlo (MC) simulations. Additionally the penumbra region, defined as the fringe zone of the active ^{106}Ru layer, was investigated to characterize the usable area of different applicator types in terms of lateral dose fall off in varying depths.

Materials and methods: Using EBT2 and EBT3 radiochromic films two-dimensional dose distributions of three different applicator models (CCA, CCB and COB) were measured parallel to the central axis as well as on normal planes in depths of 3 mm, 6 mm, 8 and 9 mm in a polystyrene phantom. Additionally depth-dose profiles along the central axis as well as off-axis profiles were obtained with a newly developed synthetic single crystal diamond Schottky diode and a silicon diode (both PTW-Freiburg, Germany) in a water scanning phantom (IBA, Belgium) using the high precision step motor to accurately position the detectors. All applicators were modeled using the MCNP5 code and the calculated dose profiles were compared to the measurements and available published data (BEBIG manufacturer values and Soares *et al* 2001). By means of penumbra characteristics the actual size of the active layer was evaluated at varying depths. This allows to account for the true size of the lateral dose distribution (100 % of central dose) in order to sufficiently cover the tumor volume not only in apex height but also in its width.

Results: The film measurements showed an accuracy of absolute dose rates in a reference depth of 2 mm on the central axis of the applicator better than 10 % as compared to the manufacturer's data. For the depth-dose profiles (2 – 8 mm along central axis) the measurements yielded a reproducibility (1 SD) < 3 %, < 2.5 % and < 4 % for the investigated applicator types with the diamond, diode detector and film, respectively. To test reproducibility the measurements were repeated five times with completely independent setups. The off-axis profiles showed a precision of < 10 % in the inner part (< 5 mm) and up to 30 % across the rim. All MCNP calculations yielded a SD < 2.3 %. The experimental data sufficiently complied with the MC calculated dose distribution and data published by Soares *et al* 2001, i.e. the deviation was less than 5 %. The measured depth dose profiles showed an agreement to the manufacturer's data well within 6 % for all applicator types with all used detectors which conforms to recommended tolerances.

Conclusion: The results of the relative and absolute dose measurements of different ^{106}Ru/^{106}Rh applicators with the investigated detector systems complied very well with the data from the MC simulations as well as with reference data from the manufacturer. The presented description of reference dose rates, percent depth doses and two-dimensional dose distributions along with the determination of effective lateral applicator sizes as a function of depth will be followed by more advanced dosimetric studies with regard to three-dimensional dosimetry. This will form the basis for verification of future 3D treatment planning of ^{106}Ru/^{106}Rh eye-plaques.

(Supported by the Austrian Science Fund (FWF), project P25936)

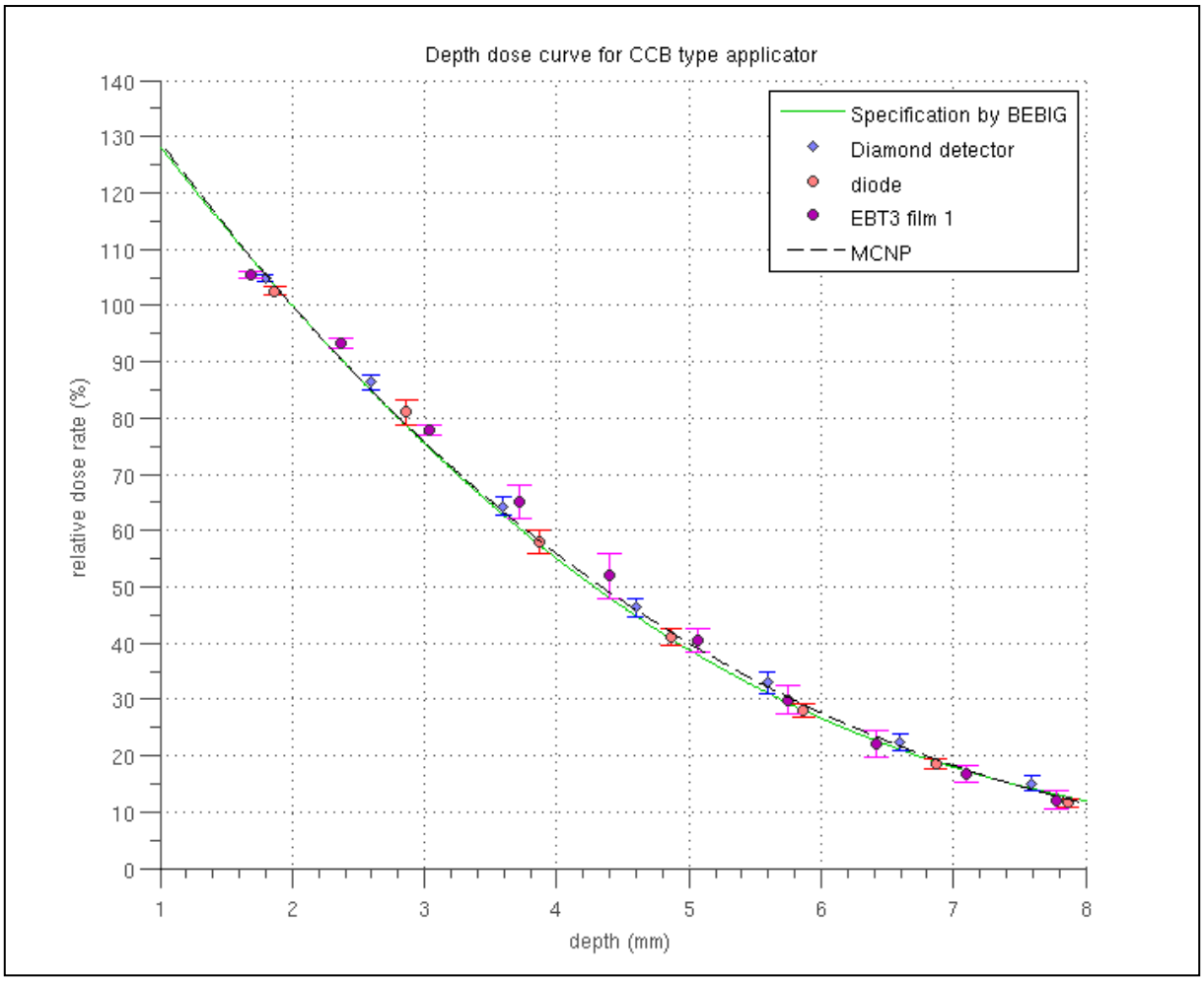

Fig. 6: Depth dose distribution of a CCB type applicator measured with different detectors.

References

[1] C.G. Soares *et al.*, "Dosimetry of beta-ray ophthalmic applicators: Comparison of different measurement methods," Medical Physics **28**(7), 1373 (2001).

Session 11 – Magnetic resonance imaging II: Modelling and Quantitation

Chairs: M. E. Ladd (Heidelberg/DE), J. R. Reichenbach (Jena/DE)

62 Introductory lecture: Quantitative Oxygen-17 MRI

M. Bock[1]
[1] Universitätsklinikum Freiburg, Radiologische Klinik-Medizin Physik, Freiburg, Germany

The energy consumption of the brain is to 90 % maintained by glucose metabolization. Therefore, oxygen (O2) is required which is taken up via the lungs, and which binds to hemoglobin in the blood to be transported into the brain. In the brain cells oxygen is metabolized into water. Many diseases are characterized by local changes in the cellular oxygen metabolism, such as Alzheimers, Parkinsons, or brain tumors. Oxygen metabolism is quantified by the measurement of the cerebral metabolic rate of oxygen consumption, CMRO2, which is given in µmol/min O2 per 1g brain tissue. For white brain matter, CMRO2 is about 0.6 µmol g-1min-1, whereas an about 2.5-fold higher value of 1.5 µmol g-1min-1 is found in gray brain matter.

Currently, CMRO2 is quantified with 15O positron emission tomography (PET). 15O-PET uses the radioactive isotope 15O, which needs to be produced in a cyclotron close to the PET system due to its short half life of only 120 s. Furthermore, for a quantitative analysis also arterial blood samples need to be taken during the exam. These disadvantages have so far hampered the use of 15O-PET studies, and only a few academic centers are performing them routinely today.

Recently, MRI with the stable isotope 17O has been proposed as an alternative to 15O PET. Oxygen-17 is a nucleus with a spin of 5/2, and it has a natural abundance of about 0.038 %. The quadrupole interaction leads to very short relaxation times on the order of a few milliseconds, which is advantageous as it enables an efficient acquisition with short repetition times, but it also requires ultra-short TE acquisition strategies to overcome the inherent T2* decay. Despite the low natural concentration and the imaging challenges, imaging studies with 17O have been performed already at natural abundance using high field MRI systems with B0 = 7 T and higher. Recently, we have shown that 17O MRI is also possible at field strengths that are more clinically available such as 3 T.

To quantify CMRO2, MRI at natural abundance alone is not sufficient; rather, the patient needs to inhale highly enriched 17O gas. During cerebral metabolization of this oxygen H217O is formed which is then detected with dynamic 17O MRI. The MR signal change after inhalation is modeled using rate equations which use CMRO2 as one fit parameter. From the data regional maps of CMRO2 can be calculated.

In this presentation the current state-of-the-art in 17O MRI is presented, and applications in particular in the diagnostics of tumors are shown.

References

[1] Zhu XH, Zhang N, Zhang Y, Zhang X, Ugurbil K, Chen W. In vivo 17O NMR approaches for brain study at high field. NMR Biomed 2005;18(2):83-103.
[2] Hoffmann SH, Begovatz P, Nagel AM, Umathum R, Schommer K, Bachert P, Bock M. A measurement setup for direct 17O MRI at 7 T. Magn Reson Med 2011;66(4):1109-1115
[3] Borowiak R, Groebner J, Haas M, Hennig J, Bock M. Direct Cerebral and Cardiac 17O-MRI at 3 Tesla: Initial Results at Natural Abundance. MAGMA 2014;21(1):95-99.

63 CPMG inter pulse delay time variation and capillary diameter quantification in muscle tissue

F. T. Kurz[1], T. Kampf[2], H.-P. Schlemmer[3], H. Sabine[1], M. Bendszus[1], C. H. Ziener[3]
[1]Heidelberg University, Neuroradiology, Heidelberg, Germany
[2]Würzburg University, Experimental Physics 5, Würzburg, Germany
[3]German Cancer Research Center, Radiology, Heidelberg, Germany

Introduction: Recently, it has been shown that blood transverse relaxation rate increases with inter-echo time using multi-spin-echo Carr-Purcell Meiboom-Gill (CPMG) sequences due to ^{1}H nuclear spin diffusion around or exchange with erythrocytes containing paramagnetic deoxyhemoglobin [1]. This can be applied to **s**keletal muscle tissue, where the effects of denervation or aging are linked to a remodeling of the underlying capillary network [2,3]. The resulting susceptibility differences of capillaries and surrounding tissue are used to provide a means of quantifying microstructural parameters such as capillary radius and diffusion D.

Materials and methods: Magnetic field inhomogeneities in capillary networks are due to susceptibility differences of capillaries that contain deoxygenated blood cells and the surrounding tissue. Within the well-known capillary model of Krogh [4], diffusion-dependent spin trajectories are restricted to a dephasing cylinder around each capillary where the radius is chosen such that the regional blood volume fraction $\kappa = R_c^2/R^2$ remains constant (see Fig.1). Measured transverse relaxation rates $R_2 = R_{2,0} + \Delta R_2$ with intrinsic and diffusion-dependent transverse relaxation rate $R_{2,0}$ and ΔR_2, respectively, are treated in the weak field approximation of Jensen and Chandra [5] where ΔR_2 can be expressed in terms of a correlation function K. In close analogy to [6], a spectral expansion of K leads to an expression for ΔR_2 that is only dependent on correlation time $\tau = R_c^2/D$, external magnetic field induced susceptibility-dependent frequency shift $\Delta\omega$ and inter-echo time τ_{180}.

Results: In Fig. 2, ΔR_2 is visualized for $\Delta\omega\tau$ = 0.1 and limiting cases for $\tau_{180} \to 0$ and $\tau_{180} \to \infty$ are considered. Results for R_2 were fitted to experimental data of Damon *et al.* [7] who examined CPMG relaxation rates in excised plantaris muscles of Sprague-Dawley rats at 4.7 Tesla field strength (Fig. 3). The resulting parameters $\Delta\omega$ = 421.58 µs and $R_{2,0}$ = 19.67 s^{-1} are in close agreement with those obtained from the Luz-Meiboom (LM) chemical exchange model [7,8] (τ^{LM} = 470 µs and $R_{2,0}^{LM}$ = 21.07 s^{-1}[1]). With D = 2 µm^2/ms, the capillary radius follows as R_c = 0.92 µm.

Conclusion: The presented model can be used to quantify capillary diameters and/or nuclear spin diffusion around capillaries based on measurements of CPMG T_2 relaxation time in muscle tissue. Model behavior of transverse relaxation rate $R_2 = 1/T_2$ agrees well with experimental data (Fig.3), however, predictions for rat muscle capillary radius slightly underestimate the radius ~1.5-2.5 µm given in [9] due to experimental shortcomings like postmortal blood loss, increased vessel wall permeability and therefore pericapillary tissue swelling.

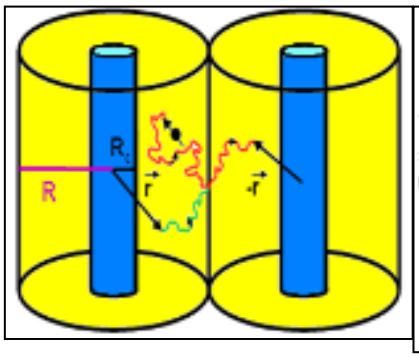

Fig. 1: Schematic view of two parallel capillaries with supply areas (yellow) and a corresponding ^{1}H nuclear spin trajectory (red) that is replaced by a reflected version (red-green in the left capillary).

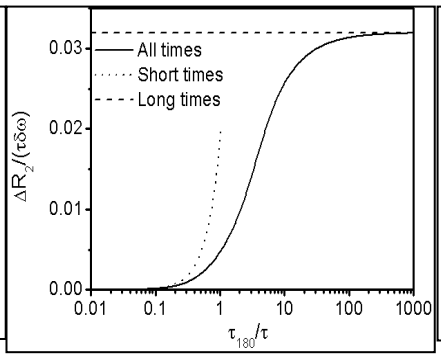

Fig. 2: CPMG relaxation rate ΔR_2 in depen-dence of inter-echo time τ_{180}. For small τ_{180}, ΔR_2 increases quadratically with τ_{180} to reach a plateau for large τ_{180} .

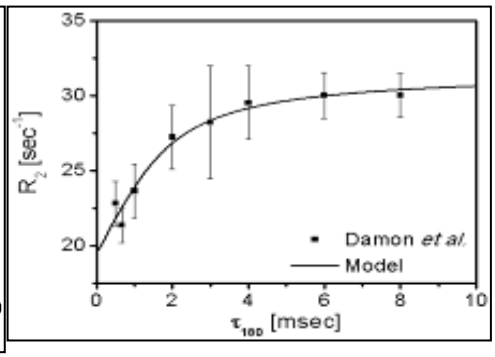

Fig. 3: Comparison of model and experimental results for rat muscle tissue [7]. Model parameters are $\Delta\omega$ = 421.58 µs, $\kappa\Delta\omega$ = 941.58 s^{-1} and $R_{2,0}$ = 19.67 s^{-1}.

References

[1] Borisov, *et al.*, Anat Rec 2000;285:292-304
[2] Harris BA, Acta Physiol Scand 2005;185:89-97
[3] Gardener AG, *et al.*, Magn Reson Med 2010;64:967-974
[4] Krogh A, J. Physiology 1919;52:457-474
[5] Jensen JH, *et al.*, Magn Reson Med 2000; 44:144-156
[6] Ziener CH, *et al.*, J Magn Reson 2010;202:38-42
[7] Damon BM, *et al.*, Proc. ISMRM 2002; 48:97-104
[8] Luz, *et al.*, J Chem Phys 1963;39:366
[9] Sexton WL, *et al.*, Am J Physiol 1994;266:H1502-11

64 Quantification of myocardial microstructure by T2* relaxation in a capillary model

C. H. Ziener[1], F. T. Kurz[2], T. Kampf[3]
[1]German Cancer Research Center, Radiology, Heidelberg, Germany
[2]Heidelberg University, Neuroradiology, Heidelberg, Germany
[3]Würzburg University, Experimental Physics 5, Würzburg, Germany

Introduction: Susceptibility-sensitive cardiovascular magnetic resonance imaging is a powerful tool to noninvasively detect coronary artery stenosis [1,2]. It has been shown that myocardial T_2^* relaxation time is affected by vasodilatators through their influence on regional blood volume [3]. Susceptibility differences of myocardial capillaries and surrounding tissue induce a pericapillary magnetic field in which the dephasing of nuclear spins occurs. The T_2^* relaxation time can be used to quantify microstructural parameters such as capillary radius and regional blood volume in terms of a theoretical model.

Materials and methods: The well-established capillary model of Krogh is used to examine the microscopic architecture of the myocardium: capillaries are regularly arranged such that their ensemble can be reduced to a single capillary with a surrounding supply cylinder [4]. Due to susceptibility differences around each capillary, a local dipole field is induced where dephasing and diffusion occur (see Fig. 1). Theoretically, transverse relaxation is determined by the exact solution to the Bloch-Torrey equation for a pericapillary dipole field [5]. Yet, susceptibility effects as well as diffusion effects have to be taken into account. Analytical expressions for free induction decay and T_2^* relaxation time are obtained in dependence on the underlying microstructural parameters (capillary diameter and regional blood volume) of myocardial tissue. Experimentally, free induction decay is measured with a multi gradient echo sequence from the septal region of the myocardium (see Fig.2).

Results: In Fig. 3, experimentally acquired values of the free induction decay are compared with the theoretical model for an assumed regional blood volume of 8.4 %, capillary diameter = 5.5 µm, and intrinsic T_2-relaxation time T_2=52 ms. In comparison, the mean measured value of the T_2^* relaxation time from the septal region is 39.9 ms – this nicely coincides with the predicted model value of 42.7 ms. Susceptibility effects of the surrounding lung tissue are visible in the T_2^*-map in Fig. 4.

Conclusion: The presented model correctly predicts free induction decay and T_2^* relaxation time in the myocardium. Consequently, the relation between microscopic parameters and relaxation time of the myocardial tissue can be used to quantify capillary diameters and/or regional blood volume based on T_2^* measurements in muscle tissue. Model behavior of free induction decay agrees well with experimental data (Fig.3), however, predictions for T_2^* relaxation time are slightly overestimated most likely due to the relative uncertainty of intrinsic T_2 relaxation time values.

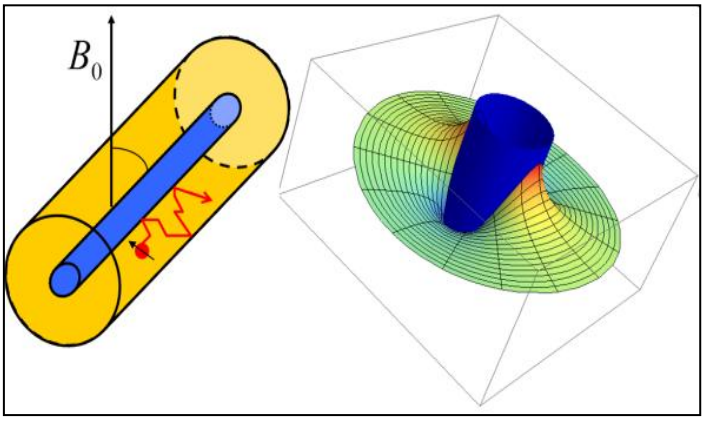

Fig. 1: Left: blood filled capillary (blue) and the surrounding supply cylinder (yellow) in which the diffusion (red trajectory) occurs. Right: pericapillary dipole field.

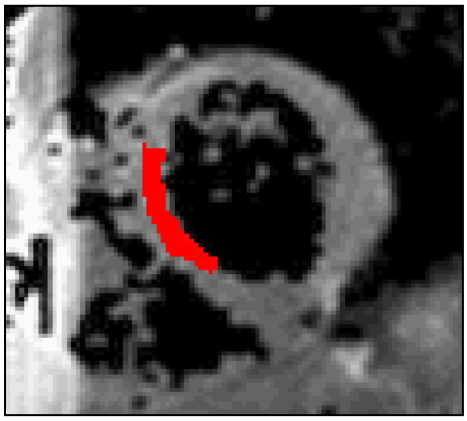

Fig. 2: Septal region of the myocardium from which free induction decay is measured. In this region, background gradients of the surrounding lung tissue are minimized.

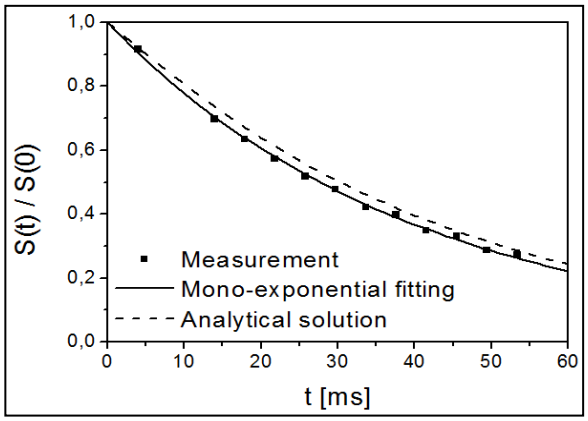

Fig. 3: Measured free induction decay at 1.5 T from the septal region and monoexponential fit (solid line). The dashed line shows the analytical solution of the mathematical model.

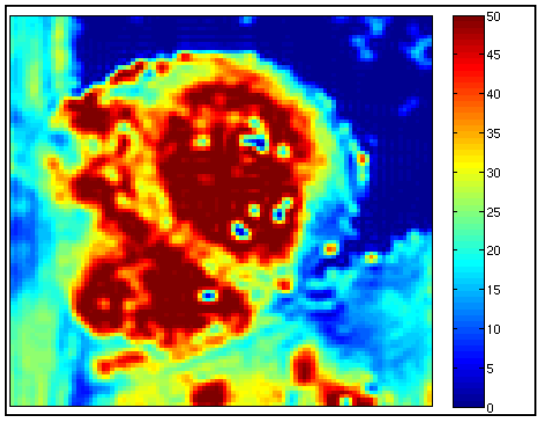

Fig. 4: T_2^* map of a short axis view. The septal region is the most homogeneous region while the surrounding lung tissue influences T_2^*-value in the anterior and posterior region.

References

[1] Bauer, *et al.*, Magn Reson Med 1999;41:51-62
[2] Friedrich MG, J Cardiovasc Magn Reson 2013;15:43
[3] Wacker CM, *et al.*, J Am Coll Cardiol 2003;41:834-840
[4] Krogh A, J. Physiology 1919;52:457-474
[5] Ziener CH, *et al.*, Phys Rev E 2012;85:051908

65 A theoretical model to determine spin-echo relaxation times of cells labeled with magnetic nanoparticles and of iron oxide agglomerations.

F. T. Kurz[1], T. Kampf[2], H.-P. Schlemmer[3], H. Sabine[1], B. Martin[1], C.H. Ziener[3]
[1]Heidelberg University, Neuroradiology, Heidelberg, Germany
[2]Würzburg University, Experimental Physics 5, Würzburg, Germany
[3]German Cancer Research Center, Radiology, Heidelberg, Germany

Introduction: Recently, diagnostic and therapeutical modalities involving magnetically labeled cells gain in importance to qualitatively characterize and treat cardiovascular and cerebrovascular diseases with MRI [1,2]. However, detailed knowledge about microstructural parameters like magnetic particle concentration and size is required to quantitatively measure the extent of the respective micro-pathological changes, for example in neurodegenerative disease or tracking of magnetically labeled cells.

Materials and methods: In close analogy to Krogh's capillary model [3], agglomerations of (super)para- or ferromagnetic particles are considered in three dimensions. For such locally distributed particles, each is thought to be contained in a cubic environment with approximately the same amount of magnetic content. For restriction of diffusion to the volume between magnetic core and cube boundaries, symmetry considerations apply and it suffices to consider a single unit cube or further a single spherical dephasing volume of radius R_D around a magnetic core of radius R (see Fig. 1). In an external magnetic field, the susceptibility difference between core and surrounding tissue creates a local field inhomogeneity that is approximately that of a magnetic dipole with Larmor frequency □(***r***)=□□$R^3(3\cos^2(□)-1)/r^3$ and equatorial frequency shift □□. Using a simple relation between gradient-echo relaxation time T^*_2, spin-echo relaxation time T_2 and correlation time □∝R^2/D [4], an expression for the spin-echo relaxation rate $R_2=1/T_2$ is derived that is only dependent on radius R of the magnetic microsphere, diffusion coefficient D, volume fraction R^3/R^3_D and frequency shift □□.

Results: Quantitative predictions for the relation of spin-echo relaxation rate and particle size are compared with experimental data from Yung [5] and Weisskoff et al. [6] (Fig. 2). Also, previous analytical descriptions of motion regime limiting cases, namely the static dephasing limit [7] and the motional narrowing limit [8] as well as the strong field approximation of Jensen et al. [9], are considered (Fig. 3).

Conclusion: Based on symmetry assumptions about agglomerations of magnetic micro-particles, corresponding spin-echo relaxation rates agree well with experimental results. In contrast to most other approaches, the presented model accounts for the whole dynamic range and, in addition, it can be applied for non-Gaussian shaped diffusion. The motion regime is determined by □ and □□ which characterize dynamic and static frequency scale, respectively. Here, spin-echo relaxation rates exhibit a maximum value for □□□≈□ and asymptotically approach minimal values in the motional narrowing limit (□□□→*0*) and static dephasing limit (□□□→∞) in contrast to gradient-echo relaxation rates that approach a maximum in the static dephasing limit [4]. Model predictions are in good agreement with limiting case considerations. Obtained results allow to quantitatively examine pathological processes in neurodegenerative disease and migration dynamics of magnetically labeled cells.

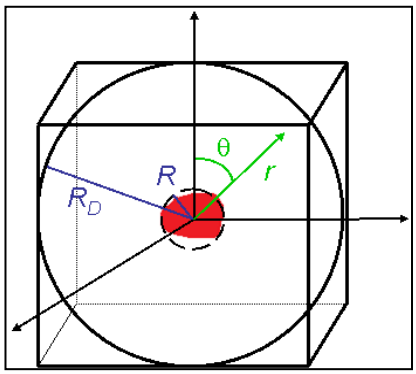

Fig. 1: Dephasing sphere with radius R_D of a unit cube contain-ing an impermeable magnetic core of radius R. Spherical coordinates are shown in green.

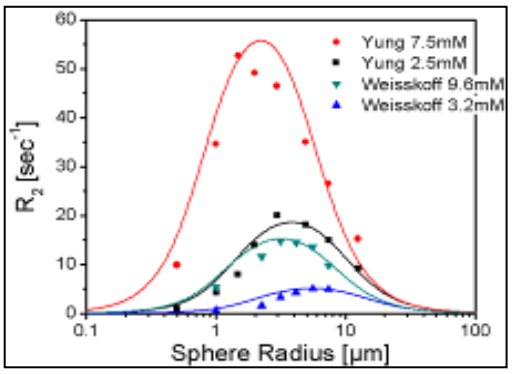

Fig. 2: Spin-echo relaxation rate R_2 dependence on different sphere radii R. Model predictions (continuous lines) are compared to experimental data [5,6] with corresponding [Dy]-DTPA concentra-tions.

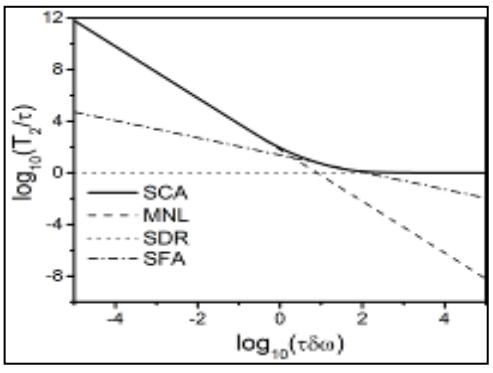

Fig. 3: Limiting cases in the strong collision approximation. Motional narrowing limit and static dephasing limit are compared with predictions by [7] (dashed line) and [8] (dotted line) as well as the strong field

References

[1] Bendszus M et al., J. Neurosci. 2003;23:10892-10896
[2] Richards JM et al., Circ Cardiovasc Imaging 2012; 5:509-517
[3] Krogh A, J. Physiology 1919;52:457-474
[4] Bauer WR et al., Magn Reson Med 1999;42:1004-1010
[5] Yung KT, Magn Reson Imaging 2003;21:451-63
[6] Weisskoff RM et al., 2004;Magn Reson Med 31:601-10
[7] Brooks RA et al., Magn Reson Med 2001;45:1014-1020
[8] Jensen JH et al., Magn Reson Med 2000;44:144-156
[9] Jensen JH et al., Magn Reson Med 2000;43:226–236

66 Impact of Bolus Dispersion on Semi-Quantitative and Quantitative Analysis of Contrast-Enhanced Myocardial Perfusion MRI

R. Schmidt[1], D. Graafen[1], K. Sommer[1], S. Weber[1], L. M. Schreiber[1]
[1]University Medical Center, Section of Medical Physics, Department of Radiology, Mainz, Germany

Introduction: Coronary artery disease is one of the main causes of death in industrialized nations. Myocardial blood flow (MBF) can be estimated based on T1-weighted contrast-enhanced first-pass magnetic resonance imaging (MRI). Therefore, the measurement of the arterial input function (AIF) is required. The AIF should be estimated inside a supplying vessel as close as possible to the tissue of interest (TOI), but in clinical practice the AIF is usually estimated from the blood pool signal of the left ventricle (LV) for technical reasons during myocardial perfusion MRI. However, dispersion (deformation) of the contrast agent bolus can occur between the LV and the myocardium. The negligence of dispersion might result in a systematic error of the MBF and the myocardial perfusion reserve (MPR), which is represented as the ratio of the MBF at pharmacologically induced stress and the MBF estimated at rest. Mathematically, the dispersion can be characterized as convolution of the AIF of the LV and a vascular transport function (VTF): $AIF_{TOI}=VTF \otimes AIF_{LV}$. The variance of this VTF σ^2 can be used as a quantitative measure of dispersion [1]. Graafen *et al.* observed an underestimation of the MBF and an overestimation of the MPR in idealized single vessel geometries considering steady [2] and pulsatile [3] flow using computational fluid dynamics (CFD) simulations. Schmidt *et al.* extended these simulations and found an underestimation of the MBF and an overestimation of MPR inside a coronary bifurcation geometry for different flow conditions inside a stenosed branch as well [4-6]. The aim of this study was to extend the investigation of the results from quantitative to semi-quantitative analysis since semi-quantitative analysis is more common in clinical practice and should therefore be examined regarding the effect of bolus dispersion.

Furthermore, subsequent simulations have been accomplished to examine the influence of different parameters on the contrast agent bolus dispersion, e.g. the non-Newtonian behavior of blood, different arrival times of the contrast agent bolus at the coronary arteries during the cardiac cycle and the influence of different diffusion coefficients. Different diffusion coefficients correspond to different kinds of contrast agent that might be used at myocardial perfusion MRI, e.g. Gd-DTPA [2-6], Gd-DOTA [7] or USPIO particles. Furthermore, the heart pumps the blood and, therefore, the contrast agent batch-wise. Due to the mixing of blood and contrast agent in the LV the concentration of contrast agent is approximately constant throughout one cardiac cycle. Simulations considering such a stepwise constant contrast agent concentration throughout one cardiac cycle have been performed to estimate the influence on bolus dispersion (Fig.1).

Materials and methods: An idealized bifurcation geometry of the left main coronary artery (LMCA) to the left anterior descending (LAD) (including a stenosis) and the left circumflex (LCX) was created [4-6]. Two sets of simulations were performed to investigate two different outflow conditions through the stenotic branch: Full autoregulation of the pressure drop across the stenosis caused by vasodilation of the downstream vessels, and limited autoregulation and therefore reduced flow through the stenotic branch [4-6, 8]. The mass fraction of contrast agent in blood was recorded at several cross-sectional positions perpendicular to the centerline with a distance of 2.5 mm within the coronary branches during the simulation to visualize and investigate the development of the bolus dispersion. CFD simulations were accomplished with the help of the Fluent software package (Fluent 14, Ansys, Darmstadt, Germany) at the High Performance Cluster ‚Elwetritsch' (RHRK, TU Kaiserslautern, Germany). The quantitative analysis of the errors in MBF and MPR due to the negligence of bolus dispersion was performed using the MMID4 model. The semi-quantitative analysis was accomplished by the measurement of the maximum upslope of the mass fraction-time curves [9]. The curves were superimposed by a random noise of typical magnitude of myocardial perfusion MRI for a more realistic evaluation. This procedure was repeated 1000 times to receive average values. The upslope of the myocardial curves, which were generated with the help of the MMID4 model, was normalized to the upslope of the curve in the LV and the curves at the LAD and LCX outlets (normalized upslope = NUS), respectively. Afterwards, the errors in the corresponding MPR index (MPRI) due to bolus dispersion were calculated [9] analog as performed for the MPR in quantitative analysis in previous work [4-6].

Moreover, several parameters of the original CFD simulations have been varied, e.g. the diffusion coefficient of the contrast agent to analyze the effect of the contrast agent particle type on bolus dispersion, respectively.

Results: A systematic underestimation of the MBF up to -16.1 % at the quantitative analysis and an average underestimation of the NUS up to -23.8 % at the semi-quantitative analysis of the results were found (Fig. 2). A consequence of the larger underestimation for rest compared to stress is an overestimation of the MPR up to 7.5 % for quantitative and of the MPRI up to 12.9 % for semi-quantitative analysis.

The diffusion coefficient of contrast agent has a larger influence on bolus dispersion compared to the influence of the non-Newtonian behavior of blood at low flow velocities as presented in Fig. 3. The stepwise constant contrast agent concentration seems to have a minor influence on dispersion (Fig. 1 and Fig. 3).

Conclusion: The MBF and NUS errors due to bolus dispersion found in this study are in the order of the interquartile range of myocardial perfusion MRI of about ±20 % in healthy volunteers [10]. This shows that bolus dispersion should not be neglected at semi-quantitative and quantitative myocardial perfusion MRI analysis. The observed overestimation of the MRP might lead to a false negative assessment of a patient. Moreover, most of the errors in NUS and MPRI for semi-quantitative analysis are considerably larger compared to the errors in MBF and MPR for quantitative analysis. This shows that semi-quantitative analysis is more sensitive with respect to bolus dispersion and confirms that quantitative analysis should be preferred.

Moreover, the bolus dispersion might vary considerably for different kinds of contrast agent depending on their diffusion coefficient. The influence of the cellular ingredients of blood on the diffusion coefficient of the contrast agent and therefore on the bolus dispersion is investigated at the moment in subsequent simulations.

Acknowledgment: This study was financially supported in part by the German Research Foundation (DFG SCHR 687/5). The support by the administrators of the High Performance Cluster Elwetritsch (RHRK, TU Kaiserslautern, Germany) is gratefully acknowledged.

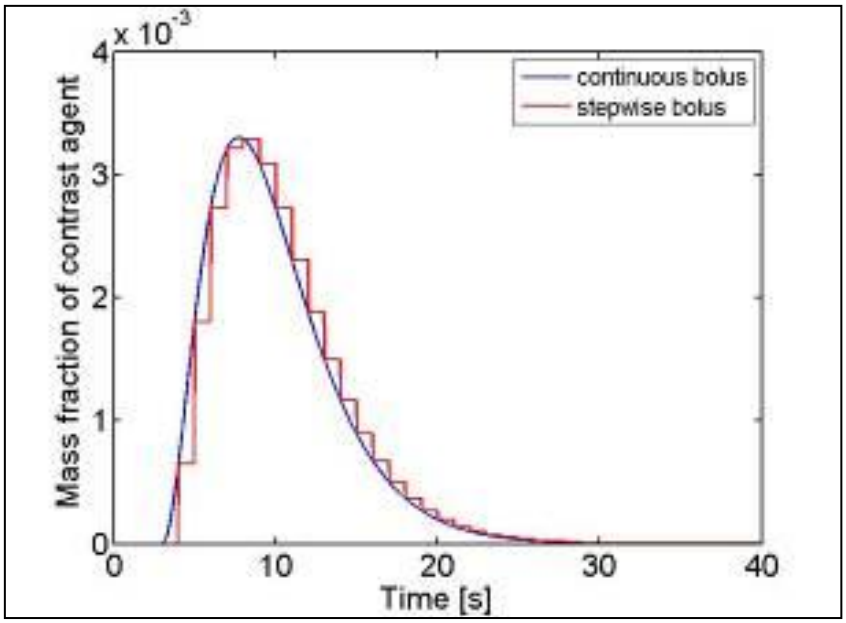

Fig. 1: Illustration of the stepwise constant contrast agent bolus (red) at the inlet of the vessel in comparison to the originally used continuous contrast agent bolus (blue).

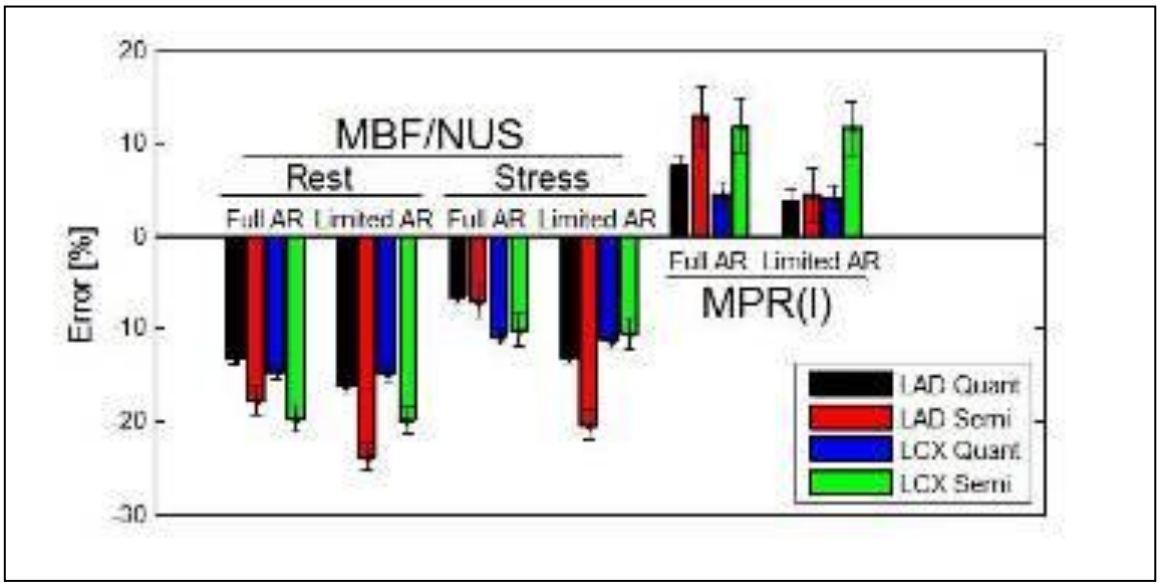

Fig. 2: Errors in the MBF/NUS and the MPR/MPRI due to the negligence of bolus dispersion. The acronym "AR" stands for autoregulation, „Quant" for quantitative analysis and „Semi" for semi-quantitative analysis.

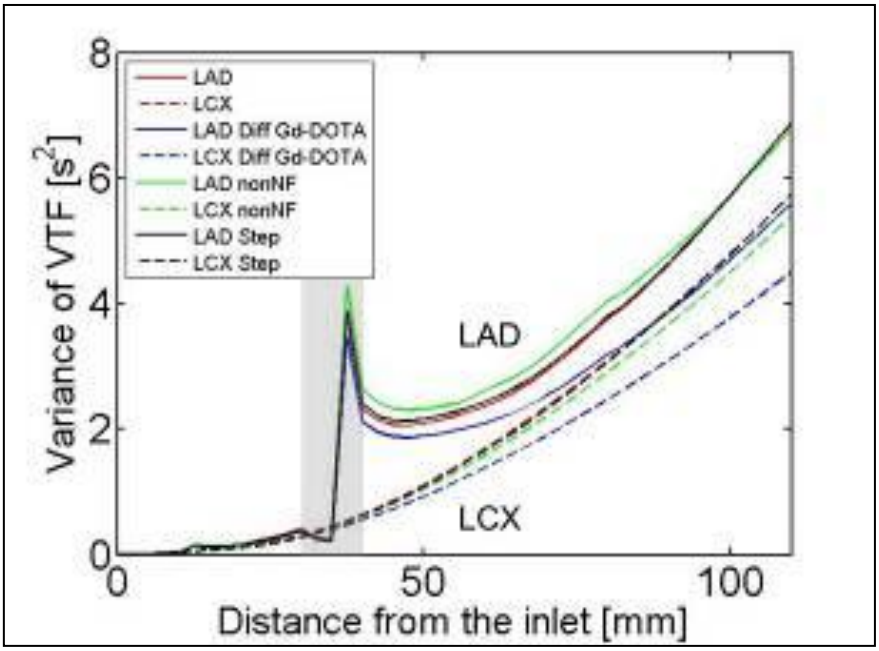

*Fig. 3: The variance of the VTF as function of the distance from the inlet for the original simulation settings (red: Gd-DTPA, D=1.5*10^{-10} m^2/s) compared to the results for a different diffusion coefficient (blue: Gd-DOTA, D=2.92*10^{-10} m^2/s), the influence of the non-Newtonian behaviour of blood (green: nonNF) and the influence of the stepwise constant concentration throughout a cardiac cycle (black: Step). The position of the stenosis is highlighted in gray.*

References

[1] Calamante, F., *et al*, Magn. Reson. Med., 2006, vol.55, no.5, pp. 1180–1185.
[2] Graafen, D., *et al*., Med. Phys., 2009. vol.36, 7, pp. 3099-3106.
[3] Graafen, D., *et al*., Phys. Med. Biol., 2011., vol. 56, 16, pp. 5167-5185.
[4] Schmidt, R., *et al*., Comput. Math. Methods. Med., vol. 2013, ID 513187.
[5] Schmidt, R., *et al.*, 21st Annual Meeting of the ISMRM, 2013, Salt Lake City, USA, number 1423.
[6] Schmidt, R., *et al.,* 44th Annual Meeting of the DGMP, 2013, Cologne, Germany, number 194.
[7] Wieseotte, Ch. *et al*.,Joint Annual Meeting of the ISMRM-ESMRMB, 2014, Milan, Italy, number 2618.
[8] Segal, J. *et al.*, J. Am. Coll. Cardiol., 1992, vol. 20, 2, pp. 276-286.
[9] Maredia, N. *et al*., Magn. Reson. Med., 2010, vol. 64, 6, pp.1616-1624.
[10] Weber, S. *et al.,* JMRI, 2008, vol. 28, 1, pp. 51-59.

Session 12 – Particle radiation therapy II: Range verification

Chairs: W. Enghardt (Dresden/DE), A. J. Lomax (Villigen, Zurich/CH)

67 Status of the Compton camera prototype for online range verification of proton beams

P. Thirolf[1], S. Aldawood[1,2], M. Böhmer[3], J. Bortfeldt[4], I. Castelhano[1,5], R. Gernhäuser[3], H. van der Kolff[1,6], C. Lang[1], L. Maier[3], D.R. Schaart[6], K. Parodi[1]
[1]Ludwig-Maximilians-University Munich, Faculty of Physics/ Chair for Medical Physics, Garching, Germany
[2]King Saud University, Riyadh, Saudi Arabia, Germany
[3]Technical University Munich, Physics Department E12, Garching, Germany
[4]Ludwig-Maximilians University Munich, Faculty of Physics/ Chair for Particle Physics, Garching, Germany
[5]University of Lisbon, Faculty of Science, Lisbon, Portugal, Germany
[6]Delft University of Technology, Delft, The Netherlands, Netherlands

Introduction: We are developing a Compton camera prototype for the position-sensitive detection of prompt rays emitted from proton- (or heavier-ion beam) induced nuclear reactions with biological samples. Alternatively, also delayed photon detection from online generated $^{+}$ emitters during the interrupts of the pulsed irradiation could be envisaged.

Materials and methods: The detector system is designed to be capable to reconstruct the photon source origin not only from the Compton scattering kinematics of the primary photon, but also to allow for tracking of the secondary Compton-scattered electrons, thus enabling a -source reconstruction also from incompletely absorbed photon events. Detailed simulation studies (using the MEGAlib simulation and image reconstruction code) resulted in the specifications of the Compton camera, based on a $LaBr_3$(Ce) scintillation crystal (50x50x30 mm^3 block crystal, read out by a multi-anode PMT) acting as absorber, preceded by a stacked array of 6 double-sided silicon strip detectors as scatterers (500 m thick, 128 strips/side, pitch 390 m). From the design simulations, an angular resolution of ≤ 2^0 and a source image reconstruction efficiency of 10^{-3} -10^{-5} (both at 2-6 MeV) can be expected.

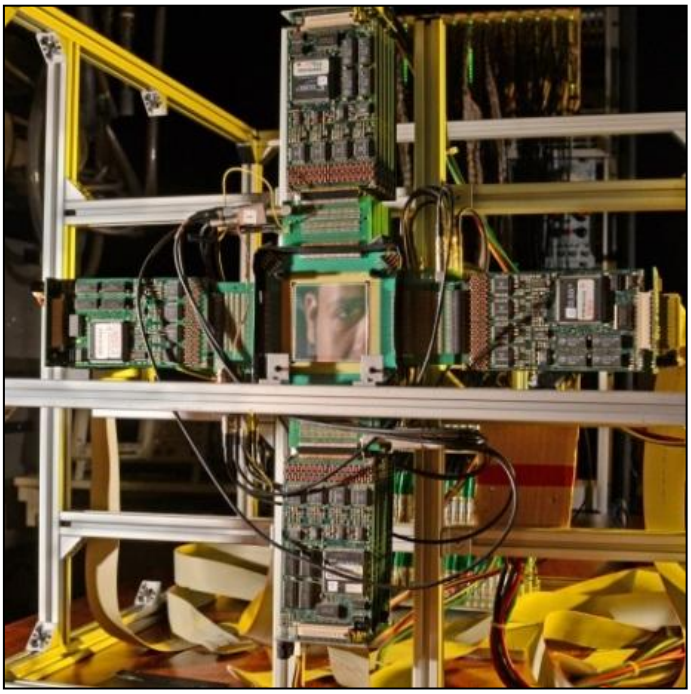

Fig. 1: Front view of the Compton-camera prototype showing the scatter component consisting of a stack of double-sided Silicon strip detectors (DSSSD). The highly integrated signal processing electronics is attached to the sides of the DSSSDs

Results: The $LaBr_3$ crystal (Fig. 2, top) has been characterized with calibration sources, both with an absorptive and a reflective side surface finish. The measurements clearly reveal the superior performance in case of the reflective surface coating. A time resolution of 273 ps (FWHM) and an energy resolution □E/E of about 3.8 % (FWHM) could be achieved (see Fig. 3). Using an intense collimated (1 mm diameter) ^{137}Cs calibration source ($E_{□}$=662 keV), the light amplitude distribution was measured for each of 64 pixels (6x6mm^2) (Fig. 4). Data were also taken with 0.5 mm collimation and 0.5 mm step size to generate a reference library of light distributions that allows for reconstructing the interaction position of

the initial photon using a k-nearest neighbor (k-NN) algorithm developed by the Delft group. The (VME-based) signal readout of the 1536 electronics channels from the silicon tracker detectors (Fig. 1 and 2, bottom) a highly-integrated electronics is based on a highly integrated, ASIC-based electronics.

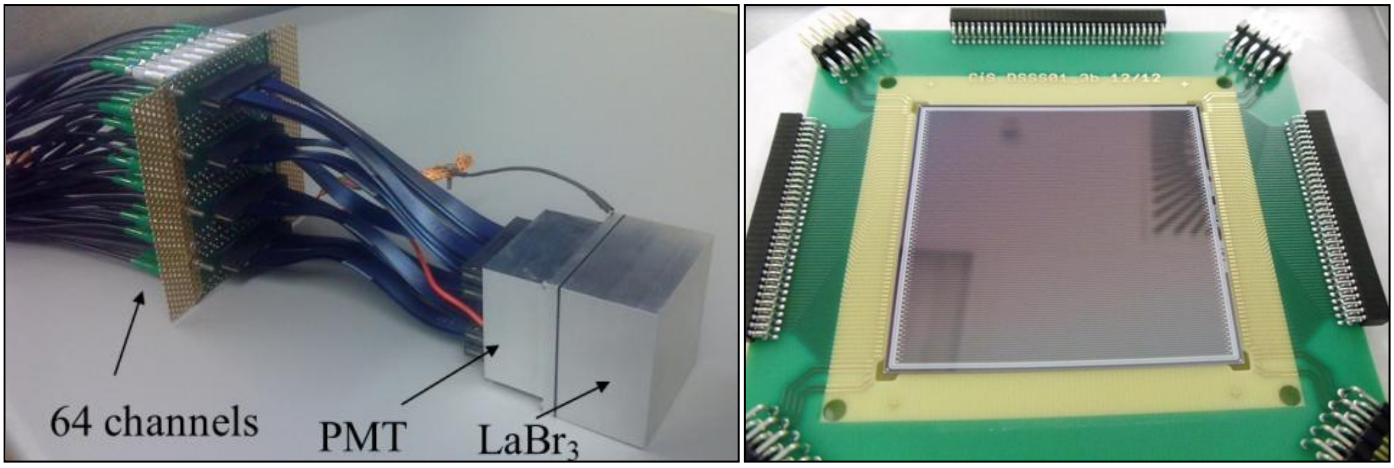

Fig. 2: Top: *Photo of the absorber crystal (fast $LaBr_3$ block crystal with position-sensitive readout by a multi-anode photomultiplier)*

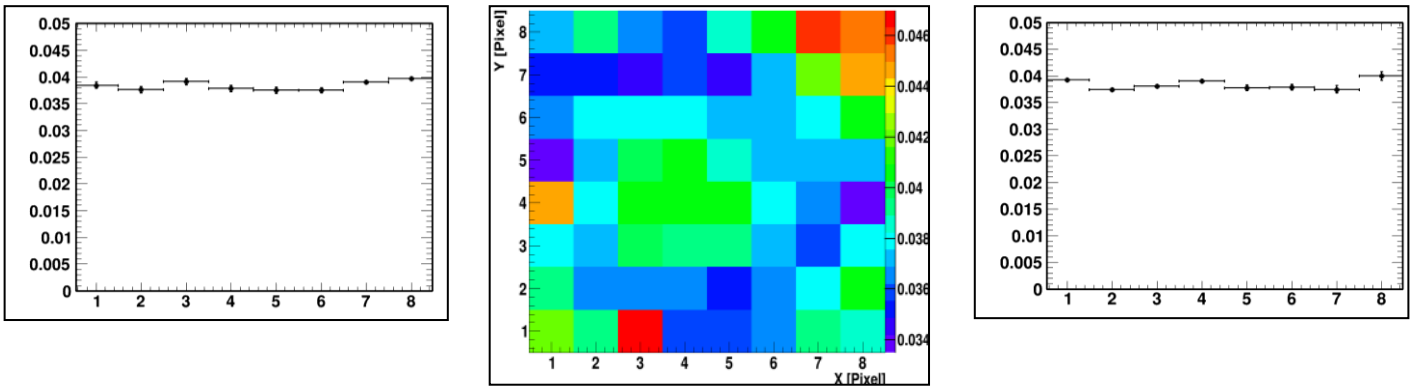

Fig. 3: Middle: *2D energy resolution map (obtained at 662 keV) with the corresponding projections on x (left) and y (right), showing the homogeneous energy resolution of ca. 3.8%.*

Conclusion: The Compton camera–based approach for prompt-□ detection from nuclear interactions of therapeutic proton and ion beams offers promising perspectives for online ion beam range verification. A Compton camera prototype module is presently being developed and characterized in Garching. Furthermore, an arrangement of, e.g., four camera modules could even be used in a '□-PET' mode to additionally detect delayed annihilation radiation from positron emitters in the irradiation interrupts (with improved performance in the presence of an additional third (prompt) photon (as, e.g., in ^{10}C and ^{14}O) [1].

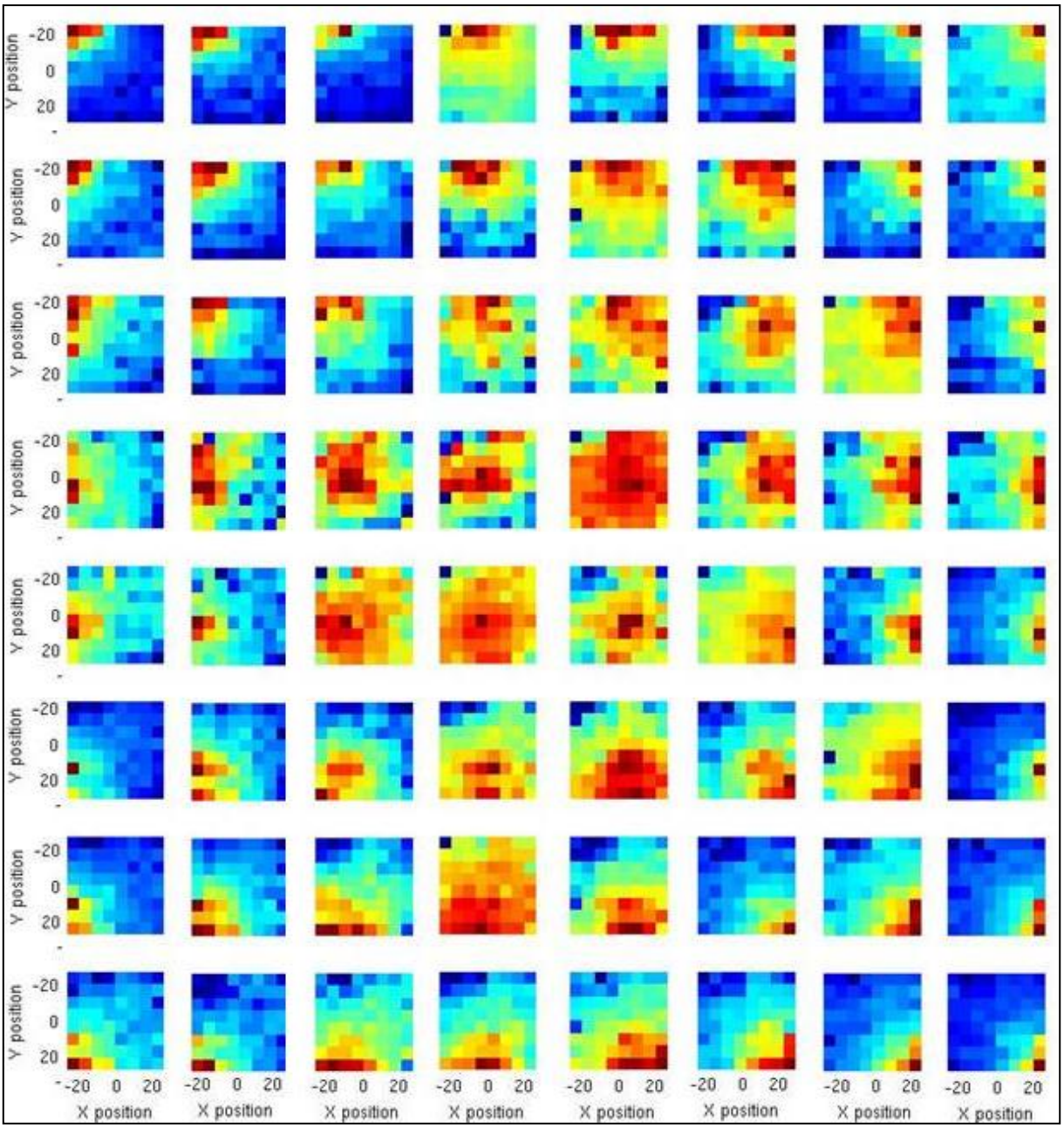

Fig. 4: Light amplitude distribution maps from a (1 mm) collimated ^{137}Cs source (662 keV), consecutively irradiating each of 8x8 pixels (6x6 mm^2).

References

[1] C. Lang, D. Habs, K. Parodi, P.G. Thirolf, Submillimeter nuclear medical imaging with increased sensitivity in positron emission tomography using □□□ coincidences, Journal of Instrumentation **9** (2014) P01008.

68 Range verification by measurement of the acoustic signal from the Bragg Peak

S. Reinhardt[1], W. Assmann[1], S. Kellnberger[2,3], M. Omar[2,3], A. Fink[1], C. Gäbisch[4], P. Thirolf[1], M. Moser[5], G. Dollinger[5], V. Ntziachristos[2,3], K. Parodi[1]
[1]Ludwig-Maximilians Universität Munich, Chair for Medical Physics, Garching, Germany
[2]Helmholtz Zentrum Munich , Institute for Biological and Medical Imaging, Munich, Germany
[3]Technische Universität Munich , Chair for Biological Imaging, Munich, Germany
[4]Munich University of Applied Science , Institute for Micro- and Nano-technologies, Munich, Germany
[5]Universität der Bundeswehr, Institute for Applied Physics and Instrumentation, Munich, Germany

Introduction: Range uncertainties are still one of the main challenges in ion beam therapy. Range verification in ion beam therapy relies to date on nuclear imaging techniques which require complex and costly detector systems and aim to exploit the not straightforward correlation between nuclear-secondary products and dose deposition [1]. A different approach is the detection of the acoustic signal due to the thermo-acoustic phenomenon. The localized energy deposition along the ion track heats the whole track region, especially the Bragg peak region. The local temperature increase yields a local thermal expansion of the absorber medium which is sufficient to generate measurable mechanical pressure waves [2, 3]. Aim of this work is to study the feasibility of determining the ion range with sub-mm accuracy using high frequency ultrasonic (US) transducers .

Materials and methods: A water phantom was irradiated by a pulsed 20 MeV proton beam with varying pulse intensity, length and repetition rate. The proton beam was stopped in a depth of 4.15 mm after passage through an air filled pipe of 83 mm with thin Kapton foils at each end used as vacuum exit and water phantom entrance window, respectively (fig. 1). The acoustic signal of single proton pulses was measured by different US detectors (3.5 MHz and 10 MHz central frequencies) placed axially with respect to the beam line.

Results: A clear signal of the Bragg peak was visible for a total energy deposition as low as 10^12 eV. The strong gradient of the energy deposition at the water/Kapton/air interface and the Bragg peak results in the formation of two separated acoustic signals. A third signal is attributed to the reflection of the original Bragg peak signal at the entrance window (Fig. 1). The signal amplitude showed a linear increase with particle number per pulse and thus, dose. Measuring the distance between signal 1 and signal 2 yields the position of the Bragg peak with an accuracy and reproducibility better than 100 micrometer in agreement with Geant4 simulations.

Conclusion: Range verification by acoustic means is a promising new technique for treatment modalities where the tumor can be localized by US imaging. Further improvement of sensitivity is required to account for higher attenuation of the US signal in tissue, as well as lower energy density in the Bragg peak in realistic treatment cases due to higher particle energy and larger spot sizes. Nevertheless, the acoustic range verification technique offers a more direct verification of the beam energy deposition than currently developed nuclear based techniques, and could open the perspective of combining anatomical US imaging with Bragg Peak imaging in the near future.

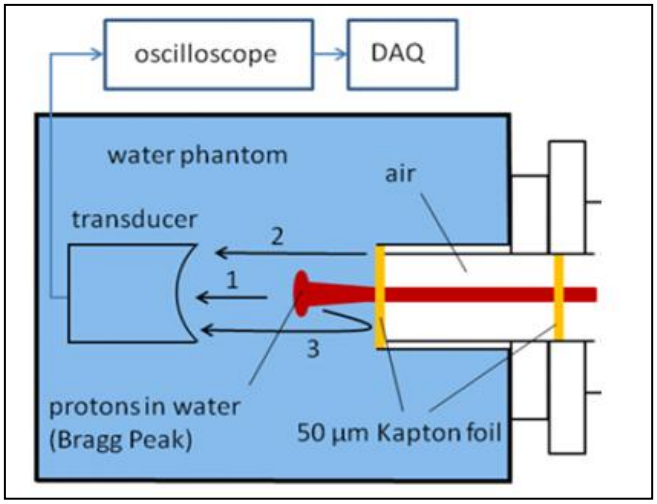

Fig. 1: Experimental setup

References

[1] Ben Mijnheer et al., In vivo dosimetry in external beam radiotherapy, Med. Phys. 40 (2013), 070903.
[2] L. Sulak et al., Experimental studies of the acoustic signature of proton beams traversing fluid media, NUCLEAR INSTRUMENTS AND METHODS 161 (1979) 203-217
[3] Marcel Toulemonde et al., Temperature and pressure spikes in ion-beam cancer therapy, PHYSICAL REVIEW E 80, 031913 (2009).

69 In-vivo Range Verification Based on Prompt Gamma-Ray Timing Measurements

C. Golnik[1], F. Hueso-Gonzalez[1], W. Enghardt[1], A. Mueller[1], F. Fiedler[2], T. Kormoll[1], J. Petzoldt[1], K. Roemer[2], P. Dendooven[3], G. Pausch[1]
[1]Technische Universität Dresden, Universitätsklinikum Carl Gustav Carus, Oncoray – National Center for Radiation Research in Oncology, Dresden, Germany
[2]Helmholtz-Zentrum Dresden-Rossendorf, Institute of Radiation Physics, Dresden, Germany
[3]University of Groningen, KVI-CART Center for Advanced Radiation Technology, Groningen, Netherlands

Background: During the 2012 AAPM Annual Meeting 33 percent of the delegates considered the range uncertainty in proton therapy as the main obstacle to become a mainstream treatment modality. Utilizing prompt gamma emission, a side product of particle tissue interaction opens up the possibility of in-beam dose verification, due to the correlation between prompt gamma-ray emission and particle-dose deposition. We verify an unconventional and simple concept towards range assessment by prompt gamma-ray (PGT) timing measurements1. Therapy particles need, dependent on their initial energy, a varying transit time to traverse the irradiated tissue, about 1-2 ns in case of protons with a range of 5-20 cm. PGT spectra are distributions of the time difference between the time of the proton bunch passing a reference position (e.g. the target entrance) and the arrival of the corresponding prompt gamma-ray at the timing detector. The measured PGT spectra comprise the proton transit-time through the irradiated material and thus the proton range information.

Methods: We performed prompt gamma-ray timing measurements at the KVI-CART accelerator facility AGOR in Groningen, The Netherlands. PMMA targets of varying thickness (5-15 cm) were irradiated with a fixed proton energy of 150 MeV. The range of 150 MeV protons in PMMA is about 13.6 cm. With increasing target thickness, the protons travel longer pathways through the material and thus the mean value (μ) as well as the standard deviation (σ) of the PGT spectra is expected to increase. Modeling of the experimental irradiation scenarios, comprising the setup geometry, detector time resolution and bunch spread of the beam (see fig. 1) have been performed.

Results: The experimental PGT spectra show the expected shift and broadening dependent on target thickness, as the increased target thickness resembles an increased proton transit-time through the irradiated material. Further, the modeling algorithm is very suitable to describe the experimental data, e.g. the spectral shape and the mean value, as it is shown in fig. 1.

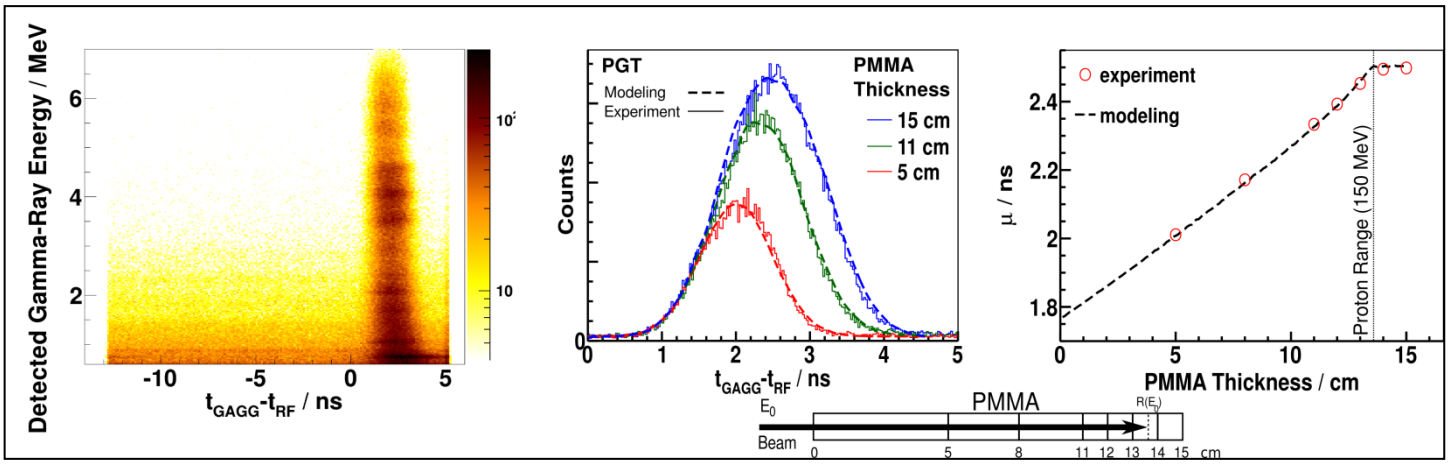

Fig. 1: Left: Time resolved prompt gamma-ray spectrum of a proton irradiated PMMA target. Middle: Experimental PGT spectra (histogram) and corresponding modeled data (straight lines). Right: Dependence of spectral parameter μ on PMMA thickness, i.e. on proton flight time. 150 MeV protons have a range of 13.6 cm in PMMA.

Conclusions: With the presented technique, which is solely based on straight timing spectroscopy, a robust and simple verification of the proton range seems to be feasible. It could be proven, that the spectral shape of PGT spectra is directly correlated to the thickness of the irradiated target. The time shift as well as the broadening of the PGT spectra was confirmed experimentally in compliance with modeled data.

Due to statistical considerations, these spectral properties (μ, σ) can be determined to a precision of a few ps within 10 s of irradiation at a beam current of 100 pA. This timing uncertainty translates to a proton range uncertainty of 2 mm. We are in preparation of experimental range dependent PGT spectroscopy at a clinical irradiation facility. Modeling of corresponding PGT spectra have been performed and predict very promising results.

70 Range Probe: a new technique to detect on-line patient misalignments

A. Hammi[1,2], L. Placidi[3,1], F. Albertini[1], M. Peroni[1], A. Bolsi[1], A. J. Lomax[1,2]
[1]Paul Scherrer Institut, Center for Proton Therapy, Villigen, Switzerland
[2]ETH, Physics, Zuerich, Switzerland
[3]Universita Cattolica Sacro Cuore, L.go Gemelli 5, Roma, Switzerland

Introduction: The advantage of proton therapy is the presence of a sharp distal dose fall-off that can be used to spare normal tissues beyond the end of the delivered field. However, due to this sharp fall-off, even small errors resulting from patient misalignments could potentially result in a significant discrepancy between the planned and the delivered dose. Therefore, to tap the full potential of proton therapy, accurate and on-line methods to verify the patient positioning and the proton range during the treatment are desirable. Here we propose and validate a fast and innovative technique for determining rotational positional uncertainties for proton therapy using what we call 'range probes' [1]. A range probe is a narrow, high energy proton pencil beam that shoots through the patient and can be detected on exit and for which the residual range and shape of the Bragg peaks (BP) can be measured using a range telescope or multi-layer-ionisation-chamber (MLIC). By the use of a number of carefully selected range probe positions, the ranges and shapes of the detected BP's can uniquely define the orientation of the patient, as the ranges and shapes of the BP's change depending on the orientation of the density heterogeneities through which they pass.

Material und methods: To validate this approach, an anthropomorphic phantom has been used, and a planning CT acquired with a slice separation of 2mm. From this, 500 new CT's were generated, assuming different rotations along each axis (interval of ±2° and resolution δ_{CT}=0,5°). Five low dose (10mGy) range probes with energy 177 MeV were then simulated to pass through all these CT data sets using the VMCPro Monte Carlo code, with the residual Bragg peaks of each range probe (simulated in a homogenous 'detector' positioned at the exit side of the head) being stored in a database to which experimentally measured range probe BP's can be compared. The phantom was then placed on an in-house developed rotation device (precision δ_{RD}=0.09°) and three new CT's with pseudo-randomly generated rotations were acquired, representing three possible daily positioning's of the patient. To determine these 'daily' rotational positioning errors, range probes were simulated through these 'daily' CT data sets, and the results compared to the pre-calculated data base, from which the actual 'daily' rotational error could be determined (see Figure 2).

Results: In Table 1 the comparison between the predicted rotations and the daily errors are reported for the three studied cases**.** The calculation performed shows that a rotational positioning errors of the phantom can be detected with a resolution of about δ_{error}=1°.

Discussion/conclusion: With this phantom study we have demonstrated the possible use of a small number of proton range probes for detecting on-line, residual rotational misalignments of patients with a high level of accuracy. The technique is fast (less than 0.5s to detect the best fit) and can effectively reconstruct three-dimensional positioning errors (rotations) from a single proton beam angle.

Even if further investigations and measurements are required before the method can be applied in clinical routine, our simulations have shown the feasibility of the approach, and the next step will be to measure true range probes in the phantom using a MLIC type detector.

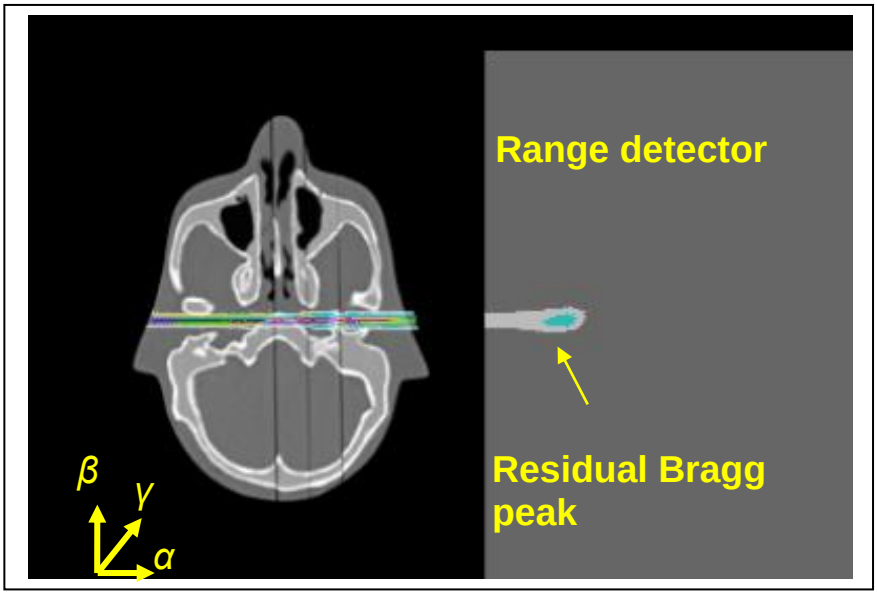

Fig.1: Model of the range probe setup.

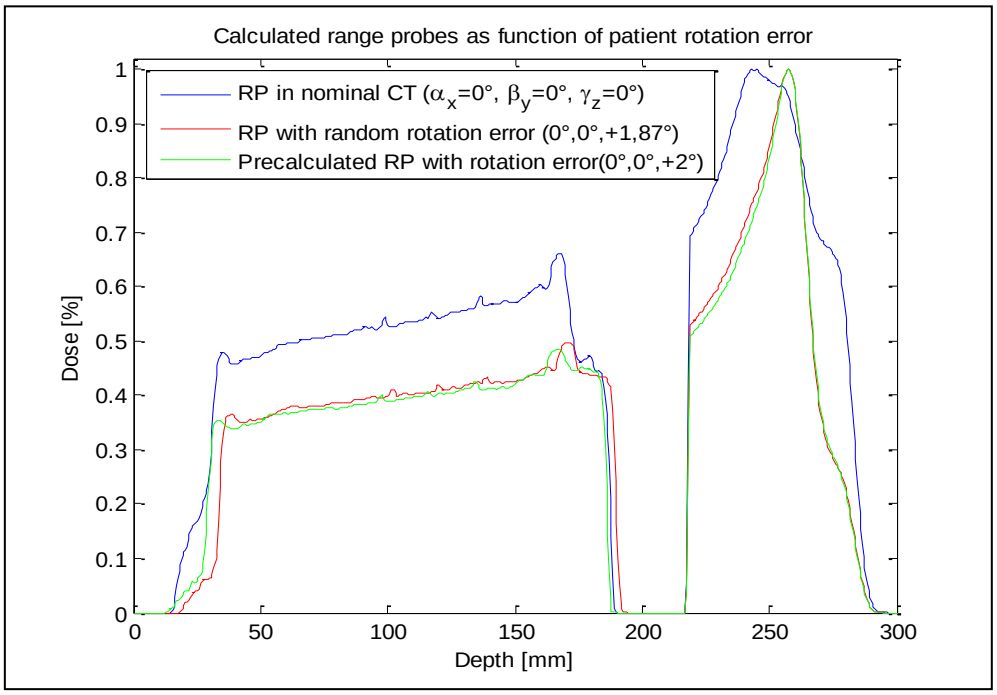

Fig. 2: VMCPro calculated integral depth dose of RP.

	One degree of freedom α_x; β_y; γ_z	Two degree of freedom α_x; β_y; γ_z	Three degree of freedom α_x; β_y; γ_z
"Daily" error	0°; 0°; +1,84°	+1,44°; -1,77°;0°	-1,35°; -2,09°; -1,35°
Predicted error	0°; 0°; +2,00°	+2;00°;-2,00°; 0°	-2,00°;-1,00°; -1,00°

Tab. 1: Evaluation of the rotation error utilized in the experiment.

References

[1] Mumot M., Algranati C., Hartmann M., Schippers J., Hug E., & Lomax A.J., 2010, Proton range verification using a range probe: definition of concept and initial analysis. Phys. Med. Biol, 55 (16), 1-13.

71 Detectability of proton range shifts in heterogeneous targets with prompt gamma based range monitoring

M. Priegnitz[1], F. Fiedler[1], S. Helmbrecht[2], G. Janssens[3], J. Smeets[3], F. Vander Stappen[3], W. Enghardt[1,2]
[1]Helmholtz-Zentrum Dresden-Rossendorf, Dresden, Germany
[2]OncoRay, TU Dresden, Faculty of Medicine Carl Gustav Carus, Dresden, Germany
[3]IBA Medical Accelerator Solutions, Louvain-la-Neuve, Belgium

Purpose: To make optimal use of the advantages of proton beams in tumor therapy a precise knowledge on their range is required. Recently, a slit camera has been developed using prompt gamma rays emitted during irradiation. First investigations in homogeneous media have shown that the position of the distal falloff of the prompt gamma ray profiles is closely correlated with the Bragg-peak position [1]. Now, heterogeneous targets are under investigation and first results on detectability of range shift as well as range retrieval precision will be presented.

Materials and methods: From real patient CTs simplified 1D-profiles in beam direction have been derived representing clinical relevant cases, e.g. base-of-skull (Fig. 1) and lung tumor. Tissue types have been assigned based upon the HU [2]. These CT profiles served as input for the simulation of prompt gamma ray profiles with the dedicated Monte Carlo software PENH [3], fig. 2. For experimental verification of these simulations phantoms have been built from tissue equivalent materials according to the derived CT profiles. They will be irradiated with monoenergetic proton pencil beams. The emitted prompt gamma rays will be measured with a passively collimated camera consisting of a tungsten slit collimator and a LYSO detector. Different range modification scenarios are investigated, like deviations in proton energy or cavity filling. Introduced range shifts are determined from the prompt gamma ray profiles by applying the distal slope matching algorithm which was originally developed for particle therapy PET [4].

Results and conclusion: The precision of range shift estimation in heterogeneous media strongly depends on the specific target composition. Generally range can be retrieved within few mm precision. However, especially in close vicinity to steep density gradients the shape of the prompt gamma ray profile is deteriorated and range retrieval becomes difficult.

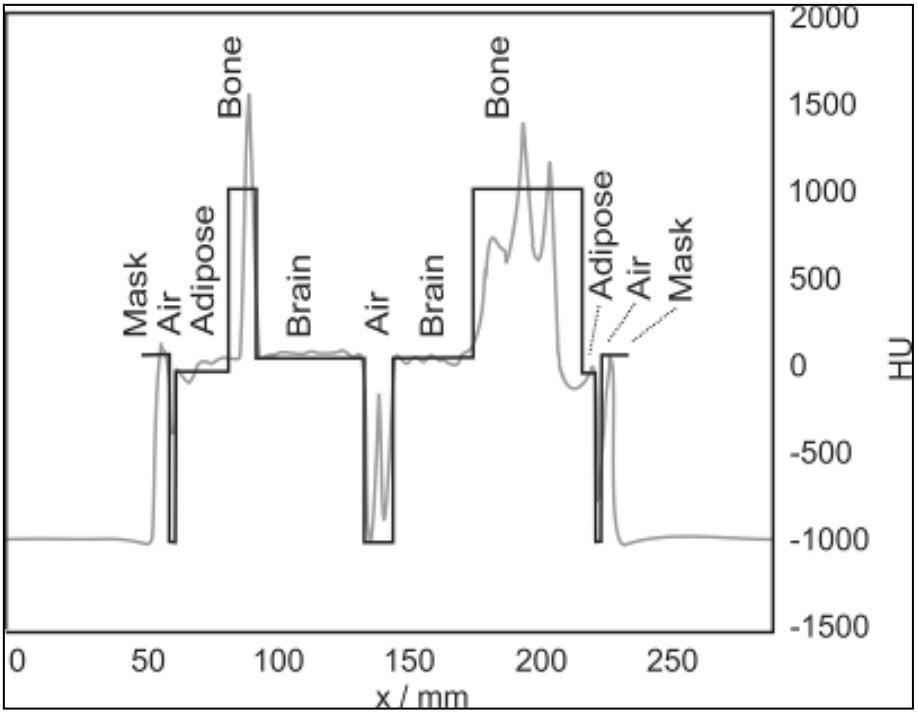

Fig. 1: Real (gray) and idealized (black) CT profile for a base-of-skull irradiation.

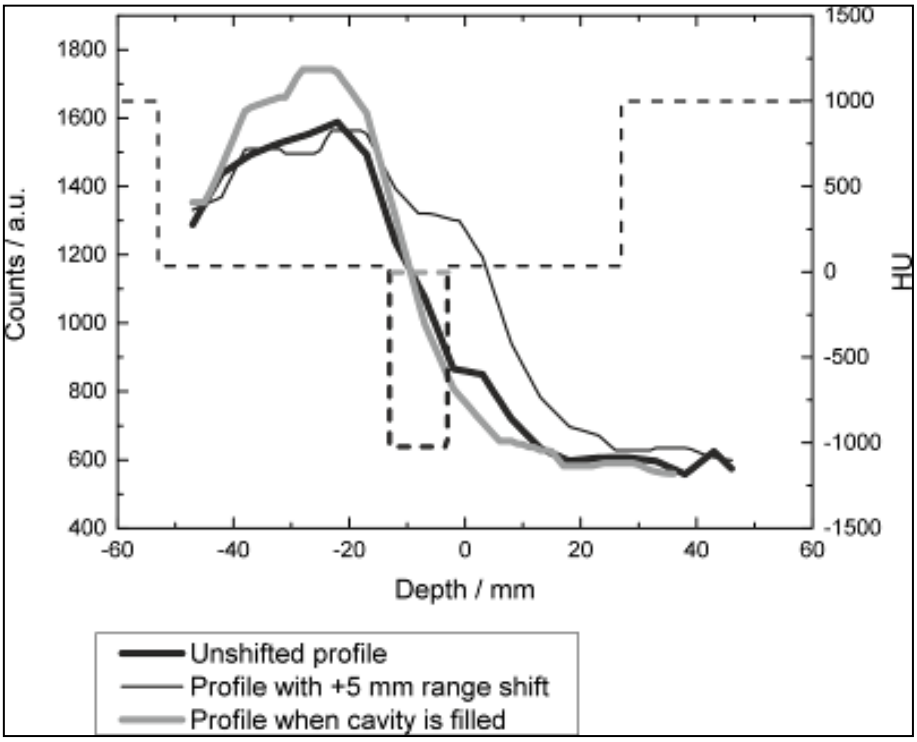

Fig. 2: Simulated prompt gamma profiles (solid line) of a base-of-skull irradiation (thick black) with an introduced 5 mm shift (thin black) and a cavity filling (gray). The correspondent HU of the CT profiles are given as dashed lines. Depth 0 denotes the isocenter of the detector, which is aligned with the Bragg-Peak of the unshifted profile.

References

[1] Smeets J et al., Phys Med Biol 57, 3371-405, 2012
[2] Schneider W et al., Phys Med Biol 45, 459-78, 2000
[3] Sterpin E et al., Med Phys 40, 111705, 2013
[4] Helmbrecht S et al., Phys Med Biol 57, 1387-97, 2012

Session 13 – Adaptive radiation therapy

Chairs: P. Winkler (Graz/AT), S. Nill (London/GB)

72 Introductury lecture: Challenges and new approaches in adaptive radiation therapy

S. Nill[1]
[1]London, Great Britain

73 Characterization of deformation vector fields for the registration of dose distributions in adaptive treatment planning and sequential boost protocols

K. Stützer[1], A. Jakobi[1], R. Haase[1], A. Bandurska-Luque[1], S. Löck[2], M. Krause[3,4,5,6], K. Zöphel[7], D. Zips[8], J. Kotzerke[7], J. Steinbach[9], M. Baumann[3,4,5,10,6], C. Richter[1]
[1]OncoRay, Technische Universität Dresden, High Precision Radiotherapy, Dresden, Germany
[2]OncoRay, Technische Universiät Dresden, Medical Radiation Physics, Dresden, Germany
[3]University Hospital Carl Gustav Carus, TU Dresden, Department of Radiation Oncology, Dresden, Germany
[4]German Cancer Consortium (DKTK), Dresden, Germany
[5]German Cancer Research Center (DKFZ), Heidelberg, Germany
[6]Helmholtz-Zentrum Dresden – Rossendorf, Institue of Radiation Oncology, Dresden, Germany
[7]University Hospital Carl Gustav Carus, TU Dresden, Clinic and Policlinic for Nuclear Medicine, Dresden, Germany
[8]University Hospital Tübingen, Department of Radiation Oncology, Tübingen, Germany
[9]Helmholtz-Zentrum Dresden – Rossendorf, Institute of Radiopharmaceutical Cancer Research, Dresden, Germany
[10]OncoRay, Technische Universität Dresden, Dresden, Germany

Introduction: Adaptive treatment and sequential boost protocols in radiotherapy rely on several treatment plans. These are often optimized not only on the initial but also on an updated computed tomography (CT) scan taken during therapy. Commonly, the different plans are approved separately in clinical routine. However, there is a strong dosimetric interest to calculate one cumulative dose distribution for verifying the observance of dose constraints for several regions of interest (ROIs). Since patient geometry might be different in the two CT scans (e.g. due to loss of weight, tumour shrinkage or imprecise patient positioning) the dose distributions cannot be simply summed up but have to be registered before adding. When performing non-rigid registration by applying deformation vector fields, their precision is often unclear and their suitability needs to be verified. For head and neck cancer patients a diffeomorphic demon registration algorithm is evaluated by assessing contour- and dose-specific characteristics.

Materials and methods: Starting in 2006, a prospective imaging trial including patients with advanced head and neck cancer was conducted at the University Hospital Carl Gustav Carus, TU Dresden [1]. Amongst others, the patients received an initial CT scan prior to their treatment and a second one about four weeks after starting radiochemotherapy. Based on the CT scans from 47 patients a treatment planning study including adaptation and boost concepts for photon and proton beams is currently under way. On the initial CT scans, the target volumes and a remarkably large number of anatomical contours (≈30) have been delineated by a radiation oncologist. The delineated contours on the second CT scan include only ROIs that are relevant for treatment planning. Four different dose distributions are generated on the second CT scan of each patient and are registered by the following procedure to the initial CT scan for creating a total dose distribution.

Registration parameters were determined with the open source software 3D Slicer [2] utilizing the two CT image data sets. After a manually performed rigid alignment by translation, a diffeomorphic demon algorithm [3] was applied to calculate the deformation vector field. In a first step, results have been checked by visualising the vector field with the in-house software Geisterr and visualising the deformed CT scan with 3D Slicer (Fig.1).

For a quantitative analysis, the vector field was applied to the structure set of the second CT scan including spinal cord, brain stem, left and right plexus brachialis, left and right parotid gland and the mandible. The deformed ROIs were compared to those contoured on the initial CT scan by calculating absolute values of volume differences, Dice coefficient, Hausdorff distance and mean contour distance. In an ideal case, both ROIs would exactly match with a Dice coefficient of 1 and volume difference as well as Hausdorff and mean contour distance of 0.

Furthermore, the retrieved vector field was applied to the dose distributions planned on the second CT scan. Changes of several dose values like maximum and mean dose within the above mentioned ROIs (as drawn by the physician on the second and the initial CT scan) are determined and rated by paired t-tests with a 0.05 p-value level of significance.

The open source software Plastimatch (version 1.5.14) was utilized for deformation of contours and dose distributions. The calculation of the contour- and dose-specific characteristics was done by using The Computational Environment for Radiotherapy Research (CERR) in MATLAB R2010b.

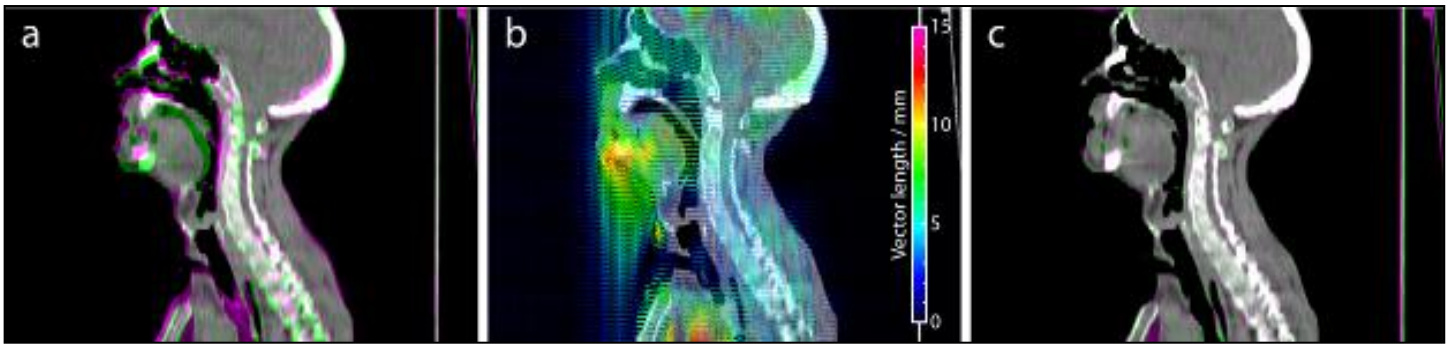

Fig. 1: Illustration of deformable registration for a selected sagittal slice: (a) Overlay of the initial CT scan (green) and the rigidly aligned CT scan taken during therapy (magenta). Grey regions represent same Hounsfield units on both CT scans. (b) Deformation vector field overlaid with the second CT scan to which the deformation will be applied. The deformation direction is indicated by the line directions and the deformation magnitude by the length and colour of the lines. (c) Overlay of initial (green) and deformed (magenta) CT scan.

Results: From the visual investigation of the deformed CT scans (Fig.1c) the diffeomorphic demon algorithm was found to deal nicely with obvious tumour shrinkage and positioning deviations for the advanced head and neck cancer patients. The vector field visualisation (Fig.1b) revealed in some cases non-physiologic deformation magnitudes in the brain or lungs. However, these do normally not affect the drawn ROIs.

Quantitative analysis has been done so far for 40 out of the 47 patients. Some preliminary results are summarized in Tab. 1. Largest differences in the contour volumes are found for spinal cord and brain stem. This might be caused by slightly different lengths of the contoured ROIs if the evaluated CT scan sections do not match exactly. The branching plexus structures are quite complex and thus, difficult to delineate especially taking into account the CT slice thicknesses of 3 – 5 mm. Therefore, the Dice coefficients for the plexuses (0.58) is obviously lower compared to the other ROIs (>0.78) and the Hausdorff distance is slightly increased. The mean contour distances are within similar ranges for all considered ROIs.

The maximum and mean dose values in the evaluated ROIs before and after registration were averaged over all deformed dose distributions. The largest changes are observed for the parotid glands. They are known to undergo shrinkage during radiotherapy which might not always be correctly reflected by the deformation vector field. Although the p-values from paired t-tests indicate significant changes of dose values for some ROIs when applying the deformable registration the typical changes are clearly below 0.5 Gy.

Conclusion: A desired verification of deformation vector fields in radiotherapy has been established not only based on visual investigation but also on quantitative contour- and dose-specific characteristics. For the advanced head and neck cancer patients, the diffeomorphic demon algorithm is feasible to account for changed patient geometry when registering CT scans, but the vector fields should be checked individually for non-physiologic deformation in the dosimetrically relevant areas. The quite small changes of mean and maximum dose values within the investigated ROIs seem to be acceptable for creating reasonable cumulative dose distributions for adaptive treatment and sequential boost protocols.

References

[1] Zips D, Zöphel K, Abolmaali N, Perrin R, Abramyuk A, Haase R, Appold S, Steinbach J, Kotzerke J, Baumann M (2012) Exploratory prospective trial of hypoxia-specific PET imaging during radiochemotherapy in patients with locally advanced head-and-neck cancer. *Radiother Oncol* 105(1):21-8.

[2] Fedorov A, Beichel R, Kalpathy-Cramer J, Finet J, Fillion-Robin J-C, Pujol S, Bauer C, Jennings D, Fennessy F, Sonka M, Buatti J, Aylward SR, Miller JV, Pieper S, Kikinis R (2012) 3D Slicer as an Image Computing Platform for the Quantitative Imaging Network. *Magn Reson Imaging* 30(9):1323-41.

[3] Johnson H, Zhao Y (2009) BRAINSDemonWarp: An Applicaton to Perform Demons Registration. *Insight Journal* URL: http://hdl.handle.net/1926/1517.

	Spinal cord	Brain stem	Left plexus brachialis	Right plexus brachialis	Left parotid gland	Right parotid gland	Mandible
Volume difference / ml	4.9 ± 3.1	5.2 ± 5.5	0.8 ± 0.6	1.1 ± 1.2	2.0 ± 1.6	2.4 ± 1.7	4.0 ± 3.7
Relative volume difference	0.21 ± 0.15	0.22 ± 0.23	0.14 ± 0.18	0.20 ± 0.24	0.07 ± 0.06	0.09 ± 0.09	0.07 ± 0.06
Dice coefficient	0.81 ± 0.04	0.78 ± 0.10	0.58 ± 0.13	0.58 ± 0.15	0.86 ± 0.03	0.85 ± 0.04	0.85 ± 0.04
Hausdorff distance / cm	0.86 ± 0.93	0.98 ± 0.51	1.18 ± 0.71	1.36 ± 0.90	0.71 ± 0.19	0.78 ± 0.24	0.84 ± 1.15
Mean contour distance / cm	0.10 ± 0.06	0.22 ± 0.14	0.15 ± 0.10	0.18 ± 0.20	0.10 ± 0.03	0.10 ± 0.03	0.07 ± 0.03
D_{max} before registration / Gy	9.6 ± 3.8	4.3 ± 5.2	15.1 ± 8.2	16.1 ± 7.8	15.9 ± 9.1	16.0 ± 8.7	21.1 ± 5.6
D_{max} after registration / Gy	9.7 ± 3.9	4.3 ± 5.2	15.1 ± 8.2	16.1 ± 7.9	15.5 ± 9.0	15.5 ± 8.6	21.1 ± 5.5
Difference of D_{max} / Gy	**0.10 ± 0.96**	**0.09 ± 1.24**	**0.01 ± 0.52**	**0.04 ± 0.61**	**-0.38 ± 0.73**	**-0.49 ± 0.92**	**-0.07 ± 0.87**
p-value of paired t-test for D_{max}	0.19	0.37	0.85	0.40	< 0.01	< 0.01	0.28
D_{mean} before registration / Gy	3.6 ± 2.4	1.0 ± 1.8	4.8 ± 4.4	5.4 ± 4.7	4.8 ± 3.9	4.9 ± 4.3	8.1 ± 4.3
D_{mean} after registration / Gy	3.8 ± 2.4	1.1 ± 1.8	4.9 ± 4.3	5.6 ± 4.8	4.9 ± 4.0	5.0 ± 4.3	8.1 ± 4.3
Difference of D_{mean} / Gy	**0.19 ± 0.39**	**0.00 ± 0.50**	**0.11 ± 0.72**	**0.21 ± 0.80**	**0.15 ± 0.59**	**0.12 ± 0.76**	**0.07 ± 0.36**
p-value of paired t-test for D_{mean}	< 0.01	0.94	0.07	< 0.01	< 0.01	0.05	0.02

Tab. 1: Preliminary results for the selected ROIs in 40 patients. The upper part (first 5 lines) shows contour-specific characteristics when comparing the deformed structures with those drawn on the initial CT scan. The lower part shows dose-specific characteristics (D_{max} and D_{mean}): as they have been determined during treatment planning on the second CT scan (before registration), as they are found after dose deformation and applying the contours from the initial CT scan (after registration), the difference of both values and the p-values from paired t-tests. Except for the p-values, the cells contain the mean and standard deviation when averaging over all 40 patients (upper part) or all 4×40 deformed dose distributions (lower part).

74 A Software Tool for Quality Assessment, Visualization and Documentation of Deformable Image Registration

T. Brandt[1,2], K. Anderle[3], D. Richter[1,2,3], J. Wölfelschneider[1,2], C. Graeff[3], C. Bert[1,2,3]
[1]University Clinic Erlangen, Radiation Oncology, Erlangen, Germany, Germany
[2]Friedrich-Alexander-University Erlangen-Nürnberg, Faculty of Medicine, Erlangen, Germany, Germany
[3]GSI – Helmholtz Centre for Heavy Ion Research, Dept. of Biophysics, Darmstadt, Germany, Germany

Introduction: Registration of digital images is gaining more and more importance in radiation therapy. Techniques such as 4D dose calculation and optimization rely on deformable image registration (DIR) and therefore are affected by its uncertainties. Although many parameters are available to assess or quantify registration quality, including false-color-overlays and the Jacobian determinant of the transformation vector-field, identifying acceptable and unacceptable registrations is not obvious. Typically, a single parameter is not sufficient to judge the registration result. Although tools are already available to compute and visualize individual parameters, checking a whole set of parameters for a single registration is often tedious, time consuming and not feasible on a routine basis. Therefore, a software tool is implemented that allows to automatically compute and visualize a range of parameters for a set of registrations and create registration quality reports which can be inspected or saved for later use.

Materials and methods: Based on the free open-source software 3D Slicer (http://www.slicer.org), a registration quality assessment extension (Slicer Registration QA) was developed. The calculations were implemented as modules using the Insight Segmentation and Registration Toolkit (ITK, http://www.itk.org).
Visual inspection of registration results is provided by four modalities: flicker-overlay, false color, checkerboard and absolute difference filters. For “Flicker”-overlay, fixed and warped images are shown alternately at a selectable frequency. At the same time, the user can scroll through the images in all spatial directions so that differences caused by improper registration are easily visible. For false color overlay, the images are displayed in two channels with complementary color scales so that differences appear colored while similar regions are grey. The checkerboard filter combines the two images in an alternating pattern making differences visible at the edges of the checkerboard tiles. The absolute difference filter visualizes image differences using the absolute difference of corresponding voxels in both images.
Moreover, two options were added, which operate entirely in the vector field domain: a filter calculating the Jacobian determinant of the vector field and a filter assessing the inverse consistency of the registration. The Jacobian determinant describes local volume changes caused by tissue compression or shrinking, which enables an identification of unphysical volume changes caused by unacceptable registration vector fields. For inverse consistency, the pre-calculated vector field for the inverse registration is used. Combining both transformations results into a residual vector field, which should be close to the identity transformation. Deviations are visualized as image overlay indicating the magnitude of the residual vector field.

Results: A 3D Slicer extension was implemented which assists the user in assessing the quality of DIR. The software can be used in an interactive step by step manner but is also scriptable and can therefore be easily integrated in an automated workflow. It further creates registration quality reports and includes infrastructure for integrated handling of 4DCT data sets and related DIR. This software was successfully tested with various registrations of CT and MR images. Especially when checking registration of all phases of a 4DCT onto a reference phase, automation of the workflow makes the process much less time consuming, so the user can focus on the QA results. Furthermore, registration quality is assessed in a more consistent way.

Conclusion: A software module was implemented to assess, visualize and document the quality of DIR in a flexible and efficient way. Initial tests with existing datasets were conducted and showed promising results differentiating between successful and unacceptable registrations. Tests with more datasets of registrations in different body regions as well as usability tests are ongoing.

75 A novel approach to estimate the dosimetric influence of anatomical changes in head and neck cancer patients undergoing proton therapy using daily CBCT imaging

G. Landry[1,2], G. Dedes[1], J. Handrack[1], G. Cabal[1], R. Nijhuis[2], M. Söhn[2], M. Reiner[2], U. Ganswindt[2], C. Thieke[2], G. Janssens[3], J. Orban de Xivry[3], C. Paganelli[4], F. Kamp[5], M. Riboldi[4], J. J. Wilkens[5], G. Baroni[4], C. Belka[2], K. Parodi[1]
[1]LMU Munich, Faculty of Physics, Department of Medical Physics, Garching, Italy
[2]LMU Munich, Department of Radiation Oncology, Munich, Germany
[3]Université Catholique de Louvain, IMagX group, ICTEAM institute, Louvain-la-Neuve, Belgium
[4]Politecnico di Milano, Dipartimento di Elettronica, Informazione e Bioingegneria, Milano, Italy
[5]Technische Universität Munich, Klinikum rechts der Isar, Department of Radiation Oncology, Munich, Germany

Related questions: The excellent dose conformity of proton therapy entails a higher degree of sensitivity to range shifts caused by anatomical patient variations over the course of treatment. One of the goals of image-guided radiotherapy is to minimize the uncertainties stemming from anatomical changes by monitoring such changes and estimating their impact on dosimetry.

The aim of this project is to develop techniques allowing the utilization of daily Cone-Beam Computed-Tomography (CBCT) imaging of head and neck (H&N) cancer patients to recalculate proton therapy dose distributions in the anatomy of the day. As CBCT image quality does not yield the required accuracy in the estimation of the water equivalent path length (WEPL), we aim to use deformable image registration (DIR) techniques to morph the planning CT WEPL map onto the anatomy observed from CBCT imaging.

Material and procedure: Clinical data of H&N cancer patients undergoing Intensity Modulated Photon Radiotherapy (IMRT) with weekly CBCT imaging was used in this study. In addition to the planning CT (pCT) contoured by a radiation oncologist, the patients underwent two re-planning CT scans (rpCT) which were also contoured.

The REGGUI software platform was employed to perform DIR to adapt the pCT anatomy onto the CBCT anatomy, yielding a virtual CT (vCT) [1]. A multi-scale implementation of the Morphons algorithm [2] was used. This image based method is insensitive to the typical absolute intensity differences of pCT and CBCT. Contours from the pCT were also morphed to yield contours for the vCT.

Deformation accuracy was evaluated using the adaptive scale invariant feature transform (aSIFT) method of [3] to extract corresponding features in the pCT vs CBCT and vCT vs CBCT. The preservation of CT numbers was evaluated by comparing CT number distributions between the pCT and vCT from corresponding contours of homogeneous anatomical regions.

Scanned pencil beam simultaneous integrated boost (SIB) proton plans using 4 fields were generated using a research TPS based on CERR [4]. Dose per fraction were 1.8 Gy and 2 Gy for the 54 Gy and 60 Gy CTVs respectively. Plans were exported to Geant4 where Monte Carlo (MC) dose recalculations were performed on the pCT, vCT and rpCT. For validation purposes, dose-volume-histogram (DVH) indices of pairs of vCT and rpCT closest in time, and for which no significant anatomical variations were observed, were compared.

Result: Fig. 1 presents the pCT, vCT and CBCT along with aSIFT features for a case presenting significant anatomical changes. For this case the mean distance between corresponding features extracted by the aSFIT algorithm between the pCT and CBCT (not shown in Fig. 1) were 3.7 mm with interquartile range of 2.9 mm, while for the vCT and CBCT they were reduced to 1.6 mm and 2.2 mm. Mean CT number differences for corresponding contours between the pCT and vCT were negligible. Fig. 2 presents a single field MC dose distribution in the pCT and vCT, with observable range shifts caused by weight loss and different airway shapes.

Preliminary DVH metric comparison (D_{95} for the 1.8 Gy and 2 Gy CTVs) between vCT and rpCT close in time (around mid-treatment) for a typical case showed differences of less than 2 %. Comparing the same CTV metrics between pCT and rpCT shows differences of up to 8 % in the 2 Gy CTV, likely due to the sensitivity of proton beams to inter-fractional variations. These preliminary results suggest that the vCT method allows for evaluation of the daily dose distribution.

Summary: A new approach has been developed, which allows estimating the dosimetric impact of daily anatomical changes, as observed using CBCT imaging, in proton therapy. The DIR of pCT onto CBCT for generation of a vCT has been evaluated by comparing automatically identified features and by comparing mean CT numbers in corresponding homogeneous anatomical regions. Further validation will be performed by comparing the vCT contours obtained from DIR to contours drawn by a radiation oncologist on the vCT and by assessing organs at risk DVH metrics. The method will be applied to a larger number of cases, and corresponding results will be presented.

Parts of this work were supported by the Federal Ministry of Education and Research (BMBF) Germany, grant number 01IB13001 (SPARTA) and DFG Cluster of Excellence: Munich-Centre for Advanced Photonics.

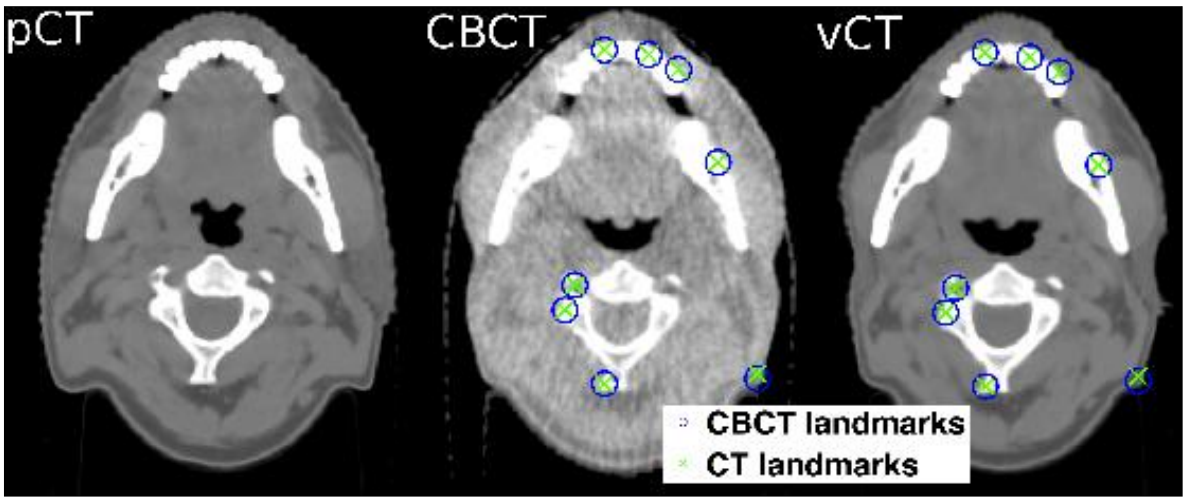

Fig. 1: Comparison of pCT, CBCT and vCT for a late treatment fraction. The corresponding features (crosses and circles) between the CBCT and vCT obtained from aSIFT are presented for a typical slice.

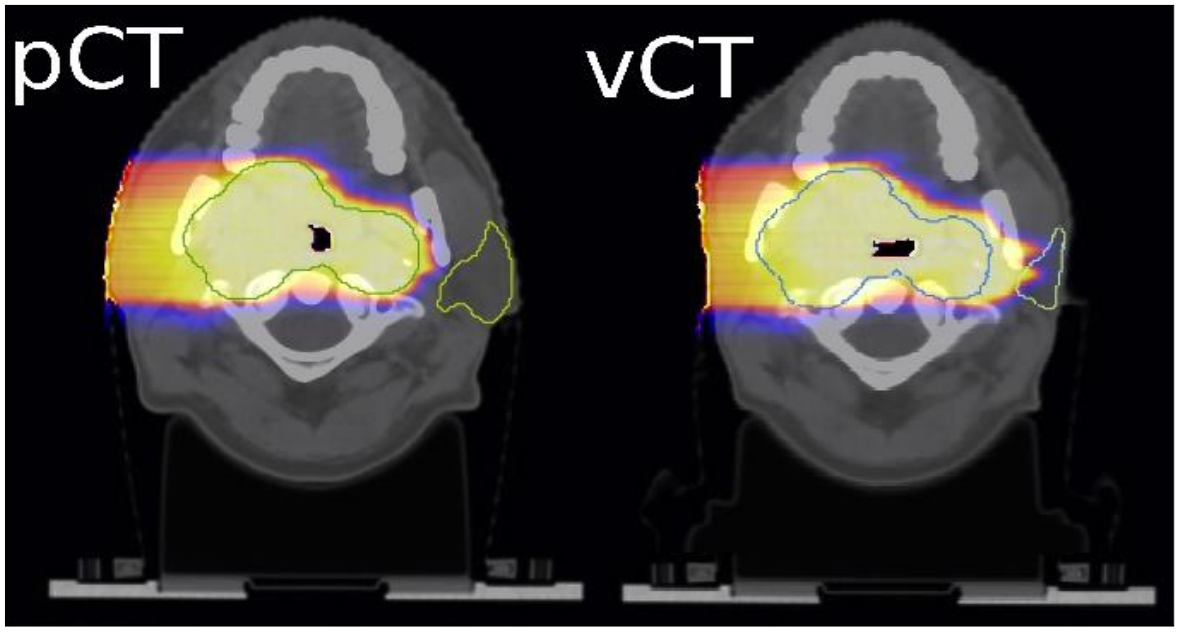

Fig. 2: Optimized on the pCT. In the vCT case, weight loss causes the beam to overshoot the PTV edge into the parotid gland contour obtained from DIR. For ease of illustration only the high dose PTV was optimized. A different slice than in Fig. 1 is shown.

References

[1] Peroni. M.: Automatic segmentation and online virtualCT in head-and-neck adaptive radiation therapy. Int. J. Radiat. Oncol. Biol. Phys. 84 (2012), p.427-33

[2] Janssens, G.: Diffeomorphic registration of images with variable contrast enhancement. Int J Biomed Imaging (2011) p. 891585

[3] Paganelli C.: Quantification of organ motion based on an adaptive imaged-based scale invariant feature method. Med. Phys. (2013) p.111701

[4] Schell. S.: Advanced treatment planning methods for efficient radiation therapy with laser accelerated proton and ion beams. Med. Phys. 37 (10) (2010) p.5330-40

76 Monte Carlo study on the sensitivity of positron and prompt-gamma imaging to proton range variations due to inter-fractional anatomical changes in head and neck and prostate cancer patients

G. Dedes[1], G. Landry[1], J. Handrack[1], G. Cabal[1], R. Nijhuis[2], M. Söhn[3], M. Reiner[3], C. Thieke[2], U. Ganswindt[2], F. Kamp[4], J. J. Wilkens[4], C. Belka[2], K. Parodi[1]
[1]LMU Munich, Faculty of Physics – Department of Medical Physics, Garching, Germany
[2]LMU Munich, Department of Radiation Oncology, Munich, Germany
[3]LMU Munich, Department of Radiation Oncology, Medical Physics, Munich, Germany
[4]Technische Universität Munich, Klinikum rechts der Isar, Department of Radiation Oncology, Munich, Germany

Related questions: One of the main advantages of proton therapy over conventional photon therapy is the high dose conformity. As the physical dose distribution of massive particles has a steeper gradient and is also more sensitive to density changes than that of photons, delivery uncertainties, patient positioning, organ motion, as well as anatomical changes can have a large impact on dose distribution variations, as compared to the initial treatment plan. Therefore, (quasi-) real-time range verification is essential in order to fully exploit the potential of proton therapy.

In this study, we focus on comparing the sensitivity of positron emission tomography (PET) and prompt-gamma emission (PG) to proton range variations due to inter-fractional anatomical changes of real head and neck and prostate cancer patients.

Material and procedure: The study is based on planning CTs (pCT) and available CBCTs of head and neck and prostate cancer patients undergoing IMRT treatment. Using the REGGUI [1] software platform, the high quality pCT is deformed to adapt to the CBCT daily anatomy of the patient, creating a virtual CT (vCT). This procedure has been evaluated in a separate study for head and neck patients [2]

Based on the pCT, proton treatment plans are calculated using the CERR research analytical TPS platform [3]. The proton plans as well as pCT and vCT are imported into Geant4 for dose recalculation. Furthermore, emitted positron and prompt gamma three-dimensional maps are obtained. The correlation of the positron and prompt-gamma maps to the proton range variations due to clinically observed anatomical changes is investigated with a dedicated MATLAB-based program

The proton range is determined as the distance from the entrance into the patient to the 90 % level at the distal falloff of the proton dose distribution along each pencil beam. In order to identify relative range shifts in the positron and prompt-gamma maps, the highest 30 % of the points in each one dimensional profile in beam-eye-view is averaged, to obtain a normalization value. This normalization level defines the distal falloff region of the positron or prompt-gamma distributions, and the 50 % of this falloff is used as the point correlated to the proton range for each pencil beam within the irradiated field.

Result: Initial results show that the positrons and prompt-gamma maps could be utilized for the identification of dose range variations due to inter-fractional anatomical changes. An example is shown in Figure 1 for a head and neck cancer patient. In regions where there was either sub-millimeter or no range variation at all in the dose map (1mm±1mm), positron and prompt-gamma maps identified a 1mm±3mm range shift, which is dominated by the intrinsic statistical error. In the case of a larger 12mm±1mm shift in dose, illustrated in Figure 1 as the region where the dose enters the contoured left parotid gland, a range shift of 12mm±3mm and 11mm±3mm was identified by means of the positron and prompt-gamma maps, respectively.

Summary: We have developed a new software framework which allows quantitatively investigating the sensitivity of positron and prompt-gamma emission maps to dose variations calculated in-silico for real clinical anatomical changes. A systematic investigation on the robustness of the method is ongoing and will be presented. Further investigations taking into account detector effects on the simulation of PET and prompt gamma distributions will be performed.

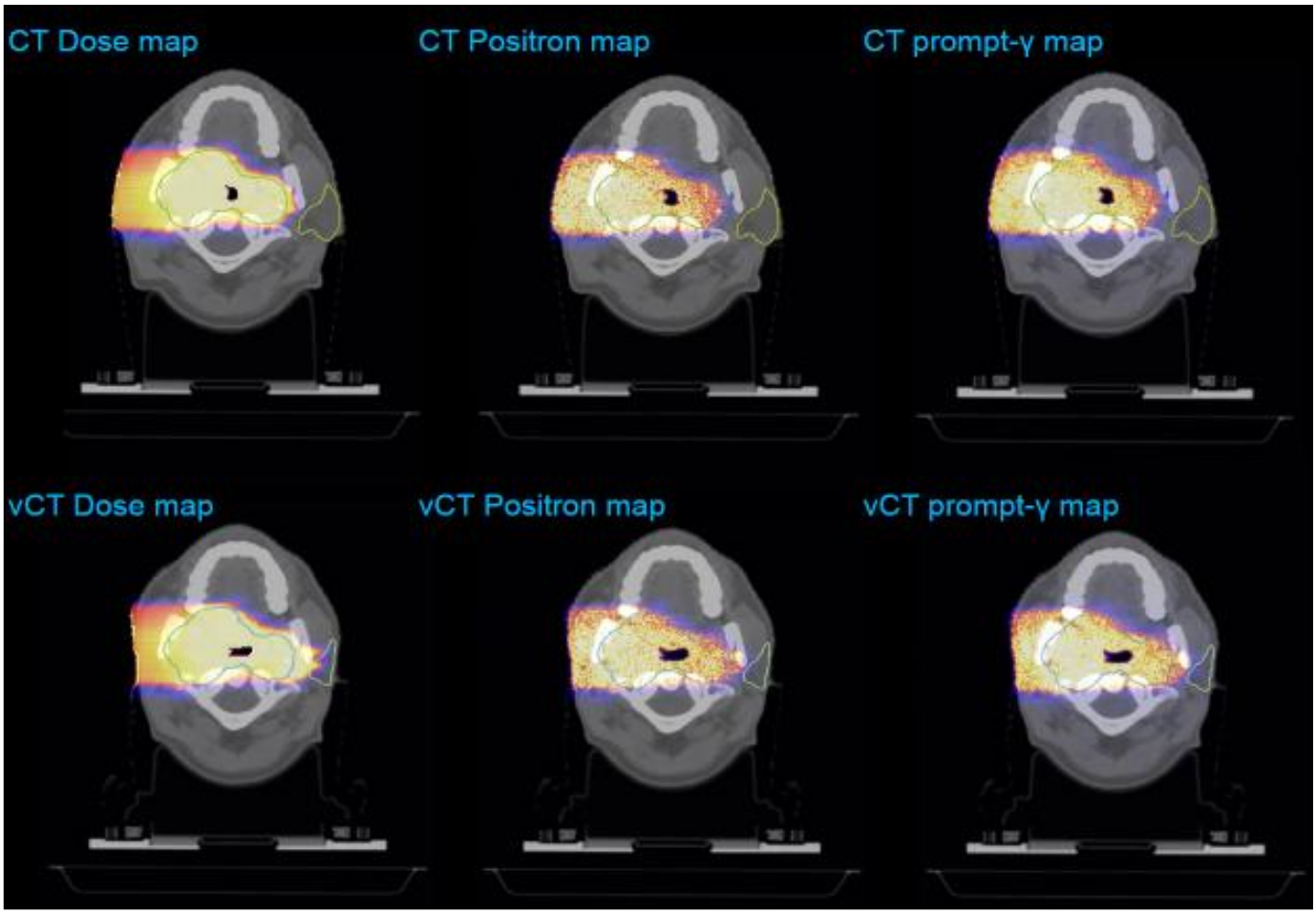

Fig. 1: For a single proton field, comparison of MC-simulated dose, positron and prompt-gamma 2D maps for a planning CT and a virtual CT of a head and neck cancer patient exhibiting inter-fractional anatomical changes (weight loss)

References

[1] Janssens, G.: "Diffeomorphic registration of images with variable contrast enhancement". Int J Biomed Imaging (2011) p. 891585

[2] Landry, G: "A novel approach to estimate the dosimetric influence of anatomical changes in head and neck cancer patients undergoing proton therapy using daily CBCT imaging". Submitted as an abstract to this conference

[3] Schell. S.: Advanced treatment planning methods for efficient radiation therapy with laser accelerated proton and ion beams. Med. Phys. 37 (10) (2010) p.5330-40

Session 14 – Quality assurance for medical radiation applications I: Machine QA

Chairs: G. Kohler (Basel/CH), H. W. Roser (Basel/CH)

77 Introductory lecture: Risk management in diagnostics and radiotherapy

M. Buchgeister[1]
[1]Beuth University of Applied Sciences, Department of Mathematics, Physics & Chemistry, Berlin, Germany

“Risk” in general is a very subjective term and usually negatively connoted. The Spanish word “risco” can mean a “cliff that is to avoid”. Risks linked to travel by e.g. car, railway or aircrafts are well known to the public and are accepted in everyday life. Continuous efforts are taken to reduce these risks with great success, if one compares to the situation 50 or even more years ago.

Risks are naturally also present in the healthcare system, where the human being is direct subject of diagnostic or therapeutic measures. High risks have been identified in e.g. surgical, intensive care or baby delivery/neonatal stations. Here procedures of risk management have been developed and established following general international norms like ISO 31000 “risk management – principles and guidelines” [1], that successively are extended to all components of the healthcare systems including the IT-network that is dealt with in an extra norm EN 80001 [2]. For the case of radiology and radiotherapy already exist extensive quality assurance procedures have been developed for the imaging and treatment equipment involved, since the application of e.g. X-rays have been identified soon after the discovery as potentially dangerous to both, patient and radiologist. The ALARA-principle (administer ionising dose” as low as reasonably achievable” for the given purpose) was established and is continuously valid as “golden rule of radiology”. Nevertheless, all quality assurance measures on e.g. the dose applied or the image quality yielded focuses only on the technical side of the risk linked to the administration of radiation. The personal operating these machines follow organized procedures and are faced by the workload given in relation to the workforce provided by the institution. Actions and decisions are taken, that may impose also risks to patients not covered by the above mentioned quality assurance systems of the machines. This is also subject of a risk management that comprises quality management and control as a part.

The goal of risk management in an healthcare system is to reduce risks linked to patients , to continuously improve the quality of the healthcare and safety of the patient, but also to prevent the institution as well as the people working there from unjustified claims of patients. This is of economical value to the institution as insurance premiums are calculated according the level of risk of insurance claims. The general procedure setting up a risk management is first to have full support by the leading authorities of the institution as risk management requires additional resources in workforce and money that have to be provided. The next step in implementing a risk management is usually following the method of “healthcare failure mode and error analysis” (hFMEA)[3]. This starts with the identification of possible sources of risks in all procedures involved. This is best done by a internal team of experts from the institution itself knowing all related facts, that is accompanied by an external expert for risk analysis. Risks are then categorised according their potential frequency of occurrence and severity of consequences in form of a risk or hazard scoring matrix (Table 1), where scoring values or colors (red, yellow, green) can be used to classify the associated risk. From this risk matrix priorities have to be set for measures to control and reduce these risks if possible. As last step of a risk management, a continuous process of regular audits has to be set up to ensure the effectiveness and completeness of the system as well as a critical incident reporting system (CIRS). Experience from the history of fatal accidents tells, that those critical accidents often have shown up before as critical incidents, that have been prevented just before major harm or damage occurred due to the alertness of someone. If the information of this incident is given to the risk management team, preventive measures can be developed to improve safety by e.g. adapting checklists used in this procedure or adding new elements to the training of the personal. Crucial to this step is an open culture of dealing with errors indicated by someone him- or herself. They should be seen as valuable indicators for improvement and not as sources of punishment of the person involved. This is – besides the error reducing design of the hard- and software involved – one of the most critical topics in a successful risk management. Anonymity is an important prerequisite necessary in such an error or incident reporting system. These CIRS have also been already established on international levels for the field of radiotherapy by the ROSIS project [5] maintained by an ESTRO working group and the new SAFRON [6] project, that is part of the radiation protection of patients (RPOP) website by the IAEA at Vienna. For radiology there are currently no comparable efforts known, but nevertheless exist potential risks of e.g. applying unnecessary high levels of dose in interventional procedures or missing important facts for the diagnoses from the images of a patient.

Risk or hazard scoring matrix		**Serverity of effect**			
Likelihood or probability of event		**Catastropic:** **e.g. death or injury**	**Major:** **e.g. permanent lessening of body function**	**Moderate:** **e.g. increased length of stay at hospital**	**Minor:** **no injury, increased length of stay nor increased level of care**
	Frequent: **e.g. several times per year**	**16**	**12**	**8**	**4**
	Occasional: **1-2 times per year**	**12**	**9**	**6**	**3**
	Uncommon: may happen in 2 to 5 years	**8**	**6**	**4**	**2**
	Remote: **unlikely, may happen in 5 to 30 years**	**4**	**3**	**2**	**1**

Tab. 1: Example of a risk or hazard scoring matrix according to [4].

References

[1] DIN ISO 31000: Risikomanagement- Grundsätze und Leitlinien (ISO 31000:2009), Entwurf 2011, Beuth Verlag Berlin.

[2] DIN EN 80001-1: Anwendung des Risikomanagements für IT-Netzwerke, die Medizinprodukte beinhalten – Teil 1: Aufgaben, Verantwortlichkeiten und Aktivitäten (IEC 80001-1:2010); Deutsche Fassung EN 80001-1:2011 und DIN EN 80001-1-5: Anwendung des Risikomanagements für IT-Netzwerke, die Medizinprodukte beinhalten – Teil 2-5: Anleitung für verteilte Alarmsysteme (IEC 62A/816/NP:2012), Beuth Verlag, Berlin.

[3] www.patientsafety.va.gov/media/hfmea.asp, 30.07.2014

[4] www.patientsafety.va.gov/docs/joe/hfmea_intro_jm_may14.doc, 30.7.2014

[5] www.rosis-info.org/index.php, 30.07.2014

[6] rpop.iaea.org/RPOP/RPoP/Content/News/safron.htm, 30.07.2014

78 Comparison of different methods for assessing imaging performance in dental cone-beam computed tomography

C. Steiding[1,2], D. Kolditz[1,2], W. A. Kalender[1,2]
[1]University of Erlangen-Nürnberg, Institute of Medical Physics, Erlangen, Germany
[2]CT Imaging GmbH, Erlangen, Germany

Introduction: Dedicated cone-beam computed tomography (CBCT) scanners are increasingly used for 3D oral and maxillofacial imaging [1,2]. However, to date there is still a lack of transnational consensus on acceptance and constancy testing for image quality (IQ) and dose of these systems. The aim of this work was to implement, validate, and compare procedures for routine IQ evaluation in dental CBCT. We focused on the German standard DIN 6868-161 [3] issued in 2013 and on conventional IQ metrics according to the well-established standard IEC 61223-3-5 [4] of clinical CT x-ray equipment**.**

Materials and methods: The approximated in-plane modulation transfer function (MTF), the so-called uniformity-indicator (UI*), and the contrast-to-noise-indicator (CNI) were determined in accordance with [3] employing the new DIN-compliant phantom (Fig. 1 (a)). Image noise, contrast-to-noise ratio (CNR), the CT value uniformity index (UI), and the 3D MTF were measured using a recently proposed quality assurance (QA) framework [5] conforming to the IEC standard [4]. For this, a modular phantom was used featuring contrast, homogeneous, and spherical test inserts (Fig. 1 (b)). All experiments were performed on a clinical dental CBCT unit. Both phantoms were scanned with predefined standard clinical protocols. In order to evaluate the effect of the phantom location and, in consequence, the severity of cone-beam artifacts, every measurement setup was executed at two different z-positions (z = 0 cm and z = 6 cm). To allow for automated QA procedure, all IQ evaluation methods and phantom-specific detection algorithms were implemented in a dedicated computer program.

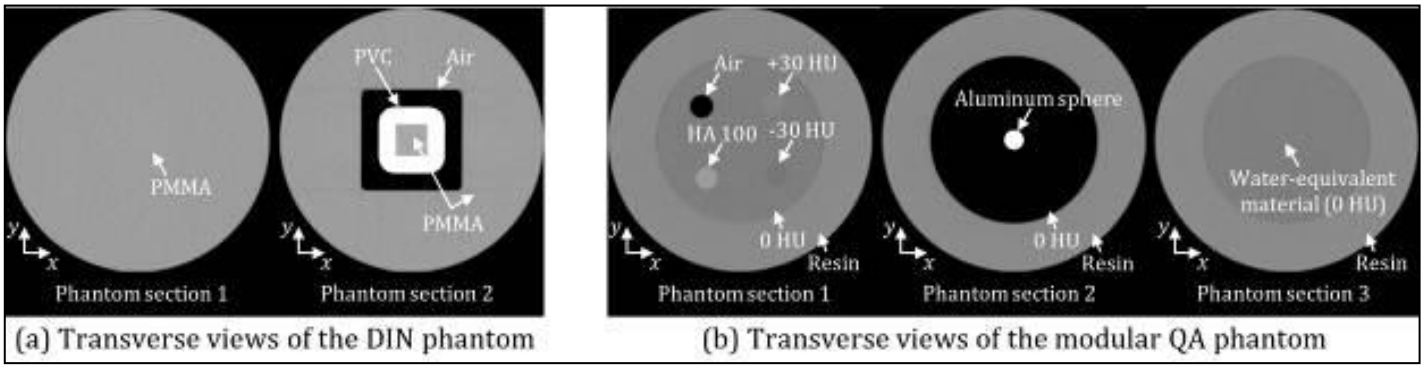

Fig. 1. Schematic representation of the (a) new DIN-compliant phantom and (b) the modular IEC-compliant phantom.

Results: The position and orientation of the phantoms were detected automatically in all of the measurements. Thus, a reproducible placement of the evaluation regions and volumes was provided. The IQ parameters determined in this study are summarized in Table 1. In-plane 50 % and 10 % MTF values from the approximated and the exact MTF calculation procedure agreed to within 5 %. With increasing axial distance from the center of the field of measurement, UI* and CNI dropped by 30 % and 19 %, respectively. Conventional IQ parameters showed higher sensitivity for cone-beam artifacts; i.e., UI and CNR were reduced by about 197 % and 37 %.

Conclusion: The implemented automated QA routines compatible with both the DIN and the IEC approach offer reliable and quantitative tracking of imaging performance in dental CBCT for clinical practice. However, equivalence between the recently proposed metrics [3] and the well-established CT IQ assessment is not given. In addition, direct measurements of physical image characteristics such as image contrast and noise, uniformity, and axial resolution are not supported by the new concept according to DIN 6868-161.

IQ parameters	z = 0 cm	z = 6 cm	Difference / %
Uniformity			
UI* (new)	27.42	19.19	-30.0
UI (conv.) / %	4.09	-3.98	-197.3
Image contrast			
CNI (new)	26.96	21.84	-19.0
CNR (conv.)	3.97	2.52	-36.5
Resolution			
$MTF_{50\%,xy}$ (new) / cm^{-1}	4.78	4.43	-7.3
$MTF_{10\%,xy}$ (new) / cm^{-1}	8.20	8.50	3.7
$MTF_{50\%,xy}$ (conv.) / cm^{-1}	4.75	4.65	-2.1
$MTF_{10\%,xy}$ (conv.) / cm^{-1}	8.57	8.41	-1.9
$MTF_{50\%,z}$ (conv.) / cm^{-1}	4.75	4.18	-12.0
$MTF_{10\%,z}$ (conv.) / cm^{-1}	9.04	8.97	-0.8
Image noise			
σ (conv.) / a.u.	33.01	38.83	17.6

Tab. 1: IQ parameters according to [3] (new) and IEC-compliant procedures (conv.) measured at the axial positions z = 0 cm and z = 6 cm.

References

[1] M. W. Vannier, "Craniofacial computed tomography scanning: technology, applications and future trends," Orthod. Craniofac. Res., 6 (2003), 23-30

[2] C. Holberg, S. Steinhäuser, P. Geis and I. Rudzki-Janson, "Cone-beam computed tomography in orthodontics: benefits and limitations," J. Orofac. Orthop., 66 (2005), 434-444

[3] DIN Report No. 6868-161: Image quality assurance in diagnostic X-ray departments – Part 161: RöV acceptance testing of dental radiographic equipment for digital cone-beam computed tomography, 2013, Berlin: Beuth Verlag

[4] IEC Report No. 61223-3-5: Evaluation and routine testing in medical imaging departments – Part 3-5: Acceptance tests – Imaging performance of computed tomography X-ray equipment, 2004, Berlin: Beuth Verlag

[5] C. Steiding, D. Kolditz and W. A. Kalender, "A quality assurance framework for the fully automated and objective evaluation of image quality in cone-beam computed tomography," Med. Phys., 41 (2014), 031901

79 Landolt rings for acceptance and annual tests in digital mammography and breast tomosynthesis

H. de las Heras[1], F. Schöfer[1], M. Chevalier[2], O. Weinheimer[3], G. Zwettler[4], F. Semturs[4], A. M. Acosta Roa[5], S. Pedersen[5], M. Rivas[6]
[1]QUART GmbH, Research and communication, Zorneding, Germany
[2]Complutense University, Radiology department, Madrid, Spain
[3]University Hospital of Heidelberg, Department of Diagnostic and Interventional Radiology, Heidelberg, Germany
[4]Medical University Vienna, Vienna, Austria
[5]Norwegian Radiation Protection Authority, Østerås, Norway
[6]Servicio Aragonés de Salud, Zaragoza, Spain

Introduction: Current methods for image quality tests in x-ray breast imaging rely either on visual, subjective methods or on software-based measurements that avoid human observers. In fact, both are complementary in practice. Visual methods are required to test all parameters involved in the imaging chain, including device performance, processing and visualization. Software-based measurements enable frequent evaluations to early detect changes in the device performance.

This paper demonstrates the use of Landolt C rings (Fig. 1) and measurements of signal difference to noise ratio as an alternative method for image quality checks during acceptance and constancy tests.

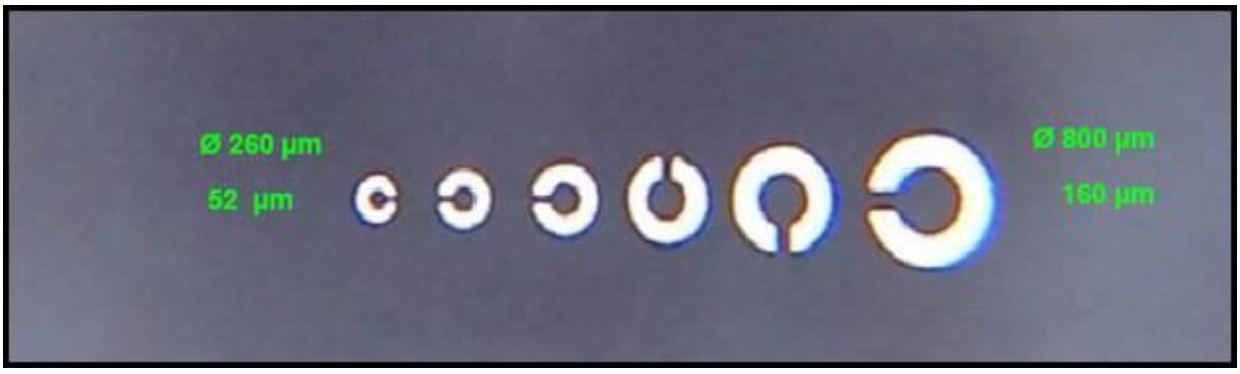

Fig. 1. Microscopic image of a group of six Landolt rings.

Materials and methods: A phantom containing Landolt rings in a Titanium background within a step wedge (presented at the DGMP annual meeting in 2012) was used to obtain mammography and tomosynthesis images from systems by all major manufacturers. The analysis of the Landolt test (4-alternative forced-choice) was performed visually and corrected by dedicated software. An overall score, $Landolt_7$, was obtained by adding the results from the seven thickest steps (equivalent breast thicknesses from 32 to 82.5 mm). In addition, automatic evaluations of signal difference to noise ratios (SDNR) calculated using the titanium strip on the same steps were added to obtain a corresponding $SDNR_7$ score. These scores were compared to the methods described in the European guidelines and the German PAS 1054 by analysing images of the phantoms obtained with the same exposure parameters. The Landolt and SDNR tests were performed on both raw and processed images.

Results: The Landolt test showed superior sensitivity to the tests described in the European guidelines and the German guidelines (Fig. 2 and table 1). It also enabled the definition a *common limiting value for the image quality of mammography projections* (both for raw and processed images) and *tomosynthesis reconstruction planes*: Landolt7 = 19 (Figs. 3 and 4). This value was obtained by comparison to the threshold thickness described in the European guidelines for the 0.1 mm-disc and confirmed for all tested devices including a CR system (Fig. 5). The decisive role of this disc was confirmed for all systems available (CR systems Toshiba Sophie, Siemens Mammomat 3000 Plus, Hologic Lorad, GE DMR, GE Senographe 600T and digital systems by Siemens, Hologic and GE) except for one model of one manufacturer (Fuji Amulet).

Conclusions: The Landolt ring test on processed images (for presentation) should be recognised as an alternative quality control tool for acceptance and annual tests of image quality in mammography and tomosynthesis. Complementarily, software measurements of signal-difference-to-noise ratio on raw images (for processing) have been proved to be a very sensitive tool for easy and early detection of performance changes, thus ideal for constancy tests.

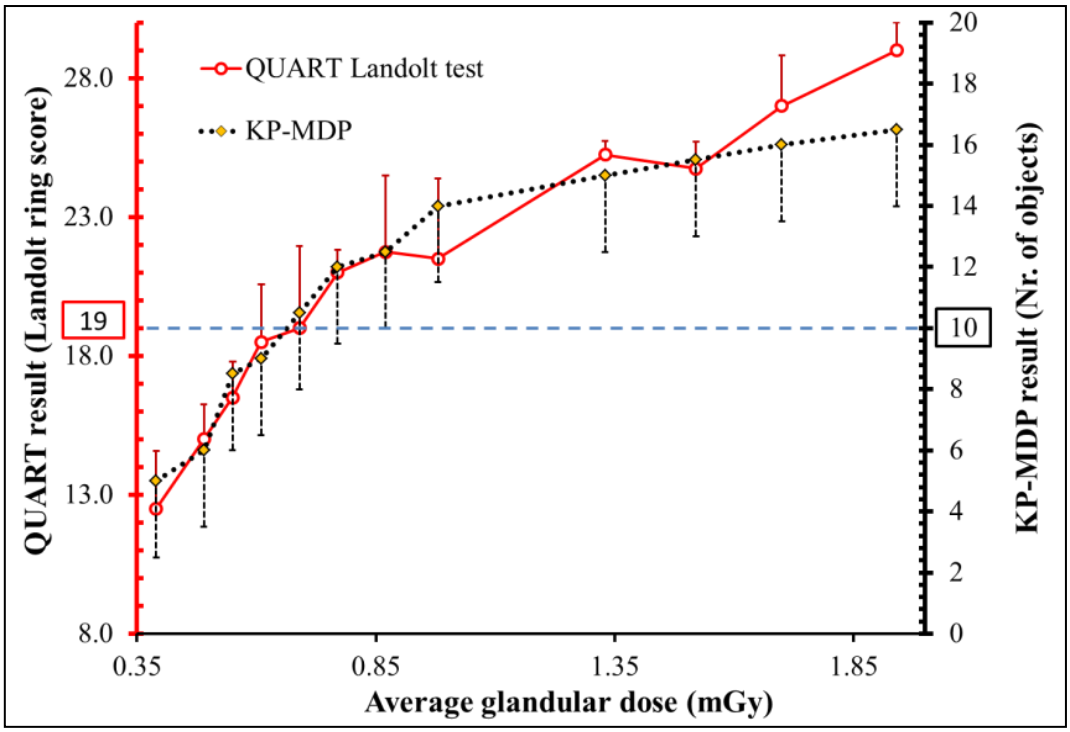

Fig. 2. The Landolt score (left axis) and the KP-MDP score (right axis) as a function of average glandular dose. A horizontal line represents the acceptable limiting value defined in the European guidelines for the 0.1 mm-diameter disc. The error bars are shown only in one direction for the sake of clarity.

	Wide range (1.5 mGy)	**0.3 mGy around CDMAM acceptability**	**0.3 mGy around ACR acceptability**	**Higher dose range (AEC)**
AGD range (mGy)	0.4-1.9 ACR: 0.2 – 1.7	0.55-0.85	0.2 – 0.5	1.35-1.95
Landolt ring score	5.4 ± 0.5	8.1 ± 1.1	17.6 ± 1.5	6.3 ± 2.0
$SDNR_7$	17.0 ± 0.8	25.2 ± 1.9	30.1 ± 1.5	10.6 ± 1.1
CDMAM (0.1 mm disc)	4.3 ± 0.8	7.0 ± 1.1	-	2.4 ± 1.8
ACR	1.3 ± 0.2	-	5.1 ± 1.1	0.7 ± 0.3
KP-MDP	2.8 ± 0.4	5.5 ± 0.6	7.9 ± 1.7	0.99 ± 0.05

Tab. 1: Score sensitivity (mGy^{-1}) values for different AGD ranges. All results were obtained with the same device (Siemens Mammomat Inspiration). Data regarding the phantoms CDMAM and ACR were taken from de las Heras et al, Phys Med Biol 2013;58:L17–L30 and reproduced here for comparison.

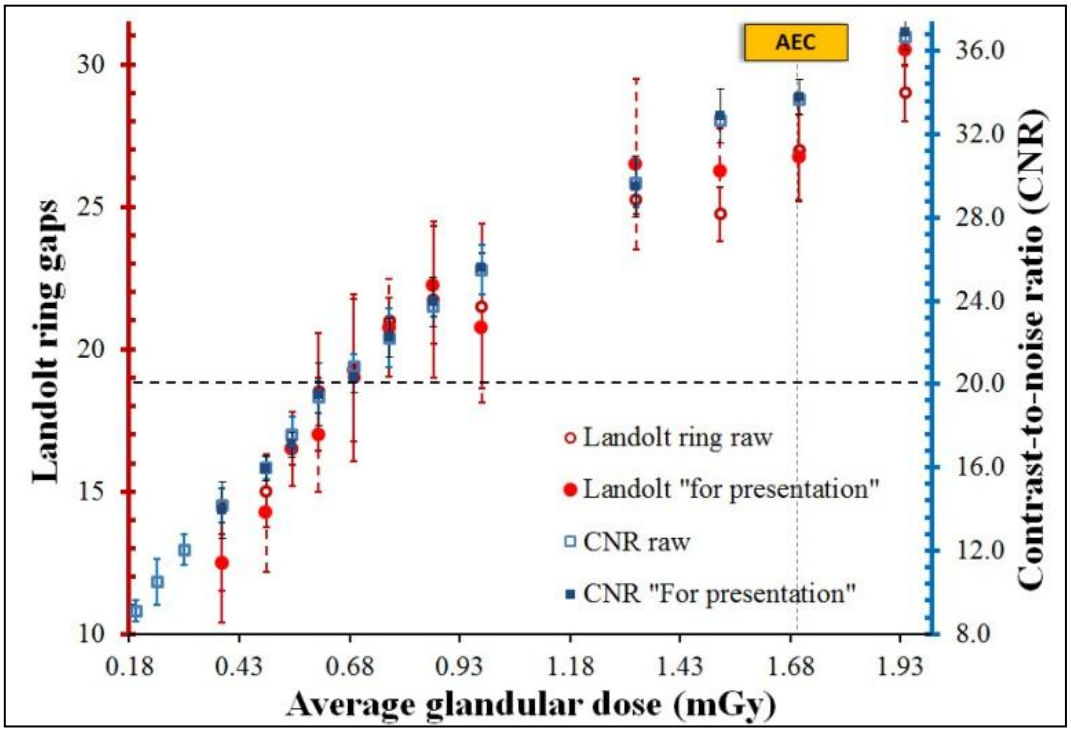

Fig. 3: Image quality as a function of average glandular dose for raw (left) and processed (right) images from a Siemens system. The AEC exposure is shown with a vertical line around 1.70 mGy. The AEC-determined kilovoltage and anode/filter combination (29 kVp and W/Rh) were kept constant.

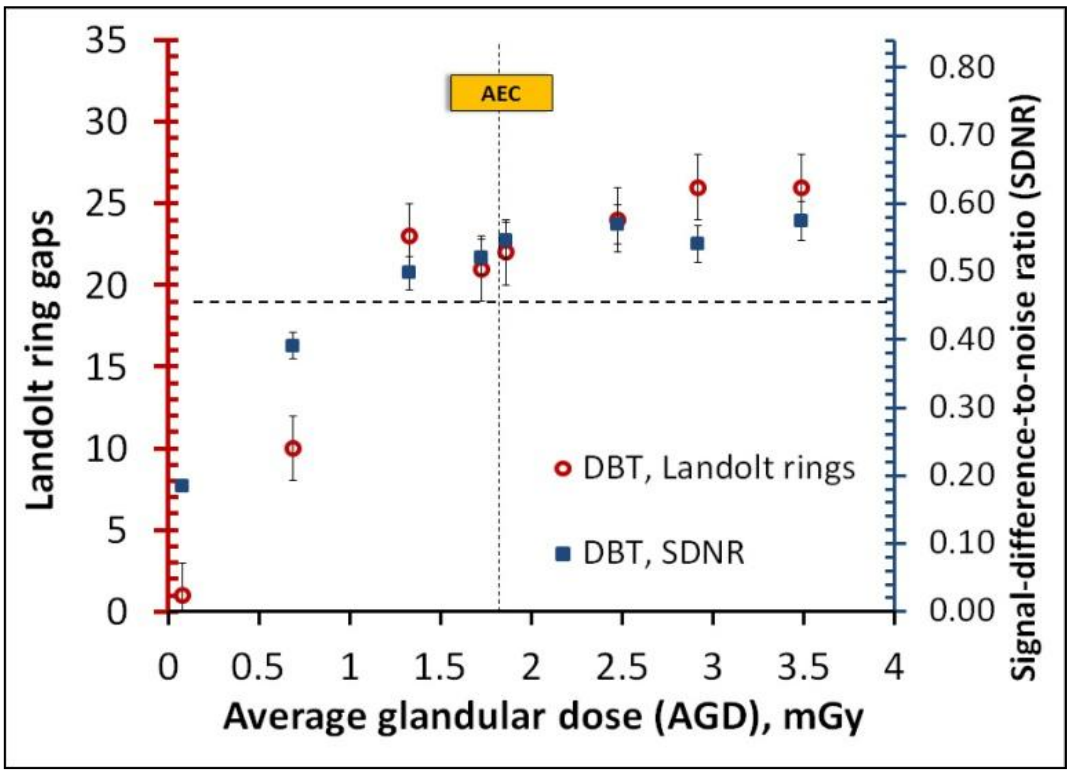

Fig. 4: Image quality as a function of average glandular dose for tomosynthesis reconstructions from a Hologic system. The AEC exposure is shown with a vertical line at 1.73 mGy. The AEC-determined kilovoltage and anode/filter combination (31 kVp and W/Al) were kept constant.

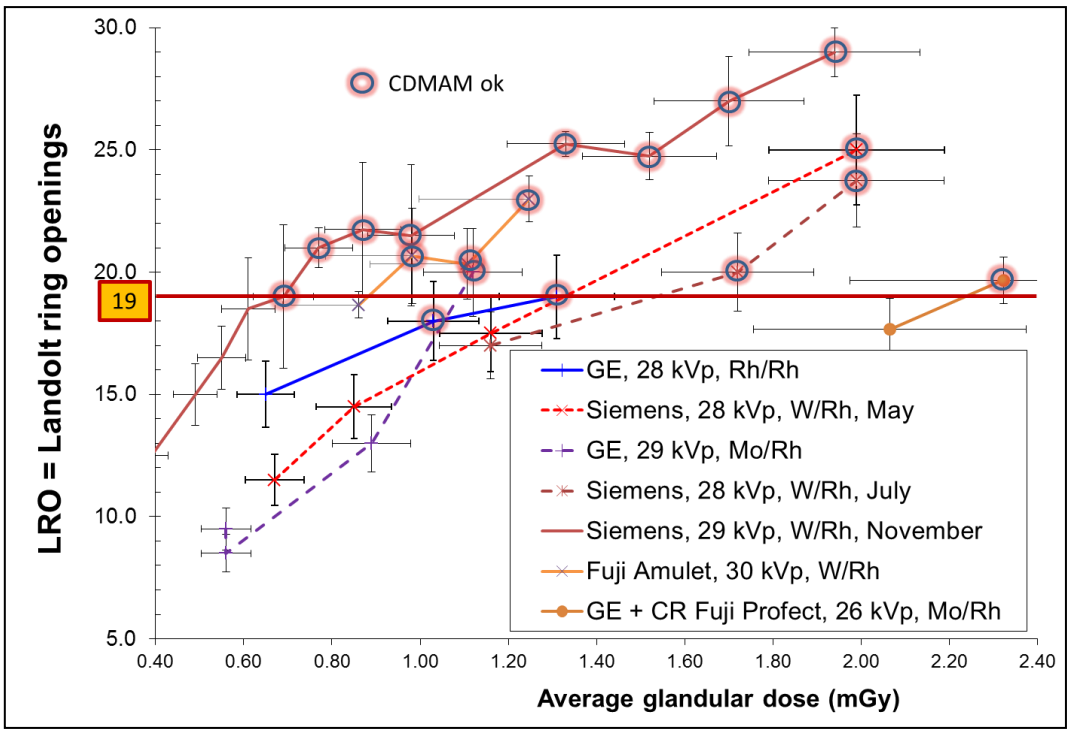

Fig. 5. Landolt$_7$ score as a function of average glandular dose for systems by different manufacturers including a CR system. The data points corresponding to a CDMAM test within tolerance for the 0.1 mm disc are marked with a circle.

80 Implementation of Technical Quality Assurance for the Austrian Mammography Screening Program: Our experiences in the pilot phase and country-specific challenges

A. Osanna-Elliott[1], S. Menhart[1], G. Zwettler[1], S. Wildner[1], M. Kaar[1], F. Semturs[1]
[1]Österreichische Agentur für Gesundheit und Ernährungssicherheit GmbH – AGES, Vienna, Austria

Introduction: On 01.01.2014, the Austrian Mammography Screening Program has started nationwide. In this program, invitations for a screening mammography are sent to women aged 45-69 years every two years. In order to assure that all women receive the best possible care while at the same time minimizing radiation dose, all mammography machines have to be certified according to Guidelines of the European Reference Organisation for Quality Assured Breast Screening and Diagnostic Services (EUREF) which are called EPQC (European Protocol for Quality Control, [1]). A pilot project to implement EUREF technical quality control (EUREF-Ö TQC) had been running since 2007 (Reference Center for Technical Quality Control of the Medical University of Vienna, RefZQS-MUW). As per 01.04.2014, the RefZQS has been incorporated into the AGES (Österreichische Agentur für Gesundheit und Ernährungssicherheit, Austrian Agency for Health and Food Safety, [2]). The pilot project started with 7 radiology institutes; by the end of 2013, the number had increased to 151 and should reach 201 by 30.09.2014. By that date, all participating radiologists will have to be certified by the RefZQS that they are fully compliant with EUREF-Ö TQC.

This presentation focusses on the challenges due to special Austrian circumstances, such as the fact that about 43 % of Austrian radiologists use computed radiography (CR) systems. In order to optimizes CR systems within EUREF-Ö tolerances, additional tests and adjustments are usually necessary, which require more time than for direct radiography (DR) systems. Also, in the Austrian screening program breast sonography is part of the screening examination. Therefore, QC for sonography equipment has been developed [3] and a sono testing process has been implemented [4].

Materials and methods: The European (EPQC) guidelines have been expanded to include requirements specific to Austria (as for example required by ÖNORM, [5]). The complete set is called “EUREF-Ö” and is maintained by the RefZQS. The main points exceeding EPQC are: Measurement of Y-60, use of reference cassette set, Initial Test for CR systems, TQC of sonography equipment. In particular, EUREF-Ö tolerances for Average Glandular Dose are identical to EPQC tolerances. On 12.07.2014, an ordinance was issued by the Austrian legislative authority [6] that EUREF-Ö is superior to ÖNORM requirements and ÖNORM testing (for mammography) can be omitted once a system has been certified as EUREF-Ö compliant.

In order to facilitate EUREF-Ö certification, a rigorous testing process has been developed and implemented. Particularly for CR systems, one or several adjustment steps may be necessary to bring the systems within EUREF tolerances. One or more "Initial Tests" are performed, where a range of possible T/F/kV settings are obtained that balance sufficient image quality and acceptable dose levels. In agreement with the radiologist, the optimal set of T/F/kV settings is defined and implemented by the system technical support staff. Only then Acceptance testing is started. Overall, this adjustment process on CR system usually takes many weeks, in some cases up to 4-6 months.

Results: As already indicated, CR systems usually present a special challenge for EUREF-Ö TQC: It has been shown that CR systems will have acceptable (comparable) image quality to DR systems, provided the images are taken at higher dose compared to DR [7, 8]. In any case, the necessary dose has to be within EUREF-Ö tolerances.

As of 31.03.2014, on 161 Austrian mammography systems (71 CR and 90 DR) EUREF-Ö TQC has been implemented. Without our optimization process, almost all CR systems and even some DR would have failed the EUREF-Ö TQC requirements, due to the fact that they were administering too little dose to reach EPQC image quality tolerance.

Conclusion: By 01.10. 2014, all women in Austria participating in mammography screening can be assured that they receive high quality screening mammography with the lowest dose necessary, as well as quality-assured sonography, so that a sufficient cancer detection rate can be reached.

References

[1] www.euref.org
[2] www.ages.at
[3] S Wildner *et al.*, "Technische Ultraschall-Qualitätssicherung im Rahmen des österreichischen Mammographie-Screening-Pilotprojektes nach EUREF-Ö: Konzept und praktische Durchführung". Radiopraxis **6** (2013)
[4] S Wildner *et al.*, "Technical quality assurance in mammasonography within the Austrian mammography-screening pilot project: concept and first results". Proceedings ECR 2014, to be published.
[5] ÖNORM S 5240-12, S 5240-7
[6] TQS-Erlass des Bundesministeriums für Gesundheit, 12.07.2013
[7] H Bosmans *et al.*, "Technical and clinical breast cancer screening performance indicators for computed radiography vs. direct digital radiography." European Radiology **10** (Oct 2013)
[8] AM Chiarelli *et al.*, "Digital compared with screen-film mammography: performance measures in concurrent cohorts within an organized breast screening program." Radiology **268** (Sep 2013)

81 Quality Assurance for Irradiation Systems in Radiation Therapy: A Set of General Empirical Rules

G. Kunz[1], R. Walter[1], J. Jean-Joseph[1], A. Liebhold[1], Z. Roushan[1], S. Gutser[1], T. Janzen[1], J. Kopp[1], G. Stüben[2]
[1]Klinikum Augsburg, Medizinische Physik und Strahlenschutz, Augsburg, Germany
[2]Klinikum Augsburg, Strahlenklinik, Augsburg, Germany

Introduction: The medical physicist is amongst other responsible for acceptance and quality assurance of the physical-technical section of irradiation systems intended for use at humans. Modules, interfaces and gateways of e.g. linacs or afterloaders become more and more complex because of new features and add on components of the irradiation system. Each (new) module running in clinical routine has to pass an acceptance test and has to undergo a routinely repeated quality control. Many of them are described in national and international guidelines (i.e. DIN, ICRU, SGSMP recommendations, etc.) [2-5] or are recommended by the manufacturer. Because of the usual time interval between a new module is put into clinical use and guidelines and recommendations are published the user himself is responsible to set up quality assurance procedures. In that case some general rules could help to do that [1]. The described general rules are depending each other and are derived empirically from already existing modules with their guidelines. Of course as soon as guidelines are published the initial quality assurance routine has to be replaced or adapted.

Materials and methods:

A) Check objects: each irradiation module and its interfaces, which is used clinically. The functionality of each module with influence on position accuracy and dosimetry, safety of patient and operator has to be investigated. Additionally the measurement equipment, i.e. ionization chamber, electrometer, water phantom, level etc. must be calibrated by an institute and/or routinely checked to ensure that effects measured origin from the irradiation system and are not caused by any instability of measurement equipment.

B) Check frequency: As long as published guidelines are absent checks must be performed at least after hard- and software upgrades, maintenance and after repairs. The frequency of testing can be taken from guidelines dealing with similar topics, taking into account the requirements on accuracy of patient positioning, dosimetry, safety and security.

C) Check methods: Sometimes there are two concurrent methods. On one side “end to end” check of a total workflow chain, on the other side a “point to point” check of every module of the chain. The problem of overall system tests is widely discussed in Germany these days arising from a publication of the German Radiation Protection Commission (SSK) [5]. In overall system tests errors can on the one hand compensate each other but result in an overview of the whole process chain. Point to point measurements detect errors in small steps of the working process, but also the error propagation has to be investigated.

Results: Of course a published guideline always leads to the application of its rules, measures and frequencies. In other case empirical rules can help.

A) Constancy rule: In a quality assurance procedure each parameter and the complete equipment including the setup must be kept constant. This rule holds especially to those objects, whose influence on a measurement is not known.

B) Completeness rule: The quality assurance procedure should take into account all variable parameters with their degrees of freedom. It should not be questioned whether a parameter has to be checked or not but only how often. If a parameter is not checked this decision must be based on an important and rational reason. If neither the physicist nor the service engineer exactly knows the influence of a performed change of a machine parameter all parameters that can depend on the adjustment have to be checked.

C) Independence rule: Any physical value should be measured independently, i.e. by two institutes, two people, two measurement methods or two single measurements (i.e. absolute dosimetry (MTK), adjustment of MU chamber response or other readouts from linacs, MU check of a plan etc.). This rule can operate as some kind of backup system. Parameters depending on each other can only be measured iteratively or alternately. Independent parameters can be measured sequentially.

D) Interpolation rule: At least the minimal and the maximal possible value of a parameter should be checked. The clinically occurring values should be inside the screened range, so values can be interpolated and not extrapolated.

E) Traceability rule: Each measured value should be traceable to the original value measured with calibrated equipment. It should be clear which result is the reference and which one is measurement derived or secondary value.

F) Competence rule: The more an irradiation component is understood in detail the more accurate and focused a check can be performed. This is especially true for functional correlations between different parameter, e.g. a) linear correlations of two parameters: origin, scale, orientation of the scale; b) orthogonal axes of a system: origin, scale, orientation of the

scale, perpendicularity, independence of axes and so on. If components and there influenced parameters are not known in detail, the whole parameter field has to be checked.

Action levels for a new parameter can often be determined from known parameters taking their uncertainties into account e.g. patient positioning accuracy and dose or determined by machine working range.

Conclusion: Even if totally different new irradiation modules have to be brought into clinical routine a set of rules can be applied and helpful to set up an appropriate quality assurance system.

References

[1] Norbert Licht, Universitätsklinikum des Saarlandes, private communication, Bericht der Arbeitsgruppe “Qualitätssicherung von Strahlentherapiesoftware”, AK "Computer in der Radioonkologie", 2008
[2] DIN: NA 080 Normenausschuss Radiologie (NAR)
[3] SGSMP (http://www.sgsmp.ch/recrep-m.htm#rec; request at 25.03.2014)
[4] Task Group 142 report: Quality assurance of medical accelerators: Med. Phys. 36, 9, 2009, p. 4197-4212
[5] Physikalisch-technische Qualitätssicherung in der Strahlentherapie – Vorschläge zur Prüfung des gesamten Behandlungssystems, Empfehlung der Strahlenschutzkommission; 241. Sitzung 28./29. April 2010; (http://www.ssk.de/SharedDocs/Beratungsergebnisse_PDF/2010/2010_03.pdf); request at 25.03.2014)

82 Quality Assurance of an Infrared Controlled Hexapod Couch Top on a Linac with X-ray CBCT

G. Kunz[1], G. Albert[2], J. Jean-Joseph[1], T. Janzen[1], A. Liebhold[1], S. Gutser[1], R. Walter[1], Z. Roushan[1], J. Kopp[1], G. Stüben[3]
[1]Klinikum Augsburg, Medizinische Physik und Strahlenschutz, Augsburg, Germany
[2]Elekta, PSC SchwabMunich, Medical Intelligence Medizintechnik GmbH, SchwabMunich, Germany
[3]Klinikum Augsburg, Strahlenklinik, Augsburg, Germany

Introduction: Until now there is no official guideline to routinely check a hexapod couchtop for high precession radiation therapy i.e. stereotaxy. The investigated HexaPOD™ evo RT System [3, 4] with the included iGUIDE® tracking system™ requires a daily check. Here we try to give recommendations for quality assurance in expansion the DIN [1, 2] and other publications [6, 7].

Material and methods: The investigated HexaPOD™ evo RT System is mounted on an Elekta Synergy Precise Table™ and allows 6 degrees of freedom (6 DoF): 3 orthogonal translations and 3 rotation directions (roll, pitch, yaw) around the radiation isocenter. In clinical use the hexapod couchtop position is controlled by an infrared camera evaluating the reflected signal of passive spheres which are located at the iGUIDE® reference frame™ at the couchtop. According to DIN [1, 2] the relevant control criteria can be separated into mechanical, radiation and safety tests.

In the mechanical part origin and orientation of the scale, perpendicularity and independency of axis movement are checked. To evaluate we used a precise level (clinotronic plus electronic level™; WYLER AG, Winterthur / Switzerland). We recommend checking these criteria on a yearly basis with the maximal table load allowed by the manufacturer according to [1, 2]. For safety reasons the limit switches of the 6 axes should also be checked yearly.

In the radiation test it is to check the isocenter of the hexapod couchtop and its congruence both with the X-ray-ConeBeamCT including matching processes and with the linac including the portal imaging system. We used the MIMI™ phantom (Standard Imaging, 3120 Deming Way Middleton WI 53562-1461 USA) and the Ball Bearing phantom™ (Elekta) to perform these tests. We recommend controlling these points monthly up to weekly dependent on the results and aimed accuracy of high precision radiation therapies. Distortions of the couchtop were not taken into account. According to the acceptance test we defined action levels at errors bigger than ±0.4 mm and ±0.2° [5, p. 19] for all axes.

Results: The proposed QA routine can be understood as an addition and expansion of the stereotaxy DIN [2] to 6 DoF couches. The positioning accuracy of the hexapod couchtop is within submillimeter range and ±0.2°. The accuracy of iGUIDE® tracking system™ including X-ray CBCT with matching software 1 mm in each direction and ±0.6°.

Conclusion and outlook: Because of the importance of the couchtop for positioning accuracy the daily necessary check of the iGUIDE® tracking system™ recommended by Elekta should be extended. Some additional weekly/monthly and yearly checks are necessary to build up a complete quality control system for 6 DoF hexapod couchtops.

In future the isocenter of the linacs with portal imaging, X-ray CBCT and hexapod couchtop should be done with one phantom put at one position of the couchtop. An improvement of the iGUIDE® tracking system™ could be achieved if the reference frame and camera is replaced by a more accurate couch control. The actual reference frame is neither patient nor user friendly. The 3 translation directions and the isocentric couchtop rotation (yaw) could be transferred to the couch table. In this case the couchtop would have to perform only roll and pitch. Another improvement could be reached if the CBCT match software would be able to match phantoms with a less number of structures.

References:

[1] Norm DIN 6847-5: Medizinische Elektronenbeschleuniger-Anlagen – Teil 5 Konstanzprüfungen von Kennmerkmalen, Oktober 2013, Berlin: Beuth Verlag
[2] Norm DIN 6875-2: Spezielle Bestrahlungseinrichtungen – Teil 2: Perkutane stereotaktische Bestrahlung – Konstanzprüfungen, November 2008, Berlin: Beuth Verlag
Flächenmodellierung. 2. Aufl. München: Hanser, 2003 – ISBN 3-446-22380-0
[3] Elekta AB (Publ), Box 7593, SE-103 93 Stockholm, Sweden; Medical Intelligence, D-86830 Schwabmünchen
[4] Elekta, Precision radiation therapy, User Manual, HexaPOD™ evo RT System; iGUIDE® 2.0
[5] Elekta, Precision radiation therapy, Customer Acceptance Test, HexaPOD™ evo RT System; iGUIDE® 2.0
[6] Winey,B.: Quality assurance for the commissioning of 6 dof robotic couch image guidance system for stereotactic radiosurgery, Journal of Radiosurgery & SBRT, 2013 Supplement 2.1, Vol.2 , p. 87-88
[7] D. Schmidhalter, M.K. Fix et al.: Evaluation of a new six degrees of freedom couch for radiation therapy, Medical Physics, 2013,40(11) 111710-1 – 111710-11

83 QA for rotational treatment delivery using the Octavius 4D Phantom

K. Schubert[1], B. Rhein[1], M. Seurig[1], S. Klüter[1], D. Oetzel[1], J. Debus[1]
[1]Universitätsklinikum Heidelberg, Abt. Radioonkologie u. Strahlentherapie, Heidelberg, Germany

Introduction: During the delivery of a rotational IMRT treatment plan on a conventional C-arm linac multiple parameters, such as gantry speed, dose rate or leave positions, are changing. In most institutions these treatment plans are recalculated to a verification phantom, which is later on used to measure the dose at the treatment unit. Some institutions avoid an individual verification measurement, by performing a second independent dose calculation on the patient anatomy. This procedure, however, is only detecting errors introduced by the dose calculation algorithm. Therefore, the machine QA in such institutions must be extended.

In this work we investigated, how the time resolved measurements with the Octavius 4D Phantom can be used to perform machine QA for rotational treatment delivery.

Materials und methods: One arc of a VMAT treatment plan for a patient with a target volume in the Head and Neck region serves as the basis of this QA test. It has 89 control points and uses 350 degrees of a rotation to modulate the dose. For the measurement of the dose distribution, the Octavius 4D Phantom is positioned in the isocenter of the treatment machine and a normal plan verification is performed. The Octavius 4D Phantom includes an inclinometer, which is positioned at the gantry, to rotate the phantom in such a way, that the Octavius detector array inside the phantom is always perpendicular to the central beam line. The detector uses 729 cubic ion chambers with a dimension of 5x5x5 mm^3 and a spacing of 10 mm from center to center, to measure a two dimensional dose distribution. The dose to the ion chambers and the value of the inclinometer are stored every 200 ms. This data is used to compare two measurements, one being an initial reference measurement and one being a routine QA test.

For the QA of the gantry speed and gantry position, the readings of the inclinometer are compared. For every 200 ms interval the reference position of the gantry is subtracted from the corresponding gantry angle of test procedure. The gantry speed is calculated by subtracting two consecutive gantry angles and dividing them by the 200 ms measurements interval. Corresponding gantry speeds are compared.

To compare the dose rate of the linac, the maximum dose value over all ion chambers for every measurement interval is analyzed. The concept of the maximum dose per time interval should ensure that the dose rate of the linac is observed and effects like the coverage of an individual ion chamber by a leaf are ignored. The dose rates of the reference procedure are compared against the dose rates of the test procedure at corresponding times.

In addition, the dose rate and the cumulative dose of the central ion chamber of the array are analyzed. Again, the dose measured in each interval of 200 ms of the reference procedure is subtracted from the dose measured during the corresponding interval of the test procedure. And finally, the difference of the cumulative dose is compared between reference and test procedure.

Results: Using the inclinometer of the Ocatvius 4D Phantom the deviations of the gantry positions between a test and a reference procedure could be studied in 200 ms intervals. A mean deviation of 0.4° ±0.6° with a maximum 2° was observed (Abb. 1). The mean deviation in gantry speed was 0.0035°/s ± 0.7°/s, while the maximum difference was 3.5°/s for a short interval of 200 ms.

The comparison of the maximum dose rate per time interval showed a mean deviation of 0.006 cGy ± 0.1 cGy per 200 ms, with a maximum deviation of 0.85 cGy per 200 ms (Abb. 2).

In the test procedure the central ion chamber collected 0.5 cGy less than during the reference procedure. This corresponds to 0.87 % of the total dose measured by this chamber. The mean deviation of the cumulative dose to the central chamber was 0.16 cGy ± 0.26 cGy with a maximum deviation of 0.75 cGy (Abb. 3). For the differential dose, the mean deviation was 0.0054 cGy ± 0.23 cGy and the maximum deviation was 2.4 cGy (Abb. 3). In the graph of the differential dose deviation sequences of positive and negative peaks can be observed. Most likely those peaks are related to deviations in the movement of MLC leaves.

Conclusion: The time resolved measurements with the Octavius 4D Phantom are a very helpful tool to study the dynamic behavior of the treatment unit during the delivery of a rotational IMRT plan. The movement of the gantry can be studied directly via the independent inclinometer of the phantom. The variation of the dose rate can be observed by the cumulative and differential measurements of the ion chambers of the array. While the view on the complete ion chamber array controls the dose rate of the linac, the view on single ion chambers has the potential to study the movements of the single leaves of the MLC. Probably a specific MLC test procedure should be developed to test the MLC in detail.

Since all results in this study are related to a reference procedure, only conclusions regarding a constancy check of the system can be made.

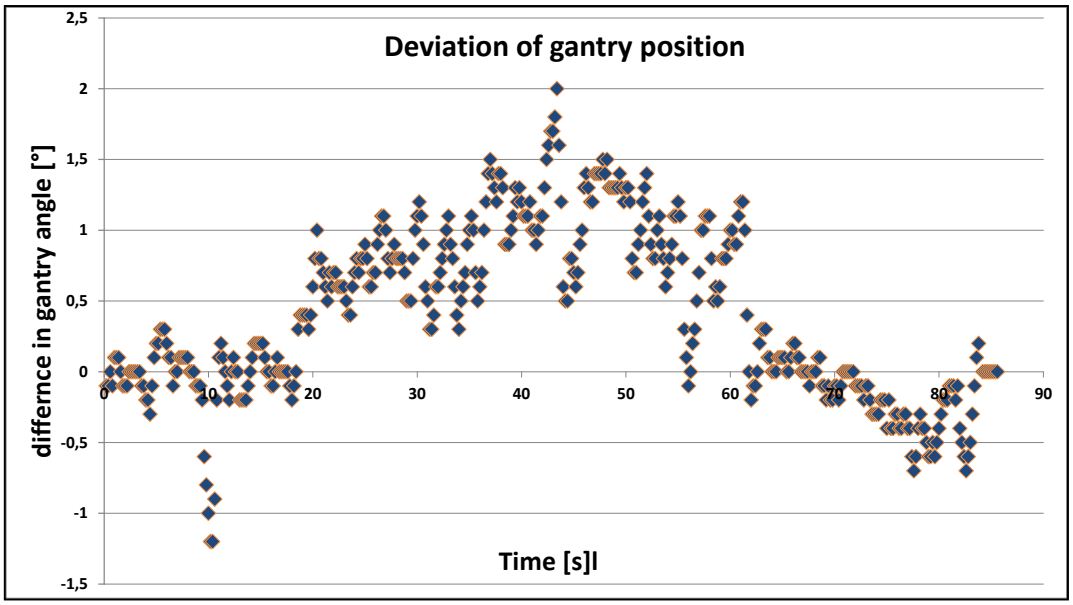

Fig. 1: Deviation of the gantry position (read from the independent inclinometer of the phantom) between test and reference procedure

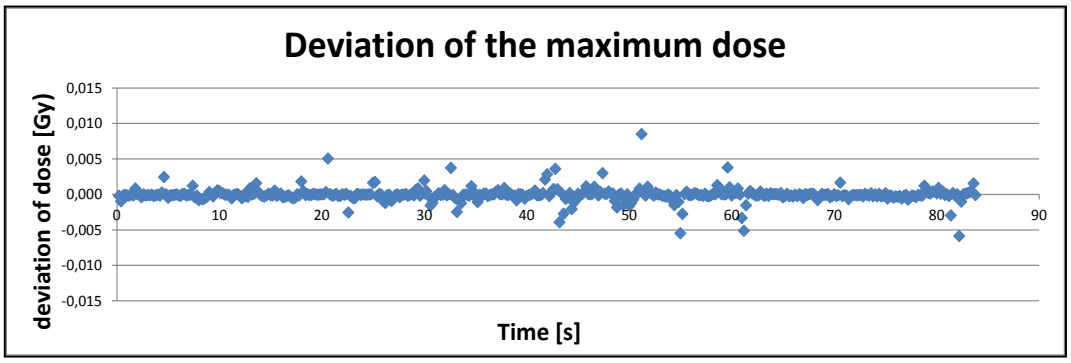

Fig. 2: Deviation of the maximum dose of all ion chambers of the array between test and reference procedure

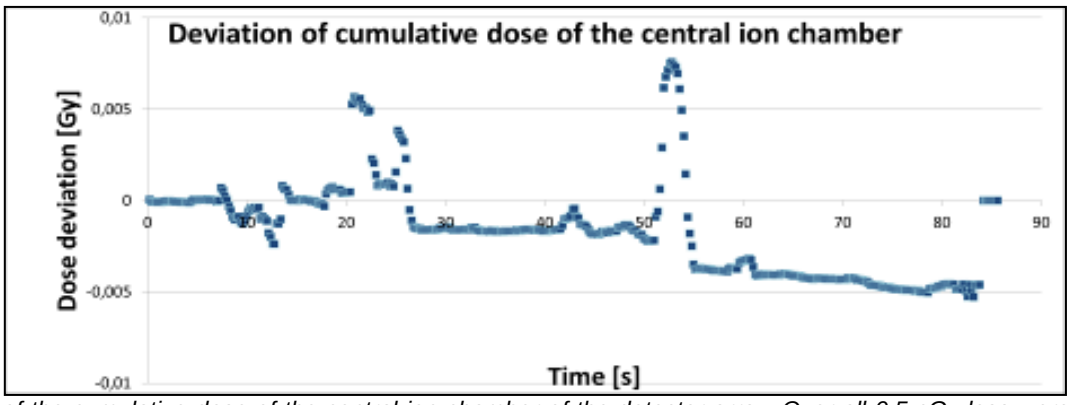

Fig. 3: Deviation of the cumulative dose of the central ion chamber of the detector array. Over all 0.5 cGy less were measured in the test procedure.

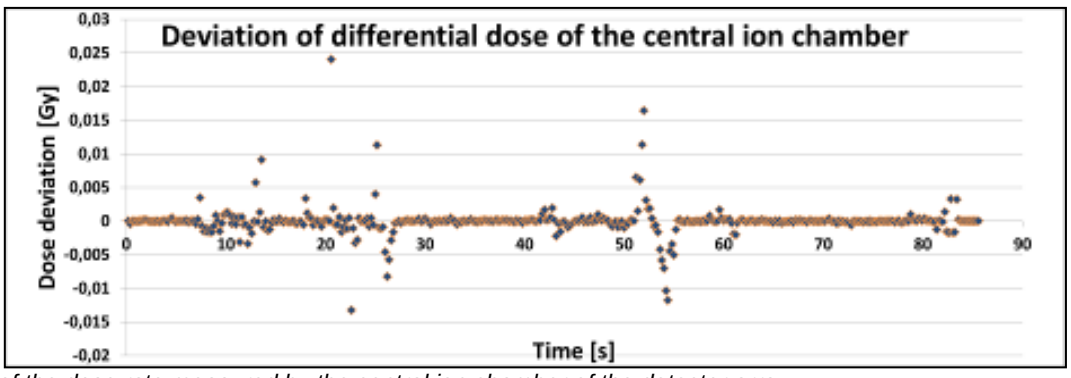

Fig. 4: Deviation of the dose rate measured by the central ion chamber of the detector array

Session 15 – High precision and stereotactic radiotherapy

Chairs: S. Klöck (Zurich/CH), H. Treuer (Cologne/DE)

84 Introductury lecture: The need for high precision and accuracy in radiotherapy

P. Manser[1]
[1]Division of Medical Radiation Physics and Department of Radiation Oncology, Inselspital, Bern University Hospital, and University of Bern, Switzerland

The success of radiotherapy depends strongly on both, precision as well as accuracy. It is worth to mention that these terms have different meanings, and it is one aim of this introductory lecture to point out this difference. From a physics point of view, geometric as well as dosimetric issues need to be discussed with respect to accuracy and precision. And it is well known that in recent years, several improvements have been realized. Some of these improvements did not only improved clinical treatments but lead even to totally new treatment modalities, which are currently available in clinical routine. However, there is still room for improvement and research and development are still needed in order to bring accuracy and precision to even higher levels. The presentation is describing the conducted and ongoing improvements and is covering not only accurate dose delivery but also dose computation treatment planning.

85 Introductury lecture: Physics essentials of stereotactic radiotherapy

A. Mack[1]
[1]Zurich, Switzerland

Introduction: High precision and stereotactic radiotherapy in general refer to the delivery of high doses of radiation in very few sessions to a small volume of tissue within the body. Therefore, the accuracy of the irradiation position is of vital importance. Many different irradiation systems claim to have submillimeter precision in hitting the target point and also offer features to treat moving targets in the body.

Material and methods: All factors and demands of high precision radiotherapy and modern radiosurgery are illuminated and discussed. A focus is set to the imaging, to the dose planning and to the exact application of the dose. Methods of QA to proof and to verify the quality of the complete setup are introduced.

Results: Very many techniques are capable of delivering precise dose distributions using small fields generating high dose gradients. The key factors for high precision or stereotactic radiotherapy are nearly distortion free 3D imaging modalities, accurate algorithms, small fields generating high dose gradients and end to end results finding accuracies of <1mm

Conclusions: High precision techniques e.g. radiosurgery are becoming increasingly important because they can achieve precise dose distributions. Thus it is possible to give more dose to the lesion per fraction and possibly achieve a better tumor control.

86 Robotic Radiosurgery for Lung Tumors: Technical Considerations and Treatment Outcome

O. Blanck[1,2], B. Scharf[3], M. Chan[4], S. Wurster[2], R. Pahl[1], M. Ayadi[5], A. Schweikard[3], D. Rades[1], G. Hildebrandt[6], J. Dunst[1], N. Andratschke[6,7]
[1]University Clinic Schleswig-Holstein, Kiel/Lübeck, Germany
[2]CyberKnife Center Northern Germany, Güstrow, Germany
[3]University of Lübeck, Lübeck, Germany
[4]University of Hong Kong, Hong Kong, Hong Kong
[5]Centre Léon Bérard, Lyon, France
[6]University Clinic Rostock, Rostock, Germany
[7]Universitaetsspital Zurich, Zurich, Germany

Introduction: Various lung tumor treatment techniques are available for the robotic CyberKnife system (Accuray, USA). Ideally, direct non-invasive lung tumor tracking with adaptive motion compensation (XLT = XSight Lung) is preferable, yet not feasible for all patients. Alternative treatment strategies consist of fiducial based tracking (FID), or spinal tracking combined with an internal target volume (ITV) concept (XST = XSight Spine). To facilitate clinical decision making on which motion compensation strategy to use, we developed a decision tree and present our clinical outcome data for lung tumor treatments.

Materials and methods: Our lung tumor decision tree was constructed as follows: 1) XSight Lung simulation. If not successful, then 2) XSight Spine with ITV margin, if tumor motion < 5mm and stable position with spine. If not given, then 3) Fiducial Tracking, if patient health justifies fiducial implantation. If not possible, then 4) XSight Spine with ITV and setup uncertainty margin or 5) treatment with potential alternatives (e.g. CBCT with gating on Linac). Primary planning CT was at end expiration (XLT, FID) or free breathing (XST) and ITV margin definition was performed on 4D CT or on regular end expiration and end inspiration CT. GTV to CTV margin was 2mm and CTV/ITV to PTV margin was 3mm (XLT, FID, XST < 5mm motion) or 5mm (XST > 5mm motion). Dose calculation and plan optimization was based on MonteCarlo simulation on the primary CT and generally 60Gy mean GTV dose in 3 fractions were prescribed resulting in 39-54Gy delivered to 95 % of the PTV depending on size and location of the tumor.

Results: We treated 42 primary and 67 secondary lung tumors in 96 treatments from 2011 to 2013 with our method. Out of 96 treatments 41 (43 %) were treated with XLT (3 tumors close to the tracked one were treated simultaneous with a differential motion margin concept; *see Fig1. and Fig2.*), 31 (32 %) with XST (< 5mm), 4 (4 %) with FID and 20 (21 %) with XST (> 5mm). PTV doses ranged from 20-54Gy (mean BED10 = 112Gy) in 1-5 fractions and GTV mean dose over all treatments were 30Gy (26-36Gy, 1 fraction), 60Gy (42.5-73.5Gy, 3 fractions) and 65Gy (62-69Gy, 5 fractions). Dose simulation with the still routinely used RayTrace algorithm revealed dose overestimations of 2.5-45.7 % (mean 15.9 %). Out of 20 treatments with XLT (> 5mm) 16 (80 %) were suitable for the new single x-ray 2D lung tracking system (LOT). After a mean follow up of 18.8 months (4-37 months) 24/76 patients died (88.2 % OS 1 year) due to tumor progression (10) or comorbidities (14). Out of 109 tumors 1 local failure after treatment with XST (> 5mm) was documented and re-treated with XLT. Side effects from fiducial implantation were in 2 cases (50 %) a self-recovering pneumothorax. Side effects from radiosurgery grade 2 (CTCAE version 4) were in 2 cases pneumonitis (XLT > 5mm and FID after pre irradiation) and in 1 case a rib fracture (XLT). Grade 3 or higher side effects were not noticed.

Conclusion: Our decision tree for lung tumor treatments with the CyberKnife was developed to avoid fiducial implantation and hence to reduce the risk of side effects. While some questions regarding quality assurance and treatment validation of non-direct target tracked CyberKnife treatments remain unanswered due to lack of tumor motion data during treatment and due to potential baseline shifts in respect to the spine, our clinical results demonstrate excellent efficacy with very few side effects given careful patient handling. Newer tracking algorithms may further decrease setup and motion uncertainty, but long term validation and the implementation of dedicated quality assurance programs are strongly warranted.

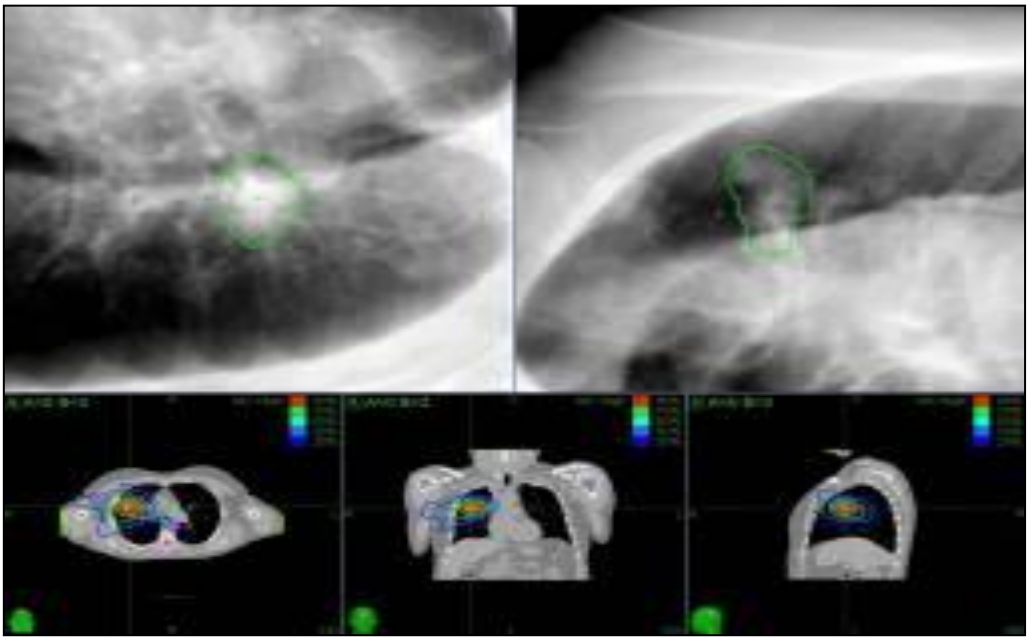

Fig. 1: XSight Lung Treatment Case

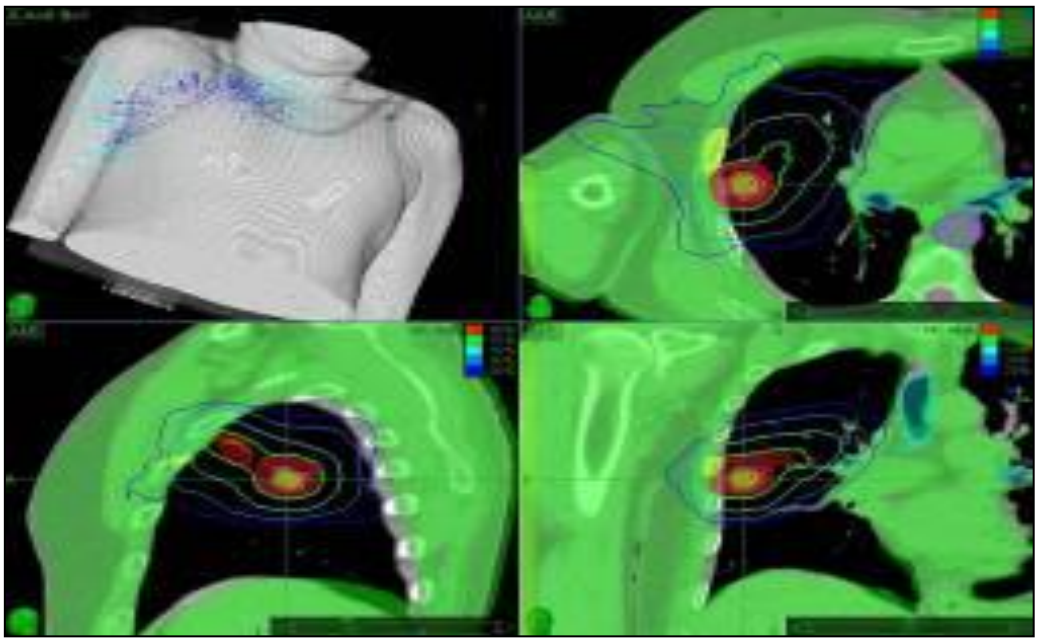

Fig. 2: Differential motion margin concept for secondary tumor close to the tracked one (see Fig. 1)

87 Cyberknife versus Linac-Radiosurgery – A comparison in geometrical accuracy

M. Hoevels[1], H. Treuer[1], K. Luyken[1], A. Hellerbach[1], M. Kocher[2], M. Ruge[1]
[1]University of Cologne, Stereotaxy, Cologne, Germany
[2]University of Cologne, Radiotherapy, Cologne, Germany

Introduction: In the first hand the Cyberknife has been designed by the neurosurgeon John Adler for the treatment of intracranial lesions. Thus the overall accuracy of the whole system has to meet the specific requirements for radiosurgery. The manufacturer (Accuray, Sunnyvale, CA USA) specifies this geometrical accuracy with less than 0.95 mm.

To establish and maintain this accuracy the cyberknife-system provides a special, very well designed test procedure, the End-to-End (E2E)-test. To perform this E2E-test, two gafchromic films are positioned in the so called ballcube phantom as shown in fig. 1, which in turn is placed in the head-neck-phantom. By the use of these films, which are perfectly aligned to the border of the phantom, two rectangular planes from the dose distribution can be analysed at once.

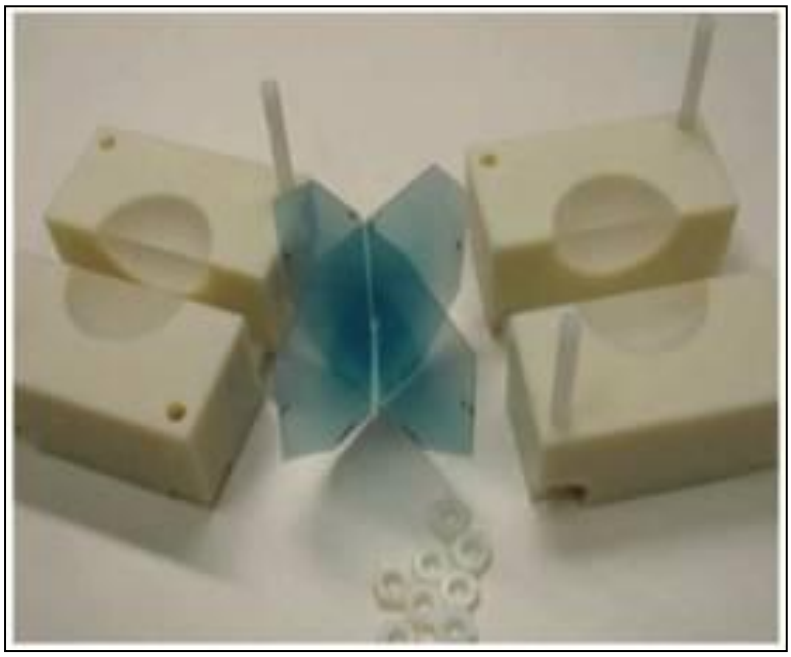

Fig. 1: the ballcube phantom

Fig. 2: the head-neck-phantom

This phantom undergoes the same steps as performed in a common patient treatment procedure, including imaging, definition of the target volume and dose delivery. Finally the irradiated films are analysed in a standard procedure. In this study this test procedure is applied to the cyberknife system as well as to the linac, in order to achieve comparable results.

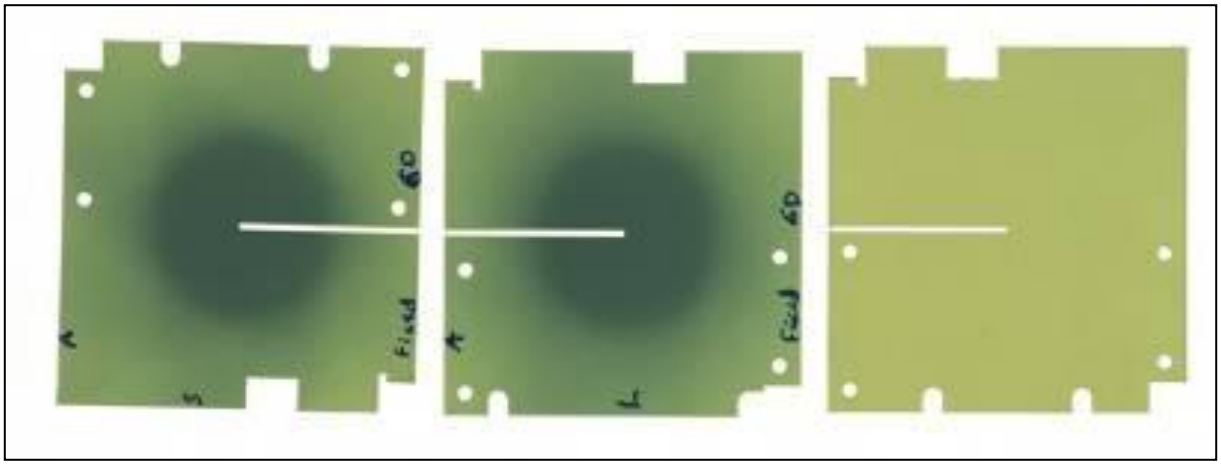

Fig. 3: gafchromic films showing the symmetric dose distribution

Materials and methods: The cyberknife system supports the user during this E2E-test in several ways:

1. The treatment planning system **Multiplan** provides optimal support for the definition of the ballcube as target volume
2. and for the alignment of dose distribution onto the target volume
3. The standardised analysis of the films is achieved by an external program

Item 1 and 2 have to be replaced with our own software module to make it work on the linac, whereas the analysis is done the same program in order to maintain a maximum of comparability.
The dose delivery is performed by the use of a micro-multileaf-collimator and therefore the dose distribution is calculated by the **VIRTUOS**-radiosurgery module as in fig. 5.

*Fig. 4: dose distribution in **Multiplan***

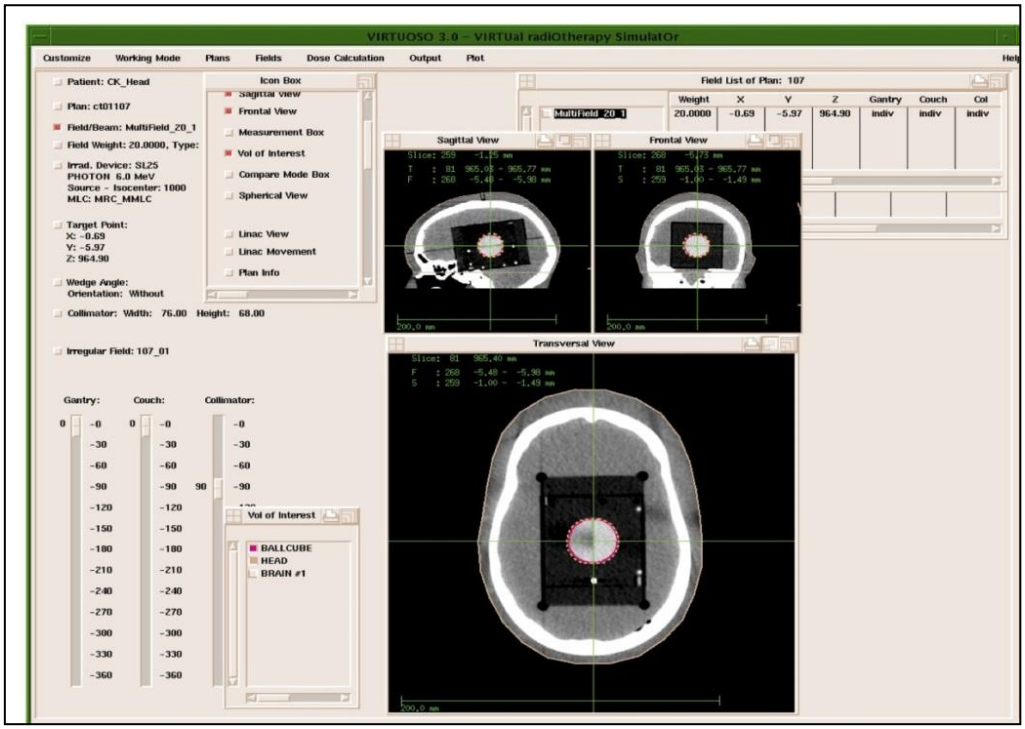

*Fig. 5: dose distribution in **VIRTUOS***

The major part of efforts is bound to the alignment of the dose distribution, which is performed in a loop. The primary target point of the isocentric field in the linac radiosurgery is the center of gravity of the target volume. We consider the borders of the resulting dose distribution with respect to the target volume and calculate delta values for the displacement in three dimensions. These are applied to the target point and the whole procedure is repeated until these delta values are below 0.1 mm as in fig. 6.

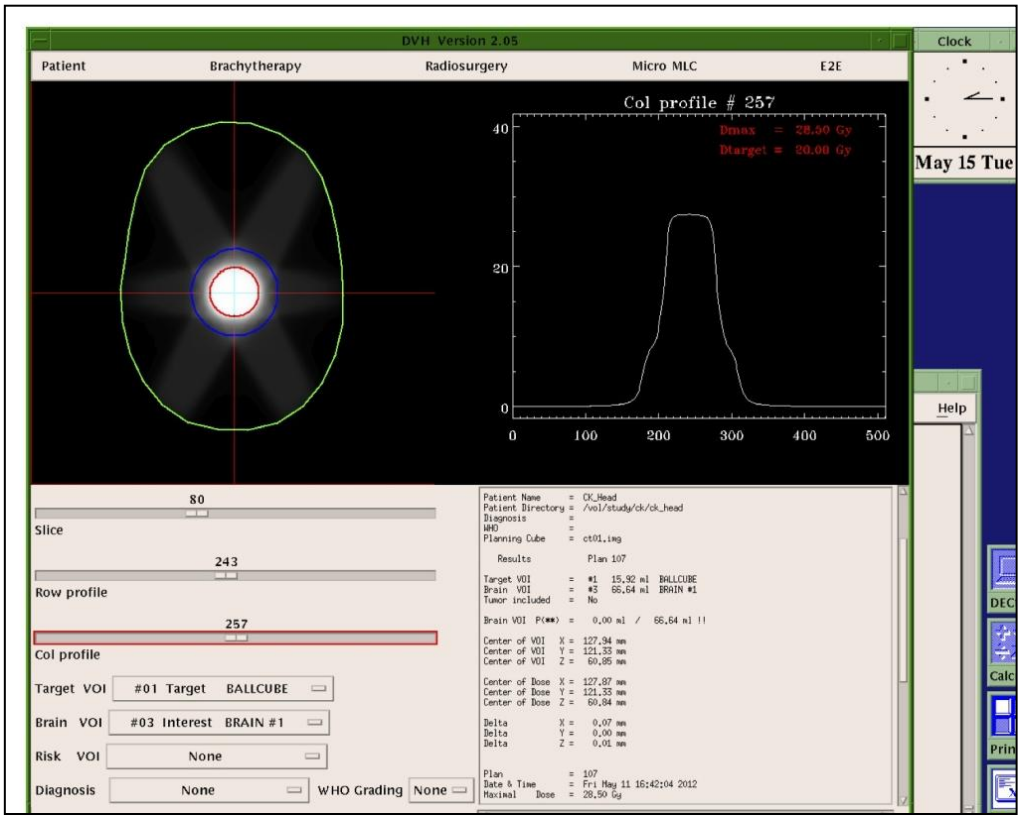

Fig. 6: dose alignment

Results: By this methodology the determination of accuracy, which is performed on the cyberknife by the E2E-test, is made available in a nearly equivalent manner for the use on the linac. This way quantitative comparisons under standardised and realistic conditions for both modalities can be achieved.

References

[1] Treuer, H. et al., *On isocentre adjustment and quality control in linear accelerator based radiosurgery with circular collimators and room lasers.* Phys Med Biol, 2000. **45**(8): p. 2331-42.

[2] Anthony K. Ho et al., *A STUDY OF THE ACCURACY OF CYBERKNIFE SPINAL RADIOSURGERY USING SKELETAL STRUCTURE TRACKING*, Neurosurgery 60[ONS Suppl 1]:ONS-147–ONS-156, 200

88 Dosimetric and geometric end-to-end tests in stereotactic Radiosurgery – Evaluation of a new end-to-end procedure on a NovalisTx and a TrueBeamSTx stereotactic radiosurgery system

P. Schmelzer[1], S. Scheib[1], D. Schmidhalter[2], S. Lang[3], J. Krayenbühl[3]
[1]Varian Medical Systems, Baden, Dättwil, Switzerland
[2]Inselspital, Medical Radiation Physics and Radiation Oncology, Bern, Switzerland
[3]University Hospital, Radiation Oncology, Zurich, Switzerland

Introduction: With the increasing clinical interest in stereotactic radiosurgery (SRS) and stereotactic ablative body radiotherapy (SABR), geometric and dosimetric accuracy is important. The overall accuracy in SRS is typically measured by means of an End-to-End (E2E) test, encompassing the entire treatment chain: plan image acquisition, data transfer, segmentation and registration, planning, dose calculation, positioning and monitoring on the treatment device and finally dose delivery [1]. Recently an E2E test procedure was developed including a new E2E phantom, which is being part of the new SRS platform EDGE™ from Varian Oncology Systems. This E2E test procedure consists of dosimetric and geometric tests. In this work these tests were executed on a NovalisTx (NTx) system and a TrueBeamSTx (TBSTx) system from Varian. This study should demonstrate the ability of the E2E test with the proposed phantom to verify geometric and dosimetric sub-mm accuracy.

Material und methods: The new E2E test phantom consists of a polyurethane cube (density of 0.45 g/cm^3) with a dimension of 15x15x15 cm^3. Various densities (0.25 g/cm^3, 1.4 g/cm^3), 16 ceramic balls (5 mm diameter) and three Calypso transponders are embedded. The phantom is equipped with an exchangeable polyurethane inner cube with a dimension of 7x7x7 cm^3 and a density of 1.05 g/cm^3. Different inner cubes are used depending on which dosimetric or geometric test is performed. For geometric verifications an insert with a steel/tungsten ball (5 mm diameter) in the center of the cube is used for Winston-Lutz tests [2]. For dosimetric verifications various inserts for radiochromic films in different single layers as well as crossed layers are used. The phantom was positioned using reference images similar to a patient positioning workflow. Treatment planning was performed using iPlan for NTx and Eclipse for TBSTx. A planning CT with slice thickness and spacing of 0.75 mm and an in-plane resolution of 0.75 mm was acquired. For phantom positioning the ExacTrac system was used on the NTx and a 3D/3D (CBCT) and 3D/2D match for the TBSTx.

The isocenter of the geometric set up plan was in the center of the steel/tungsten ball. A steel ball was used on the NTx, a tungsten ball on the TBSTx. After positioning, MV images with a square field (20x20 mm^2) defined by the Multi-Leaf Collimator (MLC) were acquired with the EPID (resolution of 0.392mm) for various gantry, collimator and couch angles. A Matlab based research software was used to determine the shift between the steel/tungsten ball center and the center of the field outline.

Several patient verification plans with different modalities (RapidArc and IMRT on TBSTx, HybridArc, DynamicArc and IMRT on NTx) and different energies (6X, 6XFFF, 10XFFF on TBSTx and 6X-SRS and 6X on NTx) were used on both systems to perform the dosimetric tests. The radiochromic EBT3 film of each test case was scanned with an EPSON 10000XL scanner using the FilmQA Pro software and the dose distribution was determined using triple channel analyzes. The scanned dosed distribution was matched to the corresponding calculated dose distribution base on the known isocenters. By using dose profiles, isodose lines and the gamma evaluation pass rate (3 % max. dose, 1 mm DTA) the geometrical shift between the two dose distributions is determined in two orthogonal directions.

Results: Figure 1 shows an example of a measured and calculated dose profile as well as percentage isodose lines. The results shown in Table 1 are the average radial shifts, the standard deviations, the minimum, the maximum radial deviations and the number of measurements for both types of tests. The results indicate that the E2E test is able to determine sub-mm geometric and dosimetric accuracy for both systems.

Conclusion: This study proved the capability of the E2E test with a dedicated phantom to show the sub-mm dosimetric and geometric accuracy of both SRS systems, NTX and TBSTx. Furthermore it has been shown that the E2E phantom and the Matlab based research software is a valuable tool for the analysis of the E2E test.

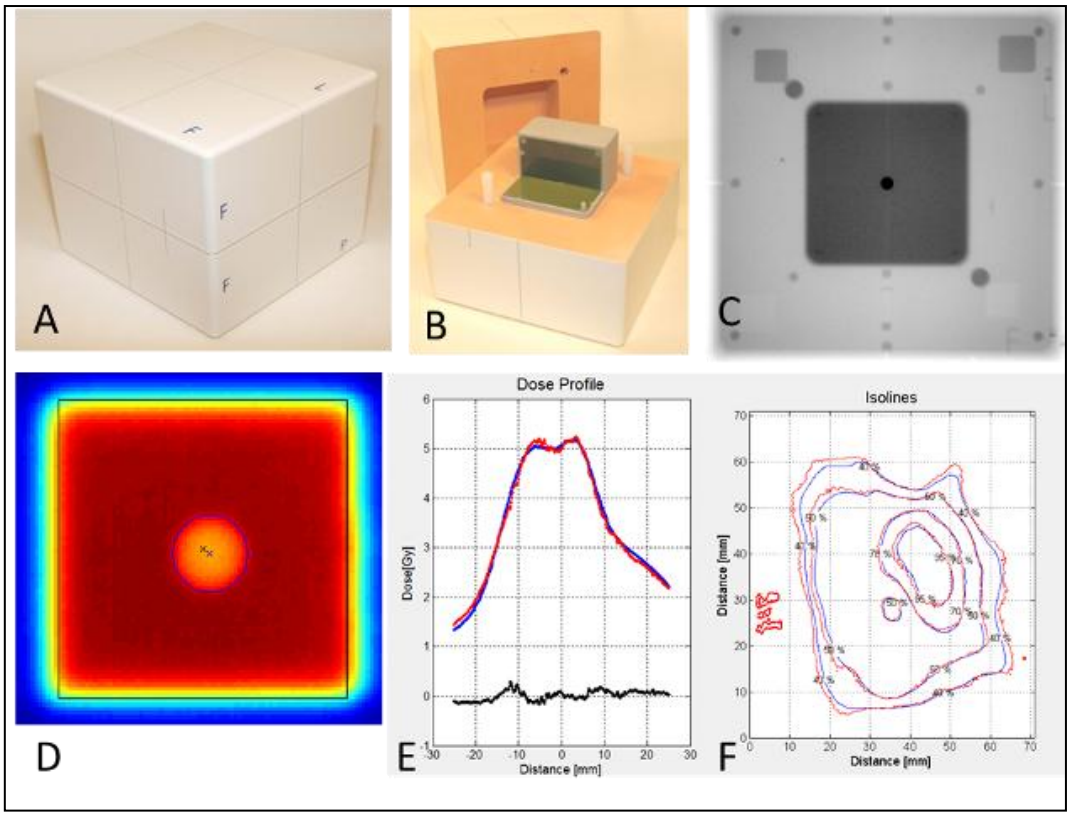

Fig. 1: (A) E2E Test phantom (B) opened E2E Test phantom with inserted crossed film (C) MV, 6XFFF, 3MU image with tungsten ball insert, 14 ceramic BB, Calypso Beacons, pegs, letters and different density areas (D) geometric verification, ball center vs. outline field center (E) dosimetric verification, vertical dose profile through measured (red) and planned (blue) dose distributions (F) dosimetric verification, various percentage isodose lines of measured (red) and planned (blue) dose distributions.

System – Type of test	Mean shift ± std. deviation	Min. shift	Max. shift	Number of Measurements
NTx – geometric	0.58 ± 0.14 mm	0.26 mm	0.73 mm	13 MV images
TBSTx – geometric	0.42 ± 0.18 mm	0.08 mm	0.71 mm	15 MV images
NTx - dosimetric	0.48 ± 0.27 mm	0.15 mm	0.76 mm	6 different planes/plans
TBSTx - dosimetric	0.40 ± 0.20 mm	0.21 mm	0.71 mm	12 different planes/plans

Tab. 1: Geometric and dosimetric results for both stereotactic radiosurgery systems NovalisTx and TrueBeamSTx

References

[1] Norm DIN 6875-1: Spezielle Bestrahlungseinrichtungen – Teil 1: Perkutane stereotaktische Bestrahlung, Kennmerkmale und besondere Prüfmethoden , Ausg. 2004-01, Berlin: Beuth Verlag

[2] Lutz W, Winston KR, Maleki N. A system for stereotactic radiosurgery with a linear accelerator. Int J Radiat Oncol Biol Phys. 1988; 14(2):373–81.

89 Is there an optimal prescription isodose for stereotactic radiotherapy?

W. W. Baus[1], H. Treuer[2]
[1]University Hospital of Cologne, Radiotherapy, Cologne, Germany
[2]University Hospital of Cologne, Stereotaxy, Cologne, Germany

Introduction: Using inverse treatment planning, the optimization algorithm takes care of the dose gradient between target volume (PTV) and organ(s) at risk (OAR). However, the question is not yet answered how much the maximal gradient is influenced by other parameters, e.g. the prescription technique or other technical parameters. This is also of general interest, though of paramount interest for stereotactic treatment of lesions located in the near vicinity of important OAR (comp. Fig. 1). In external beam radiotherapy the standard for dose prescription was (and is) set by ICRU 50 [1]. According to that, every treatment plan has a point (the reference point) to which 100 % of the dose (that is, the prescription dose) is designated to. Then ICRU recommends a range of dose heterogeneity within the PTV of -5 and plus +7 % of that prescription dose. Regarding the era of conformal radiotherapy using blocks or MLC to limit relatively large, flattened fields, and applied to PTVs which do not necessarily enclose macroscopic tumour (e.g. in the postoperative setting) this restriction seems reasonable. (However, in the case of intensity modulated treatment planning (IMRT) the application of these principles is somewhat relaxed). Stereotactic treatment, on the other hand, started historically from other assumptions. The aim was to create necrosis in small tumours within the cranium by using large single doses (sometimes called radiosurgery), therefore dose homogeneity (or, maximum dose within the target) was often not of primary concern. A dose prescription referring to 50 % or even less is common to Gamma Knife users, for example. In extracranial stereotactic body radiotherapy (SBRT) the case is somewhat mixed: sometimes single dose treatments are used for small lesions with a rationale similar to cranial radiosurgery, but most of the treatment is applied to relatively large tumours (large compared to small intracranial lesions) using hypofractionation. The prescription method is mixed accordingly: in the CyberKnife community, for example, the prescription varies between the 65 to 80 % isodose line encompassing the PTV (100 % being the dose maximum). The reasons for a specific choice, however, are not always obvious.

Therefore, we investigated the dose gradient in various planning situations. We started with straightforward situations such as single fields and a model used for calculation of fixed field arc treatment dose distributions [2]. These findings we compared with dose distributions of patient plans.

Materials and methods: We compared the gradient at beam edge of several types of single beams, namely open fields of different size of a Truebeam linac (Varian Medical Systems, Palo Alto, CA, USA), both flattened and flattening filter free, and of a CyberKnife (Accuray, Sunnyvale, CA, USA; fixed circular collimators). The profiles were measured in a water phantom with a diode as detector.

With the CyberKnife fields as an input we calculated dose profiles for isotropic convergent beam irradiation according to

$$Dose(R) = 2\pi * \int d\Theta \sin\Theta * OAF(R\sin\Theta) \quad (1)$$

with R = radial distance, □ = rotational angle, and OAF = Off Axis Function, to study the influence of collimator size to the gradient in the case of multiple fields (a rotational field, in this case). [2] The calculation was done with Mathematica v. 7 (Wolfram Research, Champaign, IL, USA). Additionally, we also calculated so-called isocentric plans with Multiplan (v. 4.6; Accuray, Sunnyvale, CA, USA) for the CyberKnife. The patient plans were calculated either with Multiplan (CyberKnife) or with Eclipse v. 10 (Truebeam). All relative dose values refer to 100 % at dose maximum.

Results: Some of the results are summarized in Fig. 2. Not surprisingly, a single field shows the steepest gradient, though unflattened beams perform somewhat worse. The CyberKnife beams, which are also without flattening filter, are somewhat better off: the gradient ranges from 22 to 17 %/mm for collimator diameter from 10 to 60 whereas the gradient peaks at 52 to 40 % of dose.

For the so-called isocentric plans (one isocenter, one collimator) the same holds: as larger the collimator used, as gentler the gradient, from 18 %/mm for the 10 mm collimator to 13 %/mm for the 30 mm collimator (Maximum again at 52 to 40 % of dose).

In the case of patient plans the observed gradients are generally much smaller, being in the range of 10 %/mm in the high gradient region of a CyberKnife plan (see fig. 1 and 2) and even lower for conventional IMRT plans (ca. 5 %/mm for the example of a prostate plan, see fig. 2). The maximum gradient as can be seen from fig. 2 is located at about 90 % for the prostate plan and at 65 % for the vertebral lesion treated at the CyberKnife. (Since the plan was originally planned with 80 % prescription isodose one would in retrospect assume the 65 % as a better choice.)

Conclusions: Recent treatment techniques make a dose prescription to a certain point questionable. The isodose distribution achieved with inverse planning optimization algorithms is in general quite inhomogenous and volume statistics

seem more adequate to describe dose distributions for these cases. This leads to the concept of prescribing to the isodose line which encompasses the PTV (comp. fig. 1). For stereotactical treatment using small collimators (or fields) a low isodose around 65 % leads to a steep dose gradient, whereas for larger collimators a higher isodose can be more appropriate, especially for conventional IMRT-fields.

References

[1] ICRU Report No. 50, Prescribing, Recording and Reporting Photon Beam Therapy, 1993
[2] U. Treuer, H. Treuer, M. Hoevels et al., Phys. Med. Biol. 43 (1998) 49-64

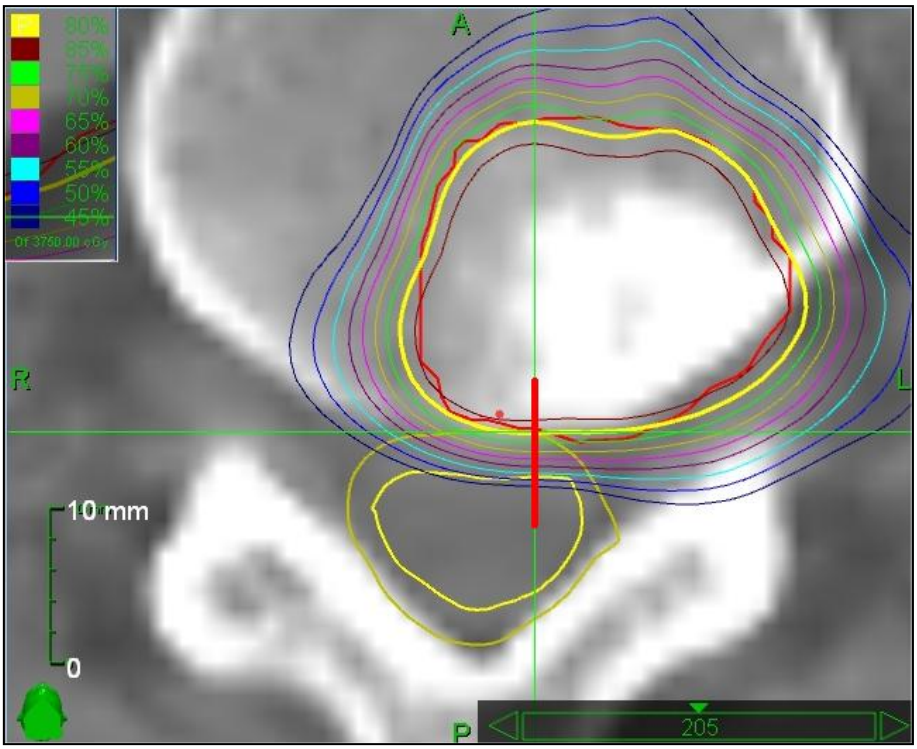

Fig. 1: CyberKnife treatment: vertebral metastasis with steep dose gradient, Collimators used: 10 and 15 mm. Isodoseline steps are 5 % (starting with 45 % up to 85 %; yellow: 80 % prescription isodose). Red bar: position of the dose gradient (comp. Fig. 2).

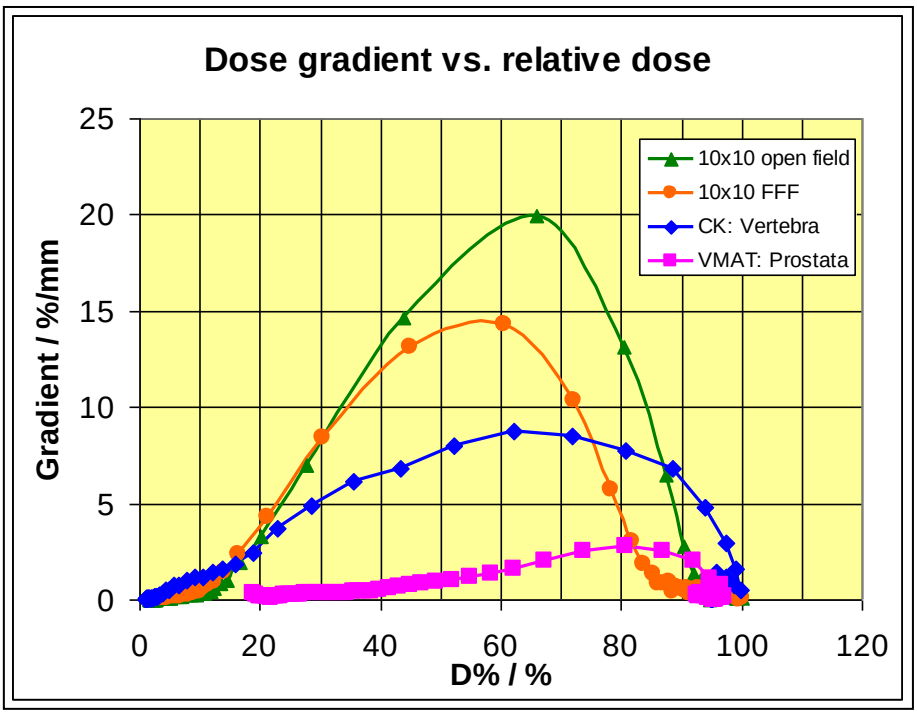

Fig. 2: Various gradients: CyberKnife treatment plan (blue; comp. Fig. 1), conventional linac VMAT plan (pink), 10x10 cm² measured reference field (6 MV) profile (green), and measured 10x10 cm² FFF-field (6 MV). The symbols represent data points, the lines are merely guides to the eye.

90 Treatment Planning for Cardiac Radiosurgery: Initial Human Simulations

O. Blanck[1,2], S. Ipsen[3,4], B. Oborn[4], R. Bruder[3], R. Werner[5], F. Bode[1], P. Hunold[1], G. Liney[6], D. Rades[1], J. Dunst[1], A. Schweikard[3], P. Keall[4]
[1]University Clinic Schleswig-Holstein, Lübeck, Germany
[2]CyberKnife Center Northern Germany, Güstrow, Germany
[3]University of Lübeck, Lübeck, Germany
[4]University of Sydney, Sydney, Australia
[5]University Medical Center Hamburg-Eppendorf, Hamburg, Germany
[6]Ingham Institute for Applied Medical Research, Sydney, Australia

Introduction: Atrial fibrillation (AF) is the most common cardiac arrhythmia in humans and is usually treated with minimally-invasive catheter ablation techniques. Radiosurgery has recently been proposed for alternative non-invasive AF treatment and dose escalation studies in animals demonstrated the need for 30Gy single fraction doses. We now analyzed human treatment planning for two radiosurgery systems including their not yet clinically implemented non-ionizing non-invasive real-time tracking capability for cardiac radiosurgery.

Materials and methods: Initially we investigated published literature and current AF ablation resp. radiosurgery practice on lesion definition and target motion and dosimetric critical structure limitations for hypothetical cardiac radiosurgery. We then obtained 3 human CT datasets of AF patients scheduled for catheter ablation and investigated treatment planning for robotic radiosurgery with transthoracic ultrasound (US) tracking and for linac-based radiosurgery with magnetic resonance imaging (MRI) tracking. For US tracking we simulated the influence on fewer beam entry possibilities of the robotic radiosurgery system due to the US-probe position on the patient's chest. For MRI tracking we simulated the influence of a 1T magnetic field during beam delivery using the Geant4 Monte Carlo algorithm.

Results: Our experience suggests that the optimal radiosurgery lesion for paroxysmal AF is located circumferentially at the pulmonary vein (PV) antrum where a human generally has four PVs; two on each side of the left atrium. The observed target motion ranged between 5-20mm (respiratory) and 1-5mm (cardiac). The PVs appear to move differently with respect to each other. Differential motion of more than 10mm was observed in some cases. The limiting factor for cardiac radiosurgery is the esophagus which is closer than 3mm to the target area in more than 50% of the patient population and which has an estimated maximum dose limit of 19-22Gy (versus 30Gy prescription dose). Initial planning studies demonstrated that safety margins smaller than 3mm are needed to maintain the critical structure dose limits in the optimal patient population (with the esophagus located centrally at the left atrium). Thus real-time target tracking is necessary (regardless of the delivery system). The plan quality influence of US-probe position (beam entry blocking) is small *(Fig.1)* and the magnetic field has also little impact on the dose distribution during linac-based radiosurgery *(Fig.2)*.

Conclusion: Our results suggest that cardiac radiosurgery for AF is technically feasible. However, the patient population for this treatment is small. Accuracy estimation and clinical implementation of US- and MRI tracking are under investigation.

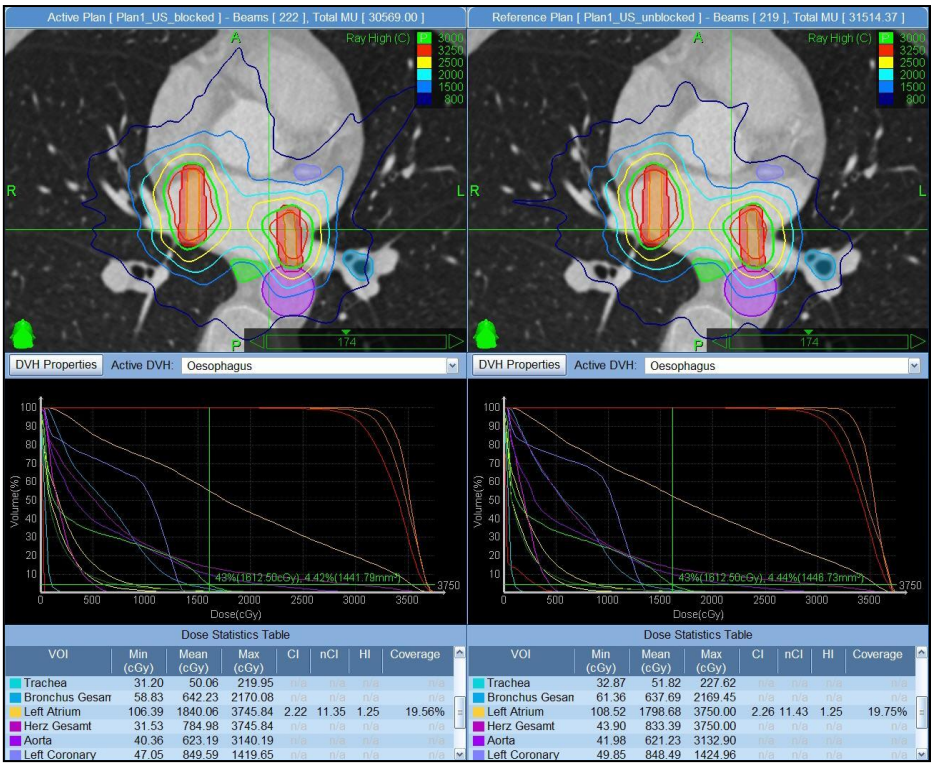

Fig. 1: Robotic radiosurgery treatment plan with and without ultrasound tracking

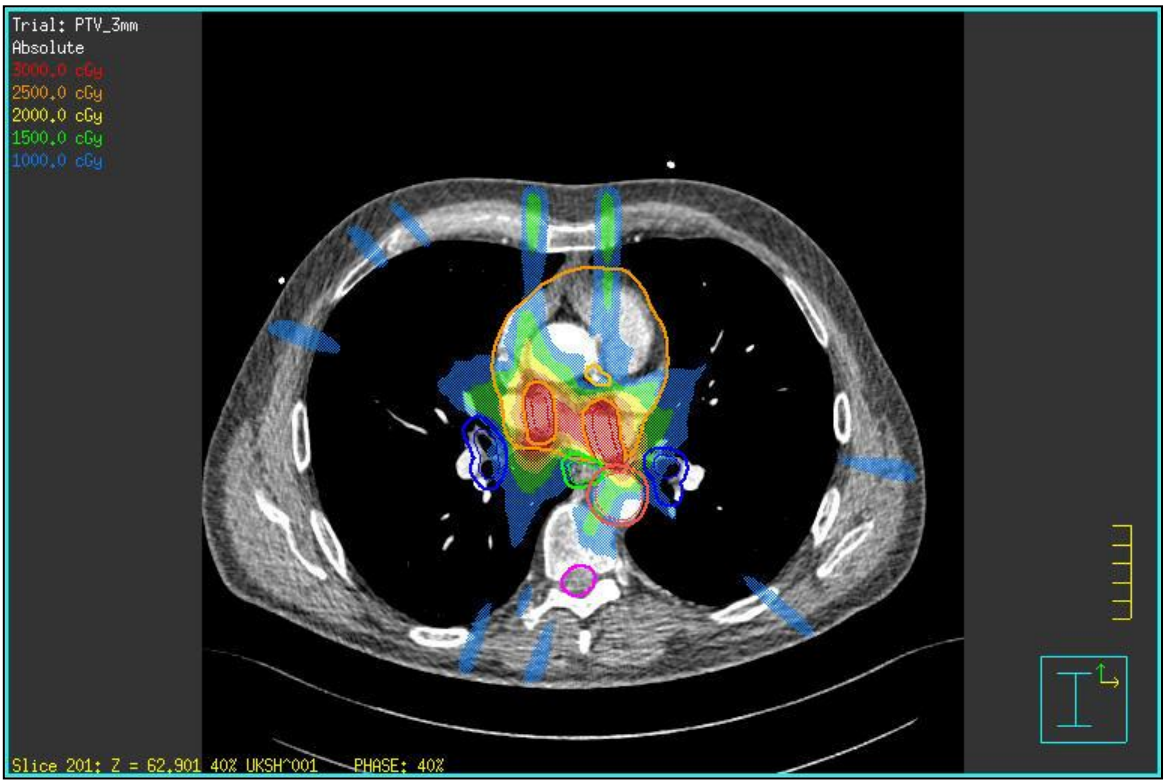

Fig. 2: Linac-based treatment plan with 10 IMRT fields

91 International Multi-Institutional Treatment Planning Bench Mark Trial for Robotic Radiosurgery

O. Blanck[1,2], L. Wang[3], T. Lacornerie[4], W. Baus[5], J. Nilsson [2], S. Luchkovskyi[6], I. Palazon[7], Z. Shou[8], M. Ayadi[9], H. Treuer[5], R. Virad[10], M. Chan[11], A. Movahed[12], F.-A. Siebert[1], B. Poppe[13], J. Dunst[1], G. Hildebrandt[14], P. Romanelli[15], R. Semrau[5], E. Lartigau[4], S. Soltys[3], A. Schweikard[16]
[1]University Clinic Schleswig-Holstein, Kiel/Luebeck, Germany
[2]CyberKnife Center Northern Germany, Guestrow, Sweden
[3]Stanford University School of Medicine, Stanford, United States
[4]CLCC Oscar Lambret, Lille, France
[5]University Clinic Cologne, Cologne, Germany
[6]CyberClinic Cancer Center Spizhenko, Kiev, Ukraine
[7]Hospital Ruber Internacional, Madrid, Spain
[8]CyberKnife Center Tampa Bay, Tampa Bay, United States
[9]Centre Léon Bérard, Lyon, France
[10]AQUILAB, Lille, France
[11]University of Hong Kong, Hong Kong, Hong Kong
[12]Pomona Valley Hospital Medical Center, Los Angeles, United States
[13]Pius Hospital Carl v. Ossietzky University, Oldenburg, Germany
[14]University Clinic Rostock, Rostock, Germany
[15]Centro Diagnostico Italiano, Milano, Italy
[16]University of Luebeck, Luebeck, Germany

Introduction: Hallmarks of Stereotactic Radiosurgery (SRS) include the accurate, conformal delivery of high dose radiation to tumors while minimizing normal structure doses via steep dose gradients. Inverse treatment planning (ITP) with computerized optimization algorithms is now routine practice, yet many aspects of the ITP remain user-dependent. We performed an international, multi-institutional ITP bench mark trial to study variability in ITP and to seek consensus on preferable ITP practice for robotic radiosurgery with the CyberKnife (Accuray Inc., Sunnyvale, CA).

Materials and methods: For this study, a single, complex-shaped, previously irradiated spinal tumor was chosen *(Fig.1)* with a conservative SRS dose of 21Gy in 3 fractions and primary ITP constraints for spinal cord (D14 < 1cc, D18 < 0.1cc) and planning target volume (PTV coverage > 95 %). ITP was performed by 10 CyberKnife centers on a single dedicated and remotely accessible ITP system (MultiPlan Version 4.5, Accuray Inc.). The resulting treatment plans were analyzed with ARTIVIEW (Version 2.8, AQUILAB, Lille, France) and ranked on a scale from 1 (excellent) to 4 (poor) in 5 different categories (constraint compliance, optimization goals, low dose regions, treatment planning complexity, and clinical acceptability) by a blinded, independent review panel. Finally we compared the reviewer ranking against a mathematical ranking based on computed plan indexes.

Results: The resulting treatment plans varied substantially in coverage (91.4-96.3 %), conformity (1.3-2.1 CI), monitor units (29500-74280 MU), homogeneity (1.19-1.44 HI) and critical structures doses (e.g. spine max dose 17.1-20.8 Gy) among the participating CyberKnife centers. The reviewers' ranking assessment also varied substantially with 8/10 treatment plans rated excellent (rank = 1) in at least one category by at least one reviewer. The mean overall rank for each treatment plan ranged from 1.2 to 4.0 (avg. 2.6) with standard deviations of 0-1.05 (avg. 0.72). The overall rankings revealed that a plan with a balanced trade-off among all planning objectives (which was generated using a simple ITP method) was preferred by most participants and reviewers. The reviewer ranking agreed well with the mathematical index ranking in 7/10 plans *(Fig.2)*.

Conclusion: This multi-institutional study illustrates the different ITP approaches and treatment preferences for spinal robotic radiosurgery. The results demonstrate that ITP systems need to be capable of exploring trade-offs among planning objectives to avoid unbalanced results. The participants' and reviewers' agreement on the preferable treatment plan and ITP techniques indicate that bench marking and consensus guidelines could improve the consistency of treatment planning.

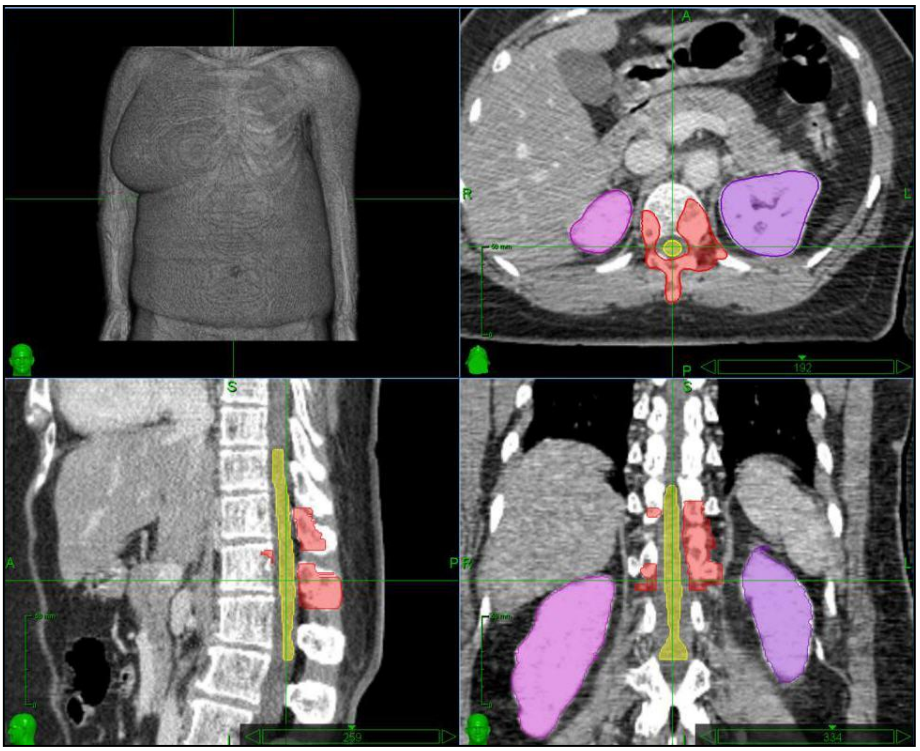

Fig. 1: Treatment Planning Bench Mark Case

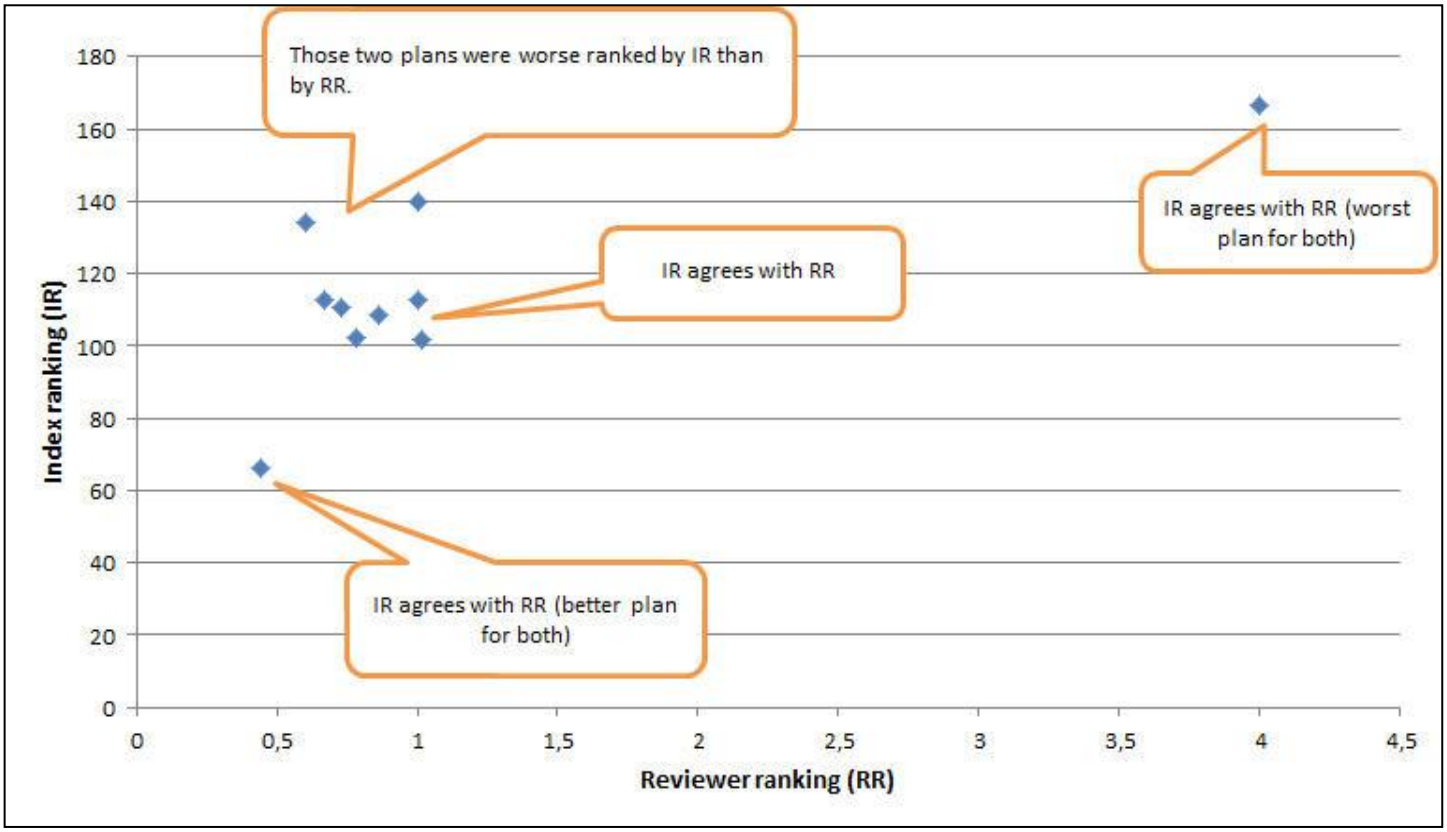

Fig. 2: Reviewer Ranking versus Mathematical Index Ranking

Acknowledgments: The authors would like to thank Etienne Lessard (Accuray Inc, Sunnyvale, CA) for maintaining the MultiPlan planning system and the remote access to that system.

Session 16 – Dosimetry in radiation therapy II: Detectors I

Chairs: D. Frauchiger (Bern/CH), K. Zink (Giessen, Marburg/DE)

92 Introductury lecture: Recent developments in dosimetry

K. Zink[1]
[1]Institut für Medzinische Physik und Strahlenschutz, Technische Hochschule Mittelhessen, Giessen, Germany

93 Primary Metrology for Proton Therapy Dosimetry using Water Calorimetry

J. Mulder[1], O. Kavatsyuk[1], A. Van 't Veld[1], M. Schippers[2], J. de Pooter[3], D. Twerenbold[4], S. Brandenburg[5]
[1]University Medical Center Groningen, Radiation Oncology, Groningen, Netherlands
[2]Paul Scherrer Institut, Villigen, Switzerland
[3]Dutch Metrology Institute VSL, Delft, Netherlands
[4]Federal Institute of Metrology METAS, Bern, Switzerland
[5]KVI – Center for Advanced Radiation Technology, Groningen, Netherlands

Related questions: Proton Therapy offers very high conformity of the dose distribution with the tumour volume, because of the finite penetration depth. The primary benefit of Proton Therapy is an expected decrease in complications due to reduced irradiation of healthy tissue. However, high-accuracy dose delivery is essential to realize the potential advantage of protons over X-rays. We are developing an absolute primary measurement standard for dosimetry of scanned proton beams. This standard should reach the same level of uncertainty (less than 1 %) as the current primary standard for photons, which is based on ^{60}Co, and should allow a direct comparison with the primary standard for X-rays.

Material and procedure: Experiments were performed at the AGOR superconducting cyclotron at KVI-CART that can deliver various beams: protons (energy ≤ 190 MeV) and light ions until carbon (energy ≤ 90 MeV/A) in air and vacuum. In the case of protons, irradiation fields of up to 70 mm can be produced. With 150 MeV protons a homogeneity of ± 2 % (70 mm diameter field) is routinely achieved. Proton pencil beams with a FWHM of 7 mm at 150 MeV have been obtained. The facility is routinely used for proton therapy related experiments, radiobiology, dosimetry and radiation damage studies.

The dose to water is directly measured by calorimetry (temperature increase) in a water phantom at 4°C. The magnitude of the temperature signal is about 0.24 mK/Gy. Because of the small signals thermal shielding is necessary. The temperature sensors are encapsulated into glass probes which are placed in a glass cell (App. A) containing ultra-pure water. Major systematic effects occur due to radiation induced chemical reactions in the water and heat transfer occurring on the high gradients of the dose distribution. The systematic effects due to heat transfer within the calorimeter have been studied using 4D finite elements simulations. LET-dependent reaction rates have been used to calculate the contribution of all relevant radiation induced chemical reactions. Water mixtures with some amount of dissolved Hydrogen and Oxygen gas have been used to experimentally validate the radiation chemistry calculations.

Result: Correction factors for heat transfer in the water have been obtained for different irradiation conditions. The contribution of the chemical reactions to the temperature increase (heat defect) has been calculated for various initial conditions and irradiation regimes. Comparison of experiments (App. B) with radiation chemistry modeling indicate that the model correctly predicts the sequence of reactions that takes place. On the basis of this agreement we conclude that the model prediction that dissolving a significant amount of hydrogen stabilizes the chemistry is credible.

Summary: Water calorimetry is an established method for absolute X-ray dosimetry. However, its application for proton beams relies upon the possibility to quantitatively calculate and verify the corrections needed to compensate the effects of heat transfer and radiation chemistry. These correction factors are very sensitive to the dose gradients, the scanning and irradiation sequence, dose rate and LET. Special water preparation techniques and pre-irradiation sequences are required to achieve the overall steady state needed to perform reliable measurements.

Fig. 1: Glass cell with ultra-pure water thermistors.

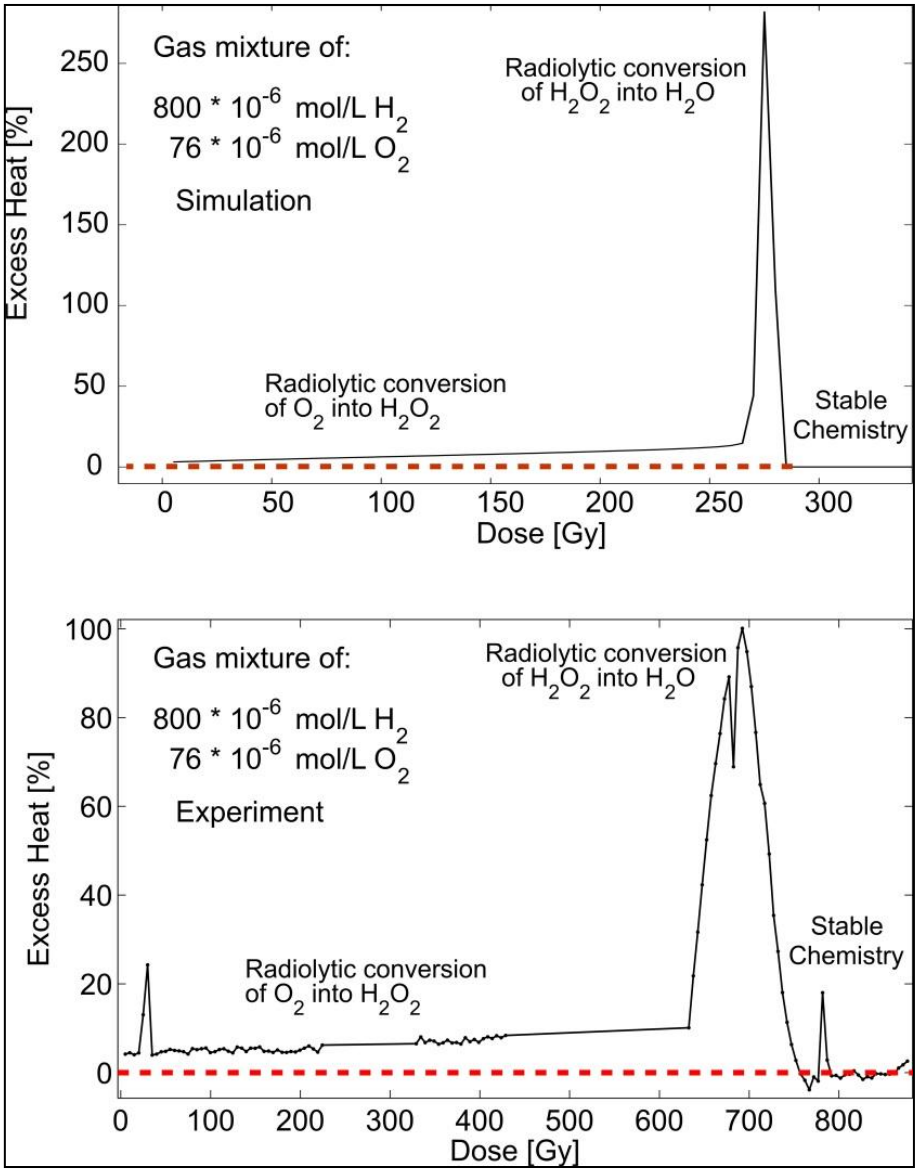

Fig. 2: Comparison of radiation chemistry modeling and experiment showing the effect of added Oxygen with a surplus Hydrogen.

94 Measuring depth profiles with multi-layer ionization chambers in proton therapy

C. Bäumer[1], B. Koska[1], J. Lambert[1]
[1]UK Essen, WPE, Essen, Germany

Aim: Quality assurance and commissioning in proton therapy centers require accurate and efficient acquisition of dose profiles. This can be solved in beam direction by multi-layer ionization chambers (MLIC). We present our measurement and simulation results for two MLIC devices: the small-electrode MLIC measures percent depth dose under broad field conditions mimicking a point-by-point measurement with an advanced Markus chamber in water. A prototype MLIC with large electrode acquires integral depth profiles similar to a Bragg Peak Chamber in a scanning water phantom. The current work evaluates the similarity of MLIC acquisitions to the respective profiles in water.

Materials and methods: Pristine depth profiles have been acquired with both MLIC devices. Profiles obtained with the small-electrode MLIC have been compared with point-by-point acquisitions with an advanced Markus chamber in a water phantom. The acquisitions with the large-electrode MLIC have been compared with the results of large plane-parallel chambers in water with 4.1 cm radius and 6.0 cm radius, respectively. For interpretation of the results we modelled these experiments with the FLUKA Monte-Carlo code. Spread-out Bragg Peaks have been measured with the small-electrode MLIC and are overlayed with the respective measurements in water.

Results: The energy dependence of proton interactions in the MLIC material components lead to small distortions of the dose reading which can be corrected for by uniformity calibration at start of a measurement series. A linear function can be used to transform between MLIC channels and

depth in water. These calibrations are sufficient for clinical quality assurance. The user of the investigated commercial MLIC devices has to take care of small distortions in the dose domain if the acquired depth profiles are used as input data for a treatment planning system. The large-electrode MLIC offers the possibilities of a fast quality assurance and a simple probe for water equivalent thickness. Acquisitions with this device are equivalent to scans with a large integrating chamber with 6.0 cm radius in water, which in turn lacks about 2% geometrical efficiency with respect to a 10.0 cm radius chamber.

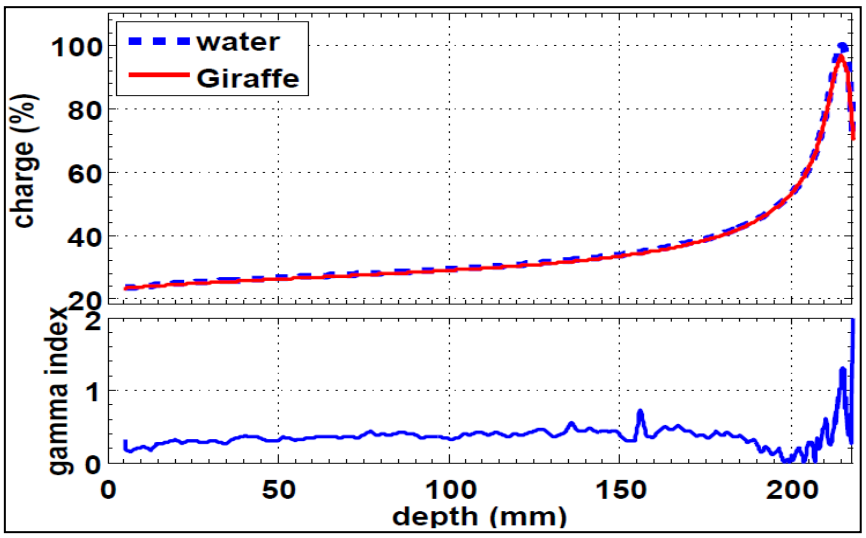

Fig. 1:Percent depth dose acquired with large-electrode MLIC (brand name "Giraffe") as compared to water (1 mm/1% □-index)

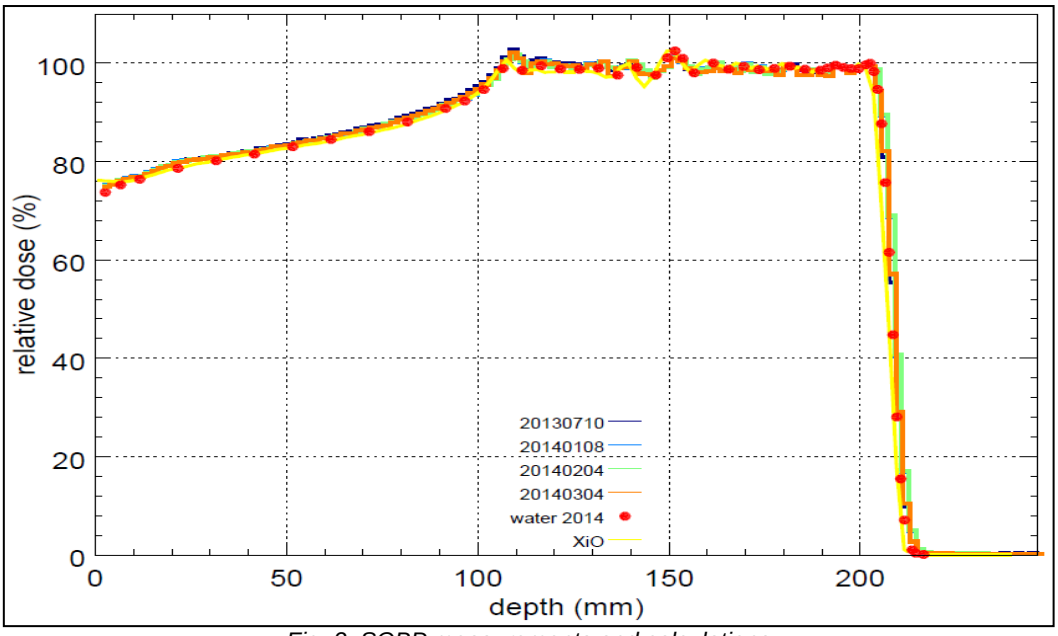

Fig. 2: SOBP measurements and calculations

References

[1] Dhanesar S, Sahoo N, Kerr M, Taylor M B, Summers P, Zhu X R, Poenisch F & Gillin M, Medical Physics 40 (2013) 092102
Mustermann, M.: Musterbuch, Z. f. Metallkunde, 38 (1999) 5, S. 538-547

[2] Grevillot L, Bertrand D, Dessy F, Freud N & Sarrut D, Physics in Medicine and Biology 56 (2011) 5203

[3] Pedroni E, Scheib S, Bhringer T, Coray A, Grossmann M, Lin S & Lomax A, Physics in Medicine and Biology 50 (2005) 541

[4] Sawakuchi G O, Mirkovic D, Perles L A, Sahoo N, Zhu X R, Ciangaru G, Suzuki K, Gillin M T, Mohan R & Titt U, Medical physics 37 (2010) 4960

95 Fluence verification for patient specific quality assurance in ion beam therapy. Use of an amorphous silicon flat panel detector

J. Horn[1], B. Ackermann[1], M. Ellerbrock[1], S. Brons[1], S. Lahrmann[1], C. Lampe[1], O. Jäkel[1,2,3]
[1]Heidelberger Ionenstrahl-Therapie Zentrum, Heidelberg, Germany
[2]Universitätsklinikum Heidelberg, Abteilung Radioonkologie und Strahlentherapie, Heidelberg, Germany
[3]Deutsches Krebsforschungszentrum, Abteilung Medizinische Physik in der Strahlentherapie, Heidelberg, Germany

Introduction: Regarding the complexity of dose distributions produced by active rasterscanning each dose distribution has to be verified prior to patient treatment. At the Heidelberger Ionenstrahl Therapie-Zentrum (HIT) patient specific dose verification is currently performed using ionization chambers [1]. Due to the limited spatial resolution (~ 14 mm) of this system, the present study investigates a high resolution (~ 0.2 mm) flat panel detector to supplement these dose measurements.

Materials and methods: A method is presented to convert the detector signal into fluence maps after suitable calibration. Martišíková et al. have already presented a usability study of fluence verification using a flat panel detector (RID 256L, Perkin Elmer, Germany) [2]. In contrast to this study, in the present investigation the fluence measurements were realized using patient relevant accelerator settings. Additionally, the newest state of the art flat panel detector (XRD 0822 without scintillator, Perkin Elmer, Germany) was investigated with respect to signal quality and mandatory image corrections. After each measurement, the generated fluence maps are checked against expected fluence maps calculated from the respective beam parameters.

Results: A specific protocol to process flat panel raw data was established. It contains necessary offset, gain and bad pixel corrections. Furthermore, to quantify the agreement between the measured and calculated fluence maps a gamma-index criterion (5 % dose deviation and 1 mm distance to agreement) was used: Averaged over all energies for each field, the gamma-index criterion was met in more than 97 % of the pixel values for protons and more than 91 % for carbon ions in all investigated patient plans.

Conclusion: Based on two-dimensional high resolution fluence measurements in the dose plateau area of the depth dose distribution it is now possible to provide enhanced and supplementary information to conventional dose measurements prior to patient treatment. The corrected and calibrated detector signal shows promising results compared to the calculated data. However, before using this protocol in clinical routine, further studies, especially towards irradiation damage of the detector, have to be performed. So far, within this work no further bad pixels have been detected.

References

[1] Karger, C. et al.: A system of three-dimensional dosimetric verification of treatment plans in intensity-modulated radiotherapy with heavy ions, Med. Phys., 26 (1999), S. 2125-32
[2] Martišíková, M. et al.: High-resolution fluence verification for treatment plan specific QA in ion beam radiotherapy, Phys. Med. Biol., 58 (1013), S. 1725-1738

96 Perturbation corrections for parallel plate chamber in clinical electron beams – a reiteration of a historical experiment

P. von Voigts-Rhetz[1], D. Czarnecki[1], K. Zink[1,2]
[1]Institute for Medical Physics and Radiation Protection – IMPS, University of Applied Sciences, Giessen, Germany
[2]University Medical Center Marburg, Department of Radiotherapy and Radiation Oncology, Marburg, Germany

Introduction: International dosimetry protocols [1,2] request well-guarded parallel plate ion chambers for electron dosimetry. For the Markus chamber, which has a vanishingly small guard-ring a perturbation factor p_{cav} based on experimental investigations by Van der Plaetsen et al [3] is reported. Aim of this study is a reinvestigation of the perturbation factor p_{cav} of the Markus parallel plate chamber applying Monte Carlo simulations.

Materials and methods: Based on the experimental setup used by Van der Plaetsen et al. [3] Monte Carlo simulations with the EGSnrc code system [4] were performed to determine the perturbation correction p_{cav} for the Markus chamber. For that purpose, four models of parallel plate chambers (Roos, Markus, NACP, Adv. Markus) were modelled in detail according to the information given by the manufacturer (PTW, Freiburg, Germany), and the dose ratio D_{det}/D_{Markus} was calculated for all chambers and for 13 different electron spectra (E_0 = 6 – 21 MeV), respectively. For all simulations the chambers were positioned with their reference point at the depths z_{max} and z_{ref} in a water phantom with a volume of 30x30x30 cm³. The beam size at the phantom surface was 10x10 cm^2, and the source surface distance (SSD) was 100 cm. For all simulations the threshold/cut-off energies of electrons and photons in the EGSnrc user_code egs_chamber [5] were set to *AE=ECUT*=521keV and *AP=PCUT*=10keV, all other transport parameters were set to their defaults. To avoid the calculation of the stopping power ratios, all chambers were filled with “low density water” [6], i.e. water with the density of air and a density correction of normal water.

Results: The calculated dose ratio D_{det}/D_{Markus} (D_{det}: D_{Roos}, D_{NACP}, $D_{Adv.Markus}$) as a function of the mean electron energy $E_{mean}(z)$ at depth z is quite similar for all three chambers and shows the same trend as published by Van der Plaetsen. But, in comparison to Van der Plaetsen’s experimental values our Monte Carlo data reveal smaller deviations from unity (see fig. 1 and 2). This is true for both depths investigated here (z_{max} and z_{ref}). According to all dosimetry protocols the ratio for the NACP chamber D_{NACP}/D_{Markus} is interpreted as the fluence perturbation correction p_{cav} for the Markus chamber. Values below unity are commonly interpreted as the dose contribution due to the “in-scattering effect” present in the guard-less Markus chamber.

The total perturbation correction p for all chambers, calculated as the dose ratio D_w/D_{det} is also given in figures 1 and 2. The simulations show that compared to all well-guarded chambers (Roos, NACP, Advanced Markus) the guard-less Markus chamber reveal the smallest total perturbation correction p at both investigated depths and moreover, p is almost energy independent.

Conclusion: Our Monte Carlo simulations in principle reproduce the experimental data published by van der Plaetsen. These data are presently interpreted as the fluence perturbation correction p_{cav} of the Markus chamber, which has to be accounted for in electron reference dosimetry. According to the mentioned dosimetry protocols, p_{cav} is the only perturbation correction which has to be considered for the Markus chamber, for the well guarded chambers (Roos, NACP, Advanced Markus) the relevant perturbation corrections p_{cav}, p_{wall} are both assumed to be unity. Considering the calculated doses ratios D_w/D_{Markus}, i.e the total perturbation correction p, the presented Monte Carlo results are obviously in contradiction to the recommendations given in all dosimetry protocols.

The simulations show that, in contrast to the assumptions, the impact of the flucene perturbation factor p_{cav} is lower for the guard ring less Markus chamber than a well-guarded parallel plate chambers.

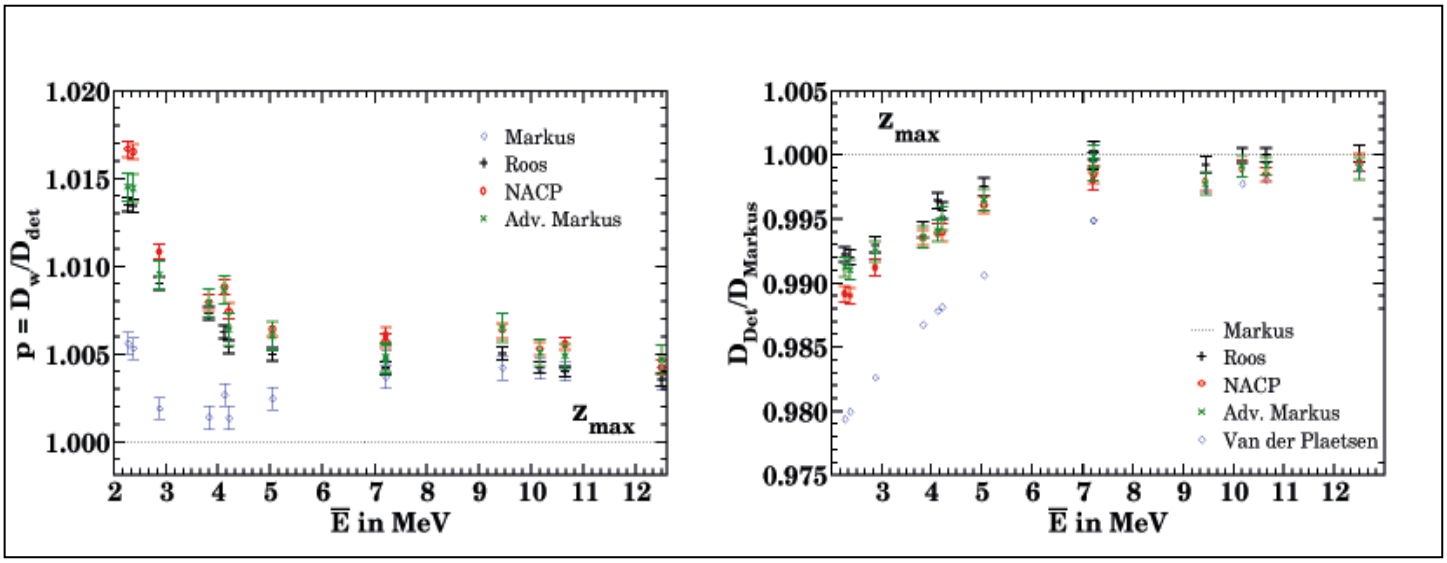

Fig. 1: Total perturbation correction $p=D_w/D_{det}$ (left) and dose ratio D_{det}/D_{Markus} (right) as a function of the mean electron energy at water depth z for four different parallel plate chambers. For all electron energies the chambers were positioned with their reference point at the depth of the dose maximum z_{max}.

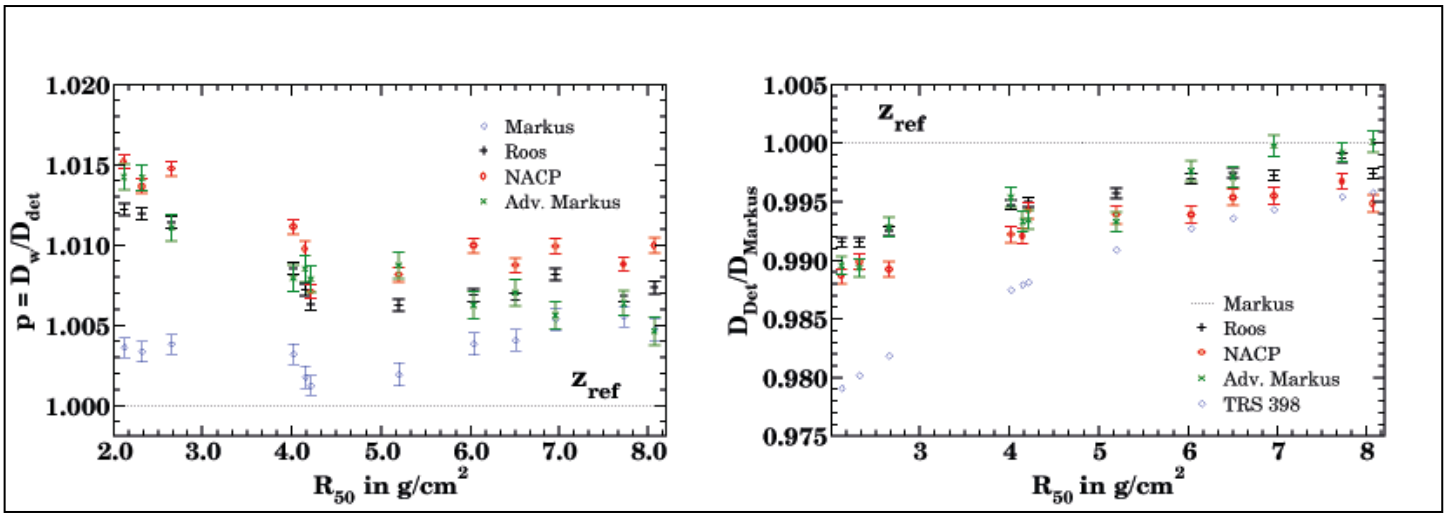

Fig. 2: Total perturbation correction $p=D_w/D_{det}$ (left) and dose ratio D_{det}/D_{Markus} (right) as a function of the beam quality specifier R_{50} for four different parallel plate chambers. For all electron energies the chambers were positioned with their reference point at the reference depth z_{ref} in water.

References

[1] Almond PR, Biggs PJ, Coursey BM, Hanson WF, Huq MS, Nath R, Rogers DW. AAPM's TG-51 protocol for clinical reference dosimetry of high-energy photon and electron beams. Med Phys 1999;26(9):1847–70.

[2] Andreo P, Burns DT, Hohlfeld K, Huq MS, Kanai T, Laitano F, SmythV, Vynckier S. Absorbed dose determination in external beam radiotherapy. An international code of practice for dosimetry based on standards of absorbed dose to water, Technical Reports

[3] Van der Plaetsen A, Seuntjens J, Thierens H, Vynckier S. Verification of absorbed doses determined with thimble and parallel-plate ionization chambers in clinical electron beams using ferrous sulphate dosimetry. Med Phys. 1994;21(1):37-44.

[4] Kawrakow I, Mainegra-Hing E, Rogers DWO, Tessier F, Walters BRB. The EGSnrc Code System: Monte Carlo Simulation of Electron and Photon Transport, NRCC Report PIRS-701, National Research Council of Canada 2011.

[5] Wulff J, Zink K, Kawrakow I. Efficiency improvements for ion chamber calculations in high energy photon beams. Med Phys 2008;35(4):1328–36.

[6] Wang LLW, Rogers DWO. Calculation of the replacement correction factors for ion chambers in megavoltage beams by Monte Carlo simulation. Med. Phys 2008:35, 1747–1755.

97 Monte-Carlo-based calculation of perturbation factors for parallel-plate ionization chambers in high-energy photon beams

N. Jach[1], D. Czarnecki[1], K. Zink[1,2]
[1]University of Applied Sciences Mittelhessen, Institute of Medical Physics and Radiation Protection, Gießen, Germany
[2]University Medical Center Marburg, Department of Radiotherapy and Radiation Oncology, Marburg, Germany

Purpose: In current dosimetry protocols ([1], [2]) parallel-plate ionization chambers are mainly recommended for dose measurements in electron beams. However, due to their construction, parallel-plate chambers may also be advantageous for precise measurements of depth dose curves in high energy photon beams**.** Currently the information about perturbation corrections of parallel-plate chambers in high energy photon beams given in literature is sparsely. Therefore, the aim of the present study is the Monte Carlo based determination of relevant perturbation factors for parallel-plate chambers which are used in clinical photon dosimetry.

Methods: The perturbation factors p_{wall}, p_{cav} and the total perturbation correction p of four parallel-plate chamber types (Roos, Markus, Advanced Markus, NACP-02) were calculated by using the EGSnrc Monte Carlo code system [3]. The chambers have been modelled in detail according to the information given by the manufacturer. To avoid the calculation of the necessary stopping power ratios for the materials water and air, the cavities of all chambers were filled with „low density water“ [4]. All calculations were performed with the EGSnrc user code *egs_chamber* [5]. The perturbation corrections were calculated according to the following equations:

$$p = \frac{D_w}{D_{chamber}} \quad (1)$$

$$p_{wall} = \frac{D_{cav}}{D_{chamber}} \quad (2)$$

$$p_{cav} = \frac{D_w}{D_{cav}} \quad (3)$$

Herein D_w describes the dose to water determined in a small water voxel with dimensions r = 0.2 cm, h = 0.02 cm positioned at a depth of 10 cm within a water phantom, $D_{chamber}$ is the dose calculated in the active volume of the chamber and D_{cav} is the dose inside the cavity of the wall-less chamber. According to the recommendations of all present dosimetry protocols regarding reference dosimetry, the chamber's reference point (centre of the gas filled cavity's entrance window) was positioned at a depth of 10 cm in a water phantom (30x30x30 cm^3). The field size at the phantom surface was 10x10 cm^2 and the source-to-surface distance (SSD) was 100 cm. Different high energy photon spectra from clinical linear accelerators available in literature [6] were applied. The calculations have been performed with the *egs_chamber* code including photon cross section enhancement (XCSE) and intermediate phase-space storage (IPSS) [5]. The beam quality specifier $TPR_{20/10}$ was calculated using a water voxel (r = 0.05 cm, h = 0.05 cm) positioned at a depth of 10 cm and 20 cm in the water phantom, with a SSD of 90 cm and 80 cm respectively.

Results: Figure 1 shows the calculated perturbation factors p, p_{wall} and p_{cav} for the different chambers as a function of the beam quality specifier $TPR_{20/10}$. As can be seen, the total perturbation correction p for the Roos, Markus and Advanced Markus chamber is almost independent on beam quality and its value p=1.02 is within the statistical uncertainty of our calculations identical for these chambers. In contrast, the perturbation correction p for the NACP chamber reveals a small decrease with increasing $TPR_{20/10}$. For small photon energies (small values of $TPR_{20/10}$) the perturbation factor p for the NACP chamber is about 1 % larger in comparison to the other parallel plate chambers. This is obviously due to the larger wall perturbation correction of this chamber (see fig. 2). This behavior may eventually be explained by the larger backscatter deficiency due to the massive graphite back-wall present in the NACP chamber. This will be investigated in further simulations.

In 2006 Buckley and Rogers [7] already published Monte Carlo based data for the wall perturbation correction concerning the Roos, Markus and NACP chamber (see fig. 2). Except for the NACP chamber both data sets are in good agreement. For the NACP chamber there are deviations up to 0.4 % especially for small photon energies. This may be explained by small differences in chamber geometry used for the Monte Carlo simulations [8, 9].

Conclusion: To our knowledge, this is the first study presenting the perturbation corrections of plane parallel chambers in high energy photon beams. The results show, that for the widely used Roos, Markus and Advanced Markus chamber the total perturbation corrections are in good approximation independent on the beam quality specifier $TPR_{20,10}$, and the numerical values for these chambers are identical (p= 1.02) within the statistical uncertainty of our simulations.

The corresponding data for the NACP chamber reveal a small dependency on the photon energy and the total perturbation correction is about 0.5 – 1 % larger in comparison to the other chambers investigated in this study. This may be due to the chamber's massive rear wall made of graphite, which results in a larger backscatter deficiency in comparison to the other chambers.

To provide the beam quality correction k_Q, necessary to perform reference dosimetry in high energy photon fields also with parallel plate chambers, in a further step, corresponding data in a ^{60}Co field will be calculated.

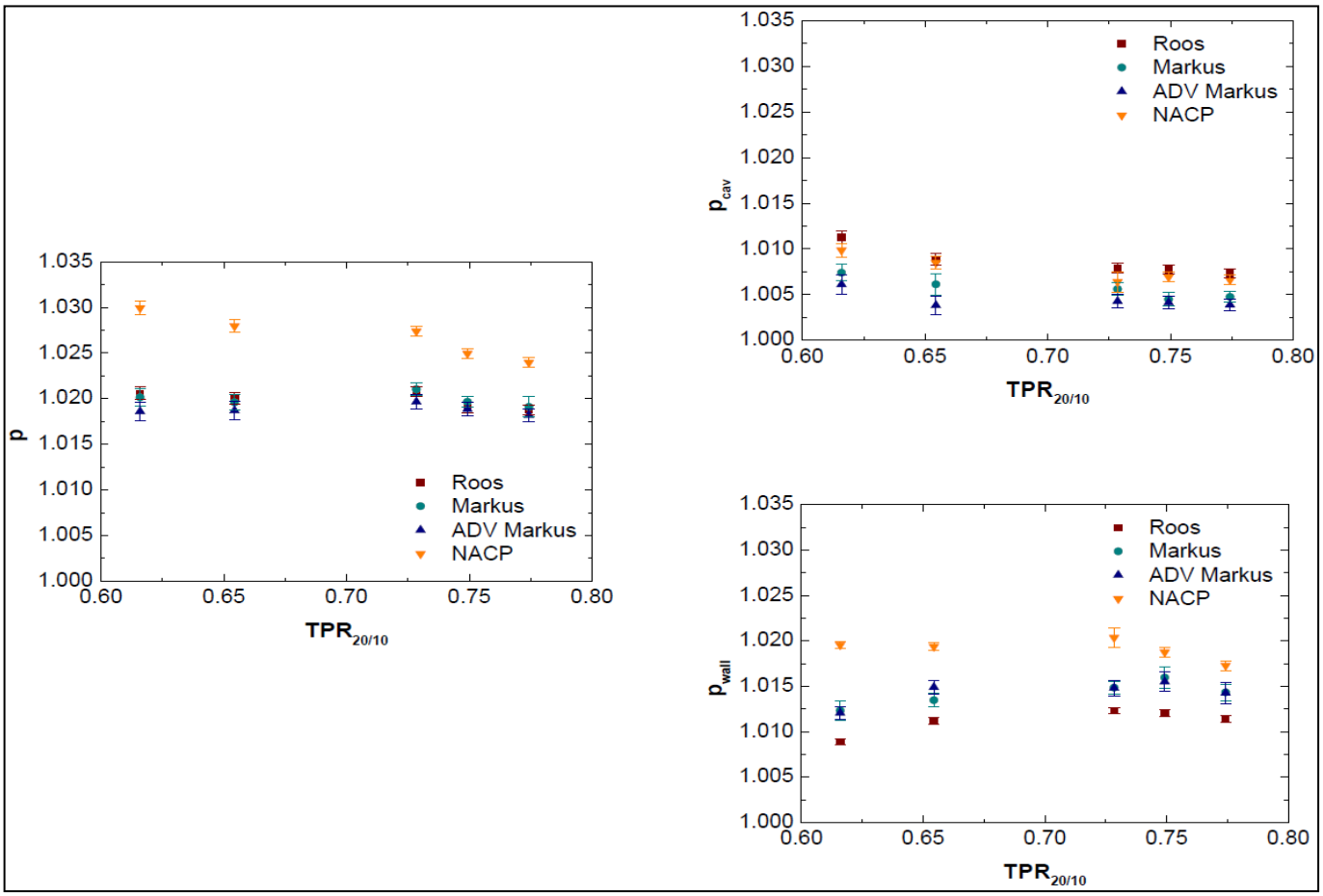

Fig. 1: Perturbation corrections p, p_{wall} and p_{cav} for the Roos , Markus , Advanced Markus and the NACP chamber as a function of the beam quality specifier $TPR_{20/10}$. The error bars represent the statistical uncertainty of the Monte Carlo results (1□).

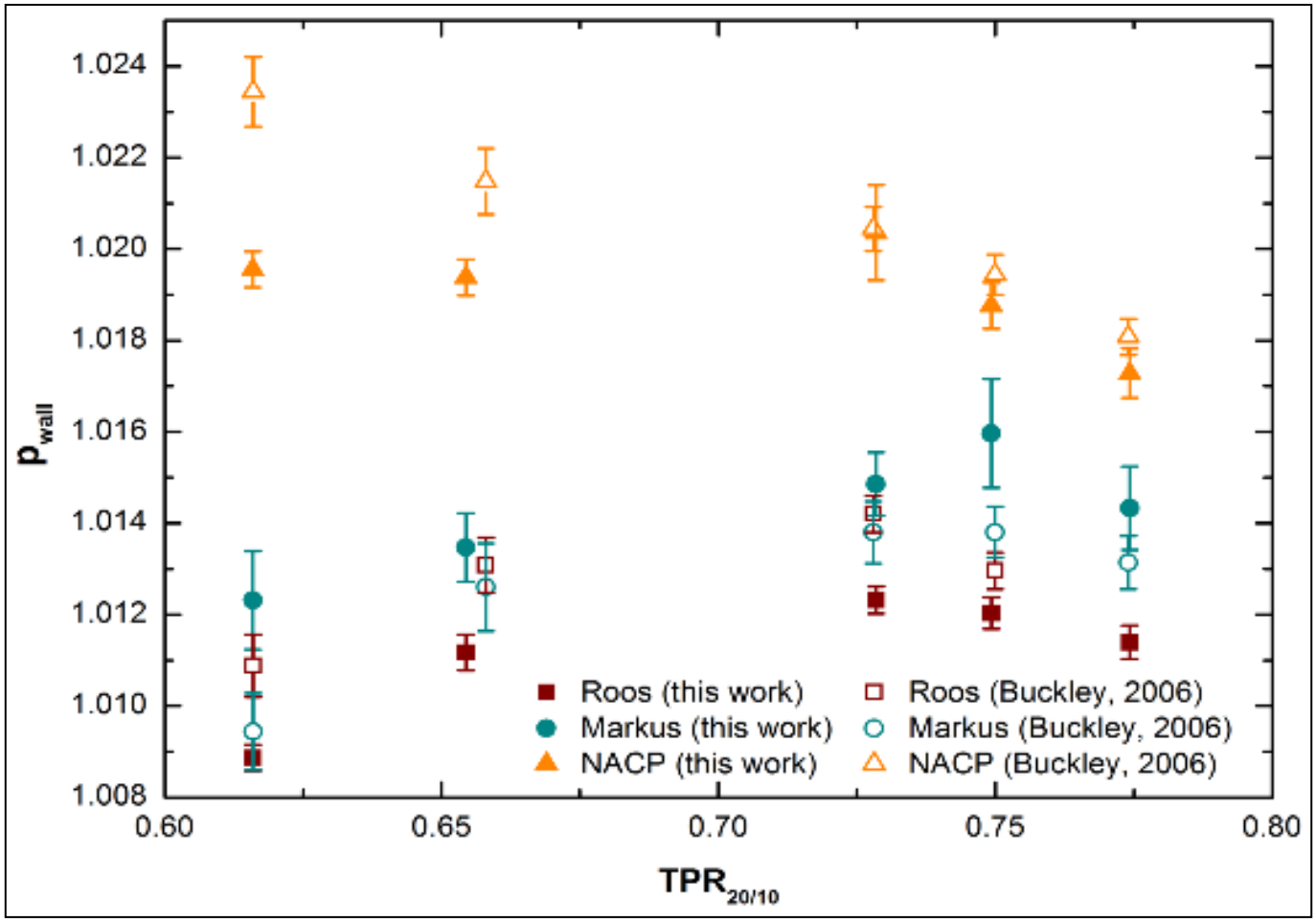

Fig. 2: Comparison between the perturbation correction p_{wall} achieved in this work and published by Buckley and Rogers [7]. The error bars represent the statistical uncertainty of the Monte Carlo results (1□□).

References

[1] DIN 6800-2: Procedures of dosimetry with probe type detectors for photon and electron radiation –Part 2: Ionization chamber dosimetry of high energy photon and electron radiation, 2008.

[2] Andreo P, et al: IAEA TRS-398 – Absorbed Dose Determination in External Beam Radiotherapy: An International Code of Practice for Dosimetry based on Standards of Absorbed Dose to Water. International Atomic Energy Agency, 2001.

[3] I. Kawrakow, E. Mainegra-Hing, D. W. O. Rogers, F. Tessier, and B. R. B. Walters. The EGSnrc code system: Monte Carlo simulation of electron and photon transport. National Research Council of Canada, Report PIRS-701, 2013.

[4] Wang L.L.W., Rogers D.W.O. Calculation of the replacement correction factors for ion chambers in megavoltage beams by Monte Carlo simulation. Med. Phys., 35(5), 1747–1755, 2008.

[5] J. Wulff, K. Zink and I. Kawrakow. Efficiency improvements for ion chamber calculations in high energy photon beams. Med. Phys., 35(4), 1328–1336, 2008.

[6] Ali ESM, Rogers DWO. Functional forms for photon spectra of clinical linacs. Phys. Med. Biol, 53(11):2823–36, 2008.

[7] Lesley A. Buckley and D. W. O. Rogers. Wall correction factors, *P*wall, for parallel-plate ionization chambers. Med. Phys., 33(6), 1788–1796, 2006

[8] Chin E, Shipley D, Bailey M, Seuntjens J, Palmans H, Dusautoy A and Verhaegen F. Validation of a Monte Carlo model of a NACP-02 plane–parallel ionization chamber model using electron backscatter experiments. Phys. Med. Biol. 53 N119–26, 2008.

[9] Zink K, Wulff J. Beam quality corrections for parallel-plate ion chambers in electron reference dosimetry. Phys. Med. Biol. 57, 1831-1854, 2012.

Session 17 – Radiation biology and biological modeling

Chairs: M. Pruschy, T. Streller (Zurich/CH)

98 Introductury lecture: Challenges for radiation biology in times of radiati on physics

M. Pruschy[1]
[1] University Hospital Zurich, Department of Radiation Oncology, Laboratory for Molecular Radiobiology, Zurich, Switzerland

The development of technology for the delivery of radiotherapy has been paralleled in recent years by a greatly-improved understanding of the biology of radiotherapy itself. Clinical prognostic factors like tumor stage, size, type and location have long played a role in determining applied treatment parameters like total dose, dose per day (fractionation) and overall treatment time. In recent years radiobiologists have now begun to understand how tumor radiosensitivity is affected by the complex regulatory network of molecular processes in tumor cells and the microenvironment of the tumor tissue. However, an active translation of these insights into the clinics is still missing. Furthermore several additional significant technological advancements could be implemented during the last decade of radiotherapy to achieve its present level of effectiveness. The therapeutic end results of these developments are Intensity Modulated Radiation Therapy (IMRT), Image Guided Radiotherapy (IGRT), Stereotactic Body Radiotherapy (SBRT), including high-dose rate irradiation. However, these technological achievements have again outpaced radiation biology and at the same have opened relevant novel areas for radiation biology-oriented research. Radiation biology is challenged by these new technological advancements which not only allow very precise targeting of a specified tumor site but also allows irradiation with single high doses up to 30Gy/fraction. For example, preclinical research will have to analyse in depth whether high dose irradiation induces a similar treatment response on the molecular, cellular and tumor physiological level - relative to a classic fractionated radiotherapy regime - or whether a “New Radiation Biology” will have to be defined.

Likewise, molecular radiobiological research has only started to enter the field of hadron therapy. For example, the rapid introduction of proton therapy worldwide contrasts with the scarcity of radiobiologic evidence to support the expansion of new clinical indications. A generic RBE value of 1.1 has been defined for high energy, low LET proton radiotherapy - even though we are well aware that the RBE can vary significantly depending on the tissue, cell line or end point investigated. With the increasing numbers of proton therapy centers, in-depth studies are now required to understand the differential response to the two types of IR on the molecular and cellular levels, also taking the genetic background of the irradiated cells into consideration. Future studies will have to investigate whether the differential response patterns to proton versus photon irradiation can be translated into biology-based rationales to choose between proton- and photon-based radiotherapy.

Radiotherapy can be looked at as one of the most personalized medicine with each patient receiving an individualized treatment but based on the most sophisticated delineation of the 3D tumor volume for each individual patient. We slowly begin to understand the tumor response to IR on the molecular, cellular, tumor physiological and normal tissue level. However, we can only minimally link the treatment response to radiotherapy to the individual genetic make-up of a tumor. As radiation biologist we are also challenged to make substantial contributions in the future towards a personalized radiotherapy based on biology-based strategies.

99 Differential Response to Proton versus Photon Radiotherapy: Response Mechanisms and New Combined Treatment Concepts

A. Fontana[1], M. Pruschy [1], A. Sartori[1], N. Grosse[1], M. Augsburger[1], A. Lomax[2]
[1]University Hospital and University of Zurich, Zurich, Switzerland
[2]Paul Scherrer Institute, Villigen, Switzerland

Purpose/objective(s): The 10 % higher efficacy of proton- versus photon-irradiation (IR) is already implemented in the clinics. But little is known about the radiobiology of this RBE. We previously investigated this higher efficacy of proton-IR in genetically-defined chinese hamster ovary cells (CHO) cells. Surprisingly homologous recombination (HR)-deficient cells were significantly more sensitive to proton IR when compared to the wild type cells, whereas non-homologous end joining (NHEJ)-deficient cells did not show any significant differences in response to these two types of IR. These results have now been investigated on the molecular level in these CHO cells and in human cancer cells deficient in specific proteins of HR.

Materials and methods: Experiments were performed with an HR-proficient and -deficient CHO cell line pair, NHEJ-deficient CHO cells and the corresponding genetically reconstituted wild-type cells, a human ovarian tumor cell pair (BRCA2-deficient and wildtype, respectively) and the mammary carcinoma MDA-MB-436 (BRCA1-deficient) and MDA-MB-231 (BRCA1-wildtype) cells.

Results: In contrast to NHEJ-deficient cells, HR-defective Irs1sf cells and CHO-wildtype cells, depleted of Rad51, showed an increased RBE_{10} in comparison to their corresponding wildtype cells (RBE_{10} of 1.44 and 1.52 vs 1.33, respectively). This difference in the RBE could be reversed when cells were irradiated in plateau phase (RBE_{10}: AA8=1.29; Irs1sf=1.27), indicating a critical role of HR. Likewise, human BRCA2-deficient cells were markedly hypersensitive towards proton irradiation. Furthermore, transient inhibition of ATM in MDA-MB-231 cells by the potent ATM-inhibitor KU60019 significantly sensitized them to proton- vs photon irradiation. Quantification of residual chromosomal aberrations in wildtype and HR-deficient cells revealed a slightly enhanced total amount of chromosomal aberrations in the HR-deficient cells in response to both types of IR. Proton-irradiation resulted in more fragments but also more complex chromosomal aberrations, especially in the HR-deficient cells, with a shift from chromosome- to more chromatide-type aberrations in HR-deficient cells.

Conclusions: Our data demonstrate an enhanced susceptibility of HR-deficient cells to proton-irradiation. The enhanced RBE is not due to an increased amount of induced DNA DSBs, but might be linked to the slower repair kinetics in HR-defective cells due to a differential quality of DNA damage induced by proton- versus photon-irradiation. This might become relevant for clinical stratification of patients carrying mutations in the DNA damage response pathways.

100 A computer model to simulate the radiation response of hypoxic tumors

I. Espinoza[1,2], P. Peschke[3], C. P. Karger[1]
[1]German Cancer Research Center, Medical Physics in Radiation Oncology, Heidelberg, Germany
[2]Pontificia Universidad Católica de Chile, Physics , Santiago de Chile, Chile
[3]German Cancer Research Center, Clinical cooperation Unit Radiotherapy, Heidelberg, Germany

Background: Hypoxic tumors are known to be highly resistant against radiation. To integrate information on tumor oxygenation into treatment planning, the radiation response of hypoxic tumors has to be predicted. For this, a simulation model was developed, which describes the main biological aspects of spatial-temporal development of hypoxic tumors under radiation treatment [1].

Materials and methods: The simulation model consists of two sub-models: the *T*issue *O*xygenation *M*odel, TOM [2], and the *T*umor *R*esponse *M*odel, TRM [1]. The TOM simulates the oxygen distribution for a reference volume based on an assumed vascular architecture and a vascular fraction by solving the diffusion-reaction equation for oxygen under stationary conditions. With this model, oxygen histograms are precalculated for different settings of the vascular fraction and the number of viable tumor cells. The TRM simulates the radiation response of the tumor including the following six radiobiological processes: (i) proliferation of tumor cells, (ii) hypoxia-induced angiogenesis, (iii) Cell exchange between voxels leading to tumor growth, (iv) radiation response based on the linear quadratic model extended by the oxygen enhancement ratio, (v) resorption of dead cells, and (vi) Cell exchange between voxels leading to tumor shrinkage. Step (ii) and (iv) depend on the oxygen distribution and are considered by evaluating the oxygen histograms calculated with the TOM. Prior to the simulation of the tumor response, the initial status of the tumor has to be characterized by specifying the tumor and normal tissue contours, the number of tumor cells and vascular fraction per voxel as well as the radiation response parameters. In addition, dose and fractionation parameters from treatment planning are taken into account.

Result: The simulation model describes the spatio-temporal development of hypoxic tumors under radiation treatment and for each voxel, it provides the number of viable and dead cells as well as the vascular and hypoxic fractions, from which the oxygen distribution may be obtained. Tests in a number of cases showed that the model describes the most important feature of the radiation response. The model includes three mechanisms of reoxygenation of which tumor shrinkage appears to be most important. Simulating dose response curves for a squamous cell carcinoma for different vascular fractions (7.2 vs 3.6 %) revealed a clinically significant shift of the dose response curve of 17.4 Gy.

Conclusion: The developed voxel-based multi-scale model simulates the spatio-temporal development of hypoxic tumors. On a microscopic scale it describes the oxygen distribution, which is incorporated on a voxel-scale to determine the radiation response. On a macroscopic scale morphometric parameters such as tumor size, shape as well as the presence of hypoxic regions may be assessed. The model allows studying the relative importance of different radiobiological effects, and in the future, it might also be used in treatment planning to improve the estimation of the response of clinical tumors. Clearly, the validity of the predictions depends on the correctness of the implemented radiobiological mechanisms as well as on reliable values for the input parameters. Both have to be validated in future studies using preclinical [3] as well as clinical data on tumor response. As the model is voxel-based, it offers the chance to characterize the initial status of the tumor prior to irradiation by morphological and functional imaging.

References

[1] Espinoza Bornscheuer IG: Computer simulation of the radiation response of hypoxic tumours. Dissertation Naturwissenschaftl.-Mathematische Gesamtfakultät, Universität Heidelberg, (2013).
[2] Espinoza I, Peschke P, Karger CP. A model to simulate the oxygen distribution in hypoxic tumors for different vascular architectures. Med Phys 2013;40:081703
[3] Karger CP, Peschke P, Scholz M et al. Relative biological effectiveness of carbon ions in a rat prostate carcinoma in vivo: comparison of 1, 2, and 6 fractions. Int J Radiat Oncol Biol Phys 2013;86:450-455.

101 *In vivo* dose response to laser driven electron beams

M. Oppelt[1], M. Baumann[2,1,3], R. Bergmann[2], E. Beyreuther[2], K. Brüchner[2,1], J. Hartmann[1], M. Kaluza[4], L. Karsch[1], M. Krause[2,1,3], L. Laschinsky[1], E. Lessmann[2], M. Nicolai[4], M. Reuter[4], A. Sävert[4], M. Schnell[4], M. Schürer[1], J. Pawelke[2,1]
[1]OncoRay – National Center for Radiation Research in Oncology, Faculty of Medicine and University Hospital CGC, TU Dresden , Dresden, Germany
[2]Helmholtz-Zentrum Dresden – Rossendorf , Dresden, Germany
[3]German Consortium for Translational Cancer Research (DKTK) , Dresden, Germany
[4]Institute of Optics and Quantum Electronics, Friedrich-Schiller – Universität , Jena, Germany

Purpose: The novel technology of particle acceleration by ultra-high intensity lasers promises the realization of compact and economic proton and ion accelerators for cancer therapy that can be integrated in already existing clinics. In comparison to conventional accelerators used in clinical routine, the new acceleration technology based on high intensity lasers leads to ultra-short beam pulses with ultra-high pulse dose rate. Prior potential clinical application possible biological consequences of the particular beam properties have to be investigated. Within the German joint research project “onCOOPtics” we already performed extensive *in vitro* dose response studies with laser driven electron [1] and proton [2] beams as a first translational step. We now report on the first experiments comparing laser and conventional accelerated particle beams *in vivo*.

Materials and methods: A mouse tumor model suitable for the available, still low energy (up to ~ 20 MeV) of laser accelerated protons [3] was established for human squamous cell carcinoma FaDu. Cells grown in cell culture were suspended in PBS (phosphate buffered saline) and injected subcutaneously onto the right ear of NMRI nude mice. Subsequently a tumor development to a size of ~ 2.5 mm was awaited. This model was applied using laser accelerated electrons, since laser driven particle acceleration and homogenous dose delivery to the tumor is easier to achieve with electrons than with protons. Radiobiological experiments with laser accelerated electrons likewise provide information about the biological consequences of ultra-short pulsed beams. The *in vitro* established irradiation technology which included real time and absolute dose determination [4] was further enhanced for the 3D tumor irradiation in terms of beam transport, beam monitoring, dose delivery, and dosimetry in order to apply a prescribed dose to each tumor. A system for precise tumor positioning and position verification at the irradiation site was realized [5]. Human FaDu tumors were irradiated at the 30 Terawatt Titanium:Sapphire laser system JeTi operated at Friedrich-Schiller-University Jena. Laser pulses of 700 mJ energy and 28 fs duration were focused into a hydrogen gas jet with a frequency of up to 1 Hz accelerating electrons to energies of up to a few 10 MeV. Prescribed doses of 3 Gy and 6 Gy were delivered with mean dose rates of ≥ 1 Gy/min by applying electron pulses of ~35 mGy mean dose per pulse [6]. Control animals were 0 Gy mock irradiated. Reference electron irradiation was performed with the same setup and dosimetry system at a conventional therapy LINAC. The radiation induced tumor growth delay was determined.

Results and conclusion: Dose response curves have been obtained for the direct comparison of ultra-short pulsed laser accelerated and conventional continuous electron beams. This world wide first full scale animal study with laser accelerated particles demonstrates the reliability and stability of all implemented components and methods. Moreover, no significant difference in biological effectiveness of the two electron beam modalities was observed. The realization of *in vivo* studies with laser driven proton beams is now under preparation.

This work was supported by BMBF, grant nos. 03ZIK445 and 03Z1N511.

References

[1] Laschinsky et al. (2012) Radiobiological effectiveness of laser accelerated electrons in comparison to electron beams from a conventional linear accelerator. J Radiat Res 53:395-403
[2] Zeil et al (2013) Dose controlled irradiation of cancer cells with laser accelerated proton pulses. Appl Phys B 110:437- 444
[3] Brüchner et al. (2014) Establishment of a small animal tumour model for in vivo studies with low energy laser accelerated protons. Radiat Oncol 9:57
[4] Richter et al. (2011) Dosimetry of laser-accelerated electron beams used for in vitro cell irradiation experiments Rad Meas 46(12):2006-2009
[5] Schürer et al. (2012) Irradiation system for pre-clinical studies with laser accelerated electrons. Biomed Tech 57(Suppl 1):62-65
[6] Nicolai et al. (2013) Realizing a laser-driven electron source applicable for radiobiological tumor irradiation. Appl Phys B doi:10.1007/s00340-013-5747-0

102 Variance-based Sensitivity Analysis to Quantify the Impact of Biological Model Uncertainties in Carbon Ion Therapy

F. Kamp[1], J. J. Wilkens[1]
[1]Technische Universität Munich, Klinikum rechts der Isar, Department of Radiation Oncology, Munich, Germany

Introduction: In carbon ion therapy, treatment planning and evaluation are frequently based on biological models to estimate the relative biological effectiveness (RBE) or the equivalent dose in 2 Gy fractions (EQD2). Within the framework of the linear-quadratic model, these quantities are functions of the radiosensitivity parameters for the reference x-ray radiation (α_x, β_x) and the ion (or particle) radiation (α_p, β_p) as well as the physical dose d_p. Biological models, for example the Repair-Misrepair-Fixation (RMF) [1] model or the Local Effect Model (LEM) [2], can be used to extrapolate the biological effect of x-rays to the biological effect of ions. The used radiosensitivity parameters are not directly measurable and subject to large (relative) uncertainties of up to 20-40 % or even more. Therefore it is necessary to estimate the resulting uncertainties in e.g. RBE or EQD2 caused by the uncertainties of the biological (input) parameters and the biological models.

Materials and methods: The presented sensitivity analysis (SA) approach was implemented in a research treatment planning system which allows biological optimization for three dimensional patient geometries for carbon ion therapy. The mechanism-based RMF model is used for the biological modeling of the different biological effects of carbon ions as well as their fragments. We employ the variance-based sensitivity analysis approach as described in [3] as "Factor Priorization" to access uncertainties in RBE(α_x,β_x,α_p,β_p,d_p) and EQD2(α_x,β_x,α_p,β_p,d_p). In this Monte Carlo SA approach a function is evaluated n = 10^4 to 10^6 times. For each of those runs all input parameters are changed simultaneously, using random numbers according to their associated uncertainties. Variance-based statistic formalisms then rank the input parameter/uncertainty pairs according to their impact on the result of the function (quantification of the impact of the uncertainties). The presented analysis accounts for uncertainties in α_x, β_x, α_p, β_p, d_p as well as the used biological model.

Results: Assigning normal distributions with a relative standard deviation of 10 % to the input parameters already results in great deviations in RBE and EQD2. The used variance-based SA approach, with the performed quantification, enables the generation of three dimensional, voxel-based sensitivity maps. They illustrate the impact of variations in the input parameter on calculated RBE or EQD2 values and hence treatment plan evaluation. Different treatment scenarios, uncertainties and patient cases are evaluated.

Conclusion: Even small variations in the input parameters result in significant uncertainties of RBE and EQD2 in carbon ion therapy. The presented SA is able to rank the influence of different input parameter uncertainties on the output variation. This allows conclusions about the importance of uncertainties of different input parameters. The implementation in a three dimensional treatment planning system allows the examination of sensitivity values with respect to dependencies on treatment depth and geometry. The presented SA offers the potential for a comprehensive uncertainty analysis, needed in carbon ion therapy treatment planning and evaluation.

Acknowledgement: This work was supported by DFG grant WI 3745/1-1, DFG cluster of excellence: Munich-Centre for Advanced Photonics and a fellowship from the German Academic Exchange Service (DAAD).

References

[1] Carlson DJ, Stewart RD, Semenenko VA, Sandison GA. Combined use of Monte Carlo DNA damage simulations and deterministic repair models to examine putative mechanisms of cell killing. Rad Res 2008: 169; 447–459.
[2] Scholz M, Kellerer AM, Kraft-Weyrather W, Kraft G. Computation of cell survival in heavy ion beams for therapy. Radiat Environ Biophys 1997: 36; 59–66.
[3] Saltelli A, Ratto M, Andres T, Campolongo F, Cariboni J, Gatelli D, Saisana M, Tarantola S. Global sensitivity analysis. Chichester, England. John Wiley 2008.

103 Biological optimization for carbon ion therapy planning based on the Equivalent Uniform Dose (EUD)

S. Brüningk[1], F. Kamp[1], J. J. Wilkens[1]
[1]Technische Universität Munich, Klinikum rechts der Isar, Department of Radiation Oncology, Munich, Germany

Introduction: Biological treatment plan optimization based on the concept of equivalent uniform dose (EUD) has successfully been applied to IMRT treatment plan optimization [1]. Due to variations of the relative biological effectiveness (RBE) in carbon ion therapy, the biological impact of the irradiation has inevitably to be taken into account making it very attractive to relate also the optimization to a biologically meaningful end point. To facilitate EUD-based optimization for carbon ion therapy, we implement two different EUD concepts that are applicable to ion therapy and use them as a basis for biological optimization.

Materials and methods: In addition to the classical EUD concept, which calculates a generalized mean over the RBE-weighted absorbed dose, we propose an equivalent uniform effect (EUE) to simplify the optimization process of carbon therapy plans. The EUE is defined as the biologically equivalent uniform effect yielding the same probability of injury as the inhomogeneous effect distribution under consideration. Its mathematical formulation is implied by a generalized mean over the distribution of the biological effect ($E = \alpha D + \beta D^2$, with α and β the linear quadratic model parameters) in the respective organ. For both EUD concepts, objective functions were implemented into the research treatment planning system CERR in a flexible way allowing for each structure to choose between biological effect constraints per voxel and EUD objectives. To analyze the impact of the underlying mathematical objective function on the optimization results apart from the influence due to EUD- or voxel-based optimization, all objective functions were available as quadratic or logistic implementation.

For a head-and-neck patient treatment plans yielding a uniform RBE-weighted dose distribution in the target were calculated for multiple combinations of objective functions for the organs at risk (OARs). All plans were evaluated regarding dosimetric and biological criteria as the final EUD (based on RBE x dose) and the corresponding normal tissue complication probabilities (NTCP) for the OARs. The impact of the underlying biological parameter for the EUD calculation on the optimization was tested by a systematic variation and the deviations in the resulting EUD values were related to the voxel-based optimization outcome.

Results: In agreement with the results from EUD-based IMRT treatment plan optimization, EUD-based optimization for carbon ion therapy resulted in a slightly better sparing of the OARs in terms of EUD compared to a simple voxel-based optimization approach. This conclusion was independent of the underlying EUD-concept and mathematical implementation of the objective function. Depending on the architecture of the organ under study, i.e. its degree of parallelism or serialism, the gain in OAR sparing is pronounced differently with respect to logistic or quadratic objective functions on a voxel basis. Regarding the biological outcome, it was more intuitive to handle EUD-based objective function terms, since voxel-based approaches are rather try-and-error processes. Especially in the case of very inhomogeneous dose distributions in OARs, where it was difficult to meet the voxel-based effect constraints, the optimization could easily be steered in the desired direction by applying EUD constraints.

It could be shown, that an EUE-based objective function holds the capability of yielding the same treatment plan as RBE-weighted EUD-based optimization. This approach may thus be favorable for future EUD-based optimization for radiation therapy treatment planning for different irradiation modalities.

Conclusion: Our investigation proposes that EUE-based optimization for carbon ion therapy is a useful tool to optimize more specific in the sense of biological outcome. However, due to steeper dose gradients for carbon ion irradiation compared to IMRT, the gain in normal tissue sparing by EUD-based optimization is less pronounced as for EUD-based IMRT optimization and is strongly correlated to the used biological parameters.

Acknowledgements: Supported by DFG grant WI 3745/1-1 and DFG cluster of excellence: Munich-Centre for Advanced Photonics.

References

[1] Wu, Q.: Int. J. Radiation Oncology Biol. Phys., 52 (2002) 224-235

104 Homologous Recombination in the View of the MHR-Model

S. Scheidegger[1], N. Grosse[2], R. M. Füchslin[1]
[1]ZHAW School of Engineering, Zurich Universtity of Applied Sciences, Winterthur, Switzerland
[2]University Hospital Zurich, Laboratory for Molecular Radiobiology, Zurich, Switzerland

Introduction: The repair of radiation-induced lesions is based on the interaction of repair-proteins and DNA. The impact of ionizing radiation is not limited to the DNA. Protein-related radiation damages may alter the cellular repair capability in general. The different repair pathways may have specific sensitivities to radiation-induced damages, related to stability of proteins, complexity and redundancy in the signaling pathway and the spatial distribution of energy deposition. The last point may be from special interest regarding the differences found between photons and protons by Grosse et al. [1]. To model the aspect of protein-DNA interaction and the impact of radiation-induced damages of the repair system, the Multi-Hit-Repair- (MHR-) model [2] can be used. This model covers a large variety of radio-biological observations such as linear-quadratic-linear behavior for large doses per fraction [3], apoptotic vs. non-apoptotic cell death [4] and dose rate dependencies as well [5]. With a similar approach, also low-dose hypersensitivity can be reproduced [6]. For sensitivity tests and identification of parameters (possibly) related to homologous recombination, a fit of the experimental data of Grosse et al. [1] was carried out.

Materials and methods: The MHR- model is based on a chain of cell populations which are characterized by the number (i) of radiation induced damages (hits). Cells can shift downward along the chain by collecting hits and upward by a repair process. The corresponding equations describing the rates of change of the cell populations (N = population size of the cells in the mitotic cycle; L_i = size of population with i hits) is given by [2]:

$$\frac{dN}{dt} = -\alpha RN + c_r e^{-\mu\Gamma} \cdot L_1$$

$$\frac{dL_1}{dt} = \alpha RN - \left(\alpha R + c_r e^{-\mu\Gamma} + c_e\right) \cdot L_1 + c_r e^{-\mu\Gamma} \cdot L_2$$

$$\frac{dL_i}{dt} = \alpha RL_{i-1} - \left(\alpha R + c_r e^{-\mu\Gamma} + c_e\right) \cdot L_i + c_r e^{-\mu\Gamma} \cdot L_{i+1}$$

Here, R is the dose rate (the cell killing term αRN or αRL_i represents a Poissonian process, α is a radiation sensitivity coefficient describing the baseline in the case of no enhanced repair: We assumed here, that HR (homologous recombination)-deficient cells determine the baseline defined by $\log S = -\alpha D$ and the repair constant c_r is zero (no "enhanced" repair; only limited repair included in the parameter α). A separated baseline (value of α) for protons and photons was chosen. The repair process is governed by a repair probability ($c_r e^{-\mu\Gamma}$) which depends upon a state variable Γ (transient dose equivalent) used for a simplistic description of the impact of radiation onto repair proteins. It is assumed that this transient dose equivalent increases linearly with the dose rate R and will fade away by a fist order repair process: $d\Gamma / dt = R - \gamma\Gamma$ (for more details, see [2]). In addition to repair or collection of further hits, damaged cells can be eliminated (elimination rate $c_e L_i$). For fitting the experimental data, an evolutionary optimization algorithm has been applied [2].

Results: The values of the parameter α are computed from the survival data of the HR -deficient CHO cells which exhibit a linear logarithmic cell survival. The resulting values are given in Tab. 1. We compared the other parameter values with previously evaluated values by fitting different experimental data sets gained from different cell lines [2]. There, a value of 1.45 h^{-1} was found for γ. We evaluated this value by performing parameter optimization runs with and without fixed values for γ (Tab. 1). With a fixed value, the optimization algorithm found only for the photon data (dose rate R = 60 Gy/h) a converging set of parameters. For proton data (dose rate R = 4 Gy / s = 14400 Gy/h), no convergence was found with fixed γ although the fitted curves matched the data within the error bars. However, allowing γ to be adjusted by the evolutionary process yielded estimates for all parameters. The parameter μ turned out to be more or less identical for all settings. The parameter c_r and c_e seem to be correlated – this behavior is in agreement with previously found results by fitting other cell lines [2].

Discussion and conclusion: The model is able to fit the data well. But based on the number of parameters and the available data, it is problematic to select a parameter set as the "right one". One reason is the fact that we measure the number of surviving cells in the limit of long times after irradiation. Mathematically, this implies that all constants with units not containing a time can be determined in an absolute manner, whereas parameters with units containing times are only fixed up to a constant that represents the time scale. The strength of the MHR model is the fitting of dose rate dependent cell survival: Therefore, clonogenic survival experiments with varying dose rates are needed to assess the parameter values more appropriately. Beside this aspect, the value of μ is remarkably stable between 0.15-0.16 Gy^{-1} for all fits. This is in agreement with the findings using other cell lines for fitting, where a possible range of 0.03-0.5 Gy^{-1} has been identified for this parameter. Furthermore, our stable findings for μ are well in accordance with the mathematical fact that the unit of μ is Gy^{-1} and therefore, since it contains no time unit, should be determined down to a single value. The choice of a separate baseline for protons and photons (value of α) implies that the basic repair (possibly due to NHEJ-repair) is not equal for protons and photons. Another interpretation could be an additional dose rate dependency since the protons are irradiated at a remarkably higher dose rate. However, the term $c_r e^{-\mu\Gamma}$ in the model seems to cover the effect of homologous recombination in an appropriate manner.

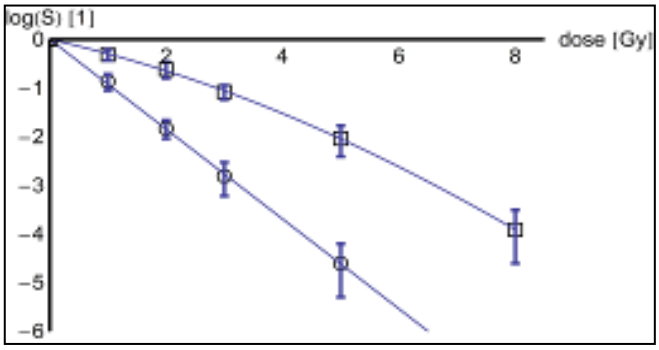

Fig. 1: Fit of surviving fraction S in case of protons

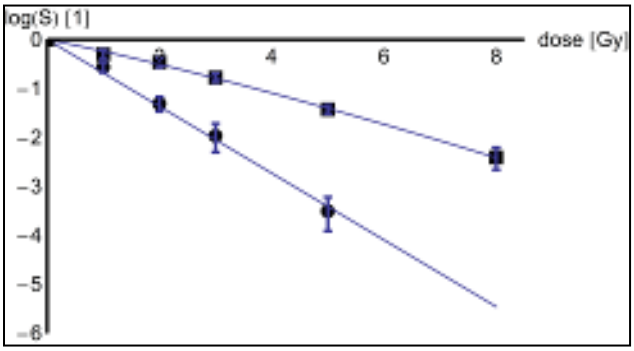

Fig. 2: Fit of surviving fraction S in case of photons

	Proton	Proton with fixed γ	Photon	Photon with fixed γ
α / Gy^{-1}	*0.923*	*0.923*	*0.682*	*0.682*
c_r / h^{-1}	12.58	Not conv.	4.245	2.522
c_e / h^{-1}	5.15	Not conv.	2.081	1.234
μ / Gy^{-1}	0.155	Not conv.	0.150	0.153
γ / h^{-1}	0.960	*1.45*	2.320	*1.45*

Tab. 1: Parameter values for the different cell lines found by fitting the experimental data by the MHR model. The italic numbers were fixed (predefined) values and therefore not gained by evolutionary optimization.

References

[1] Grosse N, Fontana AO, Hug EB, Lomax A, Coray A, Augsburger M, Paganetti H, Sartori AA, Pruschy M: Int J Radiation Oncol Biol Phys, 88 (2014) 1, 175-181
[2] Scheidegger S, Fuchs HU, Zaugg K, Bodis S, Füchslin RM: Computational and Mathematical Methods in Medicine, 2013, http://dx.doi.org/10.1155/2013/587543
[3] Guerrero M, Li XA: Phys Med Biol 49 (2004), 4825-35
[4] Harrigan Hardenberg P, Hahnfeldt P,Hlatky L, Takemoto C, Shimamura A, McGill G, Fung CY, Bodis S, Fisher DE: Int J Radiat Oncol Bio Phys 43(1999) 3, 601-5
[5] Wells RL, Bedford JS: Radiat Res 94(1983), 105-34
[6] Scheidegger S, Füchslin RM: Proc. of ASIM 2011 (full papers, ISBN 978-3-905745-44-3)

Session 18 – Image guided radiation therapy/hybrid systems

Chairs: R. Müller (Erlangen/DE), D. Vetterli (Biel/CH)

105 Introductory lecture: Systems of image guidance for radiation therapy

G. Sroka-Perez[1]
[1]Universitätsklinikum Heidelberg, Klinik für Radioonkologie und Strahlentherapie, Heidelberg

Introduction: Imaging methods have been used in the treatment room for a long period of time. The aim was to get detailed information on the patient anatomy in treatment position right before or during treatment. During the last years several systems have been developed, where imaging modalities are directly connected or integrated into radiation delivering systems. If so we talk about hybrid systems. Those systems are used to improve treatment accuracy both interfractional and intrafractional.

What do we intend to achieve? Applying IGRT using hybrid systems will provide a variety of information depending on the system and method used. Main interest could be to improve the positioning of the patient and logically consistent reduce margins of the planning target volume (PTV). Furthermore it may be of interest to image changes in tumor size and shape as well as changes in organs at risk. Systems can provide information on intrafractional motion of the target that can be applied for gating or tracking. All those information can be used to adapt plan and dose to the patient.

Imaging modalities of hybrid systems in IGRT: Ceiling and floor mounted systems in most cases use X-ray tubes and digital flatpanel detectors. Gantry-mounted systems on conventional C-arm linear accelerators come up with both kV- and MV cone beam CTs. Therefore either X-ray tubes or the therapy beam, sometimes with reduced energy, are used. Gantries designed as a tomotherapy system provide fan beam CTs with the therapy beam of reduced energy. Data is acquired with a detector ring similar to conventional CT. Newest developments try to integrate magnetic resonance imaging into radiation delivering systems. All imaging modalities used in radiotherapy with photons mentioned above are theoretically thinkable for protons and ions.

Choice of image guidance modality depending on clinical objective: Using hybrid systems for patient repositioning is possible for all technologies mentioned above. Additional dose delivered to the patient by using IGRT devices has to be taken into account and needs to be discussed with respect to patient age and presence of organs at risk in the imaging area. To gain information on tumor growth or shrinkage during the course of therapy or adapting beam delivery with respect to soft tissue borders, image quality plays an important role. In order to eliminate additional dose by using radiation for imaging and improving image quality especially for soft tissue situation, hybrid systems based on MR imaging are being developed.

Conclusion: The introduction of in-room digital imaging provides new opportunities to further improve treatment accuracy and precision. At the same time, it presents new challenges for its efficient and effective implementation. Each IGRT method has its strengths and limitations. The user needs to match the clinical objective with the appropriate technology. Bounds of validity for each method have to be evaluated carefully and must be taken into account before application.

References

[1] Accuray product brochure for CyberKnife System, Accuray document P/N 500500.A.
[2] Fenwick JD et al. Quality Assurance of a helical tomotherapy machine. Phys Med Biol 2004, 49:2933-2953.
[3] Kamino Y et al. Development of a four-dimensional image-guided radiotherapy system with a gimbaled X-ray head. Int J Radiat Oncol Biol Phys 2006;66:271–8.
[4] ExacTrac Vero Clinical User Guide, version 3.1, BrainLab AG Germany, 2012, 253.
[5] Raaymakers B W et al. Integrating a 1.5 T MRI scanner with a 6 MV accelerator: proof of concept Phys. Med.Biol. 2009, 54 N229–37
[6] Hunsche S et al. Combined x-ray and magnetic resonance imaging facility: application to image-guided stereotactic and functional neurosurgery. Neurosurgery. 2007 Apr;60(4 Suppl 2):352-60; discussion 360-1.
[7] Yan H et al. Hybrid MV-kV 3D respiratory motion tracking during radiation therapy with low imaging dose. Phys Med Biol. 2012 Dec 21;57(24):8455-69. doi: 10.1088/0031-9155/57/24/8455. Epub 2012 Nov 30.
[8] Srinivasan K et al. Applications of linac-mounted kilovoltage Cone-beam Computed Tomography in modern radiation therapy: A review. Pol J Radiol. 2014 Jul 3;79:181-93. doi: 10.12659/PJR.890745. eCollection 2014.

106 Introductory lecture: Details on technical and clinical implementation of image guidance systems

M. Stock[1]
[1]EBG MedAustron GmbH, Medical Physics, Wiener Neustadt, Austria

A tremendous amount of different technology is available for image guidance during therapy. The approaches can be either grouped as kV or MV imaging modalities as well as 2D or 3D imaging, CBCT vs. FBCT imaging or due to the way they are installed: Rail-track mounted, Ceiling-floor mounted or gantry mounted systems. Based on one clinical experience the necessary steps for the clinical implementation for two examples, kV CBCT imaging and stereoscopic imaging, are highlighted. From the physics point of view the implementation covers different parts. First the technical implementation (like the commissioning and acceptance), the development of a regular quality assurance procedure and secondly the setup of clinical protocols including image parameter optimization or imaging frequency optimization combined with setup correction protocols.

During the technical implementation the physicist should assure the mechanical and geometric precision and accuracy, as well as image quality verification, workflow and documentation. Parameters reported during acceptance like kV/MV isocenter concordance, imaging dose, spatial resolution or image contrast serve as baseline values for the further periodic QA programs. The needs for a clinical implementation are highly depending on the intention of an IGRT protocol. IGRT should support mainly stereotactic treatments where geometrical miss can have serious consequences as well as IMRT/VMAT or whenever margin reduction is aimed for. Stereotactic treatments should always be accompanied by imaging prior and in some cases also during or after the fraction. For highly conformal normal fractionated treatments (like IMRT/VMAT) the margin is determined by the IGRT and setup correction protocol. A margin reduction concept is demonstrated for VMAT prostate treatments using fiducial markers and stereoscopic imaging. Of importance is also the additional dose for IGRT together with its impact on dose to the patient and hence on imaging frequency of respective IGRT protocols. Finally some comments on additional equipment like a robotic couch or the communication with the TPS or the treatment machine and archiving are given.

All together IGRT has become part of the success of radiotherapy and is therefore a nice example of how technology development is supporting a better therapeutic ratio if implemented properly.

107 Dose Contribution of different imaging systems for frequently image guided radiotherapy (IGRT) protocols – 3D-dose-calculations with the treatment planning system and measurements in a phantom

T. Koch[1], T. Hauschild[1], K. Freundl[1]
[1]Sozialstiftung Bamberg, Klinik und Praxis fuer Strahlentherapie und Radioonkologie, Bamberg, Germany

Introduction: The daily use of IGRT systems like kilovoltage Cone Beam Computer Tomography (kV-CBCT) or Megavoltage Computer Tomography (MVCT, Tomotherapy) is essential for modern treatment planning strategies. The modern radiotherapy high precision treatment techniques like Intensity modulated Radiotherapy (IMRT) and Tomotherapy makes it necessary to verify the patient position very accurate immediately before the treatment. The goal is to target the high dose very exactly to the tumor and to reduce the damage of normal tissue close to the Tumor. Furthermore there is the possibility to observe anatomical changes during treatment. However the additional dose contribution has to be considered for the daily use.

Material and procedure: Measurements of the depth dose curves and the profiles as well as the absolute dose of the image beams for the Elekta Synergy kV-CBCT system and the Tomotherapy HiArt system were performed. For both datasets basic models were created and commissioned for our Pinnacle^3 treatment planning system (Version 9.6). The modeled and the measured depth dose curves and the profiles show a quite good agreement (Fig. 1 and 2). The models were checked by measurements in a solid state phantom (Octavius, PTW). For these measurements we used an ion chamber array (PTW729) as well as single ion chambers in different positions. The models were used to calculate the dose distributions and dose volume histograms (DVH) of the imaging systems in a real CT-Dataset of a patient with prostate cancer. For the CBCT an optimized in-house protocol with lower dose (weighted CTDI: 5 mGy) was applied instead of the Elekta standard protocol (weighted CDTI: 20 mGy). For the Tomotherapy MVCT we used the normal mode (slice thickness 4mm). The data were compared with the dose contribution of former IGRT protocols: Orthogonal Megavoltage (MV) isocenter control fields and double exposure used with conventional box techniques on an amorphous silicon based electronic detector (EPID).

Result: The basic dose calculations models of the CBCT and the MVCT show a sufficiently good agreement to the measurements. They are not suitable for high precision dose calculation but they could be used for an estimation of the dose contributions of the IGRT systems. The DVH calculation of different organs like rectum, bladder, femoral head and the whole body indicates, that a weakly double exposure with EPID yields the highest cumulative dose contribution for the whole series over 7 weeks (3 to 5 Monitor Units (MU) for the opened fields). For the prostate itself, that means 160cGy more as can bee seen in the DVH (Fig. 3). With weekly orthogonal isocenter fields (3 MU per field) the additional dose can be reduced to 40 cGy (Fig. 3). The lowest additional dose contribution can be achieved with kV-CBCT with our in-house protocol. The daily use of kV-CBCT yields 27 cGy mean dose more in the prostate for the whole series of 35 fractions (Fig. 4). The daily use of MVCT (Tomotherapy) produces an additional mean dose in the prostate of 43 cGy (Fig. 4), that is comparable to weekly isocenter checks with orthogonal fields (Fig. 5, 6). The other organs like rectum (Fig.5, 6)., bladder, femoral head are affected in a similar way.

Summary: The main purpose in modern radiotherapy is the concentration of the high dose area to the target and to avoid high dose exposure of the normal tissue and the organs at risk close to the targets. The weekly IGRT protocols with EPID images are insufficient, because for 80 % of the whole series, there is the risk of misalignments. A more frequently use is very critical because of the additional dose contribution. Moreover the EPID images are not suitable to account for anatomical changes during the treatment series. IGRT protocols which can be used daily are mandatory, especially when modern treatment techniques like IMRT or Tomotherapy are applied. It could be shown, that the kV-CBCT of Elekta and the MVCT of Tomotherapy have considerably low dose contributions. They can be used daily to align the patient with high precision.

Fig. 1: Measured and calculated Depth Dose curve for the CBCT dose calculation model

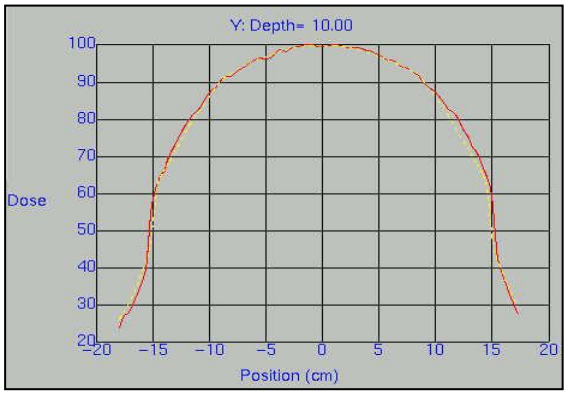

Fig. 2: Measured and calculated Inplane Profile for the CBCT dose calculation model

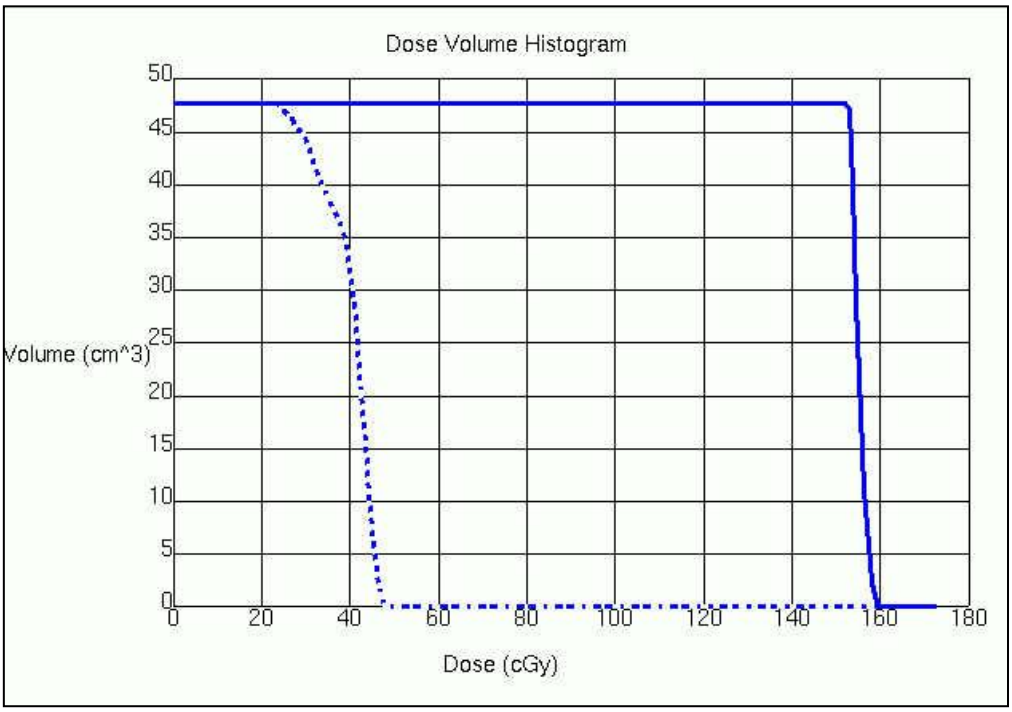

Fig. 3: Cumulative DVH for the prostate with weekly double exposure (solid) and weekly orthogonal isocenter fields

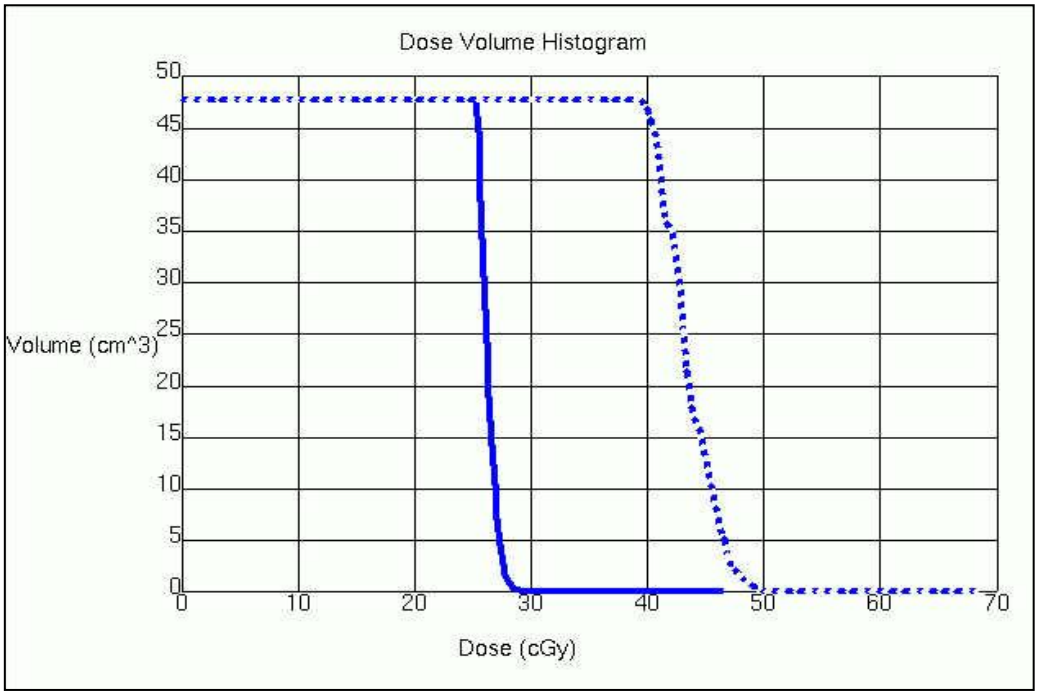

Fig. 4: Cumulative DVH for the prostate with daily CBCT (solid) and daily MVCT

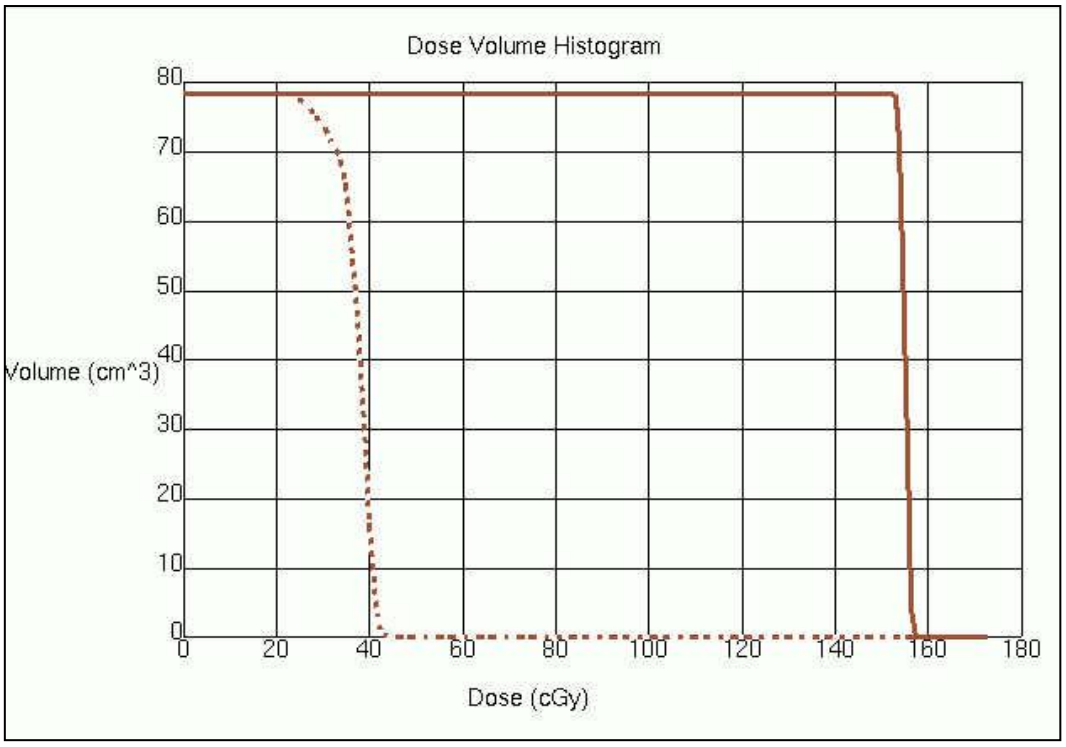

Fig. 5: Cumulative DVH for the rectum with weekly double exposure (solid) and weekly orthogonal isocenter fields

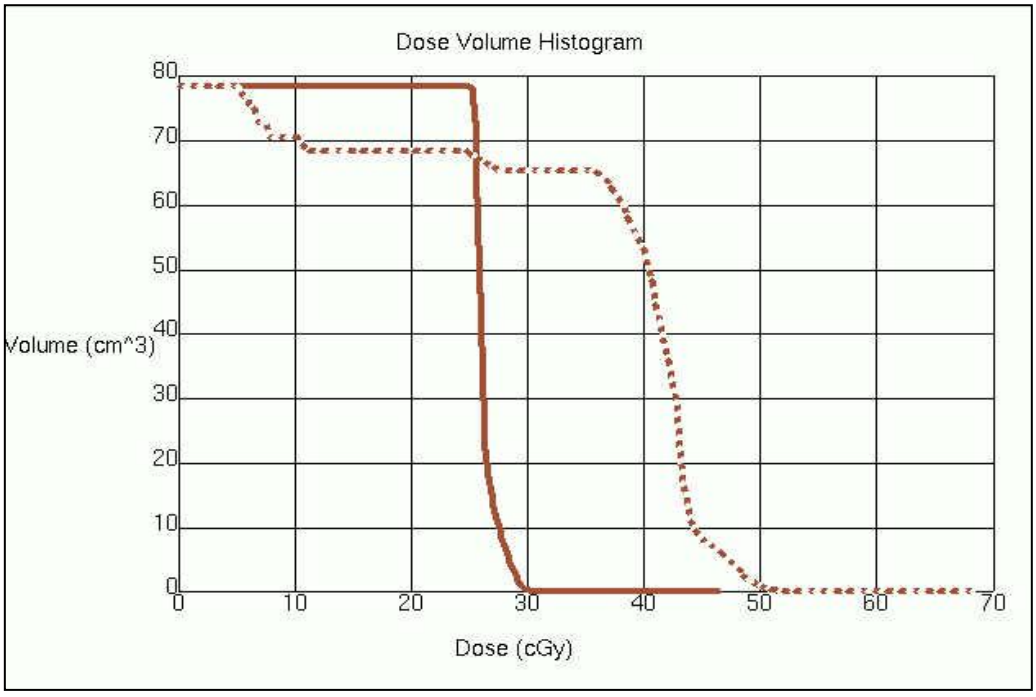

Fig. 6: Cumulative DVH for the rectum with daily CBCT (solid) and daily MVCT

108 System Integrity Quality Assurance for Image Guided Patient Position with 3D Ultrasound in External Beam Radiotherapy (EBRT)

D. S. K. Sihono[1], S. Kegel[1], H. Wertz[1], J.-B. Heggemann[1], F. Lohr[1], F. Wenz[1]
[1]University Medical Center Mannheim, University of Heidelberg, Department of Radiation Oncology, Mannheim, Germany

Related questions: 3D ultrasound (US) provides a radiation-free method for soft tissue detection and positioning and allows online intermodality image registration at treatment planning CT. As for all high precision patient positioning systems geometric performance parameters such as robustness of isocenter placement/alignment accuracy play a major role. As part of the quality assurance (QA) program, an end to end test is an ideal tool to check the overall system accuracy and integrity. In this study, system integrity quality assurance with an end to end test based on a phantom study was performed for the 3D ultrasound system Clarity (Elekta, Canada) for image guided radiotherapy to check if the system meets common criteria and requirements.

Material and procedure: The Clarity system consists of 3D ultrasound devices in both the CT-Simulator (Clarity-Sim) and treatment rooms (Clarity-Guide). To quantify the accuracy of the implicit registration between CT and US image and also positioning and tracking of Clarity system, the Clarity QA phantom was scanned in CT and US at the same position in CT-simulator room. Two different probes were used: transabdominal ultrasound (TAUS) and transperineal ultrasound (TPUS) probe. TPUS is a motorized probe positioned (robotic solution) at the patient's perineum that can track the prostate and surrounding anatomy during treatment. Two positions of the phantom were used for TPUS, the vertical and the horizontal position. CT and US datasets were implicitly registered in the Clarity workstation. The differences in registration were analyzed for left-right (LT/RT), anterior-posterior (ANT/POST), and inferior-superior (INF/SUP) directions. The reference positions for positioning and tracking were defined in the Clarity workstation. Several positions/shifts of the phantom were acquired using Clarity-Guide. The differences in positioning and tracking were analyzed for LT/RT, ANT/POST, and INF/SUP directions.

Result: The geometric positioning tolerance for Clarity-Sim and Clarity-Guide is 1 mm according to the manufacturer's specifications. The results showed that all phantom and probe combinations met this criterion. The mean results and standard deviations for the positioning errors are shown in table 1.

Probe and phantom position	Clarity	LT/RT (mm)	ANT/POST (mm)	INF/SUP (mm)
TAUS – vertical	Clarity-Sim	0.2 ± 0.3	0.2 ± 0.3	0.2 ± 0.4
TPUS – vertical	Clarity-Sim	0.2 ± 0.3	0.1 ± 0.2	0.4 ± 0.5
TPUS – horizontal	Clarity-Sim	0.4 ± 0.5	0.3 ± 0.5	0.6 ± 0.4
TAUS – vertical	Clarity-Guide	0.1 ± 0.1	0.2 ± 0.2	0.2 ± 0.1
TPUS – vertical	Clarity-Guide	0.4 ± 0.3	0.2 ± 0.1	0.3 ± 0.3
TPUS – horizontal	Clarity-Guide	0.2 ± 0.2	0.3 ± 0.2	0.3 ± 0.1
TPUS – horizontal	Clarity-Guide tracking	0.3 ± 0.2	0.2 ± 0.1	0.1 ± 0.1

Tab. 1. The accuracy of Clarity system

Summary: The system tests based on the standard QA phantom showed that the overall geometric accuracy of the Clarity 3D ultrasound system fulfilled the requirements and were inside the acceptance criteria. From a technical point of view the system seems to be a suitable alternative method for precise image guided patient positioning without additional imaging dose.

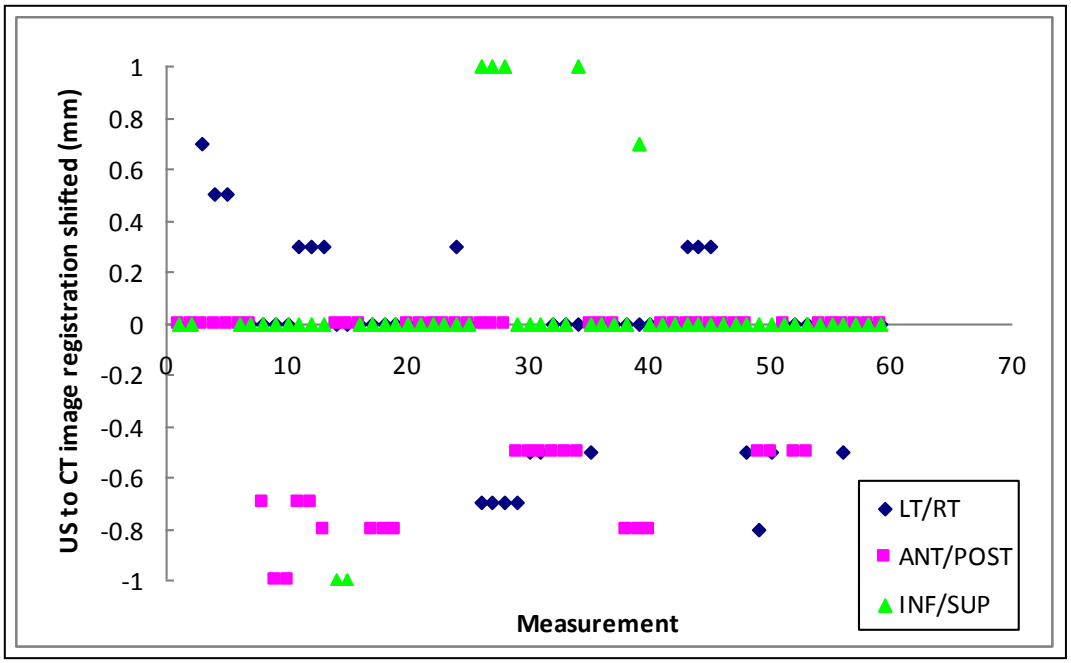

Fig. 1: US to CT image registration shifted of vertical phantom scanned by TAUS

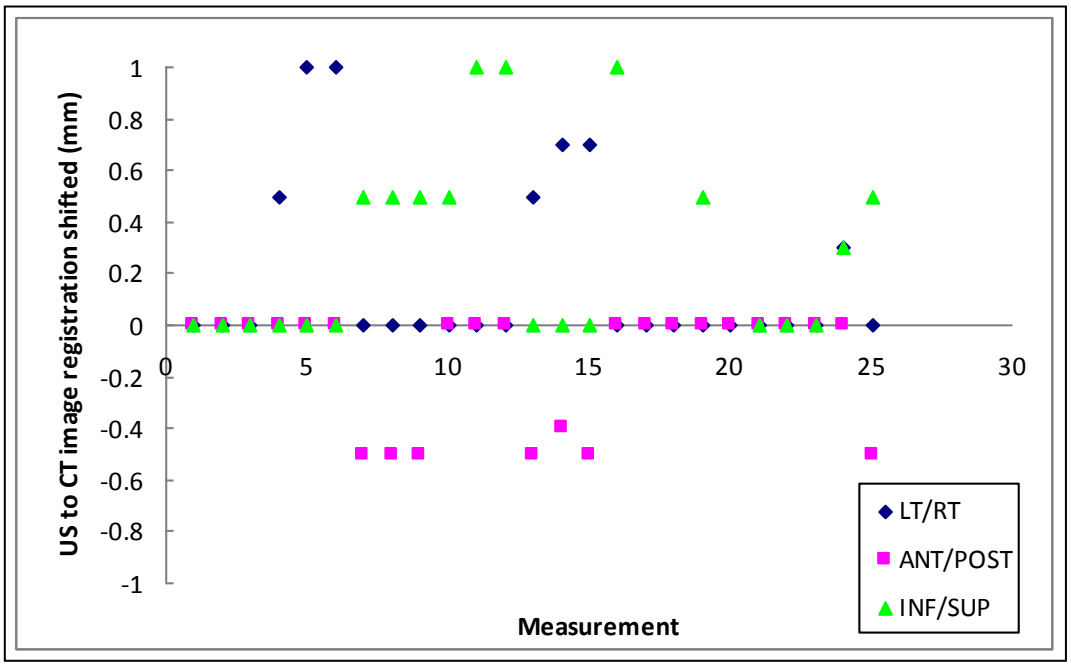

Fig. 2: US to CT image registration shifted of vertical phantom scanned by TPUS

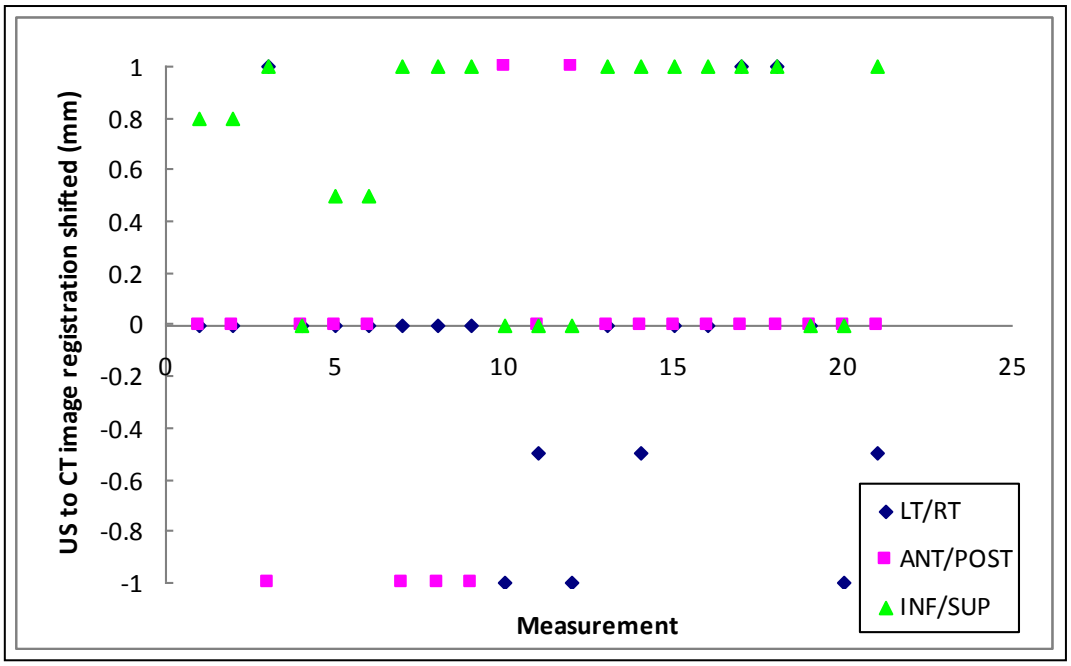

Fig. 3: US to CT image registration shifted of horizontal phantom scanned by TPUS

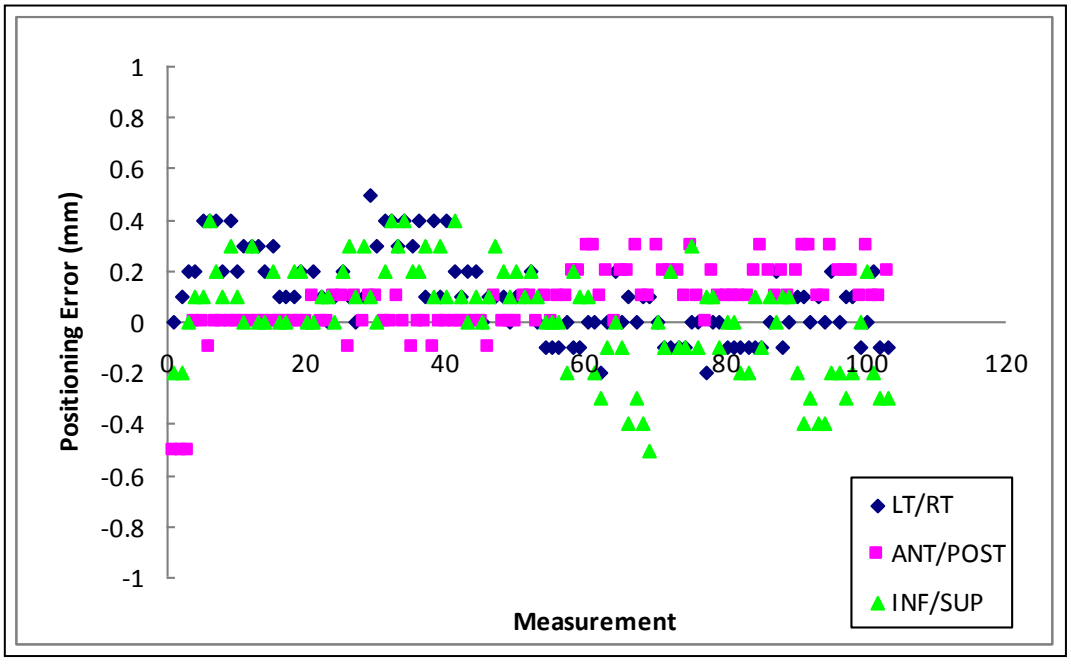

Fig. 4: Positioning errors of vertical phantom scanned by TAUS in treatment room

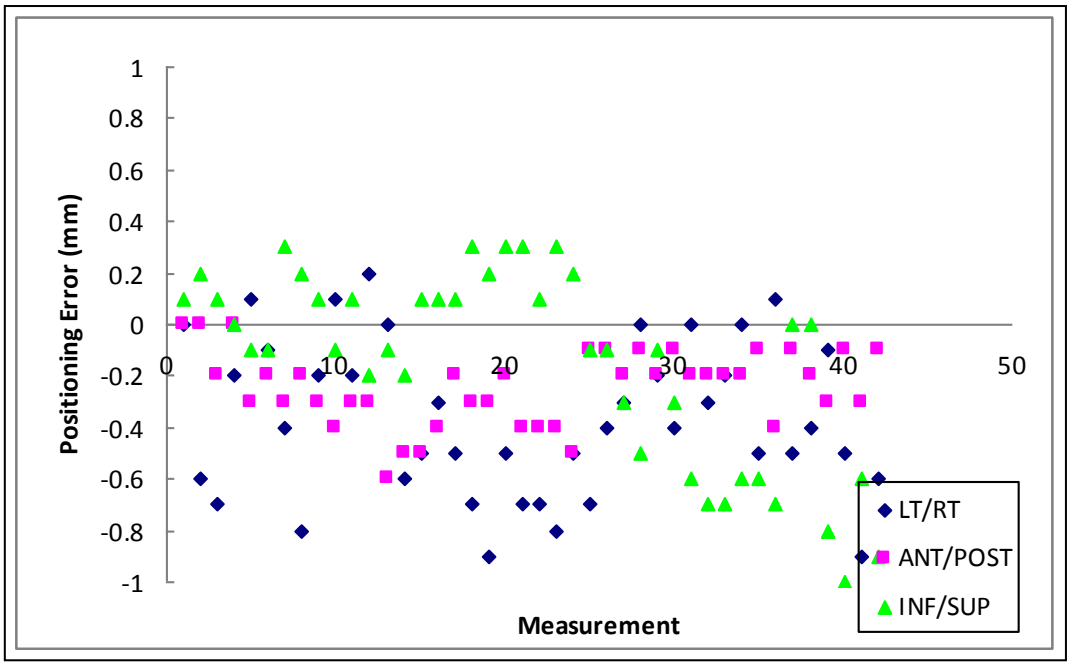

Fig. 5: Positioning errors of vertical phantom scanned by TPUS in treatment room

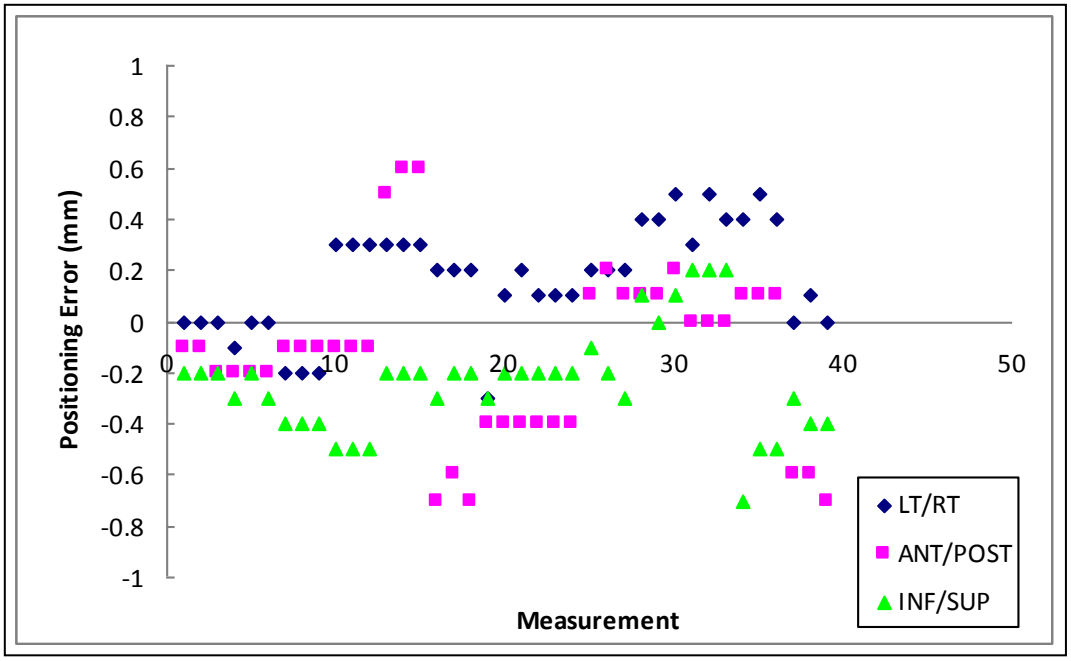

Fig. 6: Positioning errors of horizontal phantom scanned by TPUS in treatment room

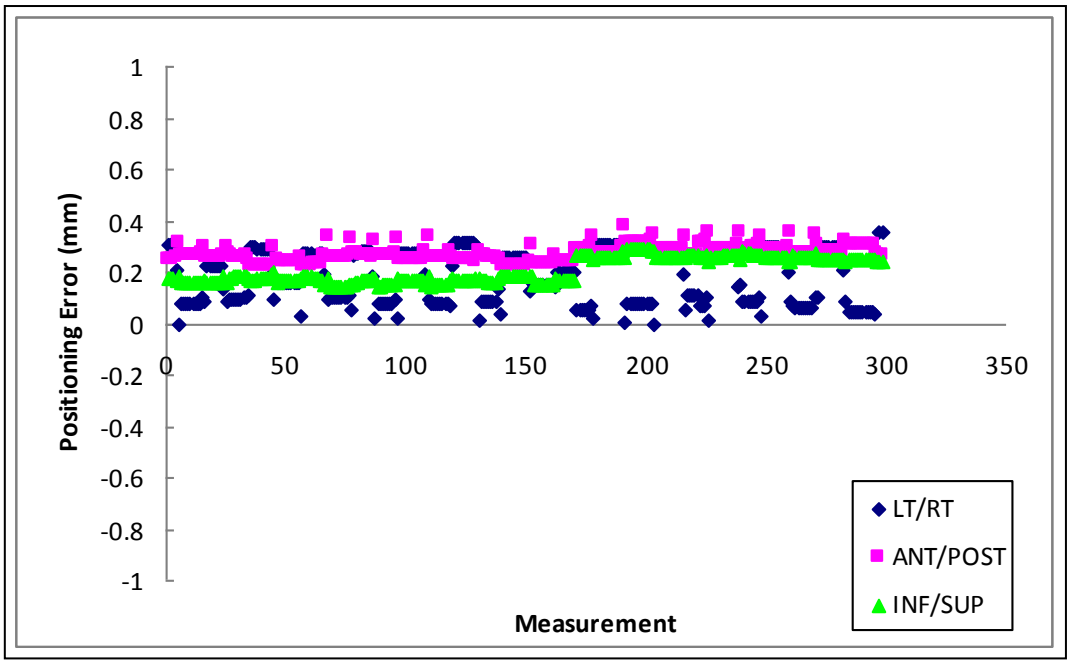

Fig. 7: Tracking position errors of horizontal phantom scanned by TPUS in treatment room

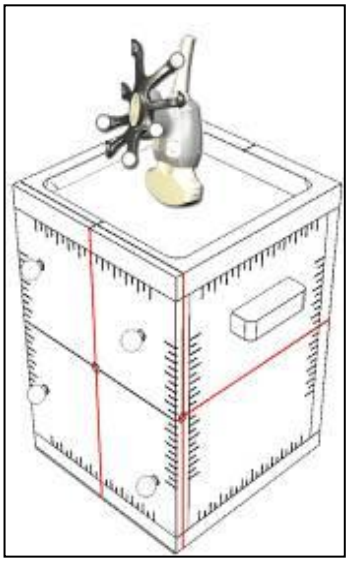

Fig. 7: Vertical phantom with TAUS

Fig. 8: Vertical phantom with TPUS

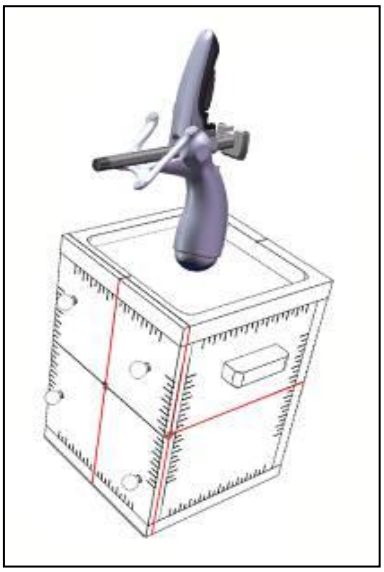

Fig. 9: Horizontal phantom with TPUS

References

[1] Wolfgang A. Tome and Nigel P. Orton. Quality assurance of ultrasound imaging systems for target localization and online setup corrections. Int. J. Radiation Oncology Biol. Phys., 71 (2008), S53-S56.

[2] Clarity Software Version 3.0 User Guide, Elekta Ltd, Montreal, Canada, 2012

109 Implementation of the workflow for an MR-guidance study

A. Pfaffenberger[1], T. Bostel[1,2], G. Echner[1], M. Stoll[1], P. Mercea[1], P. Haering[1], G. Grossmann[1,3]
[1]German Cancer Research Center (DKFZ), Heidelberg, Germany
[2]University Hospital, Heidelberg, Germany
[3]Ortenau Klinikum, Offenburg-Gengenbach, Germany

Objective: Several groups worldwide have started to pursue the realisation of magnetic resonance image-guided radiation therapy (MRgRT). Its potential arises from the excellent soft-tissue contrast of MR imaging and its lack of ionising radiation combined with the possibility to perform time-resolved examinations and monitor physiology. Dedicated devices have been designed that integrate MRI with linear accelerators [1,2,3] or cobalt sources (ViewRay Inc., USA) while other approaches use a trolley (shuttle) from the MR-scanner to the linear accelerator [4] or a mobile magnet solution [5], aiming to learn more from and adapt the treatment to daily variations in morphology and physiology of both the tumour and surrounding healthy tissues. Recently, we have launched a clinical study to evaluate the safety and clinical feasibility of daily shuttle-based MRgRT, compare it with our standard kV-CBCT-guided workflow, analyse suitable MR sequences, evaluate support and immobilization devices, acquire daily diffusion-weighted images to find indications of physiological modifications connected to tumour response, acquire perfusion images of cancerous tissues under therapy and assess the possibilities of using MR-guidance for adaptive radiation therapy [6]. Moreover, methods of automated image registration and evaluation are being investigated. First experiences from the implementation of the clinical workflow are presented in this contribution.

Materials and methods: Both the treatment planning CT as well as the daily fraction CBCTs are supplemented with 1.5T MR images (all Siemens Healthcare, Germany) in treatment position. The patients are immobilised by means of a vacuum mattress that is fixed to a PMMA frame connected to a Zephyr MR Patient Transport Stretcher (Diacor, USA). The PMMA frame is equipped with an “A”-shaped hose filled with contrast agent visible both in CT and MR images that is located posterior to the patient. Fig. 1 displays the frame and its T2 image in the coronal plane. A second, anterior frame is fit over the patient, containing another “A”-shaped hose to which PinPoint® markers (Beekley Medical, USA) are added to evaluate the feasibility of automated image registration between CT and MR images based on these different structures. Additionally, PinPoint® markers are placed on defined points on the patient skin, such that uncertainties of patient re-positioning based on the marks on the external frame as well as on the skin marks can be assessed. MR sequences selected for the first patients having pelvic tumours, are T2-SPACE and a diffusion weighted sequence, and a built-in 3D distortion correction algorithm is applied.

Results: At the time of abstract submission, four patients with tumours of the pelvis have successfully been treated within the study. The additional MR scans prior to the CBCT and subsequent radiation treatment were well tolerated by the patients. Using the T2-SPACE sequence, imaging voxel sizes of $(1mm)^3$ were achieved within around 6 minutes of imaging time for the entire 3D data set. Due to the superior soft tissue contrast of the T2 images, changes could be observed that are not properly visible in the CBCT images as shown in fig. 2, where the organ delineation of the planning CT image is propagated to the registered CBCT and T2 images of different treatment sessions. Also the diffusion weighted images show variations over the course of treatment. A prototype for automated detection of the PinPoint® markers has further been developed and is ready for evaluation with the patient data. Images from testing the prototype on phantom data are displayed in fig. 3.

Summary: The workflow for a study on the potential of magnetic resonance image-guided radiation therapy has been successfully implemented in our institute. The first images acquired within the study are promising that our protocol involving daily MR imaging will reveal valuable additional information to our standard CBCT-guided protocol. Thorough evaluation will be performed in the coming months, encompassing the quantification of uncertainties associated with immobilisation, transport and image registration as well as from residual MR image distortions. In addition, tools will be developed and evaluated for reliable image registration and contour propagation, and both the workflow and its individual components will be further optimised.

Fig. 1: PMMA frame used in immobilisation and for image registration (left) and its T2 image (right).

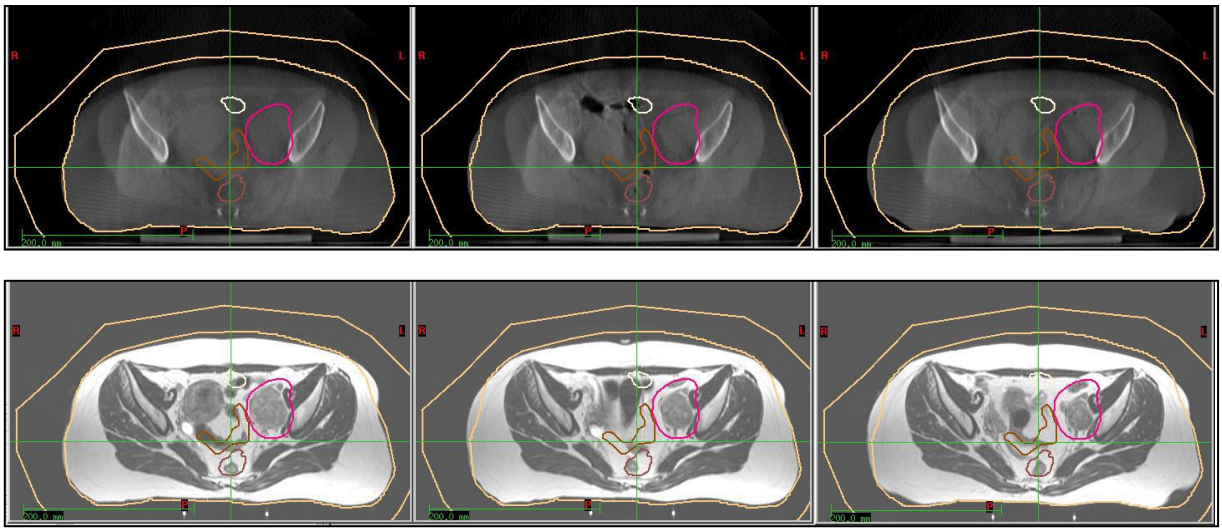

Fig. 2: CBCT (top) and MR T2 (bottom) images of treatment sessions 6, 11 and 16 (from left to right), where the contours are propagated from the treatment planning CT.

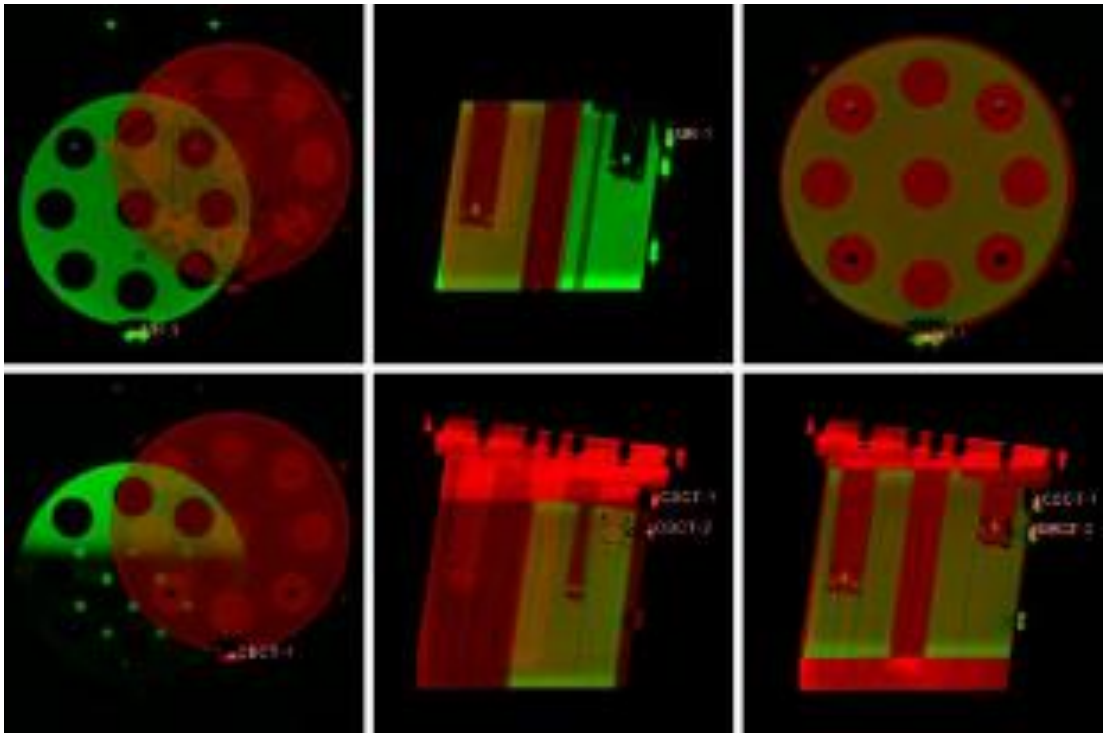

Fig. 3: Phantom registration based on the detection of PinPoint® markers.

References

[1] B.W. Raaymakers et al. Integrating a mri scanner with a 6 mv radiotherapy accelerator: dose deposition in a transverse magnetic field. Phys Med Biol, 49:4109-4118, 2004.

[2] B. Fallone et al. Development of a linac-mri system for real-time art. Med Phys, 34:2547, 2007.

[3] D.E. Constantin et al. A study of the effect of in-line and perpendicular magnetic fields on beam characteristics of electron guns in medical linear accelerators. Med Phys, 38(7):4174-4185, 2011.

[4] M. Karlsson et al. Dedicated magnetic resonance imaging in the radiotherapy clinic. Int. J. Rad. Onc. Biol. Phys., 74 (2): 644–651, 2009.

[5] D.A. Jaffray et al. Image-guided radiation therapy: emergence of MR-guided radiation treatment (MRgRT) systems. Proc. SPIE 7622, Medical Imaging 2010: Physics of Medical Imaging.

[6] T. Bostel et al. MR-guidance – a clinical study to evaluate a shuttle-based MR-linac connection to provide MR-guided radiotherapy. Radiation Oncology 9:12, 2014.

110 Proton Radiography as a Tool for Imaging in Proton Radiotherapy

N. Ghazanfari[1], M.-J. van Goethem[2], M. van Beuzekom[3], T. Klaver[3], J. Visser[3], S. Brandenburg[1], A. Biegun[1]
[1]KVI-CART, Mathematic and Science, Groningen, Netherlands
[2]UMC Groningen, Groningen, Netherlands
[3]Nikhef, Amsterdam, Netherlands

Related questions: In radiotherapy with proton beams high conformity of the dose distribution with the tumor volume can be achieved because protons deposit most of the dose at the end of their trajectory. Due to this high conformity the dose deposited in healthy tissue can be up to a factor of 2 to 5 lower than in conventional X-ray radiotherapy [1]. The quality of the treatment with protons critically depends on accurate predictions of the proton stopping powers of the traversed tissues. Nowadays, proton treatment planning is based on stopping power information derived from X-ray Computed Tomography (CT) images. The conversion of HU values from the CT to proton stopping powers has systematic uncertainties in the calculated proton range in a patient of approximately 3-4 % and even up to 10 % in regions containing bone [1-7]. The inaccuracies may in certain cases lead to no dose at all in parts of the tumor or a very high dose in Organ-At-Risks (OAR) and other normal tissues [2, 8]. A direct measurement of the proton stopping power by transmission radiography of high-energy protons will make it possible to reduce these uncertainties significantly and will thereby improve the quality of dose delivery, which is expected to have a positive impact on treatment outcome (higher tumor control, less serious complications).

Materials and methods: Several studies theoretically showed that the best way to obtain a sufficiently accurate radiography image is by tracking individual protons traversing the phantom (patient) [2, 7]. In our studies we take benefit of the novel gas-filled time projection chamber (GridPix), being developed at the National Institute for Subatomic Physics (Nikhef) in The Netherlands, to track a single proton entering and exiting the phantom. For current studies the dimension of the prototype detector is 3x3x1.4 cm^3, which will be later enlarged to a size required in clinics. A BaF2 calorimeter has been used to measure the proton residual energy. To obtain transmission radiographs, different phantom geometries and materials have been irradiated with a 3x3 cm^2 scattered proton beam with the energy of 150 MeV, produced by the AGOR cyclotron facility of the University of Groningen. The experiment was simulated using the Geant4-based simulation package TOPAS [9]. Exploiting the multiple Coulomb scattering, energy straggling and the initial energy of a proton beam can affect the radiography image quality in terms of contrast and spatial resolution both the energy and scattering angle radiographs have been studied.

Result: First results for both energy and scattering angle radiographs, for different geometries and materials, show a good agreement between simulated (App. 2.a) and experimental (App. 2.b) energy radiographs, as presented in the example for the trapezoid brass wedge phantom with a polycarbonate (PC) cylindrical inserts (App. 2.d). Exploiting the multiple Coulomb scattering that affect the position resolution of the proton traversing the tissue, a simulated scattering angle radiograph has been also analyzed. It also represents well the shape of the phantom (App. 2.c). The sharp edge of the phantom and the transition between the brass and PC material are clearly seen in both types of radiograph.

Summary: We conclude that the first results of the simulated and experimental energy radiographs, where single protons are detected before and after the phantom, are in a good agreement. The first approach to obtain a scattering angle radiograph has been done as well and it is being further developed. The analysis merging both types of radiograph is ongoing to finally obtain the accurate values of stopping powers, which are critical in proton therapy treatment. More complex geometries will be studied in the future.

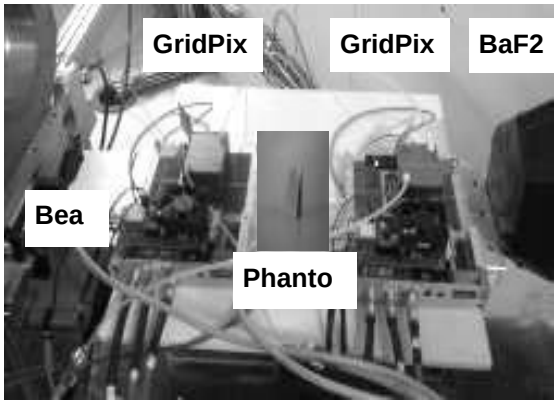

Fig. 1: The experimental set-up of proton radiography experiment. Two position detectors (GridPix1 and GridPix2) together with the calorimeter (BaF2) are shown. The phantom is placed between the position detectors.

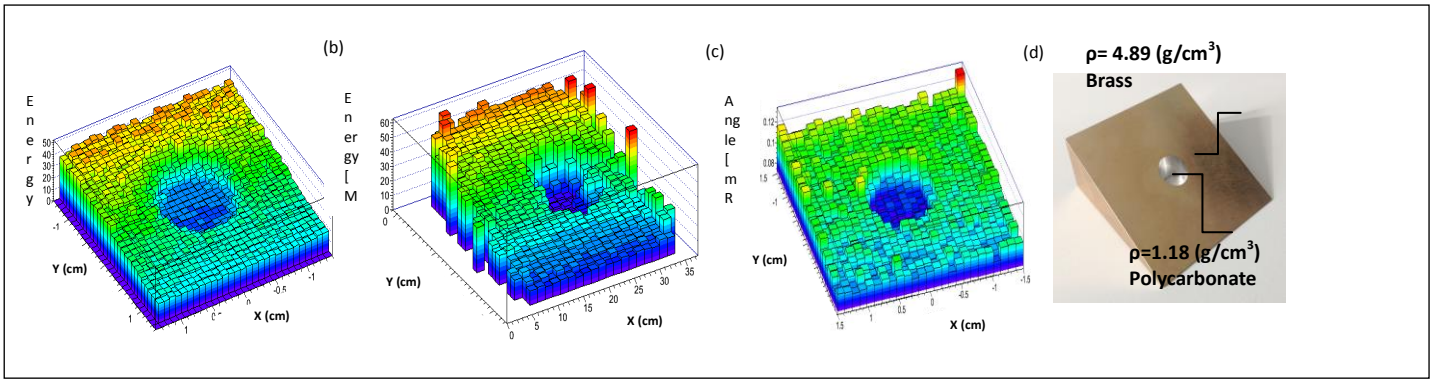

Fig. 2: Simulated (a) and experimental (b) energy radiographs and scattering angle radiograph (c) from the brass trapezoid phantom with polycarbonate (PC) cylinder insert in the middle (d).

References

[1] Schneider, U., Pedroni, E.: Proton radiography as a tool for quality control in proton therapy, Med. Phys. 22(4) (1995) 353-363

[2] Plautz, T. et al.: 200 MeV Proton Radiography Studies with a Hand Phantom Using a Prototype Proton CT Scanner, IEEE NSS/MIC (2012) R04-R24

[3] Schneider, U., Pedroni, E., Lomax A.: The calibration of CT Hounsfield units for radiotherapy treatment planning, Phys. Med. Biol. 41 (1996) 111-124

[4] Schneider W., Bortfeld T., Schlegel W.: Correlation between CT numbers and tissue parameters needed for Monte Carlo simulations of clinical dose distributions, Phys. Med. Biol. 45 (2000) 459-478

[5] Paganetti, H.: Range uncertainties in proton therapy and the role of Monte Carlo simulations, Phys. Med. Biol. 57 (2012) R99-R117

[6] Landry, G. et al.: Deriving concentrations of oxygen and carbon in human tissues using single- and dual-energy CT for ion therapy applications, Phys. Med. Biol. 58 (2013) 5029–5048

[7] Cirrone, G. et al.: The Italian project for a proton imaging device, Nuclear Instruments and Methods in Physics Research Section A: Accelerators, Spectrometers, Detectors and Associated Equipment, 576 (2007) 194-197

[8] Knopf, A-C., Lomax, A.: In vivo proton range verification: a review, Phys. Med. Biol. 58 (2013) R131-R160

[9] Perl, J. et al.: TOPAS-An innovative proton Monte Carlo platform for research and clinical applications, Med. Phys. 39 (2012) 6818-6837

111 TOF-PET scanner configurations for quality assurance in proton therapy: patient case studies

P. Dendooven[1], F. Diblen[1,2], T. Buitenhuis[1], D. Oxley[1,3], A. Biegun[1], S. Brandenburg[1], A. van der Schaaf[4], A. van der Borden[4], A. van 't Veld[4], S. Vandenberghe[2]
[1]University of Groningen, KVI-Center for Advanced Radiation Technology, Groningen, Netherlands
[2]Ghent University-IBBT-IBiTech, MEDISIP, Department of Electronics and Information Systems, Ghent, Belgium
[3]Paul Sherrer Institut, Center for Proton Therapy, Villigen, Netherlands
[4]University Medical Center Groningen, Department of Radiation Oncology, Groningen, Netherlands

Related questions: To evaluate the clinical benefit of positron emission tomography (PET) for in-vivo dose delivery verification in proton therapy (see e.g. [1] for an overview of this subject), we simulated patient irradiation plans and subsequent PET imaging in order to compare in-situ with in-room time-of-flight (TOF) PET.

Material and procedure: Geant4-based [2] Monte-Carlo simulations of the treatment plan of typical patient cases were performed to obtain the distribution maps of the production of the 7 most relevant PET isotopes. Radioactive decay during irradiation is taken into account; biological washout is not. GATE [3] is used to simulate PET imaging, with coincidence resolving time (CRT) and limited angular coverage (in case of the in-situ partial-ring scanner) applied to the GATE output data.

Both in-room and in-situ scanner geometries and scan protocols were investigated. The in-room scanner is modeled after a state-of-the-art full-ring PET scanner. Two in-situ scanner geometries were considered: a partial-ring scanner that is, apart from the limited angular coverage, identical to the in-room scanner, and a flat-panel dual-head scanner placed close to the patient. Identical PET block detectors containing 4x4x22 mm^3 LSO crystals and the same axial length (18 cm) were considered for all scanners. A scan duration of 120 s is considered in all cases. For the in-situ options, scans start with zero delay after the end of the irradiation; for the in-room option, delays of 30 and 60 s are considered.

The quality of the PET images is quantified by means of the Pearson Correlation Coefficient (PCC) between the PET image and the PET isotope decay activity distribution; it is a measure of the fidelity of an image with respect to the activity distribution that is imaged.

Result: For the typical head-and-neck case investigated, the maximum number of detected coincidences, 3.36 million for a Spread-Out-Bragg-Peak physical dose of 0.46 Gy in one posterior treatment beam, is obtained for the full-ring in-situ clinical scanner (note that this is not a practical geometry due to the need for proton-beam access to the patient). The flat-panel dual-head scanner detects only 23 % less coincidences, a number comparable to that of a full-ring in-room scanner with a delay after irradiation of about 45 s. An in-situ clinical scanner needs an angular coverage of about 3/4 to acquire the same number of coincidences as the dual-head scanner. For a CRT of 150 ps, a value close to what has recently been obtained with laboratory detector setups [4], similar image quality is obtained in all cases (App. 1).

The PCC vs. CRT (App. 2) is quite constant for the full-ring scanner. For the other, limited-angle, configurations, a better CRT improves the fidelity of the images, more so for the flat-panel dual-head configuration as it has a smaller angular coverage (1/2) than the 2/3 partial-ring scanner. For a CRT of 150 ps, all situations yield the same image fidelity. This results from the fact that time-of-flight information mitigates limited-angle imaging artifacts.

Summary: We conclude that, for a typical head-and-neck case, both an in-situ flat-panel dual-head and an in-room full-ring clinical TOF-PET scanner deliver comparable image quality: they detect a comparable number of coincidences and state-of-the-art TOF capability can eliminate the limited-angle image artifacts of the dual-head scanner. The in-situ dual-head configuration has the advantage of minimizing the effect of biological washout. Given that its detector area is just 1/6th that of a full-ring clinical scanner, it is an economic solution as well. The original treatment plan was also simulated for patients with artificially introduced anatomical changes. The ability to see the effect of the anatomical changes at the distal edge of the irradiation in the TOF-PET images and its relation to scanner geometry, scanning protocol and scanner timing resolution is under investigation. An identical study of other patient cases is in progress.

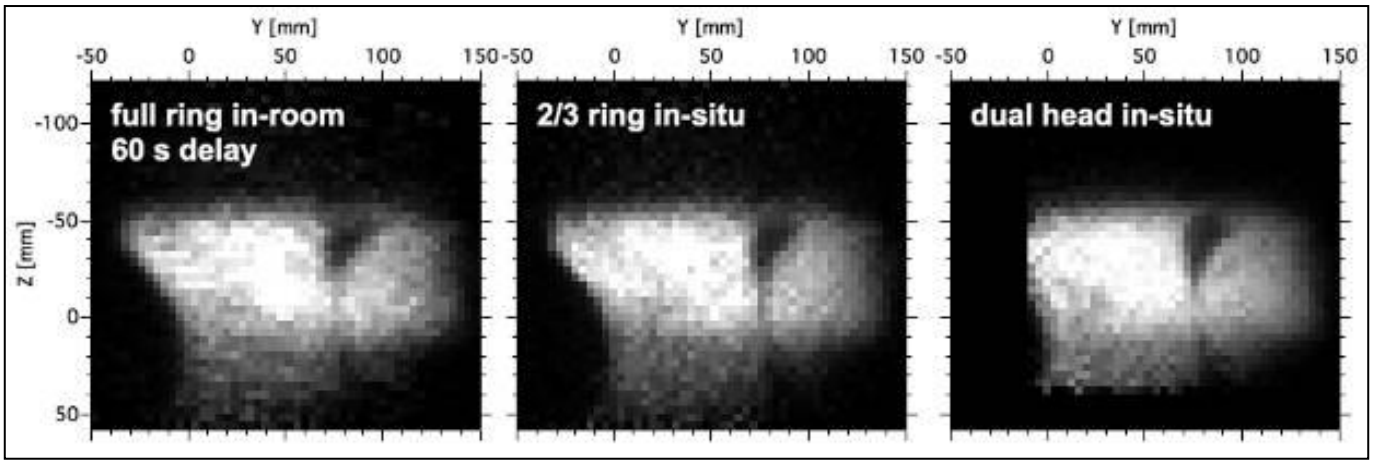

Fig. 1: Sagittal slice through the PET images for different PET scanner geometries/scan protocols for a coincidence resolving time (CRT) of 150 ps. On the left in each image, the outline of the back of the neck is seen. The dark area in the right upper part of the images corresponds to the oral cavity. The dual-head image is somewhat cut on the left and bottom due to the limited field-of-view of the scanner.

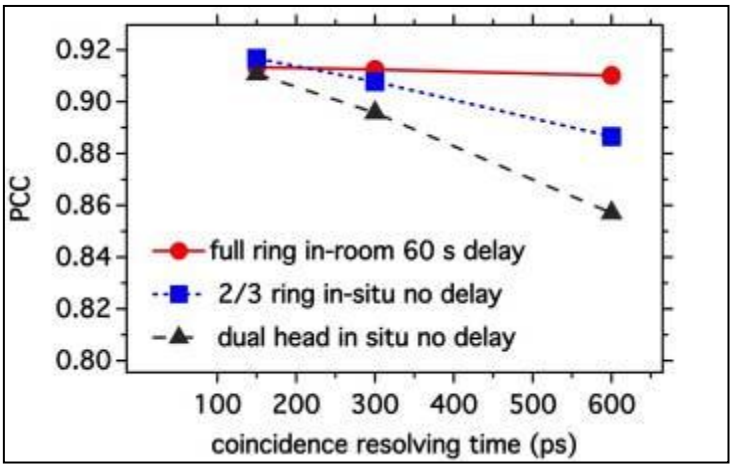

Fig. 2: Pearson Correlation Coefficient (PCC) between PET image and PET isotope decay activity distribution as function of PET scanner coincidence resolving time for different PET scanner geometries/scan protocols.

References

[1] Parodi, K., In vivo dose verification, Proton Therapy Physics (Series in Medical Physics and Biomedical Engineering), ed. H. Paganetti (2011, Boca Raton: CRC Press) p 489

[2] Agostinelli, S. et al.: GEANT4 – A simulation tool kit, Nucl. Instrum. Meth. Phys. Res. A, 506 (2013) S. 250-303

[3] Jan, S. et al.: GATE V6: a major enhancement of the GATE simulation platform enabling modeling of CT and radiotherapy, Phys. Med. Biol. 56 (2011) 881901

[4] van Dam, H. et al.: Sub-200 ps CRT in monolithic scintillator PET detectors using digital SiPM arrays and maximum likelihood interaction time estimation, Phys. Med. Biol. 58 (2013) 3243

Session 19 – Treatment planning and dose calculation in radiation therapy II: Clinical applications

Chairs: M. K. Fix (Bern/CH), U. Wolf (Leipzig/DE)

112 Introductory lecture: On the comparison of dose calculation algorithms

M. K. Fix
Inselspital, University Hospital, and University of Bern, Bern Division of Medical Radiation Physics and Department of Radiation Oncology, Switzerland

The comparison of dose calculation algorithms is one of the main tasks of medical physicists in radiotherapy. These comparisons mainly concern the resulting dose distributions but also include quantities like efficiency. The development of advanced delivery techniques such as intensity modulated radiotherapy or volumetric modulated arc therapy leads not only to more complex dose distributions but also to an increased complexity of the dose comparisons. Additionally, the dose distributions are compared in more than one domain, e.g. the dose domain and the spatial domain. These demands and the use of an increasing number of points to be compared led to numerous metrics. Apart from dose difference and distance to agreement, the gamma index is a very common quantity used for comparing dose distributions, especially for the verification of the complex delivery techniques in radiotherapy.

However, the handling of the gamma index is not trivial. Although it is expected that in dose comparisons a certain fraction of points will typically fail some test criteria, the result of the gamma analysis depends critically on the settings of the parameters for the evaluation. Among others these parameters include the normalization of the dose distribution, the spatial resolution, the analyzed volume of interest and the software implementation. In this introductory lecture some basic approaches used for the comparison of dose calculation algorithms will be provided. Especially some limitations of the gamma index will be presented in order to demonstrate the importance that its settings are carefully applied.

In general, for these comparisons the metrics and the settings of its parameters should be selected such that the purpose of what should be tested can be achieved.

113 Evaluation and implementation of the Acuros XB dose calculation algorithm for clinical radiation therapy treatment planning

M. Buschmann[1], S. Odreitz[1], W. Sprengel[2], P. Winkler[1]
[1]Medical University of Graz, Therapeutic Radiology and Oncology, Graz, Austria
[2]Graz University of Technology, Institute of Materials Physics, Graz, Austria

Introduction: In modern external radiation therapy treatment planning, the dose distribution in a patient is calculated based on a three-dimensional CT scan. The Acuros XB dose calculation algorithm is a new algorithm, which is based on the solution of the linear Boltzmann transport equation and has recently been implemented in the Eclipse treatment planning system (Varian Medical Systems, Palo Alto, CA, USA).

Materials and methods: The algorithm was configured by adjusting the physical parameters, which model the radiation source. The accuracy of the algorithm was evaluated by comparing dose calculations to dosimetric measurements and well-established algorithms. The measurements were performed with ionization chambers and radiochromic films in heterogeneous phantoms upon exposure to 6 MeV photon radiation. The dosimetric impact of using the Acuros XB algorithm for treatment planning in clinical cases was assessed by calculating dose distributions on datasets of real patients and comparison to two established superposition/convolution algorithms (AAA, CCCS).

Results: The dose calculations of Acuros XB in inhomogeneous phantoms were in very good agreement with the measurements. The performance of Acuros XB was equal or better compared to the established AAA algorithm in the same treatment planning system. Especially after air gaps Acuros XB had better agreement than AAA, which overestimated the dose. However, the Acuros XB algorithm showed tendencies to underestimate the dose in some material environments, e.g. in bone tissue. The results of the dosimetric study on clinical cases suggest that the mean dose calculated by Acuros XB in the target volume and the surrounding organs of head and neck tumor patients is 1-3 % lower compared to the two established algorithms. The dose conformity to the target volume in lung tumor patients did not show any significant change when recalculated by Acuros XB.

Discussion: The investigations in this study showed that the Acuros XB algorithm is able to calculate dose distribution with high accuracy in the presence of heterogeneous media, even near interfaces of materials with high density differences. If Acuros XB is used for treatment planning, more dose will be delivered to the tumor assuming that the prescribed dose remains the same. Whether this change would have clinical impact, is subject to further research.

114 Comparison of Intensity-Modulated Radiation Therapy (IMRT) vs. Volume Modulated Arc Therapy (VMAT) Treatment techniques for Breast Cancer: a planning, dosimetric and statistical study

S. C. Chaganty[1,2], C. Willomitzer[2], M. Krüger[2], G. A. Zakaria[3]
[1]Martin Luther University/Anhalt university of applied sciences, Biomedical Engineering, Halle(Saale)/Köthen, Germany
[2]Praxis für Strahlentherapie und Radio-Onkologie,Ruppiner Kliniken, Brandenburg an der Havel, Germany
[3]Akademisches Lehrkrankenhaus der Universität Cologne, Abteilung für Medizinische Strahlenphysik, Gummersbach, Cologne, Germany

Introduction: The purpose of this study is to compare VMAT (RapidArc) plans for Breast cancer patients with intensity-modulated radiotherapy (IMRT) using dosimetric and statistical analysis.

Materials and methods: Simultaneous integrated boost (SIB)-IMRT and SIB-VMAT treatment plans were created for 40 patients (group1) with prescribed dose for PTV1 (boost) as 66 Gy in 33 fractions (2 Gy/fraction) and for PTV2 as 56 Gy in 33 fractions (1.69 Gy/fraction). The treatment plans without boost were created for 40 patients (group2) with prescribed dose 50 Gy in 25 fractions (2 Gy/fraction).Treatment plans were normalized to higher dose PTVs receiving 100 % mean dose. The dosimetric parameters such as conformity index (CI), homogeneity index (HI), uniformity index (UI), dose distributions to the planning target volumes (PTVs) and organs at risk (OARs), normal tissue complication probabilities (NTCPs), tumor control probabilities (TCPs), and secondary tumor mortalities were recorded and analyzed for plan quality evaluation.

Result: For the patient group1, with the use of IMRT technique there were improvements in CI, HI, UI, TCP (%) for the PTV, and NTCP (%) for total lung (ipsilateral+contralateral) when compared to VMAT. On average, the V_{20Gy} (volume receiving more than 20 Gy) of total lung was 16.2$\pm$ 2.9 % for IMRT and 17.5 $\pm$ 4.3

% for VMAT technique. The mortality due to secondary malignancy in normal tissue also showed higher values with VMAT when compared to IMRT. In contrast, for the patient group2 with the use of VMAT, CI, HI, TCP (%) for the PTV and NTCP (%) for total lung (ipsilateral+contralateral) showed improvements. While, the UI decreased, when compared to IMRT. On average, the V_{20Gy} (volume receiving more than 20 Gy) of total lung was 14.4 $\pm$ 5.4 % for IMRT and 12.6 $\pm$ 2.5% for VMAT technique. The mortality due to secondary malignancy was more with IMRT when compared to VMAT. 3D-dose distributions showed that the contralateral breast is receiving more doses with VMAT than with IMRT for both groups. However, the NTCP (%) for other surrounding organs did not show significant differences with both treatment techniques for both patient groups, except for lungs.

Summary: IMRT for breast cancer treatment may be suitable in the case of SIB with 66 Gy as prescribed dose, in comparison to VMAT, which can increase the TCP (%) and reduce NTCP (%); while, VMAT is feasible in the case of 50 Gy as prescribed dose without boost, which can reduce the treatment time and can improve the treatment outcome.

115 First clinical application of mARC treatment

Y. Dzierma[1], F. Nüsken[1], N. Licht[1], J. Palm[1], S. Kremp[1], C. Rübe[1]
[1]Universitätsklinikum des Saarlandes, Klinik für Strahlentherapie und Radioonkologie, Homburg, Germany

Introduction: The Siemens mARC technique [1,2] has recently been introduced as an analogue to volume modulated arc therapy (VMAT, [3,4]), but with a somewhat different philosophy and technical implementation. In contrast to continuous mode delivery as achieved by VMAT, the mARC beam is switched on only around the optimization points while the MLC remains static and the gantry moves along an arclet of a few degrees, the maximum width of which is determined by the user ("burst mode" [10]). At the end of the arclet, the beam is turned off while the MLC and gantry move to the next configuration. Depending on the monitor units to be irradiated in each arclet, the Artiste firmware automatically adjusts gantry speed, dose rate, and arclet length (within the defined upper limit) to provide an optimum between speed and accuracy.
The mARC upgrade was installed at the Department of Radiation Oncology of the Saarland University Medical Center at the end of 2012. After extensive dosimetric testing and plan evaluation, the technique was applied to clinical practice and has been in use since then. The aim of this work is to present the commissioning and validation of the system, and examples of the clinical applications. To our knowledge, this is the first presentation of patient treatment with this technique.

Materials and methods: Treatment planning at our institution is usually performed in the Philips Pinnacle TPS; however, at installation, only the Prowess Panther TPS v5.1 provided mARC planning. We therefore followed two approaches: a) commissioning of Prowess Panther, b) development of an algorithm to convert Pinnacle IMRT plans into mARC [5].

Dosimetric verification was made in two steps: firstly, the accuracy of mARC dose delivery was assessed by comparison with step-and-shoot plans. Secondly, the agreement of the TPS calculated dose with the delivered dose was verified by measurements of the 3D dose distribution by PTW Octavius 729 2D-Array with rotation unit.

We present the first 12 patients treated with mARC at our institution, providing a heterogeneous collective including different tumour entities and planning methods.

Results: For symmetrical target volumes (e.g., brain metastases, prostate), a single arc with optimization points spaced every 10° or 12° yields conformal plans with short treatment times. In more complicated cases, the spacing of the optimization points needed to be decreased or hybrid fields were added, which interrupt the arc to deliver several segments from one gantry angle (similar to step-and-shoot). Very complex target volumes such as in the head-and-neck region require more than one arc to achieve a good dose distribution, resulting in treatment times comparable to IMRT.

For mARC treatment, we could create highly conformal dose distributions of comparable or better quality than our alternative IMRT or 3DCRT backup plans, and a reduction in monitor units as compared with IMRT treatment. The treatment time ranges between 2 and 5 minutes for a single arc (depending on the choice of 6 MV or FFF 7 MV energy and the inclusion of hybrid fields), similar to the observations from a retrospective study [6].

Plan verification measurements of the 3D dose distribution were carried out for each patient before treatment using the 3D gamma index. For all single arcs tested at our institution, over 95 % of the points passed the 3D-gamma criteria of 3 % local dose deviation and 3 mm to agreement (above 20 % maximum dose).

Conclusions: The mARC offers a rotational IMRT treatment option for Siemens linear accelerators. Although treatment times are still longer than for VMAT/RapidArc, mARC offers faster treatment delivery than IMRT, with single-arc treatments of only a few minutes achieving comparable dose distributions to IMRT plans taking up to twice as long.

References

[1] Kainz K, Chen GP, Chang YW, Prah D, Qi XS, Shukla HP, Stahl J, Li XA (2011) A planning and delivery study of a rotational IMRT technique with burst delivery. Med Phys 38(9):5104-5118.
[2] Salter BJ, Sarkar V, Wang B, Shukla H, Szegedi M, Rassiah-Szegedi P (2011) Rotational IMRT delivery using a digital linear accelerator in a very high dose rate 'burst mode'. Phys Med Biol 56:1931-1946.
[3] Otto K (2008) Volumetric modulated arc therapy: IMRT in a single gantry arc. Med Phys 35(1):310-317.
[4] Teoh M, Clark CH, Wood K, Whitaker S, Nisbet A (2011) Volumetric modulated arc therapy: a review of current literature and clinical use in practice. Brit J Radiol 84:967-996.
[5] Dzierma Y, Nuesken F, Licht N, Ruebe Ch (2013) A novel implementation of mARC planning with automated gantry angle optimization for hybrid fields. Radiat Onc 8:193.
[6] Spahn U, Prott FJ (2013) Erste Erfahrungen mit der modulierten Rotationsbestrahlung mARC amd Linearbeschleuniger ARTISTE. Strahlenther Onkol Suppl 1:62-63.

116 mARC treatment planning using three different treatment planning systems – a comparison

Y. Dzierma[1], F. Nüsken[1], K. Bell[1], N. Licht[1], C. Rübe[1]
[1]Universitätsklinikum des Saarlandes, Klinik für Strahlentherapie und Radioonkologie, Homburg, Germany

Introduction: The modulated arc (mARC) technique [1,2] has recently been introduced to Siemens ARTISTE linear accelerators as an alternative implementation of volume modulated arc therapy (VMAT). In contrast to VMAT treatment, which continuously delivers dose while the MLC and gantry move [3,4], the mARC separates phases of MLC travel from the irradiation of “arclets” with stationary MLC, while the gantry moves continually at variable speed (“burst mode” [2]).

At the time of writing, only two treatment planning systems are certified for mARC planning: Prowess Panther and RayStation; Varian Eclipse will incorporate mARC treatment in the next release. In addition to this, an in-house software was developed to convert IMRT plans from any treatment planning system into mARC format. The purpose of this study is to present differences in planning workflow and plan quality for the three different planning modalities available at our institution, namely Prowess Panther, Varian Eclipse, and Pinnacle with conversion algorithm.

Materials and methods: The mARC was installed at the Department of Radiation Oncology of the Saarland University Medical Centre at the end of 2012. Since then, three different techniques for mARC treatment planning have been implemented in practice:

1. Prowess Panther dedicated mARC planning, with clinical treatment of a number of patients with different tumour entities and a planning study focusing on prostate cancer patients,
2. Varian Eclipse evaluation of the mARC planning module, in direct comparison with the Prowess Panther plans, and
3. Philips Pinnacle IMRT planning using 30-36 beams and 30-40 segments (similar to Quasi-IMAT presented in [5]), converted into mARC format by an in-house algorithm [6], used for comparison with the Prowess plans and for clinical treatment of a small number of patients.

We present the overall planning workflow, which differs between the three systems. We assess the overall plan quality and treatment time for example patients with prostate cancer, brain metastases, head-and-neck cancer and lung cancer.

Results: All three planning methods offer good results for plan quality. Overall, the workflow is clearly most complicated in the case of the Pinnacle IMRT plans with subsequent format conversion. Both Prowess and Eclipse offer direct mARC planning, with several differences in their approach to arc optimization. In particular, the restrictions on optimization point spacing and arclet lengths result in very different rotational scenarios; however, both achieve highly conformal dose distributions. In our experience, Eclipse plans require more monitor units than Prowess, and tend to have somewhat longer treatment times (within one minute) – an effect that decreases when mARC is combined with the high dose-rate flattening-filter-free energy. For some examples, we find that this slight increase in treatment time is offset by increased plan conformality (and better sparing of organs at risk) in the Eclipse plans. Whether this effect is due to the optimization algorithm, arc settings, or the user-friendly planning workflow is still unclear.

Conclusions: We present three different options for mARC treatment planning: IMRT planning with subsequent format conversion into mARC, and direct mARC planning in Prowess Panther and Varian Eclipse. All three methods differ substantially in workflow, restrictions on the arc properties, and overall philosophy. Still, all of them are able to create good quality treatment plans applicable to the clinical practice.

References

[1] Kainz K, Chen GP, Chang YW, Prah D, Qi XS, Shukla HP, Stahl J, Li XA (2011) A planning and delivery study of a rotational IMRT technique with burst delivery. Med Phys 38(9):5104-5118.
[2] Salter BJ, Sarkar V, Wang B, Shukla H, Szegedi M, Rassiah-Szegedi P (2011) Rotational IMRT delivery using a digital linear accelerator in a very high dose rate ’burst mode’. Phys Med Biol 56:1931-1946.
[3] Otto K (2008) Volumetric modulated arc therapy: IMRT in a single gantry arc. Med Phys 35(1):310-317.
[4] Teoh M, Clark CH, Wood K, Whitaker S, Nisbet A (2011) Volumetric modulated arc therapy: a review of current literature and clinical use in practice. Brit J Radiol 84:967-996.
[5]. Alvarez Moret J, Kölbl O, Bogner L (2008) Quasi-IMAT Study with Conventional Equipment to Show High Plan Quality with a Single Gantry Arc, Strahlenther Onkol 185(1):41-48.
[6] Dzierma Y, Nuesken F, Licht N, Ruebe Ch (2013) A novel implementation of mARC planning with automated gantry angle optimization for hybrid fields. Radiat Onc 8:193.

117 Total Body Irradiation (TBI) with TomoDirect TM

H. Salz[1], B. Bohrisch[1], N. Banz[1], T. Wiezorek[1]
[1]Universitätsklinikum Jena, Klinik für Strahlentherapie, Jena, Germany

Background: Modern methods of radiooncology, like IMRT, are used for an increasing number of indications because of better results in conformity, dose homogeneity and dose sparing for organs at risk. For total body irradiations (TBI) such methods are limited because of the large target sizes.
The TomoTherapy® system goes beyond some limitations of classical linacs and allows the use of the advantages of IMRT even for the irradiation of the total body. First experiences using the helical mode have already been reported by other groups [1].
With the new TomoDirect™ modality, the TomoTherapy® system offers a non-rotational option with discrete beam angles. We have investigated this mode for TBI, including treatment planning, dosimetric accuracy and practical aspects. This work describes the new method and discusses initial results of our investigations.

Methods: CTs were performed at a wide-bore CT-Scanner Optima CT580W (GE Comp.). For patients with a body length larger than 1,40 m two CT-Scans are necessary: one head-first and one feet-first. The reasons are the limited range of table motion of the CT and the TomoTherapy® system as well.
Contouring has been done with Oncentra® (Elekta AB), treatment planning has been performed with TomoHD™, Version 1.2.1. The following structures have been created: body, PTV as body without skin (distance to the surface 5mm), eyes, spinal cord, lung, inner lung (distance to thoracic wall 10mm for adults). Additionally, a second target was defined which contains safety margins near the shoulder and superior of the head. If the irradiation is split into a head-first and a feet-first part, two “overlap regions” covering a length of 6 cm are added. Their related position is defined by markers on the upper leg. Up to now six patients have been planned in total (5 adults, 1 child).
Measurements have been done on the TomoTherapy® system to evaluate the range of table motion depending on the height of the virtual isocenter. Furthermore, extensive dosimetric studies have been performed with an Alderson phantom and thermoluminescent rods as well as with an ion chamber Exradin A1SL (Standard Imaging Inc.) and Delta4® (Scandidos AB) for the lower part.
The prescribed dose for the total body is usually 12 Gy, the dose per fraction is furthermore 2 Gy for children (twice daily) or 3 Gy for adults (one fraction per day). The prescribed lung dose is 8 Gy, the mean lung dose has to be less than 9 Gy. Hot spots >110 % in the spinal cord and in the eyes are not accepted.

Results: The treatment plans of six patients show the following results for the head-first plans:
total body: mean dose = 12,09 – 12,33 Gy (average 12,25 Gy), D2 = 12,7 – 13,1 Gy (av. 13,0 Gy), D98 = 11,2 – 11,6 Gy (av. 11,5 Gy). *Inner lung:* mean dose left = 8,29 – 9,03 Gy (av. 8,73 Gy), right 8,22 – 9,11 Gy (av. 8,66 Gy)
A critical point may be the duration of treatment planning. The generation of the beamlets needs 4 to 8 hours, even simple changes of plan parameters are time-consuming. A feasable solution was the introduction of standardized optimization parameters. In our measurements, 12 beams with equally spaced angles are used (small children: 8 angles).
The treatment times (calculated for 2Gy) amount to 29,1 min for the child and 30,5 – 45,9 min (mean 37,9 min) for the adults (n=5). Additional plans in feet-first position are applied faster and amount to 8,2 to 9,8 min for 2 Gy. Because of the fact that for adults normally 3 Gy per fraction are prescribed, the treatment time increases accordingly.
The dosimetric results of the detectors in the Alderson phantom (25 positions) show a deviation of 0,55% (mean). At 15 of 25 positions the accuracy was better than 2 %, the maximum deviation (and the only one >4%) was 4,40 % overdosage in the phantom.

Discussion: The new technique allows a homogeneous dose distribution even near the lung and is very comfortable for patients. The treatment time is acceptable and shorter than our well established linac-based translation method.
Additionally DVH curves can be calculated for the different organs. If head-first and feet-first plans are needed, overlap regions allow a gradual and well defined dose decrease to avoid underdoses between the targets.
As a precaution to mispositioning of the patient or external patient movement, the treatment plan was prepared to allow a positional error of 5 mm – 2 cm in many regions without underdosage in the target. However, the use of TomoDirect ™ demands an accurate immobilization of the patient in a vacuum cushion.
Even if the results of the pre-treatment and the TLD in-vivo measurements on representative as well as on critical position (1 time per patient) are very good, the clinical results should be observed carefully.
Because of the good dosimetric results and the feasible procedure, the TomoDirect ™ modality is used for TBI in our department since January 2014 as the standard technique.

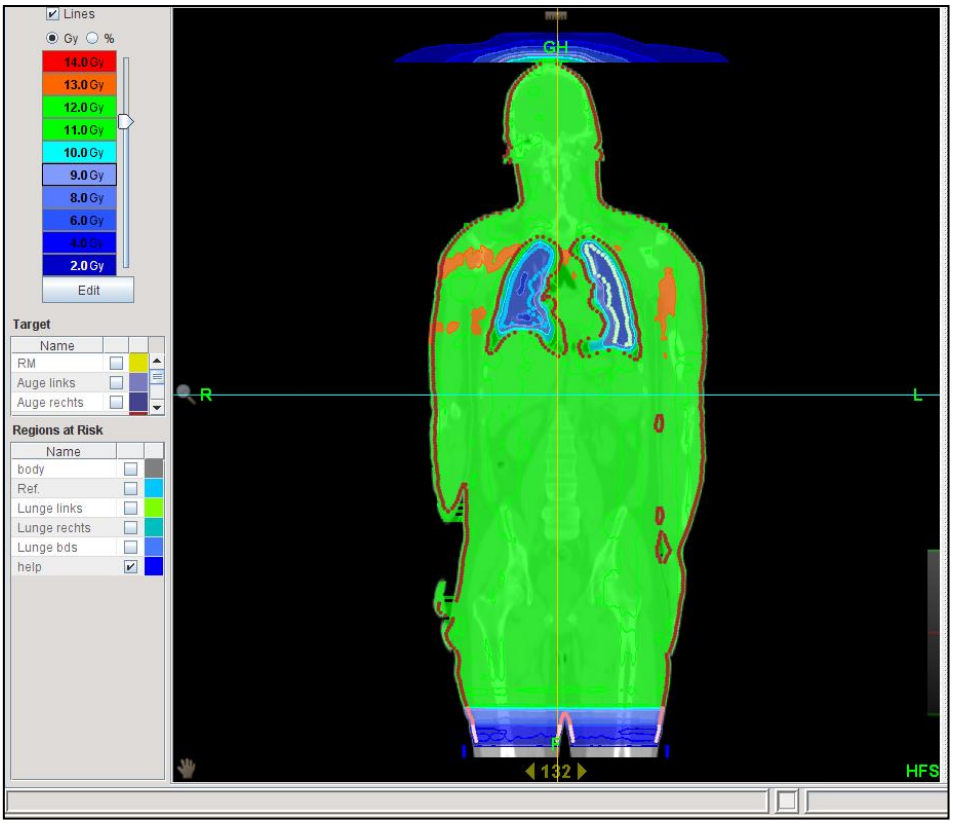

Fig. 1: dose distribution of TBI plan

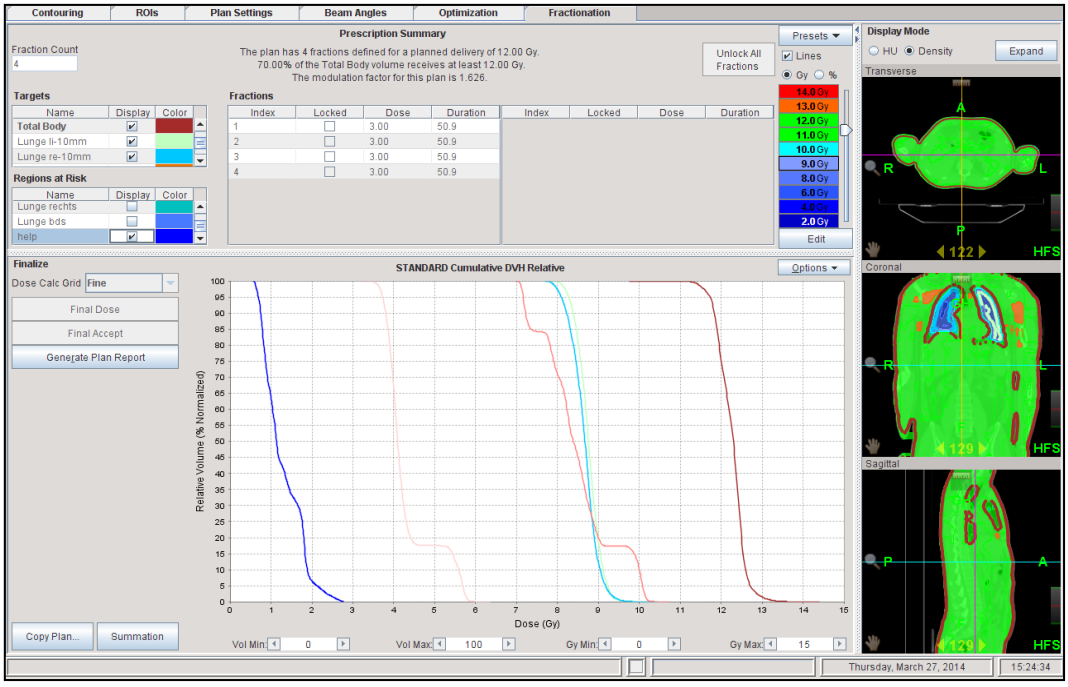

Fig. 2: dose volume histogram of a TBI plan. Colors: red-brown: target, green and light blue – inner lung, pink – overlap (8 and 4 Gy demanded), blue – region beyond the target and overlap regions.

References

[1] Gruen, A. et al: Total Body Irradiation (TBI) using Helical Tomotherapy in children and young adults undergoing stem cell transplantation. Radiation Oncology 8 (2013)

118 A treatment planning solution for Helium ion beam therapy

H. Fuchs[1], B. Knäusl[1], K. Dieckmann[2], M. Alber[3], T. Schreiner[4], D. Georg[1]
[1]Medical University of Vienna/AKH Vienna, Department of Radiation Oncology & Christian Doppler Laboratory for Medical Radiation Research for Radiation Oncology, Vienna, Austria
[2]Medical University of Vienna/AKH Vienna, Department of Radiation Oncology, Vienna, Austria
[3]Aarhus University Hospital, Department of Oncology, Aarhus, Denmark
[4]PEG MedAustron GmbH, Wr. Neustadt, Austria

Purpose:To present a treatment planning solution for scanned helium ion beam therapy (^{4}He) based on the treatment planning system (TPS) Hyperion and to benchmark the results against scanned proton beam therapy.
^{4}He is a promising candidate and its superior biological and physical characteristics compared to protons could potentially improve treatment plan quality. However, ^{4}He was recently not investigated intensively in comparative planning studies, mainly due to the lack of a suitable TPS including a dose calculation algorithm for scanned beam delivery and an appropriate biological model. To investigate the potential benefits of ^{4}He pediatric patients were chose since they would proffer most from a more conformal treatment. The clinical implementation of ^{4}He would be feasible at synchrotron based ion beam facilities and by using a dedicated ion source and by retuning of the beamline and magnets.

Materials: A pencil beam (PB) algorithm for proton therapy (PT) and ^{4}He was developed and implemented in the TPS Hyperion, enabling PB scanned treatment planning for protons and helium ions [1]. The algorithm was based on the theory of fluence weighted elemental pencil beam (PB) kernels. Using a real-time splitting approach, a minimization routine selects the optimal shape for each sub-beam. Dose depositions along the beam path were determined using a look-up table (LUT). Materials other than water were incorporated by using water-equivalent depth scaling. Lateral beam spreading caused by multiple scattering was accounted for by implementing the Highland-Lynch scattering formula. A nuclear correction was modeled using a Voigt function and implemented by a LUT approach.
To model the biological properties of ^{4}He historical data from early Berkley experiments were evaluated [2,3] and also more recent data from cell experiments were taken into account [4]. The RBE model for ^{4}He employed a 'zonal' model based on different LET regions, ranging from 1.1 in the beam entrance area up to 1.3 at the Bragg-Peak. The resulting RBE model was implemented into the TPS Hyperion enabling biological optimized treatment planning for ^{4}He. For PT a constant RBE value of 1.1 was employed in accordance with clinical practice.
Validation of the physical dose calculation was performed employing MC simulations using GATE 6.1. Homogeneous and heterogeneous phantoms were simulated with initial particle energies ranging from 50 to 250 MeV/A and a flux of 107 ions per beam. For comparison a gamma index evaluations were performed for dose distributions employing a gamma index criteria of 2 %/2mm.
In a first planning study 11 pediatric Neuroblastoma (NB), 9 Hodgkin Lymphoma (HL) and 4 Wilms (WT) patients treatment plans based on PB scanning were created. The same beam configuration (1-3 beams from anterior-posterior or lateral direction) was used for ^{4}He and PT. Furthermore, employing the same conceptual dose calculation algorithm for both ions enables a precise comparison without having to account for deviations within algorithms.
The CTV_{NB} and CTV_{WT} included the preoperative GTV and areas of local lymph node enlargement, whereas for WT a boost CTV was defined additionally on macroscopic tumor remainder after surgery. The CTV_{HL} encompassed the involved lymph nodes at diagnosis adapted to post-chemotherapy anatomy. Dose prescription to the PTV (CTV + 0.8-1.5 cm margin) was 21 Gy(RBE) (NB), 14.4 Gy(RBE)+10.8 Gy(RBE) (WT) and 19.8 Gy(RBE) (HL). For patients younger than 14 the vertebral body plus a 5 mm margin was included in the PTV. The PTV size ranged from 220–753 (NB),443-1521 (HL) and 674–548 (WT) cm^3. The WT Boost Volume ranged from 297–566 cm^3.
Depending on the tumor position myelon, kidneys, liver, heart, lungs, breasts and thyroid were considered as OARs.
Treatment plan quality analysis was based on dose difference maps, conformity and homogeneity index (CI, HI), $V_{95\%}$, $D_{2\ \%}$, $D_{98\%}$ and $D_{50\ \%}$ (ICRU83). For OARs DVH related parameters ($D_{2\ \%}$, $D_{50\ \%}$ and V_d values) were investigated.

Results: Results of the gamma index evaluation between MC and PB calculated dose distributions showed very good agreement. For more complex phantoms using laterally arranged bone-air slabs, the γ -index criterion was exceeded in some areas giving a maximum γ -index of 1.75, a γ_{mean} of 0.19 with 4.9 % of all voxels having γ -index values larger than one.
In the treatment planning study more stringent OAR constraints could be used for ^{4}He plan optimization compared to PT. 95 % of the PTV was covered by at least the 95 % isodose. $D_{50\ \%}$ fulfilled the PTV dose prescription in all treatment plans. $D_{2\ \%}$ never exceeded 107 % of the prescribed dose and $D_{98\ \%}$ was always above 90 %. For PT and ^{4}He the CI for NB and HL was 0.90±0.02 and 0.88±0.03 respectively. The HI was comparable for both indications with 0.13±0.01.

In NB $D_{50\ \%}$ for the ipsilateral and the contralateral kidney ranged from 0.5-21.5 Gy(RBE) and 0.1-10.1 Gy(RBE), respectively. On average ^{4}He delivered 13 % less dose to the kidneys$_{NB}$ compared to PT. The liver was spared equally well with an average $D_{50\ \%}$ of 2.1±3.2 Gy(RBE). Regarding the PT plans for 10/11 NB patients 1.6-23.1 % of the voxels received a higher dose than in the corresponding ^{4}He plan (difference > 1 Gy(RBE)). Dose weighted difference maps showed reduced entrance doses for ^{4}He for both indications (see Figure 1 for a representative NB patient).
For HL and WT patients, due to the large PTV sizes, ^{4}He and PT performed comparable with a smaller ^{4}He dose, although differences were not always significant. On average HL patients received more dose to 3.8 ± 4.6 % of all voxels and WT patients to 7.5 ± 2.4 % of all voxels.

Conclusions: The presented treatment planning solution based on the TPS Hyperion was suitable to conduct a treatment planning comparison between PT and ^{4}He. The dose distribution outside the PTV was notably different, especially in the beam entrance region. An improved OAR sparing was observed for ^{4}He for all OARs, which was more pronounced for OARs in the vicinity of target structures. The results motivate a thorough investigation of ^{4}He. Biological experiments need to be performed in order to improve biological dose optimization.

References

[1] Fuchs et al (2013) MedPhys 39: 6726.6737
[2] Raju et al (1971) ActaOncol 10: 353-357
[3] Todd et al (1974) Cancer 34: 1–5
[4] Kase et al (2006) Radiat Res 166(4).

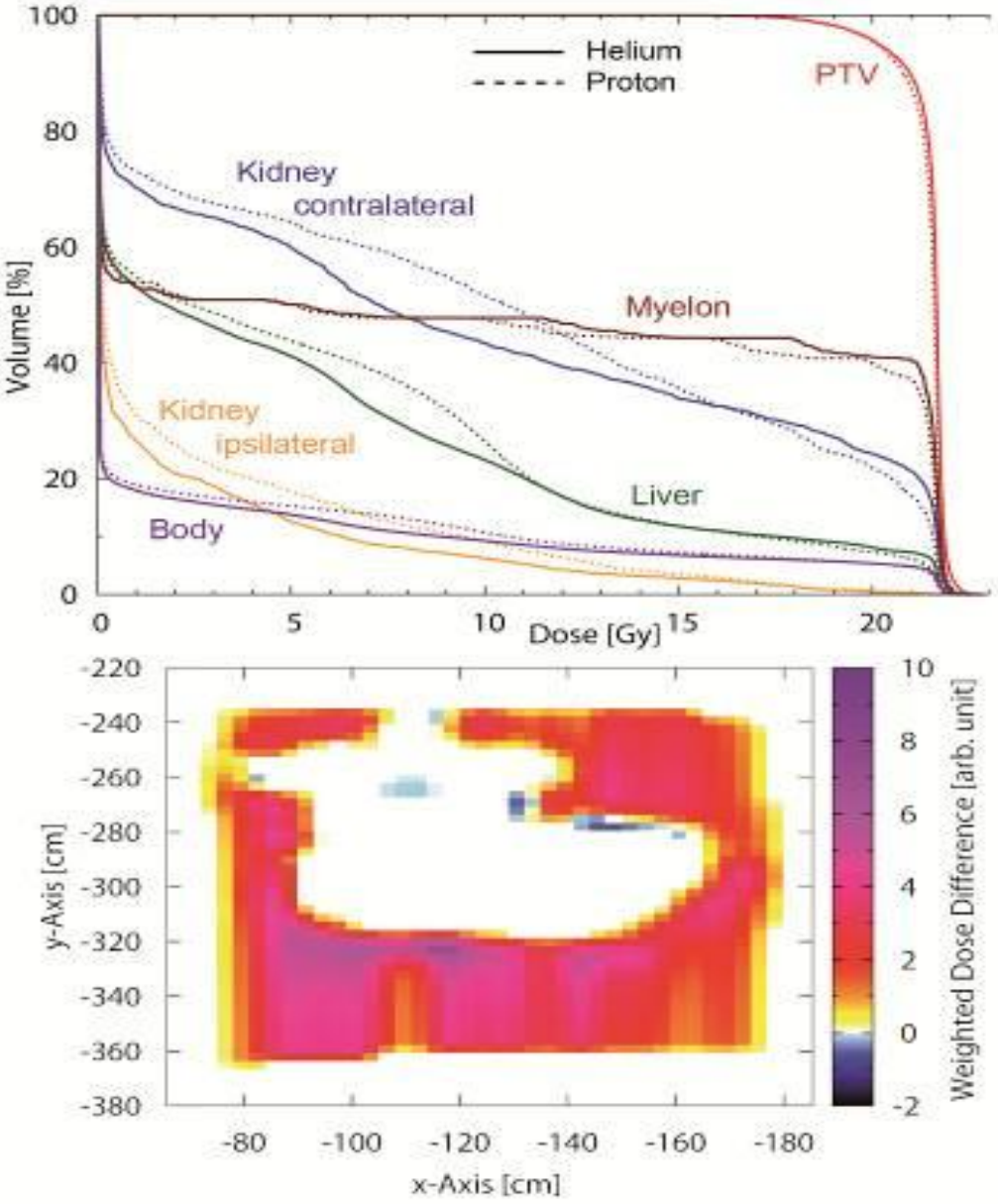

Figure 1: upper: DVH curves for PTV and OARs (kidneys, liver, myelon,body) for a representative NB patient. lower: weighted dose difference map of a proton and helium ion treatment plan slice. Positive values (red) indicate a higher proton dose while negative values (blue) indicate a higher helium dose.

Session 20 – Dosimetry in radio diagnostics and nuclear medicine II: radio diagnostics

Chairs: F. Bochud (Lausanne/CH), G. Stücklschweiger (Graz/AT)

119 Introductory lecture: Dosimetry in diagnostic imaging for radiology and nuclear medicine

G. Dobrozemsky[1]
[1]Vienna, Austria

The aim of diagnostic imaging is the production of data that, when presented to the physician, contains the relevant information for a correct diagnosis. In contrast to the therapeutic application of ionising radiation, any further effect is an unwanted one.
This requires a thorough application of the ALARA principle, which, in it's own course yields low doses, and (mostly) low dose rates.
We therefore have to deal with stochastic effects, where the outcome of radiation on the individual no longer can be predicted-unless a serious accident occurred.

While the dosimetric methods in diagnostic radiology and nuclear medicine are similar to those in the interventional and therapeutic counterparts, some crucial differences apply.

In this lecture the basic methods of dosimetry in diagnostic imaging will be described. Furthermore, the decisive differences between nuclear medicine and radiology, like source strength and exposure time, and their effect on the imaging process and effective dose will be discussed.

The abstract concepts will be examined in the context of specific imaging methods like nuclear medical bone scans, PET scans with nuclides with short and long half-lives, CT scans and tomosynthesis for mammography.

120 Dosimetry of on board imager (OBI) systems – are approaches from CT systems transferrable?

M. Borowski[1], F. Wetzel[1], B. Alikhani[2], L. Büermann[2]
[1]Klinikum Braunschweig, Institut für Röntgendiagnostik, Braunschweig, Germany
[2]Physikalisch-Technische Bundesanstalt, Fachbereich 6.2, Braunschweig, Germany

Motivation: There are numerous systems on the market to produce tomographic images. Beside real computed tomography (CT) systems these are an increasing number of cone beam CT (CBCT) systems, e.g. digital volume tomography (DVT)-systems, angiography units or on board imager (OBI) of radiotherapy systems. Until now there are still partially different measured quantities used in CT and CBCT systems to estimate patient dose, e.g. dose area product (DAP) and computed tomography dose index (CTDI). Further it is an ongoing debate how the CTDI should be measured for wide beam collimations. Within this study the applicability of different approaches to measure the CTDI for OBI was tested in comparison to CT systems. Further, the patient doses as calculated from the CTDI and dose length product (DLP) values were compared for studies covering the same body part.

Materials & Methods: We performed dosimetric studies for full fan and half fan protocols of an OBI (Varian Clinac DHX) and compared the results to those of a CT system with up to 16 cm beam collimation. The dose measurements have been performed using a single and a triple CTDI-phantom setup and 100 mm as well as 300 mm ionization chambers. Free in air measurements have been performed in addition. CTDI values have been calculated and compared a) for the standard setup using a single CTDI-phantom, b) for the setup using a triple phantom and a 100 mm and 300 mm Ionization chamber, c) for the approach to determine the CTDI as specified in IEC 62B/804/CD [1]. From the CTDI and corresponding DLP values estimates for patient doses were calculated using a standard software tool [2] in the actual release.

Results: For both fan modes and phantom sizes reliable values for the CTDI were found up to largest beam collimations when using the IEC approach. The dose portion from overbeaming was found to be larger for the OBI compared to the reference CT system. Dose estimates using the triple phantom and 300 mm chamber were found to be higher by about 30 % compared to the IEC. The dose values displayed along the studies by the OBI system deviated clearly from the measured ones. The reason therefor is an approach used by the company, which deviates clearly from the standard. Patient dose from a single study was found to be around 5 mSv for the half fan and below 1 mSv for the full fan studies.

Conclusion: The applicability of the different approaches to determine the CTDI was tested for one representative OBI system. It was found that the IEC approach is well suited to determine CTDI for this type of system. With the values obtained it was possible to compare the dose to the patient from studies performed at the OBI with corresponding studies from a reference CT system. Using this approach an evaluation of the risk associated with OBI studies is possible on the level of single organ exposures.

References

[1] IEC 62B/804/CD:2010; Medical electrical equipment – Part 2-44: particular requirements for the basic safety and essential performance of X-ray equipment for computed tomography
[2] CT-expo – a novel program for dose evaluation in CT

121 Monte Carlo software for dose calculation in CT examinations

C. Adrien[1], A. Croc De Suray [1], J.-C. Garcia-Hernandez[1], S. Dreuil[2], J. Plagnard[1], B. Poumarède[1], C. Le Loirec[1], J.-M. Bordy[1]
[1]CEA, LIST, Gif-sur-Yvette, France
[2]Institut Gustave Roussy, Villejuif, France

Introduction: The significant rise of medical imaging exams in the past few years has led to an increase of collective doses. The medical physics community agreed that this increase must be accompanied by a better understanding of the origin of the radiation doses and their associated risks. A controversial article announced that around 1.5 % of all cancers in the United States may be due to radiation from Computed Tomography (CT) [1]. Even if this is overestimated, it points out the necessity of using the appropriate tools for evaluating the doses associated to medical exams. Several applications/software have been developed; they provide the usual dose indexes (CTDI, DLP) and effective dose [2]. But only a few research groups are currently developing more specific tools providing organ or tissue absorbed dose [3]. Despite the numerous tools already available, most of them only provide common dose index and effective dose rather than absorbed dose to organs. Therefore our goal is to develop a predictive tool to obtain the best compromise solution for a CT exam exposure with low organ absorbed doses and high image quality.
In this paper, the first stage of this work is presented, that is to say the radiation dose estimations are presented. For that purpose, a Monte Carlo (MC) tool, PENELOPE C++, based on the PENELOPE simulator developed by Salvat *et al* [4] is used. This tool should ultimately enable CT exam simulations in a voxelized numerical phantom mimicking the human anatomy.

Materials and methods: The GE Lightspeed VCT 64 CT tube was modeled by using the method proposed by Turner *et al* [5].
First of all, equivalent spectra were determined for 100 kVp and 120 kVp by using experimental half-value layers (HVL). Measurements were then performed is static mode with a CdTe detector associated with an unfolding method developed by the French national laboratory of metrology for ionizing radiations (LNHB) to achieve experimental spectra and validate the tube model.
Then, equivalent bowtie filter shapes were established by using the Turner method [5].
Ultimately, the axial and helical rotation of the X-ray tube was implemented in the MC tool. To improve the efficiency of the simulation, 2 variance reduction techniques were used: a circular and a translational splitting. The splitting algorithms allow a uniform particle distribution along the gantry path to simulate the continuous gantry motion in a discrete way. To validate the calculation, simulated sinograms are compared with the expected ones and the particle distribution along the gantry path is checked.
The MC tool and the X-ray tube model were then validated for dosimetric purposes. The calculated dose values are expressed in eV/g/shower and then converted into gray as presented in the following equation:
$Dose(Gy) = A * s * 1000 * Dose(eV/g/shower)$
with A, the tube current and s, the exposure time. Experimental dose length product (DLP) were first obtained in a static mode with an Unfors calibrated pencil ionization chamber in a PMMA phantom and compared with simulations for different positions and setups. Validations for rotational modes are in progress.

Results: Equivalent Turner spectra and experimental data obtained with a pediatric body scan field of view (SFOV) are reported in Figure 1 for 120 kVp. Computed and measured spectra shows acceptable discrepancies which could be attributed to a misalignment during measurements (new measurement are in progress). Bowtie filter shapes are reported in Figures 2 and 3. Their equivalent shapes are in agreement with theoretical expectations.
Comparisons between measured and simulated DLP are reported in Table 1 and Table 2 for 100 kVp and 120 kVp, respectively. The experimental and simulated data are in good agreement, with less than 6 % discrepancies for all different acquisition parameters and ionization chamber positions.
Particle distribution for a single gantry rotation is plotted in Figure 4. Simulated and measured sinograms are reported in Figure 5 and Figure 6 in different configurations. The geometric validations are consistent with our expectation.

Summary: The first validations obtained for the use of PENELOPE C++ for CT dose estimations are encouraging. The validation of the rotation motion implementation is part of ongoing research on several phantoms and for several examination procedures in CT exams.

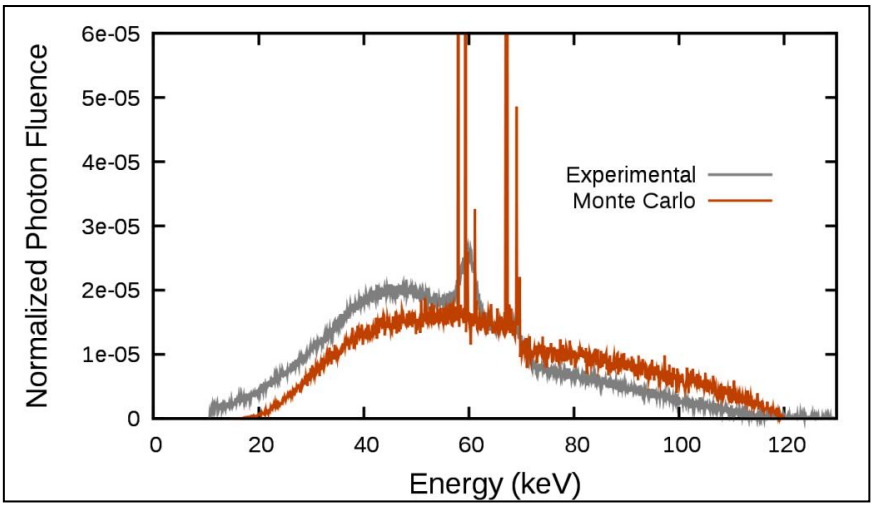

Fig. 1: Experimental and equivalent spectra 120 kVp for the Ped Body FOV.

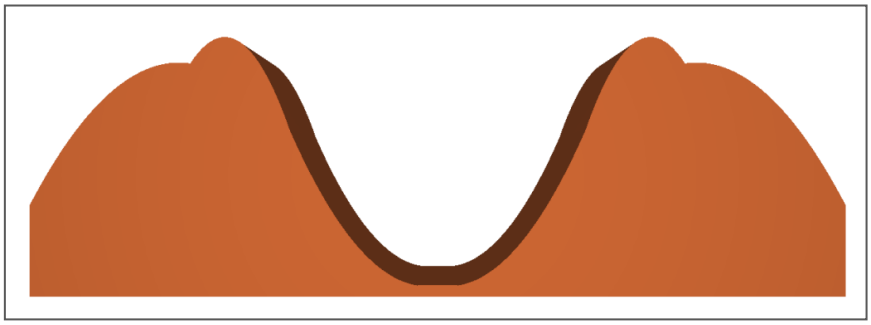

Fig. 2: Ped Body bowtie filter shapes.

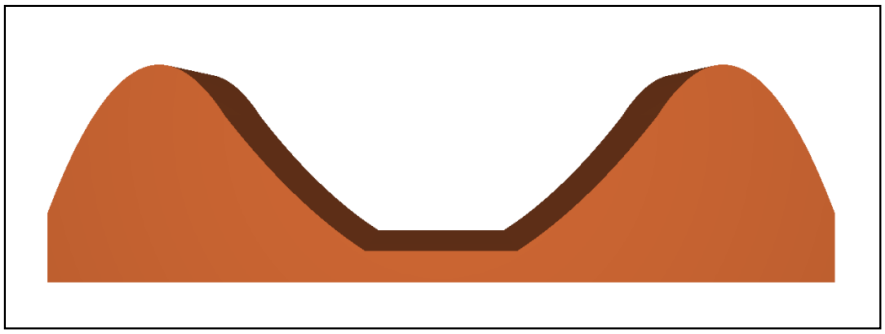

Fig. 3: Large Body bowtie filter shapes.

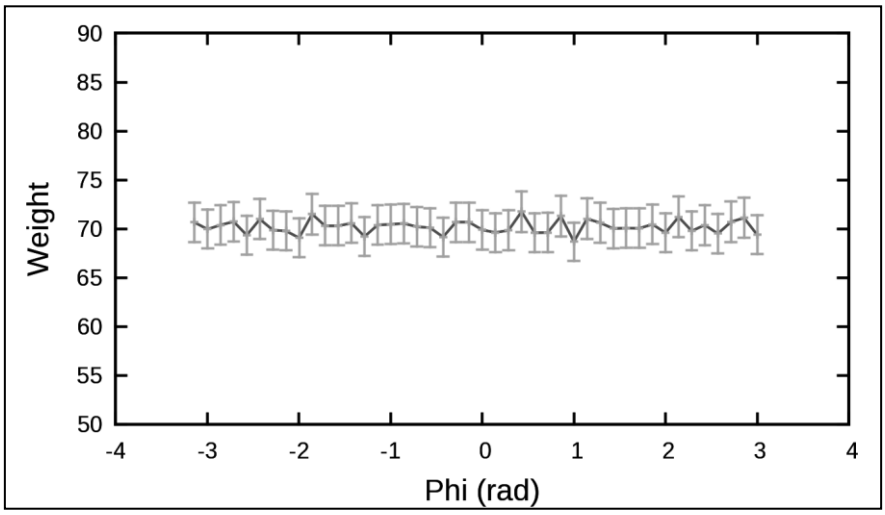

Fig. 4: Circular splitting uniformity for a single gantry rotation.

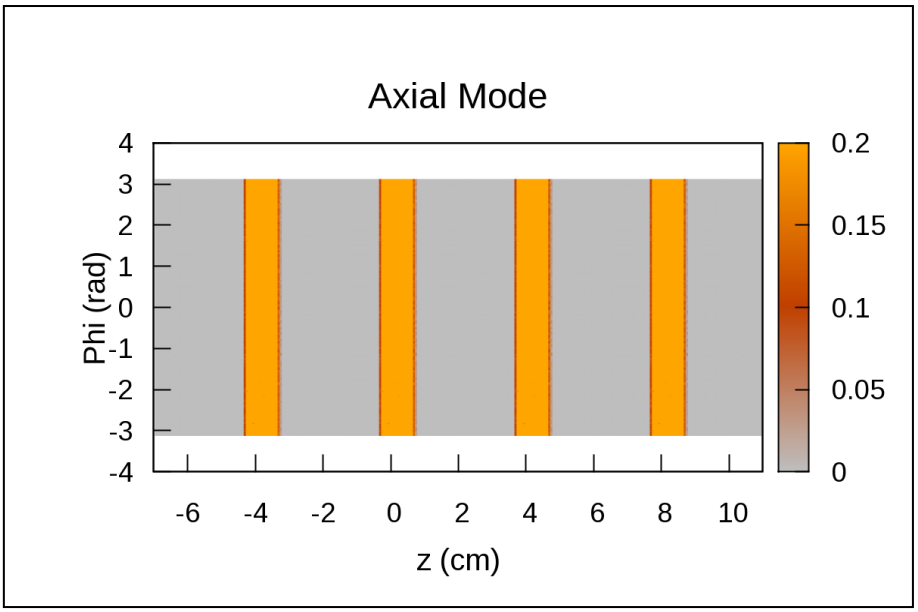

Fig. 5: Spatial particle distribution in axial mode.

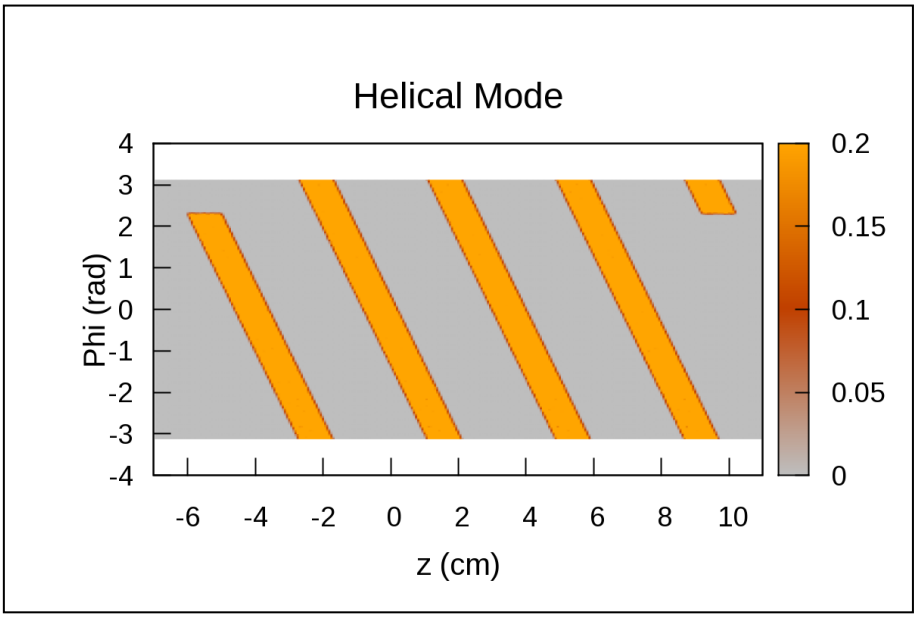

Fig. 6: Spatial particle distribution in helical mode (pitch = 0.95).

Bowtie Filter Type	Measured DLP (mGy.cm)	Simulated DLP (mGy.cm)	Deviation (%)
None	1106.0	1105.9	0.01
Ped Body	937.2	936.6	0.06
Large Body	747.4	722.9	3.27

Tab. 1: Comparison between measured and simulated DLP at 100kVp.

Bowtie Filter Type	Measured DLP (mGy.cm)	Simulated DLP (mGy.cm)	Deviation (%)
None	1063.6	1114.6	4.8
Ped Body	912.6	963.1	5.5
Large Body	763.1	764.1	0.1

Tab. 2: Comparison between measured and simulated DLP at 120kVp.

References

[1] Brenner, D.J., Hall, E.J., “Computed Tomography – an increasing source of radiation exposure”, The New England Journal of Medicine, 357, 2277-2284 (2007).

[2] Osei, E.K., *et al*, “Software for the estimation of organ equivalent and effective doses froom diagnostic radiology procedures”, J. Radiol. Prot., 29, 361-376, (2009).

[3] Li, X., *et al*, “Patient-specific radiation dose and cancer risk estimation in CT: Part I. Development and Validation of a Monte Carlo Program”, Medical Physics, 38, 397-407, (2011).

[4] Salvat, F. *et al*, “PENELOPE 2006, a code system for Monte Carlo simulation of electron and photon transport”, OECD, Barcelona, Spain, (2006).

[5] Turner, C., *et al*, “A method to generate equivalent energy spectra and filtration models based on measurements for multidetector CT Monte Carlo dosimetry simulations”, Medical Physics, 36, 2154-2164, (2009).

122 Implementation of a Monte Carlo based dose calculation model for a differential phase-contrast mammography set-up

S. Garni [1,2], S. Peter[1,2], M. Büchner[1,2], M. Fix[3], M Stampanoni [1,2]
[1] Institute for Biomedical Engineering, ETH Zurich, Switzerland
[2] Paul Scherrer Institute, Villigen, Switzerland
[3] Division of Medical Radiation Physics and Department of Radiation Oncology, Inselspital, Bern University Hospital and University of Bern, Bern, Switzerland

Introduction: X-ray imaging is a standard tool in medical diagnostics. Mammography for example is an important application for the detection and diagnosis of breast cancer, which is based on a good soft tissue contrast. Soft tissue contrast can be improved through the use of differential phase contrast imaging (DPC), which has recently been shown to improve specificity and sensitivity in Mammography [1]. An important aspect of X-ray imaging methods is the dose delivered to the patient, since in diagnostics it may be a limiting factor for instance for exposure time and thus image quality. The aim of this work was the implementation of a numerical simulation model based on Monte Carlo methods for the dose calculation of a DPC mammography set-up.

Materials and methods: Monte Carlo methods (MC) allow the calculation of dose distributions under the consideration of scattering and absorption of electrons and photons in material, making them well suited for numerical simulations of X-ray imaging. A MC model of the mammography set-up has been implemented using egs++[2], a C++ interface for the well established EGSnrc code. Different experimental parameters such as filters, tube voltage, field of view, exposure time, and a number of projections were included within the model. Relative dose distributions in phantoms were calculated for a number parameters and compared.

Results: The results show the relative dose distribution for different phantoms as a function of different set-up parameters. The comparison shows the influence of those parameters on the delivered dose and the dose distribution for several phantom materials.

Conclusion: The influence of different parameters such as filters and tube voltage on the delivered dose and the dose distribution can be determined using the presented simulation model. This allows optimization and improvement of the imaging set-up with respect to patient dose.

References

[1] M. Stampanoni et al. “The First Analysis and Clinical Evaluation of Native Breast Tissue Using Differential Phase-Contrast Mammography”, Investigative Radiology 46, 801 (2011).
[2] I. Kawrakow et al. The EGSnrc C++ class library, NRC Report PIRS-898 (rev A), Ottawa, Canada (2009)

123 Monte Carlo radiography simulation to assess the absorbed radiation dose in femur bone marrow during x-ray radiography for constant mAs technique

Z. Salehi[1]
[1]Department of ADP, KDU University, Petaling Jaya, Selangor, Malaysia

Objectives: The purpose of this study was to find the accurate absorbed dose in the femur bone marrow during the x-ray radiography for constant mAs technique

Method: The DOSXYZnrc was used to simulate two femurs based on the converted CT images to the equivalent digitalized phantom. These phantoms were modified by adding seven micrometre layers of marrow. Thirty billion particles were used in the DOSXYZ code to simulate the X-ray machine. For different filters and energies, the absorbed dose was evaluated

Result: In the head of the femur, for 2.5 mm Aluminium filtered 85 kVp with 50 mAs X-rays, the absorbed dose in the marrow was found to be 1.360 mGy, i.e. 36 % of the absorbed dose in the cortical bone. It was also found that for the constant mAs technique, the radiation dose in the marrow ranges from 0.356 mGy to 2.403 mGy, with higher dose for higher kVp. Also for the typical settings, viz. 85 kVp, 6 mAs at 48 inches SID, the bone marrow absorbed dose was found to be 0.186 mGy for the constant mAs technique.

Conclusion: The absorbed dose in the femur bone marrow for the standard settings of x-ray radiography was accurately calculated.

Advances in Knowledge: The study described a new MC simulation model to calculate the femur absorbed dose for diagnostic X-ray with less than 7 % inaccuracy.

Keywords: DOSXYZ simulation, Bone Marrow, Dosimetry

Session 21 – Functional and molecular imaging

Chairs: T. Beyer (Zurich/CH), M. Hentschel (Bern/CH)

124 Diffusion tensor imaging of the murine brain in cohort studies: an application to APP transgenic mice at 11.7T

H.-P. Müller[1], J. Kassubek[1], I. Vernikouskaya[2], A. C. Ludolph[1], D. Stiller[3], V. Rasche[2]
[1]University of Ulm, Department of Neurology, Ulm, Germany
[2]University of Ulm, Experimental Cardiovascular Imaging, Core Facility Small Animal MRI, Ulm, Germany
[3]Boehringer Ingelheim Pharma, Target Discovery Research Germany, Biberach, Germany

Introduction: *In-vivo* high resolution diffusion tensor imaging (DTI) of the mouse brain is often limited by the low signal to noise ratio (SNR) resulting from the required small voxel sizes. Recently, cryogenically cooled resonators (CCR) have demonstrated significant increase of the effective SNR [1]. It is the objective of this study to enable fast DTI of the mouse brain for cohort studies, as a proof-of-principle in β-amyloid precursor protein (APP) transgenic mice compared to wild-type (wt).

Material and methods: Twelve mice (7 APP transgenic tg2576, 5 wt) underwent DTI examination at 156^2 x 250 μm^3 spatial resolution with a CCR at ultrahigh field (11.7T). Additionally, three wt underwent the same scanning protocol with a brain array coil in order to compare the SNR. Diffusion images were acquired along 30 gradient directions plus 5 references without diffusion encoding with a total acquisition time of 35 minutes. Fractional anisotropy (FA) and fiber tracking (FT) results including quantitative tractwise fractional anisotropy statistics (TFAS – [2]) were compared qualitatively and quantitatively. At the group level, FA maps of APP transgenic mice and wild type controls were statistically compared by whole brain-based spatial statistics (WBSS).

Results: Qualitative and quantitative assessment of the FA maps (Fig. 1a) and FT results (Fig. 1b) showed SNR improvement of the CCR compared to a brain array coil and a coinciding outcome comparing 35 minute scans to the standardized 110 minute scan [3]. At the group level, FA-map showed characteristic regional patterns of differences between APP transgenic mice compared to wt (Fig. 2) with localizations associated with Alzheimer's disease in humans, such as the hippocampus, the entorhinal cortex, and the caudoputamen [4].

Conclusion: Mouse DTI at 11.7T was performed with an acquisition time of approximately 30 minutes which can be considered feasible for *in-vivo* large scale whole brain murine DTI cohort studies. In this proof-of-principle study, regions associated with amyloid-β deposition could be identified by WBSS of FA maps in APP transgenic mice vs. wt mice. Thus, both acquisition and postprocessing of DTI in the mouse brain at 11.7T by use of a CCR was demonstrated to be feasible for cohort studies.

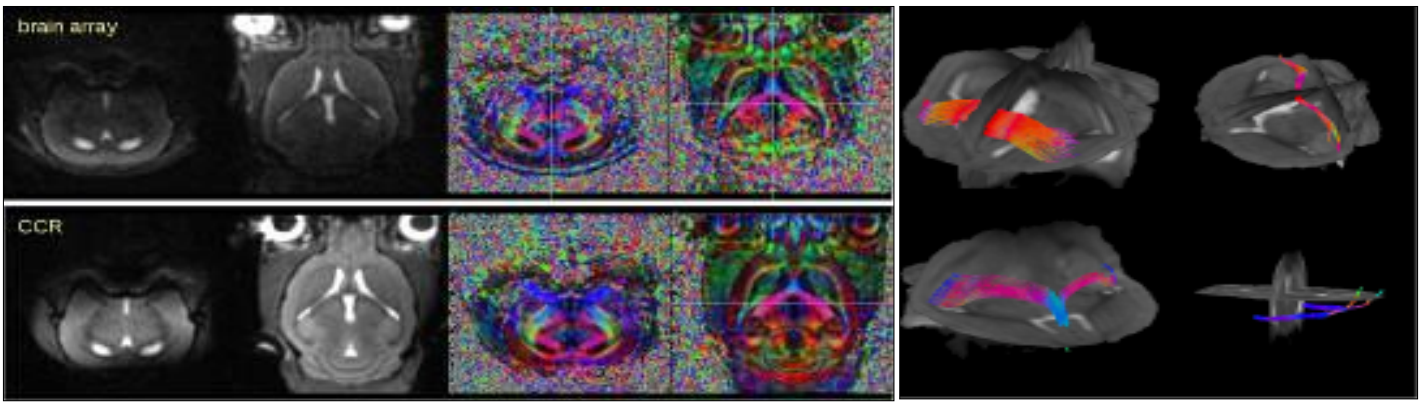

(a) **(b)**

Fig. 1: (a) Brain array coil (upper panel) vs. cryogenic cooled resonator (CCR – lower panel). Right: (b=0) anatomical images used for signal-to-noise ratio (SNR) estimation. Left: Directional encoded color maps of FA. (b) FT results for seed points in the genu and along the corpus callosum, near the lateral septal nucleus, the splenium, and in the olfactory path. display background. was (b=0)-scan.

References

[1] Vernikouskaya I, Wokrina T, Bornstedt A, Rasche V. SNR comparison for high-resolution in vivo imaging @ 11.7T: 4-element surface array coils vs. 2-element cryoprobe. In "Proceeding Annual Meeting DS-ISMRM, Ulm, Germany", 2012.

[2] Müller H-P, Unrath A, Sperfeld AD, Ludolph AC, Riecker A, Kassubek J. Diffusion tensor imaging and tractwise fractional anisotropy statistics: quantitative analysis in white matter pathology. Biomed Eng Online (2007) 6: 42.

[3] Müller H-P, Vernikouskaya I, Ludolph AC, Kassubek J, Rasche V. Fast diffusion tensor magnetic resonance imaging of the mouse brain at ultrahigh-field: aiming at cohort studies. PLoS One (2012) 7: e53389.

[4] Müller H-P, Kassubek J, Vernikouskaya I, Ludolph AC, Stiller D, Rasche V. Diffusion tensor magnetic resonance imaging of the brain in APP transgenic mice: a cohort study. PLoS One (2013) 8: e67630.

125 Automated lesion contouring in PET: Inter-algorithm-variability is a surrogate for contour accuracy

R. Haase[1], F. Lohaus[2,3,4], N. Abolmaali[1,5], K. Zöphel[6], J. Kotzerke[6], M. Krause[1,2,3,4], M. Baumann[1,2,3,4,7], C. Richter[1]
[1]OncoRay, TU Dresden, HZDR, Dresden, Germany
[2]German Cancer Consortium (DKTK), Dresden, Germany
[3]German Cancer Research Center (DKFZ), Heidelberg, Germany
[4]University Hospital Carl Gustav Carus, TU Dresden, Department of Radiation Oncology, Dresden, Germany
[5]Akademisches Lehrkrankenhaus Dresden-Friedrichstadt, Clinic for Radiology, Dresden, Germany
[6]University Hospital Carl Gustav Carus, TU Dresden, Clinic and Policlinic for Nuclear Medicine, Dresden, Germany
[7]Helmholtz-Zentrum Dresden – Rossendorf, Institute of Radiooncology, Dresden, Germany

Aim: In the field of imaging for radiotherapy planning, Positron Emission Tomography (PET) and automated PET-based contouring are increasingly applied techniques. A number of segmentation algorithms for PET have been proposed, validated and compared in the scientific literature. A standard-method is not foreseeable and there is currently no method for estimation of contour accuracy without comparing to reference contours which are often manually-defined. This work outlines a method for estimating contour accuracy by deriving it from an observer-independent measurement of inter-algorithm-variability.

Materials and methods: In a prospective study on [^{18}F]fluorodeoxyclucose (FDG)-PET as biomarker for therapy response in non-small cell lung cancer, 45 Patients were scanned using FDG-PET/CT before start of combined radiochemotherapy. For the following analysis, PET images of the thorax and corresponding PET-based gross tumour volume (GTV) contours, manually-created during radiotherapy planning, were retrieved and processed. A volume of interest (VOI) in the PET data set was defined which encloses the earlier defined GTV and surrounding tissue. For this analysis, four segmentation algorithms earlier proposed [1-4] and an additional swarm-intelligence-based algorithm, which is still in development, were applied to this VOI. The four published algorithms were developed, tested and validated using phantom experiments with homogeneous and spherical simulated target volumes. Thus, it is assumed that in similar clinical cases, the algorithms deliver similar target volume definitions. However, in clinical data sets with inhomogeneous and/or non-spherical target volumes the resulting volume definitions may differ and thus, at least one of the algorithms delivered a contour of worse accuracy. To evaluate the relationship between contour differences, or rather inter-algorithm-variability (IAV), and contour accuracy (CA), the following procedure was applied to the resulting volume definitions: From the five automatically generated contours, three volume definitions were derived: 1) the intersection volume *I* containing all voxels which were defined PET-positive by all algorithms, 2) the consensus volume *C* containing all voxels which were defined as PET-positive by the majority of the algorithms (in this case three of five), and 3) the union volume *U* containing all voxels which were defined as PET-positive by at least one algorithm. A scheme visualising these volumes is presented in Figure 1. The Jaccard-Index *J*, a relative measurement of volume overlap between these volumes, was then calculated pair-wise from the three volumes *I*, *C* and *U*. The measurements *J(U,C), J(U,I)* and *J(C,I)* are representations of IAV. Differences in these volumes may hint to the inability of single or several algorithms to segment the specific data set. Furthermore, the Jaccard-Index of each of these three volumes with the reference GTV *R* was calculated. In default of the knowledge of the true tumour volume, this reference GTV is assumed as the 'gold' standard for the CA determination. The measurements *J(U,R), J(C,R)* and *J(I,R)* are representations of CA of the contours U, C and I, respectively. To investigate the relationship between IAV and CA the Pearson correlation coefficient of the respective *J* measurements was calculated. Afterwards, the median value of IAV related *J* values was defined as a threshold to separate the data sets by their IAV in two groups. Finally, the Mann-Whitney U-test and the criterion for significance $p < 0.05$ were applied to determine if these two groups were significantly different in CA related *J* values.

Results: Exemplarily, the Pearson correlation coefficient of *J(U,R)* compared to *J(U,C)*, *J(U,I)* and *J(C,I)* were 0.71, 0.53 and 0.32, respectively. For *J(I,R)* and *J(C,R)* no better correlation coefficient than 0.68 was achieved. Thus, at least *J(U,C)* appeared to be related to *J(U,R)*. By splitting the data sets in two groups using the median of the *J(U,C)*, two groups resulted, possessing a contour accuracy of *J(U,R)*=37±24 % and *J(U,R)*=64±16 %, respectively. The differences in these two groups were significant with a p-value of 0.00003. A scatter plot visualising the observed relationship between *J(U,R)* and *J(U,C)* and a boxplot of the two groups are shown in Figure 2. Analogously separated groups using median *J(U,I)* and median *J(C,I)* were also significantly different in CA with a p-value of 0.0003 and 0.008, respectively.

Conclusion: The proposed observer-independent method of analysis of the inter-algorithm-variability allowed for estimating the contour accuracy: By measuring the volume overlap between union volume and consensus volume of the majority of the tested segmentation algorithms, a measure was available which was related to the volume overlap between the union volume and the given reference volume. Using this measurement it was possible to separate the contour data sets in two groups: one with limited accuracy of the automatically-generated contours and another with significantly higher accuracy. Thus, the presented method is recommended for automated contour quality assurance. A conceivable application is preselecting automatically-generated contours of low accuracy for review and correction.

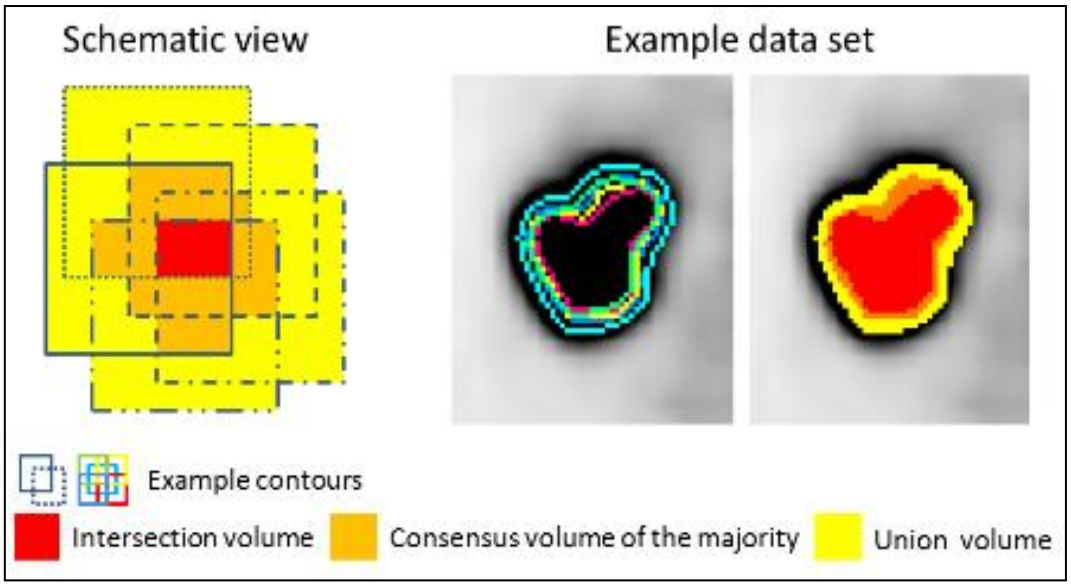

Fig. 1: Schematic view and example data set of the contours derived from five algorithms and their further processing. From the five automatically generated contours, three volumes based on the theory of sets are generated: The intersection, the union and the consensus volume including all voxels which were segmented as PET-positive by the majority of the tested algorithms. The relationship between these three volumes describes the Inter-Algorithm-Variability.

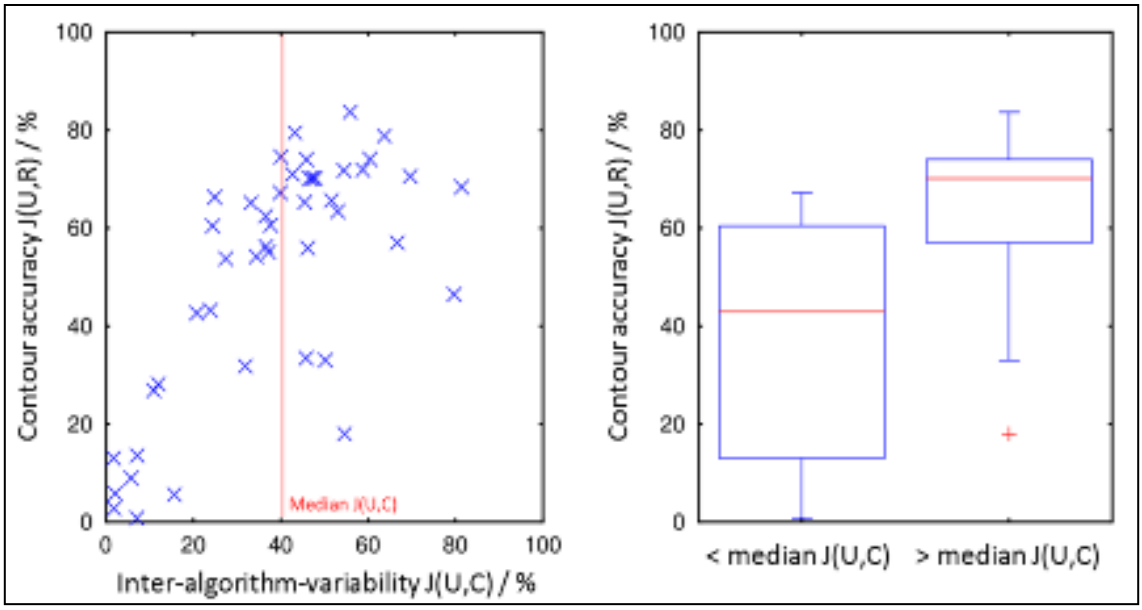

Fig. 2: The scatter plot on the left visualises the observed relationship between inter-algorithm-variability and contour accuracy. Splitting the data sets in two groups by the median J(U,C) threshold resulted in the box plot on the right visualizing the different distribution of contour accuracy in the two distinct groups.

References

[1] S. A. Nehmeh, H. El-Zeftawy, C. Greco, J. Schwartz, Y. E. Erdi, A. Kirov, C. R. Schmidtlein, A. B. Gyau, S M Larson, J L Humm. An iterative technique to segment PET lesions using a Monte Carlo based mathematical model. Med Phys., 36(10), pages 4803-4809, 2009.

[2] R. Haase, H.-J. Böhme, D. Zips, and N. Abolmaali. Swarm Intelligence for Medical Volume Segmentation: The Contribution of Self-reproduction. In KI2011: Advances in Artificial Intelligence, volume 7006 of Lecture Notes on Computer Science, pages 111-1121. Springer Berlin Heidelberg, 2011.

[3] F. Hofheinz, C. Pötzsch, L. Oehme, B. Beuthien-Baumann, J. Steinbach, J. Kotzerke, and J. van den Hoff. Automatic volume delineation in oncological pet. evaluation of a dedicated software tool and comparison with manual delineation in clinical data sets. Nuklearmedizin, 51:9-16, 2012.

[4]A. Schaefer, U. Nestle, S. Kremp, D. Hellwig, A. Grgic, H. G. Buchholz, W. Mischke, C. Gromoll, P. Dennert, M. Plotkin, S. Senftleben, D. Thorwarth, M. Tosch, A. Wahl, H. Wengenmair, C. Rübe, and C. M. Kirsch. Multi-centre calibration of an adaptive thresholding method for pet-based delineation of tumour volumes in radiotherapy planning of lung cancer. Nuklearmedizin, 51:101-10, 2012.

126 Bronchodilatation Effect on Lung Function of Asthma Patients Measured by Static and Dynamic ^{3}He MRI : First Statistical Analysis Results of Open Clinical Study

M. Terekhov[1], U. Wolf[1], K. K. Gast[1], C. Hoffmann[1], N. Bojadzic[1], C. Düber[1], L. Schreiber[1]
[1]Universitätsmedizin Mainz, Klinik und Poliklinik für Diagnostische und Interventionelle Radiologie, Mainz, Germany

Motivation: Hyperpolarized ^{3}He-MRI is known to be an efficient tool to visualize and quantify static (SV) and dynamic Ventilation (DV) of lungs. The spatial and temporal information on regional gas distribution in lungs are available. This makes both methods particularly attractive for the diagnostics of patients with obstructive lung disease, e.g. asthma and COPD. To characterize gas distribution and delivery in the lungs a set of parameters evaluated either directly from the ^{3}He-MR-images (SV) or calculated by analysis of the ^{3}He signal-time profile (DV) [1] are used. However, the relevance of these parameters for the assessment of lung physiology, as well as the statistical significance of its changes under different factors influencing the respiratory function of patient is still not established firmly. Therefore, finding out how the changes of these parameters correlate with clinically proved tests of lung function is a question of great importance for the diagnostic relevance of ^{3}He-MRI results. In the present work measurements of static and dynamic lung ventilation with HP-^{3}He-MRI were performed on bronchial asthma patients before and after bronchodilatation (BD). The particular aim was to find out if the BD-effect can be detected using parameters obtained with ^{3}He-MRI and to correlate the variation of these parameters with the changes in the key values of the pulmonary function tests (PFT).

Materials and methods: In an open monocentric clinical trial performed after approval of the local Ethics Committee 8 (of 12) patients with confirmed bronchial asthma were examined in the first visit. 4 patients finished the study with the 2nd visit (interval 1 year). Each visit comprised two 3He-MRI as well as PFT before and after BD (250µg Salbutamol). The MRI measurements were performed on a 1.5T scanner (Avanto, Siemens, Germany) using a dual-tune ^{3}He/^{19}F birdcage (Rapid Biomedical). The HP-^{3}He (polarization level p=70±2 %) was provided by centralized large scale polarization, delivery and recycling process approved by local Ethic Committee [2]. The ^{3}He:N_2 mixtures (200:300ml for SV and 200:800ml for DV) were administered using a Tedlar bag. The SV images were 14 coronal slices (10mm thickness) acquired using image matrix 128x81 at FOV=400mm. The DV ^{3}He-MR-images series were coronal 2D-projections (128x64 at 400mm FOV) continuously acquired during patient inhalation of a ^{3}He:N2 mixture. This yields ^{3}He signal-time curve $S_p(t)$ recorded at temporal resolution of 7 images per second. The $S_p(t)$ was analyzed on a pixel basis using dedicated Matlab scripts. The evaluated DV parameters were: (1) rise time (RT), denoting an interval required for $S_p(t)$ to rise from 10 % to 90 % of maximum value S_p^{max}; (2) the delivery time TD determined as ($S_p(TD)=0.9 \cdot S_p^{max}$); (3) maximal flow value FM = max($dS_p(t)/dt$). For the SV-images the amount of ventilation defects (VD) were counted in each slice and percentage of non-ventilated lung volume (%nVV) was calculated respectively. For the statistical analysis the mean values of the parameters were used. Statistical tests were performed using Matlab Statistical toolbox and SPSS.

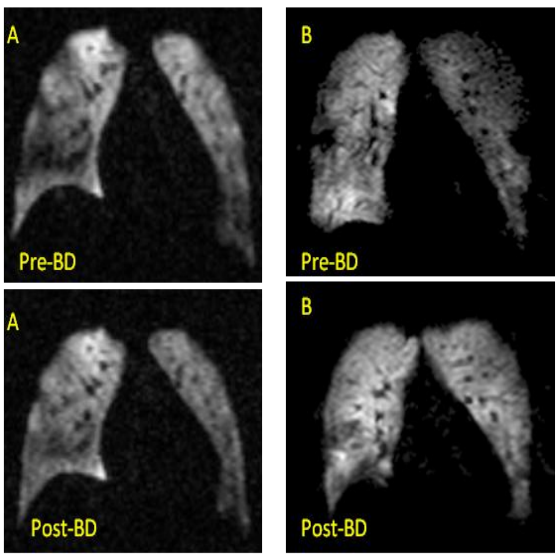

Figure 1. Static ventilation 3He-MR-images of 20 (A) and 53 (B) years old patients with pre-study FEV1= 92% and 72% respectively. Statistically significant (p=0.95) decrease of non-ventilated volume were detected in measurements performed after bronchodilatation.

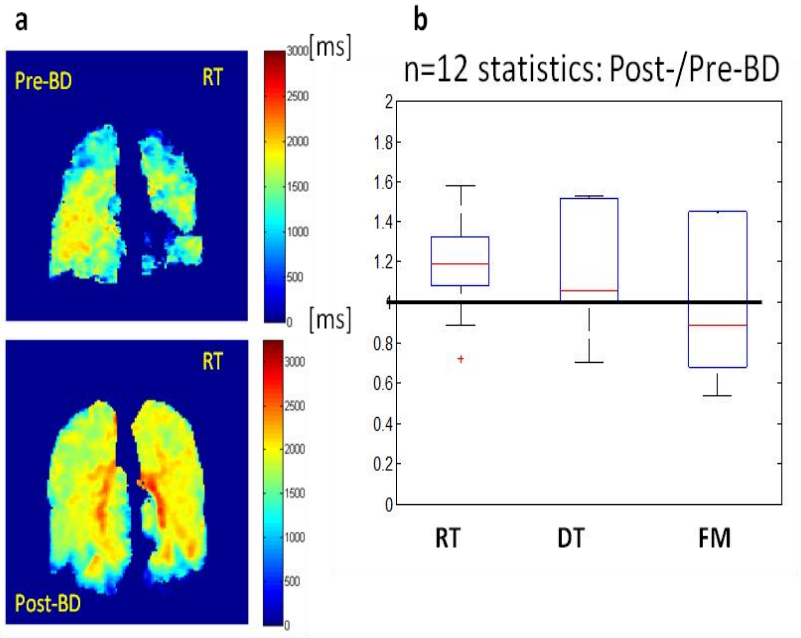

Figure 2. (a) Exemplary dynamic ventilation RT-map of patient (B). An increase of ventilated volume leads to elevation of rise and delivery time.(b) Summarized n=12 patients statistics of DV parameters. Statistically significant (α=0.01) increase for RT and less significant (α=0.2) for DT is found. The significance of maximal flow FM decrease should tested with more patient data to be acquired in further study course.

Results and discussion: Figure 1 demonstrates that the SV-measurements before (Pre-) after (Post-) BD allow for detecting substantial increase of %nVV as the result of medication. The statistical analysis (Wilcoxon test) confirms the hypothesis %nVV(Pre-BD)>%nVV(Post-BD) at α=0.05 significance level. Additionally, the hypothesis for FEV1(pre-BD)>FEV1(post-BD) is confirmed using both t-test and Wilcoxon test (at α =0.05). The results of DV-measurement show an increased mean ^{3}He signal rise time and delivery time after BD. The highest significance level (unpaired t-test, α =0.01) was found for the hypothesis RT increased post-BD. The increase of the mean DT value post-BD is less significant and can be confirmed statistically (paired t-test) only at α =0.2 level. The FM values before and after BD show the largest variance among all calculated DV parameters and its changing (in both direction) post-BD cannot be statistically proved at the significance level better than a=0.4 using actual amount of measured patients data.

Conclusion: Although the trial is not yet finished, several trends can be observed. For the patient data analyzed we confirmed that both SV and DV ^{3}He-MRI allow for detecting statistically significant differences of lung ventilation before and after bronchodilatation. For SV-images the expectable decrease of the non-ventilated volume was observed. The increase of the DV rise-up time is especially remarkable in the region of the large airways (Fig. 2a) for patients with significant initial %nVV. This observation may be explained by longer and deeper inspiration (increased FIV1 and IC).caused by BD. As a consequence, gas inflow impairment is decreased which in turn reduces the absolute maximal flow peaks (FM) within a RT-period. The statistical significance of the later findings should be confirmed in course of the Clinical Study competition.

References

[1] K.Gast et al Intrapulmonary 3He Gas Distribution Depending on Bolus Size and Temporal Bolus Placement. Invest Radiol. 2008; 43(6):439-46.

[2] S. Karpuk et al, Spin polarized 3He: From basic research to medical applications, Physics of Particles and Nuclei, 2013, 44(6): 904-908

127 Systematic Development of a Tracer Specific Cannabinoid-Type1 PET-Template of the rat brain using "DARTEL"

A. Kronfeld[1], H.-G. Buchholz[2], S. Maus[2], N. Afahaene[2], W. Müller-Forell[1], B. Lutz[3], M. Schreckenberger[2], I. Miederer[2]
[1]University Medical Center of the Johannes Gutenberg University, Institute of Neuroradiology, Mainz, Germany
[2]University Medical Center of the Johannes Gutenberg University, Clinic and Policlinic for Nuclear Medicine, Mainz, Germany
[3]University Medical Center of the Johannes Gutenberg University, Institute of Pysiological Chemistry, Mainz, Germany

Introduction: The spatial resolution of positron emission tomography (PET) is – compared to the size of brain structures – poor. This is a challenge especially for small animal PET imaging and subsequent analyses. However, an accurate and reproducible positioning of volumes-of-interest can be achieved by using a template image [1]. Thus, the aim of this study was the development of a tracer specific cannabinoid-type1 (CB1) PET-template based on coregistered magnetic resonance imaging (MRI) data. Therefore the SPM8-toolbox "DARTEL" [2] has been considered, which is already established for human use, and the optimal parameters were determined.

Materials and methods: 5 male Sprague-Dawley rats (age 12 weeks) received an MRI- and 2 days later a PET-examination. MR-imaging was conducted on a Magnetom Trio (3 Tesla, Siemens Medical Solutions, Erlangen) and a small loop coil with a diameter of 4 cm was used. Amongst others, T1- (MPRAGE) and T2- (TurboSpinecho) weighted images were acquired with a resolution of 0.3 mm^3. The measurement time was 55 min for each animal.
The PET-data was acquired using a small animal PET-scanner (Focus 120, Siemens Medical Solutions USA, Inc.). An activity of 20 MBq of the CB1-receptor tracer [18F]MK-9470 was administered and data was acquired during a period of 90 minutes. The PET-data was reconstructed by filtered backprojektion. For further processing, a summed image of the last 30 minutes was used.

After that, all PET- and MRI-images were coregistered using SPM8. To use DARTEL, the individual MRI-images were segmented into grey and white matter [3] and then combined to one dataset (Template). Possible adjustments and their combinations were compared using a covariance-analysis: clean up (no clean up, light clean up, thorough clean up), used partition (grey matter, white matter, both compartments) und regularisation form (linear elastic energy, membrane energy, bending energy)
All spatial manipulations were transferred to the coregistered PET-images.
To receive a symmetric template the original images and their mirrored images were used for the calculation of the template.

Results: SPM8/DARTEL is suitable for the calculation of small animal templates. Figure 1 shows the fused PET-MRI-Template. Visual inspection shows typical accumulations for the [18F]MK-9470-tracer in the grey matter. A pronounced dependency from the chosen SPM8/DARTEL-parameters could not be detected in the covariance-analysis.

Conclusion: A tracer-specific PET and an anatomic MRI-template for the spatial normalisation of small animal CB1-images were calculated with SPM8/DARTEL. The used method works uncomplicated and stable. The developed template allows the matching of appropriate CB1-PET-images and is the base for accurate definitions of VOI and therefore for the quantification of the PET-data.

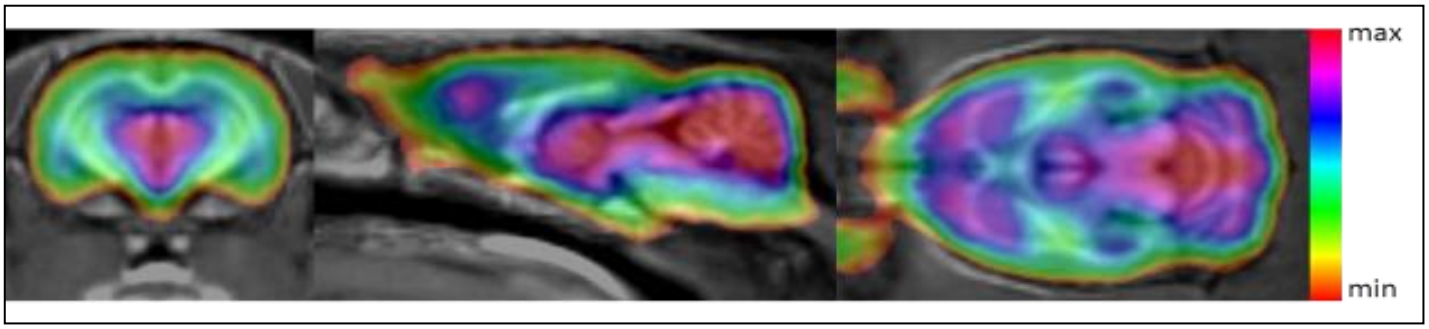

Fig. 1: Fused PET-MRI-Template in coronal, sagittal und transversal view.

References

[1] Casteels, C. et al., Construction and evaluation of multitracer small-animal PET probabilistic atlases for voxel-based functional mapping of the rat brain, J Nucl Med. 2006 Nov;47(11):1858-66.
[2] Ashburner J., A fast diffeomorphic image registration algorithm, Neuroimage. 2007 Oct 15;38(1):95-113.
[3] Caprioli, D. et al., Baseline-Dependent Effects of Cocaine Pre-Exposure on Impulsivity an dD2/3 Re-ceptor Availability in the Rat Striatum: Possible Relevance to the Attention-Deficit Hyperactivity Syndrome, Neuropsychopharmacology. 2013 Jul;38(8):1460-71.

128 Pharmakokinetic modeling and quantification of the liver function using DCE-MRI with contrast agent Gd-EOB-DTPA

P. Zylka[1], T. Denecke[2], D. Geisel[2], L. Lüdemann[1]
[1]Universitätsklinikum Essen, Klinik und Poliklinik für Strahlentherapie, Essen, Germany
[2]Klinik für Radiologie, Charité Universitätsmedizin Berlin, Berlin, Germany

Purpose: We explored the possibility of establishing a mathematical model for noninvasive and spatially resolved determination of liver function parameters using dynamic contrast-enhanced magnetic resonance imaging (DCE-MRI). We expect that, unlike other liver function tests, our approach will enable assessment of both overall hepatic function and function of hepatocytes in specific liver regions. We analyze and compare the metabolism of arterial and portal venous blood in embolized and healthy liver areas using the liver-specific contrast agent Gd-EOB-DTPA.

Introduction: All patients included in this study underwent surgical occlusion of portal venous blood flow to a liver segment because of malignant liver disease. The aim of this embolization is to reduce blood supply to the liver region harboring malignant disease, causing it to shrink while the remaining healthy liver parts start to grow. Ideally, the procedure completely suppresses sinusoidal blood flow to the target area, which normally accounts for about 75 % of blood supply, leaving only arterial supply to this area. Nonembolized liver portions retain both arterial and portal venous supply. Thus, livers treated by this embolization procedure allow good comparison of flow and metabolism in treated and untreated regions. Continuous acquisition of the concentration-time curve of the liver-specific contrast agent Gd-EOB-DTPA can be used to assess liver function expressed as the metabolic rate of the contrast medium (CM). The CM distributes in the bloodstream and is actively taken up into healthy hepatocytes. Using a two compartment model (Fig. 1) based on the indicator dilution theory [2, 4], it is possible to determine six relevant liver parameters.

Materials and methods: Here we present the results obtained in five cases. All MRI-data were acquired at 1.5T (Siemens MAGNETOM Avanto). A standard Siemens 6-channel body coil and a 6-channel table coil were used for signal readout. To record CM behavior up to 30min after bolus injection, a 3D gradient-echo keyhole sequence with a temporal resolution of 3.4s (Siemens, syngo TWIST) and parallel acquisition was used. Sequence parameters were repetition time TR=2.33ms, echo time TE=0.84ms, 24 k-space rows, central space 20 %, 20 % read-out rate of peripheral k-space, PAT factor 3, No. of averages 1, FoV 400x400mm, acquisition matrix 205x256, reconstruction matrix 256x72x265, slice thickness 2.5mm, and flip angle α=30°. Dynamic acquisition was performed over approx. 30 minutes. Within this time frame, dynamic and anatomic images were acquired in turns, resulting in gaps in the dynamic data as shown (Fig. 3). As the sequence was designed to allow free breathing for the patient throughout the examination, retrospective correction for liver motion had to be performed. Motion correction was done locally by exploiting the “normalized mutual information” routine using a high-resolution reference image (Fig. 2, left). The computation was performed using the Amira visualization software (FEI Visualization Sciences Group). To derive the concentration information from the MRI data, we used the method of Li et al. [1], equations (1) and (2), implemented in Amira – to convert signal intensities to relaxation rates. The change in the relaxation rate is directly proportional to the contrast agent concentration.

S(α) equals the acquired MR signal of a static image with defined flip angle α. Both R1 and M0 are identified experimentally by performing several acquisitions with different flip angles. All of these variables are used in eq. (2) to compute the relaxation rates successively for each voxel. S(0) is the signal intensity without contrast agent and S(t) the signal at a specific time t after bolus injection. After subtraction of the baseline relaxation rate, the converted relaxation maps are proportional to the contrast agent concentration with a proportionality factor 1/K (eq. 3).

$$S(\alpha) = \sin(\alpha) \cdot M_0 \frac{1-e^{-T_R \cdot R1_0}}{1-\cos(\alpha) \cdot e^{-T_R \cdot R1_0}} \tag{1}$$

$$R1(t) = \frac{-1}{T_R} \cdot \ln\left(\frac{1-(A+B)}{1-\cos(\alpha)\cdot(A+B)}\right) \qquad A = \frac{S(t)-S(0)}{M_0 \cdot \sin(\alpha)} \qquad B = \frac{1-e^{-T_R \cdot R1_0}}{1-\cos(\alpha)\cdot e^{-T_R \cdot R1_0}} \tag{2}$$

$$C_T(t) = \frac{R1(t) - R_0}{K} \tag{3}$$

The resulting motion-corrected concentration maps (Fig. 2, right) were used to extract the concentration-time curves of ROIs placed in the aorta (C_{AIF}), the portal vein (C_{PVIF}), and the examined liver area (C_T). The used rate equations include two enhancing compartments and two inputs. The first compartment represents the sinusoids, while the other compartment represents hepatocytes. The simplex optimization algorithm is used to fit the following parameters: *overall sinusoidal flow* (F_G), *sinusoidal mean transit time* (MTT), *hepatic uptake / extraction rate* (K_I / K_E) as well as the *compartment volumes* (v_S / v_H) (Fig. 1). To reduce the number of free parameters, two parameters were fixed. First the arterial time delay between aorta and liver was fixed between 3 and 9 sec depending on the data. Second, the overall sinusoid flow was separated into 25 % arterial and 75 % portal venous blood flow when non occluded liver areas were evaluated.

Results and discussion: The computations resulted in stable regressions for all patients in healthy liver areas. The means and standard deviations of the determined parameters over all five patients are presented in Table 1. All calculated parameters are within the range of expected physiological parameters and of published data [4]. The contrast agent's uptake is at about 5 %/s, whereas the extraction rate is only approximately 0.8 %/s, resulting in hepatic accumulation. The mean transit time of the sinusoids is 5-8 sec. In agreement with the literature, hepatocytes constitute approximately 70 % of the total liver volume, whereas the sinusoids account for less than 10 %. Although the calculated means are in agreement with technical literature, averaging data of patients with different liver malignancies results in high deviations of up to 40 % (F_G, K_E). The low signal-to-noise-ratio in the dynamic sequence is most likely due to acquisition during free breathing. The accuracy of the regression might depend on the fixed values used in the rate equation for fitting. In contrast to earlier work on the pharmacokinetic modeling of Gd-EOB-DTPA [3, 4], we used both liver inlets for calculations as well as an image acquisition over up to 30 minutes. This results in accurate fitting of contrast medium behavior up to the point of maximum accumulation. Additionally, using a two-compartment approach was especially important for proper description of arterial and portal venous phases of contrast medium enhancement.

Conclusion: The model introduced here allows spatially resolved quantification of hepatocyte function via the metabolic rate of Gd-EOB-DTPA in the liver using data from healthy liver segments. This approach has the potential to enable noninvasive liver function analysis. The computation provides stable regressions for all patients that are consistent with physiologic parameters.

References

[1] K.-L. Li et al., Improved 3D quantitative mapping of blood volume and endothelial permeability in brain tumors, J Mag Res Imaging 12: 347-357 (2000)

[2] S. Sourbron and D. Buckley, Tracer kinetic modelling in MRI: estimating perfusion and capillary permeability. Physics in Medicine and Biology 57 (2012) R1-R33

[3] H. Nilsson et al., Assessment of hepatic fraction and input relative blood flow using dynamic hepatocyte-specific contrast-enhanced MRI, J Mag Res Imaging 29:1323-1331 (2009)

[4] S. Sourbron et al., Tracer-kinetic analysis of Gd-EOB-DTPA in the liver with a dual-inlet two-compartment uptake model, Proc. Intl. Soc. Mag. Reson. Med. 18:4583 (2010)

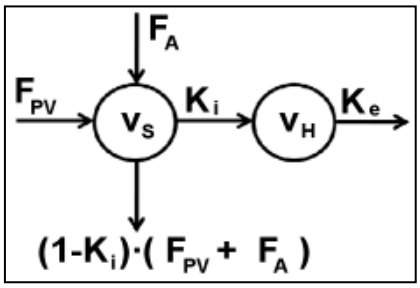

Fig. 1: Two-compartment liver model of contrast agent Gd-EOB-DTPA

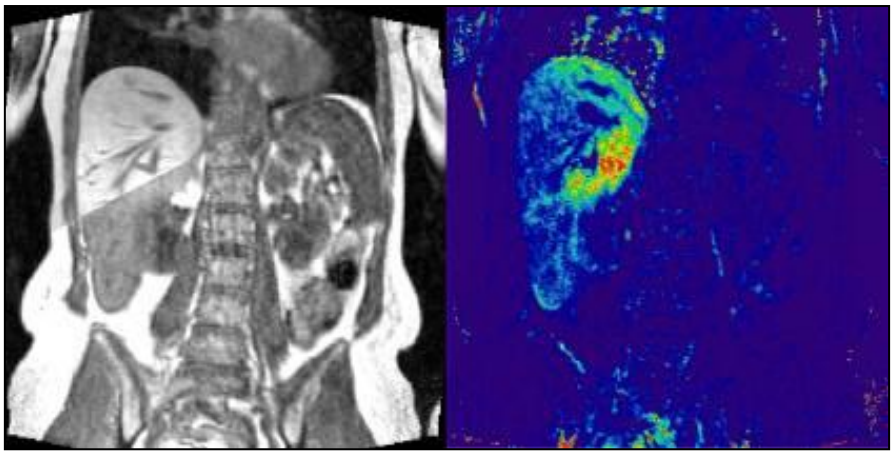

Fig. 2: Motion correction using a high-resolution reference image (left), motion-corrected concentration map (right)

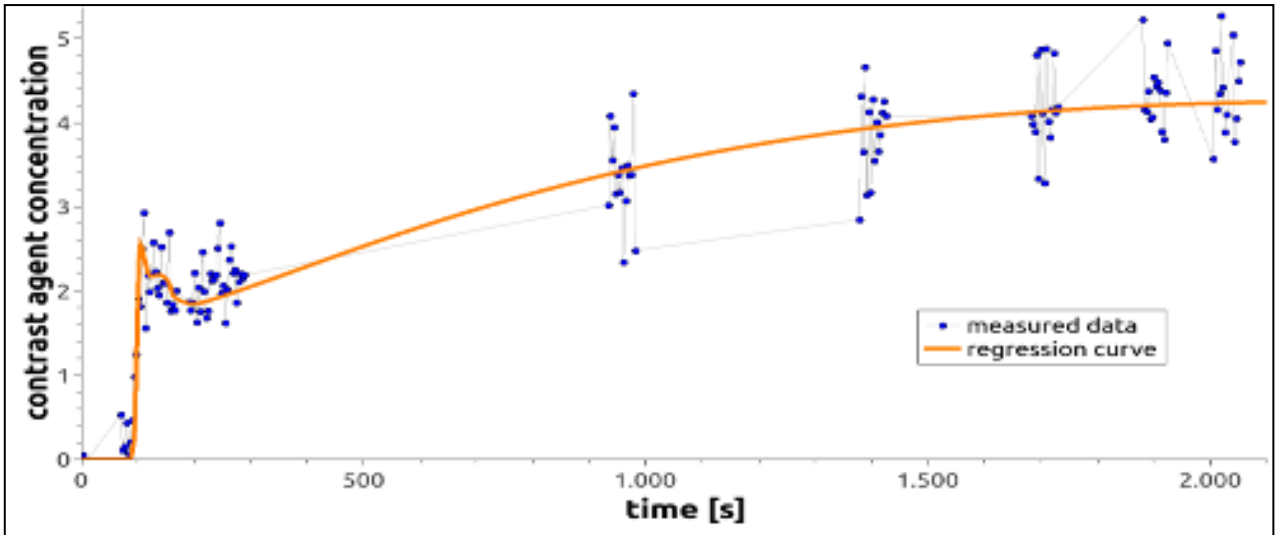

Fig. 3: Using a simplex-algorithm, the regression curve is measured data to identify the model's unknown

	$\frac{1}{K} \cdot F_G$	v_S [%]	v_H [%]	K_I [%/s]	K_E [%/s]	MTT [s]
mean	$4{,}43 \cdot 10^{-4}$	3,20	66,20	5,09	0,82	6,79
sd	$1{,}92 \cdot 10^{-4}$	0,94	4,55	1,18	0,32	1,17

Tab. 1: Means and standard deviations (sd) of the free parameters taken from all five patients, ROI in healthy liver areas

Session 22 – Motion management in imaging and radiation therapy II

Chairs: S. Lang (Zurich/CH), K. Parodi (Munich/DE)

129 Introductory lecture: Intra-fractional motion management for lung tumors

R. Moeckli[1]
[1]Lausanne, Switzerland

130 Influence of respiratory motion amplitude und phase on dosimetric margins in radiotherapy

L. Gunasekaran[1,2], J. Lenz[1,3], E. Becker[1,4], G. A. Zakaria[5,2], A. Block[1]
[1]Klinikum Dortmund, Institut für Medizinische Strahlenphysik, Dortmund, Germany
[2]HS-Anhalt University of Applied Sciences, Biomedical and Clinical Engineering, Köthen, Germany
[3]TU Dortmund, Experimentalphysik V, Dortmund, Germany
[4]University of Applied Sciences, Biomedizinische Technik, Münster, Germany
[5]Gummersbach Hospital, Department of Radiation Physics, Gummersbach, Germany

Purpose: Respiratory and cardiac motions in the thoracal and abdominal region induce displacement of the tumor volume as well as various internal organs during the treatment. Amplitude, period and form of these motions show wide varity, There are no basic patterns, they are patient-specific. Vedam et al. [1] were the first who proposed the idea that lung tumors in the vicinity of the diaphragm move with the same magnitude and phase as the diaphragm. This concept was adapted of other groups [2]. When introducing respiratory patterns to the calculation of dosimetric margins, the amplitude of the respiratory cycle and its time dependence have been assumed as the most important parameters. While these relations have been thoroughly examined in the literature, considerably less attention has been spent on the phase of the respiratory pattern, which also varies with time. According to the report of AAPM Task Group 76 [3] amplitudes can vary from a couple of millimeters to a few centimeters. In this work, we start by analyzing the influence of the respiratory amplitude of both, tumor and diaphragm, on the dose distribution and subsequently expand our enquiries towards phase dependency.

Materials and methods: For the current investigation the patient's respiratory signal and target motion were recorded for about 36 seconds from the Real-time Position Management System (Varian Medical Systems) and the fluoroscopic screen being part of the therapy simulator (Varian Medical Systems). The clinical linear accelerator Saturne-43 (E_{peak}=6 MeV and E_{peak}=6 MeV) was used for the measurements. Respiratory signal and target motion were imported to ORAT [4] where the patient's respiration and tumor motion is analyzed. The initial investigation was done using the in-house developed software ORAT (Organ Respiration Analysis Tool) to analyze the individual movement of the lung tumor frame by frame.

To investigate the influence of the periodic motion has on two dimensional dose distribution first of all four regular patterns with different amplitudes and periods were analyzed:

- Pattern 1: A = 18 mm, T = 5.3 s
- Pattern 2: A = 3.9 mm, T = 4.0 s
- Pattern 3: A = 6.0 mm, T = 2.4 s
- Pattern 4: A = 16.4 mm, T = 3.9 s

All of these patterns were derived from different patient-individual motions. The last pattern is a periodic curve derived from a current motion curve (tumor upper edge motion, see below), the other patterns are regular motion curves derived from other patient's motions of former studies ([5], [6]). They were chosen as a basis of comparison for the current periodic motion.
To investigate the influence of irregular motion on two dimensional dose distribution some lung patient-specific motion sequences were chosen. The four different patterns are motion of the tumor upper edge, motion of the tumor lower edge and motion of the left and the right diaphragm. The characteristic motion data of these patient patterns are:

- tumor upper edge motion: A_{mean} = 16.4 ± 0.2 mm, T_{mean} = 3916.7 ± 589. ms
- tumor lower edge motion: A_{mean} = 18.4 ± 0.1 mm, T_{mean} = 3994.0 ± 410.4 ms
- diaphragm motion I: A_{mean} = 21.8 ± 0.3 mm, T_{mean} = 3972.2 ± 300.1 ms
- diaphragm motion II: A_{mean} = 37.3 ± mm, T_{mean} = 3986.1 ± 284.0 ms

Diaphragm motion is also object to the investigation as it is used as a common representative for tumor motion [1], [2|.

In order to investigate the influence of different motion parameters the tumor upper edge motion was converted into periodic curves and compared with the irregular motion pattern. The converted curves are:

- Periodic curve with a mean amplitude and a mean period
- Periodic curve with a mean amplitude, a mean period and a baseline shift
- Periodic curve with one mean amplitude and different periods
- Periodic curve with one mean period and different amplitudes

The device used for measurements of two-dimensional dose distribution is a two-dimensional diode array called MapCHECK2 (Sunnuclear Corp.) kept on top of the XY/4D motion table named MotionSim (Sunnuclear Corp.). The table acts as a motion phantom being able to simulate the patient's respiratory and tumor motion.

The patient individual motion data obtained from ORAT and the designed periodic patterns derived from them are given as input to the XY/4D
simulation table. The measurements were taken with the field size of 10 cm x10 cm, with response to tumor motions as well as in rest positions. They were then analyzed by using the supporting software SNC Patient to measure the extent of different isodose areas in the direction of motion (y-direction in MapCHECK2-coordinates).
Results: To quantify which motion has the influence on two-dimensional dose distribution, the extent of two isodose areas were determined: the 90 %-isodose area is chosen as representative for high dose area, the 10 %-isodose area as representative for low dose area. The extents for the current study and previous studies are listed below. The differences measured between the isodose extents (target at rest and target in motion) were normalized to the corresponding extend at rest and 100 %.

The turning point of motion influencing the distribution was found to be near 50 % of the relative dose. However, it is the dose value in the middle of maximum and minimum dose. Within this turning point motion does not change the dimension of the corresponding isodose area. This is important as the dimension of 50 %-isodose is to define the physical field size. As it does not change in case of motion field size it cannot be taken as a tool to quantify motion effects two dimensional dose distributions.

Periodic motion

For all measurement conditions (different energies, different amplitudes and different periods) a shrinkage of 90 %-isodose areas and broadening of 10 %-isodose areas could be detected. Increasing amplitude can be correlated with increasing influence on dose distributions, in other words increasing shrinkage of 90 %-isodose areas and increasing broadening of 10 %-isodose areas. Otherwise demonstrates the results in table 1 the influence of the cycle time, comparable amplitudes (16.4 mm and 18 mm) with different cycle times (3.9 s and 5.3 s) yields to a large difference in the shrinkage of the 90 %-isodose (73.12 % and 92.47 %).

	Dimension 90 %-Isodosearea (in relation to value at rest)	**Dimension 10 %-Isodosearea (in relation to value at rest)**
Target at rest (E_{peak} = 6 MeV)	100 %(reference)	100 % (reference)
Target in motion (E_{peak} = 6 MeV A = 18 mm, T = 5.3 s, direction: y)	91.40 %	104.30 %
Target in motion (E_{peak} = 15 MeV A = 18 mm, T = 5.3 s, direction: y)	92.47 %	106.99 %
Target in motion (A = 3.9 mm, T = 4.0 s, direction: y, E_{peak} = 15 MeV)	99.03 %	104.62 %
Target in motion (A = 6.0 mm, T = 2.4 s, direction: y, E_{peak} = 15 MeV)	93.33 %	107.63 %
Target in motion (A = 16.4 mm, T = 3.9 s, direction: y, E_{peak} = 15 MeV)	73.12 %	119.36 %

Tab. 1: 90 %- and 10 %-Isodose dimensions for different periodic motions [percentage value in relation to value at rest]

Irregular motion patterns

Another subject to the investigation were irregular patterns. At first the four irregular motion sequences described above were compared to each other. Comparing irregular tumor motions and diaphragm motions with target at rest perceptions gained by previous data are approved: 90 %-isodose area dimensions shrink under motion, 10 %-isodose area dimensions broaden in presence of motion. Differences between isodose area dimensions of target at rest and target in motion increase with increasing amplitude. But what has to be pointed out is the fact that the amplitude of diaphragm motion II is more than twice as big as those of both tumor motions. Also diaphragm motion I is considerably larger than tumor motions. The usage of diaphragm motion as a representative for tumor motion seems therefore difficult as far as amplitude considerations are concerned.

	Target at rest	lower edge tumor motion	upper edge tumor motion	Diaphragm motion I	Diaphragm motion II
Dimension 90 % Isodose area (in relation to value at rest)	100 % (reference)	91.20 %	90.10 %	87.91 %	73.62 %
Dimension 10%-Isodosearea (in relation to value at rest)	100 % (reference)	105.78 %	104.95 %	107.43 %	117.35 %

Tab. 2: 90 %- and 10 %-Isodose dimensions for irregular motion patterns (tumor motions and diaphragm motions) [percentage value in relation to value at rest]

Next one irregular motion pattern was chosen to be looked at in detail (lower edge tumor motion). Regarding the periodic motions derived from the patient individual motion of the upper tumor edge a few discoveries can be made. Comparing dimensions of 90 %- and 10 %-Isodose areas of dose distributions measured under usage of irregular motion with different periodic motions shows least changes. The largest influence on isodose extents is found when using the periodic motion with the same amplitude but varying periods (Same Amplitude: SA, Different Phase: DP, Tab. 3 /Fig. 1). Periodic motions using same amplitude and different period (SA, DP, Tab. 3 /Fig. 1), one mean amplitude with one mean period and a baseline shift (Basline shift, Tab. 3 /Fig. 1) and same phase and different amplitudes (SP, DA, Tab. 3 /Fig. 1) show variations in isodose dimensions about the same range. Variations are bigger compared to those linked with irregular motion but smaller compared to periodic motion of different periods. Incident to periodic motion of same amplitude but different periods it has to be mentioned that the standard deviation of mean period T_{mean} = 3916,7 ms is б = 589,6 ms. This is 15,1 % of T_{mean}. Comparing this to the mean amplitude you find: A_{mean} = 16.4 ± 0.2 mm, which is 1,3 % of A_{mean}.

	Target at rest (mm)	Irregular motion (lower edge tumor motion)	Periodic motion (mm)
Dimension isodose area (y-direction) 90 %	100 % (refernce)	91.20 %	73.62 %
Dimension isodose area (y-direction) 10 %	100 (refernce) %	105.78 %	114.87 %

	Baseline shift (mm)	Same amplitude, diff. periods (mm) (SA, DP)	Diff. amplitude, same periods (mm) (SP, DA)
Dimension isodose area (y-direction) 90 %	74.72 %	64.83 %	74.72 %
Dimension isodose area (y-direction) 10 %	114.87 %	126.44 %	116.52 %

Tab. 3: 90 %- and 10 %-Isodose dimensions for lower edge tumor motion and different derived periodic motions [percentage value in relation to value at rest]

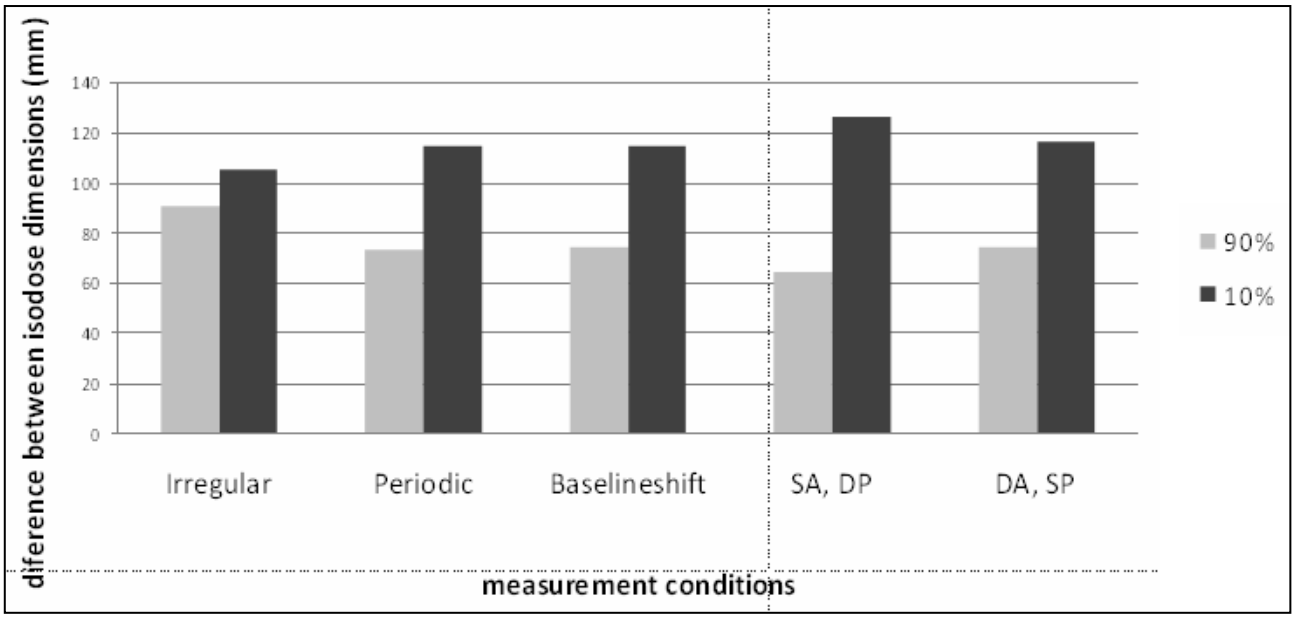

Fig. 1: Differences between isodose dimensions of target at rest and target at different motions regarding 90%- and 10 %-isodose areas

Conclusions: Regarding periodic motion of different amplitudes there is one prominent observation: increasing amplitudes involve increasing influence on isodose area dimensions. The higher the amplitude the smaller is the 90%-Isodose extent and the broader is the 10%-Isodose. Having a look at irregular motion patterns this tendency is approved for both tumor motion and diaphragm motions. But two issues have to be pointed out: At a certain point it is doubtful to choose diaphragm motion as a representative for tumor motion as the amplitude deviates numerously from tumor motion amplitude; in other case deviated periodic motion influences two-dimensional dose distribution more than the original irregular motion does. This is important as periodic motions are chosen as representative for patient patterns which is not adequate according to the current data. The irregularity can be expressed in terms of standard deviations. The standard deviation of the breathing phases is ten times higher then the standard deviations of the amplitude. Therefore varying periods induce a stronger influence on isodose dimensions in the direction of motion than any other parameter of derived periodic motions. Our research indicates that the phase of the respiratory cycle might have great influence on dosimetric margins. To calculate an effective margin for an individual patient tumor a precise investigation of the respiratory pattern is necessary and the amplitude, phases and its standard deviations should be paid more attention. Why deviated periodic motion seems to have more influence on isodose area dimensions than irregular motion and how current results can be connected with margin concepts are topics under discussion.

References

[1] S. S. Vedam, P. J. Keall, V. R. Kini, R. Mohan: Determining parameters for respiration-gated radiotherapy; Med. Phys. 28 (10), 2139 – 2146 (2001)

[2] L. I. Cerviño, A. K. Y. Chao, A. Sandhu and S. B. Jiang: The diaphragm as an anatomic surrogate for lung tumor motion, Phys. Med. Biol. 54 (2009) 3529–3541

[3] P. J. Keall, G. S. Mageras, J. M. Balter et al: The management of respiratory motion in radiation oncology report of AAPM Task Group 76; Med. Phys. 2006; 33:3874-3900

[4] A. Block, R. Bauer: Ein Auswerteprogramm zur visuellen und quantitativen Erfassung der intrafraktionellen Organbewegung; Med. Physik 2004, 342-343

[5] J. Lenz: Dosimetrische Messungen an bewegten Targets mit einem halbleiter-basierten 2D-Array, Diplomarbeit, TU Dortmund/ Institut für Medizinische Strahlenphysik und Strahlenschutz am Klinikum Dortmund, 2012

[6] E. Becker: Dosimetrische Messungen in der Hochvolt-Strahlentherapie an bewegten Targets unter Einfluss der Wahl des Gatingfensters auf die 2-dimensionale Dosisverteilung, Bachelorarbeit, Fachhochschule Münster/ Institut für Medizinische Strahlenphysik und Strahlenschutz am Klinikum Dortmund, 2012, S.10-25

131 Evaluation of the Interplay Effect during VMAT Treatments for Different Treatment Sites

S. Ehrbar[1,2], S. Lang[1], S. Stieb[1], O. Riesterer[1], S. Klöck[1]
[1]University Hospital Zurich, Radiation Oncology, Zurich, Switzerland
[2]Eidgenössische Technische Hochschule Zurich, Physics, Zurich, Switzerland

Purpose: Respiratory motion is a non-negligible source of uncertainty in radiotherapy. A common treatment approach is motion encompassing delineation of the target volume (internal target volume (ITV)-concept), where the irradiation plans are calculated on the average reconstruction of the four-dimensional computed tomography (4D-CT) scans. The authors investigated the extent of the interplay effect in the dose distribution caused by interaction between dynamic dose delivery and respiratory motion, which is neglected in the clinical practice of treatment planning using the ITV-concept.

Methods: 4D-CT scans of 18 patients with 20 cancer lesions (7 liver, 6 adrenal glands and 7 lung lesions) were used for the analysis. All patients were treated with volumetric modulated arc therapy (VMAT). The dose distributions and optimizations were calculated on average reconstructions of the 4D-CT. The original treatment plans were split into 10 sub plans for the 10 breathing phases using Matlab (MathWorks). A steady breathing cycle of 3.4 s was assumed for the splitting of the plans for all patients and over the entire treatment fraction. These sub plans were then imported back into the planning system and assigned to according breathing phases. The dose distributions were calculated for the individual breathing phases on the corresponding phase sorted 3D-CTs. The resulting 10 dose distributions from the 10 sub plans were added up and displayed on the average CT. The dose to the planning target volume (PTV) and the organs at risk (OARs) from the original plan calculated on the average CT and the plans calculated on the 3D-CTs of the breathing phases were compared.

Results: The differences in dose delivered to the PTV were calculated for the minimum, maximum and mean dose in the PTV. For the evaluation the absolute values of these differences were taken. The mean difference with standard deviation (maximum) averaged over all patients was 0.78% ± 0.40% (1.75%) for the minimum dose to the PTV, 0.80% ± 0.54% (1.94%) for the maximum and 0.74% ± 0.49% (1.94%) for the mean dose values to the PTV. The amount of volume of the PTV getting 100% of the prescribed dose (V_{100}) changed by 1.76% ± 1.74% (7.21%). Averaged over liver patients only, the results were: 0.69% ± 0.29% (1.08%) for the minimum dose to the PTV, 0.62% ± 0.43% (1.05%) for the maximum and 0.55% ± 0.39% (0.88%) for the mean dose to the PTV. The V_{100}-value changed by 2.47% ± 2.77% (7.21%). For adrenal gland patients the results were: 0.49% ± 0.20% (0.88%) for the minimum, 0.79% ± 0.36% (0.93%) for the maximum and 0.74% ± 0.28% (0.98%) for the mean dose in the PTV. The V_{100}-value changed by 1.36 ± 0.70% (1.78%). For lung patients the results were: 1.12% ± 0.39% (1.75%) for the minimum, 0.98% ± 0.75% (1.94%) for the maximum and 0.94% ± 0.67% (1.94%) for the mean dose in the PTV. The V_{100}-value changed by 1.38% ± 0.78% (2.28%).

The relative changes in the doses to the OARs are shown in figure 1. For liver, kidney and lung the mean doses of the organs were compared. For myelon and ribs the maximum dose values were taken for the comparison. The mean of differences in dose stayed below 1% for all OARs. The maximal dose difference was 2.02% and occurred in the ribs of one patient treated for a lung tumor.

In 86% of all taken values, the dose was underestimated in the dose calculation on the averaged 4D-CT.

The sub plans were also calculated on the average reconstructions of the 4D-CT to verify the equivalency of the sum of the sub plans to the original irradiation plan. A maximum deviation in the displayed dose of 0.08% was found.

Conclusion: The approximation of calculating the dose on the average 4D-CT, instead of on the respiratory phases, gives acceptable results. The interplay effect results in dose variability in the range of 0.5-2%.

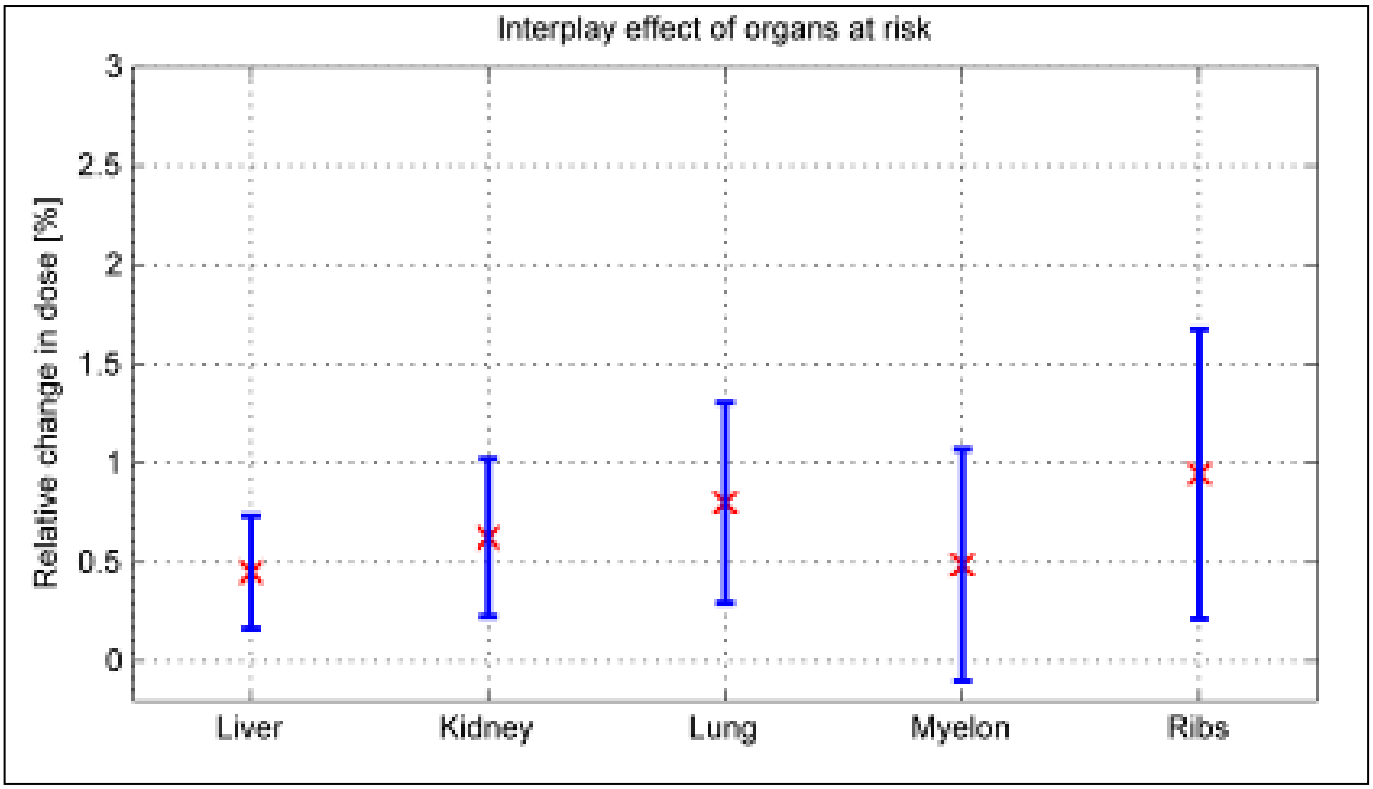

Fig. 7: This figure shows the amount of the interplay effect for OARs comparing irradiation plans calculated on the average 4D-CT to the same treatment plans calculated on the corresponding 3D-CTs of the respiratory phases. The mean values (red crosses) and standard deviations (blue bars) were calculated from dose values of 11 liver, 9 kidney, 11 lung, 20 myelon and 6 rib volumes.

132 Clinical Workflow for gated treatment of the left breast using Deep Inspiration Breath Hold (DIBH) technique

C. Hoinkis[1], F. Tillner[1,2], S. Appold[1], F. Lohaus[1,3], R. Perrin[2,4], C. Richter[2], K. Stützer[2], M. Baumann[1,2,3,5], M. Krause[1,2,3,5]
[1]University Hospital Dresden, Radiotherapy, Dresden, Germany
[2]OncoRay Nationales Zentrum für Strahlenforschung in der Onkologie, Dresden, Germany
[3]Deutsches Konsortium für Translationale Krebsforschung (DKTK), Dresden, Heidelberg, Germany
[4]Paul Scherrer Institut, Villigen, Germany
[5]Institut für Radioonkologie, Helmholtz-Zentrum Dresden-Rossendorf, Dresden, Germany

Introduction: For treatments of carcinomas in the left breast a benefit concerning heart protection is expected by using the technique of Deep Inspiration Breath Hold (DIBH). Especially the left anterior descending (LAD) coronary artery seems to be very sensitive to irradiation and, therefore, a prognostic risk factor for radiation-induced cardiac diseases. A suitable signal is necessary for triggering the linear accelerator, at best surveying the position of the patient and the level of deep inspiration. At our clinic the surface monitoring system AlignRT (VisionRT) has been implemented into the clinical workflow for positioning of breast cancer patients and for triggering the linear accelerator for the DIBH technique. Physical investigations of the AlignRT system have been done using an in-house built phantom [1, 2]. The clinical workflow from imaging, planning, verification and application of the treatment will be presented.

Materials and methods: In general, for each patient selected as potential beneficiary of a DIBH treatment two treatment plans are prepared. These two plans are based on a free-breathing CT (FB-CT) and a DIBH CT, respectively.. In addition, a 4D-CT is acquired using the tool GateCT (VisionRT) in order to extract the patient position in end-exhalation phase (Ex-CT) using the tool GateCT (VisionRT). Those three data sets are located within the same coordinate system. Treatment planning is done in the Oncentra Treatment Planning software (Elekta) in two so called “cases”: case DIBH and case FB. Both cases contain the Ex-CT as a secondary dataset. This dataset supplies the reference patient outer contour in exhalation and is used for defining the anatomical reference point in both cases. Thus the positioning for both cases is the same, no matter if the treatment finally will be delivered in free breathing or DIBH. The offset of the isocentre relative to the anatomical reference point is defined identical for both cases, so finally the patient gets one marking for both plans. Treatment planning is done for both cases and the following DVH-parameters are evaluated for plan comparision: Coverage of the PTV and CTV in terms of D98% and V95%, D_{max} of the LAD, D_{mean}, V_{40Gy} and V_{20Gy} of the heart. Medical plan evaluation also includes distribution of the isodoses with special attention to the boost region and is performed by two experienced clinicians. In case of decision for DIBH technique, treatment plans of both cases are transferred to the Record- and-Verify System Mosaiq (Elekta), since the FB case serves as breakdown backup. At the time of the first fraction at the linear accelerator (Artiste, Siemens) the patient undergoes the procedure of Virtual Simulation. Positioning of the patient is done in the End-Exhalation position using the gated option of positioning within the AlignRT module, i.e. the patient surface is monitored for several seconds determining the End-Exhalation surface position. After having the patient at the right position on the treatment table, the reference surface for the DIBH case is loaded. Patient breathing is supported with goggles showing only the “Coaching bar” of the AlignRT screen. Thus the correct amplitude of the DIBH-level is verified and radiation is only enabled if the deep inspiration level is reached by the patient. Visual verification of the main treatment fields is done by Electonic Portal Images compared to reference DRRs from the treatment planning system. In case of a breakdown of the AlignRT or the regarding accelerator, the patient can be treated at another machine with the Free-breathing plan using the same skin marking as for the DIBH-plan.

Results: Up to March 2014 six patients have gone through the procedure of comparative planning. Two of them have been selected for DIBH treatment due to a clear benefit evaluated from DVH parameters as well as isodose distribution. The D_{max} of the LAD could be significantly reduced from 45,5 Gy to 3,4 Gy and from 49,3 Gy to 12,3 Gy without compromising the coverage of the PTV and CTV. As an example, Figure 1 shows the sparing of the LAD and the heart for the DIBH plan compared with the FB plan for the ventrolateral field.

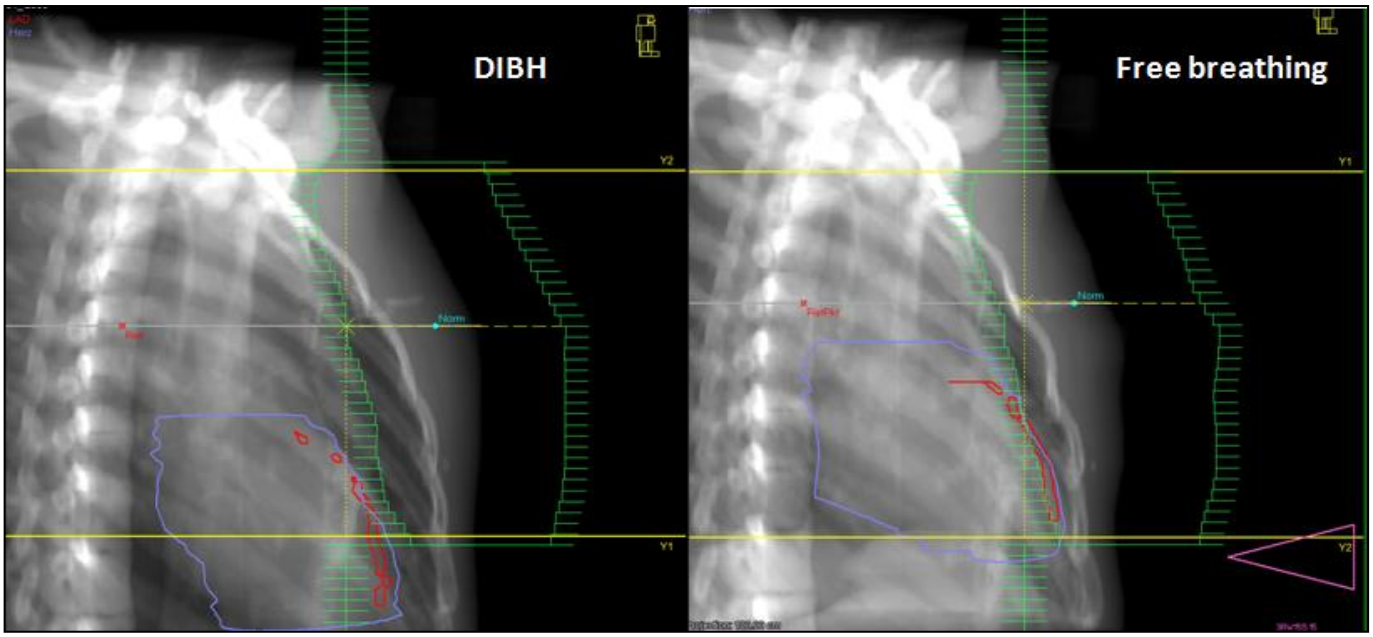

Fig. 1: Example for a ventrolateral field sparing the heart in the DIBH-technique (left), whereas part of the heart (blue) and LAD (red) lies within the treatment field for the Free-breathing technique (right).

Conclusion: The clinical workflow for DIBH treatments including reliable verification of patient positioning and verification of the DIBH level has been implemented successfully. Defining criteria and parameters for patient selection is part of our future work.

References

[1] C. Hoinkis, G. Rothe, P. Zahn, P. Geyer, W. Enghardt: Entwicklung eines Phantoms zur Verifikation der getriggerten Bestrahlung in Tiefer Einatmung bei Mammakarzinom (Deep Inspiration Breathhold), DGMP-Tagung 2013, Cologne

[2] Herold, J.: Implementierung der Gating-Technik „Deep Inspiration Breathhold“ am Universitätsklinikum Carl Gustav Carus, Masterarbeit, 2013

133 Decomposition of interfractional deformations of head & neck patients using principle component analysis

M. Stoll[1], K. Giske[1], R. Bendl[1,2]
[1]German Cancer Research Center (DKFZ), Division of Medical Physics in Radiation Oncology , Heidelberg, Germany
[2]Heilbronn University, Faculty of Medical Informatics, Heilbronn, Germany

Introduction: Due to its flexibility the head and neck anatomy is affected by intense interfractional deformations, which can be compensated by the use of safety margins. These margins are usually of constant width. Approaches to calculate margins having a width adapted to deformability of their location are subject of current research and scientific discussion [1]. In this work we use principle component analysis (PCA) to find main directions of deformations at specific landmarks. This allows including the direction of deformations in the margin calculation. Further we decompose the correlated landmark deformations of the whole head & neck region to find a low-dimensional representation to enable deformation model based plan evaluations, similar as proposed for pelvic area in [2].

Materials and methods: 503 daily kV control CTs of 19 patients are analyzed in this retrospective study. 24 landmarks in easily identifiable bony structures are manually selected in the planning CT image of each patient. A fully automatic correspondence finder, based on normalized cross correlation, which is part of a deformable image registration [3], localizes all landmarks in each control CT (12,072 positions in total). A statistical analysis of distances between landmarks creates a geometric model and detects outliers. Procrustes analysis for a subset of the landmarks, located on the skull, finds a transformation rigidly matching the landmarks positions of the control CT to corresponding positions of the planning CT. The transformation is applied on all 24 landmarks to eliminate translation and rotation and to use the skull as reference region for deformation analysis. PCA is used to find main directions of each individual landmarks remaining displacement, which is now representing a deformation in respect to the skull. In addition a probabilistic PCA is used to find the first five eigenvectors of all combined landmark displacements. The probabilistic approach allows including datasets with missing data (outliers). The achievable reconstruction quality of this approach is measured.

Results: Correspondences between planning CT and control CT are automatically found for all landmarks, except in cases of a reduced field of view. The geometric model is able to detect outliers due to mixed up structures of similar shape (e.g. vertebrae). Procrustes analysis matches the skull landmarks sufficiently with a mean error of less than 1 mm. The landmark-wise PCA shows, that the main axis of the deformation can be different from anteroposterior, dorsoventral or left-right direction especially near the shoulders (see fig. 1 and fig. 2). The probabilistic PCA of all combined landmark displacements enables a reconstruction of the deformation with a mean difference between reconstructed and original data of 1.3-3.4 mm (depending on patient), when linear combining only the first five eigenvectors (five DOF, last row of Tab. 1).

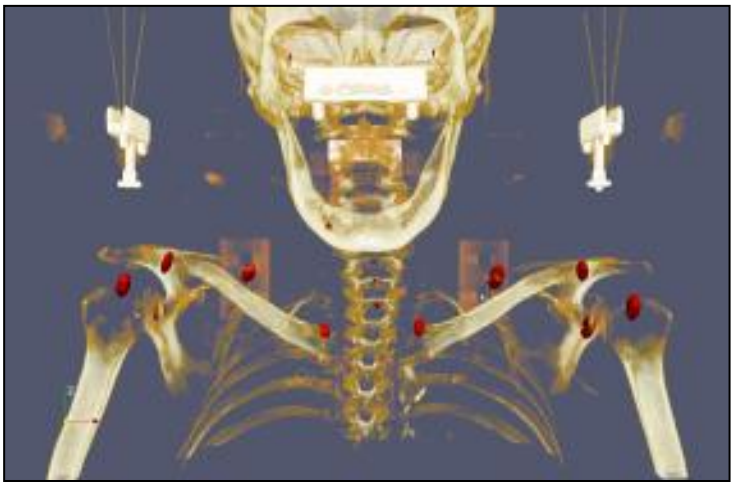

Fig. 1: Ellipsoids having axes rotated to principle components of local deformations visualized together with volume rendering of a planning CT (frontal)

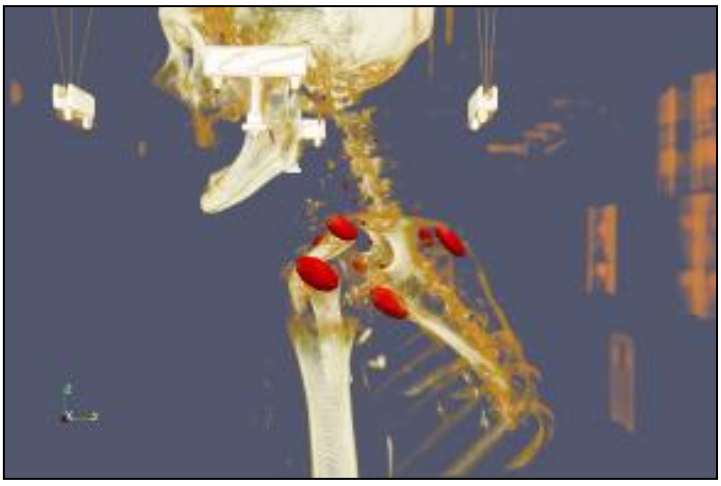

Fig. 2: Ellipsoids having axes rotated to principle components of local deformations visualized together with volume rendering of a CT (lateral)

Conclusion: Landmark-wise PCA allows measuring directions of deformations. For some landmarks this direction is different from anteroposterior, dorsoventral or left-right and should be included in margin generation to reduce the required margin size. Further a decomposed deformation of all combined landmarks displacements allows reconstructing the deformation with five degrees of freedom for each fraction (residual error 1.3-3.4 mm). This dimensionality reduction allows representing interfractional deformation in a compact model and allows inter- and extrapolating new samples together with their probability. These samples could be combined with an appropriate interpolation technique to allow plan evaluations, plan-of-the-day strategies or robust planning approaches.

Acknowledgement: This research was carried out with the support of the German Research Foundation (DFG) as part of project C02, SFB/TRR 125 Cognition-Guided Surgery.

#DOF	Patient# 1	2	3	4	5	6	7	8	9	10	11	12	13	14	15	16	17	18	19
0	3.8	4.3	4.1	5.8	3.3	7.6	3.2	7.7	3.6	6.3	3.6	4.5	7.1	2.7	3.7	3.8	4.5	5.4	4.7
1	2.7	3.0	2.5	3.4	1.8	4.4	2.8	5.0	2.2	3.7	3.3	1.6	3.5	2.9	3.2	2.8	3.0	4.6	3.5
2	2.6	3.0	2.5	3.2	1.8	4.2	2.8	4.9	2.0	3.5	2.9	1.6	3.4	2.7	3.1	2.7	2.8	3.4	3.2
3	2.3	2.7	2.3	2.9	1.7	3.7	2.5	4.3	1.9	3.2	2.7	1.4	3.0	2.1	3.0	2.6	2.7	3.1	3.0
4	2.2	2.4	2.0	2.7	1.5	3.6	2.4	4.0	1.7	2.9	2.4	1.4	2.8	1.8	2.8	2.4	2.6	2.5	2.5
5	2.1	2.2	1.9	2.2	1.4	3.4	2.3	3.0	1.7	2.6	2.3	1.3	2.4	1.6	2.6	2.3	2.5	2.3	2.5

Tab. 1: Reconstruction quality of a (probabilistic) PCA for combined landmark displacements: Mean distance in [mm] between reconstructed landmark position and original data depends on the number of eigenvectors being used (degrees of freedom = DOF*).*

References

[1] Yang J., Garden A. S., Zhang Y., Zhang L., & Dong, L: Variable planning margin approach to account for locoregional variations in setup uncertainties. Medical physics, 39.8 (2012), 5136-5144.

[2] Söhn M, Birkner M, Yan D, Alber M: Modelling individual geometric variation based on dominant eigenmodes of organ deformation: implementation and evaluation. Physics in medicine and biology, 50.24 (2005), 5893-5908.

[3] Malsch U., Thieke C., Huber P. E. & Bendl R.: An enhanced block matching algorithm for fast elastic registration in adaptive radiotherapy. Physics in medicine and biology, 51.19, (2006). 4789-4806.

Session 23 – Quality assurance for medical radiation applications II: Therapy Plan QA

Chairs: T. Künzler (Feldkirch/AT), P. Pemler (Zurich/CH)

134 On the accuracy and efficiency of different verification methods for modulated electron radiotherapy treatment plans

D. Henzen[1], C. Chatelain[1], D. Vetterli[1], P. Manser[1], D. Frei[1], W. Volken[1], H. Neuenschwander[2], A. Joosten[1], K. Loessl[1], D. Aebersold[1], M. Fix[1]
[1]Division of Medical Radiation Physics and Department of Radiation Oncology, Inselspital, Bern University Hospital, and University of Bern, Bern, Switzerland
[2]Clinic for Radiation-Oncology, Lindenhofspital, Bern, Switzerland

Related questions: Applying modulated electron radiotherapy (MERT) for superficial tumors allows sparing distal organs at risk. Previously, a Monte Carlo (MC) based framework was developed in order to create treatment plans for MERT using the photon MLC as an electron beam shaping device. This framework includes an electron beam model, a forward and inverse planning algorithm [1,2]. In this work, different verification techniques for MERT plans are explored in terms of accuracy and efficiency.

Material and procedure: The developed direct aperture optimization was used to create MERT treatment plans for a whole breast, a chest wall and a squamous cell skin carcinoma. In order to reduce the degradation of the penumbra due to the electrons scatter in air, the plans are created for a source to surface distance (SSD) of 70 cm. These plans consist of 6-12 electron beam segments, which employed energies between 6 and 18 MeV. For verification purposes, for all segments of each plan dose distributions were measured using a stand-alone electronic portal imaging device (EPID) [3] placed at an SSD of 70 cm, the in-build EPID of the linear accelerator at an SSD of 100 cm and films in a solid water phantom at an SSD of 70 cm. All measurements were carried out using a gantry rotation of 0°. These measured dose distributions were then compared to calculated dose distributions in a homogenous water phantom employing the developed MC framework at SSD of 70 cm as well as 100 cm. Using an in-house developed analysis software, the measured and calculated dose distributions were compared and evaluated in terms of the gamma analysis.

Result: All of the proposed measurement techniques led to excellent agreement to the calculated dose distributions. The gamma analysis using 2% / 2 mm criteria and a 10% dose threshold for the comparison of the EPID measurements and the calculations resulted in passing rates above 99% for all cases and both SSDs. The analogous comparison with the film measurements led to passing rates between 92% and 100% depending on the case considered.

Whereas the film measurements are the least efficient to be carried out, the positioning of the EPID at SSD of 100 cm is the most efficient one, since this can be performed by the built-in EPID. On the other hand, the measurement at SSD of 70 cm requires a stand-alone EPID which is less efficient but more close to the clinical patient situation.

Summary: While all measurement methods are viable in terms of accuracy, the two EPID solutions are favorable regarding the efficiency.

References

[1] D. Henzen et al “Monte Carlo based beam model using a photon MLC for modulated electron radiotherapy”, Med. Phys. 41(2), 021714 (10 pp.) (2014).
[2] D. Henzen et al “Using the Swiss Monte Carlo Plan for inverse treatment planning of MERT”, SARSO Meeting 2013, Davos.
[3] C. Chatelain et al. “Dosimetric properties of an amorphous silicon EPID for verification of modulated electron radiotherapy”, Med. Phys. 40(6) 061710 (14 pp.) (2013).

135 Improved quality assurance in deep hyperthermia with a new 3D E-field scanning phantom

D. Marder[1], N. Brändli[1], L. Nicoletta[1], N. R. Datta[1], O. Timm[1], G. Lutters[1]
[1]Kantonsspital Aarau, RadioOnkologieZentrum, Aarau, Switzerland

Introduction: The BSD-2000/3D system is used to treat deep seated tumours with hyperthermia (to temperatures of 41-43°C) in combination with radiotherapy. Tissue heating is caused by the electromagnetic field and its absorption in tissue. In this study a phantom and measurement system (**D**ynamical **E**lliptical **E**-field **P**hantom – DEEP) developed at the KSA is presented. It allows visualisation of E-field distributions in tissue equivalent saline solutions for improved quality control.

Materials and methods: The phantom consists of a tube elliptical in diameter connected to a water tank filled with saline solution of variable NaCl concentrations to simulate tissue equivalent electrical properties. The tube is inserted either into the BSD-2000/3D SigmaEye or Sigma60 applicator which differ in size. A measurement probe aligned with the main electrical field component can be placed and moved freely inside the tube by a mechanical arm. The position of the probe is controlled in 3 dimensions by a commercial CNC software which allows scanning of the probe on predefined routes. The probe used in this study was a white LED with a diameter of 3mm. This diode was connected to a 100 Ohm resistor causing a current flow when placed in an electromagnetic field E-field. The leads of the resistor were used as antennas to pick up the electromagnetic field and were aligned with the main component of the E-field in the applicator. Light is emitted by the diode above a certain E-field threshold. Above this threshold the light is proportional to the strength of the E-field. Images of the field distribution were obtained using a digital camera with its shutter open while scanning a predefined route inside the applicator.

Results: Images of the E-field can clearly be seen inside the applicator centre where field strength is expected to be highest. The size of the illuminated area increases when increasing the total applied power to the applicator. Steering the focal spot in the applicator is achieved by shifting the phases of the individual antennas and can clearly be seen in the images (Fig. 1). The relationship between BSD coordinates and focus displacement was determined by comparing the position of the centre of the illuminated ellipse for BSD coordinates ranging from -6 to +6 in x and y-direction. For the Sigma60 applicator the relation of the measured focus shift to the BSD coordinate settings were found to be: 1.08±0.28 cm per BSD coordinate in x-direction and 1.06±0.14 cm per BSD coordinate in y-direction. The improved visualization of the focal spot imaged with the new DEEP device, as compared to typical images obtained with the older lamp phantom described by Wust et. al.[1], allows the center of the focal area to be determined more easily. By scanning in two orthogonal planes the shape and size of the focus can be visualized in three dimensions.

Conclusion: Because of the single diode scanning method used in this study with the new DEEP device, variations in light intensities from multiple lamps as seen in other lamp phantoms can be avoided. This allows the focus of the E-field and therefore the heated area to be determined more accurately. The uncertainty found in positioning the focus area corresponds to the uncertainty in applying the correct phase shift to the individual antennas for the BSD2000/3D hyperthermia system. The design of the phantom also allows other sensor types e.g. SAR probes to be used inside the hyperthermia applicators and these will be tested in the future.

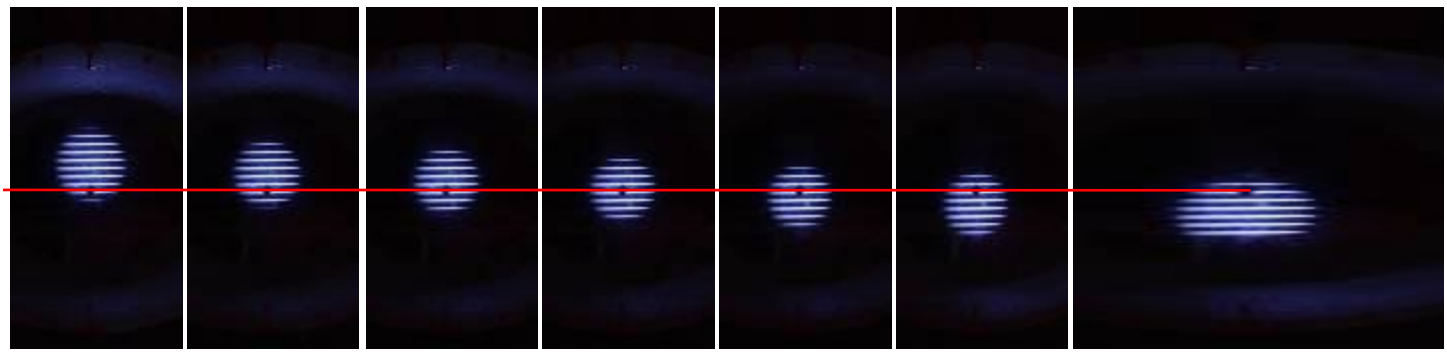

Fig. 1: shift of the focus area in y-direction; scanned lines are 1cm apart

References

[1] P. Wust, H. Fähling, A. Jordan, J. Nadobny, M. Seebass, R. Felix: Developement and testing of SAR visualization phantoms for quality control in RF hyperthermia; International Journal of Hyperthermia, 1994, vol. 10, no. 1, 127-142

136 Delivery Quality Assurance with a High Resolution Liquid Filled Ion Chamber Array for Robotic Radiosurgery

S. Adamczyk[1], M. Chan[2], T. Stelljes[3], D. Schmitt[4], A. Skrobala[1], D. Poppinga[3], M. Adamczyk[1], B. Pawalowski[1], G. Hildebrandt[5], B. Poppe[3], O. Blanck[6,7]
[1]Greater Poland Cancer Centre, Poznan, Poland
[2]University of Hong Kong, Hong Kong, Hong Kong
[3]Pius Hospital Carl v. Ossietzky University, Oldenburg, Germany
[4]Center for Radiosurgery, Frankfurt, Germany
[5]University Clinic Rostock, Rostock, Germany
[6]University Clinic Schleswig-Holstein, Kiel/Luebeck, Germany
[7]CyberKnife Center Northern Germany, Guestrow, Germany

Introduction: In this work a 2D liquid filled ion chamber array (Octavius 1000 SRS, PTW, Freiburg, Germany) was evaluated with a robotic CyberKnife (Accuray Inc, Sunnyvale, CA) and first experiences regarding sensitivity and usability in clinical practice are presented.

Materials and methods: The Octavius 1000 SRS comprises of 977 liquid filled ion chambers using microLion (PTW) technology, which are arranged on a 10 cm x 10 cm field with 2.5 mm spacing in the central 5 cm x 5 cm field. Analysis has been done with VeriSoft (Version 6.0, PTW). For evaluating the geometric accuracy of the Octavius 1000 SRS a single vertical beam with the CyberKnife robot pointed to the central ion chamber (reference) was delivered and the robot was moved in 0.1 mm steps in all directions with repeating beam delivery. We then registered the reference to the shifted measurements using the auto-alignment function in VeriSoft and compared the real versus the detected shifts. For evaluation of error detection during treatment we created a C-shaped dose distribution and deleted beams in a specific region of the treatment plan with total MU of 1%, 1.5%, 2.5% and 3%. We then delivered all plans to the Octavius 1000 SRS and compared the results to the calculated dose distribution from the original non-modified treatment plan. To verify the clinical impact and to justify the implementation of correcting angular sensitivity differences of the 1000 SRS we performed a Gamma-Index analysis of 20 extracranial and 20 intracranial clinical treatment plans.

Results: The measured shifts with VeriSoft agreed within the measurement uncertainty to the real shifts of the CyberKnife robot demonstrating excellent geometric detection accuracy of the Octavius 1000 SRS. The missing beams test showed 95.5%, 92%, 87.4%, 82.3% and 80.7% pixels passed gamma (1% local dose difference LDD, 1mm distance to agreement DTA) when removing 0%, 1%, 1.5%, 2.5% and 3% of the total MU (Fig. 1) demonstrating similar error detection accuracy compared to our gafchromic film based analysis [Blanck et al. DGMP 2013]. The clinical cases generally showed good agreement with the planned dose distribution with gamma (2% LDD, 1mm DTA) passing rates of mean 96.3% (min 84.5%, max 100%, SD 4.0%) for intracranial and mean 89.1% (min 75.9%, max 99.4%, SD 6.3%) for extracranial CyberKnife treatments. As for extracranial cases more beams are irradiated from lateral directions, the currently uncompensated beam angle dependent errors with the Octavius 1000 SRS result in lower passing rates. Detailed analyses of the treatment plan beam directions and of the Octavius 1000 SRS angular response for the CyberKnife are under investigation and will be presented.

Conclusion: We demonstrate that a high-resolution array of ion chambers (Octavius 1000 SRS) can be a precise dosimetric tool for delivery quality assurance for robotic radiosurgery.

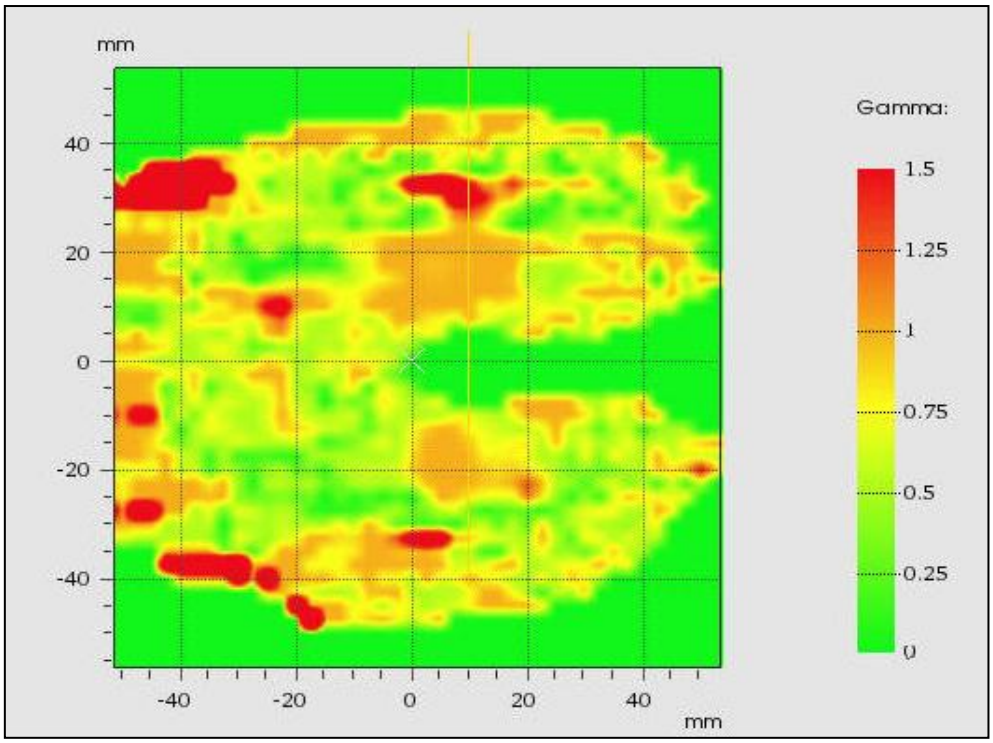

Fig. 1a: Gamma Map (1% LDD, 1mm DTA) of original the C-shaped treatment plan without beam removal. All lateral beams are pointed at the top part of the C.

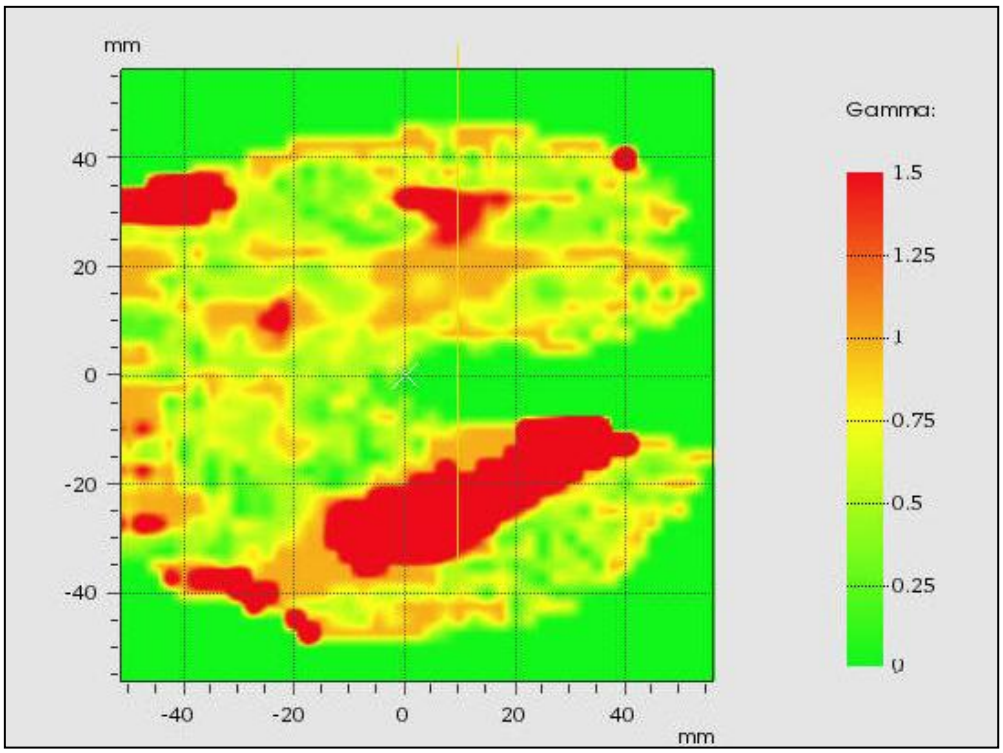

Fig. 1b: Gamma Map (1% LDD, 1mm DTA) of delivered plan with missing beams of 1.5% total MU in the lower part of the C.

References

[1] Poppe B, Stelljes TS, Looe HK, et al. Performance parameters of a liquid filled ionization chamber array. Med Phys 2013;40(8):082106.

[2] Blanck O, Masi L, Damme MC, et al. Film-Based Delivery Quality Assurance for Robotic Radiosurgery: Commissioning and Validation. Med Phys 2014. Submitted.

137 Determination of reference levels for quality assurance of flattening filter free beams

G. Nicolini[1], E. Vanetti de Palma[1], A. Clivio[1], M. F. Belosi[1], L. Cozzi[1], G. Bolard[1], P. Fenoglietto[1], H. Krauss[1], A. Fogliata[1]
[1]Oncology Institute of Southern Switzerland, Radiotherapy, Bellinzona, Switzerland

Purpose/Objective: New definitions for some dosimetric parameters to be used for quality assurance of flattening filter free (FFF) beams generated by medical linear accelerators have been suggested. The present study aims to validate these suggestions and to propose possible reference levels.

Material and methods: The main characteristics of FFF photon beams were investigated in terms of: field size, penumbra, unflatness, slope and peak-position parameters. Data were collected for 6 and 10 MV-FFF beams from three different Varian TrueBeam linacs, and a Varian Clinac iX upgraded to FFF capability for its 6 MV. Measurements were performed with a 2D-array (Starcheck system from PTW-Freiburg), with a linear array (LA48 system from PTW-Freiburg) and with the portal dosimetry method GLAaS utilizing the build-in portal imager of TrueBeam.

Results: All the parameters suggested to characterize the FFF beams were measured and evaluated. Little variation was observed among the different linacs. Referring to two reference field sizes of 10x10 and 20x20cm2, at SDD=100cm and d=dmax, from the portal imaging data converted into dose map with the GLAaS method, the following results were obtained, averaged on X and Y profiles. Field size: 9.95±0.02 cm and 19.98±0.03 cm (including all energies. Penumbra: 2.7±0.3 mm and 2.9±0.3 mm for 6MV-FFF; 3.1±0.2 mm and 3.3±0.3 for 10MV-FFF. Unflatness: 1.11±0.01 and 1.25±0.01 for 6MV-FFF; 1.21±0.01 and 1.50±0.01 for 10MV-FFF. Slope: 0.320±0.020 %/mm and 0.43±0.015 %/mm for 6MV-FFF; 0.657±0.023 %/mm and 0.795±0.017 %/mm for 10MV-FFF. Peak Position: -0.2±0.2 mm and -0.4±0.2 mm for 6MV-FFF; -0.3±0.2 mm and 0.7±0.3 mm for 10MV-FFF. Results would depend upon measurement depth.

With thresholds set to at least 95% confidence level from the measured data, and to account for possible variations between detectors, methods and experimental settings, a tolerance set of: 1 mm for field size and penumbra, 0.04 for unflatness, 0.1 %/mm for slope and 1 mm for peak position could be proposed from our data.

Conclusion: The parameters introduced to characterize the FFF profiles (in particular the unflatness, the slope and the peak position) appear to be a viable solution for routine checks, also presenting strong similarity to the conventional parameters widely used for flattened beams. The results from three different TrueBeams and a Clinac-iX machine suggested the robustness of the methods and the possibility to use general tolerances for the parameters. The data suggested also the reproducibility of beam characteristics among different systems (of the same vendor) and could therefore be possibly generalized.

138 Development of an EPID-Dosimetry Tool for IMRT Plan QA

S. Fink[1], O. Sauer[1]
[1]Uniklinikum Würzburg, Klinik und Poliklinik für Strahlentherapie, Würzburg, Germany

Purpose: The increasing complexity of the IMRT plans demands for increasing quality assurance effort. Different approaches are available as commercial solutions. In general a phantom capable to measure dose distributions in 3D is used. Existing systems suffer from a low spatial resolution or an obscure relation between measured deviations and dose to PTV or OARs. Goal of this project is to develop an IMRT quality assurance tool for patient specific plan QA based on EPID dosimetry. A review of EPID-dosimetry was given by Van Elmpt et al [1].

Materials and methods: All measurements were made using an Elekta Synergy equipped with the Agility MLC, with 6MV and 10MV X-rays. The fields and therefore the dose planes were measured with the standard EPID, the iViewGT™. The iViewGT™ is the aSi-EPID of the LINAC with 1024x1024 pixels of size 0.4x0.4 mm^2 corresponding to a pixel size of 0.25x0.25 mm^2 in the plane of the isocenter. The treatment plans and respective planar dose distributions were calculated with the treatment planning system Pinnacle 9.6 and evaluated using in-house developed software based on MATLAB (MathWorks Inc.). The measured grey values from the EPID were calibrated to dose by applying the quotient of the output in water to the EPID signal for quadratic homogeneous fields. For the comparison a gamma criterion was used with 3 mm Distance-To-Agreement (in the isocenter plane) and 3 % Dose-Difference. To test the procedure, IMRT-fields with intentional errors were measured and compared to the original plan. One of the intentional errors was a shift of one segment edge by 5 mm, the other was a segment containing 5 % less dose.

Results: The EPID dosimetry tool showed a good correlation between the measurement and the expected dose level. The unaltered plan had a pass rate (Gamma 3%/3mm, dose threshold 10% of planned dose) of 98 %. The intentionally introduced errors are visible on the gamma maps (Fig. 2). Although the shifted edge is clearly visible (Fig. 2 middle), the pass rate dropped only marginally to 97 %. The plan including the dose deviation failed the gamma criterion with a pass rate of 83 % (Fig. 2 right).
Conclusion: An EPID dosimetry tool was developed for IMRT quality assurance. Intentionally introduced errors were well detected by our procedure.
Next step is to compare the performance of the EPID dosimetry tool to the standard QA tools at our clinic, i.e. the OCTAVIUS 4D (PTW) and ArcCheck (Sun Nuclear).

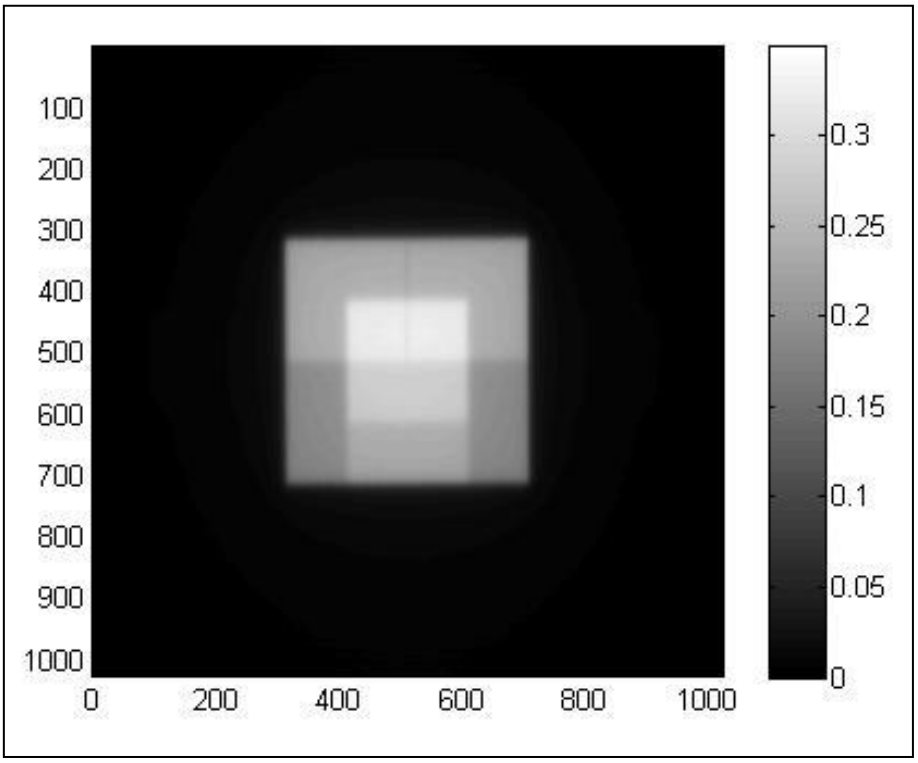

Fig. 1: Dose Map of the unaltered Plan [Gy]

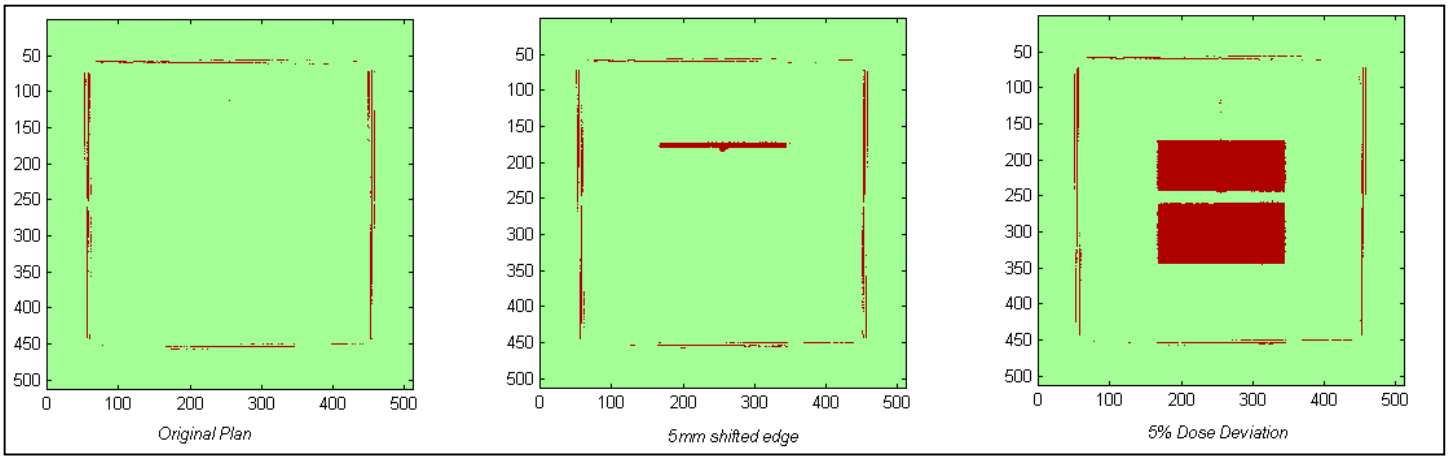

Fig. 2: The passed (green/light) and failed (red/dark) points of the Gamma criterion are shown for the different examples of introduced errors in comparison with the original plan.

References

[1] van Elmpt, W.: A literature review of electronic portal imaging for radiotherapy dosimetry, Radiotherapy and Oncology 88 (2008) S. 289–309

139 Assessment of and clinical experience with a novel system for 3D radiation treatment plan QA intended for independent dose calculation for VMAT.

P. Winkler[1], A. Uller[1], S. Odreitz[1], K. Maier[2], W. Sprengel[2]
[1]Medical University of Graz, Therapeutic Radiology and Oncology, Graz, Austria
2Graz University of Technology, Institute of Materials Physics, Graz, Austria

Background: Individual quality assurance for intensity modulated treatment plans has become an elaborate task in a medical physicist's daily routine. The advancement from static IMRT to volumetric modulated arc technique (VMAT) has prolonged this requirement. Consequently, we are seeking efficient QA protocols with the demand to ensure the highest level on safety. Measurement-based QA for individual treatment plans is essential and should be obligatory when new treatment modalities are implemented and the experience is limited. With increasing experience, many clinics change their QA-protocols to a process based on independent dose calculation, complemented by some additional machine-related QA-measurements. For the latter approach, a number of different software tools are commercially available. The system Mobius3D (Mobius Medical Systems, USA) appears novel in several aspects.

Aim of this work is to present the results of the assessment and the first clinical experience with this system in a multi-vendor environment.

Materials and methods: Mobius3D (M3D) performs independent dose calculation for various types of treatment plans based on the patient's CT-data in three dimensions. It uses a collapsed-cone dose calculation algorithm. The vendor supplies a generic beam model for a variety of common machine / energy / MLC-combinations, requiring only one single input-parameter from the user. M3D calculates a dose comparison with the usual metrics (dose-difference, gamma-criterion) and displays, besides other parameters, DVH-comparisons and statistics for dose coverage and dose to all contoured structures.

We have three different treatment planning systems (TPS) with a total of five dose calculation algorithms in use for the calculation of intensity modulated treatment plans (IMRT and VMAT): Acuros XB and AAA algorithms in Eclipse (Varian Medical Systems), CCC-Superposition inPinnacle (Philips), Monte Carlo and Pencil Beam in iPlan (Brainlab).
We compared the generic beam models from M3D with the in-house measured beam data for three energies (6MeV, 18MeV and 6 MeV SRS mode) and two multi-leaf collimators (Millenium, HD) for Clinac iX and Novalis Tx accelerators (Varian Medical Systems) and re-calculated reference- and standard field configurations. In the next step of the assessment we re-calculated twenty-five clinical VMAT-plans from our three TPS with M3D. Reference-point dose and gamma-criterion passing rates for the full dose matrix and the PTVs were evaluated (tolerance level settings: 3% dose difference, 2mm distance-to-agreement).

Results: The generic beam models from M3D agreed well with the models from our TPS. Almost all measured points in standard- and reference fields showed deviations less than 1%. Deviations exceeding 1% were found only for very small fields (<2x2cm²) and a depth in phantom of more than 20 cm.
For clinical VMAT-plans (calculated in M3D on the patient's CT-datasets) we found 1.2% average deviation in the dose at the reference point (max.: 2.8 %). Average Gamma-index passing rates were 98.7 % for the full dose matrix and 93.6% for the PTV, respectively. For air cavities and low-density regions significant dose deviations were observed between M3D and TPS for the AAA and CCC algorithms (figure 1), and to a lesser extent for the Acuros XB and Monte Carlo Algorithms.

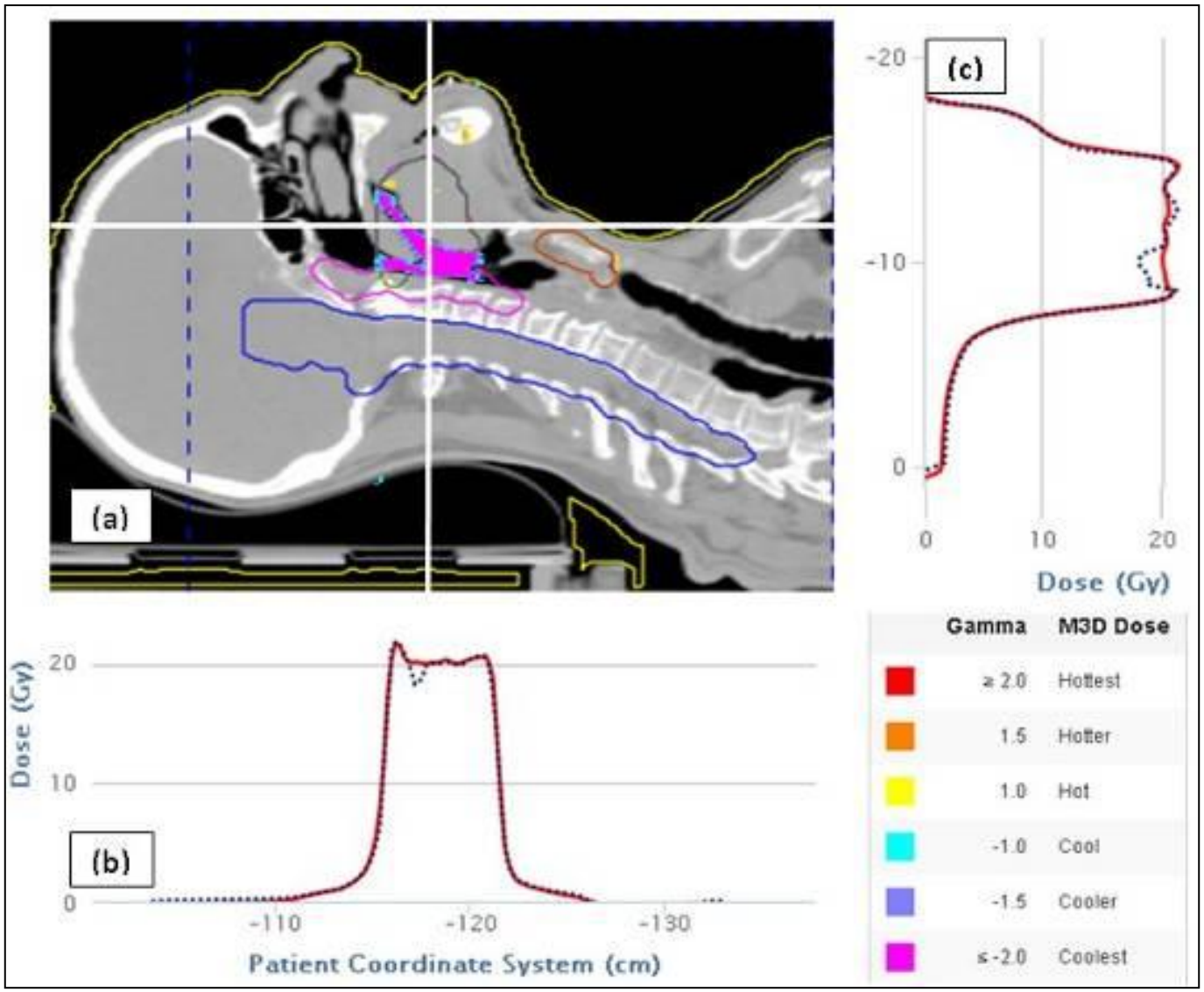

Fig. 1: Gamma evaluation using M3D for a VMAT-plan calculated with Eclipse AAA algorithm. (a) sagittal gamma-map (b) horizontal dose profile (c) vertical dose profile.

Discussion: Mobius3D is a very powerful tool for independent dose calculation in VMAT-QA. It can be well integrated in a QA concept that relies primarily on re-calculations. Using this system shifts the focus of plan analysis and plan QA towards more complex issues: while simple systems for independent dose-calculation are normally used for checking the dose and a few representative points, it is now possible to study the influence of parameters like tissue heterogeneities or body contouring on the robustness of dose calculation.

140 A multi-institutional QA study for VMAT benchmark plans

M. Pasler[1,2], J. Kaas[3], T. Perik[3], J. Geuze[3], R. Dreindl[4,2], T. Künzler[5], D. Georg[2], F. Wittkamper[3]
[1]Gemeinschaftspraxis für Strahlentherapie, Friedrichshafen, Germany
[2]Medical University Vienna, Department of Radiotherapy and Christian Doppler Laboratory for Medical Radiation Research for Radiation Oncology, Vienna, Austria
[3]The Netherlands Cancer Institute, Department of Radiation Oncology, Amsterdam, Netherlands
[4]EBG MedAustron GmbH, Wr. Neustadt, Austria
[5]Landeskrankenhaus Feldkirch, Institute of Medical Physics, Feldkirch, Austria

Introduction: Machine specific quality assurance (QA) is an important prerequisite to safely deposit the prescribed dose to the target volume (Bedford et al 2009, Haga et al 2009). The purpose of this study is to create VMAT QA benchmark plans and to obtain a systematic overview of dynamic parameter uncertainties at four different institutes. Furthermore we demonstrate the validity of geometrical errors indicated by logfiles by evaluating dosimetric accuracy for single control points of VMAT plans.

Methods: VMAT test plans were generated using iComCAT (Elekta) and delivered by 14 Elekta linacs (9 Synergy with MLCi, 5 Agility) in Friedrichshafen1, Amsterdam2, Vienna3 and Feldkirch5. Test plans were based on square field shapes with varying field size (0.5x0.5cm2 to 24x24cm2) and a full gantry rotation. Control points were composed to vary dose rate, MLC, Jaw and gantry speed.

Planned vs. actual position of individual leaves, jaws and gantry were quantified by analyzing the linac's log files. Delivery robustness in terms of dose rate stability and delivery time was investigated for each of the 14 linacs and subsequent a inter-linac comparison was performed.

Dosimetric verification in terms of intra-linac consistency was performed at one institute (Amsterdam) using the OCTAVIUS 4D system and the Verisoft 6.0 evaluation software (both PTW). Relative dose differences were assessed by mean gamma (1mm/1%) for each control point and compared to the results of the log file evaluation (Stock et al 2005).

Results: The mean leaf error during plan delivery was 0.28±0.15mm for all linacs. The maximum errors for leave and jaw positions were found at control points where the moving direction reversed: up to 6.7mm deviation were detected between planned and actual positions (range 2.9mm to 6.7mm). A correlation between MLC speed and error was observed, the errors increased for higher MLC speed.

Delivery time for the same plan varied from 80s to 128s, depending on the linac's ability to keep a constant low dose rate for those arc segments demanding maximum leaf speed. For linacs with poor low dose rate stability, poor delivery robustness was found. However, exact coordination of dynamic parameters was observed for all linacs: dose rate decrease coincided very accurately with leave and gantry deceleration.

Dosimetric evaluation of delivery robustness for plans including all control points resulted in a mean gamma of 0.68±0.19, indicating very accurate VMAT plan reproducibility. Control point resolved analysis correlated very well with log file analysis, as shown in fig.1. A mean gamma of 0.49±0.30 was found for single control points with coinciding leaf positions (deviation <1mm). For positional leaf deviations >1mm, the mean gamma value increased up to a hundredfold, tracing very low agreement for two plans at the same control point.

Conclusion: Although VMAT delivery robustness regarding delivery time and dose rate stability varied, overall MLC errors were comparable. Observation of log files enables a better understanding of linac limitations in terms of maximum MLC speed and low dose rate stability.

The dosimetric evaluation for single control points provides strong evidence that log file indicated errors have an impact on delivery accuracy for small arc segments. Log file analysis is a valuable tool for proactive VMAT QA in terms of troubleshooting, long-term stability checks and linac intercomparison.

References

[1] Bedford JL, Warrington A. Commissioning of volumetric modulated arc therapy (VMAT). Int J Rad Onc Biol Phys 2009;73:537-545.
[2] Haga A, Nakagawa K, Shiraishi K et al. Quality assurance of volumetric modulated arc therapy using Elekta Synergy. Acta Oncol 2009;48:1193-1197.
[3] Stock M, Kroupa B, Georg D. Interpretation and evaluation of the gamma index and the gamma index angle for the verification of IMRT hybrid plans. Phys Med Biol 2005;50:399-411.

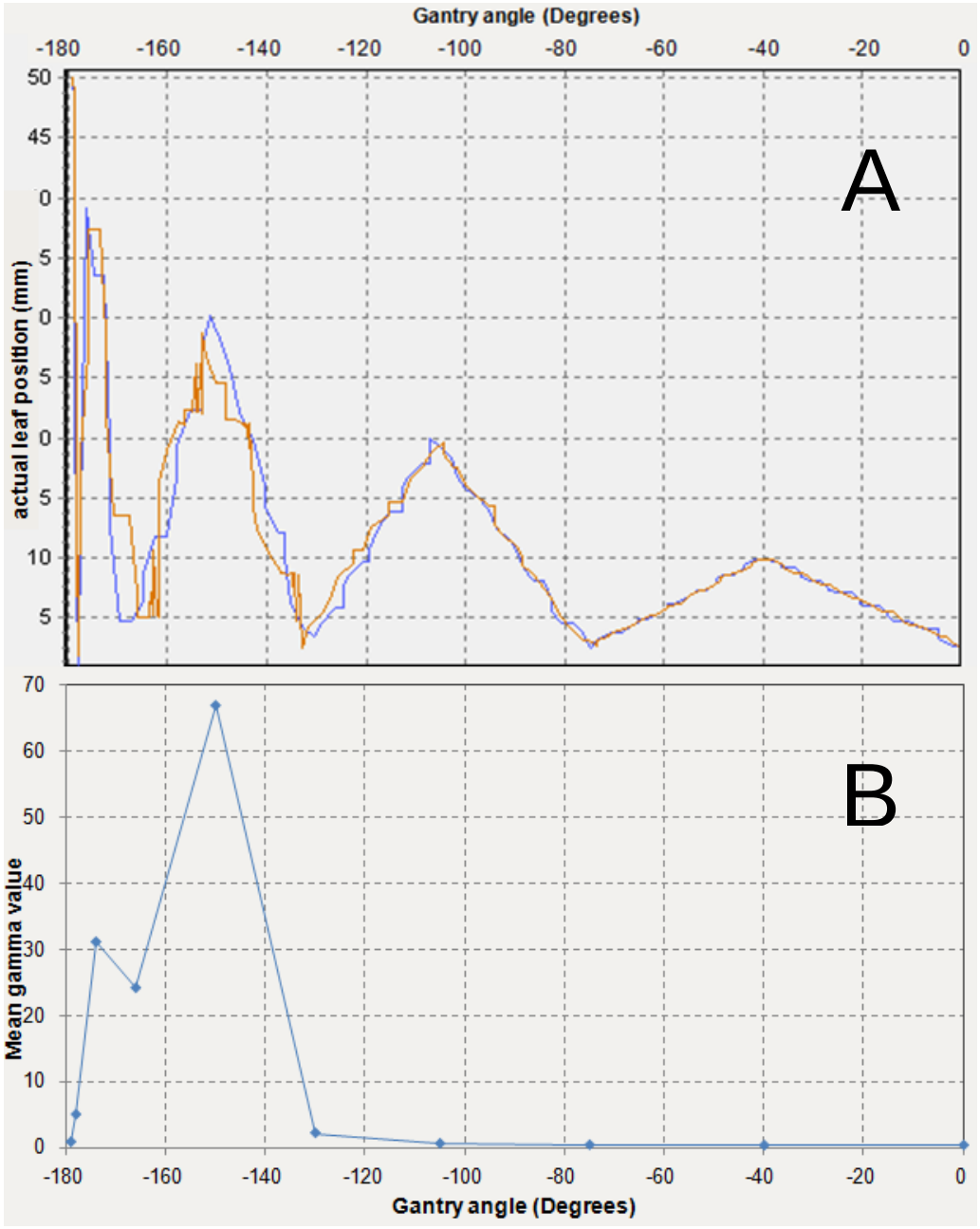

Fig. 8 Example of the correlation between deviation in leaf position and high gamma value at gantry angle 150° is shown: Actual leaf position of one single leaf for the same plan and two consecutive plan deliveries (A) and the corresponding gamma value (B).

Session 24 – Magnetic resonance imaging III: Experimental Applications

Chairs: M. E. Ladd (Heidelberg/DE), J. R. Reichenbach (Jena/DE)

141 Validation of quantitative blood flow by DCE-MRI two-compartment analysis using blood pool contrast medium in swine muscle

S. Hindel[1], A. Sauerbrey[1], M. Maaß[2], L. Lüdemann[1]
[1]University Hospital Essen, Department of Radiotherapy, Essen, Germany
[2]Evangelisches Krankenhaus Wesel, Wesel, Germany

Introduction: We evaluated the use of a two-compartment model for the quantification of arterial and capillary muscular blood flow in large mammals using blood pool contrast media and a 3D gradient-echo sequence with keyhole technique. The exact determination of blood flow is crucial to the assessment of existing pharmacokinetic models such as the Tofts model [1] and gives clear insights into physiological situations.

Materials and methods: A total of three female pigs (56-60 kg body weight) were investigated. An ultrasonic Doppler probe (Transonic Systems Inc., USA) was attached to the right femoral artery to determine the total flow in the hind leg musculature [2]. The femoral artery was catheterized to enable continuous local administration of adenosine. The continuous adenosine injection resulted in steady blood flow levels up to four times the baseline level. In this way, three different stable perfusion levels were induced. The MR protocol included a 3D gradient-echo sequence with a temporal resolution of approximately 1.3 seconds and the following parameters: TR = 2.69 ms, TE = 0.86 ms, α = 30°, voxel size of 2.89 × 4.5 × 2.9 mm3 , 160 × 48 × 128 reconstruction matrix. 100 frames were recorded with distribution of peripheral k-space lines to several images with keyhole technique (region A and B both 20%). After the fifth acquisition of the first dynamic sequence, 0.1 mL/kg body weight of blood pool contrast medium (0.25 mMol/mL gadofosveset trisodium) was injected via the central venous catheter, delivery rate: 5 mL/s. Time dependent maps of relaxation rate changes ΔR(t) were computed using the method of Li et al. [3]. A veterinary physician created virtual segmentations of the hind leg with the 3D visualization software Amira 5.2 (see Figure 1).

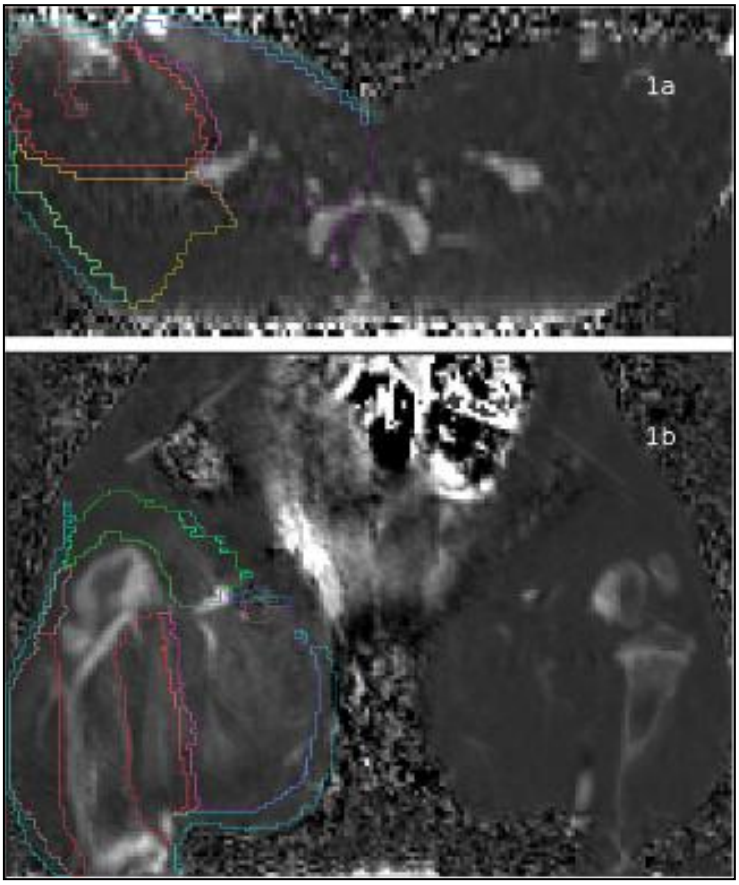

Fig. 1: relaxivity rate mchange based blood volume map creatd from the 3D gradient-echo imgages and segimentation examples for the hind leg musculature in axial (a) and coronal (B) view.

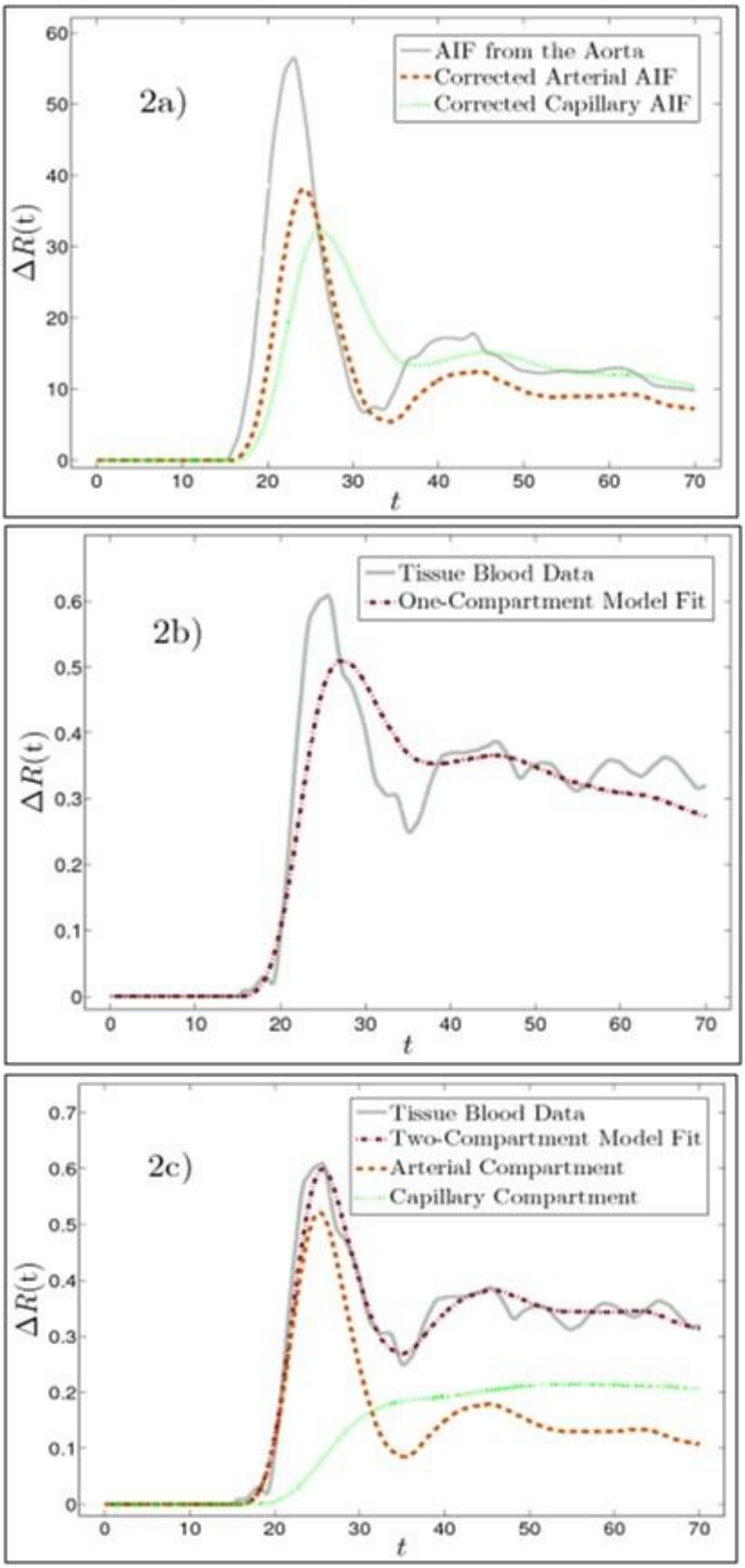

Fig. 2: The estimated AIF measured in the aorta and the delay and dispersion corrected AIFs for the lower leg segment (a). Tissue blood relaxivity change curves and the resulting model fits for the one (b) and two (c) compartment model in the respective segment. Due to the large bolus fraction in the lower leg curve the one-compartment model leads to an underestimation of the steepness and height of the bolus and thus to an underestimation of the flow.

The labeled segments were: medial, cranial, lateral and pelvis thigh muscles, lower leg, bones, skin and fat. The first 80 seconds of the relaxation change time-curves of the voxels in these segments were used for model fitting. Beforehand the curves time resolution was increased to 0.1 seconds. Just as we proceeded with the arterial input function (AIF) Caest(t) measured in the aorta. The flow determination is influenced not only by height, but mainly due to the steepness of the tissue curve. Thats why single-compartment approaches often lead to underestimations in high flow situations (see figure1b). Therefore, the perfusion of the different anatomic regions was calculated using one- and two-compartment models with delay and dispersion corrected AIFs. The design of the models was based on the indicator dilution theory and required the deconvolution of the tissue blood concentration time curve in tissue capillaries, Cb(t) [4]:

$$C_b^i(t) = F^i \cdot C_a^i(t) * R^i(t).$$

Where i = a, c indicates the respective compartment (arteriel or capillary), Fi are the perfusions and Ri(t) are the respective residue functions with mean transit times Ti:

$$R^i(t) = e^{-t}/T^i.$$

To calculate the AIFs Cia(t) for the two single compartments we corrected Caest(t) for delay δti and dispersion times 1/βi:

$$C_a^i(t) = C_a^{est}(t + \delta t^i) * h^i(t).$$

Where

$$h^i(t) = \beta^i \cdot e^{-\beta^i t}$$

are the vascular transport functions, which describe the bolus dispersion during the effective transit times 1/βi from the site of AIF measurement to the input to the particular region of interest. Finally, the sum

$$C_b(t) = \sum_i C_b^i(t)$$

gave the total tissue blood concentration time curve in the considered region of interest. Fixing Fa=0 represented the one-compartment model. By calculating the ratio of the washout region (75-95 seconds) of the tissue blood concentration curves of all considered voxels and of the washout of the AIF, blood volume maps were created. Appropriate starting values for the capillary and arterial compartment were estimated by fitting the one compartment model to the portion of each anatomic segment which had a blood volume of 3.5% or lower and 10% or higher, respectively. The F-test for model comparison was used to decide whether to use the results of the one or two compartment model fit. We calculated the total flow by integrating the volume weighted perfusion values over the whole measured region.

Results: The resulting values of delay, dispersion, blood volume, mean transit time and flow were all in physiologically and physically reasonable ranges. In 29 of 72 ROIs the blood signal was separated into a capillary and an arterial signal contribution, proven by the F-test. The overall flow of the hind leg muscles, as measured by the ultrasound probe, highly correlated with the total flow from the MRI measurement, P <0.001 (see Figure 3). The correlation coefficient between the two measurement methods is 0.91. Linear regression yielded a slope of 1.2 and a y-axis intercept of 322 ml/min. The flow offset and the flow overestimation can be explained by the increase of the capillary flow fraction and the superimposition of the arterial and capillary curve component.

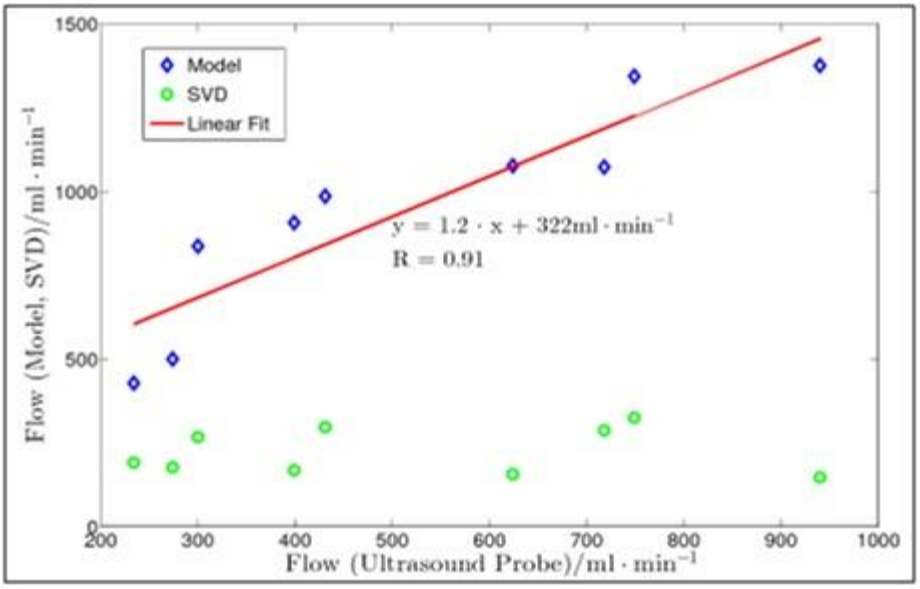

Fig. 3: Correlation of the entire hind leg flow measured with DCE-MRI with the flow measured with the Doppler ultrasound probe at the femoral artery of the supply region in question. Three different stable flow levels of the three pigs were induced and measured. The correlation coefficient between the two measurement methods is 0.91. The Comparison with results of the singular value decomposition (SVD) method [5] showed that the SVD underestimates the flow and was not able to detect its increase in low perfused muscle tissue.

Summary: The DCE-MRI technique of the present study in combination with the two-compartment model allows for the absolute quantification of the muscle perfusion as well as the separate determination of the bone perfusion. The results show that the technique has sufficient accuracy and reproducibility in order to evaluate existing pharmacokinetic models.

References

[1] Tofts, et al., JMRI 1999; (10: 223-32)
[2] Sauerbrey, et al., BioMed Res Int 2014; (ID 300506)
[3] Li, et al., JMRI 2000 (12:347-357)
[4] Calamante et al., JMRI 2005; 22:718-722
[5] Ostergaard, et al., MRM 1996; (36:715-725)

142 Retrospective four-dimensional analysis of magnetic resonance imaging data in lung ventilation studies

R. Etzel[1], M. Fiebich[1]
[1]Technische Hochschule Mittelhessen, Institut für Medizinische Physik und Strahlenschutz, Gießen, Germany

Introduction: The aim of this study was to develop a new ImageJ plugin to get a simple and easy to handle tool for a four-dimensional analysis of magnetic resonance imaging data to visualize and quantify lung ventilation. The analysis was based on change of pixel intensities during variation of the oxygen concentration to use the contrast enhancing characteristic of oxygen in functional lung MRI [1-3]. The visualization should be realized by providing a characteristic result image for each slice and enable a time-dependency quantification based on a pixel-precise graphical representation of grey values.

Materials and methods: A plugin was developed and programmed by using the tool Fiji, which is an image processing package based on ImageJ. The test experiments were all conducted on previously recorded 1.5T magnetic resonance images of narcotized and mechanically ventilated pigs, whose lungs were partially blocked mechanically. The MRI images were recorded in both dorsal and transversal plane, with a slice thickness of 8 mm and 32 images per slice. The oxygen concentration of the pigs' breathing was alternated periodically from 21 to 100 percent and backwards within an eight seconds interval.

After importing the MR sequence into Fiji the tool could be started automatically with pre-set or manually adjusted parameters. The plugin analyzed all pixels of each image temporally to detect the variation of gray values related to the temporal change in oxygen rate.

Results: First results could already be seen after a simple subtraction of two images, one with an oxygen rate of 21 percent and another with 100 percent, of the same slice (Fig. 1). Areas with a higher change in pixel values resulted in a higher signal in the subtraction image. The mechanically blocked and in this way lower ventilated lung areas could be identified easily.

To realize the four-dimensional analysis of MRI data the change in value and time-to-peak of output signal were stored for all pixels while alternating the oxygen rate periodically. The quotient of these two parameters was displayed in a new image to create a characteristic result image for each slice. In addition the stored data was printed out in curves for each pixel. Figure 2 shows the time-dependent change in value of pixel intensity for a representative pixel, which is located in the lung. This curve was smoothed with a gliding average filter.

The new ImageJ plugin is able to detect time-dependent changes in signal intensity during dynamic examination of the lung. Change of pixel intensities and time-to-peak of the output signal showed a significant relation between oxygen rate and gray value of the stored data and the generated images and curves. The blocked lung areas could be identified in the result images since pixels located in these regions representing less signal in contrast with other regions.

Conclusion: A simple and easy to handle tool for time-dependency analysis of MRI data was successfully developed in this work. The intended visualization and quantification of lung ventilation could be realized in a useful and highly diagnostic way.

This work confirmed the ability of oxygen to be used as contrast media in magnetic resonance imaging. The developed and tested ImageJ plugin for a four-dimensional analysis of MRI data has demonstrated the significance of a quantification of lung ventilation based on oxygen-induced change in output signal.

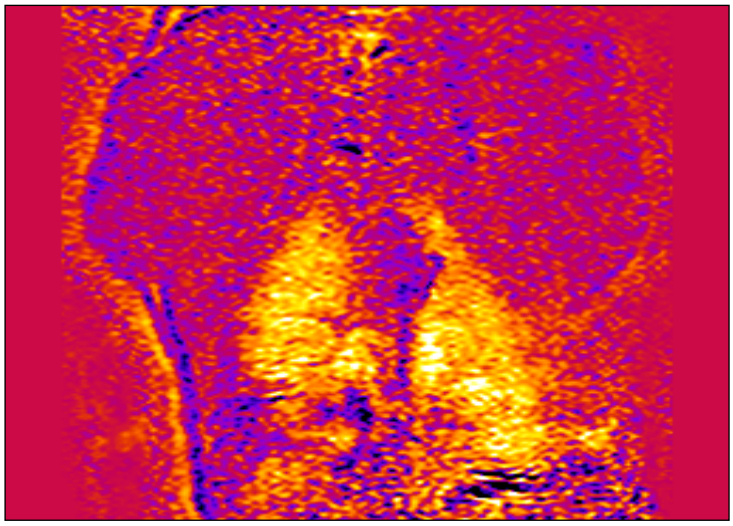

Fig. 1: Subtraction of two MRI images of the pigs' lung

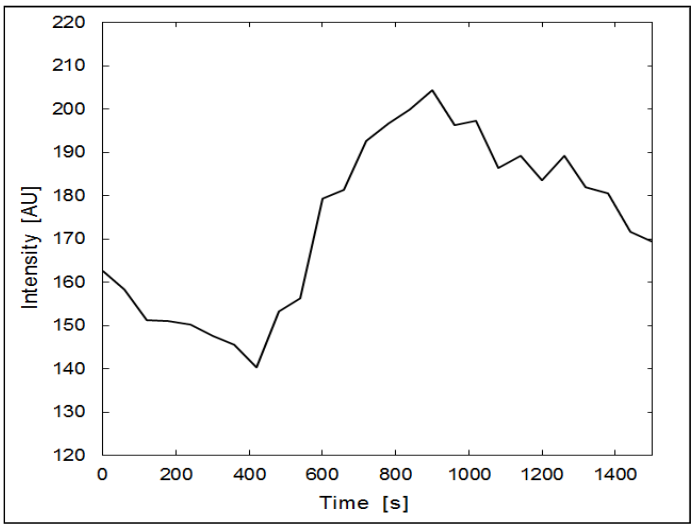

Fig. 2: Time-dependent change of pixel intensity

References

[1] Beer M., Stäb D., Oechsner M., Hahn D., Köstler H., Hebestreit H., Jakob P.: *Sauerstoffverstärkte funktionelle MR-Lungenbildgebung*, Radiologe 49 (2009), S. 732-738

[2] Takenaka D., Puderbach M., Ohno Y., Risse F., Ley S., Sugimura K., Kauczor H.: *Oxygen-enhanced lung magnetic resonance imaging: influence of inversion pulse slice selectivity on inversion recovery half-Fourier single-shot turbo spin-echo signal*, Jpn J Radiol 29 (2011), S. 244-250

[3] Stadler A., Stiebellehner L., Jakob P., Arnold J., Bankier A.: *T1-Maps und O_2-verstärkte MRT der erkrankten Lunge*, Radiologe 46 (2006), S. 282-289

143 Comparison of Three Ultrashort Echo Time Sequences for MRI of an Ancient Mummified Human Hand

A. Özen[1], U. Ludwig[1], L. Öhrström[2], F. Rühli[2], M. Bock[1]
[1]University Medical Center Freiburg, Radiology – Medical Physics, Freiburg, Germany
[2]Institute of Anatomy, University of Zurich, Centre for Evolutionary Medicine, Zurich, Switzerland

Introduction: Ancient mummies are unique objects of human history, and therefore non-invasive and non-destructive examination technologies are favored for paleopathology studies. X-ray based imaging methods such as computed tomography (CT) are very useful to study mummies and other valuable ancient remains non-destructively. Recently, feasibility of magnetic resonance imaging (MRI) of mummified tissue has been shown [1]. MRI of the de-hydrated mummy is challenging due to the low water content and the very short transverse relaxation times T_2*. To overcome the signal loss associated with the short T_2*, pulse sequences with very short echo times (TE) are used. The objective of this study was to compare 3 different short-TE pulse sequences: ultra-short echo time (UTE), point-wise encoding time reduction with radial acquisition (PETRA), and single point imaging (SPI).

Materials and methods: To compare the three short-TE pulse sequences, a mummified left hand of an embalmed ancient Egyptian mummy (ca. 1500 – 1100 BC) was used (Fig. 1a). MR images of a mummified hand were acquired with all 3 sequences at clinical MRI field strengths of 1.5 T and 3 T (Siemens, Erlangen) using home-made solenoid Tx/Rx RF coils. Dedicated Tx/Rx switches were also constructed.
In 3D UTE imaging [2], a nonselective rectangular RF pulse of 60 □s duration was applied. The following other imaging parameters were used: TE = 70 □s, 50000 radial spokes, acquisition bandwidth: 639 Hz/pixel, TR = 10 ms, flip angle □ = 10^o, FOV: $(206\ mm)^3$, isotropic voxel size: $(0.9\ mm)^3$, total scan time: 10 min. In PETRA [3], the excitation is not non-selective. Due to the time delay between the RF pulse and the start of the acquisition, center of the k-space is missing which is compensated by single point acquisition of the k-space center at the end of the radial acquisition. The imaging parameters for PETRA sequence was set to the same as UTE. In SPI [4], a single k-space data point is acquired at each TR, and 3D k-space is acquired onto a Cartesian grid. SPI was performed with a larger voxel size of 1.7x1.7x3.4 mm^3 due to system hardware limitations. The following other imaging parameters were used: FOV: $(212\ mm)^3$, □ = 2^o, acquisition delay: 300 □s, TR = 2 ms. For 64 x 128 x128 points it takes 35 min in total. For SPI in 3T, voxel size was reduced to 1.6x1.6x3.2 mm^3, and the acquisition delay to 280 □s s, because the gradient hardware of the 3T system is stronger.
Differences in the imaging parameters were accounted for in signal to noise ratio (SNR) calculations [5]. UTE sequence is also used for relaxation time measurements, and MATLAB® is used for the computations.

Results: In all MR images tissue differentiation was feasible; major anatomical structures such as bones, tendons and muscles could be identified (Figure 2). Skin with embalming resin shows a very high signal, whereas it appears iso-intense to the neighboring tissues in CT. PETRA offers higher SNR, yet it fails to display small anatomical structures due to image blurring. Due to longer acquisition delay (i.e., echo time), SPI has a lower SNR especially for the anatomical structures with shorter T_2^* values, however it is not affected by blurring artifacts.T_2^* varies between 40 – 600 □s and T_1 varies between 30 – 400 ms. Metacarpal spongy bones have very low SNR, therefore, T_2^* value could not be calculated.

Fig. 1: (a) Left hand of the Egyptian mummy. Yellow line shows the corresponding slice taken into consideration in the image analysis. (b) Mummy hand placed in the solenoid coil which is put on a holder to place the sample in iso-center

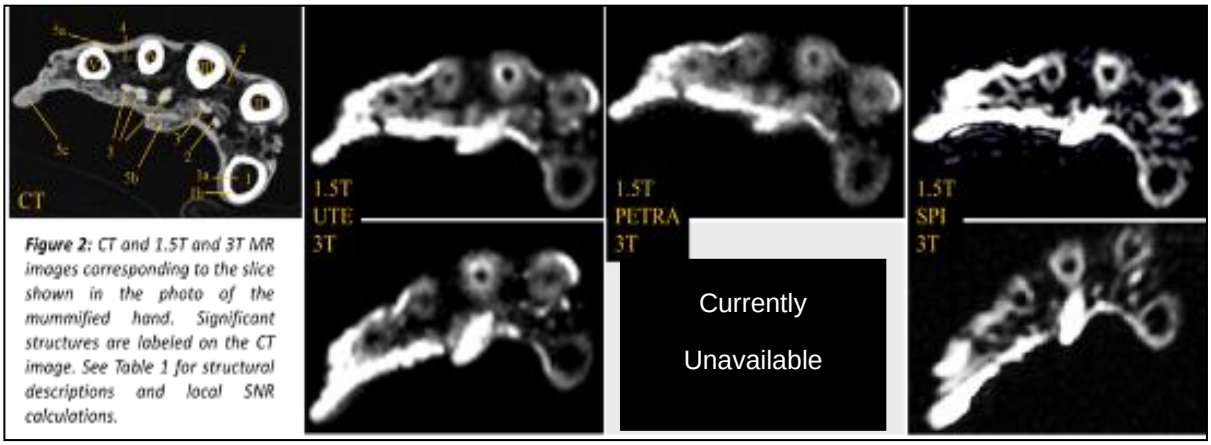

Figure 2: CT and 1.5T and 3T MR images corresponding to the slice shown in the photo of the mummified hand. Significant structures are labeled on the CT image. See Table 1 for structural descriptions and local SNR calculations.

Discussion: Radial sequences are more prone to artifacts due to signal decay during the image acquisition. If these sequences were used clinically (for example for bone imaging in combined PET/MR systems) PETRA and SPI are very silent due to continuous gradient ramps. However, SPI with its long scan durations is not suitable for most clinical exams. UTE and PETRA have similar scan times, which are in the clinically acceptable range as long as TR is kept short and low flip angles are used. SPI image does not suffer from blurring artifacts, therefore anatomical structures better distinguished and localized. Spatial localization in 3D is best performed with UTE, which is perfectly non-slice-selective, whereas PETRA and gradient-ramped SPI introduce some spatial selectivity due to the presence of a slice selection gradient during RF excitation.

References

[1] Öhrström LM et al. “Scenes from the Past MR Imaging versus CT of Ancient Egyptian Mummified Tissues”, RadioGraphics, pp. 291–296, 2013.

[2] Holmes JE et al. MR imaging with ultrashort TE (UTE) pulse sequences: Basic principles. *Radiography*, *11*(3), 163–174, 2005.

[3] Grodzki DM et al. Ultrashort echo time imaging using pointwise encoding time reduction with radial acquisition (PETRA). Magn Reson Med, 67(2):510–518, 2012.

[4] Balcom BJ et al. Single-point ramped imaging with T1 enhancement (SPRITE). J Magn Reson A, 123:131–134, 1996.

[5] Edelstein, W et al. The intrinsic signal-to-noise ratio in NMR imaging. *Magnetic Resonance in Medicine*, *3*(4), 604–618, 1986.

144 High-Resolution ex-vivo diffusion imaging and tractography of the human brain

C. Wieseotte[1,2], L. Wald[3], L.M. Schreiber[1]
[1]Johannes Gutenberg University Mainz Medical School, Section of Medical Physics, Mainz, Germany
[2]Max Planck Graduate Center, Mainz, Germany
[3]Massachusetts General Hospital, Athinoula A. Martinos Center, Boston, United States

Introduction: Diffusion weighted magnetic resonance imaging (DWI) serves as the basis for neuronal fiber tracking methods such as diffusion tensor imaging (DTI), diffusion spectrum imaging (DSI), q-ball imaging (QBI) and many more. Spatial resolution for in-vivo studies is mainly limited by long acquisition times, especially for high angular resolution protocols.
Ex-vivo studies, however, do not suffer from this limitation and thus can achieve significantly higher spatial and angular resolution while being intrinsically free of motion artifacts.

A major challenge of ex-vivo imaging is that tissue samples have to be fixed, often in Fomblin or Formalin, which decreases relaxation times and water diffusivity (Fig. 1). This leads to significantly lower SNR and diffusion contrast compared to in-vivo studies.

The purpose of this study was to evaluate the feasibility of high-resolution ex-vivo diffusion weighted imaging and tractography of the human brain, using a purpose-built 60 channel coil array and very high b-values.

Materials and methods: In order to minimize the distance between sample and receive coils, thus maximizing SNR, a special, closely fitting 60 channel coil array was developed for this study (Fig. 2). Diffusion imaging was performed on the Connectome MRI system at the Athinoula A. Martinos Center in Boston which is equipped with a 300 mT/m gradient system [1]. This enabled the use of very high b-values (b=12000 s/mm^2) necessary to achieve sufficient diffusion contrast while maintaining a relatively short echo time of 58 ms. Images were acquired using a segmented 3D EPI sequence.

Results: Our results show, that even with b=12000 s/mm^2 and 0.5 mm isotropic resolution the SNR in the center of the hemisphere with a single acquisition is sufficient to see contrasts between different diffusion encoding directions. QBI reconstruction of the fiber tracts of a dataset with 60 diffusion directions (Fig. 3) shows two exemplary fiber bundles originating in the corpus callosum.

Conclusion: Diffusion weighted images of an ex-vivo human hemisphere with an isotropic resolution of 0.5 mm were acquired using a segmented 3D EPI sequence. Although TE was in the range of T_2 and a very high b-value was used, the SNR and diffusion contrast of a single acquisition are sufficient to perform tractographic analysis. Strategies to further increase the resolution are currently developed and are subject to future studies.

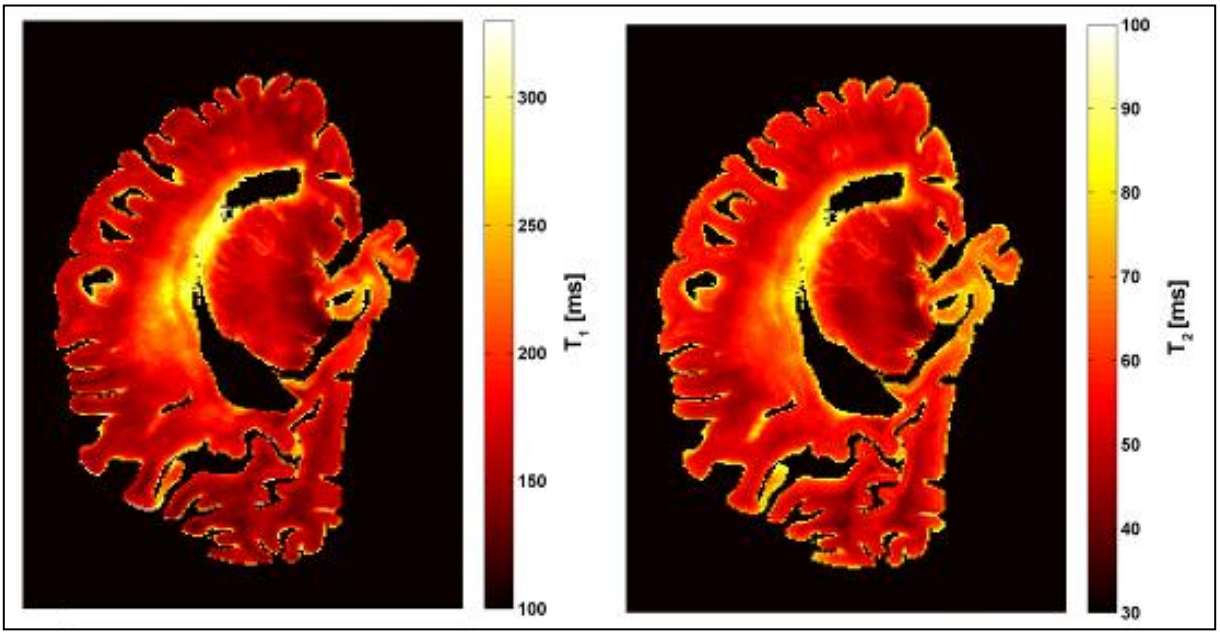

Fig. 1:T_1 and T_2 maps of the ex-vivo brain sample

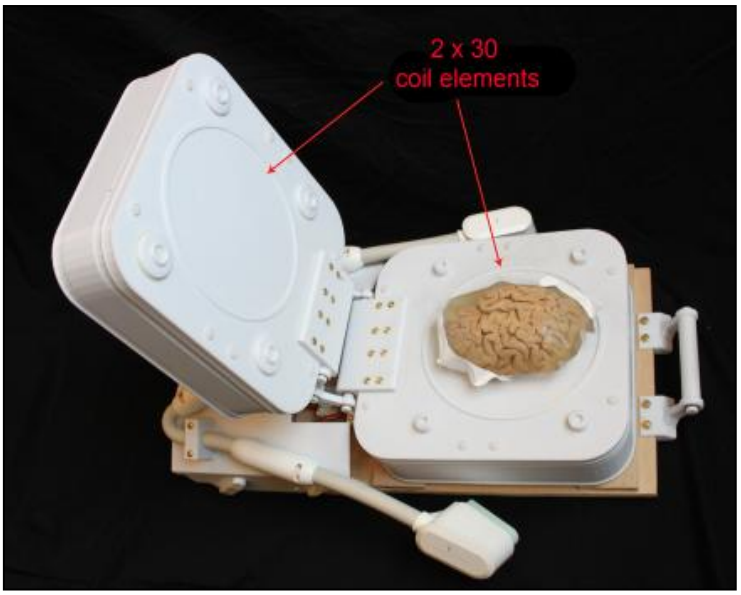

Fig. 2: Purpose-built 60 channel coil array

Fig. 3: Exemplary fiber tracts originating in the corpus callosum, reconstructed from 60 diffusionencoding directions with b=12000 s/mm^2

References

[1] Setsompop, K.: Pushing the limits of in vivo diffusion MRI for the Human Connectome Project, NeuroImage, 80 (2013), S. 220-233

145 APT-CEST MR imaging of formalin fixed C6 glioma in the rat brain at 7 T

M. Salehi Ravesh[1], A. Moussavi[1], K. Koetz[1], M. Huhndorf[1], S. Boretius[1]
[1]Christian-Albrechts-University, Section Biomedical Imaging, Department of Diagnostic Radiology and Neuroradiology, Kiel, Germany

Target audience: Scientists and physicians interested in CEST, cancer MR imaging and spectroscopy.

Introduction: Glioblastoma multiforme (GBM) is a highly aggressive brain cancer characterized by uncontrolled proliferation, resistance to cell death, extensive induction of angiogenesis, and vascular edema1. Chemical exchange saturation transfer (CEST) MRI2 has emerged as an innovative technique generating contrasts dependent on the tissue microenvironment composition of small molecules as well as mobile peptides and proteins3. The purpose of this study was to investigate the effect of formalin as a fixation medium on the tumor and normal tissue with respect to the APT-CEST contrast.

Materials and methods: The brain of a male Wistar rat (6 weeks) was fixed in 4% paraformaldehyde for two days and stored in phosphate buffered saline at 4°C on day 21 after injection of 100.000 C6 glioma cells into the right basal ganglia4. MRI was performed at 7 T (ClinScan, Bruker BiosSpin, Ettlingen, Germany) using a transmit/receive volume coil (inner Ø=3.8 cm). During the MR measurement the temperature of the fixed brain was kept constant at 37.0 ±0.5°C. Single-slice chemical exchange saturation transfer (CEST) MR-imaging was performed using pulsed RF saturation followed by a 2D FLASH (Fast Low Angle SHot) readout [TR/TE: 32,123/5 ms, FOV: 35mm, matrix: 256×256, slice thickness: 2 mm]. Z-spectra were acquired by application of one (Tsat=22.6 ms) and five repetitive (Tsat=113 ms) RF pulses of 430° at 201 frequency offsets up to ±5 ppm (scan time=27.27/105 min). B0 inhomogeneity was corrected on a voxel-by-voxel basis by centering of the z-spectra. Saturation transfer was quantified by magnetization transfer ratio: MTR=100× [S0-Ssat(ω)]/S0, and by asymmetry analysis: MTRasym=100×[Ssat(-ω)-S(+ω)]/S0 at frequency offsets corresponding to the maximized intensity difference between the signal intensities from the ROIs in the tumor and healthy tissue at ω=±4ppm. Ssat(ω) and S0 are the signal intensities with and without frequency selective excitation, respectively. In the rat brain, two ROIs of the same size were selected inside the tumor (on the right side of the rat brain, (Fig. 1, white arrow)) and the contralateral normal appearing brain region (Fig. 1, green arrow).

Results and discussion: Figure 1 shows the z-spectra (left) and MTRasym spectra (right) of the tumor and contralateral normal brain tissue for the short (green/red line) and long (blue/black line) saturation scheme. The z-spectra of the tumor and the contralateral tissue acquired with the short saturation time had a narrow spectral line width of about 1 ppm and overlap each other. In contrast to that, a strong asymmetry broadening of the z-spectra line shape can be seen at longer saturation time between 0.5 to 3 ppm downfield of the water signal. This asymmetry appeared different between tumor and normal tissue. At 4 ppm the chemical fixed normal tissue exhibited a negative MTRasym that could not be seen in the tumor. On the other hand, in the tumor a strong asymmetry was observed at about 1.5 ppm resulting in a positive MTRasym value, which was about 8% higher than those of the normal tissue. Fig. 2 shows the corresponding maps of MTR and MTRasym at 1.5, -1.5, +4, -4 ppm as well as the obtained S0 and Ssat(at -4 ppm) images. The tumor appeared with a clear reduction of MTR, both at 4 and -4 ppm which is in line with previous observations in vivo. In contrast to in vivo data, no z-spectra asymmetry was detectable between 5 and 3 ppm indicating a loss of APT-effects in fixed tissue. Conclusion: The strongest contrast between glioma and brain tissue in formalin-fixed brain could be achieved by macromolecular magnetization transfer, rather than chemical exchange from mobile protons. While the contrast alteration on the MTR map was comparable to those in vivo, the observed CEST-effect clearly differed from in vivo data of tumor and normal tissue.

References

[1] Haskins W.E., et al., Front Oncol, 3:182, (2013). [2] Ward K.M.,et al., MRM, 44:799-802, (2000). [3] Zhou J., et. al., Nat Med, 8:1085-1090, (2003) [4] Benda P., et al., Science, 161:370-371, (1968). [5] Zhou J., et al., MRM, 70:320-327, (2013)

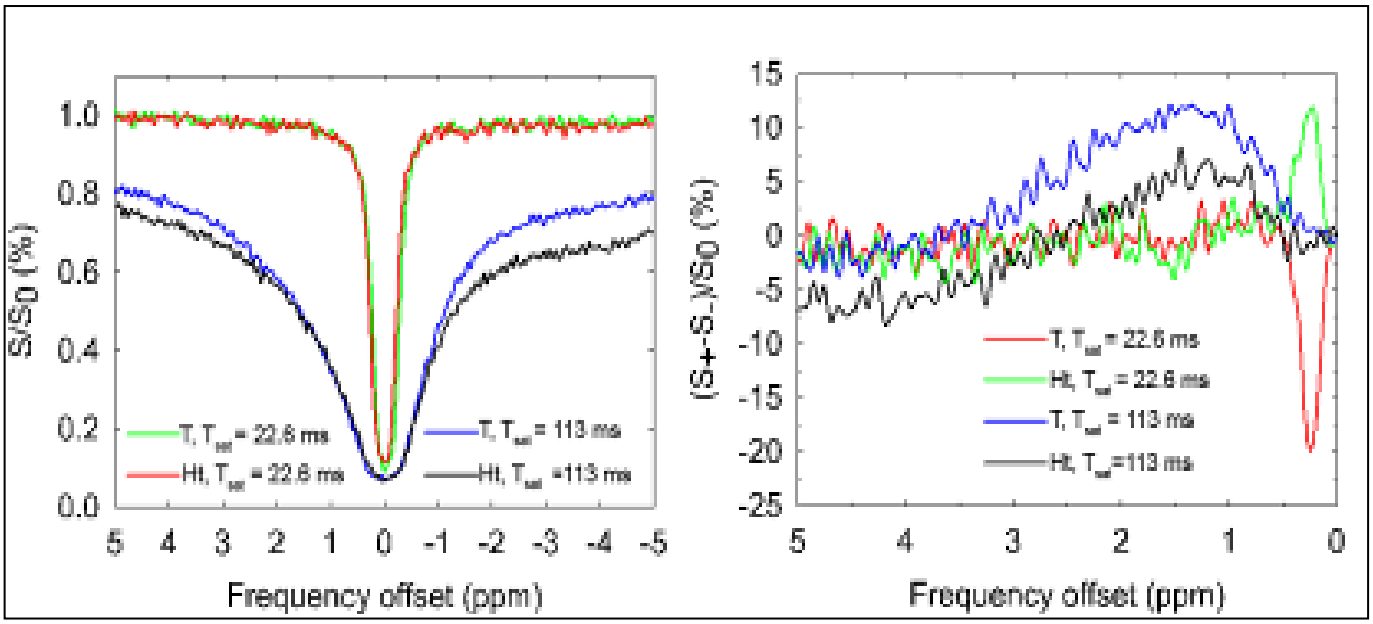

Fig. 1: Normalized z-spectra (left) and MTR_{asym} spectra (right) of the brain tumor and the contralateral normal brain tissue as a function of frequency offset at two different saturation periods T_{sat}=22.6 ms and 113 ms. The words tumor and healthy tissue were abbreviated to T and Ht.

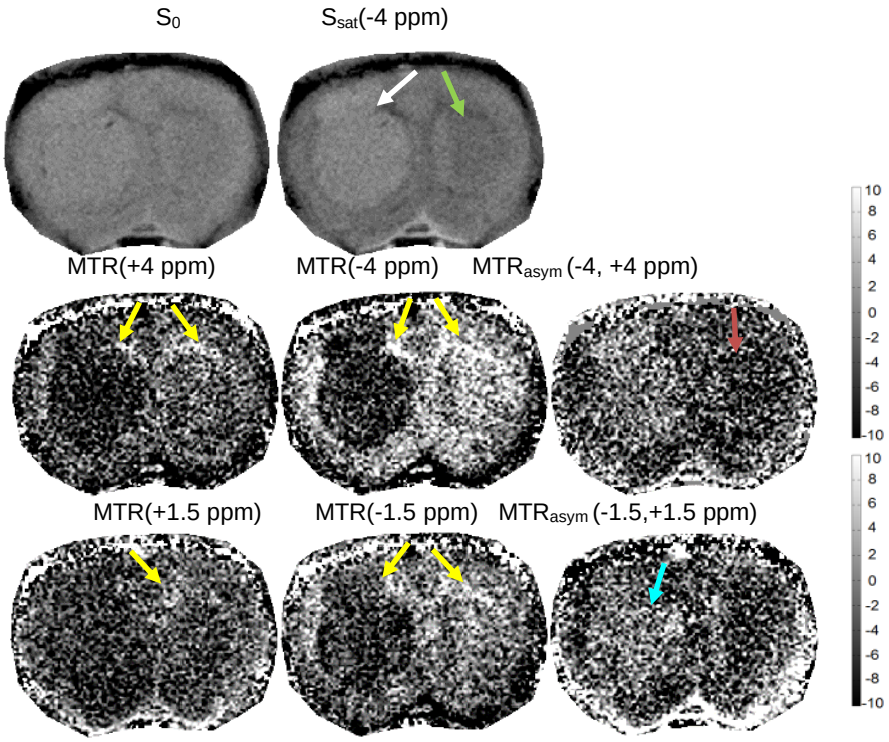

Fig. 2: The obtained S_0 and S_{sat}(at -4 ppm) of the in formalin-fixed rat brain tumor by a saturation period of T_{sat} = 113 ms and the MTR and MTR_{asym} at 1.5, -1.5, +4, -4 ppm. The gray scale of both maps shows the values from -10% to 10%. The white and green arrows show the tumor (left) and normal brain tissue (right), the yellow, orange and blue arrows show white brain matter, normal tissue and tumor on the MTR and MTR_{asym} maps, respectively.

Session 25 – Dosimetry in radiation therapy II: Detectors II

Chairs: D. Frauchiger (Bern/CH), K. Zink (Giessen, Marburg/DE)

146 Experimental comparison of different detector types for small field electron dosimetry

V. Spöring[1], B. Zeeb[2], S. Tsitsekidis[2], D. Thorwarth[1], O. Dohm[2]
[1]University Hospital Tübingen, Section for Biomedical Physics, Tübingen, Germany
[2]University Hospital Tübingen, Department for Medical Physics, Tübingen, Germany

Introduction: While dosimetry of small fields is quite well understood for photons this is not the case for Electrons. In this work we investigated the properties of various detectors at small fields for electrons to get an overview of the behavior and the limits of them. In our case we used the Roos ionization chamber, Advanced Markus ionization chamber and the E-Diode silicon detector all from PTW-FREIBURG.
The aim was to find out the best detector for small field dosimetry of electron irradiation using fields under a size of 4x4 cm^2.

Materials and methods: All measurements were carried out on an Elekta SL15 linear accelerator (Elekta, Crawley UK) having electron energies of 4, 6, 8, 10, 12 and 15 MeV. For this work we limited ourselves to an electron energy of 10 MeV. The used detectors in this work were Roos (Type 34001) ionization chamber, Advanced Markus (Type 34045) ionization chamber, E-Diode (Type 60017) silicon detector and as reference detector a Semiflex 0.3 cm^3 (Type 31013) ionization chamber (all detectors PTW-Freiburg, Freiburg, Germany). Furthermore we made use of Gafchromic™ EBT3 Radiochromic Films. Depth dose curves and profiles were recorded in water using a MP3 Water phantom (PTW-Freiburg, Freiburg, Germany) at a source surface distance SSD = 100 cm with the sofware Mephysto mc2 (PTW-Freiburg, Freiburg, Germany). Output factors were measured with an UNIDOS*webline* Universal Dosemeter (PTW-Freiburg, Freiburg). The 10x10 cm^2 square field was used as a reference.
The measurements were carried out according to DIN 6800-2 [1]. First of all depth dose curves were recorded with the different detectors for the field sizes of 1x1, 2x2, 3x3, 4x4, 5x5, 6x6, 10x10, 14x14 and 20x20 cm^2. The field sizes 6x6, 10x10, 14x14 and 20x20 were generated with applicators of Elekta. The field sizes from 5x5 cm^2 down to 1x1 cm^2 were generated by using self-made end frames (composition of Pb, Bi and Sn) which were installed on the 6x6 cm^2 applicator. The depth dose curves of each detector and each field size was measured at 10 MeV. We installed the Roos chamber and Advanced Markus chamber so that the irradiation comes orthogonal on the entrance window and the E-Diode detector parallel to the irradiation direction.
We assumed that the Roos chamber is the “Goldstandard” and according to PTW-FREIBURG the Roos chamber can be used to a field size of 4x4 cm^2. The shift of the Roos chamber of the effective point of measurement is well known [2]. So we adapted depth dose curves of Advanced Markus chamber and E-Diode detector to the shifted Roos chamber and get the depth dose curves in the effective point of measurement and the shifts of Advanced Markus chamber and E-Diode detector.
From the shifted depth dose curves we took the half value depth (R_{50}) and determined z_{ref} [1]: Furthermore we took the depth of the dose maximum (D_{max}) of each depth dose curve. Next step was to measure profiles in D_{max} and output factors in z_{ref} and compare the results of the different detectors with each other.
The measurement with the Gafchromic™ EBT-3 Radiochromic film was more difficult. For that we used a self-made mini water phantom with a modified holder which positioned the film parallel to the radiation axis. It was after an irradiation of 3 Gy scanned with an Epson 10000xl and analysed with Mephysto mc2.
For the field sizes smaller than 6x6 cm^2 we adapted depth dose curves of the Advanced Markus and E-Diode to the depth dose curves of the film. So we get the shifts of these two detectors at the field sizes 1x1, 2x2, 3x3, 4x4 and 5x5 cm^2. We also done this for the field sizes 6x6 cm^2 and compared the shifts with the results of adapting to Roos chamber.

Results: The depth dose curves of Advanced Markus chamber and E-Didoe detector at the field size 6x6 cm^2 shifted by the value which can be seen in table 1 for the effective point of measurement, are in good agreement to the shifted Roos chamber and film. But this is not the case for the field sizes under 6x6 cm^2. Table 1 also shows the penumbra of the fields measured in D_{max} with the different chambers. It can be seen, that the Roos chamber measures the largest penumbra width because of its large diameter of the measuring volume. The other two detectors are in good agreement.
The measured output factors in z_{ref} can be seen in figure 1. Output factors of Advanced Markus chamber are in good agreement with the output factors of E-Diode detector, but the Roos chamber begins to deviate at a field size of 5x5 cm^2 and smaller.

Discussion and conclusion: While PTW states, that the Roos type chamber can be used down to 4x4 cm² fields our results show that its usage should be limited to a 6x6 cm² field. For smaller fields the volume effect [3] is getting too dominant. Our measurements also show that the Advanced Markus chamber and E-Diode detector have a sensitive volume which is small enough to measure small fields with a negligible volume effect, not only for profiles, but also for output factors of the small fields.
For the E-Diode there is a energy dependent shift of effective point of measurement [4] but also field size dependent shift of effective point of measurement has to be taken into account (table 1). Also Advanced Markus chamber shows an increase of the shift of the effective point of measurement with decreasing field size (field size < 6x6 cm^2) (table 1). As a result we took Roos as reference and adapted the depth dose curves of Advanced Markus chamber and E-Diode detector to Roos chamber, but this works only down to a field size of 6x6 cm^2. For smaller fields Roos chamber can't be used as a reference because of the volume effect. So we took the depth dose curve of the EBT-3 Gafchromic™ film and adapted depth dose curves of the Advanced Markus chamber and E-Diode detector to that curves of the film. That's the way we got the shift of this two chambers for the small fields and could find out D_{max} and R_{50} for z_{ref}.
Dosimetry in small fields is a difficult and time-consuming method. There is no standard detector which can be used for measurements in fields under the size of 4x4 cm^2 like Roos chamber for fields greater than 6x6 cm^2 and no standard measuring procedure. It's difficult to maintain the measuring accuracy at small fields

References

[1] DIN Deutsches Institut für Normung e.V.: Dosismessverfahren nach der Sondenmethode für Photonen- und Elektronenstrahlung – Teil 2: Dosimetrie hochenergetischer Photonen- und Elektronenstrahlung mit Ionisationskammern, DIN 6800-2 (2008)

[2] H. K. Looe, D. Harder and B. Poppe.: Experimental determination of the effective point of measurement for various detectors used in photon and electron beam dosimetry , Phys. Med. Biol., 56 (2011), S. 4267-4290

[3] M.Schwedas, M. Scheithauer, T. Wiezorek, T. G. Wendt: Strahlenphysikalische Einflussgrößen bei der Dosimetrie mit verschiedenen Detektortypen, Z. Med. Phys., 17 (2007), S. 172-179

[4] H. Song, M. Ahmad, J. Deng, Z. Chen, N. J .Yue and R. Nath: Limitations of silicon diodes for clinical electron dosimetry, Radiation Protection Dosimetry, 120 (2006), S. 56-59

	1x1	2x2	3x3	4x4	5x5	6x6	10x10	14x14	20x20
D_{max}	Penumbra [mm]								
Roos			9.7	10.94	12.18	13.13	13.34	14.16	13.72
E-Diode	3.59	4.93	6.18	7.62	9.27	10.11	10.59	11.8	10.58
Advanced Markus		5.44	6.45	7.41	9.2	10.58	10.53	11.82	10.65
	shift of effective point of measurement [mm]								
Advanced Markus (adapted to film)		1.1	2.01	2.35	1.34	0.05			
Advanced Markus (adapted to Roos)		1.9	1.9	0.7	0.4	0.15			
E-Diode (adapted to Film)	1.45	3.08	4.37	3.82	2.8	1.53			
E-Diode (adapted to Roos)		3.77	3.57	2.07	1.37	1.27			

Tab. 1: Penumbra and shift of effective point of measurement

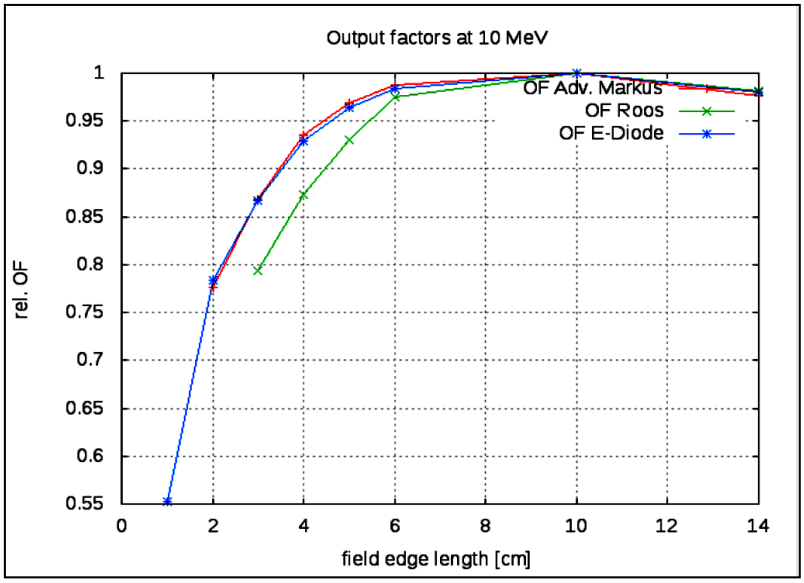

Fig. 1: Output factors at 10 MeV

147 Commissioning of the Octavius detector 1000SRS for the quality assurance of linear accelerators and treatment plans especially for stereotactic radiotherapy

T. Hauschild[1], T. Koch[1]
[1]Sozialstiftung Bamberg, Klinik und Praxis fuer Strahlentherapie und Radioonkologie, Bamberg, Germany

Introduction: Volumetric modulated arc therapy will become the preferred technique in modern radiotherapy. This applies not only standardized large volume irradiations with single doses of 1,8Gy to 2,0Gy but also small-volume stereotactic irradiations with single doses of 5,0Gy to 15,0Gy or higher.
For the quality assurance of stereotactic irradiations there are special dosimetry arrays. The Octavius detector 1000SRS (PTW-Freiburg, Germany) was examined to determine the dosimetric and physical properties, whether it is appropriate for the particular task of quality assurance of stereotactic irradiations.

Material and procedure: The Octavius detector 1000SRS is a two-dimensional ionization chamber array with 977 liquid-filled ionization chambers. The chambers are mounted on a square area of 11x11cm² with a regular grid of 0,5cm. A high-resolution area of 5,5x5,5cm² is located centrally on the detector array. The regular grid spacing in this range is 0,25cm.
The measurements were performed with the Octavius phantom and a slab phantom consisting of RW3 material at an Elekta Synergy and a Tomotherapy HiArt accelerator. The dose rate dependence, linearity, directional dependence and the dependence of field width were determined by comparing the measurement of the central chamber of the array with the dose measured with a Semiflex 31010 ionization chamber. The spatial resolution of the array was determined by varying the diaphragm of the accelerator. Dose profiles measured with the array and the Star Check (PTW-Freiburg, Germany) were compared. For an overall assessment as to the suitability for quality assurance of patient plans several patients plans were measured on both accelerators and compared with the calculations.

Result: The results show that the detector array has a directional dependency. The resolution is very good so that the evaluation criterion is fulfilled for the verification of stereotactic irradiation plans with a gamma index of 2% / 2mm over 95% of the measurement points (Fig. 1). Irradiation plans with a standardized fractionation could be very well reproduced with a gamma index of 3% / 3mm.

Summary: The detector 1000SRS was examined with regard to its properties on the ability to measure stereotactic treatment plans and quality assurance particular for small fields. Therefor dosimetric properties such as linearity, dose rate dependence and directionality were verified experimentally. In addition real radiation plans were verified for a clinical introduction.
For quality assurance purposes especially stereotactic irradiation plans the Octavius detector 1000SRS is sufficiently accurate and very suitable. The machine-related quality assurance can be equally well performed with this detector particularly for small field dosimetry.

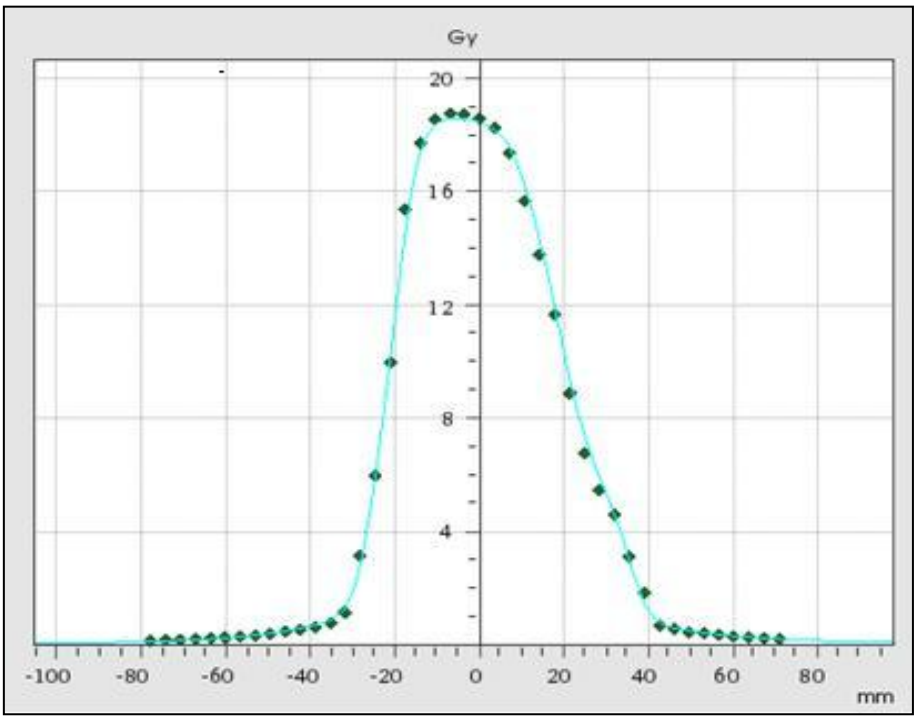

Fig. 1: Measured (dotted) and calculated (solid) profile for stereotactic case. For a gamma criterion of 3%/1mm the result was 99,7%

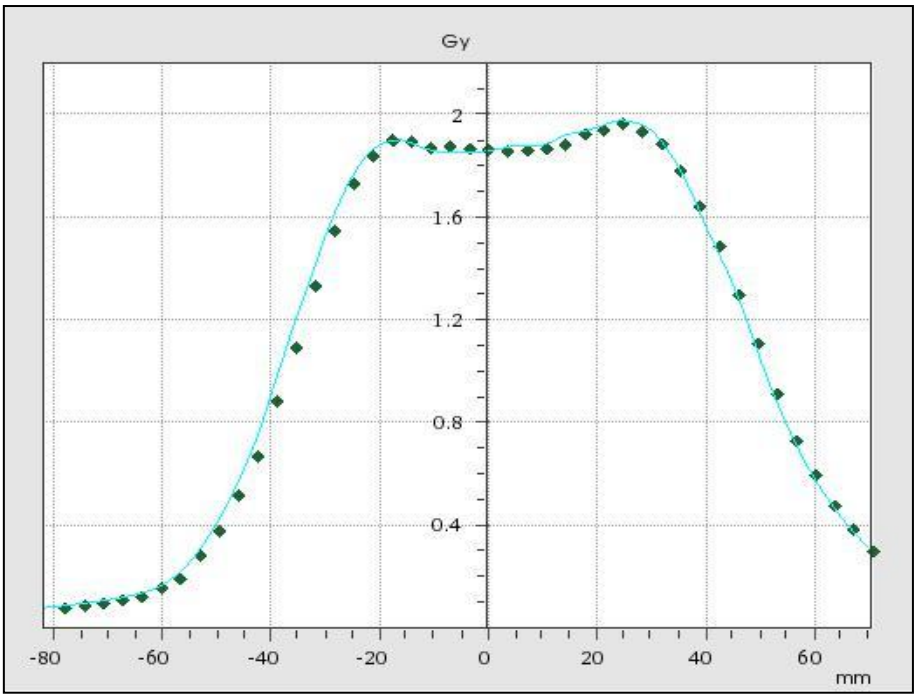

Fig. 2: Measured (dotted) and calculated (solid) profile for a prostate case. For a gamma criterion of 3%/3mm the result was 99,5%

148 Dealing with the angular dependence of the PTW Octavius II System in clinical routine

K. Schlemm[1], F. Fischer[1]
[1]Strahlentherapiepraxis Dr. Guttenberger, Medizinische Physik, Fürth, Germany

Introduction: The Octavius II System is designed for 2D Pre-Treatment QA for rotational IMRT. To compensate for absorption in the body of the ion camber array the bottom part of the phantom contains a cavity. The dimensions of the cavity have been optimised for the 2D-Array729 in Namur, Belgium, in 2007 [1]. A similar response curve for two arrays with spread was shown again in St. Gallen 2011 [2] and on other sites [3,4]. In 2012 the 2D-Array729 was followed by the Octavius Detector 729 with a new design of the housing and with different absorption characteristics. The correction of the absorption in the body of the phantom by a cavity of 2 cm is now critically reviewed, espacially with regard to using higher energies for intensity modulated arc therapy. We compared 3 procedures to evaluate computed dose and measured dose to the Octavius Detector 729 in the Octavius Phantom: a) with the “Artifact-free” CT-scan of PTW and the Linac-Bottom Part [5]; b) with a home CT-scan and the Linac-Bottom Part; c) a density-modified home CT-scan and the CT-bottom part.

Our goal was to obtain a relative dose difference between measured and calculated dose of less than 2% for each Gantry angle.

Materials and methods: For dose measurements we placed the Octavius II System with the measurement window facing the Gantry of an Elekta Synergy Linac at 90°. Static fields of the size 26x26 cm² were irradiated to the phantom with Gantry spacing of 5° CCW to a Gantry angle of 270°. We assumed, that the array behaves symmetrical [3]. Dose readings of the central chamber were corrected for air density. We acquired two sets of dose readings for each energy, 6 MV and 15 MV Photons. One with the Linac-Bottom part of the Octavius Phantom and another with the CT-Bottom part. With this setup we did not irradiate through the carbon treatment couch.

Dose calculations were performed with Pinnacle³ TPS 9.4 on 3 data sets:

1) PTW-CT scan with artifical housing of the Octavius Detector 729 and a ROI to set the density of the body of the array to 1,9 g/cm³

2) home made CT scan with the Octavius Detector 729 and no adaption

3) home made CT scan with ROIs to correct for the angular response of the central chamber of the Octavius Detector 729.

Relationship between measured and calculated dose is given in radiation angle to the array and relative dose difference, normalized to vertical irradiation at 0°.

Results: Using the Linac bottom part of the Octavius phantom relative dose difference of <2% is achievable with both CT data sets, the PTW scan and the home made scan, in an angular range of 0° (vertical on the array) to 60° and 140° to 180°(vertical from the back) for both energies.

In the remaining segment of 80° maximum deviation is seen at an angle of 110° with 5,3% (06 MV), 4,6% (15 MV) and 6,4% (6 MV), 5,6% (15 MV) for the PTW-scan and the home made scan respectively (fig. 1+2). This segment includes several steep changes in density: front of the detector housing with a density of 1,9 g/cm³, the measuring plane with 5mm air and 5mm chamber housing, back of detector housing, the air-filled cavity. Each gives a point of discontinuity in the angular response curve. These discontinuities are less for dose measurements with the homogeneous CT-Bottom part.

With the CT-Bottom part we choose to correct for absorption in the body of the detector array by adding a slab of density 1 to the phantom during dose calculation. In a similar way dose deviation >2% can be corrected by implementing ROIs of density 0 or 1 for dose calculation in areas of too little or too big response respectively (fig. 3). These ROIs can be designed energy specific.

With these ROIs we reduced the segment with deviation >2% to 10°to 15° around an angle of 90° and 95° to the array for 6 MV and 15 MV.

Conclusion: With a home made CT-scan it is possible to get very similar results to the PTW CT-Scan. The artifacts on the back of the detector housing material are of no relevance. Assigning the density of 1,04 g/cm³ (Polystyrene) to the chamber area and the front of the housing reduces the relative dose difference at 80° from 3,5% to 2% for 15 MV Photons. The home CT scan can be acquired with the phantom feet used inhouse, with a data set big enough to place the carbon treatment couch and in diagonal orientations, all is not supplied by the PTW scan.

Further reductions of relative dose deviation to approximately 1% can be achieved with energy specific ROIs of the density 0 or 1, except for an angular range of 10° to 15° around 90° to the array.

In comparison of the literature reviewed and the behaviour of our Octavius Detector 729 we assume individual behaviour of the detector which will be further investigated.

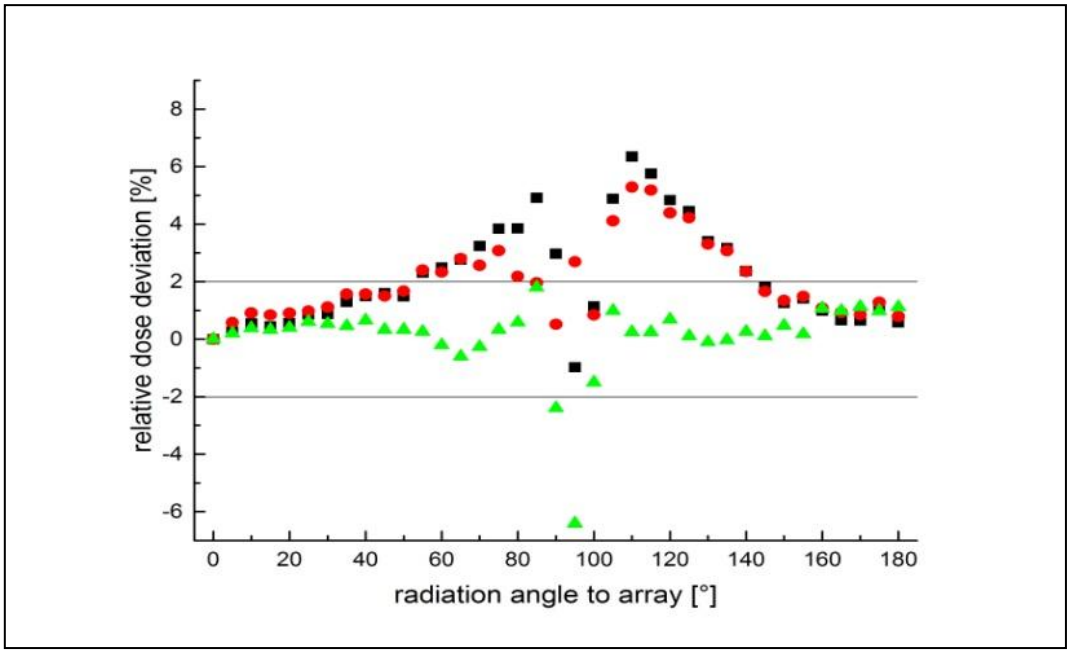

Fig. 1: relative Dose difference of dose measurement and calculation for 6 MV on the PTW scan and Linac bottom part (red dots), home scan and Linac bottom part (black squares) and density modified home scan and CT-bottom part (green triangles).

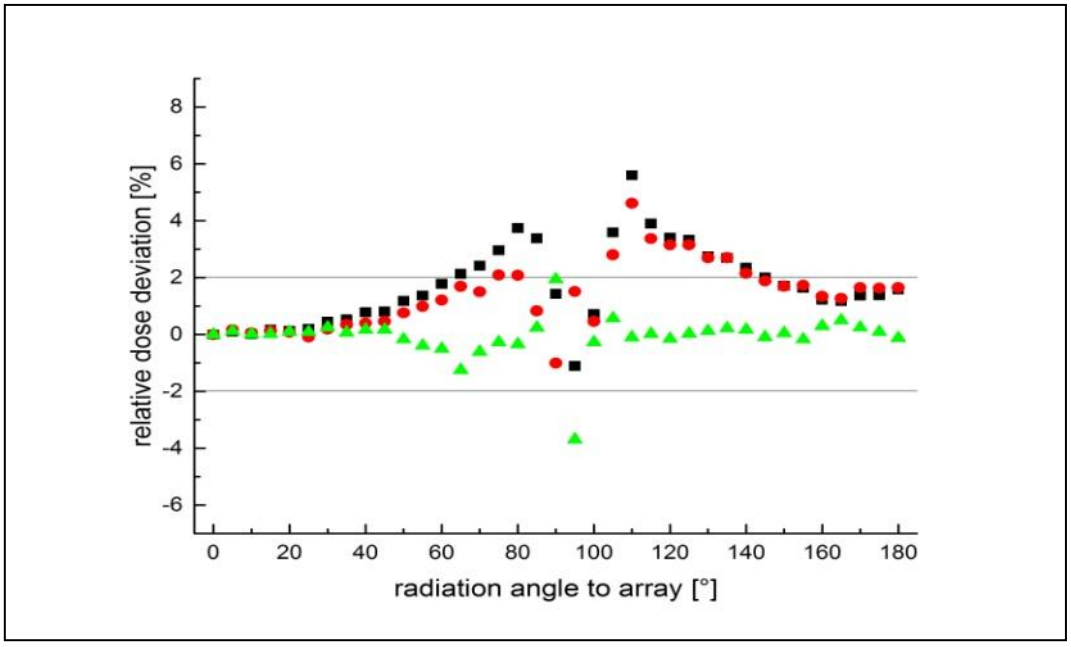

Fig. 2: relative Dose difference of dose measurement and calculation for 15 MV on the PTW scan and Linac bottom part (red dots), home scan and Linac bottom part (black squares) and density modified home scan and CT-bottom part (green triangles).

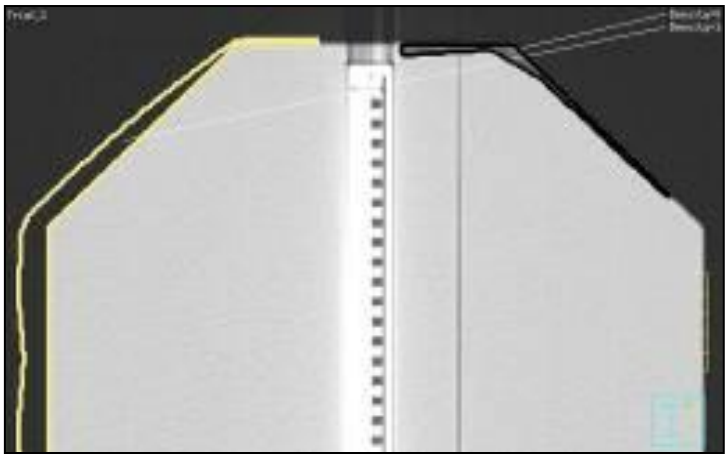

Fig. 3: correcting ROIs for 15 MV Photons, left density 1, right density 0

References

[1] "On-line quality assurance of rotational radiotherapy treatment delivery by means of a 2D ion chamber array and the Octavius phantom". Ann van Esch et al, 2007, Medical Physics, Vol 34, No 10, pp. 3825-3837

[2] „Zwei Methoden zur Verbesserung der IMRT Qualitätssicherung mithilfe des PTW Octavius-Systems". W. Seelentag et al, Poster P10.15, Dreiländertagung der ÖGMP, DGMP, SGSMP 2011

[3] „A critical evaluation of the PTW 2D-ARRAY seven29 and OCTAVIUS II phantom for IMRT and VMAT". Hussein et al, 2013, Journal of Applied Clinical Medical Physics, Vol 14, No 6.

[4] „Characterization of Responses of 2D-Array Seven29 Detecor and Its Combined Use with Octavius Phantom for the Patient Specific Quality Assurance in Rapid Arc Treatment Delivery". Kumar et al, Med.Phys. 37, 3236 (2010)

[5] „Using a predefined OCTAVIUS II CT scan". PTW Technical Note 913.200.01/00

149 Thermoluminescence dosimetry (TLD): New findings on the energy correction factor k_E for X-ray photons between 30 kV and 280 kV

A. Schwahofer[1], H. Georg[2], W. Schlegel[1]
[1]German Cancer Research Center, Medical Physics in Radiation Therapy, Heidelberg, Germany
[2]PTW, SSDL Calibration Laboritory, Freiburg, Germany

The raised use of X-ray imaging in radiation therapy (IGRT) in terms of cone beam CT (CBCT) put in the claim of highly accurate dose determination methods in order to estimate the additional dose to the patient. Thermoluminescence dosimetry (TLD) is chosen due to very good spatial resolution and thus the potential of 3D dose distribution detection in anthropomorphic phantoms. For this reason existing literature [1-3, 5-8] about energy dependence of TL-Detectors was questioned critically and found to vary a lot quantitatively as well as methodically. Hence energy dependence of TLD600 and TLD700 (Harshaw) for X-ray photons is determined in order to define energy correction factors k_E. For the dose-to-water based measurements PTW Germany provided their X-ray tube and the fixed setup including absolute reference dose with calibration quality of a secondary standard laboratory. The determined energy dependence in the range between 30 kV and 280 kV is depicted in Fig. 1 a) and the comparison to the previous findings of other authors in Fig. 1 b).

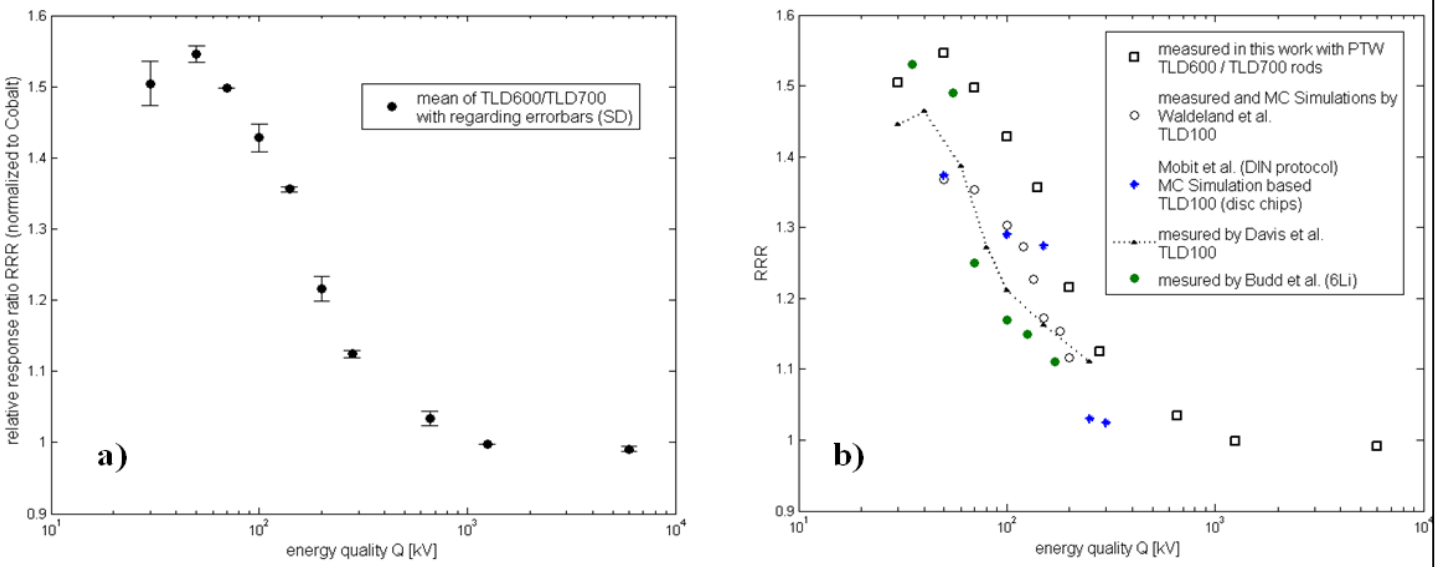

Fig. 1: Energy dependence measured a) in this work at the PTW and b) compared to several results of previous authors among others the values given in the DIN protocol based on the results of Mobit et al.

The responses of the TL-Detectors at each energy level is normalized to the response at the calibration energy at ^{60}Co. This is called the relative response ratio (RRR). The energy correction factors k_E are then created by the inverse of the RRR. In summary, it can be stated that the results of this work are highly accurate, since even the low energy qualities like 30 kV and 50 kV are determined with standard errors between ± 1.16 and ± 3.03 %. When comparing to the data of other authors it is conspicuous that indeed the shape of the curves is similar but quantitatively there are big differences. But there are some obscure parameters which make a comparison almost impossible. E.g. nearly all other authors measured with TLD100, some compared rods with chips, some made just Monte Carlo Simulations and some compared dose-to-water calibrations at the reference energy to air-kerma based measurements at the kV energy range. The correct specification of the energy at the point of measurement is the most challenging part for the comparison of different author´s data. Since photons out of an X-ray tube are distributed in a spectrum and the latter in turn changes its composition due to interaction processes in different materials. The correction factors of this work are tested in a clinical phantom study at the X-ray tube of a Linac with 70 kV, 100 kV and 120 kV. The calculated dose values (following Eq. (1)) $D^i_{w,Q}$ for the i-th TL-Detector with its individual calibration factor N^i_w including the utilization of k_E fitted very well (see Tab. 1) and thus are assessed as reliable.

$$D^i_{w,Q} = (M_i - M_0) \cdot N^i_w \cdot k_E \quad (1)$$

TLD700, all values in unit [mGy]				
D_w^{IC}	5	10	30	100
$D_{w,Q}^{i}\ (70kV)$	4.8 ± 0.01	10 ± 0.60	28.3 ± 1.20	93.0 ± 1.17
$D_{w,Q}^{i}\ (120kV)$	5.1 ± 0.10	9.0 ± 0.36	29.2 ± 0.88	98.8 ± 2.70

Tab. 1: Results of dose measurements with an X-ray tube mounted at the Linac in a fluoroscopic mode exemplary with energy levels 70 and 120 kV, absolute reference dose determined with an ionization chamber (TM31010, PTW). Standard errors are referred to the intra-TL-uncertainty averaged over 3 repetitions.

Concluding, it is not recommended to use the k_E values (X-ray photons) given in the DIN protocol for dose-to-water measurements with TL-Detectors, moreover it is necessary to revise this chapter of the DIN protocol.

References

[1] P. Bassi, G. Busuoli, and O. Rimondi. *Calculated energy dependence of some RTL and RPL detectors.* Int J Appl Radiat Isot, 27(5-6):291–305, 1976.

[2] T. Budd, M. Marshall, L. H. Peaple, and J. A. Douglas. *The low- and high-temperature response of lithium fluoride dosemeters to x-rays.* Phys Med Biol, 24(1):71–80, Jan 1979.

[3] S. D. Davis, C. K. Ross, P. N. Mobit, L. Van der Zwan, W. J. Chase, and K. R. Shortt. *The response of LiF thermoluminescence dosemeters to photon beams in the energy range from 30 kV x rays to 60 Co gamma rays.* Radiat Prot Dosimetry, 106(1):33–43, 2003.

[4] DIN 6800-2 Dosismessverfahren nach der Sondenmethode für Photonen- und Elektronenstrahlung. *Teil 2: Dosimetrie hochenergetischer Photonen- und Elektronenstrahlung mit Ionisationskammern*. 2008

[5] DIN 6800-5 Dosismessverfahren nach der Sondenmethode für Photonen- und Elektronenstrahlung. *Teil 5: Thermolumineszenzdosiemtrie.* 2005

[6] A. F. McKinlay. *Thermoluminescence Dosimetry - Medical Physics Handbooks 5*. Adam Hilger Ltd, Bristol, 1981.

[7] P. N. Mobit, A. E. Nahum, and P. Mayles. *A monte carlo study of the quality dependence factors of common TLD materials in photon and electron beams*. Phys Med Biol, 43:2015–2032, 1998.

[8] E. Waldeland and E. Malinen. *Review of the dose-to-water energy dependence of alanine and lithium formate EPR dosimeters and LiF TL-dosimeters in comparison with monte carlo simulations.* Radiat. Meas., 46:945–951, 2011

150 Dose-dependent transmission of polarized light through EBT3 radiochromic films

A. Schoenfeld[1,2], D. Harder[3], B. Poppe[1,2]
[1]Carl von Ossietzky Universität Oldenburg, Medical Radiation Physics, Oldenburg, Germany
[2]Pius Hospital Oldenburg, Radiation Therapy, Oldenburg, Germany
[3]Georg-August Universität Göttingen, Medical Physics and Biophysics, Göttingen, Germany

Purpose: The optical properties of radiochromic EBT3 films achieved by exposure to high-energy photons have been experimentally studied. This study entailed the investigation of the dose-dependent transmission of polarized light through the films in order to reveal the scattering properties of the films and to verify the applicability of the theory of light scattered from rod-like structures.

Materials and methods: An optical table setup was used to study the transmission of a narrow, homogeneous light beam through EBT3 radiochromic films exposed to doses between 0 Gy and 10.5 Gy. A Linos Halogen lamp including a condenser (Linos Richtleuchte type 030123, Linos, Göttingen, Germany) was used as a source of white light, and its slight preference for horizontal polarization was measured and eliminated by a numerical correction. Two apertures in combination with a light diffusing glass were used to form upon the film a homogeneously illuminated spot of white light with adjustable light intensity. A linear polarizer (here called the front polarizer, FP) type 10K-036323 (Spindler & Hoyer, Göttingen, Germany) served to polarize the incident light.

The films were positioned with their long side horizontal. The 0° polarization of the FP corresponded to an electrical vector of the incident light parallel to the short side of the film; accordingly, 90° corresponded to an electrical vector parallel to the long side. A second polarizer of the same type (here called the rear polarizer, RP), was placed behind the film. The light current of the transmitted light was measured in the red channel of a Nikon D5100 DSLR (Nikon Corp., Tokyo, Japan) camera with sigma macro lens type 105/2.8 EX Macro DG OS HSM (Sigma Corporation, Kawasaki-shi, Japan) focused upon a light diffusing glass placed behind the second polarizer. The camera shutter was triggered by remote control. The images were taken in Nikon NEF raw format using the Adobe DNG (Adobe, San José, CA, USA) converter. Further evaluation was performed in Matlab (Mathworks, Natick, MA, USA). The polarization dependence of the transmission of light through the film was investigated by rotating the FP from 0° to 180°. The RP was placed in three different setups relative to the FP by a) omitting the RP, b) orienting the RP parallel to the FP and c) orienting the RP perpendicular to the FP.

Results: The transmission of linear polarized incident light peaks at 90° when the polarization is perpendicular to the coating direction of the film. A deeper insight was obtained in setups b) and c) using pairs of front and rear polarizers. Relatively sharp transmission maxima are obtained at polarization angles of 90° for a parallel oriented pair of polarizers. Two sharp peaks occur for a crossed pair of polarizers at front polarizer angles 45° and 135° with a local minimum at 90°. In all cases, the peaks become more prominent with increasing dose. These results agree with those of Klassen et al 1997 who studied the optical properties of MD-55 Radiochromic films. Two lower peaks of transmission already occur on unexposed films at polarizer orientations of 0° and 180° polarization of the incident light for parallel polarizers and at 45° for crossed polarizers.

Conclusions: The measured patterns of light transmission as a function of the polarization direction of the incident light match the theory presented by Rhodes and Stein (Rhodes & Stein, 1969) predicting a $cos^2\alpha$ dependence of the parallel-polarized component of light scattered from a rod-like structure and a $sin\alpha\ cos\alpha$ dependence of the crossed-polarized component of scattered light, when the direction of maximal polarizability of the scattering oscillators is preferently the 90° direction. Thus the preferred direction of the oscillators in EBT3 films is orthogonal to the coating direction. The dose dependent increase of the transmitted intensity indicates that the underlying oscillators are formed during a radiation-induced polymerization process. According to Rink (2008), these oscillators have been identified as conjugated double bonds between the lithium pentacosa-10,12-diynoate (LiPCDA) monomers of the radiochromic film.

The observed strong dependence of the transmitted light current upon the polarization direction and its consistence with the theory of light scattering from rod-like structures has to be weighted as the proof that radiation-exposed EBT3 radiochromic films are not only attenuating the light offered by a photometer, but also produce scattered light, whose interaction with the properties of the usual flatbed scanners gives rise to the well-known artefacts known as the orientation effect and the parabola effect.

References

[1] Klassen, N. V., van der Zwan, L. & Cygler, J., 1997. GafChromic MD-55: Investigated as a precision dosimeter. *Medical Physics,* 24(12), pp. 1924-1934.
[2] Rhodes, M. B. & Stein, R. S., 1969. Scattering of Light from Assemblies of Oriented Rods. *Journal of Polymer Science Part A-2: Polymer Physics,* **7**(9), pp. 1539-1558.
[3] Rink, A., 2008. *Point-based Ionizing Radiation Dosimetry Using Radiochromic Materials and a Fibreoptic Readout System.* Toronto: University of Toronto.

Session 26 – Particle radiation therapy III: Plan QA/ InVivo dosimetry

Chairs: W. Enghardt (Dresden/DE), G. Kragl (Vienna/AT)

151 Current status of dosimetric quality assurance of the ion beam Gantry at HIT

B. Ackermann[1], S. Brons[1], N. Chaudhri[1], S. Ecker[1], M. Ellerbrock[1], P. Heeg[1], K. Henkner[1], J. Horn[1], S. Lahrmann[1], H. Latzel[1], J. Naumann[1], H. Prokesch[1], M. Winter[1], O. Jäkel[1,2,3]
[1]Heidelberger Ionenstrahl-Therapie Centrum (HIT), Medizinische Physik, Heidelberg, Germany
[2]Universitätsklinik, Radioonkologie und Strahlentherapie, Heidelberg, Germany
[3]Deutsches Krebsforschungszentrum, Medizinische Physik in der Strahlentherapie, Heidelberg, Germany

Introduction: In October 2012, the Ion Beam Gantry at the Heidelberg Ion Therapy Center (HIT) [1], which features active beam scanning, started clinical operation. Until end of February 2014, 222 patients have been treated with protons or carbon ions. For clinical operation, the medical physics team developed and performed comprehensive acceptance and periodic quality assurance tests to ensure that the clinical dose distributions are within the respective specifications for all applied beam parameters at all applied gantry angles.

Materials and methods: For each ion species and gantry angle, beam position and beam width can be adjusted for 255 different energy levels and 4 different focus levels by the accelerator physics team. For certain parameters, interpolation between sampling points is employed. Therefore, a reasonable amount of measurement points were determined in the beam parameter phase space and test protocols with appropriate tolerance levels were developed.

Different detectors, which are used for the acceptance and periodic quality assurance tests, will be presented. This includes a multi wire proportional chamber (Siemens PT, Erlangen) for measuring beam position and beam width, radiographic films for measuring dose homogeneity of scanned fields, an air filled ionisation chamber array (Starcheck, PTW Freiburg) for scanned field dose profile measurements and a farmer chamber for monitor calibration. All these detectors are mounted on a rotating device connected to the patient positioning robot to allow measurements at each gantry angle.

Results: For the tests mentioned above, the beam position and beam width are within +/- 1 mm and +/-20% relative to given reference values, respectively. The field dose homogeneity is better than +/-5%. The scanned field dose profiles show 1d gamma-index values below 1.0 for settings of 1.5 mm distance to agreement and 5% dose deviation, normalized to the maximum dose. The monitor calibration shows differences of less than 0.5% for different gantry angles. The results of further quality assurance tests will be presented as well.

Conclusion: For protons and carbon ions the measurement results of acceptance and periodic quality assurance tests at different gantry angles are well within tolerances. Currently, the physics team focuses on making arbitrary gantry angels available for clinical operation. Moreover, there is still a need to further accelerate the measurement procedures. In order to achieve this, we are currently implementing an amorphous silicon flatpanel detector [2], which is already in use for beam adjustment and problem investigation, into the quality assurance program.

References

[1] Haberer T. et al.: The Heidelberg Ion Therapy Center. Radiother Oncol. 2004 Dec; 73 Suppl 2:S186-90.
[2] Hartmann B. et al.: Investigations of a flat-panel detector for quality assurance measurements in ion beam therapy. Phys. Med. Biol. 2012 Jan 7;57(1):51-68

152 An enhanced approach to beam delivery verification in ^{12}C ion-beam therapy based on secondary ion direction and energy loss information

C. K. Spindeldreier[1], B. Hartmann[1], M. Reinhart[1], J. Jakubek[2], O. Jäkel[1,3,4], M. Martisikova[1,3]
[1]German Cancer Research Center, Medical Physics in Radiation Oncology, Heidelberg, Germany
[2]Czech Technical University in Prague, Institute of Experimental and Applied Physics, Prague, Czech Republic
[3]Universitätsklinikum Heidelberg, Heidelberg, Germany
[4]Heidelberger Ionenstrahl-Therapiezentrum, Heidelberg, Germany

Introduction: In heavy ion radiotherapy the highly localized dose deposition in the Bragg peak area represents an important advantage over conventional photon beam therapy. At the same time, however, the sensitivity to small deviations in the dose delivery, such as inaccuracies in the patient positioning, is increased. Therefore, non-invasive dose delivery verification would be highly desirable. The only method currently available in clinics are PET measurements, which suffer from low signal, biological washout processes and long acquisition times [1]. To overcome these drawbacks, a different approach for heavy ion beam delivery verification based on monitoring of prompt secondary ions leaving the patient has been investigated. Gwosch et al. showed that e.g. beam range differences of down to 2 mm can be detected by tracking of secondary ions [2]. In continuation of these initial studies it is now investigated if information on the energy loss of the detected ions in the detector system can be exploited to enhance the beam delivery verification.

Materials and methods: The experiments were performed at the Heidelberg Ion-Beam Therapy Center with carbon ion pencil beams of energies typically used in patient treatments. A cylindrical PMMA phantom of head-size was placed in the isocenter. Behind the phantom a stack of three Timepix detectors [3] was positioned at an angle of 30° against the beam axis (see Fig. 1). The employed semiconductor detector system allows for detection of single particles due to its high spatial resolution.

In the first detection layer the energy deposition of the particles in the 300 µm thick silicon sensor layer was measured. The rear detector layers were used to obtain the particle arrival time and match coincident events. In this way, the trajectories of the secondary ions in the detector were determined and back-projected into the initial beam plane. The correlation of the gained profiles of intersection points in the beam plane and the corresponding energy loss information with the initial beam range was studied.

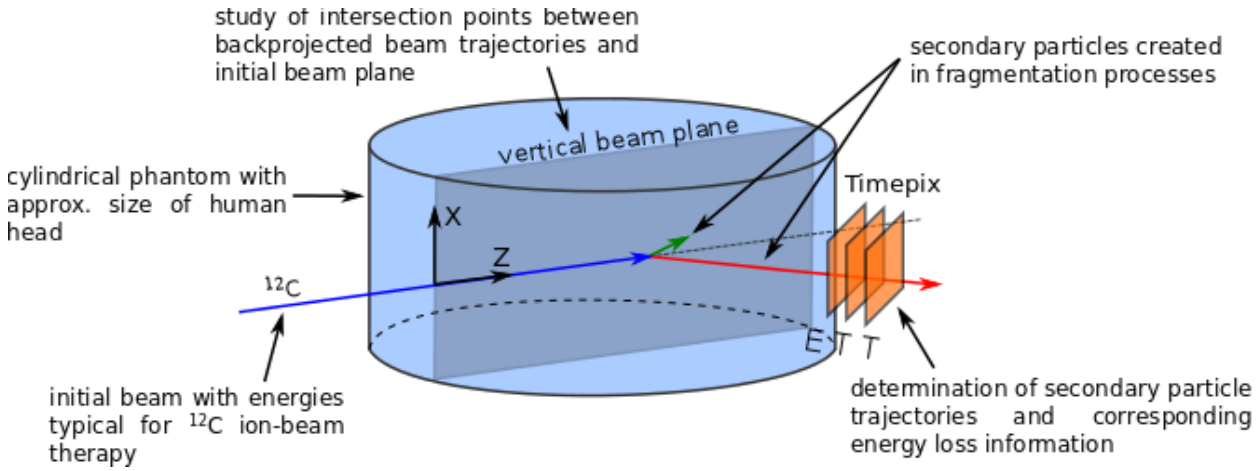

Fig. 1: Schematic illustration of the used measurement set-up and principle of evaluation.

Results: The analysis of the back-projected particle trajectories and the corresponding ion energy loss information revealed promising correlations of the obtained signal distributions to the initial beam range. Further measurements using different initial ion energies have been made. Detailed investigations on a possible improvement of the precision in beam range verification exploiting the energy loss information will be presented.

Conclusion: The possibility to match information on the particle trajectories and the energy loss of the respective ions enables enhanced evaluation methods for beam monitoring by means of prompt secondary charged particles in carbon ion-beam therapy. The first results are promising to improve the initial method [2] based solely on particle trajectory information. Further analysis to quantify the precision in beam range verification achievable with this novel approach will be made.

References

[1] Knopf, *Phys. Med. Biol., 2009*
[2] Gwosch, *Phys. Med. Biol., 2013*
[3] Llopart, NIM A, 2007

153 Range-modulation effects of carbon ion Bragg peaks in porcine lungs

M. Witt[1], U. Weber[2], R. Engenhart-Cabillic[3], K. Zink[1,3]
[1]Technische Hochschule Mittelhessen, Institut für Medizinische Physik und Strahlenschutz (IMPS), Gießen, Germany
[2]Rhön-Klinikum AG, Marburg, Germany
[3]Universitätsklinikum Marburg, Klinik für Strahlentherapie und Radioonkologie, Marburg, Germany

Introduction: When a heavy ion Bragg-peak is measured after traversing an inhomogeneous, porous material range modulation effects of the Bragg-peak occur. There are two main causes for the modulation.

One reason was well described by Urie et.al. (1986) [1]. In large heterodense structures with simple configuration, the Bragg-peak degradation can be explained by superimposing the residual ranges of beam parts traversing different tissue / material thicknesses, or being split at high density gradients like bone edges.

The second effect is caused by multiple and complex heterodense structures like porous microstructures (e.g. alveolar septa and alveoli in the lung) and results in a modulation of the particle ranges. The observed modulation is comparable to the modulation caused by Ripple-filters [2]. In this study these second modulation effects are measured, analyzed and quantified in tissue substitutes and organic lung-tissue. A simple method is described to recalculate a modulated Bragg peak after traversing lung tissue.

Materials and methods: Residual range measurements of a 200 MeV/u and 270 MeV/u C-12 beam were performed using a water column (PTW PEAKFINDER). Two lung substitutes with different densities and a fresh porcine lung were used as samples. The organic lung was irradiated on different locations resulting in different path lengths and different oxygen filling states. A statistical model was introduced to describe the passage of particles through the porous material. The microstructure of the lung (pulmonary alveoli separated by alveolar septa) is represented in a simplified structure by randomly distributed voxels of water (tissue) and air.

The particles traversing this model structure hit a randomized number of solid voxels. The probability distribution can be described in good approximation by a normal distribution where σ is the width and μ the mean value for the water equivalent path length through the whole model target. This distribution is called “lung modulation function” (see fig. 1 lower part).

It could be observed that by a convolution of the reference Bragg peak measurement (no sample in beam path) with that lung modulation function the measured lung Bragg curves can be well reproduced (see fig. 1 upper part). An inverse optimization procedure was used to fit the parameters σ, μ of the modulation function.

The modulation effect of the introduced voxel model depends on the size of the voxels. This allows to draw inferences on the geometrical micro structures of the measured samples from the fitted values σ and μ.

Results: The introduced, simplified statistical model describes the modulation in both lung substitutes and porcine lung properly. The convolution of the so called lung modulation function with the reference measurement reproduces the measured lung Bragg curve with good accordance (see fig. 1).

In some of the organic lung measurements a superposition of degradation and modulation effects is visible. This was attributed to macroscopic structures from the respiratory system such as bronchi tubes being hit by the beam.

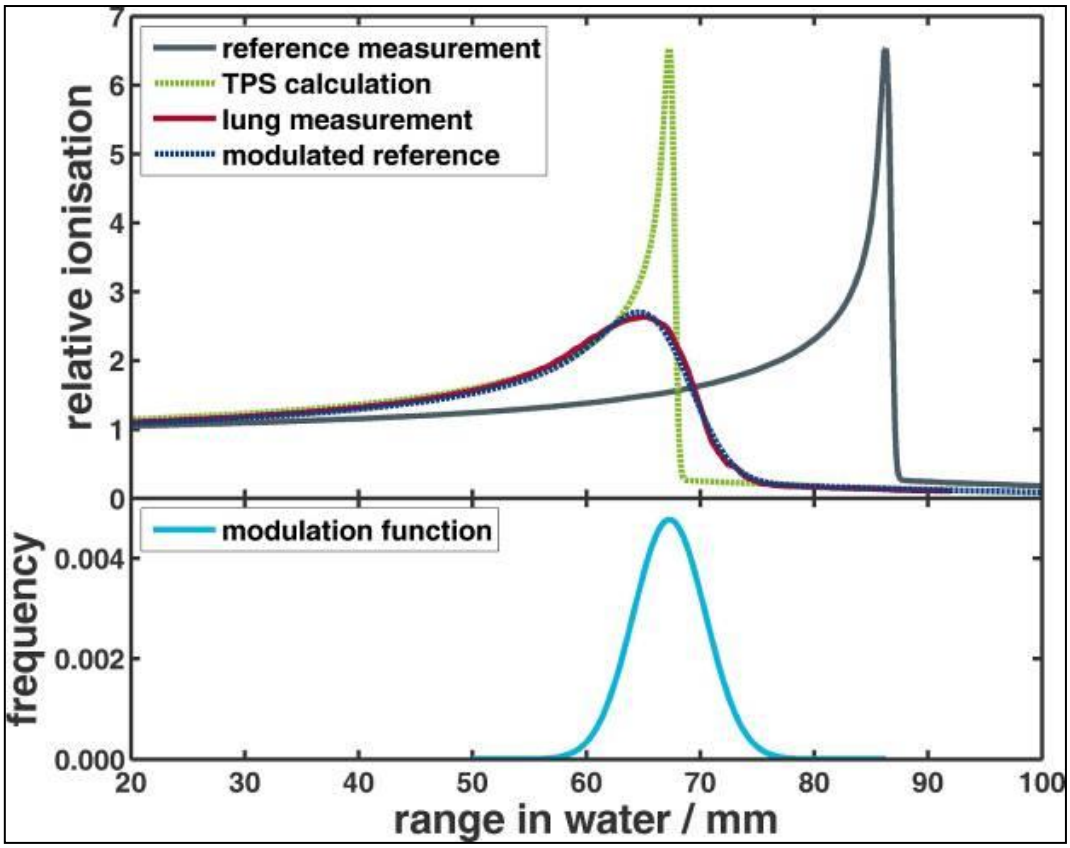

Fig. 1: Top: depth dose profile of a 200 MeV/u C-12 beam. Reference measurement (gray, no sample in beam path) and porcine lung measurement (red). The dark blue dotted line is the result of the convolution of reference and lung modulation function (bottom). The position of the modulation function (bottom, light blue) is relative to the Bragg peak position of the reference measurement. The green dotted line is the reference curve shifted by the mean area density corresponding to a Bragg-peak a TPS would calculate.

The green Bragg-peak in fig. 1 shows the result, a treatment planning system (TPS) would calculate in a treatment situation similar to the experimental setup. The reference curve is shifted by the amount of the mean area density derived from the modulation function. A great difference is visible between measurement and TPS calculation, due to the fact, that current TPS do not consider modulation effects.

Table 1 summarizes the different parameters for lung tissue and substitutes.

Especially the distal dose fall off shows the strong modulation effect of the lung tissue. The fall off increases from 0.5 mm in case of the reference curve to 4.3 mm ± 1.7 mm in the lung tissue measurements.

	modulation function					
	σ [mm]	μ [mm]	Δ [mm]	"Modulation Power" σ/√Δ [1/√mm]	thickness [mm]	$D_{90\%-20\%}$ [mm]
lung1	**3,17**	**67,3**	**19,01**	**0,726**	**50**	**4,8**
lung2	**3,05**	**66,8**	**19,46**	**0,692**	**50**	**4,9**
lung3	**1,98**	**77,8**	**8,49**	**0,680**	**70**	**2,5**
lung4	**1,85**	**77,8**	**8,45**	**0,636**	**70**	**2,4**
lung5	**3,11**	**68,5**	**17,80**	**0,736**	**100**	**5,5**
lung6	**3,08**	**66,8**	**19,49**	**0,698**	**100**	**5,4**
lung7	**1,29**	**81,7**	**4,64**	**0,600**	**50**	**2,2**
lung8	**1,21**	**81,9**	**4,37**	**0,579**	**50**	**1,8**
lung9	**4,22**	**65,2**	**21,15**	**0,919**	**70**	**7,1**
lung10	**3,73**	**59,6**	**26,69**	**0,723**	**70**	**5,3**
LN300	**2,66**	**69,9**	**87,78**	**0,284**	**70**	**5,2**
LN450	**2,14**	**80,9**	**76,75**	**0,245**	**70**	**4,2**

Tab. 1: Parameters for all measured lungs and tissue substitutes (from left to right): σ = width of the modulation function, μ = expectation value of the modulation function, Δ = mean area density (center of mass of the modulation function, thickness = length of beam path through the lung, $D_{90\%-20\%}$ = distal dose fall-off of the modulated Bragg curve

Conclusion: Strong modulation effects of range occur in organic lungs. A simple statistical model was introduced which allows to recalculate the modulation.

Although the statistical model describes the modulation in high accordance, the geometrical parameters resulting from the model are greater than expected. This aspect will be further investigated.

A strong difference between measurement and TPS calculation is visible. This difference has to be taken into account when lungs are being radiated or lie within the beam path.

References

[1] M. Urie, M. Goitein, W. R. Holley, and G. T. Y. Chen, “Degradation of the Bragg peak due to inhomogeneities”, Phys. Med. Biol. 31, 1–15 (1986).

[2] U. Weber and G. Kraft, “Design and construction of a ripple filter for a smoothed depth dose distribution in conformal particle therapy”, Phys. Med. Biol. 44 (11), 2765–2775 (1999).

154 Experimental validation of beam quality correction factors for proton beams

C. Goma[1], B. Hofstetter-Boillat[2], S. Safai[1], S. Voros[2]
[1]Paul Scherrer Institut, Villigen PSI, Switzerland
[2]Federal Institute of Metrology METAS, Bern-Wabern, Switzerland

Introduction: This work presents a method to experimentally validate the beam quality correction factors (k_Q) tabulated in IAEA TRS-398[1] for proton beams and to determine the k_Q of non-tabulated ionization chambers, based on the already existing values.

Materials and methods: The ratio between the k_Q of two ionization chambers can be expressed as a function of their reading in ^{60}Co (M_{Co60}) and in a proton beam of quality Q (M_Q), as it follows:

$$\frac{k_Q}{k_Q^{ref}} = \frac{M_{Co60}/M_Q}{M_{Co60}^{ref}/M_Q^{ref}}$$

In this work, we studied 4 ionization chamber models: IBA FC65-G Farmer, PTW 31010 Semiflex, PTW 23343 Markus and PTW 34045 Advanced Markus—the latter has no tabulated k_Q in IAEA TRS-398. The ^{60}Co and proton beam measurements were all performed according to IAEA TRS-398 reference conditions. The ^{60}Co-beam measurements were performed in a Primary Standards Dosimetry Laboratory. The proton beam measurements were performed in the middle of a 10x10x10 cm^3 spread-out Bragg peak of residual range (R_{res}) 6 g/cm^2.

Result: Table 1 shows a comparison between the k_Q values tabulated in IAEA TRS-398 and the k_Q values experimentally determined in this work—taking the k_Q of the Markus chamber as reference. We found the differences between the experimental and the tabulated k_Q values were -0.7% for the Farmer chamber and +0.3% for the Semiflex. The k_Q of the Advanced Markus, for R_{res} = 6 g/cm^2, was found to be 0.997.

Summary: The k_Q of the PTW 34045 Advanced Markus chamber was experimentally determined. The differences between the experimental k_Q values determined in this work and the tabulated values in IAEA TRS-398 are within the uncertainty of the latter (σ=1.7%)[1]. The method described in this work is not only applicable to proton beams, but to any kind of radiation beam quality.

		IAEA TRS-398	**Experimental**
IBA FC65-G	Farmer	1.040	1.033
PTW 31010	Semiflex	1.029	1.032
PTW 23343	Markus	1.002	n/a
PTW 34045	Advanced Markus	-	0.997

Tab. 1: Theoretical and experimental k_Q for R_{res} = 6 g/cm^2 for different ionization chambers. The k_Q of the Markus chamber is taken as reference.

References

[1] Andreo P, Burns DT, Hohlfeld K, Huq MS, Kanai T, Laitano F, Smythe VG, Vynckier S. Absorbed dose determination in external beam radiotherapy: an international code of practice for dosimetry based on standards of absorbed dose to water (IAEA Technical Report Series No. 398), 2000, Vienna: International Atomic Energy Agency

155 Individualized patient selection for particle therapy: ReCompare

A. Lühr[1,2], S. Löck[1], K. Roth[1], S. Helmbrecht[1], A. Jakobi[1], U. Just[2,3], M. Krause[1,2,3,4], M. Baumann[1,2,3,4], W. Enghardt[1,3,4]
[1]Technische Universität Dresden, OncoRay – National Center for Radiation Research in Oncology, Dresden, Germany
[2]German Cancer Research Center (DKFZ), German Cancer Consortium (DKTK), Dresden, Germany
[3]University Hospital Carl Gustav Carus, Radiation Oncology, Dresden, Germany [4]Helmholtz-Zentrum Dresden-Rossendorf, Institute of Radiation Oncology, Dresden, Germany

Introduction: Particle therapy offers some patients a higher chance of cure with fewer side effects than state-of-the-art photon therapy. The identification of these patients is essential to guarantee a fair and sufficient access to this specialized and limited resource. However, expertise on particle therapy is usually concentrated at particle therapy centers, while the (initial) treatment decision for most patients is made at a non-particle radiotherapy institution. Therefore, an individualized patient selection requires networks of particle and non-particle radiotherapy centers that establish (1) the exchange of relevant patient information and expertise on particle therapy as well as (2) procedures for a well-founded decision process. In this work, we contribute a novel concept addressing these two aspects.

Materials and methods: We proposed a practical concept that allows a non-particle radiotherapy institution to select individual patients for photon or particle beam therapy [1]. It bases on patient-specific, remote treatment plan comparison as schematically shown in Fig. 1. The non-particle radiation institution sends a photon treatment plan (that does not comply with the constraints) to the particle therapy center where a corresponding particle treatment plan is produced on the same data. The particle plan is sent back and the final treatment decision at the non-particle radiotherapy institution bases on a comparison of the pair of plans. We have translated this concept by developing the web-based software tool ReCompare (REmote COMparison of PARticlE and photon treatment plans), which realizes remote and safe patient data transfer. Also, we have established a clinical workflow, an IT infrastructure solution, and a legal framework.

Results: We demonstrated the feasibility of the proposed concept by exchanging photon and particle treatment plans for the same patient between remote radiotherapy institutions. The software ReCompare enables non-particle radiotherapy institutions to directly compare photon and particle radiotherapy plans in their photon treatment planning system (Fig. 2). The treatment decision remains with the attending physician at the non-particle radiotherapy institution using their standard treatment planning software. Thereby, the concept is thought to integrate into the clinical workflow of the participating radiotherapy institutions. We have initiated a testing phase with external non-particle radiotherapy institutions.

Conclusion: Our concept supports non-particle radiotherapy institutions with an individual treatment decision on the optimal irradiation modality. It may improve and standardize this personalized treatment decision. We believe that especially patients but also non-particle and particle therapy centers will profit from the proposed (pre-) selection of patients. The software ReCompare will be available when proton therapy is operational in Dresden.

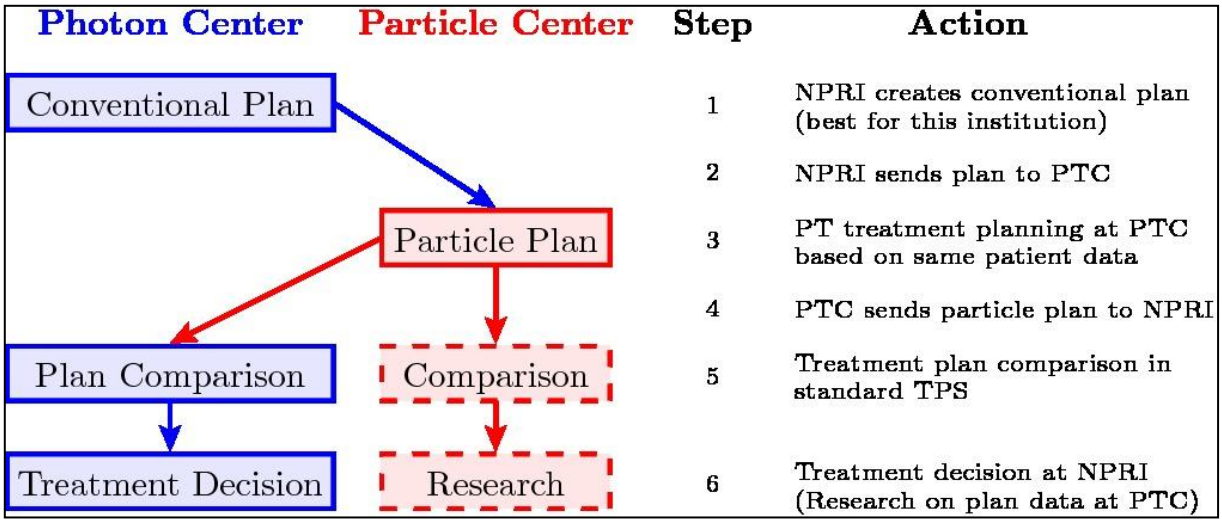

Fig. 1: Individual treatment decision process based on remote plan comparison for photon and particle irradiation. NPRI: Non-particle radiotherapy institution, PT(C): Particle therapy (center), TPS: Treatment planning system.

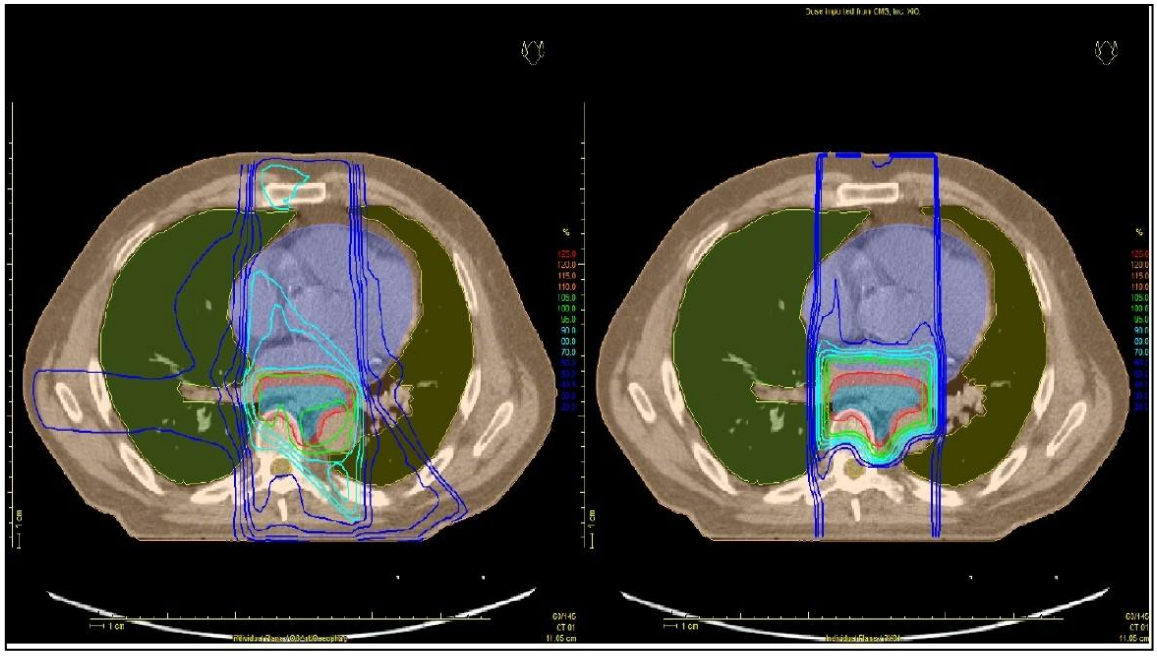

Fig. 2: Comparison of photon (left) and proton (right) treatment plans for the same esophagus cancer patient. Plan exchange was performed with ReCompare. Protons: XiO, photons: Masterplan.

References

[1] Lühr A, Löck S, Roth K, Helmbrecht S, Jakobi A, Petersen J B, Just U, Krause M, Enghardt W and Baumann M: Concept for individualized patient allocation: ReCompare—remote comparison of particle and photon treatment plans, Radiation Oncology 9 (2014), p. 59.

Poster session I – Advanced techniques in radiation therapy

Chair: H. Treuer (Cologne/DE)

P 1 Dose distributions calculated on cone-beam-CT compared to normal CT: limitations for clinical routine

T. Streller[1], M. D. Herraiz Lablanca[1]
[1]Unispital Zurich, Radioonkologie, Zurich, Switzerland

Purpose: To evaluate differences between dose distributions of intensity modulated treatment plans calculated on CT and kV-cone beam CT (CBCT).

Materials and methods: The scanning protocols of the kV-cone-beam-CT (CBCT) of two linacs (OBI 1.4. Trilogy, and TrueBeam 1.6, Varian Medical Systems) and the planning CT (PCT) (Siemens Definition AS) were calibrated by means of a CatPhan® phantom, resulting in nearly identical Hounsfield – electron density – relations. 22 patients treated with intensity modulated radiotherapy, received a CBCT (12 with OBI Trilogy, 10 with the TrueBeam system) and a PCT on the same day. The original treatment plan was calculated on both the CBCT and PCT. The resulting axial, coronar, and sagittal dose planes with different extensions (5x5cm and 30x30cm around the isocenter) were extracted. The corresponding CBCT and PCT dose distributions were compared by means of the Gamma-Index (1 mm distance to agreement, 3% or 5% dose difference, accepted percentage of points passing the Gamma index: >90%). Further, the isocenter dose values were compared to the values of the original plan.

Results: For the 30x30cm planes which contain the whole body, the dose distributions were comparable in all 3 planes for 3 patients (0 for OBI Trilogy vs. 3 for TrueBeam) with respect to the Gamma-Index (1mm, 3%) and for 13 patients (5 vs 8) with respect to Gamma-Index(1mm,5%). For the 5x5cm planes, the dose distribution was comparable for 17 patients (7 vs 10) with respect to Gamma-Index(1mm,3%). The remaining 5 cases of comparison failure could be explained by artefacts limiting the CBCT image quality due to metal, air cavities and large body size. The relative mean isocenter dose difference (CBCT vs PCT) was 1.3±2.0% (OBI Trilogy) and 0.4±1.3% (TrueBeam), whereas the relative mean isocenter dose deviation (absolute unsigned difference) was 1.5% (OBI Trilogy) and 1.0% (TrueBeam).

Conclusions: The improved of comparability of CBCT and PCT based dose calculations with limited dose matrix extension (5cm vs 30cm) is likely caused by body surface effects. Thus, the CBCT based dose calculation may be used during treatment for dose verification with 3% confidence, unless the image quality is limited by density-gradient artifacts. This might explain the different comparison results for the two CBCT systems: the Truebeam patients were treated in brain, head/neck and pelvis, whereas the Trilogy patients were also treated in the mediastinum. Finally, the deviation between means of original and absolute (unsigned) isocenter dose differences suggests that calculation differences between PCT and CBCT include systematic and stochastic components. These systematic effects need to be investigated further in order to improve the CBCT dose calculation.

P 2 CBCT-IGRT use to implement adaptative treatment: comparative study of CT- and CBCT-based dosimetries using the CIRS phantom and the gamma index

G. Guibert[1], P. Cossmann[2], C. Tamburella[1], M. Notter[1], P. Weber[1]
[1]Hôpital Neuchâtelois, Service Radiothérapie, la Chaux-de-Fonds, Switzerland
[2]MTCc, Zug, Switzerland

Related questions: CBCT images taken during radiotherapy treatments offer potential – and often non exploited – possibilities for adaptative radiotherapy treatments (ART). IGRT provides information about the positioning of the patient, tumor and organs at risk evolution compared to the reference CT exam. Some anatomical, biological and functional changes can be observed during treatment. The CBCT images can thus be used to recalculate the dosimetry and assess the real delivered dose throughout the treatment, providing a supplementary help to decide for a replanification on a new CT exam or for a retrospective assessment (cumulative dose).

Material and procedure: The use of CBCT images for dosimetry calculation requires a CT-number versus-density calibration curve. The implementation of this calibration curve on our XVI system 4.5 (Elekta Agility) was performed in Pinnacle 9.2 by using the phantom CIRS (Model 062MA CBCT). This CIRS phantom was also used for testing the dosimetry quality. Different types of plans (3DRT, VMAT) and different localisation (pelvis, Head&Neck, chest) are calculated from the CIRS and recomputed on the CIRS CBCT for comparison. Many parameters are available to compare CT and CBCT dosimetries: minimum dose, maximum dose, mean dose, DVHs etc. Nevertheless some of them could be sensitive to geometric considerations (position, countouring) and may not be so representative. Using the gamma index as a comparison parameter offers interesting possibilities in dose quality assessment.

Result: For every localisation (H&N, pelvis) and type of plans (3DRT, VMAT), the comparison of CT-based and CBCT-based dosimetries shows that more than 95 % of the considered voxels pass the criteria of 2mm and 2%. Nevertheless, one has to pay attention for lung or dense bone similar tissues that could have 4% difference locally observed, for the lower dose and when the mean dose parameter is used.

Summary: In conclusion, CBCT can be used to replanning a dosimetry and evaluate the effect of movement or shrinkage changes during treatment. It is a relevant tool to decide for a replanification based on a new CT scan.

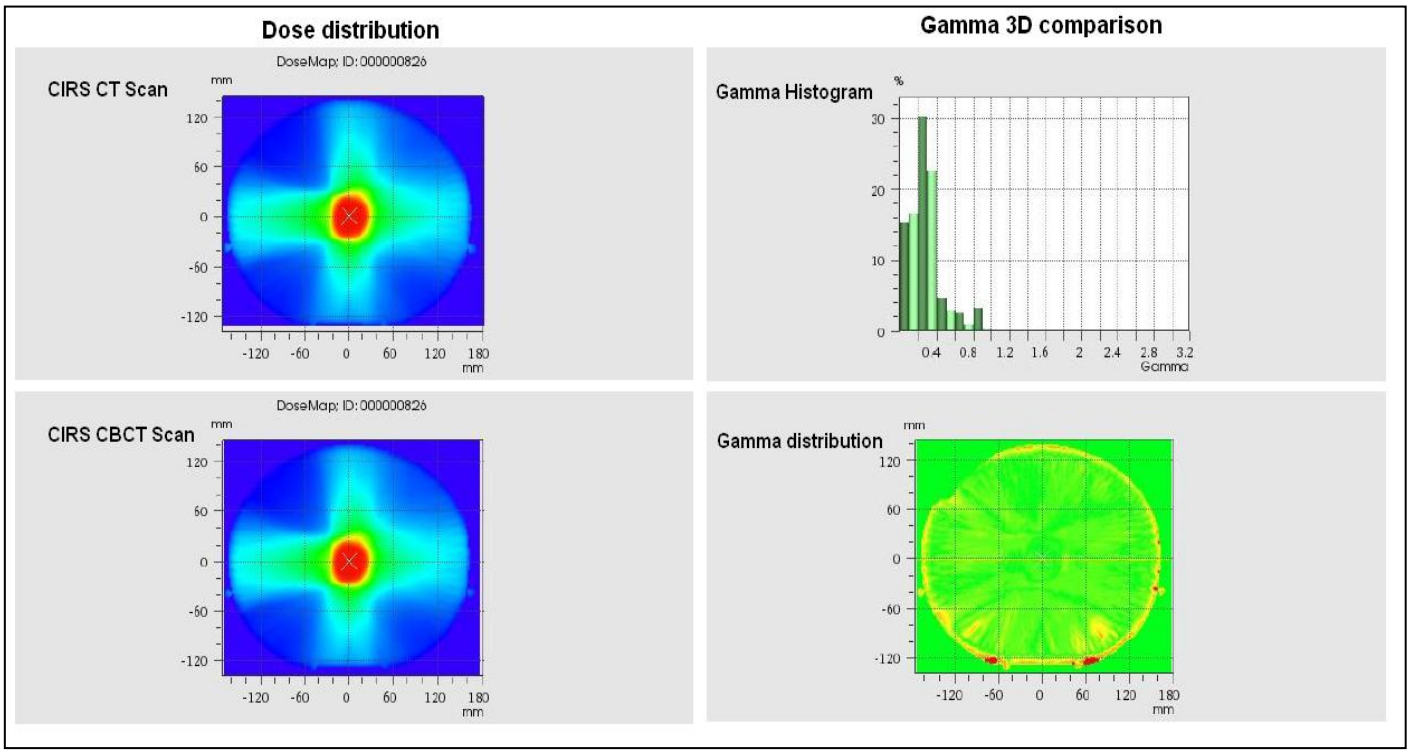

Fig 1: Comparison of dose calculated on CIRS CT Scan and recomputed on CBCT CIRS scan, showing that more 95 % of the voxels pass the 2mm and 2% criteria.

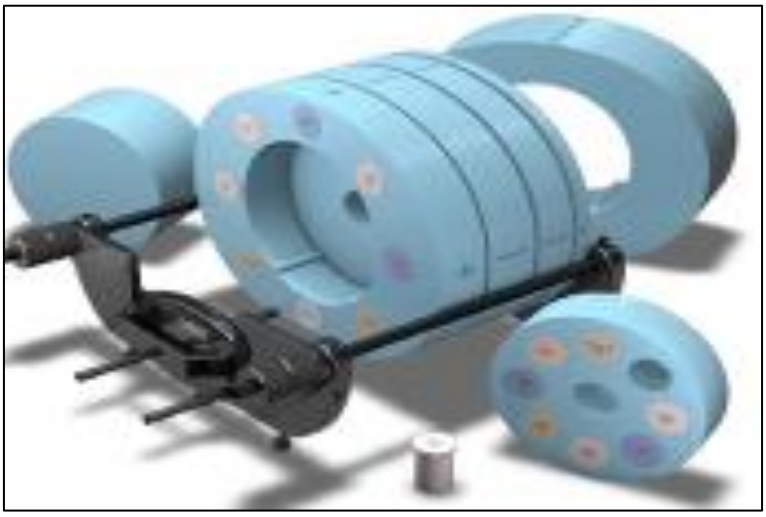

Fig 2: CIRS phantom model 062MA

References

[1] George X. Ding et al. A study on adaptative IMRT treatment planning using kV cone-beam CT. Radiotherapy and Oncology 85 (2005) 116-125.

[2] Y. Rong et al. Dose calculation on kV cone beam CT images:an investigation of the Hu-density conversion stability and dose accuracy using the-specific calibration. Med. Dosim. 35 (2010) 195-207.

[3] PH. Cossmann, V. Varchena] A novel phantom design for the electron density calibration of a linac CBCT option.Zeitschrift fuer Medizinische Physik (submitted)

[4] PH Cossmann et al. Characterisation of a Linac Cone-Beam-CT Option: What is the Future Potential for Treatment Planning? SU-GG-T-536, Medical Physics. 35 6 (2008).

P 3 Comparison and evaluation of dose distributions of 3D-conformal and IMRT plans with organ movement

V. Preylowski[1], T. Weihrich[1]
[1]KH Buchholz und Winsen, Strahlentherapie, Buchholz, Germany

Introduction: Due to the high conformality and the better sparing of normal tissue intensity-modulated radiotherapie (IMRT) is superior to conventional 3D-conformal radiotherapy [1-3]. For radiation of lung tumors often a compromise of lung dose and dose of the spinal cord or other organs at risk has to be made. So the use of IMRT planning for lung cancer or other diseases in the thoracal region could simplify the planning and could improve the quality of treatment. However due to the high organ movement by breathing the high conformality could be decreased and cold- and hotspots might occur [4-5]. The aim of this study is the evaluation of IMRT-plans with organ movement compared to conventional 3D-conformal plans.

Materials and methods: Conducting the irradiation a Varian Clinac DHX 2100 C/D (Varian Medical Systems) with a 120-leaf Millennium MLC is used. The IMRT fields are used in sliding window technique. For measurements an IMRT plan with five fields and a comparable 3D-conformal plan with similar irradiation directions are applied.

The 3D-dose distribution of the IMRT and the 3D-conformal plans is measured at characteristic places of the distribution using a dosimetry diode/ionization chamber (PTW). The measurements are made with and without movement. To avoid statistical errors due to the phase of the movement, all dose values are measured several times to simulate the complete fractionation of treatment. For these measurements a symmetric phantom of solid water with inhomogenities (EasyCube) and a water phantom containing a moveable air cavity to simulate a breathing patient are used. Evaluating the blurring of the dose distribution a 2D-array is used.

To evaluate the two different techniques the maximum, the minimum and the mean dose of the 2D-array in the area of tumor can be compared with the static case. Further the standard deviation and the mean value of the measured places of the 3D-dose distribution can be evaluated.

Discussion: By the time of the submission of this abstract the phantom with the moveable air cavity is still in progress.

Regarding the maximum, the minimum and the mean values of the dose distribution of the IMRT and the 3D-conformal plan can be compared and the stability of the dose over the various fractions interpreted. Hence, the advantage of the superior calculated dose distribution of the IMRT in the static case can be evaluated.

References

[1] Berbeco et al., Measurement of the interplay effecting lung IMRT treatment using EDR2 films, Journal of Applied Clinical Medical Physics, Vol 7,No 4, pp. 33–42 (2006)
[2] Wolff et al., Volumetric modulated arc therapy (VMAT) vs. serial tomotherapy, step-and-shoot IMRT and 3D-conformal RT for treatment of prostate cancer, Radiotherapy and Oncology 93 (2009) 226–233
[3] Arbea et al., Intensity-modulated radiation therapy (IMRT) vs. 3D conformal radiotherapy (3DCRT) in locally advanced rectal cancer (LARC): dosimetric comparison and clinical implications, Radiation Oncology 2010, 5:17 doi:10.1186/1748-717X-5-17
[4] Dzierma et al., Visualisation of Respiratory Tumour Motion and Co-Moving Isodose Lines in the Context of Respiratory Gating, IMRT and Flattening-Filter-Free Beams, PLOS ONE, January 2013, Volume 8, Issue 1, e53799
[5] Gierga et al., Quantification of respiration-induced abdominal tumor motion and its impact on IMRT dose distributions, Int. J. Radiation Oncology Biol. Phys., Vol. 58, No. 5, pp. 1584–1595, 2004, doi:10.1016/j.ijrobp.2003.09.077

P 4 Analysis of breathing patterns – curves during lung and liver SBRT

M. Weichel[1], R. Werner[1,2], C. Petersen[1], T. Gauer[1]
[1]Universitätsklinikum Hamburg-Eppendorf, Klinik für Strahlentherapie und Radioonkologie, Hamburg, Germany
[2]Universitätsklinikum Hamburg-Eppendorf, Institut für Computational Neuroscience, Hamburg, Germany

Introduction: In radiotherapy of lung and liver tumors, the internal target volume (ITV) is meant to compensate for the uncertainty in tumor position, which primarily depends on breathing motion. The breathing motion is accessed by 4D-CT imaging. For 4D-CT reconstruction, breathing curves are measured by surrogate systems. Thus, variations of surrogate breathing curves are likely to result in variations of the tumor trajectories and hence affect the correct sizing of the ITV.

This investigation is a first attempt to gain detailed knowledge of the intensity and the properties of breathing irregularity of free-breathing patients in radiotherapy. Irregularities in breath amplitudes and cycle lengths are explored, as well as baselineshifts. They are studied at intra-fractional and inter-fractional level. In total, this study considers 59 breathing curves of 10 participants, splitting up into two groups: Five patients with liver or lung tumors, plus five healthy volunteers.

Materials and methods: The breathing curves of five patients who undergo 4D-CT imaging and SBRT treatment are acquired and analyzed. Three of them suffer from liver tumors and two from lung tumors. The course consists of one imaging session and five treatment fractions. Recording is done during 4D-CT acquisition in the imaging session (SIEMENS Somatom AS Open combined with the VARIAN RPM respiratory gating system) and right after irradiation on each treatment fraction (VARIAN TrueBeam STx with integrated RPM). In case of the fractions, each breathing curve covers about one to two minutes, which corresponds to the timespan of 4D-CT.

Furthermore, breathing curves of five healthy volunteers at the age of 20 to 30 are recorded (RPM) to observe the longer-term properties; each curve's duration is about 10 minutes. Six curves per volunteer are recorded, to add up with the number of curves per patient. All participants are asked to breathe regularly, but no coaching or bio-feedback is used.

The RPM is a surrogate system that tracks a retroreflective infra-red marker positioned on the abdomen. In case of the patients, a proper position between tip of the sternum and navel is found by the clinical personnel. This surrogate position stays the same over the full course for each patient. In case of the healthy volunteers, the marker is always placed medial, immediately superior to the navel.

The anterior-posterior (a-p) breathing curves from the surrogate systems are parametrically analyzed by self-developed MATLAB routines. Parameters are breath amplitude (peak-to-peak amplitude of one period of the surrogate signal), cycle length (duration of a period of the surrogate signal) and baseline (shift).

The intra-fractional variability of breath amplitudes and cycle lengths is explored based on the span of values per fraction (or session). Inter-fractional variability is explored based on the spans of minima, maxima and mean values. Furthermore, both are regarded relatively (span-to-mean-ratio in percent). The general character of the distribution of breath amplitudes and cycle lengths is examined in outlines. Typical baselineshifts under clinical conditions are determined for short timespans in patients, plus for longer timespans in healthy volunteers.

Results: The breathing curves demonstrated intra- and inter-fractional irregularity in breath amplitudes and cycle lengths (Fig. 1).

The analysis of the irregularity's intensity establishes:

- The intra-fractional spans of the breath amplitudes are in the range of 3 mm – 19 mm in case of the patients and 9 mm – 36 mm in case of the healthy volunteers, or (span-to-mean-ratio:) 25 % – 300 % and 81 % – 620 %, respectively.
- Inter-fractional spans of the mean values of the breath amplitudes are 2 mm – 4 mm (patients) and 3 mm – 6 mm (healthy volunteers), or (span-to-mean-ratio:) 26 % – 50 % and 27 % – 62 %, respectively. For the maxima they are 5 mm –14 mm and 3 mm – 17 mm. For the minima they are 2 mm – 6 mm and 1 mm – 10 mm.
- All breath amplitudes of the patients are in the range of 2 mm – 22 mm. Those of the healthy volunteers are all in the range of 0 mm – 42 mm.

The intra-fractional spans of the cycle lengths are in the range of 0.5 s – 4.9 s in case of the patients and 2.0 s – 12.9 s in case of the healthy volunteers, or 13 % – 103 % and 55 % – 255 %, respectively.

- Inter-fractional spans of the mean values of the cycle lengths are 0.6 s – 3.9 s and 0.5 s – 2.0 s, or 16 % – 67 % and 16 % – 39 %, respectively. For the maxima they are 1.0 s – 5.3 s and 1.6 s – 5.0 s. For the minima they are 0.6 s – 2.7 s and 0.3 s – 2.7 s.

- All cycle lengths of the patients are in the range of 2.2 s – 9.5 s. Those of the healthy volunteers are all in the range of 0.8 s – 14.6 s.

- The baselineshifts of the patients amount to -2.9 mm – +1.3 mm in range, during about one to two minutes recording length, after lying on the couch for about ten to fifty minutes. Those of the healthy volunteers amount to -6.7 mm – +5.5 mm in range, during recording lengths of about ten minutes with a lay-time before recording of approximately one minute.

The analysis of the irregularity's properties establishes:

- Individual tendencies/peculiarities can be found. Each participant shows a typical range of values.

- Chronological trends (rising or falling of any value) over the full course cannot be found. The connection between fractions and values seems random.

- Minimum and, especially, maximum values sometimes vary significantly stronger than mean values.

- Longer observation periods lead to larger spans per fraction but have no impact on the inter-fractional spans of mean values, minima or maxima.

- Large intra-fractional spans of the cycle length go hand in hand with large inter-fractional spans of the mean values of the cycle lengths.

- For longer observation periods the values show a tendency towards the Gaussian distribution, which is hardly recognized during short observation periods.

- Systematic baselineshifts resulting from the impact of gravity towards the surrogate can be fitted using decay functions.

- Apart from the systematic shift, random short term (breath to breath) variations of the baseline can be found. They are in the size of total baselineshifts found during one or two minutes, if the participant has been lying on the couch for some minutes before.

Conclusions: Analysis of breathing variability of lung and liver patients revealed considerable irregularity over the course of 4D-CT acquisition and treatment. Observed breathing signal variability possibly translates into tumor motion variability, which is not accounted for in conventional 4D-CT-based ITV delineation.

Clinical benefit of bio-feedback on patient breathing to reduce variability is currently under debate. In addition, approaches to extend ITV delineation for compensation of breathing irregularity should be taken into consideration.

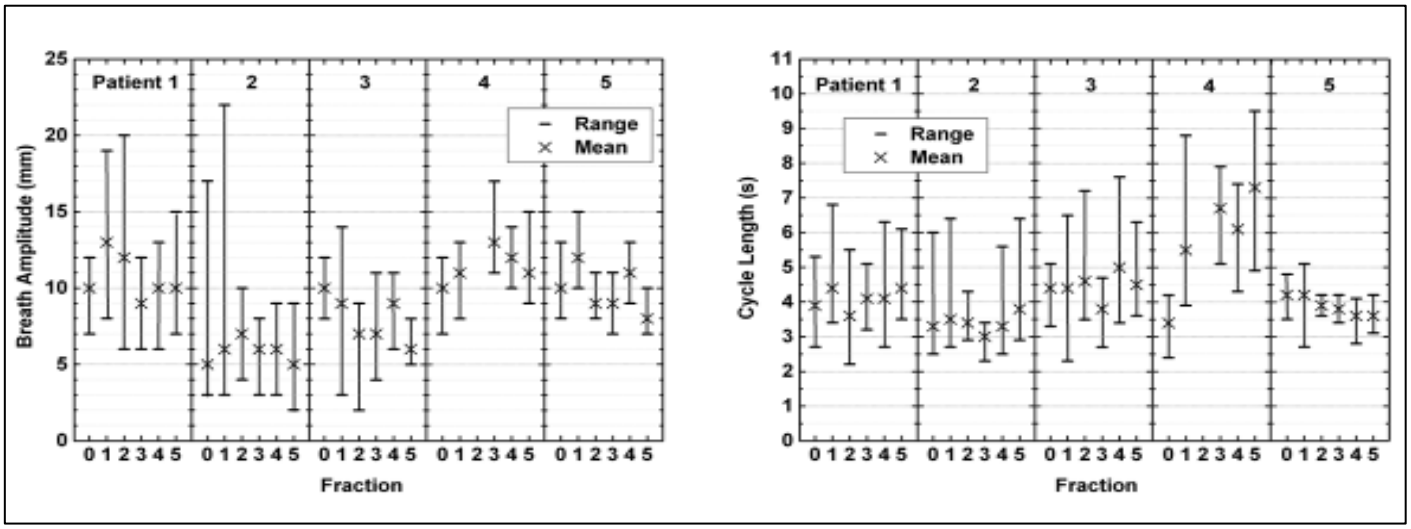

Fig. 1: The patient's breath amplitudes (left) and cycle length (right) from the a-p breathing curves. Fraction 0 refers to the 4D-CT imaging session. The span of values per fraction is an indicator for the intra-fractional irregularity. The variation of the minima, maxima and mean values shows the inter-fractional variability. (On the 2nd fraction of patient 4, no curve was recorded, for clinical reasons.)

P 5 Practicability of the Elekta Agility-MLC versus Elekta add-on MLC Apex for stereotactic radiosurgery

Y. Avcu[1], H. Petermann[1], G. Kohler[1]
[1]Unispital Basel, Radioonkologie, Basel, Switzerland

Introduction: Since Winston et al. [1,2] work in 1988, stereotactic radiosurgery with linear accelerators (linac) has improved considerably. Whilst applicators were self-built by clinics for stereotactic radio therapy, nowadays linacs with built-in multi leaf collimators (MLC) with and without add-on MLC, are in vogue to enable high precision therapy.

In 2012, Elekta introduced their new built-in MLC called Agility consisting of 160 tungsten leaves, each 5 mm wide, with a leaf speed of up to 6.5 cm/sec and an exceptionally low leaf transmission with less than 0.5% across the entire field. Therefore Agility is suitable for stereotactic therapy. On the other hand, Elekta presented their new add-on MLC Apex for stereotactic radio therapy in 2011 with a leaf width of 2.5 mm in isocenter and 112 dual-focusing leaves, which produces a sharp penumbra. A steeper dose gradient and smaller leaf width can be generated by collimation close to the patient. Furthermore, due to the divergent beam, the closer the collimation is done, the smaller is the resulting leaf width in the isocenter plane. However, as a disadvantage add-on MLCs have to be attached and removed from the base linac, which can lead to variations in mounting. Moreover, a special quality assurance (QA) has to be implemented in addition to the basic linac QA.

The current investigation aims at a comparison of the new Agility MLC and the add-on Apex MLC. This is especially of interest for institutions where both MLCs are available.

Materials and methods: For the purpose of the investigation, Linac Elekta Synergy (Elekta, Crawley, UK) with built-in Agility MLC, Elekta Apex add-on MLC were implemented. The measurements were carried out with a photon energy of 6 MV and for field sizes between one to six centimeter. The single field dose distributions were analyzed with EBT3 GafChromic films (Ashland Inc., Convington, KY). The films were scanned with Epson 10000XL scanner. The scanner response to the dose values was determined using protocol proposed by Lewis et al. [3] with the Film pro QA software. The reproducibility of leaf positioning was measured using Elekta iView EPID and analyzed with the open source software suite ImageMagick (www.imagemagick.org).

Results: The leaf positioning reproducibility of both MLCs was below 0.2 mm. The mounting reproducibility of the Apex MLC was significantly accurate, i.e. below 0.1 mm. The influence of the weight of the Apex MLC to the gantry sag was 0.2 mm in gantry target direction; influences in the other directions could be neglected. As expected, the add-on Apex MLC provided a sharper penumbra in cross plane direction compared to the built-in Agility MLC. However, reproducibility of the leaf positioning was almost the same with both MLCs. Based on preliminary tests we expect for small field sizes between 1 cm and 4 cm a penumbra of 3 mm with the Apex add-on MLC. By contrast, the Agility MLC has a penumbra of 6 mm. In the in-plane direction the penumbra of both MLCs led to almost similar results, with a 5 mm width between the 20% and 80% isodose. In the next months we will perform the measurements for accurate results.

Conclusion: The Agility MLC proves to be useful for stereotactic radio therapy treatments in most cases with an advantage of interchangeability between different linacs of the same type and the speed of usage. The Apex MLC, on the other hand, provides very sharp penumbras and is excellent suited for high irregular shaped target volumes in radio surgery.

References

[1] Lutz, W.: Winston, K.: A system for stereotactic radiosurgery with a linear accelerator, Int. J. Radiation Oncology Biol. Phys.1988, Vol 14. pp. 373-381.
[2] Winston, K.: Lutz, W.: Linear Accelerator as a Neurosurgical Tool for Stereotactic Radiosurgery, Neurosurgery 1988, Vol 22, No. 3
[3] Lewis D et al.: An efficient protocol for radiochromic film dosimetry combining calibration and measurement in a single scan. Med Phys. 2012 Oct;39 (10):6339-50.

P 6 A comparative study of different dose calculation algorithms for small photon fields

R. Schmitz[1], P.-H. Mackeprang[1], D. Henzen[1], D. Schmidhalter[1], D. Terribilini[1], P. Manser[1], M. K. Fix[1]
[1]Division of Medical Radiation Physics and Department of Radiation Oncology, Inselspital, Bern University Hospital, and University of Bern, Switzerland, Bern, Switzerland

Introduction: In recent years, stereotactic radiotherapy has been of growing interest. Hence, it is important to study and understand the accuracy and behaviour of commonly used dose calculation algorithms for the regime of small fields. Previous studies have dosimetrically compared Acuros XB and AAA and found a good reliability for both methods regarding quadratic fields down to a field size of 0.8x0.8 cm^2 [1]. The aim of this work is to extend this comparison to a broader spectrum of dose calculation algorithms and to put emphasis on a detailed analysis within artificial, well-understood setups considering a larger set of different field sizes and shapes in order to identify differences between the algorithms and study the influence of field size and shape, collimation technique and beam energy.

Materials and methods: The following commercial dose calculation algorithms have been included in this study: AAA and Acuros XB (Eclipse v11, Varian Medical Systems), as well as the pencil beam and Monte Carlo (MC) technique within the treatment planning system iPlan (Brainlab). Furthermore, Monte Carlo calculations have been conducted using the Swiss Monte Carlo Plan (SMCP) [2], employing VMC++ and EGSnrc dose calculation algorithms. The statistical uncertainty for all MC calculations is about 1%. Voxel sizes of $(0.25\ cm)^3$ and $(0.1\ cm)^3$ have been chosen. All data refer to a Novalis TX system at 6X or 15X. Fields collimated using jaws, together with high-definition multi-leaf collimator (HD120 MLC) and block shaped fields have been applied to a homogeneous water phantom as well as a number of heterogeneous setups, both at a source to surface distance of 100 cm. For the latter, a 16 cm thick layer of either air or lung or a 6 cm thick layer of bone tissue, each starting at a depth of 5 cm in water, is introduced into the water. These setups have been irradiated by a set of quadratic and rectangular fields with side lengths ranging from 0.25 to 10 cm.

Results: All investigated dose calculation algorithms show virtually the same results for all situations considered when the different beam modifiers are used to shape the field sizes. For a field size of **5x5** cm^2 and the homogeneous water phantom, a very good agreement is found amongst all algorithms considered. This situation changes with decreasing field size. For very small fields (0.5x0.5 cm^2) Acuros XB tends to show equally spaced, unphysical kinks along the depth dose curve if a voxel size of 0.25 cm^3 is chosen and this behaviour is even more emphasized along the off-axis depth dose curves. A possible reason could be the interconnection of voxel size and angular discretization when solving the Boltzmann transport equation in Acuros XB. AAA, on the other hand, shows to be more robust with respect to changes in voxel sizes from 0.1 cm^3 to 0.25 cm^3.

For the inhomogeneous phantom with a layer of air or lung, the algorithms show various differences in dose deposition. Whilst the relative dose distribution in the first water layer is virtually the same for all dose calculation algorithms, there arise considerable differences, particularly in the first centimeters inside the low density tissue. These differences are enhanced for small and elongated fields, which might be understood as an effect of electron disequilibrium at the beam edges**.**

Conclusion: For sufficiently large fields, the various methods show a very good agreement, as expected. For small stereotactic fields, however, the results suggest that Acuros XB is more sensitive to the voxel size compared to the other dose calculation algorithms. The shape of depth dose curves can be affected by the voxel size, even though the former consider a much larger spatial scale than the side length of a voxel.

In the case of the heterogeneous phantoms, particularly with low density material inhomogeneities, further differences between the dose calculation algorithms can be found. These differences might relate to the different handling of secondary electron transport. They are considerably more prominent for small or elongated fields and high beam energy.

References

[1] A. Fogliata, G. Nicolini, A. Clivio, E. Vanetti, and L. Cozzi: Accuracy of Acuros XB and AAA dose calculation for small fields with reference to RapidArc® stereotactic treatments, Medical Physics 38 (2011), p. 6228
[2] M.K. Fix, P. Manser, D. Frei, W. Volken, R. Mini, and E.J. Born: An efficient framework for photon Monte Carlo treatment planning, Physics in Medicine and Biology 52 (2007), p. N425

P 7 Evaluating the Optimum radiation dosimeter for Small field photon dosimetry via Audit Methodology

A. Yousuf[1], S. Mushkin[1], A. Hussain[1], M. Naqvi[1]
[1]Aga Khan University Hospital, Radaition Oncology, Karachi, Pakistan

Title: Evaluating the Optimum radiation dosimeter for Small field photon dosimetry via Audit Methodology

Objective: The aim of this study is to investigate the optimum radiation dosimeter for small photon fields, define by multileaf collimator (MLC) and to perform an audit of treatment planning system for small field output factor dataset against standard dataset produced by radiological physics center (RPC).

Material and procedure: In this study multiple small field size output factor datasets were measured and calculated for 6 MV x-ray beams using the RPC recommend methods. These beam datasets were measured at 10 cm depth and 100cm SSD for secondary jaws setting 10 × 10 cm2 with MLC defined field sizes of 6 × 6, 4 × 4, 3 × 3, 2 × 2 and 1x1 cm2. The measurements were made with Landauer's nanoDot OSLDs, Gafchromatic EBRT3 and PinPoint® ion chamber. The measured output factors were also compared with those calculated by Eclipse™ treatment planning software.

Result: The spread of multiple dosimeter measured value was (standard deviation) on average, 1.5%. When compared to treatment planning system-calculated and RPC's standard dataset max deviation range 3% and 2% respectively. OSL found to be more reliable and efficient dosimeter for small field photon dosimetry having max deviation of 1 % with RPC and 2 % with TPS dataset.

Summary: OSLDs are simple, durable, and accurate tool to verify doses that delivered using small photon beam fields down to a 1 x 1cm2 field sizes. The study emphasizes that the treatment planning system should always be evaluated for small field out factors for the accurate dose delivery in clinical setting.

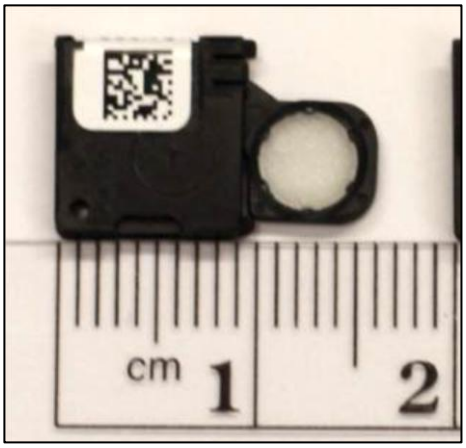

Fig. 1: OSLDs Nanodot and its Jacket

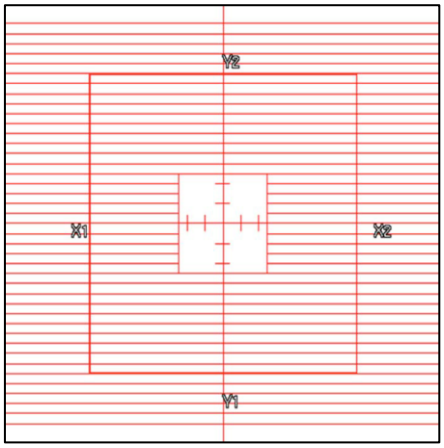

Fig. 2: A sample MLC-defined aperture within a larger jaw setting. This field of 5_5 cm2 within a jaw-defined field of 10_10cm2

Open	MLC define aperture	Deviation with RPC dataset			Deviation with TPS		
10x10		OSL	EBRT3	Pinpoint	OSL	EBRT3	Pinpoint
	6x6	0.99 %	1.0 %	0.78 %	0.7 %	0.0%	1.0 %
	4x4	1.01 %	1.5 %	1.48%	1.3 %	1.0 %	1.6 %
	3x3	1.00 %	1.7 %	1.76%	2.5%	2.0 %	2.0 %
	2x2	0.99 %	2.6 %	1.84%	2.4 %	4.0%	4.7 %
	1x1	------	-------	------	1.0 %	2.0 %	4.8 %

Tab. 1: Shows the deviation of multiple dosimeter with RPC and TPS dataset.

References

[1] Pham, Christopher, "CHARACTERIZATION OF OSLDS FOR USE IN SMALL FIELD PHOTON BEAM DOSIMETRY" (2013).

[2] David S. Followill, The Radiological Physics Center's standard dataset for small field size output factors. 2012, PACS number: 87.53.Bn

[3] Parham Alaei & Patrick Higgins "Effect of multileaf collimator-defined segment size on Sc" , 2010 American Association of Physicists in Medicine. DOI: 10.1118/1.3431997

[4] Measuring output factors of small fields formed by collimator jaws and multileaf collimator using plastic scintillation detectors, 2010 American Association of Physicists in Medicine. DOI: 10.1118/1.3488981_

P 8 Geometrical accuracy of stereotactic cranial radio-surgery improved to 0.5 mm with patient dedicated QA procedures

H. Petermann[1], G. Kohler[1]
[1]Universitsetsspital Basel, Institute of Radiooncology, Basel, Switzerland

Introduction: In cranial radio-surgery geometrical accuracy depends on the interplay of different tolerances: cone beam CT for patient positioning, radiation field positions at different gantry and collimator angles and isocentric couch rotation. QA procedures were developed that (a) have high geometric resolution and reproducibility (b) cover the complete chain of tolerances from patient positioning to beam delivery and (c) can be done in a reasonable time in the clinical routine.

Materials and methods: Cranial radio-surgery is done on ELEKTA Synergy with an-add-on-MLC with leaf width of 3mm. Two phantoms are used for the QA:

1) A self-developed PMMA phantom for positional accuracy of the cone beam CT: The drilled hole is (a) aligned to the laser, (b) used to align the phantom in the cone beam CT and (c) used to mark the laser position on the GafChromic® film with a needle prick.
2) The ball bearing phantom delivered by ELEKTA for cone beam CT calibration is used to evaluate deviation of laser to radiation field for different gantry and couch angles.

The phantom position relative to laser is documented with a digital camera. The images are taken parallax free and have minor geometric distortions. Distance of cone beam CT position to laser is evaluated manually with the standard ELEKTA software. The excellent contrast of the drilled hole allows determination of CT position very precisely. Star shot is irradiated on GafChromic Film. The position of the laser is marked with a pin prick on the film.

The relative position of laser to radiation field is evaluated for 13 gantry and 13 couch positions for clockwise (CW) and counterclockwise (CCW) rotation. The distance between the center of gravity of the ball is evaluated relative to the center of gravity of the radiation field using Image Magick procedures. Overall analysis delivers the combined misalignment of: cone beam CT position ↔ laser ↔ radiation field isocenter ↔ axis of isocentric couch rotation. Analysis for patient positioning is done on the gantry- and couch angles of the patient plan. Precise couch adjustment is possible with the internal couch position items accessible in service mode.

Results: Positioning the phantoms with accuracy below 0.1 to 0.2 mm is not possible without digital camera, with zoomed digital images the accuracy is below 0.1 mm. The reproducibility of the cone beam CT, the gantry and the couch position is about 0.1 mm, 0.05 mm and 0.1 mm respectively.

The position of the radiation field ↔ ball differs for CW and CCW gantry rotation. Crossplane variation is up to 0.3 mm. Inplane position of the radiation field is very stable for one linac but on another linac differrence between CW and CCW rotation is up to 0.4 mm, reasons for which could not be ascertained. The position of the ball to the radiation field differs up to 0.4 mm for CW and CCW isocentric couch rotation respectively. The position of cone beam CT evaluation differs by 0.5 mm, when cone beam CT is recorded CW or CCW. Using our calibration, position evaluated by the cone beam CT has an inplane offset of 0.5 mm relative to the radiation field isocenter. The axis of isocentric couch rotation should coincide with radiation field isocenter. However, this is difficult to achieve because the position of the rotation axis of the couch can only be adjusted with coarse tools. The residual offset is about 0.5 mm. QA procedures evaluate the overall misalignment of these components. Positioning a patient to an optimized spot between the radiation isocenter and the axis of isocentric couch rotation minimizes deviation of radiation delivery from isocenter position in the patient. Exploiting the internal couch position items, patient can be positioned to 0.2 mm on a regular couch top.

Conclusion: QA using digital camera and Image Magick procedure is precise. Sub millimeter misalignment of XVI position ↔ laser ↔ radiation isocenter ↔ isocentric couch rotation can be determined reliably. The differences between CW and CCW rotations of couch and gantry are reproducible. Positioning of the patient is possible to 0.2mm on a regular couch top. An accuracy of 0.5 mm in patient is achievable and the deviation is mainly caused by the gantry sag.

P 9 Absorbed dose to water measurements in a clinical carbon ion beam using water calorimetry – Project outline and preliminary experiments

J.-M. Osinga[1,2], S. Greilich[2], O. Jäkel[2,3,4], U. Ankerhold[1], A. Krauss[1]
[1]Physikalisch-Technische Bundesanstalt, Dosimetry for Radiation Therapy and Diagnostic Radiology, Braunschweig, Germany
[2]German Cancer Research Center, Medical Physics in Radiation Oncology, Heidelberg, Germany
[3]Heidelberg Ion-Beam Therapy Center , Heidelberg, Germany
[4]University Hospital of Heidelberg, Radiation Oncology, Heidelberg, Germany

Introduction: Until now, the dosimetry of heavy ion beams with ionization chambers has not reached the same level of accuracy as the dosimetry of conventional high-energy photon beams. The standard uncertainty associated with carbon ion dosimetry is about a factor of 3 higher as compared to high-energy photons [1]. This is mainly caused by the weak knowledge of the so-called $k_{Q,Q0}$ factor, which corrects for the different response of the ionization chamber to the actual user beam quality Q (e.g. ^{12}C) compared to the reference beam quality Q_0 (^{60}Co**).** A significant discrepancy between fluence-based and ionization-based dose measurements in clinical carbon ion beams was shown in a previous study [2], which could indicate an inaccurate $\boldsymbol{k_{Q,Q0}}$ factor. Due to the lack of experimental data, the $k_{Q,Q0}$ factor is, up to now, determined by calculations based on Monte-Carlo transport simulations and asks for experimental verification. Experimentally, the $\boldsymbol{k_{Q,Q0}}$ factor of ionization chambers can be determined by use of a primary standard for absorbed dose to water that allows for a direct calibration of the chamber in the actual user beam quality Q. In a cooperation between PTB and HIT, a project has been started to perform absolute dose to water measurements in carbon ion beams by means of water calorimetry [3] with the aim to determine the $\boldsymbol{k_{Q,Q0}}$ factor with a lower standard uncertainty.

Materials and methods: Since the measurements with the water calorimeter at HIT are performed under special conditions, namely (1) the irradiation with a pulsed beam using the raster-scan method and (2) the off-isocenter position of the calorimeter, a number of investigations are required in order to determine and optimize the irradiation parameters at the effective measurement position. Firstly, the irradiation time needs to be as short as possible in order to minimize heat conduction effects occurring during the calorimetric measurements. At the same time, a homogenous and reproducible dose distribution is necessary to achieve a low standard uncertainty in the later calorimetric measurements. Therefore, the size of the beam spot in the effective measurement position, the distance between adjacent spots and the spot pattern has to be investigated and optimized. Based on the optimal beam parameters found in the first part of this project together with corresponding Monte-Carlo simulations, reliable corrections factors for the subsequent calorimetric measurements, *e.g.* for perturbation effects or for heat conduction effects will be determined. This allows a first estimation of the resulting standard uncertainty for the experimental determination of the $k_{Q,Q0}$ factor.

Results: An experimental set-up was designed to mimic the real measurement condition of the water calorimeter by means of a water-equivalent slab phantom. This set-up offers a high flexibility in order to perform the measurements regarding the optimization of the beam parameters in the effective measurement position. The phantom design, the optimized beam parameters as well as corresponding calculations of the induced heat transport effects for the water calorimeter will be presented.

Conclusion: We investigated optimized irradiation conditions enabling accurate calorimetric measurements in a scanned carbon ion beam. The results of these experiments and simulations form the basis for the subsequent application of the water calorimeter to experimentally determine the $k_{Q,Q0}$ factor for ionization chambers and to achieve low standard uncertainties.

References

[1] International atomic energy agency. Absorbed dose determination in external beam radiotherapy. Technical Reports Series No. 398. IAEA, 2000.
[2] Osinga, J.-M., Brons, S., Bartz, J.A., Akselrod, M.S., Jäkel, O. and Greilich, S.: Absorbed dose in ion beams: comparison of ionization- and fluence-based measurements. Rad. Prot. Dos., doi:10.1093/rpd/ncu004, 2014.
[3] Krauss, A. and Kapsch R.-P.: Calorimetric determination of k_Q factors for NE 2516 and NE 2571 ionization chambers in 5 cm x 5 cm and 10 cm x 10 cm radiotherapy beams of 8 MV and 16 MV photons. Phys. Med. Biol. 52:6249-59, 2007 and Phys. Med. Biol. 53:1151-2, 2007.

P 10 Electron Beam Dose Distribution in a Solenoid Magnetic Field

S. M. Varzar[1], A. S. Osipov[1], A. P. Chernyaev[1], A. V. Belousov[1], A. Ehtesham[2,1]
[1]Lomonosov Moscow State University, Moscow, Switzerland
[2]University of Bern, AEC – LHEP University of Bern, Bern, Switzerland

Objective: The results of simulation of irradiation of tissue-equivalent target by 20-MeV electron beam in the presence of solenoid magnetic fields are discussed and compared with the corresponding data obtained without magnetic fields. The data obtained can be used to solve beam therapy problems.

Methods: In the previous jobs, it was shown in detail how a magnetic field can affect deep dose distributions under target irradiation. Here the Monte Carlo simulation is performed using the GEANT4 package, which makes it possible to obtain the energy losses of different types of particles in materials, taking into account all known physical processes; in this case, one can also take into account the presence of magnetic fields of specified configuration. We consider the field of a solenoid, which can be represented as a superposition of longitudinal and radial fields at any point and space.

Results: In this study, we investigated the effect of a solenoid magnetic field on the distribution of the electron beam dose as a function of the depth of their penetration into a tissue-equivalent medium. Results indicate that switching on the solenoid magnetic field up to 2-3 T, leads to displacement of the peak in the distribution of absorbed energy into the detector bulk (up to 1.5 cm) and significantly changes the magnitude and shape of this maximum.

P 11 The determination of relative depth doses in kilovoltage beams

P. Zucchetti[1], L. Vugts[2], T. Götzfried[1], R. Seiler[1], M. M. Aspradakis[1]
[1]Luzerner Kantonsspital, Radiation Oncology, Luzern 16, Switzerland
[2]Academic Medical Centre, Amsterdam, Netherlands

Introduction: In most dosimetry codes of practice low energy photon beams are broadly classified in a low energy range (beams from tube potentials typically below or equal to 100kVp) or and in medium range (for beams from tube potentials equal to or greater than 100kVp). Uncertainties in reference dosimetry at kV energies are estimated to be as high as 5% [1]. The determination of relative depth dose in water (RDD) poses challenges due to the lack of suitable detector for these measurements. Common practice has been the measurement of relative depth ionisation (RDI) in polystyrene or PMMA, which are not water-equivalent materials [2], or the interpolation of data from published data tables [3]. In this work, the determination of RDD curves in kV beams was carried from measurements using different detectors and phantoms. Results were compared with published data.

Materials and methods: Measurements were carried out on the T200 x-ray therapy system manufactured by Wolf-Medizintechnik GmbH, in radiation beams ranging from 30kV/0.45mmAl HVL to 200kV/1.78mmCu HVL and for nine field sizes with equivalent diameters ranging between 20mm and 133mm**.** RDIs were measured in liquid water using two types of cylindrical ionization chambers (PTW 30013/0.6cm^3 and IBA IC-15/0.13cm^3) and in solid water-equivalent plastic (Plastic Water® DT manufactured by CIRS) with the 0.6 cm^3 ionization chamber and with radiochromic film (GAFCHROMIC® EBT3 manufactured by Ashland). Measurements in liquid water with the chambers' geometric centre at the depth of measurement were acquired only up to the depth of 10mm below the water surface. RDI measurements with cylindrical chambers were assumed to equal RDDs, because these ionization chambers are known to have a flat energy response (better than 1%) and beam quality and perturbation corrections that do not vary significantly with depth [4, 5]. Fifth order polynomial fitting was carried out to the measured data, in order to determine RDD values close to and at the surface. Earlier investigations on the measurement of RDDs using a plane-parallel ionization chamber (IBA NACP-02/0.16 cm^3) had shown that measurements with this type of chamber agreed to within **±**1% with measurements with cylindrical chambers at energies down to 60kV/2.31mmAl HVL. At lower energies and at shallow depths measurements with this chamber differed by more than **±**2% from those with cylindrical chambers. These findings were consistent with the findings of Li et al (1997). Measurements with the NACP-02 were not further investigated in this work.

The water equivalence of PWDT in the determination of relative dose at the kV beams was examined in a separate investigation and is within **±**1% in the medium kV range, but water equivalence worsens with decreasing kVp and at increasing depths (within **±**3%).

To investigate the validity of the measurements in water at shallow depths, measurements with EBT3 film in PWDT were limited at 50kV/1mmAl and at 150kV/0.69mmCu**.** The response of EBT3 film in kV beams is reported to be energy dependent [6]. Therefore in this work, investigations with film included the dependence of calibration curves on irradiation conditions (energy and at the depths of 0, 5, 20 and 40mm in PWDT) as well as on the choice of irradiation geometry (orientation of the film with respect to the beam central axis). Exposed films were scanned with an Epson Expression 10000XL (Epson America, Inc.) flat-bed scanner and the film analysis was carried out with the FilmQA Pro software developed by Ashland.

Results: Measurement of RDDs in water with two different cylindrical chambers agreed at all depths beyond 10mm to within ±0.5%.

At 50kV/1mmAl, optical densities (OD) from the three colour channels and at different depths, differed by -1.5% from the values at 0mm and for doses up to 4Gy. At 150kV/0.69mmCu, differences in OD from the values at the depth of 20mm were not more than ±2% for doses up to 11Gy. The comparison of calibration curves at 50kV and 150kV showed that, irrespective of depth of calibration, differences in the two calibrations increased with applied dose, with the optical densities at 50kV being consistently higher than the corresponding values at 150kV. For the measurement of RDDs, films were calibrated at the geometric depth in PWDT which was closer to the depth in water where reference dose is being determined; namely at the surface for the low energy range and at 20mm for the medium energy range.

Measurements of RDDs with the film placed parallel to the beam central axis (CAX) showed large deviations at shallow depths from measurements where the film was placed orthogonally to CAX. With the film irradiated parallel to CAX it could not be excluded that the film itself attenuates the beam and there were uncertainties involved in setting up the film on CAX under this irradiation geometry. For this reason, measurements of RDD with film were further investigated with the film placed only orthogonal to CAX.

Comparisons of the RDD data measured in water with data from BJR Supplement 25 [3] showed differences greater than ±5%. For example at 50kV/1mmAl values in BJR25 differed by -5.5% at 10mm depth in water and by 9% at 50mm depth, whereas the corresponding values from measurements in PWDT were 1.4% and -3.7% (all data normalized at the depth of 20mm). At the medium range, differences between datasets from BJR-25 and measurements in water and PWDT were within ±5%, but with the published data having the largest deviations from the measurements in water.

Conclusions:

- To calibrate EBT3 films for use kV beams it is not appropriate to measure a calibration curve at a single beam energy. Separate calibrations are required at each kV beam and it is appropriate to measure these at a depth close to that at which reference dosimetry is carried out.
- For the measurement of RDDs with film it is not recommended to expose the film parallel to the beams' CAX.
- RDDs determined in water from measurements with cylindrical ionisation chambers and a polynomial fit to this data differ by ±2**%** from the measurements with EBT3 film. This confirmed the data between the surface and at 10mm depth in water obtained through polynomial curve fitting.
- Published RDD data should not be used to represent RDD values in water for clinical beams because the origin of this data in terms of beam filtration and collimation as well as measurement methodology used (detectors and irradiation medium) is unknown.

References

[1] IAEA, TRS-398: Absorbed dose determination in external beam radiotherapy: An international code of practice for dosimetry based on standards of absorbed dose to water. 2000, Vienna.
[2] Hill, R., et al., The water equivalence of solid phantoms for low energy photon beams. Med Phys, 2010. 37(8): p. 4355-63.
[3] BJR-25, Central Axis Depth Dose Data for Use in Radiotherapy. British Journal of Radiology, 1996. Suppl. 25.
[4] Li, X.A., et al., Measurement of percentage depth dose and lateral beam profile for kilovoltage x-ray therapy beams. Phys Med Biol, 1997. 42(12): p. 2561-8.
[5] Ma, C.M. and J.P. Seuntjens, Mass-energy absorption coefficient and backscatter factor ratios for kilovoltage x-ray beams. Phys Med Biol, 1999. 44(1): p. 131-43.
[6] Villarreal-Barajas, J.E. and R.F. Khan, Energy response of EBT3 radiochromic films: implications for dosimetry in kilovoltage range. J Appl Clin Med Phys, 2014. 15(1): p. 4439.

P 12 Dosimetry of a kilovoltage radiotherapy device: going beyond the reach of detectors

O. Nwankwo[1], F. Schneider[1], S. Clausen[1], F. Wenz[1]
[1]Klinik für Strahlentherapie und Radioonkologie, Mannheim, Germany

Introduction: The INTRABEAM® system consists of a 50 kV radiation source. An applicator is placed over the source during treatment. The applicator is in direct contact with the patient during treatment and there are several types and sizes. The needle applicator is used for the treatment of spinal metastases in a technique that is referred to as Kypho-IORT[1]. The reference depth-dose data for the source (provided by the device manufacturer) starts at 3.0 mm from the isocentre (tip) of the source. The depth-dose information of the needle applicator starts at 3.5 mm from the isocentre of the source. This corresponds to a distance of 2.9 mm from the surface of the applicator. The geometry of ionization chambers and need to waterproof makes it impossible to accurately estimate the dose on the surface of the source or needle applicator. This study is motivated by the need to go beyond the reach of reliable detector and estimate the dose rate at the isocentre of the source and surface of applicators.

Methods: A virtual source model (VSM) of the INTRABEAM® source for accurate and fast Monte Carlo dose calculation was described in our previous publication[2]. The model can estimate the 3D dose that results from the placement of the source in a given experimental geometry. Relevant geometries were modeled in Geant4 and the VSM was used to simulate the dose to water around the source and applicator. The result of the simulation provided the dose rate information at the isocentre of the source and surface of the needle applicator. The results were compared to reference data (when available) from the device manufacturer.

Results: When the depth-dose curve of the bare probe is normalized to the dose at 3.0 mm from the isocentre of the source (i.e. first point of ionization chamber measurement = 100% dose), the dose rate at the isocentre of the source is 6100%. When the depth-dose curve of the needle applicator is normalized to the dose at a depth of 3.5 mm from the isocentre of the source (2.9 mm from the surface of the applicator), the dose rate on the surface of the needle applicator is 1460%.

Conclusion: Monte Carlo simulation was used to determine the dosimetric properties of the INTRABEAM source and needle applicator beyond the reach of detectors. This knowledge is useful for a better understanding and estimation of the biological effectiveness of this therapeutic device.

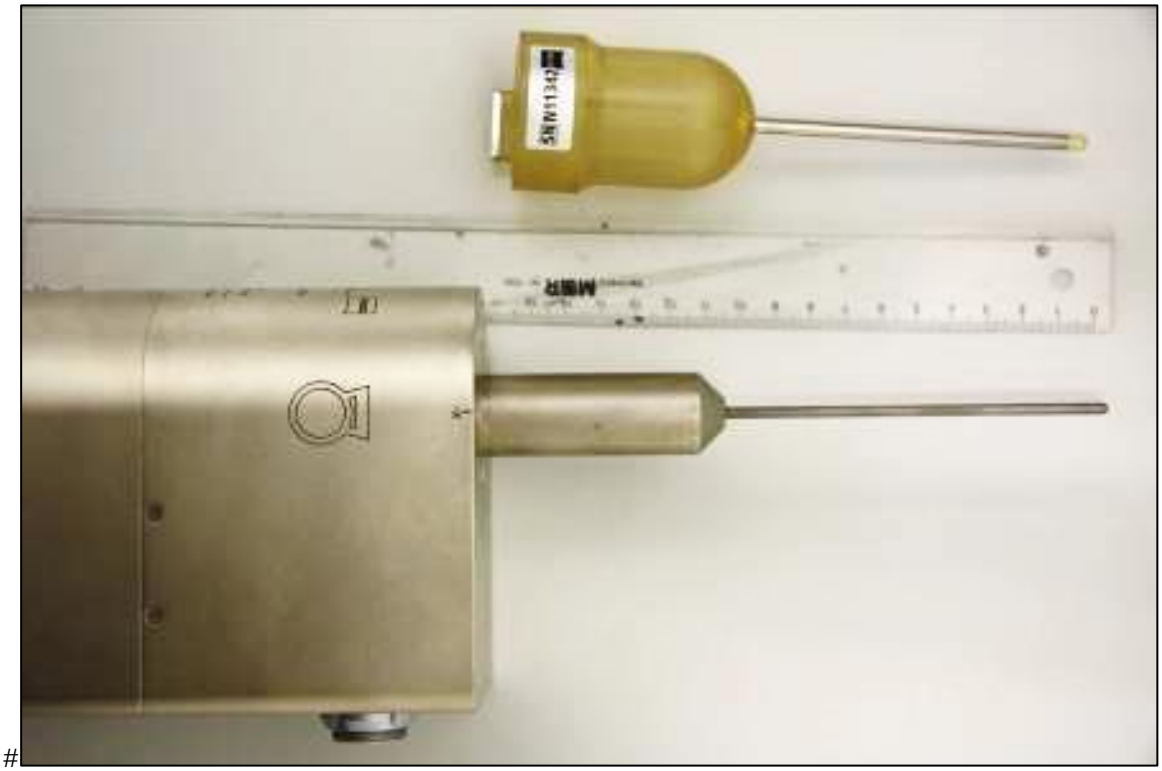

Fig. 1: The INTRABMEAM® source and needle applicator

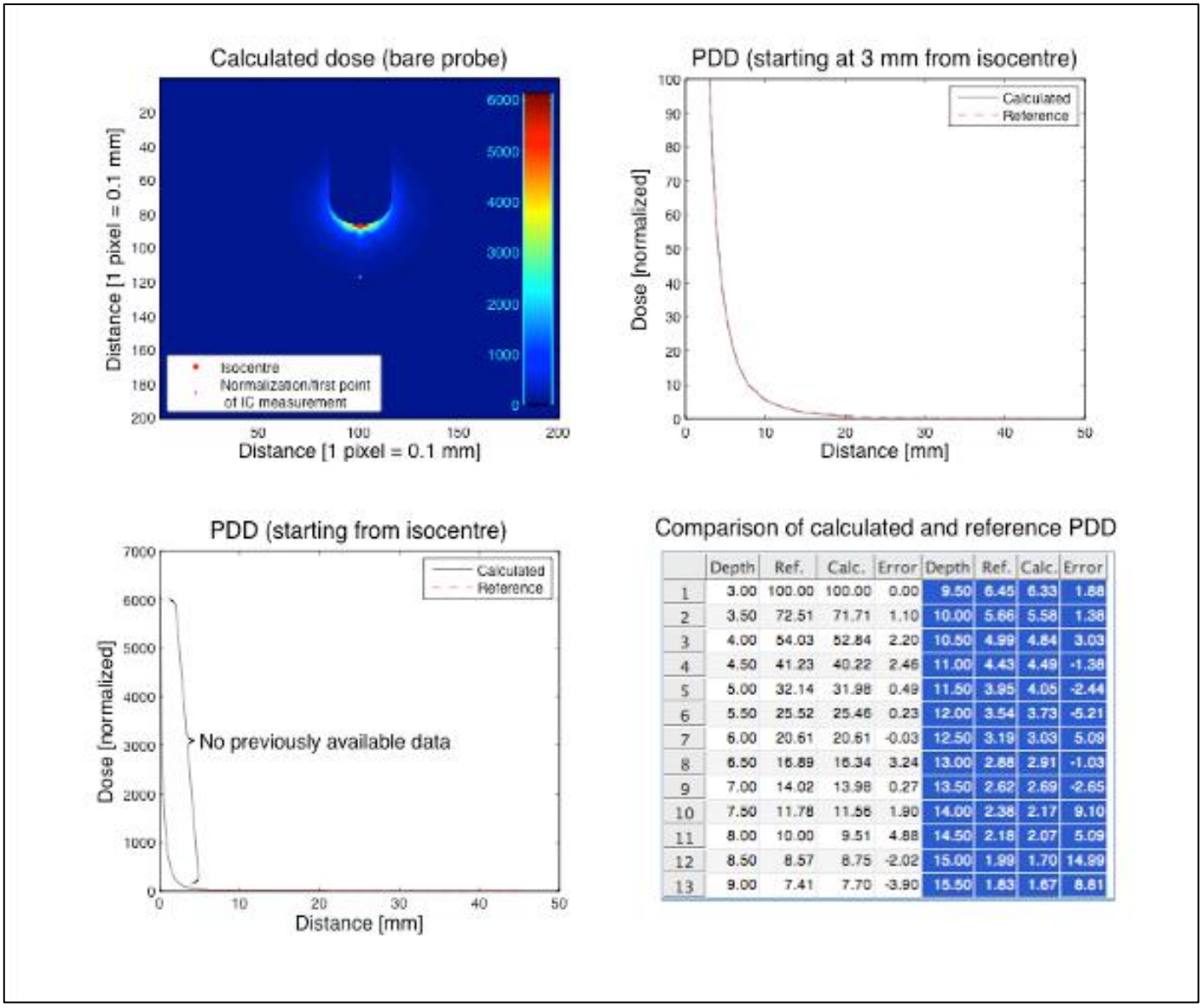

	Depth	Ref.	Calc.	Error	Depth	Ref.	Calc.	Error
1	3.00	100.00	100.00	0.00	9.50	6.45	6.33	1.88
2	3.50	72.51	71.71	1.10	10.00	5.66	5.58	1.38
3	4.00	54.03	52.84	2.20	10.50	4.99	4.84	3.03
4	4.50	41.23	40.22	2.46	11.00	4.43	4.49	-1.38
5	5.00	32.14	31.98	0.49	11.50	3.95	4.05	-2.44
6	5.50	25.52	25.46	0.23	12.00	3.54	3.73	-5.21
7	6.00	20.61	20.61	-0.03	12.50	3.19	3.03	5.09
8	6.50	16.89	16.34	3.24	13.00	2.88	2.91	-1.03
9	7.00	14.02	13.98	0.27	13.50	2.62	2.69	-2.65
10	7.50	11.78	11.56	1.90	14.00	2.38	2.17	9.10
11	8.00	10.00	9.51	4.88	14.50	2.18	2.07	5.09
12	8.50	8.57	8.75	-2.02	15.00	1.99	1.70	14.99
13	9.00	7.41	7.70	-3.90	15.50	1.83	1.67	8.81

Fig. 2: Comparison of the calculated and measured dose for the INTRABEAM source.

Dept-dose data of the INTRABEAM source

Depth from Isocentre	Measured dose (%)	Calculated Dose (%)	Percentage error
0.000	NA	6123.600	NA
0.500	NA	1778.900	NA
1.000	NA	782.710	NA
1.500	NA	407.990	NA
2.000	NA	235.230	NA
2.500	NA	149.290	NA
**3.000	100.000	100.000	0.000
3.500	72.515	71.714	1.104
4.000	54.033	52.844	2.201
4.500	41.235	40.220	2.461
5.000	32.138	31.981	0.489
5.500	25.522	25.462	0.233
6.000	20.607	20.614	-0.032
6.500	16.887	16.340	3.236
7.000	14.021	13.984	0.270
7.500	11.780	11.557	1.895
8.000	10.002	9.514	4.881
8.500	8.572	8.745	-2.018
9.000	7.409	7.699	-3.901
9.500	6.453	6.332	1.877
10.000	5.659	5.581	1.380
10.500	4.994	4.843	3.034
11.000	4.432	4.494	-1.382
11.500	3.954	4.051	-2.445
12.000	3.545	3.729	-5.208
12.500	3.191	3.029	5.089
13.000	2.885	2.915	-1.035
13.500	2.617	2.687	-2.649
14.000	2.383	2.166	9.105
14.500	2.177	2.066	5.093

15.000	1.995	1.696	14.991
15.500	1.833	1.671	8.806
16.000	1.688	1.670	1.098
16.500	1.559	1.471	5.647
17.000	1.443	1.306	9.483
17.500	1.339	1.242	7.229
18.000	1.244	1.173	5.761
18.500	1.159	1.251	-7.944
19.000	1.081	0.977	9.686
19.500	1.011	0.861	14.838
20.000	0.946	0.832	12.045
20.500	0.887	0.757	14.714
21.000	0.833	0.778	6.574

*NA = Not available** = normalization point*

Dept-dose data of the needle applicator

Depth from surface	Depth from Isocentre	Measured dose (%)	Calculated Dose (%)	Percentage error
0.000	0.600	NA	1463.100	NA
0.500	1.100	NA	1088.300	NA
1.000	1.600	NA	548.750	NA
1.500	2.100	NA	311.260	NA
2.000	2.600	NA	196.790	NA
2.500	3.100	NA	131.770	NA
**2.900	3.500	100.000	100.000	0.000
3.400	4.000	73.514	72.167	1.832
3.900	4.500	55.485	54.162	2.384
4.400	5.000	42.848	43.881	-2.411
4.900	5.500	33.761	34.005	-0.723
5.400	6.000	27.077	27.284	-0.766
5.900	6.500	22.059	22.870	-3.676
6.400	7.000	18.222	18.772	-3.021
6.900	7.500	15.240	16.257	-6.675
7.400	8.000	12.886	12.975	-0.690
7.900	8.500	11.004	10.928	0.688
8.400	9.000	9.480	9.627	-1.551
8.900	9.500	8.232	8.094	1.674
9.400	10.000	7.200	7.258	-0.812
9.900	10.500	6.338	6.765	-6.740
10.400	11.000	5.612	5.555	1.023
10.900	11.500	4.996	5.280	-5.680
11.400	12.000	4.470	4.537	-1.504
11.900	12.500	4.017	4.127	-2.745
12.400	13.000	3.625	3.793	-4.633
12.900	13.500	3.284	3.317	-1.012
13.400	14.000	2.986	2.833	5.130
13.900	14.500	2.724	2.866	-5.234
14.400	15.000	2.493	2.599	-4.254

14.900	15.500	2.287	2.257	1.329
15.400	16.000	2.105	2.121	-0.779
15.900	16.500	1.942	1.941	0.047
16.400	17.000	1.796	1.506	16.110
16.900	17.500	1.664	1.493	10.315
17.400	18.000	1.546	1.499	3.021
17.900	18.500	1.439	1.107	23.073
18.400	19.000	1.341	1.280	4.571
18.900	19.500	1.253	1.104	11.841
19.400	20.000	1.172	1.090	6.981
19.900	20.500	1.098	0.936	14.744
20.400	21.000	1.031	0.818	20.609
20.900	21.500	0.969	0.911	5.929
21.400	22.000	0.912	0.985	-8.058
21.900	22.500	0.859	0.759	11.637
22.400	23.000	0.810	0.632	22.070
22.900	23.500	0.765	0.598	21.852
23.400	24.000	0.724	0.680	6.064

*NA = Not available ** = normalization point*

References

[1] Schneider F, Greineck F, Clausen S, Mai S, Obertacke U, Reis T and Wenz F 2011 Development of a novel method for intraoperative radiotherapy during kyphoplasty for spinal metastases (Kypho-IORT) *Int. J. Radiat. Oncol. Biol. Phys.* 81 1114–9

[2] Nwankwo O, Clausen S, Schneider F and Wenz F 2013 A virtual source model of a kilo- voltage radiotherapy device *Physics in Medicine and Biology* 58 2363

Poster session II – Detectors for radiation therapy

Chair: D. Frauchiger (Bern/CH)

P 13 Introduction of epoxy-resin plastics for routine dosimetry in the clinic

M. M. Aspradakis[1], A. von Deschwanden[1], R. Seiler[1], T. Götzfried[1], P. Zucchetti[1]
[1]Luzerner Kantonsspital, Radiation Oncology, Luzern, Switzerland

Introduction: The reference medium for dosimetry in the clinic is liquid water. The use of solid plastics for reference dosimetry is discouraged; but provided the relationship between dosimeter readings in plastic and liquid water has been established, these could be used for routine dose measurements [1]. Solid phantom materials vary in elemental composition, mass, electron and relative densities. Several report on evaluations of commercial water-equivalent phantoms for dosimetry [2-4]. Due to differences between different types of materials and possible changes in manufacturing between batches of the same material, it is necessary to assess the suitability of solid phantoms prior to their introduction into clinical use.
The purpose of this work was to characterise and commission the routine use of the epoxy-resin plastic slabs Plastic Water Diagnostic Therapy (PWDT®) manufactured by CIRS, in the clinic of radiation oncology at the cantonal hospital of Lucerne (LUKS).

Materials and methods: PWDT® slabs were initially assessed for their geometric and physical properties. They were weighed and measured to confirm their specified physical properties. From computer tomography (CT) imaging, using a 120kV scanning protocol, relative electron densities were also derived from CT numbers as given on the CT scanner console and by the treatment planning software (Eclipse™). Computed relative electron densities from CT numbers were compared with the values stated by the manufacturer and in the literature.

Dosimetric measurements were carried out in 6 and 18 megavolt (MV) photon beams, in 6, 9, 12, 16, and 20MeV electron beams on an Varian Clinac and in a range of kilovolt (kV) photon beams (30kV/0.45mmAl HVL to 200kV/1.78mmCu HVL) on a T200 x-ray therapy system (by Wolf-Medizintechnik GmbH). The detectors used for measurements were a PTW 30013/0.6cm^3 cylindrical ionisation chamber and a NACP-02/0.16 cm^3 plane-parallel ionisation chamber. The field sizes on the linear accelerator beams were set at a source to surface distance (SSD) of 100cm. The field size examined on the kV treatment unit was 6cm × 8cm at SSD of 40cm as defined by the treatment applicator.

For reference dose measurement, the water equivalence of the PWDT® slabs was accessed in MV and MeV beams. The formalism to convert ionisation chamber readings to dose in water is described by [5] and [6]. According to this, the dose to water can be related to the dose at a water equivalent depth in the solid plastic by correcting the detector signal in plastic at scaled distances with detector-specific phantom-correction factors. Depth scaling factors were determined from measurements of tissue-phantom ratios (TPR) in MV beams and from depth ionisation curves in MeV beams in both liquid water and PWDT®. Chamber phantom-correction factors were defined as the ratio of detector signals at the reference distance in liquid water and at the equivalent distances in PWDT® for the same number of monitor units.

Depth profiles measured in PWDT® were compared with those in liquid water in MV, MeV and kilovoltage beams. The assessment also included a comparison of output factors measured in the two media.

Results: From the physical assessment of the PWDT® slabs at LUKS the calculated average mass density was 1.037 g/cm^3 and the relative electron density was 1.001 electrons/cm^3. These values are in good agreement with the values reported by Araki (2009) (1.039 g/cm^3 and 1.003 electrons/cm^3 respectively). The average relative electron density determined from CT numbers as reported by the CT scanner and the TPS software was 0.990 electrons/cm^3 and this was -0.7% different from the value reported for liquid water, which was scanned in the same imaging procedure with the PWDT® slabs. The value reported in the literature for this material 1.002 electrons/cm^3.

In terms of reference dosimetry, depth scaling factors determined at the depth of 50mm in PWDT were 0.990 for 6MV and 0.993 at 18MV. That is, the equivalent depth in water is 50.5mm at 6MV and 50.4mm at 18MV. The phantom correction factors for the **PTW 30013 chamber at** this depth were 0.997 at 6MV and 1.006 at 18MV. Depth scaling and phantom scaling factors determined at beam reference depths for the NACP-02 chamber and for the range of electrons beams examined were also within 1%.

For routine beam output checks, the measurement of output at scaled depths in plastic was considered not practical and for this reason a composite correction factor to the absorbed dose to water calibration coefficient of the detector to be applied to detector readings at the geometric depth was determined instead. Relative dose measurements in MV and MeV beams at the same geometric distances in liquid water and PWDT® agreed with each other to within 0.5%. In kV beams the agreement in relative dose measured in the same geometric distances in the two media was within 3% for the range of energies and depths investigated.

Conclusions

- The differences in Hounsfield numbers between PWDT® and liquid water was less than 10HU. In terms of treatment planning a difference of more than 10HU would be needed to cause differences of the order of 0.5% in the calculated primary photon fluence at 10cm depth in water in 6 - 18MV photon beams.

- The PWDT® solid slabs acquired at LUKS were shown to be water-equivalent in MV and MeV beams to within 1%. Reference dosimetry could be carried out in these, provided the appropriate depth scaling and phantom correction factors are used.

- For routine beam output checks in MV and MeV beams a composite correction factor to the detector reading in PWDT® was determined which accounts for differences from reference calibration conditions.

- PWDT® solid slabs can be directly used for relative dosimetry for most of the beam energies available in our clinic.

References

[1] IAEA, TRS-398: Absorbed dose determination in external beam radiotherapy: An international code of practice for dosimetry based on standards of absorbed dose to water. 2000, Vienna.
[2] Fujita, Y., et al., Depth scaling of solid phantom for intensity modulated radiotherapy beams. J Radiat Res, 2010. 51(6): p. 707-13.
[3] McEwen, M.R. and D. Niven, Characterization of the phantom material virtual water in high-energy photon and electron beams. Med Phys, 2006. 33(4): p. 876-87.
[4] Ramaseshan, R., et al., Dosimetric evaluation of Plastic Water Diagnostic-Therapy. J Appl Clin Med Phys, 2008. 9(2): p. 2761.
[5] Seuntjens, J., et al., Absorbed dose to water reference dosimetry using solid phantoms in the context of absorbed-dose protocols. Med Phys, 2005. 32(9): p. 2945-53.
[6] Araki, F., et al., Monte Carlo calculations of correction factors for plastic phantoms in clinical photon and electron beam dosimetry. Med Phys, 2009. 36(7): p. 2992-3001.

P 14 Commissioning of an In-Vivo Diode Dosimetry System for External Beam Radiotherapy

D. Blumer[1], U. Schneider[2,3], J. Besserer[3]
[1]Radiotherapie Hirslanden, Aarau, Switzerland
[2]Universität Zurich, Zurich, Switzerland
[3]Radiotherapie Hirslanden, Zurich, Switzerland

Introduction: In-vivo dosimetry has been demonstrated to be a valuable quality assurance tool to verify the delivered dose, patient position and the quality of the inhomogeneity correction of the treatment planning system (TPS) [1]. When diodes are used, the calibration and the determination of the correction factors are essential to make in-vivo dosimetry a reliable instrument for routine use.
In this work, a method of acquiring the correction factors by the use of a verified TPS instead of ionization chamber measurements is described and the consistency with patient measurements is checked.

Materials and methods: A diode set consisting of two PTW 6MV(T60010MP), two PTW 16 MV (T60010HP) and two Sun Nuclear ISORAD 6-12 MV diodes was investigated for energies of 4 MV, 6 MV and 16 MV on a Varian IX and a beam matched Varian TrueBeam. The correction factors were determined without ionization chamber measurement, by comparing the diode dose on a RW3 phantom to the dose given by the TPS on a virtual water phantom with the same irradiation parameters. A set of 260 patient measurements were analyzed to detect systematic errors. 157 of those measurements are from breast irradiation fields.

Results: The correction factors were found to be in agreement with manufacturer's specifications with the exception of the angular correction factor, which exceeded the specifications by more than 2% for oblique beams with angles of incidence larger than 45° [2, 3]. This difference can be explained by the different definition of the angular correction factor.

The patient measurements showed over all energies and diodes a mean deviation of -0.12% (σ=1.75%) relative to the ICRU dose (Fig. 1). For the breast patient measurements, the mean deviation was -0.29% (σ=1.94%) relative to the ICRU dose (Fig. 2).

Conclusion: Correction factors of in-vivo diodes can be obtained without ionization chamber measurement to a good accuracy. Even for breast irradiation where oblique fields with high gradients are used, the angular dependence is well modeled.

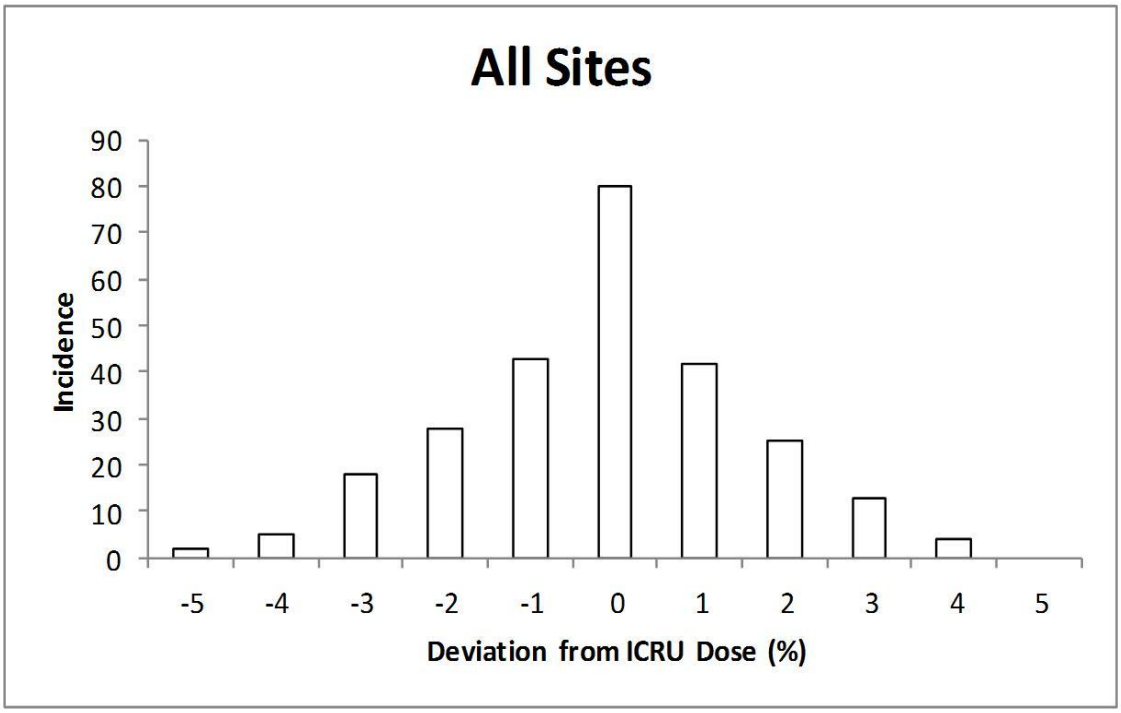

Fig. 1: Histogram of n=260 in-vivo measurements of all sites and energies (mean= -0.12%, σ= 1.75%).

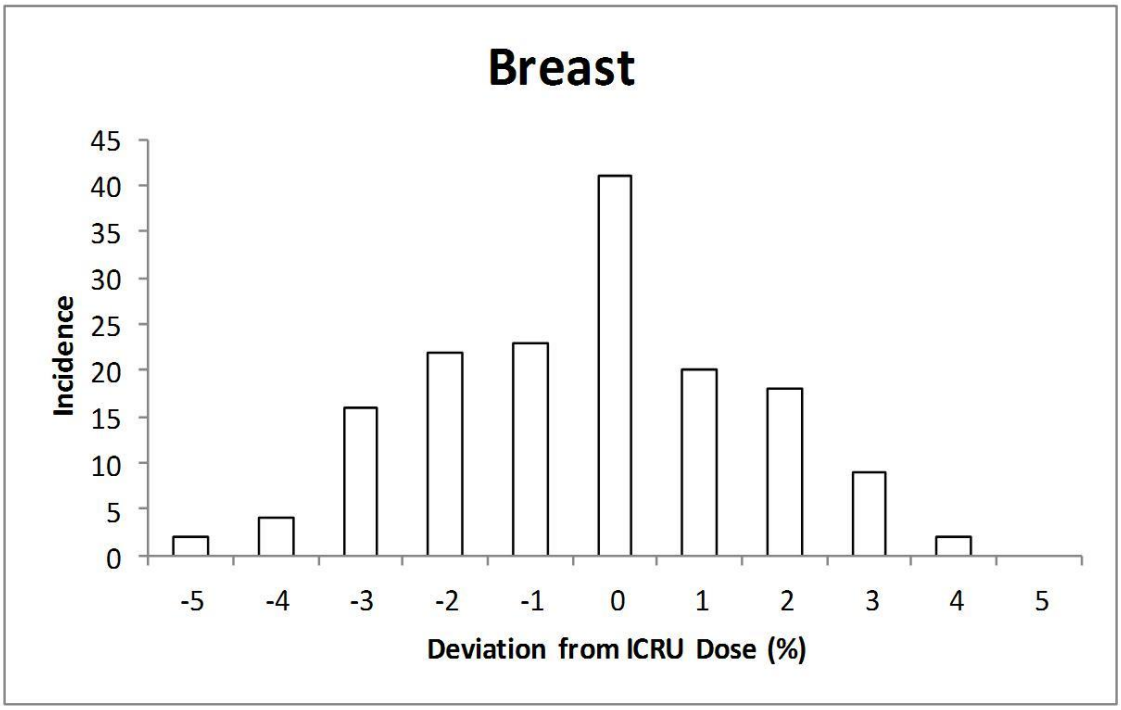

Fig. 2: Histogram of n=157 in-vivo measurements of breast patients (mean= -0.29%, σ=1.94%).

References

[1] Essers, M.: „In vivo Dosimetry during external photon beam radiotherapy“, International Journal of Radiation Oncology Biology Physics 43:245-249 (1999).

[2] „IsoRad Detector User's Guide“, Sun Nuclear, Rev G, 2009

[3] „Gebrauchsanweisung In-vivo Halbleiter Messsonde T60010MP, T60010HP, T60010L, T60010RO und T60010EP ab SN200“, PTW (2010)

P 15 Commissioning of the Leksell Gamma Plan convolution algorithm by means of A1SL ionisation chamber

M. Zeverino[1], F. Bochud[1], J. Bourhis[2], M. Levivier[3], R. Moeckli[1]
[1]CHUV, Medical Physics, Lausanne, Switzerland
[2]CHUV, Radiation Oncology, Lausanne, Switzerland
[3]CHUV, Neurosurgery, Lausanne, Switzerland

Related questions: The aim of this work was to evaluate the dose calculation accuracy of the convolution algorithm implemented within the Leksell Gamma Plan (LGP version 10.1) treatment planning system (TPS) by using the A1SL (Standard Imaging, WI, USA) cylindrical ionization chamber.

Material and procedure: An electron density phantom (Catphan, The Phantom Laboratory, USA) with different insert materials was CT scanned for calibration purpose. Hounsfield units corresponding to different insert materials of the phantom were measured by ImageJ software. The calibration curve was then imported in the LGP TPS to enable the convolution-based calculations.
Two distinct CTs of the spherical polystyrene phantom (Elekta Instruments AB, Sweden) were acquired: one with the film cassette insert and one with the A1SL ionization chamber placed at ist centre.

The two CTs were then co-register by means of LGP in order to perform the dose calculation on the phantom CT with the film insert while keeping spatial information on the position of the A1SL. 7 plans were designed in total: 3 single shot plans, one for each collimator size, placed at the centre of the A1SL volume; 3 seven shots plans, one for each collimator size, where one shot was placed at the centre of the A1SL volume and the remaining six were placed symmetrically apart a distance equal to the half of the collimator size along every orthogonal axis; 1 composite shots plan using 15 shots with different collimator sizes.

The prescription dose for each plan was 1 Gy to the 50% isodose, thus giving the maximum dose equal to 2 Gy. For dose comparison purposes, the active volume of the A1SL was contoured on the LGP TPS and the mean dose resulting from its DVH for every plan was taken as the calculated dose value. For each plan, dose calculation was performed using both the convolution algorithm and the TMR10 algorithm, this latter does not take into account any density inhomogeneity and it assumes the density to be water-equivalent. Absolute dosimetry was performed using the TomoElectrometer (Standard Imaging, WI, USA) which was calibrated together with the chamber, only the correction for temperature and pressure was then applied to the dose measurements. The A1SL chamber was also used to evaluate the transit dose due to the movement of the sources to be aligned with the centres of collimators.

Result: Concerning the single shot plans the dose measurements were 2.5% and 2.9% for the 16 mm and 8 mm collimator, respectively, higher than the convolution dose calculation. The equivalent TMR10 dose calculations were -0.6% and -0.05% for the 16 mm and the 8 mm collimator sizes, thus showing a better agreement with the measurements. The dose measured for the 4 mm collimator size was 16.3 % and 19.5 % lower than the convolution and the TMR10 dose calculation, respectively.

The dose measurements arising from the 7 shots plans were 3.2%, 5.4% and 12.1% lower than convolution calculated values for the 16 mm, 8 mm and 4 mm collimator sizes, respectively. When compared to the TMR10 calculation, such dose differences were 5.8%, 8.3% and 15.9%. The composite shots plan dose measurement was 1.9% higher than the convolution predicted dose and 0.3% lower than the TMR 10 predicted dose. The transit dose measured for was 0.002 Gy the 16 mm collimator size, while the A1SL was not able to measure it for the smaller collimator sizes. As a consequence, the measured dose was corrected for the transit dose only for plans using the 16 mm collimator size shots.

Summary: A1SL has been declared by its vendor able to accurately measure field size down to 6 mm. This was considered in the design of the presented study and it was expected to be accurate at least for the 16 mm and 8 mm collimator size. If we consider the response of the A1SL reliable for such field sizes, then the convolution algorithm should be considered not accurate as it was expected. Our results showed the good agreement between measurements and TMR10 for the single shot plans having the 16 mm and 8 mm collimator sizes. For such plans the convolution algorithm underestimated the dose by an amount of almost 3%.

Due to the design of the 7 shots plans, the A1SL lies on the penumbra of the displaced 6 shots thus the underestimation of the measured dose is expected.

Finally, for the composite shots plan the TMR10 algorithm is able to predict better the dose than the convolution algorithm. This latter, however, underestimated the dose by the 2 % which can still be considered acceptable.

In order to investigate the influence of the detector on the results, further measurements should be performed using a different detector able to measure the dose accurately even for such small fields. Future work will imply the use of the radiochromic films.

P 16 Dosimetric properties of the two-dimensional ionization chamber array Octavius Detector 1500

T. S. Stelljes[1,2], A.-K. Harmeyer[2], J. Reuter[2], H. K. Looe[1,2], N. Chofor[1,2], D. Harder[3], B. Poppe[1,2]
[1]Pius-Hospital Oldenburg, Clinic for Radiation Therapy, Oldenburg, Germany
[2]Carl von Ossietzky University, WG Medical Radiation Physics, Oldenburg, Germany
[3]Georg August University, Prof. em., Medical Physics and Biophysics, Göttingen, Germany

Introduction: Detector arrays have become a widely used tool for daily quality assurance and IMRT plan verification.[1, 2] In this work the dosimetric properties of the newly introduced two-dimensional ionization chamber array Octavius Detector 1500 (PTW-Freiburg, Germany) are investigated. The array consists of 1405 vented ionization chambers with an entrance area of 4.4 x 4.4 mm² and a height of 3 mm resulting in an ionization volume of 0.058 cm³. The chambers are supplied with a voltage of 1000 V and are arranged in a checkerboard pattern with a chamber to chamber distance of 10 mm in each row which results in a sampling frequency of 0.1 mm^{-1} in each row and 0.14 mm^{-1} along the diagonals. By merging two measurements which are shifted by 5 mm in longitudinal or lateral direction the sampling frequency along each row can be doubled to 0.2 mm^{-1} and thus fulfil the Nyquist sampling theorem for typical IMRT dose distributions.[3]

Materials and methods: All measurements were performed with an Elekta Synergy or a Siemens Artiste linac equipped with 160 leaf MLCs. The detectors were placed in RW3 slab phantoms. The stability, linearity and output factors were assessed by using either a Semiflex 31010 or a Semiflex 31013 ionization chamber as a reference detector. For field sizes smaller than 5 x 5 cm² output factors were additionally measured with a diode type 60012. The effective point of measurement was determined by comparing measured TPR curves with the array and a Roos chamber type 34001 with known effective point of measurement. The energy dependence was assessed by measuring the signal ratio of the array and a Semiflex 31010 ionization chamber at an SSD of 100 cm. The photon spectrum at the effective point of measurement was changed by varying the depth of measurement (2, 10, 15 and 20 cm) and field size (4 x 4 cm², 10 x 10 cm², 20 x 20 cm²). The readings of the Semiflex chamber were corrected for non-reference conditions following Chofor *et al*.[4, 5] The lateral dose response function of a single chamber of the array was investigated by measuring the dose profile of a 1 cm slit beam formed by tertiary lead collimators with a diode 60012 and the array following Looe *et al*.[6] The lateral dose response function was determined by searching the σ-value of a Gaussian convolution kernel, which, convolved with the diode measured profile, yields the array measured profile. An intensity modulated dose distribution was measured with the array's central chamber placed at the isocentre and with a longitudinal shift of 5 mm in target direction. Both measurements were merged with a self-written MATLAB (The MathWorks, Natick-MA, USA) script to double the sampling frequency. By application of gamma index passing rates, the merged array measurement was compared to TPS calculations, an EBT3 film measurement and the same film measurement convolved with the σ-values of the lateral dose response function of the array.

Results: The signal of the OD1500's central chamber was stable within ± 0.15 % without preirradiation. The array's readings were linear within 1% in comparison to Semiflex 31013 readings from 5 to 1000 MU. The effective point of measurement was determined to be 8.2 mm beneath the array's surface. Output factors measured with the OD1500 array showed deviations from Semiflex 31010 measurements smaller than 0.77 % for fields ranging from 5 x 5 cm² to 27 x 27 cm². For a 2 x 2 cm² field deviations from the diode were -2.33 % and -1.7 % at 6 and 15 MV respectively. As to be expected, due to the volume effect for the smallest field size of 1 x 1 cm², the deviations of the OD1500 output factors from the diode output factors caused by the lateral response function of a single array chamber were highest (-24 % at 15 MV and - 26 % at 6 MV). For 6 and 15 MV the array showed a maximum deviation of ± 1.5 % from the reference condition (10 x 10 cm² at d=10 cm) when changing the photon spectrum at the effective point of measurement. Taking into account the σ-value of the diode, the σ-value of an array chamber was found to be σ6MV = (2.07 ± 0.03) mm and σ15MV = (2.09 ± 0.03) mm. Gamma index passing rates of a merged OD1500 measurement were 96.2 % for a 2 mm / 2 % local gamma-index criterion compared to TPS calculations and 90.09 % for an EBT3 film measurement. Convolving the EBT3 film measurement with the lateral dose response function of the array yielded an increased passing rate of 98.3 %.

Conclusions: The first measurements with the OD1500 array show the applicability of the array for clinical dosimetry. The possibility to double the sampling frequency to 0.2 mm-1 in all directions and to increase the coverage of a dose distribution with sensitive areas of ionization chambers by merging two measurements is a welcome addition for dose patterns to be measured at a high level of spatial resolution.

References

[1] Beach KW, Leotta DF, Zierler RE. Carotid Doppler velocity measurements and anatomic stenosis: correlation is futile. Vasc Endovascular Surg. 2012 Aug;46(6):466-74.

[2] AlHuzaimi A, Al Mashham Y, Potts JE, De Souza AM, Sandor GG. Echo-Doppler assessment of arterial stiffness in pediatric patients with Kawasaki disease. J Am Soc Echocardiogr. 2013 Sep;26(9):1084-9.

[3] Voges I, Jerosch-Herold M, Hedderich J, Pardun E, Hart C, Gabbert DD, et al. Normal values of aortic dimensions, distensibility, and pulse wave velocity in children and young adults: a cross-sectional study. J Cardiovasc Magn Reson. 2012;14:77.

[4] Rusconi C, Sabatini T, Faggiano P, Ghizzoni G, Oneglia C, Simoncelli U, et al. Prevalence of isolated left ventricular diastolic dysfunction in hypertension as assessed by combined transmitral and pulmonary vein flow Doppler study. Am J Cardiol. 2001 Feb 1;87(3):357-60, A10.

[5] Markl M, Wallis W, Strecker C, Gladstone BP, Vach W, Harloff A. Analysis of pulse wave velocity in the thoracic aorta by flow-sensitive four-dimensional MRI: reproducibility and correlation with characteristics in patients with aortic atherosclerosis. J Magn Reson Imaging. 2012 May;35(5):1162-8.

P 17 The response of pMOS dosimeters up to high absorbed doses

G. Ristic[1], M. Andjelkovic[1], A. Jaksic[2]
[1]University of Nis, Faculty of Electronic Engineering, Applied Physics Laboratory, Nis, Serbia
[2]Tyndall National Institute, Cork, Ireland

Abstract: The pMOS dosimeters, known as RADFETs, having extremely small sizes of sensor elements (≈ 1 mm × 1 mm), and allowing the dose measurement in vivo in real time, are specially important for radiotherapy. The dependence of threshold voltage shift (ΔV_T) on dose, representing sensitivity to the ionizing radiation, is investigated up to absorbed dose of 1330 Gy(H_2O). In addition, the behaviors of fixed traps and switching traps, induced by irradiation, are considered.

Introduction: The radiation sensitive p-channel metal-oxide-semiconductor transistors (pMOS dosimetric transistors) known as *pMOS dosimeters* or *RADFETs* (Radiation-Sensitive Field Effect Transistors) allow the measurement of absorbed radiation dose using the threshold voltage shift, ΔV_T, which is caused by radiation-induced oxide charge and interface traps. Irradiation results in the trapping of holes (generated by the radiation) in the SiO, and the creation of interface states at the Si/SiO_2 boundary. The sensitivity increasing to the radiation could be achieved increasing the gate oxide thicknesses. pMOS dosimeters have extremely small sizes, and allow dose measurements *in vivo* in real time, which is specially important for radiotherapy (Figs. 1 and 2). Besides the many advantages, one of disadvantage of pMOS dosimeters is non-linearity, i.e., the saturation of dosimetric parameter ΔV_T, which is very important for their repeatedly use. In this paper, the dependence of ΔV_T on absorbed dose D to relatively high dose of 1330 Gy(H_2O) is investigated. In addition, the behaviors of fixed traps in SiO_2, and switching traps near and at the SiO_2/Si interface, during irradiation without gate bias has been considered.

Material and procedure: The experimental samples were *Al*-gate dosimetric pMOS transistors (RADFETs), manufactured by Tyndall National Institute, Cork, Ireland, with the oxide thicknesses of t_{ox} = 400 nm. The transistor gate oxide has been grown at temperature of 1000 ˚C in dry oxygen and annealed for 15 minutes in nitrogen. The post-metallization annealing has been performed at 440 ˚C in forming gas for 60 minutes. The irradiation was performed in the Radiation and Environmental Protection Laboratory, Vinca Institute of Nuclear Science, Belgrade, Serbia. The experimental samples were irradiated at room temperature without gate bias (zero bias regime), V_G = 0 V (all pins were grounded), using the ^{60}Co ionizing source up to absorbed dose of D = 1330 Gy(H_2O) at the absorbed dose rate of DR = 121 Gy/h. The irradiation was lasting 11 hours, while the distance between the source and samples was 186 mm. Zero bias regime corresponded to a small positive gate bias of V_{wf} = 0.33 V due to a work function difference between *Al* gate and n-type silicon substrate, giving low external electric field in the oxide of $E_{wf} = V_{wf}/t_{ox}$ = 0.825 V/μm, which has a direction towards the oxide/substrate (SiO_2/Si) interface.

The midgap-subthreshold technique (MGT) for determination of the densities of fixed traps (FTs), and switching traps (STs), has been used [3]. The FTs represent the traps created in the gate oxide, and STs represent the traps created near and at the oxide/substrate (SiO_2/Si) interface (Fig. 3). The STs created in the oxide, near SiO_2/Si interface, are called the slow switching traps (SSTs) or border traps, while the STs created at this interface are called either the fast switching traps (FSTs) or true interface traps (or only interface traps). FTs represent traps in the gate oxide that do not exchange the carriers from the channel, while the SSTs and FSTs, forming the STs, represent the traps that do exchange (communicate with) the carriers from the channel within the time frames of electrical characteristic measurements. FTs and SSTs are also known as the oxide trapped charge, and FSTs as the interface traps. The electrical characteristics were measurements in the reader-circuit (RC) configuration (Fig. 4).

The contributions of FTs (ΔV_{ft}) and STs (ΔV_{st}) to the net threshold voltage shift ΔV_T of pMOSFETs in MGT could be expressed as

$$\Delta V_T = \Delta V_{ft} + \Delta V_{st}\,, \tag{1}$$

where ΔV_{ft} and ΔV_{st} are the components of threshold voltage shift due to FTs and STs, respectively.

Result: In Fig. 5, the dependences of ΔV_T, as well as of ΔV_{ft} and ΔV_{st}, on dose D, are shown. The basic concept of pMOS dosimeter is to convert the threshold voltage shift, ΔV_T, induced by radiation, into absorbed radiation dose, D. The relation between threshold voltage shift and dose ($\Delta V_T/D$) represents sensitivity which in this case is not constant, and has values between 78.1 and 12.73 mV/Gy for dose range from 30 to 1330 Gy.

The dependence of ΔV_T on D is usually expressed in the form:

$$\Delta V_T = AD^n\,, \tag{2}$$

where $\Delta V_T = V_T - V_{T0}$, V_T is the threshold voltage after irradiation, V_{T0} before radiation, A is a constant, and n is the degree of linearity. n depends on oxide thickness, electric field and absorbed dose. Ideally, this dependence is linear, i.e., $n = 1$, and then A represents the sensitivity, S, of MOS dosimeter. The fitting of ΔV_T by eq. (2), gives the values of constants A and n of 0.45 and 0.66, respectively (dashed line in Fig. 5).

It was shown that eq. (2) is not suitable for ΔV_{ft} fitting, and more physical sense has the following equation [3]:

$$\Delta V_{ft} = a - \frac{a}{1 + bD^c}, \tag{3}$$

where a, b and c represent the fitting constants (a also represents the saturation voltage). A very good fitting of ΔV_{ft}, as well as of ΔV_{st}, using eq. (3), could be seen in Fig. 5. In addition, the sum of fitting values of ΔV_{ft} and ΔV_{st} fits the ΔV_T very well (eq. 1).

During irradiation, the electron – hole (e^--h^+) pairs are created, and the released electrons quickly sweep out the oxide, while the holes remain, moving towards one of the interface, depending on the direction of electric field in the oxide [4]. In our case, there is a small gate oxide electric field due to a work function difference between *Al*-gate and n-type silicon substrate (external electric field), having a direction towards the oxide/substrate (SiO_2/Si) interface. It causes the holes moving to the SiO_2/Si interface, where they are trapped, creating positively charged FTs (PCFTs). The electrons could be also trapped at the amphoteric trapping centers, creating negatively charged FTs (NCFTs), but the probability for this event during irradiation is small. In the most cases, including ours, PCFTs dominate over NCFTs, representing the net effect of FTs.

The PCFTs increase the internal electric field in the oxide that has the opposite direction of external electric field. It causes the decrease of hole moving to and trapping at SiO_2/Si interface. Since the external electric field is very low, the internal electric field overcomes the external electric field. Having in mind a huge value of ΔV_{ft}, it means that the significant number of holes is trapped in the bulk of gate oxide. They holes, although far from SiO_2/Si interface, obviously have significant influence of the carriers in the channel.

Fig. 6 shows the differences in the sensitivity between the pMOS dosimeters with gate oxides of 100 nm [3] and 400 nm, and it is higher more than ten times in latter case. The fitting of ΔV_T for 100 nm pMOS dosimeter using the sum of fitting values of ΔV_{ft} and ΔV_{st} is also very good.

Summary: The sensitivity of pMOS dosimeters during irradiation with ^{60}Co gamma-ray source to dose of 1330 Gy(H_2O), is investigated. It was shown that the threshold voltage shifts, as well as its components, induced by fixed traps and switching traps, saturate. Up to dose of 700 Gy, ΔV_{ft} is higher than ΔV_{st} , but after that ΔV_{ft} slowly saturates, but ΔV_{st} continues to increase. The saturation values of ΔV_{ft} and ΔV_{st} are a = 9.51, and even 17.06 V, respectvely. The buildup and saturation of FT density is limited by the field collapse and could be expected, in theory, to occur at the voltage corresponds the external electric field. However, the saturation voltage value of ΔV_{ft} is higher, because the bulk trapped hole density is high and its influence on channel carriers is not negligible. The fixed trap density is probably much higher than swithing trap density, but the influence of STs on channel carriers is much higher, because they are closed to the chanel, giving very high saturation value of ΔV_{st}.

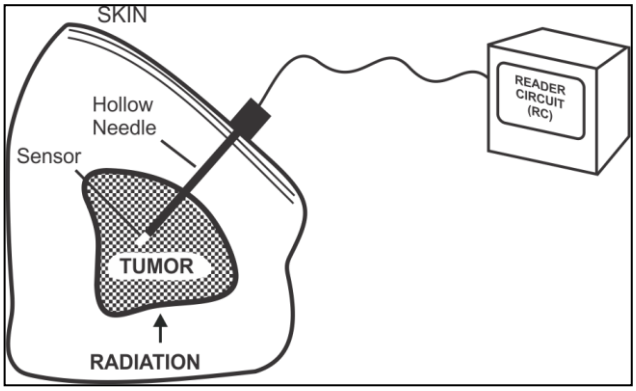

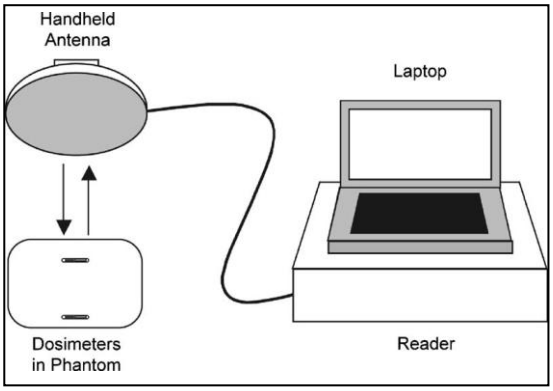

Fig. 1: An application of pMOS dosimeters in radiotherapy [1] Fig. 2: An implantable wireless pMOS dosimeter for radiotherapy [2]

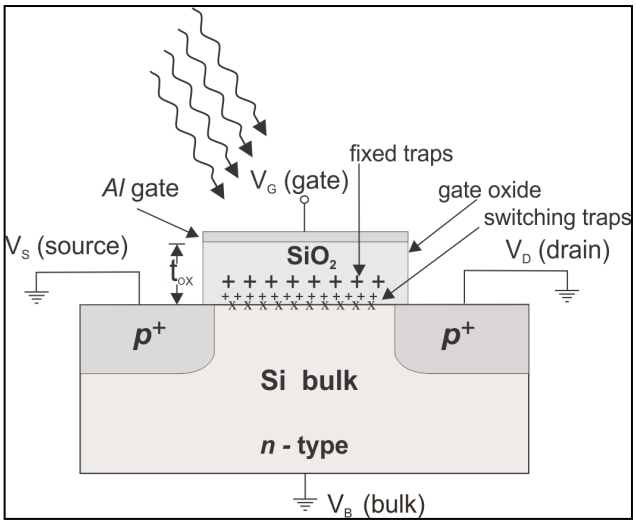

Fig. 3: Cross section of pMOS dosimeters after irradiation measurements

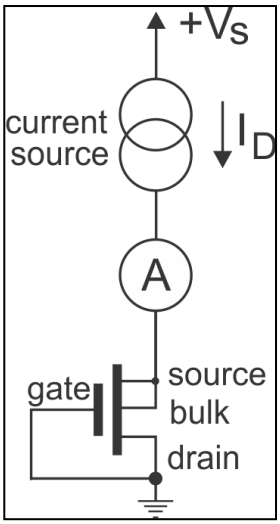

Fig. 4: The reader-circuit (RC) configuration for electrical characteristic

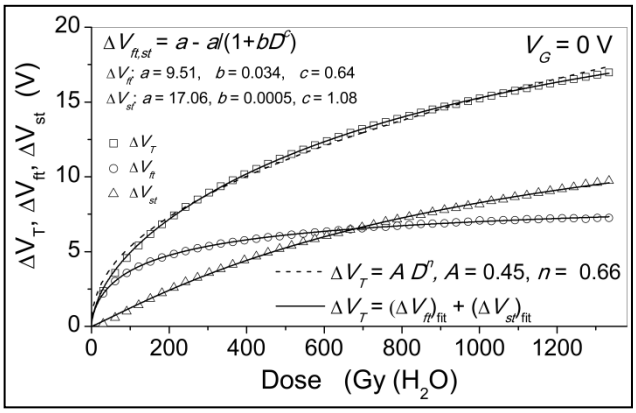

Fig. 5: The threshold voltage shift and its components during fitted by eqs. (2) and (3).

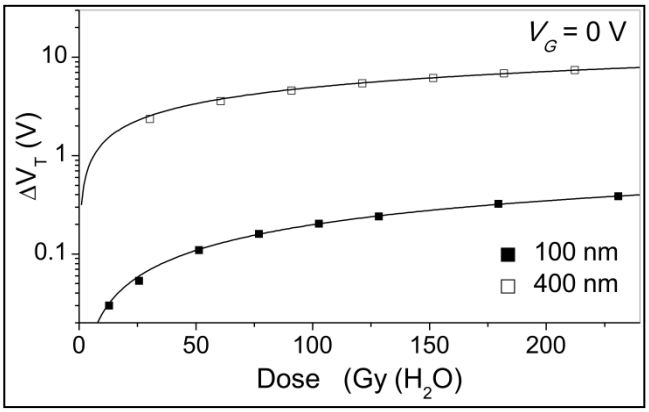

Fig. 6: The differences in sensitivity between 100 nm and irradiation, 400 nm thick gate oxides

References

[1] Holmes-Siedle, A: From space to therapy - the radiation sensitive silicon fet (RADFET), in: Proceedings of the Technology Transfer Workshop, European Space Agency, ESA SP-364, ESA/ESTEC, Noordwijk, the Netherlands, 87–90, 1994.

[2] Briere, T.M., Beddar, A.S., Gillin, M.T.: Evaluation of precalibrated implantable MOSFET radiation dosimeters for megavoltage photon beams, Med. Phys. 32 (11), 3346 – 3349, 2005.

[3] Ristić, G.S., Vasović, N.D., Kovačević, M., Jakšić, A.B.: The sensitivity of 100 nm RADFETs with zero gate bias up to dose of 230 Gy(Si), Nucl. Instrum. Methods Phys. Res. B, 269, 2703 – 2708, 2011.

[4] Ristić, G.S.: Influence of ionizing radiation and hot carrier injection on metal-oxide-semiconductor transistors, J. Phys. D: Appl. Phys., Topical Review, 41, 02300-1-19, 2008.

P 18 The microDiamond TM60019 – Experimental determination of its lateral dose response function

D. Poppinga[1,2], H. K. Looe[1,2], N. Chofor[1,2], T. S. Stelljes[1,2], A. A. Schoenfeld[1,2], J. Meyners[1,2], B. Delfs[1,2], J. Fischer[1,2], D. Harder[3], B. Poppe[1,2]
[1]University of Oldenburg, Medical Radiation Physics, Oldenburg, Germany
[2]Pius Hospital, Oldenburg, Germany
[3]University of Goettingen, Goettingen, Germany

Purpose: The aim of this study is to determine the lateral dose response function K(x) of the novel single crystal microDiamond detector (TM60019, PTW-Freiburg, Germany) by comparing narrow slit beam signal profiles measured with the microDiamond and with an unshielded Si diode detector (TM60012, PTW-Freiburg, Germany).

Methods: All measurements were performed at an Elekta Synergy linac equipped with Agility MLC at 6 MV. Two 10 cm thick lead blocks, acting as tertiary collimators, were positioned on the accessory holder directly below the MLC, forming a narrow slit only 10 paper sheets (1 mm) wide. The linac's secondary collimator was set to 2 x 10 cm2 to minimize the amount of transmission and scattered radiation reaching the detector plane. The surface of the water phantom (MP3 phantom, PTW-Freiburg, Germany) was positioned at a distance of 10.5 cm below the lower edge of the lead blocks. Slit beam signal profiles were measured at 5 cm water depth and 0.1 mm step size with both the microDiamond detector and the Si Diode. Detectors were arranged with their symmetry axes parallel to the central beam axis and were scanned across the slit beam. Using a 90 degree rotation of the secondary and tertiary collimators, a slit beam could be scanned in the left/right and the gun/target direction.

In order to determine the lateral dose response function, the diode profile was numerically convolved with normalized one-dimensional Gaussian kernels of varying standard deviation σ. The best fit between the resulting convolution product and the microDiamond signal profile was used to determine σ.

Results: As shown in Fig. 1, the FWHM of the slit-beam beam profiles measured with the TM60019 are slightly wider, which corresponds to its larger sensitive detector area (2.2 mm diameter) compared with that of the TM60012 Si diode (diameter 1.1 mm).

The best fit was obtained when the TM60012 diode slit beam profiles were convolved with an area-normalized Gaussian kernel with σ = 0.58 mm for both the gun-target and left-right scan directions (see fig. 1). This result was corrected for the spatial resolution of the Si diode itself, characterized by a Gaussian kernel with σ = 0.30 mm [1]. The final □ value of the diamond TM60019 was calculated by adding in quadrature the two □ values mentioned above , which resulted in σ = 0.65 mm for the TM 60019. This experimental value agrees with the results obtained by Monte Carlo simulation in a previous study [2]. The deviations between the full black and the dashed red curves are plotted below.

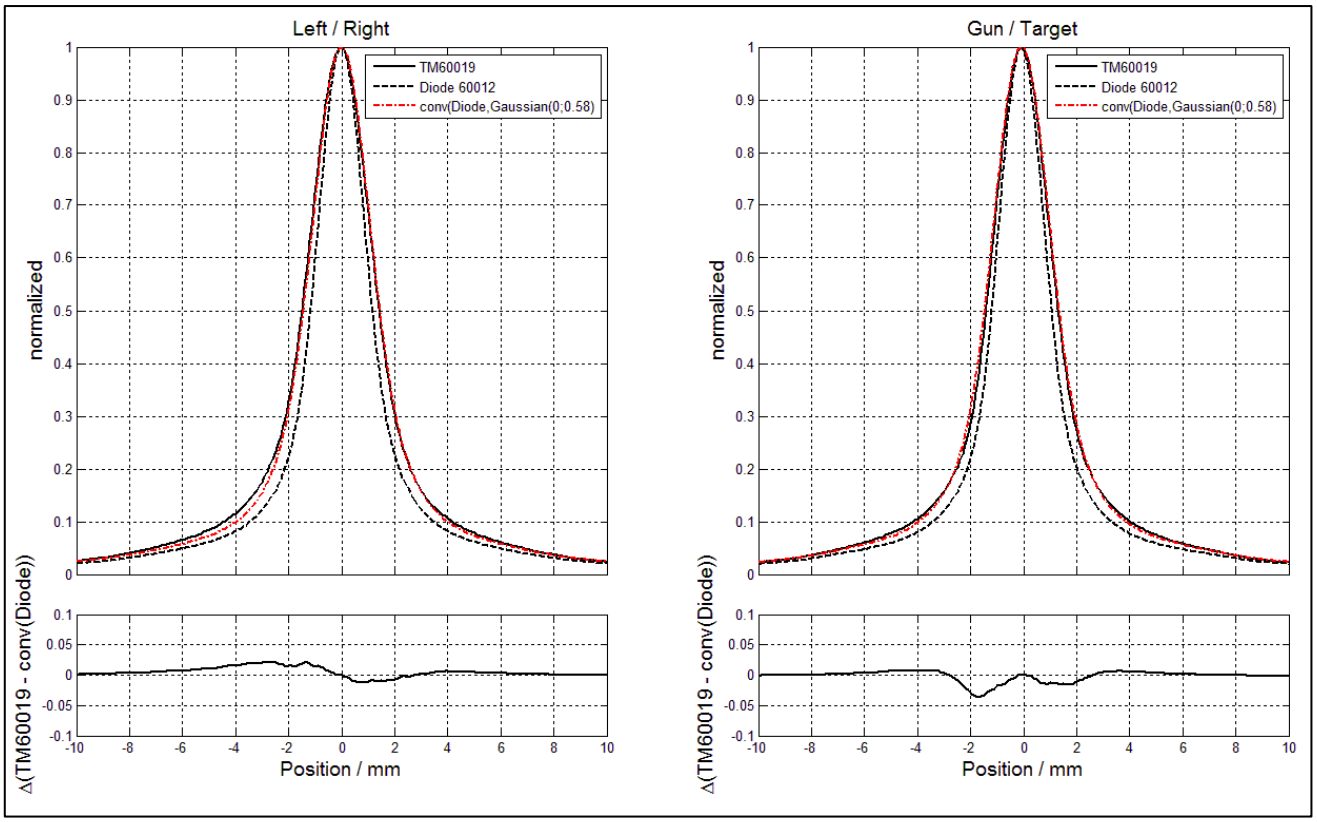

Fig. 1 Relative slit-beam beam signal profiles measured with the MicroDiamond TM60019 (full black curve) and the Si diode TM 60012 (dashed black curve) at 6 MV. By convolving the signal profile of the Si diode TM60012 with a 1D Gaussian distribution with standard deviation = 0.58 mm, a close approximation (dashed red curve) to the signal profile of the MicroDiamond TM60019 was achieved.

Conclusions: In this study, the spatial resolution of the novel microDiamond detector TM60019 has been characterized by its lateral dose response function which turned out to be a Gaussian function with σ = 0.65 mm, in agreement with the result of a previous Monte Carlo study of the same detector [2]. Owing to its high spatial resolution, the microDiamond is suitable for measurements of very narrow photon field dose profiles but possesses lower energy dependence of its response than high Z semiconductor detectors [3].

References

[1] H.K. Looe, T. S. Stelljes, S. Foschepoth, D. Harder, K. Willborn, B. Poppe, Z Med Phys. 23 (2013) 129-43
[2] H. K. Looe, N. Chofor, D. Poppinga, T. S. Stelljes, J. Meyners, J. Fischer, A. Schönfeld, D. Harder, B. Poppe: Klinische Erfahrungen mit dem neuen Diamant-Detektor (DGMP 2013, PTW Lunch-Symposium)
[3] N. Chofor, D. Harder, B. Poppe, Z Med Phys 24 (2014) 27-37.

P 19 First implementation of a multi-wire ionization chamber at an Elekta Synergy linac with Agility 160-leaf MLC for the in-vivo dose verification of VMAT

M. S. Danpullo[1], T. S. Stelljes[1], J. Becker[1], N. Chofor[1], B. Poppe[1], H. Looe[1]
[1]University of Oldenburg/Pius Hospital, AG Medizinische Strahlenphysik.Campus Pius-Hospital, Oldenburg, Germany

Introduction: The DAVID system is a multi-wire transmission detector, which is mounted on the accessory holder of the linear accelerator (linac), with the measurement wires aligned beneath each multi-leaf collimator (MLC) leaf pair. The system is used for the in-vivo verification of advanced intensity-modulated treatment deliveries. Since the system is usually designed to fit the specifications of the linac under use, this work presents our results of the implementation of the DAVID system at an Elekta Synergy linac.

Materials and methods: The DAVID system (T16029, PTW-Freiburg) implemented for an Elekta Synergy linac with the Agility 160-leaf MLC can be used for the in-vivo verification of both intensity modulated radiotherapy (IMRT) and volumetric modulated arc therapy (VMAT). The Elekta Synergy linac has a maximum field size of 40 x 40 cm^2, where the width of each MLC leaf is 5 mm projected on the isocenter plane. A detailed description of the DAVID system has been published by Poppe *et al* [1,2] and Looe *et al* [3]. Fig. 1 shows the DAVID chamber mounted on an Elekta Synergy linac.

Fig. 1 . The DAVID chamber attached to the Elekta Synergy linac

Before the commissioning procedure was performed, the DAVID chamber was aligned so that each measurement wire is positioned exactly underneath the assigned MLC leaf pair. The alignment was checked by measuring the response function of each wire [3] ensuring the signal is symmetrical [3].

A transmission factor is required, to correct for the radiation beam attenuation due to the presence of the chamber. Therefore, the transmission factors of the DAVID chamber were measured at 6 and 15 MV photon beams and at different field sizes (3 x 3 cm^2, 5 x 5 cm^2, 10 x 10 cm^2, 15 x 15 cm^2 and 20 x 20 cm^2) using the Octavius phantom (PTW-Freiburg) and an ionization chamber (Semiflex T31010, PTW-Freiburg). Percentage depth dose (PDD) distributions in a water phantom were measured with and without the DAVID chamber in the beam path in order to investigate its influence on the PDD shift, especially on the increase in the surface dose due to the presence of the detector acting as an absorber.

To test the stability of the DAVID system, one IMRT plan and 3 VMAT plans were measured with the DAVID system for consecutive 14 days. Artificial MLC errors were also introduced to the plans to determine the sensitivity of the system to indicate possible errors that could occur clinically. For this purpose, positional errors ranging from 1 mm to 7 mm of a single MLC leaf were introduced for one single arc VMAT prostate plan and one double arc VMAT head and neck plan.

Results: The mean transmission factors were found to be 0.939 for 6 MV and 0.953 for 15 MV at the Elekta Synergy linac for the field sizes investigated. Poppe *et al* [1] measured in an RW3 phantom (SSD 90) at a Siemens Primus linac transmission factors of 0.928 to 0.939 for 6 MV and 0.947 to 0.955 for 15 MV. The PDD measurements show a small shift of the depth of D_{max} towards the surface and an increase in the surface dose due to the presence of the DAVID chamber. These effects are attributed to the secondary electrons generated at the front and back plates of the DAVID chamber reaching the patient or phantom as reported by Poppe *et al* [3].

Fig. 2 shows the maximum deviations of each fraction for one step-and-shoot IMRT plan and 3 VMAT plans. For all plans, the maximum deviations did not exceed ±2% for all evaluated measurement wires. One could also observe that the VMAT plans show less fluctuation than the IMRT plan. Fig. 3 shows that the deviations at the measurement wire corresponding to the modified MLC leaf increase linearly with the magnitude of the artificial errors introduced.

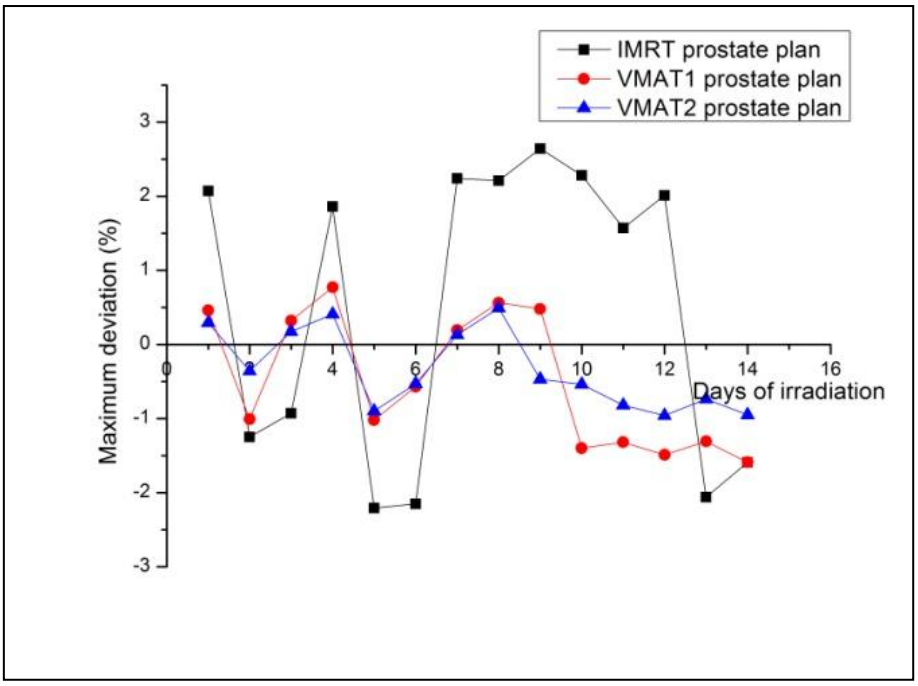

Fig. 2. Maximum deviation plot for IMRT and VMAT.

Figure 2 shows the maximum deviations of each fraction for one step-and-shoot IMRT prostate plan and 2 VMAT prostate plans. For all plans, the maximum deviations did not exceed ±2% for all evaluated measurement wires. It could also be observed that the VMAT plans show less fluctuation than the IMRT plan.

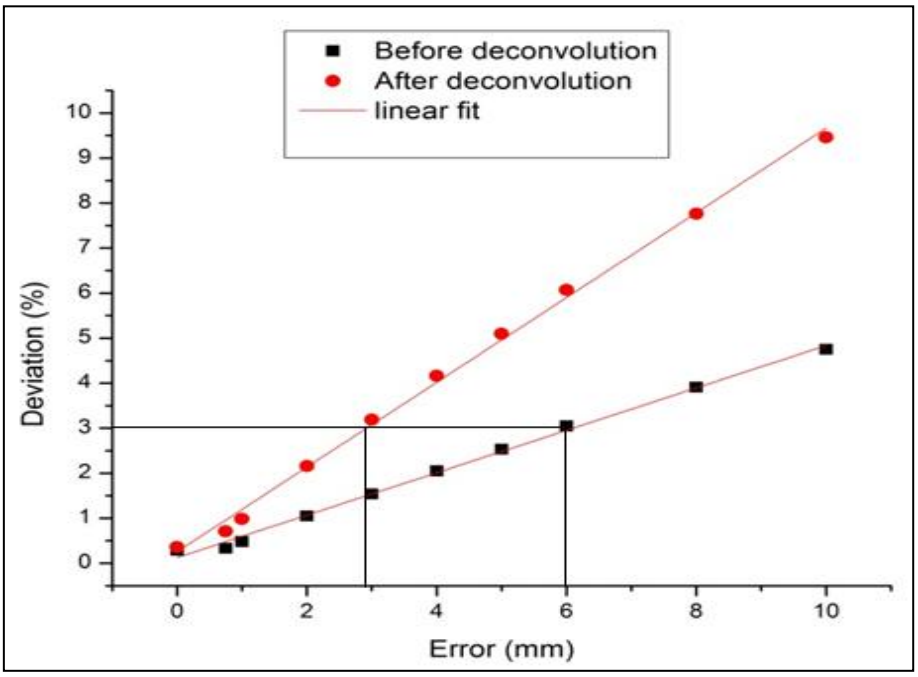

Fig. 3. Percentage deviation against MLC error plot before and after deconvolution.

Figure 3 demonstrated the improvement in the sensitivity of the DAVID system after deconvolution. The percentage changes in measured signal height due to artificial MLC leaflet errors of magnitude 0 to 10 mm for the prostate plan are plotted. The changes of the blurred signal profiles are indicated by black squares, the corresponding changes of the deconvolve fluence profiles are plotted as red circles and linearly fit is obtained. Before deconvolution 3 mm error correspond to 1.5% deviation and 5 mm error correspond to 2.5% deviation. After deconvolution 3 mm error correspond to 3% deviation and 5 mm error correspond to 5% deviation.

Discussion and conclusion: In this work, the first implementation of the DAVID system at an Elekta Synergy linac equipped with Agility MLC is described. The dosimetric influence of the DAVID chamber on the beam has been investigated. The stability of the DAVID chamber has been tested with realistic IMRT and VMAT plans. All MLC errors introduced to the plans can be detected by the DAVID system, where these deviations from the reference signals are indicated by the software to ease the detection by the users. In an ongoing work, the deconvolution of the DAVID signal is implemented in order to further increase the sensitivity of the system to detect MLC errors [3]. The sensitivity of the DAVID software is enhanced after deconvolution as can be seen from the above plots in figure 3.

References

[1] Poppe B, Thieke C, Beyer D, Kollhoff R, Djouguela A, Rühmann A, Willborn K and Harder D. DAVID-a translucent multi-wire transmission ionisation chamber for in vivo verification of IMRT and conformal irradiation techniques. Phys. Med. Biol. 2006; 51:1237-48

[2] Poppe B, Looe H K, Chofor N, Rühmann A, Harder D and Willborn K. Clinical Performance of a Transmission Detector Array for the Permanent Supervision of IMRT Deliveries. Radiother. Oncol. 2010; 95:158-65

[3] Looe H K, Harder D, Rühmann A, Willborn K and Poppe B. Enhanced accuracy of the permanent surveillance of IMRT deliveries by iterative deconvolution of DAVID chamber signal profiles Phys. Med. Biol. 2010; 55:3981-92

P 20 The influence of a novel transmission detector for 3D online IMRT-verification on 6 MV beam characteristics (with and without flattening filter)

J. Thoelking[1], Y. Sekar[1], J. Fleckenstein[1], R. Fizesan[2], J.-C. Celi[2], F. Lohr[1], F. Wenz[1], H. Wertz[1]
[1]University Medical Centre Mannheim, University of Heidelberg, Mannheim, Germany
[2]IBA Dosimetry GmbH, Schwarzenbruck, Germany, Germany

Introduction: Online IMRT-plan verification during actual treatment delivery is desirable for optimal patient safety. A full-field transmission detector may perform this task and would be, in addition, an essential part for an adaptive radiotherapy workflow, where the treatment plan could be continuously adjusted and verified within a closed feedback loop.

Since such a detector is a new device that is placed in the path of the beam, its use for in-field measurements requires a detailed analysis of the influence on the beam characteristics. We have therefore evaluated the combination of a pre-clinically released new transmission detector and the verification software COMPASS (IBA Dosimetry, Germany).

Materials and methods: Since a possible increase of the skin dose can be caused by absorbing materials in the beam, it is important to know the exact dose at the surface as well as in the build-up region if a transmission detector is used during actual patient treatments. We performed surface and build-up dose measurements with a Markus chamber (Model 329, PTW-Freiburg, Germany) from the surface to a depth of d_{max} for a 6 MV beam delivered with and without flattening filter (FFF). The over-response of the chamber was scaled down by the use of correction factors determined by Mellenberg [1].

Furthermore percentage depth dose profiles (PDD) on the central axis from d_{max} to 250 mm, off axis profiles in different depths (d_{max}, 5 cm and 10 cm) and absorption factors were measured with and without detector in the path of the beam to investigate the influence of the detector beyond d_{max}. These measurements were carried out also for a 6 MV and 6 MV FFF beam using an ionization chamber (Model CC13, IBA Dosimetry). All measurements in this study were performed for different field sizes ranging from 5x5 cm^2 to 30x30 cm^2 and different source-to-surface distances (SSD) of 80 cm and 100 cm.

Results: When the transmission detector was placed in the path of the beam, an increase of the dose at the surface and in the build-up region was detected. For small field sizes and larger SSDs, the increase of the surface dose was negligible (Table 1). However, at reduced SSD or increased field sizes, the increase in the surface dose was noticeable (Table 1). Beyond d_{max}, the influence of the transmission detector on PDDs and off-axis profiles were negligible for 6 MV and 6 MV FFF. The maximum difference between PDDs with and without transmission detector in the path of the beam was less than 1%.

For both modalities, 6 MV and 6 MV FFF, a small increase in the absorption factor was observed when the field size was decreased (Table 2). For field sizes 3x3 cm^2 and 5x5 cm^2, the attenuation can reach 10% and it was measured for different depths ranging from d_{max} to 10 cm. With field sizes larger than 10x10 cm^2 the absorption of the detector dropped to 8.3% and 8.9%, respectively, for 6 MV and 6 MV FFF beam at an SSD of 100 cm and a field size of 30x30 cm^2.

Conclusion: Since the influence of the transmission detector beyond d_{max} is negligible for 6 MV energies and only a small increase in the surface dose was observed, the detector's influence on beam characteristics would allow its clinical use. Since the differences in the absorption factors for small field sizes (3x3 cm^2 - 10x10 cm^2) are negligible, only a single absorption factor has to considered during treatment planning.

	surface dose(detector) - surface dose(open field) (%)			
	6 MV		6 MV FFF	
Field size (cm^2)	SSD = 100 cm	SSD = 80 cm	SSD = 100 cm	SSD = 80 cm
5 x 5	0,1	0,8	0,1	0,9
30 x 30	5,6	14,1	5,3	14,4

Tab 1: Differences in the surface dose for open fields with and without detector in the path of the beam. Differences are expressed as a percentage of the dose in d_{max}.

	Absorption (%)	
Field size (cm^2)	6 MV	6 MV FFF
3 x 3	10,0	10,5
5 x 5	10,0	10,5
10 x 10	9,8	10,1
20 x 20	9,2	9,5
30 x 30	8,3	8,9

Tab. 2: Absorption factor was measured for different field sizes ranging from 3x3 cm^2 to 30x30 cm^2 at SSD of 100 cm in a depth of 10 cm with an ionization chamber in a RW3 phantom.

References

[1] Mellenberg, D. E. Jr.: Determination of build-up region over-response corrections for a Markus-type chamber, 1990, Medical Physics, Vol.17, No.6

P 21 Dosimetric properties of a new commercial artificial-diamond detector

R. Fouassi[1], W. W. Baus[1]
[1]University Hospital of Cologne, Radiotherapy, Cologne, Germany

Introduction: Especially for Measurements of small fields used for e.g. IMRT or stereotactical radiotherapy one needs dosimeters with a small sensitive Volume. So called pinpoint ion chambers have a rather low sensitivity whereas dosimetry-diodes with there much smaller sensitive volume exhibit other disadvantages (e.g. radiation induced fading). Diamond detectors, on the other hand, mix the advantages of these detectors by avoiding at the same time the disadvantages: very small sensitive volume, comparatively high sensitivity, fairly good tissue equivalency and long term stability under irradiation. Until recently, a diamond detector using a natural diamond was purchasable (Type 60003, PTW Freiburg, Germany [1]). However, this detector had the disadvantage that it needed a bias voltage – together with a fatal sensitivity to voltage polarity. This product was replaced by a new detector based on an artificial diamond (Type 60019, PTW Freiburg, Germany). We tested the dosimetric properties of this new detector, especially sensitivity, linearity, dose rate dependency and dark current.

Materials and methods: All irradiations were done in a plastic water slab phantom (CIRS, Norfolk VA, USA) in a depth of 10 cm (SSD: 100 cm) with a 6 MV beam of a Truebeam accelerator (VMS, Palo Alto CA, USA). As Electrometer we used a Unidos webline (Type 10022, PTW Freiburg, Germany). The performance of the microdiamond was compared to a 0.125 cm³ semiflex ion chamber (Typ 31010, PTW Freiburg, Germany).

Results: The sensitivity of our diamond detector was 0.930 nC per Gy which is in agreement with the specification given by the manufacturer. This value was stable after 5 Gy of pre-irradiation (see fig. 1). Without pre-irradiation, however, the dose was about 1.2 % off whereas for the semiflex chamber there was only a very small effect of 0.06 %, if any. Linearity for both detectors was virtually perfect (Fig. 2) with a regression parameter of 1.000. We observed no dose rate dependency in the range from 0.5 to 3.0 Gy/min. After irradiation, the diamond detector exhibited a kind of dark current which leveled not before about 10 minutes (see fig. 3).

Conclusions: Further investigations, especially a broader range of parameters and, for example, an extensive examination of the direction dependency of the sensitivity are under way.

References

[1] Wolfram U Laub, Theodor W Kaulich, Fridtjof Nüsslin, A diamond detector in the dosimetry of high-energy electron and photon beams, Phys. Med. Biol. 44 (1999) 2183-2192

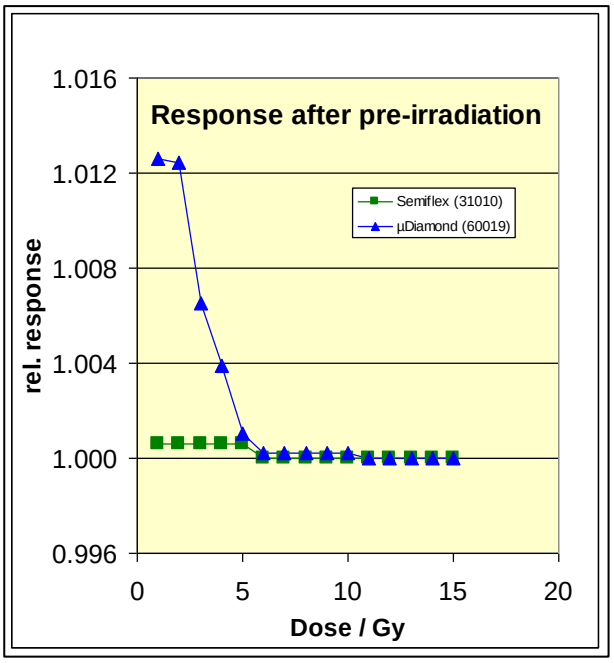

Fig. 1 Response after pre-irradiation. Comparison between µDiamond and Semiflex ion chamber, indicating the need of pre-irradiation with about 5 Gy.

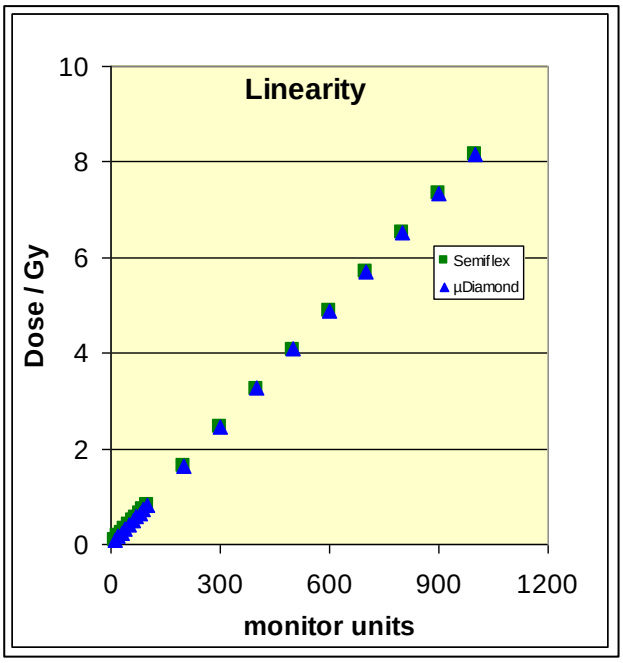

Fig. 2 Linearity of the dose response. The coefficient of a linear regression is 1.000 for both data sets.

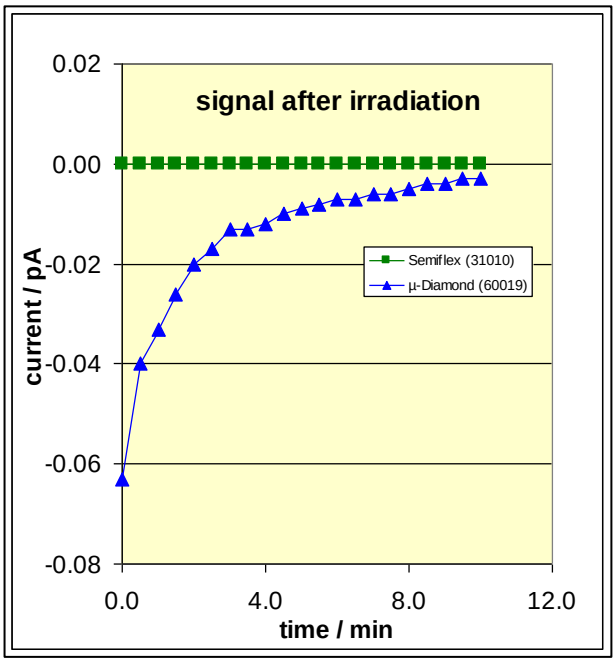

Fig. 3 Detector current after irradiation over time (zeroing of the electrometer before irradiation with 10 Gy).

P 22 Radiochromic film dosimetry with EBT3 films for low kilovoltage x-ray beams with energies between 12 kV and 50 kV

P. Pemler[1], C. Erckes[1], T. Buchsbaum[1], F. Hasenbalg[1], V. Vlachopoulou[1]
[1]Stadtspital Triemli, Radioonkologie, Zurich, Switzerland

Introduction: Low kV x-ray beams are still used by many dermatologists in Switzerland. Relative film dosimetry with EDR2 films for analyzing profiles is still common practice. To replace EDR2 film dosimetry, a robust, that means a reliable, reproducible and fast method of radiochromic film dosimetry with EBT3 films [1-3] should be established. The feasibility of using a standard flatbed scanner with standard dosimetry soft-ware without any special components was evaluated. The results were compared to standard EDR2 profiles with respect to parameters required by the BAG directive R-08-09.

Materials and methods: The feasibility of radiochromic film dosimetry with EBT3 films for low kV x-ray beams was evaluated. Films were irradiated with a Gulmay XStrahl100 with energies of 12 kV (0.03 mm Al), 20 kV (0.13 mm Al), 30 kV (0.32 mm Al), 40 kV (0.76 mm Al) and 50 kV (1.49 mm Al). The films were scanned with a flatbed scanner EPSON V700 (A4) in portrait mode and fixed with a special frame for reproducibility. All films were scanned and analyzed with PTW Mephisto Film Scan in "GAFChromic optimized" mode and analyzed with PTW Film Analyze. All films were scanned before irradiation and an individual flattening correction was stored for each film used. For evaluation, films were analyzed with and without flattening correction and with individual or standard flattening correction for the lot of films used.

For all energies calibration curves have been determined in a range between 0 and 4 Gy. All films used were irradiated with 2 Gy where the corresponding treatment time was determined with an ionisation chamber measurement.

For evaluating the robustness of the procedure, for 12 kV and 40 kV a 4 cm circular cone was irradiated on 4 films and at 6 different positions on each film. The films were analyzed with and without flattening correction. For 20 kV and 30 kV one film each was irradiated and analyzed at 4 different positions with a non-individual flattening correction. For 50 kV one film was irradiated and analyzed with the same procedure as used for 12 kV and 40 kV. For all profiles the parameters field size, homogeneity and symmetry were analyzed. As a reference, EDR2 films were irradiated with the same cone. In addition the central axis dose has been determined for each of the irradiated cones and averaged.

Results: The calibration curves are shown in figure 1. While energies between 20 kV and 50 kV exhibit a similar behavior, the lowest energy showed a significant different response. Flattening corrections have been determined for 10 individual films before irradiation. The flattening correction which is applied as a factor is between 0.975 and 1.025 if the outer 2 cm of the short side of the film and 1 cm of the long side is avoided (effective area: 20 cm x 16 cm). Rotating the film by 180° or flip the film to the other side adds another 1% error to the applied flattening correction. A response gradient of 2% over 4 cm could be observed in the center of the film. Figure 2a shows examples of profiles for 40 kV without flattening correction. The red curve is the EDR2 reference, the grey curves are the profiles of the field at 6 different positions in the direction of the long side of the film. Figure 2b shows the profiles with an individual flattening correction applied. Figure 2c is an example for 20 kV, if no individual, but a standard flattening correction is applied. As can been seen from figure 2, the profiles with EDR2 films show a slightly steeper penumbra. While the field size increases by 1-2 mm from one energy to the next for EDR2 films the field size is almost constant for all energies for the profiles taken with EBT3 films. The results for the symmetry (maximum dose ratio according to IEC 60976 evaluated within 80% of the field size determined by the 50% isodose) for EBT3 films are shown in figure 3 together with the EDR2 results. The results are similar for both directions and almost independent of whether individual flattening correction (i-FC) or no flattening correction (NFC) was applied. For 20 kV and 30 kV the results for a standard flattening correction (s-FC) are shown for illustration. Except for 12 kV, were EDR2 film dosimetry is limited, the results of EDR2 film dosimetry are clearly superior to EBT3 film dosimetry.

For absolute dosimetry, the central axis dose for each irradiated cone has been determined and averaged. The results are depicted in figure 4. In general, the values determined with flattening correction are too high, very likely because the correction is applied as a factor and not renormalized by the software afterwards. For 20 kV to 50 kV the values are acceptable within 5% tolerance level. For 12kV the value is significantly higher than expected and has to be further investigated.

Conclusion: For the system used in this evaluation, the quality of radiochromic film dosimetry with EBT3 films for low kilovoltage x-ray beams could not reach the quality of standard EDR2 film dosimetry except for the lowest energy. If a flattening correction is used, an individual correction by scanning each film before irradiation is preferable compared to a standard flattening correction for one lot of EBT3 films. If film borders are avoided, analyzing films without flattening corrections showed similar results. Absolut dosimetry was unreliable if flattening correction was used and were acceptable without flattening correction except for the lowest energy. Further investigation is needed to improve the quality of EBT3 film dosimetry for routine use in our setting.

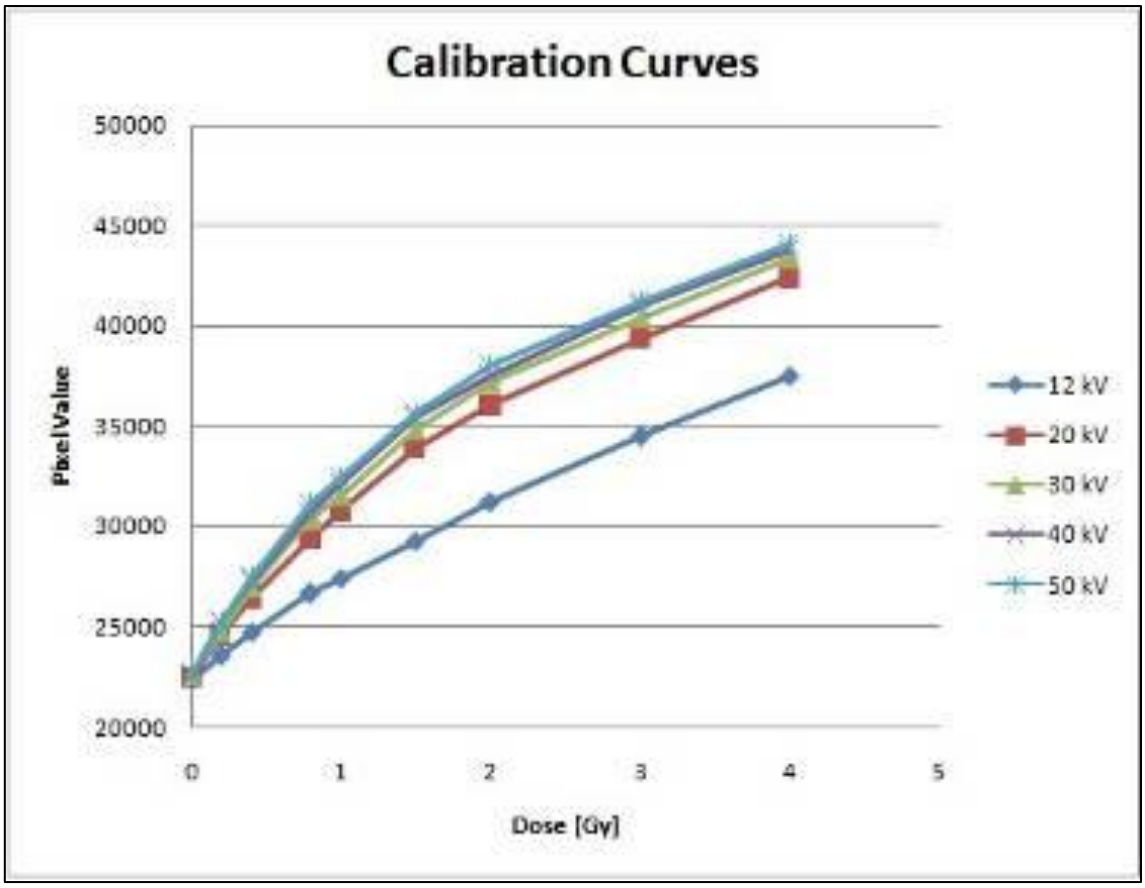

Fig. 1: Calibration Curves for EBT3 films for low kilovoltage x-ray beams

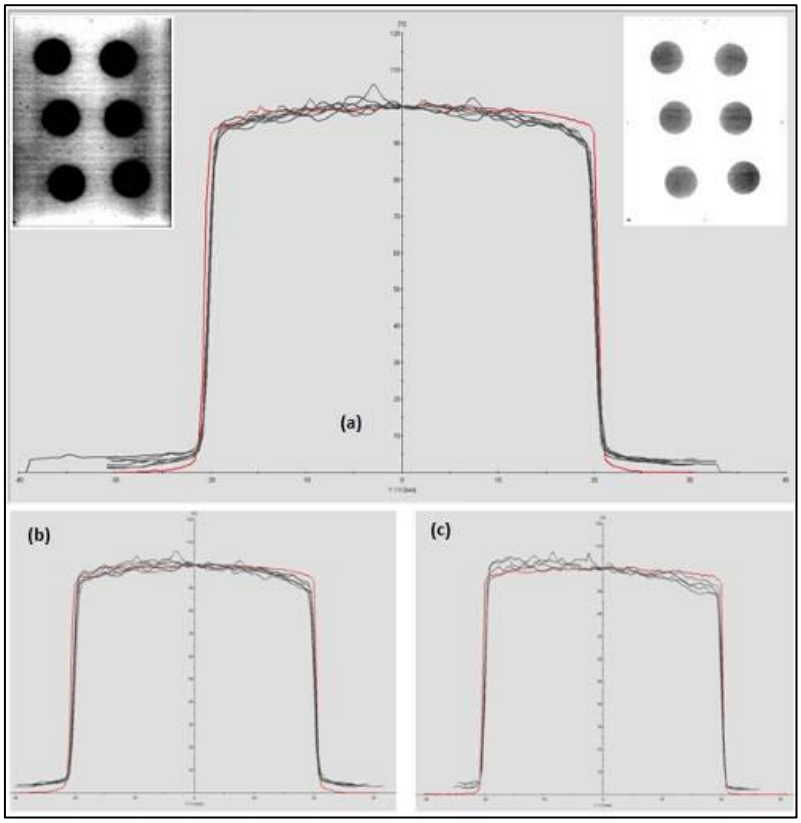

Fig. 2: Examples of profiles aquired with EBT3 films for (a) 40kV without flattening correction, (b) 40kV with individual flattening correction and (c) 20kV with a standard flattening correction. The direction of the profiles are along the long side of the film.

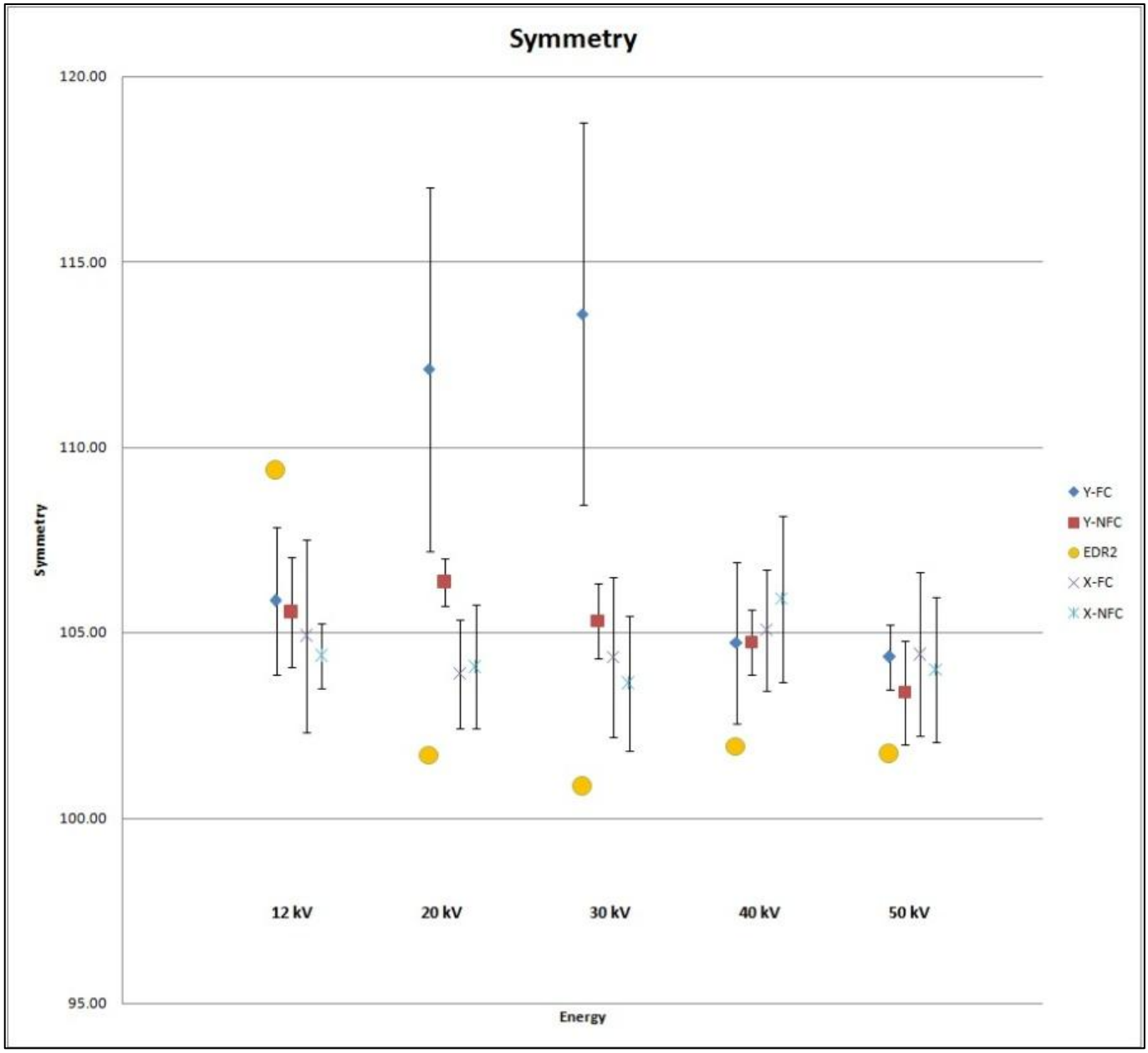

Fig. 3: Symmetry of the profiles for EBT3 films in comparison with those from EDR2 films

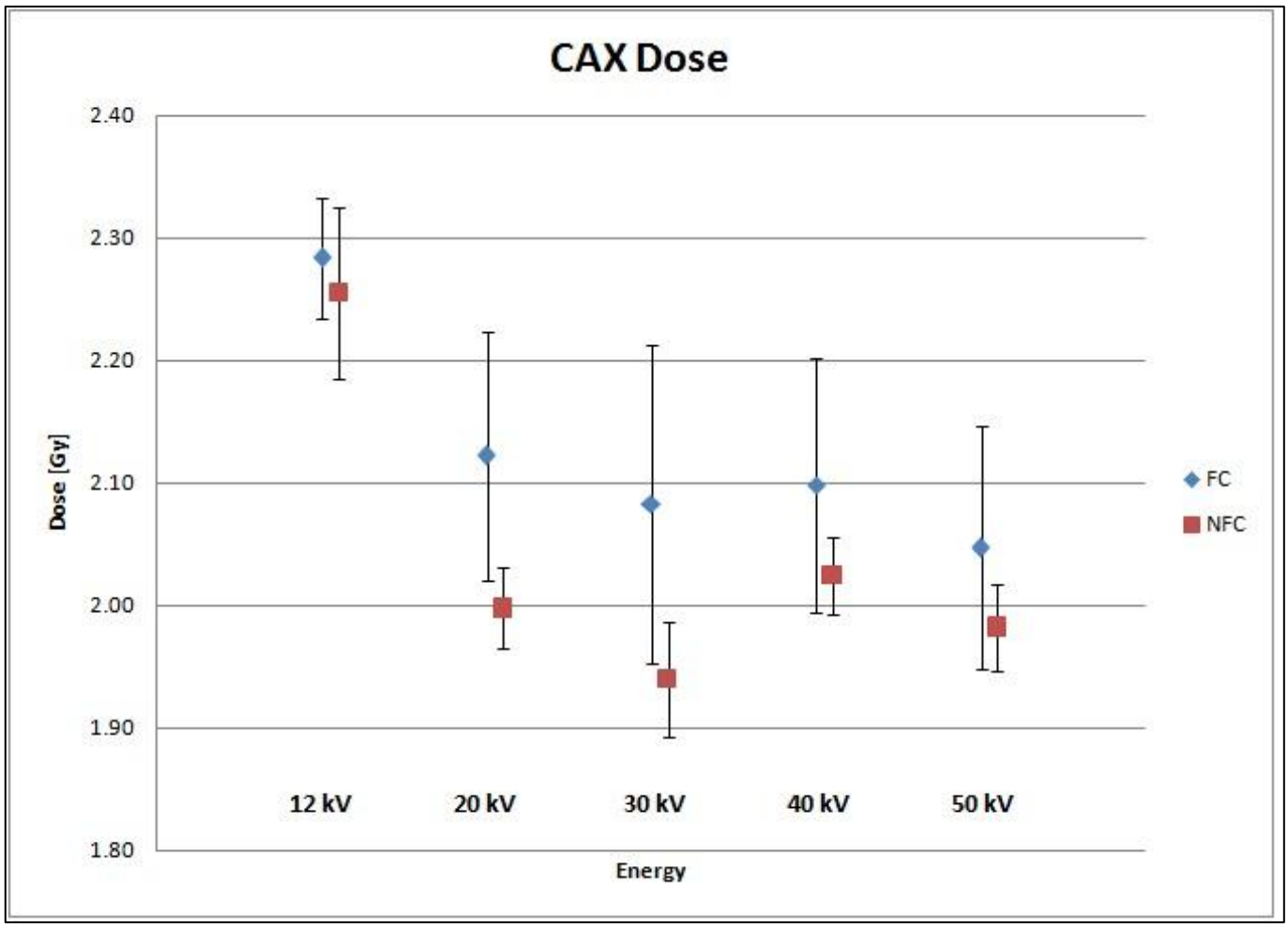

Fig. 4: Central axis dose for all energies, determined with and without individual flattening correction

References

[1] R. Hill et al.: Advances in kilovoltage x-ray beam dosimetry, Phys. Med. Biol. **59** (2014), R183-R231

[2] D. Poppinga et al.: A new correction method serving to eliminate the parabola effect of flatbed scanners used in radiochromic film dosimetry", Med. Phys. **41** (2014), 021707

[3] D. Lewis et al.: An efficient protocol for radiochromic film dosimetry combining calibration and measurement in a single scan, Med. Phys. **39** (2012), 6339-6350

P 23 Examination of surface dose enhancement using radiochromic EBT3-films in a cylindrical setup

T. Failing[1], N. Chofor[1,2], W. Kunth[2], H. K. Looe[1,2], D. Poppinga[1,2], A. Schönfeld[1,2], K. Willborn[2], B. Poppe[1,2]
[1]Carl von Ossietzky Universität, Oldenburg, Germany
[2]Pius Hospital, Klinik für Strahlentherapie und Radioonkologie, Oldenburg, Germany

Introduction: While radiochromic EBT3 films (Ashland ISP, Wayne, USA) have proven useful for surface dose measurements near high Z materials, the range of the backscattered radiation causing the surface dose enhancement has been difficult to determine. A stack of films allows precise surface dose measurements close to the probes surface, but offers a limited number of measurement points for range measurements due to the thickness of the films. Placing the film normal to the surface creates a setup enabling a high resolution range measurement, but with a limited accuracy at the probe's surface due to the cutting edges of the films.
This study was undertaken to combine at the same time a high resolution depth dose curve of the backscattered radiation and an accurate close-to-surface dose measurement using EBT3 films.

Materials and methods: A polyethylenterephthalat (PET) hollow cylinder was used to form radiochromic EBT3 films into a defined cylindrical shape with a radius of 20.75 mm. The resulting EBT3 cylinder was fixed upon the surface of a lead block (figure 1) to measure the surface dose enhancement. The setup was immersed in water and exposed to a dose of 2 Gy at 6MV acceleration voltage using a Siemens Primus linear accelerator. Water reference measurements were undertaken under equal conditions.

The films were digitized using an Epson Expression 10000 XL flatbed scanner (Epson, Suwa, Japan) with a resolution of 72 dpi. The red color channel was used for evaluation, which was performed in Matlab (The Mathworks, Natick, USA). By dividing the surface dose measurement by the water reference measurement, not only the relative dose enhancement could be measured, but also the curvature of the film was taken into consideration resulting in a high resolution depth dose measurement. Marking the touching point of the probe surface and the film is unnecessary, since it is identical with the point of maximal dose enhancement and therefore easily detectible on the films

Results: The dose distribution resulting from the backscattered radiation could be measured along the axis normal to the lead surface with a high resolution of measurement points. At a distance of 134 µm from the lead surface, a dose enhancement of 70% was measured. The data has been compared with results presented by Das et al. and is consistent within the uncertainty of the measurements (figure 2). The results are also in consistence with the results from other time-tested EBT3 setups, i.e. normal-to-beam EBT3 film stacks and parallel to beam EBT3-films, but combine their advantages while eliminating their disadvantages in one measurement setup.

Conclusion: The advantages of a stacked film setup and a parallel to beam setup could be combined such as it is possible to achieve both a high resolution depth dose curve and accurate surface dose measuring. The cylindrical film setup has proven to be very useful for surface measurements and should be tested in other applications.

References

[1] Das F. Kahn: Backscatter dose pertubation at high atomic number interfaces in megavoltage photon beams, Med. Phys. 16 (3) AAPM, 1989

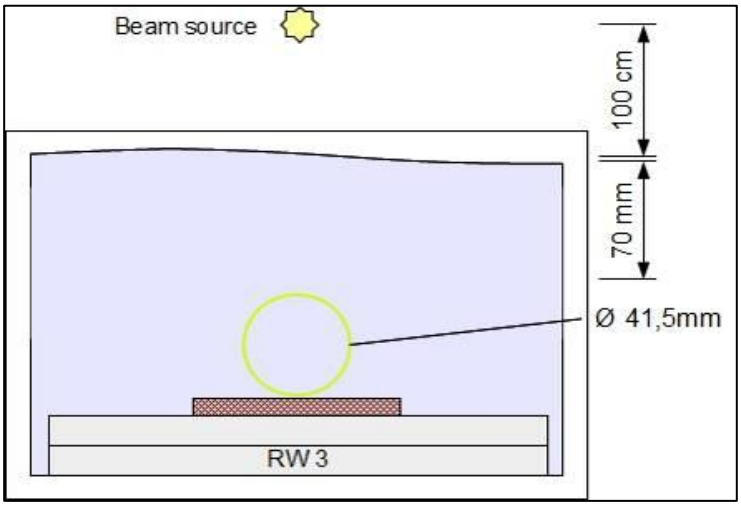

Fig. 1: Schematic view of the experimental setting within a water phantom. One stripe of EBT3-film is sufficient for measurement. The point of measurement's distance from the surface can be calculated using the radius of the cylinder.

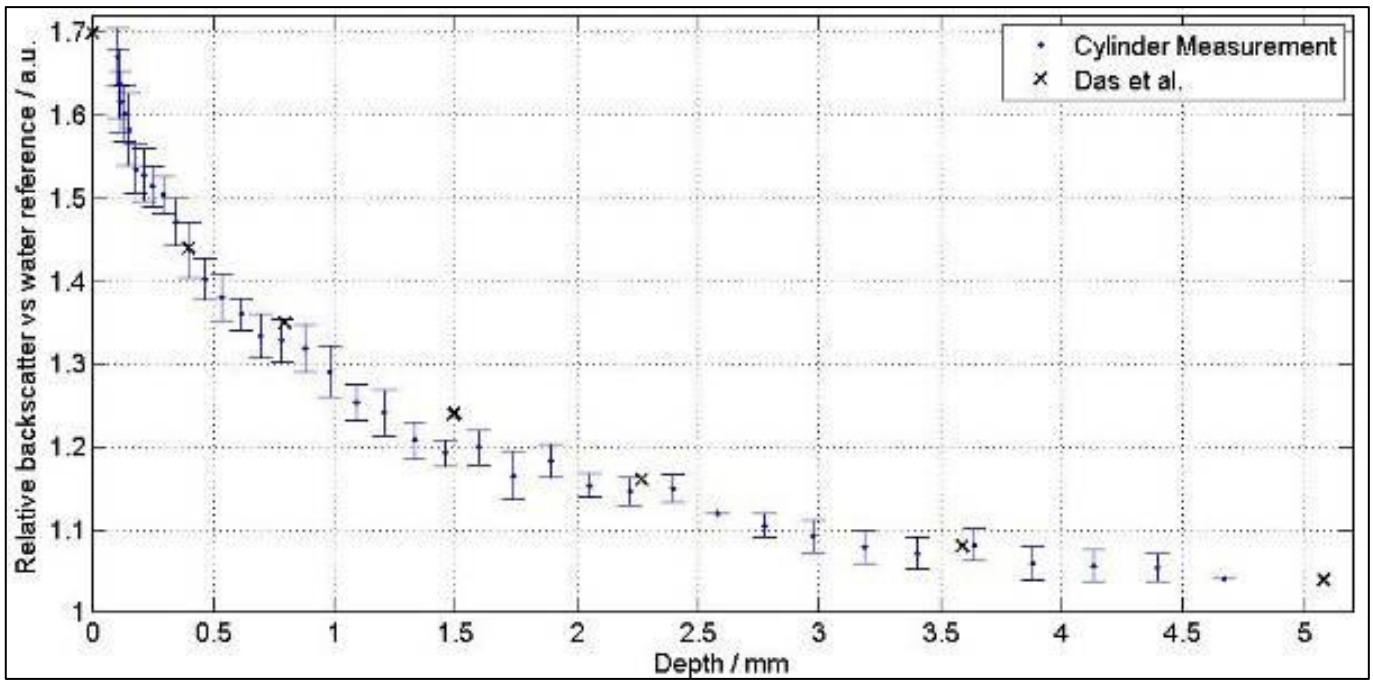

Fig. 2: Relative dose enhancement on the proximal side of lead. The results show a great conformance while the cylinder setting provides a high density of measurement points especially within the first millimeter.

P 24 Evaluating the angular dependence of dose enhancement effects at metal probe surfaces using radiochromic EBT3 films during megavoltage photon deliveries

A. Jansen[1,2], A. Schönfeld[1,2], D. Poppinga[1,2], N. Chofor[1,2], B. Poppe[1,2]
[1]Pius Hospital Oldenburg, Radiation Therapy, Oldenburg, Germany
[2]Universität Oldenburg, Medical Radiation Physics, Oldenburg, Germany

Introduction: In Radiotherapy, inhomogeneities with high atomic numbers may cause significant surface dose enhancements, which should be considered during treatment planning. In this study the relative dose enhancement at the surface of several metal materials in dependence of the angle of incidence were quantified using radiochromic EBT3 films.

Materials and methods: Several metal probes covering a wide range of atomic numbers Z were chosen for this study. Aluminum (Z = 13), titanium alloy (Z = 21.66), copper (Z = 29), silver (Z = 47), dental gold (Z = 74.23) and lead (Z = 82) were cut into 1.0 x 8.0 x 8.8mm³ slabs (figure 1) and embedded in an Octavius 4D phantom (PTW Freiburg, Germany) using several custom fitted plates of RW3. The probes were placed in the isocenter of the Phantom. For each angle of incidence an EBT3-film was positioned at the surface of the metal slab to measure the respective surface dose. The thin structure of the radiochromic EBT3 films allows dose measurements at 0.1 mm distance from the probe's surface.

The setup was exposed to a dose of 0.75 Gy at acceleration voltages of 6MV and 10MV using a 10 x 10 cm² field at angles of incidence between 0° to 90°. Water reference measurements were taken under similar conditions.

Fig. 1: A copper slab of dimensions 1.0 x 8.0 x 8.8mm³ embedded in an adapted RW3 slab for measurements within the Octavius 4D phantom.

Results: The results of the surface dose enhancement are shown in figure 2. Lead and dental gold produced the highest surface dose enhancement factor of about 1.65 for angles of incidence up to 30°. For higher angles of incidence, the surface dose enhancement dropped significantly. At an angle of incidence of 80°, the dose enhancement factor was still 1.35.

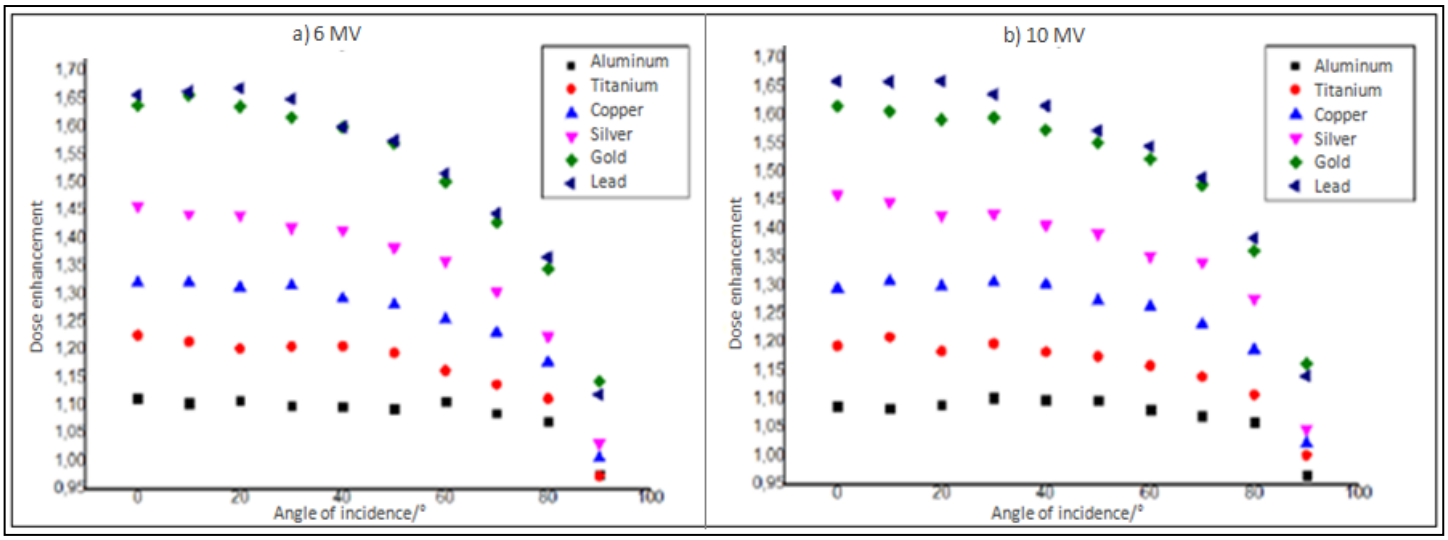

Fig. 2: The dose enhancement factor at 0.1mm from the surface of aluminum, titanium alloy, copper, silver dental gold and lead in dependence of the angle of incidence of (a) 6 MV and (b) 10 MV photon beams.

The surface dose enhancements at an angle of incidence of 0° were 1.45 for silver, 1.32 for copper, 1.22 for titanium alloy and 1.12 for aluminum. At an angle of incidence of 80°, these enhancement factors dropped to 1.22 (silver), 1.18 (copper), 1.12 (titanium alloy) and 1.06 (aluminum) respectively. The dose enhancement factors measured after irradiation either with 6MV (figure 2a) or 10MV photon beams (figure 2b) were within 2-3% for the same angle of incidence for each metal probe. In general, the surface dose enhancements at 6 MV are slightly higher than at 10 MV, which is in accordance with literature (Das et al., 1989).

The results of the measurements performed with dental gold and titanium alloy were compared to Monte Carlo simulations. For titanium, the result of the simulations was 1.24 ± 0.02 for an angle of incidence of 0°, 1.22 ± 0.06 for 30° and 1.16 ± 0.11 for 50°, which is in consistence with the measured values. For dental gold, the simulations resulted in 1.59 ± 0.03 for normal incidence at 6 MV and 1.61 ± 0.04 for normal incidence at 10 MV. The slight deviation from measurement results could stem from the unknown factors such as the exact composition of the dental gold alloy.

Conclusion: The surface dose enhancement factor drops significantly for higher angles of incidence. However, the surface dose enhancement near implant materials with high atomic numbers should be taken into consideration in radiotherapy. The dependence of the magnitude of the surface dose enhancement on the atomic number of the surface material was shown, which is in consistence with literature (Krieger, 2012).

References

[1] Indra J. Das and Faiz M. Khan, “Backscatter dose pertubations at high atomic number interfaces in megavoltage photon beams,” Med. Phys. 16(3), 1989.

[2] Krieger, Hanno: Grundlagen der Strahlungsphysik und des Strahlenschutzes, Springer Spektrum, 4th Edition, 2012.

P 25 Filmdosimetry at the tissue-air interface − The influence of the film material

R. Klepper[1], S. Höfel[1], U. Botha[1], T. Hertel[1]
[1]Praxis und Belegabteilung, Strahlentherapie, Konstanz, Germany

Related questions: Dose measurements in air as well as at the tissue-air interface are challenging, since the sensor material usually produces additional secondary electrons which affect the detected signal. Especially in MV photon beam therapy air or surface dose measurement are therefore biased. Here we assess the magnitude of this effect in the case of dosimetry with EBT3 films. Further we present a method which corrects for this effect.

Material and procedure: In the first step, the influence of the film material on the dose measurement in air was estimated by using Monte Carlo (Geant4) simulations for monoenergetic photon beams (1.49 MeV) impinging perpendicular on the film surface. Therefore a series of simulations for different film thicknesses were performed. Also the absence of any sensor material was simulated. The relation was fitted by a third degree polynomial. In the second step, corresponding dose measurements were performed with a tomotherapy 6MV beam which provides a mean photon energy of approx. 1.49 MeV. Variation of film thickness was realized by stacking several films together (1,3,5,7). Only the middle film was evaluated. Likewise, the resulting dose values were fitted with a third degree polynomial. The dose value for a sensor-free condition was obtained by extrapolation.

Result: The relationship between the dose and the film thickness is almost linear. The quadratic and cubic terms are small. Measurements and simulations yield similar results for the relative dose increase with increased film thickness. The additional dose effect of secondary electrons emerging from the film material itself could be estimated to about 49% (for our setup) of the measured dose for air. This value strongly depends on the incident angle and must be determined for a specific setup.

Summary: The described extrapolation method shows that the dose measured with EBT3 films in air is considerably higher than the actual air dose. The extrapolation method is thought to be suitable for surface dose measurements in phantoms. Thus it provides support to validate dose calculation algorithms at the tissue-air interface.

P 26 Characterization of small field size electron beams using GafChromic EBT3film dosimetry

S. Abbi[1], S. Jaquet[1], H. Petermann[1], G. Kohler[1]
[1]University Hospital Basel, Basel, Switzerland

Goal: Electron beam therapy is a well-established treatment method for near surface tumours. Although excellent treatment planning systems exist for electron beam therapy, it is still usual to perform electron beam therapy planning by the means of tables. Furthermore, it is very common among physicians to use a rule of thumb for planning. The value of energy in MeV divided by the number three gives the therapeutic depth of 80% dose. This approach works for most of the applicators. However, for small closed wall applicators the rule of thumb cannot be used any longer for several reasons. At our institution for the small targets, the beam shape is modified by employing tubular applicators (2cm, 3cm, 4 cm, 5 cm in diameter) with closed walls. In contrast to applicators without closed wall the electrons in closed wall applicators are scattered on the walls thereby increasing the proportion of low energy electrons which leads to increased skin dose and shifts maximum dose backwards to the surface. Additionally, for these tubular applicators the field size becomes shorter than the lateral scatter equilibrium of the beam [1]. Hence, an accurate dosimetry of the small beams poses a challenge. Recently, electron beams small field size dosimetry has been documented using gel dosimeter [2] and silicon and diamond diodes [3]. As pointed out by Das, Ding and Ahnesjö [4] the very presence of the detector itself is a factor contributing to the not easily quantifiable perturbative effect. Self-developing radiochromic films provide a method with small perturbation in the small field region and high spatial resolution. The results should help improving external electron beam therapy at our institution.

Material und Methods: Elekta Synergy equipped Agility MLC (Elekta AB, Sweden) capable of delivering electron energies 6, 8, 10, 12, 15, 20 MeV at dose rate of 600MU/min is used in tandem with small field closed tubular applicators provided by Elekta. GafChromic EBT3 films produced by International Specialty Products Ashland Inc. (Convington, KY) are employed in accordance with procedures described by AAPM TG-55 report [5] and were placed parallel to the central beam axis. With this approach, percentage depth dose curve (PDD) as well as off axis ratio can be extracted. The single scan protocol proposed by Lewis et al. [6] was used to evaluate the film using Film QA Pro software.

Conclusion: Preliminary measurements to check the proof of the concept were performed but the measurements on all energies and applicators still need to done. The results are expected in next two months. For the special case of tubular small field applicators 2-dimensional dose distribution and output factors will be catalogued using GafChromic films.

References

[1] Hogstrom K R and Almond R P, Review of electron beam therapy physics. Phys. Med. Biol. 51 (2006) R455-R489.
[2] Francisco G. A. Sampaio et al., 8 and 10 MeV Electron Beams Small Field-Size Dosimetric Parameters through the Fricke Xylenol Gel Dosimeter. IEEE Transactions on Nuclear Science, Vol. 60, No. 2, April 2013.
[3] Bagalà P et al., Radiotherapy electron beams collimated by small tubular applicators: characterization by silicon and diamond diodes. Phys. Med. Biol. 58 (2013) 8121–8133.
[4] Das I J, Ding G X, and Ahnesjö A, Small fields: Non equilibrium radiation dosimetry. Medical Physics 35 (1) January 2008.
[5] AAPM Report No. 63 Radiochromic Film Dosimetry. Medical Physics, 25 (11), November 1998
[6] Lewis D. et al., An efficient protocol for radiochromic film dosimetry combining calibration and measurement in a single scan. Medical Physics, 39(10), October 2012.

Poster session III – Biological modeling and treatment planning in radiation therapy

Chair: J. Wilkens (Munich/DE)

P 27 Feasibility study of MLC virtual compensation for total body irradiation at extended SAD (500 cm)

D. Marc[1], H. Markus[1], B. Susann[1], S. Frank-André[1]
[1]UKSH, Strahlentherapie, Kiel, Germany

Introduction: The main requirement for total body irradiation (TBI) is a homogeneous delivery of dose to the patient. The current method practiced at UKSH (Universitätsklinikum Schleswig-Holstein), Campus Kiel, was developed in the clinic of radiotherapy in the late 80's. 12Gy in total are delivered to the patient in 6 fractions within 3 consecutive days. During treatment, the patient lies in supine position on a couch placed at 5 meter distance from the radiation source (linear accelerator) and is irradiated by two 40 x 40 cm2 opposing lateral beams of 15 MV photons. The beams are attenuated by solid compensators made of tin granules. These compensators are computed individually for each patient by in-house software.

The method although very effective in its time has some drawbacks: high logistic efforts to manufacture the compensators and numerous sources of uncertainty; it can be modernized with today's techniques. In this context, we checked the feasibility of using virtual compensation with multi leaf collimated fields instead of solid compensation for TBI.

Materials and methods: Fluence maps equivalent to maps obtained with solid compensation were first determined in Matlab (MathWorks, Natick, MA) using a ray tracing algorithm through the solid compensator object. These maps were then imported in Varian Eclipse v10 (Varian Medical Systems, Palo Alto, CA) to calculate MLC leaf sequences for our Artiste accelerator (Siemens Healthcare Sector, Erlangen, Gemany).

Measurements of delivered fluence were performed at 5 m distance from the beam source with a Octavius 29 chamber 2D array (PTW, Freiburg, Germany) placed in a Perspex phantom at different off axis positions covering a -100 cm to + 100cm lateral range. Film dosimetry measurements with gafchromic, representatives for head, lung, and abdomen dose in an Alderson Rando anthropomorphic phantom were acquired as complementary verification.

Results: Measured fluence maps merged in a 200 x 27 cm2 matrix showed deviations of less than 5% between several virtual and solid compensators (compensator with "stair" shape, Rando phantom compensator and real patient test compensators). As observed on the fluence maps, the lateral leaf resolution of 5mm (at 100 cm), larger than the solid compensator resolution, 3 mm steps, did not impact negatively the results.

Film dosimetry measurements confirmed these results with similar dose distribution obtained with both methods along the Rando phantom axis. The specified lung dose, 16% lower than the nominal dose, was respected. The beam delivery time was only 15% larger with the virtual compensation for the Rando phantom plan.

Discussion and conclusion: The study demonstrates that TBI with virtual compensation could be an alternative to TBI with solid compensation with similar dosimetry results. The flexibility of the method, without compensator manufacturing, is of evident advantage. As a next step, the impact of patient movement vs segmented fields needs to be evaluated. The Matlab software tool developed for measurements and evaluation of TBI dose maps presents an interesting potential for plan verification before delivery.

P 28 Electrons, Cut Out Factors, Monitor Units, Depth Dose Profiles and Co.

J. M. Jensen[1], K. Malkoske[2], J. Beck[1], F.-A. Siebert[3]
[1]CCMB, Medical Physics, Winnipeg, MB, Canada
[2]RVH, Medical Physics, Barrie, ON, Canada
[3]UKSH, Medical Physics, Kiel, S-H, Germany

Introduction: In radiotherapy beside photons also in 10 % of all cases electrons are used for treatment. Protons and other exotic beam qualities are negligible with respect to number of treated patients.

Based on physical properties, such as limited range in tissue, electrons are applicable only for superficial lesions.

In the absence of suitable treatment planning systems for electrons the calculation of monitor units to apply a planned dose to a reference depth using a linear accelerator, is still done manually or semi-manually. Taking into account the geometrical size of the tumor, a cut out is designed, the appropriate electron energy is chosen, and the thickness of the bolus material is determined.

Method: Because of the influence of electron applicators and the individual cut-out shape, a cut-out factor has to be determined experimentally for the calculation of the preset number of monitor units. Different procedures have been published, showing an accuracy of about ± 3 % with respect to measurements.

Based on about 900 measurements on individual cut-outs for the energy range of 6 MeV to 20 MeV and medical linear accelerators of three different vendors, a simple procedure was designed to calculate the cut-out factor and the preset number of monitor units per fraction, resp. The physical background of the determination of field dimensions along the main axis, starting with the maximum separation, crossing the geometrical centre, and to this orthogonal axis, is the range of electrons in soft tissue or water. Cut-out factors of the original field sizes (6x6 cm^2, ... , 25x25 cm^2) in the energy range of 6 MeV to 20 MeV are the basic data set. Variations in source-skin-distance are taken into account by an inverse-square-law correction, including d_{max} and the virtual source position.

Results: Keeping some basic requirements, such as minimum field dimensions and focus-skin-distance, allows the estimation of the cut-out factor with a maximum error of ± 3 %, which is clinical acceptable. For the EXCEL® spread sheet a set of only 5 basic data is necessary to characterize the cut-out factor: Electron energy [MeV], type/size of electron applicator [6x6, ... , 25x25], reference isodose [90 % ... 100 %], minimum field dimension [cm], SSD [100 cm ... 105 cm]. Out of a list of basic and advanced data for standard (squared, rectangular, circular), original (6x6 cm^2, ... , 25x25 cm^2), eccentric and individual shaped cut-outs, the appropriate factor is determined.

Discussion and Conclusion: Although the presented procedure is very simple and relies on only one field defining parameter, the results are comparable to significantly more sophisticated techniques, such as equivalent field size method, sector integration or Monte Carlo calculation.

If the criteria 'minimum field dimension' (length L or width W) is not fulfilled, an additional experimental correction factor can account for this with respect to modified scatter conditions and electron energy spectrum. When the minimum field dimension is significantly smaller than required, $F_{L, W} < F_{min}$ -1 cm, measurement of the cut-out factor is still necessary, taking into account the shift of d_{max}. These measurements will extend and validate this model. In daily routine experimental dosimetrical checks of cut-out factors are necessary in less than 5 % of all cases.

Acknowledgement: The authors gratefully acknowledge T. Bailey *, M. Evan *, T. Bridgelall * and M. Hirt *** for measurements and data compilation.

References

[1] Chen FS : Med. Phys. 15 (1988) p. 348-50
[2] Chen, J et al : Med. Phys. 36 (2009) p. 3397-405
[3] Choi DR et al : Phys. Med. Biol. 48 (2003) p. 899-908
[4] Johnson DA, Ahmad, S : J. Xray Sci. Technol. 18 (2010) p. 309-18
[5] Jones, D et al : Br. J. Radiol. 63 (1990) p.59-64
[6] Klevenhagen SC : Physics of Electron Beam Therapy. A. Hilger Publ., Bristol 1985

P 29 Deviations of DQA-results as a function of plan parameters with helical TomoTherapy

S. Howitz[1], K. Weibert[1], T. Wiezorek[1]
[1]Universitätsklinikum Jena, Jena, Germany

Introduction: With TomoTherapy, dose application is a dynamic process with the gantry rotating around the moving couch and with constantly changing leaf patterns in the binary multi leaf collimator (MLC). Treatment plans are calculated by the TomoTherapy treatment planning system (TPS) based on a collapsed cone algorithm. Parameters that can be altered in the planning process are: dose grid resolution, pitch, longitudinal field size, and modulation factor (defined in detail in the TG 148 report [1]). However, some parameters decisive for plan quality cannot be influenced by the user, as explained in the following. In dose calculation and optimization, 51 gantry angels – projections – are modelled. This is a good compromise between accuracy and CPU calculation time [2,3]. During every projection the fluence is modelled by binary leaf motion, and there is no option to influence the number of segments or the minimum field size directly. The minimum leaf opening time is 20 ms because of mechanic and electronic latency [4,5]. However, S. Lissner (UK Heidelberg) has shown that latency has not yet been considered in minimum shutter times of leaves [6]. That means that the TPS calculates dose with leaf sequences where leaves are closed for less than 20 ms, which the MLC hardware cannot realize. The TG 148 report recommends a delivery quality assurance (DQA) [1] for each patient plan. If the dose measurement fails, the plan has to be re-calculated. Except for changes in the relative factors pitch and modulation factor, it is not possible to influence the plan quality. We have investigated the relation between DQA deviations and the TomoTherapy parameters pitch, modulation factor, gantry period, and number of gantry rotations, but have found no correlations. The aim of this study is to find a reason for deviations between dose measurement and plan calculations based on plan parameters.

Materials and methods: We used the treatment unit TomoHD with TPS software version 1.2.1.Patient quality measurements were performed with the Delta4 phantom (Scandidos, Uppsala, Sweden). The two detector planes were positioned in sagittal and coronal orientation. To pass the quality assurance test, the median dose deviation, including only detectors in the dose range above 60% of the prescribed dose, must not exceed 3%. Few plans (less than 5%) did not pass this criterion and had to be re-calculated with the following conditions: similar DVH of target and risk volumes, and no significant changes to adjustable plan parameters, because neither gantry period nor modulation factor reached their limit values in the initial plans. The corrected plans showed better results in the DQA. The optimized results of TomoTherapy plans are saved in DICOM RT plan files in the form of a sinogram: a two dimensional data table which contains information for each beamlet. A relative leaf opening time factor (LOTF) for each leaf (column) in each projection (row) describes the applied fluence, displayed as gray values. The absolute leaf opening time (LOT) can be obtained by multiplying the LOTF with the gantry period divided by the number of projections per revolution (51).

The sinogram data from the DICOM RT plan files were interpreted with a MATLAB tool developed in-house. The tool determines the dose contributions of segments in dependence of their field size. A field is defined when at least one leaf (6.25 mm in isocenter) is opened, and the field size results from the number of adjoining open leaves. The jaw opening is always 2.5 cm in the isocenter. Additionally, it was possible to determine the minimum duration of times during which a leaf is closed (close times).

Results: The evaluation of the DICOM RT plan files shows a correlation between the fluence applied through small field sizes and dose deviations in the DQA. In Fig. 1 the total opening time of each field size summed over one plan is displayed – for the plan with large deviations and the corrected one, respectively. The figure shows that the plan with large deviations has a larger proportion of fluence delivered by small fields (three or less open leaves).

Fig. 2 displays the ratio between the fluence delivered by fields with only one open leaf and the total fluence of the plan, versus the deviation between measurement and TPS calculation for five different TomoTherapy plans with different target volumes. It reveals the tendency, that plans with a smaller percentage of fluence applied through fields with only one open leaf are more robust. The lower number of small fields has mainly been achieved by less demanding optimization criteria and a smaller number of iterations.

Fig. 3 shows a correlation between dose deviations in the measurement and close times which are too short for the MLC hardware.

Conclusion:
This investigation shows that dosimetric inaccuracies of TomoTherapy plans are caused by a) a large percentage of dose delivered through small fields, and b) close times which are too small for the MLC hardware. Currently it is not possible for the user to directly influence these parameters in the TomoTherapy TPS.

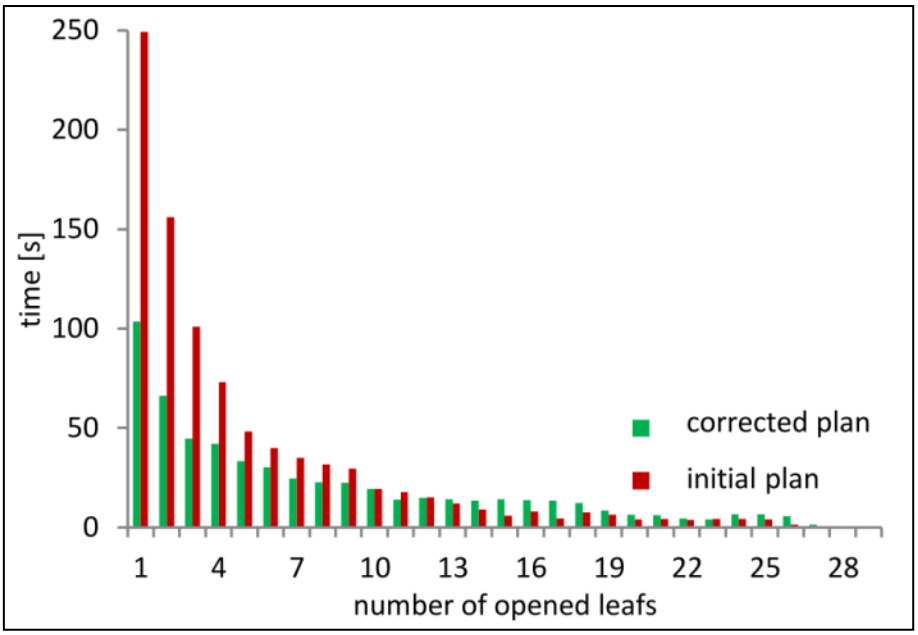

Fig. 1: Histogram showing the total opening times of different field sizes for a plan which fails the mean dose criterion in the DQA and the corrected plan, respectively.

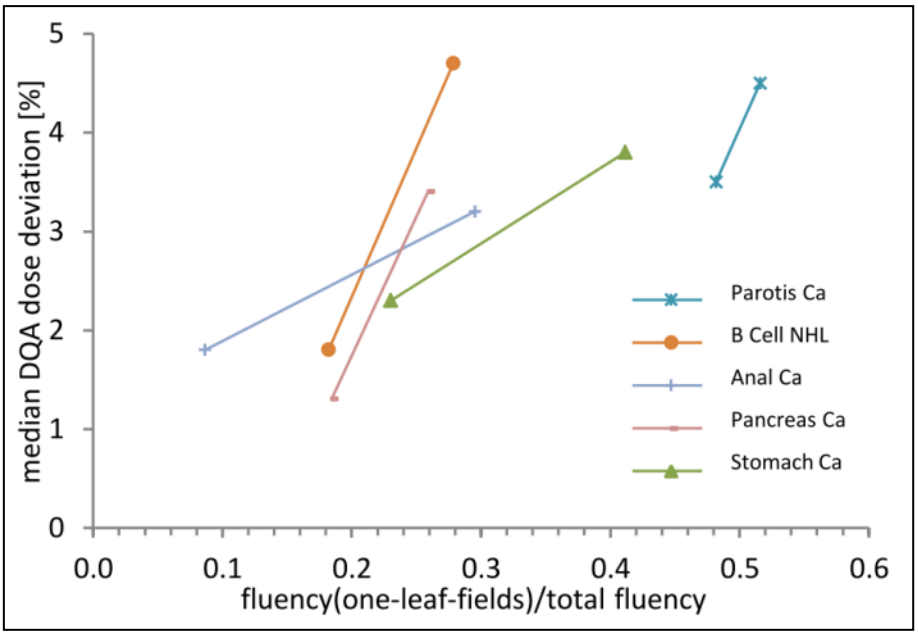

Fig. 2: Percentage of fluence delivered by fields with only one open leaf versus dosimetric error for five different indications and plans.

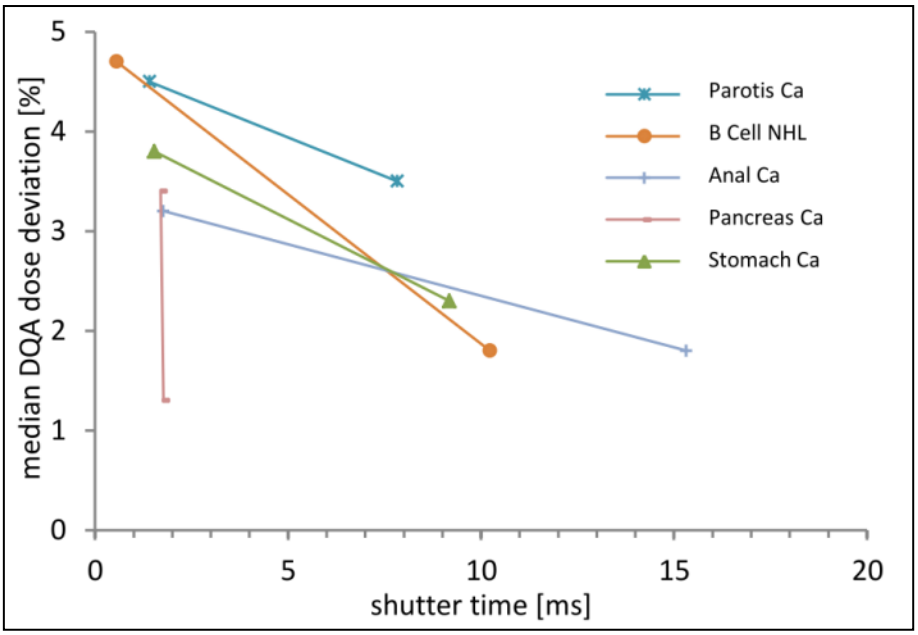

Fig. 3: Minimum close time of leaves versus dosimetric error for five different indications and plans.

References

[1] Langen KM, Papanikolaou N, Balog J, et al. QA for helical tomotherapy: report of the AAPM Task Group 148. Med Phys 2010;37:4817-4853

[2] Kissick MW, Mackie TR, Jeraj R. A delivery transfer function (DTF) analysis for helical tomotherapy. Phys Med Biol 2007;52:2355-2365

[3] Sterpin E, Verboomen C, Vynckier S. Impact of the number of discrete angles used during dose computation for TomoTherapy treatments. Medical Physics 2012;39:6947-6956

[4] Lissner S, Schubert K, Klüter S,. Untersuchung der Latencykorrektur eines binären MLC. Abstractband der 44 Jahrestagung der Deutschen Gesellschaft für Medizinische Physik 2013

[5] Lissner S, Schubert K, Klüter S, Oetzel D, Debus J. A method for testing the performance and the accuracy of the binary MLC used in helical tomotherapy. Z Med Phys 2013;23:153-161

[6] TomoTherapy User Meeting in Berlin 2014

P 30 Type B uncertainty contributions in Monte Carlo calculations caused by an X-ray target

F. Renner[1], R.-P. Kapsch[1]
[1]Physikalisch-Technische Bundesanstalt Braunschweig, Braunschweig, Germany

Introduction: At PTB`s research linear accelerator for dosimetry in radiation therapy [1] a benchmark experiment has been carried out. It aimed at the absolute verification of Monte Carlo (MC) calculations through the comparison of absorbed dose values. For the MC calculations a virtual copy of the experimental setup had to be constructed in the MC program. The uncertainty of an MC calculated result depends, among other things, on the restricted knowledge about the setup. This work deals with uncertainties in relation to the X-ray target used. The influences of the uncertainties were investigated beforehand to draw principal conclusions regarding the uncertainty of the MC calculation in connection with the benchmark experiment.

Materials and methods: For the investigations the MC program EGSnrc [2] was used. Since for general conclusions a simple rotationally symmetric geometry was adequate, the code dosrz [3] distributed with EGSnrc was used. As a radiation source a parallel beam of electrons with a radius of 0.2 cm was defined. The beam impinges perpendicularly on an X-ray target made of an alloy of tungsten and copper**.** The thickness, composition and density of the X-ray target were investigated as possible sources of uncertainty regarding absorbed dose. The absorbed dose was calculated for an air volume located 25 cm behind the target. A number of simulations were performed and their results were analysed regarding the change in absorbed dose.

Results: The results linked to the simulations regarding possible combinations of target composition and density are shown in fig. 1. The error bars represent the statistical uncertainties of the basic calculations. The first assumption was a composition of 80 % tungsten and 20 % copper (80/20) with a density of 14.47 g/cm³. Then the density was measured with high precision and a value of 14.4247(25) g/cm³ (k=2) was found. This value indicated that the composition of the material was 72/28 instead of 80/20. Another issue to investigate was the target thickness. It was determined by repeated measurements and also considered different measurement points. The result was a mean value of 3.875 mm and an experimental standard deviation s of 0.001 mm. MC simulations were performed with a target thickness of the mean value and with the mean thickness changed by $\pm 1 \cdot s$. The results and their statistical uncertainties are shown in fig. 2.

Conclusion: The results demonstrate that it is more important to know the exact composition than the density of the material of the X-ray target. Through the assumption that the composition of 72/28 is correct and by knowing the density very well, the uncertainty of the calculation of the absorbed dose is < 0.1 % and for this reason it was considered negligible in the context of the benchmark experiment. The variation of the target thickness by one standard deviation resulted in a change in absorbed dose> 0.1 %. Furthermore, the dose decreases with increasing thickness. Because of the amount of change and the systematic dependency of the dose on the target thickness, the influence of the target thickness on the uncertainty of the absorbed dose may be an important aspect regarding the uncertainty of the MC calculation in connection with the benchmark experiment.

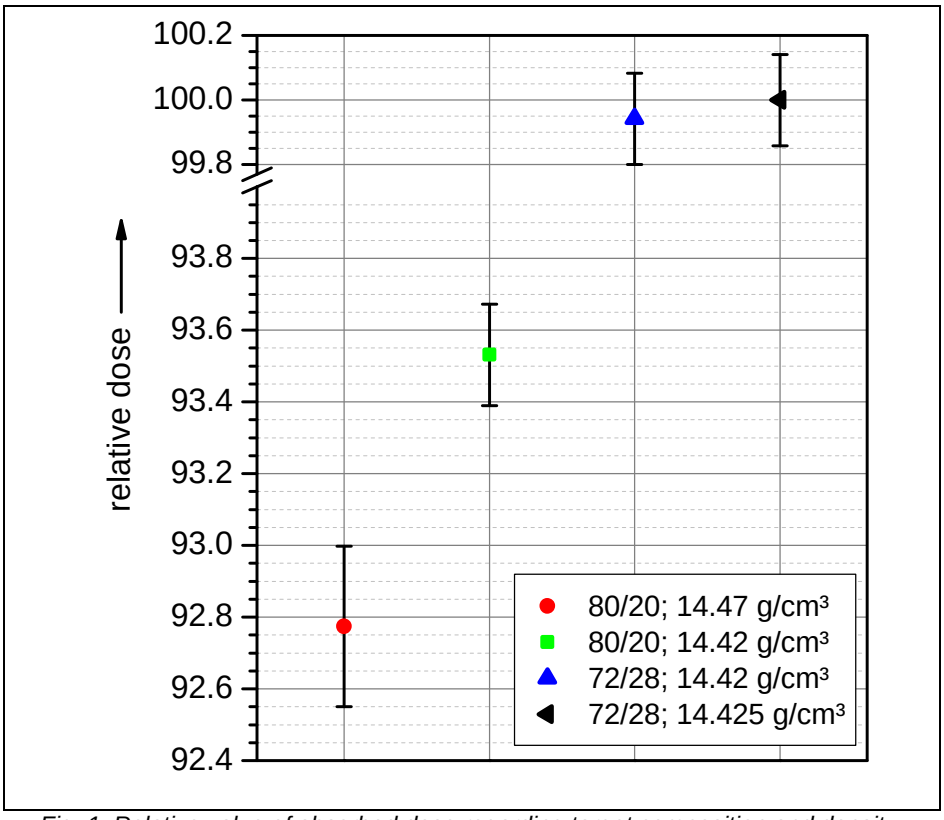

Fig. 1: Relative value of absorbed dose regarding target composition and density.

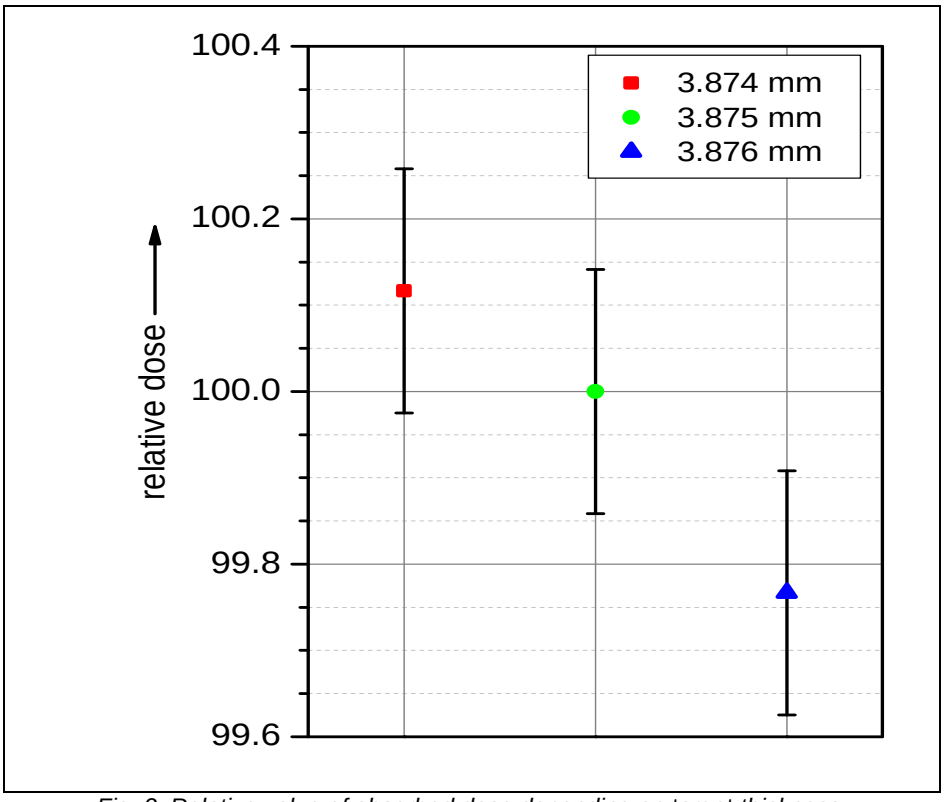

Fig. 2: Relative value of absorbed dose depending on target *thickness.*

References

[1] Derikum, K.: A Dedicated Irradiation Facility for Radiotherapy Dosimetry, in: O. Dössel and W. C. Schlegel (Eds.) WC 2009, IFMBE Proceedings 25/I, 2009, S. 53-55

[2] Kawrakow, I. et al.: The EGSnrc code system: Monte Carlo simulation of electron and photon transport, NRCC report PIRS-701, 2010

[3] Rogers, D. W. O. et al.: NRC User Codes for EGSnrc, NRCC report PIRS-702(revB), 2005

[4] International Atomic Energy Agency (IAEA): Measurement Uncertainty. IAEA-TECDOC-1585, Vienna, 2008

P 31 Comparison of the dosimetric impact of different CT datasets for stereotactic treatment planning using 3D-CRT or VMAT

M. Oechsner[1], L. Odersky[1,2], J. Wilkens[1], M. N. Duma[1]
[1]Klinikum rechts der Isar der TU Munich, Department of Radiation Oncology, Munich, Germany
[2]TU Munich, Department of Electrical Engineering and Information Technology, Munich, Germany

Introduction: In stereotactic body radiotherapy (SBRT) different concepts and CT datasets were proposed to delineate the planning target volume (PTV) [1,2]. In addition, 4D planning strategies were developed using 4DCT data and deformable image registration methods which are time consuming and not widely-used [3]. Therefore 3D planning is still clinical practice. Limited publications exist which compared the dosimetric impact of different 3DCT datasets for SBRT treatment planning [4,5].

The purpose of this study was to assess the dosimetric impact on PTV and organ dose for lung and liver SBRT by using four differently generated CT datasets for treatment planning with 3D conformal radiotherapy (3D-CRT) and volumetric modulated arc therapy (VMAT).

Materials and methods: Twenty SBRT patients, ten lung cases and ten liver cases, were retrospectively selected for this study. Each patient received a planning CT (PCT) and 4DCT scan. From the 10 phases of the 4DCT, an average intensity projection (AIP) and a maximum intensity projection (MIP) CT dataset were calculated using self-written programs in Matlab (MathWorks, Natick, MA, USA). Additionally, a mid-ventilation CT (MidV) [4] was selected by evaluating the tumor motion or diaphragm motion on the 4DCTs.

PTVs were generated by contouring the internal target volume on the phases of the 4DCT and adding a uniform margin of 5 mm. The PTVs were copied to the four generated CT datasets and lungs and liver were contoured.

For each patient two treatment plans were optimized on the AIP CT dataset using 3D-CRT (7-9 coplanar fields) or VMAT (2-3 partial arcs) techniques. The prescription dose was 5 Gy delivered in 7 fractions (prescribed to the 60% isodose level) with the 60% isodose surrounding the PTV (D_{min}) and 100% dose at the beam isocenter. Contouring and planning was performed with Eclipse 10 planning system (Varian Medical Systems, Palo Alto, CA, USA). The optimized plans were copied to the other CT datasets and doses were recalculated keeping all beam parameters and monior units unchanged.

Dosimetric parameters for PTV (D_{mean}, D_{min}, D_{max}, D_{95}), the ipsilateral lung and liver (D_{mean}, V_{20}) were determined on all CT datasets and statistical analysis was performed using paired t-test.

Results: Mean values over all patients for PTV are depicted in tab. 1. The largest differences were found for parameter D_{min} (in lung SBRT: -16.4% (MIP vs. AIP) and 23.8% (MidV vs. MIP); in liver SBRT: -6.1% (PCT vs. AIP) and 6.8% (MidV vs. PCT)). For all other PTV parameters differences between CT datasets were <3%. Nevertheless, some values showed significant differences ($p<0.05$). AIP and MidV achieved the best agreements. Overall VMAT plans resulted in smaller differences between the different CT datasets, especially for D_{min}.

Figure 1 and 2 depict D_{mean} an V_{20} for ipsilateral lung and liver dose over all patients. For the dose to the ipsilateral lung, largest differences were found in comparison to MIP (-5.5 – 7.8%). For all other CT sets, mean difference in lung dose was small (<1.3%) for both 3D-CRT and VMAT, but with standard deviations up to 7.7%. For the liver, larger differences were also found for AIP, MidV and PCT with smaller standard deviations than for the lung. MIP showed somewhat smaller differences. Only small differences appear between 3D-CRT and VMAT.

Conclusion: Except for D_{min}, only small differences were found for PTV parameters between the four CT datasets. PTV dose for VMAT plans was less affected by CT density changes than 3D-CRT plans. Larger differences were found for D_{mean} and V_{20} for lung and liver. These were especially pronounced for tumors located near to the diaphragm where breathing artifacts compromise organ contouring and tissue density is represented differently in the CT datasets.

lung SBRT	3D-CRT						VMAT					
[%]	PCT vs. AIP	MIP vs. AIP	MidV vs. AIP	MIP vs. PCT	MidV vs. PCT	MidV vs. MIP	PCT vs. AIP	MIP vs. AIP	MidV vs. AIP	MIP vs. PCT	MidV vs. PCT	MidV vs. MIP
ΔD_{mean}	-0.8 ± 0.5	1.3 ± 0.9	0.0 ± 0.3	2.1 ± 0.9	0.8 ± 0.7	-1.2 ± 0.7	-0.5 ± 0.5	1.4 ± 1.2	-0.1 ± 0.3	2.0 ± 1.0	0.5 ± 0.6	-1.4 ± 1.1
ΔD_{min}	-4.2 ± 2.4	-16.4 ± 15.7	-0.1 ± 1.1	-12.8 ± 16.1	4.4 ± 3.2	23.8 ± 25.4	-2.1 ± 1.8	-4.9 ± 7.9	0.1 ± 0.9	-2.7 ± 8.3	2.3 ± 2.2	5.8 ± 8.2
ΔD_{max}	-0.5 ± 0.5	0.7 ± 0.9	-0.1 ± 0.5	1.2 ± 1.1	0.4 ± 0.7	-0.8 ± 1.2	0.1 ± 1.0	3.0 ± 1.6	0.4 ± 0.7	2.9 ± 1.3	0.3 ± 1.4	-2.5 ± 1.7
ΔD_{95}	-1.3 ± 0.3	-1.4 ± 3.3	0.2 ± 0.4	0.4 ± 2.8	1.5 ± 0.5	1.2 ± 2.6	-0.9 ± 0.4	-0.6 ± 2.7	0.0 ± 0.4	0.3 ± 2.8	0.9 ± 0.4	0.7 ± 2.6
liver SBRT												
ΔD_{mean}	-0.5 ± 0.7	-1.3 ± 0.4	0.0 ± 0.3	-0.8 ± 1.0	0.5 ± 0.9	1.4 ± 0.3	-0.4 ± 0.5	-0.9 ± 0.7	0.1 ± 0.4	-0.8 ± 0.6	0.4 ± 0.6	1.1 ± 0.3
ΔD_{min}	-6.1 ± 5.0	-4.1 ± 3.9	0.0 ± 0.9	2.4 ± 6.9	6.8 ± 5.8	4.5 ± 5.0	-0.8 ± 1.0	-0.6 ± 1.2	0.0 ± 1.0	-0.1 ± 0.9	1.4 ± 0.9	1.6 ± 1.0
ΔD_{max}	-0.3 ± 0.5	-1.5 ± 0.6	-0.6 ± 1.0	-1.2 ± 1.0	-0.3 ± 1.4	0.9 ± 0.7	-0.3 ± 0.8	-1.1 ± 0.7	-0.2 ± 0.5	-1.3 ± 1.0	-0.2 ± 1.1	1.1 ± 0.3
ΔD_{95}	-0.7 ± 0.8	-1.6 ± 1.1	0.4 ± 0.6	-0.9 ± 1.8	1.1 ± 0.9	2.0 ± 1.3	-0.5 ± 0.4	-0.8 ± 0.6	0.1 ± 0.3	-0.6 ± 0.6	0.5 ± 0.5	1.1 ± 0.3

Tab. 1: Relative differences over all patients (mean ± standard deviation) of dosimetric values for PTV between the different CT datasets for 3D-CRT and VMAT plans.

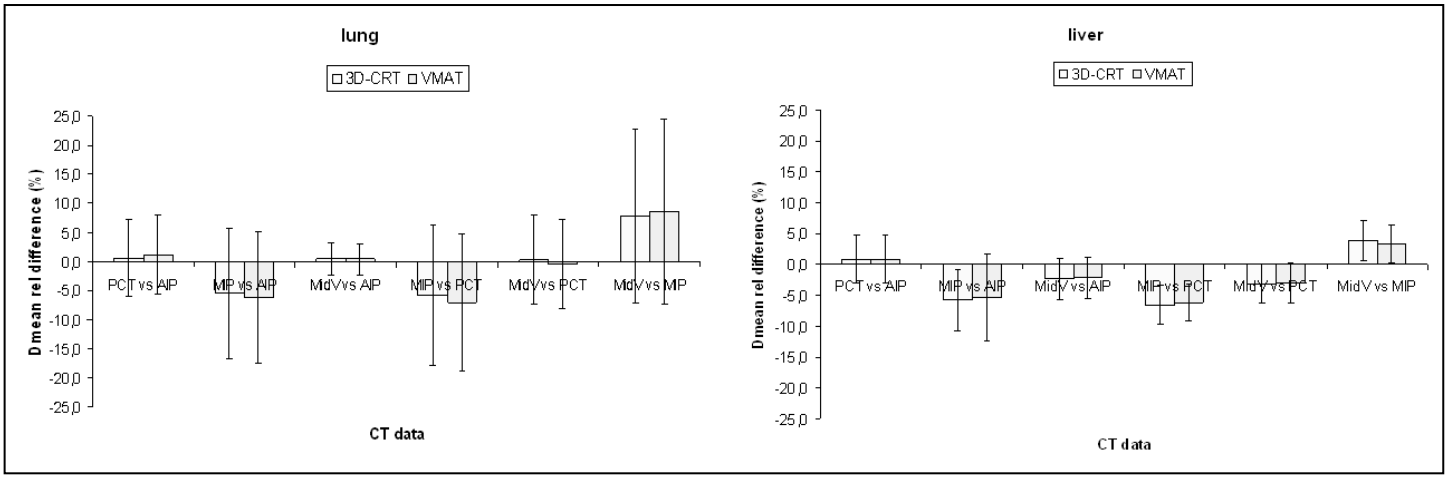

Fig. 1: Relative differences of D_{mean} over all patients (mean ± standard deviation) of the ipsilateral lung and liver dose between the CT datasets for 3D-CRT and VMAT plans.

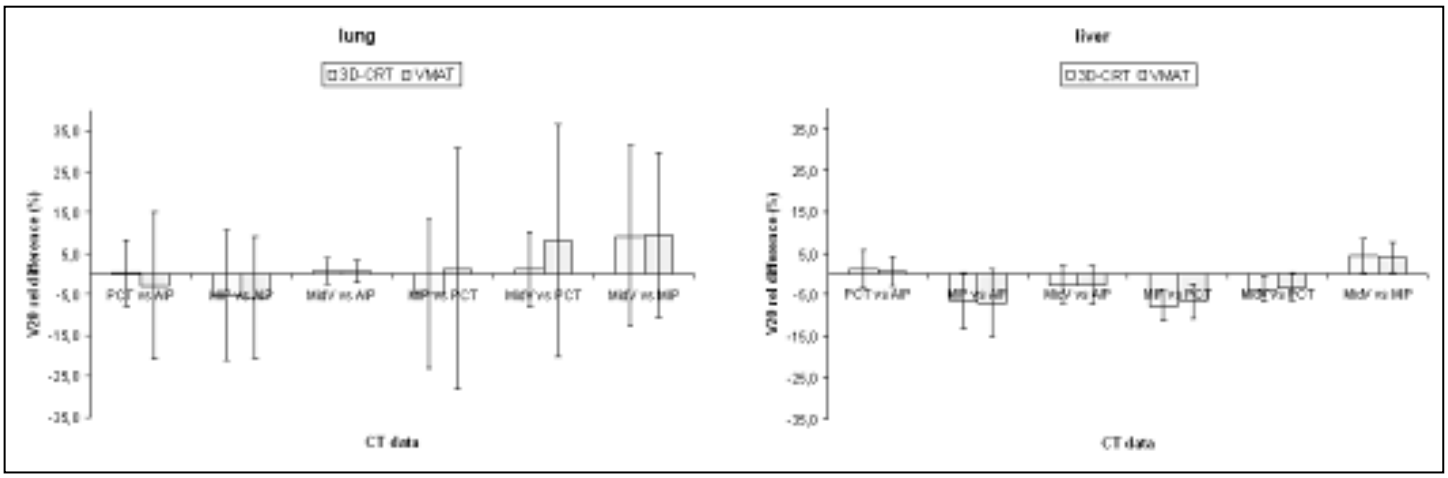

Fig. 2: Relative differences of V_{20} over all patients (mean ± standard deviation) of the ipsilateral lung and liver dose between the CT datasets for 3D-CRT and VMAT plans.

References

[1] Bradley D. et al.: Comparison of helical, maximum intensity projection (MIP), and averaged intensity (AI) 4D CT imaging for stereotactic body radiation therapy (SBRT) planning in lung cancer. Radiother. Oncol. 81, 264-268 (2006).

[2] Underberg R.W. et al.: Use of maximum intensity projections (MIP) for target volume generation in 4DCT scans for lung cancer, Int. J. Radiat. Oncol., Biol., Phys. 63, 253-260 (2005).

[3] Glide-Hurst C. K. et al.: A simplified method of four-dimensional dose accumulation using the mean patient density representation. Med. Phys. 35(12), 5269–5277 (2008).

[4] Wolthaus J.W.H. et al.: Mid-ventilation CT scan construction from four-dimensional respiration-correlated CT scans for radiotherapy planning of lung cancer patients. Int. J. Radiat. Oncol. Biol. Phys. 65(5), 1560-1571 (2006).

[5] Tian Y. et al.: Dosimetric comparison of treatment plans based on free breathing, maximum, and average intensity projection CTs for lung cancer SBRT. Med. Phys. 39(5), 2754-2760 (2012).

P 32 Application of an Elekta Precise BEAMnrc model with dynamic multileaf collimators for the Monte Carlo simulation of dynamic radiotherapy treatment plans

O. Schrenk[1], D. Czarnecki[1], K. Zink[1,2]
[1]Institute of Medical Physics and Radiation Protection, Gießen, Germany
[2]University Medical Center Marburg, Department of Radiotherapy and Radiation Oncology, Marburg, Germany

Introduction: Model based photon dose calculations used in treatment planning systems are known to be inaccurate when it comes to heterogeneities in media where the effect of electron transport cannot be accurately determined [1]. Fogliati et al. [2] state that dose calculation algorithms in treatment planning show significant discrepancies of dose in lighter materials compared to the Monte Carlo gold standard. Furthermore the impact of the inaccuracy to highly conformal dose distribution due to the combinatorial effect of many small fields and steep fluence gradients is expected to be higher [3].

Two new DOSXYZnrc sources for the 4D Monte Carlo simulation presented by Lobo et al. [4] improve the possibilities to model linear accelerator with dynamic multileaf collimators (MLC). This enables the simulation of intensity modulated radiotherapy methods (IMRT) for the examination of dose distribution with EGSnrc.

In this work a BEAMnrc beam model with dynamic MLC was validated with data calculated from a phase space file (PHSP) of the IAEA database [5]. Subsequently the validated BEAM model was used to proof the concept by calculating a dose distribution using dynamic Monte Carlo simulation of a wedge in a water phantom.

Material und Method: All Monte Carlo calculations were performed with the EGSnrc/BEAMnrc code system [6, 7]. The Elekta Precise 6 MV accelerator head was modeled in detail based on technical drawings supplied by the manufacturer. The MLC was modeled using the dynamic MLC module (SYNCMLCE) integrated into BEAMnrc. Calculations of dose profiles in 10 cm depth with source surface distance of 100 cm and the percentage depth dose were performed with egs_chamber [8,9] for a field size of 10 cm x 10 cm. Additionally the spectral distributions and energy fluence versus position were determined from PHSP with BEAMdp [7]. The BEAM results were compared with simulations using the IAEA ELEKTA_PRECISE_6mv [5] PHSP as a source located between monitor chamber and MLC.

The dose calculation of the wedge was accomplished using DOSXYZnrc [10] where the BEAMnrc model was synchronized to the DOSXYZnrc simulation. To show the possibilities of dynamic sources a dynamic wedge with 45° was simulated. The fluence for the 10x10 cm^3 field was modulated by 10 MLCs opening steadily from the mid position to one side until a field size of 10 cm was reached. The dose distribution was calculated in a 40x40x35 cm^3 phantom with source surface distance of 90 cm. ECUT was set to 0.7 MeV and PCUT to 0.01 MeV.

Results: The Elekta Precise linear accelerator model was verified with the calculations using the IAEA PHSP as source. Dose profiles and percentage depth dose of the BEAMnrc model and IAEA PHSP simulation were directly compared in figure 1. The deviations of the percentage depth dose and dose profiles are less than 0.5 %. In addition the energy fluence versus position (Fig. 1c.) and spectral distribution (Fig. 1d.) in 27.21 cm distance to the target was examined. The dynamic wedge calculation presented in figure 2 was performed with a statistical uncertainty of less than 0.5 % for all dose points greater than half of the maximum dose.

Conclusion: The results show good agreement between the BEAMnrc model and the IAEA simulations for dose profiles and percentage depth dose as well as for the spectral distribution and energy fluence. Moreover a commissioning of the model with clinical measurements is currently conducted to improve its reliability. The wedge simulation shows the feasibility of the dynamic sources in EGSnrc. The future aim of this work is the implementation of intensity modulated therapy methods with higher complexities into the BEAMnrc system to examine highly conformal dose distributions in heterogeneous media.

References

[1] Chetty et al.: Report of the AAPM Task Group No. 105: Issues associated with clinical implementation of Monte Carlo-based photon and electron external beam treatment planning, Med. Phys., vol. 34, no. 12 (Dec. 2007), pp. 4818–53
[2] Fogliata et al.: On the dosimetric behaviour of photon dose calculation algorithms in the presence of simple geometric heterogeneities: comparison with Monte Carlo calculations, Phys. Med. Biol., vol. 52 , no. 5 (Mar. 2007), pp. 1363–85
[3] American Association of Physicists in Medicine (AAPM), and Radiation Therapy Committee. Task Group 65.: Tissue Inhomogeneity Corrections for Megavoltage Photon Beams, AAPM report No. 85

[4] Lobo, J. and. Popescu, I. A.: Two new DOSXYZnrc sources for 4D Monte Carlo simulations of continuously variable beam configurations, with applications to RapidArc, VMAT, TomoTherapy and CyberKnife, Phys. Med. Biol., vol. 55, no. 16 (Aug. 2010), pp. 4431–43
[5] R. Capote.: Phase-space database for external beam radiotherapie 2011. [Online]. Available: *www-nds.iaea.org/phsp/photon1*
[6] Kawrakow et al.: The EGSnrc code system: Monte Carlo simulation of electron and photon transport, NRCC Report PIRS-701 (2003), National Research Council of Canada, Ottawa, Canada
[7] Rogers, D. W. O., Walters, B. R. B., Kawrakow, I. .: BEAMnrc Users Manual, NRCC Report PIRS-0509(A)revL (2001), National Research Council of Canada, Ottawa, Canada
[8] Kawrakow I.: NRCC Report PIRS-898, National Research Council of Canada, (2006), Ottawa, Canada
[9] Wulff, J., Zink, K., & Kawrakow, I. (2008). Med. Phys. 35(4), 1328-1336
[10] Walters, B., Kawrakow, I., & Rogers, D. W. O.: DOSXYZnrc users manual. (2005) NRC Report PIRS, 794

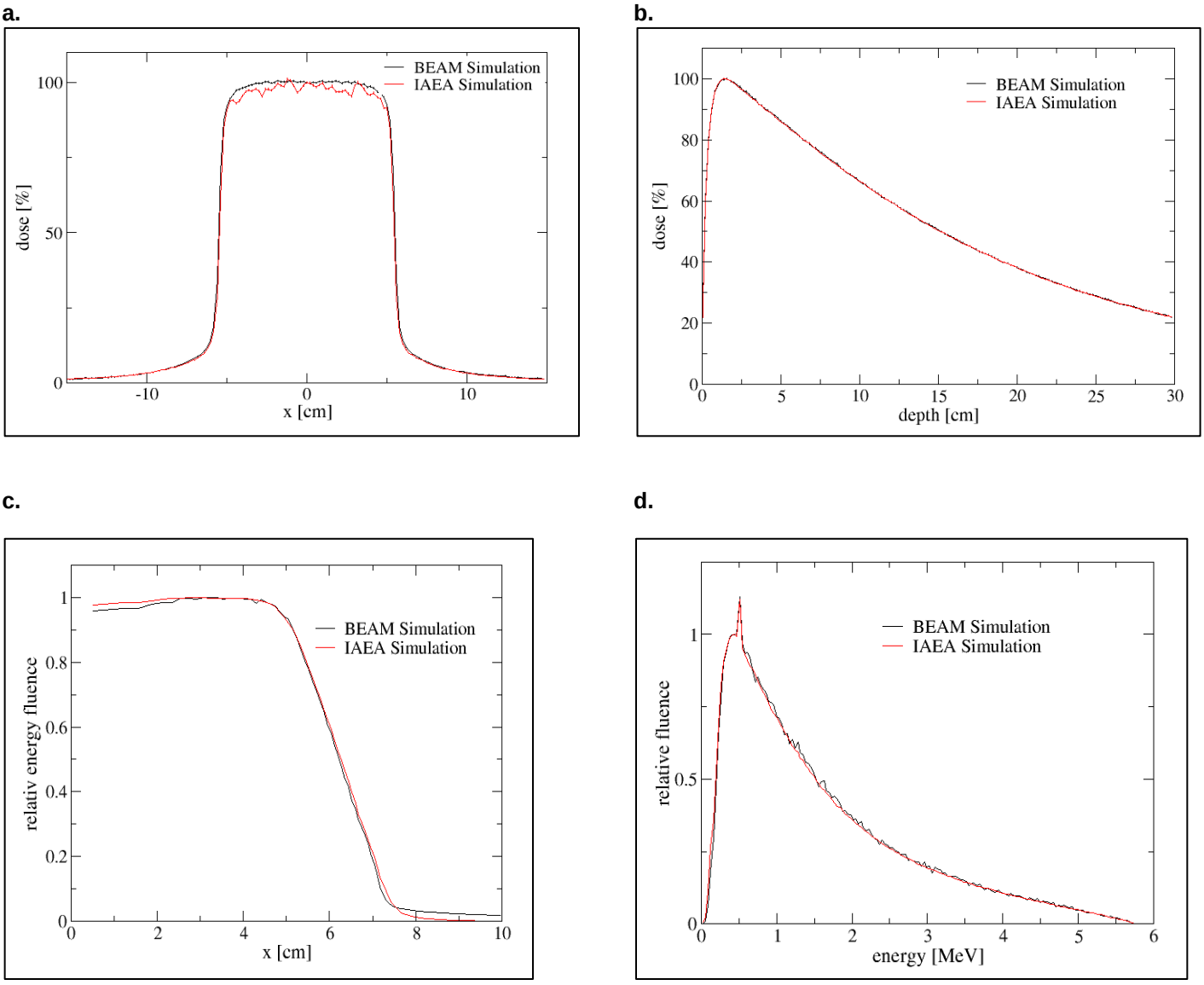

Fig. 1: Comparison of calculated data between the created BEAMnrc model (gray) and an IAEA phase pace file (red) of an Elekta Precise 6 MV-X model as beam source a.: Normalized dose cross profile in a water phantom calculated for a field size of 10 cm x 10 cm in the depth of 10 cm. b.: Percentage depth dose of a 10 cm x 10 cm field in a water phantom. c.: Spectral distribution in 27.21 cm distance to the target. d.: Energy fluence plotted versus position in 27.21 cm distance to target. All graphs show results from the BEAMnrc Elekta Precise model in 6 MV mode (gray) and results simulated with the IAEA ELEKTA_PRECISE_6mv phase space file as source (red).

P 33 *Validation of Swiss Monte Carlo Plan (SMCP) for Out-of-Field Photon Dose Calculation*

E. Marín[1], D. Henzen[1], D. Schmidhalter[1], P. Manser[1], M. Fix[1]
[1]Inselspital Bern, Zurich, Switzerland

Introduction: Currently, Swiss Monte Carlo Plan (SMCP) is validated regarding photon dose calculations in patients for in-field situations [1]. However, calculated out-of-field dose distributions still need further validation. Thus, the aim of this work is to compare calculated and measured dose profiles for various photon fields.

Materials and methods: The validation of SMCP is based on measurements using an Alderson phantom. The photon fields were setup such that their isocenter is placed in the head and neck region, typically close to the left eye. Static 6 MV and 15 MV fields with different field sizes were applied on a Novalis TX (Varian Medical Systems). The out-of-field dose was measured by an ionization chamber, which was placed at distances from 25 cm to 55 cm to the isocenter.

The corresponding situations were also simulated using the SMCP framework. The statistical uncertainty in the high dose region was 0.1% and a voxel size of 0.4 cm in all directions was chosen for the calculations.

Results: The results demonstrate that, in general, there is a good agreement between SMCP dose calculations and corresponding measurements. For distances larger than 30 cm from the isocenter, the local relative error was less than 60% for all configurations. For the 6 MV 10x10 cm^2 field configuration, the mean relative error was less than 5%. For the 6 MV 6x6 cm^2 and for the 15 MV 6x6 cm^2 configuration, the mean relative error was less than 20% for distances larger than 30 cm.

Conclusions: Although local and systematic discrepancies were observed depending on the field configuration, the SMCP calculated dose distributions provide a suitable estimation of the dose in the out-of-field situations. The observed differences indicate that there might be additional shielding components in the linac treatment head which has not been considered in the SMCP simulations so far.

Conflict of Interest: The development of SMCP has been supported by Varian Medical Systems

References

[1] V. Magaddino, P. Manser, D. Frei, W. Volken, D. Schmidhalter, L. Hirschi, M. K. Fix, *Validation of the Swiss Monte Carlo Plan for a static and dynamic 6 MV photon beam,* Z. Med. Phys. 21, 2011.

P 34 Accuracy of out-of-field dose values – comparison between measurements and calculations of two different treatment planning systems

J. Remmele[1], U. Wolf[1]
[1]Universitätsklinikum Leipzig, Klinik für Strahlentherapie und Radioonkologie, Leipzig, Germany

Introduction: Treatment planning systems (TPS) in radiotherapy are able to calculate the absorbed dose in the primary field with a high grade of accuracy. For personalized risk assessment of secondary cancers and late effects after radiotherapy, the absorbed dose outside the primary beam also has to be considered. Dose outside the primary beam results from scattering processes inside the patient, headscattered and leakage radiation [1]. These complex processes have to be modeled by the TPS to match reality. The present study investigates the reliability of two different commercial TPS in calculating out-of-field doses from simple fields and treatment plans in case of breast cancer.

Materials and methods: To investigate the dose calculation accuracy outside the primary field of the TPS Oncentra Masterplan (OTP) and Raystation (RS) two phantoms were used: a simple cubic phantom and a complex one. The simple phantom consists of RW3 with dimensions of 30x30x22cm^3. The measuring plane is an ionization chamber array from PTW (Array 729). The dose distribution is measured in 10 cm depth. This configuration allows the measurement in homogeneous case. The geometry of the simple phantom was modeled by the two planning systems. Radiation fields from a LINAC with 6 MV photons (Primus-Siemens) and field sizes of 5x5 cm², 10x10 cm², 20x20 cm², 10x20 cm² with and without wedge compensation were measured. Additionally radiation fields of 10 MV with flattening filter (FF) and 7 and 11 MV photon energy without flattening filter (FFF) from an Artiste-LINAC (Siemens) were investigated. The local differences between measured and calculated out-of-field dose values of the planning systems in crossplane direction were examined. To evaluate the reliability of the TPS in a more complex geometry a thorax phantom made of Obomodulan® was designed (figure 1), which allows the simulation of breast irradiations. Obomodulan® is based on polyurethane and is available in different densities. Three densities were used to simulate soft tissue (Obomodulan® "crème" ρ= 0.95 g/cm³), bone (Obomodulan® "sand" ρ= 1.6 g/cm³) and lung tissue (Obomodulan® "hellgrau" ρ= 0.2 g/cm³) [2]. The phantom offers the possibility to determine dose values within several inserts for different detectors. A CT-Series (Somatom Emotion, Siemens Medical systems) was used to generate three different treatment plans: a conventional plan with wedge compensation and 6 MV (Primus), a simple plan with open fields and 6 MV (Primus), as well as an IMRT plan with 7 MV flattening filter free beams (Artiste). Measurements were carried out using an ionization chamber (Semiflex 0,125 cm³, PTW Freiburg) on selected points in the thorax phantom in-field and out-of-field.

Results: The results from the measurements in the simple case with the 2D-Array are shown in figures 2, 3, 4, 5. The investigated planning systems show a different behavior in out-of-field dose calculation. While OTP tends to underestimate the out-of-field dose with increasing distance to the field border in case of experiments with Primus, RS overestimates the dose outside the primary field in case of wedge compensation. The out-of-field dose of a 10x10 cm² field is represented well by RS. The experiments using Artiste show an overestimation by OTP for beams with flattening filter and an underestimation of out-of-field dose in case of beams without flattening filter. In contrast to this, RS shows an inconsistent behavior at the tested cases on Artiste.
The results of measurements in complex geometry with the thorax phantom are shown in figures 6, 7, 8. The in-field deviations never exceed 3 % between measured and calculated values. It is clearly evident, that the two TPS under investigation show a quite contrary behavior in calculating out-of-field doses. The experiments on Primus indicate an underestimation by OTP in calculating out-of-field doses in most cases, whereas RS overestimates the local dose outside the primary beam. There is no large influence on the dose calculation accuracy in OTP with absence of wedges. On the other hand RS shows a significant improvement in accuracy, when the treatment plan is designed without wedges. This was also observed in the studies with the slab phantom. The observed local dose differences for the IMRT plan and beams without flattening filter show an improved accuracy for OTP and partly for RS. These results could be explained by the lower peripheral dose, which occurs in beams without flattening filter because of a decreased head scatter a much smaller amount of transmitted radiation [3].

Conclusion: The large discrepancies between measured and calculated values may have several reasons. First they could be explained by the individual beam commissioning process in the TPS. Second, the TPS use different algorithms for dose calculation and for describing the head scatter of the LINAC. Modelling of the peripheral dose in the TPS is only a simplified simulation of the complex interaction physics. Even with a commissioning process which is targeted on out-of-field areas, modelling of the peripheral dose through the TPS is not optimal. When using dose values of a TPS for risk assessment of secondary cancers and late effects after radiotherapy, it is necessary to understand and evaluate the potential inaccuracies of dose calculation outside the treatment field individually.

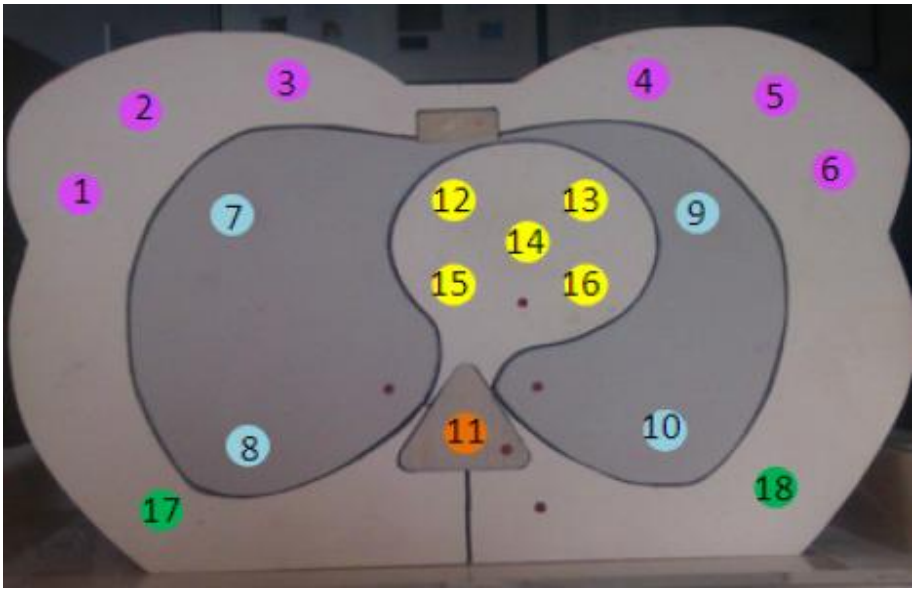

Fig. 1: Transversal slice of the thoraxphantom with possible measurement points

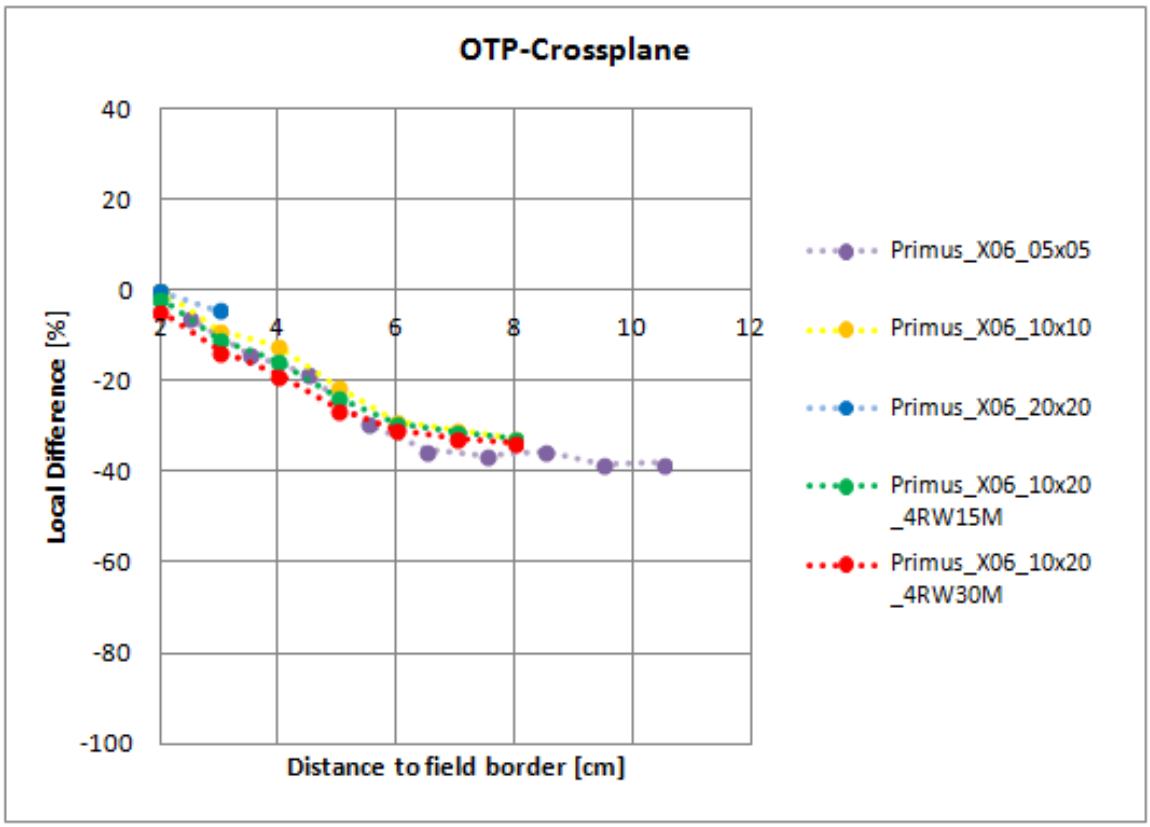

Fig. 2: Mean local differences between measurement and calculation of OTP, Primus

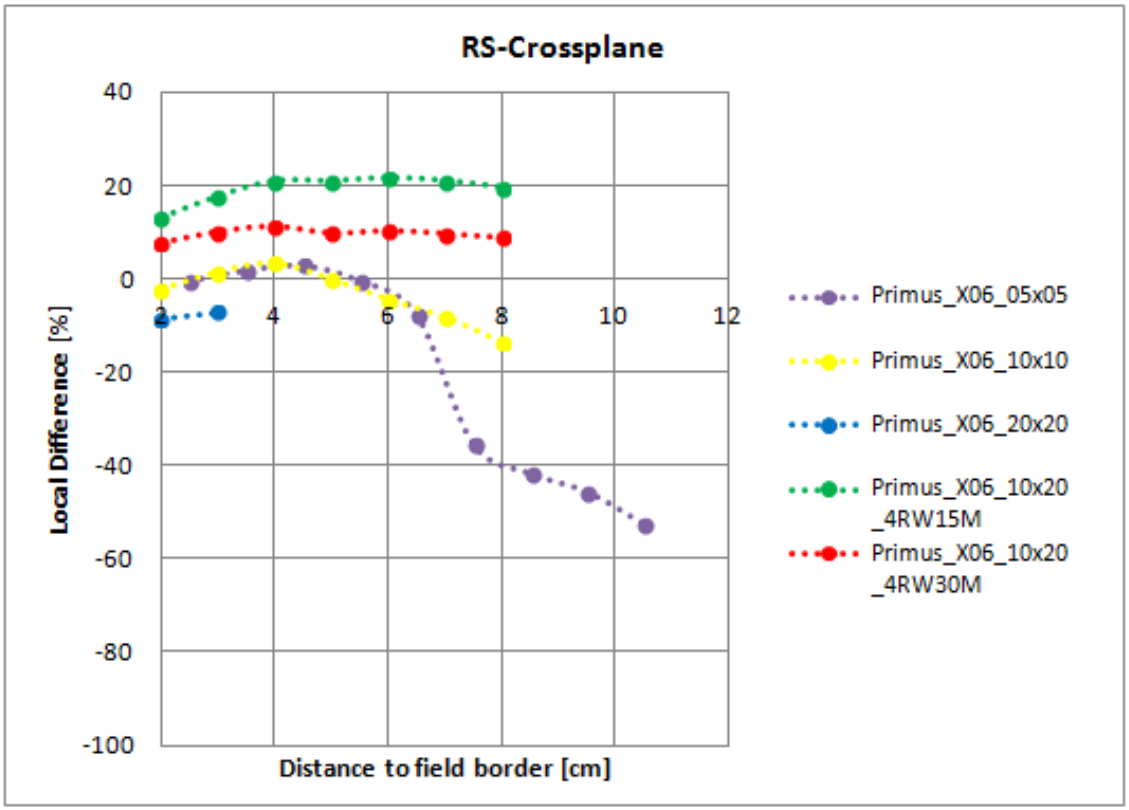

Fig. 3: Mean local differences between measurement and calculation of RS, Primus

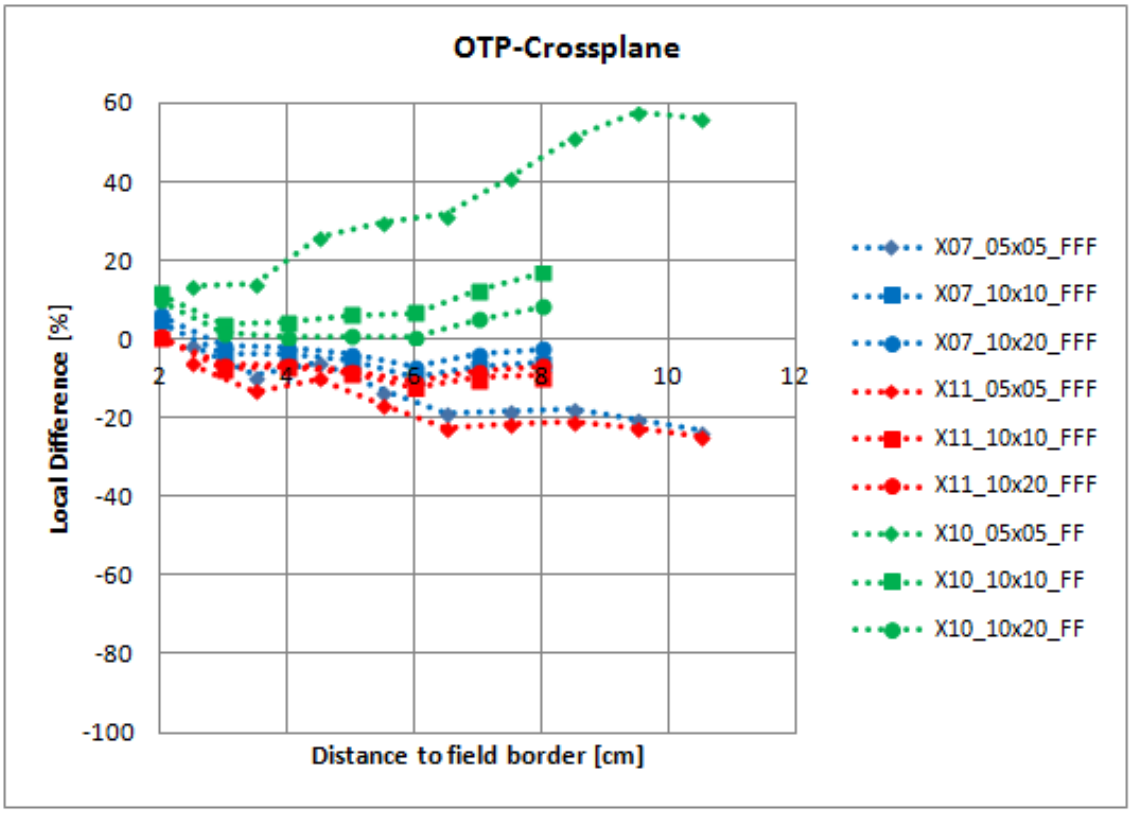

Fig. 4: Mean local differences between measurement and calculation of OTP, Artiste

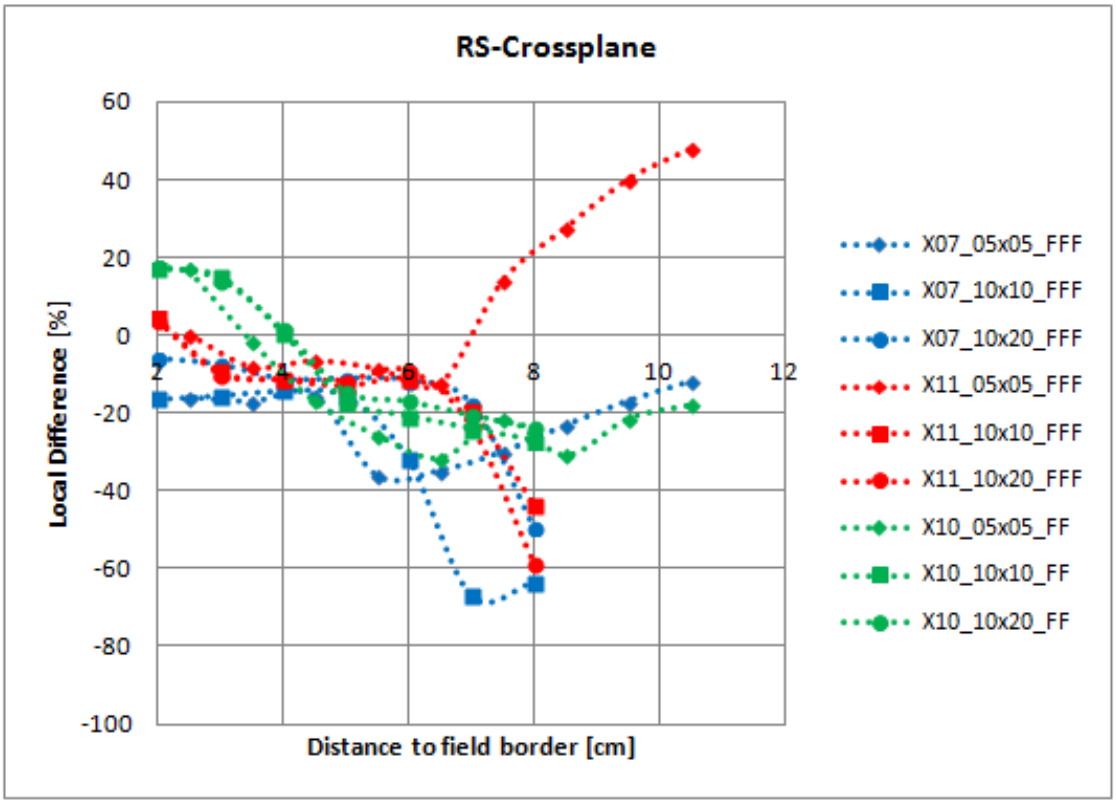

Fig. 5: Mean local differences between measurement and calculation of RS, Artiste

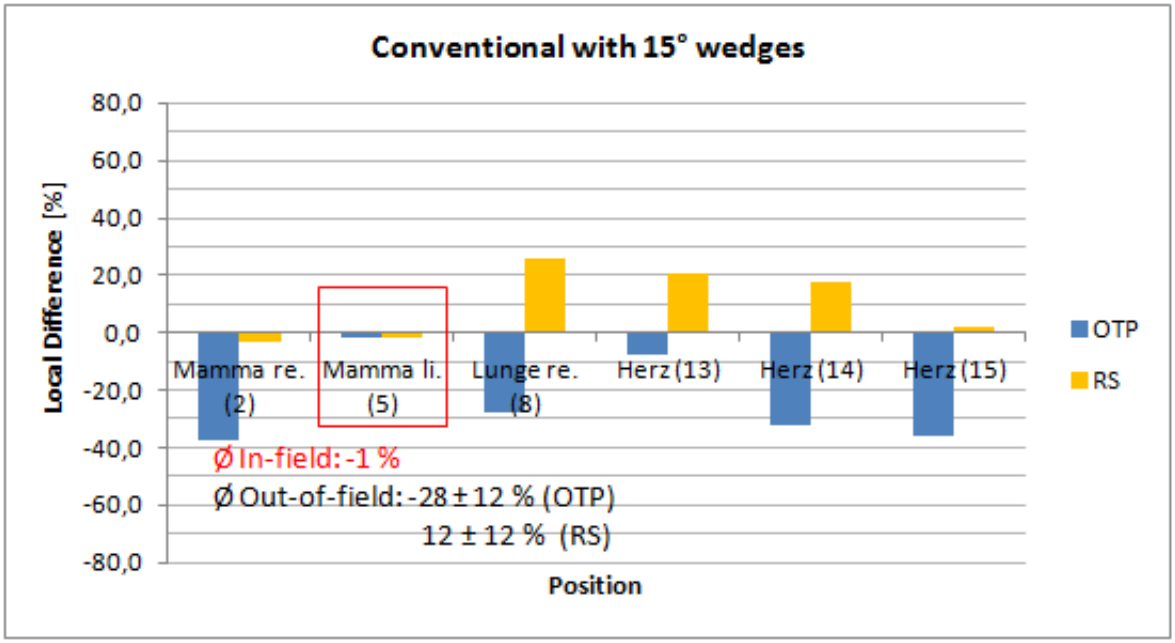

Fig. 6: Local differences between measurement and calculation in the complex case, conventional with wedges

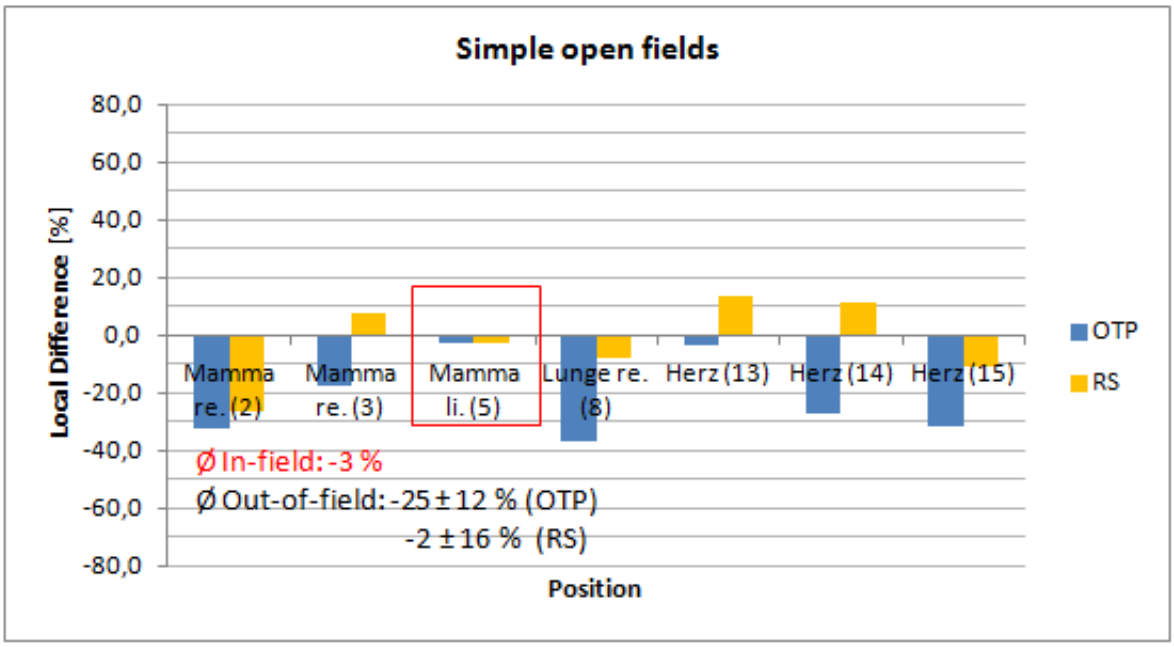

Fig. 7: Local differences between measurement and calculation in the complex case, simple open fields

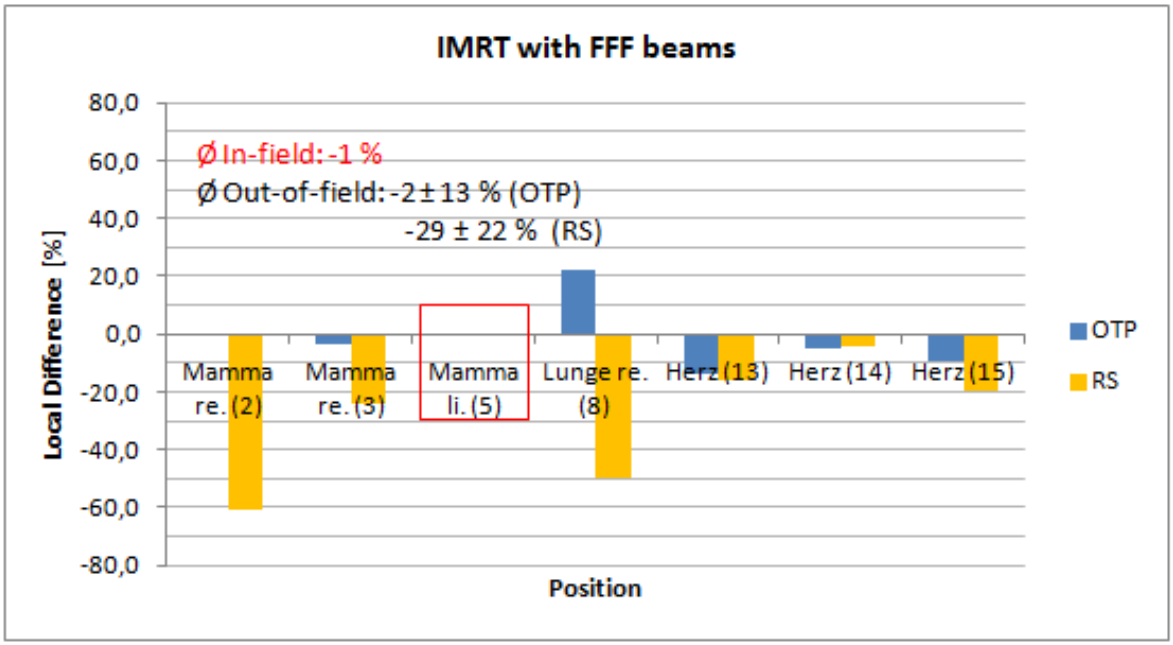

Fig. 8: Local differences between measurement and calculation in the complex case, IMRT

References

[1] Chofor, N.: Internal Scatter, the unavoidable major component of the peripheral dose in photon-beam radiotherapy. Physics in Medicine Biology, 2012, 57, 1733-1743

[2] Flyer-Obomodulan: http://www.obo-werke.de/files/obo-werke.de/pdf/obomodulan_pros_gb_10-2012.pdf

[3] Kry, S.: Out-of-field photon dose following removal of the flattening filter from a medical accelerator. Physics in Medicine Biology, 2010, 55, 2155-2166

[4] Howell, R.: Accuracy of out-of-field-dose calculations by a commercial treatment planning system. Physics in Medicine Biology, 2010, 55(23), 6999-7008

P 35 Dosimetric comparison of Acurus XB dose calculation algorithm with the Anisotropic Analytical Algorithm for different treatment sites

A. Stüssi[1], S. Lang[1], M. Zamburlini[1], S. Verlaan[1], S. Ehrbar[1], S. Klöck[1]
[1]University Hospital Zurich, Radio-Onkologie, Zurich, Switzerland

Purpose: Several authors have shown that the Acuros algorithm (Varian Medical Systems), which is based on the linear Boltzmann transport equation is more accurate in predicting the dose in inhomogeneous media compared to Anisotropic Analytical Algorithm (AAA, Varian Medical Systems) algorithm [1]. However clinical experience concerning tolerance doses to organs at risk as well as dose to the planning target volume is based on pencil beam or convolution algorithms, such as the AAA algorithm. Therefore we've evaluated the difference between the Acuros algorithm scored in water (AcurosWater), the Acuros algorithm scored in medium (AcurosMedium) and the AAA algorithm for various treatment sites.

Materials and methods: In total 33 treatment plans previously treated in our clinic using volumetric modulated arc therapy (VMAT) were recalculated using AAA and AcurosWater and AcurosMedium (all Version 11) in the Eclipse treatment planning system (Varian Medical Systems). Different anatomical regions were evaluated (5 sarcoma, 5 prostate tumours, 9 lung lesions, 8 intracranial lesions, 6 vertebral bodies). The influence of the calculation algorithm was determined by comparing the mean dose, maximum dose and minimum dose to the planning target volume (PTV) and the gross tumor volume (GTV). Additionally mean and maximum doses to various organs at risk (OAR) were compared.

Results: The dose calculated in bony structures was generally lower for AAA compared to Acuros scoring dose to water and slightly higher for Acuros scoring dose to medium. The opposite was true for the dose in lung tissue and air cavities. The differences were small in soft tissue (mean deviation less than 3%) and in lung tissue (mean deviation less than 3%), however were larger in the bony structures (a mean deviation of 15% between Acuros scoring to water and scoring to tissue). The differences in bony structures were increasing with increasing electron density (Hounsfield units).

Conclusion: The Acuros dose calculation more accurately estimates the applied dose compared to conventional algorithms. Since the tolerance doses to organs at risk as well as dose to the planning target volume is based on pencil beam or convolution based algorithms, the question arises how to implement Acuros into clinical routine. The large differences in dose to bone tissue between Acuros and the AAA Algorithm cannot be neglected and the physicians need to get used to the new estimated dose to bone and they would need to adapt their tolerance doses.

References

[1] Kan et al: Med Phys, 39 (2012), S. 4705-4714.

P 36 VMAT dosimetry comparison between 6 MV and 15 MV using Pinnacle and Elekta Agility

C. Tamburella[1], G. Guibert[1], M. Notter[1], P. Weber[1]
[1]Hopital Neuchatelois, La Chaux de Fonds, Switzerland

Introduction: In conformal 3D radiotherapy plans, the 15MV photon beam energy is mainly used for dosimetry of deep tumors or for large people. With the VMAT rotational technique, the 6MV beam is widely used to calculate a dosimetry. In this study, we try to evaluate if the 15MV VMAT can provide dosimetries with a better PTV coverage and reduce the dose to organs at risk especially for obese patients.

Materials and methods: Several plans for prostate and vertebral column were generated for some large patients on Philips Pinnacle 9.2 treatement planning system. All these plans have been delivered on the Agility linac for both 6MV and 15 MV. The dosimetry has been measured on PTW Octavius 4D, and analyzed with PTW Verisoft, using the gamma index pass fail test of 3% / 3mm.

Results: For all prostate cases, the Dose Volume Histrograms (DVH) for 6MV and 15MV dosimetry plans did not show major differences for PTV and OAR, even for larger patients. This is mainly due to the diameter of the body which becomes smaller in this region and makes no such difference of size beetween patients. A difference can be observed for vertebral columns plans on large patients, for isodoses below 30% of the maximum dose. There is clearly a contraction of these isodoses for the 15MV plan in the direction of the PTV, which can better protect critical organs surrounding the PTV volume (Figure1). All the 15 MV VMAT plans have been measured on the PTW Octavius 4D and reached the gamma index criteria of 3% and 3mm.

Summary: 15MV VMAT does not create a significant improvement in the dosimetry of prostate plans, but we did not have extremely obese patients. For tumours located in a deeper region of the body, it was possible to observe a faster decrease of the peripheral dose at 15MV, when compared to 6MV plans. However, neutron dose still needs to be measured before using 15 MV rotational techniques and may be the limiting factor using higher energies, especially if the therapeutic gain will be minimal.

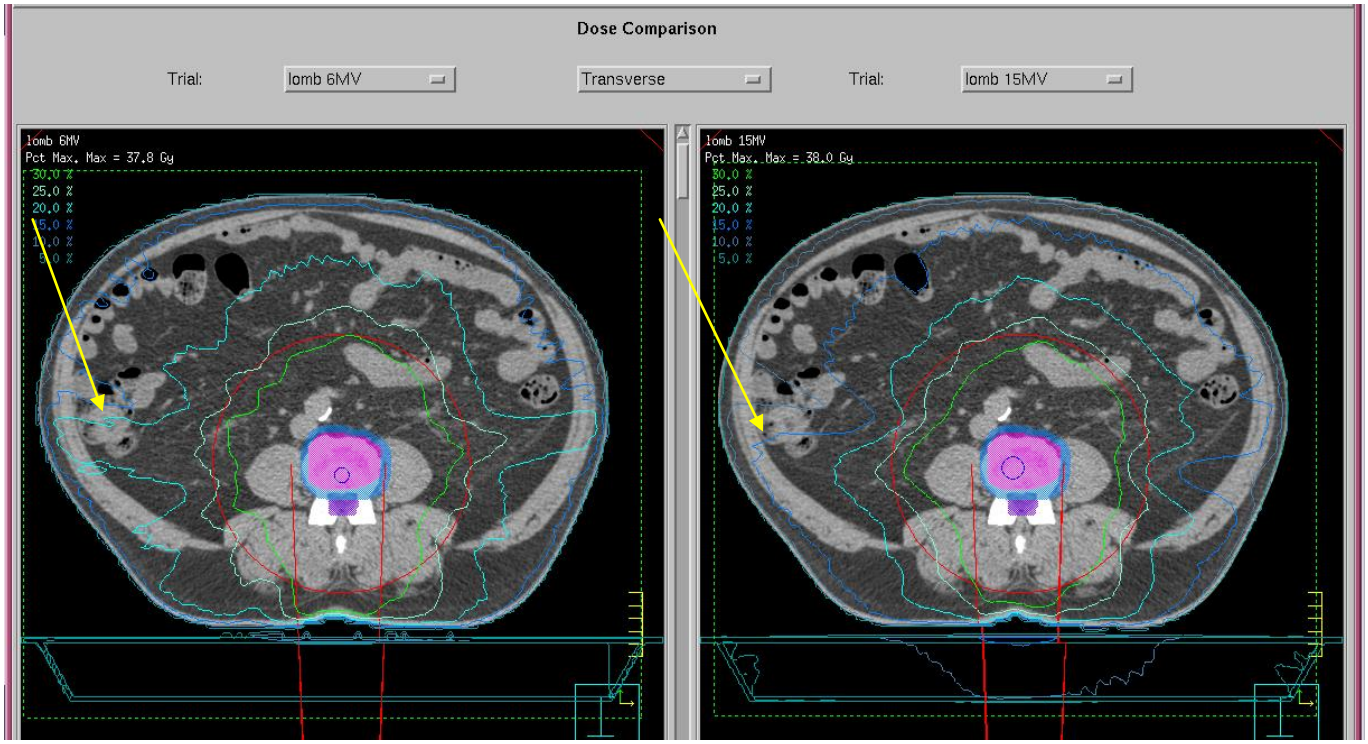

Fig 1: Dosimetry comparison between 6MV VMAT (left) and 15MV VMAT (right). Contraction of isodoses for the 15MV plan in the direction of the PTV.

P 37 Assessment of normal tissue complication risk factors and dose-volume relations in adjuvant radiotherapy of breast cancer patients: A treatment planning study

H. Rennau[1], S. Sebb[1], C. Gocke[1], G. Hildebrandt[1]
[1]Universitätsmedizin Rostock, Klinik für Strahlentherapie, Medizinische Physik, Rostock, Germany

Background: The adjuvant radiation treatment of breast cancer is known to improve the patients long-term locoregional control as well as survival. However, the increased risk of ischemic heart disease and radiation pneumonitis might potentially reduce the overall outcome of the patients cure. The PASSOS project (**http://goo.gl/0qA65L**) investigates on how the individual treatment technique and individual patient factors influences these risks such that tools for radiation oncologists can be developed in selecting **the optimal treatment technique.**

Materials and methods: A number of >100 patients with low risk breast cancer following breast conserving surgery is investigated regarding dose-distributions during adjuvant therapy. Within this project a very detailed contouring of the substructures of the heart is made which allows for a closer investigation which substructures of the heart receive high or low doses. While most patients are treated with 3D conformal tangential technique, additional IMRT treatment plans are calculated for each patient. Both treatment techniques are then compared to each other using NTCP models and DVH analysis. The dose volume distributions of several organs at risk do vary between different patients and the applied treatment technique (3D-CRT, IMRT, deep-inspiration-breathold: DIBH). The accumulated dosimetric data of this work is collected in a database which is – at a later stage of this project – used by epidemiologic modelers to develop health risk models.

Results: The collected data reveals that during adjuvant treatment of breast cancer significant deviations in doses to the heart, its corresponding substructures and further organs at risk occur. These doses depend on several factors such as whether it is left or right-sided breast cancer, the applied planning technique, the dose calculation algorithm and the individual patient-specific geometric conditions. While the volume that receives high (therapeutic) doses has been found to be smaller when applying the IMRT technique for e.g. certain substructures of the heart and axillary lymph nodes (Fig.3), the average and maximum doses to organs at risk have been found to be lower in most cases when the conformal tangential technique is applied (Fig. 1). The advantage of IMRT in reducing the volume of organs that receive high (therapeutic) doses is supported by Fig. 4 with lower NTCP for the ispilateral lung. Lower doses due to the IMRT technique in the transition area between planning target volume and ipsilateral lung is shown in Fig. 2 (right figure).

Phantom measurements conducted at the University of Rostock revealed that outside of the planning target volume the differences between the doses calculated by the treatment planning software (TPS) and measurements vary by up to +/- 60%. Dose point measurements within the planning target volume show dose underestimations of the TPS by about 0.5-2.8%.

Conclusions: The collected data analyses the quantitative and qualitative dose distributions to several organs at risk during adjuvant treatment of breast cancer such as for example thyroid, contralateral breast and oesophagus. A special focus of this work is the detailed contouring of the heart and corresponding substructures which allows to specify where high (therapeutic) doses occur and how individual geometric conditions lead to different treatment techniques. At a later stage of this project, this data will be applied in epidemiological models to estimate complication probabilities. A challenge for these models is how to treat the observed range of exposures between about 30cGy (e.g. thyroid, contralateral breast) to >4Gy (ipsilateral lung, heart,…). A second focus is the investigation of different treatment techniques and their impact on dose-volume distributions to several organs at risk which has been discussed in 'Results'. The aim of this project is to provide tools for radiation oncologists in selecting the optimal treatment technique for the individual patient.

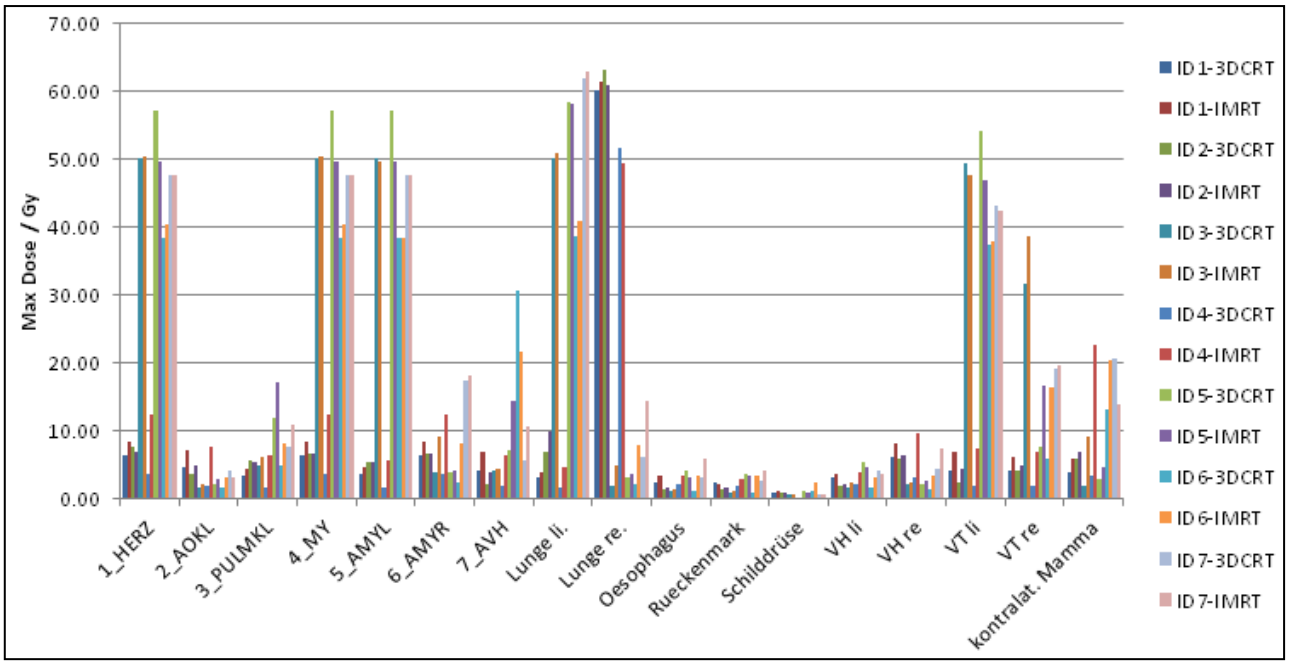

Fig. 1 Maximum dose for different organs depending on individual patient (id1-id7) and treatment technique (3d-CRT, IMRT).

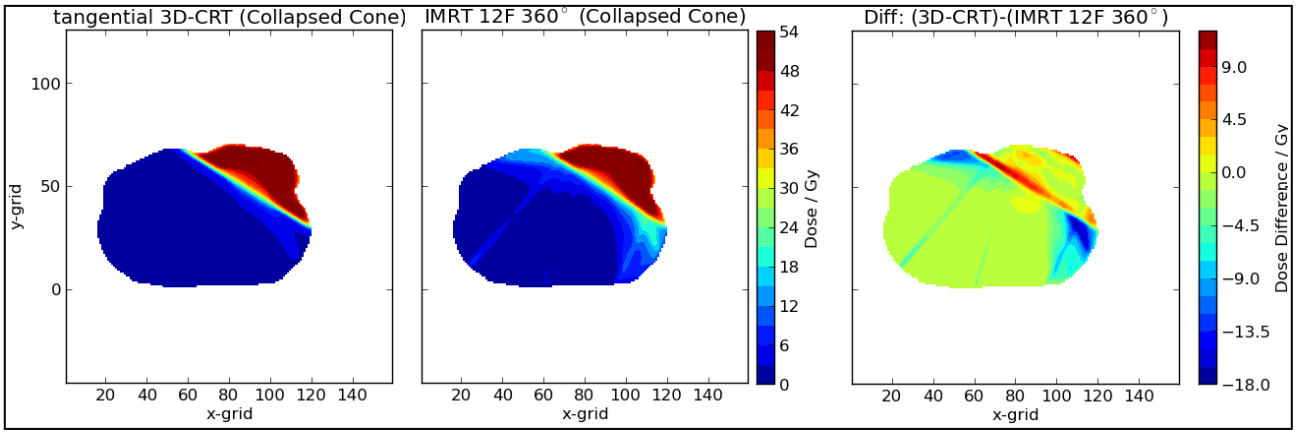

Fig. 2 Figure showing dose for tangential technique (3D-CRT, left figure) and IMRT step and shoot technique (Figure in center, 12 fields rotating in equidistant distance of 360°) in a CT-slice perpendicular to the craniocaudal axis. The right plot shows the quantitative differences of the dose of the 3D-CRT plan subtracted by the IMRT plan which demonstrates the significantly different dose distributions between the techniques.

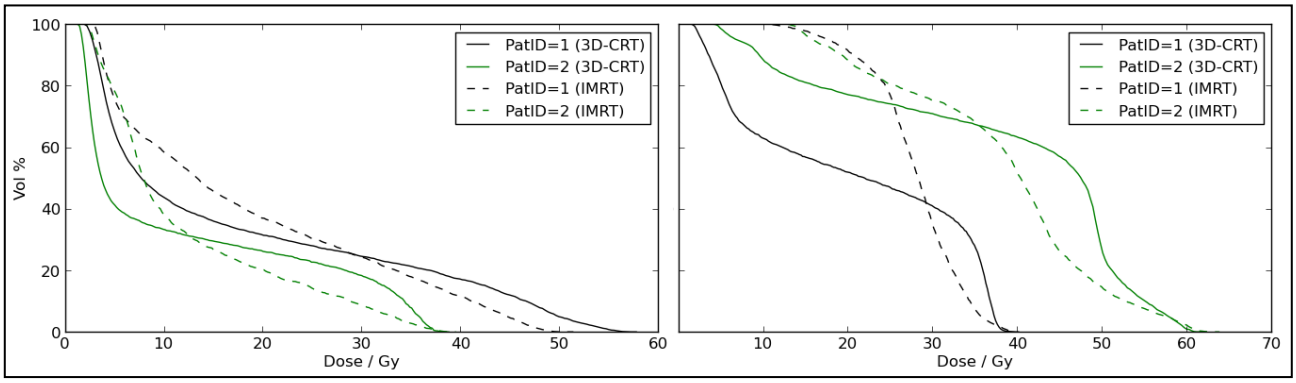

Fig. 3 Left panel showing Dose-Volume-Histogram of heart structure AMYL (AMYL includes: left anterior myocardium, main stem of coronary arteries, left anterior descending coronary artery) for two different treatment techniques (3D-CRT, IMRT) and two patients (PatID=1,2). Same figure is made for axillary lymph node level 1 (right panel) with a qualitatively similar result.

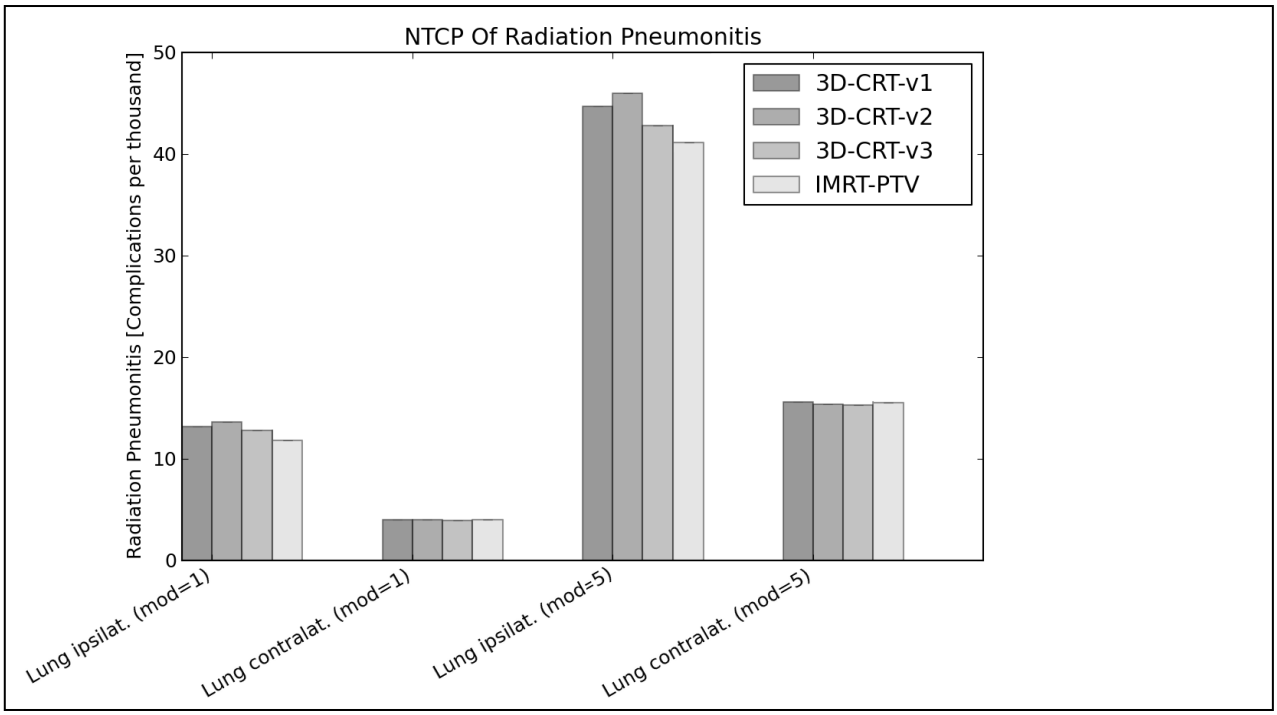

Fig. 4 NTCP complications of two different NTCP models for contralateral and ipsilateral lung. Here three different 3D-CRT plans (similar PTV covererage but made by three different planners) and an IMRT plan is compared. Both NTCP model parameter sets reveal a lower complication propability of the ipsilateral lung when IMRT is applied which is due to lower doses in the area between ipsilateral lung and PTV as shown in Fig. 2 (see red area in the right figure).

P 38 Exploring Dose Rate Dependence of Cancer Risk by a Dynamic LQ-type Model

S. Scheidegger[1]
[1]ZHAW School of Engineering, Zurich Universtity of Applied Sciences, Winterthur, Switzerland

Purpose: Modern CT units offer high dose rate with radiation pulses up to 60 Sv/h. There is a lack of knowledge about biological impact of such pulsed beams and dose rates. Different models such as linear-no-threshold (LNT), linear-quadratic (LQ)-type or linear models with threshold have been proposed. A validation of the different models based on epidemiological data is difficult. Beside this problem, the exploration of dynamic models based on a radio-biophysical rationale may help to support the discussion concerning radiation risk related to radiological examinations.

Materials and methods: Given a population with *N* healthy individuals (humans, susceptible for radiation induced cancer), the conversion rate to a population with individuals having a radiation-induced damage leading to mortal cancer (denoted by the number of individuals *L*) is assumed to be linear dependent on the dose rate *R*, the number of susceptible individuals *N* and a transient dose equivalent Γ describing the effect of previous irradiations: $dL/dt = (\kappa + \lambda\Gamma)\cdot RN = -dN/dt$. This approach is similar to the Γ-LQ model [1], but the coefficients κ and λ are related to the average cancer mortality of the irradiated population. The dose rate dependence is governed by the transient dose equivalent which is assumed to fade away due to cellular repair processes. In this work, first order kinetics is investigated: $d\Gamma/dt = R - \gamma\Gamma$. The transient dose equivalent can be calibrated by the following condition:

$$\lim_{t\to\infty}\left[\int_{-\infty}^{t}\gamma\Gamma(\tau)\cdot d\tau\right] = \lim_{t\to\infty}\left[E(t)\right] = E_{tot}$$

Here, *E* is the effective dose. In contrast to the Γ-LQ model, the transient dose equivalent is not directly linked to the absorbed dose. It represents more an average of the different tissues considered by the radiation weighting factors according ICRP103 [2]. Tissue dependent repair speeds are not considered by the kinetic constant γ. The parameter κ can be estimated using the low-dose-rate limit:

$$\left[\frac{dL}{dt}\right]_{R\to 0} = \left[\frac{dL}{dt}\right]_{\Gamma\to 0} = \lim_{\Gamma\to 0}\left[(\kappa+\lambda\Gamma)\cdot RN\right] = \kappa RN$$

Separation and integration leads to: $N = N_0 e^{-\kappa E}$ and $L = N_0 - n = N_0\cdot(1-e^{-\kappa E})$. The initial slope therefore is given by: $[dL/dE]_{E\to 0} = \kappa N_0$. This can be interpreted as the LNT-limit for low doses and dose rates.

Results: The model includes the free parameters γ, κ and λ. The parameters are estimated coarsely by using of the following conditions: For comparably low dose rates, the risk should be in correspondence to the established value of 5% per Sv [2] and dose rate independent, whereas for high dose rates, the risk should more or less double. According the (initial) disappearance of γ H2AX-foci found in CHO cells [3], the parameter for decay of the transient dose equivalent was set to $\gamma = 0.2h^{-1}$. Assuming an approximately linear relationship between effective dose and risk with 5% per Sv for the low dose rate limit and *E* < 2 Sv, a value for $\kappa = 5\cdot 10^{-2} Sv^{-1}$ is resulting. With the condition of a fix-point of 10% at a dose of 1 Sv in the high dose rate limit, the last parameter values have been determined by computer simulations: $\lambda = 5.6\cdot 10^{-2} Sv^{-2}$.

Discussion and Conclusions: All three assumption used for estimating the parameters are fraught with large uncertainties. The use of a transient dose equivalent with decay proportional to the disappearance of γ H2AX-foci (in non-human cell lines) must be seen as a very rough estimate and implicates proportionality between remaining foci and risk of induction of mortal cancer. Therefore, the model should be validated by experimental or observed data. Beside the problems of estimating the parameter values, the model exhibits some interesting general aspects (Fig.1 & 2): The mortality or cancer risk is given by a LQ-type relationship for the logarithm of mortality at high dose rates. For low dose rates, the model tends to a LNT-behavior. For *E* < 0.2 Sv, no strong dose rate dependence is observed. A remaining problem is related to the inhomogeneous dose distribution in the patient: A “biological averaging” by the effective dose for example does not refer to the deterministic effects which possibly influence the local cancer risk.

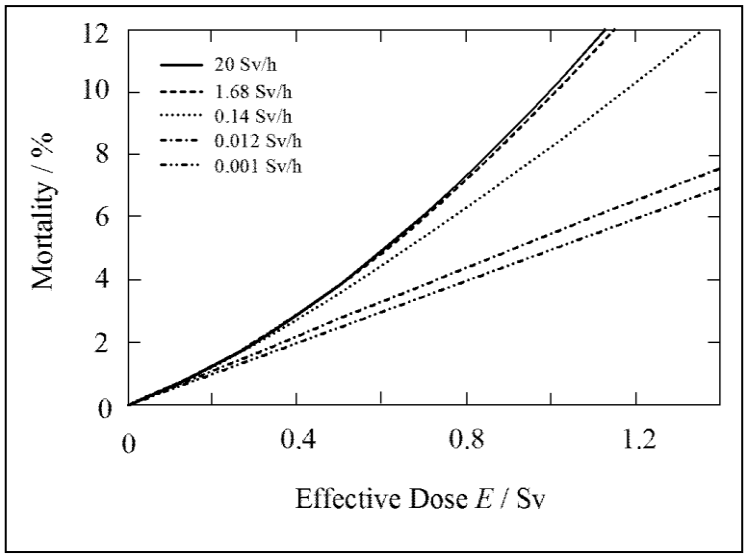

Fig. 1: Cancer mortality as function of the effective dose.

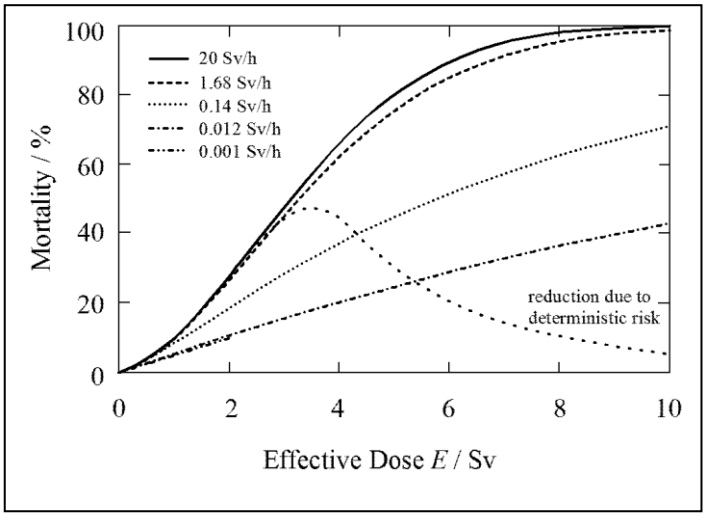

Fig. 2: Mortality in the dose range below 1.4 Sv.

References

[1] Scheidegger S., Lutters G., Bodis S. Z. Med. Phys. 21 (2011),164–173
[2] ICRP Publication 103; Oxford, New York, Frankfurt: Pergamon Press; 2008.
[3] Grosse N, Fontana AO, Hug EB, Lomax A, Coray A, Augsburger M, Paganetti H, Sartori AA, Pruschy M: Int J Radiation Oncol Biol Phys, 88 (2014) 1, 175-181

Poster session IV – Image guided radiation therapy and treatment planning

Chair: M. K. Fix (Bern/CH)

P 39 VMAT optimization for difficult lung cases: A comparison between the PRO2 and PRO3 algorithm

R. Wiehle[1]
[1]Unklinik Freiburg, Klinik für Strahlenheilkunde, Freiburg, Germany

Introduction: With the release of Eclipse 10 by Varian Medical Systems the new PRO3 algorithm for VMAT optimization was introduced into clinical practice. Its main advantage lies in the significant increase in speed compared to the former PRO2 algorithm. Furthermore, one is able to judge the achievable plan quality in an early stage of the optimization process, which can be done only close to the end when using PRO2. However, we were uncertain whether the resulting treatment plans were of the same quality.

Material and methods: In order to quantify the differences in plan quality, we chose a set of patients, who were treated at our institution. We started with the plans, which had been chosen for treatment, and did the optimization again without adjusting the objectives. For the PRO2 a single optimization was performed with a subsequent final dose calculation using the AAA10 algorithm. For the PRO3 an additional optimization was done after the final dose calculation, using its results as an input. In this second optimization only the last step was performed.
The DVH for each treatment plan was exported, and Mathematica was used to compute mean-DVHs for each of the two algorithms. Because of variations in the prescribed dose, relative dose was used. To quantify the conformance of the dose distribution a conformity function was used [1], which is defined as:

$$CF(x) = \frac{\text{Volume outside the PTV receiving } \geq x\% \text{ of prescribed dose}}{Volume\ of\ PTV}\ .$$

Results: Fig. 1 shows the averaged DVHs for the relevant structures. For the PTV they are very similar: The PRO3 yields slightly better coverage, but the overdosage is also a bit higher. Heart sparing is better with the PRO3 in the range above 50% of the prescribed dose, the spinal cord receives lower dose with the PRO2, but in a dose range, which is of no interest. For the esophagus there are no significant differences. The PRO2 algorithm yields better plans for the lungs in a dose range between 10% and 55% of the prescribed dose, which roughly corresponds to our range of interest for this organ (5Gy to 20Gy). Since our main focus apart from PTV coverage and keeping the dose to the spinal cord below 45Gy was to minimize the volume of the lung exposed to doses between 5Gy and 20Gy, we think that the PRO2 plans are better. In Fig. 2 one can see that this increase in plan quality comes at a price: The conformity of the dose distribution is worse for the PRO2 plans. For example the volume outside the PTV, which receives 95% of the prescribed dose amounts to about 15% of the size of the PTV for PRO3 plans and about 33% for PRO2 plans. Equally the CF(80%) amounts to 0.79 for the PRO3 algorithm and to 1.1 for the PRO2 algorithm.

Conclusion: We present a comparison of the outcome of optimizations using two different algorithms, but otherwise identical starting positions. The PRO2 algorithm is able to find a solution, which comes closer to our objectives, it follows our wishes more closely. However, there is a price we have to pay: The dose conformance is significantly lower. The sparing of the lung is more important in these cases, because the toxicity to the lung generally limits the dose applied to the tumor. For these cases we therefore consider the PRO2 superior, which stands in contrast to results published by Vanetti et al [2].

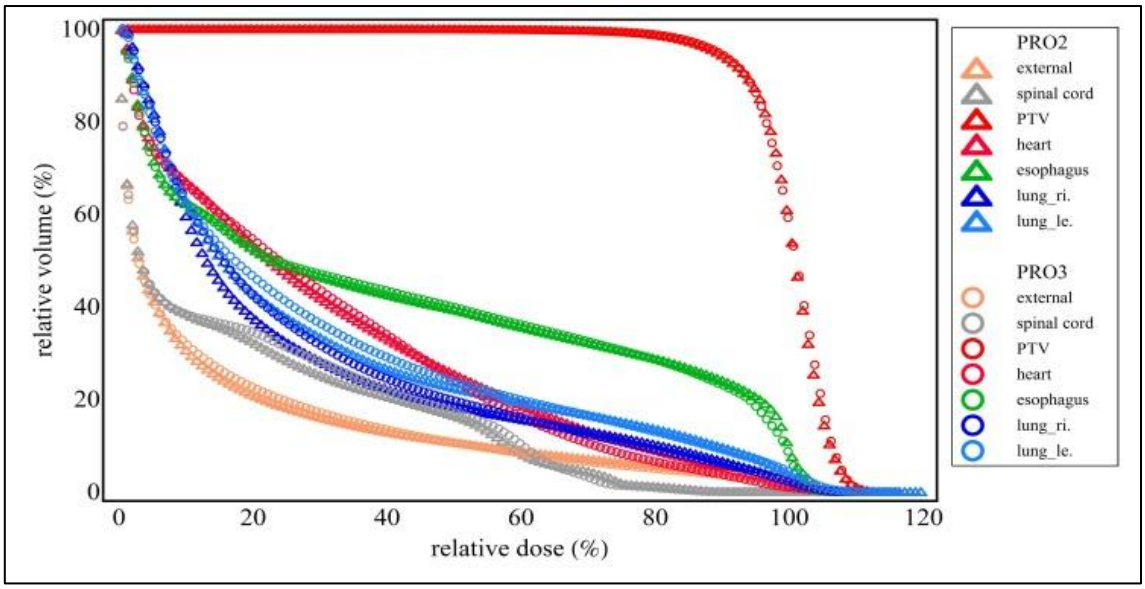

Fig. 1: mean-DVHs for the relevant structures

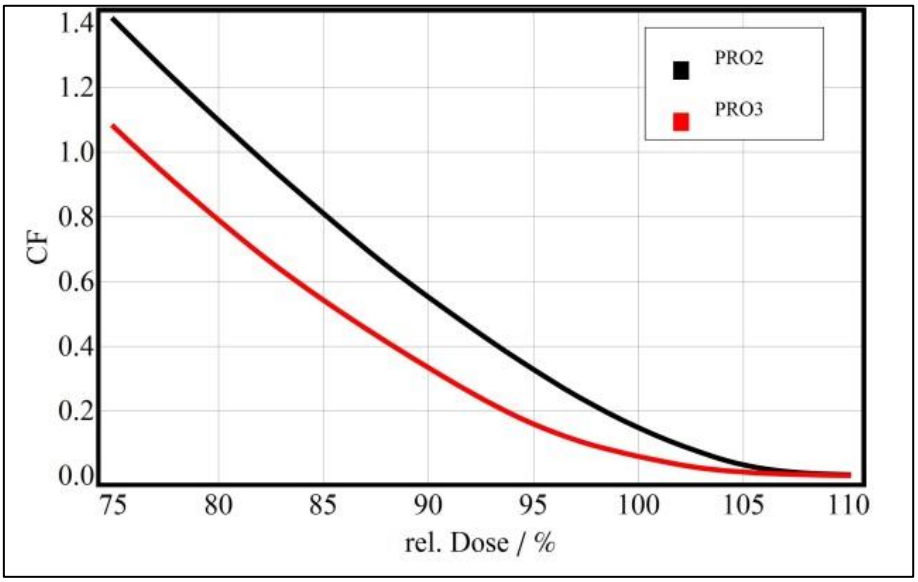

Fig. 2: conformity function for the two algorithms

References

[1] Wiehle R. et al.: Strahlentherapie und Onkologie, 187 (2011) 12, S. 820-825
[2] Vanetti E. et al.: Medical Physics, 38 (2011) 11, S. 5844-5856

P 40 Craniospinal irradiation with IMRT in the supine position

H. Blank[1], B. Sebralla[1], H. Alheit[1]
[1]Strahlentherapie Distler, Bautzen, Germany

Einführung: Die Bestrahlung des gesamten Liquorraumes von Gehirn und Spinalkanal ist Bestandteil der lokoregionären Therapie bei Meningeosis neoplastica und Hirntumoren mit hohem Potenzial zur liquorgenen Metastasierung [Sch03].
Weil die Länge des Zielvolumens die maximale Feldlänge der Bestrahlungsgeräte übersteigt, wurde als grundlegender Ansatz eine Technik mit zwei bis drei Isozentren gewählt. Die Problematik der konventionellen Techniken liegt in der Gefahr einer Überschneidung der jeweiligen Ansatzstellen der Bestrahlungsfelder. Dies ist verbunden mit der Gefahr einer Über- und Unterdosierung bei Lagerungsabweichungen. Daher werden neue Techniken wie Tomotherapie, Protonenbestrahlung, und intensitätsmodulierte Strahlentherapie (IMRT) als Alternativen diskutiert und untersucht. Für die praxisrelevanten Fälle mit Meningeosis neoplastica bei vorwiegend soliden Tumoren und Lymphomen soll eine intensitätsmodulierte Strahlentherapie für den Linearbeschleuniger in Rückenlage entwickelt werden, die sicher applizierbar ist und harte Feldgrenzen vermeidet.

Material und Methode:
*Objekt***:** An einem Alderson Rando© Man Phantom wurde eine Planungsstudie mittels multi-isozentrischer IMRT-Technik durchgeführt.
Bestrahlungsplanung: Wie die konventionelle Technik wird die IMRT mit einem multi-isozentrischen Ansatz durchgeführt. Planung und Berechnung erfolgen im TPS Monaco® Ver. 3.0 (Firma Elekta) mit dem Monte Carlo Algorithmus. Zur Ermittlung einer optimalen Planvariante wurde folgendes Vorgehen gewählt:

1) Übertragung der konventionellen Feldkonfiguration auf das TPS Monaco®
2) Variation der Feldanzahl und Einstrahlrichtungen zur Ermittlung einer optimalen Geometrie
3) Definition von geeigneten Constraints für die Fluenzmodellierung aus klinischer Erfahrung
4) Variation der Constraints zur Ermittlung der optimalen Parameter
5) Optimierung der Segmentierung

Planevaluation: Die Ergebnisse der Planoptimierung werden mit einer konventionellen Bestrahlungstechnik mittels dosimetrischer Parameter verglichen. Folgende Parameter werden genutzt:

1) *D*max, *D*mean, *D*min als maximale, mittlere und minimale Dosis im jeweiligen Volumen
2) *D*50 %, *D*90 %, *D*95 % als Dosiswerte für die Exposition von 50, 90, und 95 % des Volumens einer Struktur
3) *V*35,64Gy, *V*37,62Gy und *V*42,37Gy als Volumina des PTV, die mit der 90 %, 95 % und 107 % Isodose umschlossen sind

Gemäß ICRU83 werden als Ersatz für *D*max und *D*min die Dosen *D*2 %, *D*98 % als maximale, minimale Dosis für 2 % und 98 % eines Volumens herangezogen [ICRU83]. Um die unterschiedlichen Bestrahlungspläne zu vergleichen, werden Konformitätsindex, Homogenitätsindex, Coverage Index, Health Tissue Conformity Index, neuer Konformitätsindex **–** *newCI* ausgewertet

Ergebnisse: Bei den meisten untersuchten Parametern zeigte der Plan *CSIMRTC* die besten Ergebnisse. Die schlechteren Ergebnisse gegenüber dem Plan *CSIMRTB* im Bereich der Dosiswerte Dmax und *D*min lagen bei 0,3 %. Wichtigster Faktor für die Entscheidung zugunsten Plan *CSIMRTC* war die deutlich bessere Schonung der OAR im ventralen Bereich und die Verringerung des *D*max der Linsen, des Rückenmarkes und des Hirnstammes um teilweise über 1Gy gegenüber den anderen Varianten. Dies lag auch in der höheren Modulation begründet, die allerdings zu einer höheren Segmentanzahl und mehr ME pro Fraktion führt. Dies wird aber zugunsten der erwähnten Vorteile für die OAR als gerechtfertigt angesehen.
Der Plan stellt ein Optimum dar aus: Ganzkörperbelastung (Bestrahlungszeit)≡Modulationsgrad≡Ergebnis

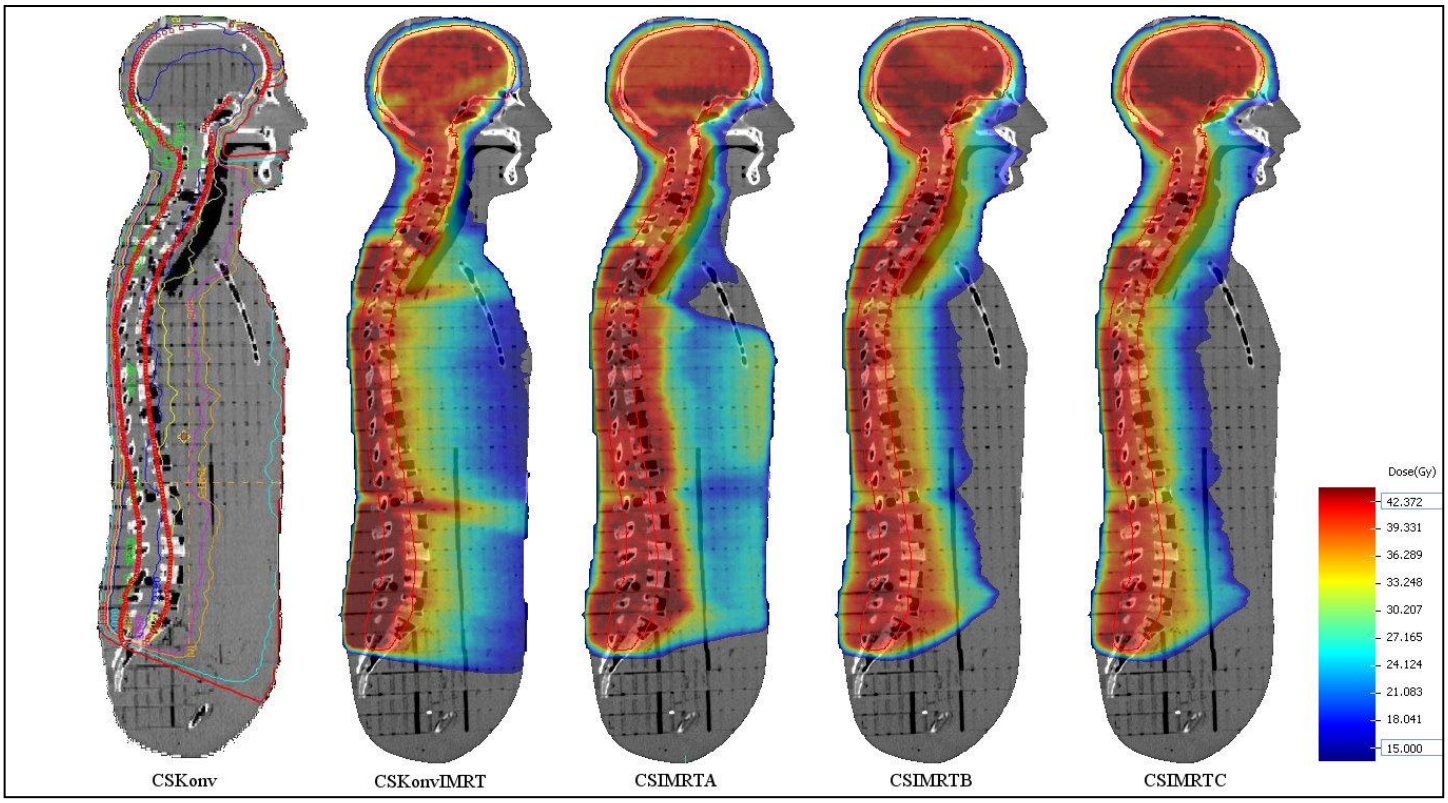

Fig. 1: Sagittale Dosisverteilung der IMRT Varianten

Diskussion: Ein Wechsel zur IMRT erschien aus planerischer Sicht sinnvoll weil die Überdosierungen im dorsalen Bereich reduziert, die OAR besser geschont und Homogenität und Konformität gegenüber der konventionellen Technik verbessert wurden. Darüber hinaus gab es keine direkten Feldansatzstellen mehr, so dass eine größere Sicherheit bei der Bestrahlungsdurchführung erwartet werden kann.

Schlussfolgerung: Bei Einsatz von IMRT-Techniken sollte ein Monte-Carlo Algorithmus bevorzugt werden. Eine Hauptorientierung der Felder von dorsal scheint die günstigsten Ergebnisse zu liefern. Für die Bewertung der erstellten Pläne empfiehlt sich neben der visuellen Beurteilung und der DVH-Analyse auch die Berechnung geeigneter Qualitätsindizes wie *HI* und *newCI*. Die Gesamtbelastung für den Patienten mit insgesamt 900ME und 100 Segmenten bei einer Gesamtbestrahlungszeit von etwa 15 min erscheint akzeptabel.

P 41 A comparative planning study for prostate cancer using IMRT vs. mARC treatment with flat and FFF beams

K. Bell[1], Y. Dzierma[1], J. Palm[1], F. Nüsken[1], N. Licht[1], C. Rübe[1]
[1]Universitätsklinikum des Saarlandes, Klinik für Strahlentherapie und Radioonkologie, Homburg, Germany

Introduction: The recently introduced mARC technique offers rotational IMRT delivery ("burst mode", [1-2]) for Siemens linear accelerators, similar to VMAT/RapidArc. Although some planning examples have been presented [3] and first patient treatments have by now been performed [4], to our knowledge, there exists no systematic planning study comparing mARC to IMRT treatment so far. Furthermore, it has not been assessed how well mARC treatment performs for flat vs. flattening-filter-free (FFF) beam energies.
Prostate cancer has been found well-suited for mARC planning using different treatment planning systems [5]: on the one hand, good bladder and rectum sparing requires sophisticated planning (IMRT/VMAT rather than 3D conformal planning), on the other, the relatively symmetrical target volume is easier to treat with a single gantry arc than highly complex targets such as head-and-neck tumours. In the following, we present a first planning study of mARC treatment for prostate cancer patients, concentrating both on the plan qualities and the treatment times, for flat and FFF beams respectively.

Materials and methods: Prostate PTV contours were drawn retrospectively on the planning CT (Philips Brilliance BigBore) for 10 patients, with a prescription dose of 76 Gy delivered in 38 fractions. The Siemens Artiste linac available for mARC at our institution is equipped with a 160 MLC and offers two beam energies: flat 6 MV and FFF 7 MV, with very similar depth-dose characteristics [6]. Treatment planning was performed in the Prowess Panther treatment planning system V5.10r2 using a collapsed cone algorithm.
For each patient, four different scenarios were considered: mARC treatment with a single gantry arc, equidistantly spaced optimization points (every 10°), 4° arclet length, with 6 MV and FFF 7MV; and IMRT treatment with 11 gantry angles and 3 segments per beam, again for both energies. The four plans have about the same number of degrees of freedom (36 for mARC vs. 33 for IMRT), so differences in quality should be caused by the treatment technique rather than the freedom in optimization. All plans were reviewed by a senior radiation oncologist and were found acceptable for treatment. Plan quality was compared based on dose distribution and dose-volume histograms. For the statistical evaluation, we considered the quality indices for PTV conformity and homogeneity and the sparing of organs at risk (OAR) as measured by V(50%) of the bladder and rectum and V(40%) of the posterior rectal wall. All plans were irradiated and treatment times were measured for comparison.
Pair-wise t-tests were made between plan scenarios if a normal distribution could be presumed (after testing with the Shapiro-Wilk test), otherwise, the paired Wilcoxon signed-rank test was applied. We use a level of significance of 5 %.

Results: All plans met the criteria for PTV coverage and OAR sparing, given in Table 1, and were acceptable for treatment based on the DVH and dose distribution.
For all measures of quality considered, no significant difference exists between IMRT and mARC plans of the same energy. In homogeneity and conformity index, the 6 MV plans are slightly better than the 7 MV plans, both for IMRT and mARC (p-values in Table 2). In the sparing of OAR, no significance is found for the comparison between IMRT plans of both energies. For mARC, the 7 MV plans perform slightly worse than the 6 MV plans, although the results are just barely significant for the rectum and posterior rectal wall. These results are in fact surprising, since they are in contradiction with the visual evaluation of plan quality. Indeed, the evaluation of dose distributions and DVHs for each individual patient showed no clear preference for the 6 MV plans. From the point of view of dose coverage and distribution (e.g., shape of medium dose isodose lines), the 7 MV plans were in fact sometimes preferred. The reason for this is that the difference between both plans is so small to evade clinical (though not statistical) significance: the comparison of dose to OAR for 6 MV vs. 7 MV mARC plans is 22.1 Gy vs. 23.5 Gy for the V(50 %, bladder), 15.6 Gy vs. 16.5 Gy for the V(50 %, rectum) and 3.6 Gy vs. 5.1 Gy for the V(40 %, post. rect. wall). For all practical purposes, the plan qualities can therefore be considered identical, even though minor differences exist.
Measured treatment times were: 5-6 minutes for 6 MV IMRT, 4-5 min for 7 MV IMRT, 3-4 min for 6 MV mARC, and 2-3 min for 7 MV mARC.

Conclusions: Although the statistical evaluation shows a slight improvement of the 6 MV over the 7 MV treatment plans, the differences are very small and lack clinical significance – from the radiation oncologist's point of view, all four planning scenarios (IMRT or mARC with 6 or 7 MV) yield equally good quality plans. Treatment times are considerably shortened both by the use of mARC and the high dose rate FFF 7 MV energy. In combination, a 7 MV mARC plan can be irradiated in less than 3 minutes, less than half the time taken for a 6 MV IMRT plan.

Organ at risk	Constraint
Bladder	V(75 Gy) < 15 %
	V(70 Gy) < 20 %
	V(50 Gy) < 50 %
Rectum	V(70 Gy) < 10 %
	V(60 Gy) < 30 %
	V(50 Gy) < 50 %
	V(40 Gy) < 70 %
	V(30 Gy) < 80 %
Posterior rectal wall	D_{max} < 60 Gy
	V(50 Gy) < 15 %
	V(40 Gy) < 30 %

Tab. 1 Planning constraints (satisfied by all plans)

Measure of quality	Comparison	p-value
Conformity index [7] $CI = \frac{(TV_{PIV})^2}{TV \cdot PIV}$	6 MV IMRT – 7 MV IMRT	0.029
	6 MV mARC – 7 MV mARC	0.004
Homogeneity index $HI = \frac{D_{PTV}(2\%) - D_{PTV}(98\%)}{D_{PTV}(50\%)}$	6 MV IMRT – 7 MV IMRT	0.010
	6 MV mARC – 7 MV mARC	0.027
Bladder V(50 %)	6 MV IMRT – 7 MV IMRT	Not significant
	6 MV mARC – 7 MV mARC	0.004
Rectum V(50 %)	6 MV IMRT – 7 MV IMRT	Not significant
	6 MV mARC – 7 MV mARC	0.049
Posterior rectal wall V(40 %)	6 MV IMRT – 7 MV IMRT	Not significant
	6 MV mARC – 7 MV mARC	0.043

Tab. 2 Measures of quality with significance levels for plan comparison. All other comparisons not shown in the table (6 MV IMRT vs. 6 MV mARC, 7 MV IMRT vs. 7 MV mARC) showed no statistical significance.TV = volume of the PTV, PIV = volume of the prescribed isodose (95 %), TV_{PIV} = volume of the PTV covered by the prescribed isodose,

References

[1] Kainz K, Chen GP, Chang YW, Prah D, Qi XS, Shukla HP, Stahl J, Li XA (2011) A planning and delivery study of a rotational IMRT technique with burst delivery. Med Phys 38(9):5104-5118.

[2] Salter BJ, Sarkar V, Wang B, Shukla H, Szegedi M, Rassiah-Szegedi P (2011) Rotational IMRT delivery using a digital linear accelerator in a very high dose rate 'burst mode'. Phys Med Biol 56:1931-1946.

[3] Spahn U, Prott FJ (2013) Erste Erfahrungen mit der modulierten Rotationsbestrahlung mARC amd Linearbeschleuniger ARTISTE. Strahlenther Onkol Suppl 1:62-63.

[4] Dzierma Y, Nüsken F, Licht N, Palm J, Kremp S, Rübe Ch, 2014. First clinical application of mARC treatment, submitted to DGMP annual meeting 2014

[5] Dzierma Y, Nüsken F, Bell K, Licht N, Rübe Ch, 2014. mARC treatment planning using three different treatment planning systems – a comparison, submitted to DGMP annual meeting 2014

[6] Dzierma Y, Licht N, Nuesken F, Ruebe Ch, 2012. Beam properties and stability of a flattening-filter free 7 MV beam – An overview, Med. Phys. 39(5):2595-2602.

[7] Paddick I, 2000. A simple scoring ratio to index the conformity of radio-surgical treatment plans. Technical note. J. Neurosurg. 93(Supp. 3):219-222.

P 42 Dosimetric comparison of tangential opposing field technique versus intensity-modulated and volumetric-modulated radiation therapy and irregular surface compensator technique at different patient position setups for left-sided breast cancer

R. Hielscher[1], I. Nikolova-Rezaie[1], S. Trappen[1], K. Delp[2], K. Hierholz[1], B. Kober[1]
[1]Klinikum Darmstadt, Institut für Radioonkologie und Strahlentherapie, Darmstadt, Germany
[2]GSI Helmholtzzentrum für Schwerionenforschung, Darmstadt, Germany

Introduction: Dynamic-modulated treatment planning for whole-breast radiation is a complex behavior that can be employed to ensure adequate dose target coverage while minimizing doses to the organs at risk as ipsilateral lung and heart. For whole-breast radiation a conventional tangential opposing field technique with wedges is often used on a breast board with arms elevated above the head as patient position setup. In our institute we use individual-formed vacuum mattresses on top of a left or right formed wedge for each patient, particularly for patients with left-sided breast cancer.

Material and Methods: This work compares four radiation treatment techniques, 3D-conventional tangential opposing fields (3D-CRT), intensity-modulated radiation therapy (IMRT), volumetric-modulated arc therapy (VMAT) and a tangential opposing intensity-modulated arrangement using the irregular surface compensator (ISC) for whole-breast radiation treatment. 20 patients with left-sided breast cancer, 10 located on breast board and 10 located on a vacuum mattress in supine position, were analyzed due to planning target volume (PTV) coverage, dose homogeneity, organs at risk (OAR) as lungs, heart and contralateral breast. Dose plans were calculated for each patient using the four different techniques 3D-CRT, IMRT, VMAT and ISC. All patients were prescribed a dose of 50 Gy in 25 fractions. The dose distributions in PTV and the dose to the OAR were compared analyzing dose-volume histograms.

Results: All four techniques offered adequate PTV coverage between $D_{98\%}$ > 95% and $D_{2\%}$ < 107%, respectively. However, dose differences were observed between the techniques in the PTV, OAR and also in the pattern of dose distribution spreading into the contralateral side. IMRT and VMAT spread more low doses into right breast and right lung than the tangential techniques. However, IMRT and VMAT plans improved distributions for the PTV, exhibiting better conformity and homogeneity in PTV and reduced high dose percentages in ipsilateral lung. The ISC dose plans did not significantly differ from the 3D-CRT plan. Nevertheless, ISC dose plans show clearly better homogeneity in PTV than in 3D-CRT and are comparable with IMRT and VMAT. The dosimetric disadvantages found in IMRT and VMAT plans did not occur in ISC plans. In addition, dosimetric differences could be observed between the two patient position setups. The dose in heart is higher in straight position. It could be shown that high dose in ipsilateral lung is reduced using the vacuum mattress.

Discussion: Considering the risk of secondary neoplasms and the relative high dose in lung and contralateral breast, we do not suggest to choose VMAT for left-sided breast cancer radiation therapy. An alternative technique could be ISC due to its dosimetric advantages and reduced beam on time compared to the other techniques.

P 43 Comparison of five different planning techniques for left breast radiation therapy treatment

M. Zeverino[1], M. Marguet[1], W. Jeanneret Sozzi[2], F. Bochud[1], J. Bourhis[2], R. Moeckli[1]
[1]CHUV, Medical Physics, Lausanne, Switzerland
[2]CHUV, Radiation Oncology, Lausanne, Switzerland

Related questions: This work aims at investigating the different dose distributions arising from five planning techniques in terms of target coverage and homogeneity as well as sparing of surrounding healthy tissues.

Material and procedure: Three left-sided breasts were used for planning comparison. The prescribed dose was 50 Gy delivered in 25 fractions. The planning techniques used were: forward planning field-in field (FiF), inverse planning step and shoot IMRT (s-IMRT), volumetric arc therapy (VMAT), helical tomotherapy (HT) and TomoDirect (TD). FiF was planned with 4 to 6 beams, s-IMRT with 4 beams, VMAT with 2 half arcs and TD with 4 beams. HT was planned without any directional or complete structure blocking. Dose to the planning target volume (PTV) was compared using the following figures of merit: dose delivered to the 98% and to the 2% of the PTV (D98% and D2%, respectively), volumes of PTV receiving the 95% and the 105% of the prescription dose (V95% and V105%, respectively). Organs at risk (OARs) evaluated were: contra-lateral breast, lungs, heart. Different figures of merit were considered for each OARs according to their clinical relevance.

Result: Concerning the PTV coverage, D98% resulted as the lowest for FiF (92.4% of the prescription dose) and as the highest for TD (94.4% of the prescription dose), while V95% reached its maximum for TD plans (97% of the PTV volume) and its minimum for VMAT (95% of the PTV volume). In terms of PTV homogeneity, D2% was the highest for s-IMRT (106.5% of the prescription dose) and the lowest for VMAT (102.6% of the prescription dose), while V105% resulted as the lowest for both VMAT and HT techniques (0.1 % of the PTV volume) and as the highest for s-IMRT (4.2% of the PTV volume).

Maximum dose delivered to the contra-lateral breast was the lowest for both FiF and TD techniques (4.7 Gy) and the highest for HT (10.6 Gy). Volume of omolateral lung receiving 10 Gy (V10Gy) was minimum for TD (18.1 %) and maximum for VMAT (33.5 %). V20Gy for contra-lateral lung was minimum for TD (10.9 %) and maximum for s-IMRT (22.9%). V5Gy for contra-lateral lung resulted as the minimum for FiF and TD (0%) and as the maximum for HT (9.6%). V10Gy for heart was minimum for FiF (4.9%) and maximum for HT (52.5%). V25Gy for heart reached its minimum for s-IMRT (0.3%) and its maximum for HT (15.1%).

All showed values were averaged over the 3 dose distributions.

Summary: The presented study showed that every RT technique is capable to deliver the dose to the PTV with an adequate level of coverage and homogeneity. However, both HT and TD resulted as the techniques able to deliver the most homogeneous dose to the PTV. Fixed gantry angle techniques (i.e. FiF, s-IMRT and TD) were able to provide a better OARs dose sparing with respect to volumetric and helical techniques. Based on the few number of plans performed in this study, TD seems to be the most appropriate technique able to produce an optimal dose delivery to the target and OARs dose sparing.

At present authors are collecting further plans in order to evaluate the statistical significance of the differences in dose distributions.

P 44 Sensitivity analysis of plan quality for hypopharynx cancer on flat vs. flattening-filter-free beam energy, beam and segment number

F. Nüsken[1], Y. Dzierma[1], J. Fleckenstein[1], P. Melchior[1], N. Licht[1], C. Rübe[1]
[1]Universitätsklinikum des Saarlandes, Klinik für Strahlentherapie und Radioonkologie, Homburg, Germany

Introduction: While highly conformal dose distributions can be achieved by IMRT planning, these plans often make use of a large number of beams or segments per beams, resulting in increased treatment times. Flattening-filter-free (FFF) beams carry the promise of reducing these times due to their high dose rate; however, to homogeneously cover extended target volumes, even more segments may be necessary. Therefore, there is a need to systematically investigate the dependence of IMRT plan quality on the three factors: number of gantry angles, number of segments, and use of flat or FFF energies.

Materials and methods: We present a planning study for IMRT treatment of hypopharynx cancer, comparing flat 6 MV and FFF 7 MV beams of the Siemens Artiste, and using three different beam arrangements (7, 11, and 18 gantry angles). Planning was performed in Philips Pinnacle³ V9.2-9.4 for eight patients, using direct machine parameter optimization and a collapsed-cone dose calculation algorithm.

We first determine inversion objectives and constraints that yield good quality plans for 6 MV and FFF 7 MV alike, when a large number of segments (70) is permitted. Starting with these constraints, segment number is reduced stepwise down to 25 and the effect on the plan quality is evaluated for the different gantry scenarios and beam energies. Different measures of quality are considered, including plan conformity index, homogeneity index, gradient index, maximum dose to the spinal cord and mean parotid dose.

Results: As long as a sufficiently large number of segments is permitted, all planning scenarios give clinically adequate results, independently of gantry angles and energy (flat or FFF). As expected, plan quality decreases with a smaller number of segments; this effect is stronger a) for fewer gantry angles and b) for FFF beams. For low segment numbers, FFF plans generally perform worse than the corresponding flat beam plans. However, they are less sensitive to a decrease in segment number if many gantry angles are used (18 beams); in this case the quality of flat and FFF beams remains comparable even for few segments.

Conclusions: Given a sufficient number of beams and segments, FFF beams yield plans of comparable quality as flat beams. However, the higher sensitivity of FFF beams to a reduction in segment number implies that the time advantage with respect to flat beams is small at least for the case of relatively large and complex PTV like hypopharynx cancer.

P 45 Comparison of 3D-CRT, IMRT and VMAT treatment plans for the irradiation of the recurrent Graves' ophtalmopathy

T. Labuznova-Lateit[1], S. Zeller[1], T. Hero[1], H. Hermani[2], I. Adamietz[1]
[1]St.Josef-Hospital Bochum, Strahlentherapie, Bochum, Germany
[2]Marien-Hospital Herne, Strahlentherapie, Herne, Germany

Background: The purpose of the current study was to compare normal tissue sparing and dose coverage using four different radiotherapy planning methods in patients with the recurrent Graves' ophtalmopathy (GO).

Methods: A total of 10 consecutive patients with endocrine orbithopathy were selected for the present study. CT-scan with 5mm slices were used. The clinical target volume (CTV) for irradiation of the Graves ophtalmopathy included the peri- and retrobulbar space with extraocular muscles. Both lenses, lacrimal glands, conjunctiva, olfactory and temporal lobe were delineated as organs at risk (OAR). For each patient, four treatment plans were generated (Two 3D-CRT, IMRT and VMAT). Irradiation was performed with a 6MeV photon beam. The planned total dose was 20 Gy in 10 fractions.

The coverage of the PTV was expressed using the isodose covering 95% of the PTV (D95), minimum dose within the PTV (Dmin) and maximum dose within the PTV (Dmax). Conformity and Homogeneity Index (CI and HI) as well as additional parameters were evaluated.

Results: In the overall comparison of four techniques, the adequate target coverage was found in almost all cases; CI nearly 1, a better mean Quality of Coverage (QC) using 3D-CRT or VMAT (0.85±0.6 and 0.89±0.4, respectively), and a lower mean HI for 3D-CRT (OF and MF) $2<HI\leq2.5$. However, the overall comparison did not demonstrate the preference of one of the techniques in individual patients.

Conclusion: 3D-CRT/MF and VMAT-technique provide more accurate coverage of the areas at risk and the dose homogenity in whole PTV (QC) (Fig.1-2) compared to 3D-CRT/OF or IMRT. Despite low total doses used, the results suggest a personalized approach for treatment planning in patients with the recurrent GO.

P 46 IGRT: Optimizing CBCT doses

E. T. Samara[1], C. Castella[1], J.-Y. Ray[1], V. Zilio[1]
[1]Hôpital du Valais, Sion, Switzerland

Introduction: Image-guided radiotherapy (IGRT) uses different imaging techniques in order to assure geometric accuracy of the radiotherapy. Cone-beam computed tomography (CBCT) is one of the techniques widely used for correcting the set-up of the patient. After the acceptance of the Truebeam machine, all standard CBCT protocols were measured and optimized. The optimization included the calculation of the CBCT effective and organ doses, so the results of our work were presented to the medical doctors in order to further optimize the global IGRT strategy.

Materials and methods: All available CBCT dose protocols were evaluated in terms of radiation and image quality. A first optimization of the available protocols was performed by reducing the image rate per second from 15 to 11 and 7. All other parameters (kV, mA, etc.) remained constant. Radiation dose was measured using two cylindrical Plexiglas phantoms of 16-cm (head) and 32-cm (body) in diameter and a 10-cm pencil ionization chamber (PTW, Germany). The PCXMC software was employed to calculate organ and effective doses [1]. Image quality was evaluated with the Catphan 600 phantom (Phantom Laboratory Inc., USA). Spatial resolution, uniformity index, signal-to-noise ratio and the number of Hounsfield units were evaluated for each protocol.

Results: Radiation dose was reduced by 27% with 11 images per second (ips) and by 47% with 7 ips compared with the initial protocol with 15ips. New optimized protocols were established for the clinical use: “High Image Quality” with 11 ips and “Low Dose” with 7ips. Hounsfield units remained constant with the new protocols. The signal–to-noise ratio decreased with the reduction of the ips and total mAs; however, the spatial resolution remained the same. Table 1 below shows the doses to the main organs after a CBCT scan at the pelvis area.

	Pelvis Default	**Pelvis High Image Quality**	**Pelvis Low Dose**
Tension (kV)	125	125	125
Intensity (mA)	60	60	60
Time (ms)	20	20	20
Image per second (ips)	15	11	7
Spead (^{o}/s)	6	6	6
Projection number	900	660	420
mAs	1080	792	504
CTDI (mGy)	14.3	10.5	6.7
Urinary bladder dose (mGy)	41	30	19
Prostate dose (mGy)	31	23	15
Colon dose (mGy)	14	10	7

Summary: New imaging protocols were introduced to the clinics. Radiation technologists were trained to use either “High Image Quality” or “Low Dose” protocols according to the different needs of patient setup. The first treatment will take place in April and clinical tries will allow us to further evaluate the optimization.

References

[1] Tapiovaara M, Siiskonen T. PCXMC, A PC-based Monte Carlo program for calculating patient doses in medical x-ray examinations (2nd Ed.)

P 47 Dosimetric Results of Image Guided Pitch Corrections for Patients with Nasopharyngeal Carcinoma

S. Stieb[1], M. Malla[1], S. Klöck[1], O. Riesterer[1], S. Lang[1]
[1]University Hospital Zurich, Department of Radiation Oncology, Zurich, Switzerland

Purpose: Conventional treatment tables of linear accelerators allow manipulations of the patient in four degrees of freedom. The rotation degrees, pitch and roll are normally not addressed. However, it has been shown in literature that patients could have a variation in pitch and roll of up to 4° during the course of radiotherapy (1, 2). In the meantime several robotic add on systems for corrections in six degrees of freedom (6DoF) are available to compensate for this deficit. In this study the question was addressed if there is any benefit of treating with a 6DoF couch instead of 4DoF. Therefore dosimetric differences in the planning target volumes (PTVs) and various organs at risk (OAR) due to a pitch of the patient of 3° are evaluated in treatment plans of nasopharyngeal carcinoma.

Methods: All six patients with nasopharyngeal carcinoma were treated using volumetric modulated arc therapy (VMAT) to deliver 66 Gy (1 case) and 70 Gy (5 cases) to the PTV in 33 and 35 fractions, respectively. Treatment planning was performed in Eclipse treatment planning system (Varian Medical Systems). Patient pitch was simulated by tilting the planning CT in cranio-caudal direction by +/-3°. For that a copy of the original CT dataset was made, identifying DICOM tags were deleted, PTV structures and structures of organs at risk were copied on the dataset and the dataset was tilted. A verification plan was calculated on the two tilted datasets. PTV coverage and mean and maximum dose to OARs were compared to the original plan. Mean differences in dose have been calculated and Box-Whisker-Plots showing the dosimetric changes have been created using the SPSS software.

Results: Figure 1 shows the changes in dose for the six nasopharyngeal carcinoma patients tilted dorsally and ventrally by 3°. A ventral pitch of 3° leads to an increased dose to the sensitive organs like the chiasm (mean dose: +4.9%), brainstem (max. dose: +1.3%; mean dose: +3.6%), lenses (mean dose: left +9.3%, right: +9.8%), myelon (max. dose: +3.1%; mean dose: -0.2%) and parotid glands (mean dose: left +4.5%, right: +5.6%). The doses to the PTV70 (max. dose: -0.2%; mean dose: -0.7%) and PTV54 (max. dose: +1.6%; mean dose: -0.1%) remained nearly stable. A dorsal pitch of 3° leads to decreased doses to the chiasm (mean dose: -4,9%), lenses (mean dose: left -6.2%, right -6.1%) and left parotid gland (mean dose: -0.4%) whereas the right parotid gland (mean dose: +3.3%) and the myelon (max. dose: +8.2%; mean dose: +0.7%) received larger doses in comparison to the original plan. The changes in maximum dose and mean dose of the PTV70 (max. dose: -0.4%; mean dose: -0.3%) and PTV54 (max. dose: +2.8%; mean dose: -0.4%) were small.

Conclusion: The PTV coverage was only slightly affected by the pitch error of the patient, but it could – depending on the case – be clinically relevant for the organs at risk. Therefore a correction is recommended for nasopharyngeal patients with a 3° pitch mismatch.

References

[1] Kaiser et al., Int. J. Radiation Oncology Biol. Phys, 2006; [2] Ahm et al., Int. J. Radiation Oncology Biol Phys., 2009

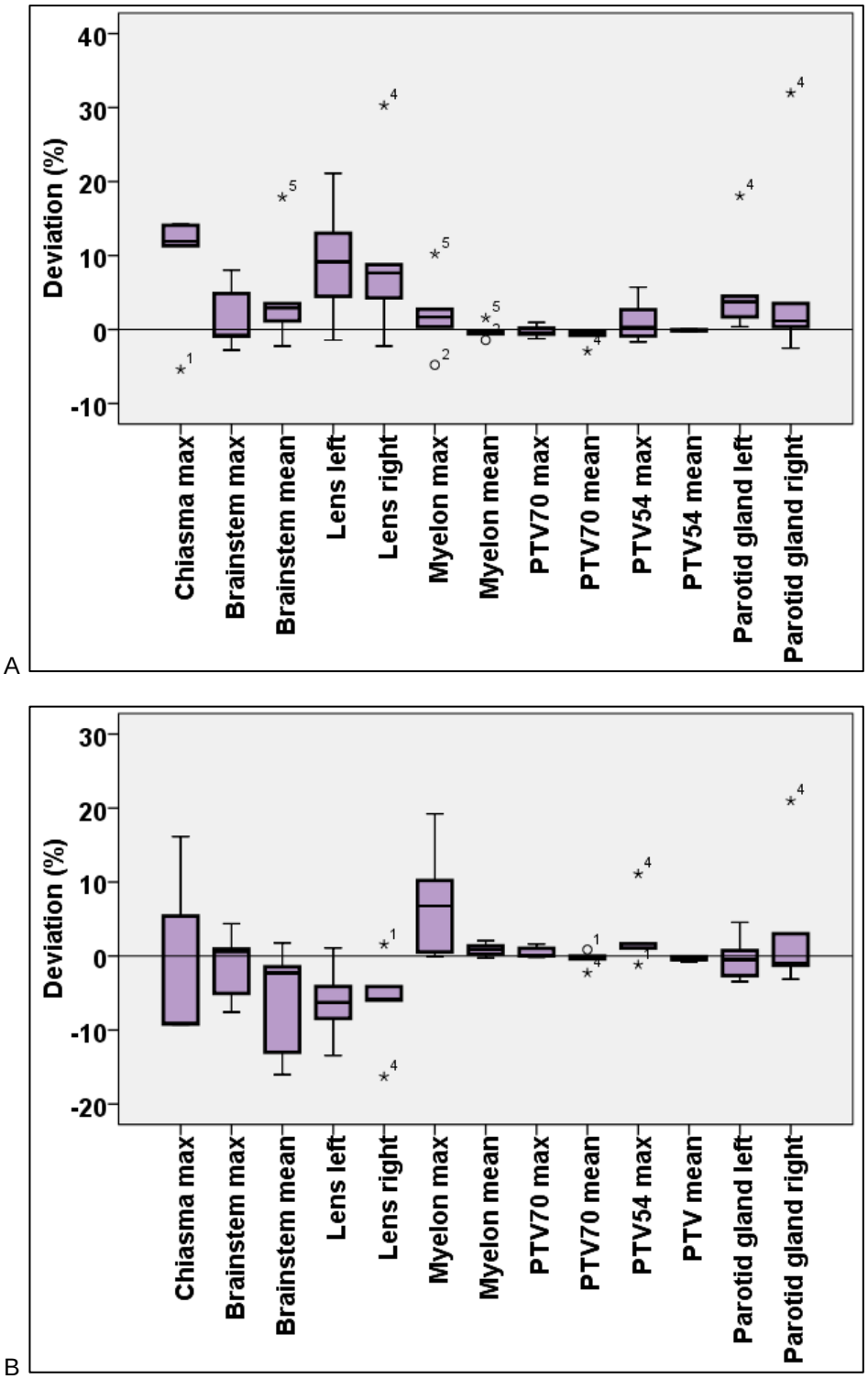

Fig. 1: Boxplots showing the changes in dose in PTV and OARs if the patient is tilted A) ventrally and B) dorsally by 3°.

P 48 Evaluation of gold marker position migration during the radiotherapy treatment course of prostate cancer

S. Kuechler[1]
[1]Uniklinik Freiburg, Klinik für Strahlenheilkunde, Freiburg, Germany

Purpose: The purpose of this study is to assess the variability of relative gold marker position due to deformation and marker migration in external beam radiotherapy for prostate cancer during the treatment course.

Materials and methods: 14 patients with localized prostate cancer who underwent primary IGRT with four implanted gold markers were chosen for this study. The gold marker implantation was carried out one week before the planning CT. The IGRT was carried out using on-board kV imaging (OBI) with CBCT and orthogonal 2d image pairs. The marker positions were identified in the kV-images (figure 1) using an in-house algorithm. In mean 22 pairs of kV-images (between 8 and 28) were evaluated per patient. The inter-marker distances were determined. If there was a longitudinal shift between first and second image that exceeded 2 mm these images were not considered in the evaluation.

Results: Relative marker position can be influenced by organ filling and migration during the course of radiotherapy. For most patients inter-marker distance variations didn't exceed 4 mm. Exemplary evaluation of a patient showed mean marker distance of 32.2 ± 11.8mm (SD). The mean marker distance variation was 0.8 ± 0.4 mm (SD). The maximal variation in inter-marker distance was 3.8 mm. For this patient 18 of 21 image pairs could be evaluated. Three image pairs showed a longitudinal inter-imaging shift that exceeded 2 mm.

Conclusion: Most of the variations in inter-marker distances seem to relate to distortion and volume changes of the prostate. For inter-marker distance variations of up to 3 mm good image matching is still feasible [1]. If the inter-marker distance variation exceeds 3 mm the matching process might become more problematic and the quality should be evaluated. Variations that exceed 4mm should be evaluated. Assessing the causation for distance variation is difficult. A CBCT gives a better estimation of organ fillings that might cause prostate deformation. A sure method to investigate if the change is related to the marker migration is only the evaluation of the following imaging.

Furthermore, if necessary, the planning CT should be repeated and the PTV margins adapted.

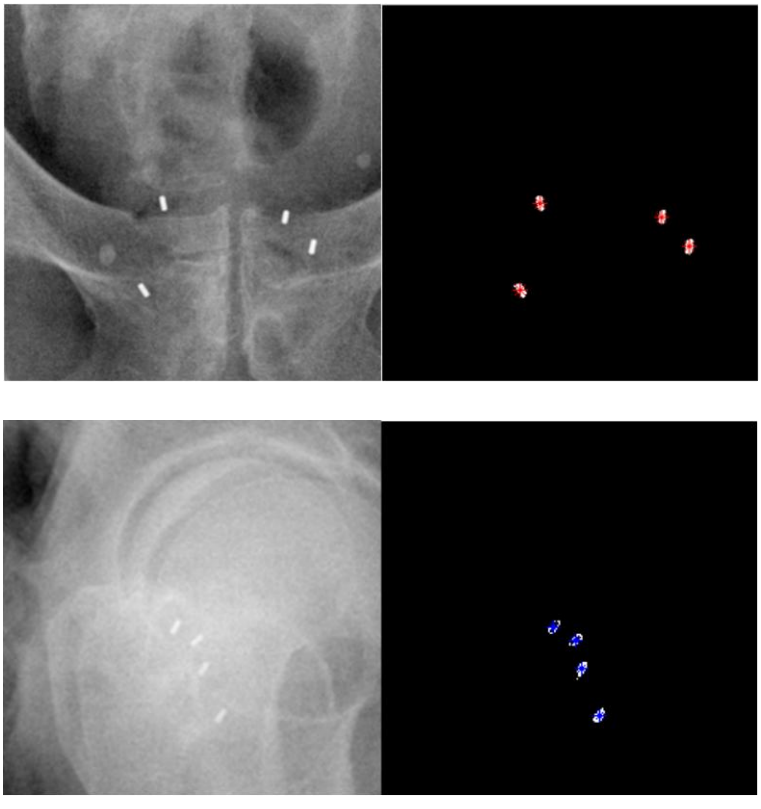

Fig. 1:Marker detection in orthogonal kV images

References

[1] Delouya G et al. „Migration of intraprostatic fiducial markers and its influence on the matching quality in external beam radiation therapy for prostate cancer“ Radiotherapy and Oncology 96 (2010) 43-47.

P 49 Dose reconstruction from EPID images using position dependent point spread functions based on Monte Carlo simulations

D. K. Uchimura Shishechian[1,2], P. Penchev[2], P. von Voigts-Rhetz[2], R. Schmidt[2], K. Zink[2]
[1]Philipps-Universität Marburg, Fachbereich Physik, Marburg, Germany
[2]Technische Hochschule Mittelhessen, Institut für Medizinische Physik und Strahlenschutz, Giessen, Germany

Introduction: The technical developments in radiotherapy, for instance intensity modulated radiation therapy (IMRT) and volumetric modulated arc therapy (VMAT), have heightened the need for an independent method which can verify the applied dose during the treatment. As Electronic Portal Image Devices (EPIDs) are mostly available in modern treatment units and its dosimetric properties were well studied in the past decade, it's obvious that the interest for employing the EPID as a dosimetric device during the treatment is increasing. So far, however, there has been little discussion about differently pronounced undesired influence of scattered particles in the image [1]. This study aims to develop and evaluate a theoretical calculation model that allows reconstructing the applied fluence from the images acquired by the EPID and which can take account of the mentioned influence while still being fast enough.

Materials and methods: The developed method requires the following information: the photon spectrum of the linac, the CT-dataset of the patient and of course the EPID image taken during the treatment. Furthermore the spectral sensitivity of the EPID, its Point Spread Function (PSF) and also that of the water phantom for different thicknesses needed to be determined once for the 6MV photon beam, which was the only spectrum used in the context of this study. In order to verify the accuracy of the mathematical model without the device specific errors or unpredictable disturbances, the research was entirely based on computer simulations using the EGSnrc Monte Carlo code system. Thus the EPID image was assumed to be the computed dose distribution in the scintillator layer of a realistic virtual model of the amorphous silicon (aSi) EPID, which primarily consists of three main layers: a Gadolinium oxysulfide based scintillator layer covered by a 1 mm thick copper plate on top of an amorphous silicon photodiode array of 512 x 384 pixels in a 40 x 30 cm^2 total sensitive surface from which results a square side length of 0.78 mm for one pixel. The geometrical setup of source-to-detector-distance (160 cm) and source-to-isocenter-distance (100 cm) as well as of the point source shape was kept identical for all simulations.

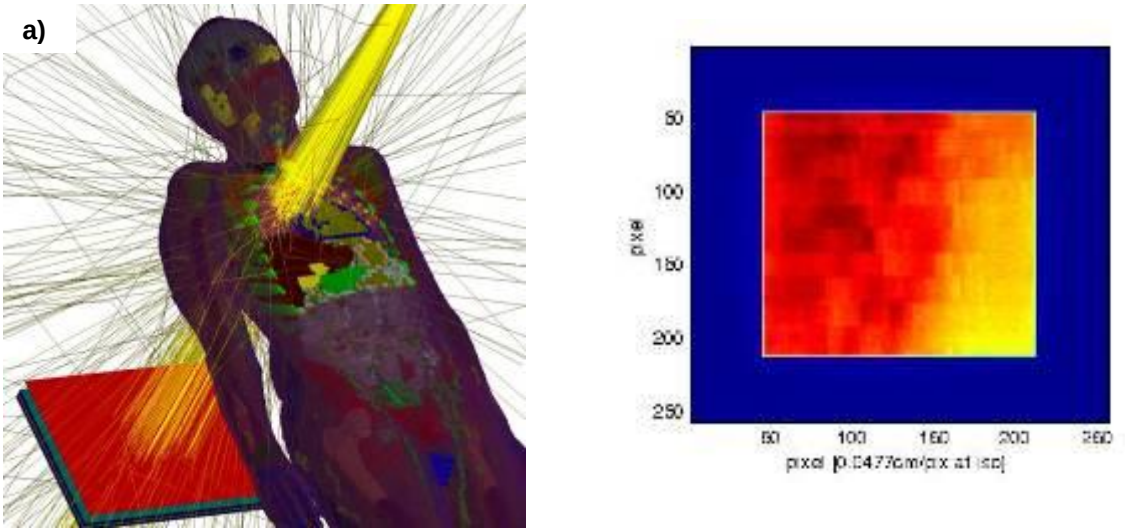

Fig. 1: a): The created simulation geometry. The chest of the phantom was opened to show the irradiated organs and the square under the ICRP phantom is the EPID model. The yellow lines represent the photon tracks and the red lines are those of the electrons. b): The resulting dose distribution from the MC simulation. Darker means a higher dose. A part of the heart is visible in the bottom right in yellow due to higher attenuation (compared to lung).

The calculation method can be described in two steps: reconstruction of the primary fluence at the detector plane and the back projection of it through the patient CT-dataset. Because of the information loss in form of image noise, which is even present in MC simulations due to their statistical uncertainty, the primary fluence is estimated by an iterative deconvolution method. This occurs typically by convolving an estimated image with a single PSF and comparing it to the observed image. The difference between them is then considered for the new estimation in the next iteration step [2]. In this work, the convolution step was modified relying on the superposition principal of position dependent PSFs but, instead of calculating pixel by pixel, the distributivity of the convolution operation was exploited to shorten the computation time (Eq. 1, 2).

$$\text{superposition principal } \Rightarrow I = \sum_{i,j}^{n\times m} I_{ij} \otimes PSF_{ij} \quad (1)$$

I is the $n \times m$ image acquired by the EPID and I_{ij} is a 2D function, which has the primary dose value of P_{ij} at the position i,j and 0 for everywhere else. PSF_{ij} is the dose kernel for the image position i,j. P_{ij} is the dose distribution without dose contribution from scattered particles.

$$I_{ij} = \begin{cases} P_{ij}, & position\ ij \\ 0, & else \end{cases}$$

$$\text{for } PSF_{kl} = PSF_{gh} \xrightarrow[Distributivity]{} I = I_{11} \otimes PSF_{11} + \cdots + (I_{kl} + I_{gh}) \otimes PSF_{kl} + \cdots + I_{nm} \otimes PSF_{nm} \quad (2)$$

The suitable PSF was determined for each pixel position by analyzing the ray path for each detector pixel through the patient CT geometry. This predicts the effective water phantom thickness that would provide the comparable PSF in the EPID image. In order to benefit from the distributivity the resulting thicknesses within the range of 0.5 cm effective water thickness were seen as the same PSF. The back projection of the primary fluence was done with just the same energy dependent linear attenuation coefficient as used for the EGSnrc simulations for the EPID image generation and taking into account the primary photon spectrum of the linac and the spectral sensitivity of the EPID model.

Results: The calculation model was applied on two different treatment scenarios: prostate and lung treatment both in anterior-posterior direction with an 8x8 cm^2 flat field employing the ICRPmale-Voxelphantom with the x,y,z resolution of about 2,2,8 mm (Fig. 1). The result was compared to the reconstruction method using the conventional deconvolution method with a single PSF. Figure (Fig. 2) shows the relative deviation of the reconstructed fluence to the actual applied fluence in the EGSnrc simulation. The method using a single average PSF produced visible position dependent error, while the method with multiple PSF's did reconstruct the fluence more accurately. The mean deviation in the 2nd and the 4th quadrants of figure 2 decreased from -1.52 and 1.01% to 0.10 and 0.13%. Both quadrants are characterized by large inhomogeneities (lung), see figure 1. The histogram in the upper panel of figure 2 shows the distribution of the deviation of the reconstructed entrance fluence.

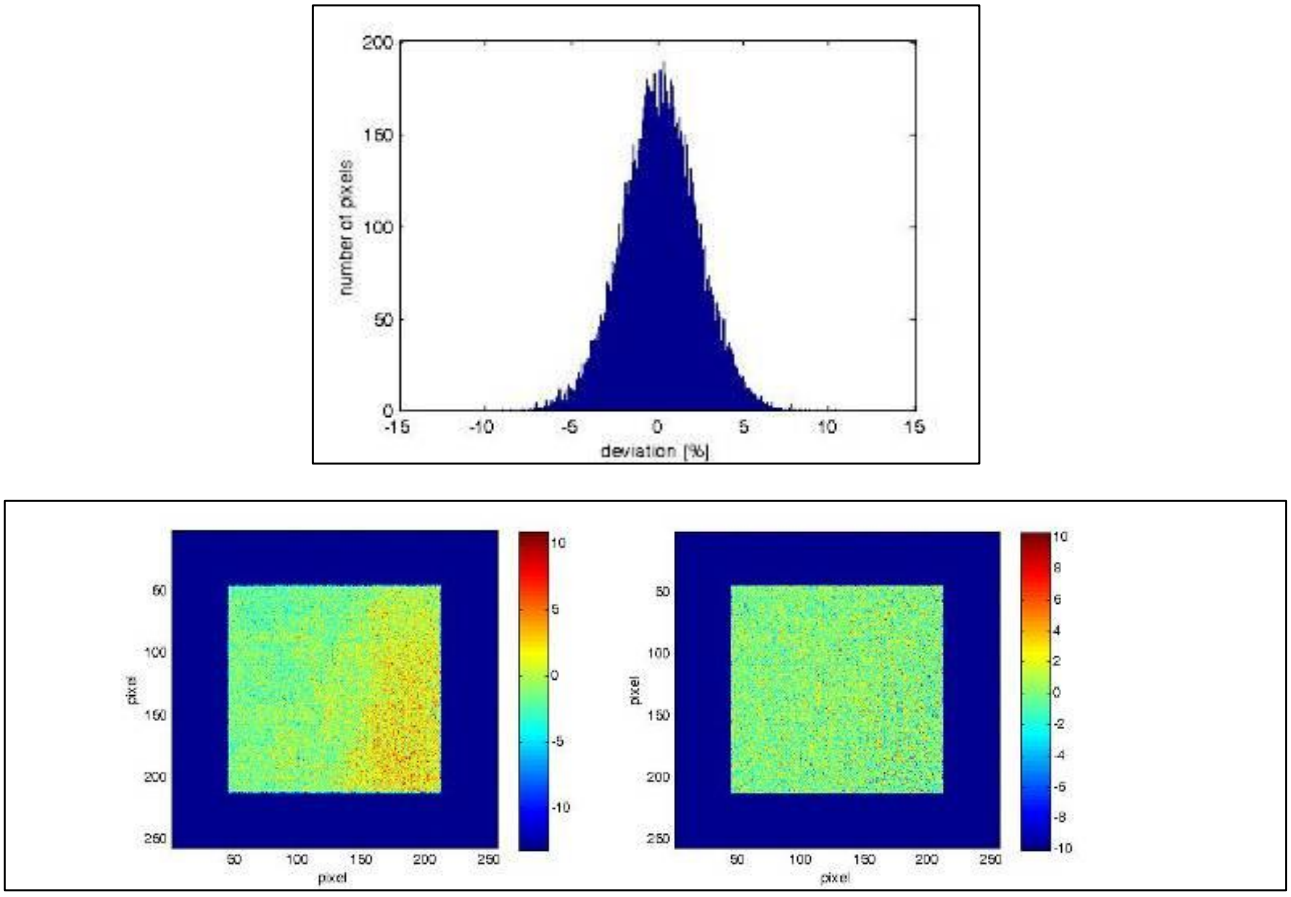

Fig. 2: Deviation of the reconstructed fluence to the actual applied fluence in percent. The upper panel shows its distribution and the lower its spatial distribution. Left: the result using the conventional deconvolution method with a single PSF. Right: using the position dependent PSFs

Discussion and outlook: A calculation method which reconstructs the entrance fluence from the EPID image using position dependent PSFs was developed and its superior accuracy compared to the simple deconvolution method applying a mean PSF could be confirmed on realistic scenarios. The shape of the resulting deviation histogram can be explained by the Gaussian distribution of the statistical noise in the simulated EPID image. The deconvolution was calculated with 29 different PSFs for the lung treatment and 16 for the prostate. It took less than 2 seconds for a 256 by 256 pixel image covering a field size of 12 x 12 cm^2 projected on iso-plane. It is imaginable to monitor the beam deliveryin quasi real time (almost simultaneously) if this algorithm is implemented in a lower level programming language and optimized instead of the MATLAB script employed here. The PSF shape was assumed to be isotropic in this study because of the small ray angle change on the detector. For the applied field size of 8x8 cm^2, this assumption seems to deliver a decent accuracy. The calculated entrance fluence can be further processed with a therapy planning system to provide the 3D dose distribution in the patient. The hardening of the beam on the field edges caused by the collimator has already been pointed out by Li et al. and might be also considered in the future with this method [3].

References

[1] Van Elmpt. W, McDermott. L, Nijsten. S, Wendling. M, Lambin. P, Mijnheer. B.: A literature review of electronic portal imaging for radiotherapy dosimetry, Radiotherapy and Oncology. (2008) 88(3):289–309.

[2] Richardson, WH. Bayesian-Based Iterative Method of Image Restoration, J Opt Soc Am. (1972) 62(1):55–9.

[3] Li. W, Siebers. JV, Moore. JA.: Using fluence separation to account for energy spectra dependence in computing dosimetric a-Si EPID images for IMRT fields, Medical Physics. (2006) 33(12):4468–80.

P 50 Imaging doses for prostate and head-and-neck patients using three different on-board imaging systems

E. Ames[1], Y. Dzierma[1], F. Nüsken[1], N. Licht[1], C. Rübe[1]
[1]Universitätsklinikum des Saarlandes, Klinik für Strahlentherapie und Radioonkologie, Homburg, Germany

Introduction: Modern radiotherapy makes increasing use of image-guidance (IGRT) to achieve good coverage of the target volume and optimal sparing of organs at risk by highly conformal treatment plans. On-board imaging techniques included with the linear accelerator offer straightforward patient positioning verification before treatment, which allows to correct for set-up errors by couch shifts. Since these imaging techniques generally make use of ionizing radiation, the improved localization accuracy comes at the cost of concomitant imaging dose delivered to the patient, which varies considerably depending on the imaging modality used. The aim of this study is to estimate the imaging doses received by the patients for three different imaging techniques available at our institution, considering two very common indications for IGRT: head-and-neck cancer and prostate cancer.

Materials and methods: Three on-board imaging techniques are available at the Department of Radiation Therapy of the Saarland University Medical Centre: the 6 MV treatment beam line, a dedicated image beam line with a nominal energy of 1 MV, and x-ray imaging at 121 kV for cone-beam CT (CBCT, with either 70 kV or 121 kV for planar images). The choice which modality is used depends both on the linac (one linac only offers 6 MV, two IBL, and one kV) and the tumour entity. All three imaging energies were measured and commissioning in the treatment planning system (TPS, Philips Pinnacle V9.2), so they can be included in the patient treatment plans (Dzierma et al., 2013, 2014).

In this study, we included 53 patients with image-guided IMRT treatment of head-and-neck cancer and 36 prostate cancer patients treated in 2013. For all patients, the number of verification images was determined, separately for planar images (two orthogonal axes) and CBCT with the energies 6 MV, IBL (1 MV) and 121 kV (for CBCT only, since the kV imaging dose for planar images is negligible in comparison with the other modalities).

The dose for each verification image was calculated in the TPS either as orthogonal static fields or as rotational fields with the gantry angle and number of monitor units or mAs-value as recorded by the record-and-verify system. We evaluated the absolute dose maximum and maximum dose to the spinal cord, lens, parotids (for head-and-neck), bladder and rectum (prostate cancer), both for the total imaging dose, and for the techniques (6 MV, IBL, kV, planar vs. CBCT) separately.

Results: Images were acquired at every second or third treatment fraction. The following maximum dose values were obtained from the TPS: For head-and-neck cancer, a median of 34.6 cGy, for prostate cancer, 70.6 cGy. The values for different organs at risk are given in Table 1.

	Total	Planar		CBCT		
		6 MV	IBL	6 MV	IBL	121 kV
Head-and-neck						
Overall max	346.4 (132.6; 920.3)	41.4 (13.0; 221.1)	81.1 (13.4; 188.7)	106.6 (33.0; 247.9)	142.3 (19.4; 369.6)	7.5 (7.2; 13.9)
Spinal cord	253.0 (102.1; 716.5)	28.9 (9.3; 122.5)	48.8 (7.6; 120.0)	69.6 (25.1; 200.3)	109.7 (15.5; 299.0)	5.3 (4.5; 8.8)
Lenses	226.7 (11.3; 743.2)	25.4 (1.9; 164.5)	40.0 (0.6; 130.2)	49.1 (7.7; 235.0)	99.1 (2.8; 306.9)	2.9 (1.1; 12,8)
Parotids	268.4 (102.0; 831.2)	27.1 (7.4; 152.3)	49.6 (6.5; 167.9)	76.6 (26.8; 220.2)	116.6 (14.9; 328.0)	5.4 (4.9; 10.1)

Prostate						
Overall max	706 (204; 2313)	69 (16; 229)	56 (13; 217)	374 (147; 771)	211 (48; 1982)	35 (14; 53)
Rectum	551 (120; 1991)	41 (8; 143)	22 (6; 90)	334 (130; 687)	199 (46; 1824)	22 (9; 30)
Bladder	559 (181; 2205)	51 (9; 190)	26 (6; 160)	343 (131; 693)	192 (46; 1917)	25 (11; 33)

Tab. 1 Maximum imaging dose to organs at risk (median (min; max), in mGy).

Conclusions: The contribution of planar images to the imaging dose is smaller than the dose due to megavoltage CBCT, but not negligible in the clinical routine due to the larger number of planar images. The kV imaging modality has very small overall contribution to the imaging dose, which mainly arises from 6 MV and IBL (the latter being more frequently employed and therefore more prominent in the dose contribution).

References

[1] Dzierma Y, Nuesken FG, Licht NP, Ruebe Ch, 2013. Dosimetric properties and commissioning of cone-beam CT image beam line with a carbon target, Strahlenther Onkol 189:566-572.

[2] Dzierma Y, Nuesken F, Otto W, Alaei P, Licht N, Rübe Ch, 2014. IJROBP 88(4):913-919.

P 51 Investigation of different ICP algorithms with respect to the registration precision of data from two different 3D surface sensors (RT-Vision, in-house built)

M. Walke[1], N. Saeednejad[2], G. Krell[2], G. Gademann[1]
[1]Clinic for Radiotherapy, University Clinic Magdeburg, Magdeburg, Germany
[2]Institute for Information Technology and Communications, Faculty for Electrical Engineering and Information Technology, Magdeburg, Germany

Questions and aims: The installation of a new optical sensor on the TomoTherapy HD modality requires the investigation of the precision of the settlement (registration) of raw data generated by this system. The applied ICP (iterative closest point) algorithm should be tested in comparison to the inherent data registration of RT Vision and additionally to the own in-house built 3D surface sensor. The action of independent and different ICP algorithms was tested on raw data for pre-defined positions of the treatment couch. In comparison to this, these ICP algorithms were also applied to data gathered by our installed in-house 3D system in the localizer room. Our aim was an assessment of the usability of different ICP algorithms. Especially an estimation of the reliability of the particular ICP method for registration should be checked.

Methods and materials: The data of two different optical sensors, the RT-Vision system (Scandidos) and an in-house built system (designed and installed by IIKT), have been compared. The registration precision of both systems has been tested on raw data. The used phantoms possess different degrees of shape uniqueness. Defined table motions were applied to simulate patient or phantom position deviations. Four different ICP algorithms were used to calculate translation and rotation vectors with respect to the supported raw data. The ICP algorithms were user delivered (open source Matlab). A routine to reconvert the output data of both 3D systems to the input format of the ICP algorithms has been written (Visual C++). Independent calculations of translations and rotations by own algorithms have been compared with the results of the commercial system.

Results und conclusions: The raw data (point clouds in 3D) of both systems have been extracted. Four different open source ICP algorithms have been applied and two different phantoms types have been used. One phantom owns four surfaces especially build to define the unique assignment with respect to the room coordinates. The other phantom was a torso phantom to reproduce a typical body surface outline. The torso phantom has a weaker uniqueness in transversal motion direction. The contour characteristic is important to define a unique motion direction. Three of four algorithms deliver good results for the test data. As expected, the deviations are slightly higher in the direction of weaker surface structure and the algorithms calculate motion components which not have been induced by the experiment for this phantom. This shows the importance of a unique curvature of surfaces for a subsequently applied registration. Restricting the number of rotation and translation parameters can improve the registration safety and is also shown in the study. Prospectively the assessment of minimum requirements of surface curvatures characteristics is a definite aim of our research to evaluate the worthwhile use of 3D surface sensors for the enhanced pre-treatment positioning of patients.

Poster session V – Medical imaging physics

Chair: E. Guni (Nuremberg/DE)

P 52 Can patients with high risk of treatment failure of selective internal radiation therapy (SIRT) be identified by image co-registration of PET, MAA and Y90?

L. Thomas[1], H. Ahmadzadehfar[1], M. Essler[1], W. Willinek[2], C. Meyer[2], L. Papp[3], N. Zsóter[3], R. A. Bundschuh[1]
[1]Universitätsklinikum Bonn, Klinik und Poliklinik für Nuklearmedizin, Bonn, Germany
[2]Universitätsklinikum Bonn, Radiologische Klinik, Bonn, Germany
[3]Mediso Medical Systems, Budapest, Hungary

Objectives: For patients with multifocal unresectable primary liver carcinoma or metastatic liver tumours selective internal radioembolization therapy (SIRT) with Yttrium 90 (^{90}Y) labelled microspheres is a promising therapy option. In SIRT radioactive microspheres are injected directly into the tumour using an intraarterial catheter. Advantage of this method is the direct deposit of the injected activity almost completely in the liver and mainly the tumor tissue. Aim of this study is the comparison of the pretreatment metabolic volume, assessed with 18F-flurodesoxyglucose (FDG)-positron emission tomography (PET) with activity distribution of therapy simulation imaging using Technetium-99m labelled macroaggregated albumin (^{99m}Tc-MAA), activity distribution of therapeutic Y90 and metabolic volume after SIRT. Especially, it is determinded if there are new or progressive metabolic areas in the post therapeutic PET/CT in areas where no SIRT activity was delivered by therapy, but a metabolic volume in the pre therapy PET/CT was present.

Material and methods: So far the study included 6 patients (2 women 4 men) with unresectabel liver metastases. Before SIRT patients underwent FDG-PET/computed tomography (PET/CT) (prePET) examination.

For therapy preparation patients underwent angiographic guided coiling of the vessels to the gastrointestinal tract. As simulation of the injection of the therapeutic Y-90 labelled spheres, a pretreatment injection of ^{99m}Tc-MAA was done followed by SPECT/CT imaging (MAA) to control if there is no collateral blood flow from the liver into the gastrointestinal tract or into the lung. 1-2 days after SIRT, Bremsstrahlung imaging was done using a SPECT/CT (Y90) to determine the distribution of the ^{90}Y. A follow-up PET/CT for staging scan was done 4 weeks after treatment (postPET). After rigid-registration of the CT-components of the prePET, postPET, GKY90 and MAA, all associated images, the two PETs and the 2 SPECTs, are automatically co-registered. Segmentation was done manually in the registered PET respectively in SPECT images. After registration the overlap values (OV) of PrePET&MAA, PrePET&Y90 and MAA&Y90 were determinded. It was visual analysed if there are any new or progressive lesions in regions where PrePET was positive and no SIRT-spheres were applied.

Results: For the comparison of overlaps we found the following values in relative differences: OV-PreaPET&MAA-> 63%± 36%, OV-PraePET&Y90-> 53%± 17% and OV-MAA&Y90 -> 47%± 40%. In all 6 patients it was seen, that in liver tissue, were PrePET was positive and Y90 negative, there was a progressive tumour increase in addition to the PrePET positive tissue. Differences in overlap values can be the result of heavy influence of respiratory movement to the liver or resulting from respiratory movement a not exact rigid registration.

Conclusion: Around pre treatment metabolic PET-positiv liver tissue, which was not treated by ^{90}Y labeled mircospheres an expansion of the PET-positive volume was determined in the post therapeutic PET-scan which can be considered as progressive disease. Therefore such patients may benefit from additional treatment directly after SIRT. In addition we found serious differences between MAA scan and Bremsstrahlung-imaging.

P 53 PET/CT-based image processing method for the determination of the Variance of Standardized Uptake Value (SUV) in assessing response to therapy of patients with bronchial carcinoma.

A. Rastädter[1], M. Fiebich[1]
[1]Technische Hochschule Mittelhessen, Institut für Medizinische Physik und Strahlenschutz, Gießen, Germany

Introduction: Hybrid systems combining CT with positron emission tomography are principal medical imaging systems for cancer care and control the therapy progress particularly bronchial carcinoma. Beside the anatomical structures of the CT, the PET enables the representation of molecular processes in vivo. The accumulation of the tracer FDG (18F-Deoxy-glucose) takes place in locations with high metabolic rate as in cases with malignant tumor, but also in the brain and is proportional to the radioactive signal that is detected by the PET. The classification of patient individual case of tumor disease is realized by the international TNM (Tumor Nodes Metastasis)-staging system. To control the progress of therapy the use of standardized uptake value (SUV) is common. SUV serves as a semiquantitative imaging biomarker for cancer response [1]. It's defined as the ratio of tissue radioactivity concentration (kBq /ml) and the amount of injected radiolabeled FDG (kBq) divided by the weight of the patient (g) [2]. The radioactivity concentration is proportional to the intensity of the detected signal given in gray values in the image. Consequently, the intensity is an important variable to calculate the SUV. It is automatically determined in this work to fascilitate and optimize SUV calculation. Kumar et al describe in their work the possible variance in clinical practice by measuring the SUV [3]. To figure out the deviation between semi-automatic and manual measurements of this value a software tool was developed in ImageJ [4].

Materials and methods: An ImageJ plug-in (SegRegLex) is written in Java for the segmentation of the lung, automatic fusion of CT and PET images and for a semi-automatic assessment of the SUV. The SegRegLex window is the main window of the plug-in which consists of a command panel to open and save DICOM-files and 3 further panels described below:

- Segmentation: In the first panel the segmentation of the lung and the body is realized by an algorithm which dilates a binary duplicate of the CT-Data and subtracts another duplicate. The result window is an outer and inner contour of the data. This dataset is added as an overlay to the CT-Data.
- Fusion: Subsequently, the fusion of the PET and CT-Dataset is done by adding a semitransparent preprocessed PET-data to the CT-data.
- SUV-Assessment: For calculating the SUV, the gray values of the tumor region have to be determined. A semi-automatic method for defining the region of interest based on a region growing approach is implemented. It is realized by demanding the user to click on the region of interest to set a starting point for the algorithm. Then a ROI is defined automatically based on fixed threshold.

For comparing the performance of the new automatic approach and the commonly used manual definition for the ROIs, 5 scans from patients involved in routine lung cancer staging, were used in a validation study. For this reason the mean gray values and the standard deviation of the defined ROIs were representatively taken into account for assessing of the SUV.

Results: A GUI was developed, which enables a look and feel appliance. As a result fast and easy processing of the fused image series is provided. Image 1 shows the defined SUVs in layers of the fused dataset drawn with manual thresholding in 2 patients. Image 2 shows determination of the SUV with the help of the semi-automatic adapted thresholding algorithm. As shown in Table 1 both SUV-assessments methods have a considerable difference of the intensity which would lead to different SUV-values. Especially in patients with inhomogeneous tumors manual definition of the ROI can lead to substantially different values of the SUV. For regions where the amount of smoothing is relatively high (Image 1, 2 right-handed), it reveals that an automatic calculated threshold is needed for accurate lesion size. Manual measuring of SUV is not as reproducible as an automatic process. Moreover the automatic SUV measuring is helpful for quantified diagnosis and results are less fluctuating and more stable.

Conclusion: The new software tool enables an automatic segmentation of the lung and the body in the datasets. Furthermore it can overlay PET/CT-datasets and allows easy modification, customization, and enhancement to the image data as it is implemented in the powerful image progressing software ImageJ. It enables further quantitative analysis, (e.g. volumetry, intensity measurements) or different graphical representation of the datasets (e.g. maximum intensity projection (MIP), anatomical planes). The semi-automatic approach for the calculation of the SUV offers a new possibility to reduce the variance of this value. The comparison between the two methods for determining the SUV shows a significant difference (Table1). Therefore it is reasonable to perform quantitative evaluation with the help of a semi-automatic software tool rather than manual definition of the ROI. It is shown that an automatic determined ROI can reduce the variance of the SUV in particular for supplying more reliable evaluation of response to therapy.

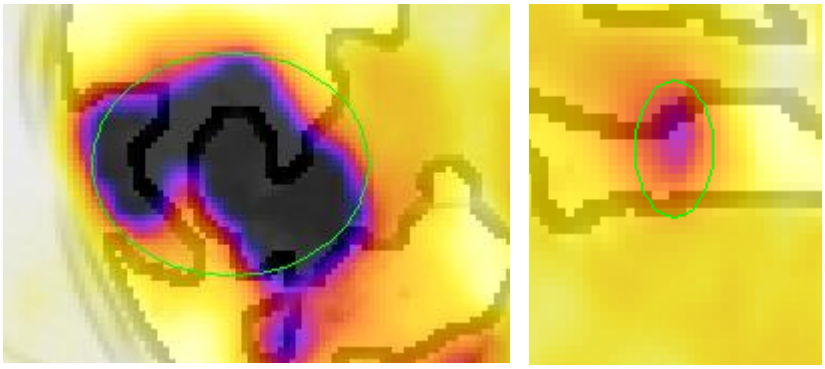

Fig 1: Fused PET/CT-Dataset with manual segmentation of the ROI (Left-handed: Patient 1, Right-handed: Patient 2)

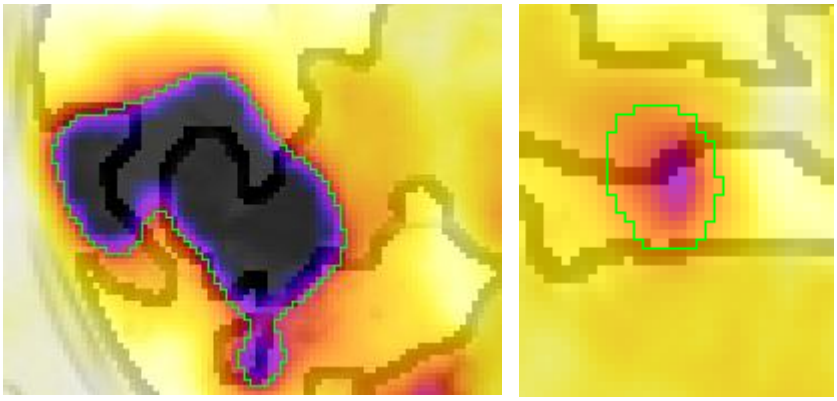

Fig. 2:Fused PET/CT-Dataset with automatic segmentation of the ROI (Left-handed: Patient 1, Right-handed: Patient 2)

Intensity of manual and automatically defined tumor regions : $\bar{I} \pm \sigma$[AU]					
	Patient 1	Patient 2	Patient 3	Patient 4	Patient 5
Manual	41,4±60,3	118,8±21,5	46,7±33,2	74,0±34,7	48,4±28,1
Automatic	21,2±28,7	141,1±26,8	43,9±29,9	72,3±31,3	53,5±28,8

Tab. 1: Intensity of the gray values including standard deviation of the segmented areas in the Images

References

[1] Berghmans et al.: Primary tumor standardized uptake value (SUVmax) measured on fluorodeoxyglucose positron emission tomography (FDG-PET) is of prognostic value for survival in non-small cell lung cancer (NSCLC): a systematic review and meta-analysis (MA) by the European Lung Cancer Working Party for the IASLC Lung Cancer Staging Project. J Thorac Oncol. 2008 Jan;3(1):6-12. doi: 10.1097/JTO.0b013e31815e6d6b.

[2] Kinahan et al.: PET/CT Standardized Uptake Values (SUVs) in Clinical Practice and Assessing Response to Therapy. Semin Ultrasound CT MR. 2010 December; 31(6): 496–505. doi:10.1053/j.sult.2010.10.001

[3] Kumar et al.: Variance of SUVs for FDG-PET/CT is greater in clinical practice than under ideal study settings. Clin Nucl Med. 2013 Mar; 38 (3):175-82. doi: 10.1097/RLU.0b013e318279ffdf.

[4] ImageJ, developed by Wayne Rasband (http :(/imagej.nih.gov/ij/docs/index.html).

P 54 ^{19}F-MRI of Different Fluor Substances for the Investigation of Drug Dissolution in the Gastrointestinal Tract

J. Friedrich[1], J. Schröder [1], S. Kindgen [2], S. Fischer [1], M. Schuppert[1], K. Gogoll [2], P. Langguth [2], L. M. Schreiber [1]
[1]University Medical Center, Section of Medical Physics, Department of Radiology, Mainz, Germany
[2]Johannes Gutenberg University , Institute of Pharmaceutical Technology and Biopharmacy , Mainz, Germany

Introduction: To investigate the transit and dissolution of oral application forms like tablets or capsules in the gastrointestinal tract, Several techniques have been developed(e.g. ultrasonic and magnetic marker monitoring).Yet another promising method is the imaging of fluor containing substances using ^{19}F-MRI. It was already shown that the visualization of perfluorocarbone and the determination of gastrointestinal transit times are feasible[1,2]. The aim of the present study is the development of an MRI technique that allows for in vivo investigation of oral applied pharmaceutical substances. Therefore, different fluor containing substances were analyzed with regard to their relaxation times and signal quality. First measurements with tablets that contained perfluoro-15-crown-5-ether and a semifluorinated alkane were performed.

Methods: All measurements were performed on a 1.5T MRI system (Siemens, Magnetom Avanto, Germany) using a purpose-built, home-made ^{19}F transmit/receive coil, that was optimized for a 1.5-mL-microcentrifugetube. The investigated substances were perfluoro-15-crown-5-ether (PFCE, ChemPur, Germany), PFCE-emulsion (40% wt/wt PFCE), commercially available toothpaste jelly (contains: NaF, $C_{27}H_{60}F_2N_2O_3$ and $C_{18}H_{38}FN$, GABA GmbH, Germany) and two novel semifluorinated alkanes (SFA) in the following referred to as SFA1 and SFA2. Further, specimens containing SFA (1.5 mL) mixed with 30 µL Gd-DOTA, a specimen containing SFA2-emulsion (40% wt/wt) and a specimen containing SFA2-gadolinium-emulsion (4.5 mM Gd-DOTA) were prepared. Spectroscopic saturation recovery sequence and spin echo sequence were utilized to determine T_1 and T_2 of all substances, respectively. Spectra and images were acquired using a FID-sequence and a gradient echo (GRE-) sequence. In addition, a porous SFA2 and a PFCE loaded tablet were imaged using a GRE-sequence and a TrueFISP-sequence, respectively.

Results: In general, all substances provide a measurable MR signal. The pure PFCE yielded the highest signal intensity in short measurement times (seconds) without signal averaging. The jelly offered poor signal in comparison to PFCE substances and SFA. The relaxation times are listed in TAB. 1. A significant influence of Gd-DOTA on the relaxation times of the pure SFA was not observed. The emulsion of SFA2 has a slightly shorter T_1 in comparison to the pure SFA2, but the difference is not significant. T_2 in comparison is considerably shortened. While the spectra of PFCE and the PFCE-emulsion showed only one resonance peak the jelly spectrum consists of at least four peaks that agglomerate to one broadened peak. In contrast, the resonance peaks of SFA1 and SFA2 separate in four and five peaks, respectively while one peak is clearly separated from the others (see exemplarily FIG.2). Tablets containing SFA2 and PFCE were successfully prepared and imaged (see FIG.1 c).

Discussion: In this study different ^{19}F containing substances were investigated in order to use the most promising substances in future studies to explore the dissolution process of oral application forms. Due to the small amount of ^{19}F-atoms inside the measured volume the jelly yielded the lowest signal intensity. A higher concentration of ^{19}F containing substances within the jelly may overcome this problem but would increase the toxicity of the jelly. The SFA were identified as the most advantageous substances for further studies of the dissolution process of oral application forms. Although PFCE provides the highest signal intensity its hydro- and lipophobic properties are disadvantageous and therefore its molecules would rather agglomerate than distribute within an examined volume. Therefore, PFCE needs to be emulsified. The SFA are biological inert and possess both a hydrophilic and a lipophilic character which makes them attractive for the use with other pharmaceutical substances. Here, first successful trials of imaging tablets loaded with pure SFA2 and PFCE are presented.

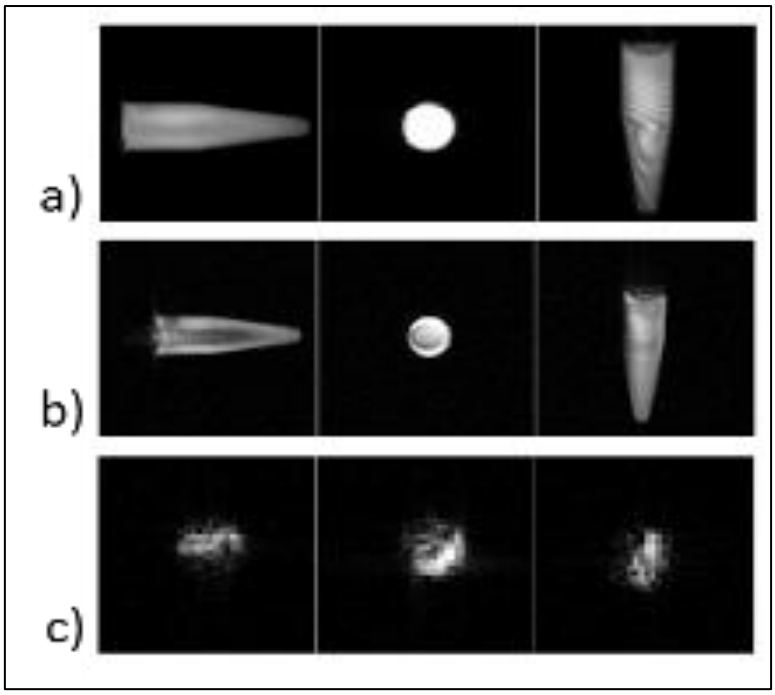

Fig. 1: Images of PFCE and SFA2 in a 1.5-mL-centrifuge-tube with a resolution of 0.6x0.6 mm. a) PFCE (SNR = 430), b) SFA2 (SNR = 50) and c) SFA2 loaded tablet (SNR= 25).

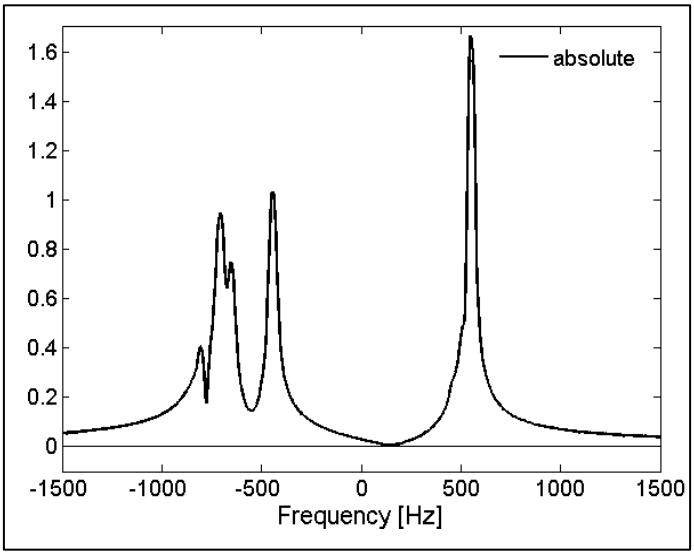

Fig. 2: Spectrum of the SFA2 loaded tablet

Substance	T_1 [ms]	T_2 [ms]	^{19}F-atoms per 1.5 mL [$\cdot 10^{21}$]
PFCE ($C_{10}F_{20}O_5$)	933 ± 3	719 ± 3	55
PFCE-emulsion	1155 ± 30	538 ± 5	13
Jelly	422 ± 19	135 ± 2	<1
SFA1	1629 ± 49	156 ± 35	36
SFA1 + Gd	1635 ± 35	153 ± 26	
SFA2	940 ± 6	150 ± 10	36
SFA2+ Gd	922 ± 10	126 ± 11	
SFA2-emuls.	896 ± 39	90 ± 7	11
SFA2-Gd-emuls.	883 ± 18	22 ± 2	11

Tab. 1: MR properties of the investigated fluor substances.

Acknowledgement: This study was supported by the German research foundation, DFG (SCHR 687/5-1, SCHR 687/5-2, SCHO 1375/1)

References

[1] Hahn T., et al., Magn Reson Med 2011;66(3):812-820
[2] Schwarz R., et al., Magn Reson Med 1999;41(1):80-86

P 55 Parametric imaging for analyses of discrepant radionuclide uptakes using NaI-131 and Tc-99m pertechnetate in patients with thyroid autonomy

U. Lützen[1], U. Karwacik[1], Y. Zhao[1], C. Winkler[1], A. Tjiong[1], M. Zuhayra[1], M. Marx[1]
[1]Klinik für Nuklearmedizin, UKSH, Campus Kiel, Kiel, Germany

Introduction: Radio iodine therapy is a common method to treat thyroid autonomies, which is detected prior to therapy using a Tc-99mO4-scintigraphy. Intratherapeutically the uptake of I-131 is also shown by scintigraphy. The aim of this study was to compare the uptake of the different tracers with a subtraction analysis and a 3D-illustration of the variations.

Material und Methods: Retrospectively the scans showing the pretherapeutical and intratherapeutical tracer uptake of 38 patients (20 women and 18 men) suffering from autonomies of the thyroid (18 unifocal, 15 multifocal, 5 disseminated) were compared. For subtraction analysis the scans were normed, the Tc-99mO4- was subtracted from the I-131-scan and displayed parametrically using an evaluation program. The distribution of the activity was calculated as an absolute value and percent wise.

Results: Through visual evaluation a differing distribution of activity could be observed in 15 of 38 cases (39,5%), the uptake of I-131 was more intense in 12 cases (31,6%), the uptake of Tc-99mO4 in 3 cases (7,9%). No significant difference could be found in 23 cases (60,5%). By calculation, a difference of activity uptake could be found in 23 cases (60,5%). The uptake was higher in 4 (10,5%) for I-131, and 19 (50,0%) for Tc-99mO4. No greater varieties could be found in 15 cases (39,5%). A division of the patients into 9 groups comparing the visual and calculated evaluation showed concordance in 10 cases (26,3%), whereas discordance could be observed in 28 (73,7%) cases.

Conclusion: A quantification of distribution of Tc-99m and I-131 activities by parametric substraction images is feasible. The discrepant results compared with visual evaluation are unexpectedly high, possibly due to differing biokinetics of both tracers. A pretherapeutical administration of I-123 could achieve less deviation to I-131 and should further be discussed for better therapeutical results and patient outcome despite of higher costs and radiation hazard.

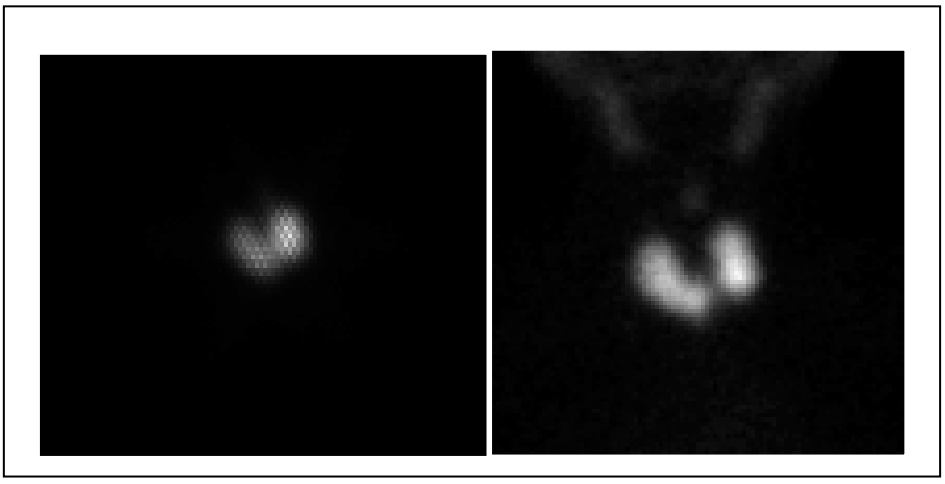

Fig. 1: I-131-scan (left), Tc-99m04-scan (right)

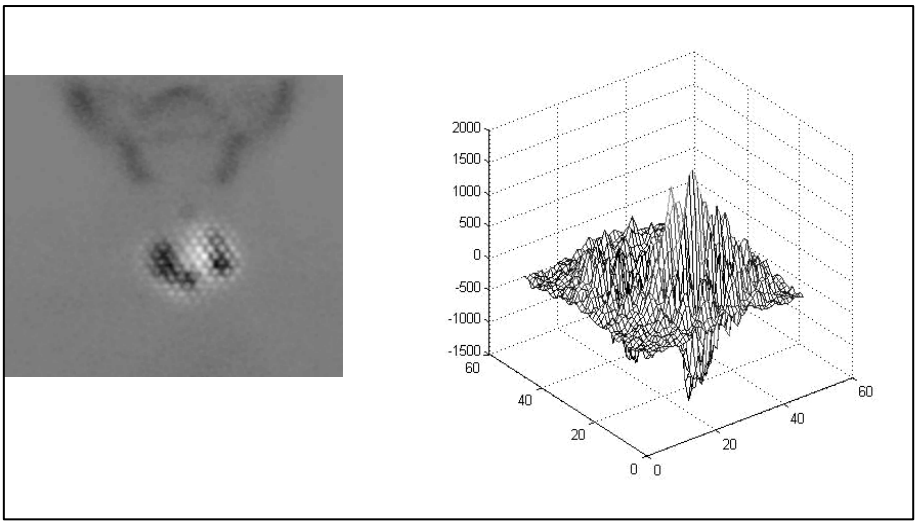

Fig. 2: Substraction image (left), 3-D-image, I-131 above, Tc-99m below (right)

	Iodine > Tc	Iodine < Tc	Iodine ≈ Tc
Scans (visual)	12	3	23
3D-image (calculated)	4	19	15

Tab. 1: Visual vs. calculated evaluation, > higher intensity, > lower intensity, ≈ equal intensity

References

[1] Quin-Sheng Chen.: Parametric imaging of patient pharmacokinetics. European Journal of Nuclear Medicine (1997); 24 (11): 1369-1373.

[2] Goris, M.L.: Parametric images as a tool for quantitative normative evaluation. Seminars in Nuclear Medicine (1987); 17 (1): 18-27.

[3] Schommartz B, Cupisti K, Antke C et al. Lokalisation von Nebenschilddrüsen-adenomen mit planarer 99m-Tc-Sestamibi-Szintigraphie: Vergleich von Subtraktions- und 2-Phasen-Technik. Nuklearmedizin 2006; 45 (3): 115-121.

[4] Gorowski T, Chomicki OA. Some comparative studies using 99m-Tc and 131-I in thyroid scanning. Nuklearmedizin 1976; 15 (6): 268-272.

P 56 Signal stability of MR sequences used for attenuation correction in PET/MR

M. Lukas[1], S. Ziegler[1]
[1]Technische Universität Munich, Klinikum rechts der Isar, Nuklearmedizinische Klinik und Poliklinik, Munich, Germany

Introduction: In contrast to non-MR related PET systems, PET/MR does not provide information about electron density that essentially is needed for quantitative emission tomography. Several concepts to solve this issue by generating synthetic attenuation maps have been proposed [1]. They generally can be categorized into *atlas-based methods* which generate pseudo-CTs by nonlinear registration of prior given CT/MR correlates [2,3,4], and *segmentation based techniques* trying to classify tissue types using their different MR contrasts [5,6,7]. Both methods depend strongly on image quality, thus it is crucial to maintain it constant. Particularly the accuracy of segmentation approaches based on different MR sequences is prone to changes in tissue contrast and signal-to-noise ratio.

Apart from imaging parameters, the image quality depends on a wide range of physical factors like temperature, subject geometry, hardware used, etc. which can vary over time [8]. Even if modern MR scanners are able to eliminate most of these influences, there are sequences which are still highly sensitive, including those which are used for attenuation correction (AC). Sequences based on ultrashort echo times (UTE) for instance, are filling k-space already during gradient ramping. Due to this, the signal is strongly affected by hardware fluctuations caused by eddy currents or gradient ramping variations [5].

In this work the course of image contrast of MR sequences currently used for PET AC (Siemens UTE-VB18, UTE-VB20, DIXON, MPRAGE) was observed under changing clinical conditions within one day, one week and over 3 months to guarantee constancy and robustness for in-house established AC methods. Investigations were done by single subject to get an idea about the diversity of possible image quality issues.

Material and methods: Acquisition: All measurements were done at a clinical scanner (3 T, Biograph mMR, Siemens AG Medical Solutions) equipped with the 16-channel head/neck coil. The same volunteer was scanned for 4 days every morning after scanner start-up and every evening immediately after the last clinical patient with Siemens MPRAGE (isotropic 1³ mm³, TR/TE/TI = 2300/2.98/900 ms, α = 9°)**,** UTE-VB18 (isotropic 1,5625³ mm³, 192³ px³, $TR/TE_1/TE_2$ = 11.94/0.07/2.46 ms, α = 10°)**,** UTE-VB20 (isotropic **1**,5625³ mm³, 192³ px³, $TR/TE_1/TE_2$ = 3.98/0.07/2.46 ms, α = 10°) and DIXON (2,343 x 2,343 x 2,73 mm³, 126 x 192 x 128 px³, TR/TE = 3.6/2.46 ms, α = 10°)**.** Afterwards the test series was continued once per week for further 12 weeks (n_{total} = 20). System and room temperature were protocolled as well as the volunteer's body temperature measured with an ear thermometer.

Image Preprocessing: For each dataset all sequences were coregistered to each other with MPRAGE as reference using Matlab (R2013a, MathWorks) and SPM8 (rev4252, University College London). Parameters were: Separation = 2/2, Histogram Smoothing = 7/7, Interpolation = 5th Degree B-Spline. For determination of tissue contrasts the MR magnitude images were segmented. To distinguish cerebrospinal fluid (CSF), grey matter (GM), and white matter (WM) SPM's segmentation tool was used to generate probability maps with the parameters: Gaussians per class = 2/2/2/4, Affine Regularisation = ICBM European brain, Frequency Cutoff = 25, Bias FWHM = 60 mm cutoff, Sampling Distance = 2. For segmentation of bone, cavital air, and background the AC maps of UTE-VB20 generated by the scanner were used. To avoid the influence of Gibbs artefacts, the background was defined to be every voxel with at least 30 mm distance to skin surface.

Analysis of data: For each segment the mean (Signal *S*) weighted by segment probability and the standard deviation (*SD*) was extracted with Matlab. To get a robust but semi-quantitative parameter for contrast which remains unaffected by unknown image post processing and Gibbs artefacts, we defined, opposed to the NEMA recommendation [9], contrast *C* to be $C = S_{segment} / S_{bkg}$. Contrasts were normalized to white matter whereupon the background signal S_{bkg} is cancelled out by definition. Due to missing sharp structures in brain, the skin-air interface was used for calculation of sharpness. Therefore the skin was extracted from most cranial slice still including the Corpus Collosum and a profile was generated as described in figure 1. After curve fitting using the sigmoidal function $\mathbf{y}(\mathbf{x}) = \boldsymbol{y_0} + \frac{1}{1+e^{-((x_0-x)/B)}}$, parameter B describes the sharpness inversely proportional.

Statistics: The datasets were analysed descriptive using SPSS (v21, IBM Corporation). The dependence of means and SD from time of day was analysed by *Mann-Whitney U test*. The means and SD and their central tendency over the weak and months was tested with *Kruskal-Wallis one-way analysis of variance by ranks test*.

Results: The room temperature was constant with 21.3 ± 0.4°C on every scan. The scanner's cooling system temperature varied between 21°C and up to 32°C after special scans. UTE sequences **(**UTE-VB18, UTE-VB20) with their radial readout were found to be much less prone to motion artefact than MPRAGE. Due to the scan time of about 5 min for MPRAGE swallowing reflexes often provoke motion artefacts in facial and neck regions.

Signal stability: The volunteer's body temperature was varying with 37.1±0.4°. The head shift over all 20 scans was X/Y/Z = ±2.1/±2.3/±12.3 mm and tilt X/Y/Z = ±1.8/±4.6/±3.01°. As seen in table 1, the signal magnitude for GM, WM, CSF, bone and cavital air are very constant for all used MR sequence. The standard deviations are much less than 3% for high signal (WM, GM, CSF) and less than 5% for low (or no) signal tissues (bone, air). That also leads to invariant tissue contrast. No time correlation to MR signal was found by statistical testing (equal distribution significance α for all cases $\alpha > 0.9$). Neither for body, room or cooling temperature nor for head position and tilt a significant impact on signal could be found.

Image sharpness: No relationship between sharpness and head shift, tilt or time for any of the used sequences was detected. In comparison to UTE-VB18, UTE-VB20 improved the sharpness and its deviations by adding calibration steps to correct for effects of eddy currents and gradient delays.

Conclusion: One volunteer was scanned 20 times for different sequences distributed over 3 months to get a prediction about tissue contrasts and stability of signal. In addition to this, the sharpness as an important parameter for accuracy of tissue classification was investigated. It was found, that the magnitude signals were very stable. Also the contrast ratios for bone, air and tissue (WM, GM, CSF) were constant and independent of head position, tilt, body temperature and time. In context of signal stability all sequences can be used unhesitatingly to generate attenuation maps with high reproducibility**.** In case of sharpness, MPRAGE delivered the highest, DIXON the lowest resolution and sharpness. UTE-VB20 as successor of UTE-VB18 provides better reproducibility and sharpness due to implemented calibration steps.

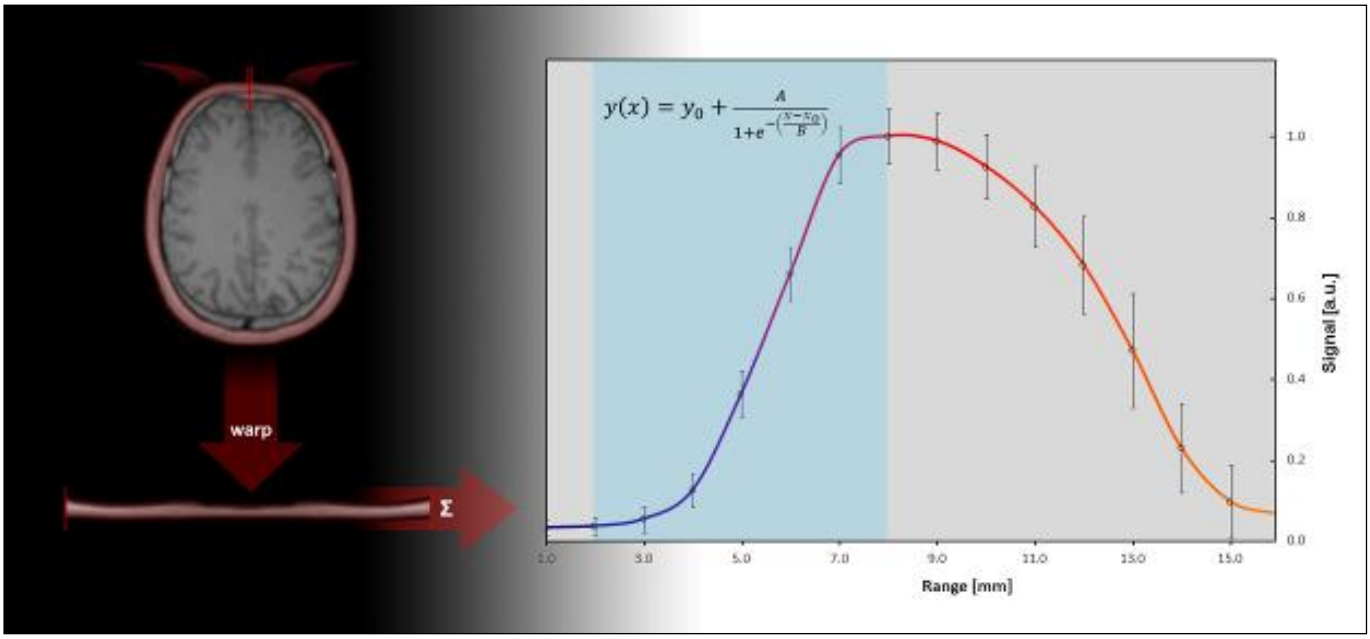

Fig. 1: Semi-quantitative analysis of sharpness. The skin was extracted by masking. After warping, the sum gives a profile that can be fitted by sigmoidal function where B describes the slope as a value for sharpness.

	MPRAGE		***UTE_{VB20} TE_1***		***UTE_{VB20} TE_2***		***UTE_{VB18} TE_1***		***UTE_{VB18} TE_2***		***$DIXON_{IP}$***		***$DIXON_{OP}$***	
	S_{Mag}	R_{WM}	S_{Mag}	R_{WM}	S_{Mag}	R_{WM}	S_{Mag}	R_{WM}	S_{Mag}	R_{WM}	S_{Mag}	R_{WM}	S_{Mag}	R_{WM}
WM	351.9 *± 1.9%*		87.5 *± 2.2%*		84.5 *± 3.7%*		297.1 *± 1.9%*		267.4 *± 4.2%*		294.4 *± 2.8%*		293.7 *± 2.9%*	
GM	241.9 *± 1.9%*	0.687 *± 0.5%*	72.5 *± 2.1%*	0.829 *± 0.1%*	70.4 *± 3.5%*	0.833 *± 0.2%*	246.9 *± 1.9%*	0.831 *± 0.2%*	227.8 *± 4.1%*	0.852 *± 0.25%*	249.8 *± 2.8%*	0.850 *± 0.20%*	247.8 *± 2.9%*	0.844 *± 0.19%*
CSF	116.4 *± 2.3%*	0.331 *± 1.2%*	70.5 *± 2.1%*	0.806 *± 0.9%*	48.3 *± 2.9%*	0.571 *± 0.9%*	238.8 *± 1.8%*	0.804 *± 1.0%*	156.5 *± 3.8%*	0.586 *± 0.7%*	190.0 *± 2.5%*	0.646 *± 0.5%*	165.5 *± 2.5%*	0.564 *± 0.6%*
BO	103.7 *± 4.5%*	0.295 *± 4.8%*	76.8 *± 2.8%*	0.878 *± 2.9%*	23.8 *± 3.2%*	0.282 *± 3.2%*	261.8 *± 2.5%*	0.881 *± 2.59%*	77.24 *± 2.6%*	0.289 *± 2.9%*	123.35 *± 2.3%*	0.420 *± 3.6%*	87.2 *± 1.9%*	0.297 *± 1.7%*
CA	49.1 *± 3.0%*	0.140 *± 3.8%*	14.9 *± 2.3%*	0.171 *± 3.7%*	12.4 *± 3.0%*	0.147 *± 3.3%*	56.2 *± 2.6%*	0.189 *± 3.32%*	41.8 *± 4.4%*	0.157 *± 6.6%*	39.8 *± 2.6%*	0.135 *± 3.8%*	38.3 *± 2.9%*	0.130 *± 3.9%*

Tab. 1: Results of signal analysis of 20 scans distributed over 3 months for white matter (WM), gray matter (GM), cerebrospinal fluid (CSF), bone (BO) and cavital air (CA). The magnitude signals (S_{Mag}) and the contrast ratios normalized to WM are very constant with low standard deviation.

	MPRAGE	***UTE_{VB20} TE_1***	***UTE_{VB20} TE_2***	***UTE_{VB18} TE_1***	***UTE_{VB18} TE_2***	***$DIXON_{IP}$***	***$DIXON_{OP}$***
B	0.36 *± 2.3%*	1.05 *± 3.4%*	0.70 *± 3.2%*	1.1 *± 5.1%*	0.81 *± 5.0%*	1.01 *± 3.1%*	3.27 *± 2.9%*

Tab. 1: Results of skin-air sharpness analyses of 20 scans distributed over 3 months. Parameter B is inversely proportional to sharpness.

References

[1] Wagenknecht G. et al: MRI for attenuation correction in PET: methods and challenges. Magn Reson Mater Phy 2013; 26:99–113

[2] Poynton C.B. et al: Probabilistic atlas-based segmentation of combined T1-weighted and DUTE MRI for calculation of head attenuation maps in integrated PET/MRI scanners. Am J Nucl Med Mol Imaging 2014; 4(2):160-171

[3] Hofmann M. et al: MRI-based attenuation correction for PET/MRI: a novel approach combining pattern recognition and atlas registration. J Nucl Med 2008; 49:1875–1883

[4] Schreibmann E. et al: MR-based attenuation correction for hybrid PET-MR brain imaging systems using deformable image registration. Med Phys 2010; 37:2101–2109

[5] Aitken, A.P. et al: Improved UTE-based attenuation correction for cranial PET-MR using dynamic magnetic field monitoring. Med Phys. 2014; 41(1):012302

[6] Delso, G. et al: Anatomic Evaluation of 3-Dimensional Ultrashort-Echo-Time Bone Maps for PET/MR Attenuation Correction. J Nucl Med. 2014; 55:1-6

[7] Keereman, V. et al: MRI-Based Attenuation Correction for PET/MRI Using Ultrashort Echo Time Sequences. J Nucl Med. 2010; 51:812-818

[8] Normalization of brain magnetic resonance images using histogram even-order derivative analysis James D. Christensen* Magn Reson Imagin 2003; 21:817–820

[9] NEMA Standards Publication MS 1-2008: Determination of Signal-to-Noise Ratio (SNR) in Diagnostic Magnetic Resonance Imaging. 2008, Rosslyn, National Electrical Manufacturers Association

P 57 Attenuation correction in PET/MR scanners with Feed Forward Neural Network and varying input information

E. Rota Kops[1], A. Santos Ribeiro[2], H. Hautzel[3], H. Herzog[1], N. J. Shah[1]
[1]Forschungszentrum Juelich, Institute of Neuroscience and Medicine, Juelich, Germany
[2]Imperial College London, Centre of Neuropsycopharmacology, Dept. of Medicine, London, United Kingdom
[3]Heinrich-Heine-University Duesseldorf, Dept. Nuclear Medicine, Juelich/Duesseldorf, Germany

Related questions: Attenuation correction (AC) of hybrid PET/MR brain images still remains an issue to be investigated. Until now different methods have been proposed to obtain the required AC map. Segmentation of MR images is one possible method yielding a high specific patient's information. All segmentation-based methods usually assign predefined attenuation coefficients to each segmented tissue class thus limiting the accuracy of the generated AC map. In this study a feed forward neural network (FFNN) algorithm is presented which yields AC maps with predefined as well as continuous attenuation coefficients depending on the input data of the learning phase.

Material and procedure: MR, PET, and CT data were acquired in 7 subjects. The dual echo MR images delivered from the ultrashort echo time (UTE) MR sequence were used as input data of the training (n=1) as well as of the classification step (n=6) for FFNN1 (Fig. 1 left), while the UTE images together with the corresponding template-based AC map [1] were used for FFNN2 (Fig. 1 middle). Furthermore, the optimal network weights of FFNN2 were obtained by guiding the network output with the corresponding CT-based AC map (FFNN3), thus leading to a continuous AC map in the classification step (Fig. 1 right). All FFNN1-3-based results were compared with the CT-based ones as gold standard. The classification results were evaluated by calculating the dice coefficient D. After reconstruction of the PET emission data with the created AC maps and normalization to the MNI brain, the influence of the segmentation was assessed by considering the volumes of interest of the AAL-atlas. Relative differences (RD) were finally calculated.

Result: The resulting Ds show similar results when only the skull region is considered, while higher values for FFNN3-based tissues are reached, particularly for bone tissue, when the facial&neck (D1=0.31, D3=0.46) and occipital (D1=0.53, D3=0.64) areas are involved. Because the Dice coefficients do not necessarily measure the segmentation goodness, segmented bone images were generate in order to have also a visual description of the segmentation (Fig. 2). The RDs calculated for FFNN3 show an overall lower value than that for FFNN1 (RD1=3.7%, RD3=4.7%).

Summary: In the presented study three different approaches of the same feed forward neural network (ffnn1, ffnn2, and ffnn3) were applied on both MR images resulting from the double echo sequence DUTE. Different supplemental information was given into the network, obtaining in each case different output images. An improvement of the Dice coefficients in all head regions, but in particular for the occipital and facial regions, was achieved from ffnn1 up to ffnn3. The occipital and facial regions are in general very difficult to segment due to the inhomogeneous tissue composition as well as to possible MR artifacts. In conclusion our results show that an enhancement of current methods can be performed by combining both information of new MR image sequence techniques and general information provided from, e.g., template techniques. Nevertheless, the number of tested subjects is statistically low and current analysis for a larger dataset is being carried

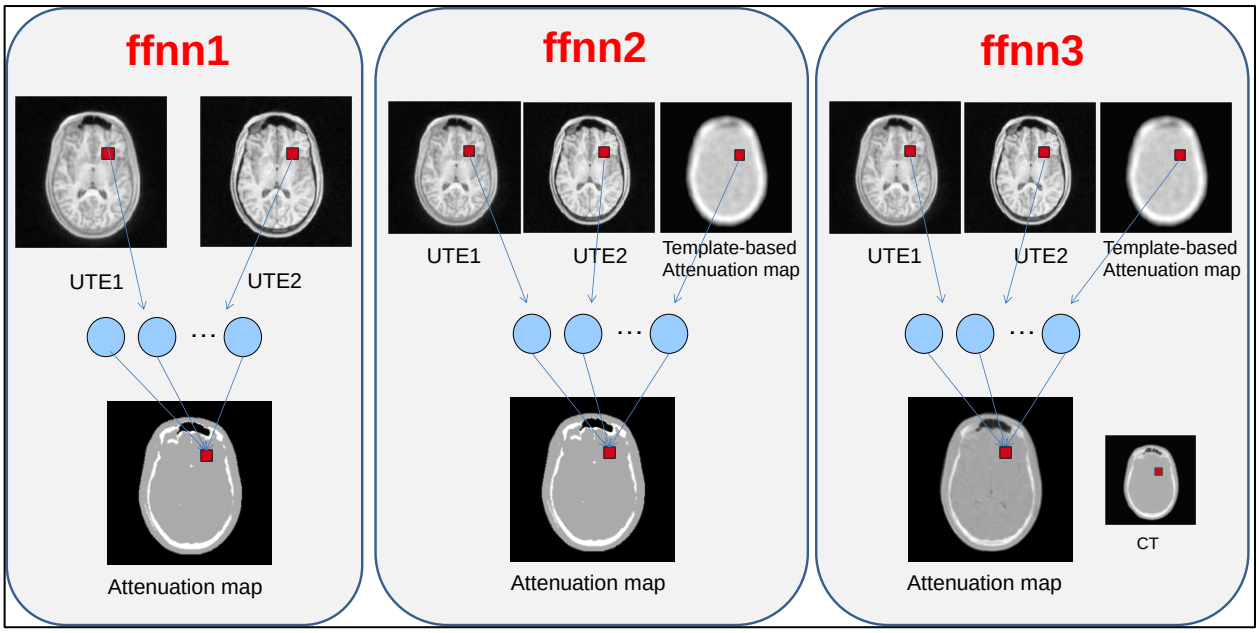

Fig. 1: Illustration of the methodology for attenuation correction of PET images with the proposed FFNN algorithms. The input features (top row) are given to the FFNN (middle row) for the calculation of the attenuation coefficient (bottom row). The generated attenuation images are then directly used for attenuation correction of PET images.

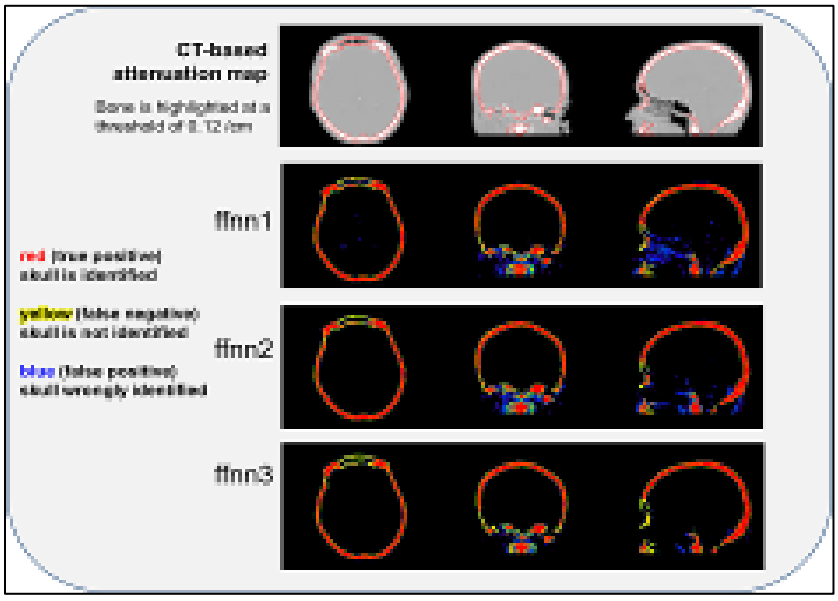

Fig.2 – Exemplarily the bone tissue images of one subject from the three different segmentation methods together with the corresponding CT-based attenuation map are shown.

References

[1] E Rota Kops, H. Herzog, IEEE NSS/MIC Conference Record, (2008) 4327-4330.

[2] A. Santos Ribeiro, E. Rota Kops, H. Herzog, P. Almeida, Nuclear Instruments & Methods in Physics Research / A 702, (2013)114–116.

P 58 First clinical evaluation of PET performance between PET/CT and PET/MR

K. Zeimpekis[1], G. Delso[2], P. Veit-Haibach[1], M. Hüllner[1], G. von Schulthess[1]
[1]University Hospital Zurich, Nuclear Medicine Division, Zurich, Switzerland
[2]GE Healthcare, Waukesha, WI, United States

Objectives: This study is a preliminary evaluation of PET performance in a new integrated PET/MR scanner compared to state-of-the-art of sequential PET/CT. The purpose of the study was to evaluate clinically two of the expected PET/MR advantages over PET/CT, which are higher sensitivity and larger axial FOV [1], based on the experience of the first months using PET/MR clinically.

Methods: A sequential ToF-PET/CT (Discovery 690, GE Healthcare) and a prototype simultaneous ToF-PET/MR (Signa PET/MR, GE Healthcare) were used. Two brain and two whole-body patients were examined with ^{18}F-FDG on PET/CT and their consent was taken for a following PET/MR examination. Mean injected activity was 220.3 MBq, mean uptake time was 60 minutes and mean interim time between PET/CT and PET/MR 15 minutes for whole body and 30 minutes for brain scan. Since PET/MR follows PET/CT the activity in the patient was further exponentially decayed, this is why PET/MR scan duration is longer than PET/CT, to acquire more signal to have sufficient image quality. Our purpose was to expose both systems to the same amount of signal so we took the decay integral between start – end of the scan for both systems. Therefore, keeping PET/CT as the clinical standard reference, a manual adjustment of the PET/MR acquisition time was performed. Since PET/MR lasts longer we could easily reduce its acquisition time and match it with the PET/CT by requiring the integrals of PET/CT and PET/MR to be equal both for single bed brain scans and multiple beds whole-body scans. Once the first fitting was achieved then we reduced both PET/CT and PET/MR acquisition to see how the systems respond to gradually lower SNR, requiring again the integrals to be equal. **Protocols :** PET/CT Head scan from 10 minutes (default) down to 1 minute with 1 minute steps. Whole-body scan from 2 minutes/bed (8-9 bed positions) down to 40 seconds with a 20 seconds step. PET/MR Head scan 20 minutes (default / reduced to 13:22 minutes to be equal to PET/CT). Whole-body scan 4 minutes/bed (5-6 bed positions) (reduced to 3:45 minutes to be equal to PET/CT).

Reconstruction: Time-of-flight, OSEM (3 iterations/18 subsets) with point spread function correction, 2mm transaxial gausian post-filter, no z-axis filter (longitudinal resolution varies between systems, so filter on z axis was not applied), 256 x 256 reconstruction matrix and 30 cm transaxial FOV, attenuation, randoms, scatter and decay corrected. Exactly same parameters used for PET/MR but with 3 iterations /16 subsets, due to the difference geometry, there was not any closer subsets value to match the PET/CT.

Results: The images were qualitatively assessed by two experienced radiology and nuclear medicine physicians. The pairs of images were set to the same window level and width. Figure 1 concerns brain scan and show saggital plane head scans of PET/MR (a) and PET/CT (b) corresponding to reduced acquisition times of 5 minutes for PET/CT (6:22 PET/MR equivalent). Figure 1 (c) and (d) show the coronal plane of the same acquisition, PET/MR and PET/CT respectively. Figure 1 PET/CT images (b) and (d) are noisier than PET/MR ones (a) and (c). The noise is more prominent near the PET/CT FOV limit due to sharp sensitivity drop. Except for noise though, there is no pertinent clinical information in both pairs of images. Figure 2 concerns whole-body scan and shows (a-b) coronal plane of PET/MR and PET/CT respectively, and similarly (c-d) axial plane at the lungs level and (e-f) axial Maximum Intensity Projection of 30 slices covering the lungs, corresponding to reduced acquisition times of 1:20 minutes/bed for PET/CT (2:30 PET/MR equivalent). For (a-b) there is lung tumor in left upper lobe with hilar and mediastinal lymph node metastases, probably also supraclavicular (N3) lymph node metastases. The metastases are blurred on the PET/CT and are not well appreciated there, compared to PET/MR. However bladder activity cancels out activity in femoral heads. For (c-d) there is lung tumor in left upper lobe. On PET/MR no clear lymph node metastases visible at this level. On PET/CT blurring of the mediastinum. For (e-f) the patient has probable lung metastases (or two primary tumors) and mediastinal metastases. Mediastinal metastases are not well seen on PET/CT due to noise.

Fig. 1

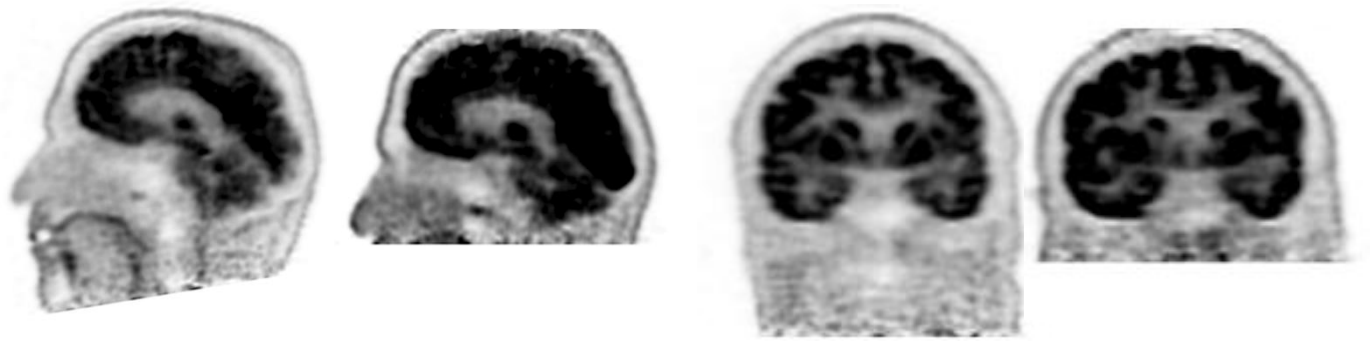

a **b** **c** **d**

Fig. 2

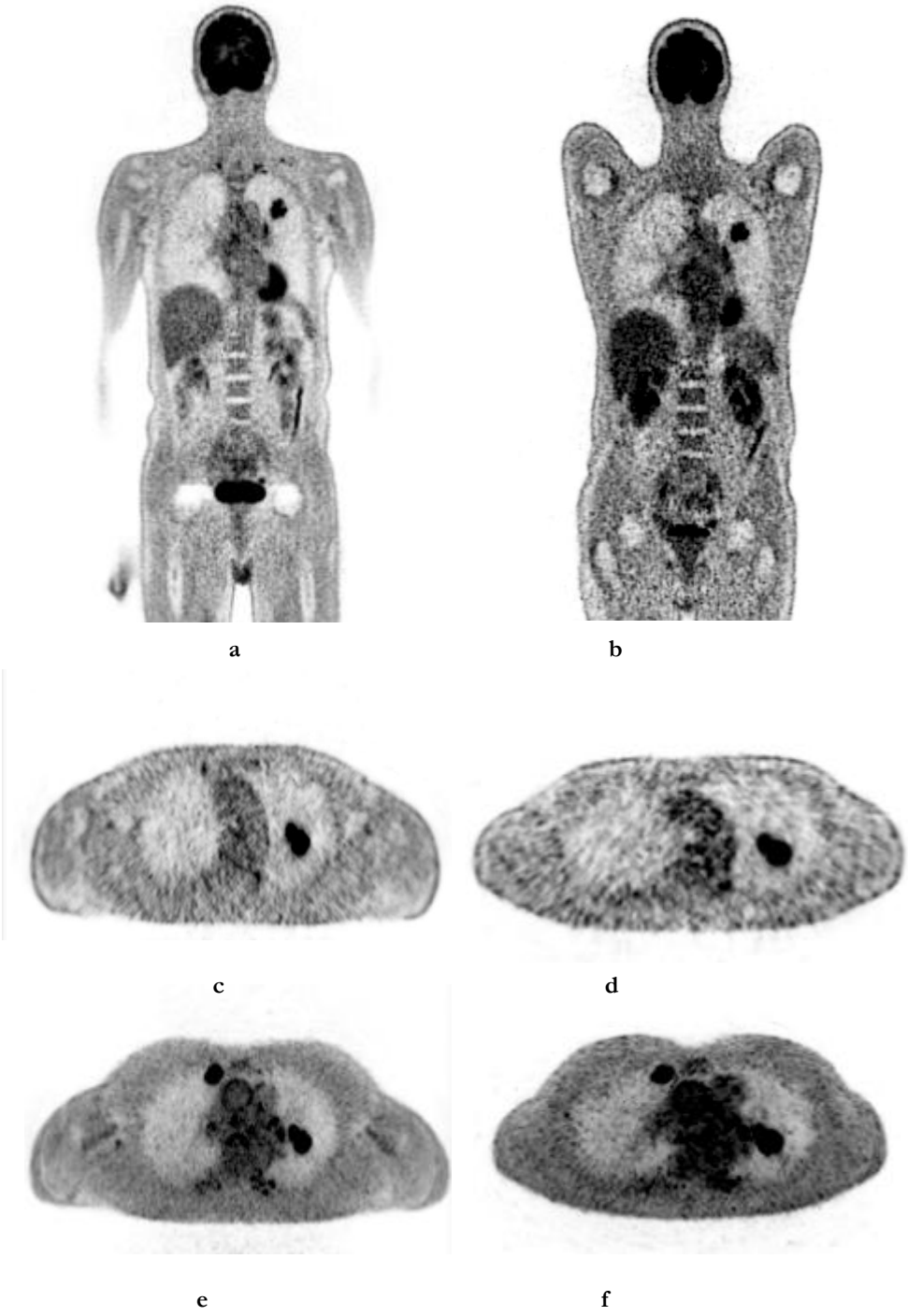

Conclusions: Preliminary results show that PET performance of PET/MR might present less noisy images than PET of PET/CT, for reduced scan times, producing images with higher diagnostic value. Larger axial FOV looks promising for better image quality in brain scans. However differences are not that significant. Further studies need to be conducted to get reliable statistics and a variety of patient body types along with different types of disease. Future plans include investigation of scan time or injected activity reduction potential taking advantage of the probable improved performance of PET component of PET/MR compared to that one of PET/CT.

References

[1] Delso et al., Medical Physics 36, 4126 (2009)

P 59 3D UTE-Cones MRI for lung parenchyma visualization and lung PET AC potential

K. Zeimpekis[1], G. Delso[2], F. Wiesinger[3], P. Veit-Haibach[1], G. von Schulthess[1]
[1]University Hospital Zurich, Nuclear Medicine Division, Zurich, Switzerland
[2]GE Healthcare, Waukesha, WI, United States
[3]GE Global Research, Munich, Germany

Objectives: This study concerns 3D ultra short-echo time (UTE) sequence investigation and comparison to LAVA sequence for lung parenchyma detection as well as MR based attenuation correction for PET lung imaging [1]. 3D UTE is advantageous over LAVA, because detection and visualization of lung parenchyma density, as studies have already shown [2], is possible. This advantage is based on its very short TE (~0.03ms) that enables signal capture from very fast signal decay-structures like lungs but also bones. Consequently, 3D-UTE besides lung parenchyma disease visualization could furthermore lead to more precise attribution of the linear attenuation coefficients of bone and lung structure for PET AC.

Methods: The study was conducted on a GE Discovery MR750w 3T scanner. Gradient echo sequences used are dual-echo Liver Acquisition with Volume Acceleration (LAVA-Flex) and 3D UTE Cones. A healthy volunteer was scanned with both sequences. For LAVA the parameters are: 15 sec breath-hold acquisition, TR/TE/FA 4.4ms/2.6ms/12 degrees, FOV 30*30*30 cm, res/slice 2mm/4mm. For Cones: 2 min prospective gated acquisition, TR/TE/FA 4.2ms/0.028ms/7 degrees, FOV 30*30*26 cm, res/slice 1.2mm/4mm. The images were normalized to LAVA's dynamic range and were set to same contrast window width (Window Lenght (WL) – Window Width (WW)).

Results: Figure 1 shows slices of both Cones and LAVA acquisitions. ROIs were drawn towards the anterior /posterior & superior/inferior parts of the lung estimating mean signals. Table 1 includes all of the ROIs mean signals. For the transaxial plane which is the scan plane, Cones presents a 443.2% (178.2/32.8 au) higher anterior and 632.5% (270.3/36.9 au) higher posterior signal. These quantified results suggest that this higher signal is due to lung density detection and could be used for attenuation correction of the lung.

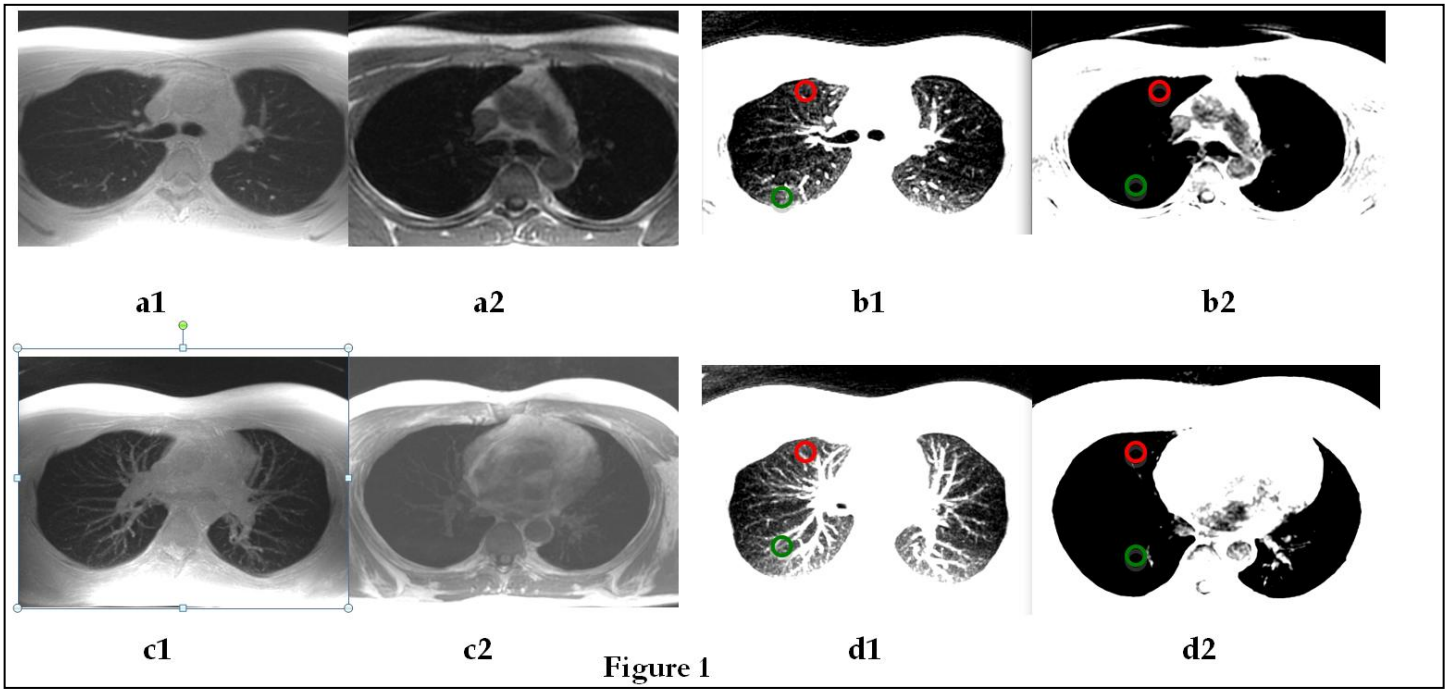

Figure 1

	b-red	b-green	d-red	d-green
1. 3D-UTE Cones	178.2	270.3	253.6	52.3
2. LAVA	32.8	36.9	364.9	58.9

Tab. 1. Mean signal extracted by the red – green ROIs drawn on Figure 1. a, b indicate the same slice with larger and narrower WL & WW respectively. Similarly, c, d indicate MIP reconstruction with larger and narrower WL-WW. Difference is more obvious using narrower WL-WW due to the parenchyma inherent low signal. Cones signal is significantly higher than LAVA for all planes.

Conclusions: First results show that 3D UTE-Cones is able of capturing more lung signal than LAVA and could be used for lung parenchyma density visualization. Further clinical studies are needed in order to strenghten this perspective that might lead to use of continuous lung structures attenuation coefficients instead of only one that it is the standard method up to date. Consequently, Cones could certainly outperform LAVA for PET AC.

References

[1] Wollenweber et al,IEEE Transactions on nuclear science, 2013; 60(5):3391:3398.
[2] Lederlin et al, J Magn Reson Imaging, Oct 2013.

P 60 Feasibility of Quantitative MRI Tissue Mapping with Balanced SSFP: Multi-Dimensional Nonlinear Parameter Optimization

A. Wunderlich[1,2], M. Beer[2]
[1]Univ.-Clinic Ulm, Sect. for Experimental Radiology, Ulm, Germany
[2]Univ.-Clinic Ulm, Dept. for Diagnostic and Interventional Radiology, Ulm, Germany

Purpose: To evaluate the feasibility of determining tissue parameters with balanced SSFP (bSSFP) MRI.

Introduction: bSSFP has proven to be the most efficient imaging sequence in MRI (*1*). In this work, we address the feasibility of determining tissue parameters T1 and T2 of abdominal organs with bSSFP in multiple breathholds.

Methods: Tissue parameters were simulated in the range of T1 from 50 ms … 1 s and T2 from 1 … 30 ms. A subset of T1/T2 combinations was also investigated with T1 ranging from 50 … 200 ms and T2 range as above. Eight different flip angles (FA) were chosen as acquisition parameters, meaning a total of eight breathholds for patient investigations, in a variety of different values ranging from 7 … 65°. Two approaches were addressed concerning TR: 1. it was kept constant at different values of 3.5, 5 and 7 ms for all FA, 2. two different TR (3.5 ms and 5, 7 or 8 ms, resp.) were chosen for two subsets of FA.

The signal S_{bSSFP} of the bSSFP sequence was simulated using the eq. given in (*1*)

$$S_{bSSFP} = S_0 \frac{\sqrt{E_2}\,(1-E_1)\sin\alpha}{1-(E_1-E_2)\cos\alpha-E_1E_2} \quad (1)$$

with S_0 meaning theoretic maximal signal, incorporating tissue magnetization, coil sensitivity and receiver gain, $E_{1/2} = e^{-\frac{TR}{T1/2}}$ and FA α.

At given S_0, random noise was added at a certain level in 1000 repetitions for each parameter combination, resulting in SNR of 15 or below, depending on TR / FA. Tissue parameters were evaluated by nonlinear Levenberg-Marquardt fit with fixed start values. If a fit did not converge, other start values were tried up to three times. Mean and standard deviation of results as well as their uncertainties from all 1000 noise simulations were stored for analysis as well as number of converged fits and parameters addressing fit quality, namely number of iterations and residual error. Single-voxel fit as well as fit for median values of ROIs containing 10 voxels were simulated. Since B1 inhomogeneity is a problem, esp. at high field strength, influence of deviating flip angles was also simulated.

With optimized parameters, MRI acquisitions have been performed in a phantom consisting of bottles containing water doped with different concentrations of $MnCl_2$. Also, a volunteer has been scanned.

Results: High uncertainties of T1 and T2 results were observed when working with a single TR. This effect was overcome when working with two different TR. In the range of T1 and T2 covered, the TR combination of 3.5 and 8 ms proves best at FA of 7, 12, 20, 32 and 50° for TR 3.5 ms and 25, 40 and 65° for TR 8 ms. This yields reliable results with deviations below 3% for most parameter combinations, cf. Fig. 1. Only for long T1 above 200 ms, T1 and T2 results deviate more than 5% from given values. In the range of reliable results, uncertainties of parameters are below 2% except for extreme short T2 values of 1 … 2 ms. To address the reduced range of T1 with 50 … 200 ms, optimized FA and TR combination with FA of 7, 10, 14, 20 and 32° at TR 3.5 ms and 17, 27 and 45° for 5 ms TR shows best performance and yields uncertainties below 2 % (data not shown).

Small deviations of flip angles increase uncertainty of results to 20-30%, but have only little influence on accuracy of evaluated tissue parameters. Real data acquired in phantom and volunteer show similar reproducibility of tissue parameters at a level of uncertainty of 40%.

Discussion: Determining tissue parameters T1 and T2 is in theory feasible based on bSSFP images. The bSSFP sequence has the advantage of high scan efficiency expressed in SNR per acquisition time unit. Also, 3D imaging is feasible in reasonable scan times. In our setting, we use the high efficiency to get short acquisition times required for breathhold abdominal imaging.

Phantom as well as volunteer results show that the method can be used in practice. It has to be figured out whether larger uncertainty of results than predicted for exact flip angles is indeed caused by B_1 inhomogeneity, of if additional sources of imperfection have to be considered. Effective flip angles applied in reality can be monitored e.g. with B_1 mapping.

a)

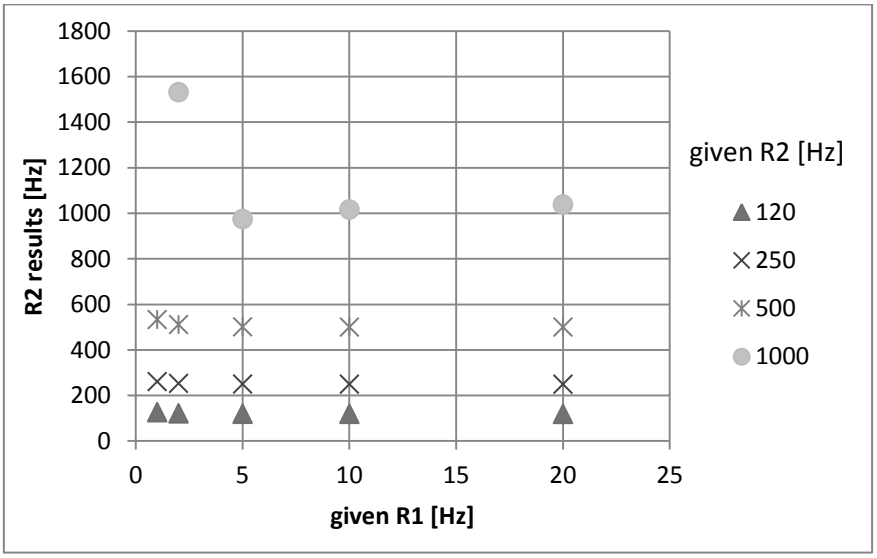

b)

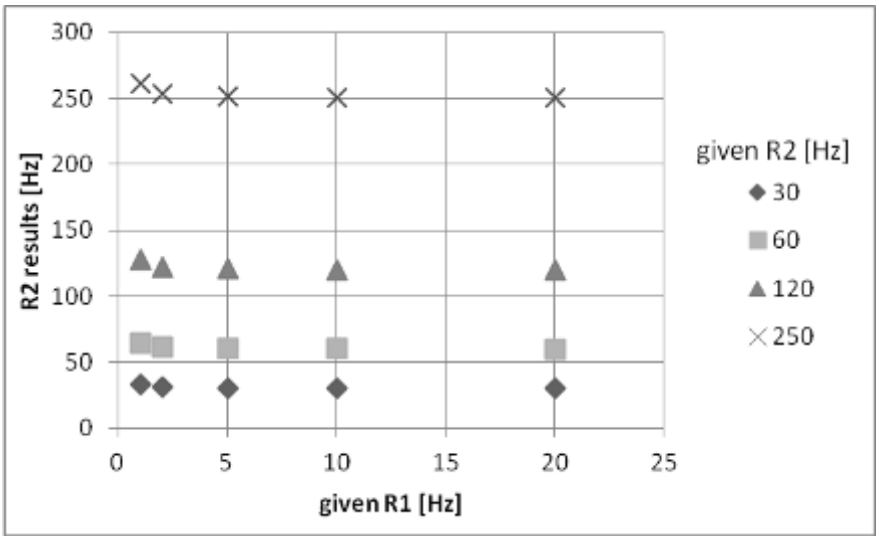

Fig. 1: R2 fit results of single-voxel fit as function of given R1 for various given R2 values.

a) shows the larger R2 values (shorter T2),
b) the smaller R2s (longer T2). Note that the combination 1/1000kHz for given R1/R2 (T1/T2 1000/1 ms) results in a large deviation of more than 200% of R2 result from given value (not shown in diagram).

For short TR and therefore TR << T1 as used in our simulation, eq. (1) can be simplified to a relation depending on the T1 / T2 ratio. Therefore, with a single TR, T1 / T2 ratio can be determined reliably, but uncertainties are large for T1 and T2. With the inclusion of two different TR, T1 and T2 can be determined at low uncertainties.

Since we worked with predefined values for S_0 and noise level in simulations, SNR varied for different TR/FA settings, giving an SNR depending on bSSFP signal. We regard this as closer to reality than assuming a certain constant SNR for all acquisition parameters.

The previously reported (*2, 3*) DESPOT approach for parameter mapping also involves bSSFP images. However, less efficient gradient echo sequences are used in this method to determine T1. Furthermore, the proposed evaluation procedure for DESPOT involves signal dependence on FA rewritten to give the form of a linear equation, thereby neglecting additive signal noise which causes deviation from theoretic behaviour. This has been overcome in our approach at the cost of time consuming nonlinear fit which isn't straightforward but prone to lack of convergence and false results.

Although we didn't address efficiency yet, we expect similar performance compared to DESPOT due to bSSFP properties. A certain disadvantage of bSSFP is that usually only one contrast is imaged in a single acquisition, whereas for eg. GRE multiple signals can be read out after one excitation resulting in a multi-contrast GRE acquisition. Some manufacturers offer multi-contrast bSSFP readout at some disadvantages: multiple gradient refocusing of signal between bSSFP excitations will introduce T2* effects in image signal, also leading to dephasing between fat and water signal. Therefore, not only one more parameter will have to be considered, but also tissue fat fraction and B_0 inhomogeniety. To compensate for these additional free parameters, a minimum of three echoes is required, but even more, if you keep in mind that echo formation is expected to be symmetric around the centre between bSSFP excitations, leading to identical signal of e.g. the first and last echo. This bunch of additional echoes required will lead to prolonged TR, which will degrade not only image quality due to off-resonance effects but also leads to a substantial increase in acquisition time.

While we focused on short acquisition times in this work to address abdominal organs subject to respiratory motion, the principle presented here may also be adapted to obtain 3D high-resolution T1/T2-maps in non-moving regions as e.g. head. Since eight acquisitions are required, it's challenging to acquire dynamic T1 maps for contrast enhanced studies, but this might be overcome taking advantage of image sparsity.

It has been shown that long T1 above 200 ms are difficult to address with the proposed method. Probably prolonged TR may be helpful, but this is not useful for clinical routine due to increased banding artefacts and prolonged measurement time. Such long T1 are observed only in few tissues and liquid, resp., which may be quantified otherwise.

This is theoretic work addressing the feasibility of rapid T1 / T2 mapping in tissues undergoing respiratory movement. In reality, bSSFP data suffer from various imaging artefacts, which contribute in first line to higher uncertainty compared to theoretic results. It has to be figured out whether adjustment of parameters regarding artefact minimization is able to improve performance in real data.

References

[1]. K. Scheffler, On the transient phase of balanced SSFP sequences. *Magnetic resonance in medicine : official journal of the Society of Magnetic Resonance in Medicine / Society of Magnetic Resonance in Medicine* **49**, 781 (Apr, 2003).

[2]. S. C. Deoni, B. K. Rutt, T. M. Peters, Rapid combined T1 and T2 mapping using gradient recalled acquisition in the steady state. *Magnetic resonance in medicine : official journal of the Society of Magnetic Resonance in Medicine / Society of Magnetic Resonance in Medicine* **49**, 515 (Mar, 2003).

[3]. S. C. Deoni, T. M. Peters, B. K. Rutt, High-resolution T1 and T2 mapping of the brain in a clinically acceptable time with DESPOT1 and DESPOT2. *Magnetic resonance in medicine : official journal of the Society of Magnetic Resonance in Medicine / Society of Magnetic Resonance in Medicine* **53**, 237 (Jan, 2005).

P 61 Dynamic T2*-Mapping using Segmented EPI with Multi-TE

K. Eickel[1], M. Günther[1], L. Lüdemann[2]
[1]Universitätsklinikum Essen / Fraunhofer Mevis, Bremen, Germany
[2]University Hospital Essen, Radiotherapy, Essen, Germany

Introduction: In Magnetic Resonance Imaging (MRI) the use of contrast agents (CA) allows to noninvasively extract physiological parameters. Especially quantification of CA-dynamics requires fast acquisition techniques in combination with sufficient robustness and spatial resolution.

The analysis of MRI-data can be performed by pharmacokinectic modelling which is commonly referred to as dynamic-contrast-enhanced MRI (DCE-MRI) and dynamic-susceptibility-contrast MRI (DSC-MRI). DSC can be used to assess information about the perfusion and tissue-geometry whereas with DCE the CA-exchange processes (extravasation) can be measured to determine e.g. blood-volume, interstitial volume or permeability [1, 2]. Leakage of CA and resulting changes in the susceptibility gradients are a main drawback of highly T1-weigthed images and a limitation for quantitative evaluation in DSC. Quantification of perfusion and extravasation required to assess physiological parameters for tumor-staging and control during therapy.

Materials and methods: The decay of transverse magnetization and thus the MR-signal in gradient-echo sequences are dominated by the T2*-decay. Others than the reversible T2-decay, the T2*-effect originating from e.g. susceptibility variations, local B-field inhomogeneities and spin-spin interaction is irreversible [3]. In presence of a contrast agent (CA), at air-tissue interfaces or other regions of a signification change in susceptibility the T2*-decay mainly determines the image contrast

A newly designed Multi-TE segmented Echo-Planar Imaging (EPI) sequence (TE= 9.5/15.4/21.3/27ms; matrix=96x128; FoV=225mmx300mm; Δz=5mm; 3 slices; TA/image=1.4s; EPI-factor=14; α=40°) is used to acquire four different T1/T2*-weighted images within a single measurement of 1.4s.

Image analysis is done with MeVisLab a development environment for image processing and visualization [4]. First the analysis of the (sub-)images (four images with different TEs/contrasts) with increasing T2*-weighting (Fig. 1) is used to calculate a dynamic M_0- and T2*-maps (Fig. 2). The resulting dynamic-image set is then overlaid with an anatomical image (PDT2-TSE; matrix=270x320; same FoV; 3slice) to select the brain structures. On the masked data-set a voxel-by-voxel analysis of the T2* dynamics is performed and the resulting curves are used for calculation of the mean T2*-values of the relevant region (Fig. 3).

As a CA-free alternative to monitor T2*-dynamics a finger-tapping experiment with both hands is carried out on a clinical 3T scanner (Skyra, Siemens Erlangen). Acoustic commands are given every 10 measurements (14s) over the experiment-duration (126s) giving an equal pattern of resting state (R) and brain-activation (A) (Fig. 3).

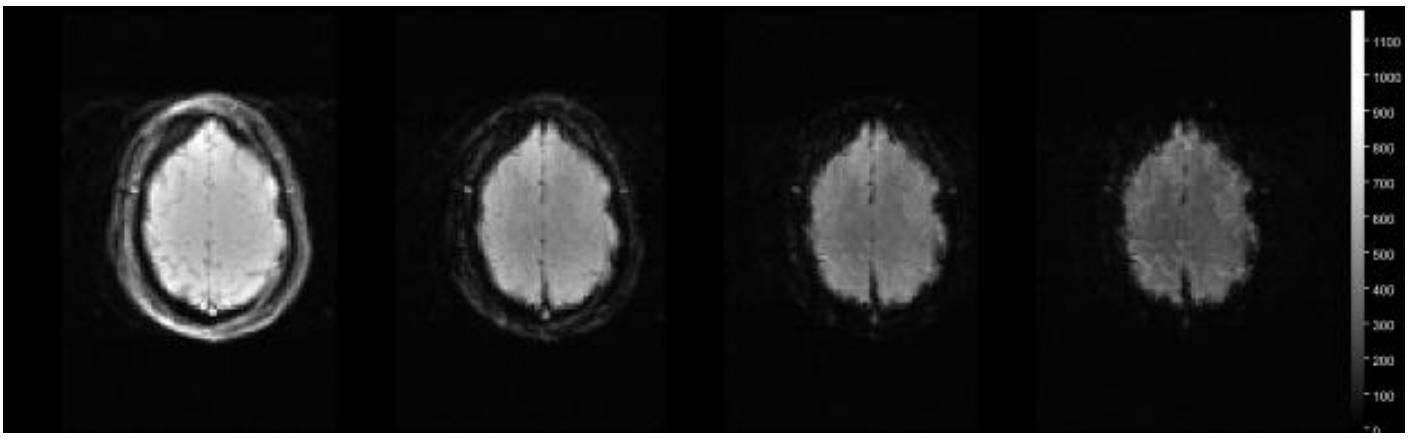

Fig. 1: With increasing echo-time the image contrast becomes more T2-weighted. The set of four images (TE=9.5/15.4/21.3/27ms) is acquired within TA<1.4s (for multiple slices) making dynamic MRI over a volume of interest possible.*

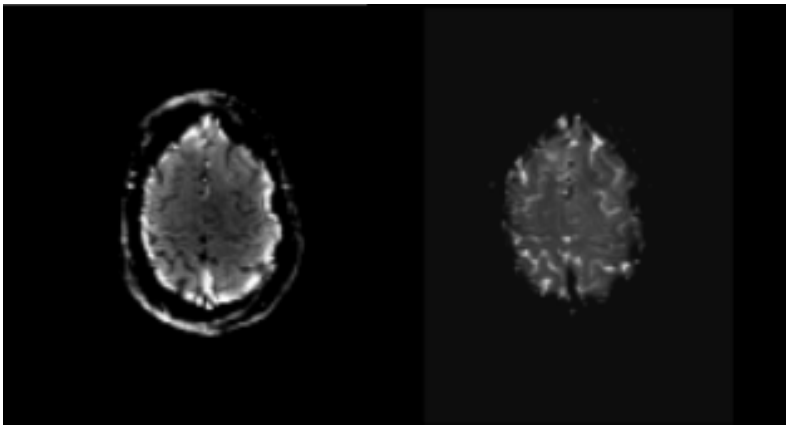

Fig. 2: For each measurement of the Multi-TE EPI sequence dynamic M_0- (left) and T2-maps (right) are calculated.*

Results: Finger-tapping increases the cerebral blood flow locally and leads to activation in the upper motor cortex (Fig. 3). During the activation phase the blood oxygen level-dependent effect is decreased (relative decrease in deoxyhemoglobin) leading to an increase in the local T2* [3]. The curve shape is clearly correlated to the tapping-pattern. On average the T2* increases by 37% during activation compared to the T2*-value at the resting state.

A tendency of increasing T2*-values is likely to be caused by the relatively short resting phase so that no full equilibrium-state of oxygen/deoxygenated blood is reached.

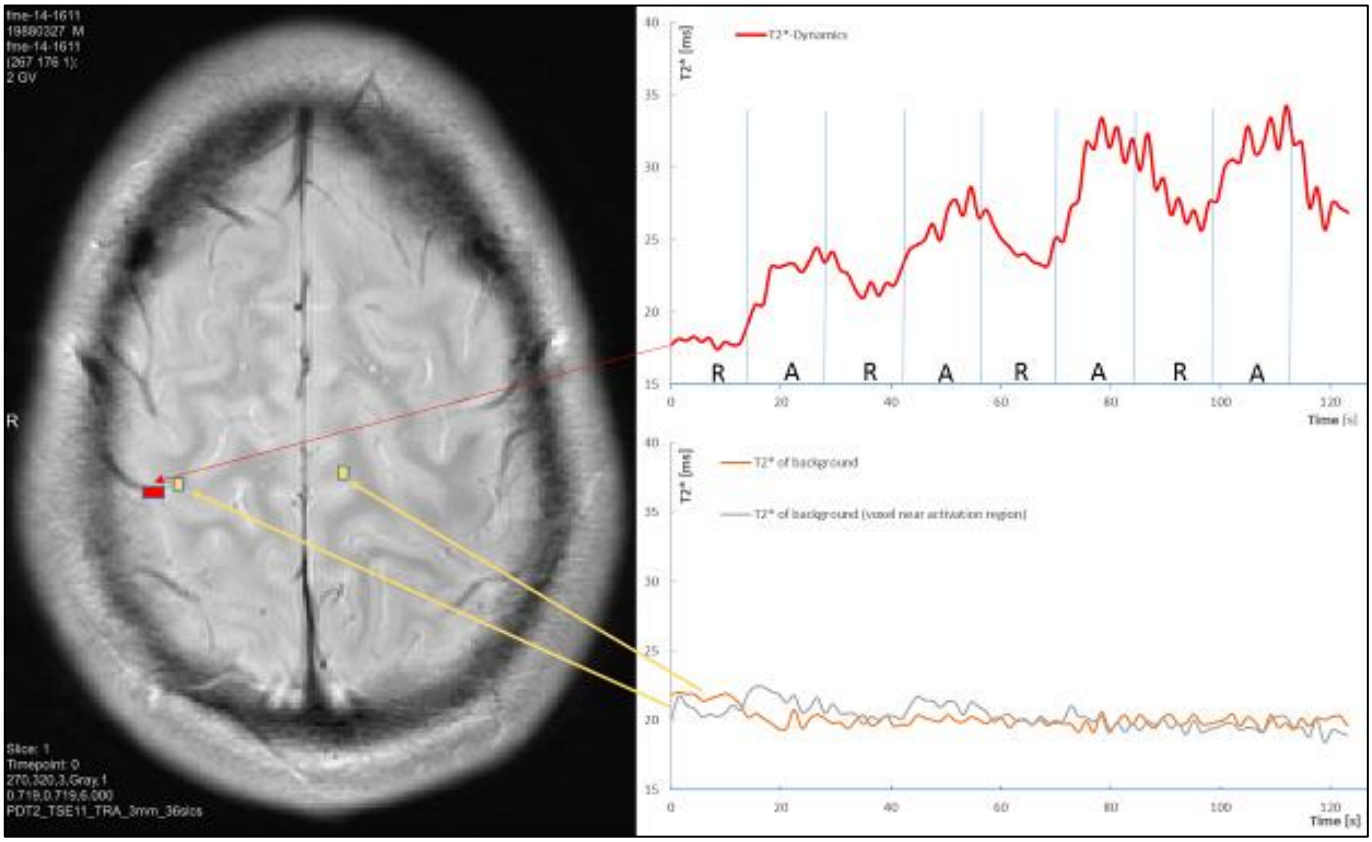

Fig. 3: Using a reference image (PDT2-TSE) with higher spatial resolution the location of the motor cortex can be verified. Here just on hand side of the activation region in the mortor cortex is shown (upper diagram). After the resting phase (R) T2 increases due to local rise in oxygenated blood during the activation phase (A). For comparison the T2*-dynamics in other regions of the brain are printed in the lower diagram. No variation of T2* corresponding to the tapping-pattern can be seen here.*

Conclusion: The presented Multi-TE EPI sequence is capable to detect changes in T2* on a rate which is suitable for e.g perfusion imaging [3]. A stronger quantitative T2* combined with simultaneous acquisition of T1-weighted images can be used for quantitative bolus-tracking [2] and for correction of changing susceptibility-gradients due to CA-leakage or other sources of error in DCE-MRI [1, 5].

References

[1] Sourbron S., Heilmann M.: T2*-Relaxivity Contrast Imaging: First Results, Magnetic Resonance in Medicine, 2013, 69:1430-1437

[2] Lüdemann L., Prochnow D.: Simultaneous Quantification of Perfusion and Permeability in the Prostate Using Dynamic Contrast-Enhanced Magnetic Resonance Imaging with an Inversion-Prepared Dual-Contrast Sequence, Annals of Biomedical Engineering, 2009, 37: 749-762

[3] Chavhan G. B.: Principles, Techniques, and Applications if T2*-based MR Imaging and Its Special Applications, RadioGraphics, 2009, 29:1433-1449

[4] URL: http://www.mevislab.de/ (31.03.2014)

[5] Sourbron S., Heilmann M.: Bolus-Tracking MRI with a Simultaneous T1- and T2*-Measurement, Magnetic Resonance in Medicine, 2009, 62:672-681

P 62 CTDI Based Effective Dose Calculations for Megavoltage Photon Cone Beam CTs

K. Duong Hoang Anh[1], M. Liebmann[1], K. C. Willborn[2], A. Rühmann[2], B. Poppe[1,2]
[1]Carl von Ossietzky University of Oldenburg, Medical Radiation Physics, Oldenburg, Germany
[2]Pius-Hospital Oldenburg, Klinik für Strahlentherapie und Onkologie, Oldenburg, Germany

Purpose: Megavoltage cone-beam computed tomography (MV-CBCT) is being frequently used in radiation therapy due to its practical performance. Since the first MV-CBCT image of the patient was obtained in 2003 [1], many clinical uses of MV-CBCT have been reported, e.g. patient positioning before dose delivery (usually used for head and neck, lung and prostate cancer) [2], monitoring of tumor growth or shrinkage [3] and supporting for Image-Guided Radiation Therapy (IGRT) strategies [4]. Along with the increase in use of MV-CBCT, the effect of the dose to organs at risk (OAR) is still a topic under investigation. The aim of this work is to determine the absorbed doses to OAR based on conversion factors from measured absorbed dose integrals like the CTDI300 and to estimate the effective dose for daily clinical MV-CBCT in comparison to other imaging techniques.

Materials and methods: The study used a medical linear accelerator model Siemens Artiste™. A commercial treatment planning system (TPS) for external beam planning, Oncentra MasterPlan 4.3 (Nucletron, Netherlands) was used for dose calculation. Patient data sets were randomly collected from the TPS database in our radiotherapy department. For calculation of organ doses, CBCT plans were generated for six different regions of the human body including: skull, head and neck, thorax, abdomen and pelvis. All CBCT procedures used a standard clinical protocol which is provided by the manufacturer: photon energy 6 MV, field size 27.4 cm x 27.4 cm, dose delivery 8 MU, gantry rotation from 260° to 100°. For head and neck (H&N) cases, due to the radiation sensitivity of the lenses of the eyes, a reduction in eye dose and effective dose is a subject of consideration. Therefore, an additional CBCT plan with a modified protocol was used: field size of 18 cm x 18 cm, was generated for this region. The modification of the field size was to minimize the directly irradiated region, but still to ensure that it was large enough for imaging (planning target volume was in field of view).

The dose calculation was executed on individual patient data and an anthropomorphic female CIRS ATOM® phantom "Irene". Based on the organ doses, conversion factors from the dose length product or CTDI300, which was measured with a special 300mm long ionization chamber, and effective doses were determined.

The chamber is a pencil type chamber, CT-Chamber Type 30017, which was designed and manufactured by PTW in Freiburg, Germany. It has a radius of 3.5 mm, an effective length of 300 mm, and features a sufficient homogeneous response over the whole length of the chamber.

In this study, the effective doses were estimated using the tissue weighting factors issued in ICRP 103 (2007) [5]. A total of 120 CBCT plans were calculated for individual patients (20 plans per anatomical region) and 7 CBCT plans calculated on the phantom were used in this study.

Results: The CTDI300 for the used CBCT protocol was measured with a 16 cm diameter PMMA Phantom of 500 mm length. For the standard protocol a CTDI300 of 60.7 mGy was determined and used for the conversion factor calculation [6]. The calculated organ doses and conversion factors for the individual OARs are shown in Table 1. Organ doses which were derived from the phantom are slightly greater than those from the patients. This is due to the smaller size of the phantom compared to the average size of the randomly chosen patients.

The estimated effective dose was lowest for the head scan (9.7 mSv) and highest for the thorax scan (35.1 mSv) as shown in Table 2. For H&N cases using the modified CBCT protocol reduces the irradiated area and therefore reduces the effective dose compared to the standard protocol while the eye dose could be reduced significantly. Based on the conversion factors maximum additional organ doses may be calculated and considered in treatment planning evaluations.

In comparison to other imaging techniques (kV-CBCT, orthogonal portal images) the organ doses and effective dose from MV-CBCT are higher than those of the same examination regions [7, 8]. For example: effective dose (mSv) of pelvis scan for MV-CBCT in this study is 14.3, while it is 5.6, 0.8 and 11.9 for kV-CBCT, kV-Images and MV-Images, respectively, as reported by V. Dufek et al. [8].

CBCT Examination Region	Organ Dose [mSv]		Standard Deviation [mSv]	Largest Standard Score	Conversion Factor [mSv/mGy.cm]
	Phantom Irene	Patients (mean value)			
Skull					
Eyes	89.7	89.0	2.72	2.19	0.0539
Brain	76.9	74.3	2.35	2.26	0.0462
Spinal cord (max.)	75.0	72.7	3.08	-2.34	0.0451
Head & Neck					
Eyes	90.7	88.6	2.53	-2.83	0.0545
Spinal cord (max.)	76.6	78.9	2.73	3.74	0.0461
Thorax					
Humeral head	61.6	49.7	11.13	-2.08	0.0370
Heart	70.0	66.0	4.80	-2.04	0.0421
Lungs	73.2	70.9	5.91	-2.20	0.0440
Spinal cord (max.)	70.2	67.1	4.32	2.22	0.0422
Abdomen					
Liver	77.6	69.4	6.13	-2.06	0.0467
Kidneys	70.0	64.3	3.71	2.20	0.0421
Spinal cord (max.)	68.7	61.8	4.80	2.31	0.0413
Pelvis					
Bladder	79.0	68.1	3.57	-1.90	0.0475
Femoral heads	71.6	69.0	2.53	-2.55	0.0430
Rectum	58.2	55.6	2.39	-2.22	0.0350
Rectal back wall	55.7	53.5	2.47	-2.35	0.0335

Tab. 1: The organ doses and conversion factors for individual organs at risk of the phantom and patients using the standard CBCT protocol

CBCT Examination Region	Effective Dose [mSv]
Skull	9.7
Head & Neck	17.0
Head & Neck (field size: 18 cm x 18 cm)	9.1
Thorax	35.1
Abdomen	29.2
Pelvis	14.3

Tab. 2: The estimated effective doses for the phantom

Conclusion: The CTDI, which is used in conventional CT, can also be applied in MV-CBCT. Conversion factors based on the measured CTDI300 can be used for the dose estimation. Greater variations in organ doses were found for organs which are irradiated partly, which effects effective dose calculations. The use of MV-CBCT in clinical imaging should be monitored and additional doses through the necessary imaging should be considered in treatment planning

References

[1] J. Pouliot, A. Bani-Hashemi, J. Chen, M. Svatos, F. Ghelmansarai, M. Mitschke, M. Aubin, P. Xia, O. Morin, K. Bucci, M. Roach, III, P. Hernandez, Z. Zheng, D. Hristov, and L. Verhey: Low-dose megavoltage cone-beam CT for Radiation Therapy, Int. J. Radiat. Oncol., Biol., Phys. 61, (2005), p.552–560

[2] O. Morin, A. Gillis, J. Chen, M. Aubin, M. K. Bucci, M. Roach, III, and J. Pouliot: Megavoltage cone-beam CT: System description and clinical applications, Med. Dosim. 31, (2006), p.51–61

[3] J. F. Aubry and J. Pouliot: Imaging changes in radiation therapy: Does it matter?, MRI 12, (2008), p.3–13

[4] M. Roach, J. Pouliot, and P. Xia, Image-guided intensity modulated radiotherapy (IGRT) for clinically localized prostate cancer: Targeting pelvic lymph nodes, in Image-Guided Radiation Therapy of Prostate Cancer, edited by R. K. Valicenti, A. P. Dicker, and D. A. Jaffray Informa Healthcare, London, (2008), p. 183–196

[5] The 2007 Recommendations of the International Commission on Radiological Protection, Annals of the ICRP. ICRP publication 103 37 (2-4), (2007), ISBN 978-0-7020-3048-2

[6] M. Liebmann et al.: Dosisausgabe an einer klinischen CBCT Anlage und Schritte zur Ermittlung von Organdosen, Fulda, (2013)

[7] Lee-Cheng Peng, Ching-Chong Jack Yang, Sang Sim, Mitchell Weiss, and Alex Bielajew: Dose comparison of megavoltage cone-beam and orthogonal-pair portal images, Journal of Applied Clinical Medical Physics, Vol. 8, No. 1, (2007), p.10-20

[8] V. Dufek, I. Horakova and L. Novak: Organ and Effective Doses from Verification Techniques in Image-Guided Radiotherapy, Radiation Protection Dosimetry (2011), p.1–4

P 63 Optimization and evaluation of eye lens protectors in computed tomography

L. Künzel[1], M. Roll[1], D. Hornscheidt[2], A. Betz[3], W. Kating[3], M. Buchgeister[1]
[1]Beuth University of Applied Sciences, Department of Mathematics, Physics & Chemistry, Berlin, Germany
[2]Somatex Medical Technologies GmbH, Teltow, Germany
[3]Military Hospital Berlin, Department of Radiology, Berlin, Germany

Introduction: The sensitivity of the lens of the eye for radiation cataracts is known for a long time. Therefore dedicated thresholds of the organ dose of the eye lens are set by legal authorities. Currently the dose to the eye lens is limited to 150 mSv/a for occupationally radiation-exposed persons in Germany according to StrlSchV §55 (2) and RöV §31 (3) and to 15 mSv/a for all other people (StrlSchV §46 (2), RöV §32 (2)), expect for medical purposes. This limitation is based on the assumption, that the radiation cataract is a deterministic radiation damage effect with a threshold dose [1]. Newer studies have questioned these thresholds and recommend a lower value of 20 mSv/a for occupationally radiation-exposed persons [2-3], which has now been adopted e.g. by the European Council Directive 2013/59/Euratom [4].

In the past the eye lens could be excluded from direct X-rays in computed tomography (CT) by tilting the CT gantry, but newer multislice CT do not offer this option anymore. The same protecting effect can be realized by an overflexion of the cervical spine, but this requires the patient's cooperation.

Different studies have shown the possibility of using in-plane shielding by eye lens protectors made of different materials [5-8]. In all of these studies the authors reported image artefacts nearby the protectors. Kalra et al. discussed the use of foam pads to reduce these artefacts in the case of in-plane Bismuth shielding for the breast [9].

In this work the effect of foam pads behind protectors using a mixture of Sb/Bi for radiation protection is investigated with respect to the eye lens dose and image artefacts and compared to commercially available protectors consisting of Bi/Sb/W/Gd without foam pad and one of $BaSO_4$ with pad. Since modern CT offer dose reduction protocols applying an angle depended X-ray tube current modulation, this was also included.

Materials and methods: The dose measurements are performed with thermoluminescence detectors (TLD) type 100h (TLD Poland MCP-100, Krakow, Poland) and an Alderson-RANDO-Phantom (Alderson Research Laboratories, USA). The relative sensitivity of each TLD has been calibrated at 70 kV. 10 TLDs are calibrated with the reference dose of approximately 12.0 mGy at 117 kV measured with a DOSIMAX plus with RQX detector (Scanditronix-Wellhöfer, Schwarzenbruck, Germany).

To evaluate the dose reduction, the dose is measured in front and behind of the protector at the position of the left and right eye lens, at the nose and in the paranasal sinuses. The commercial available eye lens protector "Gray Shield Eye Protection" distributed by e.g. Wiroma AG (Niederscherli, Switzerland), the "CT-EyeProteX" (referred to as "SomatexOld") and four different prototypes of a new protector produced by SOMATEX® Medical Technologies GmbH are examined. The protector "Gray Shield" is composed of $BaSO_4$ and is padded with 5.5 mm foam. The CT-EyeProteX consists of Bi/Sb/W/Gd, the prototypes are made of Sb/Bi and havefoam pads with thicknesses of 3 mm, 5 mm and 10 mm, respectively.

The scans are performed with a Siemens SOMATOM Definition Flash CT with parameters listed in table 1. This CT offers the organ-based tube-current modulation X-CARE reducing the tube current when the X-ray tube is facing frontal parts of the body. Additionally the effect of the combined use of protectors and the X-CARE mode is investigated for the protectors except for the 10 mm padded Somatex prototype. To this end, cranial CT-protocols with and without X-CARE are used. The protectors are also investigated for a possible use in paranasal sinuses examinations, where the scan limits are adjacent to the eyes.

To assess the image artefacts, the CT numbers are analysed at identical positions near to and more than 100 mm away from the eyes for scans with protector or the X-CARE mode option and compared to CT numbers of examinations without protector.

	Foam pad thickness / mm	CT protocol	mAs_{ges}	DLP_{ges} / mGycm	$CTDI_{vol}$ / mGy
No protector	-	CT head nativ , 120 kV, pitch 0.55, single collimation 0.6 mm	3257	693	50.11
SomatexOld	-		3335	709	51.19
Somatex	-		3581	767	50.51
Somatex3	3.0		3409	733	51.87
Somatex5	5.0		3475	742	52.21
Somatex10	10.0		3571	761	51.53
GrayShiled	5.5		3230	687	51.19
No protector	-	CT head native X-CARE, 120 kV, pitch 0.55, single collimation 0.6 mm	3551	760	50.85
Somatex	-		3664	783	50.17
Somatex3	3.0		3518	750	51.87
Somatex5	5.0		3452	732	50.85
GrayShield	5.5		3657	782	49.48
No protector	-	CT paranasal sinuses, 120 kV, pitch 0.7, single collimation 0.6 mm	382	145	13.72
Somatex	-		390	152	13.52
Somatex3	3.0		507	193	14.33
Somatex5	5.0		358	108	16.75
Somatex10	10.0		382	145	14.13
GrayShield	5.5		391	153	13.72

Tab. 1: CT parameters for head and paranasal sinus CT examinations with and without eye lens protectors and/or X-CARE CT mode.

Results: The measured dose to the eye lens in cranial CT is about 35 mGy without protection. By using eye lens protectors the dose is reduced by about 20% – 33% to 28 mGy – 23 mGy. With the X-CARE mode of the CT alone, a dose reduction of 35% is yielded. If eye lens protectors and the X-CARE mode are combined, the dose is lowered to about 17.5 mGy corresponding to a dose reduction of 50%. The measured dose to the eye lens in paranasal sinuses examinations is about 9 mGy without eye lens protectors and is decreased to 6 mGy by using protectors.

The protectors cause an increase in CT-numbers close to the protector. This effect can be reduced by adding foam pads between protector and the head, but at the same time the dose reduction is lowered as controversial effect. Areas analysed further than 100 mm away from the protectors are not affected in CT numbers. If protectors combined with the X-CARE mode are used, the artefacts are increased compared to examinations using protectors alone. If the X-CARE mode is used only, no artefacts are observed. The diagnostic image quality of the scans hasn't been assessed in this study.

Conclusions: The measured organ dose of up to 35 mGy for the eye lens in conventional head CT exceeds the threshold organ dose of 15 mSv/a already in one examination. Therefore the protection of the eye lens in CT is an important issue. The measurements reported here show that during head CT the eye lens can be effectively protected by using eye lens protectors or organ-based tube-current modulation (X-CARE). However, clearly the best result is reached according to our findings, if eye lens protectors AND the X-CARE mode are used combined, yielding a dose reduction of about 50%.

The eye lens protectors showed also a significant shielding effect for the eye lens in paranasal sinuses examinations, where no or marginal direct radiation hits the eye lens but scattered or leakage radiation from the CT.

The image artefacts caused by the protectors can be moderated by foam pads of increasing thickness, but at the cost of lowered dose reduction to the eye lens. Since the artefacts appear only close to the protectors, the diagnostically image quality should be evaluated by radiologists in test scans with an appropriate phantom, before protectors are used for this examinations with patients to meet the diagnostic requirements.

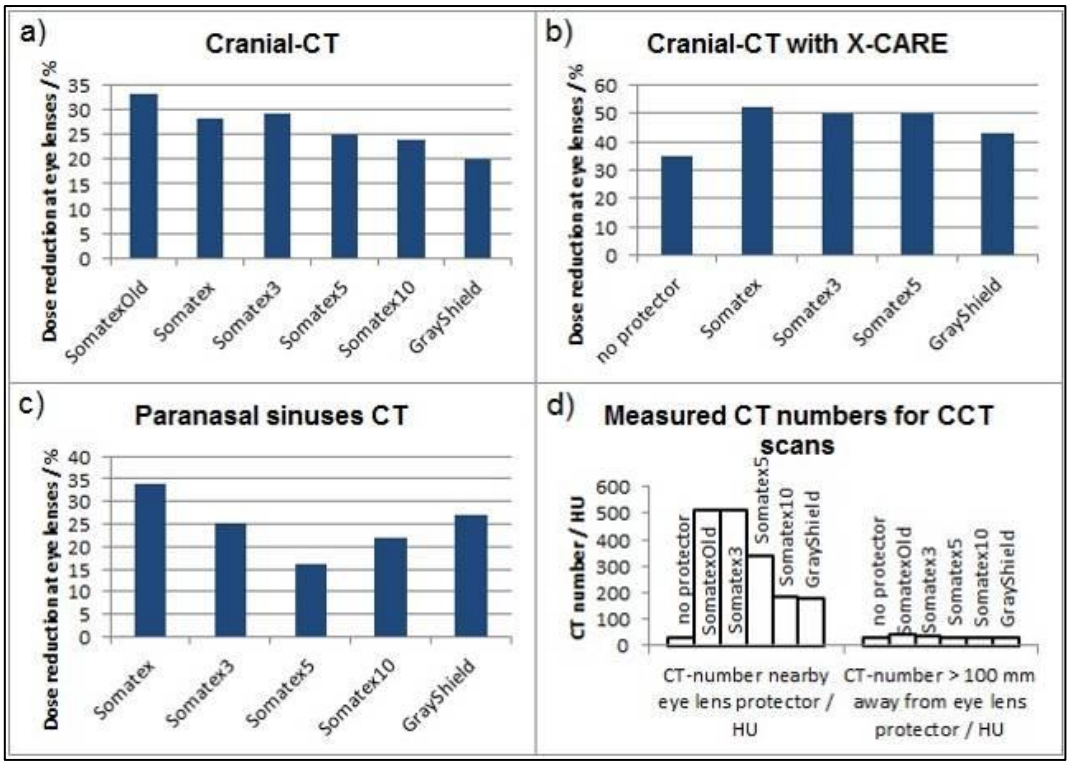

Fig. 1: Dose reduction to the eye lenses for cranial and paranasal sinuses CT examinations with eye lens protectors and/or X-CARE CT mode (a-c) and CT numbers for head CT examinations with and without eye lens protectors (d).

Acknowledgments: The authors would like to thank Mrs. Grit Hohlfeld, MTRA first sergeant, for her technical support with performing the CT scans.

References

[1] P. Mountford and D. Temperton, “Recommendations of the international commission on radiological protection (ICRP) 1990”, Eur. J. Nucl. Med., vol. 19, no. 2, pp. 77-79, 1992.

[2] Strahlenschutzkommission, “Strahleninduzierte Katarakte Empfehlungen der Strahlenschutzkommission mit wissenschaftlicher Begründung”, 2009, http://www.ssk.de/SharedDocs/Beratungsergebnisse_PDF/2009/Strahleninduzierte_Katarakte.pdf?__blob=publicationFile, accessed 30/03/2014.

[3] Strahlenschutzkommission, “Überwachung der Augenlinsendosis Stellungnahme der Strahlenschutzkommission mit wissenschaftlicher Begründung“, Verabschiedet in der 240. Sitzung der Strahlenschutzkommission am 02. Februar 2010, http://www.ssk.de/SharedDocs/Beratungsergebnisse_PDF/2010/2010_01.pdf?__blob=publicationFile, accessed 30/03/2014.

[4] Council Directive, “2013/59/Euratom of 5 December 2013: basic safety standards for protection against the dangers arising from exposure to ionising radiation”, 2014, http://eur-lex.europa.eu/LexUriServ/LexUriServ.do?uri=OJ:L:2014:013:0001:0073:EN:PDF, accessed 30/03/2014.

[5] D.J. McLaughlin and R. B. Mooney, “Dose reduction to radiosensitive tissues in CT. Do commercially available shields meet the users’ needs?”, Clin. Radiol., vol. 59, no. 5, pp. 446-50, May 2004.

[6] J. Wulff, B. Keil, D. Auvanis, J. T. Heverhagen, K. J. Klose, K. Zink, “Dosimetrische Evaluation von Augenlinsen-Protektoren in der Computertomographie – Messungen und Monte-Carlo Simulation“, Z. Med. Phy., vol. 18, no. 1, pp. 19-26, Mar. 2008.

[7] B. Keil, J. Wulff, D. Auvanis, “Protection of Eye Lens in Computed Tomography-Dose Evaluation on an Anthropomorphic Phantom using Thermo-Luminescent Dosimeters and Monte-Carlo Simulations”, RöFö, vol. 180, no. 12, pp. 1047-53, Dec. 2008.

[8] S. Diekmann, E. Siebert, R. Juran, M. Roll, W. Deeg, H.-C. Bauknecht, F. Diekmann, R. Klingebiel, G. Bohner, “Dose exposure of patients undergoing comprehensive stroke imaging by multidetector-row CT: comparison of 320-detector row and 64-detector row CT scanners”, AJNR. Am. J. Neuradiol., vol. 31, no. 6, pp. 1003-9, Jun. 2010.

[9] M. K. Kalra, P. Dang, S. Singh, S. Saini, J.-A. O. Shepard, “In-plane shielding for CT: effect of off-centering, automatic exposure control and shield-to-surface distance“, Korean J. Radiol., vol. 10, no. 2, pp. 156-63, 2009

P 64 Perception of the modulation transfer function – an underestimated concept?

K. Loot[1,2,3], A. Block[1]
[1]Klinikum Dortmund, Institut für Medizinische Strahlenphysik und Strahlenschutz, Dortmund, Germany
[2]Heinrich-Heine-Universität, Düsseldorf, Germany
[3]Technische Universität, Dortmund, Germany

Introduction: The modulation transfer function (MTF) is an established instrument for describing the resolution properties of imaging systems. It allows comparison of systems as well as analysis of individual subsystems by mapping the spatial frequency dependence of the contrast.
So far, the IEC standard for digital radiography only specifies the measurement of the detector MTF [1], thereby ignoring the contributions from geometric unsharpness, scattering, object motion, sampling effects and processing. However, these MTF components can at least be qualitatively analyzed and may be harnessed for clinical usage.

We present the measurement of several MTF components by use of standard QA equipment, along with an automated evaluation program. Based on the results, we envision the benefit and the applications arising from a more general perception of the MTF.

Materials and methods: The presampled MTF contains the contributions from the analog input, the detector response and the sampling aperture. Sampling effects (e.g. aliasing), filtering and displaying are excluded [2]. The MTF is calculated from the image of an edge device. The transition from black to white, the edge spread function (ESF), provides us with information about the image quality of the system. By a small angulation of the edge device, the information of subsequent image rows can be interlaced to produce an oversampled ESF, which is no longer quantized by the pixel spacing of the digital detector [3]. Differentiation yields the line spread function (LSF), from which the presampled MTF can be calculated via a Fourier transform.

Simulation images with known MTF curves were produced with/without noise, with/without influence of the sampling aperture, with/without geometric unsharpness (arising from a finite size of the focal spot), and with/without motion blur. These images were used to verify the results of the analysis program, explore different noise cancelling algorithms, investigate the influence of object motion and compare the MTF components of subsystems.

The analysis program was implemented using a computational software program (Mathematica, Wolfram Research), which was also used to create the simulation images. As a test device we employed the precision edge of a lead foil test (PTW Freiburg, L659048), consisting of 0.05 mm lead foil embedded in 2 mm acrylic. This deviates from the specifications in [1] and will not allow for observation of the low frequency drop, but corresponds to the translucent edge device presented in [4]. Such a device has been shown to be sufficient for qualitative analysis and has the advantage of being available in any clinical environment as part of the standard QA equipment. The experimental images were obtained with a commercial radiography system (Axiom Multix M, Siemens).

Results: The evaluation program was found to produce accurate discrete values for the presampled MTF; the Nyquist frequency was shifted to values above the clinically interesting frequency range, eliminating aliasing effects. It was shown that the averaging of several ESF representations significantly reduces the noise level in the MTF over the whole spatial frequency range without alterations of the line shape. An alternative approach using smoothing algorithms on the ESF was found to be counterproductive.

Fig. 1 demonstrates the influences of several components on the overall MTF. A simulation image featuring an edge transition similar to that of clinical radiographs was artificially exposed to the resolution degrading effects of the sampling aperture and object movements with various velocities. We observe how the sampling aperture and increasing velocities subsequently lead to a decrease of the MTF.

For experimental verification, the detector MTF of a radiography system was obtained both in horizontal and vertical direction. By elevating the test device from the detector surface, the influences of geometric unsharpness and scattering come into play. Fig. 2 compares these two components for different distances between test device and detector. It illustrates that for these measurement geometries scattering has a greater impact on the spatial resolution than geometric unsharpness.

In a second work, we further discuss the influence of motion and present the application of the MTF to the restoration of motion-blurred radiographs [5].

Conclusion: The MTF in digital radiography has more potential than just for the analysis of the detector. We showed that other components of the imaging system like scattering, geometric unsharpness and motion blur can be qualitatively examined, compared to one another and checked against their analytical description. This additional information allows a more profound assessment of the imaging system and paves the way for individual restoration of radiographic images.

Qualitative experimental results were obtained by use of a lead foil test device, which is available as part of the QA equipment in any clinical environment.

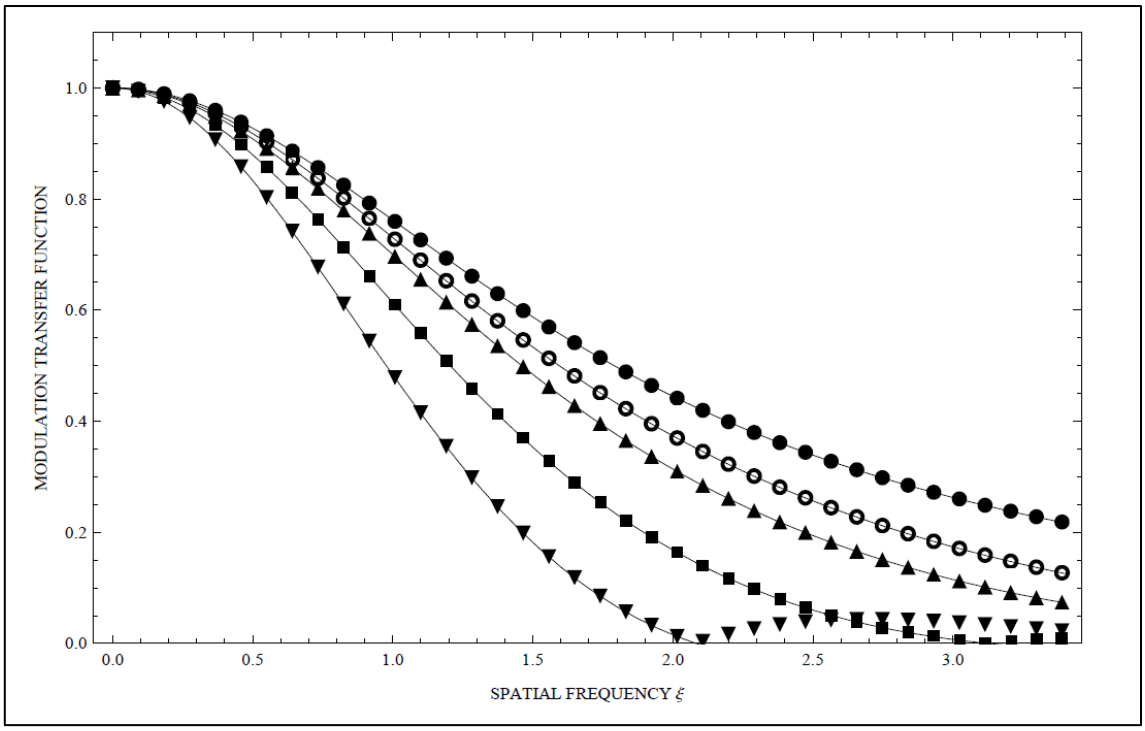

Fig. 1: MTF components derived from simulated images. Disks: Initial blur corresponding to experimental images. Circles: Additional intro-duction of sampling aperture (0.16 mm pixel spacing). Additional introduction of motion: Triangle: Blur extent of 1 pixel. Rectangle: Blurextent of 2 pixel. Upside down triangle: Blur extentextent of 3 pixel.

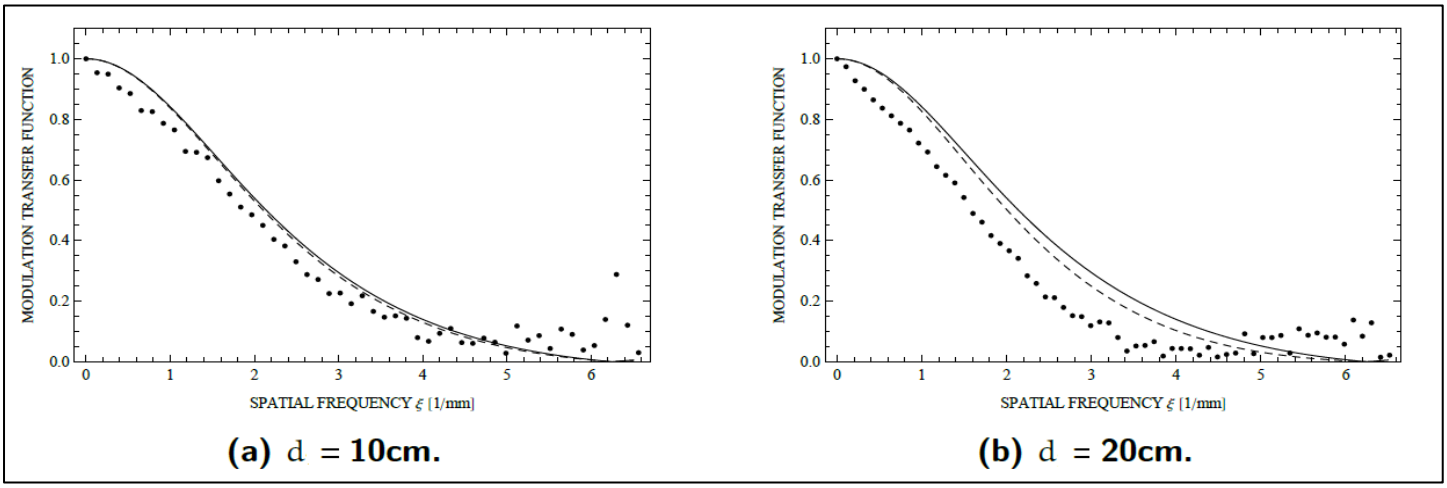

Fig. 2: Data points: MTF of the Siemens Axiom Multix M, including scattering and geometrical unsharpness, measured with test device at a distance d from detector and 125 cm – d from the x-ray source. Continuous line: Fit of detector MTF Dashed line: Analytical estimate for the detector MTF combined with geometrical unsharpness, but without scattering

References

[1] IEC 62220-1: Medical Electrical Equipment – Characteristics of Digital X-ray Imaging Devices – Part 1: Determination of the Detective Quantum Efficiency. IEC, 2003.

[2] Giger, M.L. et al.: Investigation of basic imaging properties in digital radiography – I. Modulation transfer functions. Medical Physics, 11(3), 1984.

[3] Fujita, H. et al.: A simple method for determining the modulation transfer function in digital radiography. IEEE Transactions on Medical Imaging, 11(1), 1992.

[4] Samei, E. et al.: Intercomparison of methods for image quality characterization – I. Modulation transfer function. Medical Physics, 33(5), 2006.

[5] Loot, K. and Block, A.: Restoration of motion-blurred images in digital radiography: a feasibility study; submitted to the Joint Conference of the SGSMP, DGMP, ÖGMP, 2014.

P 65 Non-invasive experimental characterization of bow tie filters in a CT scanner using a small ionization chamber and a solid state detector

B. Alikhani[1], L. Büermann[1]
[1]Physikalisch-Teschnische Bundesanstalt, Ionizing Radiation, Braunschweig, Germany

Related questions: A common method for computed tomography (CT) dosimetry is the use of Monte Carlo (MC) studies. For a correct MC simulation a precise description of scanner parameters is required. The characterization of bow tie filters (BT) which are installed in all modern CT scanners is an essential part of MC simulations. In recent years the BT filters of different scanners have been characterized [1,2]. The method used is based on a comparison of the calculated and measured air kerma attenuation profile as a function of the fan angle. The methods used hitherto resulted in the determination of an aluminium-based attenuation equivalent BT filter but with an arbitrarily assumed central ray thickness. The aim of this work was to improve these methods by the absolute determination of the central ray thickness of the BT filter. Furthermore, a procedure was developed to correct for the energy dependence of the air kerma response of the detector used for the rate profile measurements along the BT filter. It is demonstrated that the application of this correction yields almost identical aluminium-equivalent BT filter shapes when measured with an ionization chamber and a solid state detector, the first characterized by a near independence and the latter by a significant dependence of the air kerma response as a function of photon energy.

Material and procedure: The scanner used for the purpose of this work was a GE Optima 660 with two different BT filters that is installed at PTB for research purposes. A nearly energy-independent responding ionization chamber (i-chamber) of the type Radcal 10X6-0.6CT with a sensitive volume of 0.6 cm^3 and an RTI CT Dose Profiler based on a solid state detector with a significant energy dependence of the response were used to measure the air kerma rate profile along the x-axis of the CT gantry (Fig. 1). The air kerma responses of both detectors were measured in ISO narrow-spectrum radiation qualities (20 kV to 300 kV) using PTB's primary air kerma standard. A sketch of the experimental setup and the response of the detectors as a function of the photon energies are shown in Fig. 1. In order to measure the X-ray qualities of the CT scanner, the half-value layer (HVL) method has been utilized. Here, the measurements were performed in the service mode of the scanner without the gantry rotation and the first and second HVLs were determined without BT filtration. Using a program called "SpekCalc" [3], a photon spectrum with approximately identical HVLs for aluminium was calculated. The obtained spectrum is a good approach to the CT spectrum without BT filter, but with Al-equivalent inherent filtration. For the BT filter determination first of all the ratio of the measured air kerma rate profile with and without the BT filter at each fan angle was calculated:

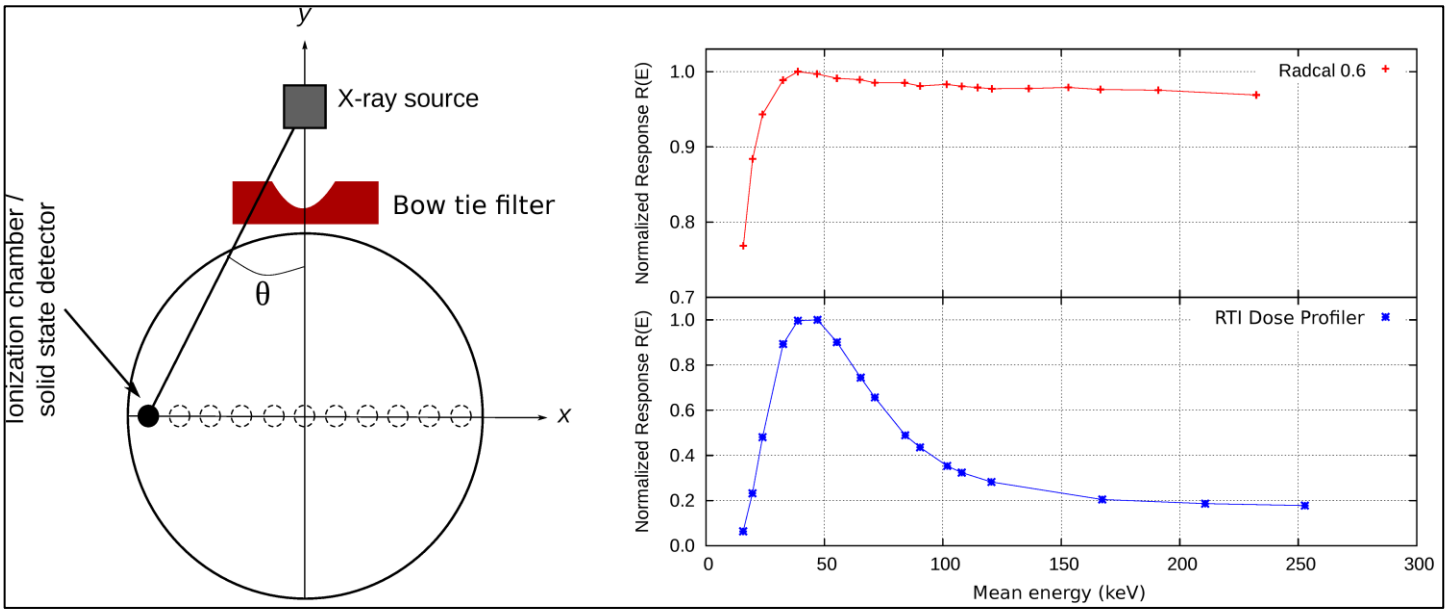

Fig. 1: (Left) Experimental setup. The measurements were performed with small, large and without BT filtration.

(Right) Normalized air kerma response R(E) as a function of the mean energy of the ISO narrow-spectrum series [4] for the i-chamber (top, red) and the solid state detector (bottom, blue)

The air kerma attenuation by incrementally increasing the thickness of aluminium was calculated until the ratio of the attenuated to the unattenuated air kerma rate profile, □$_{calc}$□□□□ was approximately equal to the corresponding measured ratio, □$_{exp}$□□□□ at each fan angle □□□These thicknesses of aluminium represent the Al-equivalent BT filters.

In order to correct the energy dependence of the response of the solid state detector (Fig. 1), the quantities □$_{exp}$□□□□were recalculated by considering the beam hardening through the different aluminium thicknesses.

Results: The measured first and second HVL in the absence of the BT filters for the X-ray tube high voltage of 120 kV were (6.9□0.1) mm Al and (8.9□0.1) mm Al, respectively. Using the corresponding X-ray spectrum obtained from the measured HVLs, the small and large BT filters installed in the GE scanner were determined. The Al-equivalent thicknesses of the BT filters are shown in Fig. 2 (Left).

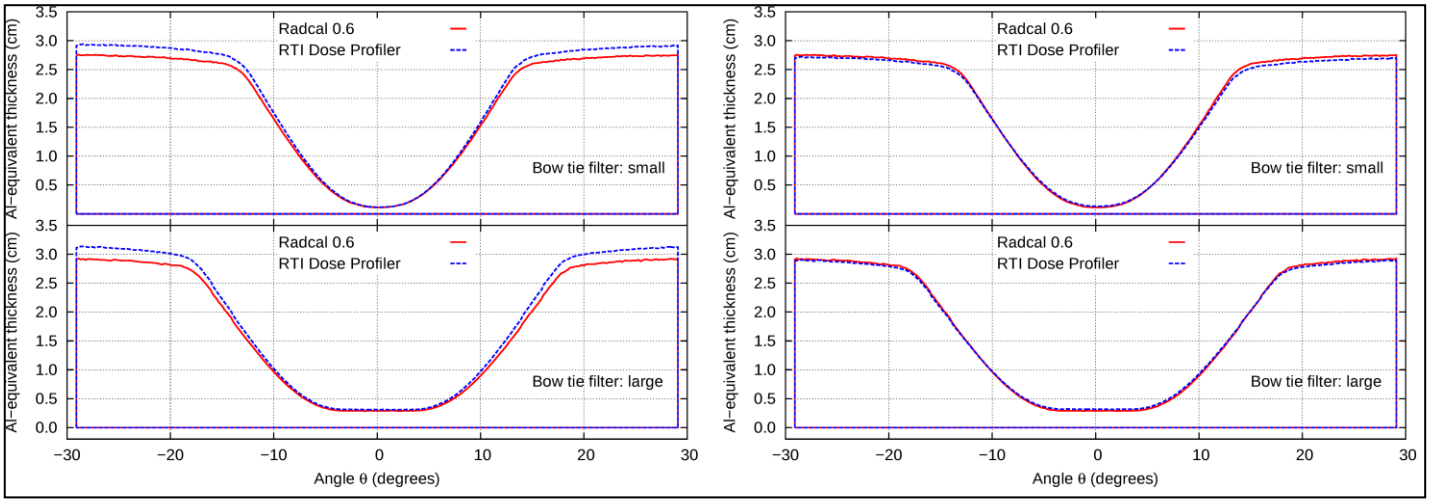

Fig. 2: (Left) Al-equivalent thicknesses of the small (top) and the large BT filter (bottom) calculated from measurements using the i-chamber (solid line, red) and the solid state detector (dashed, blue).

(Right) Al-equivalent thicknesses of the small (top) and the large BT filter (bottom) calculated from measurements using the i-chamber (solid line, red) and the solid state detector (dashed, blue).

By correcting the energy dependence of the response of the solid state detector the Al-equivalent thicknesses measured using the solid state detector matched the thicknesses obtained with the small i-chamber, Fig. 2 (Right).

Summary: In this work we determined the Al-equivalent thicknesses for the two BT filters of the PTB-CT scanner of type GE Optima 660. For this purpose the air kerma rate profile with and without BT filtration were measured. Using a Radcal i-chamber with an essentially energy-independent response and an RTI solid state detector, the thicknesses for both BT filters were determined. The use of the solid state detector needs a correction for the energy response. The results obtained with the solid state detector by correcting the changes of the response due to the beam hardening effects through the different aluminium thicknesses improved significantly and they are approximately equal to the thicknesses obtained with the i-chamber.

References

[1] Adam C. Turner et al., Med. Phys., 36 (2009), 2154-2164
[2] Kyle McMillan et al., Med. Phys. 40 (2013), 111907
[3] G. Poludniowski et al., PMB, 54 (2009), N433-N438
[4] NORM ISO 4037-1 (1996)

Poster session VI – Quality assurance for medical radiation applications

Chair: M. Buchgeister (Berlin/DE)

P 66 Investigation for the correct position of a phantom within the FOV of a SPECT gamma camera for quality assurance

R. Weise[1], W. Burchert[1]
[1]Herz- und Diabeteszentrum Nordrhein-Westfalen Universitätsklinik der Ruhr-Universität Bochum, Institut für Radiologie, Nuklearmedizin und Molekulare Bildgebung , Bad Oeynhausen, Germany

Introduction: For some years there are in Germany "Ärztliche Stellen" which checks the quality of the medical use of radiation in diagnosis and therapy to keep the radiation exposure of the patient as low as possible. Thus, for example, forms DIN 6855-2 [1], the basis for the test specification in the quality control (QC) of SPECT gamma cameras. DIN 6855-2 provides test methods for the verification of the performance parameters of a gamma camera and how often the performance parameters must be checked. In addition to many other parameters to be tested, semiannually the image quality is to check in this standard, by the visual assessment of the reconstructed cylindrical phantom uniformity and the visibility of inactive spheres in a volume phantom which are surrounded by a homogeneous radioactive solution. In a recommendation of the German Commission on Radiological Protection (SSK) from the year 2010 [2] it is required that at least 3 spheres should be determined without ring artifacts. When performing the QC with standard protocols it can be observed what is physically known, but is neglected for various reasons in the clinical routine [3] that the reliable detection of the inactive spheres is also dependent on the position of the phantom in the FOV of the gamma camera.

The recognisability of the imaged cold spheres inserted into a cylindrical phantom was the focus of the investigation.

Material and methods: In this study two SPECT gamma cameras were investigated, CardioMD and Hawkeye (SPECT-CT). The CardioMD equipped with a transmission measuring apparatus (Gd-153 line source) is a dedicated nuclear cardiac camera with fixed 90° position of the two rectangular detectors, which can be operated only in L-mode with a 180-degree arc. The Hawkeye has the ability to measure both in L-mode and in H-mode. In H-Mode the detector heads are aligned parallel to each other (360-degree arc acquisition). For the experiment a cylindrical phantom with an insert of 6 inactive spheres was filled with a homogeneously mixed solution of Tc-99m. The spheres are not radioactive and are cold objects in the radioactive solution.

The cylindrical phantom was positioned on the patient table within the FOV and the longitudinal axis of the phantom was aligned parallel to the system axis of the gamma camera. For optimal spatial resolution, the SPECT camera heads were very close to the phantom. Seven measurements per mode at each SPECT system were done. The acquisition parameters remained unchanged. Only the phantom was rotated in steps of 30° (CW for CardioMD; CCW for Hawkeye) per measurement. After the acquisition the image data set was reconstructed using an iterative computational algorithm (OSEM). The data were attenuation corrected.

Setup for measurement:

Phantom:	cylindrical phantom with an insert of 6 inactive spheres
	(Outer diameter of spheres 40; 30; 23; 20; 15; 13 mm)
Nuclide:	Tc-99m homogeneously mixed in the phantom; activity 400 MBq
Collimator:	Low Energy High Resolution parallel, for both SPECT systems

Acquisition protocol (clinical protocol):

L mode:	180-degree arc, for both SPECT systems
H-mode:	360-degree arc, only for Hawkeye
Direction of rotation:	CW for CardioMD; CCW for Hawkeye
Movement:	Step & Shoot
Angular step:	3 degrees

Matrix: 64 x 64

Acquisition time: 25 seconds per projection

Attenuation correction

Results: Inactive spheres can be well recognized in the H-mode. All six cold spheres are visible with the Hawkeye system (Fig. 1).

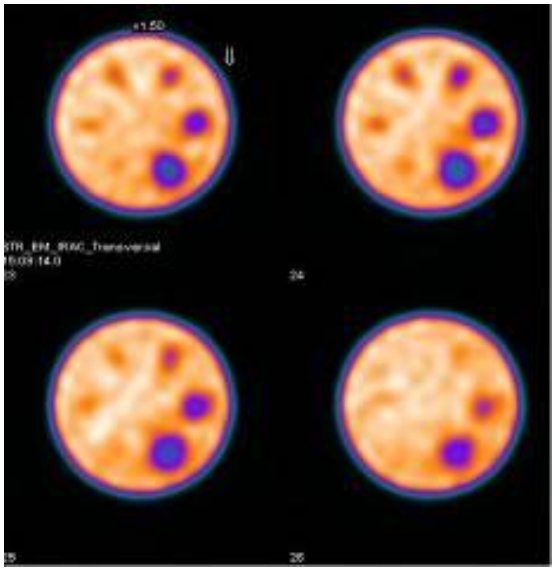

Fig. 1: Hawkeye H-Modus: Angular sampling range 360° (180° per detector) 150° position of the cylindrical phantom with insert of six cold spheres

If the identical cylindrical phantom with unchanged measuring arrangement examined in L-mode only three cold spheres are reliably detected (Fig. 2).

There are small differences in the imaged shape of the spheres compared to the H-mode.

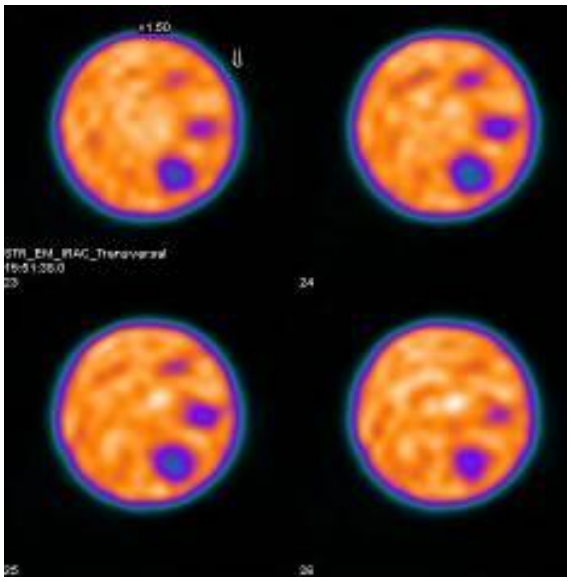

Fig. 2: Hawkeye L-Modus: Angular sampling range 180° (90° per detector) 150° position of the cylindrical phantom with insert of six cold spheres

For the CardioMD, which can be operated only in L-mode, the result for the 150° position of the cylinder phantom is shown in Figure 3.

It is possible to see the six cold spheres. However, the shape of the spheres is distorted.

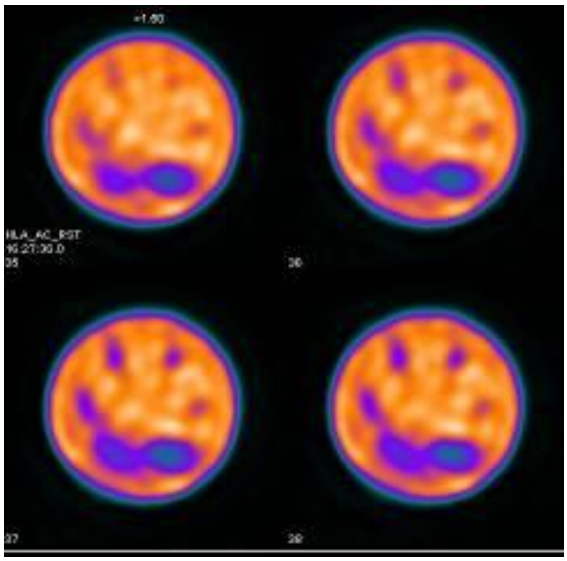

Fig. 3: CardioMDL-Modus: Angular sampling range 180° (90° per detector) 150° position of the cylindrical phantom with insert of six cold spheres

Discussion: The operation and performance parameters of a gamma camera are well known. An important performance parameter is the spatial resolution, which is essentially determined by the MTF of the collimator. The spatial resolution is different in the FOV of the gamma camera. With the distance to the detector, the spatial resolution will be worse. Therefore, the spatial resolution will be deteriorate as the radius of the camera orbit increases. There is no difference of the performance parameter of a gamma camera which operated in L-mode or H-mode. The only difference between the L-mode and H-mode is the number of projections per sampled volume. To detect an object completely a 180-degree arc is sufficient. With the H-mode is an angular range of 360 degrees possible, i.e., 180 degrees per detector. Therefore, two data sets are generated per projection direction. The advantage of this method is that with a duplicate record by averaging the loss of resolution, both radially and tangentially, can be compensated in the reconstructed image depending on the distance of the object to the detector. The spheres will be circular and completely imaged (Fig. 1). A disadvantage of the H-Mode is the duplicate acquisition time, which can often result in patient motion artifacts. That is the reason for using L-mode in the clinical routine. But the disadvantage is the deformation of the spheres because of the non-stationary spatial resolution within the FOV of a SPECT system. A reconstruction algorithm, which takes into account the transmission characteristics of the detector in the reconstruction, could overcome this deficiency.

However, since such reconstruction algorithms are not yet fully in the non-university institutions in use, this type of required quality assurance is useful to know the imaging behavior of the gamma camera.

References

[1] Norm DIN 6855-2:2013-01: Konstanzprüfung nuklearmedizinischer Messsysteme – Teil 2:Einkristall-Gamma-Kameras zur planaren Szintigraphie und zur Einzel-Photonen-Emissions-Tomographie mit Hilfe rotierender Messköpfe, 2013, Berlin: Beuth Verlag

[2] SSK 2010: Qualitätskontrolle von nuklearmedizinischen Geräten -Festlegung von Reaktionsschwellen und Toleranzgrenzen: Empfehlung der Strahlenschutzkommission verabschiedet in der 243. Sitzung der SSK am 16./17. September 2010

[3] Bushberg, Jerrold T. et al: The essential physics of medical imaging. 3rd ed. Philadelphia; Lippincott Williams & Wilkins; 2012 – ISBN 978-1-4511-1810-0

P 67 Routine analysis of Trajectory Log files on a True Beam: initial experience

M. Gainey[1], T. Rothe[1]
[1]Universitätsklinikum Freiburg, Klinik für Strahlenheilkunde, Freiburg, Germany

Indroduction: Typically patient specific QA for IMRT/VMAT comprises calculation and measurement of the patient plan transferred to the virtual measurement set-up, or independent verification of the dose distribution using a second commissioned dose engine. Both these methods verify a snapshot of the treatment on the day of measurement or verification. In order to perform an "end-to-end" QA of complex IMRT/VMAT plans it is necessary to verify that all beam and linear accelerator (linac) parameters are within tolerance for each fraction over the entire course of radiation treatment. Whilst it is possible to record an EPID image of the fluence distribution, this may not always be feasible with the patient correctly positioned *in situ* on the treatment couch due to translational shifts, and/or couch rotation. Moreover, the absorption and scatter due to the patient must be accurately accounted for. Alternatively, one can routinely record the fluence map using the EPID, prior to or after patient treatment, and compare with the predicted EPID response. However, whilst representative of the actual variation of patient treatment plan delivery at the linac, it does not record the actual clinical daily treatment parameters. On the other hand it is possible to mount a multiwire transmission detector, such as the DAVID detector (PTW Freiburg, Germany), to record daily leaf motion pattern as part of a daily constancy check. Thus, daily patient specific IMRT/VMAT QA can currently only be achieved by analysing the log files written by the linac without additional equipment [1][2].

Material and methods: The trajectory log file comprises a plurality of "snapshots" of the state of the linac axes every 20ms, for a maximum of 20 minutes, during delivery of patient plans in clinical mode: actual and expected values are recorded therein. MATLAB (R2013a, MathWorks, MA) software was developed to automatically read in and analyse the generated trajectory log files (version 1.5) for the TrueBeam™ (Varian Medical Systems Inc.) linac based upon the specification data [3]. A MATLAB software script runs each evening after patient treatments have been completed, generating PDF reports for each RapidArc™ (VMS) treatment delivered by the True Beam (VMS) linac stored on a remote network drive. The PDF reports are automatically stored in a separate directory based on the patient ID number and treatment date for subsequent embedding into Mosaiq 2.41 (Impaq Medical Systems Inc, CA) Record and Verify system. Furthermore after the script has executed a daily email summary is sent to be checked by a MPE: problematic treatment deliveries can be identified and analysed in detail by a MPE.

Results: Preliminary results indicate that actual MLC positions were within ±0.10mm of the planned position for all snapshots of the analysed fractions within a particular patient course. 57% lie within 0.01mm, 72% lies within 0.02mm and 89% of all meaured leaf positions lie within 0.05mm of their planned position, see Fig. 1 for a typical histogram of leaf position errors. Moreover, the mean leaf position deviation was found to be 0.02mm. Gantry angle variations lie in the range -0.1 to +0.3 degrees: mean 0.04 degrees (Fig 2). Furthermore, calculated fluence maps derived from the actual and expected control point sequences have been compared: initial results indicate excellent agreement (Fig. 3).

Conclusion: We have demonstrated the automatic analysis of daily trajectory log files for the routine analysis of daily fractions of complex IMRT/VMAT treatment plans, albeit that the described analysis is dependent on the manufacturer's generated data: it is not an independent verification. Once sufficient results are available we will be able to define appropriate action levels for the analysis results: perhaps even specific to the tumour localisation. Whilst this preliminary work is encouraging it is our aim to extend this work to create a DICOM RT Plan file from the actual positions recorded in the trajectory log files, for subsequent dose calculation in the Eclipse (v10.0.28) treatment planning system (VMS) using the patient CT study.

References

[1] Rangaraj D, Zhu M, Yang D, Palaniswaamy G, Yaddanapudi S, Wooten O H, Brame S and Mutic S, Catching errors with patient-specific pretreatment machine log file analysis, Practical Radiation Oncology, 3,2013, 80-90
[2] Rangaraj D, Palaniswaamy G, Yaddanapudi S, Wooten O H , Yang D, Mutic S and Santanam L Initial experience with TrueBeam trajectory log files for radiation therapy delivery verification, Practical Radiation Oncology, 2013, 3, e198-208
[3] Varian Medical Systems, TrueBeam Trajectory Log Specification: For TrueBeam 1.5 and Higher 100049068-02, August 2011.

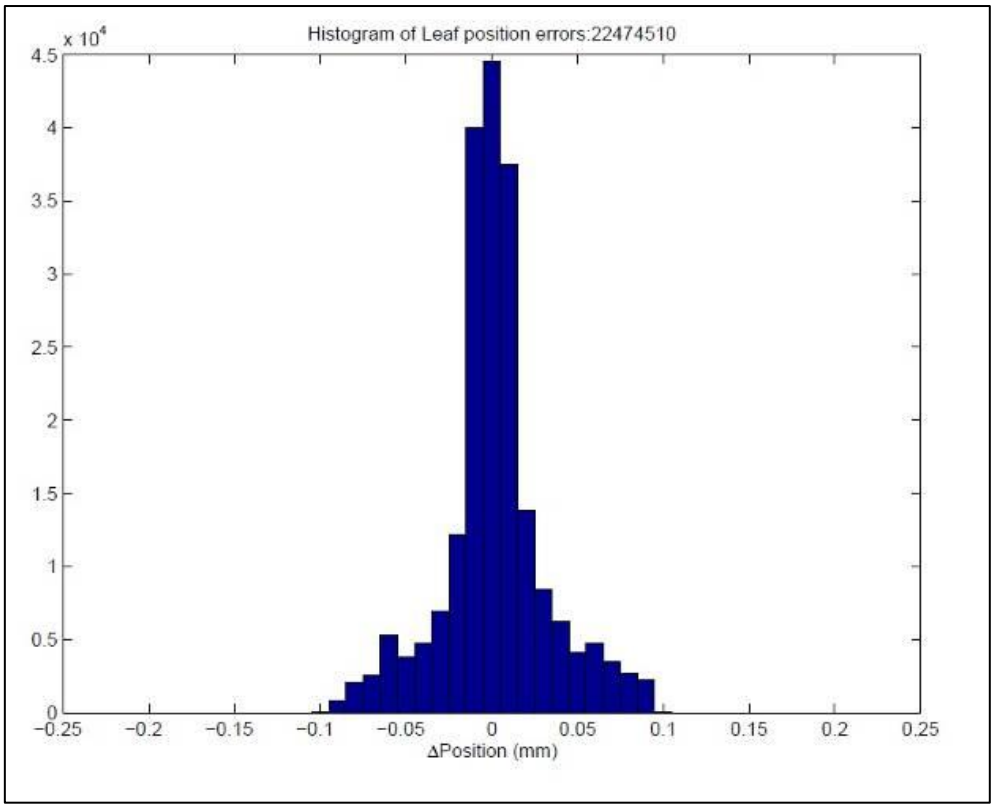

Fig. 1:Typical histogram of leaf position errors for a particular patient fraction

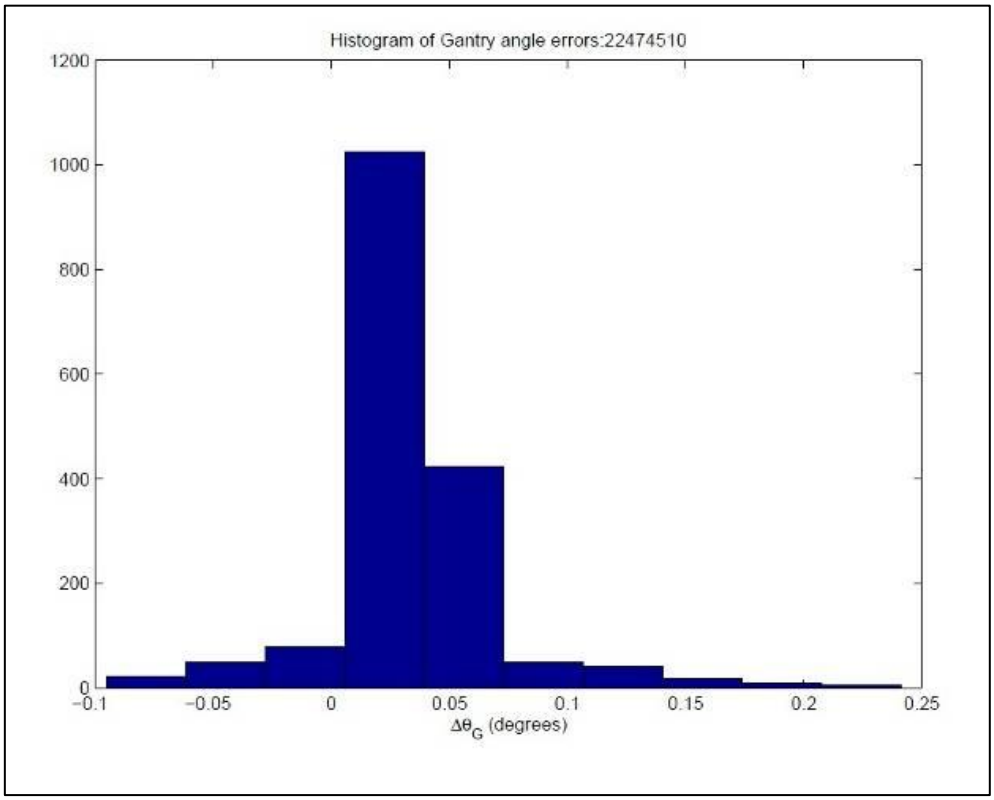

Fig. 2: Typical gantry angle errors for the same patient fraction.

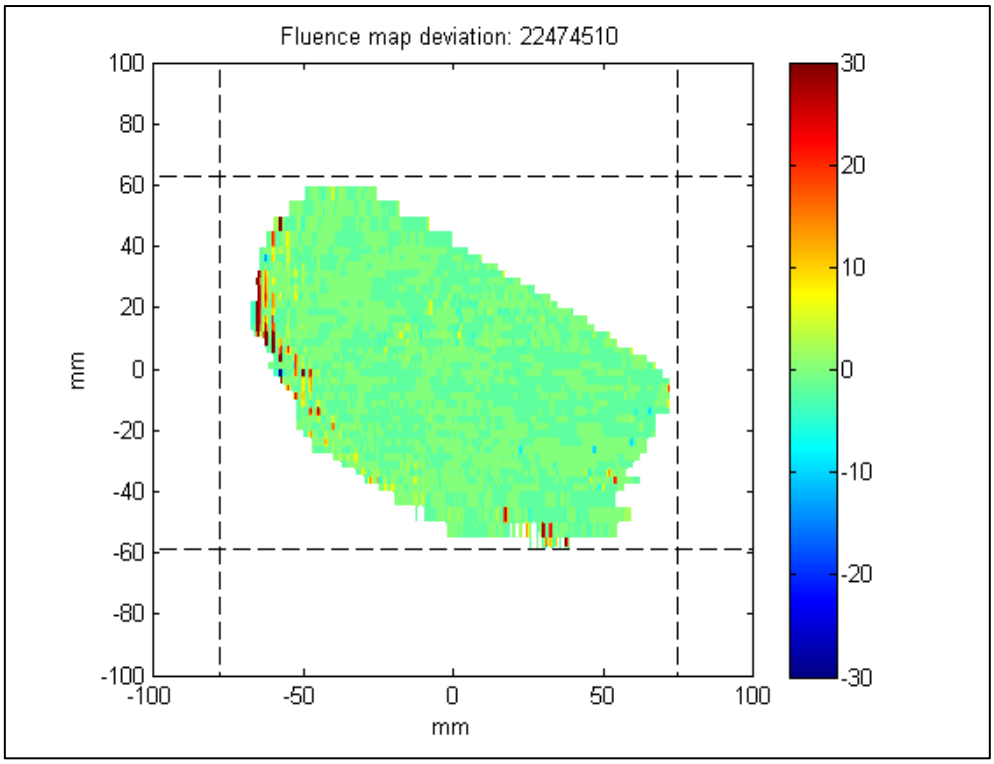

Fig. 3: Normalised fluence map deviation (planned-actual) for the same patient fraction. The dashed lines indicate the maximum jaw opening.

P 68 Testing the Machine Performance Check application

A. Clivio[1], E. Vanetti de Palma[1], G. Nicolini[1], A. Fogliata[1], M. F. Belosi[1], L. Cozzi[1], S. Rose[1], C. Baltes[1]
[1]Oncology Institute of Southern Switzerland, Radiotherapy, Bellinzona, Switzerland

Objective/Purpose: Machine Performance Check (MPC) is an application to verify that geometry and beam performances of a TrueBeam treatment unit are operating within system specifications, through automated checks based on kV and MV imaging systems installed on the Linac. In the present study, preliminary tests with MPC were analyzed using all photon beam energies available on a TrueBeam (version 1.5), comparing whenever possible with external independent checks.

Material and methods: The data acquisition comprises of a series of 40 images (12 with kV and 28 with MV detector) acquired at different predefined positions without and with the IsoCal phantom under the beam and with particular MLC pattern settings. MPC performs two kinds of checks: geometric and dosimetric. The geometric checks intend to test the treatment isocenter size and its coincidence with imaging devices, as well as the positioning accuracy of the imaging systems, the collimator, the gantry, the jaws, the MLC leaves and the couch position. The dosimetric checks refer to a reference MV image and give the beam output, uniformity and center change respect to the reference. MPC data were acquired during 10 repetitions in different consecutive days.

Alternative checks were performed for geometric checks: routine mechanical tests, and the Winston-Lutz test for treatment isocenter radius; for dosimetric checks the 2D array StarCheck (PTW, Freiburg, Germamy) was acquired just after the MPC data acquisition.

Results: Results were analyzed for 6, 10, 15 MV flattened beams, and 6, 10 MV FFF beams. In the following data are reported for 6MV flattened beams. Similar results, while not identical, were obtained for all energies. Geometric checks: treatment isocenter was evaluated of 0.27 mm with the Winston-Lutz test, compared with 0.34±0.01 mm with MPC. Coincidence of kV and MV imaging isocenters: 0.30±0.02 and 0.17±0.02 mm (0.43±0.14 and 0.32±0.24 mm with external tests). Positioning accuracy of jaws was well within 0.1 mm relative to the reference with MPC, while within 0.3 mm with independent checks. Gantry and collimator angle position was for all checks (MPC and external) within 0.2 degree in all cases. Couch positioning was within 0.4 mm in all directions for both checks.

Dosimetric tests: the output stability relative to the reference was in average 0.1±0.1 % and 0.4±0.4 % for MPC and StarCheck, respectively; beam uniformity results were 0.0±0.0 and 0.1±0.1 %.

Conclusion: MPC proved to be a reliable, fast and easy to use method for checking the machine performances on both geometric and dosimetric aspects.

P 69 Fehlerdetektion von QA-Systemen in der Strahlentherapie

T. Dressel[1], T. Gauer[1]
[1]University Medical Center of Hamburg-Eppendorf, Hamburg, Germany

Introduction: Vor Therapiebeginn müssen die Patientenbestrahlungspläne im Rahmen der Qualitätssicherung mit geeigneten Dosisverfikationssystemen überprüft werden, ob die in der Bestrahlungsplanung optimierte Dosisverteilung patientenspezifisch richtig berechnet und appliziert wird. Als Bewertungskriterium für die Planverifikation wird üblicherweise der Gamma-Index herangezogen. Die vorliegende Arbeit beschäftigt sich mit der Fragestellung, ob der Gamma-Index geeignet ist, um sowohl technische als auch menschliche Fehler in IMRT-/ VMAT-Plänen mit verschiedenen Dosimetern zu detektieren.

Materials and methods: Zur Planverifikation wurden ein EPID-System (Portal Dosimetry der Firma Varian) und ein Diodenarray (ArcCheck der Firma Sun Nuclear) eingesetzt. An einem TrueBeam-Beschleuniger der Firma Varian wurden fehlerhafte Bestrahlungspläne an den Dosisverifikationssystemen abgestrahlt und mit den initialen Plänen verglichen. Folgende Fehler wurden betrachtet: (1) Phantomdeplatzierung; (2) Verschiebung eines Bestrahlungsfeldes; (3) blockieren einer Lamelle während einer IMRT-Bestrahlung im Sliding-Window Modus (Abb. 1); (4) Verringerung der applizierten Monitoreinheiten; (5) Dosisapplikation mit falscher Dosisrate (FFF- Modus anstatt FF-Modus). Die abgestrahlten Pläne wurden mithilfe der Auswertesoftware SNC-Patient mit den geplanten Bestrahlungsplänen ausgewertet, wobei der Gamma-Index soweit verringert wurde bis weniger als 95% der Dioden das festgelegte Gamma-Kriterium erfüllen. Ferner wurde der Gamma-Index des EPID zusätzlich mit der Software Portal Dosimetry der Firma Varian bestimmt und mit den Werten aus SNC-Patient gegenüber gestellt. Als zusätzliches Kriterium zur Verifikation wurden Dosisdifferenzdarstellungen herangezogen.

Results: (1) Eine Phantomdeplazierung des ArcChecks in allen drei Raumrichtungen um jeweils 2mm konnte sowohl mittels Gamma-Index (83,4% bei einem Gamma-Kriterium von 3%/3mm) als auch durch die Dosisdifferenzdarstellung erfolgreich verifiziert werden. (2) Für die Verschiebung eines 3cm×3cm Bestrahlungsfeldes um 2mm ergab sich für das EPID ein Gamma-Index von 98,4% für 2%/3mm und beim ArcCheck von 96,2% für 2%/1mm. Anhand der Dosisdifferenzdarstellung sind Dosisabweichungen am Feldrand beim EPID jedoch deutlich zu erkennen. (3) Für die blockierte Lamelle ergibt sich ein Gamma-Index von 95,4% für 3%/3mm und beim ArcCheck von 95,1% für 2%/2mm). Mithilfe der Dosisdifferenzdarstellung konnte die deutliche Überdosierung im Bereich der Lamelle (Abb. 2) jedoch für beide Systeme erfolgreich verifiziert werden. (4) Eine MU-Verringerung von 2% ergab für beide Systeme einen hohen Gamma-Index (97,1% für 1%/2mm beim EPID und 95,2% für 3%/2mm beim ArcCheck). Auch in diesem Fall war die Verifizierung der Unterdosierung mittels Dosisdifferenzdarstellung möglich.

Conclusion: Der Gamma-Index lieferte einem für klinische Routine üblichen Kriterium von 3%/3mm unzureichende Ergebnisse zur Beurteilung von Bestrahlungsplanverifikationen in Gegenwart von technischen/menschlichen Fehlern. Eine Fehlerdetektion (Gamma-Index <95%) wurde häufig erst bei einem Kriterium von 2%/1mm erreicht, wobei das Ergebnis dann wenig aussagekräftig ist, da das Dosisberechnungsgrid der Planungssoftware 2mm beträgt. Somit scheinen zusätzlich Dosisdifferenzdarstellungen erforderlich zu sein. Ein weiteres Problem war die unzureichende Auflösung kleiner Strukturen durch das ArcCheck (z.B. 3cm×3cm MLC-Felder. Messungen bei größeren Feldgrößen könnten zu einer Verbesserung des Gamma-Index führen.

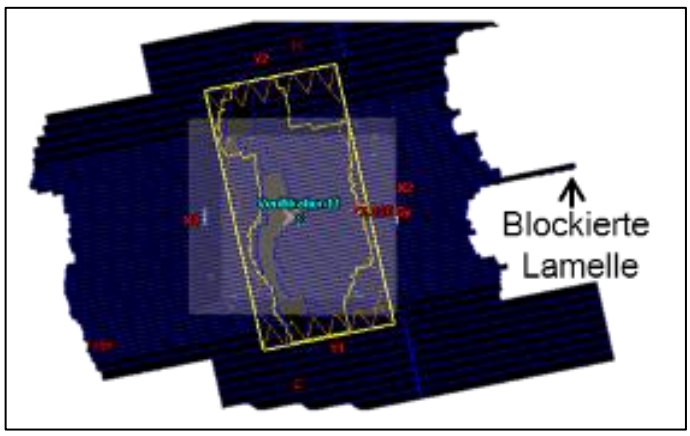

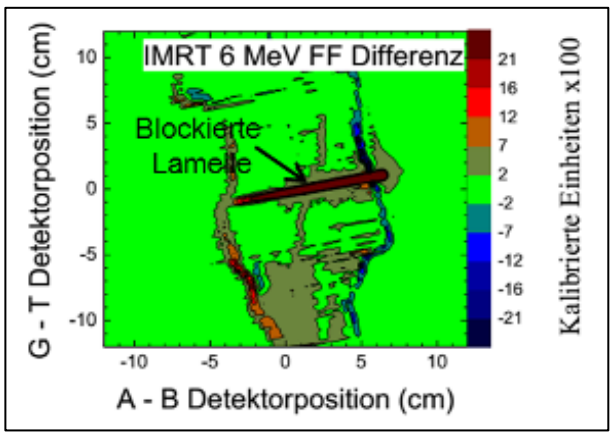

P 70 The use of the QUALIMAGIQ Platform and the Leeds Phantom TOR 18FG to check the daily geometry accuracy of the kV imaging system: results after nine months experience

C. Santinha[1], P. Huettenrauch[1], D. Wagner[1]
[1]UMG, Göttingen, Germany

Introduction: Electronic Portal Imaging Devices (EPID) are very important tools on the evaluation of patient setup/position before and during treatment (contributing for the reduction of treatment delivery errors) as well as for the quality assurance (QA) routine. For this purpose, it must be ensured that the imager is accurate and precise. Periodic QA procedures should be conducted to ensure that image quality and physical parameters remain within specified limits.

After reviewing the VARIAN Customer Technical Bulletin CTB-OB-786A *"OBI Arm Displacement From Desired Position"* a daily geometry-accuracy check of the kV imaging system was implemented. With the Isocenter cube phantom, which consists of a steel sphere placed in the center of a 5 x 5 x 5 cm^3 cube, the distance between the center of the cube (sphere) and the digital graticule was manually measured (using the Maintenance workspace of the OBI application).With this method, the distance can slightly vary from person to person. Since we have already used the QUALIMAGIQ software (QualiFormeD SARL, La Roche Sur Yon, France) and the TOR 18FG Phantom (Leeds Test Objects Ltd, North Yorkshire, UK) for an automatically monthly check to verify the image quality of the kV-OBI as well as its geometry accuracy, we decided to apply the same method for the daily check. After 9 months, the mechanical stability of the OBI system shows to be quite good.

Methods and materials: In our department are two Varian linear accelerators (Clinac 2300 CD), equipped with an On-Board Imager (OBI) system (Varian Medical Systems, Inc., Palo Alto, CA). A kV amorphous silicon detector (KVD) and a kV X-ray source (KVS) are the main parts of the OBI system.

To perform the test, the TOR 18FG Phantom was used and previously marked with a cross on the phantom's surface, to ensure the correct positioning. The phantom is placed on the top of the couch and aligned according to the laser system and the crosshair at a SSD of 100 cm. A copper filter is used on the KVS and the gantry is rotated to 90°.

The geometrical accuracy test is performed at the most used arm positions: KVS at 100/0 cm and the KVD at -50/0/0 cm. One x-ray image is acquired with the KV OBI Protocol 'Pelvis-AP-Med', and a clinical setting of 75 kV/200 mA/50 ms

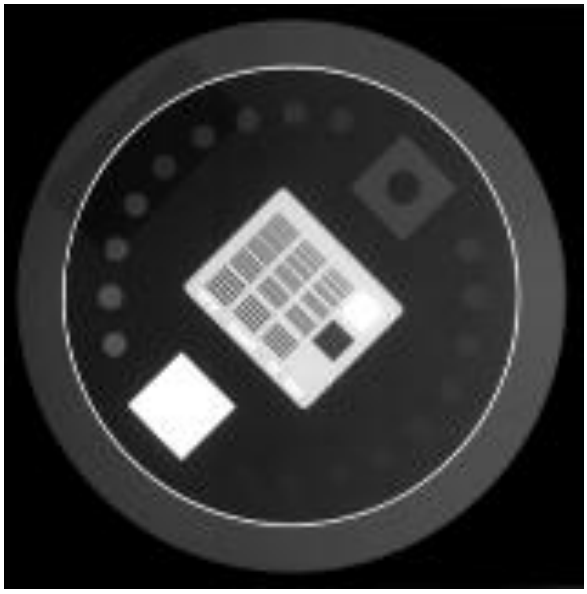

Fig. 1: TOR 18FG Phantom's acquired image.

Results: This work presents the geometry accuracy check of the kV-OBI of two medical accelerators (Varian Medical Systems, Inc., Palo Alto, CA) after a period of nine months.

The Source Imager Distance (SID) and the shifts in the longitudinal and along lateral directions were automatically evaluated on a daily basis (Figure 2). For the first kV-OBI, the average SID was 1499.44 ± 1.25 mm, the average shift along lateral direction was 0.11 ± 0.48 mm and the average shift along longitudinal direction was 1.40 ± 0.42 mm (Table 1). For the second kV-OBI, the averages were 1500.89 ± 1.03 mm, 0.23 ± 0.33 mm and 0.15 ± 0.37 mm, respectively

UMG

Klinikum - Clinac5
18FG - Daily Check SSD=100
QC:21/03/2014 Validation:21/03/2014-PrenomSu NomSu

Owner : Universitätsklinikum Göttingen
Ref User : D.WAGNER

Centering / Distortions

Mode	Control	Result	Units	Target	Min	Max	Test
75.0 KV	Flattening coeff.	1.0		1.0	0.95	1.05	Pass
75.0 KV	Max. abs. diameters deviation	0.38	mm	0.0	-1.0	1.0	Pass
75.0 KV	Max. rel. diameters deviation	0.26	%	0.0	-1.0	1.0	Pass
75.0 KV	Abs. geometric distortions	-0.03	mm	0.0	-1.0	1.0	Pass
75.0 KV	Rel. geometric distortions	-0.02	%	0.0	-1.0	1.0	Pass
75.0 KV	SID : absolute difference	-0.32	mm	0.0	-2.0	2.0	Pass
75.0 KV	SID : relative difference	-0.02	%	0.0	-1.0	1.0	Pass
75.0 KV	Source Imager Distance	1499.68	mm	1500.0	1498.0	1502.0	Pass
75.0 KV	Left / right imager shift	0.86	mm	0.0	-2.0	2.0	Pass
75.0 KV	Top / bottom imager shift	-0.34	mm	0.0	-2.0	2.0	Pass
75.0 KV	Imager / crosshair distance (at SAD)	0.61	mm	0.0	-2.0	2.0	Pass

Fig. 2: Example of a Simple Report created by the QUALIMAGIQ software.

Clinac 4: 75 kV/200 mA/50 ms		Einheit	Min	Max	Mean	SD
Centering/ Distortions	Flattening coeff.		1,00	1,00	1,00	0,00
	Max. abs. diameters dev.	mm	0,08	0,51	0,27	0,09
	Max. rel. diameters dev.	%	0,05	0,34	0,18	0,06
	Abs. geometric distort.	mm	-0,55	1,69	-0,04	0,19
	Rel. geometric distort.	%	-0,36	1,12	-0,03	0,13
	SID: abs. difference	mm	-5,47	16,85	-0,04	1,90
	SID: rel. difference	%	-0,36	1,12	-0,03	0,13
	SID	mm	1494,53	1516,85	1499,58	1,89
	Left/right imager shift	mm	-1,07	1,55	0,10	0,50
	Top/bottom imager shift	mm	-0,71	2,45	1,39	0,43
	Imager/crosshair distance	mm	0,28	1,65	1,00	0,24

Tab. 1: Evaluation of the tested parameters of 'Clinac 4'

Clinac 5: 75 kV/200 mA/50 ms		Einheit	Min	Max	Mean	SD
Centering/ Distortions	Flattening coeff.		1,00	1,00	1,00	0,00
	Max. abs. diameters dev.	mm	0,12	0,64	0,28	0,10
	Max. rel. diameters dev.	%	0,08	0,42	0,19	0,07
	Abs. geometric distort.	mm	-0,21	0,47	0,10	0,10
	Rel. geometric distort.	%	-0,14	0,31	0,07	0,07
	SID: abs. difference	mm	-2,08	4,69	1,03	1,04
	SID: rel. difference	%	-0,14	0,31	0,07	0,07
	SID	mm	1497,42	1504,69	1500,89	1,03
	Left/right imager shift	mm	-1,32	1,67	0,23	0,33
	Top/bottom imager shift	mm	-1,22	1,26	0,15	0,37
	Imager/crosshair distance	mm	0,05	1,13	0,33	0,19

Tab. 2: Evaluation of the tested parameters of 'Clinac 5'

If the phantom is not positioned exactly, the measurements can be out of tolerance. Even a slightly difference means an enormous discrepancy concerning the results and the test must be repeated.

Figure 3 shows a trend graphic, automatically generated by the QUALIMAGIQ software. Values outside the tolerance are due to a few days on which the acquired images were analysed on the next day. In such cases parameters were out of tolerance without performing a second check.

Fig. 3: Example of a SID Trend Graphic of the OBI.

Conclusions: The evaluation over a nine months period demonstrates that the two kV imaging systems have good mechanical reliability. The tests are performed by a medical-technical assistant and it could be detected that the results are individual-related. Now there is some discussion about the frequency of the checks. Nevertheless, they should be performed on a regular basis to ensure the mechanical stability of the OBI system.

P 71 Development of an efficient radiation protection software tool for linac bunkers

A. Chezzi[1], W. Volken[1], M. K. Fix[1], P. Manser[1]
[1]University Hospital, Bern, Switzerland

Introduction: In radiation therapy linear accelerators (linacs) are the equipments most commonly used. They can generate electron or photon beams with energies, which may range of 6-20 MeV. As a consequence, radiation protection is an issue and thick walls are needed in order to provide enough shielding for the staff [1]. The choice of thickness and materials is not only driven by the need of radiation protection but also associated with the optimization of costs. It is thus clear that the corresponding calculations of radiation protection must be performed efficiently and correctly such that optimization can be performed. In this work, we present an efficient radiation protection software tool for linac bunkers.

Material and methods: As a first step a software environment has been established in order to manage different linac bunker designs. The geometrical space is divided into voxels of user adjustable voxel sizes and each voxel contains the information about the materials to be considered. This information is given by the corresponding tenth-value layer, which can be assigned after considering the maximal photon energy of the linac.

As a second step a shielding barriers thickness calculation algorithm has been implemented using the ray tracing concept. The distance in the different directions of the linac bunker construction for each ray is calculated from the distance from the origin to the entry point of the shielding block and the distance from the origin to the exit point.

Finally an algorithm for the dose calculation in the voxels outside of the linac bunker has been developed. The calculation is based on a simple equation taking into account the workload (W), the use factor (U), the occupancy factor (T), the reduction factor for the dose rate (R) and the required number (n) of tenth-value layers. For this work, only two kinds of radiation were considered: the primary radiation and the leakage radiation. As regards the occupancy factor the user can easily enter the values for each voxel.

Results: The comparison of dose calculations obtained manually and those provided by the developed software tool shows perfect agreement, as expected. In addition, due to its flexibility, the software tool enables easy adaptation of both the geometry as well as the composition of the different shielding materials. Due to the use of the ray tracing method, it is possible to calculate the dose distribution outside a linac bunker in almost real time.

Summary: In this work a flexible and efficient software tool is presented. It enables to calculate and visualize the dose distribution outside of the linac bunker. Moreover several advantages have been achieved: an automatic procedure for the dose calculation reducing human errors and a substantial gain in time compared to the currently used procedures.

References

[1] Beschleunigerverordnung (814.501.513)

P 72 Linac Twins with Flatness Filter Free Option in a Radiotherapy Department

M. Treutwein[1], P. M. Härtl[1], C. Gröger[1], Z. Katsilieri[1], B. Dobler[1]
[1]Universitätsklinikum Regensburg, Klinik und Poliklinik für Strahlentherapie, Regensburg, Germany

Introduction: Having two (or more) equal treatment machines (linac twins) enables a radiotherapy department to facilitate the workflow. The major part of the German standards (DIN) regarding quality assurance of medical linear accelerators has been reworked or has been published for the first time in the recent years due to technical developments. The aim of this study is to setup a commissioning procedure and a quality assurance program for linac twins with flattening filter free option and to investigate if time required for commissioning and quality assurance can be reduced as compared to 2 linacs of different types. This includes the radiotherapy planning system (RTPS).

Material and methods: Tenders were invited to provide two linacs of the same type to replace the old Siemens Primus machines. We asked for linacs with two photon energies (6 and 15 MV), additional flatness filter free (FFF) option, capability of intensity modulated radiotherapy (IMRT) and volumetric modulated arc therapy (VMAT), and 5-6 different electron energies between 4 MeV and 22 MeV. Our requirement was that patients should be treatable at both machines with the same treatment plan. The first of the twin machines, an Elekta Synergy with Agility head, XVI Cone Beam CT, and Iview Portal Imaging has been installed and commissioned according to earlier experiences [1] and has been running in the clinical routine for several months, but initially not FFF. The second linac will be installed in April, therefore no comparative measurements are shown here but may be added for the final presentation.

Although commissioning tests, the determination of basic performance characteristics, and consistency tests for linacs according the German standards [2] have to be accomplished for each machine, they can at least be set up identically without modifications for twin machines. This is also applicable for performance characteristics and consistency testing concerning special techniques as stereotactic radiotherapy [3; 4], and IMRT [5; 6], as well as electronic portal imaging devices (EPID) [2]. For commissioning of the linac in the RTPS Oncentra 4.3 (Nucletron an Elekta Company) a set of geometrical data, absolute, and relative dose measurements is required in addition to the acceptance test of the linac. The data are processed by the company to create a model of the treatment unit, which takes several weeks according to our experience. Once the model is delivered by the company, it has to be validated by the customer. One aim of the study is to investigate, if this procedure can be reduced to the validation process for the second linac.

The draft of the German standard for consistency tests of RTPS DIN 6873 – 5 [7] requires calculations for each treatment machine. Probably part 1 of DIN 6873 for commissioning of RTPS which is in development will demand this too. Having only one treatment machine model reduces time and effort for quality assurance. The German directive “Strahlenschutz in der Medizin” [8], paragraph 2.3.4, requires a concept to ensure patient treatment even during machine down times (e.g. maintenance or breakdown). Linac twins allow shifting all patients from one machine to the other without calculating new treatment plans. The record and verify system (Mosaiq) can be configured in a manner that fields for one machine can be delivered at the other without warnings or password confirmation.

Discussion and conclusion: We expect that the time and effort for commissioning and quality assurance will be reduced for linac twins. Earlier experiences with the Siemens Primus machines (of different generations) have shown that it was possible to get equivalent dose distributions at least for standard photon energies. As much more this should be possible for linacs of the same production series.

References

[1] Dobler B, Groeger C, Treutwein M, Alvarez-Moret J, Goetzfried T; Weidner, Karin et al. Commissioning of volumetric modulated arc therapy (VMAT) in a dual-vendor environment. Radiother Oncol, 99; 2011, H. 1, 86–89.
[2] Norm, DIN 6847-6, 2012-09. Medizinische Elektronenbeschleuniger-Anlagen – Teil 6:Elektronische Bildempfänger(EPID) – Konstanzprüfung.
[3] Norm, DIN 6875-1, 2004-01. Spezielle Bestrahlungseinrichtungen – Teil 1: Perkutane stereotaktische Bestrahlung, Kennmerkmale und besondere Prüfmethoden
[4] Norm, DIN 6875 – 2, 2008-11. Spezielle Bestrahlungseinrichtungen – Teil 2: Perkutane stereotaktische Bestrahlung – Konstanzprüfungen.
[5] Norm, DIN 6875-3, 2008-03. Spezielle Bestrahlungseinrichtungen – Teil 3: Fluenzmodulierte Strahlentherapie – Kennmerkmale, Prüfmethoden und Regeln für den klinischen Einsatz.
[6] Norm, DIN 6875-4, 2011-4. Spezielle Bestrahlungseinrichtungen – Teil 4: Fluenzmodulierte Strahlentherapie – Konstanzprüfungen.
[7] Norm-Entwurf, DIN 6873 Teil 1, 2013-04. Bestrahlungsplanungssysteme – Teil5: Konstanzprüfung von Kennmerkmalen.
[8] Bundesministerium für Umwelt, Naturschutz und Reaktorsicherheit; 30.11.2011. Strahlenschutz in der Medizin – Richtlinie zur Verordnung über den Schutz vor Schäden durch ionisierende Strahlen.

P 73 Software Requirements and Prototype Development of a Web Application for Quality Assurance (QA) in Radiation Therapy- a QAlender

J. Moog[1], M. Yilmaz[2], S. Bächle[1], C. Thies[2]
[1]Universitätsklinikum Tübingen, Klinik für Strahlentherapie, Sigmaringen, Germany
[2]Reutlingen University, Computer Science, Reutlingen, Germany

Introduction: The Radiooncology Department of the University Hospital of Tübingen (UKT) operates six radiation treatment units in the main site in Tübingen and three hospital branches in the vicinity with one Linac on each site.

Today the complete technical QA is paper based according to the procedures regulated in e.g. DIN6847-5, DIN6847-6 and 6875-4. Every branch maintains a system of individual storage without a central database. This local usage of file-based documents (e.g. MS-Excel files) does not permit parallel access or interpretability of data. The current paper based administration is time consuming and inefficient.

To comply with future requirements of an efficient and practicable workflow, the QA of all radiation treatment units has to be coordinated and maintained centrally. Therefore the development and implementation of a centralized QA management system, which is easily accessible from all internal and external treatment units is essential. Thereto web based solutions allow for the use of mobile devices and efficient integration into an existing infrastructure.

Goal of this project is to design a feasible software architecture in order to optimize and simplify the current work flows which should at the same time be easily expandable to future challenges.

Material and methods: The technical demands are determined by the infrastructural and organizational structure of the UKT:

- The basic installation of the system is adaptable to different end devices
- Parallel access is possible
- Access is independent of the device (e.g. fat client or tablet)
- Check documents are presentable on web based documents
- Result data is saved in a central database
- Calendaric overview of executed and imminent QA checks for each treatment unit and graphical illustration of the follow-up interval
- Export of the results to a PDF-A File
- Storage of check files and raw data
- Currently MS-Windows is the standard operating system on clients in the UKT
- Applications and servers are virtualized via a citrix solution

The required web application consists of a central server based on a database and a web server with the corresponding application software (Fig. 1). Data is accessed via http protocol from clients with a standard web browser. For this kind of software architecture numerous framework solutions based on freeware already exist on the market [1]. The data model could be realized with the freeware database PostgreSQL. A Free Apache Tomcat Web Server could serve as a web server. PHP could be used for the application logic. All components could be easily integrated into the present software architecture and could be installed on Windows or Linux Platforms both. Therefore the usage of mobile devices via WLAN is possible independently of their operating systems since the server is accessible by generally available browsers.

As a first step the rationalization effect of such a system should be analyzed. The main effect will be a major saving of time for the staff and a much better traceability of the data by the use of Single sign on, standard access permissions and automated logging. The data and the results of QA checks will always be available from inside and outside of the UKT. This will lead to a much better performance due to intelligent user management and suitable input interfaces. Future integration of existing software such as digitized dose quality assurance into this concept is also possible. In this case three requirements have to be considered: Launching an external application, passing parameters and importing the results. All of them need the development of specific data and user interfaces. Integrating applications into an existing system is a well-known issue in healthcare information systems which is solved by open standards and middleware [2,3]. This is already part of the initial system design.

Outlook: Future developments requiring special applications such as dynamic QA measurements arise from modern and complex radiation treatment techniques such as IMRT and VMAT require. Therefore a future proof QA system must provide an open design to be extensible for new modules for instance:

- individually designed web based input interfaces instead of check documents
- Directly editable and not hardcoded input interfaces. Date should be imported in a predefined format from a precise import directory
- Automatic data import from DICOM image files via a DICOM interface. The field information should be extracted from the DICOM Header file automatically and can be compared with the automatically analyzed data of the DICOM image. The data should be presented in a pdf report.
- Automatic analysis of dynamic “DICOM Movies”.

Results: The implementation of a web based portal QA solution will lead to a high acceptance of the staff as the usage of commonly known standard software (e.g. web browser) allows intuitive handling. In the daily use a significant simplification of the workflow and performance enhancement can be achieved by easy access to the check documents.

As the data is now saved in a database it can easily be processed and long-term trends can be displayed. Therefore possible errors can be detected much easier and earlier.

By the usage of time stamps and user authentication procedures and user responsibilities are comprehensibly documented.

As the software is browser-based, integration into an existing software environment is not critical. As only technical QA data is processed, no further data security measures are necessary. A certification as a medical product is not required.

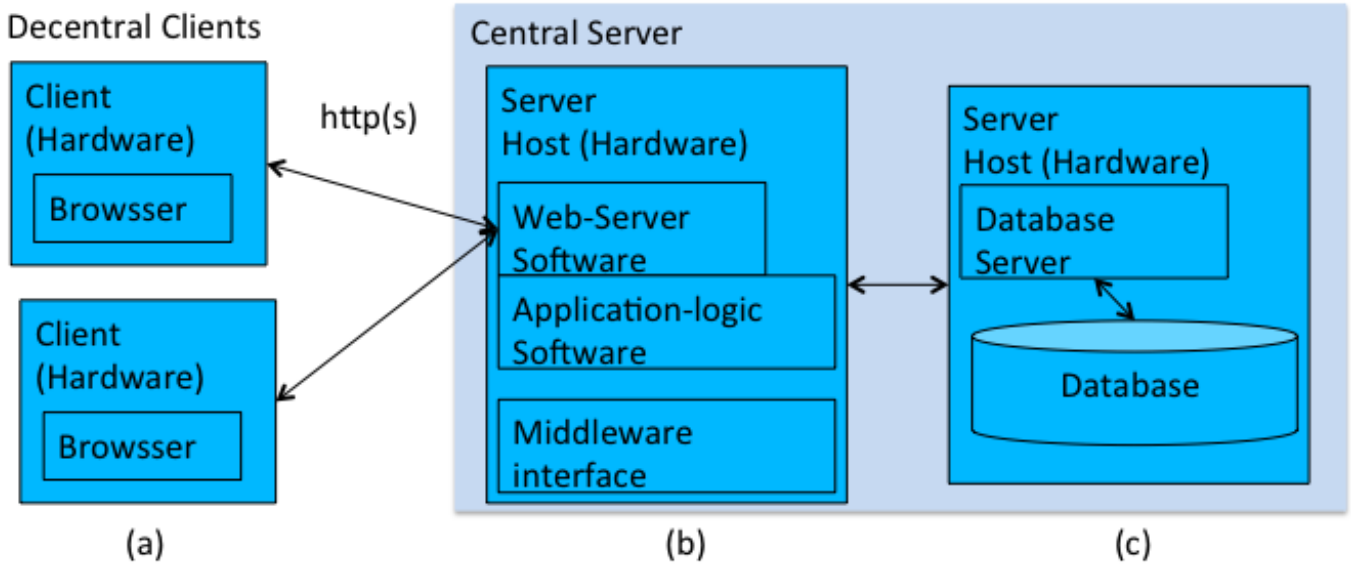

Fig. 1: In web based applications decentral clients (a) access a central server via standard http(s) protocol. Communication and application logic as well as the interfaces are hosted on a special hardware (b) from which the separate database server is accessed (c).

References

[1] Comparison of web application frameworks. In Wikipedia. Retrieved April 12, 2014 from https://en.wikipedia.org/wiki/Comparison_of_web_application_frameworks

[2] Verderio, V.; Cooper, P.: A core middleware service in H.I.S.: the experience of IC_PIDRM.Stud Health Technol Inform, (2000) 77, S 964-968.

[3] Schweiger, R.; Bürkle, T.; Dudeck, J.: Post-integration of a tumor documentation system into a HIS via middleware. Stud Health Technol Inform, (1997) 43, Pt A:6-9.

P 74 VMAT-QA using Elekta Linacs, Philips Pinnacle³ TPS and PTW Octavius 4D – A Code Of Practice including a Hole System Quality Check

U. Heinrichs[1], B. Allgaier[2], I. Brück[1], M. Caffaro[1], T. Jansen[1], I. Norton[3], M. Pasler[4], A. Schmachtenberg[1], H. Wirtz[4], M. Eble[1]
[1]Uniklinik Aachen, Klinik für Radioonkologie und Strahlentherapie, Aachen, Germany
[2]PTW-Freiburg, Marketing und Product Management, Freiburg, Germany
[3]Philips Healthcare, Amsterdam, Netherlands
[4]Strahlentherapie Singen, Medizinische Physik, Singen, Germany

Introduction: State-of-the-art linear accelerators provide a new irradiation technique called Volumetric Modulated Arc Therapy (VMAT) which is a further development of the common Intensity Modulated Radiotherapy Treatment (IMRT). This technique simultaneously changes the shape of the treatment aperture by a continuous movement of multileaf collimator leaves, the rotation speed of the gantry and the delivery dose rate. As we do for IMRT we also have to verify each VMAT patient plan before the first treatment according to DIN 6875-3 (2008) [1]. Parallel to the development of the linear accelerators the availability and complexity of the verification systems increased. While the standard IMRT verification method 2-3 years ago was to compare 2D dose distributions in one single plane, today we have the possibility to compare volumetric dose distributions as well as the dose volume histograms (DVH) of the treatment planning system (TPS) and the verification system. According to the complexity of the verification systems also their installation and commissioning becomes more and more labour-intensive.

This work will provide all users struggling with the combination of Elekta Linacs, Philips Pinnacle³ as TPS and PTW verification system Octavius 4D with a code of practice for a fast and troublefree VMAT verification work-flow.

Material and methods: Before VMAT verification becomes a standard procedure in the daily clinical work-flow the single components have to be prepared for an optimal cooperation.

Philips Pinnacle³ TPS: The first step was to acquire a CT dataset of the Octavius 4D phantom including the Elekta treatment table with 2 mm slice thickness. An alternative is to use the standard CT dataset which is delivered together with the phantom but does not include the user's treatment table. Once delivered to the TPS the phantom CT dataset has to be prepared for its use as standard QA-phantom. Therefore contours and points of interest have to be defined and the volume of the phantom must be overwritten with a predefined density because of the air cavity inside the phantom.

Elekta Linac: The Linac itself has to be perfectly optimized for VMAT treatment which is normally done by the Elekta service technicians. Within the Pinnacle³ TPS the Linac commissioning has to be checked. In our case the leaf-offset curve, the tongue-and-groove value and the inter and intra leaf leakage had to be adjusted in agreement with the results of real water phantom measurements [2].

PTW Octavius 4D: The PTW verification software VeriSoft needs a dataset of eleven measured depth dose curves which are processed by the PTW software package and finally end in a file of 27 depth dose curves for field sizes from 0x0 to 26x26 cm² which later are used for the reconstruction of the measured data. For the cross calibration and basic validation two (ap-pa) 10x10 cm² fields with the condition of a 2 Gy dose delivery in the middle chamber of the 2D ionization chamber array to verify the dose with and without treatment table and a rotational 10x10 cm² field for the rotation verification are needed [3].

Additional we planned the full rotation of the 10x10 cm² field CW and CCW as well as rotational 10x10 cm² fields for all quadrants CW and CCW.

Results:

Elekta Linac and Philips Pinnacle³ TPS: On the hardware side we made the experience that a standard VMAT machine setting according to the manufacturer's specifications is not automatically the optimal setting. There is a range fulfilling the Elekta specifications but within this range there is an optimum of the settings. In our opinion this is one of the two most critical parts on the way to an optimal VMAT behavior of the machine and it requires a lot of experience of the technician to find the Linac's optimum.

The second critical part is on the software side where the Linac needs to be implemented in the TPS. What we found were wrong values for the rounded leaf end specification provided by Elekta. Based on water phantom measurements and beam simulations in Pinnacle³ we created our own leaf offset curve for the Agility™ MLC (Fig. 1). This curve shows a different shape compared to the Elekta curve especially for leaf positions > 13 cm. Furthermore we also looked into the tongue-and-groove effect of the Agility™ MLC but we could not find this effect in our measurements. With this result it was obvious to enter a zero value for the tongue-and-groove effect in the Pinnacle³ MLC physics. But on the other hand we found that Pinnacle³ needs this value for a correct modeling of the field size perpendicular to the leaf movement.

PTW Octavius 4D Cross Calibration and basic validation: The absolute dose verification has been done by using a 0.3 ccm rigid stem ionization chamber (PTW TM23332) together with a special chamber insert plate for the Octavius phantom. For the air density correction a radioactive check device was used. Other corrections have been done according to DIN 6800-2 (2008) [4]. All measured dose values agreed with the planned values within ± 1%.

VMAT patient treatments: Since mid of December 2013 we did about 130 VMAT verifications and treatments. We have no restrictions to a special kind of tumor entities. The major part are prostate cancer treatments with 40% followed by 30% of head and neck treatments, 10% lung treatments and 7% central nervous system treatments. Our evaluation criterion is a gamma index of 3 mm / 3 % local dose. In special cases we allow up to 5 % for the dose to agreement. Over 80 % of the treatment plans fulfill the gamma criterion of 3 mm / 3 %, 15 % of the plans pass with 3 mm and 4 or 5% and the other 5 % are optimized again before they also fulfill the criterion.

Conclusion: This work shows all the critical steps in the chain of combining Elekta Linacs, Pinnacle³ TPS and PTW Octavius 4D for successful VMAT patient treatment verification. Looking to the single components the integration of the Octavius 4D system in Pinnacle³ and the workflow to get this system running and measuring is the easiest part in this chain. The most labour-intensive part is the optimizing of the real Linac and its model in the TPS. Regarding the whole patient treatment process the obtained results show a perfect quality of the complete system chain. Starting with the CT acquisition and transfer to the TPS followed by the dose planning in Pinnacle³ and plan transfer to the Linac and ending in a perfect absolute dose and VMAT plan verification the whole system was checked.

The next step is the evaluation of the DVH information in the PTW VeriSoft software in comparison with the Pinnacle³ DVH. Together with PTW we have the possibility to test this VeriSoft option before the official release in the second half of this year.

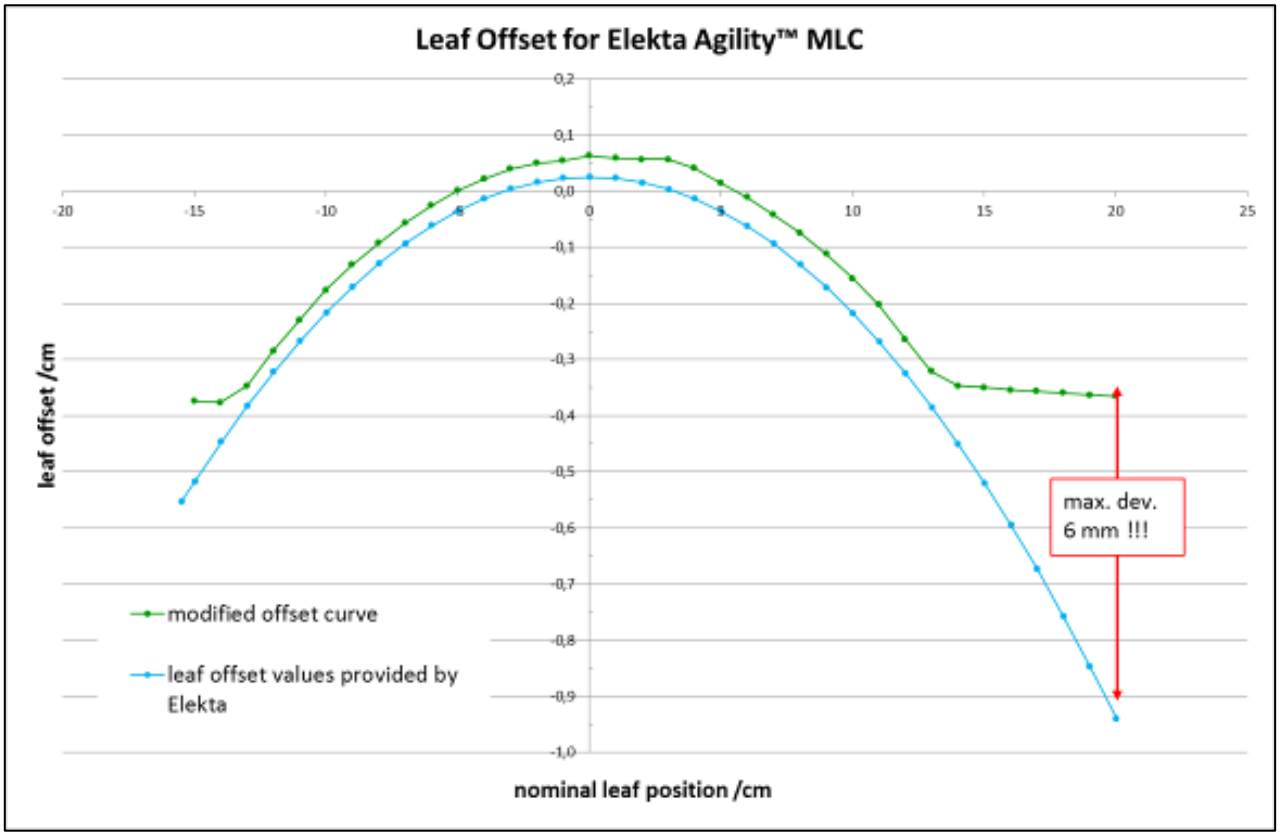

Fig. 1: Leaf offset curves for the Elekta Agility™ MLC. Values provided by Elekta (blue) and modified curve after machine specific measurements and simulations (green).

References

[1] DIN 6875-3:2008-03, Spezielle Bestrahlungseinrichtungen – Teil 3: Fluenzmodulierte Strahlentherapie – Kennmerkmale, Prüfmethoden und Regeln für den klinischen Einsatz

[2] Philips Application Note Pinnacle³ 9.0 and later – Recommended Elekta Agility™ MLC physics parameters, P/N 2012-09 Rev.B

[3] PTW Technical Note D913.200.02/00

[4] DIN 6800-2:2008-03, Dosismessverfahren nach der Sondenmethode für Photonen- und Elektronenstrahlung – Teil 2: Dosimetrie hochenergetischer Photonen- und Elektronenstrahlung mit Ionisationskammern

P 75 Magnetic resonance based polymer gel dosimetry − technical aspects in manufacturing and evaluation, restrictions, artefacts, application problems

A. Berg[1]
[1]Medical University of Vienna , Center for Medical Physics and Biomedical Engineering, MRCE, Vienna, Austria

Introduction: The 3-dimensional dosimetry of highly precise irradiation techniques as Brachytherapy using beta rays, □-knife-photons or ion beam therapy poses high challenges to the dosimeter with regard to precision, accuracy [1], tissue equivalence, spatial resolution and time-efficient measurement procedures (RTAP criterions [2]). The advantages of Magnetic Resonance Imaging based polymer gel dosimetry (MRPD) are represented by the tissue equivalence of the detector material and the fast (multi-slice) 3D dimensional imaging of the transverse relaxation time (T2) to visualize the polymerization process and subsequently the corresponding dose distribution after calibration [3, 4, 1]. In addition, high resolution at a voxel size below 1 mm in all of the three dimensions is in principle possible [5, 6, 1].

However the accuracy and reproducibility of polymer gel dosimetry is dependent on manifold conditions of manufacturing, handling, environmental state and measurement parameters. This contribution is listing in a qualitative manner some of the most important sources of errors for inaccurate or faulty determination of absolute dose levels in MRPD.

Materials and methods: The principle of polymer gel dosimetry is reliant on the production of radical carrying molecules, the concentration of which is proportional to the irradiation dose. The detector material is composed mainly of water and a monomer compound (6-10%), e.g. methacrylic acid or the copolymer system acryl amide/BIS-acrylamide, which is activated for polymerization by the presence of radical carrying molecules. Using tomographic scanners, especially optical scanners [7, 2] or parameter selective T2 Magnetic Resonance Imaging (MRI) 3D-dose images can be calculated after calibration. The MR-measurement parameter T2 is sensitive to the subsequent immobilization of the monomer and embedded water molecules [3, 4]. Gelatine serves as a carrier matrix for the initial immobilization of the multi- and polymers. The relaxation rate R2 = 1/T2 is, in many cases over large ranges, directly proportional to the irradiation dose D: R2 = R20 + + □ D (calibration). The sensitivity of the polymer gel can be varied in a wide range by different compositions [8, 9].

Oxygen suppresses the polymerization. The addition of oxygen scavenging chemicals in (mmol concentrations) as ascorbic acid [10] and THPC [11, 12] to the polymer gel allows for the manufacturing of the polymer gel dosimeters in simply equipped chemical laboratories at normal environmental oxygen partial pressure (“normoxic polymer gels”). We will restrict our discussion on these „normoxic“ polymer gels due to their wide-spread practical relevance in MRPD.

The measurement of the spatial distribution of the absolute dose is based – as a general rule – on calibration measurements of several reference samples of the same manufacturing batch. A calibration curve, correlating the measurement parameter, e.g. R2, to the dose, is obtained and the curve fitting parameters are then applied to the 3-dimensional R2-data set, from which the 3D-dose distribution is calculated. The quality of the whole quantitative dose evaluation procedure is critically dependent on identical manufacturing, handling, irradiation and evaluation conditions between calibration and 3D-dosimtry polymer gels. Several important factors and technical problems in manufacturing and evaluation of MRPD are listed and shortly discussed on a qualitative level.

Results: Variations in dose sensitivity and errors are subject to many criteria, which are subdivided in the following into mainly 4 subgroups:

1.) Polymer gel-preparation

Besides from obvious preparation parameters (temperature and course of preparation and composition), the dose response and sensitivity of polymer gels is critically connected to the concentration of oxygen scavenger incl. catalyst concentrations and their distribution. The concentration of catalyst ingredients as e.g. copper-sulphate in “MAGIC” [10] is in the order of several µmol and thus variations or impurities might have strong consequences on the dose response. Also the mixing effectiveness of the ingredients might is relevant. We experienced no dose response in the first trials with MAGIC polymer gels due to usage of a standard magnetic stirrer instead of a high velocity overhead propeller mixer. After high speed mixing the polymer gel, consisting of a mixture of monomer, gelatine, water and oxygen scavenger is developing a strong and thick foam cover, containing oxygen. The autonomous reduction of this foam may take up to one hour. We experienced in many cases tiny air bubbles left in the polymer gel, which troop together later in the measurement gel container and suppress polymerization nearby or distort the image due to susceptibility artefacts in MR-micro-imaging (see fig. 1). The oxygen permeability of the container material might be also critically relevant: During storage till irradiation oxygen penetrates through the wall and might saturate the chemical scavenging capacity of the oxygen scavenger at mmolar concentrations. The absolute free oxygen concentration in the monomer gel has to be decreased below 10-2 mg/l, in order to not suppress the polymerization process. We experienced sufficient impermeability for BAREX-type material, but still had difficulties in sealing the caps of our small containers.

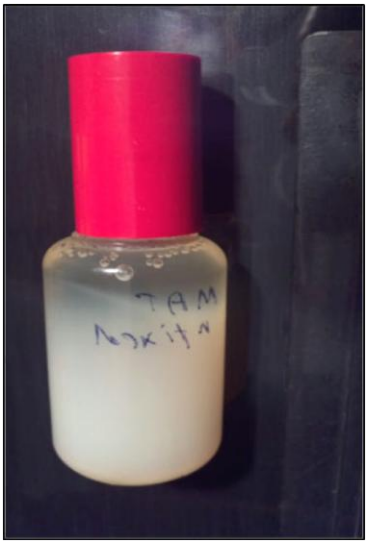

Fig. 1a Photo of a normoxic polymer gel after irradiation within a Co60 photon field (D ≅ 20 Gy). Note the air bubbles on top inside the gel container.
The oxygen present has overloaded the scavenging capacity of THPC and the polymerization is suppressed, indicated by the clear top area. Below that, in the region of effective oxygen scavenging the polymer appears turbid due to effective polymerization.

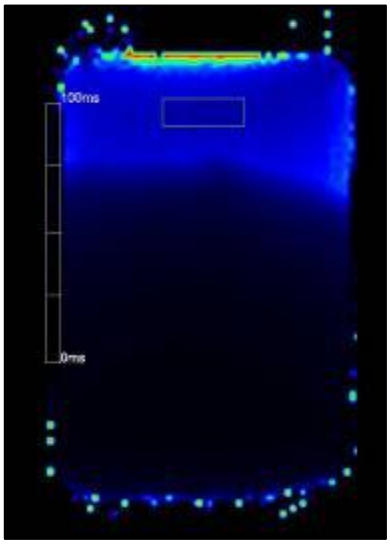

Fig. 1b T2 parameter map of the polymer gel dosimeter. The Co60 photons are applied from the bottom. Due to oxygen present in the area below the cap (see air bubbles in fig. 1a) the polymerization is suppressed. The T2 values in the rectangular ROI are significantly increased (T2 = 645 ms +- 20 ms) with reference to the central polymerized region (T2= 79,1 +-4.5 ms].

2.) Polymer gel storage

Besides from oxygen dense container material the temperature time course has a strong impact on the dose response [13]. Small calibration containers might experience a significant faster temperature drop when being stored in the refrigerator than large (l) volumes for extended radiation fields, which might result in differences in R2 of up to about 30%. Gelling, the inclusion of water in the gelatine matrix, represents a long lasting physico-chemical process up to about 8 days [14], which has a significant influence on the mobility of the water molecules and consequently the MR-measured relaxation rate R2. The process is relevant for the dose sensitivity □□and the relaxation rate at zero dose (offset: R20)) Therefore the calibration gel and the 3D-detector polymer gel are to be treated, stored and evaluated at the same conditions.

3.) Irradiations

Besides from obvious parameters, e.g. the chemical composition, the quantitative value of the dose response is dependent on the temperature due to the physico-chemical reaction process steps during polymerization and the dose rate [14, 15]. High dose rates above about 1 Gy/min [15] might result in a significant reduced dose response and subsequent deviations between the calibration gel irradiated with a (low dose rate) Co60 source and the 3D-detector polymer gel irradiated e.g. on a linear accelerator, easily exceeding dose rates of 1 Gy/min in filter free irradiation status. The MR-evaluation can be performed after finalization of the polymerization process at about 12 h for acrylamide polymer gels [1]. Also the radiation beam quality, especially the linear energy transfer (LET) affects the dose response. Particle beams exhibit a significant dose quenching in regions of a LET >~ 4 keV/µm [16].

4.) Magnetic Resonance Imaging

4.1 Several factors are strongly relevant for the relaxivity R2, as calculated from differently T2-weighted MR-images:

1) T_{meas}: the mobility of the water molecules inside the polymer and gelatine matrix is strongly dependent on the temperature. The coincidence of the temperature of calibration gels with that of the dosimeter sample is important for accuracy with absolute dose measurement.
2) The MR-measurement protocol, especially: FOV, MTX, bandwidth, echo timing: nr of echoes for evaluation, TE and its range [17].

The true spatial resolution in each imaging system might strongly deviate from the voxel or pixel size due to e.g. distortion artefacts as e.g. magnetic susceptibility differences, present in the vicinity of air bubbles. Modern highly precise radiation therapy can easily achieve dose gradients above 4Gy/mm. Consequently a pixel size as small as 1 mm might already

result in dose inaccuracy of □D = 4 Gy. It has been demonstrated that a voxel volume above 0.5 mm already results in significant dose errors in the Bragg-peak of monoenergetic particle beams [18].

Especially the gradient performance with eddy currents might result in additional dephasing of the nuclear spins, which results in significant extra relaxation □R2. The imperfection in gradient switching is especially important for high gradient strength as present in high-resolution imaging and small slice thickness and thus results in significant under-estimation of the dose as measured within the detector dosimeter, if the calibration gels are scanned with higher spatial resolution or vice versa. In dosimetric micro-imaging at very high resolution (pixel size ~ 200 µm), which is necessary e.g. for □-knife 3D-dosimetry for small sized collimators, an additional diffusion weighing is present due to the rephasing gradients, which results in an offset $R2_0$ change [5].

It is noted that accurate relative dosimetric imaging, e.g. supported by an absolute dose measurement in two single points at different dose levels, is possible as long as the linear dose response in the polymer gel detector can be guaranteed.

4.2 In addition there are several possible sources for artefacts in MRPD:

1) Magnetic susceptibility. The container material or fixation gadgets of the detector might contain compounds with a magnetic susceptibility significantly different from that of water. This results in distortions in MR-imaging especially if the bandwidth □f is chosen too small (>300 Hz/pixel]. Small tiny air bubbles present in the polymer gel might result in T2 distortion in the surrounding area even at high bandwidth (see Fig. 1).
2) An inhomogeneity in the spatial distribution of the radio-frequency field, due to e.g. too small radio-frequency (rf-) coils with reference to the field of view (FOV) results in imperfect 90°-excitation and 180°-refocusing pulses. Subsequently T2-values might be erroneous [17].

Conclusion: Quantitative accurate absolute MR-based polymer gel dosimetry is critically dependent on the identity of manufacturing process, storage conditions (especially temperature course), irradiation and MRI-evaluation of the polymer gel samples used for calibration and the dosimetric detector polymer gel. There are several sources of errors for a correct evaluation: the most important are: oxygen in the polymer gel, the temperature course during all steps of preparation and evaluation due to the sensitivity of the physico-chemical processes and a difference between calibration and measurement gels with regard to the used MR-protocol parameters. Accurate relative dosimetric imaging can be obtained with MRPD (e.g. supported by an absolute dose measurement with an ionization chamber in two single points at different dose levels), if the linear dose response in the polymer gel detector can be assured.

The lack of standardization in all the steps of preparation and MRPD evaluation requires experienced applicants involving mainly polymer gel manufacturing know-how, irradiation and dosimetric skills and in addition detailed MRI experience. MRPD (besides from optically scanned dosimeters and CT [19]) is uniquely suited for research purposes in the evaluation of highly precise modern radiation therapy techniques due to its unique combination of 3D-dosimetric imaging, visualization potential within acceptable short evaluation time, adjustable dose domains, tissue equivalence and high spatial resolution ultimately limited by the pixel size in MR-scanning. However the different possible sources of artefacts and errors for quantitative absolute dosimetry are to be considered for tolerable quantitative 3D-dosimetric results.

References

[1] Baldock C, De Deene Y, Doran S, Ibbott G, Jirasek A, Lepage M, McAuley K B, Oldham M and Schreiner L J; Polymer gel dosimetry Phys. Med. Biol. 55 R1–R63 (2010).
[2] Oldham M, Siewerdsen J H, Shetty A and Jaffray D A. High resolution gel-dosimetry by optical-CT and MR scanning Med. Phys. 28 1436–45 (2001].
[3] Gore J C, Kang Y S and Schulz R J; Measurement of radiation dose distributions by nuclear magnetic resonance (NMR) imaging; Phys. Med. Biol. 29: 1189–97 (1984).
[4] Maryanski M, Gore J and Schulz R; NMR relaxation enhancement in gels polymerized and cross-linked by ionizing irradiation: a new approach to 3D dosimetry by MRI Magn. Reson. Imaging 11 253–8 (1993).
[5] A. Berg, A. Ertl, E. Moser; High resolution polymer gel dosimetry by parameter selective MR-microimaging on a whole body scanner at 3 T; Medical Physics, 28, No. 5, 833-843 (2001).
[6] Berg A, Pernkopf M, Waldhäusl C, Schmidt W, Moser E; High resolution MR based polymer dosimetry versus film densitometry: a systematic study based on the modulation transfer function approach; Phys. Med. Biol. 49, 4087-4108 (2004).
[7] Gore J C, Ranade M, Maryanski M J M J and Schulz R J; Radiation dose distributions in three dimensions from tomographic optical density scanning of polymer gels: I. Development of an optical scanner; Phys. Med. Biol. 41, 2695-704 (1996).
[8] Senden R J, De Jean P, McAuley K B and Schreiner L J; Polymer gel dosimeters with reduced toxicity: a preliminary investigation of the NMR and optical dose–response using different monomers; Phys. Med. Biol. 51: 3301–14 (2006).
[9] Andreas Berg; Magnetic-Resonance-Imaging based Polymer Gel Dosimetry: Methodology, Spatial Resolution, Applications; World Congress of Medical Physics Munich/Germany 07.-12.09.2009. O. Dössel and W.C. Schlegel (Eds.): WC 2009, IFMBE Proceedings 25/III, pp. 451–454 (2009).
[10] Fong P M, Keil D C, Does M D and Gore J C; Polymer gels for magnetic resonance imaging of radiation dose distributions at normal room atmosphere; Phys. Med. Biol. 46: 3105-3113 (2001).

[11] De Deene Y, Hurley C, Venning A, Vergote K , Mather M, Healy B J and Baldock C; A basic study of some normoxic polymer geldosimeters; Phys. Med. Biol. 47: 3441–63 (2002).
[12] Sedaghat M, Bujold R, and Lepage M; Severe dose inaccuracies caused by an oxygen-antioxidant imbalance in normoxic polymer gel dosimeters; Phys. Med. Biol. 56 601–625 (2011).
[13] De Deene Y, Pittomvils G and Visalatchi S; On the influence of the cooling rate at the accuracy of normoxic polymer gel dosimeters; Phys. Med. Biol. 52 2719–28 (2007).
[14] Bayreder C, Georg D, Moser E, Berg A; Basic Investigations on the performance of a normoxic polymer gel with tetrakis-hydroxy-methyl-phosphonium-chloride as an oxygen scavenger: reproducibility, accuracy, stability and dose rate dependence; Med. Phys. 33 (7) 2506-18 (2006).
[15] De Deene Y, Vergote K, Claeys C and DeWagter C; The fundamental radiation properties of normoxic polymer gel dosimeters: a comparison between a methacrylic acid based gel and acrylamide based gels Phys. Med. Biol. 51 653–73 (2006).
[16] Gustavsson H, B¨ack S °A J, Medin J, Grusell E and Olsson L E; Linear energy transfer dependence of a normoxic polymer gel dosimeter investigated using proton beam absorbed dose measurement; Phys. Med.Biol. 49 3847–55 (2004).
[17] De Deene Y, DeWagter C and De Neve W; Artifacts in multi-echo T2 imaging for high-precision gel dosimetry:II. Analysis of B1 field inhomogeneity; Phys. Med. Biol. 45 1825–39 (2000).
[18] Berg, A, Wieland M, Naumann J, Jäkel O; High resolution dosimetry in monoenergetic proton beam therapy on a normoxic polymer gel: the importance of high spatial resolution for reduced Bragg-Peak-quenching; IC3DDose 04.-08.11.2012,Sydney/Australia; J.Phys. Conf. Ser. 444, 012054 (2013).
[19] Hilts M, Audet C, Duzenli C et al. (2000); Polymer gel dosimetry using x-ray computed tomography: a feasibility study ; Phys. Med. Biol. 45: 2559-2571 (2000).

P 76 Clinical validation of a new dose verification software (OmniPro-I'mRT+) for patient specific pre-treatment verification

Y. Sekar[1], J. Thoelking[1], R. Fizesan[2], J.-C. Celi[2], F. Lohr[1], F. Wenz[1], H. Wertz[1]
[1]University Medical Centre Mannheim, University of Heidelberg, Mannheim, Germany, Germany
[2]IBA Dosimetry GmbH, Schwarzenbruck, Germany, Germany

Introduction: Patient specific pre-treatment plan verification plays an important role in assuring the dosimetric accuracy in radiation therapy. The evolution of pre-treatment verification ranges from early single point ionization chamber verification to advanced planar verification using detector arrays. For the planar dosimetric verification, a reliable dose verification software tool is essential. The objective of this study was to evaluate and validate the performance of a new pre-treatment patient dose verification software OmniPro-I'mRT+ for photon beams of energies 6 MV and 10 MV with and without flattening filter (FFF). Additionally, the error detection sensitivity of the gamma algorithm in OmniPro-I'mRT+ was tested with different control point errors created in the patient plans.

Material and methods: OmniPro-I'mRT+ (pre-clinical version v. 0.3.2.0) is a new dose verification tool for patient specific IMRT QA, which is used together with the MatriXXEvolution detector array (MXX-Evo). MXX-Evo consists of 1020 air-vented pixel ionization chambers with a volume of 80 mm3, arranged in 32x32 grid with center to center distance of 7.6 mm from each center. Compared to OmniPro-I'mRT (v. 1.7b), the OmniPro-I'mRT+ has a different gamma calculation algorithm and has both the local and global gamma index.

A total of 30 patient (10 FFF cases) plans with different treatment modalities and energies were used for this study. For each case hybrid plans were created in Monaco (v. 5.0) treatment planning system. The measurements were performed with MXX-Evo positioned at the isocenter with 4 cm (3 mm inherent) build-up and attached to the gantry with a holder (source detector distance = 100 cm).The validation of the patient plans was based on the global gamma index method with a dose deviation criterion of 3% and a distance to agreement criterion of 3 mm (≥ 95% of passing gamma pixels). The plans were normalized to the dose maximum and a threshold of above 20% is applied in order to remove the low dose components from gamma. The measurement data with resolution of 0.76 cm used as the reference and compared to the isocenter dose plane of the hybrid plan with resolution of 0.3 cm.

For the error sensitivity test, a few control points (segments) in the original patient plans were removed and the dose was simulated on the MXX-Evo phantom. The error plans simulated from the planning system were compared with the measurements obtained from the original plans with the same setup mentioned above. The investigations of the error detecting capability of the gamma algorithm were based on the different dose differences and distance to agreement criteria (3%/3 mm, 2%/2 mm and 1%/1 mm).

These entire patient plans and error sensitivity tests were benchmarked against our standard clinical patient specific pre-treatmentdose verification tool i.e. using OmniPro-I'mRT with the same setup as mentioned above (however with a different resolution of 0.1 mm for both datasets).

Results: For the patient specific pre-treatment verification using OmniPro-I'mRT+, all the 30 plans had passed the clinical requirements. On comparison with OmniPro-I'mRT, the gamma map of the new OmniPro-I'mRT+ showed results with nominally higher passing rates (Figure 1).

The results for the error sensitivity in the gamma algorithm between OmniPro-I'mRT+ and OmniPro-I'mRT are presented in the Table 1. Overall, the OmniPro-I'mRT+ gamma algorithm shows comparable results with OmniPro-I'mRT with only slight deviations.

Summary: The OmniPro-I'mRT+ software provided results with slightly higher gamma passing rate in pre-treatment verification due to a different method in gamma algorithm; the new method does not require re-sampling the calculated or measured data in OmniPro-I'mRT+. Based on the gamma sensitivity test, the gamma index algorithm of OmniPro-I'mRT+ and OmniPro-I'mRT software's provided similar results. OmniPro-I'mRT+ is suitable as a dose verification software tool for patient specific pre-treatment verification of radiotherapy plans.

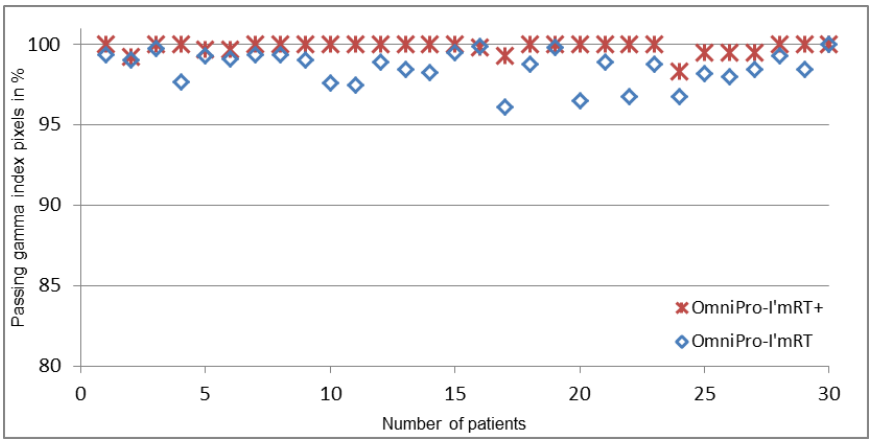

Fig. 1. Gamma index (3% dose deviation, 3 mm distance to agreement) statistics of patient plans comparing measurements and analysis from OmniPro-I'mRT+ and OmniPro-I'mRT against the dose of hybrid plan from the treatment planning system. New gamma algorithm (no need for resampling) provides higher passing rates.

		Gamma Index					
		3%/3 mm	2%/2 mm	1%/1 mm	3%/3 mm	2%/2 mm	1%/1 mm
	Plan Details	OmniPro I'mRT+			OmniPro I'mRT		
Case 1	Original	99,70%	89,50%	57,50%	99,19%	90,70%	58,94%
	5 control points missing	89,70%	78%	49,10%	88,97%	76,90%	49,16%
	7 control points missing	85,50%	75,40%	46,30%	84,99%	73,62%	45,73%
	10 control points missing	81,70%	72,60%	44,80%	81,56%	69,82%	43,22%
Case 2	Original	100%	99,20%	72,10%	99,86%	94,10%	59,58%
	7 control points missing	100%	97,50%	73%	100%	95,59%	60,83%
	10 control points missing	100%	94,30%	61,50%	99,38%	93,51%	56,68%
	15 control points missing	82,80%	65,60%	33,60%	84,48%	68,44%	34,69%

Tab. 1. Sensitivity of the gamma algorithm in OmniPro-I'mRT+ and OmniPro-I'mRT were evaluated with different dose deviation and distance to agreement criteria (3%/3 mm, 2%/2 mm and 1%/1 mm) in gamma index method for the patient plans with different control point errors.

P 77 Post irradiation quality assurance method for TBI Patients.

S. Khan[1], A. Hussain[1], A.Q. Jangda[1], S. B. S. Saeed[1], A. Y. Shaik[1], S. I. Sheikh[1]
[1]Aga Khan University Hospital , Radiation Oncology, karachi, Pakistan

Purpose: To establish an independent verification method by comparison of in vivo dosimetry and calculated dose with help of spreadsheet for total body irradiation (TBI).

Material and methods: Six patients were treated with fractionated TBI (12 Gy, 2 Gy BID) using extended SSD technique. The dose prescribes to the mid plane of the patients at the level of umbilicus. Nano Dots were placed on to the patient's skin to measure the entrance and exit doses at seven anatomical reference points (head, neck, armpit, umbilicus, groin, Knee, and ankle).

For the measurement, calibrated Nano Dots are placed simultaneously at the reference positions. The doses at entrance and exit are measured and compare to the calculated values of respective positions. Following comparison methods are used to make the study more error sensitive and effective

1. Comparison of doses on anatomical reference positions.

2. Comparison of whole treatment dose deviation.

The positions of detectors are keeping unchanged during the whole treatment by placing special marks on the reference positions.

Results: The results of in vivo dosimetry showed that the mid-plane doses are consistent with calculations using the analytical method. The average percentage dose differences are found within ±15%.

Summary: This is an easy and practicable method for independent dose quality assurance. Through this study, errors or dose deviations trace out after every fraction as well as in whole treatment. The detectors are calibrated against our standard setup and extended SSD set up to convert counts into doses. It is concluded that dose inconsistency at different reference points is within tolerance; also it is less time consuming, safe and effective QA method for TBI patients. It is also recommended for this QA method, the patients set up or the detector position must reproduce for each fraction. It will help to achieve more accurate results. It is intended to investigate further improvement in this method.

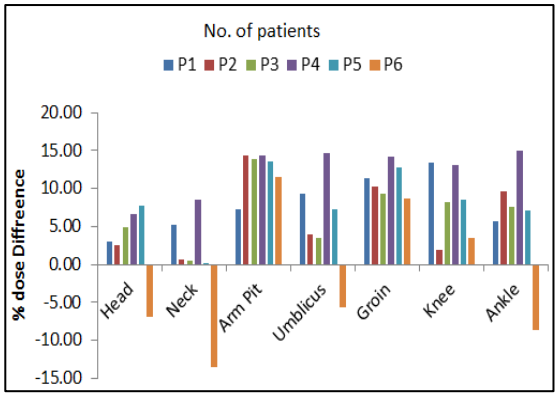

Fig. 1: Percentile dose difference on reference anatomical positions.

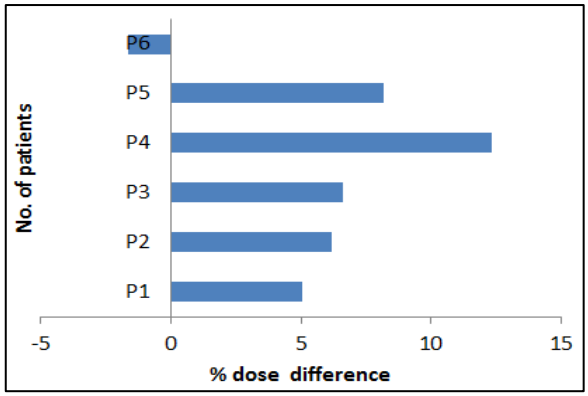

Fig. 2: Whole treatment dose percentile difference for 6 TBI patients

References

[1] Khan FM. The physics of radiation therapy. Philadelphia, PA: Lippincott Williams & Wilkins; 2010.
[2] Yigit CECEN, Bora SINDIR, M. Gamze AKSU, Beyza S. OZDEMIR, Aylin F. KORCUM, Nina TUNCEL, Melek N. YAVUZ, Total Body Irradiation Using a Modified Standing Technique: In Vivo Dosimetry with Semiconductor Diodes ULUSLARARASı HEMATOLOJI-ONKOLOJI DERGISI 2013.
[3] Podgorsak EB and Podgorsak MB. Special procedures and techniques in radiotherapy. In: Podgorsak EB, ed. Radiation oncology physics: a handbook for teachers and students. Vienna, Austria: IAEA; 2005.
[4] Tina Marie Briere,Ramesh Tailor, Naresh Tolani,Karl Prado, Richard Lane, Shiao Woo, Chul Ha, Michael T. Gillin, and A. Sam Beddar, Patient dosimetry for total body irradiation using single-use MOSFET detectors JOURNAL OF APPLIED CLINICAL MEDICAL PHYSICS, VOLUME 9, NUMBER 4, FALL 2008.

Poster session VII – From applied radiation physics in imaging to radiation protection

Chair: R. Simmler (Aarau/CH)

P 78 Routine estimation of effective patient dose for SPECT-CT and PET-CT hybrid cameras in nuclear medicine diagnostic

S. Kerschbaumer[1], G. Stücklschweiger[2], H. Kvaternik[1], C. Gstettner[1], H. Guss[2], R. Aigner[1]
[1]Medical University of Graz, Nuclear Medicine, Graz, Austria
[2]General Hospital Graz, Competence Center for Medical Physics, Graz, Austria

Aim of the Study was to define and evaluate an algorithm to estimate effective dose due to diagnostic procedures on SPECT-CT and PET-CT scanners in nuclear medicine. The recent development of hybrid cameras leads to reduced amounts of radiopharmaceuticals applied because of an increased sensitivity of detection on one hand – on the other hand the CT modality adds significant additional exposure.

The required dose of imaging systems in nuclear medicine is based on the statistical nature of radioactive decay. In contrast to the absorbed and furthermore the effective dose (ED), the radioactivity can be directly and easily measured. For the calculation of the ED in a patient an assumption of the average kinetics and distribution of the radiopharmaceutical must be defined as well as the patient itself. Therefore, it is possible to derive an estimate of ED delivered to the reference person. This implies the hypothesis that the applied kinetic model reflects the individual subject within acceptable spread also in cases of different pathologies. The provision of ED estimates for radiopharmaceuticals in routine requires a patient-specific determination of the administered activity. The ED is calculated from the activity multiplied by conversion factors from the applied radiopharmaceuticals. Literature on the available biokinetics and dosimetry data was systematically reviewed, mostly using PubMed (www.ncbi.nlm.nih.gov/pubmed) and secondary literature cited within the articles found. The complete collection of conversion factors for effective dose for several radiopharmaceuticals can be found in Annals of the ICRP Publication 53 (1987), Publication 62 (1991), Publication 80 (1998) and Publication 106 (2008). The CT component was calculated based on a simplified algorithm from the European Guidelines for Multislice Computed Tomography (EUR 16262 EN) using a normalized coefficient appropriate to the anatomical region and the patient's age multiplied by the dose-length product (DLP). Especially for PET-CT but also for SPECT-CT – unlike radiological examinations – extended scan ranges for partial-body and whole-body scans are required due to attenuation correction (Siemens Biograph mCT, Siemens Medical Solutions USA, low dose CT: 120kV, 40 mAeff, CARE dose, 5mm slice thickness, pitch 1,3).

As a result the ED was calculated according this algorithm for adult male and female patients for the common examinations of SPECT-CT and PET-CT. The radiopharmaceutical was applied proportional to patient weight according EANM dosage card or (if not listed there) from dedicated guidelines. The standard deviation only considers the difference based on the patient's weight; therefore methodical uncertainties are not included. The DLP of partial-body and whole-body scans are taken from the dose report including scout view.

Bone Scintigraphy 99mTc DPD (0,0057mSv/MBq) for 43 female patients (75±13kg) leads to 2,7±0,2mSv, for 43 male patients (81±21kg) leads to 2,7±0,3mSv. Leucocyte Scintigraphy 99mTc HMPAO (0,0093mSv/MBq) for 43 female patients (74±17kg) leads to 4,3±0,3mSv, for 43 male patients (84±18kg) leads to 4,5±0,4mSv. Scintigraphy with 123I-Iodid (0,11mSv/MBq) for 17 female patients (76±16kg) leads to 2,1±0,2mSv, for 16 male patients (84±18kg) leads to 4,5±0,4mSv. Receptor Scintigraphy 111In Octreotid (150MBq for 70kg Patient) 0,054mSv/MBq) for 43 female patients (65±11kg) leads to 7,7±0,4mSv, for 43 male patients (86±13kg) leads to 8,1±0,1mSv.

PET 18F-FDG (0,019mSv/MBq) for 43 female patients (75±13kg) leads to 3,5±0,4mSv, for 43 male patients (80±15kg) leads to 3,7±0,2mSv. PET 18F-FDOPA (0,05mSv/MBq) for 31 female patients (67±13kg) leads to 3,4±0,3mSv, for 31 male patients (82±10kg) leads to 3,7±0,1mSv. PET 18F-Fluorid (0,017mSv/MBq) for 43 female patients (64±13kg), leads to 3,1±0,3mSv, for 43 male patients (83±19kg) leads to 3,3±0,1mSv. PET 18F-FCHOLIN (0,02mSv/MBq) for 43 male patients (87±16kg) leads to 3,8±0,1mSv.

A low dose partial body scans down to the tights (0,015mSv/Gy.cm) for 16 female patients leads to 4±1mSv, for 16 male patients it leads to 3,5±0,9mSv – for the total body (0,012mSv/Gy.cm) applied to 16 female patients leads to 5±1mSv, for 16 male patients it leads to 5,2±0,8mSv.

Radiation exposure in nuclear medicine diagnostic procedures remains within the range of annual natural radiation exposure. The activity used for procedures in nuclear medicine is a compromise between radiation safety and image quality. There are several ways to minimize radiation exposure. The most important way of assuring quality in any procedure is a strong quality-control program. Comprehensive knowledge encompassing the indications for the study, adequate acquisition and processing, and the final quantification and interpretation of its results are of great importance. If the patient accepts prolonged data acquisition, the quality of the image is improved. For most diagnostic radiopharmaceuticals dosimetry data are available, although the data collection and calculation methods are heterogeneous, particularly for pediatric applications. Furthermore, the calculated ED for SPECT-CT and PET-CT examinations is not an individual patient dose, but represent the stochastic health risk.

P 79 Evalution of an alternative measurement method for the statutory determination of the activity of the therapy capsules used for radioiodine therapy to reduce radiation exposure for the medical staff

U. Lützen[1], A. Tjiong[1], T. Imme[1], Y. Zhao[1], M. Marx[1], M. Zuhayra[1]
[1]Klinik für Nuklearmedizin, UKSH, Campus Kiel, Kiel, Germany

Introduction: Radioiodine therapy is a common and well-established therapy for the treatment of benign and malign diseases of the thyroid. Determination of radioactive activity of the therapy capsule is statutory for the performance of treatment, but resulting in a significant radiation exposure for the medical staff involved in the measurement process. The aim of our study was to evaluate a new method of measurement which enabled the capsule to remain inside of the transport lead shielding and therefore to achieve a reduction of radiation hazard, whilst generating reliable and sufficient results.

Material and methods: Two capsules with different start activities (2000 MBq and 6000 MBq) were measured in two different sizes of lead containers (size I and II). The time of measurement was chosen the way that the activities measured was covering the range between 300 – 2000 MBq for the lead containers of size I and 2000 – 6000 MBq for the size II. For the measurement of the capsule activity a well-type counter and an uptake measurement probe were used. To determine the local dose rate (LDR) thermoluminescent dosimeter (TLD) were used. The count rates from the measurement of the capsule inside of the containers were correlated with the capsule activity at the corresponding time to create a calibration curve between the capsule activity [MBq] and the count rate of the used device [IPS]. Capsels with activities covering the range of calibration were measured in four additional containers of the appropriate size to evaluate the calibration curves.

Results: According to the two sizes of the lead containers the calibration of the two devices used for the measurement of the capsule activity inside of the transport lead containers resulted in two calibration lines for each device with regression coefficients R2>99,99. The total relative uncertainties of the measurement method were for the well-type counter 5.47% (size I) and 5.43% (size II) and for the uptake-measuring probe 5.44% (size I) and 5.44% (size II) respectively. The maximum equivalent dose measured at the surface of the lead shielding was 2.99 µSv/s per GBq for size I and 0.27 µSv/s per GBq for size II. The local dose rate (LDR) of the I-131-therapy capsule in ten-centimeter distance without shielding was 46.18 µSv/s per GBq. This means that the radiation exposure caused by the measurement of the capsule activity while the capsule remains inside of the transport lead shielding could be minimized 15.4-fold (93.53%) for size I and 171- fold (99.42%) for size II compared to the common conservative measurement of the capsule activity.

Conclusion: The application of the new technique for the statutory pre-therapeutic measurements of the radioiodine capsules correlates with a reduction of radiation exposure for the medical staff of 93.53% for container I, and a reduction of 99.42% for container II regarding the necessary handling. This measuring method for radioactive Iodine 131 capsules can reduce the radiation exposition for the medical staff to a minimum which is important especially under consideration of the ALARA principle, whilst a sufficient and reliable activity determination is still guaranteed.

References

[1] Grigsby, Siegel, Baker, Eichling, Radiation Exposure From Outpatient Radioactive Iodine (131I) Therapy for Thyroid Carcinoma, JAMA Vol. 283 No.17, pp. 2272, 2000
[2] Strahlenschutz in der Medizin. Richtlinie zur Verordnung über den Schutz vor Schäden durch ionisierende Strahlen (Strahlenschutzverordnung – StrlSchV) vom 30. November 2011. Gemeinsames Ministerialblatt, 62. Jahrgang, Nummer 44-47, ausgegeben zu Berlin am 30. November 2011
[3] Hendee, Edwards, ALARA and an integrated approach to radiation protection, 1986
[4] Schicha, Schober, m. Dietlein, Eschner, Kopka, Weckesser, Wellner, Nuklearmedizin Basiswissen und klinische Anwendung, Schattauer, 5. edition, pp. 12, 92, 93,2003

P 80 Measurements of fingers doses to Nuclear Medicine Staff

S. Allehyani[1,2], R. Hassan[1,2]
[1]Umm ALQura University, Physics (Medical Physics Group), Makkah, Saudi Arabia
[2]Umm ALQura University, Physics, Makkah, Saudi Arabia

Method: In this study, finger doses were measured for five different nuclear medicine staff occupational groups for which heavy irradiation of the hands was suspected. Finger doses were measured for Nuclear medicine physicians, technologists, nurses and physicists. The nuclear medicine staff working with the radioactive materials wear two TLD dosimeter during the whole period, which lasted from 1 to 4 weeks. staff perform their work on a regular basis throughout the month, and mean annual doses were calculated for these groups.

Results: The doses to the fingers for the ^{99m}Tc technologists and nurses of groups 2,3 were observed to be 30.24 ± 14.5 (mean ± SD) and 30.37 ± 17.5 uSv/GBq, respectively. Similarly, the dose to the fingers for the 3 ^{131}I technologists in group 5 was estimated to be 126.13 ± 38.2 uSv/GBq. Finger doses for the physicians could not be calculated per unit of activity because they did not handle the radiopharmaceuticals directly. Their doses were reported in millisieverts that accumulated in 1 wk. The doses to the fingers of the physicist were 16.3 ± 7.7 uSv/GBq. The maximum average finger dose in this study was to the technologists handled therapeutic ^{131}I (2.8 mSv).

Conclusion; We conclude that the maximum expected annual dose to the extremities appeared to be less than the annual limit (500 mSv/y).

P 81 The Euratom BSS for medical exposures – the Swiss way

B. Ott[1]
[1]Bundesamt für Gesundheit, Abteilung Strahlenschutz, Bern, Switzerland

The current Swiss radioprotection ordinance in force since 1994 is based on the ICRP 60. Since then, the new ICRP 103 has been published and EURATOM has published its directive laying down basic safety standards for protection against the dangers arising from exposure to ionising radiation (BSS). That is why in 2011 a large project aiming at the overall revision of the Swiss radioprotection legislation was started. The project is conducted with the involvement of the three affected authorities and multiple radioprotection experts. It is grouped in several sub-projects, one of them covering medical exposures. The new legislation is planned to be in force by 2016.

In this contribution, we will present the major changes in the adapted legislation for medical exposures and show the Swiss way of transposing the Euratom BSS. For example how we lay down the legal basis for conducting clinical audits, proceedings that are currently not yet implemented in Switzerland. Also dose constraints for cares and comforters are defined as well as for individuals taking part in biomedical or medical research that do not benefit directly from the research project. The justification principle and its three levels according to ICRP 103 is introduced. The involvement of Medical Physics Experts in medical exposures is described more precisely. Also rules for conducting non-medical imaging (formerly known as medico-legal procedures) are fixed. The obligation of notification of accidental and unintended medical exposures is enlarged beyond radiation therapy. And finally the rules for data collection required for the establishment of national diagnostic reference level and the monitoring of the population dose are defined.

P 82 Patient dose in coronary CT angiography: results of a nationwide survey

A. Schegerer[1], H.-D. Nagel[2], G. Stamm[3], G. Adam[4], G. Brix[1]
[1]German Federal Office for Radiation Protection, Medical and Occupational Radiation Protection, Neuherberg, Germany
[2]Fa. Sascrad, Buchholz, Germany
[3]Medizinische Hochschule, Hannover, Germany
[4]Universitätsklinikum, Hamburg-Eppendorf, Germany

Aim: The aim of the study was to determine representative dose values applied in coronary CT angiographic (cCTA) examinations in daily clinical practice.

Material and methods: Based on a nationwide survey on CT practice in Germany in 2012/2013, dose parameters such as the CT dose index (CTDIvol) and the dose length product (DLP) were derived from user-specified cCTA protocols. Protocols with prospective EKG-triggering (pCTA) and retrospective gating (rCTA) were separately evaluated. Considering the tissue weighting factors of ICRP Publication 103, effective dose values (Deff) were computed using the program CT-Expo (v2.2) [1-2].

Results: In total, 47 pCTA and 54 rCTA protocols were evaluated. Examinations with bypass implementation were not considered. For pCTA and rCTA, the median as well as the 1st and 3rd quartile of CTDIvol were 15.9 (8.6 / 31.6) mGy and 29.7 (21.5 / 44.4) mGy, respectively. Correspondingly, DLP values were 305 (140 / 587) mGy cm and 559 (324 / 783) mGy cm resulting in effective doses Deff of 5.4 (2.5 / 10.5) mSv and 10.0 (5.8 / 14.0) mSv, respectively. The differences between the dose parameters determined for pCTA and rCTA were statistically significant ($p<0.01$).

Conclusion: In contrast to the studies of Arnoldi et al. (2009) and Horiguchi et al. (2009) where a dose reduction potential of more than 60% were found for pCTA as compared to rCTA within a single institution [3-4], a dose reduction potential of 46% were determined in this multi-center study. As compared to the nationwide survey of Brix et al. (2002) [5], where rCTA protocols were solely evaluated (median: DLP = 589 mGy cm, CTDIvol = 45.6 mGy, Deff = 10.6 mSv), the CTDIvol of rCTA protocols have been decreased by 33% on average. This decrease is mainly due to recent technological developments of CT scanners (including detectors). The DLP, however, has not been changed accordingly which can only be explained by larger CT scan lengths used.

References

[1] International Commission on Radiological Protection (ICRP). The 2007 Recommendations of the International Commission on Radiological Protection. Valentin, J., ed. 2007; ICRP Publication 110. Ann. ICRP 39 (2).
[2] Stamm, G., & Nagel, H.-D.: CT-EXPO [computer program]. Version 2.2. Hannover/Buchholz, Germany, 2013.
[3] Arnoldi, et al., Eur. Radiol., 19 (2009), p. 2147-
[4] Horiguchi, et al., Eur. Radiol., 19 (2009), p. 2363-
[5] Brix, G., et al., Eur. Radiol., 13, 1979 (2003), p. 1979-

P 83 Eutempe-RX, an EC supported FP7 project for the Training and Education of Medical Physics Experts in Radiology

M. Borowski[1], M. Fiebich[2], C. Caruana[3], H. Bosmans[4], P. Sharp[5]
[1]Klinikum Braunschweig, Institut für Röntgendiagnostik, Braunschweig, Germany
[2]Technische Hochschule Mittelhessen, Institut für Medizinische Physik und Strahlenschutz, Gießen, Germany
[3]University of Malta, Faculty of Health Science, Msida, Malta
[4]KU Leuven, Department of Imaging & Pathology, Leuven, Belgium
[5]European Federation of Organisations for Medical Physics (EFOMP) , York, United Kingdom

Motivation: The core activity of the medical physics expert (MPE), as defined by the EU BSS [1], is to ensure optimal use of ionising radiation in patient healthcare and to bring new knowledge and expertise from physics into healthcare. It is therefore essential that these healthcare professionals are trained to the highest level. This level has been defined as EQF level 8 by the EC [2]. The knowledge, skills and competences (KCS's) going along with an expertise of EQF level 8 for MPE are specified in the accomplished EU funded 'Guidelines for the MPE' [3] project. These Guidelines have developed a harmonized qualification framework for Europe and a curriculum development model linking curriculum content to professional role.

Materials and methods: The main objective of the EUTEMPE-RX project is to provide a training scheme that allows the medical physicist in Diagnostic and Interventional Radiology in the countries of the European Union to reach EQF level 8. This is necessary because in many European countries financial and organizational considerations will preclude the development of local training schemes. In addition, not all expertise may be available locally. A European network of partners was brought together in a new FP7 EC project to ensure sufficient expertise in all fields of study and to create a harmonized program of courses. The learners that are targeted by the project are medical physicists in Diagnostic and Interventional Radiology (hospitals), in the medical device industry and in regulatory authorities.

The EUTEMPE-RX project will develop 12 courses at EQF level 8, with radiation safety and diagnostic efficacy being prevalent subjects. Some of the topics covered will be: professional issues (legal aspects, communication, leadership etc.), quality assurance, advanced performance measurements, CT imaging, breast cancer screening, high dose interventional procedures, phantoms (anthropomorphic), dosimetry (for the conceptus, infants, adolescents and adults), radiation biology, personnel and correlated patient risk in Diagnostic and interventional radiology as well as Monte Carlo simulation techniques.

Courses will be designed using a blended learning scheme. Each course will last about 2 weeks, nearly equally divided between a preparation phase at home via online learning and an onsite training phase at different centers around Europe. As part of this scheme, e-learning education and teaching sessions (courses) will be developed. This will, in particular, help support medical physicists that cannot be released from their duties for long periods, especially those with childcare responsibilities. After a successful test at the end of each course the participants receive certificates for the successful achievement of EQF level 8 within the KSCs covered by the content of the course.

A business plan will be developed to ensure the sustainable continuation of this programme of courses following the end of the project. While the project will be limited to the area of Diagnostic and Interventional Radiology, it is recognized that this work should be built upon to extend the training to other areas, such as Nuclear Medicine and Radiation Oncology.

Results: The EUTEMPE-RX project started successfully in August 2013. Details of the course content have been specified. The intended learning outcomes cover the great majority of KSCs to be found in the 'European Guidelines for the MPE'. First courses will be held in early 2015. The whole curriculum will be delivered until mid 2016. News on the project are presented at the website www.eutempe-rx.eu.

Conclusion: A standardized qualification program for MPE to reach EQF level 8 has been established. In the framework of the EUTEMPE-RX program 12 courses on the major topics will be developed. The courses are set up using a blended learning scheme, each course lasting approximately 2 weeks (1 week preparation, 1 week on site training). First courses will be delivered in spring 2015. A business plan will be developed to ensure sustainability of the qualification program beyond the end of the EC funded project.

References

[1] European Commission: COUNCIL DIRECTIVE 2013/59/EURATOM
[2] European Parliament Council: Recommendation of the European Parliament of the Council of 23 April 2008 on the establishment of the European Qualification Framework for lifelong learning
[3] European Commission: European Guidelines on Medical Physics Expert, http://www.efomp.org/index.php/documents

P 84 Is the EANM-SOP model optimal for the calculation of the time-integrated activity coefficient of I-131 in the thyroid?

G. Glatting[1], E. Brauner[1], A. Buck[2], M. Lassmann[2], H. Hänscheid[2]
[1]Medizinische Fakultät Mannheim, Universität Heidelberg, Medizinische Strahlenphysik/Strahlenschutz, Mannheim, Germany
[2]Universität Würzburg, Klinik für Nuklearmedizin, Würzburg, Germany

Introduction: The aim of this study was to find the optimal modelling method for reproducible and observer-independent calculation of the time-integrated activity coefficient of I-131 in the thyroid gland prior to radioiodine therapy of benign thyroid disease. This determination of the time-integrated activity coefficient of I-131 in the thyroid gland prior to radioiodine therapy is an important variable for determining the therapeutic activity [1, 2].

Usual practice is to measure thyroid uptake data and pre-correct it before fitting to a mathematical model (for example by subtraction of the background from the values measured in the thyroid). In contrast to this, in this study, we apply a more general modelling and evaluation method, which directly adapts the corresponding model to integrate all raw data (without pre-corrections). To what extent these mathematically improved description leads to different time-integrated activity coefficients was determined by comparing the two corresponding evaluation methods.

Material and methods: The 72 complete sets of patient measurement data after oral administration of about 1 MBq of I-131 included background measurement, the capsule activity, and 5 thyroid and femoral measurements after 2, 6, 24, 48 and 96 (n = 52) h or 120 (n = 20) h. Six patients with suspected measurement error in at least one of the measured values were excluded from the model comparison.

A general two-compartment model consisting of a blood and a thyroid compartment in conjunction with a theoretically complete description of the measured raw data was developed. From this, 7 simplified models were generated by setting different parameters to zero. All 8 models were fitted to the measurement data using GraphPad Prism (version 6.02 for Windows, La Jolla California, USA, www.graphpad.com). The optimal model was selected for each patient based on the corrected Akaike information criterion (AICc) [3, 4]. Subsequently the corresponding time-integrated activity coefficients were calculated (evaluation method 1) and compared to the corresponding values obtained according to the current EANM standard operating procedure (EANM-SOP) [1] (evaluation method 2). The EANM-SOP first converts the 12 measurements into 5 relative thyroid uptake values before fitting to a simplified two-compartment model.

Results: The thyroidal time-integrated activity coefficients were 112 h ± 46 h (range 33 h to 207 h) for evaluation method 1. The corresponding values after applying the EANM SOP (evaluation method 2) were 110 h ± 43 h (range 32 h to 206 h). The relative deviations in the time-integrated activity coefficients between both evaluation methods in each patient were -0.6% ± 7.1% (range: -28% to 15%). In 11 patients, the deviation was larger than 10%.

Conclusion: The average differences between the two evaluation methods are relatively small. In individual cases the deviations were relevant. However, this can also be caused by errors when measuring the patients. In view of the other uncertainties in the determination of the therapeutic activity, the EANM SOP provides a good estimate of the retention of radioactive iodine in the thyroid gland; a more general model is not necessary.

References

[1] Hänscheid H, Canzi C, Eschner W, Flux G, Luster M, Strigari L, Lassmann M. EANM Dosimetry Committee Series on Standard Operational Procedures for Pre-Therapeutic Dosimetry II. Dosimetry prior to radioiodine therapy of benign thyroid diseases. Eur J Nucl Med Mol Imag 2013: 1-9.
[2] Hänscheid H, Lassmann M, Reiners C. Dosimetry prior to I-131 Therapy of Benign Thyroid Disease. Z Med Phys 2011; 21: 250-7.
[3] Glatting G, Kletting P, Reske SN, Hohl K, Ring C. Choosing the optimal fit function: Comparison of the Akaike information criterion and the F-test. Med Phys 2007; 34: 4285-92.
[4] Kletting P, Glatting G. Model selection and inference in pharmacokinetics: The corrected Akaike information criterion and the F-test. Z Med Phys 2009; 19: 200-6.

P 85 Applicability of high spatial resolution detectors for CTDI- and Dose-Profile-Measurements

M. Liebmann[1,2], B. Poppe[1,2], H. von Boetticher[3]
[1]Carl von Ossietzky University Oldenburg, Medical Radiation Physics, Oldenburg, Germany
[2]Pius-Hospital, Clinic for Radiation Therapy and Radiooncology, Oldenburg, Germany
[3]Klinikum Links der Weser, Center of Radiology and Nuclear Medicine and Academy of Radiation Protection, Bremen, Germany

Introduction: The growing use of CBCT and CT in radiation therapy has waken the interest in dosimetry in the kV-range by physicists usually working with MV beams. Since there is no applicable norm for CBCT dosimetry current publications [1,2] usually use point dose measurements or CTDI values. CTDI is also the most important measured parameter for CT dosimetry. It is used for effective dose estimations based on conversion factors from Monte Carlo calculations [3] and is routinely measured and recorded for every CT-scanner. Usually this is done with a dose-length-product ionization chamber of 100 mm length. For more accurate effective dose or organ dose calculations more dosimetric parameters, e.g. geometric efficiency or overbeaming factors [4] of the used CT-scanner are needed. These values can only be determinded by the usage of spatial resolving detectors.

The aim of this work was to investigate the applicability of detector types usually available at radiation therapy departments including a new diamond detector (T60019, PTW Freiburg) dose-profile-measurements and CTDI calculations.

Material and methods: Based on a previous study [5] the energy response of the new T60019 MicroDiamond was measured free in air in comparison to the reported data of the T60008 dosimetry diode (PTW Freiburg) and T31010 SemiFlex ionization chamber (PTW Freiburg).

The T60019 is a synthetic diamond detector with a sensitive volume of 1.1 mm radius and 1 µm thickness. With a sensitive volume of 1 mm² x 2.5 µm the p-type Si diode T60008 is even smaller. A back-side guarding electrode improves energy response for high energy photon and electron beams but is not optimized for low energy photons. The T31010 ionization chamber has a nearly spherical sensitive volume of 0.125 cm³, an aluminium central electrode and graphite wall electrode.

Dose profiles at a Siemens SOMATOM Sensation 64 multi-slice CT scanner were measured with the same detectors at the center and periphery position (1 cm depth) of a 32 cm diameter, 300 mm length body phantom [6] for multi-detector use. A scanning profile without table movement, 120 kV and various total collimations from 7.2 mm up to 28.8 mm were used for irradiation while the detectors were moved remotely through the phantom. Two methods for calibration were investigated. All profiles were either normalized to the absorbed dose at the center of the primary beam or to the CTDI100 measured with a 100 mm pencil type chamber in the center position of the phantom at 120 kV and 28.8 mm total collimation. A derived CTDI100 value was calculated for each profile measurement and compared with the measured reference value.

Results: The relative detector response (Tab. 1) for peak voltages from 50 kV up to 125 kV free in air for the T60019 is strongly dependent on the orientation of the detector. For the intended axial irradiation the energy response only weakly depends on the photon energy. If the irradiation is performed in lateral direction the energy dependence is increased significantly. A possible reason for this may be found in the increased secondary electrons emission from electrical contacts.

The energy response for the shielded diode T60008 is around 50%. As the photon spectrum within an axial profile changes significantly this detector is not suited for profile measurements.

Dose profile examples are shown in Fig1. The diamond detector and ionization chamber profiles show a good agreement. Compared to the very symmetrical T31010 profile the T60019 measured profile showed a smaller penumbra region due to its very small sensitive volume of 0.004 mm³.

The shape of the profile for the T60008 is strongly deformed. Probably this is caused by the back-side internal shielding of the diode. This was pointed out by a mirrored measurement setup which showed a profile deformation changing accordingly. This diode should therefore not be used for profile measurements.

Although there is a considerable difference in energy response between all investigated detectors the calculated CTDI100 only differs 2.8% on average for CTDI-normalization and 2.4% on average for point-dose-normalization (Tab. 2, 3).

Conclusion: In this study dose profiles have been measured with conventional radiotherapy detectors. CTDI100 values have been derived and compared to reference measurements. The study supports the possible application of smaller ionization chambers and the new MicroDiamond for these measurement tasks. Shielded diodes may show the effects described in fig 1and should therefore not be used for profile measurements.

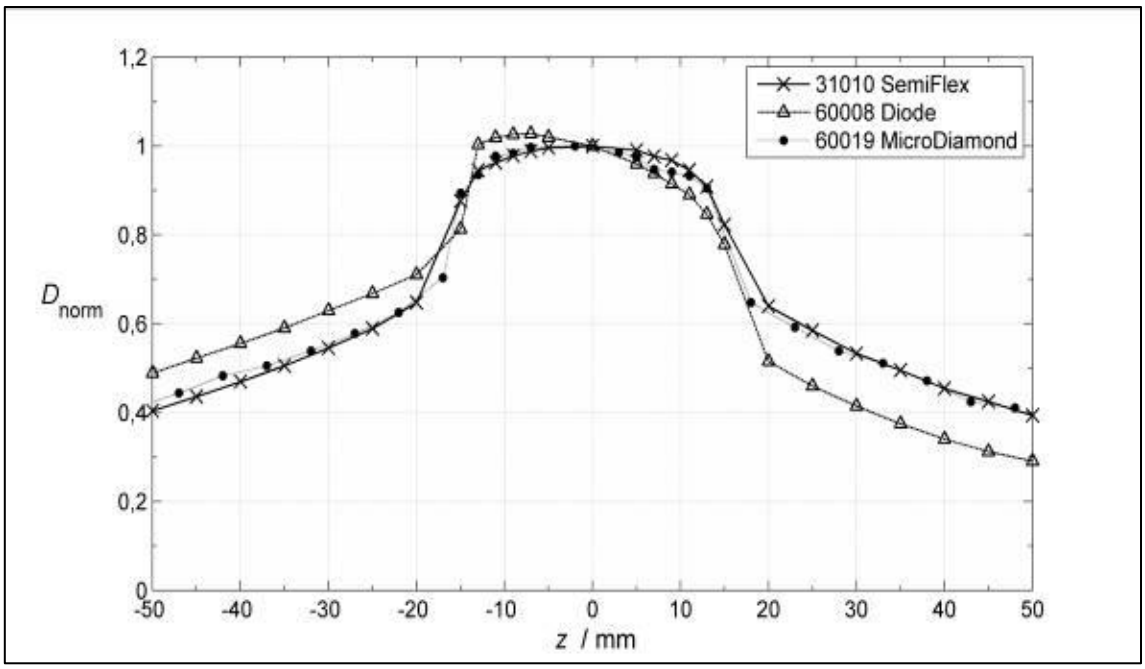

Fig. 1: Measured dose profiles from a Siemens SOMATOM 64 scanner at 120 kV, 28.8 mm total collimation in the center of a 32 cm CTDI body phantom with a PTW 31010 small volume ionization chamber, PTW 60008 dosimetry diode and the new PTW 60019 MicroDiamond.

Maximum energy response variation	31010	60008	60019	
			axial irrad.	lateral irrad.
	0.8%	50.7%	5.9%	10.3%

Tab. 1: Calculated maximum energy response variation for the investigated detectors free in air in the energy range from 50 kV up to 125 kV.

total collimation / mm		31010	60008	60019	$CTDI_{100}$
28.8	**center**	**100.0%**	**100.0%**	**100.0%**	**100.0%**
	periphery	174.9%	177.9%	174.4%	179.5%
14.4		113.5%	110.1%	113.3%	112.1%
10.0		91.2%	95.4%	94.7%	90.8%
7.2		130.9%	133.4%	132.0%	129.1%

Tab. 2: Comparison of the measured standard $CTDI_{100}$ with pencil type chamber and CTDI calculation through integration of dose profile measurements. Dose profiles were normalized to the calculated $CTDI_{100}$ at 120 kV, 28.8 mm total collimation in the center position of a 300 mm length body phantom.

total collimation / mm		31010	60008	60019
28.8	**center**	**100.0%**	100.3%	99.6%
	periphery	174.8%	178.5%	173.7%
14.4		113.5%	110.5%	112.9%
10.0		91.1%	95.7%	94.3%
7.2		130.8%	138.1%	131.5%

Tab.3: Comparison of the calculated $CTDI_{100}$ of each detector with point-dose-normalization at the center of the primary beam at 120 kV and 28.8 mm total collimation in the center position of a 300 mm length body phantom.

References

[1] Dixon, R. L. et al.: Analytical equations for CT dose profiles derived using a scatter kernel of Monte Carlo parentage with broad applicability to CT dosimetry problems, Med. Phys., 38 (2011) 7, S. 4251-4264

[2] Dixon, R. L. et al.: Experimental validation of a versatile system of CT dosimetry using a conventional ion chamber: Beyond CTDI100, Med. Phys., 34 (2007) 8, S. 3399-3413

[3] Schlattl, H. et al.: Dose conversion coefficients for CT examinations of adults with automatic tube current modulation, Phys. Med. Biol., 55 (2010) 20, S. 6243-6261

[4] Lüllau, T. et al.: Measurement of X-Ray Beam Width and Geometric Efficiency in MDCT Using Radiochromic Films, 54th AAPM Annual Meeting, Charlotte, NC 2012

[5] Liebmann, M. et al.: Strahlentherapie-Dosimetriesysteme in der CT-Dosimetrie – Energieabhängigkeit und Einsatzgebiete, 43. Jahrestagung der DGMP, Jena, 2012

[6] Liebmann, M. et al.: Comparison of different methods for measuring CT dose profiles with a new dosimetry phantom, 13th International Radiation Protection Association (IRPA) Congress, Glasgow, 2012

P 86 The influence of scan length and collimation on the CTDIvol measurement in case of helical CT

I. Özden[1], S. Scheidegger[21]KSA, Aarau, Switzerland
[2]ZHAW School of Engineering, Zurich University of Applied Science, Einterthur, Switzerland

Purpose: Legal requirements concerning optimization of X-ray based imaging modalities lead to a certain need of an appropriate methodology for assessing a baseline regarding image quality and radiation exposure. Especially for CT scanners, the rapid development of large detectors and implementation of cone beam (CB) geometries is triggering the requirements for measurement concepts and methods: Existing methods [1-3] for quantifying radiation exposure via dose-length products (DLP) and computed tomography dose index (CTDI) are dedicated to check the calibration of the CTDI- and DLP-indication of the scanner in a technical mode. In the framework of Article 74 StSV, we focus on optimization of clinical CT protocols. Therefore the measurements were performed with automatic exposure control (e.g. Dose Care 4D). The comparison between measured and indicated CTDI-values exhibits deviations dependent upon scan-length. It was also observed that the measurements with ionization chamber at the same position within the phantom have a difference of up to 40% when the scan length was small. Therefore, a rash of measurements were undertaken to find the reason for those variations, and to improve the validity of the method for CTDI assessment.

Material and methods: The measurements were performed in helical mode with CTDI100 method on a Siemens Somatom Sensation Open. The Dose Care 4D was activated, which deviates from the standard procedure for CTDI measurement. But it is important for an assessment of a baseline for clinical protocols. A CTDI body phantom according to standards IEC 61223-3-5, IEC 61223-3-6 and IEC 60601-2-44, and a UNIDOS type 10001 dosimeter with an ionization chamber TM 30009 – 00733 from PTW were used. An abdomen protocol was used with two different collimations to investigate the effect of different scan widths. The CTDIvol was calculated at first without over-ranging (CTDIm) and then with over-ranging (CTDI+ov). Both values were compared with displayed CTDIvol (CTDId) values. We calculated the total scan length l1 by the scan time ts and the rotation time tr: l1 = (ts/tr)*dz with the table distance increment per rotation dz. The total scan length l1 can be defined as the sum of the input scan length l2 and the over-ranging contribution lov: l1 = l2 + lov. The CTDIvol is calculated by: CTDIvol = DLP/l1,

Results: The measurements with collimation 24x1.2mm exhibit a strong dependence on the scan length, although a homogeneous phantom was used. For the measured dose length products (DLPm), such an increase is not observed (see appendix). The deviation between CTDI+ov and CTDId increases and the deviation between CTDIm and CTDId decreases with an increasing scan length. To obtain stable measurements at the peripheral measurement positions of the phantom, a collimation of 40x0.6mm was chosen. The scan time was set to an integer multiple of rotation time. With this method the variation of the measurements in the peripheral positions of the phantom was only 4-5%. With a collimation of 24x1.2mm the measurements were stable after deactivating the Dose Care 4D or after reducing the pitch from 1 to 0.5. That means the CT is not able to adjust the current automatically when the table advance per rotation is 2.88cm. The variations of the measurements were not observed at the displayed CTDId.

Conclusions: For a CT which has no adaptive beam-collimation/ filtration for limiting exposure due to over-ranging, it is possible to get stable measurements if the scan time is an integer multiple of the rotation time. To measure as much as possible of the scattered radiation, a small scan length should be selected. This will support the quantitative comparison between displayed and measured CTDI. The measurements show that the calibration method of the CT and the automatic adaptation of the tube current at the different scan lengths and different collimations should be independently verified. Because of the beam widths of the new CT units it is better to perform phantom and ionization chamber measurements with a minimum length of 30 cm.

collimation	24x1.2mm			40x0.6mm		
length [cm]	2.80	5.75	8.65	1.70	2.95	4.20
$CTDI_d$ [mGy]	12.56	14.71	16.15	12.55	12.65	12.77
$CTDI_m$ [mGy]	30.18	20.07	16.02	22.80	17.33	14.92
$CTDI_d$/CTDIm	58.38%	26.72%	-0.82%	44.96%	27.01%	14.40%
$CTDI_{+ov}$ [mGy]	11.27	11.04	10.38	10.50	10.35	10.12
$CTDI_d/CTDI_{+ov}$	-11.49%	-33.18%	-55.59%	19.54%	22.28%	-26.21%

Tab. 1: The measurements with collimation 24x1.2mm show that the displayed $CTDI_d$ depends strongly on scan length, although a homogeneous phantom was used. In case of 40x1.2mm the scan time is selected *as* an integer *multiple of rotation time to get stable measurements. For the collimation 24x1.2mm the measurements were stable after deactivating the Dose Care 4D or after reducing the pitch from 1 to 0.5.*

References

[1] AAPM Task Group 23 (2008): The measurement, reporting and management of radiation dose in CT. AAPM Report No. 96

[2] Edyvean S, Lewis MA, Britten AJ, Carden JF, Howard GA, Sassi SA (1998): Type testing of CT scanners: methods and methodology for assessing image performance and dosymetry. MDA 98/25 Evaluation Report

[3] J Geleijns, M Salvadó Artells, P W de Bruin, R Matter, Y Muramatsu, and M F McNitt-Gray (2009): Computed tomography dose assessment for a 160 mm wide, 320 detector row, cone beam CT scanner. *Phys Med Biol*. **54**(10): 3141–3159. doi:10.1088/0031-9155/54/10/012.

P 87 Pediatric and Adult Abdomen CT Dose Estimations: A Comparison between On-Site Equipment Calculations and SSDE (Size-Specific Dose Estimates) as Given in the AAPM Report No. 204

C. Marx[1], K.-U. Kasch[1], S. Kodlulovich[2]
[1]Beuth Hochschule für Technik Berlin, Berlin, Germany
[2]Commisao Nacional de Energia Nuclear, Rio de Janeiro, Brazil

Objective: It is a common misunderstanding in Computed Tomography (CT) to equal the Computed Tomography Dose Index (CTDI) displayed on the console with patient dose. Therefore, in 2011 the American Association of Physicists in Medicine (AAPM) suggested a Size-Specific Dose Estimates (SSDE). The latter is based on correction factors applied to the CTDI depending on the effective (i.e. geometric) patient diameter. The study presented here compares the on-site equipment calculation of patient dose and SSDE. Assuming the SSDE as the more realistic approximation of real patient dose the extent of over- or underestimation given by the console readings was evaluated. In a further step effective patient diameter was substituted by its water-equivalent diameter to investigate a potential improvement of the correction factors and, eventually, patient dose estimation.

Material and methods: To verify the CTDIvol as given by the scanner console Polymethyl methacrylate (PMMA) phantoms were used to measure the respective output. Subsequently, data of 50 pediatric and 45 adult patients were evaluated. Every patient's effective diameter was obtained as the mean of anterior-posterior and lateral diameter measured using digital calipers. The water-equivalent diameter was derived by assuming a water cylinder with equal average attenuation as the body region being scanned.

The SSDE were then calculated using two different sets of correction factors: first based on the effective patient diameter and secondly based the water-equivalent diameter. Bothe sets of SSDE values were then compared to the respective CTDIvol.

Results: Following the AAPM protocol (using effective patient diameter) the evaluation shows a maximum CT-console-based dose underestimation of 38 % for adult and 10 % for pediatric patients, respectively. A detailed analysis of SSDE results based on the water-equivalent diameter indicates an even more patient-specific dose estimation compared to the AAPM approach.

Conclusion: SSDE proves to be a more patient-specific dose estimation compared to simple CTDI values as given by the machine consoles. Further improvements of the method could derive from using the water-equivalent diameter instead of the simple patient geometry, i.e. effective patient diameter.

P 88 Influence of surrounding material on CTDI values

R. Schmidt[1], J. Wulff[1], K. Zink[1]
[1]Technische Hochschule Mittelhessen, Institut für Medizinische Physik und Strahlenschutz, Gießen, Germany

Introduction: A key quantity in CT dosimetry for quality assurance and risk estimation is the CTDIa,100 [1]. It is the integral measured air kerma K along 100 mm along the rotational axis z of the CT. The resulting dose length product of one rotation is divided by the nominal collimation/ slice thickness T to obtain the CTDIa,100.

$$\mathrm{CTDI}_{a,100} = \frac{1}{T}\sum_{-50}^{50} K(z)dz$$

A related quantity is the CTDIvol value which requires additional measurements in a PMMA (polymethylmethacrylat) phantom at several positions (central, peripheral). This value also takes the shift per rotation (pitch p) into account.

$$\mathrm{CTDI}_{vol} = \frac{1}{p}\cdot\frac{1}{3}\left(\mathrm{CTDI}_{PMMA,100,central} + 2\cdot\mathrm{CTDI}_{PMMA,100,peripheral}\right)$$

An estimation of organ doses or effective dose for a defined body region could be estimated with conversation factors, either based on CTDIa,100 (pitch corrected) or CTDIvol values.

The practical measurement is generally provided by an ionization chamber positioned free-in-air or inserted in a cylindrical PMMA phantom (DIN EN 61223-2-6). The surrounding material (here: air or PMMA) should not affect the dose measurement, i.e. the response of the ion chamber should be independent on the surrounding material. The higher numbers of secondary electrons released in the PMMA are supposed to be absorbed by the chambers air equivalent wall material (typical graphite) to achieve the required secondary charged particle equilibrium.

The aim of the work was to quantify the influence of the surrounding material on the measurement quantity air kerma and the impact on CTDI values to estimate a possible systematic error introduced. This was achieved by Monte Carlo simulations of a realistic CT source model with and without an ionization chamber geometry.

Material and methods: The modeled chamber was a 10 cm long standard CT chamber (type 30009, PTW, Freiburg, Germany), which is commonly used for CTDI measurements. Geometric data were taken from the user manual. The top and the stem were simplified by a PMMA cylinder. The central electrode was modelled as aluminum and the chamber wall as 1 mm PMMA with 0.1 mm inner graphite coating.

The Monte Carlo simulations were performed with the EGSnrc code system [2], which is generally suitable for chamber simulations in the radiology diagnostic energy range [3]. First, to simulate the measurement quantity air kerma secondary particle transport was disabled (ECUT= 100 MeV) and simulations were performed without the chamber geometry. The dose scoring air region was set to chambers dimension (10 cm in z-direction). In a second step the chamber model was inserted into the simulation geometry and the dose was scored within the active chamber volume. Secondary particle transport was activated (global ECUT= 512 keV) for the latter and photons were simulated down to 1 keV in all simulations. Rayleigh scattering was activated beside all other EGSnrc defaults (v V4-r2-4-0). Simulations were carried out for the free-in-air setup and within a CTDI standard phantom (32 cm) at the center and outer position for both scenarios (chamber, no chamber).

A radiation source model was adapted from a Siemens Definition AS CT according to the method from Turner et al. [4] with a focus isocenter distance of 595 mm and a collimation of 5 mm. In brief, the filtration was adapted from half value measurements and the model of the beam shaping filter was adapted from free-in-air attenuation measurements without rotation (scout scan mode). Spectra were created with the program SpekCalcGUI [5, 6]. Two spectra for 80 and 120 kVp were considered. Calculated values were normalized to the free-in-air simulation. Comparisons were performed between chamber /no chamber simulations of center and peripheral positions as well as CTDIvol values.

Results: The modelled ionization chamber is shown in figure 1.

The 120 kVp ratios against free-in-air for center and peripheral value of about 0.22 and 0.42 were in good agreement to published data by the impact group [7] (center: 0.23 and peripheral: 0.41), pointing to an adequate source and geometry model.

The differences between chamber and no chamber calculations between -1.15 % and 1.5 % (tab. 1) are small but mostly significant. The influences on CTDIvol values are in the same order and also energy dependent systematic with an underestimation of calculated chamber doses in PMMA for 80 kVp and overestimation for 120 kVp.

Conclusion: The effect of different surrounding materials on chamber response could be demonstrated in the case of CTDI measurement. For practical clinical purposes the effect of about 1 % is most likely negligible compared to other sources of uncertainties and well within the manufacturer's specified tolerances. For precise verification measurements the effect could be corrected to improve accuracy.

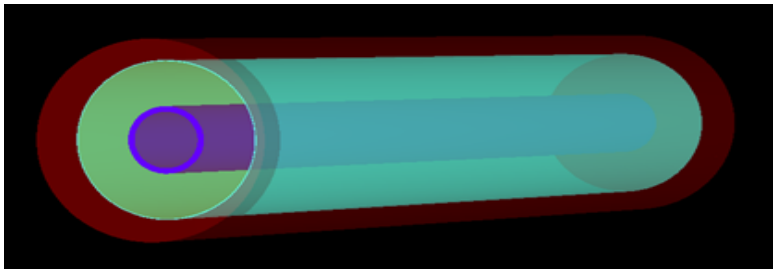

Fig. 1: Created ionization chamber model with the central electrode (aluminum, blue), the inner (graphite, green) and outer (red, PMMA) chamber wall. The sensitive volume has a length of 10 cm and is located between central electrode and chamber wall (material: air with a density of 0.0012048 g/cm^3)

		80 kVp		120kVp	
		normed	stat. unc. [%]	normed	stat. unc. [%]
no chamber	$CTDI_{central}$	0.169	0.19	0.224	0.16
	$CTDI_{peripheral}$	0.383	0.16	0.418	0.15
	$CTDI_{vol}$	0.312	0.14	0.354	0.12
chamber	$CTDI_{central}$	0.168	0.77	0.228	0.63
	$CTDI_{peripheral}$	0.378	0.45	0.421	0.42
	$CTDI_{vol}$	0.308	0.39	0.357	0.36
		diff [%]	stat. unc. [%]	diff [%]	stat. unc. [%]
ratio	$CTDI_{central}$	-0.87	0.79	1.52	0.65
chamber vs.	$CTDI_{peripheral}$	-1.21	0.48	0.70	0.44
no chamber	$CTDI_{vol}$	-1.15	0.42	0.88	0.38

Tab. 1:Calculated CTDI values with and without chamber geometry for 80 and 120 kVp. Values were normalized to the actual free-in-air simulation. Ratios were calculated chamber vs. no chamber. Statistical uncertainties express 1σ values.

References

[1] TRS 457: Dosimetry in diagnostic radiology: An international Code of Practice (2007), IAEA

[2] Kawrakow, I., Mainegra-Hing, E., Rogers, D.W.O., Tessier, F., Walters, B.R.B.: The EGSnrc Code System: Monte Carlo Simulation of Electron and Photon Transport NRCC Report PIRS-701 (2010), National Research Council of Canada Ottawa

[3] Ubrich F., Wulff J., Kranzer R., Zink K.: Thimble ionization chambers in medium-energy x-ray beams and the role of constructive details of the central electrode: Monte Carlo simulations and measurements. Phys Med Biol (2008), S. 4893–4906.

[4] Turner A.C., Zhang D., Kim H.J., DeMarco J.J., Cagnon C.H., Angel E., et al.: A method to generate equivalent energy spectra and filtration models based on measurement for multidetector CT Monte Carlo dosimetry simulations, Medical Physics (2009) 36, S. 2154–2164

[5] Poludniowski, G.G., Evans, P.M.: Calculation of x-ray spectra emerging from an x-ray tube. Part I. electron penetration characteristics in x-ray targets, Med Phys 34 (2007), S. 2164-2174

[6] Poludniowski, G.G.: Calculation of x-ray spectra emerging from an x-ray tube. Part II. X-ray production and filtration in x-ray targets, Med Phys 34(2007), S. 2175-2186

[7] CEP, center for evidence based purchasing: Comparative specifications, 64 slice CT scanners, technical specifications. CEP 08027 (2009), NHS PASA

Poster session VIII – Miscellaneous topics

Chair: C. Kirisits (Vienna/AT)

P 89 Comparison of several lumbar intervertebral fusion titanium cages with respect to their backscattering properties

T. Failing[1], N. Chofor[1,2], W. Kunth[2], H. K. Looe[1,2], D. Poppinga[1,2], A. Schönfeld[1,2], K. Willborn[2], B. Poppe[1,2]
[1]Carl von Ossietzky Universität, Oldenburg, Germany
[2]Pius Hospital, Klinik für Strahlentherapie und Radioonkologie, Oldenburg, Germany

Introduction: Using radiochromic EBT3 films, this study aim to investigate the proximal dose enhancement with regards to structure and geometry of the surface material as another backscatter dose factor [1].

Material and methods: Several laser-sintered titanium alloy cages were tested for their backscattering properties in this study. The tested cages include both prototypes, as well as established products (AditusV GmbH, Berlin, Germany) of bone fusion treatment [2]. The four implants are shown in figure 1 a) – d).

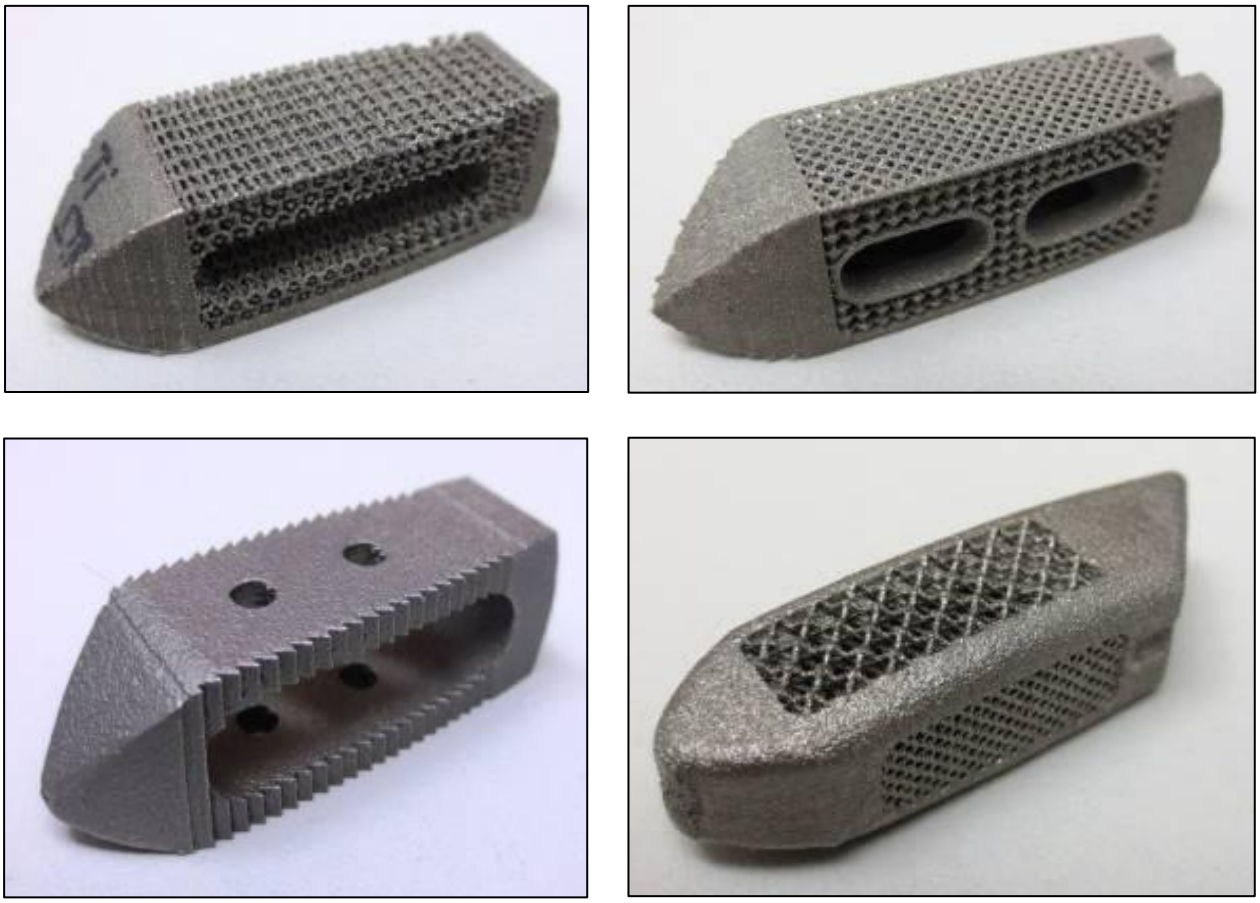

Fig. 1: The several titanium fusion cages which were used in this study:
a) TLIF cage prototype with rough mesh structure;
b) established TLIF cage with fine structure. Successor of the prototype;
d) solid TLIF cage;
c) oblique cage with mesh structure.

A stacked geometry with a set of four radiochromic EBT3 films on top of the probe's surfaces was used to measure the range and the magnitude of the expected surface dose enhancements, which is due to secondary electron release from the probe material. The stacked setup together with the small thickness of radiochromic EBT3 films allowed the dose measurement at distances of 0.1 mm, 0.9 mm, 1.7 mm and 2.5 mm from the probe surfaces. The setup was placed in a water phantom at a depth of 7.1 cm and irradiated with a dose of 1.5 Gy using a Siemens Primus Linear Accelerator (Siemens, Erlangen, Germany) at an acceleration voltage of 6MV and a 10 x 10 cm² field size.

Water reference measurements were taken under equal conditions, in order to allow the calculation of the relative dose enhancement at the surface of a probe. An Epson Expression 10000 XL ® flatbed scanner was used for digitization.

Results: Solid, sintered titanium showed a dose enhancement factor of 1.22 at the surface of the material due to backscattering. The surface dose enhancement factor can be reduced to less than 1.10 by utilizing mesh structures. In both cases, the dose enhancement factor decreased to less than 1.03 at a distance of 1.7mm.

Conclusion: Mesh structures were introduced to improve bone fusion with the implant structure but also have another advantage like a significantly reduced surface dose enhancement. Backscattering of titanium cages should be considered in treatment planning, especially when the cages are located close to organs at risk. The small range of the dose enhancement indicates a relatively low energy of scattered electrons.

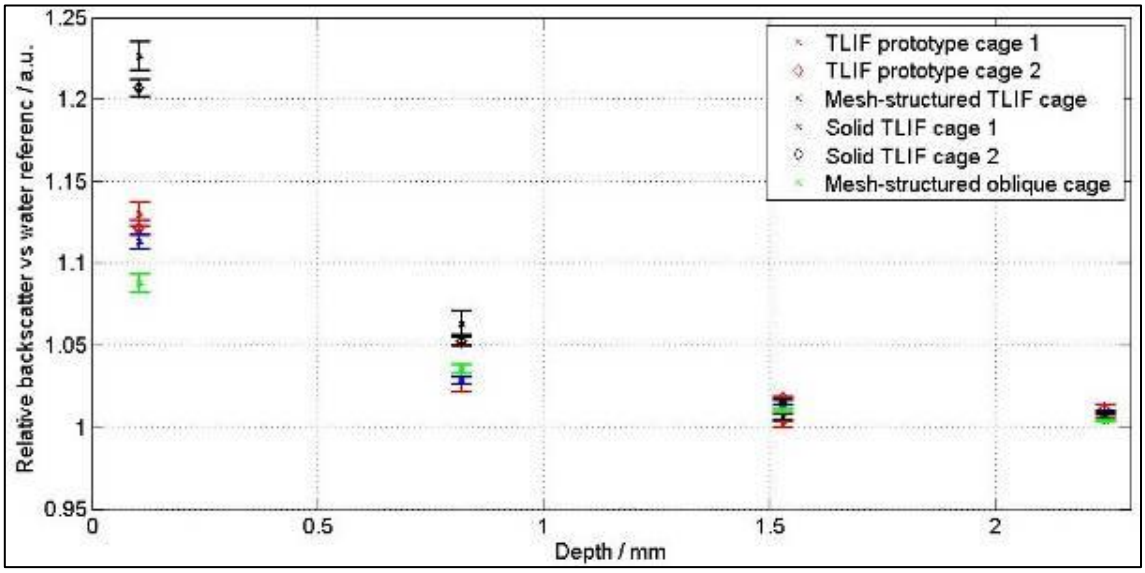

Fig. 2: Relative dose enhancement at proximal distances.

References

[1] Das,F. Kahn: Backscatter dose pertubation at high atomic number interfaces in megavoltage photon beams, Med. Phys. 16 (3) AAPM, 1989.

[2] AditusV (Publ.): Laser – sintering with TITAN (Präsentation der Firma AditusV, 2013)

P 90 Physical properties and clinical utility of a mechanical Multileaf Collimator for the use in Cobalt-60 teletherapy

M. Langhans[1,2], G. Echner[2], A. Runz[2], M. Baumann[2], S. Ueltzhöffer[3], M. Xu[4], R. Schwandtner[5], W. Schlegel[2]
[1]Radiologie Vechta, Strahlentherapie, Vechta, Germany
[2]German Cancer Research Center, Medical Physics in Radiation Oncology, Heidelberg, Germany
[3]Precisis AG, Heidelberg, Germany
[4]BEST Theratronics, Ottawa, Canada
[5]Evangelisches Krankenhaus Witten, Klinik für Strahlentherapie, Witten, Germany

Question: According to the DIRAC directory there are 2268 Cobalt-60 (Co-60) teletherapy units worldwide, most of them in low and middle income countries, compared to 10802 clinical accelerators [1]. The reasons for the rare use of linear accelerators in low and middle income countries are the high costs in purchase and maintenance [2], the need of well trained staff for its operation [3] and the lack of an electricity grid free of interference [4]. So the treatment with Co-60 is still an important part as developing countries represent 85 % of the world's population [5]. There are various authors [4,6-7], who stated that high quality Co-60 therapy is possible, but this purpose needs improved technology, especially a well-designed beam blocking system. To improve teletherapy with Co-60, a mechanical Multi-Leaf Collimator, marketed under the name CobraLeaf® was developed, which is not dependent on electricity supply and works with pneumatic pressure. The project was realized as a co-operation between the German Cancer Research Center and the medical technology company Precisis AG, Heidelberg. The subjects of this poster are the physical properties and clinical utility of the presented mechanical Multi-Leaf Collimator.

Material and methods: In order to evaluate the collimator's characteristics, various measurements concerning its penumbra, output factors, percentage depth doses, field sizes, interleaf- and end-to-end leakage were done with film (Kodak XV and Kodak EDR2) and ionization chamber (PTW TN31010) dosimetry respectively. All measurements were performed at an Equinox teletherapy unit and at a Theratron.

Results: The leakage strongly depends on the fieldsize of the therapy unit due to scatter effects. The maximum transmission measured at the location 2.5 cm next to the end-to-end gap, within a field size of 20 cm x 30 cm at 80 cm SAD, was 4.16 %. Within a field size of 10 cm x 10 cm the end-to-end leakage was at 6.5 %(see app. 2). With reference to IEC's (International Electrotechnical Commission) 5 % criteria for non IMRT MLCs, it is clinical acceptable. Results in penumbra can be seen in Tab. 1. Within the poster comparisons to traditional blocks and modern MLCs, regarding its physical properties, will be drawn.

Summary: The Cobra Leaf MLC approved its clinical utility during the measurements concerning all relevant clinical properties like penumbra and leakage. Considering this, it's a way to make modern radiotherapy, with conformal fields, possible in low-infrastructure environments, using gantry based Co-60 therapy units.

Fig. 1: CobraLeaf mounted on a Best Theratronics Gammabeam 100-80 (Phoenix) Co-60 treatment device

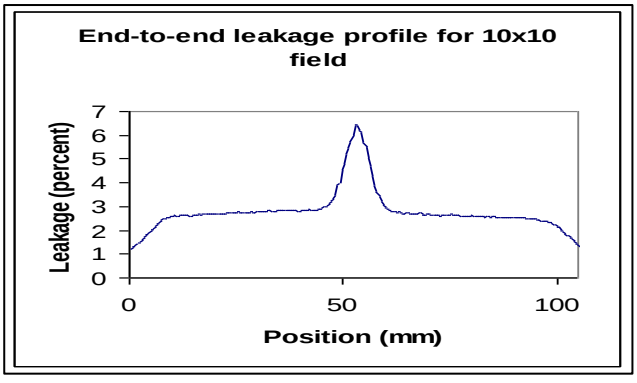

Fig. 2: Measured End-to-end leakage values

	Penumbra [cm]					
	Along Leaf			Across Leaf		
Depth [cm]	4x4	10x10	16x16	4x4	10x10	16x16
0.5	0.457	0.483	0.508	0.457	0.508	0.508
5	0.559	0.660	0.838	0.610	0.635	0.787
10	0.686	0.914	1.219	0.686	0.838	1.092

Tab. 1: Penumbra measurements at 80 cm SSD

References

[1] DIRAC (Directory of Radiotherapy Centres) database, status 03/2014, IAEA
[2] van der Giessen, P.-H., A comparison of maintenance costs of cobalt machines and linear accelerators, Radiotherapy and Oncology 20, p. 64-65 (1991)
[3] Barthold-Beß, S. et al: CoRA: A new Cobalt Radiotherapy Arrangement with multiple sources. A fensibility study, Physica Medica 19, p. 13-26 (2003)
[4] Adams, E.J. and Warrington A.P.: A comparison between cobalt and linear accelerator-based treatment plans for conformal and intensity-modulated radiotherapy, British Journal of Radiology 81, p. 304-320 (2008)
[5] Levin, V. et al: Improving Cancer Care – Increased need for the radiotherapy in developing countries, IAEA Bulletin 43, p. 25 – 32 (2/2001)
[6] van Dyk, J. and Battista, J.J.: Cobalt-60: An old modility, a renewed challenge, Current Oncology 3:8-17, 1996
[7] van der Giessen, P.-H., Design, construction, and performance of an asymmetrical collimator for a cobalt unit, Int. J. Radiation Oncology Biol. Phys. Vol. 49 No. 1, p. 265-271 (2001)

P 91 Electrochemical synthesis of biological active compounds from herbal raw materials with antioxidant properties

N. Jakipbekova[1], S. Sakibaeva[1], G. Pusurmanova[1], B. Talgatbek[2]
[1]South Kazakhstan State University named after M.Auezov, Chemistry, Shymkent, Kazakhstan
[2]Institut National Polytechnique de Lorraine, Nancy, France

The Republic of Kazakhstan has little of its pharmaceutical industry. Almost 90% of medicines are imported from far and near abroad, on a national scale spent huge sums in foreign currency. Moreover, the quality of imported products do not always correspond to GOST or TU as there is no corresponding control on the part of customs services, and sanitary and epidemiological stations, because strict control of each batch of drugs is almost not possible because of the transparency of the border and smuggled goods flooding the market [1,2].

Drugs made from plant material, are especially effective in the treatment of diseases caused by unfavorable environmental conditions (Baikonur Cosmodrome, the Semipalatinsk nuclear test site) and the high background radiation do not cause side effects when they are used and are not toxic than drugs obtained by synthesis . Perhaps that is why in recent years in developed countries such as America, Japan and the European Community for the basic components of drugs are natural products of plant and animal origin.

In Kazakhstan, there are over 20,000 species of plants, 6,000 of them contain biologically active substances. Of the six thousand six hundred species can be used as an intermediate product for the production of drugs, and from more than 500 species can be ready to receive drugs [3,4]. But the existing technology of medicines are very complicated and many-stage, energy-intensive and costly process. In addition, the purity of the products is poor, so they are not competitive on the world market [5].

In Shymkent chemical-pharmaceutical plant from plant material obtained by extraction of drugs: morphine, codeine, papaverine, etc., and related alkaloids are in the blade, as some of them exhibit the toxicity, while others are ineffective, and some do not possess physiological activity. To date, these side products are in warehouses unsold. But the structure of these alkaloids can get from them is already known or new biologically active compounds by modifying their structure, by introducing new functional groups-OH, – OCH_3,-OC_2H_5,-NO_2, etc.

These biologically active agents are effective in the treatment of cancer and have antioxidant properties. To determine the molecular formula of compound chromatographically pure samples of the final products were subjected to qualitative and quantitative elemental analysis for carbon, hydrogen, nitrogen, bromine, according to the method. The molecular weight determined by cryoscopic method in glacial acetic acid. The melting point was determined by the device TAP (TU25-II-II44-76).

Belonging to a class of products com tions revealed the following way. The content of unsaturated C = C bonds was determined by micro-Gorbaha, carbonyl groups according to the method. Quantitative analysis on the methoxy group was carried out by the modified method Tseyzelya-Fibeka.

Thin-layer chromatography on non-aluminum dioxide layer of II degree of activity (by Brockmann) was used for separation and to identify and quantify substances. Plates with a sorbent (200h80mm) were prepared according to. For the elution experiments have been used experimentally selected solvent system.Establishing the structure of the obtained compounds was carried out by removing the IR, NMR – and mass spectra.

IR spectra were recorded on the instrument "Specord" (GDR) on the plate tinah of KBr, NaCl (thickness of the cell – $1*10^{-5}$ M), solvent-free crystals deposited in the form of a liquid film iki. To remove the NMR spectra of the devices used "Varian-S-100XL" (USA) with a frequency of 100 MHz. And "Hitahi" (Japan) -60 MHz. Spectra were taken at t = 25°C and a concentration of 20-30 mg/0.5 mL of $CHCl_3$ or D_2O. Mass spectra were recorded on the mass spectrometer "Varian-MAT-313" in the field strength E 60 eV and t = 25 ° C without solvent. Results of the analysis carried out physico-chemical methods, are shown in Table 1.

№	Substance	Molecular weight	Elemental composition of			IR	NMR
			c	H	N	COOH	COOH
1.	The substance-1 (disstruktsiya)						
	Found	250,11	72,39	9,89	11,04	-	-
	Calculated	250,42	72,18	10,21	11,26	-	-
2.	Substance-2 (anabazin acid)						
	Found	234,24	76,64	11,22	11,60	+	+
	Calculated	234,68	76,92	11,11	11,21	-	-

Tab. 1: Results of the physico-chemical analysis of intermediate and end, products of electrooxidation of anabasine

The presence of the + sign. On the basis of physico-chemical analysis, IR, NMR spectroscopy revealed that the end product of electrooxidation anabasine yavlyaetsya anabazinovaya acid.

References

[1] Dzhakipbekova NO and others Predpatent RK № 10548 15.08.2001 № 8 "Biflavonid that exhibits antitumor activity and P-vitamin activity."

[2] Dzhakipbekova NO and long. Predpatent RK № 1102115 12.2001g. № 12 "Metoksianabazin and how it is received."

[3] Dzhakipbekova NO, Turebekova GZ and other studies of the process of electrochemical synthesis of alkoloydov D-sparteine with nanoelektorov / / Proc. Scientific-practical conference. St. Petersburg: -2009. -P.127-130.

[4] Dzhakipbekova NO Electrochemistry and others gidrosikvertsetina / / Proceedings of the International Conference "Auezovskie read-2. Shymkent: -2002. -C. 69-72.

[5] Dzhakipbekova NO and others. Electrochemical behavior salosadina / / in the team. "Synthesis of drugs from plant material." Penza:-2008.-p.35-38.

P 92 Behavior of mechanical properties of human milk teeth in tumor therapeutic irradiation compared to permanent teeth

H. Ulrich[1], W. Fränzel[1], R. Gerlach[2], H.-G. Schaller[3]
[1]Martin-Luther-University, Physics, Halle (Saale), Germany
[2]Martin-Luther-University, Klinik und Poliklinik für Strahlentherapie, Halle (Saale), Germany
[3]Martin-Luther-University, Klinik und Poliklinik für Zahnerhaltung und Paradontologie, Halle (Saale), Germany

Introduction: In addition to the surgical intervention and chemotherapy, irradiation often forms an indispensable part of the oncological treatment protocol [4, 8]. This also applies to children, who have tumors in their head and neck region within the first 15 years of life, and it occurs in about every 500th case. Here the radiation – depending on the tumor type – is carried out in single doses of 1.5 to 2 Gy, but total doses of over 40 Gy are to be avoided [1, 6-7].
The present in-vitro study has investigated the effects of various doses of radiation on the hardness and elastic behavior of human deciduous teeth. The results of studies referring permanent teeth, which have been available so far, demonstrate drastic reactions of the mechanical features even at a dose of 0.5 Gy. The hardness decreased in enamel by 75 % and in dentin by 55 %. The elasticity of the enamel dropped by 60 % and of the dentine by 24 %. After a single dose of 2 Gy, usual in the treatment, almost damage was evident; from 10 Gy, a final value was reached. After a total dose of 60 Gy the hardness values of the enamel are 95 % and those of the dentin 75 % lower than the initial values. Concerning elasticity, the enamel was damaged by 93 % and the dentin, by 75 % [2, 3]. As for deciduous teeth, other effects on the mechanical qualities can be expected because of the slightly different collagen-apatite structure in comparison to permanent teeth.

Material and Methods: A total of 38 primary teeth (23 canines and 15 molars) were examined. To simulate a realistic situation as much as possible, only those teeth that were normally erupted, caries-free and freshly extracted were applied. Immediately after extraction, all the teeth were kept in a physiological solution (NaCl 0.9 %, pH 7.3) at a temperature of 6°C. Immediately after the extraction, the separation of a lamella was carried out from vestibular to palatal or lingual. The top was kept cold and was ground. In the enamel and the dentin a measurement window of 1x1 mm^2 was marked, being in the area of the coating dentin. Until the experiment was done, between the follow-up measurements and before and after irradiation, the samples were stored in a refrigerator in the medium previously mentioned at a temperature of 6°C.
For irradiation a linear accelerator (Mevatron MD-2, Siemens, acceleration voltage 6 MV) was used, the determination of the mechanical properties was performed with a NANOINDENTER II and for the final evaluation the statistical program Origin 7.5 was used.
The samples were divided into five groups. To assess the effects of lower doses, subsequent measurements were made in the first group after the initial measuring at 0.5; 1; 2; 4; 6; 10; 20 and 40 Gy. According to clinical practice, the samples were not exchanged after each single dose. After the first dose (0,5 Gy) the dose was a gradually increased by 0,5 Gy (= 1 Gy), 1 Gy (= 2 Gy), 2 Gy (= 4 Gy), 2 Gy (= 6 Gy), 4 Gy (= 10 Gy), 10 Gy (= 20 Gy) and 20 Gy (= 40 Gy).
The samples of the second group were fractionated according to the clinical situation, at a dose of 2 Gy per day, on five days per week, and were irradiated over a total of four weeks.
In the third group, the effects of the first group (with leaps from 10 to 20 Gy and 20 to 40 Gy) were to be analyzed. The samples of this group were therefore (0 Gy) irradiated with single doses of 10, 20 or 40 Gy after the initial measurement.
In the fourth group the measurements were made after the first measuring at 10, 20, 30 and 40 Gy, and all the samples of this group were fractionated up to 10 Gy and were irradiated at 2 Gy for five days. After that, additional single doses of 10 Gy (= 20 Gy), 20 Gy (= 30 Gy) and 30 Gy (= 40) were administered. This served to additionally cover the steps from 10 to 20 Gy and 20 to 40 Gy completed in the first group.
To scrutinize a possible effect of the storage medium on the tooth properties, a parallel fifth group was formed, the samples of which were not irradiated. As the survey in the four other groups extended to a maximum of six weeks, measurements were made two, three, four, five and six weeks after the initial status (week 0). Like in all other samples, the storage medium was also constantly renewed and permanently checked for a pH-value of 7.3 within this group.
Approximately 3.500 individual measurements were made on this basis.

Results: The irradiation affects the hard dental tissues permanently; even a dose of 0.5 Gy leads to dramatic changes in the mechanical properties.

The enamel elasticity decreases by 47 %, that of the dentin by 57 %. At a single dose of 1 Gy, the elasticity of the enamel is reduced by 67 % and in the dentin by 77 %. Even at a single dose of 2 Gy applied in clinical practice, the enamel loses 73 % and the dentin 74 % of its elasticity. Further dose increases have only comparatively little additional impact. From 4 Gy, the elasticity has lost 80 % of the initial value and varies only slightly in higher doses.

A trend similar in principle can be seen in the hardness. After a dose of 0.5 Gy, it decreased by 40 % in the enamel and by 60 %. in the dentin. At 1 Gy, the losses in the enamel and dentin are 60 % to 75 %. At a dose of 2 Gy, there is an approximately parallel course in hardness losses of almost 70 % both in the enamel and in the dentin. At a dose of 4 Gy, the hardness has decreased by 73 % in the enamel and in the dentin by 76 %, compared to the initial level in the enamel. At 10 Gy, there is damage of 80 %; dose increases do not cause significant value reductions.

These results are confirmed by the measurements of the second group.
In the third group, however, occurs a different result. After a single dose of 10 Gy, produced in the enamel, there is a loss of elasticity of 38 % ”only" and in the dentin, of 43 %. After a single dose of 20 Gy, the elasticity values rise again even to 72 % each of the initial level, and they remain at that level even after a single dose of 40 Gy in the dentin. In the enamel, the elasticity value is 65 % above the initial level after a single dose of 40 Gy. The situation is similar in the hardness. After administrating 10 Gy, one measures a drop of 42 % in the hardness of the enamel and of 46 % in the dentin. At a single dose of 20 Gy, the hardness values increase to 73 % (enamel) and 65 % (dentin) of the initial value respectively. This hardness value remains constant In the dentin after a single dose of 40 Gy, whereas the hardness of the enamel is 20 % above the initial value after this dose. This fact can be explained above all by a hardening and embrittlement of the hydroxyapatite. With regard to the dentin, a collapse of type I collagen must also be taken into consideration.
The results of the fourth group confirm the results of the first two groups.
An influence on the mechanical properties of the milk teeth by the storage media was not found within the study period of up to six weeks. The measured values did not change significantly from the initial value over this period. The correctness of the null-hypothesis was statistically verified for each of the individual samples and also within the overall group by t-test.

Conclusion: The administration of a single dose of 1.5 Gy, conventionally used in therapy, resulted in the 70 % damage of the hard dental substances of milk teeth. This process starts even at much lower doses. At a total dose of 10 Gy, enamel and dentin have lost 80 % of their initial values. Despite structural differences in milk teeth, an essentially similar influence on the mechanical properties of permanent teeth could be established.
It is before and during radiotherapy that an intensive prevention is therefore significant for conservative dentistry, even more so because effects on existing and subsequent permanent teeth are inevitable. In addition to thorough individual dental care and regular fluoridation, an intensity-modulated therapy concept is recommended. In this concept, the salivary glands and parts of the jawbone including the hard dental substances are to be shielded from the radiation field as completely as possible [2, 3; 5, 8].

References

[1] Bamberg, M., Molls, M., Sack, H.: Radioonkologie Band 2, München-Wien-New York, 2. Aufl. 2009, S. 992
[2] Fränzel, W., Gerlach, R.: The irradiation action on human dental tissue by X-rays and electrons – an nanoindenter study, Zeitschrift für Medizinische Physik 19 (2009), 5-10
[3] Fränzel, W. et al: Effect of tumor therapie irradiation on the mechanical properties of teeth tissue, Zeitschrift für Medizinische Physik 16 (2006), Nr. 2, 148-154
[4] Gutjahr, P.: Krebs bei Kindern und Jugendlichen – Klinik und Praxis der pädiatrischen Onkologie, Köln, 5. Aufl. 2004.
[5] Schwenzer N., Ehrenfeld M.: Zahn-Mund-Kieferheilkunde, Band 1, Allgemeine Chirurgie, Stuttgart-New York, 3. Aufl. 2000, S. 211-213
[6] Vorwerk, H., Hess, C.-F.: Tabellenbuch der Radioonkologie, München, 2. Aufl. 2007, Kap. 30
[7] Wannenmacher, M., Debus, J., Wenz, F.: Strahlentherapie, Heidelberg, 2006, S. 755-769
[8] Wiss. Stellungnahme der Deutschen Gesellschaft für Zahn-, Mund- und Kieferheilkunde: Zahnärztliche Betreuung von Patienten mit tumortherapeutischer Kopf-Hals-Bestrahlung, Strahlentherapie und Onkologie 179 (2003), 275-278

P 93 Determination of the relative response of alanine dosimeters in ^{192}Ir HDR photon fields

P. von Voigts-Rhetz[1], M. Anton[2], K. Zink[1,3]
[1]Institute for Medical Physics and Radiation Protection – IMPS, University of Applied Sciences, Giessen, Germany
[2]Physikalisch-Technische Bundesanstalt, Braunschweig, Germany
[3]University Medical Center Marburg, Department of Radiotherapy and Radiation Oncology, Marburg, Germany

Introduction: For brachytherapy dosimetry with 192Ir sources, alanine dosimetry is an established method. New experimental investigations of the energy correction factor at varying distances from the source are evaluated and compared to results of Monte Carlo simulations.

Material and methods: Experimental data were obtained at the Physikalisch-Technische Bundesanstalt (PTB). A high dose rate (HDR) source of the type Nucletron ^{192}Ir mHDR-v2 was used. The experimental setup was an iridium source inside a needle placed in the middle of a water phantom. The latter was modeled in the simulation as a cylinder with a radius of 20 cm (not shown in figure 1). Two series of measurements were performed, one with and one without an additional half sided cylindrical absorber, which is used in clinical applications to spare organs at risk like the rectum in gynecological treatments. The absorber is composed of the high Z material Densimet®. The energy response of the alanine dosimeter was determined by measurements and simulations. All simulations were performed with the software bundle EGSnrc [1]. The **r**elative response was calculated with egs_chamber [2], the mean photon and electron energies with FLURZnrc [3]. The settings for the cutoff/threshold energies for all simulations were AE=ECUT=512keV and AP=PCUT=1keV, all other transport options were set to their defaults.

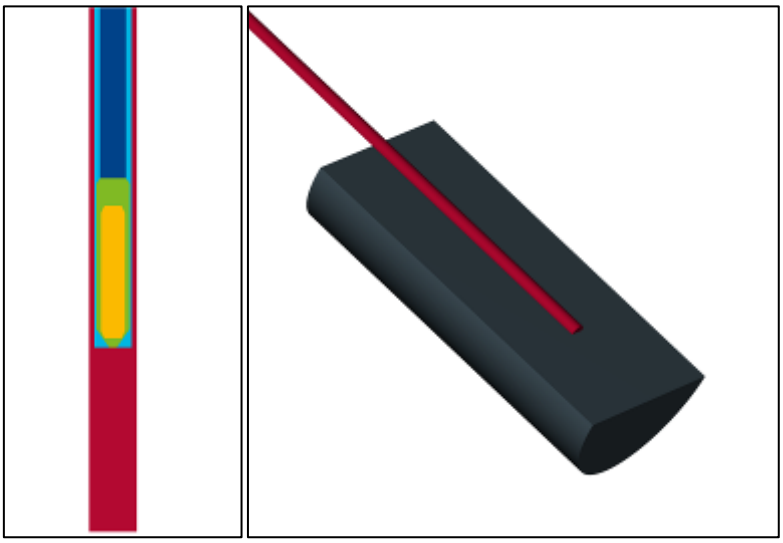

Fig 1: Measurement setup: on the left side the ^{192}Ir source (yellow) inside a steel needle-like applicator (red). The right panel shows the source embedded in the Densimet® shielding (grey). Measurements and simulations were performed at right angle with a distance d to the middle of the iridium source.

Results: The applicator insignificantly increases the mean photon energy (see figure 2) at all the depths. The experimental results of the D_W (absorbed dose to water) response of the alanine dosimeter relative to ^{60}Co from PTB and from Schaeken et al. [4] agree very well with the results of the Monte Carlo simulations (figure 2). With increasing measurement depth, the relative response of alanine decreases from 0.978 at 1 cm to 0.960 at 5 cm depth. The absorber has no significant influence on the relative response of the dosimeter. The ratio of D_w measured with alanine with and without the Densimet® absorber $D_{with\ absorber}/D_{without\ absorber}$ decreases with increasing depth (see figure 2).

Conclusion: Monte Carlo simulations are an adequate tool for the prediction of the absorbed dose to water response of alanine due to radiation from ^{192}Ir-HDR brachytherapy sources. The experimentally determined depth dependence of the relative response of alanine dosimeters in water has also been confirmed by the Monte Carlo simulations.

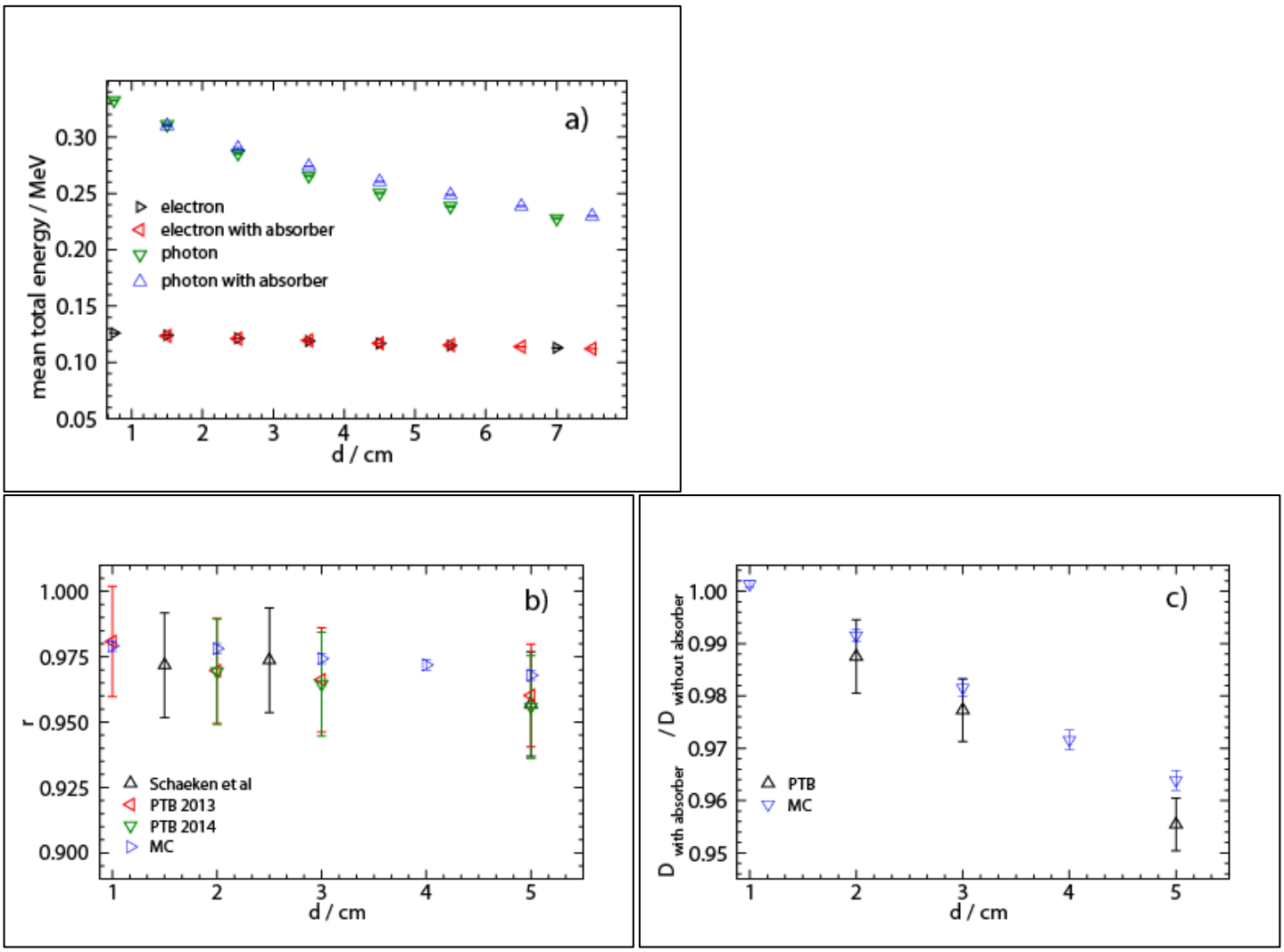

Fig 2: The top panel (a) shows the mean energy of photons and secondary electrons from the Nucletron ^{192}Ir source as a function of the depth d in water. In (b), the D_W response r of the alanine dosimeters relative to ^{60}Co, is given. In (c) the impact of the shielding material Densimet® on the alanine dose is shown as the ratio $D_{with\ absorber}/D_{without\ absorber}$ as a function of the depth

References

[1] Kawrakow I, Mainegra-Hing E, Rogers DWO, Tessier F, Walters BRB: The EGSnrc Code System: Monte Carlo Simulation of Electron and Photon Transport, NRCC Report PIRS-701, National Research Council of Canada 2011.

[2] Wulff J, Zink K, Kawrakow I: Efficiency improvements for ion chamber calculations in high energy photon beams. Med Phys2008;35(4):1328–36.

[3] Rogers DWO, Seuntjens JP, Kawrakow I, Walters BRB, Mainegra-Hing E: NRC user codes for EGSnrc, National Research Council of Canada Report PIRS-702.

[4] Schaeken B, Cuypers R, Goossens J, Van den Weyngaert D, Verellen D: Experimental determination of the energy response of alanine pellets in the high dose rate 192Ir spectrum Phys. Med. Biol. 56 (2011) 6625–6634

P 94 Quality assurance of an ^{192}Ir-afterloader by means of a fast digital compact camera

D. Flühs[1], I. Haase[1], M. Ebenau[1], L. Lüdemann[1]
[1]Universitätsklinikum Essen, Strahlenklinik / Klinische Strahlenphysik, Essen, Germany

Purpose: The quality assurance regime of a remote afterloading system, according to DIN 6853-5 [1], requires the determination of several parameters, such as the position accuracy and the transport time of the source from the storage position to an irradiation position. For this task, a precise and quick method was developed.

Material and methods: A simple set up was introduced to determine the relevant non-dosimetric data for the quality assurance of an afterloding system (Varian GammaMed Plus) by a low cost digital compact camera (Casio EX-ZR400). This camera was easy to handle and provided a zoom lens (optical zoom factor 12.5x) and a video function with a maximum frame rate of 1000 fps (frames per second). The accuracy and reproducibility of the frame rate was verified by observing an analog stopwatch with the camera.

Protected from the radiation by a lead shielding, the camera allowed for an observation of the source movement and positions, using a mirror (Fig. 1). During the measurement, the source was moved along a ruler within a source guiding tube. The source passed the ruler twice during observation: for the first time when it entered the guiding tube, for the second time when it arrived at one of the irradiation positions close to the tip of the tube. A single video recorded during 1-2 minutes displayed all relevant events, storable as a digital documentation on a hard disk. A freely available video viewer (Avidemux2.6 – 64bits) [2] was used to edit the video and find the frame number of a certain event, by scrolling through the video. The exact times of the events were calculated from the frame numbers by a spreadsheet program.

Results: With a video at a rate of typically 120 fps, a sufficiently exact determination of the source movement could be achieved. The time between the moment when the source entered the source guiding tube and the arrival at a prescribed position at the tip of the tube, i.e. approximately the source transition time, and the dwell times as well could be documented with an accuracy of 0.1 s. The spatial resolution in the 120 fps video (640 x 480 pixels) was estimated to be about 0.25 mm. With a HD video (1920 x 1080 pixels) of the same situation, a higher spatial resolution of 0.1 mm was possible (Fig. 2). The accuracy of the source position obtained in this way was comparable to values from radiographic methods.

Furthermore, the obtained data allowed for a determination the effect of source travel and dwell time inaccuracies on the delivered dose. Thus, information about the technical limitations of the remote afterloading system, with regard to the usage of very short dwell times, became available.

Conclusion: Simple set ups with fast digital compact cameras offer a cheap and quick method to determine non-dosimetric data for the quality assurance of an afterloader, such as dwell and transition times, and the positioning accuracy of the source. These systems are suitable for both the daily quality assurance and the entrance test after a source exchange. In addition, some technical limitations of an afterloading system, for example due to its dwell time accuracy, can be easily examined, if necessary.

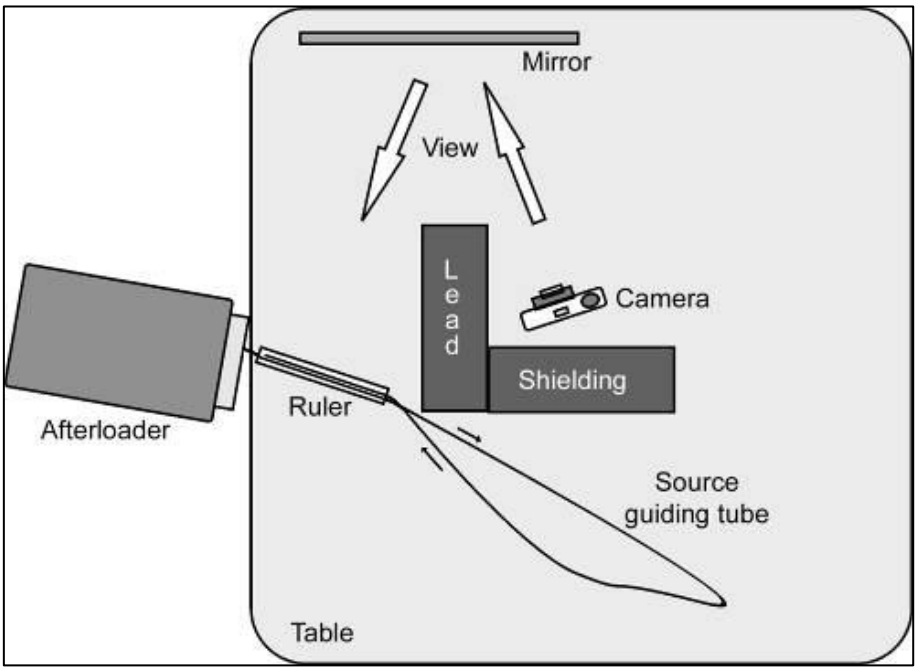

Fig. 1: Set up of the system

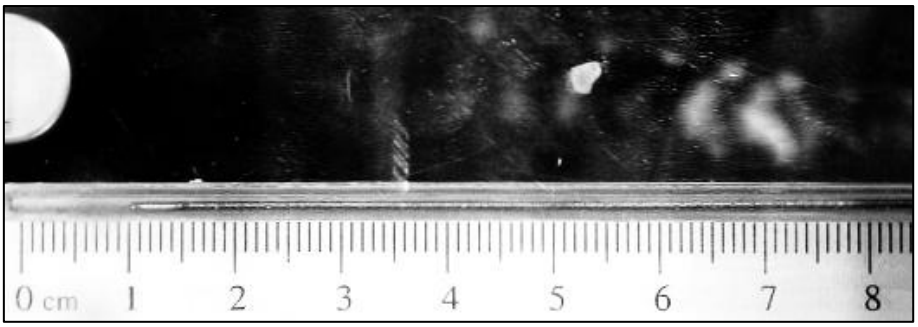

Fig. 2: Still picture from a HD video of the afterloader source during position check procedure

References

[1] DIN 6853-5: Medizinische ferngesteuerte, automatisch betriebene Afterloading-Anlagen – Teil 5: Konstanzprüfung von Kennmerkmalen, 2012-09, Berlin: Beuth Verlag

[2] http://fixounet.free.fr/avidemux/

P 95 Significance of Tissue Air Cavities during irradiation with the MammoSite® catheter

H. Hermani[1], L. Schmolinga[1], S. Ahl-Alhosseini[1], A. Ahl-Alhosseini[1], K. Fakhrian[1], M. Qweider[1], R. Schwandtner[2], T. Lateit[3], C. Demirel[4], I.A. Adamietz[1,3,2]
[1]Marien Hospital Herne, Ruhr-Universität Bochum, Department of Radiation Oncology, Herne, Germany
[2]Ev. Krankenhaus Witten, Department of Radiation Oncology, Witten, Germany
[3]St. Josef-Hospital, Ruhr-Universität Bochum, Department of Radiation Oncology, Bochum, Germany
[4]Paracelsus-Klinik, Strahlentherapie, Osnabrück, Germany

Introduction: The MammoSite® Balloon catheter represents a treatment option for the surgically removed breast cancer. The Balloon is placed inside the lumpectomy cavity after resection of the breast cancer tumour. During this procedure and after inflating the balloon air cavities may occur in vicinity of the device. The purpose of this work was to verify the influence of the air cavities by dose measurements and to compare the measured doses with the dose distribution calculated by the Treatment Planning System.

Material and methods: A MammoSite® Balloon catheter (Hologic Inc.) was filled with 60 ml of a saline solution. 9% of contrast agent (Peritrast, Dr. Franz Köhler Chemie GmbH) was added. The Balloon was placed in the centre of a small water tank. Next to the balloon a 2 cm thick plate of extruded polystyrene foam (XPS, Styrodur, Bayer) was placed. This material consists of closed cells and is characterized by a low absorption of water, being more suitable than cork or other materials. The density of XPS is 0,028 g/cm3, which is equivalent to the average density of the human lung. Thus it is the ideal material for inhomogeneity simulation.

A planning-CT of the water tank was made and transferred to the Treatment Planning System (TPS) BrachyVision 6.5 (Varian Medical Systems). A treatment plan was generated and the horizontal dose profile through the inhomogeneity was determined.

For the dosimetric verification of the treatment plan the same experimental set-up was mounted into a large 3D water phantom (Multidata Systems, Model 9760). The MammoSite® Balloon catheter was connected to an Iridium-192 Afterloader (Varian, GammMedplus). The calculated horizontal dose profile was scanned in the 3D water phantom using a waterproof semiflex ionization chamber (PTW Freiburg, Typ 31010). The scanning path was 10 cm and was scanned primarily without any inhomogeneity and secondarily with a 2 cm XPS-inhomogeneity.

Results: The primary scan performed without inhomogeneities corresponded with doses calculated by the TPS. An average difference between the calculated and measured dose was 0,05%. On contrary the measurement in the 3D water phantom using the XPS-inhomogeneity showed in average a 4,7% higher dose than calculated by the TPS.

Conclusion: When using 3D Treatment Planning for Brachytherapy we should be aware of a possible error originating from dose calculation algorithms omitting any density inhomogeneities. The treatment with the MammoSite® catheter or any other brachytherapy applicator may lead to increased doses of the organs at risk like the skin, the ribs, the lung or the heart. A standard procedure allowing a verification of complex brachytherapy treatment plans, asbeeing currently performed for IMRT treatment plans, should be developed

P 96 Treatment and Prophylaxis of Keloids in Surgical Scars

U. Retzke[1]
[1]Ostsee Institut, Flensburg, Germany

Objectives: The aim of our study is to evaluate described treatment concepts for keloids in postoperative scars. Our own experiences include 20 years of

- Excision alone
- Intralesional injection with corticoid crystal suspension
- Laser- and cryotherapy
- Compression
- Excision and silicone dressing
- Various cytostatic therapy protocols (interferone, imiquomide, retinoids…)

All of the above have unsatisfactory relapse rates of more than 50%.

Methods: A much more successful concept is the precise excision immediately followed by four daily □-irradiation fractions totaling 10 to 15 Gy. Subsequently the scar is treated with a silicone gel for three months.

Results: With a relapse rate as low as 10%, our “Flensburg Concept” outperforms all described treatment protocols by far. The treatment is illustrated with pictures taken under therapy and follow up. The risk of tumor induction within the irradiated region increases by 0.1 to 0.3% over the next 30 years and therefore is insignificant.

Conclusion: The described Flensburg Concept is recommended for treatment and relapse prophylaxis of surgically induced keloids.

References
To date, the Flensburg Concept has not yet been published.

P 97 Quality of Education of Medical Physics and Biomedical Engineering at Gono University in Bangladesh

H. Anupama Azhari[1]
[1]Kreiskrankenhaus Gummersbach Teaching Hospital of the University of Cologne, Dept. of Medical Radiation Physics, Gummersbach, Cologne, Germany

Medical Physicist personnel is an integral part of cancer treatment. In Bangladesh the first activities of Medical Physics education started in 1994 at the Physics Department of the Bangladesh University of Engineering and Technology (BUET). Five seminars/workshops were organized in Bangladesh in the years 1996, 1997, 1998, 1999 by the Task Group 16 “Medical Physics in the Developing Countries” of the German Society for Medical Physics (DGMP). In 2000 a fullfledged “Department of Medical Physics and Biomedical Engineering” (MPBME) was founded at Gono Bishwabidyalay (GB, Gono University) in Savar, Dhaka initiated by Prof. Dr. Golam Abu Zakaria who was also one of the organizators of the above seminars. Till now the Gono University is one and only university offering this course in Bangladesh. Till inception, the department is continuously pursuing a high quality in education in all aspects like course curriculum, teaching methods, local and international collaboration, research, practical class, encouragement of the students in this field, development of teaching staff, maintenance of standard of thesis work, level of Study at International Standard for development as well as to maintain its quality. Further emphasis has been taken regarding national and international collaboration (Germany, India) with this Department. Just from the beginning, a teacher/student exchange program for Medical Physics was established between the Gono University and the University of Heidelberg including the German Cancer Research Center (DKFZ) with the financial support of DAAD (2003-2006). Recently in May 2012 another collaboration is materialized between Manheim Medical Center, Heidelberg University and Gono University under DAAD financial support. The main aim of this cooperation is to improve the quality of the faculty staffs through training and doctoral program. At present, the passed graduates are working in the radiotherapy department of almost all of the public and private hospitals and also in teaching areas in Bangladesh. The establishment of the Department Medical Physics und Biomedical Engineering in Gono University is a success story for Bangladesh. We would like to develop continuously in the future strong and advanced Medical Physics and Biomedical Engineering education and research by incorporating the latest developments of imaging and radiotherapy.

P 98 FEM simulations supporting critical diagnostic applications in medical infrared imaging of the porcine thorax

C. Siewert[1], I. Hennig-Pauka[2], A. Menzel[3], H. Seifert[1]
[1]University of Veterinary Medicine Hannover, Institute for General Radiology and Medical Physics, Hannover, Germany
[2]University of Veterinary Medicine Vienna, Clinic for Swine, Vienna, Austria
[3]University of Veterinary Medicine Hannover, Clinic for Swine, Small Ruminants, Forensic Medicine and Ambulatory Service, Hannover, Germany

Introduction: Respiratory diseases in pigs affecting pork production worldwide have an impact on consumer protection, live stock trade and animal welfare. Next to diseases of the gastrointestinal tract they cause highest economic losses on pig farms in Europe and are one of the most frequent indication for using antibiotics in pigs [3]. Porcine respiratory tract diseases are mainly of multifactorial origin with several different bacterial and viral pathogens being involved in various combinations [12],[2].

The further development of diagnostics and therapy of respiratory diseases in pigs is therefore necessary for the improvement of pig health and pork quality. While animals showing clinical symptoms can be rejected before the slaughtering process subclinically and chronically diseased animals mostly show no clinical symptoms so that lung alterations are not noticed until slaughtering [6].

The early, non-invasive detection of lung disorders would be a valuable tool for the maintenance of respiratory health in pig herds. A promising approach might be the quantification of the skin surface temperature of the thoracic cavity, which is mainly determined by the heat exchange between skin and environment, metabolic activity, blood circulation and anatomical structures beneath the skin close to the body surface. Zapoudrina, et al. [22] demonstrated as part of a human medical study the good reproducibility of temperature distribution patterns in the central body area of 16 test persons.

The diagnostic fields of application of passive infrared imaging [14], [20] (at present mostly in the scope of research projects) are, above all, early detection of breast cancer [7], recognition of vascular malformations (e.g. haemangioma [14]) and blood circulatory disorders close to the body surface. By combining the mammography with the IR imaging the sensitivity regarding breast cancer recognition rises significantly [7]. A FEM-simulation (Finite Elements Method) for calculation the temperature distribution of a female breast with a tumor 2 cm below the skin (Ø = 2 cm) found an elevated skin temperature of 1.5 °C on the surface of the skin [4],[5]. Studies determining nasal path and nasal cavity pathology are currently underway at the University of Veterinary Medicine Hannover [9]. The body surface temperature of the thorax might even be influenced in the case of purulent pleuropneumonia resulting from reduced ventilation [17] if suitable environmental and biophysical parameters are chosen.

Imaging techniques for the detection of lung alterations have been evaluated for pigs but are of no practical relevance:

- Thorax-CT: lung lesion scores correlate (Spearman's rank correlation coefficient) with CT scores ($\rho = 0.82$, $p < 0.0001$), [1]
- Thorax-X-ray: lung lesion scores correlate with radiographic scores (= 0.47, p = 0.012), [1]

hypothetically Infrared-thermal imaging (IRT) fulfils the requirements of a high throughput screening method, which would be applicable in swine herds in a large number of individuals. Up to now IRT of the thorax is a possible but critical diagnostic method for the swine lung [17], [10], [11]. FEM-simulation (Finite Elements Method) for calculating the temperature distribution [19], [18] could help to optimize infrared imaging including biophysical parameters.

Material and methods: For taking the thorax anatomy into consideration tissue profiles with transversal scross sections (Fig. 1b) have been carried out.

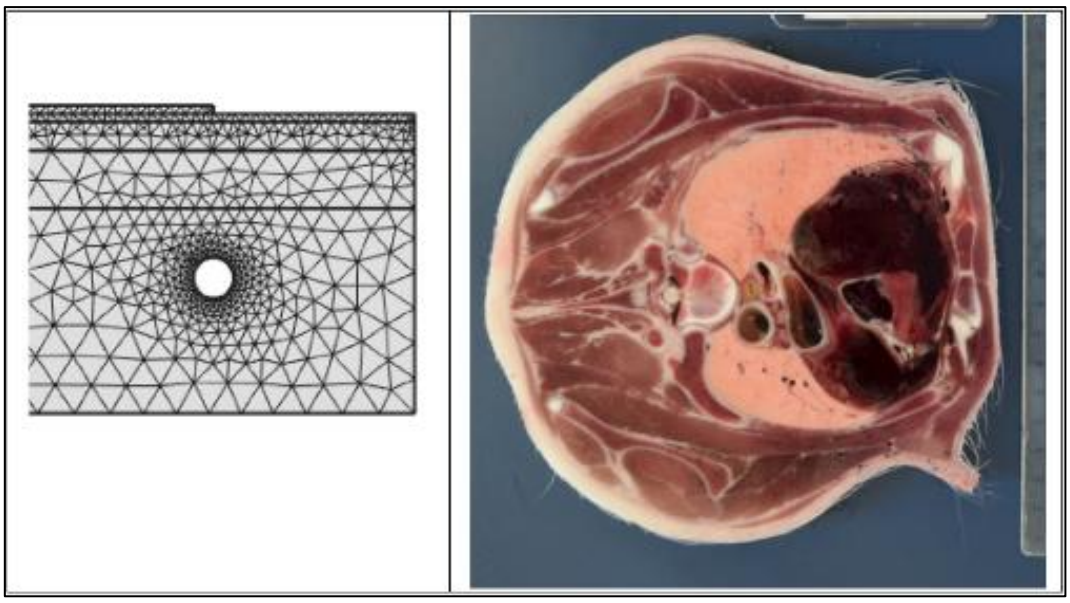

Fig. 1: Modelling

1a: FEM-grid with tissue layers (top → down: bristle, skin, subcutaneous fat layer, muscle layer with ribs, well perfused tissue; cylindrical heat sink)

1b: Anatomy of the porcine thorax (cross section, young pig), layer thicknesses for FEM-model taken from [10]

Modelling by FEM-calculations

The biological heat conduction equation (1) [13] considers the effect of the blood perfusion rate ω on the temperature distribution within the tissue.

$$\nabla \; k\nabla T + \omega \, \rho_b \, c_b \, (T_b - T) + Q_m = 0 \qquad (1)$$

∇ := Nabla operator a vector differential operator

Parameters: Thermal conductivity k: Subcutaneous fat tissue has a thermal conductivity of k = 0.16-0.2 $Wm^{-1}K^{-1}$ and muscle tissue approx. k = 0.42 $Wm^{-1}K^{-1}$ [23] consequently k_{muscle} is approx. twice as high as the value in subcutaneous fat tissue. T is the local tissue temperature.

Constants: ρ_b and c_b are the density and the specific heat of the blood [4] and are practically constants in the ambient temperature range (14 – 22 °C) and a constant blood temperature is defined by T_b. Cell meta-bolism produces heat, which is included in the parameter Q_m.

The parameters ambient temperature Ta and blood perfusion rate ω have been adapted during FEM-calculations (Comsol Multiphysics V4.3a incl. Heat Transfer Module, Fa. Comsol Multiphysics GmbH, Göttingen). The blood perfusion rate ω_{relax} was assumed to be 0.00018 ml/s/ml [4] and adapted stepwise. Further parameters were taken from [4], [8], [21].

Results: The calculated temperature distribution (Fig. 2b,d) confirms the temperature reduction in the skin layer resulting from a cylindrical heat sink at two different ambient temperatures (14˚C /18˚C).

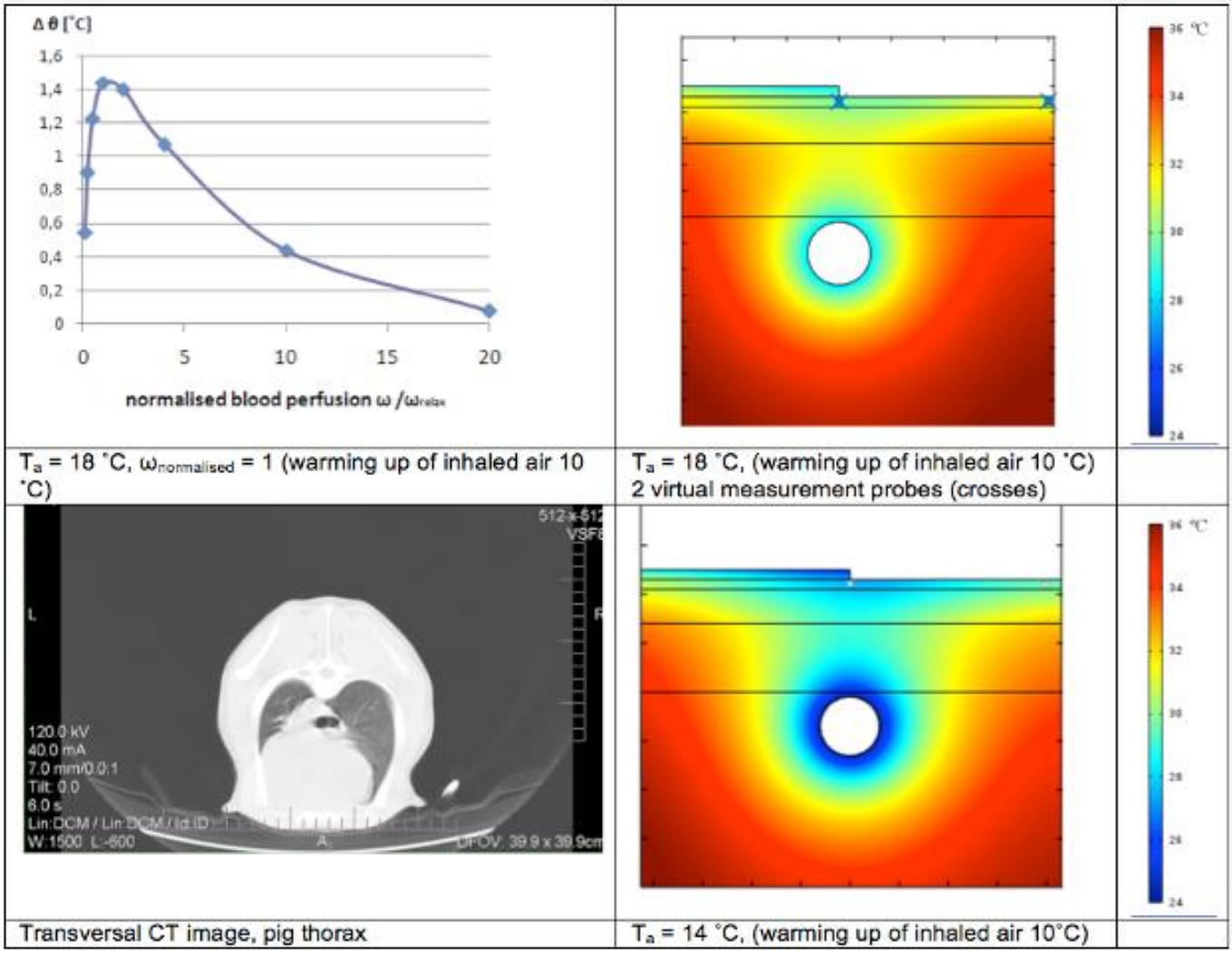

Fig. 2: Calculated temperature distribution in tissue cross-section (top → down): bristle, skin, subcutaneous fat layer, muscle layer with ribs, well perfused tissue; cylindrical heat sink (white circle area) simulates an air path (Ø = 12 mm).
2a: Calculated temperature difference $\Delta\vartheta_{probes}$ for different ambient blood perfusion rates (without error-constant, s. eq. (2))
2b,d: Calculated temperature distribution, T_a = 18 ºC and 14 ºC ambient temperature; thicknesses of layers: bristles: 2 mm, skin layer: 2 mm, subcutaneous fat layer: 7 mm, muscle layer (ribs included): 14 mm, layer of well perfused lung tissue above the airways: approx. 1 mm, cylindrical heat sink (white circle area) simulates an airway (Ø = 12 mm).
2c: Pig thorax CT, transversal (in the region of the heart)

A reduction of the temperature difference caused by an increased blood perfusion exists as simulated in the finite element model shown in Fig. 2a. The extension of the right lung layer is larger compared to the left lung layer (Fig. 2c). FEM simulations as shown in fig 2b and 2d indicate the influence of a cylindrical airway (Ø = 12 mm, approx. 22 mm below the body surface) onto the skin surface temperature. The surface temperature cooled down by approximately 1.4 °C according to eq. 1 (Fig. 2b,d). For FEM-simulation, ambient air temperature was chosen to be 18 ˚C and 14 ˚C, respectively, while the air temperature within the respiratory tract was estimated to be increased by 10-12 ˚C [15].
Conclusion: Two virtual measurement probes (crosses, Fig. 2b) are inserted in the skin layer in a distance of 40 mm. One measurement probe is located exactly above the heat sink (airway). The warming up of inhaled air was assumed to be 10 ˚C. The extent of impreciseness resulting from the physiological fluctuation-range can not precisely be assessed. An elevated body core temperature ϑ_r was assumed to increase the temperature of inhaled air resulting (eq.4) in a decrease of temperature difference $\Delta\vartheta_{probes}$ with rising ambient temperature (eq.3).

Twelve FEM simulations in the ambient temperature range (15-22 ˚C, $\omega \rightarrow \omega_{relax}$) have been calculated and 8 FEM simulations with different values for normalised ω_n ($\omega > \omega_{relax}$):

$\Delta\vartheta_{probes}$ (T_a , $\omega_n = 1$) ~ $-0.18\ T_a$ {term A} (2a)

$\Delta\vartheta_{probes}$ ($T_a = 18$˚C, ω_n) ~ f (T_a) · ($0.003\ \omega_n^2 - 0.14\ \omega_n + 1.67$); $\{R_{Polynom}^2 = 0.99\}$ {term B} (2b)

$\Delta\vartheta_{probes}$ (T_a , ω_n) ~ term A + term B – error constant (3)

error constant := (ϑ_r - 38.5 ˚C) + pa_correction (4)

The parameter pa describes the warming of air inside the respiratory system taking the physiological fluctuation range into account (pa = 10…12 ˚C, ϑ_r = rectal temperature). pa_correction is a function of pa. The surface temperature cooled down by approximately 1.4 °C (Fig. 2a), this results confirms the findings of [10] that the lung layer thickness correlates (Spearman's rank correlation coefficient: = 0.47, p = 0.038) to a temperature difference on the right thorax side and the thickness of tissue layer (muscle, ribs and skin) correlates negativ (= -0.64, p = 0.002) also. For a more precise calculation the temperature of exhaled air should be measured in a future experiment with a sufficient number of animals in the temperature range 14-18 ˚C. Results from IR thermography in swine might also be of value for human medicine. A further development of IRT imaging in paediatrics might allow the tracking of lung pathologies without x-ray imaging.

References

[1] Brauer C, Hennig-Pauka I, D. Hoeltig, F. F. Buettner, M. Beyerbach, H. Gasse, G.-F. Gerlach and K.-H. Waldmann, Experimental Actinobacillus pleuropneumoniae challenge in swine: Comparison of computed tomographic and radiographic findings during disease *BMC Veterinary Research* (2012), 8:47 2012 online publication: doi: 10.1186/1746-6148-8-47

[2] Done S, White M, Porcine respiratory disease and complexes: the story to date. In Practice (2003) 25, 410-414

[3] Fraile L, Alegre A, Lopez-Jimenez R, Nofrarias M, Segales J, Risk factors associated with pleuritis and cranio-ventral pulmonary consolidation in slaughter-aged pigs, Vet J (2009), doi:10.1016/j.tvjl.2009.03.029

[4] Gonzalez FJ, Thermal simulation of breast tumors, Revista Mexicana de Fisica (2007), 53 (4), 323-326

[5] Gonzalez FJ, Non-invasive estimation of the metabolic heat production of breast tumors using digital infrared imaging, Quantitative InfraRed Thermography Journal (2011), Vol 8, Issue 2, p. 139-148, 201

[6] Hennig-Pauka I, Seifert H, approved DFG-grant, HE 6419/1-1, personal notification (2012)

[7] Keyserlingh JR, Ahlgren PD et al. Functional Infrared Imaging of the Breast: Historical Perspectives, Current Applikation, and Future Considerations, In Nicholas A. Diakides, Joseph D. Bronzino, Medical Infrared Imaging, Boca Raton: CRC Press, 2008

[8] Klauenberg BJ, Miklavcic D, Radio frequecy radiation dosimetry and its relationship to the biological effects of electromagnetic fields, NATO science series, 3. High Technology, (2000), Vol. 82, Kluwer Academic Publishers

[9] Krogbeumker B, Siewert C, Bienert A, Staszyk C, Ohnesorge B, Seifert H, The passive infrared thmography as addition to diagnostics of diseases in the head region of the horse – first results. In: Dössel, O.; Schlegel, W. C. (Hrsg.): IFMBE Proceedings 25 (II) 11th World Congress on Medical Physics and Biomedical Engineering, (2009), Berlin Heidelberg New York, 221-224,

[10] Menzel A, Siewert C, Gasse H, Seifert H, Höltig D, Hennig-Pauka I, Infrared thermography of the pig thorax: an assessment of selected regions of interest by computed tomographic and anatomical parameters, Anatomia histologia embryologia (2014) 43

[11] Menzel A, et al., Hennig-Pauka I, experimental Actinobacillus pleuropneumoniae challenge in swine: diagnostic of lung alterations by infrared thermography, personal notification (1Q2014)

[12] Palzer A, Ritzmann M, Wolf G, Heinritzi K, Associations between pathogens in healthy pigs and pigs with pneumonia, Vet Rec. (2008), 162, 267-71

[13] Pennes HH, Analysis of tissue and arterial blood temperatures in the resting human forearm, J.Appl.Physiol.1(1948) 93-122

[14] Saxena AK, Willital GH, Infrared thermography: Experience from a decade of pediatric imaging, Eur. J. Pediatr. (2008), 167(7): 757-64

[15] Schoknecht G, Stock B, The Technical Concept for Evidential Breath Testing in Germany, Alcohol, Drugs and Traffic Safety (1995), vol.1

[16] Siewert C, Dänicke S, Kersten S Brosig B, Rohweder D, Beyerbach M, Seifert H. Difference method for analysing infrared images in pigs with a lipopolysaccharid induced hypertermia. In: Z. Med. Phys. 24 (2014) 6-15

[17] Siewert C, Hoeltig D, Brauer C, Seifert H, Hennig-Pauka **I,** Medical infrared imaging of the porcine thorax for diagnosis of lung pathologies. In: Proceedings of the 21st International Pig Veterinary Society Congress**,** Vol. II, **(**2010), Vancouver**;** p. 663

[18] Siewert C, Staszyk C, Bienert-Zeit A, Ohnesorge B, Seifert H, Einfluss der Parameter Umgebungstemperatur und Durchmesser der nasalen Luftwege auf die Temperaturverteilung am Pferdekopf. 3 Ländertagung der ÖGMP, DGMP, SGSMP, (2011), Wien (28.9.-1.10.2011), http://www.medacad.org/medphys/2011MedphysAbstracts.pdf

[19] Siewert C, Staszyk C, Seifert H. Einfaches FEM-Modell zur Berechnung der Temperatur-verteilung am frontalen Pferdekopf – Erste Ergebnisse. In: 41. Wissenschaftliche Tagung der Deutschen Gesellschaft für Medizinische Physik (DGMP), (2010), (Hrsg.: N. Hodapp, J. Hennig, M. Mix). Freiburg, Tagungs-CD; 610-612

[20] Vollmer M, Möllmann KP, Infrared Thermal Imaging**,** Weinheim: Wiley-Vch, 2010

[21] Wu Z, Liu HH, Lebanowski L, Liu Z, Hor PH, A basic step toward understanding skin surface temperature distributions caused by internal heat sources, Phys. Med. Biol. 52 (2007) 5379–5392

[22] Zapoudrina N, Varmavuo V, et al. Reproducibility of infrared thermography measurements in healthy individuals, Physiol. Meas. (2008) ;29:515–524

[23] Zheng L, Wen-Jei Y, Whole body heat balance during the thoracic hyperthermia, Med. Biol. Eng. Comput. 28 (1990) (2), 171–181

P 99 Beam reckon algorithm for irradiation – BRAIN

M. Felix[1], J. Fleckenstein[2], S. Kirschner[3], M. A. Brockmann[3,4], F. Wenz[2], F. A. Giordano[2], G. Glatting[1]
[1]Universitätsmedizin Mannheim, Medical Faculty Mannheim, Heidelberg University, Medical Radiation Physics/Radiation Protection, Mannheim, Germany
[2]Universitätsmedizin Mannheim, Medical Faculty Mannheim, Heidelberg University, Department of Radiation Oncology, Mannheim, Germany
[3]Universitätsmedizin Mannheim, Medical Faculty Mannheim, Heidelberg University, Department of Neuroradiology, Mannheim, Germany
[4]University Hospital Aachen, Department of Diagnostic and Interventional Neuroradiology, Aachen, Germany

Purpose/objective(s): In many pre-clinical studies with animal models radiotherapy is not considered, although radiotherapy represents one of the key pillars of cancer treatment. As this is mainly due to an anticipated technical complexity and the lack of an accurate tool for dose estimation, we developed the treatment planning system BRAIN (beam reckon algorithm for irradiation) for our IGRT capable small animal irradiation device.

Material and methods: A steel tube system (5 mm bore) for collimation of the primary beam was mounted on **a** micro-CT cabinet **Y**.Fox (YXLON GmbH, Hamburg, Germany)**.** An ionization chamber 31010 (PTW Freiburg GmbH, Freiburg, Germany)**,** water-equivalent RW3 slab phantoms **(**PTW) and GAFCHROMIC® EBT-films (ISP, Wayne, NJ, USA) were used for the measurement of the base data set for the planning system**.** Validation of the planning system was performed with anatomical mouse phantoms made of RW3 slab phantoms.

The graphical user interface, which provides the possibility to select arbitrary beam angles (0-360°) and assign different weights, was programmed in C++ combined with Qt 4.8.5. For the localization of the planning target volume (PTV) a verification image and a CT scan with a marker were performed. Regarding the CT scan the user has to define the PTV and the corresponding reference point. BRAIN calculates the beam-on time and the position of the mouse for each beam via superposition of the central beams. The calculation is based on the length of the surface to the reference point for every beam angle and the position of the marker.

To validate the geometric and dosimetric accuracy of the algorithm a fixed target volume within a murine phantom was defined and three different investigators delivered 116 cGy with three, four and five beams using BRAIN. Radiochromic films were placed at the center of the phantom**.**

Results: At the isocenter in a depth of 5 mm the symmetry, the flatness, the full width at half maximum and the penumbra were (116 ± 3)%, (101 ± 2)%, (11 ± 0.3) mm and (450 ± 80) µm, respectively.

Irradiations by three different investigators showed a geometric reproducibility of the differences between lengths of 5 selected isodose profiles of **(**0.2 ± 0.1) mm. Relative dose deviations at the reference point were (99 ± 3)% for three beams, (103 ± 3)% for four beams and (101 ± 3)**%** for five beams.

Conclusions: Due to the uniform flatness and symmetry as well as the sharp penumbra of the system, it is possible to treat the target volume with a homogeneous dose distribution and a high conformity. The treatment planning system BRAIN is able to determine the necessary beam-on time and the position of the mouse for the chosen beam angles and weightings with a very good reproducibility. Furthermore, BRAIN is a simple and self-explanatory treatment planning system, which can easily be used.

P 100 Computer simulation of electrical currents during the stunning of African catfish

W. Hörnig[1], M. Lüpke[1], J. Hellmann[2], D. Steinhagen[2], H. Seifert[1]
[1]University of Veterinary Medicine Hannover, Institute for General Radiology and Medical Physics, Hannover, Germany
[2]University of Veterinary Medicine Hannover, Fish Disease Research Unit, Institute of Parasitology, Hannover, Germany

Introduction: The interest in fish as a healthy and tasty food has grown during the past years. The expanded demand for fish cannot be met solely by customary fishing. For this reason the production of fish in aqua cultures has increased. Besides trout, salmon and carp the food industry has discovered the African catfish (Clarias gariepinus) as a fish with an excellent meat quality. The Animal Welfare Act stipulates that vertebrate animals have to be stunned correctly before killing [1].

Electrical stunning, carbon dioxide stunning, percussion and administration of substances with anaesthetic effects are allowed stunning methods for fish in Germany [1]. Due to the fact that the demand for meat of the African catfish is increasing, a uniform industrial effective stunning method is necessary. For this fish no consistent regulation regarding stunning during slaughtering exists. As the electrical stunning is a good method for industrial slaughter to avoid pain [2] it makes sense to also use it for the African Catfish. In the past it was difficult to achieve a sustained loss of consciousness by electrical stunning. The aim of the present study was to develop a computer model to simulate electrical current density through the catfish using the finite element analysis. The result of this in silico experiment will help to understand why it is virtually impossible to stun African catfish with electricity. In addition, the simulations will help to optimise the stunning process.

Material and methods: One fish was dissected to gain a better view of the brain and the adjacent structures.

Two more fish were euthanised and scanned with a CT (Philips brilliance 64 channel Ct-scanner) and MRI (Philips achieva 3.0T TX) device under administration of a contrast medium. The CT-scanning was performed with a resolution of 0.29 x 0.29 x 0.33 mm³ and the MRI-scanning with a resolution of 0.6 x 0.3 x 0.3 mm³. The volume data sets of CT and MRI were registered by anatomical landmarks.

Based on the CT- and MR-datasets an anatomically correct 3-D model of the catfish's head was constructed (Fig. 1). For this purpose different tissues in each slice were segmented, based on Hounsfield units and intensity values, respectively (software AMIRA, version 5.5.0, Visualization Sciences Group).

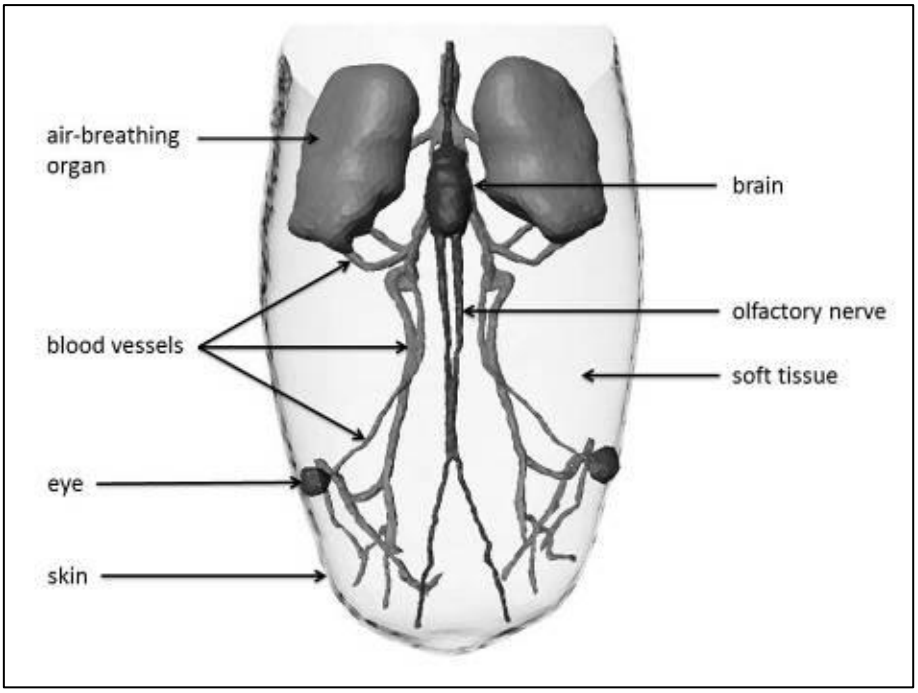

Fig. 1: 3-D model of the head with selected anatomical structures (dorso-ventral view).

Afterwards, the model was simplified for the finite element calculations. The electrical properties for each tissue were assigned and the boundary conditions were chosen.

Several computations were performed using different frequencies from 50 to 10000 Hz and voltages from 50 to 10000 volts. In addition, the type and the position of the electrodes were varied.

Results: The dissection showed that the brain of the African catfish was embedded by a fat-like substance. This mass was surrounded again by a strong bone cave.

The computer simulation (software COMSOL Multiphysics, version 4.3a, COMSOL AB, Stockholm, Sweden) demonstrated that the current density in the brain tissue was low compared to other soft tissues. The simulation showed that the current primarily flowed through the tissues around the brain which had a higher conductivity than the bones and the fat (Fig. 2).

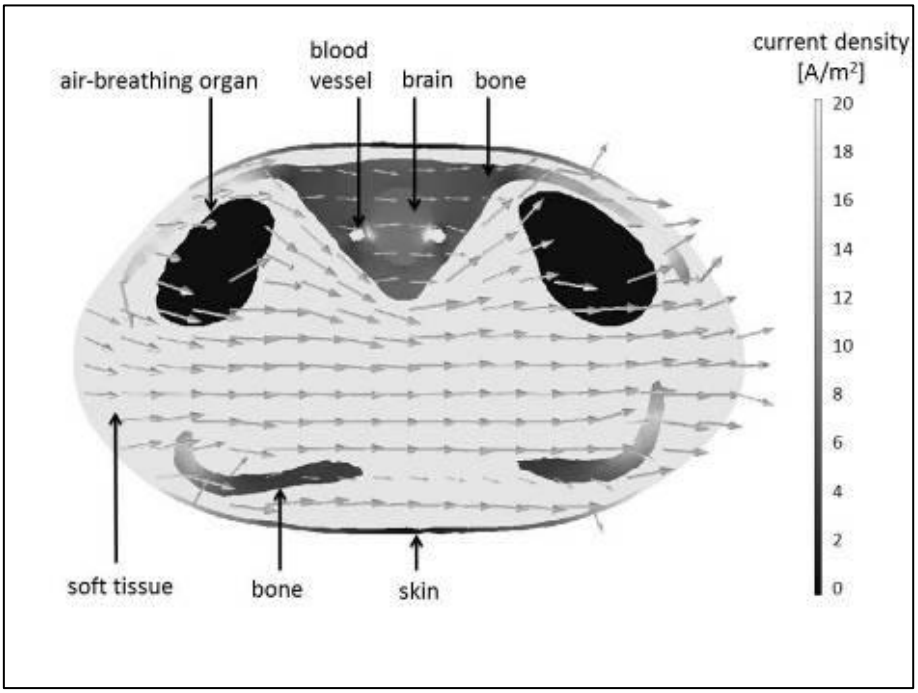

Fig. 2: Distribution of the current density in a transversal slice of the 3-D model. The arrows mark the flow direction of the current and the shading the different current densities.

Varying the positions of the electrodes resulted in small differences in the current density. Computations with higher frequencies than 50 Hz or higher voltages than 100 volts led to a slight increase in the current density inside the brain.

Conclusion: Since it is known that the electrical conductivity of fat and bones is low, it can be concluded that this could be the reason for low current density in the brain. The brain is excellently protected by the fat-like substance and the bones. Also, only small currents may enter the brain via the nerves and blood vessels.

Therefore, it is difficult to use electrical stunning for the African catfish. Only very high voltage could guarantee a sufficient loss of consciousness and sensibility. Due to occupational safety such high voltage cannot be used. The results of the computer simulation should be verified in animal experiments using EEG derivation.

References

[1] Tierschutz-Schlachtverordnung 20. December 2012 (BGBl. I S. 2982)
[2] Lines, J.A., Robb, D.H., Kestin, S.C., Crook, S.C., and Benson, T. (2003). Electrical stunning: a humane slaughter method for trout. Aquac. Eng. 28, 141-154.

P 101 Speech intelligibility and speech detection thresholds for male and female target speech in different speech-based maskers

W. Schubotz[1,2], T. Brand[1,2], S. D. Ewert[1,2]
[1]Universität Oldenburg, Oldenburg, Germany
[2]Exzellenzcluster "Hearing4all", Oldenburg, Germany

Introduction: Speech signals are the basis of human communication, in daily life speech is often perceived within a background noise that acts as a masker to the target speech signal. Speech reception is therefore hampered by individual physical parameters of the masker such as frequency content, energy distribution and temporal gaps and their interactions. The influence of these interactions can be summarized in three masker characteristics: energetic, amplitude modulation and informational masking (EM, AM, IM). Energetic masking occurs when masker energy covers the energy of the target signal within the same auditory filter [1]. When temporal amplitude modulations of the masker hide those of the target signal, this is termed amplitude modulation masking [2]. In case of confusions and similarity between target and masker signal (e.g. speech-on-speech masking), the term informational masking is used [1,3], explaining excess masking compared to EM. This study examined the influence of the three types of masking on speech intelligibility and speech detection. Different background maskers were generated to address the different characteristics in a systematic manner. In order to investigate the informational masking more closely, both male and female target signals were used within the different maskers which were derived from female speech.

Material and methods: The stimuli that were presented to the listeners were composed of target sentences from the Oldenburger Satztest OLSA [4] and six different background maskers. The female target sentences were taken from a version of the OLSA that was presented by K. Wagener at the 40. Jahrestagung für Akustik (DAGA) in 2014. The background maskers are to be separated in two categories: four are based on a speech-shaped stationary noise (SSN), the other two are intact speech maskers. The SSN was derived from the International Speech Test Signal (ISTS, [5]) thus both masker categories have the same spectral content. For the second masker, the SSN was multiplied with a 8-Hz sinusoid, introducing a regular modulation to the background noise (SAM-SSN). The SSN was also multiplied with the Hilbert envelope of a broad-band speech signal, introducing temporal gaps that reflect the modulations of intact speech. This was the third masking condition, BB-SSN. The amplitude modulations in the SAM- and BB-SSN conditions were applied to the entire frequency range of the maskers, yielding a co-modulation of all auditory channels. In contrast, the fourth SSN-based masker was created by filtering the SSN into 32 auditory channels within a frequency range of 50Hz-12kHz. Four adjacent channels were modulated with the same envelope. The envelopes were random parts from the same Hilbert envelope used for the BB-SSN condition. As a consequence coherent modulations were introduced only in those parts of the masker spectrum that belong to the four adjacent auditory filters, yielding across-frequency shifted modulations (AFS-SSN). Overall there were eight different modulations applied to the 32 bands and no co-modulation across the entire masker spectrum. Regarding the masking effects, the SSN is thought to account for energetic masking only, AM is introduced for the other SSN maskers. The two intact speech maskers were the ISTS, which is a mixture of six female talkers (see [5] for details), and a single female talker (ST). The ISTS consist of non-sense speech in different languages, the ST was composed of OLSA sentences. Both speech maskers are thought to provide most IM in this setup.

For speech intelligibility measurements an adaptive procedure was used to change the level of the target signal in order to determine the signal-to-noise ratio (SNR) where 50% of the words in a presented sentence were understood correctly. This SNR is termed speech reception threshold (SRT). Speech detection thresholds were measured by a 1up-2down, 2-interval alternative forced choice (AFC) method in order to determine the SNR at the 70.7% correct point of the psychometric function. One of the two presented intervals contained a full OLSA sentence embedded in the masker, the other interval contained only the masker. Listeners had to choose the interval containing the target sentence. Eight listeners participated in the measurements with the male OLSA sentences, six of them participated also in the measurements with the female target material. The statistical evaluation was done by using a one-way repeated-measures analysis of variance (ANOVA), regarding the different masking situations. As post-hoc test pairwise comparisons using Fischer's LSD with Bonferroni correction were performed.

Results: Fig. 1 shows the mean $SRT_{50\%}$, speech detection thresholds and the corresponding standard deviations for the male target material. Fig. 2 shows the same for the female target sentences. For both setups the ANOVA yields significant differences in masking condition for the speech intelligibility measurement. For the male target material the F values are $F(5,40) = 170.23$ ($p < 0.001$), for the female targets they are $F(5,30) = 59.32$ ($p < 0.001$). Considering the SSN-based maskers in both figures, the thresholds are very similar for both targets materials, the largest masking occurs for SSN and AFS-SSN. Post-hoc pairwise comparisons revealed that these two conditions are significantly different ($p<0.001$) from all other masking conditions in Fig. 1. For data in Fig. 2, SSN and AFS-SSN are only significantly different from the SAM-SSN. With the coherent modulations introduced to the masker (BB- and SAM-SSN) the SRTs decrease which is a known masking release for such modulated maskers. The more regular the modulations are across frequency, the lower the thresholds are which can be seen when comparing the results for all AM maskers.

This is similar to psychoacoustic experiments on co-modulation masking release (CMR). This effect is found in experiments on perception of tones in modulated maskers [e.g. 6] and describes a decrease in detection thresholds for a test tone when the masker has coherent amplitude modulations across frequency. Considering the intact speech maskers ISTS and ST, intelligibility thresholds do not differ by much for both target materials. This is in contrast to the assumption that IM is mostly ruled by similarity between the target and the masker. Besides, there is no difference whether the speech masker consists of one (ST) talker or more of talkers (ISTS). ISTS is additionally non-sense speech. IM could have been expected to be more prominent for the single talker, as meaningful sentences were spoken.

The detection measurements yield a very similar pattern when compared to the results of the intelligibility measurements, however at lower SNRs. A one-way repeated-measures ANOVA showed again a highly significant main effect of masker condition: $F(5,40) = 92.81$ ($p < 0.001$) for the male and $F(5,30) = 87.26$ ($p < 0.001$) for female target material. For both targets, the highest detection thresholds occur for the SSN and AFS-SSN. For data in Fig. 1 a pairwise comparison showed that the SSN differs significantly from all other maskers except the AFS-SSN. This is different from the intelligibility measurements, where the SSN was also different from the AFS-SSN. In Fig. 2, SSN and AFS-SSN are different from all other maskers only at a level of $p < 0.01$. Thresholds decrease for both target materials as coherent modulations are introduced, however, there is hardly any difference between the BB- and SAM-SSN condition for the female target sentences. In general, the detection thresholds across both figures are very similar, showing no detection differences due to target material, as was hypothesized. Considering the competing talkers, there is no significant difference between the ISTS and ST conditions, neither for male nor for female target sentences. This agrees with findings from the intelligibility measurements.

Conclusion: The highest thresholds in speech intelligibility and speech detection appear for the SSN masker. This type of background noise causes a high amount of energetic masking without temporal gaps which could yield release on energetic masking in the time-frequency domain. Similarly high thresholds are observed for AFS-SSN where temporal gaps are not coherent across frequencies. When coherent amplitude modulations are introduced to the masker, thresholds decrease, which is known as masking release. This is only significant if amplitude modulations in the masker are coherent across frequencies, indicating a co-modulation masking release for experiments on speech intelligibility, similar to the effects found in psychoacoustic experiments. These findings occur for both kinds of target material and give rise to the assumption that EM and AM characteristics have the same influence on the speech material, regardless if target and masker have spectral similarities or not. There are only small changes in speech intelligibility thresholds when the maskers are competing female talkers, either single talker or non-sense ISTS. In both cases SRTs are as low as for the SAM-SSN condition, indicating effective release from masking due to temporal gaps in the ST and ISTS masker. The single talker results in slightly but not significantly lower SRTs. Again SRTs are comparable for the female and male target sentences. The threshold pattern is similar for the intelligibility and detection measurements. In the latter case, the thresholds are considerable lower. In conclusion the data show little influence of informational masking, which could have been expected to be prominent when comparing male and female target material.

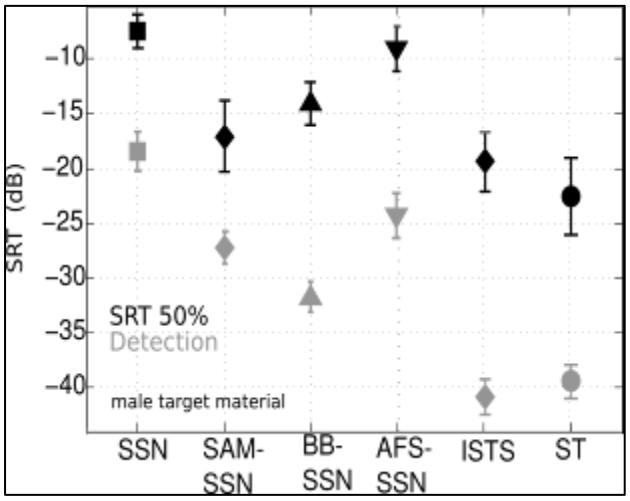

Fig. 1: Mean speech intelligibility (SRT50%) and detection thresholds including standard deviations foreight test persons. Target material were sentencesfrom the OLSA [4], spoken by a male person.

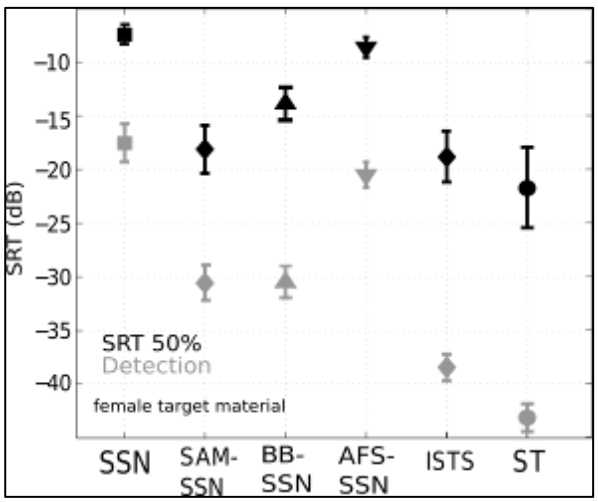

Fig. 2: Here, the target material was OLSA sentences spoken by a female talker. The figure shows mean values of speech intelligibility and detection thresholds across six test persons, including the corresponding standard deviations.

This work was supported by the Deutsche Forschungsgemeinschaft, Sonderforschungsbereich “Das aktive Gehör” (DFG SFB/TRR31).

References

[1] Durlach, N.I., Mason, C.R., Kidd, G. Jr., Arbogast, T.L., Colburn, H.S., Shinn-Cunningham, B.G.: Note on informational masking, J. Acoust. Soc. Am, 113, 2003, 2984-2987

[2] Houtgast, T.: Frequency selectivity in amplitude-modulation detection, Acoust. Soc. Am. 85(4), 1989, 1676-1680

[3] Stone, M. A., Füllgrabe, C., and Moore, B.C.J.: Notionally steady background noise act primarily as a modulation masker of speech, J. Acoust. Soc. Am. 132(1), 2012, 317-326

[4] Wagener, K. und Brand, T. und Kollmeier, B.: Entwicklung und Evaluation eines Satztests für die deutsche Sprache III: Evaluation des Oldenburger Satztests, Zeitschrift für Audiologie,1999, 38:86-95

[5] Holube, I., Fredelake, S., Vlaming, M., and Kollmeier, B.: Development and analysis of an International speech Test Signal (ISTS), Int. J. Audiol. 49, 2010, 891-903

[6] Hall, J.W.,III, Grose, J.H., and Haggard, M.P.: Effects of flanking band proximity, number, and modulation pattern on comodulation masking release, J. Acoust. Soc. Am. 87 (1),1990, 269-283

P 102 Measuring Partial Volume Artifacts using dynamic T1-weighted 3D Gradient Echo Sequence

N. Verbeek[1], S. Hindel[1], A. Sauerbrey[1], L. Lüdemann[1]
Radiation and Tumor Clinic, Essen, Germany

Related questions: Perfusion quantification using dynamic contrast enhanced MRI (DCE-MRI) requires measuring the arterial input function (AIF). In practice, partial volume artifacts (PVA) are unavoidable, because one requires a compromise between spatial and temporal resolution. As the concentration of the contrast agent (CA) increases, the vector of the complex blood signal follows a spiral like trajectory [1] in dynamic susceptibility contrast MRI. In region of full blood shows a signal with spiral center close to the origin of the complex plane. Partial-volume-voxels contain blood and tissue. PVA result in a spiral-center shift. Our aim was to develop a method for voxel-based partial volume artifact correction for DCE-MRI.

Material and Methods: All experiments were performed on a Siemens Magnetom 1.5T. We used a T1-weighted keyhole 3D Gradient Echo Sequence (Twist) with repetition time TR=2.69 ms, echo time TE=0.86 ms, flip angle □=30°, voxel size: 2.85x4.5x2.85mm^3, matrix size: 160x48x128mm^3,slice thickness: 4.5mm, Field of View: 456x356mm^2, a body coil was used as receiver and Gadoteric acid as contrast agent. We measured the partial volume artifacts in sedated female pigs (weight: 45-65kg) at the aorta [3]. The complex blood signal, $\vec{S} = M \cdot e^{i\Phi}$ [2], with M as magnitude and Φ as phase angle, follows a spiral trajectory. After plotting these data points in the complex plain, the data were fitted by a logarithmic-spiral-fit in the shape of $\vec{S} = a \cdot M \cdot e^{i \cdot b \cdot \Phi}$ using two parameters, a and b, to calculate the spiral center. The logarithmic spiral has constant polar gradients, meaning that the spiral has the same cutting angle. Every spiral center line intersects the spiral in the same angle. Therefore the geometric center calculation of the logarithmic spiral is based on constant heading change.

Results: We determined the complex trajectory center, as expected, in voxels full of blood spread in the area of 0 to 40 signal units around the complex origin (Fig. 1). Distances from the origin(cod), which were larger than 40 signal units, were allocated to voxels including partial volume artifacts (Fig. 2). For the evaluation of the fit and the calculated trajectory we used the root mean square-value (rms). Fits with a too massive rms were not involved.

Summary: We were able to illustrate the signal shift in partial volume effects voxels in living tissue using DCE-MRI under clinical conditions. This method is about to help correcting partial volume artifacts that affect measurements of the arterial input function.

Fig. 1: Full blood voxel

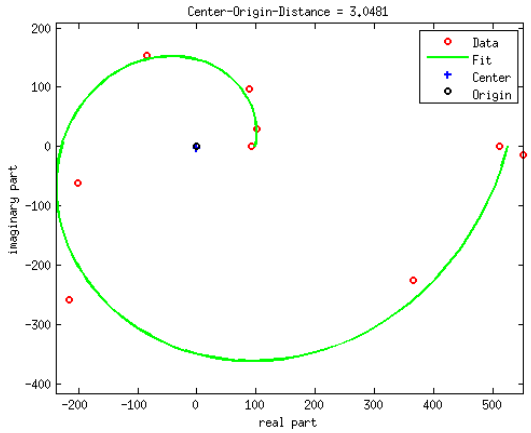

Figure1: Voxel of pure blood with COD=3.0481su

Fig. 2: Partial volume blood voxel

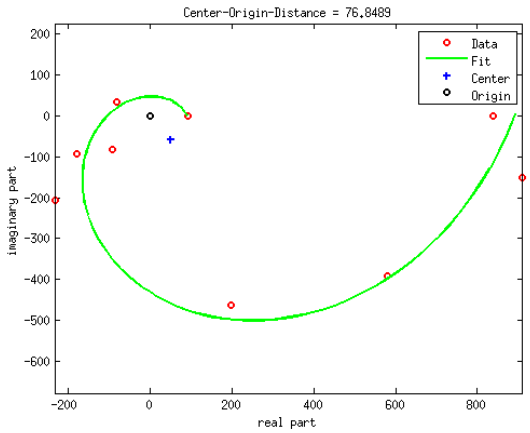

Figure2:Partial volume voxel with COD=76.8489su

Literature

[1] Osch, M.: Measuring the Arterial Input Function With Gradient Echo Sequences, Magnetic Resonance in Medicine 49:1067-1076(2003)
[2] Osch, M.: Correcting Partial Volume Artifacts of the Arterial Input Function in Quantitative Cerebral Perfusion MRI, Magnetic Resonance in Medicine 45:477-485(2001)
[3] Sauerbrey, A.: Establishment of a Swine Model for Validation of Perfusion Measurement by Dynamic Contrast-Enhanced Magnetic Resonance Imaging, BioMed Research International, Volume 2014, Article ID 390506

P 103 19F-Phase-Contrast-MRI of Fluorine Gases under Constant and Oscillating Flow

J. Friedrich[1], D. Feldmann[1], M. Terekhov[1], L. Krenkel[1], C. Wagner[1], L. M. Schreiber[1]
[1]University Medical Center Mainz , Section of Medical Physics, Department of Radiology, Mainz, Germany

Introduction: Protective ventilation strategies are of high importance in intensive care medicine. Besides ensuring a sufficient gas exchange in the lungs a so called ventilator induced lung injury (VILI) needs to be minimized or even prevented. An understanding of the gas transport mechanisms in the airways is necessary to be able to adjust the ventilation parameters according to the patients' individual affliction. A protective ventilation method, mainly used for patients suffering from the acute respiratory distress syndrome (ARDS), is high frequency oscillatory ventilation (HFOV). It uses a high distending pressure (about 20 cmH_2O) that keeps the alveoli open. This pressure is superposed by a pressure oscillation between 70 and 80 cmH_2O. Here, the used frequency ranges from about 3 Hz up to 15 Hz, which equals 210 to 900 breathing cycles per minute. Until today the detailed gas transport mechanisms of this ventilation strategy are not completely understood. Here, flow measurements using magnetic resonance imaging can help to obtain insights in these complex processes. The typically used nuclei for lung MRI in research is ^{3}He. However, ^{3}He is hardly available these days and consequently very expensive. An alternative to ^{3}He are fluorinated gases. They possess a relatively large amount of MR active ^{19}F nuclei, which provide nearly the same sensitivity as ^{1}H.
The aim of the current study was the development of a method that enables the gas flow measurement of fluorinated gases during HFOV using ^{19}F-MRI. Therefore, initial studies on constant flow in a straight pipe geometry were performed and compared to correlated numerical simulations. The developed method was subsequently adopted for first measurements under HFOV in the same geometry.

Methods: All measurements were performed on a 1.5T MRI system (Siemens, Magnetom Sonata, Erlangen, Germany) using a ^{19}F transmit/receive coil (RAPID Biomedical, Würzburg, Germany). A long straight pipe geometry served as measurement phantom. It had an inner diameter similar to the human trachea (D = 2.5 cm).
Two-dimensional maps of the axial velocity component were measured in constant, turbulent pipe flows using a flow sensitive gradient echo sequence. These flow measurements were performed at three different flow rates resulting in a Reynolds number of $Re = \{10254, 15744, 21306\}$. The integral flow rates were validated against digital flow meter measurements and direct numerical simulations (DNS).
After upgrading the HFOV device with a trigger output, which allows for phase correct measurements according to the HFOV cycle, axial velocity components were measured pixel wise at different stages of a 4-Hz-ventilation.

Results: The measurement of the axial velocity components for all three constant flow rates was carried out successfully and a good agreement with the results of the DNS was achieved. The measured and the simulated velocity profiles of all three flow rates are shown in FIG.1. The flow profiles appear flattened for all three measurements. This is caused by the relatively high degree of turbulences correlated with the high molecular mass of the gas.
During the 4-Hz-Ventilation, the axial velocity profiles at different stages of the ventilation cycle could be measured successfully as well. In FIG.2 three of 14 measured velocity profiles are shown. To characterize oscillating flow, the so called Womersley number Wo is used [2]. It describes the frequency of an oscillating flow independent of the used fluid. It was shown that for flows with $Wo >> 1$, the velocity profiles are strongly flattened and possess a strong gradient at the wall region [2]. This behavior could be reproduced with our 4-Hz-measurement ($Wo \approx 50$).

Conclusion: PC-MRI using ^{19}F gas is capable of spatially resolved velocity measurements in turbulent pipe flows at clinically relevant Reynolds numbers. Thus, the developed method provides a novel clinically useful measurement technique to further investigate unsteady and turbulent flows as they occur, e.g. in the larger airways under conditions of certain ventilation strategies.

Attachement 1

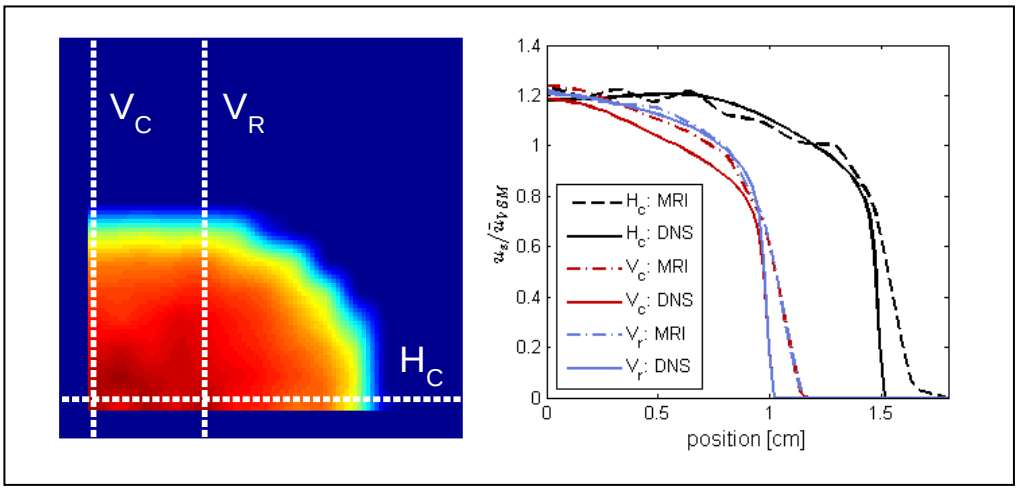

FIG.1: *Measured axial velocity profiles at three different positions inside the straight pipe geometry in comparison with velocity profiles obtained by direct numerical simulations.*

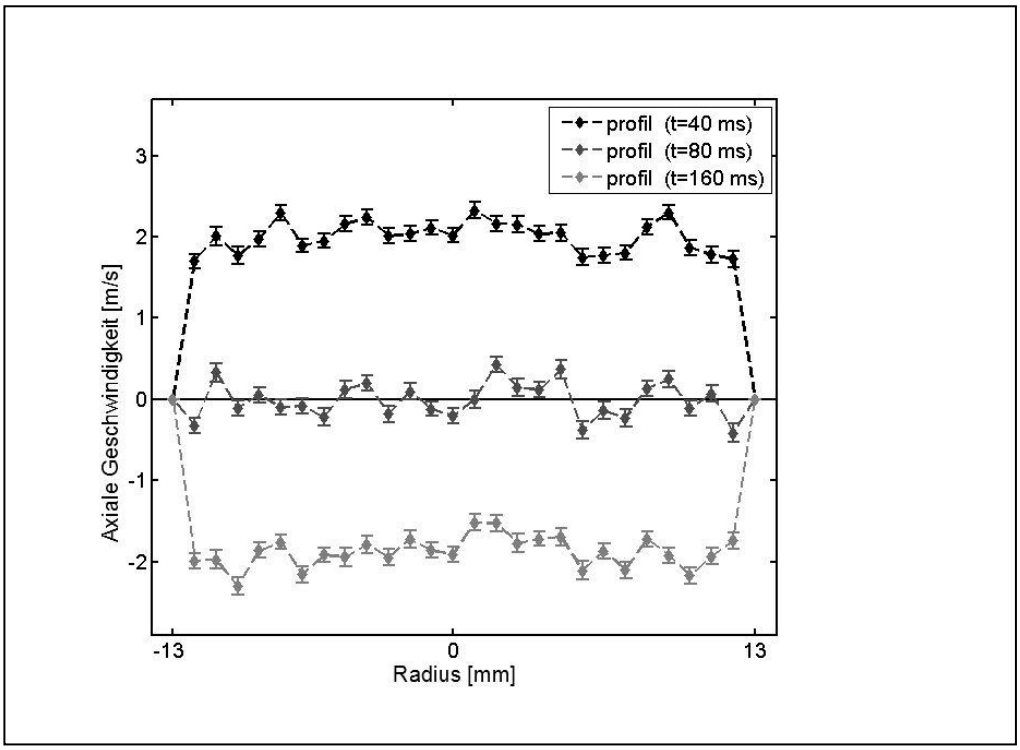

FIG.2: *Three of 14 exemplarily shown axial velocity profiles at different stages of a 4-Hz-ventilation.*

Acknowledgement:
This study was supported by the German research foundation, DFG (SCHR 687/5-1, SCHR 687/5-2, SCHO 1375/1)

References:

[1] Muders F., Pfeifer M., Müller T., Intensivmedizin und Notfallmedizin 2003, 40(6):515-522.
[2] Womersley JR.. J Physiol-London 1955;127(3):553-563.